

N. Janardhana Raju *Editor*

Geostatistical and Geospatial Approaches for the Characterization of Natural Resources in the Environment

Challenges, Processes and Strategies

Geostatistical and Geospatial Approaches for the Characterization of Natural Resources in the Environment

N. Janardhana Raju

Editor

Geostatistical and Geospatial Approaches for the Characterization of Natural Resources in the Environment

Challenges, Processes and Strategies

Editor

N. Janardhana Raju
School of Environmental Sciences
Jawaharlal Nehru University
New Delhi, India

Co-published by Springer International Publishing, Cham, Switzerland, with Capital Publishing Company, New Delhi, India.

Sold and distributed in North, Central and South America by Springer, 233 Spring Street, New York 10013, USA.

In all other countries, except SAARC countries—Afghanistan, Bangladesh, Bhutan, India, Maldives, Nepal, Pakistan and Sri Lanka— sold and distributed by Springer, Haberstrasse 7, D-69126 Heidelberg, Germany.

In SAARC countries—Afghanistan, Bangladesh, Bhutan, India, Maldives, Nepal, Pakistan and Sri Lanka—printed book sold and distributed by Capital Publishing Company, 7/28, Mahaveer Street, Ansari Road, Daryaganj, New Delhi, 110 002, India.

ISBN 978-3-319-18662-7 ISBN 978-3-319-18663-4 (eBook)
DOI 10.1007/978-3-319-18663-4

Library of Congress Control Number: 2015957595

Springer Cham Heidelberg New York Dordrecht London

© Capital Publishing Company 2016

This work is subject to copyright. All rights are reserved by the Publisher, whether the whole or part of the material is concerned, specifically the rights of translation, reprinting, reuse of illustrations, recitation, broadcasting, reproduction on microfilms or in any other physical way, and transmission or information storage and retrieval, electronic adaptation, computer software, or by similar or dissimilar methodology now known or hereafter developed.

The use of general descriptive names, registered names, trademarks, service marks, etc. in this publication does not imply, even in the absence of a specific statement, that such names are exempt from the relevant protective laws and regulations and therefore free for general use.

The publisher, the authors and the editors are safe to assume that the advice and information in this book are believed to be true and accurate at the date of publication. Neither the publisher nor the authors or the editors give a warranty, express or implied, with respect to the material contained herein or for any errors or omissions that may have been made.

Printed on acid-free paper

Springer International Publishing AG Switzerland is part of Springer Science+Business Media (www.springer.com)

Welcome Message for IAMG2014 Participants in New Delhi

Good morning everyone, ladies and gentlemen, dear friends,

On behalf of the International Association for Mathematical Geosciences (IAMG), I would like to extend my warmest welcome to all participants of this conference! I sincerely congratulate and thank Professor N.J. Raju, the Chair of the conference and his local organizing committee for hosting this event. I also want to thank the Ministry of Earth Sciences, J. Nehru University of India, the School of Environmental Sciences, and many other organizations for their generous support. I should give special thanks to Dr Raju and the visa offices, both in Toronto and Beijing, for the big help on getting my visa on time to come to India twice this year.

This year is the first time that our annual conference is being held in India since the start of the IAMG annual conferences 20 years ago. The mission of our association is to promote development of mathematics, statistics, and computer informatics in geosciences. I am convinced that this event will further promote IAMG in India and that it will result in more new contributions to MG because of the following three aspects:

First, Indian scientists traditionally and continuously make very important contributions to mathematics, statistics, and science in general. There are well-known examples of developments in mathematics and statistics that were advanced by Indian mathematicians. Just to name a few, as early as in the fourteenth to sixteenth centuries, in attempting to solve astronomical problems, Indian mathematicians at the Kerala school of Astronomy and Mathematics developed series expansion for trigonometric functions which today are pervasive not only in pure mathematics but also in applied mathematics such as frequency analysis for characterizing cyclical phenomena across many applications in the mathematical geosciences. A more recent example is the Mahalanobis distance, developed in the 1930s by an important Indian scientist and applied statistician, Prasanta Mahalanobis. This M-distance is a multidimensional generalization of standard Euclidean distance. The Mahalanobis distance is widely used in many disciplines of science and engineering including mathematical geosciences. Distance is an important mathematical property of geological features and is the fundamental

mathematics for prediction, estimation, classification, and interpolation in geoscience. Many innovations in mathematical geoscience such as Aitchison distance dealing with compositional data, Kriging as a generalization of the moving average technique, spatially weighted multivariate analysis derived from traditional multivariate analysis, fractal geometry from ordinary geometry, multifractal density derived from geo-complexity and non-Gaussian theory, and local singularity analysis from stationary analysis are all becoming part of essential mathematical theory and techniques useful not only for geoscience but also for other disciplines.

Secondly, from a geoscientific point of view, India has a diverse geology from Indian Craton to orogenic mountains and plateaus. Mineral deposits of great variety and fossil energy resources are found on the subcontinent in large quantities. The mining industry in India is a major economic activity which contributes significantly to the economy of India providing multimillion job opportunities for individuals. The Indian plate is the fastest-moving plate on Earth causing various geo-environmental hazards including earthquakes and tsunamis generated by earthquakes. Just like many other developing nations, it faces serious challenge of water resources and environmental pollution. Resourcing future generations and solving environmental issues remain major challenges and opportunities for India and Indian geoscientists.

Thirdly, from geoinformatics point of view, the Government of India has been taking numerous initiatives promoting development and applications of computer technology and spatial information technology. For example, the Indians have successfully operated Indian National Satellites (INSAT) for communication services and Indian Remote Sensing (IRS) satellites for management of natural resources. These two satellite series have become important satellite systems in the Asia-Pacific region and across the globe that continue to provide services and imageries in a variety of spatial resolutions which can be utilized for solving the geo-problems within the region. India has also set up National GIS Organizations and Geoinformatics programs in many educational institutions. Computer information technology including geoinformatics is growing in India and attracting many young talents.

To utilize mathematical methods in conjunction with geoinformatical techniques and big data to solve geoscientific problems has attracted a great deal of attention at this IAMG conference. It represents a trend of general frontier research in the geosciences. My belief is that this annual conference will lead to more promotion for IAMG within the next few years in the region including the 36th International Geological Congress (IGC) to be held in New Delhi in 2020. Our association holds joint meetings at IGCs. I look forward to see more individuals from this part of the world actively participating in IAMG.

Finally, best wishes for the success of this conference! I wish everyone a wonderful stay in India! Thank you for your attention!

President, International Association for Mathematical
Geosciences (IAMG)
New Delhi, India

Qiuming Cheng

Foreword

It is my exceptional pleasure to welcome you in New Delhi (capital of India) to the 16th IAMG annual conference at Jawaharlal Nehru University during 17–20th October 2014. For the first time in India, IAMG conference is being held since the start of IAMG annual conferences 20 years back. The organizers proposed this place because New Delhi is the hub of educational institutions and better infra-structural facilities to organize this type of prestigious event. Since it is first ever large mathematical geosciences conference, this event will further promote and will result in more new contributions to mathematical geosciences in Indian subcontinent. Indian plate is the fastest-moving plate on Earth causing various geo-environmental hazards. This century we will be mostly faced with serious problems of natural disasters due to climate change, i.e., heavy rains and floods like in Uttarakhand and Jammu and Kashmir due to cloud bursts and also similar disasters in other parts of the world. Therefore, today's research is focused on fundamental process on natural resources and proper utilization of geostatistical and geospatial technologies for the sustainable resources management. Utilization of mathematical methods in conjunction with geoinformational techniques to solve geoscientific problems has attracted a great deal of attention at IAMG2014 and will remain a trend of general research in the geosciences especially in India. Computer information technology including geoinformatics is growing and attracting many young talents in India.

With these new efforts this IAMG conference on *Geostatistical and Geospatial Approaches for the Characterization of Natural Resources in the Environment: Challenges, Processes, and Strategies* intends to bring together international specialists: (i) to exchange fundamental results of recent research, (ii) to present progress and processes in technical innovations, (iii) to discuss global strategies to synchronize natural resources and hazards, and (iv) to consider the priorities of future challenges and remedies.

Consequently the conference proceedings cover the following sections:

- Mathematical geosciences and geostatistics
- Environmental geochemistry and pollution
- Tectonic activity and natural disasters
- Modeling and simulations
- Remote sensing and geoinformatics
- Meteorology and climate change through invited papers and oral and poster presentations

The papers peer reviewed and published in the conference proceedings reflect the quality of the science at this conference. I thank all the reviewers for their efforts, which have greatly improved the quality of this publication and also sponsors who have supported to organize this event in a grand way.

I am confident that the inspiring ambience of New Delhi and IAMG2014 conference itself will favor the exchange of ideas and sharing of valuable information with eminent scientists/researchers for making future collaboration research programs.

Chairman, IAMG2014
New Delhi, India
October 2014

N. Janardhana Raju

Scientific Committee, Local Organizing Committee and Sponsors

Scientific Committee

A.K. Singhvi, India	Jef Caers, USA	Richard Sinding-Larsen, Norway
Alexander Kolovos, USA	Jesús Martínez Frías, Spain	Robert Marschallinger, Austria
Andras Bardossy, Germany	JiaxueWu, China	Ryoichi Kouda, Japan
Anil Kulkarni, India	Joel Carrillo Rivera, Mexico	Sambasiva R. Patchineelam, Brazil
Bhabesh C. Sarkar, India	John H. Schuenemeyer, USA	Sanjay Srinivasan, USA
B.S. Daya Sagar, India	Juan José Egozcue, Spain	Saumitra Mukherjee, India
Cedric Griffiths, Australia	Katsuaki Koike, Japan	Shakel Romshoo, India
D.M. Banerjee, India	K.R. Murali Mohan, India	Shilpa Pal, India
Daniel M. Tetzlaff, USA	M.P. Singh, India	T.V. Krishna Reddy, India
David M. Carttar, USA	M. Sudhakar, India	Talat Ahmad, India
Frits Agterberg, Canada	Maria T. Schafmeister, Germany	Tapan Mukerji, USA
Gang Liu, China	Mrinal Sen, India	U. Saravana Kumar, India
Hans Wackernagel, France	P Rajendra Prasad, India	VP. Dimri, India
Hari S. Pandalai, India	Peter Wycisk, Germany	V. Subramanian, India
Harsh Gupta, India	Pierre Goovaerts, USA	Vera Pawlowsky-Glahn, Spain
J.A.Vargas-Guzmán, Saudi Arabia	Qiuming Cheng, Canada	Wolfgang Gossel, Germany
Jaime Gómez-Hernández, Spain	R. Mohan Srivastava, Canada	
Jan Harff, Poland	R. Ramesh, India	
	Ricardo Olea, USA	

Local Organizing Committee

N. Janardhana Raju (*Chairman*), New Delhi

S. Sreekesh, New Delhi

AL Ramanathan, New Delhi

Dinesh Mohan, New Delhi

Jayant K. Tripathi, New Delhi

Arun K. Srivastava, New Delhi

Sponsors

Jawaharlal Nehru University (JNU), New Delhi

International Association for Mathematical Geosciences (IAMG), USA

Ministry of Earth Sciences (MOES), New Delhi

Department of Science and Technology (DST), New Delhi

Coal India Limited (CIL), Kolkata

Oil and Natural Gas Corporation Limited (ONGC), Dehradun

National Mineral Development Corporation (NMDC), Hyderabad

Reliance Industries Limited (RIL), Mumbai

Indian Meteorological Society (IMS), New Delhi

Saudi Arabian Oil Company, Saudi Arabia

Council of Scientific and Industrial Research (CSIR), New Delhi

GITAM University, Visakhapatnam

Contents

Part I Mathematical Geosciences and Geostatistics

1	Singularity-Based Geo-Information Extraction for Characterizing Mineralization-Associated Geological Processes in Gejiu Mineral District, China	3
	Wenlei Wang, Jie Zhao, and Qiuming Cheng	
2	Compositionally Compliant Contact Analysis	11
	R. Tolosana-Delgado, U. Mueller, and K.G. van den Boogaart	
3	Kernel Principal Component Analysis in the Application of Geochemical Comprehensive Feature Extraction	15
	Bingli Liu, Ke Guo, and Li Zhang	
4	Abnormal Extraction of Geochemical Data Based on Kalman Filter and SVM	21
	Ke Guo, Bingli Liu, and Fei Wu	
5	Summed Area Table for Rapid Local Singularity Mapping	29
	Z. Chen and Q. Cheng	
6	Application of a Coherent Multi-Dimensional Technique to the Central Part of the Mexican Volcanic Belt	35
	Srendra P. Verma	
7	Multivariate Grid-Free Geostatistical Simulation of Natural Phenomena	39
	Y. Zagayevskiy and C.V. Deutsch	
8	Semianalytical Solutions for Multispecies Transport Coupled with a Sequential First-Order Reaction Network Using GITT Techniques	45
	Heejun Suk, Byung-Gon Chae, and Junghae Choi	

9	Compositional Statistical Analysis of Inter-Laboratory Comparisons of Geothermal Water	51
	Mahendra P. Verma	
10	Fractal Characterization via Morphological Analysis	57
	Raghvendra Sharma and B.S. Daya Sagar	
11	Geostatistical Analysis of Functional Compositions: Characterization of Soil Particle-Size Curves through the Aitchison Geometry	65
	A. Menafoglio, A. Guadagnini, and P. Secchi	
12	Classical Statistical Techniques for Deciphering the Origin and Evolution of Volcanoes at Volcanic Front of the Central Part of the Mexican Volcanic Belt	71
	F. Velasco-Tapia and S.P. Verma	
13	Forecasting of Hollows in Abandoned Shallow Coal Mines in a Zone of Intensive Weathering	77
	V. Palchik	
14	Metallurgical Variable Re-expression for Geostatistics	83
	J.L. Deutsch, J. Szymanski, and T.H. Etsell	
15	Parameter Estimation and Sensitivity Analysis in Clastic Sedimentation Modeling	89
	A. Acevedo, A. Khramtsov, H.A. Madhoo, L. Noomee, D. Tetzlaff, and P. Burgess	
16	Study on Chaotic Time Series and Its Application on Forecasting Water Inrush in Mines	95
	Yang Yongguo, Chen Yuhua, and Cheng Qiuming	
17	p-T Computation Schemes for Thermodynamic Properties of Pure Water: A Comparative Evaluation of IAPWS-95 and IAPWS-IF97 Formulations	101
	Mahendra P. Verma	
18	Statistical Lobe Hierarchy Constraint in Surface-based Reservoir Modeling	105
	Siyao Xu and Tapan Mukerji	
19	Transport of Molecular Fluids through Three-Dimensional Porous Media	111
	A. Pazdniakou and P.M. Adler	
20	Statistical Scale-up of Reservoir Properties and Dispersivities in Heterogeneous Reservoirs	115
	Vikrant Vishal and Juliana Y. Leung	

21	Sediment Concentration Prediction at Gangotri in the Himalayas Using Artificial Neural Networks	121
	Nandita Singh and G.J. Chakrapani	
22	Lacunarity Analysis of Fracture Intensity Maps: Are they Multifractals?	129
	Ankur Roy and Edmund Perfect	
23	Modified Tetrahedral Mesh Subdivision Method and Its Application in 3D Geological Body Discrete Analysis	135
	Gang Liu, Zhengping Weng, Zhiting Zhang, and Qing Zhou	
24	High Performance Computing of Hydrothermal Ore-Forming Systems: An Approach Based on the Lattice Boltzmann Method	141
	Wei Qiang and Hui Cao	
25	Resurrecting GSLIB by Code Optimization and Multi-core Programming	147
	Oscar Peredo and Julián M. Ortiz	
26	Distribution Law for Mineral and Chemical Constituent Fractions in Rocks and Ores	153
	B.K. Sahu	
27	Comparison of Spatial Interpolation Methods for Mapping Rainfall in Indian Himalayas of Uttarakhand Region	159
	Madhuri Kumari, Ashoke Basistha, Oinam Bakimchandra, and C.K. Singh	
28	A Time Series Analysis of Spatial and Temporal Distribution of Rainfall at Pampa River Basin, Kerala, India	169
	N.A. Mayaja and C.V. Srinivasa	
29	Rainfall Statistics Change in West Bengal (India) from Period 1901-2000	173
	Sourav Mukhopadhyay, Sneha Kulkarni, Pallavi Kulkarni, and Samiran Dutta	
30	Groundwater Fluctuation and Trend in Amritsar, Punjab, India	183
	Gopal Krishan, A.K. Lohani, M.S. Rao, C.P. Kumar, and K.S. Takshi	

Part II Environmental Geochemistry and Pollution

31	Groundwater Quality Appraisal in Parts of Dun Valley Aquifers in the Terai Region, Central Nepal	191
	N. Janardhana Raju, Deepa Gurung, and Priyanka Patel	

32	GIS and Geostatistical Assessment of Groundwater and Its Pollution in Kuwait	199
	R.S. Divi and F. Al-Ruwaih	
33	Geomorphological Influence on Groundwater Quality and Arsenic Distribution in Parts of Brahmaputra River Basin Adjoining Eastern Himalayas	207
	Swati Verma and Abhijit Mukherjee	
34	Vulnerability of Ground Water Quality to Changing Climate: A Case Study from Kalpitiya Peninsula, Sri Lanka	213
	Samanmali Matharaarachchi, Ranjana U.K. Piyadasa, and Deepthi Wikramasinghe	
35	Hydrogeochemical Assessment to Explore the Extent, Nature and Source of Fluoride Contamination within the Groundwaters of the Panda River Basin, Sonbhadra District, Uttar Pradesh, India	221
	Sangita Dey and N. Janardhana Raju	
36	Presence of Uranium in Groundwater of Punjab: An Overview	231
	A. Diana Sharma and Madhuri S. Rishi	
37	Groundwater Sources in Semi-Arid Regions and Their Vulnerability to Climate Change: Drâa Catchment, Morocco	237
	S. Ouyse, José Joel Carrillo-Rivera, G.J. Hernández-Garcia, and M. Ramirez-Beltrán	
38	Assessment of Groundwater Recharge due to Monsoon in Ozar Watershed of Maharashtra State Using Isotopic Technique	245
	S.K. Verma, S.P. Rai, M.S. Rao, and C.P. Kumar	
39	Application of Statistical Techniques to Identify the Hydrogeochemical Processes in Coastal Aquifers of Pondicherry Region, Tamil Nadu	251
	R. Thilagavathi, S. Chidambaram, C. Thivya, S. Pethaperumal, K. Tirumalesh, and M.V. Prasanna	
40	Isotope Hydrogeological Factors Control Transport of Radon-222 in Hard Rock Fractured Aquifer of Bangalore, Karnataka	259
	Md. Arzoo Ansari, Archana Deodhar, U. Saravana Kumar, Deljo Davis, and R.K. Somashekar	
41	Groundwater Arsenic Contamination Affecting Different Geological Domains in India: Its Relation to Fluvial Geomorphology and Quaternary Stratigraphy	267
	Babar A. Shah	

42	Ground Water Sustainability in Varanasi District, Uttar Pradesh: Current Situation and Need for Effective Strategies	275
	Prahlad Ram and N. Janardhana Raju	
43	Discharge Pattern in the Gunt Valley, Western Pamir, with respect to $\delta^2\text{H}$, $\delta^{18}\text{O}$ and Hydrochemistry	281
	C. Meier, M. Knoche, M. Brehme, R. Merz, and S.M. Weise	
44	Environmental Isotope Investigation to Understand the Groundwater Recharge from Irrigation Tanks in Thirumal Area, Madurai	285
	Noble Jacob, Diksha, Ajay Jaryal, and A. Gurunathan	
45	Quantitative Provenance Analysis of Sediments in the Changjiang (Yangtze) River (China)	293
	G. Vezzoli, M. Limonta, E. Garzanti, and S. Yang	
46	Textural Variation of Sediments in the Course of a Small River: A case study from Khurar River, Khajuraho, Chhaterpur District, Madhya Pradesh, India	301
	S. Kanhaiya and B.P. Singh	
47	Particle Size Characteristics of Ramganga Catchment Area of Ganga River	307
	M.Y.A. Khan and G.J. Chakrapani	
48	Spatial and Temporal Variability in Grain Sizes of Alaknanda River	313
	S. Panwar and G.J. Chakrapani	
49	Characterization of the Rainfall of Central Mozambique Based on Isotopes of Water	321
	F. Steinbruch and S.M. Weise	
50	Control of Deteriorating Water Quality in Extracted Boreholes by Flow Systems Definition	327
	José Joel Carrillo-Rivera and Antonio Cardona	
51	Canal Irrigation and Its Impact on Spatial and Temporal Variation in Groundwater Level: A Case Study in Indira Gandhi Canal Project Stage I Command Area	333
	Sandhya and S. Sreelesh	
52	Impact of Canal Recharge on Groundwater Quality of Kolayat Area, District Bikaner, India	341
	Sumant Kumar, N.C. Ghosh, R.P. Singh, Rajesh Singh, and Surjeet Singh	

53	Domestic Wastewater Treatment Using Tanfloc: A Tannin Based Coagulant	349
	Rajesh Singh, Sumant Kumar, and Megha Garg	
54	Persistent Pesticides in Fluvial Sediment and Their Relationship with Black Carbon	355
	Musarrat Parween, A.L. Ramanathan, N. Janardhana Raju, and P.S. Khillare	
55	Relationship between Physicochemical Parameters and Toxicity of Leachate from Municipal Solid Waste Landfill Site in Delhi . . .	361
	Anshu Gupta and R. Paulraj	
56	Effects of Coal Mining Activities on Soil Properties with Special Reference to Heavy Metals	369
	Bhanu Pandey, Madhoolika Agrawal, and Siddharth Singh	
57	Coal Mining and Organic Pollutants: A Case of Mahanadi Basin Coalfields, India	373
	Amiya Shankar Naik	
58	Impact of Tillage and Residue Management Practices on Soil Aggregates and Soil Organic Carbon	381
	P. Singh, J. Heikkinen, S. Mitra, and K. Regina	
59	Effect of Land Cover on Soil Particle Size and Organic Carbon in the Plough Layer	385
	Poushali Roy and S. Sreekesh	
60	Sodicity Status of Salt-Affected Soils of Israna, Haryana, India	391
	Seema and R. Paulraj	
61	Characterizing and Quantifying the Effect of Aerosol Optical Depth over North Indian Plain during Harvesting Season	397
	Prasenjit Acharya and S. Sreekesh	
62	Evaluation of Urban Air Pollution Distribution in the Colombo Municipal Council Area, Sri Lanka	405
	Samanmali Matharaarachchi, L. Manawadu, and Jagath Gunatilake	
63	Platinum, Palladium and Rhodium in Road Dust/Top Soils from Major South Indian Cities: Implications on Environment and Human Health	415
	V. Balaram, C.T. Kamala, A. Sreenivasa Rao, M. Satyanarayanan, K.S.V. Subramanyam, and S.S. Sawant	
64	Longer Growing Season Decreases Peak Summer Vegetation Productivity in North American Ecosystems	421
	B.R. Parida and W. Buermann	

65	Species Diversity and Regeneration Status in Sabaiya Collaborative Forest, Nepal	427
	Bikash Kumar Mishra and S.C. Garkoti	
66	Treatment of Coke Oven Effluents by Duckweeds Ponds – A Laboratory Scale Study	435
	Subodh Kumar Maiti and Arindam Halder	
Part III Tectonic Activity and Natural Disasters		
67	Zonal Crustal Movement	443
	Xin Xian-wu	
68	Tectonic Setting of Basic Rocks of Borborema Province, Brazil, Inferred from Multi-Dimensional Discrimination Diagrams	449
	Sanjeet K. Verma and Elson P. Oliveira	
69	Tectonomagmatic Origin of Igneous Rocks from the Western Mexican Volcanic Belt	455
	Surendra P. Verma and Kailasa Pandarinath	
70	Global Sub-Crustal Stress Field	461
	R. Tenzer and M. Eshagh	
71	A Blind-wavelet Algorithm and Its Application to the Metal Mine Seismic Data Processing	467
	Zhongli Zhou, Bin Liu, Feilong Qin, and Guangxin Huang	
72	Study of <i>N</i>-dimensional Matrices and Its Application in Geology	475
	Wei Shen and Haiyan Du	
73	Small- to Large-Scale Rock Fracture Patterns as Indicators of Shock-Related Fragmentation	483
	Md. Sakawat Hossain and Jörn H. Kruhl	
74	Distribution Study of Ore-Sourced Elements from a Long Drill-Core in a Loess-Covered Area	491
	Deyi Xu, Bang Qin Feng, Changhai Tan, and Qiuming Cheng	
75	Hydrothermal Activity in the NE Portion of the Sewell Rise, Central Andaman Trough: Evidences from Multibeam and Petrographic Studies	497
	S. Varghese, K.K. Bhat, and N. Subhash	
76	Studies on the Seismicity in Garhwal Himalaya, India	503
	Arun K. Shandilya and Anurag Shandilya	

77	Shear Seam in Dam Foundation System	513
	Abhishek Singh and Shilpa Pal	
78	Geothermobarometry and Barrovian Metamorphism of Darjeeling-Mangpu Region, Eastern Himalaya	523
	Suparna Tewari and Divya Prakash	
79	High Pressure and Ultrahigh Temperature Metamorphism at Diguva Sonaba, Eastern Ghats Mobile Belt (India): New Constraints from Phase Equilibria Modelling	527
	Divya Prakash and Deepak	
80	Spatial Distribution of Seismic Site Coefficients for Guwahati City	533
	Jagabandhu Dixit, S.T.G. Raghukanth, and Sujit Kumar Dash	
81	Application of GIS-Based Weights of Evidence Method for Metallogenic Prediction to Copper Resources in Western Region of Zhejiang, China	539
	Wei Shen and Haiyan Du	
82	Application of Fuzzy Gamma Operator in Landslide Susceptibility Mapping along Yercaud Ghat Road Section, Tamil Nadu, India	545
	V. Ramesh, Thanchuipou Phaomei, M. Baskar, and S. Anbazhagan	
83	A Benchmark Synthetic Dataset for Fractured Reservoir	555
	Yongduk Shin, Ankur Roy, Orhun Aydin, Tapan Mukerji, and Jef Caers	

Part IV Modelling and Simulations

84	Three-Dimensional Metallogenic Prediction in Tonglushan Region Based on Digital Ore Deposit Model	565
	N. Li Cheng and Liu Bing-li	
85	The Integration Model of Deep Structure and Ore-Forming Systems of the Pechenga District (Baltic Shield)	571
	K.V. Lobanov, M.V. Chicherov, I.A. Chizhova, and N.V. Sharov	
86	Joint Conditional Simulation of an Iron Ore Deposit Using Minimum or Maximum Autocorrelation Factor Transformation	577
	N.L. Mai, O. Erten, and E. Topal	
87	Digital Modeling in the Study of Heavy Mineral Placers	583
	N.P. Laverov, I.A. Chizhova, D.P. Khrushchov, A.V. Lalomov, and E.A. Remezova	

88	Working with Hierarchical Databases in R to Model Geometallurgical Data	589
	S. Matos Camacho and K.G. van den Boogaart	
89	Application of Empirical Model Decomposition and Independent Component Analysis to Magnetic Anomalies Separation: A Case Study for Gobi Desert Coverage in Eastern Tianshan, China	593
	Chengbin Wang, Jianguo Chen, and Fan Xiao	
90	3D Modeling of Urban Geological Body Based on the KDA Method for Beijing City, China	599
	Chen Jian-ping, Tian Yi, and Chen Yu-Chen	
91	Generalized Compensation Model for the Gravimetric Moho Recovery	605
	R. Tenzer and W. Chen	
92	Colloidal Transport under Nonlinear Sorption in a Single Variable Fracture Aperture	609
	Nikhil Bagalkot and G. Suresh Kumar	
93	A Markov Chain Monte Carlo-based Particle Filter Approach for Spatiotemporal Modelling of an Environmental Process	617
	L. Linguet and J. Atif	
94	Using Stratigraphic Forward Modeling to Model the Brookian Sequence of the Alaska North Slope	623
	Alina Christ, Oliver Schenk, and Per Salomonsen	
95	Numerical Simulation of Migration of Seismic Activity (On the Example of Kamchatka)	627
	A. Naumovich Chetyrbotsky	
96	Comparative Performance of Thirteen Single Outlier Discordancy Tests from Monte Carlo Simulations	631
	Mauricio Rosales-Rivera, Lorena Díaz-González, and Surendra P. Verma	
97	3D Crustal Temperature Modeling over Japan for Geothermal Resource Assessment	637
	Bingwei Tian and Katsuaki Koike	
98	A Nonstationary Nonlinear Geostatistical Model and Its Application in a Beach Sand Deposit for Recoverable Reserve Estimation	643
	M. Thakur, B. Samanta, and D. Chakravarty	

99	Contextualized Geographically Weighted Principal Components Analysis for Investigating Baseline Soils Data on the North Wyke Farm Platform	651
	P. Harris, N.J.K. Howden, S. Peukert, V. Noacco, K. Ramezani, E. Tuominen, B. Eludoyin, R. Brazier, A. Shepherd, B. Griffith, R. Orr, and P. Murray	
100	Downscaling of Precipitation in Mahanadi Basin, India Using Support Vector Machine, K-Nearest Neighbour and Hybrid of Support Vector Machine with K-Nearest Neighbour	657
	Manjula Devak and C.T. Dhanya	
101	A Precipitation-Runoff Simulation Model for Flood Forecasting of River Tel, Odisha, India	665
	Prabeer Kumar Parhi	
102	Dynamics of Overland Flow under Changing Cropping Pattern: A Spatial Modeling Approach in Penganga Sub-watershed	671
	Abira Dutta Roy and S. Sreekesh	
103	Challenges of Including Groundwater Depth in a Liquefaction Loss Model	679
	T. Ancheta and Seung-Jae Lee	
104	Stochastic Quantification of Low-Resolution Geocoding Uncertainty and Its Application to Catastrophe Modeling	685
	Seung-Jae Lee and David Carttar	
105	An Improvised Effective Oceanography Monitoring Using Large Area Underwater Sensor Networks	691
	Burla Rajesh and K. Aanandha Saravanan	
Part V Remote Sensing and Geoinformatics		
106	The Extraction of Oil and Gas Information by Using SAS Imagery in the Jimusaer Field, Xinjiang-Clay Alteration Minerals	703
	Peng Tao and Wang Maozhi	
107	Characterization of Sampling Error in Instantaneous Orbital Data Products of TRMM over Indian Subcontinent	711
	J. Indu and D. Nagesh Kumar	
108	Estimation of Regional Groundwater System in a Granitic Body by 3D Permeable Zone Modeling and Flow Simulation	715
	T. Kubo, N. Matsuda, K. Kashiwaya, C. Liu, and K. Koike	

109	Hyperspectral Image Classification Using a New Dictionary Learning Approach with Structured Sparse Representation	719
	Zhen-tao Qin, Wu-nian Yang, Xiao-pin Wu, and Ru Yang	
110	Estimating Land Surface Temperature and its Lapse Rate over Kashmir Valley Using MODIS Data	723
	Mohammd Rafiq, Irfan Rashid, and Shakil A. Romshoo	
111	Combining Quantitation of Remote Sensing Information of Local Structures and Calculation of Structural Stress Field . . .	729
	Wu-nian Yang, Xin Yang, Han-hu Liu, Zhen-tao Qin, and Xiao-ping Wu	
112	Research on GIS-Based 3D Prospectivity Mapping and a Case Study of Jiama Copper-Polymetallic Deposit in Tibet, China	735
	Keyan Xiao, Nan Li, Alok Porwal, Eun-Jung Holden, Leon Bagas, and Yongjun Lu	
113	Inferring Land Surface Processes from Watershed Characterization	741
	Gowhar Meraj, Shakil A. Romshoo, and Sadaf Altaf	
114	Investigation of Seepage Channel Using Remote Sensing Technique in Jodhpur City, Rajasthan	745
	Birendra Pratap, N. Janardhana Raju, and G.S. Yadav	
115	Monitoring Snow Cover Area Using Different Algorithms on Indian Remote Sensing Data	749
	Farjana Birajdar, Gopalan Venkataraman, and Hrishikesh Samant	
116	Optimization of Neural Networks for Multisource Classification in a Glaciated Terrain	755
	Aparna Shukla and Bisma Yousuf	
117	Generation of Stream Length Gradient Index Map Using Visual Basic Program – A Case Study from South India	761
	A.C. Dinesh, Vipin Joseph Markose, and K.S. Jayappa	
118	Three Dimensional Quantitative Extraction and Integration for Geosciences Information: A Case Study of Nannihu Mo Deposit Area	767
	Li Ruix, Wang Gongwen, Zhu Yanyan, and Qu Jianan	
119	Multi-Classifer Fusion for Land Use Land Cover Mapping in Jharia Coal Field	773
	Sumit Kumar Chaudhary, Dheeraj Kumar, and M.K. Jain	
120	Land Use and Land Cover Changes and Their Impacts on Floods in Pampa River Basin in Kerala: A Remote Sensing Based Analysis	779
	N.A. Mayaja and C.V. Srinivasa	

121	Spatio-Temporal Study of the Distribution of Land Use and Land Cover Change Pattern in Chandigarh, India Using Remote Sensing and GIS Techniques	785
	Neelam Sidhu, Madhuri S. Rishi, and Rakhi Singh	
122	Development of Technique to Characterize TROF	791
	Vidit Mohan, Ashwin P. Ramesh, and Anirudh Toshniwal	
123	Study of the Urban Green Space Planning Using Geographic Information Systems and Remote Sensing Approaches for the City of Colombo, Sri Lanka	797
	M.S.P.M. Sirirwardane, Jagath Gunatilake, and S. Sivanandarajah	
124	Prediction of Crop Suitability of Certain Indian Spices – A GIS Approach	801
	Utpala Parthasarathy, O.P. Nandakishore, K. Jayarajan, K.V. Saji, and K. Nirmal Babu	
125	Morphometric and Hydrological Study of Alaknanda and Bhagirathi Basins	809
	Vikas Kamal, Ritesh Sipolya, Rajesh Kumar, and S. Mukherjee	
126	Role of Remote Sensing Data in Geoenvironmental Mapping: Case Studies from Syria	817
	Mohamad Rukieh	
127	Integrating Smart Platforms to Analyze Energy Patterns in Academic Building	823
	Prasad A. Pathak, Bakul Budhiraja, and Deepika Mann	
128	An Integrated Golden Spike Information Portal Enabled by Data Visualization and Semantic Web Technologies	829
	Xiaogang Ma, Linyun Fu, Peter Fox, and Gang Liu	
129	Web-based Facility Management System Using Open Source GIS	835
	P. Naga Vineet and L. Gnanaphazzam	

Part VI Meteorology and Climate Change

130	Estimation of Wind Speed in the Suburban Atmospheric Surface Layer	843
	Tanja Likso	
131	Role of Arabian Sea Surface Pressure on Indian Northeast Monsoon	849
	Ramesh Kumar Yadav	
132	Effect of Dust on the Indian Summer Monsoon	855
	P. Maharana, A.P. Dimri, and A. Choudhary	

133	Study of Physical and Dynamical Processes in the Ionosphere at Equatorial Anomaly Crest Region during Magnetic Storm for High and Low Solar Activity Period	861
	Bornali Chetia, M.K. Barman, M. Devi, and A.K. Barbara	
134	Winter Hailstorm over New Delhi, India	867
	A. Chevuturi, A.P. Dimri, and U.B. Gunturu	
135	Spatio-Temporal Variability of Rainfall and Temperature in Northeast India	873
	S. Sreekesh and Manasi Debnath	
136	Surface Energy and Mass Balance on the Ablation Zone of Chorabari Glacier, Central Himalaya, India	881
	Kapil Kesarwani, D.P. Dobhal, Alok Durgapal, Indira Karakoti, and Manish Mehta	
137	Monitoring the Status of Siachen Glacier Using Multi Temporal Remote Sensing Approach	887
	Snehmani, Mritunjay Kumar Singh, Krishnanjan Pakrasi, Anshuman Bhardwaj and A. Ganju	
138	Monitoring Glacial Parameters in Parts of Zaskar Basin, Jammu and Kashmir	893
	Iram Ali, Aparna Shukla, and Junaid Qadir	
139	An Analysis of Pattern of Changes in Snow Cover in the Upper Beas River Basin, Western Himalaya	899
	Seema Rani and S. Sreekesh	
140	Stream Flow Changes and Glacier Recession in the Upper Indus Basin	905
	Nahida Ali and Shakil A. Romshoo	
141	Hydrological Modeling and Streamflow Characterization of Gangotri Glacier	909
	Manohar Arora, Rakesh Kumar, Naresh Kumar, and Jatin Malhotra	
142	Abundance of <i>Cycladophora davisiana</i> Used as an Indicator for Paleoenvironment of Kerguelen Plateau, Southern Ocean Region	917
	Girish Kumar Sharma and Sheetal Kanojia	
143	Conservation Agriculture – A New Paradigm for Climate Change Mitigation in Rainfed Indian Agriculture	923
	G. Pratibha, G.R. Korwar, I. Srinivas, K.V. Rao, B.M.K. Raju, M. Maheswari, A.K. Indoria, K. Srinivasa Rao, D.K. Choudhary, and B. Rama Devi	

144	Perspective of the Agriculture Development of the Mountain Areas in Modern Condition of Climate Change	931
	I. Normatov, P.I. Normatov, and A. Muminov	
145	In the Face of Changing Climate: Groundwater Development through Artificial Recharge in Hard Rock Terrain of Kumaun Lesser Himalaya	937
	M. Tripathi	
146	Sustainable Biochar - A Tool for Climate Change Mitigation, Soil Management and Water and Wastewater Treatment	949
	Dinesh Mohan, Abhishek Kumar, and Charles U. Pittman	
147	Modelling Paleo-Geomorphology of Wave-Dominated Sandy and Tide-Influenced Muddy Coastal Embayments on the Decadal to Centennial Scale: A Comparative Study	953
	J. Deng, J. Harff, Y. Li, and W. Zhang	
148	A First-order Non-linear Differential Equation Characterizing Multiple Types of Probability Distributions	959
	Q. Cheng	
	Author Index	965

Part I
Mathematical Geosciences and
Geostatistics

Chapter 1

Singularity-Based Geo-Information Extraction for Characterizing Mineralization-Associated Geological Processes in Gejiu Mineral District, China

Wenlei Wang, Jie Zhao, and Qiuming Cheng

Abstract Singularity theory is an efficient way to quantify spatial variations of physical/chemical properties caused by geological processes. This study demonstrates several applications of singularity-based geo-information extraction. Choosing hydrothermal mineralization in Gejiu mineral district, China as an example, different singularity index estimation methods are employed to analyze controlling factors of the mineralization. At the end, this study introduces a fault-oriented singularity index estimation method. In comparison with the original singularity index, the new singularity index estimation method is able to describe anisotropy of geochemical/geophysical properties; meanwhile, controlling effects of fault activities on the hydrothermal mineralization can be quantified accordingly.

Keywords Geo-Information Extraction • Mineral Exploration • Geo-Processes • Anomaly • Spatial Variation

1.1 INTRODUCTION

From geologic theory, mineralization is a complex and cascade geo-process dominated/associated by/with various geo-processes. Geological features produced by mineralization related geo-processes often demonstrate irregular signatures in

W. Wang (✉)

Institute of Geomechanics, Chinese Academy of Geological Sciences, Beijing, China

e-mail: wenleiw@163.com

J. Zhao

State Key Lab of Geological Processes and Mineral Resources,
China University of Geosciences, Beijing, China

Q. Cheng

State Key Laboratory of Geological Processes and Mineral Resources,
China University of Geosciences, Wuhan, China

Faculty of Earth Resources, China University of Geosciences, Wuhan, China

comparison with their surroundings. Geologic interpreters often employ spatial and/or frequent analysis methods to locate these anomalous areas to delineate patterns indicative to mineral potentials. Among great numbers of geo-anomaly analysis approaches, singularity as an efficient manner to characterize spatially varied geological, geophysical and geochemical anomalies has been successfully employed in support of various fields of geosciences especially the exploration of hydrothermal mineralization [1].

1.2 STUDY AREA AND GEO-EXPLORATORY DATASETS

The Gejiu mineral district is well known for its world-class Sn-Cu polymetallic products (Fig. 1.1). Locating in the suture zone of the Indian Plate and the Eurasian plate on the southeastern of China sub-plate, well developed tectonic-magmatism produced a mineralization favored environment [2]. Providing spaces for transportation and precipitation of ore-forming material, faults are shown in an annular structure around the centre of the study area. Being sources of heat and ore-forming materials, the Yanshanian granitic intrusions possessing low magnetism and low density can be measured by geophysical data [3]. The Middle Triassic Gejiu formation is the main ore-bearing strata, the contract zones of which with the intrusions are believed as mineralization favored locations in this area. Geo-exploratory datasets including geological data indication location information

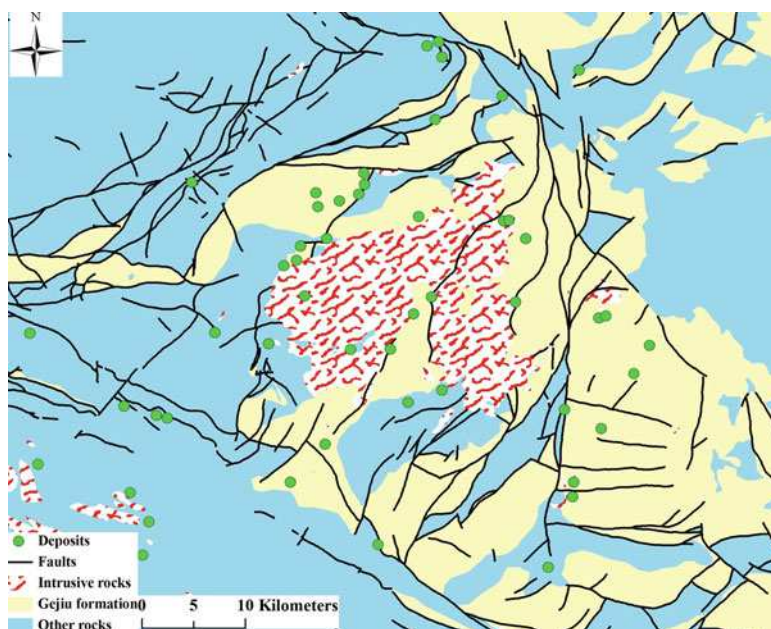


Fig. 1.1 A simplified geological map of Gejiu mineral district, China

of geological occurrences, geochemical and geophysical data demonstrating physical and chemical signatures of this area will be used to investigate spatially varied ore-controlling geo-processes.

1.3 SINGULARITY THEORY

Singularity theory to characterize irregular geo-processes accompanied by energy release and/or material accumulation within a two dimensional spatial interval (A) can be expressed as:

$$\langle \mu(A) \rangle = cA^{\alpha/2} \quad (1.1)$$

$$\langle C(A) \rangle = cA^{\alpha/2-1} \quad (1.2)$$

where, c is a constant determining magnitude of these two functions; $\mu(A)$ and $C(A)$ represents amount and concentration of released energy or accumulated materials; α is the singularity index to characterize variations of the energy or materials quantitatively and qualitatively. In general, there are three groups of singularity indices: (1.1) $\alpha = 2$ implying that $C(A)$ is independent of area A and the energy or materials are homogeneously or linearly distributed; (1.2) $\alpha < 2$ termed as positive singularity implying a “convex” property of $C(A)$ within A and the materials are accumulated within the interval A ; (1.3) $\alpha > 2$ termed as negative singularity implying a “concave” property of $C(A)$ within A and the materials are diffused within A (i.e., depletion). From the view point of signal processing, α can be considered as a high-pass filter transformation with an advantage of scale independence to characterize spatial variations of signals (e.g., geophysical fields).

$$\alpha = \frac{d\mu(A)}{dA} \cdot \frac{2}{C(A)} \quad (1.3)$$

The α corresponds to the first derivative transformation of signal $\mu(A)$. Considering anisotropy of geochemical, geological and geophysical signatures caused by cascade geo-processes, the frequently used isotropic square window-based method may not satisfy the intention to this concern. By a fault-oriented method, faults are divided into segments with equal length r . By using rectangular windows with sizes of $r \times \varepsilon_i$, an updated model is in a 1-dimensional scenario expressed as:

$$\langle C(r \times \varepsilon_i) \rangle = c\varepsilon_i^{\alpha_r-1} \quad (1.4)$$

$\alpha_r < 1$ is termed as positive singularity corresponding with continuous enrichment of materials during approaching to the fault space, while $\alpha_r > 1$ is termed as negative singularity corresponding with gradual depletion of metals during approaching to the fault space.

1.4 RESULTS AND DISCUSSION

According to singularity theory, fault length density $I(A)$ follows a power-law relationship with A :

$$\langle I(A) \rangle = cA^{\alpha/2-1} \quad (1.5)$$

$\alpha < 2$ can characterize spatially varied fault density (i.e., intensely developed fault systems). Employing singularity theory to analysis fault intensity of the Gejiu mineral district, China, areas with well developed fault systems are clearly depicted that greatly improved the characterization regarding fault intensity (Fig. 1.2). Through the high-pass filter technique (Eq. 1.3), negative singularity indices (i.e., $\alpha < 2$) of these two geophysical data are indicative to granitic intrusions (Fig. 1.3). The delineation is more flexible to the changes of observation scales (i.e., scale independency) in comparison with traditionally used band-pass filtering. By employing the singularity theory, the Middle Triassic Gejiu Formation with high contents of Ag, Cu, Pb, Sn, Zn, CaO and MgO, low content of SiO₂, K₂O, and Na₂O can be investigated to characterize their geochemical behaviors, and specific locations of mineralization within the strata can be inferred that is prior to traditionally used methods (Fig. 1.4). In comparison with old singularity method (Fig. 1.5), controlling effects of different fault segments are evaluated; meanwhile, anisotropy of geochemical behaviors can be investigated by fault-oriented singularity methods (Fig. 1.6).

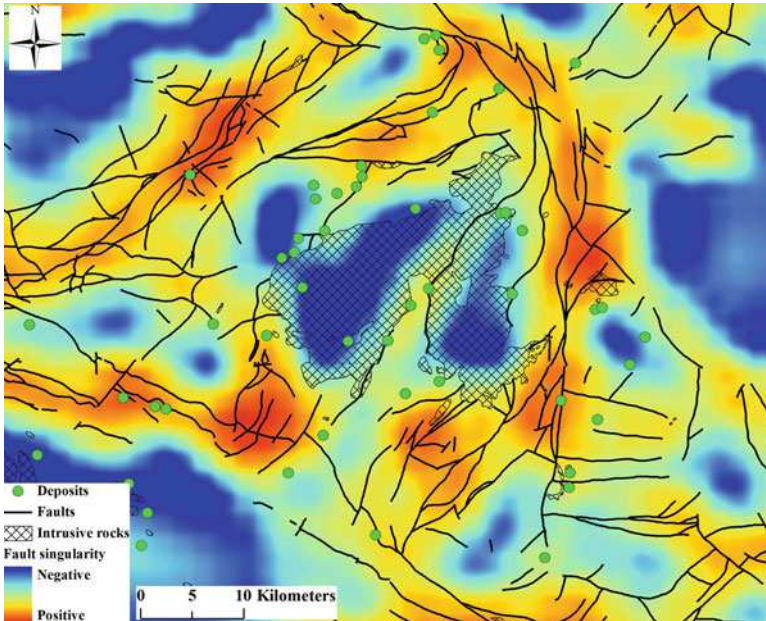


Fig. 1.2 Fault intensity characterized by singularity mapping technique

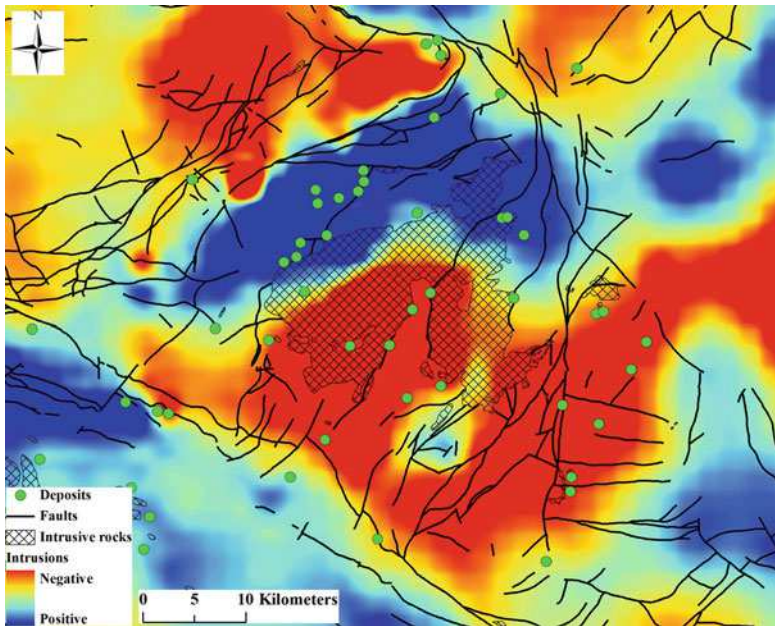


Fig. 1.3 Granitic intrusions identified by singularity mapping technique

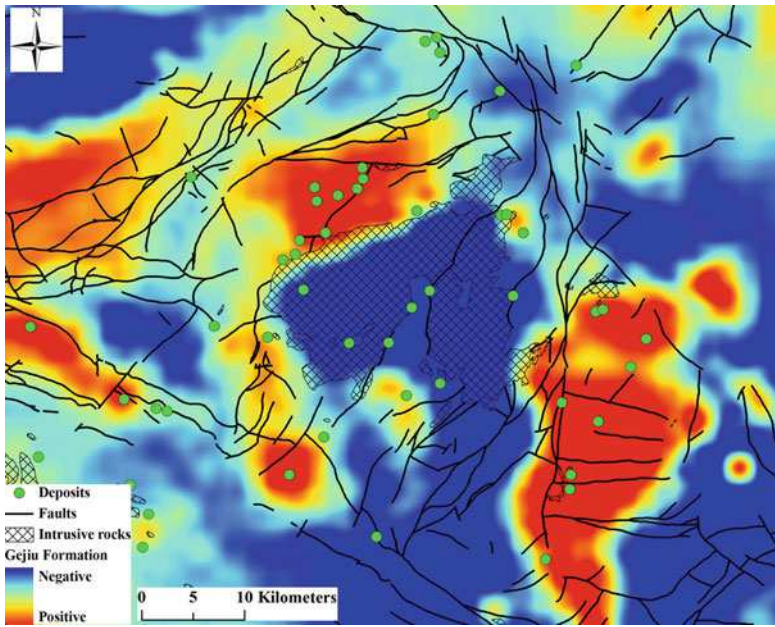


Fig. 1.4 The Gejiu Formation identified by singularity mapping technique

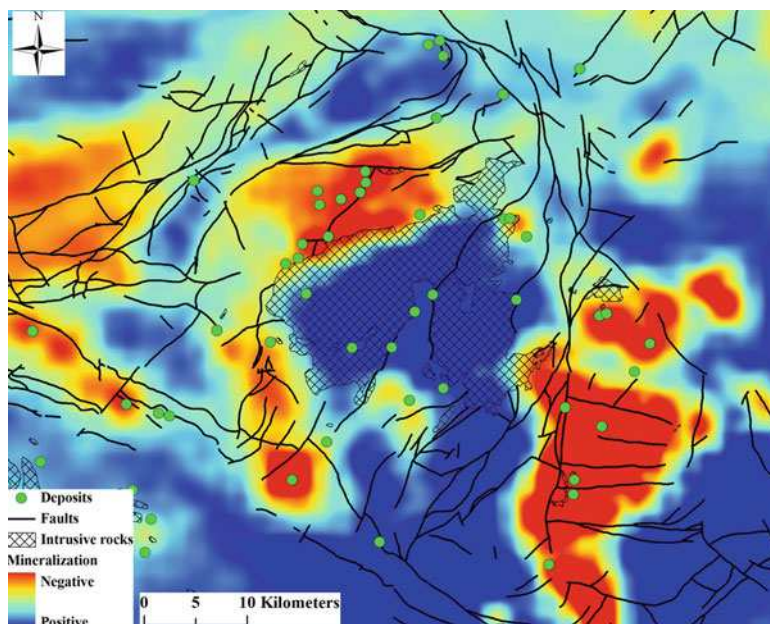


Fig. 1.5 Mineralization identified by singularity mapping technique

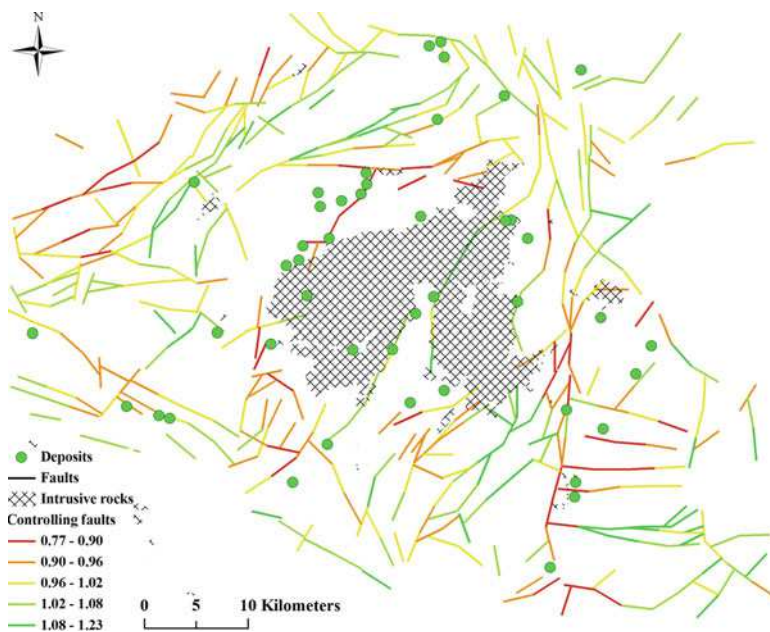


Fig. 1.6 Controlling effects of faults identified by new singularity mapping technique

1.5 CONCLUSIONS

This study demonstrate a series of applications of singularity theory to characterized spatial variations of signatures caused by mineralization associated geological features, results of which are not only beneficial to mineral potential mapping, but also usable to interpret geo-processes dominating the formation of hydrothermal mineralization in Gejiu mineral district, China.

REFERENCES

1. Cheng, Q. and Agterberg, F.P.: Singularity analysis of ore-mineral and toxic trace elements in stream sediments. *Comp Geosci*, 35, 234–244 (2009)
2. Zhuang, Y., Wang, R., Yang, S. and Yi, J.: Geology of Gejiu tin-copper polymetallic deposit. Earthquake Publishing House (1996)
3. Xiong, G. and Shi, S.: Physical-geological model of the Gejiu tin district and its application. *Geo Rev*, 40, 19–27 (1994)

Chapter 2

Compositionally Compliant Contact Analysis

R. Tolosana-Delgado, U. Mueller, and K.G. van den Boogaart

Abstract Contact analysis assesses the evolution of the average value along boreholes of a given variable at increasing distances from the contact between two facies or domains. The concept is long established in the geostatistical literature and software, albeit for studying the behavior of a single variable. This contribution explores practical ways for studying this transient behavior of a set of variables forming a composition, in such a way that spurious correlation effects are avoided. This is obtained with contact diagrams for each possible pairwise logratio of two components, as well as with a contact analysis of the centered-logratio transformed components. This approach is particularly promising when the set of components considered account for a considerable amount of the total mass, or dilution effects are suspected to have affected only a subset of the components. These concepts are illustrated with data from Murrin Murrin, WA, a Ni-Co laterite deposit where intensive remobilization of both value and deleterious components is known to have occurred.

Keywords Domaining • Facies • clr • Variation Matrix • Geometallurgy

2.1 INTRODUCTION

In deposits where supergenic enrichment zones or lithotypes occur in a complex association in such a way that it is not reasonable to consider them as separate domains, it is usual to first characterize the nature of the transition of the variable

R. Tolosana-Delgado (✉)

HIF, Helmholtz Institute Freiberg for Resource Technology, Freiberg, Germany

e-mail: rtolosana@hzdr.de

U. Mueller

ECU, Edith Cowan University, Joondalup WA6027, Australia

K.G. van den Boogaart

HIF, Department of Modelling and Valuation, Helmholtz Institute Freiberg for Resource Technology, Freiberg, Germany

TUBAF, Institute of Stochastics, Technical University “Bergakademie”, Freiberg, Germany

under consideration near the contact between the several enrichment zones. Sometimes known as *contact analysis*, this can be obtained as a diagram of the expected value of the studied variable as a function of the distance from the contact between two zones of interest. If this mean can be shown to be stationary or vary smoothly in the vicinity of the contact (a “soft” contact), then the variable can be treated considering both zones together. If the mean shows a sharp change near/at the contact (a “hard” contact”), then it is recommended to treat the two zones as separate domains for future variography or interpolation/simulation procedures [1]. These concepts have been established for one variable or a set of variables, but always real-valued ones. However, when a composition is considered, one might expect spurious correlation effects [2] to arise in contact analysis. In this paper, a composition is a set of variables that jointly describe the relative mass of the geochemical elements forming the rock samples. It is known that the components of a composition sum up to a constant. This closure to constant sum propagates actual changes in one component to apparent changes in all other. For example, in a system with two zones (facies, lithotypes, enrichment zones, etc) A and B, where the only difference between the zones is an enrichment on one element in zone B, a hard contact A-B for this component will result in apparent hard contacts for the remaining elements, even though they show the same behavior in both zones. To avoid these inconsistencies, some ideas of compositional data analysis can be borrowed. Aitchison [2] was the first to realize that compositions carry only relative information, and that this can be expressed in the form of (log)-ratios of components. Compositional data analysis proposes to use classical methods on the logratio transformed data. This contribution explores this alternative contact analysis.

2.2 COMPOSITIONAL CONCEPTS

A regionalized D -part compositional data set is a family of observations $\{\mathbf{z}(x_1), \mathbf{z}(x_2), \dots, \mathbf{z}(x_N)\}$ of a multivariate random function $\mathbf{Z}(x)$ such that $Z_i(x) \geq 0$ for all $i = 1, 2, \dots, D$ represents the *relative importance* of component i in the mass of the volume at x , and as such $Z_1 + Z_2 + \dots + Z_D \leq 100\%$. Without loss of generality, we will assume in this contribution that the last component is the complementary of all variables considered, so that $Z_1 + Z_2 + \dots + Z_D = 100\%$. The key idea of compositional analysis is the use of logratios of components, resulting in some real scores that are suitable to be modeled by any multivariate method. Two of these transformations are relevant here, the pairwise logratio (pwlr), and the centered logratio transformation (clr) [2]:

$$\text{clr}(\mathbf{z}) = \ln \frac{\mathbf{z}}{D \sqrt{\prod_{i=1}^D z_i}}$$

Means and variances can be extracted from the transformed scores and studied and interpreted in the usual ways.

2.3 CONTACT ANALYSIS

Assume a data set recorded along boreholes crossing between two domains A and B. A contact diagram is a plot of the conditional mean $E[Z_i(h) | h \pm \Delta h]$ against the signed distance h from the contact [1]. This conditional mean can be estimated by the method of moments (a classical choice), but also quantiles of $[Z_i(h) | h \pm \Delta h]$ for each fixed h can be calculated. In the case of a compositional data set, a compositionally-compliant contact analysis would be to consider the quantiles and the mean of $\ln(Z_i(h)/Z_j(h))$ and/or of $\text{clr}(\mathbf{Z})$.

2.4 THE MM23 DATA SET

Murrin-Murrin is a Ni/Co-laterite deposit from Western Australia [3, 4]. This is supposed to be formed by intense chemical weathering of ultramafic rocks. A zoned weathering profile is typical, in which mobile elements are effectively removed – and less mobile ones redistributed. Fe, for example, is residually enriched in the ferruginous zone by the leaching of Mg. Ni and Co, the major value elements, are accumulated in the smectitic or saprolitic zones between fresh (ultramafic parent rock) and weathered zones (ferruginous zones). The assessment of the contacts between these different zones (or supergenic enrichment) is the focus of this study. Ten geochemical variables (plus the rest, $D=11$) are considered, and the study focuses on the transition from saprolitic to ferruginous zones. A classical contact analysis of these 11 variables show either a hard contact (Al, As, Fe, Mg, rest) or a soft contact with a significant increase of variability around the contact (Co, Cr, Cu, Mn, Ni, Zn). A similar picture is derived with a clr analysis. On the other hand, a pwlr analysis is much richer. All logratios between Cr, Cu, Fe and As (and partly also Zn or Al) show either no contact at all or a soft contact without apparent increase of variance around the contact. The same can be said of the ratio Mn/Ni, while Co, Mg and the rest show quite an individual behavior, either showing a soft contact with increases variance (Co, rest) or a hard contact (Mg). These results suggest that a logratio-geostatistical framework [5] might consider both domains as equivalent within the subcompositions (Cr, Cu, Fe, As, Zn, Al) and (Mn, Ni), while it might be necessary to model the variables Co, Mg and the rest in each domains separately, as they are responsible for most of the “sharpness” of the contact. From a geological point of view, these results suggest that perhaps only Mg and the rest might be significantly mobilized (Fig 2.1).

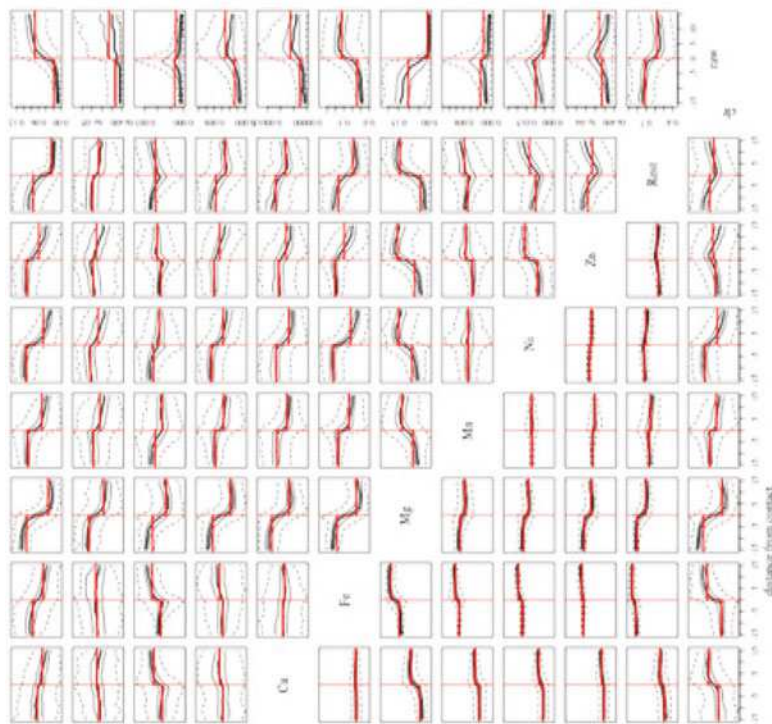


Fig. 2.1 Contact diagrams of all pairwise logratios, of clr-transformed data and of raw data from saprolitic to ferruginous zone. Lower triangle diagrams share a vertical scale. Red lines show mean values at each side of the contact. Dashed lines represent 95% probability bands and solid lines 50% probability bands. Thick line is the local median.

REFERENCES

1. Vargas-Guzmán, J.A.: Transitive Geostatistics for Stepwise Modeling Across Boundaries between Rock Regions. *Mathematical Geosciences*, 40, 861–873 (2008)
2. Aitchison, J.: The Statistical Analysis of Compositional Data. Chapman and Hall. London (1986)
3. Fazakerley, V.W. and Monti R.: Murrin Murrin nickel-cobalt deposits. In: Beriman D.A., Mackenzie D.H. (eds) *Geology of Australian and Papua New Guinean Mineral Deposits*, p. 329–334. The Australasian Institute of Mining and Metallurgy. Melbourne (1998)
4. Murphy, M., Bloom, L.M. and Mueller, U.A.: Geostatistical optimisation of mineral resource sampling costs for a Western Australian nickel deposit, in Bayer, U. et al. (eds) *IAMG 2002 Proceedings of the 8th Annual Conference of the International association for Mathematical Geology*, 105–110. Terra Nostra. Berlin. (2002)
5. Tolosana-Delgado, R. and van den Boogaart, K.G.: Geostatistics for compositions. In: Pawlowsky-Glahn V., Buccianti, A. (eds.) *Compositional data analysis: Theory and Applications*, p. 73–86, Wiley, Chichester (2011)

Chapter 3

Kernel Principal Component Analysis in the Application of Geochemical Comprehensive Feature Extraction

Bingli Liu, Ke Guo, and Li Zhang

Abstract Principal component analysis is a kind of effective method of extracting comprehensive geochemical data feature. By constructing a new comprehensive variable to instead of the original variables, the new can effectively reflect the compositive information of original variables; it also could indicate the pargenetic assemblage and genetic relationship of exploration geochemistry. But it is based on the hypothesis premise of the normal (liner) distribution of the sample data. However, the complexity of geological systems and multiple stage mineralization stage often lead to the nonlinear distribution of multivariate geochemical data. Therefore, compared with the traditional principal component analysis, the nonlinear principal component analysis is more suitable for extracting of the multivariate geochemical data. This paper introduces the principal component analysis basing on kernel function. With the help of a “nuclear techniques”, implicitly map the input space to a nonlinear characteristics space. In this space, we carry out principal component analysis of geochemical data. The algorithm is in line with the exploration geochemistry data features. Through the experimental analysis of Tibet Daewoo stream sediment data, the principal components analysis based on kernel function is compared with the conventional PCA can better complete the comprehensive exploration geochemistry data feature extraction.

Keywords KPCA • Feature Extraction • Geochemical Data

B. Liu

Institute of Geophysical and Geochemical Exploration, Chinese Academy of Geoscience,
Langfang, China

Key Lab of Geomathematics of Sichuan Province, Chengdu University of Technology,
Chengdu, China

K. Guo (✉) • L. Zhang

Key Lab of Geomathematics of Sichuan Province, Chengdu University of Technology,
Chengdu, China

e-mail: guoke@cdut.edu.cn

3.1 INTRODUCTION

In geochemical prospecting work, the comprehensive information of each element is very important. The Geochemists differentiate an abnormality is ore causing or not, and estimate the stand or fall of the miner genetic condition, mainly relying on comprehensive information rather than just depend on a mineral element anomaly. The formation of a large mine, went through a very complicated geological process. Many elements will be involved, follow the principle of element enrichment. In the end there will be forming a unique multi-element anomalies - comprehensive anomaly. As we know, geological data is nonlinear data, so Looking for a nonlinear method to pickup the geochemical anomaly is necessary. Principal component analysis is an effective method of comprehensive geochemical data feature extraction, which is constructed a new variables instead of the original variables. It can effectively reflect the compositive information of original variables, and indicate the exploration geochemistry of magmatite and genetic relationship. However, the complexity of geological systems and multiple stage mineralization stage often lead to the nonlinear distribution of multivariate geochemical data. Therefore, compared with the traditional principal component analysis, the nonlinear principal component analysis is more suitable for extracting of the multivariate geochemical data.

3.2 STUDY AREA AND HYDROGEOLOGY

The study area is located in the north of the Yarlung Zangbo River suture, Xietongmen country, Tibet autonomous region, Lielang-Tanghe-Jila river multi-metal workspace. It is located in the eastern section of Gangdese acid complex, south edge of butuo - savonarola – nanmuqie compound synclinal, duoxionggraben basin is southern neighbor, belonged to the mountain tectonic belt in South Asia. At the same time, it also located in the junction between Angren- Shigatse tectonic zones to the gangdise tectonic belt [1–3] (Fig. 3.1).

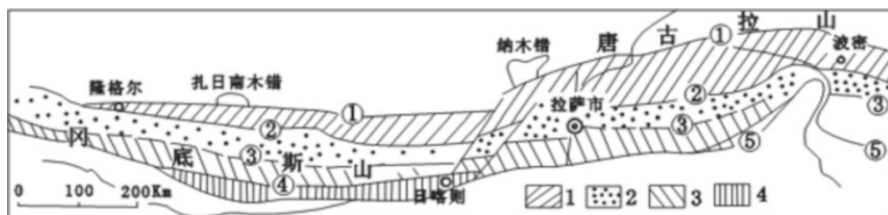


Fig. 3.1 Tectonic division of the Gangdese terrestrial sources volcanic rock - magmatic belt (According to Duguangshu,1993 modification) ①the north; ②the middle; ③the south; ④the Yarlung Zangbo River plate junction zone.

3.3 MATERIAL AND METHODS

5 of 1:50000 groundwater samples were collected in the study area. The principal component analysis basing on kernel function, with the help of a “nuclear techniques” implicitly map the input space to a nonlinear characteristics space. In this space, we carry out principal component analysis of geochemical data [4–6]. The algorithm is in line with the exploration geochemistry data features.

3.4 RESULTS AND DISCUSSION

The standard deviation, variation coefficient of Cu、Pb、Zn、Au are large change. It shows that there were stronger capacity of the enrichment intensity and enrichment capacity of elements in soil. According to the variation coefficient of each element, we determined the enrichment ability of the soil elements, and sorted them from lowest to highest: : Pb>Au>Cu>Ag>Zn (Table 3.1).
The skewness and kurtosis of the normal distribution curve for the raw data are higher. So, with the traditional multivariate statistical methods to extract the anomaly characteristics of the element is not suitable, in view of this, this paper uses kernel principal component analysis to extract the geochemical elements integrated information (Table 3.2 and Figs. 3.2 and 3.3).

Table 3.1 Characteristic parameter table of the stream sediment measured data

	Au	Ag	Cu	Pb	Zn
Sample Size	1019	1019	1019	1019	1019
Min	0.30	0.05	7.30	3.10	6.90
Max	75.00	2.68	1046.00	1690.00	458.00
Mean Value	2.36	0.15	31.97	20.23	43.41
Median	1.30	0.13	26.70	15.40	40.20
25 % Tantile	0.90	0.11	20.40	11.40	30.30
50 % Tantile	1.30	0.13	26.70	15.40	40.10
75 % Tantile	2.00	0.17	34.50	20.40	51.70
Mode	0.90	0.12	19.40	15.90	36.20
Standard Deviation	5.07	0.12	41.50	56.51	24.14
Variance	25.74	0.01	1721.96	3192.89	582.64
Skewness	8.90	14.10	17.51	26.13	6.29
Kurtosis	102.94	268.80	385.96	754.36	92.30
Variable Coefficient	2.15	0.78	1.30	2.79	0.56

Note: element unit: ω (Au) / 10^{−9}, ω (Ag)/10^{−6}, ω (Cu)/10^{−6}, ω (Zn)/10^{−6}, ω (Mo)/10^{−6}

Table 3.2 Comparison of accumulating contribution rate between PCA and KPCA

Sequence Number	PCA			KPCA		
	Eigen value	Rate of Contribution	Accumulating Contri. Rate	Eigen value	Rate of Contribution	Accumulating Contri. Rate
1	2.02	40.399%	40.399%	0.115	82.2%	82.2%
2	1.26	25.273%	65.672%	0.0142	10.14%	92.32%
3	0.843	16.866%	82.538%	0.0098	7%	99.32%
4	0.547	10.94%	93.478%	0.0009	0.68%	100%
5	0.326	6.522%	100%	0	0	0

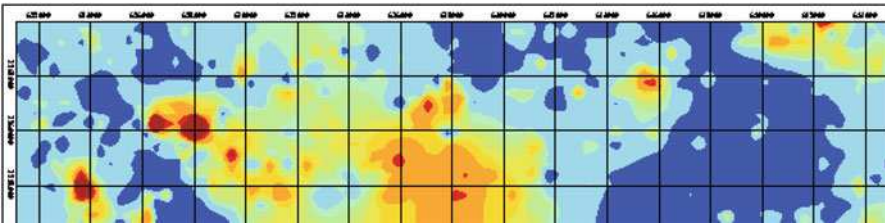


Fig. 3.2 Anomaly chart of 1:50000 stream sediments survey integrated information by PCA.

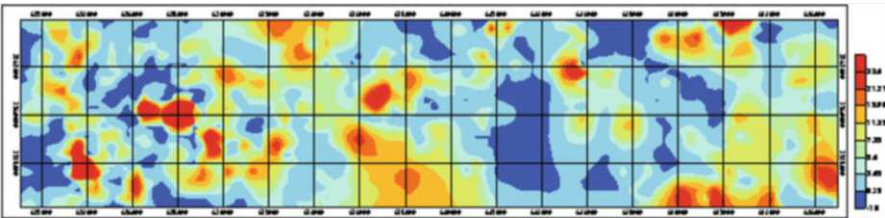


Fig. 3.3 Anomaly chart of 1:50000 stream sediments survey integrated information by KPCA.

3.5 CONCLUSIONS

Extracted integrated information of the regional geochemical five kinds of ore-forming elements (Au, Ag, Cu, Pb, Zn) by principal component analysis and kernel principal component analysis, then used the S-A model to differentiate the comprehensive regional geochemical anomaly. According to the comparative analysis between the comprehensive anomaly extraction and geochemical map for superposition of single element, it shows that the kernel principal component analysis can reflect more comprehensive information, it not only can fully embody the superposition of single elements nested part but also show the comprehensive

information that the superposition of single element can't reflect. And this part has more guiding significance to exploration prospecting.

ACKNOWLEDGEMENTS This research benefited from a research project by China Geological Survey (No.12120114002001), and the National Natural Science Foundation of China (No. 41272363).

REFERENCES

1. Tang, J.X.: The geology study report of Xietongmen County, Tibet autonomous region JiLapoly metallic ore, Chengdu University of Technology (2006)
2. Tang, J.X.: The geology study report of Xietongmen County, Tibet autonomous region TangHepolymetallic ore, Chengdu University of Technology (2006)
3. Tang, J.X.: The geology study report of Xietongmen County, Tibet autonomous region LieLangpolymetallic ore, Chengdu University of Technology (2006)
4. Cho, J.H.: Fault identification for process monitoring using kernelprincipal component analysis. *Chemical Engineering Science*, 60, 279–288 (2005)
5. Choi, S.W. and Lee, C.: Fault detection and identification of nonlinear processes basedon kernel PCA, *Chemo metrics and Intelligent Laboratory Systems*, 75, 55–67 (2005)
6. Lee, J.M. and Yoo, C.K.: Nonlinear process monitoring using kernel principalcomponent analysis. *Chemical Engineering Science*, 59, 223–234 (2004)

Chapter 4

Abnormal Extraction of Geochemical Data Based on Kalman Filter and SVM

Ke Guo, Bingli Liu, and Fei Wu

Abstract Exploration geochemistry integrating anomaly characteristics is an important index of mineral prediction. Mineralizing process is complex. Because of the superposition of the primary environment and the evolution of the secondary environment, the dispersion of geochemical model presents complex features. Effective method of comprehensive abnormal extraction is especially important. In recent years, information fusion technology is a focal point of research. And it has achieved great success in signal and image processing. Information fusion technology offers a new way for comprehensive abnormal extraction. It is a processing method of multi-order, multi-aspects and multi-level for multi-sensor information, so as to get some new efficient information. Kalman filtering is one of the typical representatives. Kalman filtering is a kind of optimal estimation algorithm and it take for linear, unbiased and the minimum variance as the criterion, and the algorithm thought correspond to the comprehensive characteristics. The introduction of Kalman filter for exploration geochemistry integrating anomaly can provide a new method of exploration geochemical prospecting.

Keywords Geochemical Data • Kalman Filter • Support Vector Machine

4.1 INTRODUCTION

Distribution of geochemical elements in natural systems measurement is the main form of geochemical exploration, the natural material has soil, stream sediment and rocks, and the target is associated with mineralization and ore deposit geochemical

K. Guo • F. Wu

Key Lab of Geomathematics of Sichuan Province, Chengdu University of Technology, Chengdu, China

B. Liu (✉)

Institute of Geophysical and Geochemical Exploration, Chinese Academy of Geoscience, Langfang, China

Key Lab of Geomathematics of Sichuan Province, Chengdu University of Technology, Chengdu, China

e-mail: liubingli-82@163.com

anomaly. Adopt the reasonable exploration technology is very necessary. In order to find elements anomaly area more intuitively and accurately, it is necessary to adopt reasonable mathematical methods for data analysis. At past, the geochemical data processing method is always based on normal distribution, such as cluster analysis, factor analysis, discriminant analysis, these algorithms has made a lot of research results, but its limitations are increasingly exposed. In recent years, the nonlinear characteristics of geochemical data are taken seriously by expert. More and more nonlinear method has been widely used. In view of this, the author proposed in comprehensive anomaly, and pay attention to the role of geological metallogenic regularities, realize the fusion in the true sense, strive to provide mineral exploration with an important prediction method, and application practice, the study of exploration geochemistry data analysis has very important significance.

4.2 STUDY AREA

The study area is located in the Rong Matownship, Xietongmen country, Tibet autonomous region. Mining area's geographical location: West $29^{\circ}21'30'' \sim 29^{\circ}24'00''$, East $88^{\circ}23'45'' \sim 88^{\circ}26'30''$. The central location exploration area: West $29^{\circ}22'30''$, East $88^{\circ}25'30''$. The distance between the east and west is about 4.5 km long, The distance between the south and north is about 4.5 kilometers long, the area of about 12.91 square kilometers can be explored, the mining area is about 4 square kilometers (Fig. 4.1).

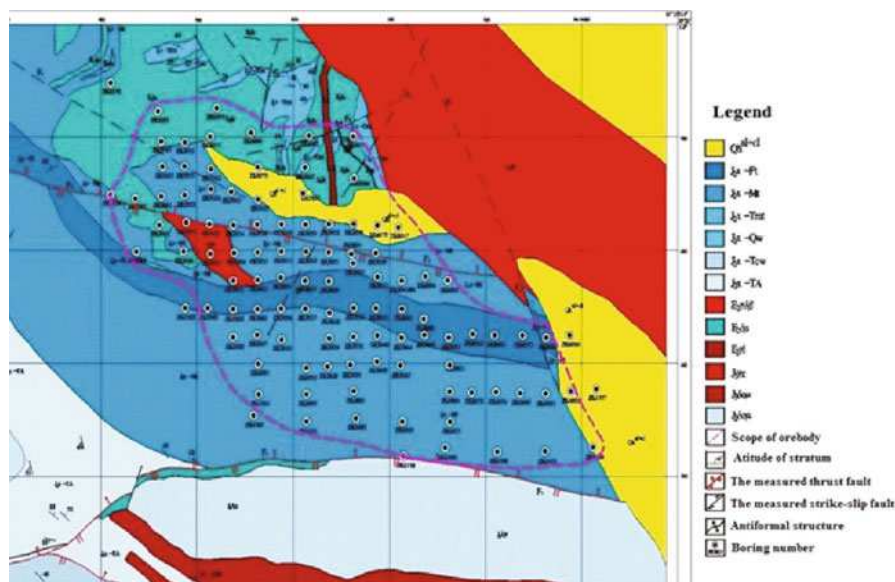


Fig. 4.1 Xionggun copper mining area geological diagram.

4.3 MATERIAL AND METHODS

1:10000 soil data were collected in the study area. The principal component analysis basing on kalman filter, with the help of SVM implicitly map the input space to a nonlinear characteristics space. In this space, we carry out data fusion and threshold extraction of geochemical data. The algorithm is in line with the exploration geochemistry data features.

4.4 RESULTS AND DISCUSSION

4.4.1 Raw Data Analysis and Comprehensive Anomaly

Making the distribution of original data in the form of exponential histograms (Figs. 4.2, 4.3, 4.4, 4.5 and 4.6)

According to the distribution, normal distribution curve of the measured data in the study area has higher kurtosis and skewness, that suggests the measured data are basically satisfy the normal distribution without any method to transform, and it shows the nonlinear characteristics. Therefore, the article chose to take logarithm of the measured data by natural method, distribution of the data after the transformation, the result shows that individual elements basically met the logarithmic normal distribution. Based on measured data part of the surveyed area as an example, Firstly, data fusion based on Kalman filter to get comprehensive information, then adopt the method of SVM learning to get the anomaly threshold. Lastly, the article get the anomaly contour map of fusion data by the software Map GIS and compared with the anomaly contour map adopted the method of cumulative frequency (Figs 4.7 and 4.8).

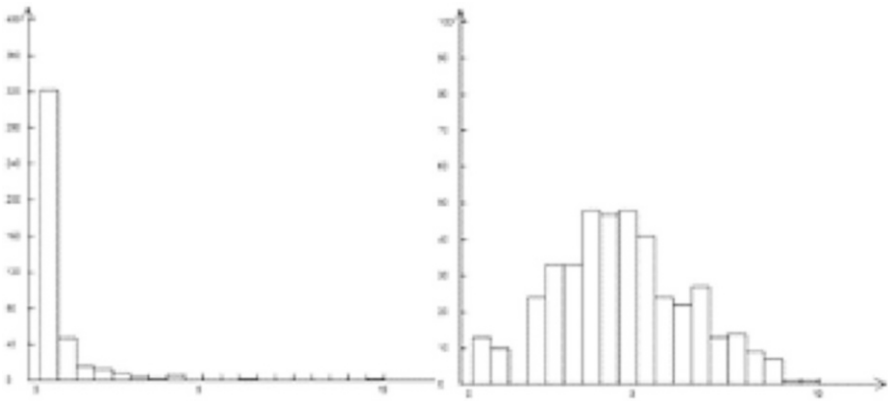


Fig. 4.2 Au original data and the exponential histogram.

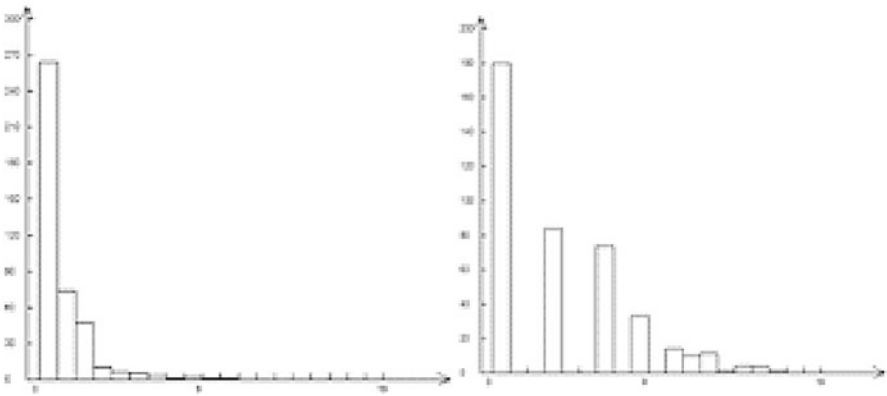


Fig. 4.3 Ag original data and the exponential histogram.

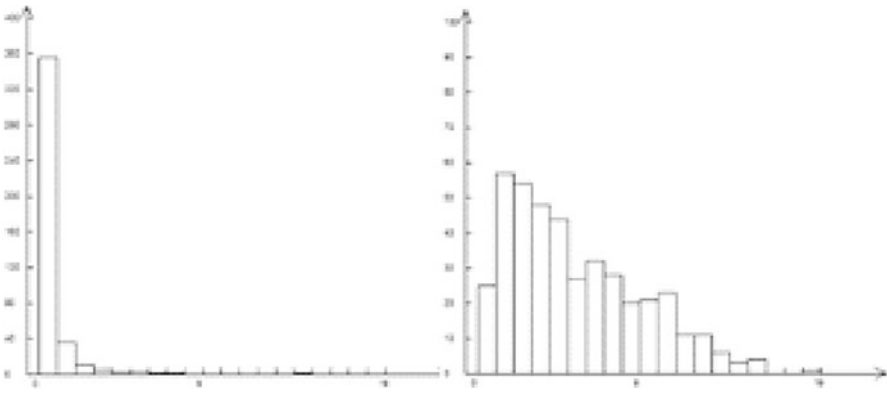


Fig. 4.4 Cu original data and the exponential histogram.

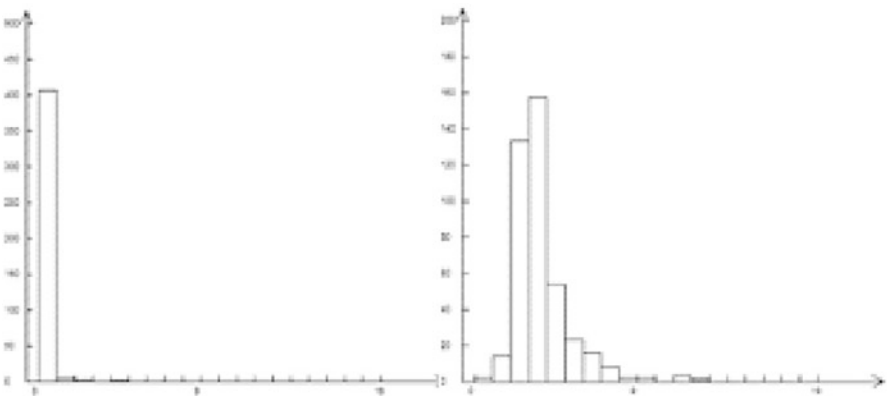


Fig. 4.5 Pb original data and the exponential histogram.

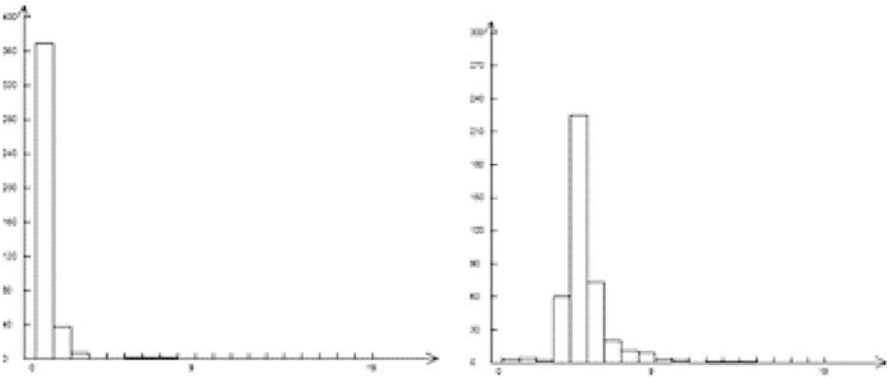
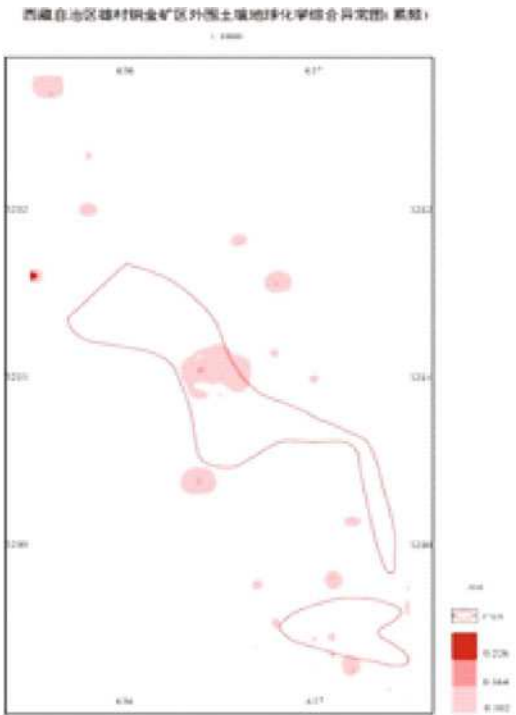


Fig. 4.6 Zn original data and the exponential histogram.

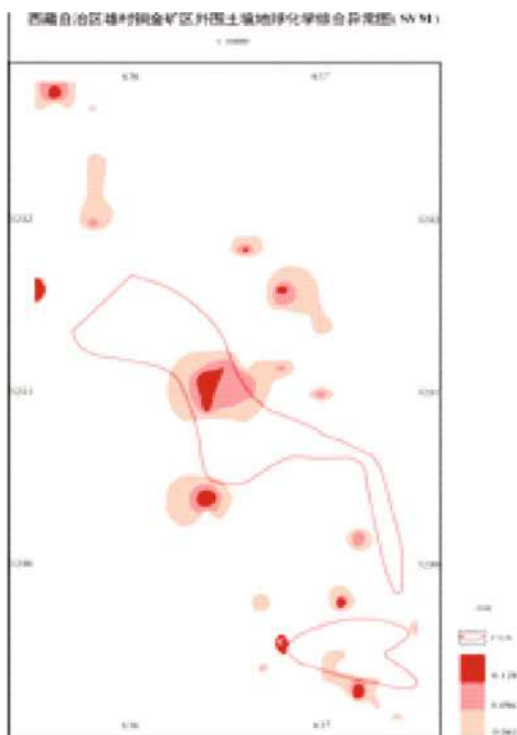
Fig. 4.7 Comprehensive anomaly map (cumulative frequency) (SVM).



4.4.2 Results Analysis

The merged data abnormal picture showed that enrichment is obvious, and mineralized bodies showed clear, comprehensive anomalies delineated the form better. At the same time, Adoptingthe method of support vector machine (SVM) to get the

Fig. 4.8 Comprehensive anomaly map.



result showed that the treatment of anomaly range tired frequency form better, framed by the abnormal and anastomosed with the mine mineralized bodies distribution accords with the practice of the field anomalies.

4.5 CONCLUSIONS

Based on the Xiongcun 1:10000 soil geochemical data as the research object, take the method of Kalman filter and SVM combining of geochemical comprehensive anomaly and determined the threshold for delineating elements. Through the theoretical research as well as the example, takingthe method of Kalman filter to extracting the comprehensive anomaly is feasible. And the theory and application effect the fusion data based on the kalman filter has more advantages than conventional method.

ACKNOWLEDGEMENTS This research benefited from a research project by China Geological Survey (No. 12120114002001), the National Natural Science Foundation of China (No. 41272363).

REFERENCES

1. Qin, Y.: Thekalman filtering and integrated navigation principle, Xian, Northwestern polytechnical university press (1998) (in Chinese)
2. Fu, M. and Deng, Z.: Kalman filtering theory and its application in the navigation system, Bei Jing, Science press (2003) (in Chinese)
3. Denaro, R.P. and Loomis, P.: GPS Navigation Processing and Kalman Filtering, AGARD, 161 (1989)
4. Grewal, M.S.: Kalman filtering: Theory and application using Matlab (Second Edition), New York, A Wiley-Interscience Publication (2008)
5. Sorenson, H.W.: Kalman filtering: Theory and application, New York, IEEE Press (1985)

Chapter 5

Summed Area Table for Rapid Local Singularity Mapping

Z. Chen and Q. Cheng

Abstract The local singularity model based on multifractal theory suggested by Cheng has gained significant attention in characterizing mineralization and predicting mineral deposits. Chen et al. developed an iterative approach of local singularity analysis to get the final singularity index. However the computational efficiency need to be improved, because the moving average with several scales are calculated for each cell of an raster dataset in the conventional algorithm. Summed area table (SAT), also called as integral image, was first prominently used within the Viola-Jones object detection framework in computer vision. We introduced SAT in local singularity mapping in this study. Once computed using SAT, any one of the rectangular sum can be computed at any scale or location in constant time. SAT is used in geochemical stream sediment survey data applications. A wide variety of scale changes for non-iterative or iterative approach are adopted to calculate the singularity index values efficiently, and then we compare the results and generate optimal singularity mapping.

Keywords Summed Area Table (SAT) • Local Singularity • Iterative Approach • Lanping

Z. Chen (✉)

State Key Laboratory of Geological Processes and Mineral Resources, China University of Geosciences, Wuhan, China

Faculty of Earth Resources, China University of Geosciences (Wuhan), Wuhan, China

e-mail: chenzhijuncs@163.com

Q. Cheng

Earth and Space Science and Engineering, York University, 4700 Keele Street, Toronto, Canada, M3j1P3

State Key Lab of Geological Processes and Mineral Resources,
China University of Geosciences, Beijing and Wuhan, China

5.1 INTRODUCTION

The concept of singularity is used for characterizing the anomalous amounts of energy release or material accumulation within a narrow spatial-temporal interval [1]. The local singularity model based on multifractal theory suggested by Cheng [2, 3] has gained significant attention in characterizing mineralization and predicting mineral deposits. Especially, this model has had impressive successes in the weak anomaly identification, interpolation for exploration geochemical/geophysical data [4]. However the computational efficiency need to be improved, because the moving average with several scales are calculated for each cell of an raster dataset in the conventional algorithm. To estimate the local singularity index α , we usually calculate the average densities on a series of windows centered at the given location and these averages versus scales on log-log plot. The singularity index map is made when we repeat the above process by gliding windows. Summed area table (SAT), also called as integral image, was brought forward to speedup the computation of the singularity analysis.

5.2 LOCAL SINGULARITY ANALYSIS

According to [5] local scaling behaviour, taking the example of exploration geochemical data, the average element concentration $\langle \rho(B_x(\varepsilon)) \rangle$ follows the following power-law relationship [5]:

$$\langle \rho(B_x(\varepsilon)) \rangle = \mu(B_x(\varepsilon)) / \varepsilon^E = c(x) \varepsilon^{\alpha(x)-E} \quad (5.1)$$

with respect to the scale ε where $\varepsilon = l/L$ is the ratio of the largest-scale L to window size l . Denote:

$$\Delta\alpha(x) = E - \alpha(x) \quad (5.2)$$

Using $\Delta\alpha$ is easier to understand than α in the exploration geochemical data:

$$\begin{cases} \Delta\alpha(x) < 0 \Leftrightarrow \text{local depletion} \\ \Delta\alpha(x) > 0 \Leftrightarrow \text{local Enrichment} \\ \Delta\alpha(x) = 0 \Leftrightarrow \text{local Background} \end{cases}$$

[5] proposed an iterative approach to obtain improved the $\Delta\alpha$ estimates. Let $c^{(-1)} = \rho$ (original dataset) and denote $\Delta\alpha^{(k)}(x) = E - \alpha^{(k)}(x)$ where k is iterative times. If $k = 0$ is ordinary non-iterative approach. Eq(5.1) can be given by

$$\langle \rho(B_x(\varepsilon)) \rangle = c(x) \varepsilon^{-\Delta\alpha(x)} \quad (5.3)$$

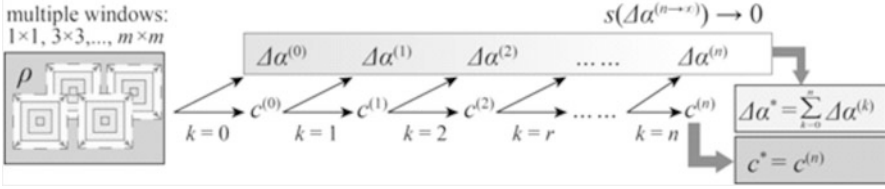


Fig. 5.1 Illustration showing the processes of the iterative approach for the local singularity analysis

If k is big enough, the standard deviation of $\Delta\alpha^{(k)}$ is approach to 0, then the final delta singularity index $\Delta\alpha^*(x)$ and the final coefficient $c^*(x)$ are

$$\begin{aligned}\Delta\alpha^*(x) &= \Delta\alpha^{(0)}(x) + \sum_{k=1}^n \Delta\alpha^{(k)}(x) = \sum_{k=0}^n \Delta\alpha^{(k)}(x) \\ c^*(x) &= c^{(k)}(x)\end{aligned}\quad (5.4)$$

Figure 5.1 shows the idea of the iterative approach. The average for ρ or c raster data will be done $m \times n \times p$ times where m is number of the multiple windows, n is the iterative times and p is the total calculating locations of the raster data. The heart of the matter of the iterative approach is to find a rapid algorithm to evaluate the gilding average or sum.

5.3 SUMMED AREA TABLE

Summed area table (SAT), also called as integral image, is a data structure and algorithm for quickly and efficiently generating the sum of values in a rectangular subset of a grid. It was first introduced to computer graphics by Frank Crow in 1984 for use with mip maps [6] and was first prominently used within the Viola-Jones object detection framework in 2002 [7]. Historically, this principle is very well known in the study of multi-dimensional probability distribution functions, namely in computing 2D (or ND) probabilities (area under the probability distribution) from the respective cumulative distribution functions [8]. Instead of recomputing sums of rectangles at every re-scaling, SAT computes all possible rectangular areas of the image $[\rho(i,j)]_{w \times h}$ in the beginning and save them for future computations using a recurrence formula:

$$\begin{aligned}s(i, j) &= s(i, j-1) + \rho(i, j) \\ SAT(i, j) &= SAT(i-1, j) + s(i, j)\end{aligned}\quad (5.5)$$

or, to put it simple,

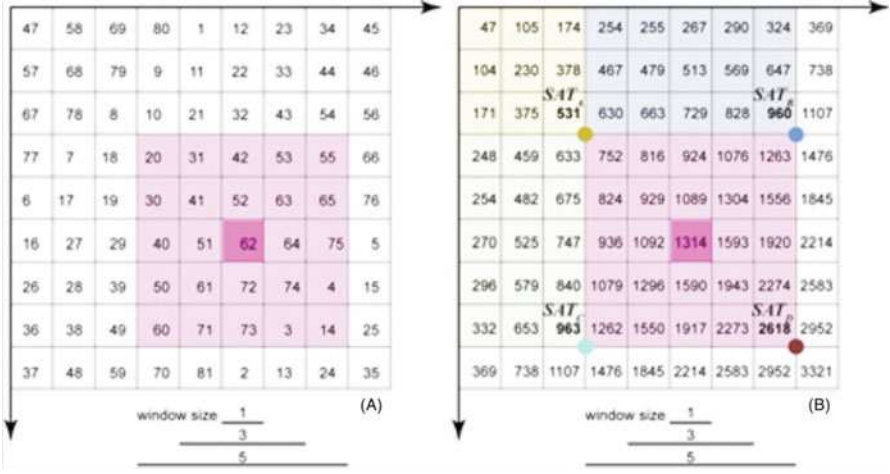


Fig. 5.2 Calculation of summed area from table. (A) input raster data produced by magic square of order 9 constructed from the integers 1 through 81. The block with pink color is centered at (6,6) and size is 5x5; (B) summed area table(SAT). The sum within pink-color shaded area can be computed as $(SAT_D + SAT_A) - (SAT_C + SAT_B) = 2618 + 531 - (963 + 960) = 1226$ and mean is 49.04

$$SAT(i, j) = \rho(i, j) + SAT(i-1, j) + SAT(i, j-1) - SAT(i-1, j-1) \quad (5.6)$$

with $SAT(-1, j) = SAT(i, -1) = 0$. For the missing data problem, we can labeled those locations and set missing data = 0. In a summed area table, the area for any rectangular region in the image can be computed by using only 4 array accesses in constant time independently of the size of the region; effectively reducing the computational complexity from $O(n)$ to $O(1)$ [8]. The local singularity analysis of the raster dataset commonly uses rectangular windows on different scales which can be computed efficiently with SAT. Figure 5.2 above may hopefully help in illustrating this point.

For example, the sum within any windows size 1×1 centered at (6,6) can be easily calculated by the formula: $\mu(1) = (SAT_D + SAT_A) - (SAT_C + SAT_B)$, and then we have

$$\mu(l) \left[(l^2 / L^2 N(l)) \right] = c(x) (l/L)^{\alpha(x)} \quad (5.7)$$

where $l = 1, 3, 5, 7, \dots, L$. $l = 1$ means the input original data, $N(l)$ is count of the valid data within window $l \times l$, if all the elements of the data are valid, Eq (5.7) can be as simple as

$$\mu(l)/L^2 = c(x) (l/L)^{\alpha(x)} \quad (5.8)$$

When $c(x)$ replaces the input original raster data, we calculate the new SAT for the $c(x)$. And the final singularity index $\alpha^*(x)$ or delta index $\Delta\alpha^*(x)$ can be fast obtained by the iterative approach.

5.4 CASE STUDY

The geochemical dataset from was sampled from stream sediments in Lanping area, Yunnan province, China where is well-known for Pb-Zn poly-metallic mineralization. To explore the influences of the different window parameters to the local singularity analysis. We set 8 suites of windows whose number is from 5 to 12:

$$\begin{aligned} B[5] &: 1 \times 1, 3 \times 3, \dots, 9 \times 9; \\ B[6] &: 1 \times 1, 3 \times 3, \dots, 9 \times 9, 11 \times 11; \\ &\dots \\ B[12] &: 1 \times 1, 3 \times 3, \dots, 9 \times 9, 11 \times 11, \dots, 23 \times 23. \end{aligned}$$

The iterative approach was adopted to calculate $\Delta\alpha$, the loop will be stopped if $\Delta^{(k)}\alpha < 0.01$ and iterative time > 10 . We use weights of evidence to calculate the t-value (t-statistic) to measure the significance of the spatial relationship between the high $\Delta\alpha$ value and the occurrences of Pb-Zn-Ag ore deposits. SAT technique is valid to to accelerate the computation of the singularity analysis. Fig. 5.3 show the singularity analysis for Zinc data. With the calculation of different suites of windows, tcures obtained by the traditional non-iterative approach are relatively

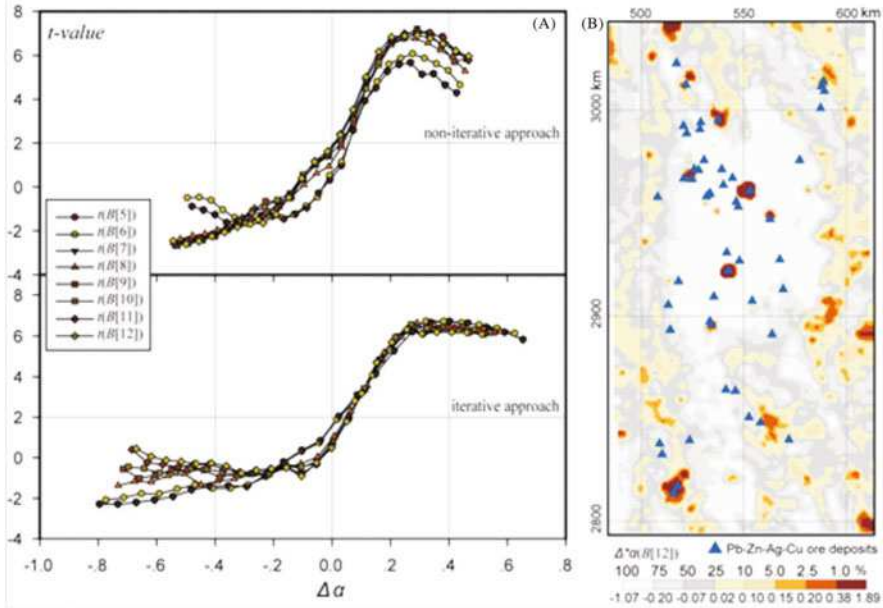


Fig. 5.3 Singularity analysis for Zinc data. (A) $\Delta\alpha$ - t charts for Zn with eight suites of windows: from $B[5]$ to $B[12]$, $\Delta\alpha$ estimated using non-iterative approach (top) and $\Delta\alpha$ -values estimated using iterative approach (bottom). (B) The optimal $\Delta\alpha$ mapping by windows setting $B[12]$ using iterative approach

dispersed, while they obtained by the iterative approach are relatively close to each other when $\Delta\alpha > 0$. Pb, Ag, Cu, Cd, Hg associated with Zinc-Lead-Silver mineralization got the similar behaviors of $\Delta\alpha$ -t charts. It means that the windows setting has an impact on the results using non-iterative approach and while it has very little impact for the iterative approach. Our results support the conclusion that the iterative method is more robust and superior to traditional non-iterative method of identifying anomalies.

5.5 CONCLUSIONS

SAT for the local singularity analysis allows for very rapid and efficient local anomaly detection. SAT gave us unlimited possibilities for designing optimal parameters in the local singularity analysis. The iterative approach will be more practical for large dataset. The case study indicated the iterative approach has the quality of multi-scale self-adaptive to obtain the optimal results.

REFERENCES

1. Cheng, Q.: Mapping singularities with stream sediment geochemical data for prediction of undiscovered mineral deposits in Gejiu, Yunnan Prov., China. *Ore Geology Reviews*, 32, 314–324 (2007)
2. Cheng Q.: Multifractality and spatial statistics. *Computers & Geosciences*, 25, 949–961 (1999)
3. Cheng Q.: A new model for incorporating spatial association and singularity in interpolation of exploratory data. In: Leuangthong D. and Deutsch C.V. (Eds.): *Geostatistics Banff 2004*. Dordrecht, the Netherlands, Springer, pp. 1017–1025 (2005)
4. Cheng, Q.: Modeling local scaling properties for multiscale mapping. *Vadose Zone Journal*, 7, 525–532 (2008)
5. Chen, Z.J., Cheng, Q.M., Xie, S.Y. and Chen, J.G.: A novel iterative approach for mapping local singularities from geochemical data. *Nonlin. Processes Geophys.*, 14, 317–324 (2007)
6. Crow, F. C.: Summed-Area Tables for Texture Mapping, in *SIGGRAPH '84: Proceedings of the 11th Annual Conference on Computer Graphics and Interactive Techniques*, 207–212 (1984)
7. Viola, P. and Jones, M.: Robust Real-Time Object Detection. *International Journal of Computer Vision*, 57(2), 137–154 (2002)
8. Phan, T., Larson, E., Sohoni, S. and Chandler, D.: Performance-analysis-based acceleration of image quality assessment. *IEEE Southwest Symposium on Image Analysis and Interpretation* (2012)

Chapter 6

Application of a Coherent Multi-Dimensional Technique to the Central Part of the Mexican Volcanic Belt

Srendra P. Verma

Abstract A combination of logratio transformation (additive logratio) and linear discriminant analysis (LDA) is a powerful experimental data-handling coherent multi-dimensional probability-based statistical technique, which is superior to the use of conventional bi-variate or ternary diagrams. Application of this procedure is illustrated with three subsets of compositional data for 2270 igneous rock samples from the central part of the Mexican Volcanic Belt (MVB). A combination of isometric logratio transformation and LDA will be used in future to test these and other sub-compositions on an updated worldwide compilation of geochemical data, which will enable us to achieve newer sets of more versatile, efficient, and coherent diagrams and related probability estimates.

Keywords Log-Ratio Transformations • Geochemistry • Tectonic Setting • Petrogenesis • Mexico

6.1 INTRODUCTION

Recently (2006-2013), natural logarithm-ratios of three sets of sub-compositions of igneous rocks from different tectonic settings have been used in conjunction with linear discriminant analysis (LDA) to arrive at 50 new multi-dimensional discrimination diagrams for all kinds of magmas ([1] and references therein). Although the traditional additive logratio (alr) transformation of Aitchison [2], instead of the more recent and mathematically more appropriate isometric logratio (ilr) transformation of Egozcue et al. [3], was used, LDA renders, as expected, identical discriminant functions DF1-DF2. These 50 diagrams were grouped in three sets of five diagrams each for basic and ultrabasic rocks [4-6], three sets for intermediate rocks [7] and four sets for acid rocks [1, 8]. The conventional approach of using compositional variables

S.P. Verma (✉)

Departamento de Sistemas Energéticos, Instituto de Energías Renovables, Universidad Nacional Autónoma de México, Priv. Xochicalco s/no., Col. Centro, Apartado Postal 34, Temixco, Mor., Mexico
e-mail: spv@ier.unam.mx

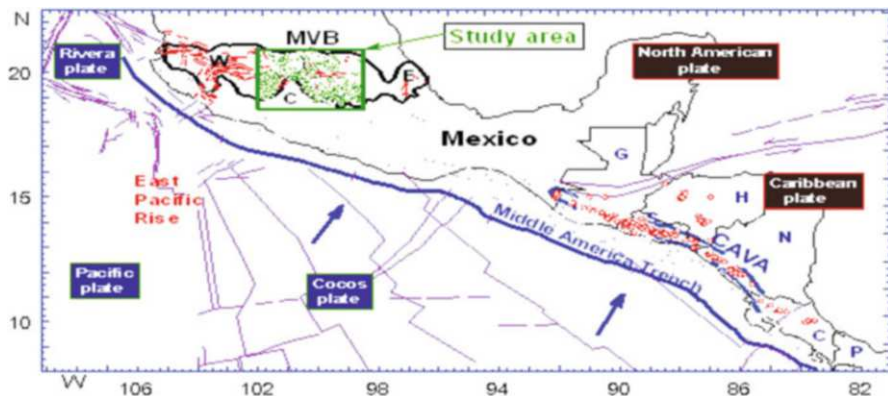


Fig. 6.1 Schematic location of samples (open circles) in the Mexican Volcanic Belt (MVB) and Central American Volcanic Arc (CAVA); the abbreviations are: W—western; C—central; E—eastern; G—Guatemala; S—El Salvador; H—Honduras; N—Nicaragua; C—Costa Rica; and P—Panama.

in bi-variate or ternary diagrams has already been shown to perform less well [8, 9]. A compilation of geochemical data for 2270 igneous rock samples from the central (C) part of the Mexican Volcanic Belt (MVB—an approximately east-west Miocene to Recent, ~1000 km long volcanic province; Fig. 6.1) is used to illustrate an application of these statistically coherent tectonomagmatic discrimination diagrams. Their good functioning is also confirmed from CAVA samples (Fig. 6.1).

6.2 EQUATIONS AND PROBABILITY ESTIMATES

One hundred DF1-DF2 equations for three sub-compositions of 50 diagrams were listed in the respective papers [1, 4–8]. These sub-compositions consist of: (1) all 11 major-elements or oxides; (2) selected major and trace elements; and (3) selected trace elements. The probability-calculations are the same as those reported earlier [1, 6–8]. As an example, two equations for the first diagram (IAB-CRB-OIB-MORB) of [4], based on adjusted major-element logratios, are

$$\begin{aligned}
 DFI_{(IAB-CRB-OIB-MORB)m2} = & -4.676 \times \ln(TiO_2/SiO_2) + 2.5330 + \ln(Al_2O_3/SiO_2) \\
 & -0.388 \times \ln(Fe_2O_3/SiO_2) + 3.969 \times \ln(FeO/SiO_2) + 0.898 \times \ln(MnO/SiO_2) \\
 & -0.583 \times \ln(MgO/SiO_2) - 0.290 \times \ln(CaO/SiO_2) - 0.270 \times \ln(Na_2O/SiO_2) \\
 & + 1.081 \times \ln(K_2O/SiO_2) + 0.184 \times \ln(P_2O_5/SiO_2) + 1.544
 \end{aligned}
 \tag{1}$$

Table 6.1 Results for basic and ultrabasic magmas from the central part of the MVB [4-6]

Fig. [ref.]	Samples (%)	Predicted tectonic affinity and number of discriminated samples (%)				
		IAB	CRB+OIB	CRB	OIB	MORB
[4]	585 (100)	71 (12)	---	408 (70)	26 (4)	80 (14)
[5]	110 (100)	0 (0)	20 (---)	79 (72)	16 (14)	15 (14)
[6]	370 (100)	49 (13)	40 (---)	155 (42)	68 (18)	98 (27)

Table 6.2 Results for intermediate [7] and acid [8, 1] magmas from the C-MVB

Samples	Number of discriminated samples {Total probability values} [% probability]				
	IA+CA	IA	CA	CR+OI	Col
[7] (1) 7000	309 {210.15} [---]	345 {226.92} [5.1%]	2041 {1395.40} [31.4%]	1095 {779.17} [15.6%]	3210 {2401.38} [47.9%]
[7] (2) 3820	128 {83.31} [---]	206 {121.54} [5.2%]	760 {485.12} [20.9%]	989 {732.28} [27.8%]	1737 {1215.66} [46.1%]
[7] (3) 1195	54 {32.54} [---]	43 {25.40} [3.4%]	404 {266.74} [35.4%]	255 {185.81} [22.2%]	439 {326.35} [39.0%]
[8] (1) 3780	597 {548.64} [---]	1384 {1054.93} [44.4%]	1093 {876.54} [36.9%]	205 {150.93} [4.9%]	501 {420.40} [13.8%]
[1] (1) 3780	591 {537.45} [---]	441 {303.89} [12.2%]	1815 {1643.58} [65.9%]	501 {375.28} [11.8%]	432 {321.26} [10.1%]
[1] (2) 2090	318 {242.94} [---]	114 {65.68} [5.4%]	992 {777.06} [64.6%]	231 {185.88} [12.0%]	435 {278.53} [18.0%]
[1] (3) 915	166 {139.46} [---]	39 {25.91} [4.4%]	489 {436.70} [73.5%]	59 {50.85} [6.6%]	162 {119.90} [15.5%]

$$\begin{aligned}
DF2_{(IAB-CRB-OIB-MORB)m2} = & 0.675 \times \ln(TiO_2/SiO_2) + 4.590 \times \ln(Al_2O_3/SiO_2) \\
& + 2.090 \times \ln(Fe_2O_3/SiO_2) + 0.851 \times \ln(FeO/SiO_2) - 0.433 \times \ln(MnO/SiO_2) \\
& + 1.483 \times \ln(MgO/SiO_2) - 2.363 \times \ln(CaO/SiO_2) - 1.656 \times \ln(Na_2O/SiO_2) \\
& - 0.676 \times \ln(K_2O/SiO_2) + 0.413 \times \ln(P_2O_5/SiO_2) + 13.164.
\end{aligned}
\tag{2}$$

6.3 RESULTS AND DISCUSSION

After ascertaining the magma types as basic or ultrabasic, intermediate, and acid varieties, the appropriate tectonomagmatic discrimination diagrams were applied and respective probabilities were calculated. The basic rocks from the C-MVB clearly indicate a continental rift setting (CRB; Table 6.1), whereas the acid rocks are more consistent with an arc or a transitional arc to collision setting (Table 6.2). The intermediate rocks indicate a transitional arc to collision setting. The

discrimination diagrams should be used in conjunction with the evaluation of petrogenetic processes. The origin of these different C-MVB rock varieties cannot be linked through simple magmatic processes; the strongest argument comes from the significant differences among Sr, Nd, and Pb isotopic ratios.

These isotopic data indicate that the basic and acid rocks from the C-MVB originated in the mantle and continental crust, respectively, whereas the intermediate rocks likely represent a hybrid origin of mantle and crust. Application of these diagrams to rocks from the Central American Volcanic Arc (CAVA; Fig. 6.1) consistently shows an arc setting for all three magma types, confirming thus their good functioning for an expected arc setting. The origin of CAVA rocks can be related to each other by simple fractionation processes because the radiogenic isotope ratios (the most important geochemical constraints) do not show any statistically significant differences among them. Finally, it is clear that in future the ilr transformation technique [3] should be used with LDA to test these and other sub-compositions in multivariate discordant outlier-free transformed geochemical data, which is likely to provide more versatile, efficient, and coherent diagrams and related probability estimates.

ACKNOWLEDGEMENTS This work was supported by DGAPA-PAPIIT grant IN104813.

REFERENCES

1. Verma, S.P., Pandarinath, K., Verma, S.K. and Agrawal, S.: Fifteen new discriminant-function-based multi-dimensional robust diagrams for acid rocks and their application to Precambrian rocks. *Lithos*, 168-169, 113–123 (2013)
2. Aitchison, J.: The statistical analysis of compositional data. Chapman and Hall, London (1986)
3. Egozcue, J.J., Pawłowsky-Glahn, V., Mateu-Figueras, G. and Barceló-Vidal, C.: Isometric logratio transformations for compositional data analysis. *Math. Geol.*, 35, 279–300 (2003)
4. Verma, S.P., Guevara, M. and Agrawal, S.: Discriminating four tectonic settings: five new geochemical diagrams for basic and ultrabasic volcanic rocks based on log-ratio transformation of major-element data. *J. Earth Sys. Sci.*, 115, 485–528 (2006)
5. Agrawal, S., Guevara, M. and Verma, S.P.: Tectonic discrimination of basic and ultrabasic rocks through log-transformed ratios of immobile trace elements. *Int. Geol. Rev.*, 50, 1057–1079 (2008)
6. Verma, S.P. and Agrawal, S.: New tectonic discrimination diagrams for basic and ultrabasic volcanic rocks through log-transformed ratios of high field strength elements and implications for petrogenetic processes. *Rev. Mex. Cienc. Geol.*, 28, 24–44 (2011)
7. Verma, S.P. and Verma, S.K.: First 15 probability-based multi-dimensional discrimination diagrams for intermediate magmas and their robustness against post-emplacement compositional changes and petrogenetic processes. *Turk. J. Earth Sci.*, 22, 931–995 (2013)
8. Verma, S.K., Pandarinath, K. and Verma, S.P.: Statistical evaluation of tectonomagmatic discrimination diagrams for granitic rocks and proposal of new discriminant-function-based multi-dimensional diagrams for acid rocks. *Int. Geol. Rev.*, 54, 325–347 (2012)
9. Verma, S.P.: Statistical evaluation of bivariate, ternary and discriminant function tectonomagmatic discrimination diagrams. *Turk. J. Earth Sci.*, 19, 185–238 (2010)

Chapter 7

Multivariate Grid-Free Geostatistical Simulation of Natural Phenomena

Y. Zagayevskiy and C.V. Deutsch

Abstract Conventional geostatistical simulation techniques require an upfront definition of the simulation locations – normally a regular grid. If simulation is performed with different simulation locations, previously simulated values may not be reproduced. A two-step grid-free simulation (GFS) approach is proposed to represent a realization as a function of the simulation location coordinates. Unconditional simulations are generated with turning bands, where 1D line simulations are presented as a function of the simulation location by Fourier series simulation (FSS) technique, and later conditioned to the data by dual kriging. The FSS is framed after the linear model of regionalization (LMR). The independent random factors of the LMR and their coefficients are derived by decomposing the covariance function of the line process into a sum of weighted covariances of random factors in cosine form, where weights are Fourier series coefficients of target 1D covariance function. Multivariate modeling is achieved with the linear model of coregionalization. The GFS implementation is demonstrated with a case study.

Keywords Grid-Free Simulation • Fourier Series • Turning Bands • LMC

7.1 INTRODUCTION

Natural phenomena are usually modeled by geostatistical techniques on regular grids [1]. Sometimes, the simulation locations have to be distributed irregularly, or additional simulation has to be performed at new locations. It is not guaranteed that previously simulated values are reproduced at new locations by conventional techniques. Spectral and fractal simulations based on the fast Fourier transformation require regular simulation grid [2]. Turning bands (TB) can represent a 2D/3D realization of the system as a function of the simulation location as long as corresponding 1D-line simulations can be continuously resolved [3]. The two-step grid-free simulation (GFS) approach is proposed to represent the simulated variable as a spatial continuous function.

Y. Zagayevskiy (✉) • C.V. Deutsch

Centre for Computational Geostatistics, University of Alberta, Edmonton, Canada T6G 2W2

e-mail: zagayevs@ualberta.ca

7.2 THEORETICAL BACKGROUND

Consider a natural phenomenon, properties of which form a multivariate system Y characterized by K spatially distributed random functions $Y = \{Y_k, k = 1, \dots, K\}$. It is assumed that relationship between these random functions can be described by a multi-Gaussian distribution. The value of any Y_k is defined in the space through the coordinate u , and is referred as a random variable $Y_k(u)$. The GFS is proposed to model the system Y . It is a two-step conditional simulation algorithm: unconditional realizations are conditioned to the data by dual kriging as presented in Eq. (7.1) [3]. The dual form is chosen (Eqs. 7.2, 7.3) to reduce computational time by eliminating recurrent matrix multiplication.

$$Y_i^s(u) = Y_i^{su}(u) + \left(Y^*(u) - Y_i^{*|su}(u) \right) \quad (7.1)$$

$$Y^*(u) - Y_i^{*|su}(u) = [c_Y(u)]^T \cdot \nu_i \quad (7.2)$$

$$C_Y \cdot \nu_i = Y^d(u_d) - Y_i^{su}(u_d) \quad (7.3)$$

where i is the realization index, $i = 1, \dots, N_R$; N_R is the total number of realizations; $Y_i^s(u)$ and $Y_i^{su}(u)$ are the $K \times 1$ column vectors of i th realization of conditional simulation and unconditional simulation at location u , respectively; $Y^*(u)$ and $Y_i^{*|su}(u)$ are the $K \times 1$ column vectors of kriging estimates at location u conditional to data values Y^d and i th realization of unconditional simulation at data locations u_d , respectively; C_Y is the $N_D \times N_D$ data covariance matrix; $c_Y(u)$ is the $N_D \times 1$ column covariance vector between data and simulation locations; N_D is the total number of the data; and ν_i is the dual kriging weights for i th realization.

The unconditional realizations are simulated by using the linear model of coregionalization (LMC). It dictates how a multivariate system Y is represented by weighted independent random factors $X = \{X_p, p = 1, \dots, P\}$, each having a unique covariance structure [2]. The nugget effect, $p = 0$, is handled separately.

$$Y_i^{su}(u) = \sum_{p=1}^P A_p \cdot X_{p,i}(u) \quad (7.4)$$

$$X_{p,k,i}(u) = \frac{1}{\sqrt{N_L}} \sum_{l=1}^L X_{p,k,l,i}^{(D)}(u \cdot \hat{u}_l) \quad (7.5)$$

$$B_p = A_p \cdot [A_p]^T, \forall p \quad (7.6)$$

$$C_Y(h) = \sum_{p=1}^P B_p \cdot C_{X_p}(h) \quad (7.7)$$

where $X_{p,i}(u)$ is the i th realization of p th random factor $K \times 1$ column vector at location u , it is simulated by means of TB as shown in Eq. (7.5); $X_{p,k,l,i}^{(1D)}(u \cdot \hat{u}_l)$ is the simulated 1D random process on l th line at projected location $u \cdot \hat{u}_l$, relationship between $X_{p,k,i}$ and $X_{p,k,l,i}^{(1D)}$ can be found in [4]; \hat{u}_l is the unit vector of l th line's direction; N_L is the total number of simulation lines; A_p is the p th $K \times K$ lower triangular matrix with LMC coefficients, which are derived by LU decomposition of the p th covariance contribution matrix B_p ; B_p is related to target covariance $K \times K$ matrix $C_Y(h)$ of the simulated system as shown in Eq. (7.7). The 1D line process $X_{p,k,l,i}^{(1D)}$ will be generated with the Fourier series simulation (FSS). Assuming a linear model of regionalization (LMR) with infinitely large number of random factors $q \in (-\infty, \infty)$, which is similar to LMC with $K = 1$, the $X_{p,k,l,i}^{(1D)}$ can be presented as in Eq. (7.8), the covariance function of which is related to independent random factors $X_{p,k,l,q,i}^{(F)}$ as in Eq. (7.9). Seeing Eq. (7.9) as the Fourier series decomposition of symmetric even function, covariance contribution coefficients b_q and covariance function $C_{X_{p,k,l,q,i}^{(F)}}(h)$ will have form as in Eqs. (7.10) and (7.11) [5]. It turns out that $X_{p,k,l,q,i}^{(F)}$ in Eq. (7.12) has cosine covariance function as in Eq. (7.11). Simulation is performed by randomly drawing phase values $\phi_{p,k,l,q,i}$ between 0 and 2π . The relationship between LMR coefficients a_q and covariance contribution coefficients b_q is shown in Eq. (7.13). In practice, only limited number of a_q is required $q \in (-Q, Q)$.

$$X_{p,k,l,i}^{(1D)}(u \cdot \hat{u}_l) = \sum_{q=-\infty}^{\infty} a_q \cdot X_{p,k,l,q,i}^{(F)}(u \cdot \hat{u}_l) \quad (7.8)$$

$$C_{X_{p,k,l,i}^{(1D)}}(h) = \sum_{q=-\infty}^{\infty} b_q \cdot C_{X_{p,k,l,q,i}^{(F)}}(h) \quad (7.9)$$

$$b_q = \frac{1}{2 \cdot S} \int_{-S}^S C_{X_{p,k,l,i}^{(1D)}}(h) \cdot \cos(\pi \cdot q \cdot h/S) \cdot dh \quad (7.10)$$

$$C_{X_{p,k,l,q,i}^{(F)}}(h) = \cos(\pi \cdot q \cdot h/S) \quad (7.11)$$

$$X_{p,k,l,q,i}^{(F)}(u \cdot \hat{u}_l) = \sqrt{2} \cdot \cos(\pi \cdot q \cdot (u \cdot \hat{u}_l)/S + \phi_{p,k,l,q,i}), \phi_{p,k,l,q,i} \in [0, 2\pi] \quad (7.12)$$

$$a_q = \sqrt{b_q} \quad (7.13)$$

where S is the covariance periodic domain, it should be larger than simulation domain and the longest variogram range to avoid periodicity in realizations.

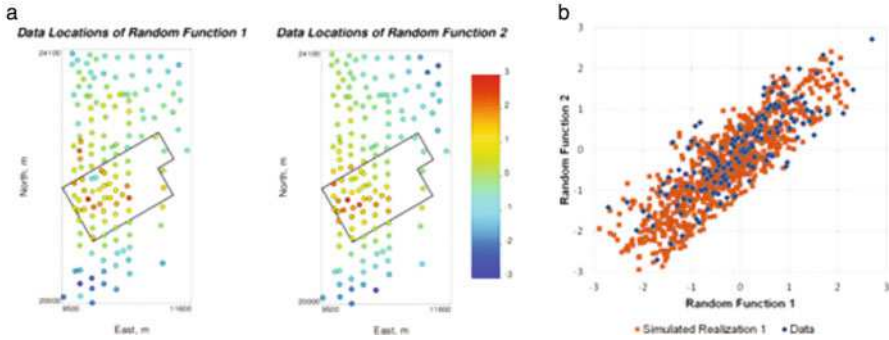


Fig. 7.1 (a) Data location maps of random functions 1 and 2. (b) Scatter plots between data values (black rhombs) and simulated realizations (brown squares)

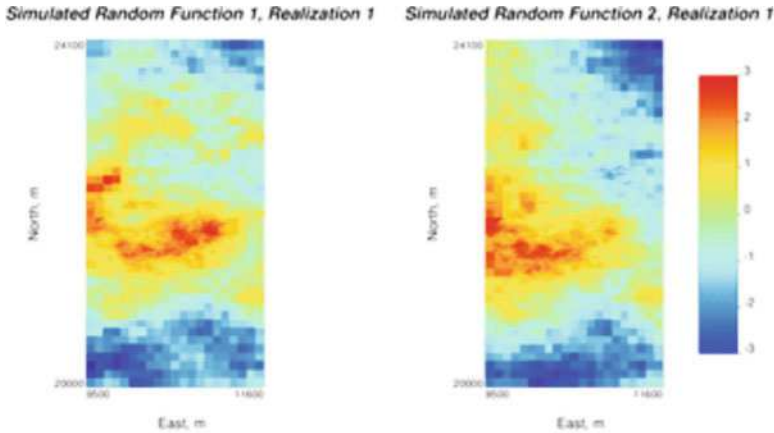


Fig. 7.2 Maps of simulated realizations of random functions 1 and 2 at varying resolution

7.3 CASE STUDY

One hundred realizations of a bivariate system are simulated in normal space on a 2D grid of varying resolution with anisotropic spherical variogram model conditional to $N_D = 2 \cdot 148 = 296$ data shown in Fig. 7.1. The grid resolution is $10 \text{ m} \times 10 \text{ m}$ within the polygon and $100 \text{ m} \times 100 \text{ m}$ outside. Two random functions are distributed normally with 0.82 correlation coefficient, and their simulated distribution matches the data (Fig. 7.1). First realizations of the simulated system are shown in Fig. 7.2. The variogram model is reproduced at shorter ranges and experimental variograms are reproduced at longer ranges (Fig. 7.3).

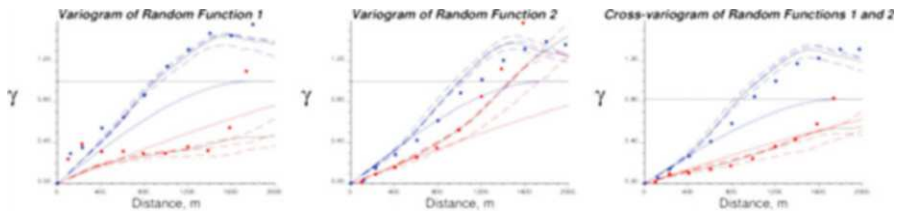


Fig. 7.3 Experimental variogram (dots), variograms from three realizations (dashed lines), average of 100 realization variograms (black lines), and variogram model (solid lines) of random functions 1 and 2 for major $N90^\circ$ (red) and minor $N0^\circ$ (blue) continuity directions

7.4 CONCLUSIONS

The GFS algorithm is a novel geostatistical simulation algorithm that allows presenting conditional simulation of the multivariate system as a function of the simulation location coordinates, data values, and imposed spatial structure.

REFERENCES

1. Deutsch, C.V. and Journel, A.G.: *GSLIB: Geostatistical Software Library and User's Guide*. 2nd ed. Oxford University Press, New York (1998)
2. Chiles, J.-P. and Delfiner, P.: *Geostatistics – Modeling Spatial Uncertainty*. Wiley, New York (1999)
3. Journel, A.G. and Huijbregts, C.J.: *Mining Geostatistics*. Academic Press, New York (1978)
4. Journel, A.G.: Geostatistics for Conditional Simulation of Ore Bodies. *Econ. Geol.*, 69, 673–687 (1974)
5. Bracewell, R.N.: *The Fourier Transform and Its Applications*. 3rd ed. McGraw Hill, New York (2000)

Chapter 8

Semianalytical Solutions for Multispecies Transport Coupled with a Sequential First-Order Reaction Network Using GITT Techniques

Heejun Suk, Byung-Gon Chae, and Junghae Choi

Abstract The paper presents a semianalytical method to solve the multispecies reactive solute-transport equation coupled with a sequential first-order reaction network under spatially or temporally varying flow velocities and dispersion coefficients. This method employs the generalized integral transform technique (GITT) and general linear transformation method by Clement [2001] to transform the set of coupled multispecies reactive transport equations into a set of independent uncoupled equations and to solve these independent equations for spatially or temporally varying flow velocities and dispersion coefficients, as well for temporally varying inlet concentration. The proposed semianalytical solution is compared against previously published analytical solutions of Srinivasan and Clement [2008] and van Genuchten [1985]. We show a practical implementation of the solution to an actual field, single-well push-pull test (PPT) example designed to obtain the concentration distribution of reactants consumed and products formed at the end of the injection phase.

Keywords Semianalytical Solution • First-Order Reaction • Multispecies Transport • Heterogeneous Medium • Transient Condition

8.1 INTRODUCTION

Many analytical or semianalytical solutions have been proposed of the multispecies advection-dispersion transport equations coupled with sequential first-order kinetics [1,5,7,8]. However, most analytical solutions are limited to steady-state flow conditions involving constant velocities and dispersion coefficients. Therefore, the objective of this study is to present solutions of the multispecies transport equations coupled with

H. Suk (✉) • B.-G. Chae • J. Choi
Groundwater Department, Korea Institute of Geoscience and Mineral Resources,
Daejeon, South Korea
e-mail: sxh60@kigam.re.kr

sequential first-order reaction networks assuming spatially or temporally varying flow velocities and dispersion coefficients, as well as for temporally varying boundary conditions. In this study, a combination of the general linear transformation methods by Clement [1] and GITT [2] is used to solve the multispecies transport equations for the above conditions.

8.2 PROBLEM FORMULATION AND INTEGRAL TRANSFORM SOLUTION

The general one-dimensional mass balance equations for a saturated aquifer, which predict the fate and transport of multispecies coupled with sequential first-order reactions, can be written as

$$R(x)\theta(x)\frac{\partial C_i}{\partial t} + \frac{\partial}{\partial x}[\theta(x)\nu(x,t)C_i] - \frac{\partial}{\partial x}\left[\theta(x)D(x,t)\frac{\partial C_i}{\partial x}\right] = y_i k_{i-1}\theta(x)C_{i-1} - k_i\theta(x)C_i \quad \forall i = 2, 3, \dots, N. \quad (8.1)$$

where $\theta(x)$ is the porosity; $\nu(x,t)$ is the seepage velocity [$L T^{-1}$]; $D(x,t) = \alpha_L(x)n(x,t)$; $D(x,t)$ is the dispersion coefficient [$L^2 T^{-1}$]; $\alpha_L(x)$ is the longitudinal dispersivity [L]; $R(x) = 1 + \frac{\rho_b k_d}{\theta(x)}$; $R(x)$ is the retardation factor; ρ_b is the porous medium bulk density [$M L^{-3}$]; k_d is an empirical distribution coefficient [$M^{-1} L^3$]; C_i is the concentration of species i [$M L^{-3}$]; y_i is the stoichiometric yield coefficient for the reaction of species $i-1$ to produce species i [$M M^{-1}$]; k_i is the first-order decay-rate constant of species i [T^{-1}]; L is the length of the porous medium [L]; and N is the total number of species. In equation (8.1), it is assumed that retardation factors of all species are the same, while $\nu(x,t)$ and $D(x,t)$ are assumed to be arbitrary functions of space x and time t . The semianalytical solution is derived according to linear system theory [3].

$$T^i(t) = \exp(-A^{-1}B^i t) T^i(0) + \int_0^t \exp[-A^{-1}B^i(t-\tau)] A^{-1}G^i(\tau) d\tau \quad (8.2)$$

$\forall i = 1, 2, \dots, N$

where

$$A_{nr} = \int_0^L \frac{\varphi_n(x)R(x)\theta(x)\varphi_r(x)}{N_n^{1/2}N_r^{1/2}} dx \quad (8.3)$$

$$B_{nr}^i(t) = \frac{1}{N_n^{1/2} N_r^{1/2}} \left[\varphi_n(L) \theta(L) v(L, t) \varphi_r(L) - \int_0^L \frac{d\varphi_n(x)}{dx} \theta(x) v(x, t) \varphi_r(x) dx \right. \\ \left. \int_0^L \frac{d\varphi_n(x)}{dx} \theta(x) D(x, t) \frac{d\varphi_r(x)}{dx} dx \right] + \frac{1}{N_n^{1/2} N_r^{1/2}} \left[k_i \int_0^L \varphi_n(x) \theta(x) \varphi_r(x) dx \right] \quad (8.4)$$

$$G_n^i(t) = -\frac{1}{N_n^{1/2}} \frac{dg_i(t)}{dt} \int_0^L \varphi_n(x) R(x) \theta(x) dx - \frac{1}{N_n^{1/2}} k_i g_i(t) \int_0^L \varphi_n(x) \theta(x) dx \\ - \frac{1}{N_n^{1/2}} [\varphi_n(L) \theta(L) v(L, t) - \varphi_n(0) \theta(0) v(0, t)] g_i(t) + \frac{1}{N_n^{1/2}} g_i(t) \int_0^L \frac{d\varphi_n(x)}{dx} \theta(x) v(x, t) dx \quad (8.5)$$

in which N_n and $\varphi_n(x)$ are the n th Norm and eigen-function, the matrices **A** and **B**, and vector **G** can be changed depending on the flow condition (steady state or transient flow) and aquifer heterogeneity (homogeneous or heterogeneous porous medium). Once the set of coupled first-order differential equations for $T_r^i(t)$ is solved, the inverse formula in GITT can be calculated, after which the transformed independent and uncoupled solutions are calculated [2]. Finally, the substitution process [1] is employed to obtain $C_i(x, t)$. While Eq. (8.2) in general has to be solved numerically, in some cases an analytical solution is possible.

8.3 VERIFICATIONS

To show a practical application of the proposed semianalytical solution to a real field problem, a single-well push-pull test (PPT) example was designed. PPTs have been employed to quantify various microbially mediated processes in the subsurface [4]. In this example, the proposed solutions and 2DFATMIC [9] are used only during the injection phase to obtain the concentration distributions of the reactants and products, leading to quantitative information on in-situ microbial processes. Injection rates and period were assumed to be 30 m³/day and 5 days, respectively, to obtain a steady state flow field in the homogeneous aquifer. Velocities around the injection well were obtained as following [6].

$$v(x) = \frac{Q}{2\pi B \theta x} \quad (8.6)$$

where Q is the injection or pumping rate depending upon injection or withdrawal phase, B is the aquifer thickness, and x is the distance from the well. As shown by Eq. (8.6), the velocity around the well is spatially varying in a steady state

Table 8.1 Transport and reaction parameters used in single-well push-pull test example

Parameters	Values
Injection rate	30.0 m d ⁻³
Aquifer thickness	10.0 m
Porosity	0.1
Longitudinal dispersivity	0.1 m
Retardation factor	1.0
k_1, k_2, k_3, k_4	0.075 d ⁻¹ , 0.05 d ⁻¹ , 0.02 d ⁻¹ , 0.01 d ⁻¹
Yield y (all of them)	1.0
Initial cond. (all of them)	0.0 mol m ⁻³
Inlet concentration on flux bound. – species 1	1.0 mol m ⁻³
Inlet concentration on flux bound. – species $i = 2-4$	0.0 mol m ⁻³
Porosity for Clay	0.2
Domain Length	10 m
Simulation time	5.0 d

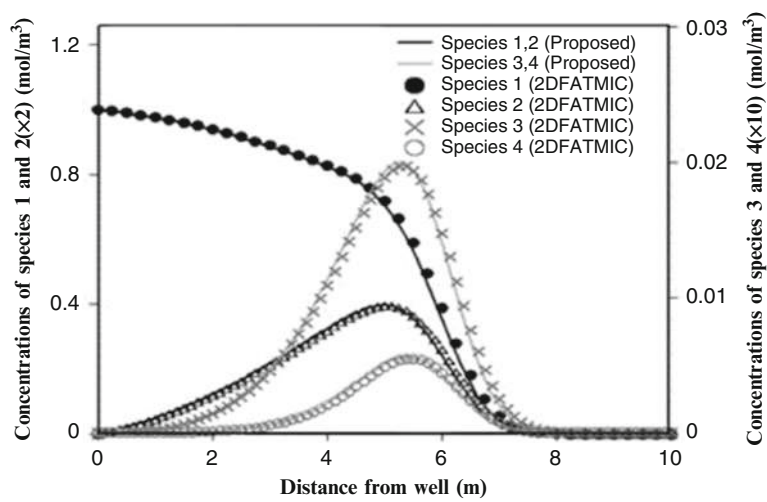


Fig. 8.1 Comparison of the proposed semianalytical solution against the numerical solution obtained with 2DFATMIC (concentrations of species 2 are magnified twice and those of species 4 ten times to visualize more clearly the two solutions)

condition. Since the velocity at the well position ($x=0$) is singular, the left boundary is assigned to a location very close to the well. Other parameters used for the simulation are listed in Table 8.1. Figure 8.1 shows that the proposed semianalytical solution and the numerical results of 2DFATMIC matched very well.

8.4 RESULTS AND DISCUSSION

This study presents a semianalytical solution of the multispecies transport equation coupled with a sequential first-order reaction network assuming spatially or temporally varying flow velocities and dispersion coefficients. One major new feature of the proposed semianalytical method is that it can solve complex reactive transport problems for transient or heterogeneous conditions involving arbitrary temporal or spatial functions of the velocity and the dispersion coefficient, time-dependent temporal concentrations at the inlet boundary, and arbitrary initial concentration distributions of the species in the decay chain. Despite of its advantages, the method cannot be used for multispecies transport problems with different retardation factors. Extension to multi-dimensional multispecies transport problem is relatively straight-forward using the general linear transformation and GITT methods.

ACKNOWLEDGEMENTS This work was supported by the Radioactive Waste Management of the Korea Institute of Energy Technology Evaluation and Planning (KETEP) grant funded by the Korea government Ministry of Knowledge Economy (2011 T100200152).

REFERENCES

1. Clement, T.P.: Generalized solution to multispecies transport equations coupled with a first-order reaction network. *Water Resour. Res.*, 37, 157–163, doi:[10.1029/2000WR900239](https://doi.org/10.1029/2000WR900239) (2001)
2. Liu, C., Szecsody, J.E., Zachara, J.M. and Ball, W.P.: Use of the generalized integral transform method for solving equations of solute transport in porous media. *Adv. Water Resour.*, 23(5), 483–492, doi:[10.1016/S0309-1708\(99\)00048-2](https://doi.org/10.1016/S0309-1708(99)00048-2) (2000)
3. Rugh, W.J.: *Linear system theory*. Prentice-Hall, Englewood Cliffs, N.J. (1996)
4. Snodgrass, M.F. and Kitanidis, P.K.: A method to infer in situ reaction rates from push-pull experiments. *Ground Water*, 36(4), 645–650, DOI: [10.1111/j.1745-6584.1998.tb02839.x](https://doi.org/10.1111/j.1745-6584.1998.tb02839.x) (1998)
5. Srinivasan, V. and Clement, T.P.: Analytical solutions for sequentially coupled one-dimensional reactive transport problems – Part II: Special cases. *Adv. Water Resour.*, 31, 219–232, doi:[10.1016/j.advwatres.2007.08.001](https://doi.org/10.1016/j.advwatres.2007.08.001) (2008)
6. Strack, O.D.L.: *Groundwater Mechanics*, Prentice-Hall, Englewood Cliffs, N.J. (1989)
7. Sun, Y., Petersen, J.N. and Clement, T.P.: Analytical solutions for multiple species reactive transport in multiple dimensions. *J. Contam. Hydrol.*, 35, 429–440, doi:[10.1016/S0169-7722\(98\)00105-3](https://doi.org/10.1016/S0169-7722(98)00105-3) (1999)
8. Van Genuchten, M.T.: Convective-dispersive transport of solutes involved in sequential 1st order decay reactions. *Computers Geosci.*, 11, 129–147, doi:[10.1016/0098-3004\(85\)90003-2](https://doi.org/10.1016/0098-3004(85)90003-2) (1985)
9. Yeh, G.T. and Cheng, J.R.: 2DFATMIC: User's manual of a two-dimensional subsurface flow, fate and transport of microbes and chemical model version 1.0., EPA/600/R-97/052, U.S. Environmental Protection Agency, Washington, D.C. (1997)

Chapter 9

Compositional Statistical Analysis of Inter-Laboratory Comparisons of Geothermal Water

Mahendra P. Verma

Abstract Statistical evaluation of the results of inter-laboratory comparisons (1976-2012) suggests an overall measurement uncertainty of $\pm 13\%$ and serious problems in the measurements of total Si and HCO_3^- in geothermal waters. The reasons for the dispersion among the results of participating laboratories are: inappropriate analytical procedure, limited number of digits in the calibration equation and errors in the calculation procedure of individual laboratory.

Keywords Compositional Data Analysis • Inter-Laboratory Comparison • Water Chemistry • Total Si and Carbonic Species

9.1 INTRODUCTION

For statistical analysis of n-valued compositional data subject to the constant sum constraint, a (n-1) dimensional sample vector space is developed with log-ratio transformations [1-3]. In fluid compositional analyses the compositions of dissolved species in water are only measured; thus all the measured compositional parameters are independent and form the vector space. In 1976 Ellis [4] conducted the first worldwide inter-laboratory comparison of geothermal water chemistry and found high dispersion among the measured values for each parameter. Verma [5] compiled the results of inter-laboratory comparisons (1976-2012). The statistical evaluation of these results suggested an overall measurement uncertainty of $\pm 13\%$, and a serious problem in the measurements of total Si and HCO_3^- . This study presents the statistical evaluation of the results of the inter-laboratory comparisons to highlight the reasons of high dispersion in the determinations of total Si and carbonic species.

M.P. Verma (✉)

Geotermia, Instituto de Investigaciones Electricas, Reforma 113, Col. Palmira, Cuernavaca, Morelos 62490, Mexico

e-mail: Mahendra@iie.org.mx

9.2 INTER-LABORATORY COMPARISONS OF GEOTHERMAL WATER CHEMISTRY

To further investigate on the analytical data quality assurance for the measurements of total Si and carbonic species, Verma and coworkers [6-10] conducted the inter-laboratory comparisons for carbonic species in different types of waters.

9.2.1 Carbonic Species

Figure 9.1 presents a summary of the statistics of HCO_3^- concentration determinations in thirteen water samples, analyzed in each participating laboratory during the IAEA inter-laboratory comparison programs. Apparently, there is an improvement in the analytical quality for HCO_3^- with time (Fig. 9.1c). However, if we also include the concentration of carbonic species in the statistical analysis (i.e., a relation between HCO_3^- , RSD and time), the improvement in the data quality in the successive comparisons is not well defined. The volumetric acid-base titration is the only reliable method for the determination of carbonic species concentration in natural waters. It is classified in three methods: (1) *Hydrologist's method*, (2) *Geochemist's method*, and (3) *initial pH and total alkalinity method*. The high dispersion among the results reported by the individual laboratories was associated with the inappropriate analytical procedure, limited number of digits in the calibration equation, and errors in the calculation procedure of individual laboratories [10].

9.2.2 Total Si

Figure 9.2 shows the relation between laboratory number and total Si-concentration for (a) natural geothermal waters and (b) synthetic waters. The uncertainty has been reduced from $\pm 70\%$ to $\pm 10\%$ [9].

Despite the high scatter in the data, there is an improvement in the analytical data quality of Si-analysis with time (Fig. 9.3c). The synthetic samples were analyzed only in 2002 and 2012; so, it is difficult to define a trend for them. Additionally, the synthetic samples fall within the trend for the natural geothermal water samples. Thus it is difficult to predict if the analytical data quality is better for synthetic waters or not. All the three analytical techniques (i.e. CO, AAS, and ICP) are proved to be equally consistent and reliable for the determinations in natural geothermal waters [11]. Similarly, it is feasible to improve the analytical accuracy (i.e. trueness and/or precision) better than $\pm 5\%$, implementing the analytical and statistical procedure described by [11].

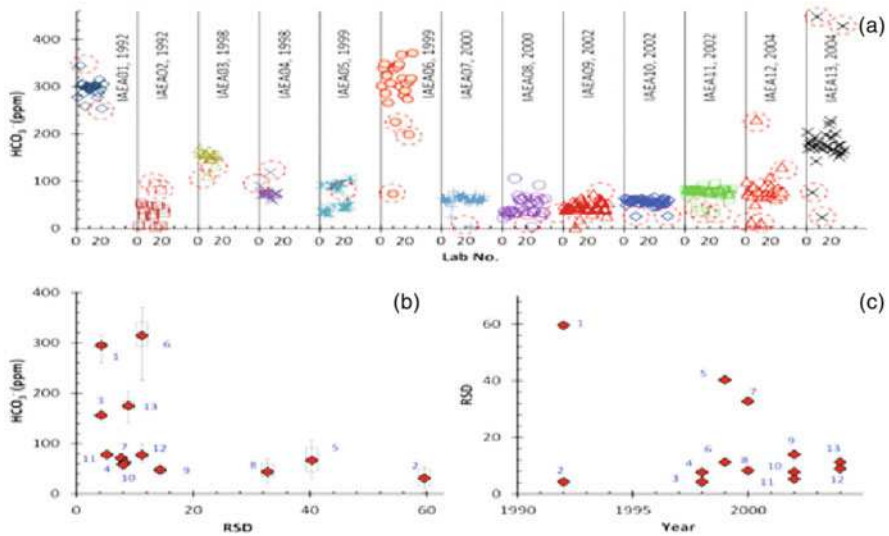


Fig. 9.1 Inter-laboratory comparisons of HCO_3^- in geothermal waters: (a) Behavior of individual laboratory data, (b) Whisker plot for HCO_3^- and RSD (% relative standard deviation) and (c) Time evolution of RSD. The outliers, marked with dashed circles, were not considered in the statistical data evaluation.

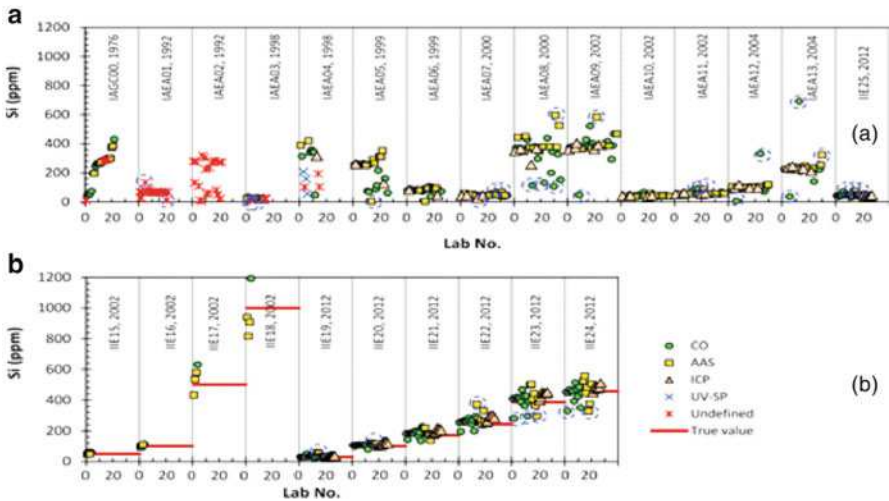


Fig. 9.2 Relations between laboratory number and total Si-concentration of inter-laboratory comparisons: (a) Natural geothermal water and (b) Synthetic waters prepared from commercial standards. The outliers are marked with dashed circles.

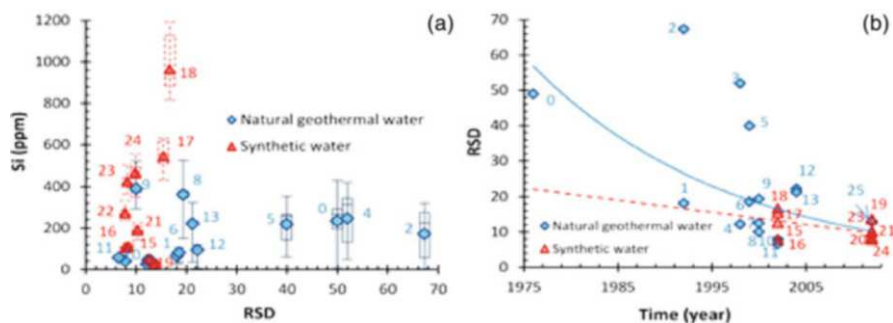


Fig. 9.3 (a) Whisker plot of Si-concentration of each sample and its relation with % relative standard deviation (RSD). (b) Evolution of RSD in the analytical values of total Si-concentration of individual laboratory of each sample with time. The trends for natural and synthetic waters are shown with solid and dashed curves, respectively.

9.3 CONCLUSIONS

The inter-laboratory comparisons of geothermal water chemistry have provided a framework to ensure high analytical data quality worldwide. Presently, the reasons of dispersion among the results of participating laboratories are: inappropriate analytical procedure, limited number of digits in the calibration equation and errors in the calculation procedure of individual laboratories. In the geochemical modeling of hydrothermal systems the analytical uncertainty propagation must be incorporated.

ACKNOWLEDGEMENTS This work was supported by the grant “FONDO SECTORIAL CONACYT-SENER SUSTENTABILIDAD ENERGÉTICA IIE-CEMIE-GEO-P14”.

REFERENCES

1. Aitchison, J.: The statistical analysis of compositional data. Chapman and Hall (1986)
2. Buccianti, A., Pawlowsky-Glahn, V.: New perspectives on water chemistry and compositional data analysis. *Math. Geol.*, 37, 703–727 (2005)
3. Pawlowsky-Glahn, V., Egozcue, J.J., Tolosana-Delgado, R.: Lecture notes on compositional data analysis. <http://www.sediment.uni-goettingen.de/staff/tolosana/extra/CoDa.pdf> (2007)
4. Ellis, A.J.: The IAGC inter-laboratory water analysis comparison programme. *Geochim. Cosmochim. Ac.*, 40, 1359–1374 (1976)
5. Verma, M.P.: IAEA Inter-laboratory Comparisons of Geothermal Water Chemistry: Critiques on Analytical Uncertainty and Accuracy, and Geothermal Reservoir Modeling. *J. Iberian Geol.*, 39, 57–72 (2013)
6. Verma, M.P.: A revised analytical method for HCO_3^- and CO_3^{2-} determinations in geothermal waters: an assessment of IAGC and IAEA interlaboratory comparisons. *Geostand. Geoanal. Res.*, 28, 391–409 (2004)

7. Verma, M.P.: Revised analytical methods for the determination of carbonic species in rain, ground and geothermal waters. *Proceedings*, WGC, Antalya, Turkey (2005)
8. Verma, M.P., Birkle, P., Sánchez, D.: Theoretical and Analytical Aspects of Carbonic Species Determination in Rain, Ground, Geothermal and Petroleum Waters. *Proceedings*, WGC, Congress, Bali, Indonesia (2010)
9. Verma, M.P., Izquierdo, G., Urbino, G.A., Gangloff, S., Garcia, R., Aparicio, A., Conte, T., Armienta, M.A., Sanchez, M., Gabriel, J.R.P., Fajanela, I.D., Renderos, R., Acha, C.B.A., Prasetyo, R., Grajales, I.C, Delgado, L.R., Opondo, K., Esparza, R.Z., Panama, L.A., Salazar, R.T., Lim, P.G. and Javino, F.: Inter-laboratory comparison of SiO₂ analysis for geothermal water chemistry. *Geothermics*, 44, 32–42 (2012)
10. Verma, M.P., Portugal, E., Gangloff, S., Armienta, M.A., Chandrasekharam, D., Sanchez, M., Renderos, R.E., Junaco, M., van Geldern, R.: Determination of carbonic species concentration in natural waters - Results from a worldwide proficiency test. *Geostand. Geoanal. Res.* (2014) in press
11. Verma, M.P., Izquierdo, G., Sangloff, S., Reyes-Delgado, L., Armienta, M.A., Sanchez, M., Garcia, R. and Turdiaman, D.: Proficiency testing statistics on Si-determinations in geothermal waters. *Geostand. Geoanal. Res.* (2014) submitted

Chapter 10

Fractal Characterization via Morphological Analysis

Raghvendra Sharma and B.S. Daya Sagar

Abstract In this paper, we provide an approach based on mathematical morphological operators to quantify the complexity of thematic information (map) or binary image object as a quantitative index that is scale invariant, but shape-dependant. We demonstrate the applicability of this approach on a binary Koch quadric fractal. We define a shape-size based fragmentation technique for both foreground and background of the considered deterministic fractal. Further, we utilize this technique to: a) quantify the roughness of binary fractal, b) explore possible relations between the results generated via this fragmentation technique and fractal dimension. This exercise was further extended to draw the results for a binary random Koch quadric fractal.

Keywords Fractal Dimension • Morphological Transformations • Fragmentation • Skull • Hull

10.1 INTRODUCTION

Data relevant to many natural phenomena and processes now have been available at multiple spatial and temporal scales. Numerous filtering, segmentation, and classification techniques are in place to precisely map the noise-free thematic information from such spatiotemporal data. Popular concepts from the theory of fractal geometry provide various tools to quantitatively characterize such thematic information. Fractal dimension computed through classical box counting method that quantifies roughness of an object is in use. Fractal dimension of an object or a collection of objects represented in the form of thematic maps provides scale invariant characteristics. Numerous approaches are available to quantify the spatial complexity of a phenomenon spread across spatial positions. The phenomenon which we refer here is a theme mapped from multi-valued spatial data. Such a theme, which is in noise-free form, depicts theme (foreground) and no-theme (background), in other words foreground in white and background in black shades. In the material that follows,

R. Sharma (✉) • B.S. Daya Sagar
Systems Science and Informatics Unit, Indian Statistical Institute, Bangalore, India
e-mail: raghvendra.sharma@gmail.com

the terms thematic information and binary image are used interchangeably and are denoted as X . The focus of this short-paper is to compute the spatial complexity of X . From the fields of fractal geometry [4], and mathematical morphology [1], several techniques have been proposed to compute the spatial complexity as quantitative indexes. Fractal geometry offers computation of fractal dimension, whereas mathematical morphology offers granulometric index. Fractal dimension is a scale invariant measure; whereas granulometric index is scale invariant but shape-dependent. In this paper, we adapted multi-scale morphological openings and closings [1–3] based fragmentation to compute complexity or roughness as scale invariant but shape-dependent quantitative index. The organization of this paper is as follows: Basic morphological transformations followed by their multi-scale versions are explained in section 10.2. The later part of section 10.2 provides the core ideas involved in systematic fragmentation of X and its background via skull and close-hull based decomposition respectively. In section 10.3, application of multi-scale morphological operations to quantify the complexity of thematic information is provided with results.

10.2 IMAGE FRAGMENTATION VIA SKULL AND CLOSE-HULL BASED DECOMPOSITION

Mathematical morphology defines the geometrical complexity of a two-dimensional thematic or image object with reference to an object of simple shape and size, termed as structuring element. The image object could be represented in a continuous space or in a sampled discrete space. We focus only upon discrete binary finite image objects and discrete binary structuring elements containing origin for further discussion in this document. The morphological transformations primarily are interactions of image object with structuring element. Morphological erosion and dilation are most basic transformations, which geometrically shrink and expand the image object respectively. Erosion of an image X by structuring element B , denoted by $X \ominus B$, is an antiextensive transform; while dilation of an image X by structuring element B , denoted by $X \oplus B$, is an extensive transform, i.e. $X \ominus B \subseteq X \subseteq X \oplus B$. In fact, morphological transforms are defined against symmetric set of B with respect to origin, denoted by B^s . Refer [1] for geometric and algebraic definitions, and other details of morphological transforms. With the same spirit of definitions as in [1], we refer simply $X \ominus B$ and $X \oplus B$ respectively as erosion and dilation of X by B in this document. Erosion of an image followed by dilation is defined as opening transform, and dilation of an image followed by erosion is defined as closing transform. Opening denoted by $X \circ B$ is an antiextensive transform; while closing denoted by $X \bullet B$ is an extensive transform, i.e. $X \circ B \subseteq X \subseteq X \bullet B$. The roughness or complexity of an image is reduced at cost of its contraction in morphological opening transform. Similarly, the roughness of image background is reduced at cost of its expansion in morphological closing transform. Thus, iterative openings

and closings with unit increment in size of structuring element will result in complete removal of the roughness of image. Complete removal of roughness in case of opening indicates no contraction of image in further cycles of openings with any bigger size of the structuring element. However, notice that image may vanish in this course of further openings well before or after complete removal of roughness. Similarly, complete removal of roughness in case of closing indicates no expansion of image (assuming enough big background) in further cycles of closings with any bigger size of the structuring element. Based upon this approach of quantifying roughness or complexity of image and its background by iterative openings and closings respectively; we define a shape-size based systematic fragmentation technique for image and its background in coming sub-sections. We demonstrate a use-case in section 10.3 to quantify a roughness index derived from this fragmentation technique. Also we relate this scale invariant, but shape-dependant quantitative index with fractal dimension.

10.2.1 Skull Fragments of Image Foreground

A skull $X \circ NB$ of finite image X is obtained at iteration count N of opening, with B being the unit structuring element; if condition (10.1) is satisfied.

$$\{X \circ NB = X \circ (N + 1)B\} \wedge \{X \circ (N - 1)B \neq X \circ NB\} \quad (10.1)$$

Here, an iteration count n ($n \geq 0$) indicates that structuring element ‘ nB ’ is used for opening. The range of iteration starts from $n=0$ and ends at N_{\max} , where:

$$N_{\max} = n | \{ (X \circ nB \neq \Phi) \wedge (X \circ (n + 1)B = \Phi) \} \quad (10.2)$$

Clearly, there may be one or more iterations N_i ($0 \leq N_i < N_{\max}$) satisfying (10.1), each indicating a skull, with ‘ i ’ being a positive integer indicating skull count. Observe that if $N_1=0$, i.e. the first skull of image is obtained at iteration count 0; condition in (10.1) is reduced to $X=X \circ B$.

We define Skull Fragment Pattern Spectrum (SFPS) of image X as follows:

$$SFPS_i(X) = \begin{cases} A(X) - A(X \circ N_1B), & i = 1 \\ A(X \circ N_iB) - A(X \circ N_{i-1}B), & 2 \leq i \leq M \\ A(X \circ N_MB), & i = M + 1 \end{cases} \quad (10.3)$$

where $SFPS_i$ is i^{th} skull fragment pattern spectrum of image X , N_i is the iteration count for which i^{th} skull is obtained, M is the (maximum) number of skulls of image, and $A(.)$ indicates area of finite image under consideration. Notice that there are $M+1$ skull fragments of an image having M skulls, as the last (i.e. M^{th}) skull itself is a fragment.

10.2.2 Close-Hull Fragments of Image Background

A close-hull $X \bullet KB$ of finite image X is obtained at iteration count K of closing, with B being the unit structuring element; if condition (10.4) is satisfied.

$$\{X \bullet KB = X \bullet (K + 1)B\} \wedge \{X \bullet (K - 1)B \neq X \bullet KB\} \quad (10.4)$$

Again, an iteration count n ($n \geq 0$) indicates that structuring element 'nB' is used for closing. The range of iteration starts from $n=0$ and ends at K_{\max} , where:

$$K_{\max} = \text{minimum } n | \{(nB \odot X) \neq \Phi\} \quad (10.5)$$

Clearly, there may be one or more iterations K_i ($0 \leq K_i < K_{\max}$) satisfying (10.4), each indicating a close-hull, with 'i' being a positive integer indicating close-hull count. Observe that if $K_1=0$, i.e. the first close-hull of image is obtained at iteration count 0; condition in (10.4) is reduced to $X=X \bullet B$.

We define Hull Fragment Pattern Spectrum (HFPS) of image X as follows:

$$HFPS_i(X) = \begin{cases} A(X \bullet K_1 B) - A(X), i = 1 \\ A(X \bullet K_i B) - A(X \bullet K_{i-1} B), 2 \leq i \leq M \end{cases} \quad (10.6)$$

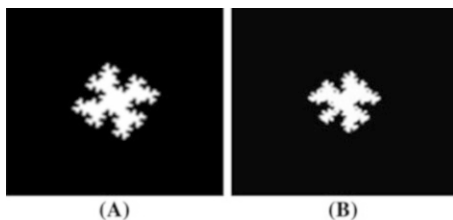
where $HFPS_i$ is i^{th} hull fragment pattern spectrum of image X , K_i is the iteration count for which i^{th} close-hull is obtained, M is the maximum number of close-hull of image, and $A(\cdot)$ indicates area of finite image under consideration. There are M close-hull fragments of an image having M close-hulls.

10.3 CASE STUDY – QUANTITATIVE INDEX FOR COMPLEXITY OF IMAGE

10.3.1 Skull Fragment Based Roughness Index of Image

We applied skull based fragmentation as defined in (10.3) on deterministic binary Koch quadric fractal of Fig. 10.1(a) with base structuring element as unit rhombus; and resultant fragments are shown in Fig. 10.2 (a) to (g).

Fig. 10.1 (a) Deterministic and (b) non-deterministic binary Koch quadric fractals.



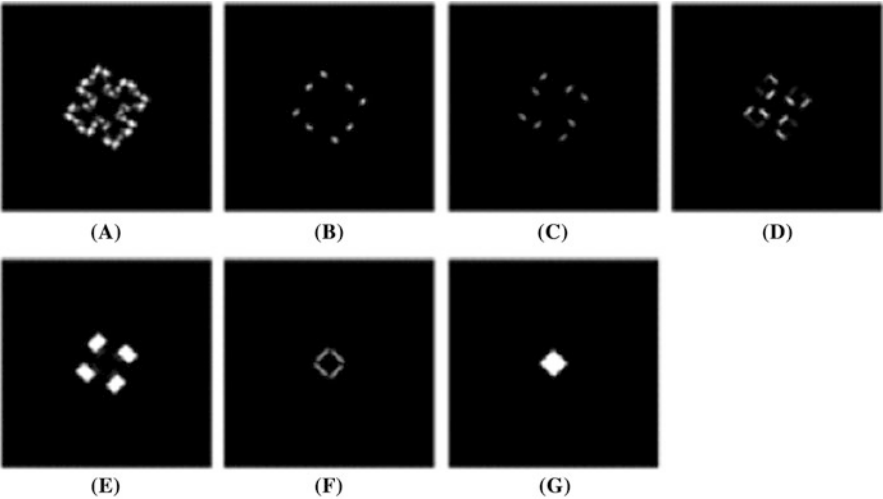


Fig. 10.2 (a) to (g):1st to 7th skull fragments (in order) of deterministic binary Koch quadric fractal of Fig. 10.1(a).

Table 10.1 (a) and (b): Skull fragment pattern spectrums and corresponding roughness of binary Koch quadric fractals of Fig. 10.1(a) and 10.1(b) respectively. Note that there are (M+1) fragments out of M skulls of fractal

a				b			
Skull No. i	N _i	SFPS _i	Roughness of skull fragment	Skull No. i	N _i	SFPS _i	Roughness of skull fragment
1	12	23826.75	0.53053	1	19	18366	0.52982
2	20	3227	0.21154	2	21	105.375	0.01968
3	26	2316	0.16845	3	37	15449.625	0.52746
4	36	5753.125	0.30511	4	41	1530.625	0.16057
5	41	19696.125	0.51974	5	47	46.875	0.00992
6	58	2715	0.18813	6	49	194.5	0.03269
		9099.5	0.39225			11440.125	0.49579

Tables 10.1(a) and 10.1(b) respectively show the iteration count N_i for which i^{th} skull of deterministic and non-deterministic binary Koch quadric fractal of Fig. 10.1(a) and 10.1(b) is obtained, corresponding $SFPS_i$ values of generated skull fragments, along with roughness of each fragment.

Figures 10.3 (a) and (b) are obtained by employing the data of Table 10.1(a) for the deterministic fractal. From the graphical relationship shown in Fig. 10.3 (a), the crossover scales between skull fragment wise roughness values and skull wise iteration number are very obvious. The respective crossover scales for skull based relationships include 12, 26, 41, and 58. The graphical relationship of Fig. 10.3 (b) between cumulative areal roughness of skull fragments computed through pattern spectra analysis and skull wise iteration number yields a scale-invariant power-law. The power-law value computed for this relationship is 0.0343. This

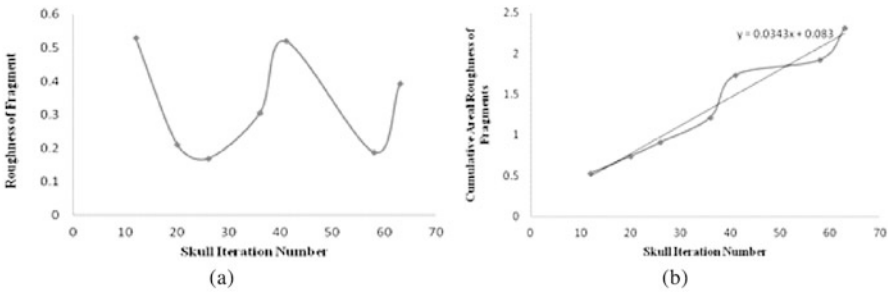


Fig. 10.3 (a) Fragment wise foreground roughness pattern; (b) Skull fragment based roughness index.

Table 10.2 (a) and (b): Hull fragment pattern spectrums and corresponding roughness of binary Koch quadric fractals of Fig. 10.1(a) and 10.1(b) respectively

a				b			
Close-hull No. i	K_i	HFPS _i	Roughness of closehull fragment	Close-hull No. i	K_i	HFPS _i	Roughness of closehull fragment
1	11	17283.125	0.48101	1	14	7403.75	0.51675
2	19	1689.5	0.22353	2	27	4866.75	0.52092
3	25	1116	0.16845	3	33	1322.875	0.29455
4	35	3786.375	0.36370	4	46	2275.125	0.39708
5	42	8049	0.50037	5	49	384.75	0.12784
6	62	185.625	0.04298				

scale-invariant power-law is shape-dependant and the absolute value of logarithm of this power law value yield 1.46, which is close enough to the analytical fractal dimension (i.e. 1.5) of deterministic binary Koch quadric fractal. This observation needs further investigation. The scale invariant power-law characteristic holds good for non-deterministic Koch quadric fractal also.

10.3.2 Hull Fragment Based Roughness Index of Image Background

We applied close-hull based fragmentation as defined in (10.6) on deterministic binary Koch quadric fractal of Fig. 10.1 (a) with base structuring element as unit rhombus; and resultant visible fragments are shown in Fig. 10.4 (a) to (e).

Tables 10.2(a) and 10.2(b) respectively show the iteration count K_i for which i^{th} close-hull of deterministic and non-deterministic binary Koch quadric fractal of Fig. 10.1(a) and 10.1(b) is obtained, corresponding HFPS_i values of generated close-hull fragments, along with roughness of each fragment.

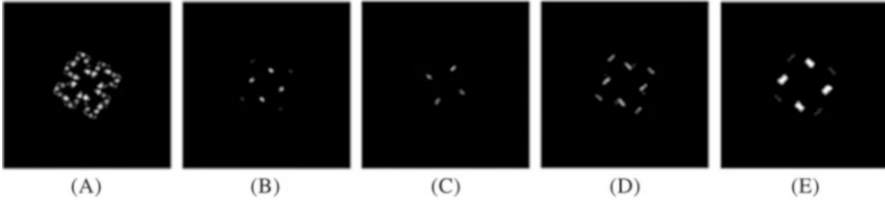


Fig. 10.4 (a) to (e): 1st to 5th close-hull fragments (in order) of deterministic binary Koch quadric fractal of Fig. 10.1(a). The 6th fragment is almost invisible (refer HFPS₆ value in Table 10.2(a)).

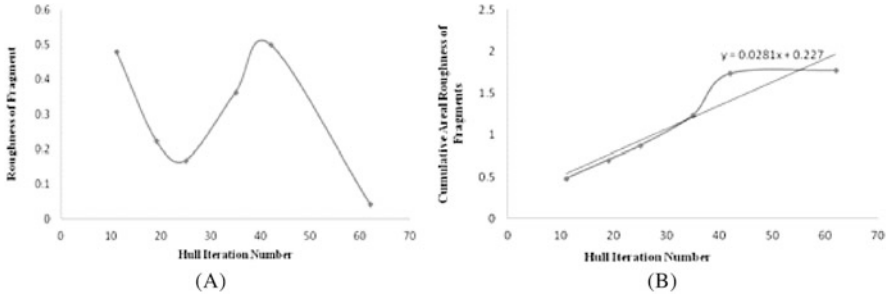


Fig. 10.5 (a) Fragment wise background roughness pattern; (b) Hull fragment based roughness index.

Figures 10.5 (a) and (b) are obtained by employing the data of Table 10.2(a) for the deterministic fractal. The graphical relationship of Fig. 10.5 (a) indicates respective crossover scales for close-hull based relationships including 11, 25, 42, and 62. The graphical relationship of Fig. 10.5 (b) between cumulative areal roughness of hull fragments and hull wise iteration number yields a scale-invariant and shape-dependant power-law. The computed power-law value is 0.0281. The absolute value of logarithm of this power law value yield 1.55, which again is close enough to the analytical fractal dimension (i.e. 1.5) of deterministic binary Koch quadric fractal. Notice symmetric pattern of skull and hull fragments of Fig. 10.2 and Fig. 10.4, and almost co-incident skull and hull based cross-over scales obtained from Fig. 10.3 (a) and Fig. 10.5 (a) respectively; which is because of perfect symmetry of deterministic fractal as well as convexity of used structuring element (rhombus) in this example. This observation requires more investigation and validation.

10.4 CONCLUSIONS

This paper provides a simple morphology-based methodology to compute the complexity of foreground and background regions of a thematic map. Skull and close-hull based fragmentation approaches are proposed for computation of foreground and background complexity respectively. Systematic use of number of

fragmented zones and corresponding areas of these decomposed fragmented zones via the two aforementioned ways yield results that provide quantitative complexity indexes of thematic maps. These approaches are demonstrated on Koch quadric fractal of both deterministic and random types.

ACKNOWLEDGEMENTS We wish to thank Indian Statistical Institute, Bangalore for funding and support of this research work.

REFERENCES

1. Serra, J.: Image analysis and mathematical morphology. London: Academic Press (1982)
2. Maragos, P. and Schafer, R.W.: "Morphological skeleton representation and coding of binary images." *IEEE Trans. Acoust., Speech, Signal Processing*. vol. ASSP-34, pp. 1228–1244 (1986)
3. Maragos, P.A.: Pattern spectrum and multiscale shape representation, *IEEE T Pattern Anal*; 11 (7): 701–716 (1989)
4. Mandelbrot, B.B.: *Fractal Geometry of Nature*. W.H. Freeman & Co.: New York, p. 468 (1982)

Chapter 11

Geostatistical Analysis of Functional Compositions: Characterization of Soil Particle-Size Curves through the Aitchison Geometry

A. Menafoglio, A. Guadagnini, and P. Secchi

Abstract We focus on the geostatistical characterization of the spatial distribution of soil particle-size curves (PSCs) within an alluvial aquifer. We consider as data object the entire PSC with a Compositional Data Analysis (CoDa) approach. Data are viewed as a point in the infinite-dimensional Hilbert space of functional compositions. The latter is endowed with the Aitchison geometry and enables us to derive a Functional Compositional Kriging (FCK) predictor. We demonstrate the methodology on a set of PSCs observed within an alluvial aquifer in the Neckar river valley in Germany.

Keywords Geostatistics • Compositional Data • Functional Data • Particle-Size Curves • Groundwater

11.1 INTRODUCTION AND MOTIVATIONS

Environmental studies often require the analysis of georeferenced infinite-dimensional objects, such as curves or images. These constitute typical examples of functional datasets associated with a structure of spatial dependence. Most of the techniques which are commonly employed in Functional Data Analysis (FDA, [5]) are not adequate in the presence of constrained data, such as functional compositions. In this context, the development of new geostatistical tools to overcome such limitations is critical from an application viewpoint. Here, we focus on the problem of providing a geostatistical characterization of the spatial distribution of soil

A. Menafoglio (✉) • P. Secchi
MOX-Department of Mathematics, Politecnico di Milano, Milano, Italy
e-mail: alessandra.menafoglio@polimi.it

A. Guadagnini
Dipartimento di Ingegneria Civile e Ambientale, Politecnico di Milano, Milano, Italy
Department of Hydrology and Water Resources, The University of Arizona,
Tucson, AZ, USA

particle-size curves (PSCs) within an alluvial aquifer. These data are relevant to applications related to groundwater hydrology, soil science, geophysics, petroleum engineering and geochemistry, with emphasis on applications oriented towards modeling physical and chemical processes occurring in heterogeneous earth systems.

The Motivating Example. The data we consider are part of the dataset collected within an alluvial aquifer with thickness of about 5 m near the city of Tübingen, Germany. We focus on the 60 particle-size curves (PSCs) collected at one of the monitoring wells at the site. In each location s_i , $i = 1, \dots, 60$ the PSC X_{s_i} expresses the relative amount $X_{s_i}(t)$ of particles within a given soil sample having size smaller than or equal to t where $t \in T = [t_{\min}, t_{\max}]$ (e.g., [6] and references therein). PSCs describe the distribution of grain sizes within the soil sample. In this application they are reconstructed through grain sieve analysis performed on the basis of 12 sieve diameters. The aim of the study is to assess the entire field of PSCs from the geostatistical analysis of the available data.

11.2 THE METHOD: KRIGING FUNCTIONAL COMPOSITIONS

In this Section, we briefly revise the geostatistical methodology introduced by [4] upon considering as data object the entire PSC [3]. The key idea is to interpret PSCs X_{s_1}, \dots, X_{s_n} as cumulative distribution functions and analyze their densities Y_{s_1}, \dots, Y_{s_n} as functional compositional data. These are the infinite-dimensional counterparts of compositional data, i.e., multivariate data whose components are proportion or relative amounts of a whole according to a given domain partition. Indeed, probability density functions are functional and compositional data, i.e., they are infinite-dimensional objects which are constrained to be non-negative and to integrate to unity.

The Aitchison Geometry for Particle-Size Distributions. We model particle-size densities Y_{s_i} , $i = 1, \dots, n$ as functional compositions. In this context, a proper geometry upon which the statistical analysis is grounded needs to be selected. To this end, we consider the Aitchison geometry for functional compositions [2]. We first note that two compositions f, g are equivalent if they are proportional, i.e., $f = \alpha \cdot g$ for $\alpha > 0$. We thus call $A^2(T)$ the space of (equivalent classes of) non-negative real functions on T with square integrable logarithm. As proved in [2], $A^2(T)$ can be provided with a Hilbert structure if endowed with the perturbation and powering operations

$$f \oplus g = \frac{fg}{\int_T fg}, g \in A^2; \alpha \odot f = \frac{f^\alpha}{\int_T f^\alpha}, \alpha \in \mathbb{R}, f \in A^2$$

and the inner product

$$\langle f, g \rangle = \int_T [\log f \cdot \log g] - \frac{1}{|T|} \int_T \log f \int_T \log g, f, g \in A^2$$

Kriging Functional Compositions. Prediction of the spatial field of PSCs from the sample Y_{s_1}, \dots, Y_{s_n} is based on the assumption that these are the partial observation of a stochastic process $\{Y_s, s \in D\}$ valued in A^2 . The space being Hilbert, all the results presented in [4] can be applied.

Supported by prior knowledge of the field site (e.g., [6] and references therein), we assume the process to be represented by a globally second-order stationary model with trace-covariogram and trace-semivariogram γ , i.e., for all $s, s_i, s_j \in D$,

$$\begin{aligned} \mathbb{E}[Y_s] &= m; C(h) = \text{cov}(Y_{s_i}, Y_{s_j}) = \mathbb{E}[Y_{s_i}, Y_{s_j}], h = \text{dist}(s_i, s_j) \\ \gamma(h) &= \text{Var}(Y_{s_i}, Y_{s_j}) = \mathbb{E}[\|Y_{s_i} \ominus Y_{s_j}\|^2], h = \text{dist}(s_i, s_j). \end{aligned}$$

Thus we consider the Ordinary Kriging predictor $Y_{s_0}^* = \bigoplus \lambda_i^* \odot Y_{s_i}$ of Y_{s_0} , which is found by solving the optimization problem:

$$\begin{aligned} (\lambda_1^*, \dots, \lambda_n^*) &= \underset{\lambda_1, \dots, \lambda_n \in \mathbb{R}}{\text{argmin}} \quad \text{Var}_{A^2} \left(Y_{s_0}^\wedge \ominus Y_{s_0} \right) \text{s.t. } \mathbb{E}_{A^2} [Y_{s_0}^\wedge] = m \\ Y_{s_0}^\wedge &= \bigoplus \lambda \odot Y_{s_i} \end{aligned}$$

This is well-posed under mild conditions on the sampling design.

Proposition 1 [Menafoglio et al. (2013)] *Assume that $\Sigma = (C(h_{i,j})) \in \mathbb{R}^{n \times n}$, $h_{i,j} = \text{dist}(s_i, s_j)$, $i, j = 1, \dots, n$, is a positive definite matrix. Then problem (1) admits a unique solution, $(\lambda_1^*, \dots, \lambda_n^*) \in \mathbb{R}^n$ which is obtained by solving:*

$$\begin{pmatrix} C(h_{i,j}) & 1 \\ 1 & 0 \end{pmatrix} \begin{pmatrix} \lambda_j \\ \zeta \end{pmatrix} = \begin{pmatrix} C(h_{i,0}) \\ 1 \end{pmatrix}$$

ζ being the Lagrange multiplier associated with the unbiasedness constraint. The ordinary kriging variance of predictor $Y_{s_0}^*$ is then an estimate of the trace-covariogram C , or, equivalently, of the trace-semivariogram γ is required to solve above system. To this end, a discretized method of moment (MoM) estimator $\hat{\gamma}$ can be employed and a valid variogram model can be then calibrated against observations. We refer to [3] for further details.

11.3 INTERPRETATION OF FIELD DATA

We illustrate the results obtained with our approach on the field case study illustrated in Section 1. Computation of density functions from grain-sieve data is grounded on the smoothing procedure based on Bernstein polynomials described in [3]. Smoothed particle-size densities are depicted in Fig. 11.1a. These are then

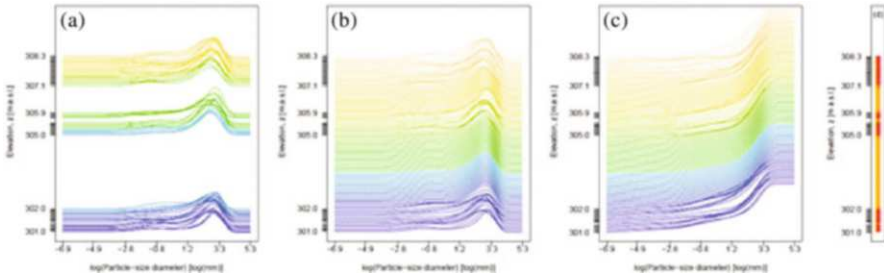


Fig. 11.1 Field case study. (a) Particle-size densities data; (b) kriged particle-size densities; (c) predicted PSC; (d) kriging variance, ranging between 0 (darkest shade) and 2.53 (lightest shade). Vertical coordinates correspond to the data (sampled or predicted) locations. Adapted from [4].

embedded in the Hilbert space A^2 of functional compositions and the methodology introduced in Section 11.2 is applied. Fig. 11.1b-11.1c depicts our prediction results. Cross-validation suggests that these are satisfactory, evidencing a median and mean sum of squared error lower than 0.2%. Tests performed to assess the local quality of kriging predictions evidence that our methodology proves to be fairly accurate in predicting the local features of particle-size distributions. We finally remark that a key advantage of our approach lies in the possibility of obtaining predictions of the entire particle-size curve at unsampled locations, as opposed to classical [1] or compositional kriging techniques [7] which allow only finite-dimensional predictions, based on a set of selected features (or synthetic indices) of the curve. The information content provided by the full PSC is critical to the proper modeling of several physical and chemical processes occurring in heterogeneous earth systems and which are affected by the local composition of the host soil/rock matrix.

REFERENCES

1. Cressie, N.: Statistics for Spatial data. John Wiley & Sons (1993)
2. Egozcue, J.J., Díaz-Barrero, J.L. and Pawlowsky-Glahn, V.: Hilbert space of probability density functions based on Aitchison geometry. *Acta Math. Sin. (English Ser.)*, 22(4), 1175–1182 (2006)
3. Menafoglio, A., Guadagnini, A. and Secchi, P.: A Kriging Approach based on Aitchison Geometry for the Characterization of Particle-Size Curves in Heterogeneous Aquifers. *Stoch. Env. Res. Risk A.* DOI: [10.1007/s00477-014-0849-8](https://doi.org/10.1007/s00477-014-0849-8) (2014)
4. Menafoglio, A., Secchi, P. and Dalla Rosa, M.: A Universal Kriging predictor for spatially dependent functional data of a Hilbert Space. *Electron. J.Stat.*, 7, 2209–2240 (2013)
5. Ramsay, J. and Silverman, B.: Functional data analysis (Second ed.). Springer, New York (2005)

6. Riva, M., Guadagnini, L. and Guadagnini, A.: Effects of uncertainty of litho facies, conductivity and porosity distributions on stochastic interpretations of a field scale tracer test. *Stoch. Environ. Res. Risk A.* 24, 955–970 (2010)
7. Tolosana-Delgado, R., van den Boogaart, K.G. and Pawlowsky-Glahn, V.: Geostatistics for Compositions, Pawlowsky-Glahn & Buccianti edn. John Wiley & Sons, Ltd, 73–86 (2011)

Chapter 12

Classical Statistical Techniques for Deciphering the Origin and Evolution of Volcanoes at Volcanic Front of the Central Part of the Mexican Volcanic Belt

F. Velasco-Tapia and S.P. Verma

Abstract New geochemical data for the Sierra de Las Cruces are combined with the published data from this volcanic range and the Sierra de Chichinautzin. Both Neogene-Quaternary ranges are located at the volcanic front of the central part of the Mexican Volcanic Belt (MVB). These geochemical data were statistically evaluated to establish central tendency and dispersion estimates for different magma types from basic to acid, which were compared with worldwide arcs and rifts. UDASYS software was used for this purpose. Similarly, multi-dimensional diagrams recently proposed (2006-2013) were also applied to decipher the tectonic setting. These statistical techniques provide further constraints on the origin of the MVB.

Keywords Multivariate Analysis • Mass Balance • Geochemistry • Volcanism • Mexican Volcanic Belt

12.1 INTRODUCTION

Several conventional mineralogical, geochemical, and isotopic tools based on a limited number of variables (e.g., bivariate, trilinear, multi-element, and semi-logarithmic diagrams), have been applied to establish qualitative or semi-quantitative views of igneous petrological processes [1]. However, a quantitative assessment can be obtained from multivariate statistical techniques although its application remains limited mainly for classification purposes [e.g., 2].

F. Velasco-Tapia (✉)

Facultad de Ciencias de la Tierra, Universidad Autónoma de Nuevo León, Linares, N.L., México

e-mail: velasco@fct.uanl.mx

S.P. Verma

Departamento de Sistemas Energéticos, Instituto de Energías Renovables, Universidad Nacional Autónoma de México, Temixco, Mor., Mexico



Fig. 12.1 Satellite image of the central part of the Mexican Volcanic Belt (Google Earth 2014). Strato volcanoes: Iz = Iztaccíhuatl, Po = Popocatepetl, NT = Nevado de Toluca.

On the other hand, an igneous petrology study would be to include the tectonic regime affinity. Nevertheless, conventional tectonic discrimination diagrams [1] display strong limitations as a result of statistically deficient treatment of compositional data, eye-drawn subjective boundaries for different tectonic fields, and lack of representation of the entire statistical population [3]. However, to solve these problems, new discriminant-function-based multidimensional diagrams have been proposed for basic to acid igneous rocks from four tectonic settings (island arc, continental rift, ocean island, and mid-ocean ridge for basic-ultrabasic and island arc, continental arc, rift + ocean island, and collision for intermediate and acid magmas) [3 and references therein]. Additionally, conventional Fisher F and Student t-tests have been applied, using the UDASYs computer program [4], to statistically compare volcanic rocks from a complex tectonic regime with those erupted in arc or rift settings.

The purpose of this study is to show that the application of conventional statistical methods and discriminant-function-based multidimensional diagrams allows us to obtain a detailed petrological view for two volcanic localities (Sierra de las Cruces—SCR and Sierra de Chichinautzin—SCH; Fig. 12.1) at the volcanic front of the Mexican Volcanic Belt (MVB). This volcanic province has been considered a very tectonically-complex zone, being associated to: (a) the subduction of the Cocos and Rivera plates under the North American plate, and (b) an incipient within-plate setting.

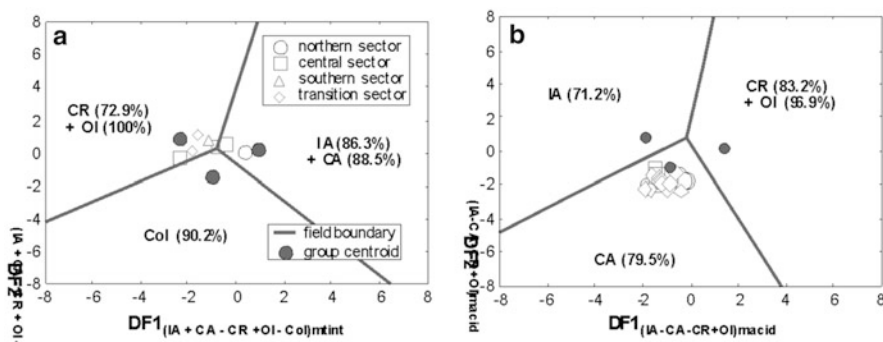


Fig. 12.2 Examples of discriminant-function multidimensional diagrams applied to SCR magmas: (a) intermediate (mtint), based on trace elements, and (b) acid (macid), based on major elements. Tectonic settings: IA = island arc, CA = continental arc, CR + OI = continental rift + ocean island, and Col = Collision.

12.2 SIERRA DE LAS CRUCES [5, 6]

This is a Pliocene-Pleistocene volcanic range, with a NNW-SSE direction for ~65 km, constituted by porphyritic lava flows. A cluster analysis of geochemical data (82 samples) has identified three groups: (a) dacite, (b) dacite with disequilibrium features, and (c) andesitic enclaves. This evidence confirms that magma mingling/mixing processes have played significant role in the evolution of this volcanic range. Multidimensional discrimination diagrams suggest a transitional continental arc to within-plate setting (Fig. 12.2). Dacite was derived from the upper continental crust, with a continental arc affinity, after being interacted by intermediate magma (spheroidal enclaves) generated in deeper levels of the crust in an extensional setting. Discordancy and significance tests have shown that evidence does not exist of a geochemical contribution of several major and trace elements from the subducting Cocos plate to the SCR magma genesis.

12.3 SIERRA DE CHICHINAUTZIN [7-9]

This volcanic range comprises over 220 Quaternary monogenetic volcanic centers, shield volcanoes and domes distributed along E-W oriented normal faults, which show active N-S extension and a strike-slip component. An extensive geochemical database (289 samples) has revealed that about 15% of erupted material corresponds to mafic magmas, whereas the rest display andesitic to dacitic compositions. Multi-dimensional logratio transformed major and immobile element based diagrams suggest that near-primary mafic and evolved SCH magmas have a continental rift tectonic affinity (Fig. 12.3). This hypothesis has also been supported by statistical comparison using ANOVA tests [4].

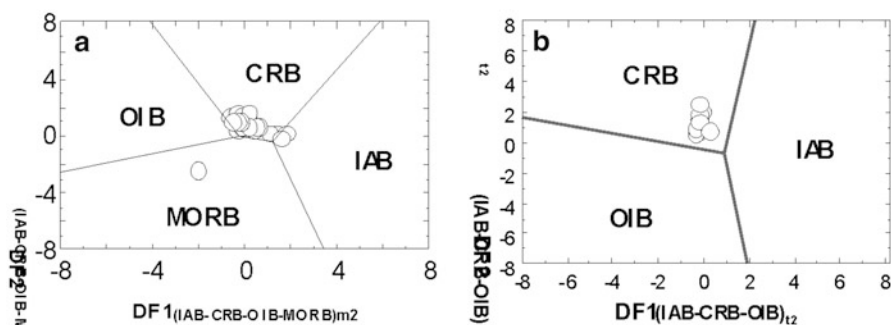


Fig. 12.3 Example of discriminant-function multi-dimensional diagrams, based on (a) major and (b) trace element log ratios, applied to mafic SCH magmas [9]. Tectonic settings: IAB = island (and continental) arc basic rock, CRB = continental rift basic rock, OIB = ocean island basic rock, MORB = mid-ocean ridge basic rock.

12.4 FINAL REMARKS

Classical statistical techniques have been successfully used as igneous petrological tools to elucidate the tectonic setting affinity of Neogene-Quaternary magmas from Central Mexican Volcanic Belt. Spatial multivariate techniques [e.g. 10] will be applied to reach a better comprehension of the volcanic phenomena.

ACKNOWLEDGEMENTS This work was supported by PAICYT-UANL grant CT786-02 and DGAPA-PAPIIT-UNAM grant IN104813.

REFERENCES

1. Rollinson, H.R.: Using of Geochemical Data: Evaluation, Presentation, Interpretation. Logman, Oxford (1993)
2. Le Maitre, R.W.: A new approach to the classification of igneous rocks using the basalt-andesite-dacite-rhyolite suite as an example. *Contrib. Mineral. Petrol.* 56, 191–203 (1976)
3. Verma, S.P., Pandarinath, K., Verma, S.K. and Agrawal, S.: Fifteen new discriminant function-based multi-dimensional robust diagrams for acid rocks and their application to Precambrian rocks. *Lithos* 168–169, 113–123 (2013)
4. Verma, S.P., Cruz-Huicochea, R. and Díaz-González, L.: Univariate data analysis system: deciphering mean compositions of island and continental arc magmas, and influence of the underlying crust. *Int. Geol. Rev.* 55, 1922–1940 (2013)
5. Velasco-Tapia, F., Rodríguez-Saavedra, P., Márquez, A., Navarro de León, I., De Ignacio, C., Marroquín Guerra, S.G., Quintanilla-Garza, J. and Rangel-Álvarez, O.M.: Mineralogical and geochemical evidence of magma mingling/mixing in the Sierra de las Cruces volcanic range, Mexican Volcanic Belt. *J. Iber. Geol.* 39, 147–166 (2013)
6. Velasco-Tapia, F.: Multivariate analysis, mass balance techniques, and statistical tests as tools in igneous petrology: application to the Sierra de las Cruces Volcanic Range (Mexican Volcanic Belt). *Sci. World J.* ID793236 (2014)

7. Verma, S.P.: Geochemistry of evolved magmas and their relationship to subduction un-related mafic volcanism at the volcanic front of the Mexican Volcanic Belt. *J. Volcanol. Geotherm. Res.* 93, 151–171 (1999)
8. Verma, S.P.: Geochemistry of subducting Cocos plate and the origin of subduction-unrelated mafic volcanism at the volcanic front of the Central Mexican Volcanic Belt (Mexico). In: Delgado-Granados, H., Aguirre-Díaz, G., Stock, J.M. (eds.) *Cenozoic Tectonics and Volcanism of Mexico*. Geol. Soc. Am. Spec. Pap., vol. 334, pp. 195–222. Geological Society of America, Boulder, CO (2000)
9. Velasco-Tapia, F. and Verma, S.P.: Magmatic processes at the volcanic front of Central Mexican Volcanic Belt: Sierra de Chichinautzin Volcanic Field (Mexico). *Turk. J. Earth Sci.* 22, 32–60 (2013)
10. Vargas-Guzmán, J.A.: Conditional components for simulation of vector random fields. *Stoch. Environ. Res. Risk Asses.* 17, 260–271 (2003)

Chapter 13

Forecasting of Hollows in Abandoned Shallow Coal Mines in a Zone of Intensive Weathering

V. Palchik

Abstract Empirical criteria ($K1-K2 > 0$ and $\eta-K3 > 0$) for predicting the presence of hollows in abandoned shallow underground workings in Donetsk city (Ukraine) located in the zone of intensive weathering are proposed. The hollows exist when both inequalities $K1-K2 > 0$ and $\eta-K3 > 0$ are satisfied. The statistical analysis has established that the value of criterion $K2$ is inversely related to rock quality designation (RQD) and that a decrease in RQD leads to a decrease in $K1-K2$ and, hence, the probability of the hollow existence is decreased. It is also established that a statistical parameter in the left-hand part of inequality $\eta-K3 > 0$ decreases according to logarithmic law with increasing standard linear intensity of weathering-induced fractures (P10). When the fracture intensity (P10) increases, the probability of the presence of a hollow is decreased. The proposed criteria confirm that a thick immediate roof and sandstone layers contribute to the existence of hollows, whereas weak alluvium, argillites and sandy shale allow a collapse of the rock mass.

Keywords Hollow • Abandoned Working • Weathered Rock • Fracture Intensity

13.1 INTRODUCTION

It is well-known [1-6] that hollows in abandoned underground workings at shallow depths represent a potential hazard for built environmental and ecology of territories above underground workings. The collapse of abandoned workings occurs due to instability within the hollows. After a mine has been deserted, the strength of the wall and roof may have deteriorated. The weight of overburden has been pressing down and squeezing the roof and walls. There is no way knowing the exact time for the rock to loosen and fall. In particular, hollows in abandoned workings at depths up to 80 m in Donetsk area (Ukraine) are potentially dangerous

V. Palchik (✉)

Department of Geological and Environmental Sciences, Ben-Gurion University of the Negev, Beer-Sheva, Israel

e-mail: vplachek@bgu.ac.il

from the point of view of the collapse of the ground surface, and therefore, require prediction [6]. In the absence of such a prediction method, it is necessary to drill a lot of boreholes to determine the existence of hollows, which results in unjustified material and labour expenses. Palchik [6] has proposed method of hollow prediction developed from back-analysis of data from boreholes which were drilled from the ground surface above underground workings. However, this method does not take into account the degree of rock weathering. For this reason, the use of this method in cases of high degree of weathering is impossible. The goal of this study is to establish modified criteria, which can provide accurate prediction of the hollows in cases where weathered rock in immediate roof is of low quality and exhibits a high intensity of weathering-induced fractures.

13.2 CONDITIONS OF WORKINGS AND DEGREE OF ROCK WEATHERING

In 19170-1951 in Donetsk city (Ukraine), dozens of coal mines used to operate at depths up to 80 m. The rock mass overlying the working in coal seams consists of layers of sandstone, argillites and sandy shale dipping at approximately 12° or less. Thickness of coal seams is between 0.9 m and 1.5 m. The workings in old mines were mainly drifts joining short (25-28 m) coalfaces. The pillars in the mined-out space and low rock pressures have created favourable conditions for the existence of hollows in abandoned mine workings. Unfortunately, the conditions of abandoned workings (working has collapsed or remains hollow) are unknown because it is impossible to enter such workings. The location of old workings at a depth up to 80 m has been generally carried out by exploratory drilling. The hollows were determined by sinking of the drilling column into the workings. If there are any hollows, free fall of the boring tool occurred. If the working had collapsed, an accelerated sinking of the boring tool was observed. The subsurface rock mass is the zone where the processes of weathering are very active. In Donetsk area, the depth of the bottom border of the weathering zone is between 55 and 85 m [7]. It is well-known (e.g. [8, 9]) that weathering exerts an adverse influence on rock strength and fracture characteristics of rock. Since rock quality designation (RQD, %) reflects the degree of weathering and fracture intensity of rock, RQD values were determined. Observations show that the RQD parameter of the rocks in immediate roof above underground working ranges from 10 to 40%. The standard linear intensity (P10, 1/m) of weathering-induced fractures along main fracture traces was measured on the lateral surface of individual pieces of core extracted within the immediate roof. It is observed that P10 value is between 14.9/m and 55.2/m. It is defined that the value of RQD tends to decrease with increasing fracture intensity (P10).

13.3 RESULTS OF STATISTICAL ANALYSIS

As a result of composite statistical analysis of the lithological composition of the rock mass, degree of rock weathering and results of exploratory boring for determining hollows in workings, it is established that hollows in abandoned subsurface mining workings in zones of intensive weathering exist when both following inequalities are satisfied:

$$K_1 - K_2 > 0 \quad (13.1)$$

$$\lambda - \ln(P10) \frac{\Sigma h_{ar} + \Sigma h_{ss}}{h_1} > 0 \quad (13.2)$$

where $\eta = 4.68$, P10 is the standard linear fracture intensity in immediate roof. Value of K_1 is computed as:

$$K_1 = \Sigma h_s + k_1 \Sigma h_{ar} + k_2 \Sigma h_{ss} \quad (13.3)$$

where ηh_s , ηh_{ar} and ηh_{ss} are the total thicknesses (m) of the sandstone, argillite and sandy shale layers, respectively, in the rock mass above an old workings; $k_1 = \eta_{ar}/\eta_s = 0.74$ and $k_2 = \eta_{ss}/\eta_s = 0.63$ are ratios between weighted mean densities (mg/m^3) of sandstone (η_s), argillite (η_{ar}) and sandy shale (η_{ss}) overlying the old workings. Value of K_2 is defined as:

$$K_2 \eta = \frac{ak_3 H}{(\text{RQD})^b} \quad (13.4)$$

where $k_3 = 1/\eta_s = 0.53$, a and b are statistical parameters ($a = 2.07$ and $b = 0.1$), H is depth of abandoned underground working: $H = \eta h_s + \eta h_{ar} + \eta h_{ss} + h_{ar}$, where h_{ar} is the thickness of alluvium.

An increase in the standard linear fracture intensity (P10) and in the value of $(\eta h_{ar} + \eta h_{ss})$ lead to a decrease in the value of the left-hand part of the inequality (13.2) and, hence, the probability of the presence of a hollow is decreased. On the other hand, an increase in the thickness of immediate roof (h_1) leads to an increase in the value of the left-hand part of the inequality (13.2) and, hence, the probability of the presence of a hollow is increased. When the maximum value of RQD = 40 %, the value of $K_1 - K_2$ is computed as:

$$K_1 - K_2 = 0.242 \Sigma h_s - 0.018 \Sigma h_{ar} - 0.128 \Sigma h_{ss} - 0.758 \Sigma h_a \quad (13.5)$$

In cases where RQD has a minimum value (RQD = 10 %), the value of $K_1 - K_2$ becomes smaller:

$$K_1 - K_2 = 0.131\Sigma h_s - 0.129\Sigma h_{ar} - 0.239\Sigma h_{ss} - 0.869\Sigma h_a \quad (13.6)$$

Comparing Eq. (13.5) and Eq. (13.6), we can see that the value of $K_1 - K_2$ for very weathered rocks ($RQD = 10\%$) is significantly smaller than that for relatively strong rocks ($RQD = 40\%$). This fact demonstrates that intensive weathering rapidly reduces the value of $K_1 - K_2$ and, hence, the probability of the existence of the hollows is decreased. Eqs. (13.5) and (13.6) also show that the probability of the existence of hollows decreases with increasing h_a , ηh_{ar} and ηh_{ss} . On the other hand, an increase in the value of h_s contributes to the existence of hollows.

13.4 CONCLUSIONS

The criteria for the prediction of hollows in abandoned underground workings located in weathered rock mass ($10\% < RQD < 40\%$ and $15/m < P10 < 55/m$) based on the result of composite statistical analysis of values of rock quality designation (RQD) and standard linear intensity of weathering-induced fractures (P10) in immediate roof of mine workings, as well as lithological composition of rock mass overlying underground workings, are proposed. These criteria can be used in cases where the preparation of rock samples for mechanical testing (for the definition of rock strength) is difficult due to friable nature of rocks in the immediate roof. According to the proposed criteria, a decrease in the values of RQD and increase in standard linear intensity (P10) of weathered-induced fractures lead to a decrease in the probability of existence of hollows in abandoned workings. The criteria confirm that the increase in thickness of the immediate roof and total thickness of relatively strong sandstone layers above an old mine working contribute to the existence of hollow, whereas the probability of the existence of hollows decreases with increasing thicknesses of very weak rock layers (alluvium, argillites and sandy shale). Such very weak rock layers do not restrain the collapse process and only exert additional weight on the roof of the underground working. The awareness of presence of hollows in abandoned shallow workings immediately before the construction of surface structures is a very important factor that allows us to use preventive measures, such as excavation and back-filling at shallow depths, barrier walls around the zone of hollows, and the filling and grouting of hollows in old mine workings within the area of surface construction.

REFERENCES

1. Waltham, A.C.: Ground Subsidence. Blackie & Son Ltd, London (1989)
2. Whittaker, B.N. and Reddish, D.J.: Subsidence: Occurrence, Prediction and Control. Elsevier, Amsterdam (1989)

3. Healy, P.R. and Head, J.M.: Construction over Abandoned Mine Workings. Construction Information and Research Association. Special Publication # 3 (2002)
4. Rueggsegger, L.R.: Manual for Abandoned Underground Mine Inventory and Risk Assessment. US Department of transportation. FHWA IF-99-007 (2009)
5. Helm, P.R., Davie C.T. and Glendinning, S.: Numerical Modeling of Shallow Abandoned Mine Working Subsidence Affecting Transport Infrastructure. *Eng. Geol.* 154, 6–19 (2013)
6. Palchik, V.: Prediction of Hollows in Abandoned Underground Workings at Shallow Depth. *Geotech. Geol. Eng.* 18(1), 39–51 (2000)
7. Palchik, V.: Influence of Physical Characteristics of Weak Rock Mass on Height of Caved Zone over Abandoned Subsurface Coal Mines. *Envir. Geol.* 42(1), 92–101 (2002)
8. Gupta, A.S. and Rao, K.S.: Weathering Indices and their Applicability for Crystalline Rocks. *Bull. Eng. Geol. Envir.* 60, 201–221 (2001)
9. Palchik, V.: In Situ Study of Intensity of Weathering-Induced Fractures and Methane Emission to the Atmosphere through these Fractures. *Eng. Geol.* 125, 55–65 (2012)

Chapter 14

Metallurgical Variable Re-expression for Geostatistics

J.L. Deutsch, J. Szymanski, and T.H. Etsell

Abstract One of the key challenges in the geostatistical modeling of metallurgical variables is their nonlinearity; estimation techniques such as kriging require that the variable of interest average linearly. By quantifying and modeling the metallurgical properties of blends, these metallurgical variables can be spatially modeled and scaled. A theoretical framework for the re-expression of these nonlinear metallurgical variables to linear variables using experimental data on the nature of blending is developed and demonstrated. The framework is developed using the power transformation family. Potential applications for this framework include mine plan optimization using high resolution spatial models and optimal decision making for processing multiple ore types.

Keywords Nonlinear Variables • Mixing • Scaling • Power Law • Geometallurgy

14.1 INTRODUCTION

The economic value of a mine is dictated not only by metal grades and ore tonnage, but also by the metallurgical performance of recovered ore. Ore hardness, throughput and recoveries will all impact the realized value of the deposit. As a deposit is mined and processed, ore types are naturally blended as material is received at the mill from multiple shovels and stockpiles. The nature of the continually changing mixture of ores is interesting. In particular, metallurgical properties such as recovery, throughput, energy consumption (related to the Bond mill work index), and reagent consumption of the ore mixture is important for process design and control. These properties are nonlinear, that is, mixing 50% of one ore type and 50% of another ore type does not necessarily lead to a mixture with a property half way between the two [1]. Quantifying and modeling the properties of ore blends allows

J.L. Deutsch (✉) • J. Szymanski

Department of Civil and Environmental Engineering, School of Mining and Petroleum Engineering, University of Alberta, Edmonton, Canada
e-mail: jdeutsch@ualberta.ca

T.H. Etsell

Department of Chemical and Materials Engineering, University of Alberta, Edmonton, Canada

for mine and mill optimization. One simple decision is whether to blend two different ore types or batch process them separately. Another application is the construction of high resolution spatial models of the metallurgical variables for enhancing mine plans and processing strategies. Understanding the nature of the blending and scaling of metallurgical variables is necessary.

The direct spatial modeling of nonlinear variables under a linear framework such as kriging would result in a bias in the resulting estimates. Geostatistical simulation is applicable since it places no requirement on the additivity of the variables; this is common in petroleum modeling applications. Nevertheless, the scaling and blending of these variables is required after simulation to derive effective properties and to quantify variability at a scale relevant for the mill. A framework that accounts for the nonlinearity is required. A power law based re-expression framework aimed at binary mixtures is developed here for the purpose of re-expressing nonlinear metallurgical variables as linear variables that permits the usage of linear geostatistical techniques including kriging for estimation and classical volume-variance relationships for addressing issues of scale. The practical challenges in the modeling of a useful re-expression framework and potential optimizations using the framework are discussed.

14.2 METALLURGICAL VARIABLE RE-EXPRESSION

Only relatively recently has much research been published in the area of understanding the mixing behaviour of mineral processing variables such as the Bond mill work index and froth floatability [1-3]. There are no theoretical mixing and scaling laws available for these variables; instead an empirical relationship is developed based on the bench scale testing of mixtures of multiple ore types. The resulting empirical models are generally not linear mass or volume fraction weighted averages due to the partially extrinsic, nonlinear behavior of the metallurgical variables. For example, Yan and Eaton observed that the Bond mill work index of blends was not the volume average of the pure Bond work indices, but was biased towards the harder ore due to mill holdback [1].

14.2.1 *Power Transformations and Mixing Frameworks*

The nonlinearity of these metallurgical variables motivates a re-expression framework which will allow the use of linear averaging techniques. In the context of estimating, scaling and blending these metallurgical variables, the goal of variable re-expression is to linearize the variable of interest permitting the use of linear weighted averages. The framework proposed here is based on the power transformation family of Tukey [4, 5] and the mixing laws of Korvin [6]. The power law

family is a widely used and flexible re-expression framework. Tukey [4, 5] defines a power transformation family with the general form:

$$y = \begin{cases} (z + c)^p & p \neq 0 \\ \log(z + c) & p = 0 \end{cases} \quad (14.1)$$

where p is the power of the transformation. The value c is a constant, often 0, which can be used to enforce $z+c > 0$. A number of modifications have been made to the original Tukey transformation, with the most notable change by Box and Cox [7] who modified the family slightly to account for the requirement of the choice of the logarithm where $p = 0$ and preserve the rank ordering of the transformed variable for $p < 0$.

The power transformation family is related to the binary mixing framework of Korvin [6]. Consider a binary mixture of two materials A and B with physical properties z_a and z_b . If the variable of interest, z , averages linearly then the property of a mixture of the materials, z_{avg} , is a linear average weighted by the proportions t_a and t_b . Korvin considered binary mixtures, but with no requirement that the property average linearly. Instead of the requirement for linearity, if the property obeys eight physical constraints the binary mixture must follow an equation with the form:

$$z_{avg} = \begin{cases} (t_a z_a^p + t_b z_b^p)^{1/p} & p \neq 0 \\ (z_a^{t_a} z_b^{t_b}) & p = 0 \end{cases} \quad (14.2)$$

where this equation is the linear average for $p = 1$, the harmonic average for $p = -1$ and the geometric average for $p = 0$. The reader is referred to Korvin [6] for the physical constraints to ensure validity of this mixing framework.

14.2.2 Re-Expression Framework

In the context of Tukey's power law re-expression and Korvin's mixing framework, a framework is proposed here to re-express a nonlinear metallurgical variable Z in terms of a linear variable, Y . This is done using a re-expression transform (such as a power law transform):

$$y = \phi(z) \quad (14.3)$$

The linear variable Y can be averaged, scaled and estimated using standard linear weighted averages. The average nonlinear metallurgical variable is calculated by inverting the transform function. The use of a power transform for the re-expression function ϕ is supported by the work of Korvin [6] although other forms could be used. Consider letting ϕ be Tukey's power transform (Eq. 14.1), and letting $c = 0$ as

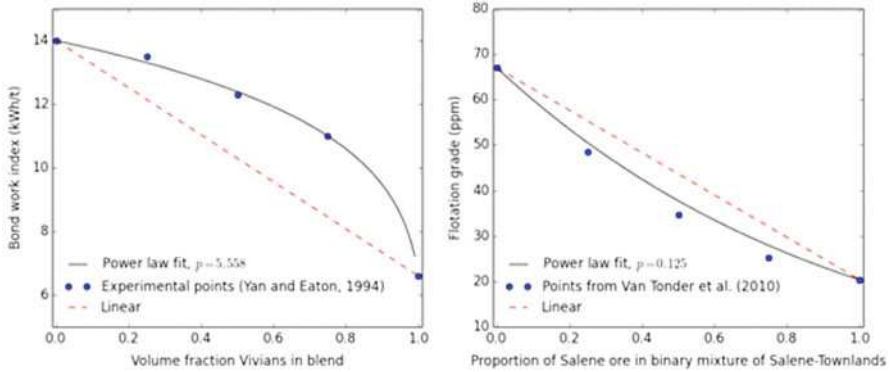


Fig. 14.1 Plot of Bond mill work index for blends (left) using the power law fit to data from Yan and Eaton [1] and a binary marginal from a ternary mixture of flotation grades (right) using a power law fit to data from Van Tonder et al. [3].

most metallurgical variables of interest (rates, work indices) are positively valued. The weighted linear average of Y and the corresponding Z are:

$$y_{\text{avg}} = \begin{cases} \sum_{i=1}^n w_i z_i^p & p \neq 0 \\ \sum_{i=1}^n w_i \log(z_i) & p = 0 \end{cases}, z_{\text{avg}} = \begin{cases} y_{\text{avg}}^{1/4} & p \neq 0 \\ \exp(y_{\text{avg}}) & p = 0 \end{cases} \quad (14.4)$$

where w are the weights applied to each component of the mixture. Tukey's power transform for re-expression is, therefore, equivalent to the general mixing law of Korvin. The weights used, generally volume or mass proportions, should be consistent with how the mixing law was established. An example fit using the re-expression framework to the experimental Bond mill work indices obtained for mixtures of Vivians and Mickey Doolans ores by Yan and Eaton [1] is shown in Fig. 14.1. A binary marginal of a ternary fit to flotation grades of blends using data from Van Tonder et al. [3] is also included. The fit to experimental data in both cases is reasonable; the power law fit to the flotation grades is fit to a ternary mixture although only a binary marginal is shown here.

14.3 DISCUSSION

The power law re-expression framework discussed here is attractive as it is theoretically correct for binary mixtures which obey a set of physical constraints. In other cases, this is an approximation, but a reasonable one in many cases including the Bond mill work index and flotation grade examples shown here (Fig. 14.1).

Experimental data on the metallurgical properties of mixtures are required to fit the re-expression framework. The first step is the identification of rock types in the ore body which will be blended at a scale relevant for processing. To understand and quantify the nature of blending, the ore could be typed by lithology, alteration, fault zones, or even different stockpiles or mineable regions. The choice of rock types will be dictated by the goal of the blending study. The framework developed here is aimed at binary mixtures, but, ternary or higher order mixtures could be used although there is a much greater sampling requirement. The value of information which could be gained from quantifying and modeling the blending relationship will need to be weighed against the time and cost of an extensive mixing study.

Using these rock types, the properties of mixtures can be analyzed. There are a number of methods for the design of experiments with mixtures and modeling the results; the interested reader is referred to Cornell [8]. If the individual rock types are available in their pure forms, a standard simplex lattice design can be used. There are a number of considerations specific to experiments with metallurgical properties. Large masses of the pure rock types are unlikely to be available for blending, particularly in the exploration and scoping phase of a mining project. In this case, the blending compositions tested may be dictated by available material to test. In the lab procedures to test the metallurgical properties of a mixture, the mixing is likely to be perfect. This perfect mixing is unlikely to hold at an industrial scale where ores may be blended by the truck load by mining multiple shovel faces or by the loading of multiple stockpiles. Depending on the scale of the mineral processing operation, the behaviour of the incompletely blended ore may differ from the behaviour expected under perfect blending in a lab. This difference will need to be reconciled by determining where the mine blending operation is on the gradient of batch processing to perfect mixing. This will be specific to each mining and mineral processing operation. Owing to material recycling within a mineral processing operation, blends will naturally arise as multiple ore types are fed to the plant.

The experimentally determined mixing law, which may be reconciled to account for the imperfect blending at the scale of a mining and mineral processing operation may then be fit using a re-expression framework. The power law based re-expression framework presented here is a theoretically attractive model, but many models are available [8]. Decisions on how to optimally process multiple rock types which may exhibit synergistic or antagonistic blending behaviour can be made using the modeled blending data.

Once the metallurgical variable is re-expressed as a linear variable, it may be spatially estimated using standard linear geostatistical algorithms such as kriging. The metallurgical data may be at a scale different from the scale of interest for modeling; the re-expressed variable can be scaled using volume-variance relationships which require linearity. After modeling the transformed linear variable, the results can be back-transformed to the original metallurgical variable. For ternary (such as the flotation grade fit here) and higher order mixtures, this may need to be done stochastically as the inversion is likely to be non-unique.

REFERENCES

1. Yan, D. and Eaton, R.: Breakage properties of ore blends. *Minerals Engineering* 7(23), 185–199 (1994)
2. Conteras, A.: Effect of ore blends on flotation of copper and molybdenum in porphyry ores. MSc thesis, University of Queensland (2013)
3. Van Tonder, E., Deglon, D.A. and Napier-Munn, T.J.: The effect of ore blends on the mineral processing of platinum ores. *Minerals Engineering* 23(8), 621–626 (2010)
4. Tukey, J.W.: On the comparative anatomy of transformations. *The Annals of Mathematical Statistics* 28(3), 602–632 (1957)
5. Tukey, J.W.: Exploratory data analysis. Addison-Wesley, Reading, PA (1977)
6. Korvin, G.: Axiomatic characterization of the general mixture rule. *Geoexploration* 19(4), 267–276 (1982)
7. Box, G.E. and Cox, D.R.: An analysis of transformations. *Journal of the Royal Statistical Society Series B (Methodological)* 26(2), 211–252 (1964)
8. Cornell, J.A.: Experiments with mixtures: designs, models, and the analysis of mixture data. Wiley, New York, NY (2011)

Chapter 15

Parameter Estimation and Sensitivity Analysis in Clastic Sedimentation Modeling

A. Acevedo, A. Khramtsov, H.A. Madhoo, L. Noomee,
D. Tetzlaff, and P. Burgess

Abstract During numeric modeling of clastic sedimentation, the modeler is faced with assigning values to several parameters that are difficult to estimate. However, proper handling of uncertainties translates to valuable uncertainty information in the output. To illustrate this process, we used a model called GPM (Geologic Process Modeler) to reproduce a deepwater turbidite system from the Campos Basin, offshore Brazil, for which good-quality 3D seismic was available. In the first stage we used a paleo-basin floor surface reconstructed from seismic and placed sediment sources at locations indicated by the inferred paleogeography. In the second stage, we varied several input parameters within a range of reasonable values while comparing results to observed data. The results of all plausible models, considered jointly, provide a picture of the uncertainty of the occurrence of observed features and sediment properties.

Keywords Stratigraphic Forward Modeling • Geologic Process Modeling • Sensitivity Analysis • Uncertainty

15.1 INTRODUCTION

In recent years geology has become increasingly quantitative. Mathematical methods and software for structural reconstruction, sediment compaction, organic matter maturation, and hydrocarbon migration are commonplace in hydrocarbon exploration, while geostatistics, reservoir flow modeling, and history matching have become essential in production. A recent addition to the geologist's set of quantitative tools has been geologic process modeling [1, 2]. This technique models

A. Acevedo • A. Khramtsov • H.A. Madhoo • L. Noomee
Schlumberger Information Solutions, Gatwick, West Sussex RH6 0NZ, U.K.

D. Tetzlaff (✉)
Schlumberger Information Solutions, Houston, TX, U.S.A.
e-mail: dtetzlaff@slb.com

P. Burgess
Royal Holloway Univ. of London, Egham Hill TW20 0EX, UK

the processes of erosion, transport and deposition of clastic sediments, as well as carbonate growth and redistribution on the basis of deterministic physical principles. This type of modeling requires several parameters, which may not be readily available from present-day data (sediment input, sediment diffusion and transport coefficients, and primary sediment properties). These parameters must be adjusted in an iterative process giving rise to more than one plausible model. The set of plausible results is used for statistical inference of model results, providing a measure of uncertainty in reservoir geometry and petrophysical parameters.

15.2 MODEL DESCRIPTION

For the work described here, an experimental package called GPM was used. It is implemented as a plugin within a major geologic modeling package. It is based on modeling principles that have been originally used in research models in the 1980’s [3]. Initially the user must specify the general basin setting by providing an approximate, location of sources, sediment types, and sea-level curve (Fig. 15.1).

The user may then select a number of processes to model, which may be run concurrently. Each process may require a several parameters. The simplest of these processes is diffusion, which is used to represent processes that occur at a sub-cell scale, such as minor slumps, soil creep, and biological activity. A more complex mechanism to model is free-surface water flow and the corresponding sediment transport. The GPM model provides for simulating both steady flow (as in rivers at normal stage) and unsteady flow (as in turbidity currents or river floods), as well as erosion, transport and deposition of sediment by flowing water. Carbonate growth is modeled using growth rates that are dependent on light, temperature and the energy of the environment, while modeling the destruction and redistribution of carbonates using the modules for flow and sediment transport. This approach enables

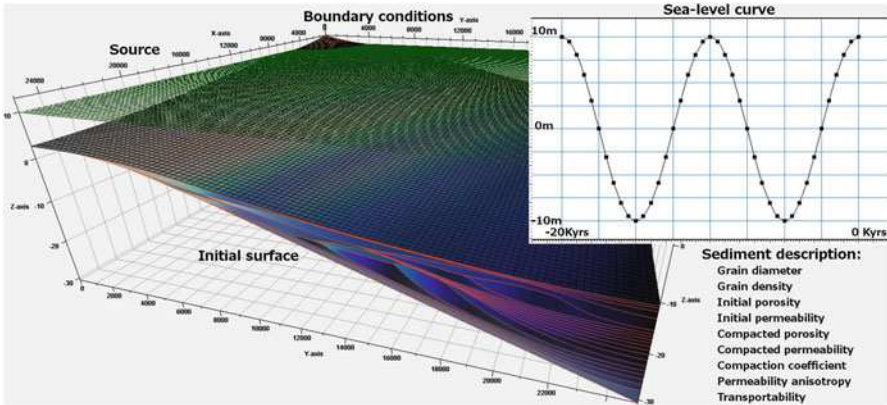


Fig. 15.1 GPM basic input.

representing in full 3D much of the complexity that is inherent in carbonate systems [4]. Tectonics can be represented as a vertical movement of the basement which raises or lowers the overlying sediments. Compaction is represented by an algorithm based on a simple load assumption. GPM is often used in conjunction with other quantitative tools for handling post depositional processes such as diagenesis and dissolution, complex structural deformation, and heat flow and hydrocarbon migration and maturation. GPM provides a detailed description of the primary depositional geometries and properties that these packages require.

15.3 APPLICATION

The case history described here involves a deepwater turbidite system from the Campos Basin, offshore Brazil, for which good quality 3D seismic was available. In this province, turbidite systems have been proven to be major reservoirs. In the first modeling stage, a paleo-basin floor surface was reconstructed from seismic and sediment sources were placed at locations indicated by the inferred paleo-bathymetry (Fig. 15.2). After adjusting the amount and type of sediment carried by turbidity currents, a reasonable match with observed seismic was obtained in terms of sequence architecture. This was assumed to represent a “base case”:

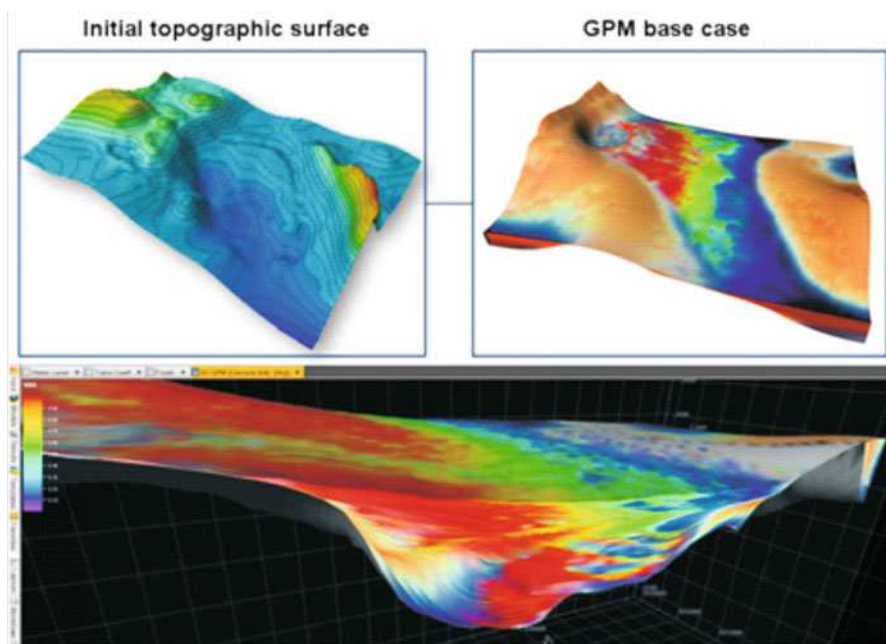


Fig. 15.2 Initial basin floor surface and base-case scenario of basin fill. Sands in the deep part of the basin represent basin floor fans deposited by turbidity currents originating in the upper end of the basin (upper left of the figure).

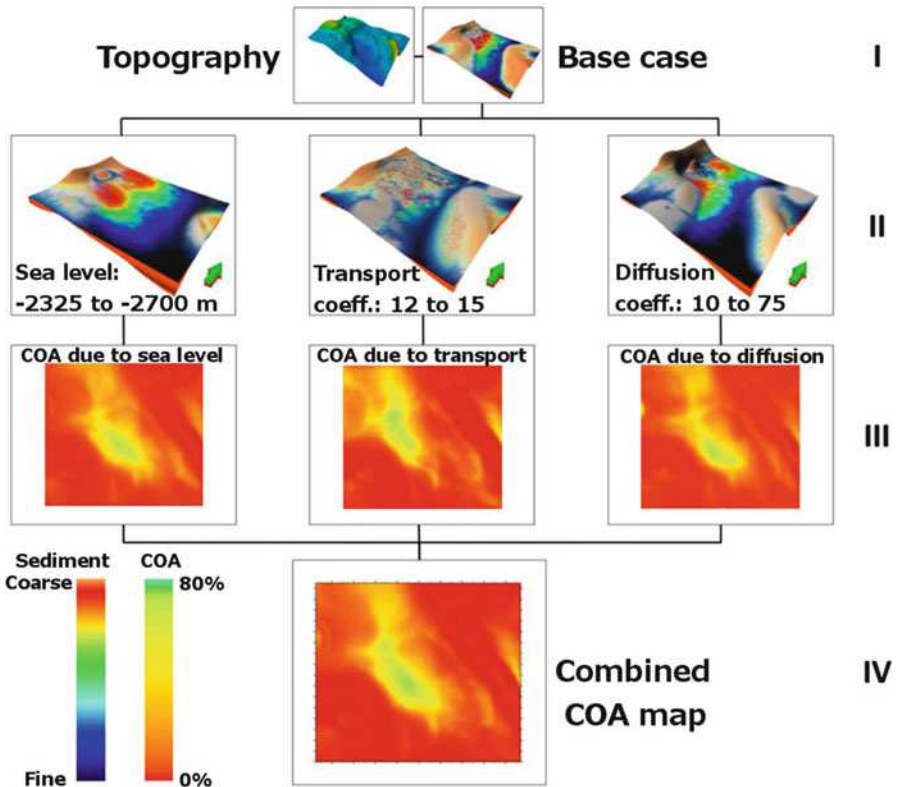


Fig. 15.3 Schematic view of workflow in which input parameters that have been varied within their ranges of uncertainty and final results combined in a probabilistic chance-of-adequacy map showing probability of success as a percentage. I. paleo-basin floor map from seismic plus base case result of GPM simulation, II. Examples of uncertainty ranges by Sea Level, Transport and Diffusion Coefficients, III. Respective Chance of Adequacy (COA) maps for each parameter, and IV. Combination of individual COA maps producing an overall COA for reservoir facies. Note: I. & II. Refer to sediment color bar; III. & IV. Refer to COA color bar.

In the second stage, sea level, transport coefficient (which determines the ease of sediment transport by water) and diffusion coefficient (which affects sediment transport due to slumps, creep, and wave action) were varied within geological ranges of uncertainty. As long as the resulting model was compatible with observed data, the varied values were considered plausible.

The result of each plausible model was individually converted to a Chance of Adequacy (COA) map to qualitatively estimate the merit of each output. For example a sand prone areas is associated with better reservoir quality, and hence is assigned a high COA (yellow to green Fig. 15.3). Although the detailed features of each realization are not certain, the joint set of all plausible models provided an estimate of the COA for reservoir presence and inferred quality in this case. Furthermore, similar estimates can provide insight into possible occurrence of

source and seal facies. “Adequacy” in this case was defined as a reservoir thickness and quality exceeding a defined industry average minimum. The workflow is briefly outlined in Fig. 15.3.

15.4 CONCLUSIONS

GPM and similar stratigraphic forward modeling tools are only a part of a growing cluster of quantitative applications used in hydrocarbon exploration and production. The results of the examples mentioned in this paper (as well as other case histories not detailed here) show that modeling of sedimentary processes is ripe for quantitative treatment. This technology provides a quantitative framework that may help either confirm or discard preexisting conceptual models. It also provides a means to quantify uncertainty in situations that were heretofore left largely to intuition, such as the chances of success under varying sea-level change conditions.

GPM does require some a priori knowledge or assumptions about paleogeographic conditions and thus is most useful if some knowledge of the basin is already available. The technology is readily applicable in exploration and early production situations, in which alternative hypotheses may have to be selected, or existing conceptual models may need quantitative refinement. At the reservoir scale, GPM can predict the general architecture, geometry and connectivity of permeable beds. Its results may be useful as training images for geostatistical methods in areas where detailed analogs may not be available.

ACKNOWLEDGEMENTS The authors would like to thank Schlumberger for permission to publish this paper and to WesternGeco for providing the seismic data. We thank also Lars Sonneland and Per Salomonsen of Schlumberger Information Solutions, Stavanger, Norway, for their support in developing the technology described herein.

REFERENCES

1. Merriam, D.F. and Davis, J.C.: *Geologic modeling and simulation, sedimentary systems*. Kluwer Academic/Plenum Publishers, New York (2001)
2. Tetzlaff, D.M. and Priddy, G.: Sedimentary Process Modeling: From Academia to Industry. In: *Geologic Modeling and Simulation, Sedimentary Systems* (Ed. by D.F. Merriam & J.C. Davis), Kluwer Academic/Plenum Publishers, New York (2001)
3. Tetzlaff, D.M. and Harbaugh, J.W.: *Computer Simulation of Clastic Sedimentary Processes*, van Nostrand – Reinhold series in Mathematical Geology, Plenum Publishing Co. (1989)
4. Burgess, P.M. and Pollitt, D.A.: The origins of shallow-water carbonate lithofacies thickness distributions: one-dimensional forward modelling of relative sea-level and production rate control. *Sedimentology*, 59, 57–80 (2012)

Chapter 16

Study on Chaotic Time Series and Its Application on Forecasting Water Inrush in Mines

Yang Yongguo, Chen Yuhua, and Cheng Qiuming

Abstract The paper focuses on chaotic time series analysis and its applications, consisting of three parts: reconstructed phase space; identification of the chaotic features of a time series, and time series prediction based on the phase space reconstructed. Based on the main shaft water inrush time series of the Wutongzhuang mine in China, a two-month of time delay for reconstruction of phase space could be obtained when calculating using autocorrelation function with an initial value of $1 - 1/e$. Mine water inrush time series model is established by Weighed first-order partial domain forecast method based on the reconstruction of phase space, and used for forecast of mine water inrushes. Results show the forecasting with a higher precision.

Keywords Chaotic Time Series • Reconstruction Phase Space • Mine Water Inrush • Forecasting

Y. Yongguo (✉)

School of Resource and Earth Science, Key Laboratory of CBM Resources and Reservoir Formation Process of Ministry of Education, China University of Mining and Technology, Xuzhou, China

Department of Earth and Space Science and Engineering,
Department of Geography, York University, Toronto M3J1 P3, Canada
e-mail: ygyang88@cumt.edu.cn

C. Yuhua

School of Resource and Earth Science, Key Laboratory of CBM Resources and Reservoir Formation Process of Ministry of Education, China University of Mining and Technology, Xuzhou, China

C. Qiuming

Department of Earth and Space Science and Engineering,
Department of Geography, York University, Toronto M3J1 P3, Canada

16.1 INTRODUCTION

As the first and foremost energy source of China, coal plays an irreplaceable role in the national economy for quite a long time. A lot of objective factors could influence the mine water inrush, such as the water contents of the aquifer, the hydraulic pressure, the thickness and strength of the aquifuge, or the faults, the earthquakes, and the human activities [1, 6]. Traditional methods and analysis theories of the time series focus on the characteristics of the mine water inrush sequence by set up autoregressive and moving average (ARMA) model of time series in time domain or frequency domain [5]. And their applications are limited. Therefore, using the chaotic theory, which integrates the single determinacy and the randomness, will be more suitable for modeling the mine water inrush [8]. The application of the chaotic time series include three sections: reconstruction phase space, chaotic identification of the time series, and prediction of time series based on the reconstruction phase space.

16.2 STUDY AREA AND DATA SOURCE

The Wutongzhuang mine field is located in the south of Fengfeng mine in Handan city, Heibei province in China. Geologically, there exist four stratum, including Ordovician, Carboniferous, Permian and Cenozoic formations. Data to be used in this research include the monthly average water inrush recorded in the main shaft at Wutongzhuang mine, and denotes as $Q(t)$, here $t=1, 2, \dots, 44$ is time. The change tendency of the main shaft water inrush discharge could be seen (Fig.16.1).

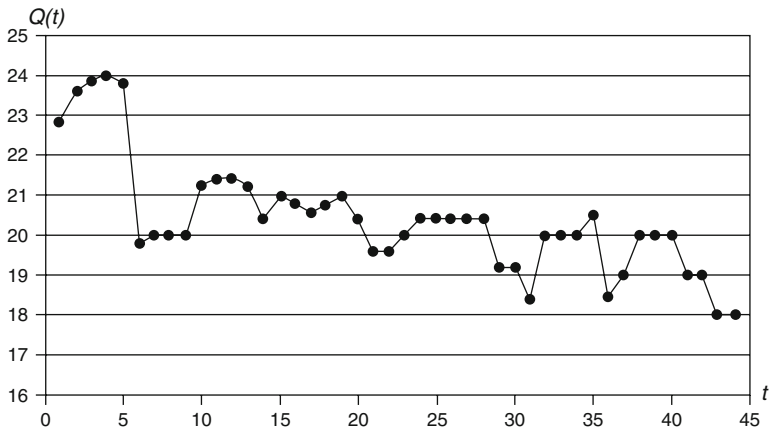


Fig. 16.1 The main shaft water inrush changes time series $Q(t)(\text{m}^3/\text{min})$.

16.3 METHODOLOGY AND APPLICATION

16.3.1 Reconstruction of Phase Space of the Time Series

According to the phase space reconstruction theory, a multi-dimensional phase space Y could be established for a time series $x(t_i)$ ($i = 1, 2, \dots, N$), using a certain time delay τ and a certain embedded dimension m . For an observed time series $x(t_i)$, if the embedded dimension is m , then the phase space vector $y(t_i)$ ($i = 1, 2, \dots, n$), built by the phase space points number $n = N - (m - 1)\tau$ will be:

$$Y(t_i) = (x(t_i), x(t_i + \tau), \dots, x(t_i + (m - 1)\tau)) \quad (i = 1, 2, \dots, n) \quad (16.1)$$

So, it is needed to properly select the time delay τ and the embedded dimension m for phase space reconstruction. For a specific time series $x(t_1), x(t_2), \dots, x(t_N)$ of the variable $X(t)$ its autocorrelation function is denoted as:

$$C(\tau) = \frac{1}{N - \tau} \frac{\sum_{i=1}^{N-\tau} (x(t_i) - \mu)(x(t_{i+1}) - \mu)}{\sigma} \quad (16.2)$$

where τ is time delay, μ and σ are the average value and the standard deviation of the time series, respectively. The time τ determined according to the tested results can also be used as the time delay for phase space reconstruction when the value of the autocorrelation function decreases down to $1-1/e$ of the initial value [3]. By calculating the time delay of mine water inrush time series should be two months.

16.3.2 Mine Water Inrush Data Chaos Recognition

If there is a chaotic time series $x(t_i)$ ($i = 1, 2, \dots, N$) whose embedding dimension is m , time delay is τ , then reconstructed phase space is (16.1). From an initial point $Y(t_0)$, given its distance to the nearest neighbor point $Y_0(t_0)$, L_0 . Tracking the evolution of these two points until the time $= t_1$, maintaining $Y(t_1)$, if the distance surpass a pre-fixed number $\varepsilon > 0$, $L'_0 = |Y(t_1) - Y_0(t_1)| > \varepsilon$, and finding another point $Y_1(t_1)$ close to $Y(t)$, making $L_1 = |Y(t_1) - Y_1(t_1)| < \varepsilon$, and the angle between them is as small as possible. Keeping on the procedure until $Y(t)$ reaches to the terminate point N , then the total iterative number is M , then the maximal Lyapunov index is:

$$\lambda = \frac{1}{t_M - t_0} \sum_{i=0}^M \ln \frac{L_i}{L_0} \quad (16.3)$$

The Lyapunov index calculated using Wolf method are all positive and the maximal is $\lambda = 0.1396$, so the main shaft water inrush time series is chaotic.

Table 16.1 Comparison of observed data with the forecasted results (m³/min)

Time	Observed Value	Forecasted Value	Relative Error(%)
31	18.4	20.24	10.00
32	20	20.43	2.14
33	20	20.42	2.11
34	20	20.58	2.91
35	20.5	20.61	0.52
36	18.5	20.43	10.43
37	19	19.99	5.19
38	20	19.92	0.42
39	20	20.53	2.64
40	20	20.55	2.76
41	19	20.52	8.02
42	19	20.51	7.96
43	18	20.48	13.77
44	18	20.31	12.83

16.3.3 *Wutongzhuang Mine Water Inrush Data Sequence Forecast*

Upon the above calculations, the maximal Lyapunov indexes in Wutongzhuang mine are positive, so the chaotic time series method can be used for prediction [3]. Weighed Zero-order partial domain method is better than Zero-order partial domain method; Weighed First-order partial domain method is better than Weighed Zero-order partial domain method [2]. Therefore, the Weighed First- order partial domain method will be used for forecasting in this paper. The forecasting model was established by using the shaft water inrush data from No. 1 to No. 30. Then forecasting effects were tested using the latter fourteen data. The results are listed in Table 16.1. From Table 16.1 it can be found that the relative errors are less than 14%, and most cases the relative errors are less than 5%. Results show the forecasting with a higher precision.

16.4 CONCLUSIONS

Chaotic characteristics of mine water inrush time series calculated by G-P correlation integral method show that the correlative dimension of Wutongzhuang main shaft water inrush time series is 2 months. The maximal Lyapunov index was obtained by Wolf method as 0.1396 implying chaotic characteristics exist in Wutongzhuang main shaft water inrush time series. Mine water inrush time series forecasting model is established by weighed first-order partial domain forecast method based on reconstruction phase space for forecasting inrush water.

ACKNOWLEDGEMENTS This work was supported by a grant awarded by National Natural Science Foundation of China (NSFC) grant (40472146, 41372342).

REFERENCES

1. Ashis, B., Ramani, R.V. and Natarajan, R.: Time Series Analysis of Coal Mine Accident Experience. *Journal of Safety Research*, 25, 229–234 (1994)
2. Istvan, B., Lucien, D., Antal, S. and Fereng, S.: Stochastic forecasting of mine water inrushes. *Advances in Water Resources*, 3, 3–8 (1980)
3. Lú, J.H., Lu, J.A. and Chen, S.H.: Chaotic time series analysis and application. Wuhan University Press, Wuhan, p 237 (In Chinese) (2002)
4. Weng, Y.C., Chang, N.B. and Lee, T.Y.: Nonlinear time series analysis of ground-level ozone dynamics in Southern Taiwan. *Journal of Environmental Management*, 87, 405–414 (2008)
5. Yang, Yong-guo, Yuan, Jian-fei and Chen Suo-zhong: R/S Analysis and its Application in the forecast of mine inflows. *J. China Univ. of Mining & Tech.* (English Edition) 16(4), 425–428 (2006)
6. Zhang, J.C.: Investigations of water inrushes from aquifers under coal seams. *International Journal of Rock Mechanics & Mining Sciences*, 42, 350–360 (2005)

Chapter 17

p-T Computation Schemes for Thermodynamic Properties of Pure Water: A Comparative Evaluation of IAPWS-95 and IAPWS-IF97 Formulations

Mahendra P. Verma

Abstract Computer codes, *SteamTables* and *SteamTablesIF97* in VB.NET were written for the thermodynamic properties of pure water, using the formulations: *IAPWS-95 for scientific use* and *IAPWS-IF97 for industrial use*, respectively. The execution time for *IAPWS-IF97* is in general 70 times less than that for *IAPWS-95*. The p and T accuracies for the both the formulations are within $T = \pm 0.1$ K and $p = \pm 0.001$ MPa. However, the steam tables contain thermodynamic inconsistencies, associated with the measurement errors of C_p near the liquid-vapor separation boundary. This causes limitation in the steam transport algorithm in a pipeline.

Keywords Steam Tables • *IAPWS-95* • *IAPWS-IF97* • VB.NET • Steam Transport

17.1 INTRODUCTION

Wagner and Prufß [1] presented a comprehensive study on the evolution of formulations for the thermodynamic properties of pure water from the first formulation (IFC-68) to the most accepted IAPWS-95 formulation. Presently, the computation schemes: *IAPWS-95 for scientific use* and *IAPWS-IF97 for industrial use* are widely accepted and have sufficient accuracy, high computing speed, numerical consistency and continuous presentation of yielded thermodynamic properties [2]. However, there is still a requirement of higher computation speed for the calculation of water thermodynamic properties in designing the steam power plant [3] and transporting steam to geothermal power plants [4], in which at least 10^6 - 10^7 calls on the subroutines for the steam thermodynamic properties are required as per job. [4] developed a linear interpolation on the p-T surface grid to accelerate the

M.P. Verma (✉)

Geoterminia, Instituto de Investigaciones Electricas, Reforma 113, Col. Palmira, Cuernavaca, Morelos 62490, Mexico

e-mail: Mahendra@iie.org.mx

calculation of the thermodynamic properties of water using the *IAPWS-95* formulation. Similarly, [3] used the *IAPWS-IF97* formulation for a spline interpolation scheme on the p-T surface grid. Thus this paper presents a comparative evaluation of both *IAPWS-95* and *IAPWS-IF97* formulations for the accuracy in the calculated properties and computational speed. Similarly, it states the reasons of the measurement errors of C_p near the liquid-vapor separation boundary.

17.2 IAPWS-95 AND IAPWS-IF97 FORMULATIONS

Using the *IAPWS-95* formulation, [5] wrote an assembly (DLL- dynamic link library), *SteamTables* in Visual Basic-6 (VB6) for 23 thermodynamic properties of water as a function of p and T. VB6 has the DLL-hell problem [6]. In .NET framework the problem is resolved with side-by-side installation of two or more versions of the assembly. Thus the present computer codes, *SteamTables-95* and *SteamTables-IF97* were written in VB.NET. Fig. 17.1 shows the comparison of execution time for the calculation of thermodynamic properties at each point. The calculation along the liquid-vapor separation boundary as function of T (Fig. 17.1a) is faster than that as function of p (Fig. 17.1b). In general, the *IAPWS-IF97* is 70 times faster than *IAPWS-95*; however, there are certain points along the critical isochor where the *IAPWS-IF97* is slower. Along the separation boundary both the formulations are accurate and consistent within $T = \pm 0.1$ K and $p = \pm 0.001$ MPa. [7, 8] pointed out the multiple values in the behavior of state functions like internal energy, enthalpy, entropy, etc., which is violation of basic laws of thermodynamics. Consequently, [9] found difficulties in solving the steam transport equations in a pipeline.

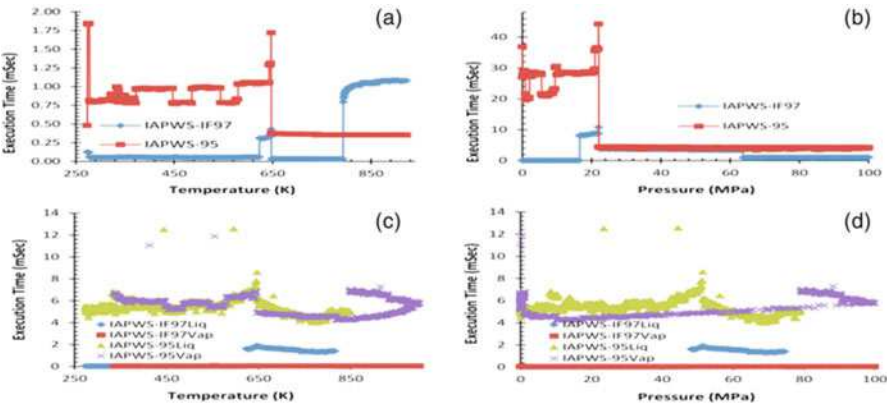


Fig. 17.1 Execution time for *IAPWS-97* and *IAPWS-IF97* formulations: (a) and (b) along the liquid-vapor separation boundary, and (c) and (d) for a given p-T in the liquid or vapor region.

17.3 EXPERIMENTAL DETERMINATION OF C_p

The values of state functions like internal energy, enthalpy, entropy, etc. are calculated from the pVT characteristics and heat capacity data of water [9]. Therefore, an analysis of the experimental data of C_p is presented here. Fig. 17.2 shows the behavior of experimental data of C_p with T at a specified pressure. The liquid-vapor separation boundary is considered as the saturation curve or critical isochor. The C_p in the compressed liquid region increases with T , while it decreases with p . The variation of C_p in the liquid region for the whole range of p and T up to 550 K is insignificant; however, there is a drastic increase in C_p above $T=550$ K, and multiple values occur just near the boundary with the vapor phase. Most of the experimental values of C_p were measured in 1956-1970 (see the database of IAPWS[2]). The experimental details for their measurements are not clearly stated in the literature; therefore, it is difficult to state precisely the reasons for such inconsistent values. The formation of vapor in the experimental setup had caused the peak in the C_p measurements (Fig. 17.2) near the separation boundary [9]. The vapor formation is associated with kinetic processes. For example, the ground surface temperatures are quite lower than that of the water boiling point at 0.1 MPa (1 atm). This means that the water at the earth surface is in the compressed liquid region, and there should not be any vapor in the atmosphere according to the thermodynamic equilibrium. Thus, the formation of atmospheric vapor is a consequence of kinetic processes. It also happens in the experimental setups for the determination of C_p .

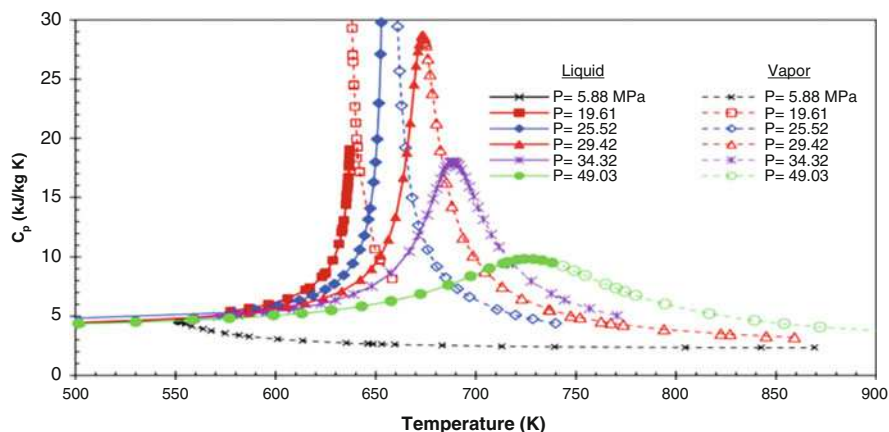


Fig. 17.2 Experimental data for the heat capacity of water at constant pressure (C_p). For a given pressure (p), the values are divided in two groups (a) for the compressed liquid region, shown by solid symbols and solid lines; and (b) for the superheated steam region, shown by empty symbols and dashed lines [9].

17.4 CONCLUSIONS

Both the formulations, *IAPWS-95 for scientific use and IAPWS-IF97 for industrial use* are sufficiently accurate. However, the thermodynamic inconsistency in the steam tables as a consequence of incorrect measurements of C_p near the liquid-vapor separation boundary is a limiting factor in the algorithm of steam transport in a pipeline. In general, the *IAPWS-IF97* is 70 times faster than *IAPWS-95*; however, there are certain points along the critical isochor where the *IAPWS-IF97* is slower. Along the separation boundary both the formulations are accurate and consistent within $T = \pm 0.1$ K and $p = \pm 0.001$ MPa.

ACKNOWLEDGEMENTS This work was supported by the grant “FONDO SECTORIAL CONACYT-SENER SUSTENTABILIDAD ENERGÉTICA IIE-CEMIE-GEO-P14”.

REFERENCES

1. Wagner, W. and Pruß, A.: The IAPWS for the thermodynamic properties of ordinary water substance for general and scientific use. *J. Phys. Chem. Ref.* 31, 387–535 (2002)
2. IAPWS: Revised release on the IAPWS industrial formulation 1997 for the thermodynamic properties of water and steam, <http://www.iapws.org>
3. Wang, X.D., An, B., Duan, Y.Y., Wang, Z.X. and Lee, D.J.: Efficient and accurate computation scheme of p-T thermodynamic properties of water and steam. *J. Taiwan Inst. Chem. Eng.* 43, 845–851 (2012)
4. Verma, M.P.: Steam Tables Grid: an ActiveX control for thermodynamic properties of pure water. *Comput. Geosci.* 37, 582–587 (2011)
5. Verma, M.P.: Steam tables for pure water as an ActiveX component in Visual Basic 6.0. *Comput. Geosci.* 29, 1155–1163 (2003)
6. Venket: .NET program execution, <http://csharp-video-tutorials.blogspot.co.uk/2012/07/net-program-execution-part-1.html>
7. Verma, M.P.: Thermodynamics, equations of state and experimental data—A review. *J. Eng. App. Sci.*, 1, 35–42 (2006)
8. Verma, M.P.: Steam Tables: an approach of multiple variable sets. *Comput. Geosci.* 35, 2145–2150 (2011)
9. Verma, M.P.: Steam transport simulation in a geothermal pipeline network constrained by internally consistent thermodynamic properties of water, *Rev. Mex. Cien. Geol.* 30, 210–221 (2013)

Chapter 18

Statistical Lobe Hierarchy Constraint in Surface-based Reservoir Modeling

Siyao Xu and Tapan Mukerji

Abstract Surface-based geomodeling produces realistic and complex stratigraphy of hydrocarbon reservoirs by imitating the underlying physics with depositional rules. However, conventional rules utilized in surface-based models are designed based on qualitative understandings, which are normally implemented with a large number of tuning parameters. The increment of tuning parameters increases workloads in model conditioning and history matching. Moreover, there is no quantitative criterion to validate reproduction of the qualitative rules in model realizations. This work aims to introduce a set of simple random walk based depositional rules for lobate environments such that the number of empirical coefficients and parameters are minimized while the realism of the model is maintained. A quantitative characterization of the qualitative concept of lobe stacking pattern is also defined based on hierarchical clustering analysis. Demonstrations show that realizations of the new model were hierarchically similar to the input lobe sequence.

Keywords Surface-Based Modeling • Random Walk • Hierarchical Clustering Analysis

18.1 INTRODUCTION

Surface-based modeling method is applied to model reservoirs where complex geometries and stratigraphy are observed. The basic idea of surface-based modeling is to imitate the physical depositional process with conceptual rules that are normally obtained from understandings about depositional processes. In most surface-based modeling algorithms, only conceptual depositional rules are implemented because of the lack of precise quantitative measurements on the intermediate conditions of the geological dynamic processes. Generally, the model is constructed based on a sequential forward workflow (Fig. 18.1). In the

S. Xu

Earth, Energy and Environmental Sciences, Stanford University, Stanford, CA, USA

T. Mukerji (✉)

Energy Resource Engineering and Geophysics, Stanford University, Stanford, CA, USA

e-mail: mukerji@stanford.edu

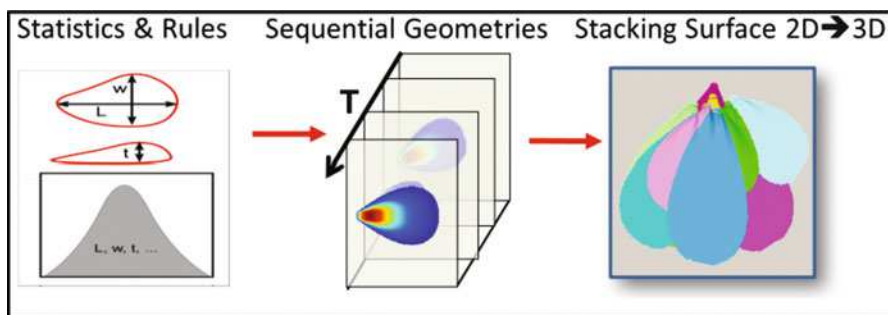


Fig. 18.1 The surface-based modeling workflow generates a sequence of geobodies by sampling geometries from prior statistics. Location of geobodies are determined by depositional rules. A 3D model is obtained by stacking all geobodies.

first step, the overall shape of geobodies in a depositional environment is represented by a shape template, which is controlled by parameters with geological interpretations, such as lobe length or width. Statistics of the geometric parameters are obtained from geological knowledge. A series of geobodies are generated sequentially with geometric parameters sampled from the input statistics. Locations of geobodies are determined based on conceptual depositional rules such as compensational stacking. The current topography is updated by adding the latest geobody onto the current topography, which is then used as topography for the next step. This procedure is repeated until a predefined criterion, such as a top surface or a volume from the seismic survey, is satisfied. The depositional rules are qualitative interpretations from geological surveys, which are difficult to quantify in most problems, linear assumptions are the most frequently starting points to utilize the rules in surface-based models. As a typical example of conceptual rules, the lobe location is determined using an artificial two-dimensional likelihood function covering the whole modeling grid. A two-dimensional likelihood function consists of three conceptual components. The first component accounts for the interpretation that a lobe is more likely to occur in the same vicinity as the basin source (Fig. 18.2 a). Likelihoods of the source components are modeled by a negative linear relationship to the distance from every cell to an assigned basin source. The second component assumes that the location of a new lobe tends to be proximate to the previous lobe (Fig. 18.2 b). Similarly, likelihoods of the previous lobe component are modeled by a negative linear relationship to the distance from every cell to the previous lobe source. The last component, or the compensational stacking (Fig. 18.2 c) rule, states that sediments tend to be deposited in regions with low relief. Likelihoods of the compensational rules are negatively correlated to the surface relief. We model the final two-dimensional likelihood function as a weighted mean of the three components (Fig. 18.2 d), representing the relative likelihood of a pixel to be the next lobe location. Finally, the location of a lobe is sampled from the two-dimensional likelihood function. The rule involves a large number of tuning parameters. This rule creates difficulties for conditioning surface-based models and for the application of surface-based models in history matching.

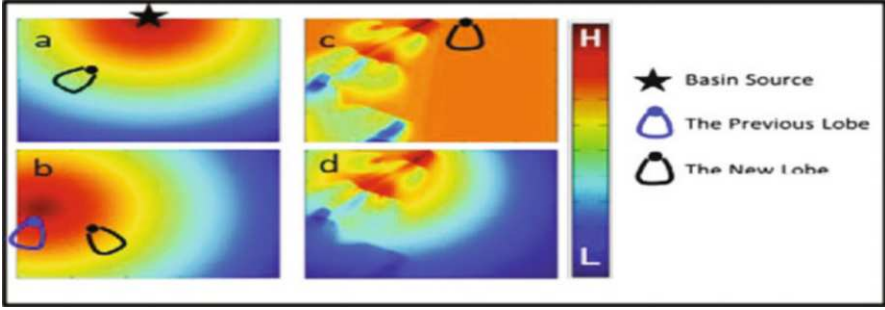


Fig. 18.2 The lobe location is determined by an artificial likelihood function over the modeling grid, which is a weighted mean of three conceptual components. The rule involves a relatively large number of parameters, which is improper for history matching. (a) The basin source component. (b) The previous lobe component. (c) The compensational tacking component. (d) The weighted mean lobe location likelihood function.

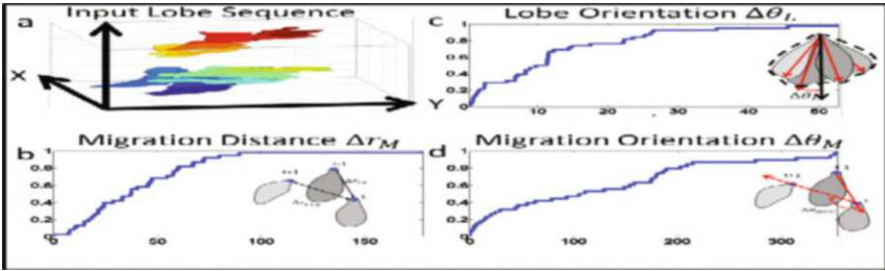


Fig. 18.3 The lobe location is determined by an artificial likelihood function over the modeling grid, which is a weighted mean of three conceptual components. The rule involves a relatively large number of parameters, which is improper for history matching. (a) The basin source component. (b) The previous lobe component. (c) The compensational stacking component. (d) The weighted mean lobe location likelihood function.

18.2 METHODOLOGY

18.2.1 The Random Walk Lobe Migration Rule

A correlated random walk (CRW)-based lobe migration rule is proposed based on the assumption of directional persistent behavior of lobe migration. This rule requires a prior lobe migration sequence to be characterized as a correlated random sequence. A sediment flow event tends to follow the channel through which the previous flow went, such that lobes tend to migrate following previous orientation. A lobe migration sequence (Fig. 18.3 a) is characterized by three parameters: migration distance, migration shifting angle and lobe orientation, which can be measured from analogues or derived from reasonably designed geomorphic experiments. The migration distance Δr from the current lobe to the next is measured as

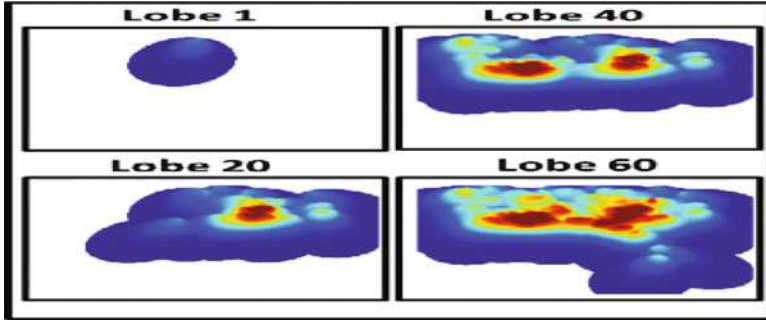


Fig. 18.4 Simulation results of a lobe migration sequence. Realistic spatial-temporal lobe clusters are produced

the stepwise lobe migration distance (Fig. 18.3 b). A migration shifting angle, $\Delta\theta_{MPP}$, is the angle between the previous migration direction and the new migration direction (Fig. 18.3 d). Lobe orientation is defined as the unit vector from lobe proximal point to the geometric centroid of a lobe. Instead of measuring it relative to the previous lobe orientation, the lobe orientation shifting angle is measured relative to the interpreted overall basin flow orientation (Fig. 18.3 c), defined by the unit vector from the basin source point to the geometric centroid of the basin. All the measurements of a lobe migration pattern are in the two-dimensional plain. However, the lower relief location is considered in the determination of lobe migration shifting angle. This strategy results in three empirical cumulative distribution functions, which are input to the surface-based lobe model. The simulation produces realistic lobe clusters (Fig. 18.4).

18.2.2 *Reproduction of the Lobe Hierarchy*

The proposed CRW-based rule constrains lobe hierarchies in realizations to the input lobe migration sequence. A distance-based measure is proposed to demonstrate the reproduction of lobe hierarchy. The hierarchy of a lobe migration sequence is quantified by a dendrogram (Fig. 18.5 b), which is explained in [1]. The hierarchical dissimilarity between two lobe migration sequences is quantified by distances between their dendrograms. The cophenetic distance is proposed to be the measure in this work. The cophenetic distance is the height where two leafs in a dendrogram merge into a branch (Fig. 18.5 a). The cumulative distribution function of cophenetic distances calculated between every pairs of leafs of a dendrogram characterizes the spatial-temporal clustering of a lobe migration sequence. Hence, the difference between cophenetic distance cumulative distribution functions of two dendrograms quantifies the hierarchical dissimilarity. Two sets of realizations are generated with respective input lobe sequences, a multidimensional scaling [2] plot demonstrates that realizations with different input lobe sequences are distinguished from the other (Fig. 18.6)

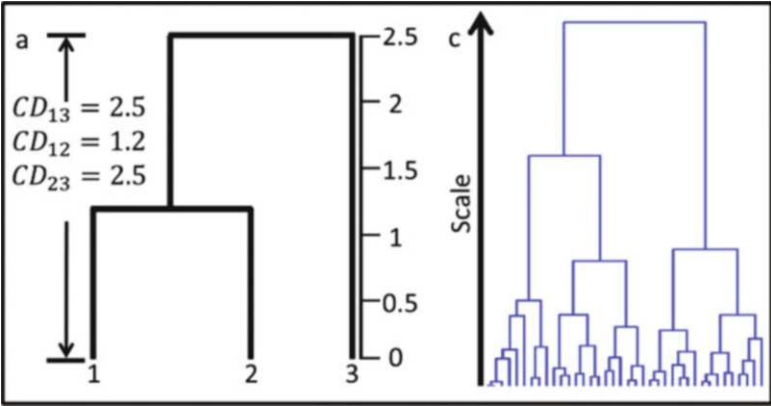


Fig. 18.5 The cophenetic distance is the junction distance between two leaves of a dendrogram, which is generated with hierarchical clustering analysis with a sequential cumulative inter lobe distance. The cumulative distribution function of cophenetic distances between every pair of leaves measures the statistical characteristics of the hierarchy of a lobe sequence. (b) The dendrogram of the lobe sequence in Fig. 18.3.a

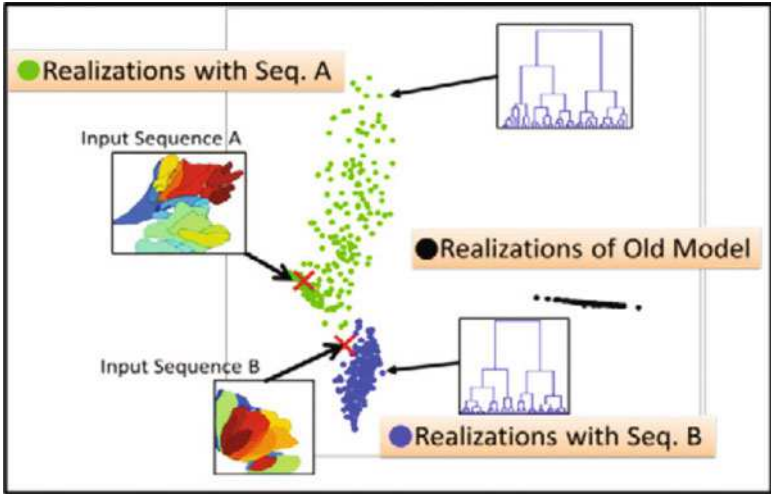


Fig. 18.6 A multidimensional scaling plot of the hierarchies of two sets of surface-based model realizations with two different input lobe migration sequences. Lobe hierarchies are differentiated.

18.3 CONCLUSIONS

The CRW-based lobe migration rule is algorithmically simple and consists of much fewer tuning parameters than the conventional conceptual likelihood function rule. This simplifies the problem of surface-based model conditioning and history

matching. The rule also constrains lobe hierarchies in model realizations to the input lobe sequence, which is demonstrated with a quantitative spatial-temporal lobe hierarchy measure based on the cophenetic distance.

REFERENCES

1. Xu, S.: PhD Dissertation, Integration of Geomorphic Experimental Data in Surface-based Modeling, Stanford University (2014)
2. Scheidt, C. and Caers, J.: A new method for uncertainty quantification using distances and kernel methods: Application to a deep water turbidite reservoir. *SPE J*, 14 (4), 680–692. doi:[10.2118/118740-PA](https://doi.org/10.2118/118740-PA) (2008)

Chapter 19

Transport of Molecular Fluids through Three-Dimensional Porous Media

A. Pazdniakou and P.M. Adler

Abstract The main purpose of this study is to extend the analysis which has been made for the double layer theory (summarized by [1]) to situations where the distance between the solid walls is of the order of several molecular diameters. The intermolecular forces and their influence on fluid structure and dynamics can be taken into account by using the mesoscopic scale models based on the Boltzmann equation. Three types of fluid particles are considered, namely the anions, the cations and the solvent. They possess a finite diameter which should be at least a few lattice units. The collision frequency between particles is increased by the pair correlation function for hard spheres. The lattice Boltzmann model is built in three dimensions with 19 velocities; it involves two relaxation times. Some preliminary applications are illustrated.

Keywords Porous Media • Nanoscale • Transport • Boltzmann Equation

19.1 INTRODUCTION

The determination of fluid flows in confined geometries at the nano-scale is of a large interest not only from a scientific viewpoint, but also for various engineering applications. When the distance between the walls in the confined geometry is of the order of several molecular diameters, the molecular structure of the fluid must be taken into account since the flow is affected by the molecular interactions. It is worth mentioning that the Navier-Stokes equation is still able to describe fluid flow correctly for geometries where the distance between the walls is of the order of a few nano-meters. However, it cannot be extended in order to take into account intermolecular interactions at the nano-scale. The molecular fluid can be simulated by considering the molecules and their interaction forces. Usually, the molecules are modelled by spheres for simplicity; however, the complex shape of real molecules can be also taken into account if necessary. The interaction between

A. Pazdniakou (✉) • P.M. Adler
UPMC Metis, Boîte 105, 4 Place Jussieu, 75252 Paris cedex 05, France
e-mail: al.pazdniakou@gmail.com

two molecules is described by a pair potential. The simplest pair potential is the hard sphere potential. The theoretical model is briefly presented in the following section. Then, some validation is given for the classical plane Poiseuille flow; a preliminary application to a three-dimensional porous medium with a realistic structure is presented.

19.2 THEORETICAL MODEL

The state of a system of N spherical particles of mass m evolving in a volume V at any time is completely described by $6N$ variables ($3N$ variables for particles positions \mathbf{r} and $3N$ variables for particles velocities \mathbf{v}). In other words, the state of the system is a point in a $6N$ -dimensional phase space and the evolution of the system can be described as a phase trajectory. In statistical physics, one can obtain the properties of the system as averages over a phase trajectory or as averages over an ensemble of systems. The description of the system can be obtained in terms of the phase space probability density distribution $f^N(\mathbf{r}^N, \mathbf{v}^N)$ which gives the probability to find the system at time t in a microscopic state described by a phase point $(\mathbf{r}^N, \mathbf{v}^N)$. The evolution of f^N is given by the Boltzmann equation. The fluid mixture is supposed to be composed by three components: anions, cations and solvent. A Boltzmann equation is written for each of them. The delicate part is the collision operator which involves fluid viscosity, electrostatic interactions and hard sphere interactions. In addition a Poisson-Boltzmann equation is written in order to calculate the local electric field. The Boltzmann equations are discretized in space and time on a lattice with 19 velocities; the collision operator is expanded on a basis of Hermite polynomial tensors as indicated by [2]. The classical part of this operator is addressed with two relaxation times.

19.3 SOME RESULTS

In order to check the system, a plane Poiseuille flow was first calculated; the fluid is flowing under the action of an external electrical field. The major physical quantities are the following. The packing density for the water phase is about 0.4 for molecules of diameter 2.8 \AA ; the viscosity is $\mu = 1.002 \text{ mPas}$. The molar density of the solute is $\rho_M = 0.1 \text{ mol/liter}$. The solid walls have a surface charge density $\Sigma = 0.8 \text{ e/nm}^2$. The electric field ΔE is equal to 100 mV . The electron charge e is $-1.602176 \cdot 10^{-19} \text{ C}$ and the dielectric constant $\epsilon_0 = 8.854187 \cdot 10^{-12} \text{ F/m}$. The main lattice units are the length δx equal to $3.4375 \cdot 10^{-11} \text{ m}$, the mass unit δm equal to $3.0150 \cdot 10^{-26} \text{ kg}$, the time unit δt equal to $6.1398 \cdot 10^{-15} \text{ s}$ and the charge unit is the electron charge e equal to $-1.602176 \cdot 10^{-19} \text{ C}$. These units are used to transform the real physical values into lattice values for the actual calculations. The density and

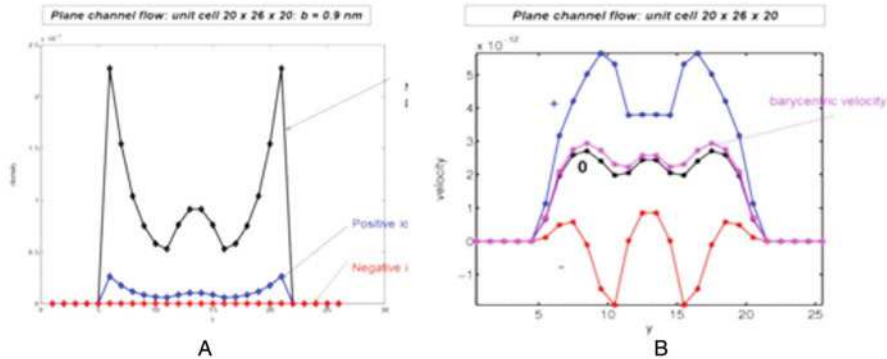


Fig. 19.1 The density (A) and the velocity (B) of the various fluid particles in a plane Poiseuille flow. The horizontal axis is perpendicular to the walls.

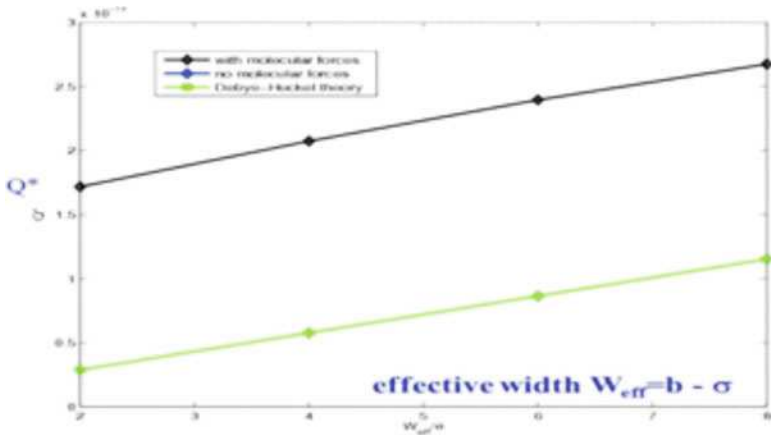


Fig. 19.2 The overall flow rate induced by an electric field as a function of the channel width for the classical double layer theory (green line) and the molecular fluid theory (black line).

the velocity in a plane Poiseuille flow are displayed in Fig. 19.1. The influence of the walls is clearly seen and it extends over distances which correspond to the size of the fluid particles. Of course, the positive ions are attracted by the negatively charged walls. The influence of the channel width was systematically investigated. Of course, the influence is limited to the wall region. The overall flow rate Q^* induced by the electric field was systematically calculated for various channel widths and some results are displayed in Fig. 19.2. It is compared to the flow rate which is predicted by the classical double layer theory as applied in [1]; the influence of the model is seen to be very important.

Calculations were extended to three dimensional porous media and a first example is displayed in Fig.19.3. The overall see pagevelocity is seen to be a linearfunction of the external electric field.

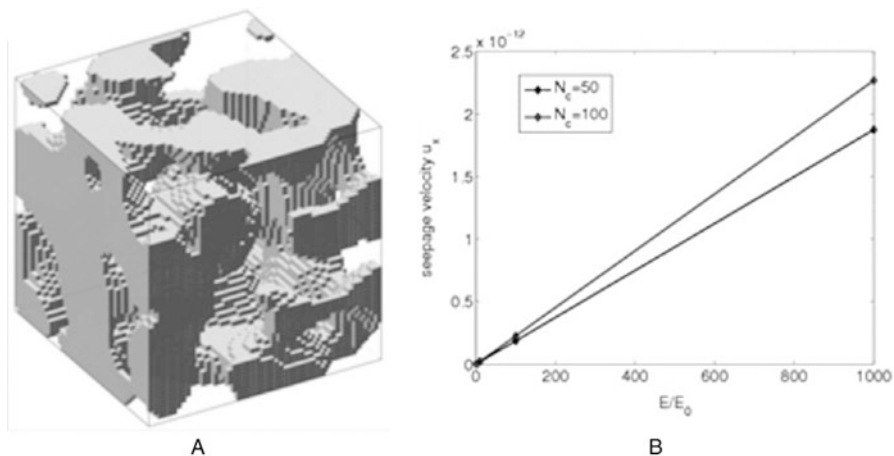


Fig. 19.3 A three-dimensional porous medium obtained by the reconstruction technique (A); the seepage velocity as a function of the external electric field for various sample discretizations.

19.4 CONCLUDING REMARKS

These preliminary calculations are presently continued and extended to realistic situations.

REFERENCES

1. Gupta, A., Coelho, D. and Adler, P.M.: Universal electro-osmosis formulae for porous media, *J. Colloid Interf. Science*, 319, 549 (2008)
2. Marconi, U.M.B. and Melchionna, S.: Kinetic theory of correlated fluids: From dynamic density functional to Lattice Boltzmann methods. *J. Chem. Phys.*, 131, 014105 (2009)

Chapter 20

Statistical Scale-up of Reservoir Properties and Dispersivities in Heterogeneous Reservoirs

Vikrant Vishal and Juliana Y. Leung

Abstract Previous works demonstrated that dispersion increases with heterogeneities and travel distance in heterogeneous reservoirs. Therefore, scale-up of input dispersivity and reservoir attributes to the transport modeling scale should account for subscale heterogeneity and its variability. A quantitative procedure to scale-up both rock and flow-related properties is presented. First, to scale-up porosity and permeability, volume variance at the transport modeling scale is computed corresponding to a given spatial correlation model; numerous sets of “conditioning data” are sampled from probability distributions whose mean is the block average of the actual measure values and the variance is the variance of block mean. Stochastic simulations are subsequently performed to generate multiple realizations at the transport modeling scale. Next, a stochastic random walk particle tracking (RWPT) method, which is not prone to numerical dispersion, is applied. Multiple sub-grid realizations illustrating fine-scale heterogeneities and of the same sizes as the transport modelling mesh size are subjected to RWPT simulation. Effective longitudinal and transverse dispersivities are computed simultaneously by matching the corresponding breakthrough concentration history for each realization with an equivalent medium consisting of averaged homogeneous properties. Probability distributions of scaled-up dispersivities conditioned to average porosity and permeability values are established. Tracer injection responses obtained with the coarse-scale models and fine-scale models are compared. Anomalous behavior is observed, and the interplay between large-scale heterogeneity and sub-scale variability is studied. Scaled-up dispersivity is shown to increase with scale. This study demonstrates that (1) accounting for variability owing to scale-up could capture the actual fine-scale behavior; and (2) the ensuing uncertainty in transport response is underestimated when sub-scale variability is ignored. It underlines the significance of quantification and integration of uncertainty in subsurface “hard” data.

Keywords Scale-up • Particle tracking • Multi-scale transport • Dispersivity

V. Vishal (✉) • J.Y. Leung

Natural Resources Engineering Facility, School of Mining and Petroleum Engineering,
University of Alberta, Markin/CNRL, Edmonton, Alberta T6G 2W2, Canada
e-mail: vvishal@ualberta.ca

20.1 INTRODUCTION

Dispersion in porous media results from the interplay between two mechanisms: convective spreading and diffusion [1]. Factors which control the dispersion are fluid velocity, pore and grain size distribution, and molecular diffusion. Presence of local velocity gradients due to multi-scale heterogeneous rock properties including porosity and permeability can enhance mixing. It has been shown that dispersivity increases with distance. This scale-dependent behavior is usually described as non-Fickian [2], characterized by early breakthrough and long-tailed effluent histories at the late times. At field scale, non-Fickian behavior can be attributed to both large-scale and unresolved sub-scale heterogeneities. Dispersion depends on heterogeneity, which varies as a function of scales [3, 4]. Several studies have discussed the inadequacies of classical advection-dispersion equation (ADE) for modeling transport behavior of non-Fickian characteristics by highlighting the systematic deviation in break through curves (BTCs) history between experimental data and ADE predictions [5]. Another issue related to numerical transport modeling is the artificial dispersion, which is the consequence of truncation error and generally overwhelms physical dispersion. An alternative is the particle tracking (Eulerian method) approach, which is essentially mesh-free and applicable in the absence of diffusion [4]. This paper presents an approach to facilitate the construction of a suite of coarse-scale realizations that capture the fine-scale variability (at the sub-grid level) in rock properties (porosities and permeability) and dispersivities (longitudinal and transverse).

20.2 FLOW AND TRANSPORT MODELING

The ADE can be formulated in terms of particle displacement according to the Itô-Taylor integration scheme [6] as

$$X_p(t + \Delta t) = X_p(t) + A(X_p, t)\Delta t + B(X_p, t) \cdot \xi(t)\sqrt{\Delta t}, \quad (1)$$

Where $X_p(t)$ is the particle position at time t ; Δt is the time step; A and B refer to the velocity vector and dispersion tensor, respectively. The function $\xi(t)$ is an independent and identically distributed (i.i.d) normal random vector with zero mean and unit variance. A formulation, RW3D-MRMT, capable of simulating advection, dispersion/diffusion, and reactive multi-rate mass transfer is adopted [7].

20.3 SCALE-UP METHODOLOGY

20.3.1 Scale-up of Reservoir Attributes

These changes in scale or volume support lead to additional uncertainty in the scaled-up models due to averaging of sub-scale heterogeneity. This uncertainty is referred to as sub-scale variability. The variance of mean of the attribute is a measure of the variability of the volume average (spatial average) at that particular volume support or scale V , and it decreases with averaging volume. Let Z be a continuous Gaussian random variable with a variance of σ^2 ; for given autocorrelation model ρ_{corr} , the variance of its linear average (\bar{Z}) over a volume V can be computed according to [8] by integrating overall possible lag distances

$$Var(\bar{Z}) = \frac{2\sigma^2}{V^2} \left(\int_V \int_V \rho_{corr}(\eta) d\eta d\xi \right). \quad (2)$$

Using a linearly-averaged scaled-up semi-variogram $\bar{\gamma}$ [9], conditional simulation is performed to establish the uncertainty estimates at locations away from conditioning data [10]. $\bar{\gamma}$ can be estimated numerically by discretizing the two volume supports (V, V'), respectively, into n and n' numbers of regularly-spaced points, and simply averaging the point-scale variogram values $\bar{\gamma}$.

$$\bar{\gamma}(V, V') = \frac{1}{V V'} \int_V \int_{V'} \bar{\gamma}(V, V') dv dv' \approx \frac{1}{nn'} \sum_{i=1}^n \sum_{j=1}^{n'} \gamma(h_{ij}). \quad (3)$$

The uncertainty in attribute value at any location away from the data location is compounded due to both sparse data and uncertainty in conditioning data. The work flow described in [10] is followed:

1. Calculate γ and variance of mean using Equation (2).
2. Compute scaled-up variogram $\bar{\gamma}$ at the coarse scale using Equation (3).
3. Sample multiple sets of scaled-up conditioning data values from distributions whose mean is the block-average of the actual measured values and the variance is the variance of the mean.
4. Perform conditional simulation at the coarse scale using scaled-up variogram and histogram (mean = fine-scale global mean; variance = variance of mean) using one sampled set of conditioning data.
5. Repeat Step #4 for other sets of conditioning data obtained in Step #3.

20.3.2 Scale-up of Dispersivities

Variability at the sub-scale also introduces uncertainty in transport-related attributes at the coarse scale and contributes to non-Fickian behavior. If all the fine-scale heterogeneities are modeled explicitly, any local (within grid cell) mixing would be represented by a Fickian model [2]. The steps can be described as follow.

1. Assign n_b bins to the histogram of $\bar{\phi}$.
2. For a given bin, perform unconditional sequential Gaussian simulation to construct n_s sub-grid porosity models of $\bar{\phi} \sim (\bar{\phi}_b, \sigma^2)$ using fine-scale variogram $\bar{\gamma}$. Permeability is computed from the collocated porosity value using the empirical relation $k = a \times \bar{\phi}_b$.
3. Construct an equivalent homogeneous model corresponding to each of the n_s sub-grid porosity models obtained from #2. Since porosity is averaged linearly, we postulate that linearly averaging is also valid in the transformed space of $(k/a)^{1/b}$; therefore, \bar{k} is estimated from $\bar{\phi}$ using the same empirical relation, assuming the transform relationship is invariant with scale [11].
4. Compute pressure and velocity distributions with the appropriate boundary conditions at steady state for n_s heterogeneous models and n_s homogeneous models generated in #2-3. Particle-based transport modeling is performed.
5. The α_L^* and α_T^* are obtained by minimizing the mismatch in breakthrough concentration profile between the heterogeneous model and the equivalent homogeneous model.
6. Steps 1 to 5 are repeated for other bins in #1.
7. Probability distributions of $P(\alpha_L^* | \bar{\phi})$ and $P(\alpha_T^* | \bar{\phi})$ such that $P(\alpha_L^* | \phi_i)$ and $P(\alpha_T^* | \phi_i)$ for $i = 1 \dots n_b$ are obtained by aggregating the scaled-up values of α_L^* and α_T^* for all $n_b n_s$ models.
8. For each coarse-scale model constructed in the previous section, α_L^* and α_T^* are assigned to individual grid blocks by sampling from the probability distributions $P(\alpha_L^* | \bar{\phi})$ and $P(\alpha_T^* | \bar{\phi})$.

20.4 CASE STUDY

Consider a synthetic 2D domain of 500 m \times 500 m with $\Delta x = \Delta y = 1$ m with $\bar{\phi}$ ranging between 0.05 and 0.35. Longitudinal dispersivity α_L at 1-m volume support is 5 m, with transverse dispersivity $\alpha_T = 0.1 \alpha_L$. The objective is to construct a set of coarse-scale 50 \times 50 models ($\Delta x = \Delta y = 10$ m) for the purpose of transport modeling. The normalized variance of mean is calculated corresponding to a volume support of 10 m \times 10 m to be approximately 0.8 using Eq. 2. Variogram calculations are shown in Fig. 20.1. To scale-up dispersivities, fine-scale 10 \times 10 models

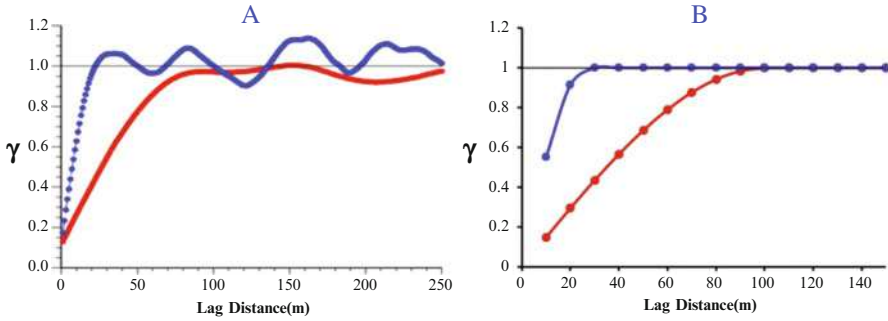


Fig. 20.1 (a) Fine scale and (b) volume-averaged variogram in the maximum direction (red) and minimum direction (blue) of continuity

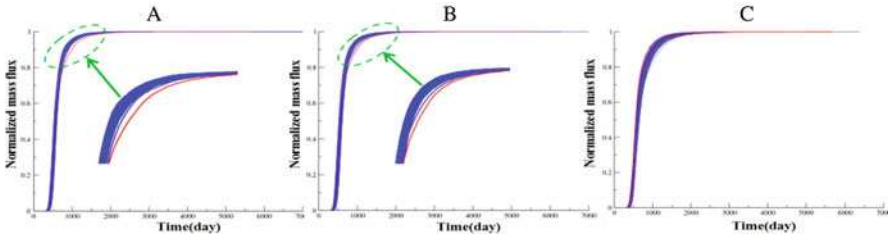


Fig. 20.2 Normalized cumulative mass flux (m/m_o) curves obtained from coarse-scale simulations: (A) no scale-up; (B) scale-up of reservoir properties only; and (C) full scale-up, where m_o is the total mass injected. Red curve represents true fine-scale response.

with $\Delta x = \Delta y = 1$ m are subjected to particle-tracking simulation where effective dispersivities are estimated as described in the methodology section.

Finally, 100 realizations at the coarse scale are constructed and subjected to particle-tracking simulation to predict solute (tracer) transport at the field scale. The results are shown in Fig. 20.2c. It is clear that the uncertainties of coarse-scale models have successfully encompassed the response from the true fine-scale model shown in red. In Fig. 20.2a, neither scale-up of reservoir attribute nor scale-up of dispersivities is performed, and fine-scale values ($\bar{\phi}$, k , α_L , and α_T) are used in the coarse-scale models. In Fig. 20.2b, reservoir attributes are scaled up according to the prescribed method, while scale-up of dispersivities is ignored. Both approaches are incapable of capturing the true fine-scale response.

20.5 CONCLUSIONS AND FUTURE WORKS

1. A new unified workflow is proposed to statistically scale-up effective dispersivities and reservoir attributes (porosity and permeability) in a consistent

manner that takes into account of sub-scale variability. Conditional probability distributions of averaged (effective) quantities representative of the transport modeling scale are established.

2. Non-Fickian transport characteristics, due to subscale heterogeneities, are observed with the ADE model where fine scale variability is integrated.
3. The proposed method can be combined with large-scale trend model to integrate sub-scale heterogeneities and large-scale geologic structures that are both contributing to non-Fickian transport behavior at field scale.

REFERENCES

1. Perkins, T.K. and Johnston, O.C.: A Review of Diffusion and Dispersion in Porous Media. *SPE Journal*, 3(1), 70–84 (1963)
2. John, A.K.: Dispersion in large scale permeable media. Ph.D. dissertation, University of Texas at Austin, USA (2008)
3. Adepoju, O.O., Lake, L.W., Johns, R.T.: Investigation of Anisotropic Mixing in Miscible Displacements. *SPE Reservoir Eval. Eng.*, 16(1), 85–96 (2013)
4. Jha, R.K., John, A., Bryant, S.L. and Lake, L.W.: Flow Reversal and Mixing. *SPE Journal*, 14 (1), 41–49 (2009)
5. Berkowitz, B., Cortis, A., Dentz, M. and Scher, H.: Modeling Non-Fickian Transport in Geological Formations as a Continuous Time Random Walk. *Rev. Geophys.*, 44(2), RG2003, doi:[10.1029/2005RG000178](https://doi.org/10.1029/2005RG000178) (2006)
6. Gardiner, C.W.: Handbook of Stochastic Methods for Physics, Chemistry, and the Natural Sciences. Springer Verlag, New York (1990)
7. Salamon, P., Fernández-García, D. and Gómez-Hernández, J.J.: Modeling Mass Transfer Processes Using Random Walk Particle Tracking. *Water Resour. Res.*, 42(11), W11417, doi:[10.1029/2006WR004927](https://doi.org/10.1029/2006WR004927) (2006 b)
8. Lake, L.W. and Srinivasan, S.: Statistical Scale-Up of Reservoir Properties: Concepts and Applications. *J. Pet. Sci. Eng.*, 44(1-2), 27–39 (2004)
9. Journel, A.G. and Huijbregts, C.J.: Mining geostatistics. Academic Press, London (1978)
10. Leung, J.Y. and Srinivasan, S.: Analysis of Uncertainty Introduced by Scaleup of Reservoir Attributes and Flow Response in Heterogeneous Reservoirs. *SPE Journal*, 16(3), 713–724 (2011)
11. Leung, J.Y. and Srinivasan, S.: Analysis of Uncertainty Introduced by Scale-up of Log-Derived Porosity in Carbonate Settings. In J. Ortiz and X. Emery (Ed.), Proceedings of Eighth International Geostatistics Congress 2, 1059–1064 (2008)

Chapter 21

Sediment Concentration Prediction at Gangotri in the Himalayas Using Artificial Neural Networks

Nandita Singh and G.J. Chakrapani

Abstract The present study explores for the first time, the possibility of modelling sediment concentration with Artificial Neural Networks at the source of Bhagirathi River in the Himalayas. Considering discharge, rainfall and temperature to be the main controlling factors of sediment concentration in the study area, seven ANN models using Feed Forward Back Propagation algorithm with different inputs have been created, trained and tested for prediction of sediment concentration. The inputs applied in the models are either the variables mentioned above as independent factors or a combination of them. Daily data of discharge, rainfall, temperature and sediment concentration for the melt period of May-October from the year 2000 to 2004, when maximum sediment movement takes place, has been used for modelling and a maximum Correlation Coefficient value of 0.89 has been obtained between observed and ANN predicted values of sediment concentration. The study has brought out that in the study area, where anthropogenic factors are minimal; discharge and rainfall taken together play a more significant role in affecting sediment concentration. Overall, ANNs perform better when multiple inputs are employed rather than single input.

Keywords ANN • Sediment Concentration Prediction • Gangotri • Himalayas

21.1 INTRODUCTION

Artificial Neural Networks (ANNs) are being used increasingly to predict and forecast water resources variables. The computational efficiency of ANNs has provided many promising results in the field of hydrology and water resources simulation [1]. In the present work, for the first time, ANN has been employed for prediction of Sediment Concentration in the Gangotri glacier of the Himalayas. The study area presents an ideal environment where maximum transport of water

N. Singh (✉) • G.J. Chakrapani
Department of Earth Sciences, Indian Institute of Technology Roorkee,
Roorkee, Uttarakhand, India
e-mail: nsingh05@gmail.com

and sediment takes place during the ablation/melt period (May to October) due to high rates of weathering with minimal influence of anthropogenic activities. In the light of watershed management, hydropower generation, frequent floods and related hazards, it becomes pertinent to model sediment concentration at the Gangotri glacier which is the source of Bhagirathi River. The Bhagirathi River itself is dotted with numerous human settlements, hydro power projects and dams which are immensely impacted by the variations in hydrologic variables like water discharge and sediment concentration.

21.2 AN OVERVIEW

ANN is a massively parallel distributed processor made up of simple processing units, artificial neurons, with a natural propensity for storing information and making it available for use [2]. It resembles the human brain in two ways, one, knowledge is acquired by the system from its environment through a learning process and two, interneuron connection strengths, known as synaptic weights, are used to store the acquired information. An attractive feature of ANNs is their ability to extract the relationship between the inputs and outputs of a process, without the physics being explicitly provided to them. Several algorithms are used for training one of which is Feed-forward Back-propagation (also used in this study). In this, training entails two passes: Forward pass, weighted inputs are summed and a transfer/activation function is applied output is obtained layer by layer, the output of one layer being input to the next and Backward pass, calculated error, difference between observed and computed output, is propagated backward through the network, to adjust weights. A good understanding of the hydrologic system under consideration is a prerequisite for successful application of ANNs.

ANNs have been used for a variety of water resource applications. Comprehensive review on the application of ANNs in the areas of water resources and hydrology is provided [3–5] rainfall-runoff processes [6–16]. ANN has often been employed for prediction of Runoff and sediment concentration by several workers like [17–23]. ANNs, however, have not been employed for modelling and prediction of sediment concentration in Gangotri, a Himalayan glacier scenario.

21.3 STUDY AREA

The Gangotri glacier is situated in the Uttarkashi district of Uttarakhand state in central Himalaya, bound between latitudes $30^{\circ}43'$ – $31^{\circ}01'$ and longitudes $79^{\circ}00'$ – $79^{\circ}17'$ (Fig. 21.1). Bhagirathi River originates from Gaumukh, the snout of the glacier, at around 4000 m.s.l elevation and joins with Alaknanda River at

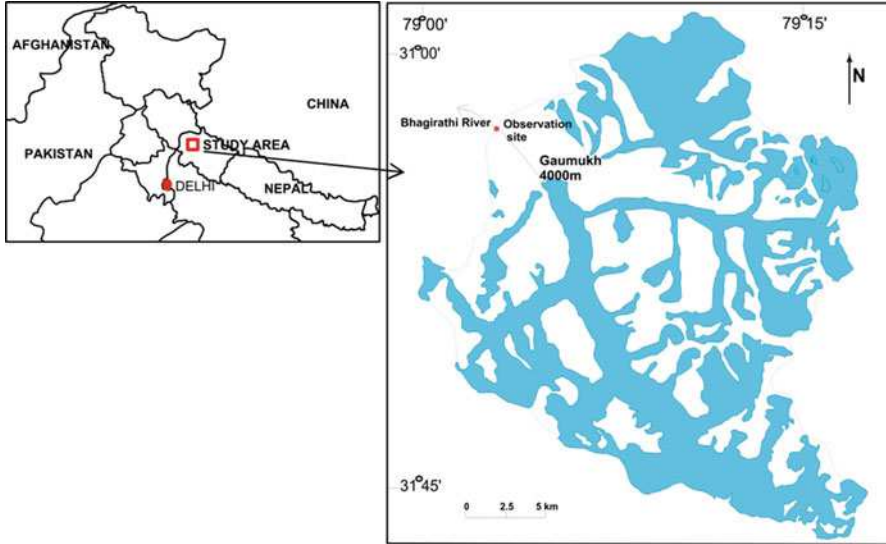


Fig. 21.1 Location of study area.

Devprayag to form the Ganges. The Gangotri glacier is a cluster of several glaciers of which the main Gangotri glacier, the trunk part of the cluster system, has a length of 30.20 km with 86.32 km² area and a gradient of 0.045 [24][25][26]. Data used in the current study is from a sampling site, situated at around 3900 m.s.l elevation about 2.0 km downstream from Gaumukh, (source-PhD Thesis U K Haritashya, DES, IITR). The total catchment area of the Gangotri glacier study basin up to the sampling site is about 556 km², out of which about 286 km² (51.4%) is ice covered [27]. The Gangotri glacier system geologically falls in the higher and Tethys Himalayan zone [28] and mainly comprises granite, mica (sericite) schist, quartzites and Phyllites. Fig. 21.1 shows the area of the Gangotri Glacier and locations of the snout and the gauging site.

21.4 DATA DESCRIPTION

In the present study daily Temperature(T), Rainfall(R) and Discharge(Q) data of the melt period (May – October) from the year 2000-2004 (Data source: Thesis of Sh U. Haritashya, DES, IITR) at a location two kms downstream from the snout of the Gangotri glacier has been used for predicting sediment concentration using ANN. Besides prediction, this study would also give better insight into dependencies of variables in an area where anthropogenic controlling factors are negligible or rather

absent. The dependence patterns of sediment concentration(S) with discharge, rainfall and temperature have been studied in detail by Haritashya et al, 2006; P. Singh et al, 2006 with the help of variation diagrams and other statistical plots. In these studies, it has been observed that, a majority of sediment is transported in the period of July to August due to intensive melting and sediment availability. In the months of May and June, the area of melting is low which lead to relatively lesser sediment load. From September to October, although melting is substantial, the sediment load is again low as most of it has been flushed out in the preceding months. The occurrence of rainstorms has a significant impact on glacier runoff as well as the sediment flux. Heavy rain occurring for short durations influences the increase of sediment in melt water more than the increase in melt runoff [29]. Sediment availability during rainstorms is also necessary for higher sediment loads.

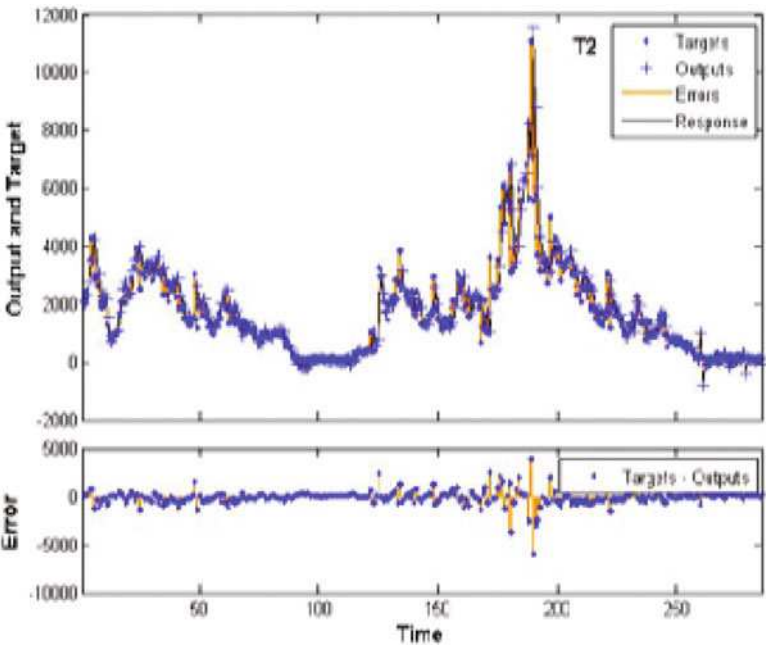
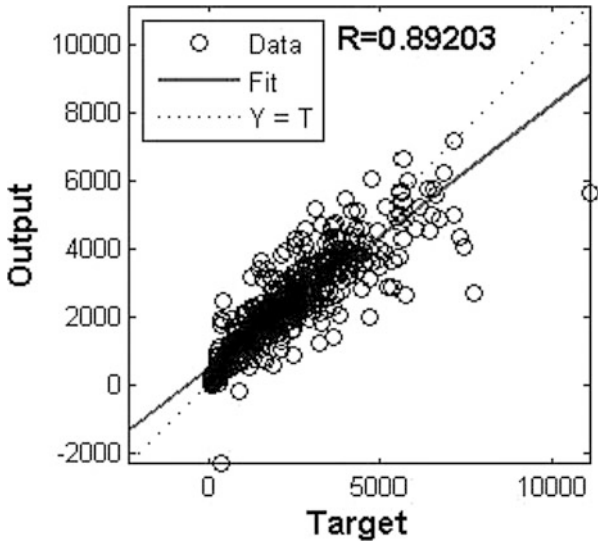
21.5 ANN MODELING

Seven Artificial Neural Networks were created using the Neural Network Time Series application in MATLAB (R2013a) to model the hydrologic flow process at Gangotri, the source of Bhagirathi River. Seven networks were trained with as many as 865 data and the goodness of fit characteristics of the computed and observed outputs were evaluated. The number of layers remained three in every case and the weights were selected randomly. Gradient Descent with momentum and adaptive learning rate (traingdx) Back Propagation Algorithm using a non-linear logsigmoidal transfer function in the hidden layer and a pure linear function in the output layer was employed. Training, validation and testing subsets were created randomly by dividing the dataset respectively into 70%, 15% and 15% of the complete dataset. The seven networks created were Model-T1: $S(t) = f\{Q(t)\}$; Model-T2: $S(t) = f\{Q(t), R(t)\}$; Model-T3: $S(t) = f\{Q(t), R(t), T(t)\}$; Model-T4: $S(t) = f\{R(t)\}$. Model-T5: $S(t) = f\{T(t)\}$; Model-T6: $S(t) = f\{Q(t), T(t)\}$; Model-T7: $S(t) = f\{T(t), R(t)\}$.

21.6 RESULTS AND DISCUSSION

In the present study, the overall performance is much better when multiple inputs are used than the cases where single input has been employed. Model T2 is, where a combination of discharge and rainfall has been used as input performs the best with the highest R value (0.89). This implies that discharge plays a relatively more important role than the other variables.

Scatter between output and target sediment conc. during testing



Observed (targets) and predicted (outputs) values of sediment conc.

21.7 CONCLUSION

It has been successfully established that despite the variations in factors involved, it is possible to predict sediment concentration in the Himalayan scenario. Daily values of discharge, rainfall, temperature for the melt period of May to October from the year 2000–2004 have been used to create seven Artificial Neural Networks for prediction of sediment concentration. It has been brought out that among discharge, temperature and rainfall, discharge and rainfall taken together affect sediment concentration the most. It is also seen that multiple inputs improve the model performance substantially. Such a study would be of great help in understanding the relationships that exist between hydrologic variables and the degree to which they affect sediment movement.

REFERENCES

1. Sudheer, K.P.: Knowledge Extraction from Trained Neural Network River Flow Models ASCE (1084-0699) (2005)
2. Haykin, S.: Neural networks: a comprehensive foundation. Mac-Millan, New York (1994)
3. ASCE Task Committee on Application of The Artificial Neural Networks in Hydrology. Artificial neural networks in hydrology I: preliminary concepts. *J. Hydrol. Engng*, ASCE 5 (2), 115–123 (2000a)
4. ASCE Task Committee on Application of The Artificial Neural Networks in Hydrology. Artificial neural networks in hydrology II: hydrologic applications. *J. Hydrol. Engng*, ASCE 5 (2), 124–137 (2000b)
5. Maier, H.R. and Dandy, G.C.: Neural networks for the prediction and forecasting of water resources variables: a review of modelling issues and application. *Environ. Model. Softw.*, 15, 101–124 (2000)
6. Dowson, C.W. and Wilby, R.L.: Hydrological modelling using artificial neural networks. *Prog. Phys. Geogr.*, 80–108 (2001)
7. Hall, M.J. and Minns, A.W.: Rainfall-runoff modeling as a problem in artificial intelligence: Experience with neural network. Proc. 4th British Hydrological Society Symp., Cardiff, UK 5.51–5.57 (1993)
8. Hsu, K., Gupta, V.H. and Sorooshian, S.: Artificial neural network modeling of the rainfall-runoff process. *Water Resour. Res.*, 31–10, 2517–2530 (1995)
9. Smith, J. and Eli, R.N.: Neural network models of rainfall runoff process. *J. Water Resour. Plann. Manag.*, ASCE 121 (6), 499–508 (1995)
10. Minns, A.W. and Hall, M.J.: Artificial neural networks as rainfall runoff models. *Hydrol. Sci. J.*, 41 (3), 399–417 (1996)
11. Shamseldin, A.Y.: Application of a neural network technique to rainfall runoff modeling. *J. Hydrol.*, 199, 272–294 (1997)
12. Tokar, A.S. and Johnson, P.A.: Rainfall runoff modeling using artificial neural networks. *J. Hydrol. Engng*, ASCE 4 (3), 232–239 (1999)
13. Sajikumar, N. and Thandaveswara, B.S.: A nonlinear rainfall runoff model using an artificial neural network. *J. Hydrol.*, 216, 32–55 (1999)
14. Gautam, M.R., Watanabe, K. and Saegusa, H.: Runoff analysis in humid forest catchment with artificial neural network. *J. Hydrol.*, 235, 117–136 (2000)
15. Chang, F.J. and Chen, Y.C.: A counter propagation fuzzy-neural network modeling approach to real time streamflow prediction. *J. Hydrol.*, 245, 153–164 (2001)

16. Zhang, B. and Govindaraju, R.: Geomorphology-based artificial neural networks (GANNs) for estimation of direct runoff over watersheds. *J. Hydrol.*, 273, 18–34 (2003)
17. Rajurkara, M.P., Kothiyari, U.C. and Chaube, U.C.: Modeling of the daily rainfall-runoff relationship with artificial neural network. *Journal of Hydrology*, 285, 96–113 (2004)
18. Nagy, H.M., Watanabe, K. and Hirano, M.: Prediction of sediment load concentration in rivers using artificial neural network model. *Journal of Hydraulic Engineering*, 128(6), 588–595 (2002)
19. Sarangi, A. and Bhattacharya, A.K.: Comparison of Artificial Neural Network and regression models for sediment loss prediction from Banha watershed in India. *Agricultural Water Management*, 78, 195–208 (2005)
20. Yitian, L. and Gu, R.R.: Modeling flow and sediment transport in a river system using an artificial neural network. *Environ. Manage.*, 31(1), 122–134 (2003)
21. Reddy, S.B.: Estimation of watershed runoff using artificial neural networks. Ph.D Thesis in Agric. Engg. (unpubl.). Post Graduate School, IARI, New Delhi.
22. Sarangi, A. and Bhattacharya, A.K.: Use of geomorphological parameters for sediment yield prediction from watersheds. *J. Soil Water Conserv.*, 44 (1–2), 99–106 (2000)
23. Kaur, R., Srinivasan, R., Mishra, K., Dutta, D., Prasad, D. and Bansal, G.: Assessment of SWAT model for soil and water management in India. *Land Use Water Resour. Res.*, 3, 1–7 (2003)
24. Boukhriassa, Z.A., Khanchoul, K., Le Bissonnais, Y. and Tourki, M.: Prediction of sediment load by sediment rating curve and neural network (ANN) in El Kebir catchment, Algeria. *Journal of Earth System Sciences*, 122(5), 1303–1312, (2013)
25. Naithani, A.K., Nainwal, H.C., Sati, K.K. and Prasad, C.: Geomorphological evidences of retreating of Gangotri glacier and its characteristics. *Current Science*, 80 (1), 87–94 (2001)
26. Singh, P., Haritashya, U.K., Kumar, N. and Singh, Y.: Hydrological characteristics of the Gangotri Glacier, Central Himalayas, India. *Journal of Hydrology*, 327, 55–67 (2006)
27. Singh, P., Kumar, A. and Kishore, N.: Meltwater storage and delaying characteristics of Gangotri glacier (Indian Himalayas) during ablation season. *Hydrological Processes*, 25, 159–166 (2011)
28. Haritashya, U.K., Singh, P., Kumar, N. and Gupta, R.P.: Suspended sediment from the Gangotri Glacier: quantification, variability and associations with discharge and air temperature. *Journal of Hydrology*, 321, 116–130 (2006)
29. Kumar, K., Miral, M.S., Joshi, S., Pant, N., Joshi, V. and Joshi, L.M.: Solute dynamics of meltwater of Gangotri glacier, Garhwal Himalaya, India. *Environmental Geology*, 58, 1151–1159 (2009)

Chapter 22

Lacunarity Analysis of Fracture Intensity Maps: Are they Multifractals?

Ankur Roy and Edmund Perfect

Abstract Lacunarity (L) is a scale (r)-dependent parameter that was developed for quantifying clustering in fractals and has subsequently been employed to characterize various natural patterns. It has been further analytically proved that lacunarity analysis invoking the gliding-box algorithm can find the correlation dimension, D_2 of multifractals. The present research empirically tests this on a set of multifractal models generated with known D_2 values. The log-transformed lacunarity values of these models, $\log L$ were plotted as a function of the log-transformed box-size, $\log r$. The slopes of these linear relations, estimated using regression analysis, were then used to calculate D_2 values that gave an approximately 1:1 relationship with the known values. Multifractal behavior can therefore, be checked without having to compute the whole spectrum of non-integer dimensions, D_q ($-\infty < q < +\infty$) that typically characterize a multifractal. The technique thus developed was applied to fracture intensity maps generated from a set of nested fracture networks from the Devonian Sandstone, Hornelen Basin, Norway in order to test if such intensity maps display multifractal behavior.

Keywords Lacunarity • Grayscale • Correlation Dimension • Multifractal • Fracture Intensity

22.1 INTRODUCTION

Lacunarity is a parameter that characterizes the distribution of spaces or gaps in a pattern as a function of scale. Originally proposed for distinguishing between monofractal patterns having the same fractal dimension but different degrees of clustering [1], lacunarity has since been used for analyzing scale-dependent clustering in natural binary data sets, both fractal and non-fractal. The gliding-box

A. Roy (✉)

Energy Resources Engineering Department, Stanford Center for Reservoir Forecasting,
Stanford, CA, USA

e-mail: royankur@stanford.edu

E. Perfect

Earth & Planetary Sciences Department, University of Tennessee, Knoxville, TN, USA

algorithm can be used to quantify the lacunarity, L , at a given scale (or box-size, r). Since values vary with box-size the results are generally reported in terms of the function: $L(r)$. It has been theoretically established that when log-transformed values of $L(r)$ and r are plotted, both fractals and multifractals result in straight lines such that the slope plus the known embedding dimension equals the box or correlation dimension, respectively [2]. Although there have been a few lacunarity studies of both synthetic and natural multifractal patterns [3, 4], there is not enough evidence to unequivocally establish that lacunarity analysis can indicate multifractal behavior in non-binary data, and that the true correlation dimension, D_2 of a multifractal can be found by employing this technique. In the present paper, we test Allan and Cloitre's theory [2] using multifractal grayscale patterns with known correlation dimensions. As an application, we focus on four fracture intensity maps (grayscale / non-binary) that have been generated from a set of nested fracture network maps (binary) from the Devonian sandstone of Hornelen Basin, Norway [5]. Since this fracture network is fractal in nature [6] it can be hypothesized that intensity maps generated from them can possibly display multifractal properties.

22.2 GENERATING MULTIFRACTAL PATTERNS

A set of 2-dimensional multifractal grayscale patterns were constructed following the steps outlined in [7]. The process is akin to generating a Sierpinski carpet, only the zeros and ones in the pattern are replaced with fractional values. The algorithm involves normalizing mass-fractions calculated from the truncated binomial distribution for an average probability, p , of retaining a cell in the generator with a scale factor, b , in successive iterations. As described in [8] the locations of the normalized mass fractions can be spatially randomized so as to create a random geometrical multifractal grayscale pattern. Eight different patterns were created from a generator with a scale factor of $b = 3$ and probability values corresponding to $p = 1/9, 2/9, 3/9, 4/9, 5/9, 6/9, 7/9$, and $8/9$ by iterating the system 5 times to produce grayscale fields of size $3^5 \times 3^5$ pixels. For each of the 8 models, 3 random realizations were constructed amounting to a total of 24 random multifractal grayscale patterns. Fig. 22.1 shows patterns corresponding to $p = 8/9, 7/9, 6/9$ and $5/9$.

22.3 LACUNARITY AND MULTIFRACTAL BEHAVIOR

Lacunarity is a scale-dependent measure of textural heterogeneity that can be quantified by employing the gliding-box algorithm [2]. Essentially, this method involves sliding a window or an interrogator box of a given length, r , translated in

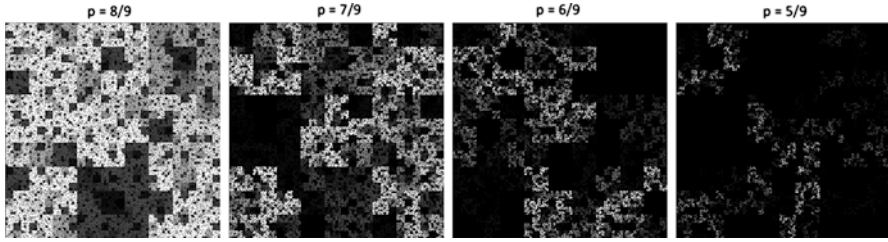


Fig. 22.1 Grayscale random multifractal patterns: $p = 8/9$ to $5/9$. Lighter phases have higher mass fractions

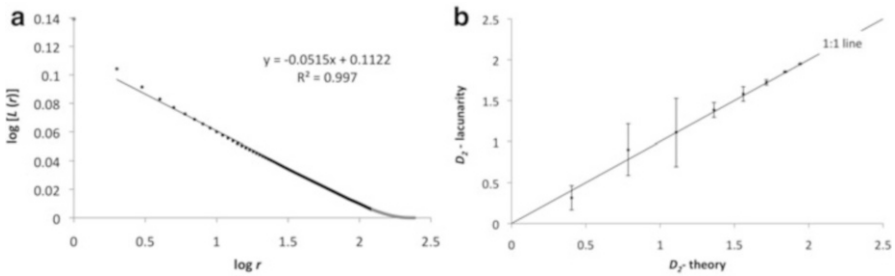


Fig. 22.2 (a) $\log L(r)$ vs. $\log r$ plot for pattern $p = 8/9$; (b) D_2 , estimated from lacunarity analysis compared to theoretical D_2 -values for 8 random multifractal fields, each point is an average of 3 realizations with bars corresponding to the 95% confidence intervals

increments of a chosen unit length (usually that of a pixel) across the whole pattern such that the total number of steps is given by $(r_f - r + 1)^2$, r_f being the length of the entire pattern. The details of this technique employed in analyzing binary patterns can be found in [9]. In the case of grayscale patterns, the mass of all pixels, $s(r)$, contained within the interrogator box at each step is calculated and a distribution of this mass at the scale r is obtained by gliding the box through all the steps. Finally, the mean, $\overline{s(r)}$, and variance, $ss^2(r)$ of this distribution are used in calculating the lacunarity, $L(r)$, at the scale r as: $L(r) = [ss^2(r) / \overline{s(r)}^2] + 1$. Typically, $L(r)$ is calculated for a range of box-sizes, r and it has been theoretically demonstrated in [15] that in the case of multifractals, $L(r)$ is related to r by a power-law such that the power-term equals $D_2 - E$, where D_2 is the correlation dimension and E the Euclidean embedding dimension. Based on this result, it is expected that the log-transformed lacunarity functions for the 2-dimensional multifractal patterns described in the previous section can be fitted with a straight line, $y = mx + c$, such that the slope is, $m = D_2 - 2$. For each of the 24 multifractal patterns, the $\log L(r)$ vs. $\log r$ values were calculated and a subset of the array of points thus obtained was fitted with a straight line. Fig. 22.2a shows one such plot for pattern $p = 8/9$ (random realization #3). In order to estimate the proper correlation dimension thus meeting a condition for multifractal behavior [2], only the relatively “straight” segment was considered for fitting a linear model to the points. For large r values,

the local slope starts to fluctuate and increases abruptly and so the points corresponding to box-sizes $r > r_t/2$ were not included in the fitting. For smaller r values, the coefficient of determination, R^2 , of the fit improved when points were sequentially excluded from the left. However, it is the first point at $r = 1$ that mostly influences the change in slope such that there was a difference of $\sim 4\%$ in the estimated slope if this point was excluded from the fit. If two or more additional points were excluded there was no more than $\sim 1\%$ difference. This is mainly because the first few points on the left hand side of the $\log L(r)$ vs. $\log r$ plot are sparsely distributed. Therefore, from the lower end, only the first point in the plot was excluded from the fitting. The points thus excluded from both ends are shown in grey. Correlation dimensions for all 24 patterns were calculated from their $\log L(r)$ vs. $\log r$ plots by employing the above protocol. An average estimated D_2 value from all three realizations of each model corresponding to a particular p -value was computed and compared to the theoretical D_2 value [7]. The results are graphed in Fig. 22.2b. The 95% confidence intervals in the computed D_2 values arising from the three random realizations for each model are shown as vertical bars. As can be seen from the figure, the computed D_2 values overlap the 1:1 line (45° slope) and are thus statistically equal to their theoretical counterparts. This analysis demonstrates empirically that an almost exact value of the correlation dimension for multifractals can be found from lacunarity analysis. It may therefore be concluded that lacunarity analysis can detect if a grayscale pattern exhibits possible multifractal behavior (on the basis of log-log linearity) and, if it does, provide an accurate estimate its correlation dimension.

22.4 FRACTURE INTENSITY MAPS

Fracture intensity may be defined as the summed fracture trace length per unit area [10]. For this study, we created four intensity maps from a subset of seven nested fracture networks that were mapped from the Devonian sandstones of Hornelen Basin, Norway [5]. These seven nested fracture maps are well studied and have been previously established as belonging to a fractal system [6]. Map 2, 4, 5 and 7 at length scales of 55m, 90m, 180m and 720m respectively, and represented by 1042 x 1042 pixels were chosen. These were converted into intensity maps by overlaying a grid with cell size 20 x 20 pixels and counting the fracture length in each cell. The bright areas indicate high fracture intensity as seen in Fig. 22.3.

22.5 RESULTS AND DISCUSSIONS

Figure 22.4 shows $\log L$ vs. $\log r$ plots for the intensity maps generated in the previous section. As seen here, plots of all four maps can be fitted by straight lines over a limited range thus confirming the hypothesis that they all display possible multifractal behavior. While the maps have somewhat similar correlation dimensions, the general trend is: larger the mapped area larger is the correlation dimension such that, map

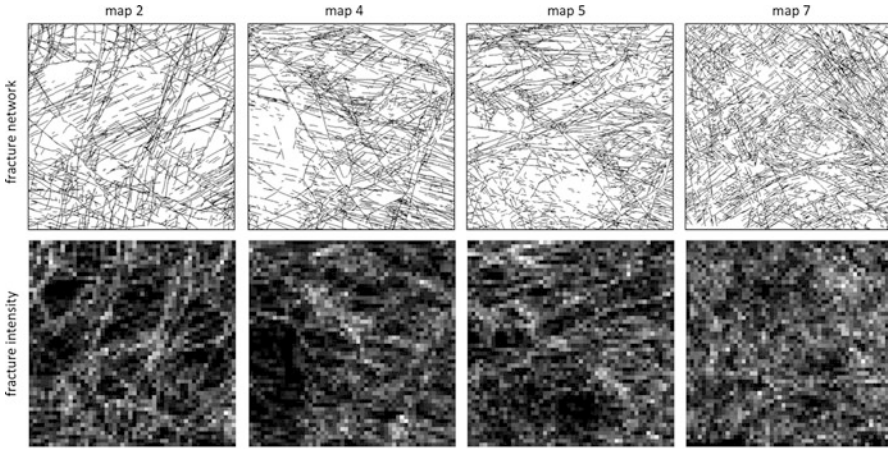


Fig. 22.3 Fracture intensity maps generated from fracture networks

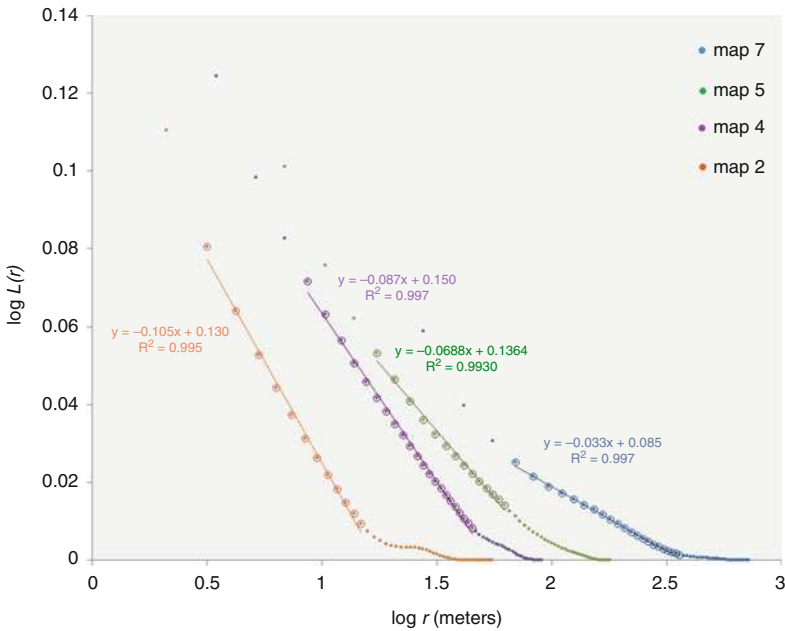


Fig. 22.4 $\log L$ vs. $\log r$ plots for intensity maps 2, 4, 5 and 7

7 (720m) has the highest dimension (least steep slope). This general observation is in agreement with the trends in box-counting dimension values of the corresponding original fractal-fracture network maps as reported in [6]. The results therefore show that lacunarity analysis can delineate possible multifractal behavior in fracture intensity maps that are associated with underlying fractal-fracture geometries.

REFERENCES

1. Mandelbrot, B.B.: The Fractal Geometry of Nature. Freeman, 1st ed. New York, NY (1983)
2. Allain, C. and Cloitre, M.: Characterizing the lacunarity of random and deterministic fractal sets. *Phys. Rev. A*, 44(6), 3552–3558 (1991)
3. Plotnick, R., Gardner, H., Hargrove, W.W., Prestegard, K. and Perlmutter, M.: Lacunarity analysis: A general technique for the analysis of spatial patterns. *Phys. Rev. E*, 53(5), 5461–5468 (1996)
4. Chen, Q.: Multifractal Modeling and Lacunarity Analysis. *Mathematical Geology*, 29(7), 919–932 (1997)
5. Odling, N.E.: 1997, Scaling and connectivity of joint systems in sandstones from western Norway. *Journal of Structural Geology*, 19(10), 1257–1271 (1997)
6. Roy, A., Perfect, E., Dunne, W.M. and McKay, L.D.: Fractal characterization of fracture networks: An improved box-counting technique. *Journal of Geophysical Research*, 112, B12201 (2007)
7. Perfect, E., Gentry, R.W., Sukop, M.C. and Lawson, J.E.: Multifractal Sierpinski carpets: Theory and application to upscaling effective saturated hydraulic conductivity. *Geoderma*, 134, 240–252 (2006)
8. Koirala, S.R., Perfect, E., Gentry, R.W. and Kim, J.W.: Effective saturated hydraulic conductivity of two-dimensional random multifractal fields. *Water Resources Res.*, 48, 1–9 (2008)
9. Roy, A., Perfect, E., Dunne, W.M., Odling, N.E. and Kim, J.W.: Lacunarity analysis of fracture networks: Evidence for scale-dependent clustering. *J. Structural Geology*, 32, 1444–1449 (2010)
10. Mauldon, M. and Zuo, G.: Fractal dimension of fracture intensity via 2-D histograms, Mining and tunnelling innovation and opportunity. Hammah, R., Bawden, W., Curran, J. and Telesnicki, M. eds, Toronto, Canada, NARMS-TAC (2002)

Chapter 23

Modified Tetrahedral Mesh Subdivision Method and Its Application in 3D Geological Body Discrete Analysis

Gang Liu, Zhengping Weng, Zhiting Zhang, and Qing Zhou

Abstract Tetrahedral mesh has excellent properties such as being easy to be edited and suitable for simulating the complex geological body. However, classical algorithms for tetrahedral mesh generation such as Delaunay tetrahedral mesh algorithm, Advancing Front Technique (AFT) and Octree algorithm still have problem of low efficiency. Here three aspects Delaunay tetrahedral mesh algorithm are modified to improve its performance in geological applications. Optimization of efficiency is divided into two parts: macro-optimization and micro-optimization. The macro-optimization is to increase efficiency through the data pre-processing. For the micro-optimization, a practical topological structure is proposed to construct the topological relationships among the points, edges and triangles to achieve more efficient search speed. On the other hand, the sliver of tetrahedral mesh will affect its quality seriously. We classify the slivers into different types and eliminate these slivers by different methods. This improved approach is applied to gold mine reserve estimation of Zijin Mine, Fujian, China. The result shows the modified algorithm is robust and its performance is better than traditional method.

Keywords Tetrahedral Mesh • Delaunay Tetrahedral Mesh Algorithm • 3D Mesh Discrete Analysis • Geological Application

23.1 INTRODUCTION

Tetrahedral mesh generation is a kind of method of three-dimensional volume subdivision method with simple structure and variable resolution. At present, among the tetrahedral mesh generation methods, Delaunay tetrahedral meshing

G. Liu (✉)

School of Computer Science, China University of Geosciences, Wuhan, China
e-mail: liugang67@163.com

Z. Weng • Z. Zhang

School of Computer, China University of Geosciences, Wuhan, China

Q. Zhou

AutoNavi Software Company Limited, No. 3 Suzhou Street, Haidian, Beijing, China

method, the AFT tetrahedral meshing method and improved octree method are widely used [1, 2]. These methods can connect the points to generate tetrahedral mesh by different ways among the point set. It is expected the mesh units are to be plump to improve the accuracy of calculation during the analysis process based on these mesh units. Delaunay meshing algorithm is the most common constrained triangular/tetrahedral mesh generation algorithm. The algorithm, with a good local operation, not only generates mesh that meet the Delaunay empty circle(ball) property, but also keep the consistency constraints to make the quality and size of generated meshes controllable [3]. Advancing Front Technique (AFT) has become one of popular general automatic mesh generation methods [3]. The AFT method, compared with Delaunay tetrahedral algorithm, has not formed mature theory basis yet. In many cases it is to solve the problem by experience, and the time complexity of the AFT algorithm is $O(N \log N)$, which is similar to the Delaunay triangulation algorithm and the constrained quadtree/octree method [4], but the quality of its mesh unit is the best of the three. In above methods, the low efficiency is a serious problem in the AFT method, because it needs to check a great deal of validity while generating new units, such as the volume check, intersection check, containment check. And generated mesh quality and success of the AFT is also largely dependent on the advancing front route. Although the octree method is simple to implement, but in the process of mesh generation a large number of point insertion and re-division will reduce the efficiency. In the 3D geological modeling application, repeated division will cause increasing large amount of inaccurate auxiliary points which will reduce the modeling accuracy. Therefore, this paper uses the method of constrained Delaunay tetrahedral generation method as the main method for geological application.

23.2 MODIFIED CONSTRAINED DELAUNAY TETRAHEDRAL MESHING METHOD

Considering algorithm itself and the characteristics of geological data, we optimize the constrained Delaunay tetrahedral mesh generation algorithm from the following two aspects.

23.2.1 *Improvement of the Algorithm Efficiency*

In general, edge is constituted by nodes, triangle is constituted by edges (or triangle is constituted by points) and tetrahedron is constituted by triangles, and they also are interknitted as network structure [5]. If using the general method to make linear search which means searching points when nodes are needed and searching edges when edges are needed, it is not only time consuming but also easy to appear incorrect matchups in complicated mutual search. To resolve this problem, HASH algorithm is adopted to build list structure, then to construct the topological relation

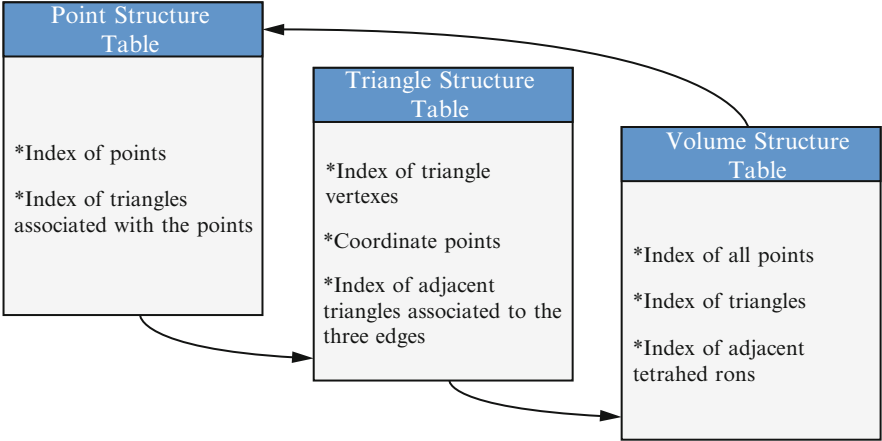


Fig. 23.1 Schematic diagram of topological structure for TEN based on HASH method.

to form speediness and effective search structure. As shown in Fig. 23.1, HASH method is adopted to the point structure table to construct HASH table (HASH here is simplified HASH table) of nodes, which include index of points and triangles associated with the points. These three structure tables build the topological relation of the whole triangular network. The index of point structure can be applied to seek out the triangles related with the points and the information of points and edges related with these triangles, and even the information of adjacent triangles, without traversal search in all triangular network data. Once the topological relationships established, spatial object search will be more stabilized than linear search and incorrect matchup will be avoided.

23.2.2 Improvement of Mesh Generation Quality

While using Delaunay algorithm in three-dimensional application, the most common problem is sliver thin unit, which will result in ill condition in engineering application and influence the computational accuracy and generate errors.

Processing method for sliver unit can be divided into several categories:

The first, the thin tetrahedron unit isn't adjacent to any other tetrahedron unit. Such thin unit will not affect entire network topological relation. This kind of unit can be deleted directly. The second, each face of the thin unit has neighboring tetrahedron, and any two of the neighboring tetrahedron have common vertexes. Then the thin unit can be eliminated by exchanging face method. As shown in Fig. 23.2, ABCD is a thin unit in tetrahedral mesh because the volume of ABCD is nearly 0, and its four vertexes are located in one plane. Tetrahedron ABCE and ACDE which are adjacent to ABCD have common vertex E. To solve this thin unit problem, the thin unit ABCD is removed first, and then the two adjacent tetrahedrons are converted to tetrahedron ABDE and BCDE.

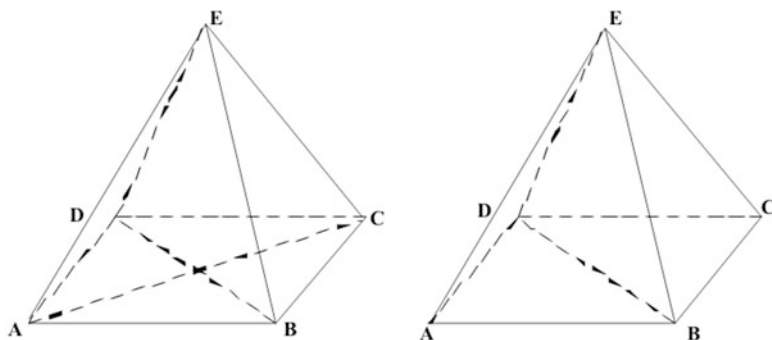


Fig. 23.2 Sliver unit elimination method.

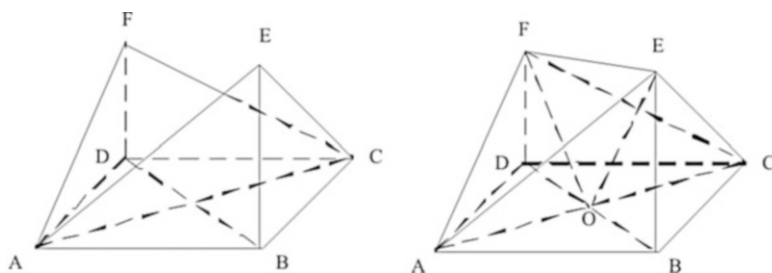


Fig. 23.3 Another type of sliver unit elimination method.

The third, there is no common vertex between four adjacent tetrahedrons of the thin unit. Then this sliver unit cannot be deleted directly because if it will influence surrounding tetrahedron units and the topological relation of entire mesh. So the handling method will be as shown in Fig. 23.3. Tetrahedron ABCD is the sliver unit, ABCE and ACDF are two adjacent tetrahedrons of the thin unit which have no common vertex. Because ABCD's four vertexes are nearly located in one plane, the point of intersection of line AC and BD can be determined as O approximately. Then, line AC and BD are broken up into line AO, OC, BO and OD, and the original tetrahedron is converted to six tetrahedrons ABOE, BCOE, AODF, CDOF, AOE, and COF. In this way, the problem of thin unit can be resolved without influencing adjacent tetrahedrons' topological relation.

23.3 APPLICATION OF IMPROVED CONSTRAINED DELAUNAY TRIANGULATION METHOD

Ore body data from Zijin Mine, Fujian, China is taken as application example. The features of data: both data range and amount are large; the distribution of gold mine is uneven, fragmented and long narrow; and the surface strata data has

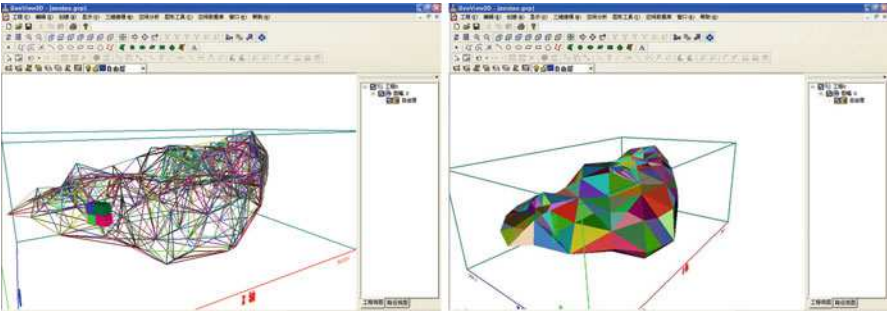


Fig. 23.4 Typical TEN mesh of part of Zijin mine ore body, China.

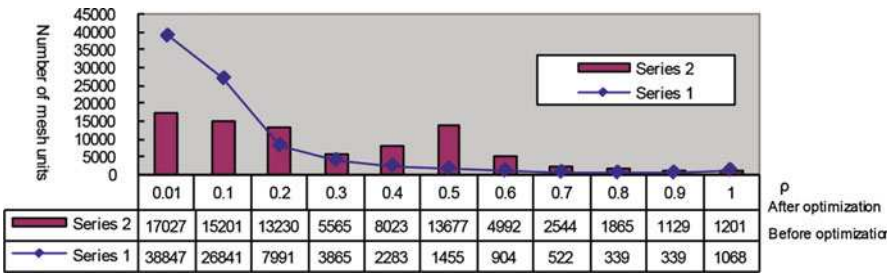


Fig. 23.5 Comparison of TEN mesh quality of ore body of Zijin Mine before and after optimization. (The series 1 is ore body data of gold mine before optimization, the series 2 is the data after optimization.)

characteristics as large range and relatively small ups and downs. In Fig. 23.4, its how part of ore body data of Zijin gold mine, overall quality of the initial mesh is at a low level.

It can be concluded from above result: when the data distributes in a large range and as narrow shape, the generated mesh quality is seriously affected. The majority of geological bodies have such kind of characteristics, so the key task is to optimize the mesh network of this data. As the amount of data of Zijin mine is large and there are pinch-outs and fragmentations in the strata data, its orebody data is taken as a typical data for mesh optimization.

In Fig. 23.5, the series 1 is the statistical results of the r value about radius ratio before mesh optimization; the series 2 is the statistical results of the r value about radius ratio after mesh optimization. Mesh sub division generates totally 84454 tetrahedral units. Comparing the data before and after optimization shows that the proportion of the mesh units with poor quality is greatly reduced after optimization, and the units with good quality are increasing and the whole mesh achieved a more balanced status.

23.4 CONCLUSIONS

Based on the constrained Delaunay tetrahedral subdivision principle and the characteristics of large amount of geological data, we study modified tetrahedral mesh subdivision method. About subdivision efficiency, three-dimensional spatial index is applied to preprocess massive data. In terms of algorithm, we mainly establish an effective and practical topological relationship by using HASH method to reduce the retrieval time. In aspect of mesh generation quality, the paper proposed three kinds of thin unit decomposition solutions to achieve application requirements of mesh quality. The optimized tetrahedral mesh can support more accurate applications such as mesh properties interpolation and 3D discrete geological analysis.

ACKNOWLEDGEMENTS This work is supported by National High Technology Research and Development Program of China (No. 2012AA121401) and NSFC (No. 41172300).

REFERENCES

1. Houlding, S.: 3D geoscience modeling: computer techniques for geological characterization. Springer-Verlag, 309 pp (1994)
2. Zlatanova, S., Rahman, A.A. and Pilouk, M.: Trends in 3D GIS development. *Journal of Geospatial Engineering*, 4(2), 71–80 (2002)
3. Wang, D. and Wan, S.: Robust Delaunay Tetrahedral Meshing Coupled with Advancing Front Method. *Journal of Southeast University* (English Edition), 18(2), 131–135 (2002)
4. Zhang, L.: A Parallel Algorithm for Adaptive Local Refinement of Tetrahedral Meshes Using Bisection. *Numerical Mathematics: Theory, Methods and Applications*, 2(1), 65–89 (2009)
5. Dong, P.: Generating and updating multiplicatively weighted Voronoi diagrams for point, line and polygon features in GIS. *Computers & Geosciences*, 34(4), 411–421 (2008)

Chapter 24

High Performance Computing of Hydrothermal Ore-Forming Systems: An Approach Based on the Lattice Boltzmann Method

Wei Qiang and Hui Cao

Abstract The lattice Boltzmann method is applied in the high performance computing of hydrothermal ore-forming systems. The scheme is highly amenable to parallelization and can deal with the multi-scalar fluid field without significant penalty. The method is implemented on a high performance computing platform with multi-processors and the paradigm of double-diffusive natural convection is used to verify the feasibility. The results are in agreement with those obtained by conventional methods. The parallelism is easily realized with the speedup ratio approaching the value of theoretical prediction. The present study provides a promising alternative to the simulation of hydrothermal ore-forming systems.

Keywords High Performance Computing • Lattice Boltzmann Method • Hydrothermal Ore-Forming Systems • Double-Diffusive Natural Convection

24.1 INTRODUCTION

The double-diffusive natural convection has been the subject of intensive researches due to its applications in the hydrothermal ore-forming systems over the past decades [1, 2]. The heat and mass transfer occurs simultaneously under the temperature and concentration gradients with different diffusivities. A wide variety of flow structures can be observed according to the physical properties of the fluid and the geometry of the enclosure [3, 4]. The phenomena are readily encountered in the large-scale fluid transportation and the mineralization in the earth's crust and mathematical models of a great diversity have been proposed to quantify the process [5]. Numerical simulation plays an indispensable role in the researches of

W. Qiang (✉)

School of Computer Sciences, China University of Geosciences, Wuhan, China

e-mail: qw@cug.edu.cn

H. Cao

Center of Information and Laboratory, China University of Geosciences, Wuhan, China

the double-diffusive natural convection. Recently the lattice Boltzmann method has developed into a highly efficient approach for simulating the dynamical processes in fluids [6]. The scheme is easier to implement than conventional computational fluid dynamic techniques, which has intrinsic parallelism and can deal with multi-scalar fluid fields and complex flow geometries without significant penalty [7]. Here, we study the double-diffusive natural convection for high Rayleigh numbers of temperature and concentration using the lattice Boltzmann method, which provides a promising alternative to the high performance computing of the hydrothermal ore-forming systems.

24.2 NUMERICAL SCHEMES

The lattice Boltzmann method originates from the lattice gas automata, a discrete particle kinetics utilizing a discrete lattice and a discrete time. The fundamental idea is to construct a simplified microscopic model to simulate the motion of fluids. The fluid particles move and collide on the lattice in discrete directions, whose ensemble average is employed to calculate the macroscopic quantities, including density and velocity. The continuous distribution functions interact locally and propagate after collision to the next neighbor node. The Boltzmann equation with the Bhatnagar, Gross, and Krook (BGK) approximation describe the evolution of the particle distribution function, which linearize the collision operator by using a single relaxation time towards the local equilibrium. The Navier-Stokes equation can be recovered from the Boltzmann-BGK equation by using the Chapman-Enskog expansion. The Oberbeck-Boussinesq approximation is adopted throughout this work, in which the density of the fluid is regarded as a constant except in the buoyancy force term. The temperature field and the concentration field are passively advected and diffuse into the main flow. The heat and concentration transport equations assume the similar form of the Boltzmann-BGK equation as that for the fluid density except for the external force term. The three dimensional 27-direction (D3Q27) lattice is used in this study [8]. In view of the translational symmetry of the system, periodical boundary conditions of velocity and passive scalars including temperature and concentration are applied in the horizontal directions. The non-equilibrium extrapolation boundary conditions are applied to the upper and lower walls.

The double-diffusive natural convection is defined as flow behavior of a fluid subject to gradients of two or more quantities with different diffusivities. The buoyancy forces due to temperature and concentration are opposing to each other in this work. The onset of the convection occurs where the temperature effect dominates over that of the concentration. The dimensionless equations are solved by the lattice Boltzmann method, including the Navier-Stokes equation, the continuous equations of mass, heat and concentration, as those in the reference [3]. We consider the enclosed fluid heated from below and cool from above that resembles the classic Rayleigh-Bénard convection. The concentration difference is also uniformly imposed on the top and bottom boundaries.

24.3 PARALLELISM

We realize the high performance computing of the double-diffusive natural convection based on the lattice Boltzmann method. The computation domain is divided into a lot of parts, which are computed on individual processor cores. The division is easy since the evolution of each lattice points is intrinsically parallel. The computation can be performed on high performance computer clusters as well as on a personal computer with a multicore processor. The algorithm with single relaxation time [6] is coded with the standard C/C++ language and the parallelism is implemented by the message passing interface (MPI). The computation is performed on the Dawning TC 5000A high performance computing cluster system. The computation parameters are summarized in Table 24.1.

24.4 RESULTS AND DISCUSSION

We perform the simulation of double-diffusive natural convection for various initial and boundary condition of temperature and concentration using the lattice Boltzmann method. A nondimensional scheme is adopted with the temperature and the concentration range between 0 to 1. The domain of the computation is defined as $384 \times 384 \times 64$. Fig. 24.1. presents the results for the Prandtl number 7.0, the Lewis number 3.0, the Rayleigh numbers of temperature 5.0×10^6 and of concentration 10^7 . The temperature and concentration field at the horizontal midplane of the fluid are shown in the upper left and upper right panels, respectively. Also the results of the Lewis number 5.0, the Rayleigh numbers of temperature 5.0×10^6 and of concentration 2.0×10^7 are shown in the lower left and lower right panels. Similar work has been reported in literatures [3], where the equations are numerically integrated with a hybrid spectral-finite difference code with laterally periodic and free-slip top and bottom boundary conditions. Here, we present only qualitative verification of the feasibility of the LBM, wherein the computation domain in our simulation is much smaller in comparison with the literature aforementioned. The parallel computer programs of non-blocking mode are designed to

Table 24.1 Computation parameters in the present implementations

Operating System	Suse Linux Enterprise 64 bit
Processor Type	AMD 2.6 GHz
Maximum Processor Number	24
Memory	32 GByte
Parallelism	MPI
Compiler	C/C++

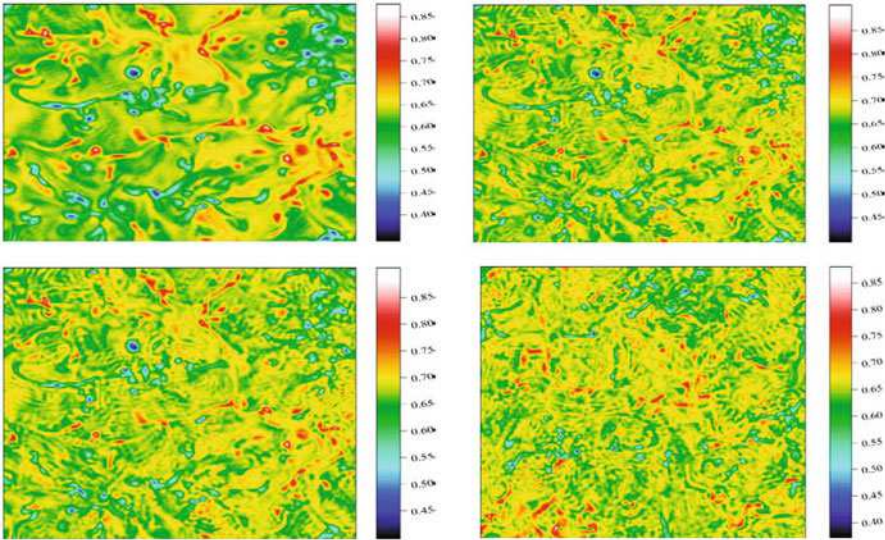
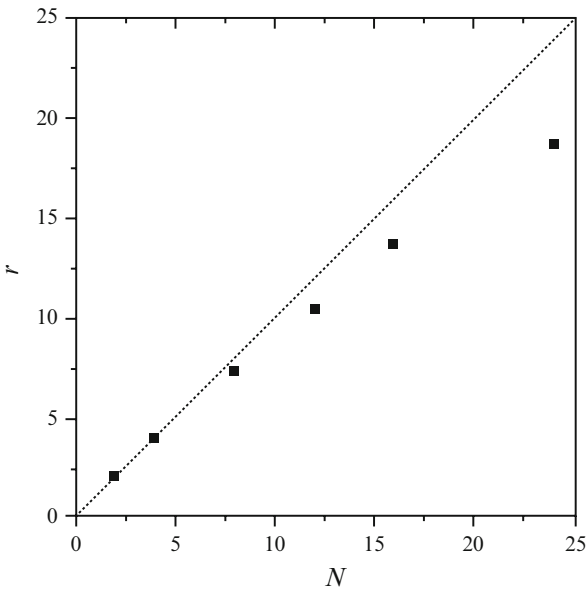


Fig. 24.1 Temperature and concentration fields at the horizontal midplane of the fluid

Fig. 24.2 Acceleration of the computation on a high performance computer with multiprocessors



verify the efficiency of the parallelism for the lattice Boltzmann method on a high performance computing platform. The acceleration of the computation approaches the value of theoretical prediction (dotted line) as shown in Fig. 24.2, wherein N is the number of processors and r is the speedup ratio.

24.5 SUMMARY

We perform a high performance computation of double-diffusive natural convection by the lattice Boltzmann method. The scheme is coded with the standard C/C++ language and the parallelism is implemented by the message passing interface. The computation is realized on the Dawning TC 5000A high performance computing clusters with the speedup ratio approaching the value of theoretical prediction. The present study provides a promising alternative to the simulation of hydrothermal ore-forming systems.

ACKNOWLEDGEMENT This research is supported in part by the National Natural Science Foundation of China (41172301) and the Fundamental Research Funds for National University, China University of Geosciences (Wuhan) (CUG090109).

REFERENCES

1. Biscoff, J.L. and Rosenbuer, R.J.: Salinity variation in submarine hydrothermal systems by layered double-diffusive convection, *Journal of Geology*, 97, 613–623 (1989)
2. Dai, B.Z., Zhao, K.D. and Jiang, S.Y.: Modern sea-floor hydrothermal activity and genesis of massive sulfide deposits: an overview. *Bulletin of Mineralogy Petrology and Geochemistry*, 23, 246–254 (2004)
3. Paparella, F. and von Hardenberg, J.: Clustering of salt fingers in double-diffusive convection leads to staircase-like stratification. *Phys. Rev. Lett.*, 109, 014502 (2012)
4. Schoofs, S., Trompert, R.A. and Hansen, U.: The formation and evolution of layered structures in porous media: effects of porosity and mechanical dispersion. *Phys. Earth Planetary Interiors*, 118, 205–225 (2000)
5. Yang, R., Ma, D., Bao, Z., Pan, J., Cao, S. and Xia, F.: Geothermal and fluid flowing simulation of ore-forming antimony deposits in Xikuangshan. *Science in China D*, 49, 862–871 (2006)
6. Shan, X.: Simulation of Rayleigh-Bénard convection using a lattice Boltzmann method. *Phys. Rev. E*, 55, 2780–2788 (1997)
7. Llewellyn, E.W.: LBflow: An extensible lattice Boltzmann framework for the simulation of geophysical flows. Part I: theory and implementation. *Computers & Geosciences*, 36, 115–122 (2010)
8. Mei, R., Shyy, W., Yu, D. and Luo, L.S.: Lattice Boltzmann Method for 3-D flows with curved boundary. *J. Comp. Phys.*, 161, 680–699 (2000)

Chapter 25

Resurrecting GSLIB by Code Optimization and Multi-core Programming

Oscar Peredo and Julián M. Ortiz

Abstract A methodology to accelerate GSLIB routines is presented, using the last updated Fortran codes as base. Minimal code modifications are added decreasing as much as possible the elapsed time of execution of the studied routines. If multi-core processing is available, the user can activate special instructions in the code to speed up the execution using all resources of the CPU. Two case studies are presented with the corresponding elapsed times and speedup results.

Keywords Groundwater Geostatistics • GSLIB • Multi-core programming • Code optimization

25.1 INTRODUCTION

The GSLIB software package, originally presented by Deutsch and Journel [1], has been used in the geostatistical community for more than 30 years. Since its original development, its routines have helped many researchers and practitioners in their studies, mainly due to the accuracy and performance delivered by this package. Many efforts have been proposed to accelerate or enhance the scope of the original package, being WinGslib [2] and SGEMS [3] the most relevant efforts. SGEMS moves away from Fortran and implements Python and C/C++ code in conventional and new algorithms. Although there is a significant gain with this change, for many practitioners and researchers, the simplicity of Fortran code and the availability of an extensive pool of modified GSLIB-based programs makes it hard to abandon this package. According to the authors' knowledge, few efforts have been reported in order to accelerate the GSLIB package by itself: analyzing, optimizing and accelerating the original Fortran routines. In this work we present case studies of accelerations performed on original GSLIB routines (in their Fortran 90 versions),

O. Peredo (✉)

ALGES Lab, Advanced Mining Technology Center, University of Chile, Santiago, Chile
e-mail: operedo@alges.cl

J.M. Ortiz

ALGES Lab, Advanced Mining Technology Center, University of Chile, Santiago, Chile
Department of Mining Engineering, University of Chile, Santiago, Chile

using advanced code optimization and multi-core programming techniques. We explain our methodology, in which a performance profile is obtained from the original routine, with the aim of identifying overhead sources in the code. After that, incremental modifications are applied to the code in order to accelerate the execution. OpenMP [4] directives are added in the most time consuming parts of the routines.

25.2 GSLIB STRUCTURE

According to GSLIB documentation [1], the software package is composed by a set of utility routines, compiled and wrapped as a static library named `gslib.a`, and a set of applications that call some of the wrapped routines. We will refer to these two sets as *utilities* and *applications*. Typically, a main program and three subroutines compose an *application*. The first subroutine is in charge of reading the parameters from the input files, the second subroutine executes the main computation and the third writes out the results using predefined output formats. Additionally, two structures of static and dynamic variables are used by the main program and each subroutine: an include file and ageostat module. The include file contains static variable declarations, like constant parameters, fixed length arrays and common blocks of variables. The geostat module contains dynamic array declarations, which will be allocated in some of the subroutines with the `allocate` instruction. *Utility* is self-contained allowing sharing variables with other utilities and applications through common block variable declarations. The above-mentioned structure is common to many applications and has advantages and disadvantages. On the one hand, the user/programmer can easily identify each part of the code and where the main computations are occurring. On the other hand, the use of implicit typing and module/include variable declarations in the applications and utilities makes it difficult to set up a data-flow analysis [5] of all the variables in any state of the execution. With this kind of analysis, the user/programmer can estimate the state of the variables in different parts of the code, being able to know if a variable is *alive* or *dead* at some point of execution (*alive* means that the variable will be used in the future after this point of execution; *dead* means that it will not be subsequently used). If the user/programmer has as final goal the computation of results and nothing more, this information can be seen as irrelevant. However, if the user/programmer is intended to re-design some parts of the code or accelerate the overall execution, the data-flow analysis is the first step into its journey. With these concepts in mind, in the next sections we show how to apply a methodology to accelerate GSLIB applications and utilities.

25.3 METHODOLOGY

The proposed methodology consists in three steps. First we have to re-design the application/utility code to identify the state of each variable, array or common block during the execution. This step is necessary to enable the user/programmer to insert OpenMP directives into the code in a smooth and easy way and also to help the profiler tool to correctly identify which lines of the code are adding overhead to the overall calculation. Secondly, we have to study the run-time behavior of the application using a profiler tool. In our case we choose the Linux-based tools `gprof` [6] and `oprofile` [7]. These tools can deliver several statistics, among the most important are: elapsed time per routine or line of code, number of calls per routine, number of cache misses per line of code and number miss predicted branches per line of code. Each of these statistics will be described in further sections. With this information, we can identify which lines of the application or used utilities are generating overhead. We can modify some parts of the code using the profiled information. For each modification, we must re-measure the elapsed time and statistics, in order to accept or reject the modification. At last, once an optimized version of the application is released, we can add Open MP directives in the most time consuming parts of the code, for example in simulation or grid loops. Each directive defines a parallel region, which will be executed by several threads, with a maximum defined by the user and bounded by the number of physical CPU cores available. For each directive the user/programmer must study the data-flow of the variables inside the parallel region, and specify if the variables will be shared or private. If original GSLIB unmodified routines are parallelized, this analysis can be very tedious and error prone. For this reason, the first step of the methodology is fundamental in order to facilitate this analysis.

25.4 PROFILING AND CODE OPTIMIZATION

As mentioned in the previous section, we perform a Linux-based profiling with the tools `gprof` and `oprofile`. In this section we will explain briefly the interpretation of these tool's outputs with the `sisim` application of GSLIB as example. The `gprof` tool gives an estimated percentage of the total elapsed time that each routine has been running during the execution. The output report can be viewed in Fig. 25.1. We can see in this report that the routine `skrige` (implemented as subroutine in `sisim`) and `ksol` (utility contained in `gslib.a` library) together consist in approximately 96% of the total elapsed time. With this information we can focus our optimization effort into these routines.

Another useful tool that allows us to obtain line-by-line statistics is `oprofile`. In Fig. 25.2 we can see an output report with the estimated number/percentage of CPU clocks cycles executed in each line of `sisim` and its associated utilities. In this figure we can see the report corresponding to `ksol` utility, which represents 50% of the

```
% cumulative self self total
time seconds seconds calls s/call s/call name
48.96 29.44 29.44 25584960 0.00 0.00 krige_
47.00 57.70 28.26 25584960 0.00 0.00 ksol_
2.11 58.97 1.27 2558496 0.00 0.00 srchnd_
...
```

Fig. 25.1 Output of gprof tool applied to sisim application

```
: subroutine ksol(nright, neq, nsb, a, r, s, ising)
...
10357 0.1186 : do i=k,nl
: ll=ii
14438 0.1654 : ii=ii+1
90551 1.0406 : ap=a(ii)*piv
: lp=lp+1
72911 0.8351 : ij=ii-kml
779008 8.9224 : do j=i,nl
: ll=ll+j
1148026 13.149 : a(ij)=a(ij)-ap*a(ll)
: end do
208109 2.3836 : do llb=k,nl,neq
: in=llb+lp+nm1
6 0.0000 : ll=llb+nm1
800864 9.1728 : r(in)=r(in)-ap*r(lll)
: end do
: end do
```

Fig. 25.2 Output of oprofile tool counting the number of CPU clock cycles executed, applied to sisim application

<pre>... 1 c 2 c MAIN LOOP OVER ALL THE SIMULATIONS: 3 c 4 5 6 7 8 9 10 11 12 13 14 15 16 17 18 19 do isim=1,nsim 20 c 21 c Work out a random path ... 22 c ...</pre>	<pre>... 1 c 2 c MAIN LOOP OVER ALL THE SIMULATIONS: 3 c 4 c\$omp parallel default(firstprivate) shared(x,y,z) 5 #ifdef _OPENMP 6 threadId = int(omp_get_thread_num()) 7 if (numThreads>1) then 8 idum=threadId*ixv(1) 9 ixv(:)=0 10 ixv(1)=idum 11 do i=1,1000 12 p = acorni(idum) 13 end do 14 end if 15 #else 16 threadId = 0 17 #endif 18 c\$omp do schedule(dynamic,1) 19 do isim=1,nsim 20 c 21 c Work out a random path ... 22 c ...</pre>
---	--

Fig. 25.3 OpenMP directives added to sisim application (left: original, right: modified). In lines 5-15 acorni's seed is modified in each thread, to generate different simulations

total CPU clock cycles. Special interest arises in three lines of this utility, which involve more than 30% of the cycles. With this information we know exactly which lines may be generating overhead.

25.5 MULTI-CORE DIRECTIVES WITH openMP

Once the target application has been re-designed and hopefully optimized, we can still accelerate it by using multiple threads of execution in critical parts of the execution. In order to do this, we can add OpenMPdirectives in some parts of the code. For example, in Fig. 25.3 we can see the required directives to split a

simulation loop into several threads of execution. A careful scope specification of the variables is needed, allowing ones to be shared and others to be private to each thread. As mentioned in Section 25.2, at this point of the methodology it is helpful to have a sketch of the data-flow of each variable in order to minimize the errors in the parallelization of the code. This data-flow analysis can be executed by the user/programmer adding and changing some parts of the code. Some of the recommended modifications are: add implicit none statement at the beginning of each routine, pass all routine's parameters as arguments (even if there are several arguments), remove unnecessary routines (even if it worsens the readability of the code) and minimize side-effects inside of routines (modification of common blocks or module variables).

25.6 CASE STUDY

The proposed methodology was applied to accelerate two GSLIB applications: sisim and gamv. We tested the final versions of the applications in two Linux-based systems: S1 with 2x8-cores Intel Xeon CPU E5-2670 0 @ 2.60GHz, and S2 with 1x4-cores Intel Xeon CPU E31225 @ 3.10GHz. Each application was tested using a small and large scenario. The results can be viewed in Tables 25.1 and 25.2. In sisim, the parallel loop corresponds to the simulations and in gamv it corresponds to the outer nodal loop. According to the obtained results, the scalability obtained is

Table 25.1 Time/Speedup results for sisim. Small scenario: $40 \times 60 \times 12$ grid nodes, 96 realizations. Large scenario: $400 \times 600 \times 12$ grid nodes, 16 realizations

#Threads	Time S1 [s] (Speedup)		Time S2 [s] (Speedup)	
	Small	Large	Small	Large
1 (base gslib)	109.2 (1.0x)	2024 (1.0x)	79.64 (1.0x)	1467 (1.0x)
1 (optimized)	94.31 (1.2x)	1739 (1.2x)	75.99 (1.1x)	1419 (1.0x)
2 (optimized)	38.53 (2.8x)	753 (2.7x)	38.44 (2.1x)	710 (2.1x)
4 (optimized)	19.59 (5.6x)	372 (5.4x)	20.45 (3.9x)	376 (3.9x)
8 (optimized)	10.7 (10.3x)	205 (9.9x)	-	-
16 (optimized)	6.37 (17.1x)	130 (15.5x)	-	-

Table 25.2 Time/Speedup results for gamv. Small scenario: 10 lags, 1 direction, 12000 data points. Large scenario: 10 lags, 1 direction, 65536 data points

#Threads	Time S1 [s] (Speedup)		Time S2 [s] (Speedup)	
	Small	Large	Small	Large
1 (base gslib)	4.97 (1.0x)	13.68 (1.0x)	4.83 (1.0x)	9.74 (1.0x)
1 (optimized)	4.94 (1.0x)	6.45x (2.1x)	4.84 (1.0x)	6.63 (1.5x)
2 (optimized)	2.47 (2.0x)	3.37 (4.1x)	2.49 (1.9x)	3.34 (2.9x)
4 (optimized)	1.27 (3.9x)	1.83 (7.5x)	1.33 (3.6x)	1.9 (5.1x)
8 (optimized)	0.67 (7.4x)	1.08 (12.7x)	-	-
16 (optimized)	0.37 (13.4x)	0.71 (19.3x)	-	-

close to linear, and in some cases superlinear (due to the code optimizations added to the application). All programs were compiled using GCC gfortranversion 4.7 with the option `-O3`.

25.7 CONCLUSIONS AND FUTURE WORK

We have shown a methodology to accelerate GSLIB applications and utilities based in code optimizations and multi-core execution with OpenMPdirectives. The methodology was tested in two well-known GSLIB applications: *sisim* and *gamv*. In both applications we have achieved almost linear (superlinearin some tests) speedup, using as base code the last updated Fortran 90 version of GSLIB. All tests were performed in Linux-based systems, however no external libraries or intrinsic operating system routines were used, so the code could be compiled and tested in other systems (Windows and Mac) without further modifications. Our final goal is to apply this methodology to all (or at least the most important) applications and utilities from GSLIB, setting the compilation scripts as general as possible, so other scientists and practitioners could benefit from this effort. We also are exploring the addition of new acceleration technologies, like Graphics Processing Units (GPU) [8] and Many Integrated Cores (MIC) [9], working as external routines into GSLIB's applications.

REFERENCES

1. Deutsch, C.V. and Journel, A.G.: *GSLIB: geostatistical software library and user's guide*. Oxford University Press, New York (1992)
2. Statios, L.L.C.: *WinGslib Installation and Getting Started Guide*. Available online <http://www.statios.com/WinGslib/GettingStarted.pdf> (2001)
3. Remy, N., Boucher, A. and Wu, J.: *Applied geostatistics with SGeMS: A user's guide*. Cambridge University Press (2011)
4. Chandra, R., Dagum, L., Kohr, D., Maydan, D., McDonald, J. and Menon, R.: *Parallel Programming in Open MP*. Morgan Kaufmann Pub. Inc., San Francisco, CA (2001)
5. Aho, A.V., Lam, M.S., Sethi, R. and Ullman, J.D.: *Compilers: Principles, Techniques, and Tools*. 2nd Edition. Addison Wesley (2006)
6. Graham, S.L., Kessler, P.B. and McKusick, M.K.: *Gprof: A call graph execution profiler*. SIGPLAN No. 39, 49–57 (2004)
7. Levon, J.: *O Profile Manual*. Victoria University of Manchester (2004)
8. NVIDIA Corporation: *Graphical Processing Units*. <http://www.nvidia.com/object/what-is-gpu-computing.html> (2014)
9. Intel Corporation: *Many Integrated Cores Architecture*. <http://www.intel.com/content/www/us/en/architecture-and-technology/many-integrated-core/intel-many-integrated-core-architecture.html> (2014)

Chapter 26

Distribution Law for Mineral and Chemical Constituent Fractions in Rocks and Ores

B.K. Sahu

Abstract Mineral and chemical constituents are multiple in numbers (say, C-dimension with $C > 3$) and are estimated as positive random fractions in open interval (0,1) of total weight/volume of measurement. Such data suffer from several drawbacks as regards their statistical analysis and inference and subsequent geological/mining applications. These defects can be listed as: (i) data are closed with spurious negative correlations among the constituents (that is data are not FULLRANK lacking unique Inverse Matrix), (ii) data are Binomial/Poisson for major/trace components where means are highly correlated to corresponding variances and Not Independent as is required for Gaussian density that is needed for conventional LINEAR statistical estimations, tests of hypotheses etc. and mean values are highly positively skewed for constituent fractions less than 0.5 ($1/C = 0.33$), (iii) variances are Not Homoscedastic over mean values as is required for Gaussian density for regression(correlation) studies, and (iv) data belong only to the interior points of C-dimensional complex excluding apices, hyper-edges, hyper-planes etc. These drawbacks can be eliminated by suitable pre-analysis nonlinear transformation, such as $\log(c(i)/1 - c(i))$ where $c(i)$ is the fractional value of the i th constituent in the rock/ore sample that was petrographically /chemically measured. The advantages of Gaussian density of constituents are LINEAR additions of random variables remain Gaussian (or, data are CLOSED or have CONSTANT SUM under summations) and hence, their second order statistics (mean, covatiance/correlation) are the only Two Non-ZERO Parameters needed for statistical characterization, as all the higher cumulants are zeros. Since rocks/ores are heterogeneous solids, a suitable volume/weight, representative elementary volume (REV), must be sampled and chemically analyses so that the resulting data are consistent, stable, unbiased and reliable. The author and his students have been using a $\log(c/1-c)$, or $\log(\text{odds})$ having multiplicative errors(NOT additive errors as given in conventional probability theory), pre-transformation for Gaussianising the geochemical data and their subsequent statistical inference since 1980s and have obtained very good geological inferences for several ores including, Au, BIF, Pb-Zn-Cu-Ag, Cu-Ag, P and associated single and multi-element mineralisations. A measure-theoretic proof of the applicability of this logarithmic pre-transform, $\log(c/(1-c))$,

B.K. Sahu (✉)

Department Earth Sciences, Indian Institute of Technology-Powai, Mumbai, India

e-mail: bas_sahu@yahoo.co.in

to obtaining Gaussian density is given. Applications of the pre-transform for Gaussianisation of fractional geochemical data for optimal grinding and beneficiation of ores, blending operations and processing to Marketable Grades, for exploration, anomaly detection, development & mine planning, and for obtaining Pathfinders of Single and Multiple-element ores are included here.

Keywords Hierarchical Geochemical Constituents • Fractional Constituents of Rocks/Ores • Logarithmic Pre-Transformation • $\log(C(I)/(1-C(I)))$ • Statistical Studies • Grade and Reserve Estimation • Path Finders for Mineral Exploration

26.1 INTRODUCTION

Mineral resources occurring in shallow crustal depths are becoming increasingly scarce that requires their intensive exploration for sustainable development needed for societal growths. Rocks and ores comprise multi-dimensional constituents, C , (usually $C > 3$) having a hierarchical structure: (Group I: minerals; Group II: chemical molecules, and Group III: chemical elements and isotopes) that are often exploited for the valuable constituents. Constituents in rocks/ores are usually represented as random positive fractions belonging to the open interval (0-1) where 1 represents, for standardization, the maximum total weight/volume/area/length/number of measured value in rock/ore sample that is studied depending on method of measurement needed/used. However, these fractional proportions have several deficiencies for statistical analyses and inferences needed for geological and mining applications. The main defects of fractional proportions include: (i) closure constraint due total sum being normalized to a constant (e.g. 1.0, 100%, 1 million, 1 billion) that induces dangerous and spurious negative correlations among the major and minor constituents and (ii) the data matrix is not of full rank (C) but possess a reduced rank of ($C-1$) or less, and its inverse is non-unique; (iii) each fractional constituent has a Binomial/Poisson distribution for major/minor and trace constituents, respectively, and hence do not possess independence of means and variances among the samples which is required for regression/correlation analyses of samples in a population (rock/ore type). However, since the fraction $(1 - c(i))$ is dependent only on $c(i)$ and happens to be independent of variations occurring in any other constituents in the rock/ore, the odds ratio $c(i)/(1 - c(i))$ is independent of variations in other constituents. Linear statistical theory can be applied to such pre-transformed data for parameter estimations, hypotheses tests, optimal decisions, etc. (iv) Variation of random mean proportions in rocks/ores are usually positively skewed and negatively skewed for low mean ($< 1/2$) and high mean ($> 1/2$). The transformed fractional constituent $c(i)$, i.e., using the $\log(c(i)/(1 - c(i)))$, varies within the real line and has a real valued mean and a variance of 4.0 [7]. The variance is 4.0 because $\log(c(i)/(1 - c(i)))$ is $2 \times (1/2) \log(c(i)/(1 - c(i)))$ which is Gaussian and possess unit variance about its population average concentration c (i) values that are independent sample values of i th constituent. The proof of this

result can be obtained by invoking Gaussianization of correlation coefficient, r , using the wellknown Fisher 's z ' = $(1/2) \log ((1+r)/(1-r))$ transform that reduces to $(1/2) \log(c(i)/(1-c(i)))$ as $c(i)$ varies from 0 to 1, unlike r which varies from -1 to +1. Gaussian distributions on real line are most useful in statistics since Gaussian distribution has only two parameters, mean and variance, and all the higher-order cumulants greater than order two are theoretically known to be zeros. Hence, after making the $\log(c/(1-c))$ or the \log (odds ratio) pre-transformation of all fractional constituent data, we can use multivariate normal distribution (MND) theory for all statistical analyses and inferences and obtain the correct estimation of parameters and decisions on hypotheses that we desire for analyses and inferences in geology.

The author (since 1980s, [6]) and many of his students have used this pre-transformation for study and inferences on many mineral deposits in India and found the results to be very useful. The deposits studied were for Au; BIF; Pb-Zn-Cu-Ag; Cu-Ag; Phosphorous (P) and associated single- and multi-metal ores. The present model of $\log(c/(1-c))$ pre-transform or logit pre-transform to Gaussian for fractional geochemical data can be considered to be very closely similar to the Correlated Topic Model (CTM) recently introduced in [2]. In the CTM model, hierarchical items such as 'topics' may be considered equivalent to our 'minerals', 'words' to our 'chemical molecules', and 'letters' to our 'chemical elements' (including isotopes) for the fractional geochemical data. A measure-theoretic proof for $\log(c/(1-c))$ or logarithmic pre-transform have been given in [3, 4, 5, 7]. The log-ratio models advanced in [1] and Aitchison's coworkers, unfortunately, do not solve the most serious problems, such as, neither the rank problem (i.e., less than full rank C), nor the negative spurious correlation problem because of closed data table, [3]. This conclusion is correct and true as geochemical data for rocks/ores belong to the set of Interior Points of C Simplex but do not include apices, edges and planar boundary surfaces of the C Simplex [11]. Mining applications of this statistical technology are useful for liberation of ore minerals by optimal grinding, blending and ore beneficiation studies, anomaly detection, identifying pathfinders for single- and multi-element ores; mine feasibility, mine development, sustainable mining etc.[10]. The statistical optimization using this pre-transform also provides optimal (maximum) profits in mining industry and makes mining industry sustainable.

26.2 Applications

Statistics is the technology of 21st century and along with current capability of computers, it will be essential, beneficial and most useful to mining and mineral processing industries. As explained earlier, a $\log(c(i)/(1-c(i)))$ pre-transform of fractional concentrations $c(i)$; $0 < c(i) < 1$ yields the desired independence sample $c(i)$ values and Gaussian pdf for each of the constituents (i) present in the rock or ore. This is necessary for characterization/estimation of parameters of each pdf, and for hypotheses tests and inference. Univariate and multivariate statistical models

are used for single and multiple pre-transformed random variables, respectively. These models are useful for geochemical exploration, mining, mine planning, mineral processing and beneficiation and for marketing such that maximal profits with minimum environmental damage can be achieved to obtain sustainable economic and societal growth. Some applications of linear statistical Gaussian technology to geosciences are listed below for getting the feel of different scenarios involved.

EXAMPLE: Estimation of ore reserves and average assays:

In the distant past, spatial distributions of assays and their pdfs were not accounted for and simple calculations yielded these quantities based on geometry of ore-body and arithmetic averaging of assays within mineable ores. Geology of syngenetic deposits produces uni- or multi-metal Binomial/Poisson distribution having homogeneous variances, whereas epigenetic deposits are likely to possess bimodal (low-assays in host rock and higher assays in ore zones) distributions that need separate treatments. A $\log(c/(1-c))$ pre-transform of fractional assays achieves linearity, Gaussianity and homoscedasticity of variance with elimination of spurious negative correlations among the constituents [8–10].

26.3 Spatially Correlated Samples on $\log(C/(1-C))$ Basis

This situation often arises in development and production stages when a large number of geochemical data becomes available. The data is having signal (mineralized assay) and noise (random errors) and time (spatial) series model separated the signal needed for average assay computation from the Gaussian noise (as $\log(c/(1-c))$ is Gaussian its linear decomposition into signal plus noise components are Gaussian too) giving the confidence limits to the average assay. Models may be non-stationary ARIMA (p, d, q) which is made stationary (ARMA(p,0,q)) by differencing d times. Integration of location data over the spatial domain gives the total volume and of signal gives the average assay. Such integration can be done blockwise to obtain block reserves and block average assays. More details of general time series modeling are given in [8]. Multidimensional time series models can be used for 2D or 3D modeling of mines assays, thicknesses, reserves etc. (see [8]).

Pathfinders include minerals, molecules, elements and isotopes and are very useful for exploration of uni- and multi-metal ores. These are characteristically easy to recognize, possess higher concentrations than sought element, higher occurrence frequency, and can be chemically analysed cheaply and easily at much less time. Correlation matrix, R, of pre-transformed fractional constituent data is then computed using R-mode analysis (cheaper and faster than Q-mode). The correlation coefficients could be strongly positive ($r > .50$), strongly negative ($r < -.50$) or weak ($-.50 < r < +.50$). Factor analysis (FA) of R (without weak r 's), provides rotated factors that are statistically significant to yield pathfinder(s) loaded strongly on high positive and/or negative correlations among constituents. Pathfinders can also be

identified through use of partial correlations but this method is computationally more intensive and decision may be confounded (non-unique).

Multi-element or multi-mineral ores would require Canonical Correlation Analysis with the mineable metals/minerals taken as criterion vector and other sets as predictor and/or control random vectors. FA in such cases may not be useful unless criterion vector has only one random constituent which is mineable. More details on finding geochemical pathfinders can be obtained from canonical correlation analysis given in [9].

REFERENCES

1. Aitchison, J.: The statistical analysis of compositional data. Chapman and Hall, London (1986)
2. Blei, D.M. and Lafferty, J.D.: A Correlated Topic Model (CTM) of SCIENCE. *Annals Applied Statistics*, 1(1), 17–35 (2007)
3. Carranza, E.J.M.: Analysis and modeling of geochemical anomalies using log-ratio transforms. *Jour. Geochemical Exploration*, 110, 167–185 (2011)
4. Le Cam, L.: Asymptotic methods in statistical decision theory. New York, Springer (1986)
5. Le Cam, L. and Yang, L.: Asymptotics in statistics. New York, Springer (1990)
6. Sahu, B.K.: Mineral deposit modeling. *Mineralium Deposita*, 17, 99–104 (1982)
7. Sahu, B.K.: Statistical Inference for geochemical and petrographic data. Proc. Rec. Res. NW India, M.S. Univ., Vadodara, Gujarat (1995)
8. Sahu, B.K.: Time series modeling in Earth Sciences. Balkema, Lisse, Netherlands (2003)
9. Sahu, B.K.: Statistical models in Earth Sciences. B.S. Publications, Hyderabad (2005)
10. Sahu, B.K.: Evaluation of Iron Ore prospect in BIF setting: A Geostatistical Approach. Intl. Sem. Iron Ore Genesis and Exploration. SGAT, Bhubaneshwar, Proc. Volume (2008)
11. Sahu, B.K.: Geochemistry applied to sustainable development of mineral resources. Intl. Sem., Souvenir Volume, ISM, Dhanbad (2013)

Chapter 27

Comparison of Spatial Interpolation Methods for Mapping Rainfall in Indian Himalayas of Uttarakhand Region

Madhuri Kumari, Ashoke Basistha, Oinam Bakimchandra, and C.K. Singh

Abstract Reliable estimation of rainfall distribution in mountainous regions poses a great challenge not only due to complex relationships between irregular topography and precipitation, but also due to non-availability of abundant rainfall measurement points. This study presents a comparison of univariate and multivariate methods for spatial interpolation of rainfall in complex terrain of Indian Himalayas in Uttarakhand region. To understand the role of topography in explaining the spatial variability of rainfall, elevation and slope calculated from DEM are incorporated as covariables in multivariate interpolation methods. Further, the study area is divided into three different regions based on variation in the elevation of topography and the performance of different spatial interpolation methods is analyzed for subdivided regions. The normal annual rainfall data of 80 rain gauge stations spread over 53,484 km² is used to generate rainfall map using different interpolation methods. Cross validation is used to compare the prediction performances of the three multivariate geostatistical interpolation algorithms: simple kriging with varying local means (SKlm), ordinary cokriging (OCK), regression kriging (RK) and two univariate techniques: inverse distance weighted (IDW) and ordinary kriging (OK). The inclusion of elevation or slope as auxiliary variables improves the prediction of rainfall in mountainous region. SKlm performs better

M. Kumari (✉)

Department of Natural Resources, TERI University, New Delhi, India

Department Civil Engg., Amity School of Engineering & Technology, Amity University, Noida, Uttar Pradesh 201313, India

e-mail: mkumari@amity.edu

A. Basistha

Hydro Power & Water Resources, Lahmeyer International (India) Pvt. Ltd., Intec House, 37, Institutional Area, Sector 44, Gurgaon 122002, India

O. Bakimchandra

Department of Civil Engineering, School of Engineering, Shiv Nadar University, Gautam Budh Nagar, Uttar Pradesh 201314, India

C.K. Singh

Department of Natural Resources, TERI University, New Delhi 110070, India

than OCK in all the cases. Residual kriging outperforms SKlm in Shivalik and Lesser Himalayas region where the correlation between rainfall and elevation is high ($r_{\text{shivalik}} = 0.79$, $r_{\text{lesserhimalayas}} = 0.5$). Also, OCK proves to be a better choice than OK only when the correlation between the rainfall and secondary variable (elevation or slope in this case) is good. When the data of Shivalik region ($r=0.79$) is considered, the RMSE of OCK is 363 and that of OK is 368. The prediction using OK and OCK yields similar result when the correlation between rainfall and elevation is moderate ($r < 0.4$). For all the cases, residual kriging outperforms OCK.

Keywords Geostatistics • Kriging • Mountainous region • Himalayas • Rainfall Interpolation

27.1 INTRODUCTION

The reliable estimation of spatial variability of rainfall is very crucial in hydrological applications such as assessment of water resources availability at basin scale, rainfall-runoff modelling and study of climate change impact on hydrological cycle. Due to economic considerations and installation challenges in complex terrain, rain gauge stations are placed irregularly and at a coarser grid in mountainous region. This poses a great challenge in accurate interpolation of rainfall. Different deterministic methods such as Thiessen polygon and inverse distance weighted (IDW) [1], estimates rainfall values at unknown points by using the values of surrounding observations. Although these methods are simple and the interpolated values can be quickly calculated, they do not account for spatial dependencies of data. The geostatistical methods includes kriging and cokriging techniques and considers the spatial dependencies of observations for interpolation process. These methods have been increasingly preferred over conventional methods [2, 3, 4, 5] as it allows inclusion of secondary information like elevation, weather radar data and are found to perform better in complex terrain with sparse data [5–7, 8]. From literature survey, inferring a best method for interpolation of rainfall is difficult. The result of different kriging techniques varies across the study area and seems to be closely related to the characteristics of data sets and terrain of the area. The objective of this study is to test the hypothesis, “Geostatistical techniques that incorporates covariables related to terrain characteristics provide better interpolated surface of rainfall in complex terrain as compared to the techniques that does not take into account any of these secondary information”. Thus, the study was carried out to evaluate the performance of different interpolation techniques when applied in mountainous region of Indian Himalayas in Uttarakhand region. To understand the role of topography in explaining the spatial variability of rainfall, elevation and slope derived from DEM are incorporated as covariables in geostatistical model. Further, the study area was divided into three different regions based on variation in the elevation of topography and the performance of different spatial interpolation

methods was analyzed for subdivided regions. In this paper, normal annual rainfall data from the Uttarakhand region are interpolated using two types of interpolation methods: (1) univariate algorithms that considers only rainfall data recorded at the meteorological stations (ordinary kriging, OK and simple kriging, SK); (2) multivariate algorithms that supplements rainfall data with secondary information (ordinary cokriging, OCK; SK with varying local means, SKlm; and regression kriging, RK). Prediction performances of the algorithms are compared using cross-validation.

27.2 STUDY AREA AND DATA USED

The study area comprises of Indian Himalayas in Uttarakhand state of India which covers an area of 53,484 km² and lies between 28°42'N to 31°28'N and 77°35'E to 81°05'E coordinates. The topography of this area is complex and rugged. The altitude varies from 175 m to 7,409 m above mean sea level (GTOPO 32). The annual rainfall in this region varies between 948 mm and 2,986 mm. Uttarakhand is divided into four physiographic zones [9]. The plain area in the foothills with an average height of 175–600 m is Terai (finer alluvium deposits) and Bhabar (deposits of pebbles) region. The second zone comprises of area with average elevation of 600 m – 1200 m and is known as Shivaliks. The third zone is known as Lesser Himalayas covering areas with average elevation of 1200 – 3000 m. The average elevation of fourth zone is 3000–7500 m and is known as Great Himalayas. For this study, normal annual rainfall data of 80 rain gauge stations were used based on the records during period 1901–1950. GTOPO32 is the digital elevation model (DEM) of 1 km spatial resolution and was used for extracting topographical variables namely, smoothed elevation and slope. Fig. 27.1 shows the spatial variability of elevation, slope and rainfall data of study area.

27.3 METHODOLOGY

The comparative study of spatial interpolation techniques was carried out in three different phases [10].

1. **EXPLORATORY ANALYSIS OF DATA:** The rainfall data was clustered into 3 different groups based on the elevation of the area. Descriptive statistics was used to describe the data distribution (Table 27.1). The correlation between rainfall and topographical variables, altitude and slope was analysed.
2. **STRUCTURAL ANALYSIS OF DATA:** In this phase, the spatial distribution of the variable was analysed. Semivariograms were plotted to quantify the spatial correlation and to understand the distribution pattern of rainfall data. Direction dependent variability was ignored due to lack of sufficient data.

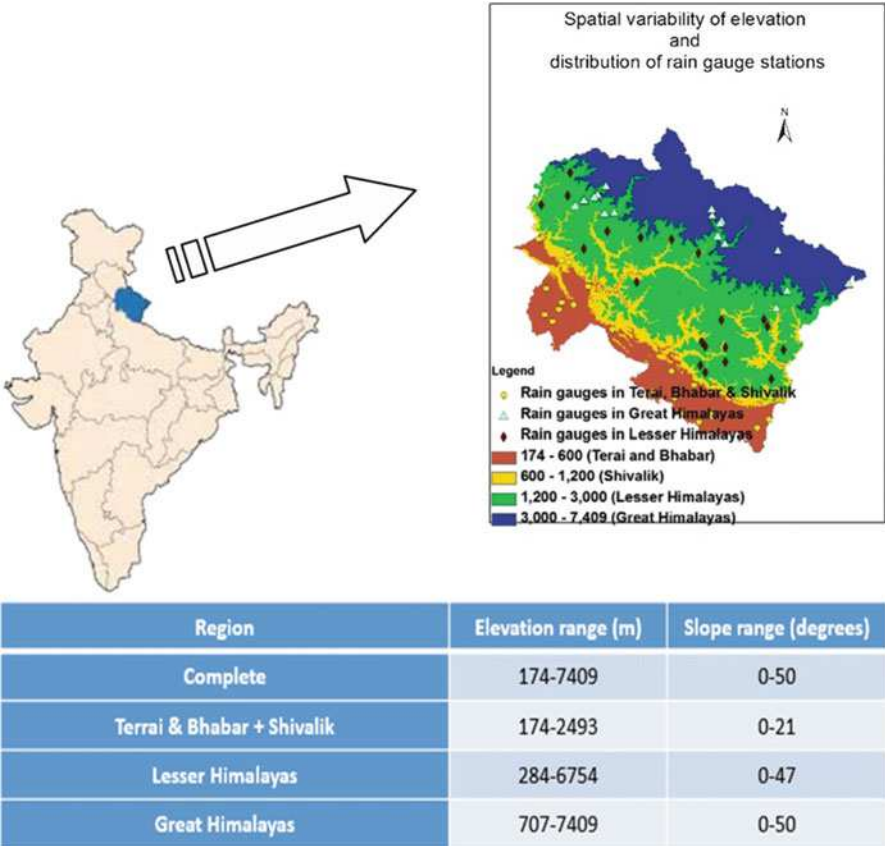


Fig. 27.1 Study Area: Spatial variability of elevation, slope and distribution of rain gauge stations in Uttarakhand

3. **INTERPOLATION:** Geostatistics offers a great variety of methods that provide estimates for unsampled locations. Kriging is considered as the best linear unbiased estimator (BLUE). The variogram model is used for calculating the weights assigned to sample data. Univariate algorithms, OK and SK, use only rainfall data for interpolation the missing values. The multivariate extension of kriging, OCK and RK, considers auxiliary information, such as altitude, together with the primary data of rainfall and it can result in better estimates. SKlm accounts for the secondary data replacing the known stationary mean by known varying local means. The cokriging approach is another possibility to incorporate secondary data which are correlated with the primary variable. In this study, two predictors are used namely altitude and slope. These variables are derived from 1 km resolution DEM of GTOPO32. Table 27.2 provides a list of seven scenarios used to compare the interpolation techniques.

Table 27.1 Descriptive statistics of normal annual rainfall (mm) data collected from 80 rain gauge stations

Type	No. of Points	Min	Max	Mean	Median	S.D	CSK	Kurtosis
Complete	80	429.3	2986	1528.8	1419.1	549.01	0.42	2.9
Terrai&Bhabar + Shivalik	33	740.8	2986	1652.6	1613	504.2	0.49	3.03
Lesser Himalayas	28	1044.8	2849.1	1668.1	1611	491.48	0.94	3.02
Great Himalayas	19	429.3	2599.3	1407.8	1522.8	649.85	−0.03	2.07

Min = minimum value; Max = maximum value; S.D = standard deviation; CSK = coefficient of skewness

Table 27.2 Scenarios for spatial modeling of rainfall using univariate and multivariate approach

Scenarios	Univariate/Multivariate	Secondary variables	Methods of Simulation
Scenario 1	Univariate case	None	OK
Scenario 2		None	SK
Scenario 3	Multivariate case	Varying local mean	SKlm
Scenario 4	Multivariate case	Elevation	OCK(E)
Scenario 5		Elevation	RK(E)
Scenario 6	Multivariate case	Slope	OCK(S)
Scenario 7		Slope	RK(S)

27.4 RESULTS AND DISCUSSIONS

The normal annual rainfall data collected over 80 rain gauge stations were explored to understand the data distribution pattern. Classical descriptive statistics was used to describe the data (Table 27.1). The normal distribution of complete data set is apparent as mean (1528.8) and median (1419.1) values are very close and coefficient of skewness (CSK) is near to zero. The data set of Shivalik region is also near to normally distributed (CSK=0.4). The data set of Lesser Himalayas are right skewed (CSK=0.94) and that of Great Himalayas are left skewed (CSK=-0.03). Kriging generates better estimate if the data set follows normal distribution [10]. The correlation between rainfall and secondary variable namely, elevation and slope was analysed for 4 different sets of data and the results are plotted in Fig. 27.2. For complete data set, correlation between rainfall and elevation is exhibited for the data sets of December-February ($r=0.4$). No evident correlation is found between rainfall and slope for complete rainfall data set ($r < 0.1$). In Shivalik region, correlation coefficient ranging between 0.4 to 0.7 for all the time periods indicates good correlation of rainfall and elevation. In Lesser Himalayas, the highest correlation between rainfall and elevation is 0.4 when annual rainfall data is considered. In Great Himalayas, correlation coefficient of 0.4 exists for data set of December-February. The correlation of rainfall and slope is not significant ($r < 0.4$) but being derivative of elevation, it was incorporated as secondary variable for comparative study.

The structural analysis was carried out for computing experimental variogram. Due to sparse data of only 80 points spread across the large study area of around 53,000 sq. km, it was difficult to arrive at the best fit theoretical variogram for spatial continuity description. Experimental variograms were computed and the spherical model provided the best fit for all the scenarios. The parameters of the variogram considered for geostatistical modeling are listed in Table 27.3.

In this study, five spatial interpolation techniques were evaluated based on exhaustive cross validation. Leave-one-out cross validation (LOOCV) was used where one rainfall data is removed at a time from the data set and the value is estimated from remaining data. Root mean square error (RMSE) was used as statistical criterion to compare the performance of spatial interpolation methods. Table 27.4 presents the error statistics of different scenarios and graphical representation of the result is shown in Fig. 27.3.

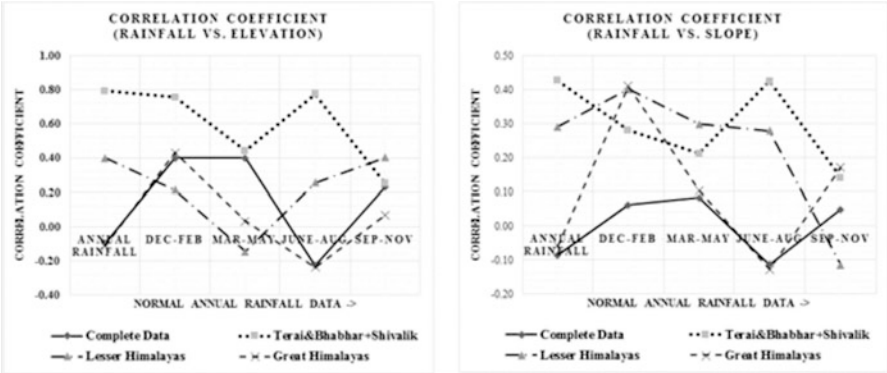


Fig. 27.2 Graphical representation of correlation coefficient variation (a) Rainfall vs. Elevation and (b) Rainfall vs. Slope

Table 27.3 Parameters of variogram used for geostatistical modeling

Model Parameters	Value
Nugget	64186
Sill	224290
Range	41846

From the cross-validation result, it is evident that the inclusion of elevation or slope as auxiliary variables improves the prediction of rainfall. However, the prediction error is similar with incorporation of either of the two variables as secondary variables for interpolation. This can be attributed to the fact that slope is derivative of elevation. IDW has maximum RMSE out of five interpolation methods used for the study. SKlm performs better than OCK in all the scenarios because it captures the local varying mean instead of global constant mean. Residual kriging outperforms SKlm in Shivalik and Lesser Himalayas region where the correlation between rainfall and elevation is high ($r_{\text{shivalik}}=0.79$, $r_{\text{lesserhimalayas}}=0.5$). Also, OCK proves to be a better choice than OK only when the correlation between the rainfall and secondary variable (elevation or slope in this case) is good. When the data of Shivalik region ($r=0.79$) is considered, the RMSE of OCK is 363 and that of OK is 368. The prediction using OK and OCK yields similar result when the correlation between rainfall and elevation is moderate ($r < 0.4$). For all the cases, residual kriging outperforms OCK. As the spatial dependence between observations weakens, the benefit of using RK over univariate method OK increases. From the results obtained, it can be concluded that geostatistical techniques that incorporates elevation or slope outperforms univariate interpolation method OK when the correlation between primary variable, rainfall and secondary variable elevation, slope is high ($r > 0.5$). In other cases, SKlm is a better choice than IDW or OK for spatial interpolation of rainfall.

This study has some limitations. The basic assumption of kriging family of spatial interpolation technique is that the data is stationary which is not true for field

Table 27.4 Cross-validation result (RMSE) for different interpolation techniques

Study Region	Univariate case		Multivariate case				
	Only rainfall		Rainfall with local mean	Rainfall & Elevation		Rainfall & Slope	
	Scenario 1	Scenario 2	Scenario 3	Scenario 4	Scenario 5	Scenario 6	Scenario 7
	IDW	OK	SKlm	OCK(E)	RK(E)	OCK(S)	RK(S)
Complete data	493	484	452	564	467	564	467
Shivalik	372	368	360	363	310	371	310
Lesser Himalayas	505	477	470	498	418	503	418
Great Himalayas	696	642	618	639	639	638	639

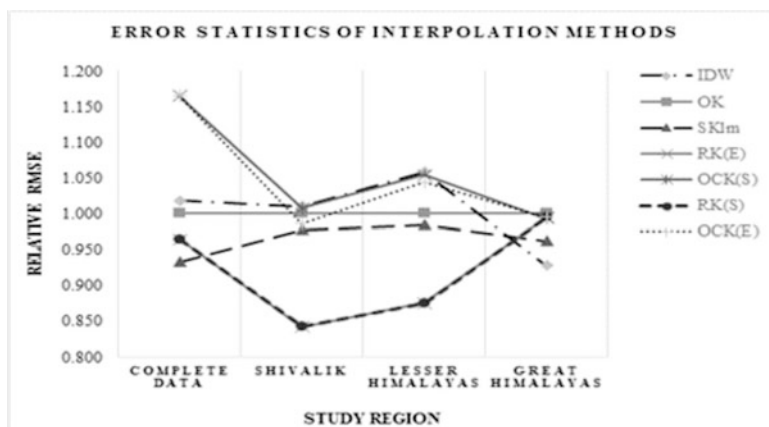


Fig. 27.3 Root mean square errors (RMSE) of estimation generated by each of the seven scenarios for study region (RMSE values are expressed relative to RMSE of OK)

data. SKlm and RK overcomes this limitation by replacing stationarity with known varying means derived from the secondary data. RK and SKlm prediction is dependent on the pattern of spatial continuity of rainfall data. Future scope of this work includes additional terrain-derived variables, vegetation information or wind circulation pattern as secondary information for spatial interpolation of rainfall.

27.5 CONCLUSIONS

The spatial interpolation of rainfall can be performed by univariate and multivariate algorithms. In this study, spatial interpolation of rainfall was performed using normal annual rainfall data derived from 80 rain gauge stations in Uttarakhand region of Indian Himalayas. The study region was divided into three different regions based on the elevation extracted from DEM to understand the spatial distribution pattern of rainfall. For comparative analysis, three multivariate geostatistical interpolation algorithms: simple kriging with varying local means (SKlm), ordinary cokriging (OCK), regression kriging (RK) and two univariate techniques: inverse distance weighted (IDW) and ordinary kriging (OK) were evaluated. The result indicates that the estimates of rainfall improves by considering secondary information like elevation and slope in multivariate interpolation techniques. The estimates using SKlm and RK resulted in the smallest RMSE than OCK in complex terrain. This indicates that the non-stationary version of kriging are potentially more appropriate for spatial interpolation of rainfall data in mountainous regions like Indian Himalayas.

REFERENCES

1. Thiessen, A.H.: Precipitation averages for large areas. *Monthly Weather Review*, 39(7), 1082–1084 (1911)
2. Goovaerts, P.: Geostatistical approaches for incorporating elevation into the spatial interpolation of rainfall. *Journal of Hydrology*, 228, 113–129 (2000)
3. Sarangi, A., Cox, C.A. and Madramootoo, C.A.: Geostatistical Methods for Predication of Spatial Variability of Rainfall in a Mountainous Region. *Transactions of the ASAE*, 48(3), 943–954 (2005)
4. Carrera-Hernández, J.J. and Gaskin, S.J.: Spatio temporal analysis of daily precipitation and temperature in the Basin of Mexico. *Journal of Hydrology*, 336(3-4), 231–249 (2007)
5. Mair, A. and Fares, A.: Comparison of Rainfall Interpolation Methods in a Mountainous Region of a Tropical Island. *Journal of Hydrologic Engineering*, 16(4) (2011)
6. Basistha, A., Arya, D.S. and Goel, N.K.: Spatial Distribution of Rainfall in Indian Himalayas – A Case Study of Uttarakhand Region. 22(10), 1325–1346 (2007)
7. Moral, F.J.: Comparison of different geostatistical approaches to map climate variables: application to precipitation. *International Journal of Climatology*, 30, 620–631 (2010)
8. Diodato, N. 2005. The influence of topographic co-variables on the spatial variability of precipitation over small regions of complex terrain. *International Journal of Climatology*, 25: 351–363.
9. Joshi, S.C.: Uttarakhand: environment and development – A geo-ecological overview. Gyanodaya Prakashan, Nainital, Uttarakhand (2004)
10. Isaaks, E.H. and Srivastava, R.M.: An Introduction to Applied Geostatistics. Oxford University Press: Oxford (1989)

Chapter 28

A Time Series Analysis of Spatial and Temporal Distribution of Rainfall at Pampa River Basin, Kerala, India

N.A. Mayaja and C.V. Srinivasa

Abstract Kerala, one of the smallest States of South India, is blessed with forty-four rivers. River Pampa is the third largest river in the State of Kerala, 176km long with a catchment area of 2235Sq.km. Recurring tropical monsoon floods during every season, causing substantial damages, is one of the perennial problems experienced in this river basin. Studying rainfall trend in the river basin and its underlying features are vital in understanding the flood phenomena and its socio-economic impacts. The present study evaluates the trend of rainfall in the Pampa river basin, utilizing the data from five gauging stations. The time series of monthly and annual rainfalls for the past twenty two years have been analyzed statistically. Significant changes have been observed in the basin rainfall features – both seasonal and annual rainfall.

Keywords Rainfall trend analysis • Time series analysis • Pampa River

28.1 INTRODUCTION

The river of Pampa - approximately 176km long- encompasses a basin area of about 2235sq.km. The basin stretches over four districts of the State of Kerala viz., Idukki, Kottayam, Pathanamthitta and Alappuzha. The area extends over dense tropical monsoon forests, semi urbanized settlements, the famous pilgrim center – Sabarimala and also a rich agricultural (rice) bowl of Kerala, called Kuttanad. The study basin lies between 76°23' to 77°20' East in longitude and 9°14' to 9°30' North in latitude. With humid tropical monsoon climate (average annual rainfall 3600mm with summer rains constituting about 10%) the basin experiences two distinct rainy seasons, South-West monsoon (June to September) contributing about 60% of the rainfall and North-East monsoon (October to December), providing about 30% of

N.A. Mayaja (✉)

Dept. of Civil Engineering, Atria Institute of Technology, Bangalore, India

e-mail: mayaja@hotmail.com

C.V. Srinivasa

Dept. of Civil Engineering, Global Academy of Technology, Bangalore, India



Fig. 28.1 The study area showing locations of rain gauge stations in the river basin

the rainfall. The peak altitude of the basin is about 1677m (at the origin of the river) and while flowing through a distance of about 176 km the river reaches the sea level and joins the Vembanad Lake and finally Arabian Sea. In this river basin there are five rain gauge stations viz., Nilackal, Kurudamannil, Chengannur, Mancompu and Alappuzha. (Fig.28.1)

28.2 DATA

Rainfall data for three stations (1991-2013) were available from Indian Meteorological Department (IMD) and for the remaining two stations (2000-2012) from Department of Irrigation, Government of Kerala. The data have been grouped into four seasons in line with the IMD classification viz: i) No-monsoon season: January to March ii) Pre-monsoon season: April to May iii) South-West monsoon season: June to September iv) North-east monsoon season: October to December.

28.3 METHODOLOGY

The linear trend of rainfall has been analyzed using SPSS 10 software. To understand the general rainfall characteristics, average *annual* rainfall data, (taking all the stations together and also individually) have been computed and compared with that of the State of Kerala (Table 28.1). Then, trend of rainfall of all the five stations have been separately analyzed for the four seasons and results are summarized in Fig. 28.2.

Table 28.1 Linear trend parameters for annual rainfall

S.No.	Station	Slope	Constant
1	Alappuzha	−20.60	3137
2	Chengannur	−63.10	3633
3	Mancompu	11.14	2780
4	Nilackal	70.07	3016
5	Kurudamannil	−42.05	3190
6	Kearala (average)	−13.18	3074

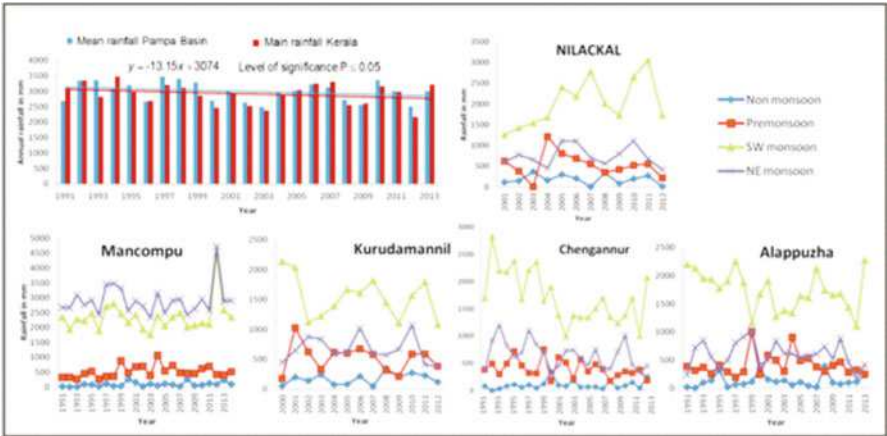


Fig. 28.2 Summary of results of rainfall trend analysis of five stations in Pampa river basin

28.4 RESULTS AND DISCUSSIONS

Recent studies have shown that monsoon as a whole is shrinking in the India [1]. A few studies related to Kerala also reported similar results [2,3,4]. The annual rainfall at the Pampa river basin also, during the period under study showed a substantial shrinkage. However, it is significant to note that this river continually received a higher rainfall compared to that of the State of Kerala, throughout the period of study. A consistent decrement in the rainfall in the river basin, though corroborating with the rainfall trend of the state, is a matter of concern, primarily considering the major monsoon dependent agricultural pattern of the basin. The shrinking rainfall trend will have a major negative impact on the agricultural prospects mainly at Kuttanad, known as the rice bowl of Kerala located in this basin. From the station wise trends provided in figure 28.2, it can be seen that the rain gauge stations located at the upstream of the river – Nilackal – have a distinctive and unique pattern and trend of seasonal rainfall. Nilackal, during the period of study recorded a minimum of 2391.6mm and a maximum of 4617.1mm of annual rainfall, which is about 10% and 30% above the Kerala average respectively. Further, this station shows a higher positive trend during the Southwest monsoon alone while the rainfall during the other seasons remains more or less stable. This is a significant observation for a gauging station on the upstream of the river, which

predominantly contributes to the recurring and severe monsoon floods in the Pampa river basin. This can be an important consideration while formulating flood mitigation measures. The rainfall pattern in the midstream and downstream stations remained stable during the pre-monsoon and no-monsoon periods, whereas, during the Southwest monsoon and Northeast monsoon periods all these stations showed a homogeneous negative trend. The shrinking monsoon rainfall can have a major negative impact on the agro-ecological sustainability of the basin, which may converge quickly to a drought. The high positive trend in monsoon rainfall of the upstream rain gauge station, read in conjunction with the severe negative trend of the downstream stations do not provide an overall prospective picture of the river performance. It is also worth to infer that in the upstream rain gauge station, namely Nilackal, the South-West monsoon rainfall intensity alone has substantially increased whereas the mean annual rainfall pattern remained stable, which testifies that the rainfall intensity during the short spell of South-West monsoon alone was escalated showing a radical change in the climatic factors.

28.5 CONCLUSIONS

This study examined the general rainfall pattern in the Pampa river basin using data from five rain gauge stations. Annual rainfall as well as seasonal rainfalls at these five rain gauge stations has been analysed. The study revealed that while the trend of rainfall in the upstream station viz., Nilackal showed an increasing trend, the rainfall at this station remained always higher than the rainfall parameters for the State of Kerala. However, in respect of other four stations the study observed significant decremending trend in annual as well as seasonal rainfall. The decreasing trend in annual rainfall may have a serious influence on the agricultural production of this lower basin, which is known as the rice bowl of Kerala. The seasonal incremental trend in the monsoon rainfall at the upstream station indicates increased flood hazards, which may require separate attention while framing hazard mitigation plans. From the whole analysis, it is clear that the present trends are more or less that of a shrinking monsoon rainfall which will not positively aid the basin development

REFERENCES

1. Ramesh, K.V. and Goswamy, P.: The shrinking Indian Summer Monsoon. CSIR report RR CM 0709 (2007)
2. Anu Simon and Mohan Kumar, K.: Spatial variability and rainfall characteristics of Kerala. *Proc. of Indian Academy of Sciences*, 113(2), 211–221 (2004)
3. Jagadeesh, P. and Anupama, C.: Statistical and trend analysis of rainfall: A case study of Brahmaputra river basin. *ISH J. of Hydraulic Engg*, Taylor & Francis (2013)
4. Raja, P.P.N. and Azeez, P.A.A.: Changing rainfall in Palakkad plains of south India. *J. Atmosfera*, 23(1), 75–82 (2010)

Chapter 29

Rainfall Statistics Change in West Bengal (India) from Period 1901-2000

Sourav Mukhopadhyay, Sneha Kulkarni, Pallavi Kulkarni,
and Samiran Dutta

Abstract The study aims to investigate rainfall trends in West Bengal, India. The paper deals with monthly, seasonal and annual general rainfall trends. The study is carried out to understanding the underlying feature for the purpose of forecasting and in identifying the changes and impact that are very crucial for an agro-based economy like the one of West Bengal, India. Here we studied using monthly data series of last 100 years (1901-2000). The methodology has been adapts various statistical approaches in order to detect the possible precipitation changes in annual, monthly and seasonal basis; including both the non-parametric tests for monotonies trend (Mann-Kendall test, Sequential version of Mann-Kendall test and Sen's estimator of slope). Maximum of the districts showed an increasing trend in annual rainfall, but only one district (South 24 Pargana), this trend was statistically significant. In case of Monsoon months (June to September) maximum number of districts shows the increasing trend but it is not statistically significant. Only three districts (Midnapur west, North 24-Parganas and South 24-Parganas) of them are statistically significant. The majority of districts show very slight change in rainfall in non-monsoon months.

Keywords Precipitation • Rainfall trend • Mann-Kendall test • India

S. Mukhopadhyay (✉) • P. Kulkarni
Department of Geography, University of Pune, Maharashtra, India
e-mail: iamsourav02@yahoo.in

S. Kulkarni
Department of Geo-information Science and Earth Observation (ITC), University of Twente,
AE Enschede, Netherland

S. Dutta
Department of Geography, National P.G. College, Lucknow, India

29.1 INTRODUCTION

Climate change is an issue for global discussion and a fast growing subject, which penetrates every aspect of human lives. Impact of climate change in future is quite severe with respect to the availability of fresh water. IPCC report signifies that there will be a reduction in the freshwater availability because of climate change. This has also revealed that by the middle of 21st century, decrease in annual average runoff and availability of water will project up to 10–30% [3]. Many studies on temperature variation on the global scale have established the fact that the earth's atmosphere has witnessed a significant warming in the last century [2–4]. The impact of climate change in future would be quite severe especially for the mega deltas in Asia and IPCC report has projected that with the rise in temperature and subsequent rise in sea level the coasts of Asia including the Indian Sundarbans in West Bengal will be exposed to increasing risks of coastal erosion [3].

Global climate changes influence long term rainfall pattern, availability of fresh water and increases the occurrence of floods and droughts. The South Asian summer monsoon is an annual wind-driven weather pattern that is responsible for 85% of India's annual precipitation and it plays a vital role for the country's agricultural sector. Changes in climate over the Indian sub-continent, particularly the South West (SW) monsoon would have a significant impact on agricultural production and water resource management. Water resource management is essential because in the monsoonal months (June–September) the subcontinent receives ample amount of rainfall however, non-monsoonal periods are severely dry.

To detect the direction of change (positive or negative) and to quantify the magnitude of such changes (if any), we analysed long-term (1901–2000) rainfall variables (annual, seasonal, monthly) using non-parametric statistical tests like Mann-Kendall. Further a Sequential Mann-Kendall test (SQ-MK) has been applied to estimate the qualitative change in the trend of annual and seasonal rainfall (monsoon, pre-monsoon and post-monsoon). The magnitudes of the trends in rainfall parameters were estimated using Sen's slope method.

29.2 DATASET AND METHODOLOGY

29.2.1 *The Regional Dataset*

The state of West Bengal (WB) (20° 31' - 27° 12' N and 85° 50' - 89° 52' E) is situated in the eastern part of India; it is only state consisting lofty peaks of the Himalaya in the north to coastal regions down south, with regions such as plateau and Ganges delta intervening in between (Fig. 29.1). Different parts of the region also experience varied climatic conditions like extremely cold winters and very hot summers with moderate to insignificant rainfall in both the climatic extremes. Heavy precipitation in the state occurs under the influence of westerly disturbances

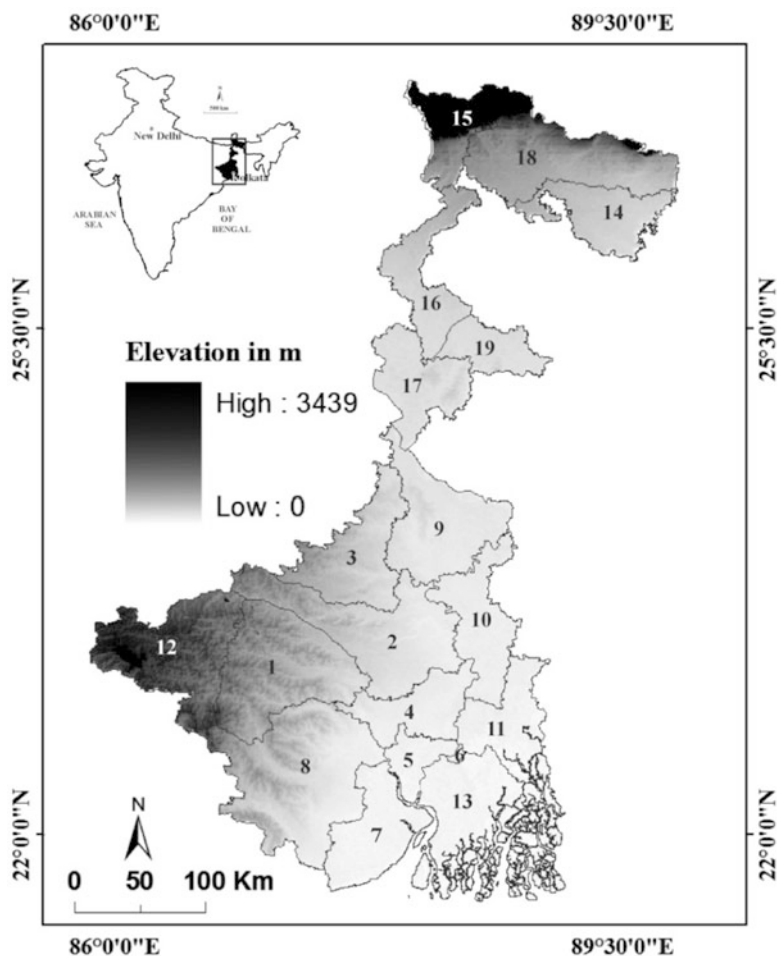


Fig. 29.1 Map of India (inset) showing the location of West Bengal. The elevation of the various districts of West Bengal (blown up) illustrates that an average elevation of ~ 3400 m is reached in the north while the south eastern end is at mean sea level: 1=Bankura, 2=Burdwan, 3=Birbhum, 4=Hoogly, 5=Howrah, 6=Kolkata, 7=Midnapur East, 8=Midnapur West, 9=Murshidabad, 10=Nadia, 11=North 24 Parganas, 12=Manbhum Purulia, 13=South 24 Parganas, 14=Cooch Bihar, 15=Darjeeling, 16=Dinajpur North, 17=Dinajpur South, 18=Jalpaiguri, 19=Malda

during the months of October to May and due to the southwest monsoon from June to September. To understand the trend of rainfall variability, 100 years (1901–2000) annual, seasonal and monthly data were collected from Indian Meteorological Department (IMD) Pune.

29.2.2 *Trend Detection Test*

The long-term trends of the time series was evaluated using nonparametric statistical techniques, such as the Mann–Kendall test [5,9,10], Sen's slope [12], and the SQ-MK test [13] and its magnitude using Sen's estimator. This method has widely been used for determining the magnitude of trend in hydro-meteorological time series and the details are available in [7,14] and references therein. The statistical significance of the trend in monthly, seasonal and annual series was analysed using the non-parametric Mann-Kendall test following [1,6]. The Mann–Kendall test checks the null hypothesis of no trend versus, the alternative hypothesis of the existence of increasing or decreasing trend. On the other hand the SQ-MK test is used for determining the approximate year of the beginning of a significant trend [8]. This test sets up two series, a progressive one $U(t)$ and a backward one $U'(t)$. If they cross each other and diverge beyond the specific threshold value of ± 1.96 , then the trend is considered statistically significant. The point where they cross each other indicates the approximate year in which the trend begins [11].

29.3 RESULTS AND DISCUSSION

29.3.1 *Rainfall Magnitude and Long Term Trend Analysis*

The rate of change in the trend of the 100 years' time series, as determined using the Sen's slope estimator, is given in Tables 29.1 and 29.2. The study revealed that the majority of the sub-divisions of WB experienced very little or no change in non-monsoon months (Table 29.1). Out of the 19 districts of WB, the maximum increase was experienced by Midnapur West in June and Cooch-Bihar in July which is statistically significant at 95% confidence level. A maximum increase in August (1.00 mm/year) with a significant positive trend was observed in South 24 Parganas. In the month of September 80% district showing increasing trend except a maximum reduction for Jalpaiguri (-1.03 mm/year). While analysing the rainfall data for the past 135 years (1871–2005), Kumar et al. found that there is an increasing trend in precipitation for the Gangetic West Bengal (maximum of 0.35 mm/year) [6].

In case of seasonal rainfall data analysis of the sub-division of WB showed that pre-monsoon rainfall increased over 9 districts; monsoon rainfall increased over 15 districts; post-monsoon rainfall increased over 15 districts and winter rainfall increased over 15 districts. In the month of monsoon the maximum increase in monsoonal rainfall was of the order of 4.37 mm/year for South 24 Parganas which is statistically significant. Whereas the decrease in monsoon rainfall was found to be maximum for Jalpaiguri (-1.66 mm/year). More than half districts have shown an increase trend in annual rainfall and remaining has shown the negative trend

Table 29.1 Sen's estimator of slope (mm/year) for monthly rainfall for 100 years of each month

Region	Jan	Feb	Mar	Apr	May	Jun	July	Aug	Sept	Oct	Nov	Dec
Bankura	0.00	-0.02	-0.01	-0.02	-0.31	0.02	0.34	0.42	0.73*	0.24	0.00	0.00
Burdwan	0.00	-0.00	-0.06	-0.08	-0.53	-0.09	0.15	0.22	0.45	-0.02	0.00	0.00
Birbhum	0.00	0.00	-0.00	0.16	-0.10	0.05	0.44	0.29	0.84	0.27	0.00	0.00
Hoogly	0.00	0.00	-0.05	0.01	-0.10	0.19	0.35	0.01	0.18	0.10	0.00	0.00
Howrah	0.00	-0.05	-0.03	-0.01	-0.15	-0.32	-0.06	0.26	1.04*	-0.03	0.00	0.00
Kolkata	0.00	0.02	-0.01	0.03	-0.23	-0.09	0.62	0.16	0.68	0.64*	0.00	0.00
Midnapur East	0.00	0.00	-0.02	0.02	-0.03	-0.10	-0.16	0.18	1.10*	0.32	0.02	0.00
Midnapur West	0.00	-0.03	0.01	0.21	0.11	0.26	0.31	0.34	0.58	0.01	0.00	0.00
Murshidabad	0.00	-0.01	-0.02	0.05	-0.22	-0.19	0.92	0.06	0.40	0.15	0.00	0.00
Nadia	0.00	-0.05	-0.14*	-0.32*	-0.66*	-0.49	0.29	-0.42	-0.38	-0.06	0.00	0.00
North 24 Parganas	0.00	0.00	-0.05	-0.09	-0.16	-0.06	0.33	0.32	0.72	0.19	0.00	0.00
ManbhumPurulia	0.00	-0.04	0.00	0.11	-0.09	0.17	-0.65	-0.39	0.55	0.19	0.00	0.00
South 24 Parganas	0.00	-0.00	-0.01	-0.03	0.16	0.09	0.93	1.00*	1.32*	0.64*	0.06	0.00
Cooch Bihar	0.00	0.00	0.03	0.33	-0.05	-0.84	3.33*	0.86	0.10	-0.17	0.00	0.00
Darjeeling	0.05	-0.03	0.03	0.23	0.18	-0.64	1.04	0.09	0.45	0.10	0.03	0.03*
Dinajpur North	0.00	-0.02	0.00	0.14	0.35	-0.24	0.29	-1.16	0.33	0.10	0.00	0.00
Dinajpur South	0.00	-0.02	-0.01	0.25	0.07	-0.13	0.32	-1.31*	0.27	0.02	0.00	0.00
Jalpaiguri	0.00	-0.01	-0.02	-0.07	-0.07	-1.03	1.39	-0.86	-1.03	-0.15	-0.01	0.00
Malda	0.00	-0.01	0.00	0.05	-0.07	-0.49	0.45	-0.20	0.47	0.05	0.00	0.00

*indicate statistical significance at 95%confidence level as per the Mann-Kendall test (+ = increase and - = decrease)

Table 29.2 Sen's estimator of slope (mm/year) for annual and seasonal rainfall of 100 years

Region	Annual	Winter (Jan, Feb)	Pre Monsoon (Mar, April, May)	Monsoon (Jun, July, Aug, Sept)	Post monsoon (Oct, Nov, Dec)
Bankura	-0.01	-0.04	-0.28	0.83	0.42
Burdwan	-0.80	-0.01	-0.84	0.40	-0.04
Birbhum	1.92	0.01	0.02	1.37	0.41
Hoogly	0.68	0.02	-0.12	1.28	0.27
Kolkata	2.07	0.04	-0.21	1.47	0.74
Midnapur East	2.19	-0.04	-0.08	1.66	0.55
Midnapur West	1.58	-0.06	0.42	1.62*	0.01
Murshidabad	1.04	-0.01	-0.21	1.67	0.23
Nadia	-0.55	-0.11	-1.13	-0.71	-0.07
North 24 Parganas	1.91	0.03	-0.37	1.87*	0.35
ManbhumPurulia	0.10	-0.13	0.10	0.12	0.38
South 24 Parganas	4.84*	0.00	0.36	4.37*	0.77
Cooch Bihar	3.94	0.01	0.40	3.59	-0.11
Darjeeling	1.31	0.01	0.33	0.55	0.29
Dinajpur North	-1.24	-0.02	0.51	-1.26	0.26
Dinajpur South	-0.90	-0.06	0.22	0.69	0.33
Jalpaiguri	-0.47	-0.02	0.37	-1.66	-0.08
Malda	-0.19	-0.04	0.05	-0.51	0.24

*indicate statistical significance at 95% confidence level as per the Mann-Kendall test
(+= increase and -= decrease)

(Table 29.2). However, rainfall trends observed are nearly very similar for the monsoonal and annual periods throughout the state of West Bengal (Fig. 29.2b).

29.3.2 Long-term Changes in the Time Series

Based on the SQ-MK test the change point detection for annual and seasonal (monsoon, pre-monsoon, post monsoon) rainfall were applied to identified the break point of the curves and therefore to detect the beginning year of the rainfall trend, that are shown in (Fig. 29.3). Yearly plots of $U(t)$ and $U'(t)$ values for the seasons of a year have been shown in (Fig. 29.3-A). An apparently decreasing trend from 1922-35 and 1950-66 is observed and the change point is detected in the year of 1966 and 1970 but it cannot be recognized as statistically significant at 0.05 level.

In the monsoonal period clear increasing trend is detected however, in the year of 1963 there is change point. Overall pre-monsoon period trend is not significant and turning points are detected in the year of 1902, 1935, 1963, 1982, but these are

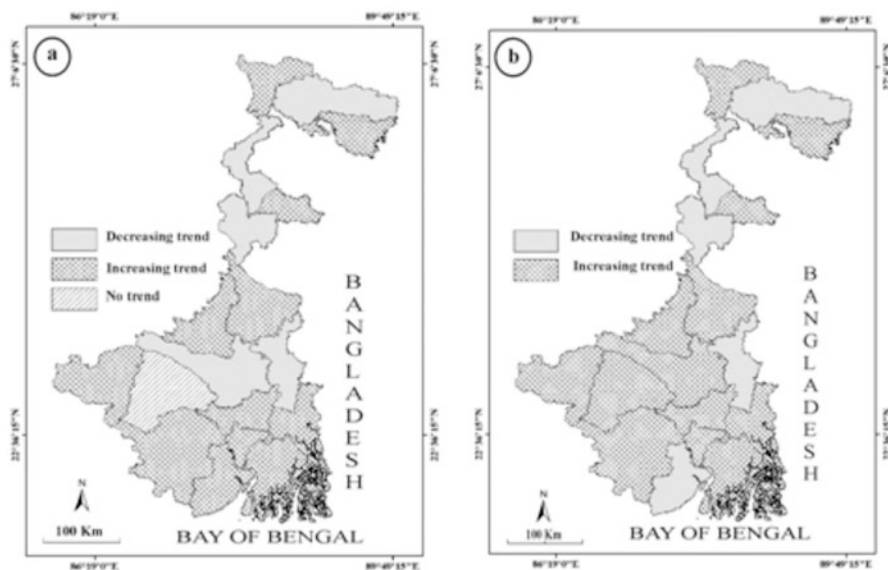


Fig. 29.2 Trends and magnitude of changes for different districts of West Bengal: (a) Annual rainfall (mean/100 years), (b) Monsoonal rainfall (mean/100 years)

not statistically significant. SQ-MK plots for post-monsoon period have been given in (Fig.29.3-D). It shows that, the $U(t)$ and $U'(t)$ curves are converging since 1901 until they intersect each other at 1902(-1.14), 1906(-0.79), 1909(-0.27), 1926 (-0.02), 1928(0.43), 1998(1.57) but these change points are not statistically significant because all are below the chosen level of significance of $p \leq 0.05$.

29.4 CONCLUSIONS

This study has examined trends in monthly, seasonal, and annual rainfall on the subdivision for the WB. Of the 19 districts, 12 are showing increasing trend in annual precipitation in the 4.84-0.1 mm/year range; while seven districts are showing decreasing trend within 1.24-0.01 mm/year range. Seasonal result shows that the pre-monsoon rainfall is increasing in nine districts, increasing monsoonal precipitation for all districts except four and during post-monsoonal period fifteen districts shows increasing trend. Statistical significance tests showed that the monsoon rainfall has a positive significant trend in South 24 Parganas. The majority of sub-divisions show increasing trends for South-west monsoon season however, only South 24 Parganas (4.37 mm/year) and North 24 Parganas (1.87 mm/year) are statistically significant. Assessment through the SQ-MK test clearly demonstrates that seasonal rainfall has increased from different time points within the considered

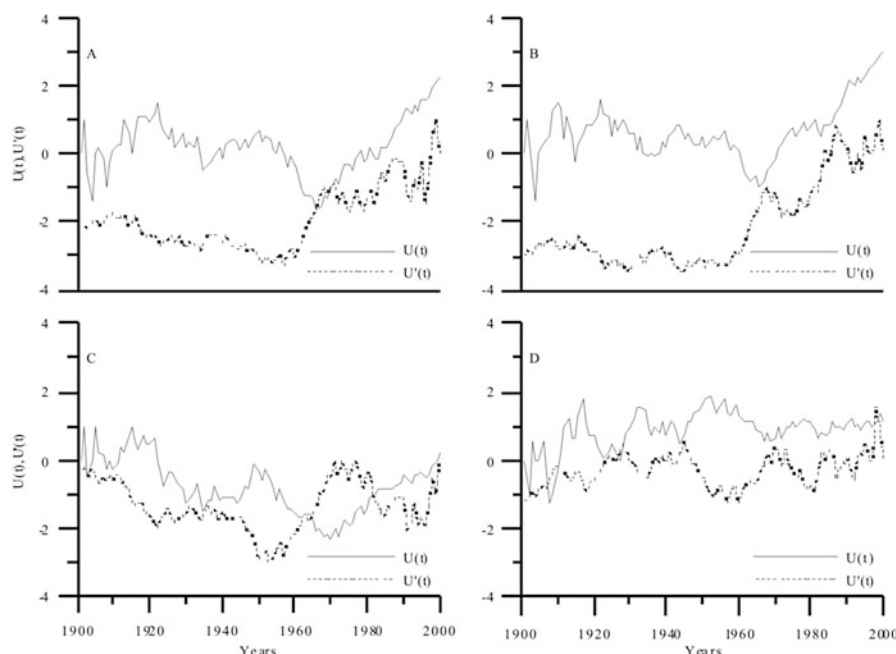


Fig. 29.3 Sequential values of the SQ-MK statistical test of annual precipitation (A), monsoon (B), pre-monsoon (C), post-monsoon (D) of West Bengal during the period 1901-2000; Solid line indicates forward series $U(t)$ and dashed line indicates backward series $U'(t)$

time period. The remarkable observation of this analysis is that no statistically significant change point is found in this seasonal rainfall series.

ACKNOWLEDGEMENTS The authors wish to express their gratitude towards India Meteorological Department (IMD) Pune, for providing the data sets for current research. The authors also extend their heartfelt thanks to Dr. Subhajit Sinha, Dept. of Geology, Durgapur Govt. College, Durgapur, West Bengal, for his advice. The authors wish to thank an anonymous reviewer, for critically reviewing an earlier version of this manuscript and for providing helpful suggestions and comments that significantly improved its content.

REFERENCES

1. Bayazit, M. and Onoz, B.: To prewritten or not to prewritten in trend analysis? *Hydrol. Sci. J.*, 52(4), 611–624 (2007)
2. Folland, C.K. and Parker, D.E.: Observed variations of sea surface temperature. In: Schlesinger ME (ed.) *Climate–ocean interaction*. Kluwer, Dordrecht, 21–52 (1990)
3. IPCC (Intergovernmental Panel on Climate Change): *Climate Change, Impacts, Adaptation and Vulnerability*. Contribution of Working Group II to the Fourth Assessment Report of the Intergovernmental Panel on Climate Change. Cambridge University Press, Cambridge, UK, 1–976 (2007)

4. Jones, P.D., Raper, S.C.B. and Wigley, T.M.C.: Southern hemispheric surface air variation: 1851-1984. *J. Clim. Appl. Meteorol.*, 25, 1213–1230 (1986)
5. Kendall, M.G.: Rank Correlation Methods, Charles Griffin, London (1975)
6. Kumar, V., Jain, S.K. and Singh, Y.: Analysis of long-term rainfall trends in India. *Hydrol. Sci. J.*, 55, 484–496 (2010)
7. Lettenmaier, D.P., Wood, E.F. and Wallis, J.R.: Hydro-climatological trends in the continental United States, 1948-88. *J. Climate*, 7, 586–607 (1994)
8. Lu, A., He, Y., Zhang, Z., Pang, H. and Gu, J.: Regional structure of global warming across China during the twentieth century. *Clim. Res.*, 27, 189–195 (2004)
9. Mann, H.B.: Non-parametric tests against trend. *Econometrica*, 13, 245–259 (1945)
10. Mitchell, J.M. (Jr), Dzerdzeevskii, B., Flohn, H., Hofmeyr, W.L., Lamb, H.H., Rao, K.N. and Wallen, C.C.: WMO Technical Note No. 79, World Meteorological Organization, Geneva (1966)
11. Mosmann, V., Castro, A., Fraile, R., Dessens, J. and Sanches, J.L.: Detection of statistically significant trends in the summer precipitation of mainland Spain. *Atmos. Res.*, 70, 43–53 (2004)
12. Sen, P.K.: Estimates of the regression coefficient based on Kendall's tau. *J. Am. Stat. Assoc.*, 63, 1379–1389 (1968)
13. Sneyres, R.: Technical note no. 143 on the statistical Analysis of Time Series of Observation. World Meteorological Organization, Geneva, Switzerland (1990)
14. Yue, S. and Hashino, M.: Temperature trends in Japan: 1900-1990. *Theoret. Appl. Climatol.*, 75, 15–27 (2003)

Chapter 30

Groundwater Fluctuation and Trend in Amritsar, Punjab, India

Gopal Krishan, A.K. Lohani, M.S. Rao, C.P. Kumar, and K.S. Takshi

Abstract Punjab state in the northwestern part of India constitutes 1.57% of total area in the country and its economy is mainly controlled by agriculture by covering 85% of geographical area with cropping intensity reaching to 184% in the central parts of the state. During last 4 decades a shift from Sugarcane-Maize-Wheat cropping pattern to Wheat-Rice cropping pattern has lead to increase in the demand for irrigation water and further putting stress on the groundwater. Groundwater level monitoring has been carried out on 4 observation wells in 4 blocks namely Ajnala, Majitha, Rayya and Tarsika of Amritsar for 7 years during January 2006 to December 2013 for assessing the groundwater level. Groundwater occurs under phreatic condition and depth to groundwater varied from 6 to 11 m (bgl) in Ajnala, 5 to 11 m (bgl) in Majitha, 14 to 19 m (bgl) in Rayya and 9 to 14 m (bgl) in Tarsika. The increased depth of 6 m was observed in Majitha and 5 m was observed in other 3 blocks. Monthly groundwater level data have been analysed which indicates that the ground water is declining in all the four blocks with variable rate. The decline of groundwater level in each block during 7 years has become an area of concern for understanding the over exploitation of groundwater scenario in the region.

Keywords Groundwater • Fluctuation • Trend • Amritsar • Punjab • India

30.1 INTRODUCTION

Groundwater is the World's largest distributed storehouse of fresh water which plays a very important role in the ecosystems sustainability and also helps the human beings in adjusting to the climate change resulted due to the variability in precipitation, soil moisture and surface water. In India, due to the rapid increase in population and human activities, the groundwater is under stress. Punjab state in the northwestern part of India constitutes 1.57% of total area in the country and its

G. Krishan (✉) • A.K. Lohani • M.S. Rao • C.P. Kumar
National Institute of Hydrology, Roorkee, Uttarakhand, India
e-mail: dr.gopal.krishan@gmail.com

K.S. Takshi
Irrigation and Power Research Institute, Amritsar, Punjab, India

economy is mainly controlled by agriculture by covering 85% of geographical area with cropping intensity reaching to 184% in the central parts of the state [1]. During last 4 decades a shift from Sugarcane-Maize-Wheat cropping pattern to Wheat-Rice cropping pattern has lead to increase in the demand for irrigation water and further putting stress on the groundwater resulting in decline of water table and deterioration in water quality [1-4]. The declining water levels are also found in Amritsar district of Punjab and the district is categorized under “Over Exploited” category. In Amritsar an average yield of wells above $150 \text{ m}^3/\text{hour}$ occur in extensive and fairly thick aquifers down to 450 meters. To assess the groundwater level fluctuations and trend in Amritsar, groundwater level monitoring has been carried out on 4 observation wells in 4 blocks namely Ajnala, Majitha, Rayya and Tarsika of Amritsar for 7 years during January 2006 to December 2013

30.2 STUDY AREA AND HYDROGEOLOGY

Amritsar district is located in northern part of Punjab state and lies between $31^{\circ}28'30''$ to $32^{\circ}03'15''$ north latitude & $74^{\circ}29'30''$ to $75^{\circ}24'15''$ east longitude and having a total area of 5056 sq.km (Fig. 30.1). The district falls in between Ravi river and Beas river. Soils in the western part of the district are coarse loamy, calcareous soils, where as in the central part of the district soils are fine loamy, calcareous and are well drained. The soils are Ustochrepts to Haplustaff type. The district forms

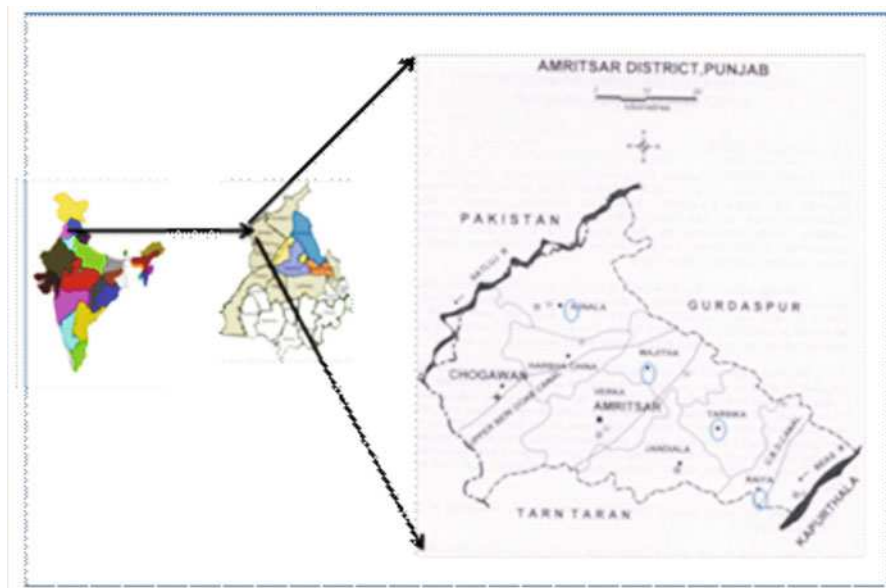


Fig. 30.1 Study area

part of Uppar Bari Doab and is underlain by formations of Quaternary age comprising of alluvium deposits belonging to vast Indus alluvial plains. Sub surface geological formations comprise of fine to coarse grained sand, silt, clay and kankar. Gravel associated with sand beds occurs along left bank of Ravi. The beds of thin clay exists alternating with thick sand beds and pinches out at short distances against sand beds.

The ground water flow direction is from north east to south west. The gradient of water table elevation is steep in the north east part and gentle in the south west part of the district. In the area around Amritsar the groundwater flow from all directions is towards city and a ground water trough has been formed in the central part of the city. The whole district is suitable for ground water development. But due to over exploitation of groundwater in all eight blocks of the district a check is required for overall ground water development.

30.3 MATERIAL AND METHODS

The monthly water level data was measured from 4 blocks namely Ajnala, Majitha, Tarsika and Rayya of Amritsar district for the 7 years i.e. 2006 to 2013. The data processing was done to remove the erroneous data before statistical analysis. The erroneous values were rectified.

30.4 RESULTS AND DISCUSSION

As evident from Fig. 30.2 and Table 30.1 that the overall depth to groundwater varied from 6 to 11 m (bgl) in Ajnala, 5 to 11 m (bgl) in Majitha, 14 to 19 m (bgl) in Rayya and 9 to 14 m (bgl) in Tarsika. The increased depth of 6 m was observed in

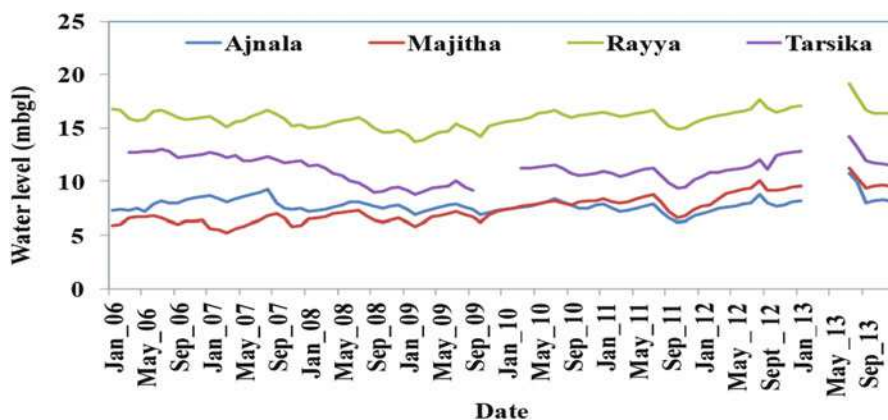
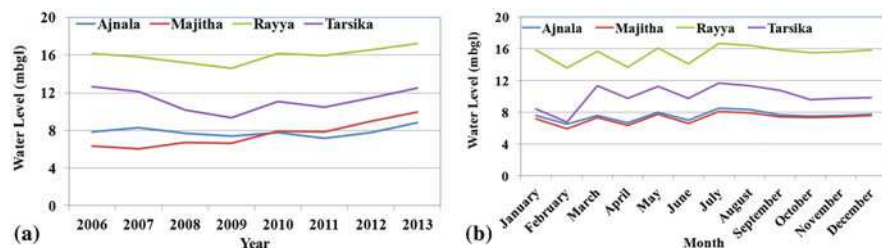


Fig. 30.2 Variations in water level during 2006-2013 in four blocks of Amritsar

Table 30.1 Statistical parameters

Blocks	Water Level (mbgl)			
	Minimum	Maximum	Average	Standard Deviation
Ajnala	6	11	7.8	0.7
Majitha	5	11	7.5	1.3
Rayya	14	19	15.9	0.9
Tarsika	9	14	11.2	1.2

**Fig. 30.3** Yearly (a) and Monthly (b) variations in water level (2006-2013) in four blocks of Amritsar

Majitha and 5 m was observed in other 3 blocks. The average maximum increase in depth of 3.55 m was observed in Majitha block during 2006-13 (Fig. 30.3) and is responsible of a decrease in water level @ 0.51 m/year, while this decrease in Ajnala and Rayya blocks was observed to the tune of 0.15 m/year. However, the groundwater level was found to increase at Tarsika block but the increase was only of 0.02 m/year.

It was observed from Fig. 30.3 that the groundwater level depth was maximum in the month of July and minimum in the month of February in all the blocks. Due to more extraction of water during June-July, the water level depth increased in July but it is minimum in February due to recharge by Monsoon rains and as well as less extraction of groundwater. Similar results were also obtained in the study carried out in Bist Doab Punjab by Krishan et al [5], where the water level depth was increasing in the months of June-July and decreasing in the months of February-March (Fig. 30.4).

30.5 CONCLUSIONS

Monthly groundwater level data have been analysed which indicated that the ground water is declining in all the four blocks with variable rate. The decline of groundwater level in each block during 7 years has become an area of concern for understanding the over exploitation of groundwater scenario in the region. Detailed

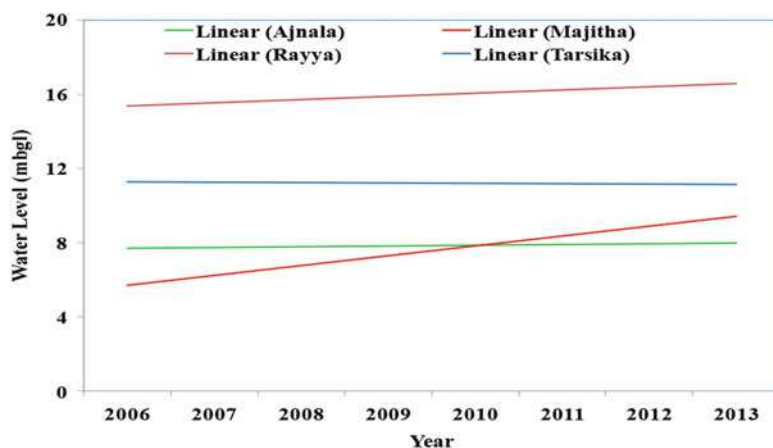


Fig. 30.4 Water level trend during 2006-2013 in four blocks of Amritsar

and high resolution monitoring is required to find out any correlation among the blocks and also there is a need to optimize the groundwater monitoring network [5-6] and accordingly suitable management measures are required [4].

AKNOWLEDGEMENTS Authors thank Director, National Institute of Hydrology for all his support and encouragement for this study.

REFERENCES

1. Gupta, S.: Groundwater Management in Alluvial Areas. Incidental Paper – 2011, CGWB, Ministry of Water Resources, Government of India, viewed on 23 November 2013, <http://cgwb.gov.in/documents/papers/incidpapers/Paper%2011%20sushil%20gupta.pdf> (2011)
2. Krishan, Gopal, Lapworth, D.J., Rao, M.S., Kumar, C.P., Smilovic, M. and Semwal, P.: Natural (Baseline) Groundwater Quality in the Bist-Doab Catchment, Punjab, India: A Pilot Study Comparing Shallow and Deep Aquifers. *Int. J. Earth Sc. Engg.*, 7, 16–26 (2014)
3. Krishan, Gopal, Rao, M.S., Kumar, C.P. and Semwal, P.: Identifying Salinization using Isotopes and Ion-chemistry in Semi-Arid Region of Punjab, India. *J. Geol. Geosci.*, 2:4 (2013), <http://dx.doi.org/10.4172/jgg.1000129>
4. Sharma, Manishi, Rao, M.S., Rathore, D.S. and Krishan, Gopal.: An integrated approach to augment the depleting ground water resource in bist-doab region of Punjab, India. *Int. J. Earth Sc. Engg.*, 7, 27–38 (2014)
5. Krishan, Gopal, Lohani, A.K., Rao, M.S. and Kumar, C.P.: Optimization of groundwater monitoring network in Bist-Doab, Punjab. In: International Conference “India Water Week 2013-Efficient Water Management: Challenges and Opportunities (IWW-2013)”, pp. 274 (2013)
6. Krishan, Gopal, Lohani, A.K., Rao, M.S. and Kumar, C.P.: Prioritisation of groundwater monitoring sites using cross-correlation analysis. *NDC-WWC Journal*, in press (2014)

Part II
Environmental Geochemistry
and Pollution

Chapter 31

Groundwater Quality Appraisal in Parts of Dun Valley Aquifers in the Terai Region, Central Nepal

N. Janardhana Raju, Deepa Gurung, and Priyanka Patel

Abstract The hydrogeochemical parameters for forty five groundwater samples of the Dun valley aquifers of central Nepal were studied to appraise the major ion chemistry and suitability of groundwater quality for domestic and irrigation uses. Geologically, the area comprises Quaternary alluvium composed of boulder, cobble, pebble, gravel and sand with intercalation of clays. Geochemical classification of groundwater shows that the majority of groundwater samples belong to the calcium-bicarbonate type. TDS values of groundwater in the study area are <1000 mg/l, therefore all groundwater evaluated are suitable for drinking and irrigation uses. The high nitrate concentration (>50 mg/l) of about 53% of the groundwater samples may be due to the local domestic sewage, leakage of septic tanks, and improper management of sanitary landfills. In general, %Na and SAR values indicate good to permissible use of water for irrigation purposes.

Keywords Groundwater quality • Hydrochemistry • Dun Valley • Aquifer • Nepal

31.1 INTRODUCTION

Groundwater quality may yield information about the environments through which the water has circulated. Each groundwater system in the area has a unique chemistry acquired as a result of chemical alteration of meteoric water recharging the system [1,2]. At present, anthropogenic activities such as industrial waste, municipal waste and intensified agriculture have deteriorated groundwater quality and creating an enormous stress on groundwater reserves [3,4,5]. Knowledge on hydrogeochemistry is very important to assess the quality of groundwater for classification of its suitability for domestic, irrigation and industrial uses. Good potential for groundwater lies in Terai region, inner valleys in hill and mountains of Nepal. Disposal of industrial effluents, agricultural residues, domestic sewage in unlined drains, dumping of garbage caused high levels of groundwater pollution in

N.J. Raju • D. Gurung • P. Patel (✉)

School of Environmental Sciences, Jawaharlal Nehru University, New Delhi, India

e-mail: prirocks11@gmail.com

the study area. Keeping the above aspects under consideration, an attempt was made to assess and interpret the hydrogeochemical characteristics of groundwater under natural and anthropogenic influences along with the spatial distribution of hydrogeochemical constituents in the study area.

31.2 STUDY AREA AND HYDROGEOLOGY

The study area lies in the Chitwan and Nawalparasi districts of Dun valley, Terai region of the Nepal. Narayani River (Fig. 31.1) is one of the biggest river of Nepal which separate two districts of Chitwan and Nawalparasi and flows north to south in the Dun valley. The study area lies between $27^{\circ}42.188'N$ - $84^{\circ}26.480'E$ and $27^{\circ}40.493'N$ - $84^{\circ}25.455'E$ covering area of 162.2 km^2 . The average annual rainfall is about 1700 mm. In west of Siwalik, the floor of the basin consists of alluvial deposits of the Narayani River which has mosaic-like landscape due to yearly flooding and riverbed migration [6]. Subsurface lithology is composed of boulder, cobble, pebble, gravel and sand with intercalation of clays as well as detritus of quaternary age in the main Dun valley aquifer. Groundwater is in unconfined types in shallow aquifers (<50 m) and semi-confined conditions in deeper aquifers (>50 m)

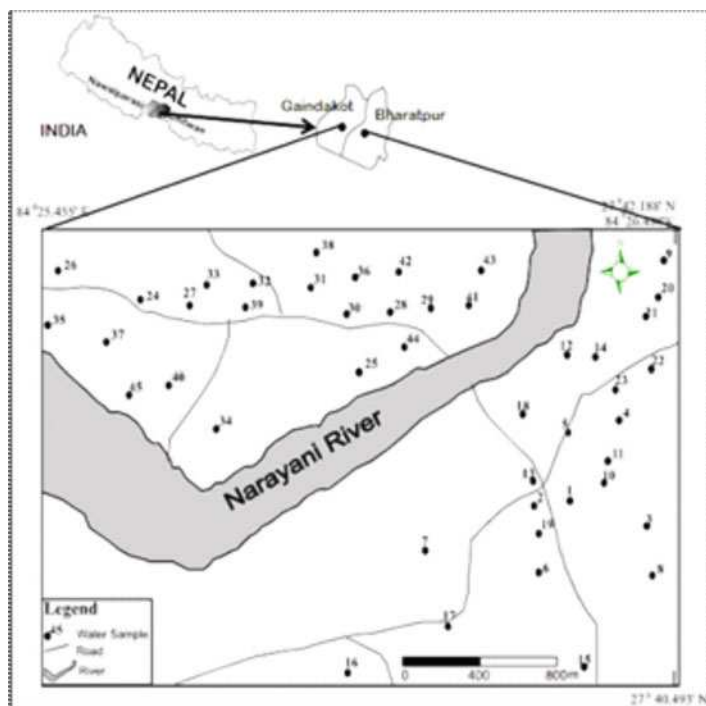


Fig. 31.1 Physiography and groundwater location map of the study area

[7]. Perched water table conditions also present in some places. The deeper aquifers are productive and have been tapped through hundreds of tube wells. The depth of deep wells ranges from 40 m to 126 m below ground level. Average water level of shallow aquifer was 3.45 m, while that of deep aquifers was 26.2 m.

31.3 MATERIAL AND METHODS

Forty five groundwater samples were collected in the month of December 2012 from dugwells and borewells of the study area. Samples were taken in properly rinsed polyethylene bottles. Parameters such as pH, EC, TDS and depth to water table were measured immediately at the time of sampling. Samples were then transported to School of Environmental Science, Jawaharlal Nehru University, New Delhi, India. The physicochemical parameters were determined using the standard analytical methods [8].

31.4 RESULTS AND DISCUSSION

31.4.1 *Groundwater Chemistry*

The statistical summary of different hydrochemical parameters determined is presented in Table 31.1. The analysis of inorganic ions showed that for the majority of samples, most parameters remain in concentrations that are not considered harmful to human health, except nitrates which form 53% exceeding permissible limits of WHO standards (Table 31.1). The pH value ranges are 5.35-7.57 (mean: 6.82). Total hardness (TH) values ranges 32-588 mg/l as CaCO_3 (mean: 224.18 mg/l as CaCO_3). TDS varies from 40-681 mg/l (mean: 251.64 mg/l) in the study area. Overall the groundwater of the study area fall in the freshwater category, since the TDS values are <1000 mg/l [9] and all groundwater evaluated is therefore suitable for drinking and irrigation purposes (Table 31.1). TDS, EC and ionic concentrations in the groundwater may be attributed to geochemical processes and anthropogenic activities [10]. Among cationic concentrations: calcium is the dominating ion ranging 20-206 mg/l (mean: 76.58 mg/l) followed by sodium 3.80 to 78 mg/l (mean: 17.80 mg/l), magnesium 1.02-23.85 mg/l (mean: 9.04 mg/l) and potassium ranges 0.4-57.5 mg/l (mean : 6.45 mg/l). The hydrochemistry of the cationic dominance pattern is in the order $\text{Ca}^{2+} > \text{Na}^+ > \text{Mg}^{2+} > \text{K}^+$. Among the anionic concentrations: bicarbonate is the dominating ion ranging 31-376 mg/l (mean: 157 mg/l) followed by chloride ranging 22-120 mg/l (mean: 56.86 mg/l), nitrate ranging 0-442 mg/l (mean: 89.6 mg/l), sulphate ranging 0.63-73.80 (mean: 14 mg/l), phosphate ranging 0.02-0.35 mg/l (mean: 0.12 mg/l) and fluoride ranging 0-0.20 mg/l (mean: 0.05 mg/l). The anionic dominance pattern is in the order

Table 31.1 Summary statistics for concentrations of chemical constituents of the study area

Parameter	Min.	Max.	Mean	SD	Permissible WHO (1997)	% sample exceeding limit
Ca ²⁺	20	206	76.58	41.46	200	2
Mg ²⁺	1.02	23.85	9.04	6.23	150	-
Na ⁺	3.80	78	19.80	17.59	200	-
K ⁺	0.40	57.50	6.45	9.75	12	16
HCO ₃ ⁻	31	376	157	96.36	600	-
SO ₄ ²⁻	0.63	73.80	14	14.90	600	-
Cl ⁻	22	120	56.86	21.57	600	-
PO ₄ ³⁻	0.02	0.35	0.12	0.10	0.1	42
NO ₃ ⁻	0	442	89.6	105	50	53
F ⁻	0	0.20	0.05	0.05	1.5	-
pH	5.35	7.57	6.82	0.45	9.2	-
EC	77.30	1368	503	293	-	-
TDS	40	681	251	146	1500	-
TH	32	588	224	125	500	4
Na %	4.02	44.18	17.8	9.64	-	-
SAR	0.09	1.96	0.56	0.41	-	-

All ions are in mg/l; EC in $\mu\text{S}/\text{cm}$, %Na and SAR in meq/l

HCO₃⁻>Cl⁻>NO₃⁻>SO₄²⁻>PO₄³⁻>F. High nitrate contamination has been spread in almost all the area and maximum content is found in the northeastern part of the study area (Fig. 31.2). High nitrate content may be due to leaching of organic and inorganic fertilizers from agricultural land by infiltration and percolation rainwater, domestic sewers and animal waste.

31.4.2 Hydrogeochemical Facies and Water Types

The concentrations of major ionic constituents in milliequivalent of groundwater samples were plotted in the Piper trilinear diagram [11] to determine the water type (Fig. 31.3). The anion diagram indicates that majority of the groundwater samples are of HCO₃ water type which is due to CO₂ and its related compounds in the atmosphere and in the unsaturated zone during precipitation and infiltration [12]. The cation diagram shows that the majority of samples belong to Ca water type which derives from reverse ion exchange in releasing alkaline earth elements in the groundwater. 53% of the groundwater samples belong to Ca-Mg-HCO₃ hydrogeochemical facies which might express mineral dissolution and recharge of freshwater by Narayani River. Around 29% of samples fall in the category of Ca-Mg-Cl i.e. carbonate alkali (primary alkalinity) exceeds 50% and depict groundwater contamination. The water-rock interactions generally include chemical weathering

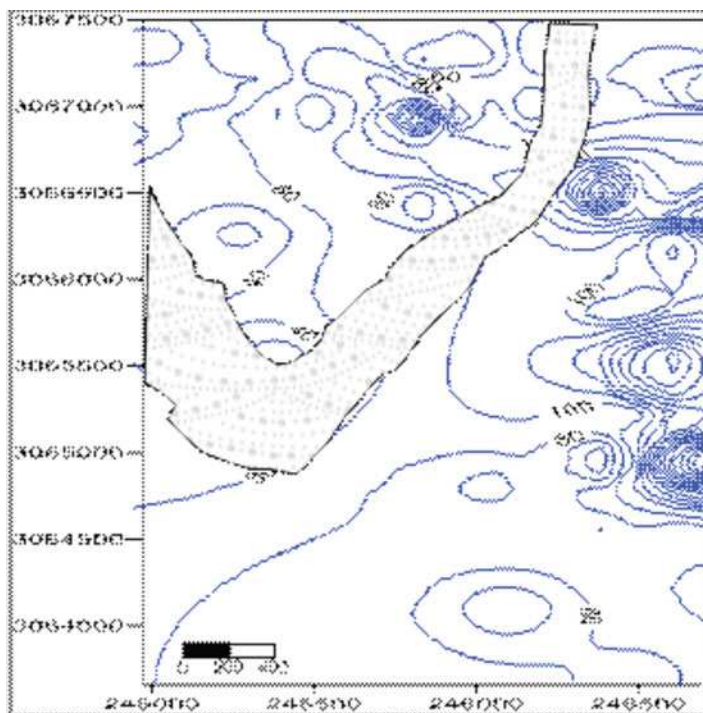


Fig. 31.2 Spatial distribution of nitrate

of rock forming minerals, dissolution–precipitation of secondary carbonates and ion exchange between water and clay minerals.

31.5 GROUNDWATER CLASSIFICATION FOR DOMESTIC AND IRRIGATION USE

Hydrochemical parameters of groundwater and their comparison [13] are summarized in Table 31.1, to evaluate the suitability of groundwater for domestic and irrigation uses. It is observed that almost all hydrochemical parameters of the groundwater samples in the study area are within the permissible limits except nitrate (53%), phosphate (42%) and potassium (16%). High salt content (high EC) in irrigation water forms saline soils leading to the loss of production in the area. High sodium content is defined by percent sodium and the calculated value of percent sodium ranges 4.02–44.18% (Table 31.1). According to Wilcox [14] plot of %Na and EC (Fig. 31.4), 82% samples fall in excellent to good category and 18% in good to permissible category. Sodium or alkali hazard in the use of water for irrigation is expressed in terms of sodium adsorption ratio (SAR). Low sodium

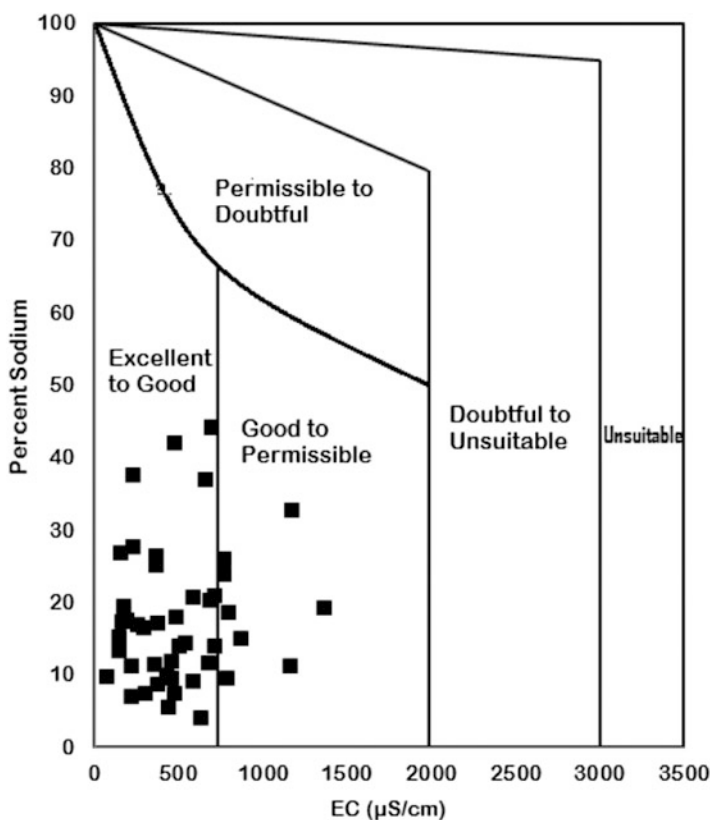


Fig. 31.3 Trilinear diagram showing the relative cation and anion composition of groundwater samples

(alkali) water can be used for irrigation on almost all soils with little danger of the development of harmful levels exchangeable sodium. SAR value in the study area varies between 0.09-1.96 meq/l (Table 31.1) and shows that all the samples are in excellent category for irrigation use.

31.6 CONCLUSIONS

The hydrochemistry of the study area shows that pH, EC and TDS is within the permissible limit but 4% of the samples exceeds the limit of hardness which could be due to anthropogenic inputs like domestic waste, poultry waste etc. The dominance of cation and anion in the study area are in the order $\text{Ca}^{2+} > \text{Na}^+ > \text{Mg}^{2+} > \text{K}^+$ and $\text{HCO}_3^- > \text{Cl}^- > \text{NO}_3^- > \text{SO}_4^{2-} > \text{PO}_4^{3-} > \text{F}^-$ respectively. Higher contaminated pockets of nitrate found in northeast part and sources could be poultry farm and

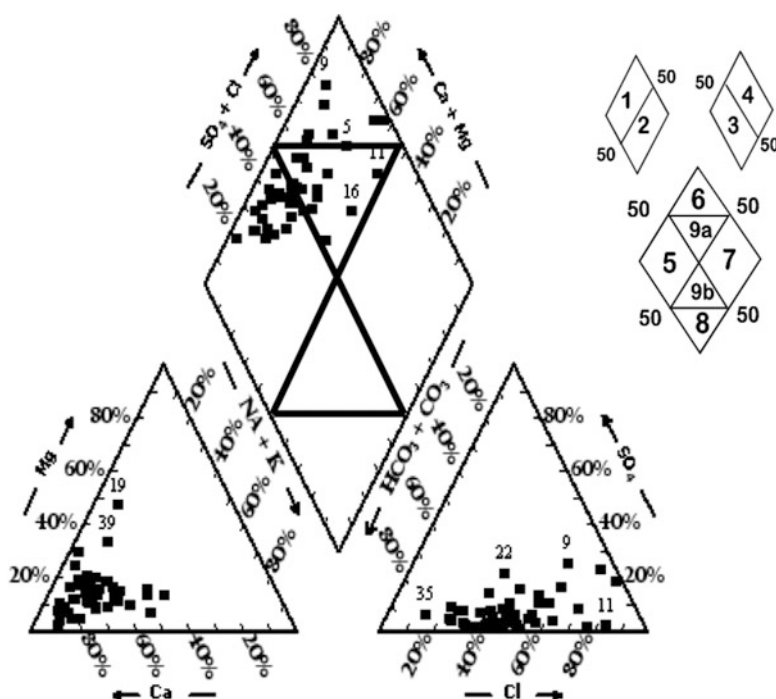


Fig. 31.4 Rating of groundwater samples on the basis of EC and % Na (Wilcox, 1948)

cattle shed waste, leakage from septic tank and fertilizers. Piper classification shows Ca-Mg-HCO₃ hydrochemical facies dominating in the study area. Suitability classification of groundwater shows that nearly all the samples are within the permissible limits except nitrate, potassium and phosphate ions for the drinking uses, and all samples are suitable for the irrigation usage.

REFERENCES

1. Raju, N.J. and Reddy, T.V.K.: Environmental and urbanization affect on groundwater resources in a pilgrim town of Tirupati, A.P., South India. *J. Applied Geochem*, 9, 212–223 (2007)
2. Wang, S.: Groundwater quality and its suitability for drinking and agricultural use in the Yandi Basin of Xinjiang Province, Northwest China. *Environ Monit Assess*, 185, 7469–7484 (2013)
3. Raju, N.J., Dey, S., Gossel, W. and Wycisk, P.: Fluoride hazard and assessment of groundwater quality in the semi-arid Upper Panda River basin, Sonbhadra district, UP, India. *Hydro. Sci.*, 57, 1433–1452 (2012)
4. Raju, N.J.: Evaluation of hydrogeochemical processes in the Pleistocene aquifers of middle Ganga plain, UP, India. *Environ. Earth Sci.*, 65, 1291–1308 (2012)

5. Raju, N.J., Prahlad, R. and Gossel, W.: Evaluation of Groundwater Vulnerability in the Lower Varuna Catchment Area, Uttar Pradesh, India using AVI Concept. *J. Geo. Soc. of India*, 83, 273–278 (2014)
6. Haffner, W.: Nepal Himalaya, Untersuchungen zum vertikalen Landschaftsaufbau zentral- und Ostnepals. *Erdwissenschaftliche Forschung*, 12, Wiesbaden (1979)
7. Neupane, R. and Shrestha, S.D.: Hydrogeologic assessment and groundwater reserve evaluation in NW parts of Dun valley aquifers of Chitwan, inner Terai. *Bulletin of the Dept of Geology*, 43–54 (2009)
8. APHA.: Standard Methods for the Exam. of Water and Wastewater, 20th edn. Washington (1998)
9. Davis, S.N. and De Weist, R.J.M.: Hydrogeology, New York: Wiley (1966)
10. Raju, N.J., Shukla, U.K. and Prahlad, R.: Hydrogeochemistry for the assessment of groundwater quality in Varanasi: a fast urbanizing center in Uttar Pradesh, India. *Environ Monit Assess*, 173, 279–300 (2011)
11. Piper, A.M.: A graphic procedure in the geochemical interpretation of water-analyses. *Trans Am Geophys Union*, 25, 914–923 (1944)
12. Jalali, M.: Salinization of groundwater in arid and semi-arid zones: an example from Tajarak, western Iran. *Environ Geol.*, 52, 1133–1149 (2007)
13. WHO.: Guideline for drinking water quality, WHO, Geneva. Health criteria and other supporting information, 2nd edn., 2, 940–949 (1997)
14. Wilcox, L.V.: The quality of water for irrigation use. *US Dept of Agriculture Tech Bulletin*, 962, 40 (1948)

Chapter 32

GIS and Geostatistical Assessment of Groundwater and Its Pollution in Kuwait

R.S. Divi and F. Al-Ruwaih

Abstract The main objectives of this study are to identify spatial correlations between groundwater and hydro geological parameters using geostatistical and subjective probability methods, towards identifying the effect of surfacial oil pollution on groundwater. The data used included multi-element chemical data for the nine groundwater field and surface and subsurface geological data. A GIS database is constructed to map the spatial variations in the geochemical and geological parameters. Geostatistical analyses consisting of variogram and kriging analyses are conducted, and the results identified the geometries of spatial correlations between the geochemical variables in the nine groundwater fields. Weights Of Evidence (WOE) model, which is based on conditional probability analysis, is used to evaluate the spatial association between pollution related to hydrocarbon contamination and groundwater fields.

Keywords Kuwait • Groundwater • GIS • Geostatistics • Pollution

32.1 INTRODUCTION

Kuwait being an arid country, has limited groundwater resources which are dwindling due to over usage and deteriorating due to oil contamination since the First Gulf War in 1991. Numerous studies on various aspects related to the groundwater resources in Kuwait have been conducted mostly by the scientists at the Kuwait Institute of Scientific Research (KISR). However, these investigations mostly used traditional graphical techniques and descriptive statistical analyses to derive basic relationships between the geological/geomorphological variables. However, the underlying relationships between groundwater parameters and the factors controlling them are complex and poorly understood. Specifically, the nature of inherent

R.S. Divi (✉) • F. Al-Ruwaih
Dept. of Earth and Env. Sciences, Kuwait University, Kuwait, Kuwait
e-mail: srdivi2006@gmail.com

‘spatial-structure’ in the variations of these factors fundamentally influences the trends in variation and estimates of the parameters, and in defining the components of the relationships between the parameters and the factors. The relationships are better analyzed and estimations more robust under geostatistical framework. GIS analysis and geostatistical methods (variogram, kriging, conditional probability) are essential for the estimation and prediction of spatially correlated groundwater variables. The objectives of this study are - compilation of groundwater and related earth science data and build a GIS database, identification of spatial correlations between groundwater and hydro-geological parameters using geostatistical methods and evaluation of the effect of surficial oil pollution on groundwater using conditional probability analysis.

32.2 STUDY AREA AND HYDROGEOLOGY

The data used consisted of 477 multi-element(13) chemical compositions of groundwater samples in 117 water-wells from the nine groundwater fields (Fig. 32.1): Al-Shagaya A, B, C, D, E; Umm Gudair; Al-Sulaibiya; Al-Raudhatain and Umm Al-Aish, and surface and subsurface geological maps. A GIS database enabled selective retrievals from the data to input into the statistical analyses. The statistical analyses consisted of distributional and correlation analyses, factor analyses, discriminant analyses, geostatistical analyses and conditional probability analyses. The results from the geostatistical and conditional probability analyses are given below.



Fig. 32.1 Groundwater fields in Kuwait

32.3 RESULTS

32.3.1 Geostatistical Analyses

The analyses include Variogram analysis which identifies the spatial structure of the variances, followed by Kriging, IDW and Simulation analyses which conduct the spatial mapping of the variables. Four types of isotropic variogram models are compared - these are Linear, Spherical, Exponential, and Gaussian. Variogram analyses of the 10 geochemical variables in each of the 9 groundwater fields in Kuwait were performed. Two examples of the models fitted are shown in Figure 32.2. High values of r^2 indicate very good fit to the data.

Interpolation by ordinary Kriging is done by using the sample point values and the variance structure (variogram model) identified from the data. The estimated value at a given location is a weighted moving average of best estimates calculated to minimize local area variance. One may choose either block or point (punctual) kriging methods for interpolation. The choice of block vs. point kriging should be made on the basis of sampling design. If samples are taken to represent point values in a field, as is the case for the groundwater wells, then punctual kriging is more appropriate. In Interpolation by Inverse Distance Weighting (IDW), estimates are made based on values at nearby locations weighted only by distance from the interpolation location. IDW does not make assumptions about spatial relationships

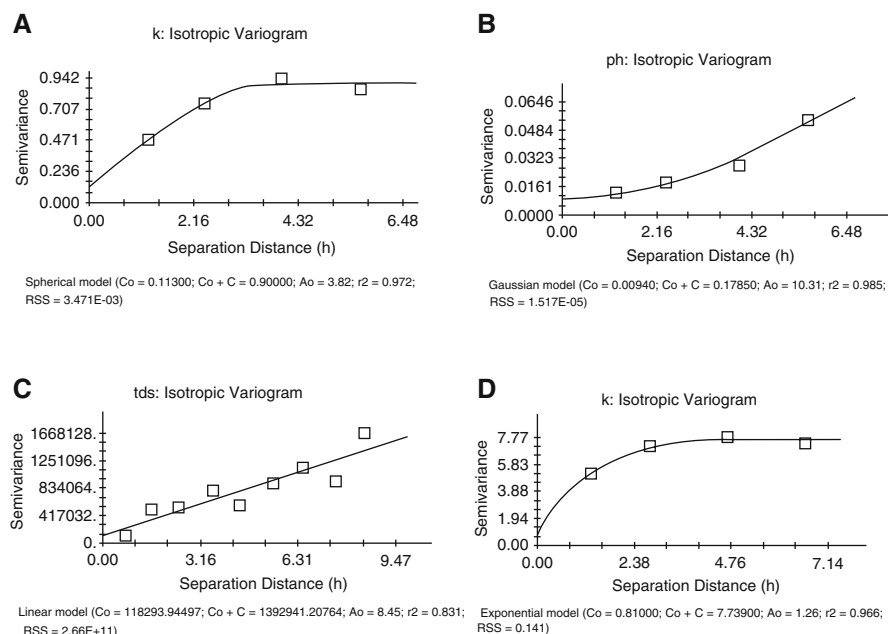


Fig. 32.2 Fitted variogram models for the groundwaters at Al-Raudhatain well: A (Spherical), B (Gaussian) and Shagaya-B well: C (Linear), D (Exponential)

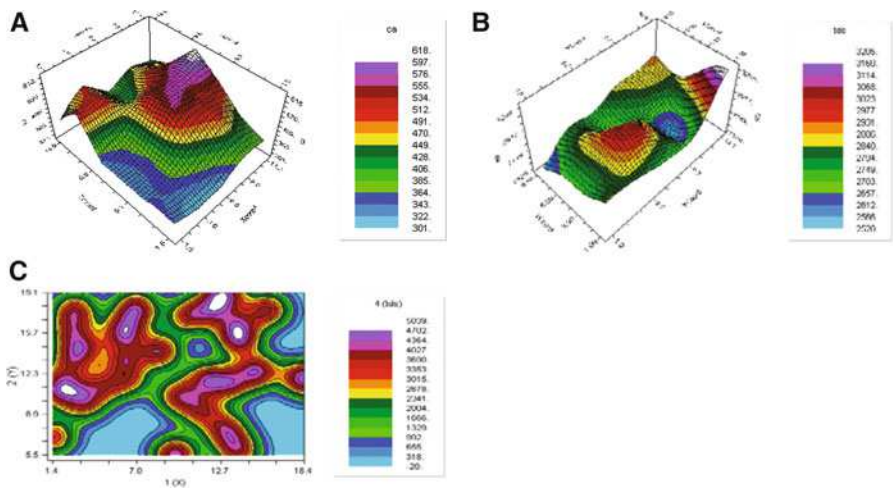


Fig. 32.3 Kriging estimation of Ca in Shagaya-E (A), TDS in Shagaya-D (B) and (C) TDS in Sulaibiya (C) groundwater fields

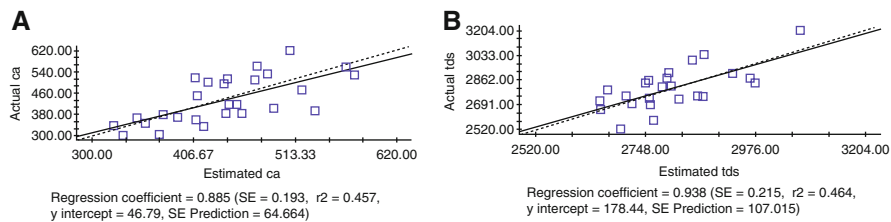


Fig. 32.4 (A) Cross validation of kriging estimates for Ca in Shagaya-E field. (B) TDS in Shagaya-D field

except the basic assumption that nearby points ought to be more closely related than distant points to the value at the interpolate location. Cross-validation analysis consists of evaluating effective parameters for kriging and IDW interpolations. In cross-validation analysis, each measured point in a spatial domain is individually removed from the domain and its value estimated via kriging or IDW as though it were never there. In this way, a graph can be constructed of the estimated vs. actual values for each sample location in the domain. In cross-validation graph, each point on the graph represents a location in the input data set for which an actual and estimated value is available. A few of the results of the Interpolation analyses (Kriging, Cross Validation and IDW) conducted on the spatial estimation of the 10 geochemical variations in the 9 groundwater fields are given in Figures 32.3A,B, C (kriging), 32.4A,B (cross validation), 32.5 (IDW) and 32.6 (simulation).

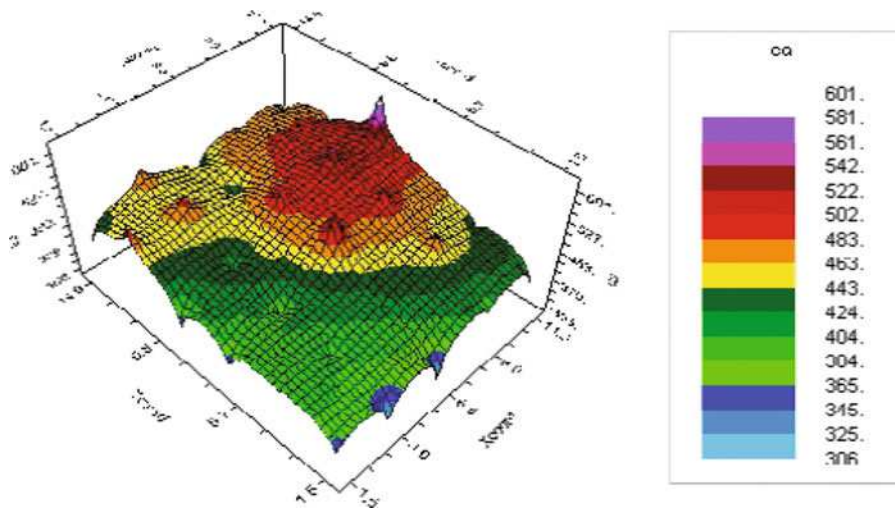


Fig. 32.5 IDW estimation of Ca in Shagaya-E groundwater field

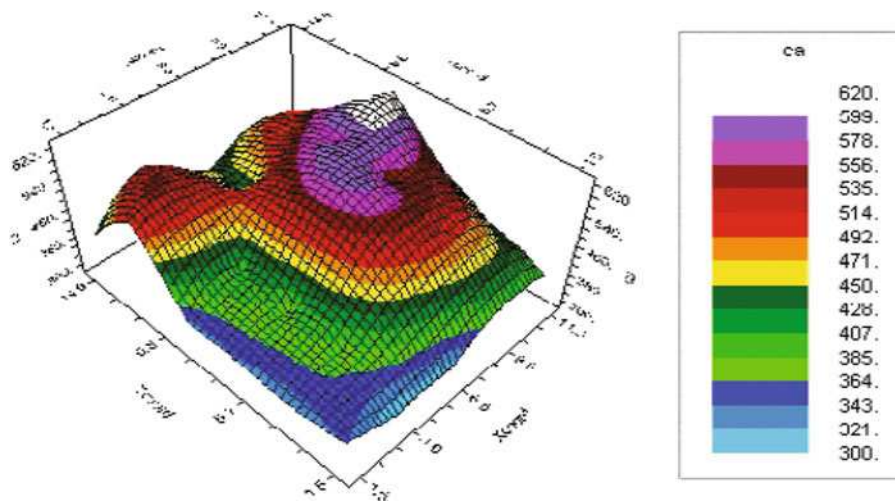


Fig. 32.6 Simulation Ca in Shagaya-E groundwater field

Table 32.1 Posterior Probability $P(E|b_1)$, Standard Deviation of Posterior Probability SD $[P(E|b_1)]$, and Studentized Posterior Probability St $[P(E|b_1)]$ for all variables

Variable	$P(E b_1)$	SD $[P(E b_1)]$	St $[P(E b_1)]$
Gh01 soil unit	0.0031	0.1605	0.0308
Ch06 soil unit	0.0471	0.0100	4.71 *
Gp20 soil unit	0.0005	0.1135	0.0044
Oil field area	0.0481	0.0105	4.625 *
Water resource area	0.0301	0.0196	1.5357

* indicates statistically significant at 95 % probability level

32.3.2 Conditional Probability Analysis

Conditional probability analysis is conducted to evaluate the association of hydrocarbon related pollution and groundwater well location's geological parameters. If the prior probability that a unit cell contains pollution is assumed to be constant over the whole study region, then from Bayes' Rule, the posterior probability that a cell contains pollution, given the presence of the j -th binary geological parameter, is:

$$P(E|B_j) = \frac{P(B_j|E) P(E)}{P(B_j|E) P(E) + P(B_j|\bar{E}) P(\bar{E})} \quad (32.1)$$

where the bar over the E refers to absence of pollution. Similarly, the posterior probability that a cell contains a pollution given the absence of pattern B_j is

$$P(E|\bar{B}_j) = \frac{P(\bar{B}_j|E) P(E)}{P(\bar{B}_j|E) P(E) + P(\bar{B}_j|\bar{E}) P(\bar{E})} \quad (32.2)$$

Then, the posterior logits (log odds) are:

$$\begin{aligned} \text{Posterior logit } (E/B_j) &= \text{prior logit } (E) + W_j^+ \\ \text{Posterior logit } (E/\bar{B}_j) &= \text{prior logit } (E) + W_j^- \end{aligned}$$

where the weights of evidence W_j (+ve or -ve) are defined as:

$$W_j^+ = \frac{P(B_j|E)}{P(B_j|\bar{E})} \quad \text{and} \quad W_j^- = \frac{P(\bar{B}_j|E)}{P(\bar{B}_j|\bar{E})}$$

Weights of evidence are computed for all the geological parameters. Using the statistically significant weights, posterior probabilities are computed for pollution. Significant highest weights are for the soil type Ch06. The associated posterior probability and its significance is given in Table 32.1. The conditional probability for pollution where soil type ch06 is present, is nine times higher than the unconditional probability.

32.4 CONCLUSIONS

Spherical variogram model fits best to the spatial variance structures of the geochemical elements in the groundwaters; robustness of Kriging estimates are validated by cross validation. Conditional probability analysis indicated hydrocarbon related pollution has strongest association with Ch06 type soil.

ACKNOWLEDGEMENTS Research Administration (RA) of Kuwait University provided the financial support, Ministry of Electricity and Water (MEW) in Kuwait supplied the groundwater data used. The Department of Earth & Environmental Sciences, Kuwait University provided general facilities.

Chapter 33

Geomorphological Influence on Groundwater Quality and Arsenic Distribution in Parts of Brahmaputra River Basin Adjoining Eastern Himalayas

Swati Verma and Abhijit Mukherjee

Abstract The present study attempts to understand the controls of geomorphological terrains on groundwater geochemistry and groundwater arsenic (As) distribution in the shallow aquifers of parts of the Brahmaputra floodplains of India. Three different geomorphologic units e.g. older alluvial (OA), younger alluvial (YA) and river channel deposits (RCD) were identified as predominant geomorphic terrains in the study area by coupled remote sensing and field observations. Groundwater compositions in the aquifers of these terrains were dominated by Ca–Na–HCO₃ and Na–Ca–HCO₃ hydrogeochemical facies. At least 60 % groundwater samples of study area have As ≥ 0.01 mg/L. The reductive dissolution of (Fe–Mn)OOH is the dominant mechanism of As mobilization in different alluvial terrains and redox transitions play major role for As mobilization in groundwater.

Keywords Geomorphology • Arsenic • Groundwater • Brahmaputra • India

33.1 INTRODUCTION

The elevated concentrations of dissolved As in groundwater, higher than the permissible limit (As < 10 µg/L, World Health Organization) have been recognized in more than twenty geological provinces around the globe [3]. In general, the distributions of the As-enriched aquifers are influenced by the geologic structure and geomorphic evolution of the basins [4]. As contamination in the aquifers of Brahmaputra river basin, mostly located in the Indian state of Assam has been largely undocumented, excluding very few publications available in the literature [1,2]. In this study, hydrogeochemistry of groundwater is being studied in the

S. Verma (✉) • A. Mukherjee

Department of Geology and Geophysics, Indian Institute of Technology,
Kharagpur, W.B., India

e-mail: swati.geo09@gmail.com

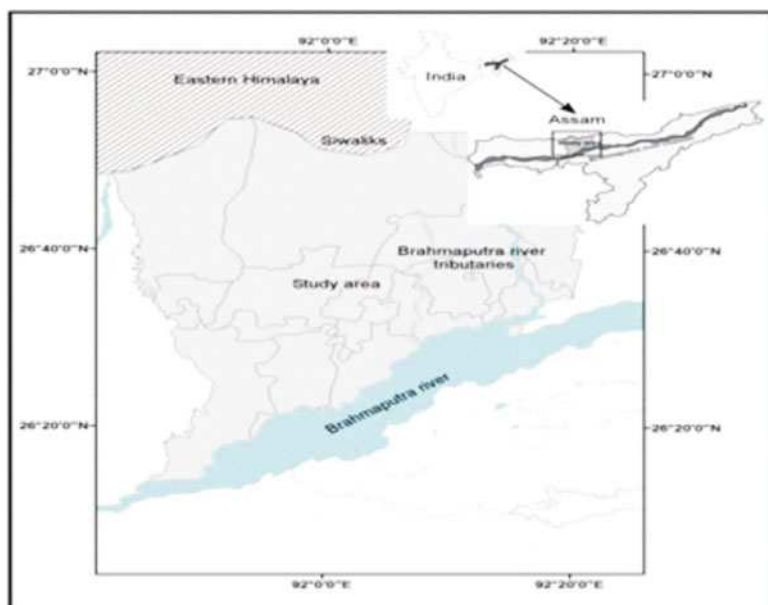


Fig. 33.1 Location map of the study area

background of the geomorphologic terrains, and their control on the distribution of As enriched aquifers.

33.2 STUDY AREA AND HYDROGEOLOGY

The study area (Darrang District), located in the northwestern parts of Brahmaputra River basin of Assam (Fig. 33.1). The Brahmaputra river basin sediments in the study area are mainly composed of alluvial deposits and it can be classified as older and younger alluvium.

33.3 MATERIAL AND METHODS

Eighty-five (85) groundwater samples from northwestern part of Brahmaputra river basin (Darrang district, Assam) were collected from hand-pumped and public water supply wells from various depths ranging from 7-60 m, between February and March, 2013. The collection of groundwater samples and field measurements were done by standard hydrogeochemical procedures [5].

Table 33.1 Statistical summary of selected parameters, solutes of the groundwater

Parameters	Unit	Min	Max	Mean	Median
Depth	m	6.39	59.15	35.72	39.63
Temp	(°C)	23.3	29.5	24.19	25.04
EH	mV	28.08	161.9	55.50	38.57
pH	-	6.77	7.71	7.19	7.71
DO	mg/L	0.25	2.72	0.85	0.52
SC	-	93	231	169.11	231
Na	mg/L	5.07	49.71	16.45	19.63
Mg	mg/L	1.49	17.84	8.18	7.99
Ca	mg/L	5.69	60.47	16.17	15.17
K	mg/L	1.03	11.02	2.93	1.58
Fe	mg/L	0.65	41.02	12.57	13.49
Mn	mg/L	0.20	5.87	1.36	0.58
As	mg/L	bdl	0.134	0.03	0.04
Zn	mg/L	0.02	0.63	0.10	0.02
HCO ₃ ⁻	mg/L	62.7	245.2	138.77	150.1
SO ₄ ²⁻	mg/L	0.13	16.6	3.58	2.34
Cl ⁻	mg/L	0.89	17.38	4.11	1.97
NO ₃ ⁻	mg/L	1.1	31.02	3.03	1.68
F	mg/L	0.29	1.19	0.53	0.91

33.4 RESULTS AND DISCUSSION

33.4.1 Groundwater Chemistry

In the study area, groundwater samples show pH values ranging from (6.8-7.7, median 7.62) indicating circum neutral groundwater (Table 33.1). Calcium (Ca²⁺) and Na⁺ are dominant cations in groundwater samples. In general, indicator of oxidizing conditions like DO and NO₃, are present in low concentration, with high concentrations of redox- sensitive solutes like (Fe, As, and Mn) in groundwater samples indicating highly reducing condition in study area.

33.4.2 Hydrogeochemical Facies and Water Types

The Piper plot (Fig. 33.2) suggests that groundwater of study area can broadly be divided into three hydrogeochemical facies: (1) Ca²⁺- HCO₃⁻; (2) Ca²⁺-Na⁺-HCO₃⁻; (3) Na⁺-Ca²⁺-HCO₃⁻.

Approximately 60% of all sampled groundwater have dissolved As concentrations ≥0.01 mg/L. Groundwater As concentrations ranged from <0.001 to 0.13 mg/L (mean 0.023 mg/L) for all samples combined.

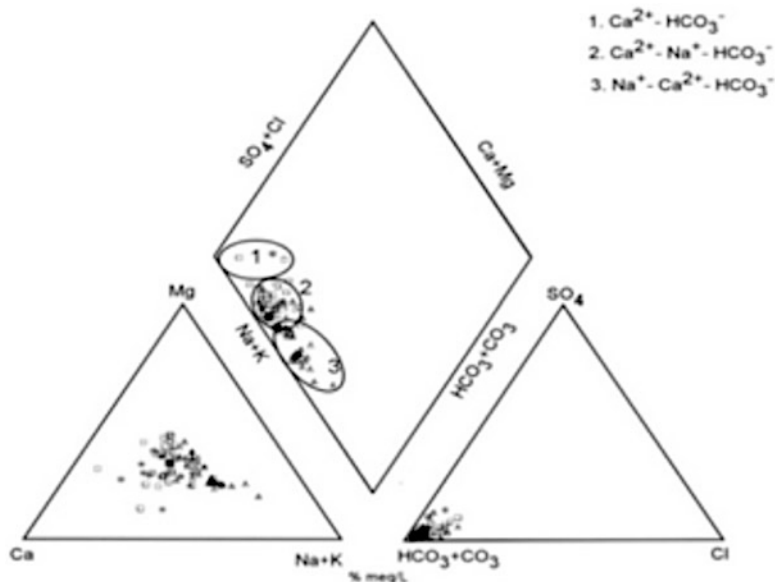


Fig. 33.2 Piper plots of groundwater samples collected from the study area

33.5 CONCLUSIONS

In the present study, plots of major ions suggested that groundwater was dominated by Ca-Na-HCO_3 and Na-Ca-HCO_3 hydrogeochemical facies, Ca^{2+} and Na^+ are dominant cations in groundwater samples. Groundwater As concentrations ranged from <0.001 to 0.13 mg/L with groundwater from OA terrain showing the highest concentration range of <0.001 to 0.13 mg/L while YA groundwater samples are least contaminated. The reductive dissolution of $(\text{Fe-Mn})\text{OOH}$ may be the dominant mechanism.

REFERENCES

1. Bhattacharya, P., Mukherjee, A. and Mukherjee, A.B.: Arsenic contaminated groundwater of India. In: Encyclopedia of Environmental Health (ed. J. Nriagu). Elsevier B.V., Netherlands, 150–164 (2011)
2. Chetia, M., Chatterjee, S., Banerjee, S., Nath, J., Singh, L., Srivastava, B. and Sarma, P.: Groundwater arsenic contamination in Brahmaputra river basin: a water quality assessment in Golaghat (Assam), India. *Environmental Monitoring and Assessment*, 173, 371–385 (2011)
3. Mukherjee, A. and Fryar, A.E.: Deeper groundwater chemistry and geochemical modeling of the arsenic affected western Bengal basin, West Bengal, India. *Applied Geochemistry*, 23, 863–892 (2008)

4. Mukherjee, A., Scanlon, B., Fryar, A., Saha, D., Ghoshe, A., Chowdhuri, S. and Mishra, R.: Solute chemistry and arsenic fate in aquifers between the Himalayan foothills and Indian craton (including central Gangetic plain): Influence of geology and geomorphology. *Geochimica et Cosmochimica Acta*, 90, 283–302 (2012)
5. Wood, W.W.: Guidelines for Collection and Field Analysis of Ground-Water Samples for Selected Unstable Constituents. US Geol. Surv. Techniques Water-Resour. Invest. Book 1 - (Chapter D2) (1981)

Chapter 34

Vulnerability of Ground Water Quality to Changing Climate: A Case Study from Kalpitiya Peninsula, Sri Lanka

Samanmali Matharaarachchi, Ranjana U.K. Piyadasa,
and Deepthi Wikramasinghe

Abstract This study presents an evaluation of ground water quality in a unique coastal ecosystem Kalpitiya, which is a low-lying peninsula in North-Western coast of Sri Lanka. In this study we assessed the physical quality of ground water in the peninsula and developed GIS maps. It was evident that pH, EC and salinity were unable to meet standards of water quality during the dry season. This condition warrants attention of the authorities since not only dry weather but also the climate change will aggravate the situation making water less available.

Keywords Ground water • pH • EC • Salinity • Kalpitiya peninsula • GIS

34.1 INTRODUCTION

Sri Lanka being an island is blessed with a wide array of coastal ecosystems. Kalpitiya peninsula, which is a low-lying area in the North-Western coast of Sri Lanka appears as a narrow strip of land which has an area of 160sq km and geographically it is bordered by the Indian Ocean from one side and Puttalam lagoon from inland. One salient feature of this landscape is that it comprises mainly of natural sand dunes. In addition, coconut, small scale commercial crops and natural scrub land dominate in the area. As for any other areas in the arid zone, Kalpitiya gets comparatively less rainfall and the annual range is 500 – 600 mm. Thus, ground water has become the main source of water supply for domestic and agricultural needs in the area. But it is increasingly evident that the ground water resources in Kalpitiya is under pressure. A very rapid exploitation and utilization of the shallow groundwater resource of the North Central, North Western and North

S. Matharaarachchi (✉) • R.U.K. Piyadasa
Department of Geography, University of Colombo, Colombo, Sri Lanka
e-mail: mataraarachchids@gmail.com

D. Wikramasinghe
Department of Zoology, University of Colombo, Colombo, Sri Lanka

Eastern regions has been taking place over the last twenty years [2]. The main impact on ground water is believed to be from the sea water intrusion and agricultural activities which are prevalent in the area [1]. Ground water is much affected by misuse and overuse of agrochemicals which results in unsustainable concentrations of nitrates and phosphates [3]. Thus, ground water resources of the peninsula is much affected during the dry season resulting water stress in the environment and severe water shortage for domestic consumptions and more on agricultural use. This study has been designed to evaluate the physical quality of ground water during the dry season. In doing so, it will also reveal the possibility of degradation of water quality in the context of climate change driven water scarcity.

34.2 STUDY AREA

Kalpitiya covers a total land area of about 160sq km. It is located between 79° 40'–79° 50' Easting longitude and 8° 20'–8° 30' Northern latitude. Figure 34.1 shows the map of study area. The climate is characterized by average annual rain fall between 500–600mm from the North East monsoon between October and January. Average annual temperature of the Kalpitaya is maximum of 31 °C to minimum of 27°C. Study area has a total area of 202sq km. Coastal and lagoon fisheries and agriculture are the main livelihood of the residents.

34.3 MATERIAL AND METHODS

Field investigations were carried out for 3 months (December 2013 to February 2014 - dry season) and water samples collected from a network of dug wells which has been located using a grid map. Figure 34.2 shows the map of grid and sample locations. Sample locations were found out the center of grid. Global Position System (GPS – Magellan exploits 620) was helped for navigation to the location (Center point of grid). Figure 34.3 shows used GPS for the find out sample location. Samples were analyzed for pH, Electrical conductivity (EC), Temperature and Salinity on site using a multi parameter (Fig. 34.4). ArcGIS 10.1 package was used to identify the spatial distribution of ground water characteristics. Inverse Distance Weighted (IDW) technique of Spatial Analysis tool was used in ArcGIS 10.1 version and maps were developed.

34.4 RESULTS AND DISCUSSION

The results of this study indicate that water quality of the Kalpitiya peninsula has degraded in physical quality. During the sampling period it was revealed that the range for the pH values was between 6.8 and 8.5 mg/L (Sri Lanka Standards for Drinking water quality pH 7.0 – 8.5; SLS 614, 1983.). Average Electrical

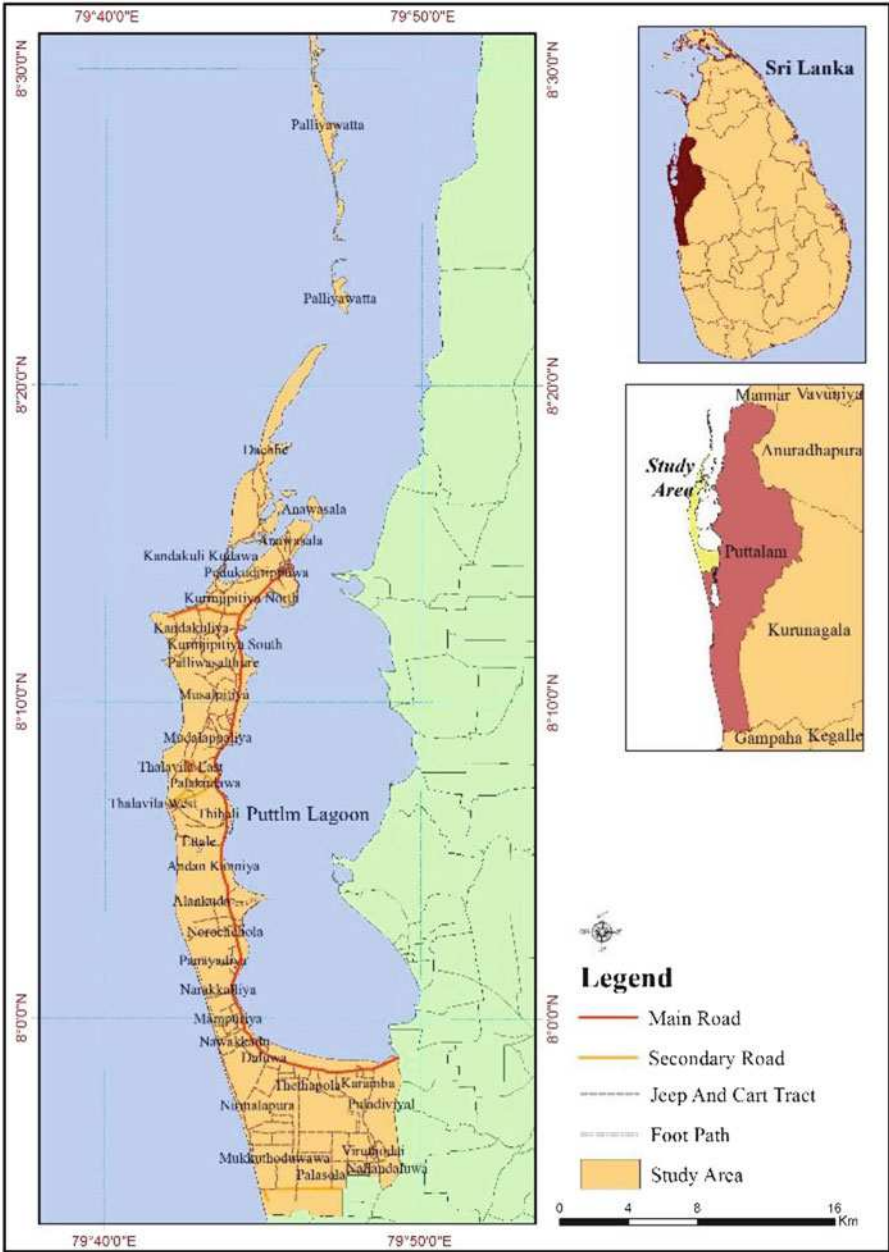


Fig. 34.1 Location map of the study area

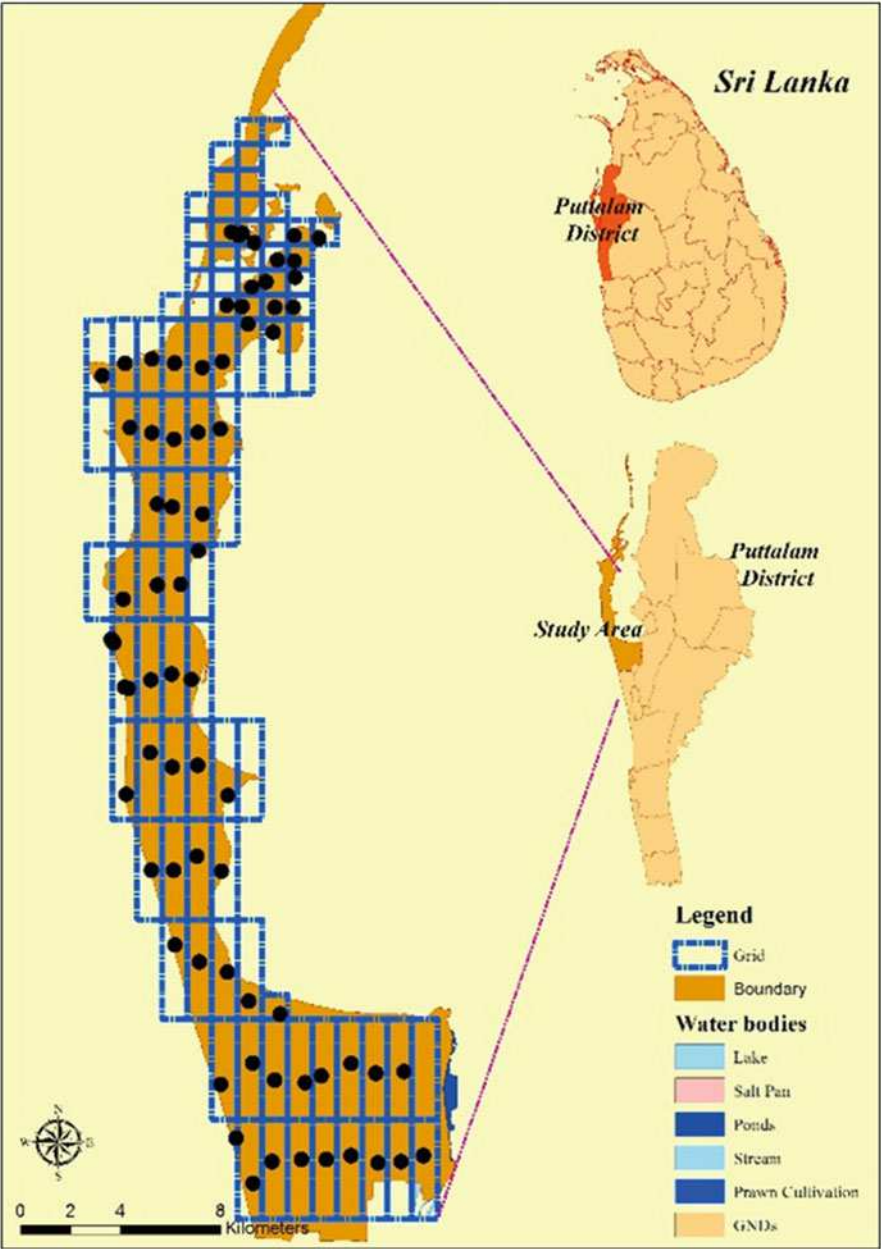


Fig. 34.2 Sample location and grid

Fig. 34.3 Magellan exploits 620



Conductivity (EC) was recorded between $103 \mu\text{S}/\text{cm}$ – $33016 \mu\text{S}/\text{cm}$. And average Salinity was recorded between recorded 0.1 ppt - 31.40 ppt during the sampling period. When considering all sample locations, Talavila area is special having much degraded water quality: the average EC recorded as $33016 \mu\text{S}/\text{cm}$ and salinity was 31.4 ppt . Similarly, pH of water too was high in that area reaching the Highest Desirable level in Sri Lankan potable water standards. Electrical Conductivity levels were greater than the $750 \mu\text{S}/\text{cm}$ exceeding Sri Lankan standards. There may be different factors affecting the water quality- overuse and misuse of agrochemicals most are of ammonia based, high evaporation rates and salt water intrusion (Fig. 34.5).

There may be different factors affecting salinity in the study area. Cleaning of vegetation that results in high rates of evaporation from soil and salt water intrusion from the sea water to the wells close to the sea which is rampant during the dry season could contribute to elevated salinity levels [4]. According to Voudouris and others [5] sea water intrusion could be caused by over pumping, water abstraction from great depths and lack of reliable water resource management. The over extrapolation of coastal aquifers always produces a lowering to the water table levels which facilitates further intrusion of sea water [6]. Since in most of the agricultural areas in the peninsula extraction of ground water is inevitable, water quality gets degraded. Figure 34.6 shows the spatial distribution of salinity in Kalpitiya peninsula.

Fig. 34.4 Multi parameter

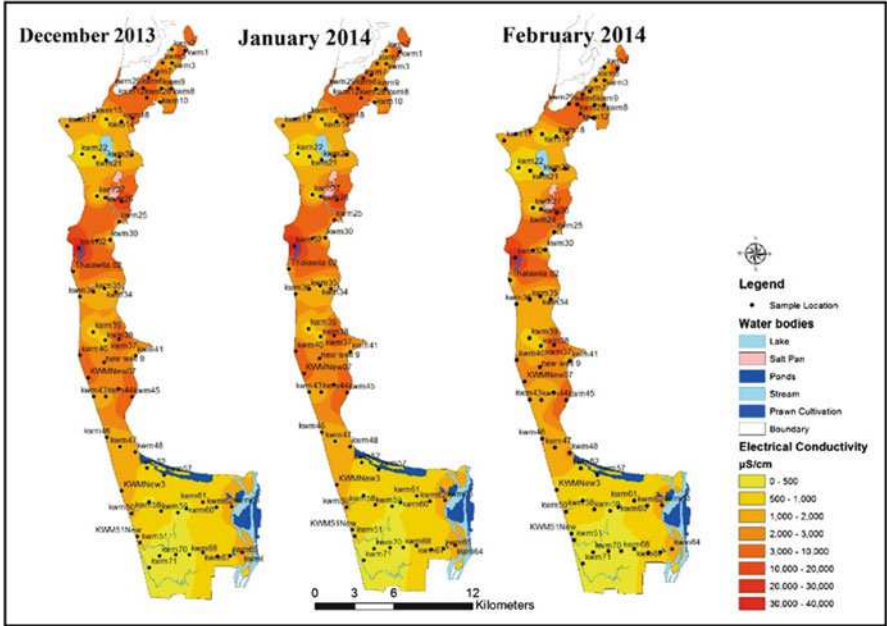


Fig. 34.5 Spatial distribution of the electrical conductivity in Kalpitiya peninsula

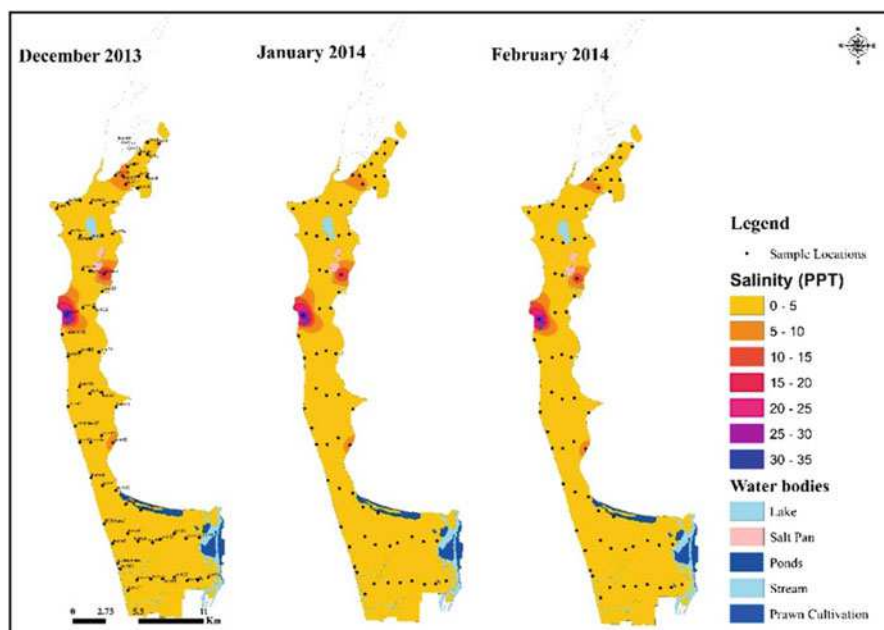


Fig. 34.6 Spatial distribution of the salinity in Kalpitiya peninsula

The pH values were recorded between 6.8 and 8.5 mg/L. Highest average pH value was recorded close to Palliyawasathurei Area which reached to 8.5 mg/L. Figure 34.7 shows the spatial distribution of pH.

In the context of climate change, where water security will be in peril due to decreased precipitation and drought conditions that are very likely to occur, this landscape will face serious problems on meeting the demands for fresh water for domestic consumption as well as for agriculture.

34.5 CONCLUSION

It is apparent that ground water in the Kalpitiya area is degraded in physical quality during the dry season. Electrical Conductivity levels were greater than the 750 $\mu\text{S}/\text{cm}$ exceeding Sri Lankan standards. Thus, it is obvious that ground water in the area could not be recommended for domestic consumptions at least during the dry season. Changing climate resulting less rainfall and sea level rise will aggravate the problem.

ACKNOWLEDGEMENT The authors are grateful to the grant from the project “Developing methods for assessing Island vulnerability to sea level rise and its effects of on livelihood options 2014” under the Ministry of Technology, Research and Atomic Energy, Sri Lanka.

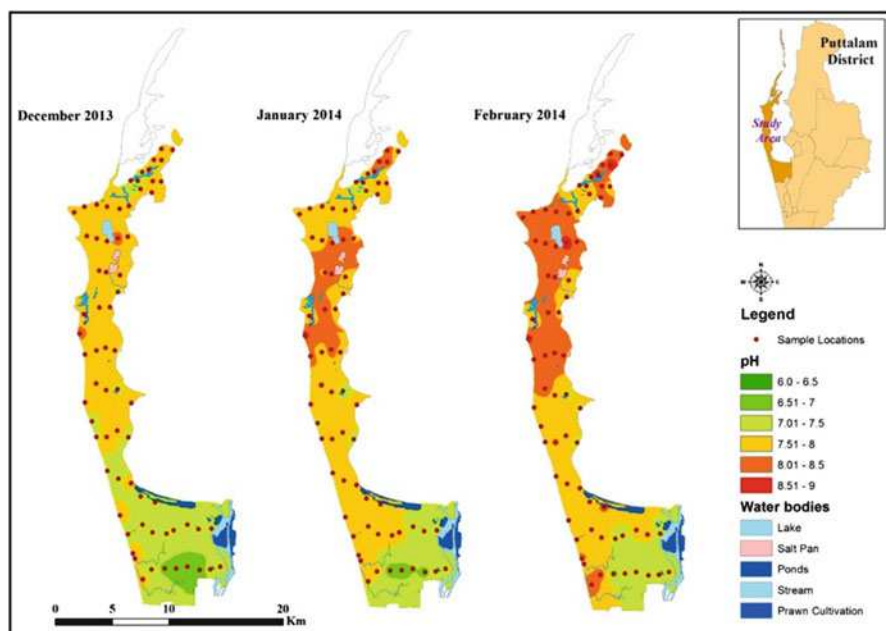


Fig. 34.7 Spatial distribution of the pH in Kalpitiya peninsula

REFERENCES

1. Kumarasinhe, K.M.S.M. and Rajapaksha, R.R.G.R.: Impact of ground water quality in Puttalam area due to over extraction and improper agricultural practices. First young water professionals symposium, Sri Lanka water partnership (Lanka Jalani), International water management institute and Unilever-Pureit, 140–145 (2012)
2. Panabokke, C.R.: Ground water conditions in Sri Lanka: A Geomorphic Perspective. National Science Foundation of Sri Lanka (2007)
3. Kumarasinghe, K.M.S.M., Rajapaksha, R.R.G.R. and De Silva, S.S.K.: Impact on Groundwater quality in Puttalam area due to over abstraction & improper agricultural practices. http://www.wrb.gov.lk/web/images/stories/BMICH_workshop_30_07_2013/b_impact_puttalam.pdf, access date 13.09.2013. Haffner, W.: Nepal Himalaya, Untersuchungen zum vertikalen Landschaftsaufbau zentral-und Ostnepals. Erdwissenschaftliche forschung, 12, Wiesbaden (1979)
4. Kumarasinge, M.S.M. and Rajapakhe, R.G.R.: Impact of anthropogenic activities on ground-water quality in Puttalam district. *Journal of Geological Society of Sri Lanka*, 15, 129–135 (2013)
5. Voudourish, S. and Antonakosa, Daskalakis: Water resources and groundwater quality in north Peloponnesus (Greece). *Global NEST Journal*, 7(3), 340–353
6. http://journal.gnest.org/sites/default/files/Journal%20Papers/paper_15_Voudouris_302.pdf (2005)

Chapter 35

Hydrogeochemical Assessment to Explore the Extent, Nature and Source of Fluoride Contamination within the Groundwaters of the Panda River Basin, Sonbhadra District, Uttar Pradesh, India

Sangita Dey and N. Janardhana Raju

Abstract Significant amounts of fluoride are found in the abstracted groundwater of the southern part of the Upper Panda River basin, Sonbhadra district, Uttar Pradesh, India. Hence groundwater with high fluoride and water mixture patterns were studied in Panda River basin through hydrochemical interpretation from 65 groundwater chemical data information from different wells for both the seasons, premonsoon and postmonsoon. The chemical relationship and Gibbs diagram suggest that the groundwaters mainly belong to freshwater, alkali type and are controlled by rock dominance; due to influence of semi arid condition and water-rock interaction. Na-HCO₃ is dominated in most part (60 % of the total number of water samples for both the seasons) of the study area. The whole environment is favorable for the fluoride dissolution as the increasing Na concentrations are observed under alkaline conditions with a subsequent reduction in Ca concentration. Major rock types of the area are phyllites and granite gneissic rocks. Geochemical study reveals that Fluor-apatite and biotite mica in the granite gneissic rock is the main source of fluoride in the groundwater through water-rock interactions. Fluoride concentrations are in the range 0.4–5.6 mg/L in the pre-monsoon season and 0.1–6.7 mg/L in the post-monsoon season. Ion exchange, dissolution, semi-arid climate, alkaline conditions and weathering are responsible for fluoride enrichment in the groundwater of the study area.

Keywords Fluoride • Groundwater • Geogenic process • Hydrogeochemistry • Panda River • India

S. Dey (✉)

Department of Geology, Banaras Hindu University, Varanasi, India

e-mail: sangitadey24@rediffmail.com

N.J. Raju

School of Environmental Sciences, Jawaharlal Nehru University, New Delhi, India

35.1 INTRODUCTION

Human health issue is largely related to fluoride intake which involves the influence of geological environment. It has adverse effect not only due to excessive intake but also to its deficiency. Human health status depends upon a delicate balance between excess and deficiency. Low intake of this element is related to dental caries (<0.5 mg/L) while experiences the high chronic levels, can lead to dental (1.5–2 mg/L) or skeletal (4–8 mg/L) fluorosis [1, 2, 3]. The hydrological factors controlling recharge and hydrogeochemical reactions that results from water–rock interaction, as well as anthropogenic interventions, are important for the chemical constituents to reach the groundwater [4, 5]. Some important fluoride bearing minerals are fluorite (CaF_2), cryolite (Na_3AlF_6), topaz, tourmaline, muscovite, biotite, hornblende and villianmite. Fluoride is also found in micas, where it occurs in combination with silicates, but particularly in association with phosphorus as fluorapatite [6, 7]. Fluoride contamination is varied even in similar hydrological environments; hence the study of the geochemical processes and unique characteristics of water that might be responsible for the assimilation of Fluoride ions is essential [5]. The habitants of the Upper Panda river basin are largely dependent on groundwater for insufficient availability of surface water and supply water. The southern part of the area shows high fluoride concentration which may increase with time if proper protective measure may not set into action. An attempt has been made here to detect extent, nature and source of fluoride through hydrochemical analysis and correlation analysis in the Upper Panda river basin, Sonbhadra district, Uttar Pradesh, India.

35.2 STUDY AREA AND HYDROGEOLOGY

Panda River is a tributary of Son River. The study area lies between $24^{\circ}15'$ – $24^{\circ}30'$ N latitude and $83^{\circ}15'$ – $83^{\circ}30'$ E longitude (Fig. 35.1). It covers an area of 216 sq. Km. The climate is characterized by a dry and hot season in March and June (avg. 47°C); a dry and cold winter from October to February (avg. 10°C); and a warm monsoon period from July to September. The average rainfall is 850 mm. Physiologically, the area is characterized by several inselbergs and torns. Small extent E-W trending hill ranges made up of quartzite are frequent. Geological formations, belong to the metasedimentary rock sequences of Parsoi Formation and Dudhi Group of Palaeo Proterozoic age. Metasedimentary rocks of Parsoi Formation mainly consists of phyllites, rest unconformably over the Dudhi Group which comprises of granite, granodiorite, and gneisses. This portion exposed in the southern parts of the study area. North and north eastern parts are covered with Meso Proterozoic thick sedimentary pile of Semri Group of Vindhyan Super Group. These rock sequences are covered with Early to Late Pleistocene Banda Alluvium Formation. The drainage shows dendritic to sub-dendritic pattern and ephemeral in

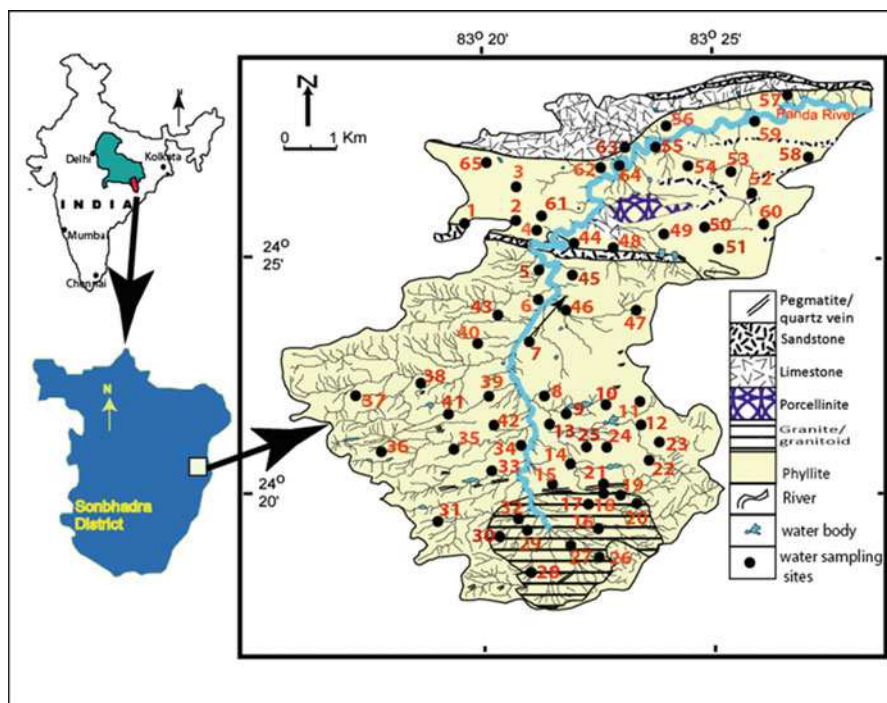


Fig. 35.1 The map showing location of well sites, drainage and geology of the Panda River basin

nature. Direct rainfall is the main recharge to aquifers of the study area. Major lithology phyllite is a low permeable rock but it can contain sufficient groundwater within it due to the presence of numerous fracture and high weathering. The granites of the area contain a number of joints and fractures, so the rock acts as an aquitard. The upper alluvium has developed good aquifer zones in the study area. The depth of the water table varies from 3m to 34.3m in premonsoon and 2.7m to 30m in postmonsoon season. The general flow directions are S-N, SW-NE, and SE-NW which is following the general topography.

35.3 METHODS OF INVESTIGATION

A well survey and groundwater collection was carried out during April-May 2006 and October 2006. Groundwater samples from 65 villages were collected for both the seasons premonsoon and postmonsoon. Pre-cleaned airtight containers of 1 liter were used for collection. The parameters pH and EC measured with pH meter and EC meter (ELICO). Na^{2+} and K^{+} were estimated by flame photometer (ELICO). Fluoride was measured by using ion selective electrode (Orion 96-09 model). Other major cations and anions were measured through titrimetric analysis. The analysis of all the samples is observed to be within the range of acceptability ($\pm 5\%$) used in most laboratory [8].

35.4 RESULT AND DISCUSSION

35.4.1 Hydrochemistry

Table 35.1 presents the statistical summary of chemical parameters of the study area. The distribution of chemical parameters can be grouped under six hydrochemical facies (Na-HCO_3 , Ca-HCO_3 , Mg-HCO_3 , Na-SO_4 , Mg-SO_4 , Ca-SO_4) on the basis of dominance of major ions. Na-HCO_3 is the most dominant facies throughout the season. pH values indicate that the groundwater of the area is slightly alkaline for both the season. Fluoride concentration shows 10.7% in premonsoon and 18.5% in postmonsoon water samples exceeding the permissible limit (1.5 mg/L) [9]. High sodium concentration can achieve through ion exchange processes and irrigation return flow. Bicarbonate may derive through weathering of parental rock [5]. According to Gibbs diagram (Fig. 35.2) [10] the groundwater chemistry is mainly acquired from weathering of parent rocks of the study area. The significance of cation exchange process is proved by the graph ($\text{Ca}^{2+}+\text{Mg}^{2+}-\text{HCO}_3^- - \text{SO}_4^{2-}$) vs. ($\text{Na}^++\text{K}^+-\text{Cl}^-$) where all the data plotted (Fig. 35.3) are close to a straight line with a slope of -0.957 and -0.953 in premonsoon and postmonsoon, respectively.

Table 35.1 Range of chemical parameters of the Upper Panda river basin

Parameter		Premonsoon (N=65)		Postmonsoon (N=65)		
	Range	Arithmetic mean	Standard deviation	Range	Arithmetic mean	Standard deviation
EC	342-1190	637.25	180.78	428-1280	703.23	177.29
pH	6.5-7.7	7.1	0.3	6.9-8.6	7.4	0.2
TDS	206-724	384.78	111.93	140-800	421.09	114.98
Na⁺	10.4-230.1	55.22	40.89	12.5-256	62.93	42.41
K⁺	1.3-3.8	2.20	0.50	1.4-4.2	2.50	0.41
Ca²⁺	6-69	27.97	11.99	14-78	42.77	12.36
Mg²⁺	10.8-56.8	29.72	11.14	4.02-59.2	23.34	11.55
Cl⁻	6-66	23.71	13.46	22-96	37.78	15.18
SO₄²⁻	10-190	97.57	40.47	25-195	111.51	41.43
HCO₃⁻	92-396	211.72	71.17	104-455	202.83	60.90
F⁻	0.378-5.6	0.98	1.02	0.08-6.7	1.17	1.09
Na⁺+K⁺/TZ	1.23-0.08	0.36	0.17	0.08-0.85	0.38	0.15
Ca²⁺+Mg²⁺ / Na⁺+K⁺	0.19-11.1	2.4	1.79	0.17-10.48	2.1	1.6

Fig. 35.2 Mechanisms controlling groundwater (after Gibbs 1970)

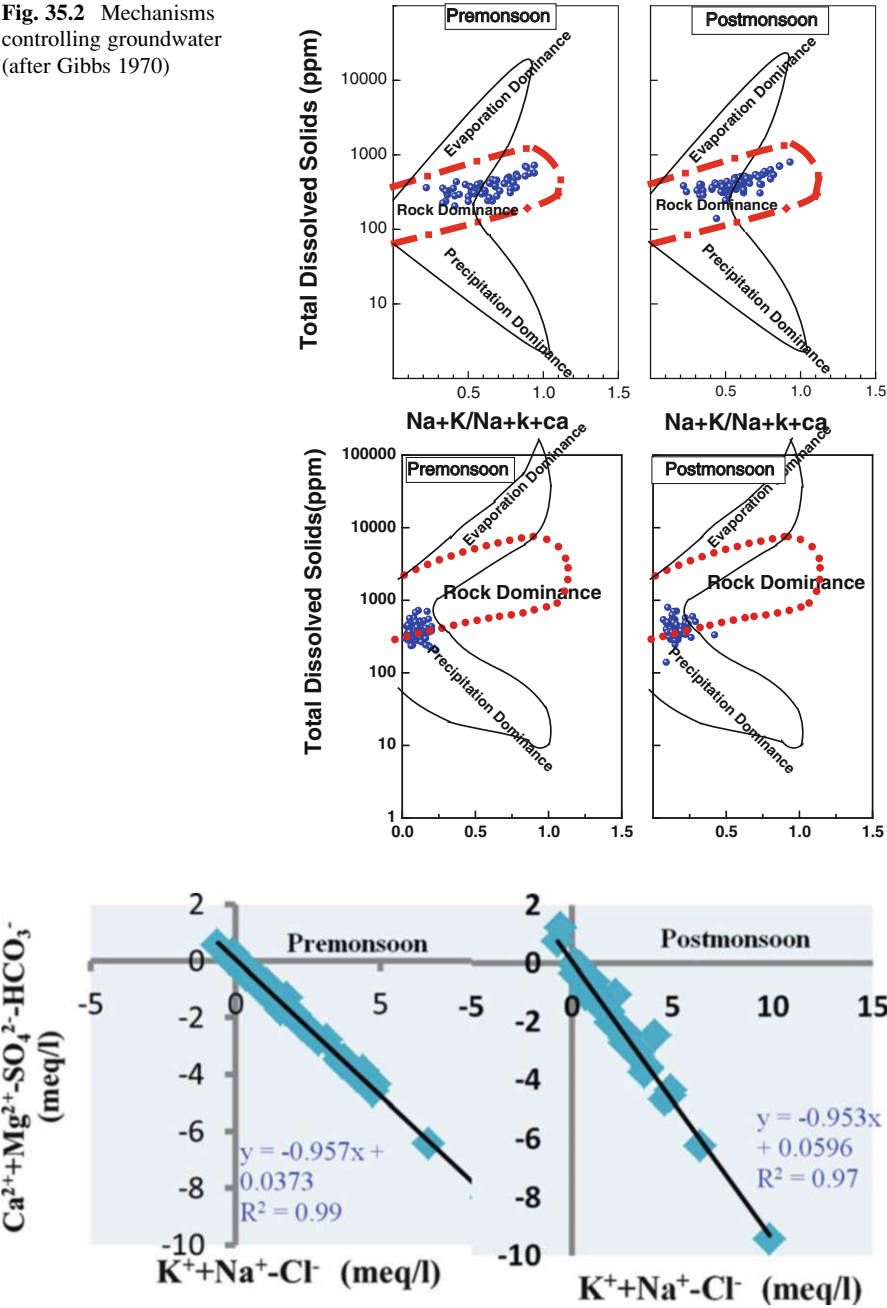


Fig. 35.3 Plot of $\text{Ca}^{2+} + \text{Mg}^{2+} - \text{SO}_4 - \text{HCO}_3$ vs $\text{Na}^+ + \text{K}^+ - \text{Cl}^-$ in the ground water of the study area

The ratio of $(\text{Na}^+ + \text{K}^+)/\text{total cations}$ (0.36 in premonsoon and 0.38 in postmonsoon) (Table 35.1) suggests that silicate weathering is dominant in the study area. But the avg. ratio $(\text{Ca}^{2+} + \text{Mg}^{2+})/(\text{Na}^+ + \text{K}^+)$ shows 2.4 in premonsoon and 2.1 in postmonsoon (Table 35.1) also indicating a little contribution of carbonate weathering on groundwater chemistry.

35.4.2 Distribution and Source of Fluoride

Fluoride distribution can be divided into three zones, that is deficient area (<0.5 mg/L), optimum area (0.5-1.5 mg/L), and enriched area (1.5-10 mg/L) (Fig. 35.4). The enriched area is identified in the southern part of the area. The area is situated above the granite gneissic complex. Most of the people in that area are suffering from dental and skeletal fluorosis [3, 5]. The distribution shows wide variation in fluoride concentration in both the seasons. The mixed seasonal variation in fluoride in space and time are primarily related the abundance of, and variation in, fluoride bearing minerals within rock formations, the different fracture system, and associated hydrochemical processes [5]. The petrological studies and XRD analysis reveals the presence of fluor-apatite and biotite within the granitic gneisses in the study region [3]. Therefore fluoride contamination in the area is due to geogenic cause and fluor-apatite and biotite are contributing minerals in that region.

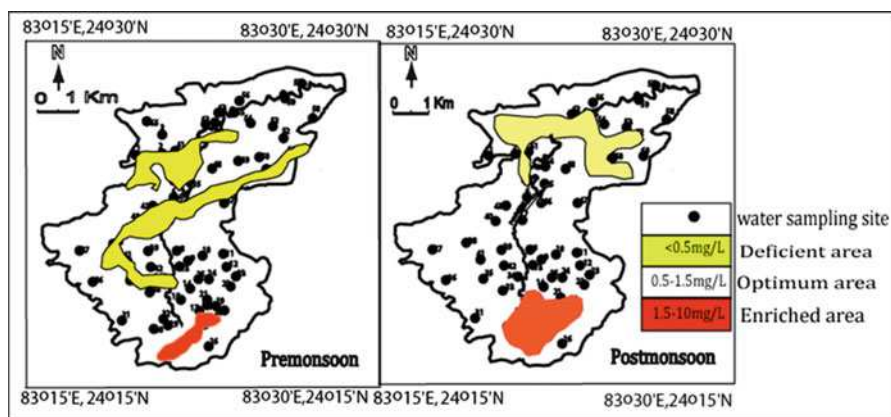


Fig. 35.4 Distribution of fluoride in the study area

35.4.3 Hydrochemistry of Fluoride

Soda-alkali environment is highly favorable for fluoride dissolution. The high pH condition replaces hydroxyl ion (e.g. biotite) with the exchangeable fluoride (biotite; $\text{KMg}_3 [\text{AlSi}_3\text{O}_{10}] \text{F}_2 + 2\text{OH}^- = \text{K} \text{Mg} [\text{AlSi}_3\text{O}_{10}] [\text{OH}]_2 + 2\text{F}^-$), increases the concentration of fluoride in the groundwater. Fluoride bearing minerals desorb fluoride ion into groundwater in presence of sodium bicarbonate type water ($\text{CaF}_2 + 2\text{NaHCO}_3 \rightarrow \text{CaCO}_3 + 2\text{Na} + 2\text{F}^- + \text{H}_2\text{O} + \text{CO}_2$). A correlation matrix (r-value at significance level of $p < 0.05$ and $p < 0.01$) for both the seasons in study area was generated for the water quality parameters to interpret the relationship among the various ions (Table 35.2). Fluoride showed positive correlation with bicarbonate (0.36 in pre- and 0.44 in postmonsoon) and sodium (0.69 in pre- and 0.60 in postmonsoon). Fluoride had a negative correlation with calcium (-0.13 in premonsoon and -0.22 in postmonsoon).

Bicarbonate ion can arrive from the hydrolysis of aluminosilicates in the hard rock aquifers that can enhance fluorite dissolution ($\text{CaF}_2 + 2\text{HCO}_3^- \rightarrow \text{CaCO}_3 + 2\text{F}^- + \text{H}_2\text{O} + \text{CO}_2$). The F^- concentration increases with increasing Na^+ content and decreases with increasing Ca^{2+} content due to the dominance of the ion-exchange process. During the ion-exchange process, calcium ions in water may exchange with sodium ions in clay minerals (sodium-montmorillonite), thus increasing the concentration of Na^+ ions in groundwater [11]. Therefore in granite dominated aquifers, dissolution of fluoride bearing minerals can be possible reason for the presence of fluoride in groundwater.

35.5 CONCLUSIONS

Groundwater is one of the important sources of drinking water in the Upper Panda river basin due to inadequate surface water. Groundwater evaluation reveals that silicate weathering along with a minute carbonate weathering contributes the major ions in to the groundwater. The southern part of the region shows high fluoride concentration. Fluoride concentrations are in the range 0.4–5.6 mg/L in the pre-monsoon season and 0.1–6.7 mg/L in the post-monsoon season. The source of high concentration of fluoride is mainly geogenic origin. The contamination is due to the dissolution of fluor-apatite and biotite of granitic gneisses. Ion exchange, dissolution, semi arid climate, alkaline conditions and weathering are responsible for fluoride enrichment in groundwater.

Table 35.2 Correlation matrix of chemical parameters of the groundwater samples of the study area

	Ca		Mg		Na		K		HCO ₃		SO ₄		Cl		F	
	Pre	Post	Pre	Post	Pre	Post	Pre	Post	Pre	Post	Pre	Post	Pre	Post	Pre	Post
Mg	−0.49#	−0.39#														
Na	−0.230	−0.38#	−0.045	−0.054												
K	0.116	0.187	−0.043	−0.27*	−0.137	−0.135										
HCO ₃	−0.169	−0.200	0.39#	0.058	0.68#	0.80#	−0.07	0.008								
SO ₄	−0.184	−0.186	0.146	0.43#	0.66#	0.61#	−0.10	−0.34#	0.194	0.34#						
Cl	0.178	−0.109	−0.077	0.135	0.51#	0.37#	−0.03	−0.082	0.242	0.166	0.32#	0.206				
F	−0.131	−0.219	−0.105	−0.109	0.69#	0.60#	−0.16	−0.094	0.36#	0.44#	0.49#	0.38#	0.37#	0.114		
EC	−0.144	−0.260*	0.30*	0.26*	0.90#	0.85#	−0.12	−0.39#	0.81#	0.68#	0.69#	0.79#	0.51#	0.43#	0.58#	0.52#

#Correlation is significant at the 0.01 level (2-tailed). * Correlation is significant at the 0.05 level (2-tailed).

REFERENCES

1. Apambire, W.B., Boyle, D.R. and Michel, F.A.: Geochemistry, genesis and health implications of fluoriferous groundwaters in the upper region of Ghana. *Environmental Geology*, 33, 13–24 (1997)
2. Edmunds, M. and Smedley, P.: Fluoride in natural waters. In: Essentials of medical geology—impacts of the natural environment on public health, Selinus, O., Alloway, B., Centeno, J.A., Finkleman, R.B., Fuge, R., Lindh, U., Smedley, P. (eds). Academic Press: Amsterdam, 301–330 (2005)
3. Raju, N.J., Dey, S. and Das, K.: Fluoride contamination in groundwater of Sonbhadra District, Uttar Pradesh, India. *Current Science*, 96 (7), 979–985 (2009a)
4. Faure, G.: Principles and applications of geochemistry. 2nd ed. Englewood Cliffs, NJ: Prentice Hall (1998)
5. Raju, N.J., Dey, S., Gossel, W. and Wycisk, P.: Fluoride hazard and assessment of groundwater quality in the semi-arid Upper Panda River basin, Sonbhadra district, Uttar Pradesh, India. *Hydrological Sciences Journal*, 57(7), 1433–1452 (2012)
6. Handa, B.K.: Geochemistry and genesis of fluoride containing groundwaters in India. *Groundwater*, 13(3), 275–281 (1975)
7. Singh, C.K., Kumari, R., Singh, N., Mallick, J. and Mukherjee, S.: Fluoride enrichment in aquifers of the Thar Desert: controlling factors and its geochemical modeling, *Hydrological Processes*, 27, 2462–2474 (2013)
8. Domenico, P.A. and Schwartz, F.W.: Physical and chemical hydrology. Wiley, New York (1990)
9. WHO (World Health Organisation): Guidelines for drinking water quality. Volume 1, Recommendations. 2nd ed. Geneva: WHO (1997)
10. Gibbs, R.J.: Mechanisms controlling world water chemistry. *Science*, 170, 1088–1090 (1970)
11. Hounslow, A.: Water quality data: analysis and interpretation, 1st edn. CRC Lewis: Boca Raton; 397 (1995)

Chapter 36

Presence of Uranium in Groundwater of Punjab: An Overview

A. Diana Sharma and Madhuri S. Rishi

Abstract Uranium is the heaviest naturally occurring element found at an average concentration of 0.0004 % in the earth's crust and in low levels within all rock, soil and water. Natural uranium is a mixture of three isotopes, ^{238}U , ^{235}U and ^{234}U and all three behave the same chemically, but they have different radioactive properties. The predominant forms of uranium are ^{234}U and ^{238}U which occurs naturally in groundwater and surface water. Its content in groundwater varies markedly depending upon geological terrain, climate, proximity of uranium deposits, as well as composition of the water. Uranium contamination of groundwater comes from the aquifer from which the water is pumped. The study area have a particular importance because of its elevated levels of uranium detected in the groundwater which may be attributed to the radioactive rich granitic rock formations of Tusham Hills (Bhiwani) of the neighboring state Haryana and from Shivalik Himalayas, parts of which are known for uranium mineralization and also through human activities like phosphate fertilizing. Being a radioactive mineral, high uranium concentration can cause impact on water, soil and health. The maximum contaminant level for uranium, recommended by the World Health Organization is 30 $\mu\text{g/L}$ and this limit is found to be exceeded in the drinking water of various regions of Punjab. This work reviews and interprets the prevailing scenario in Punjab region, focusing on uranium as an important environment contaminant.

Keywords Groundwater • Environment Contaminant • Isotopes • Radioactive

36.1 INTRODUCTION

Uranium a primordial radioelement occurs in a dispersed state with average crustal abundance of 2.8 ppm and present at a concentration of about 3.0 $\mu\text{g/L}$ in seawater [1, 4, 6, 10, 27, 28]. Uranium isotopes during their disintegration course decay into other radioactive elements and eventually decay to stable lead isotopes in the

A.D. Sharma (✉) • M.S. Rishi
Department of Environment Studies, Panjab University, Chandigarh, India
e-mail: dianasharma307@gmail.com

process emit beta and gamma radiation [8, 19]. Uranium isotopes and their specific activity are being discussed [4, 27]. The decay products of ^{238}U and ^{234}U are responsible for the presence of beta and gamma radiations in purified natural uranium. U is widespread in nature, occurring in granites and various other mineral deposits and in low concentration in all natural waters in concentrations between 0.1 and 10 $\mu\text{g/L}$, concentrations greater than 1 mg/L can occur in water associated with U-ore deposits [2, 6, 17, 20, 29]. The naturally occurring uranium concentration in drinking water sources depends on factors such as the uranium concentration in the host aquifer rock, the partial pressure of CO_2 , the presence of O_2 and complexing agents in the aquifer, the pH and the nature of the contact between the uranium minerals and water [10]. This paper states the prevailing scenario of Uranium as an environment contaminant in Punjab region and addresses new dimensions for carrying out research.

36.2 STUDY AREA AND HYDROGEOLOGY

This study was conducted for indo-gangetic alluvial plain of Punjab with particular focus on Southwest Punjab (Fig. 36.1). It lies between 3004°N and 7505°E . Its average elevation is 300 m from the sea level. The soils in the region have largely developed on alluvium deposits up to depth of thousands of feet [3].

36.3 REVIEW OF RESEARCH

Enhanced level of Uranium was detected in groundwater of Punjab and has been an issue of National importance due to its linkage with the abnormal public health conditions of the study area. Studies on U contamination in Punjab region were undertaken by many agencies but were limited to measurement of U in groundwater and profiling. The preliminary analysis is indicative that the U occurrences have been encountered not only at the shallow depth but also to a depth of around 200 mbgl. Many workers have reported concentration of U in the study area which are higher than the provisional guideline set by WHO, US EPA (MCL) of 30 $\mu\text{g/L}$ (30 ppb), and AERB, India (60 $\mu\text{g/L}$) [3, 5, 7, 14, 15, 17, 21–23, 26]. The elevated U content in ground water samples of Bathinda region may be attributed to the radioactivity rich granitic rock formations of Tusham Hills (Bhiwani) of the neighboring state Haryana, India where good correlation has been observed between uranium content and radon exhalation rate [14, 15, 21]. Basement granite rocks has been indicated as a source of U and Siwalik classic sediments controlled by redox interface, porosity permeability barriers and reductants as possible sources [7]. High TDS (above $\sim 1200 \text{ mg/L}$) has been reported in the groundwater in the Baluana village of Bathinda district which is indicative of high concentrations of Br, Sr and U elements [3, 5]. Due to high salinity, high TDS and high ionic strength

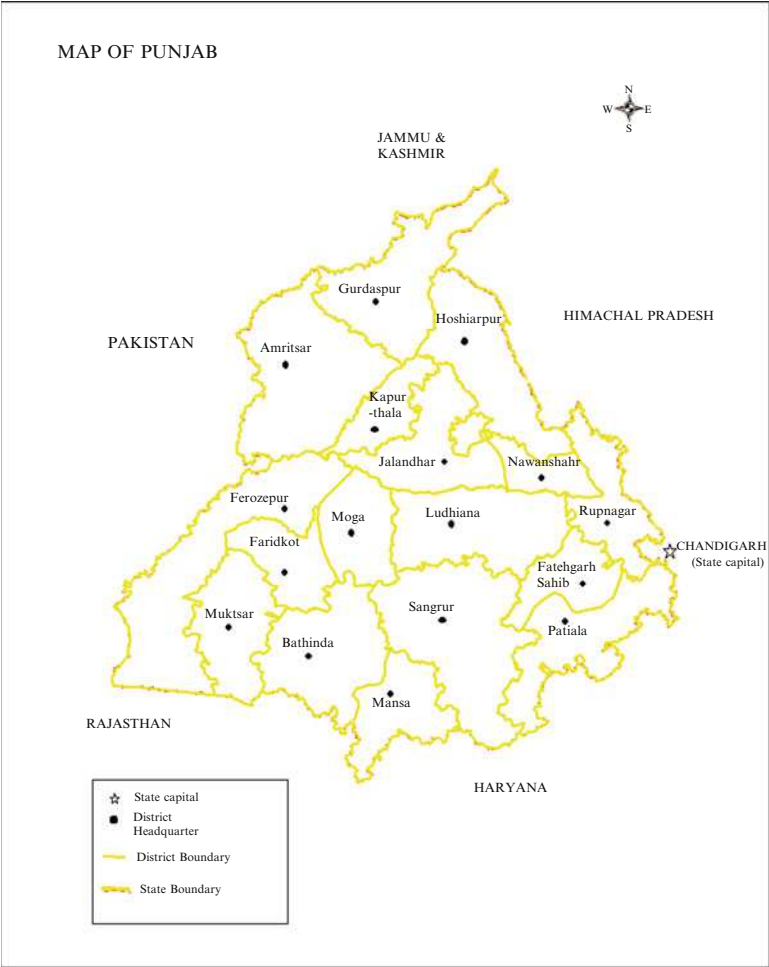


Fig. 36.1 Map showing study area

of ground water, solubility of uranium increases [17]. All ground water in the study region was found to be undersaturated with respect to U-bearing minerals indicating that minerals are responsible for controlling the uranium mobility [16]. Groundwater was classified as oxidized aquifer on normal uranium content strata (20 %) or oxidized aquifer on enhanced uranium content strata (80 %) on the basis of uranium concentration [26]. Strong correlations was observed between uranium and bicarbonate in the groundwater in Central Valley, California, USA which is quite similar with the conditions observed in the research area with rich bicarbonates, nitrate and chloride anions and soil being calcareous [13, 17]. High uranium values in drinking water samples may be due to the fact that the Punjab sediments are derived from Shivalik Himalayas, parts of which are known for uranium mineralization. It is

further reported that uranium has greater affinity for chloride and nitrate ions and established positive correlation of U with conductance, nitrate, hardness and magnesium [23]. In the oxidized environment, uranium mostly exists in the +6 state and has a strong tendency to form uranyl complexes with carbonates and bi-carbonates and is readily transportable. U remains in +4 state in reduced condition and almost precipitated quantitatively [19, 26, 31]. The solubility of uranium also depends on the mineralogical location of U in the rock. The U content in groundwater varies primarily due to recharge and discharge which would have dissolved or leached the uranium from the weathered soil to the groundwater zone. The concentration of U in groundwater is high where the oxidation reduction potential is high [6, 31]. So oxidation potential is a key factor for determining uranium concentration as stated [24]. Carbonate and phosphate ions form U-complexes, making the total dissolved U concentration much more than it would be in a carbonate and phosphate-free water [17, 31]. Studies have shown that phosphate fertilizers possess U concentration which can be transferred to agricultural systems and subsequently to ground- and running-water systems [6, 7, 18]. Groundwater, in its natural state, contains environmental isotopes. Characteristics and natural occurrence of the environmental isotopes, isotopes in groundwater has been discussed in detail by many researchers [9, 19]. Isotope hydrology acts like a useful tool as it provides complementary information on the type, origin and age of groundwater [11, 12, 25, 30].

36.4 CONCLUSIONS

As the uranium contamination of ground water is occurring over vast regions, the source is likely to be not localized one. Exposure to higher levels of uranium is of serious concern for public health due to its hazardous nature associated with internal exposure. Being an environmental contaminant further work will be carried out to validate the occurrence and release mechanism of U in groundwater using environmental isotopes.

REFERENCES

1. Agency for Toxic Substances and Disease Registry: Toxicological profile for Uranium, U.S. Department of Health and Human Services. Public Health Service. ATSDR, Atlanta, GA. A report (2011)
2. Aieta, E.M., Singley, J.E., Trussell, A.R., Thorbjarnarson, K.W. and McGuire, M.J.: Radionuclides in drinking water: an overview. *J. Am. Water Works Assoc.*, 79(4),144–152 (1987)
3. Alrakabi, M., Singh, G., Bhalla, A., Kumar, S., Kumar, S., Srivastava, A., Rai, B., Singh, N., Shahi, J.S. and Mehta, D.: Study of uranium contamination of ground water in Punjab state in India using X-ray fluorescence technique. *J. Radioanal. Nucl. Chem.*, 294, 221–227 (2012)

4. Babu, M.N.S., Somashekar, R.K., Kumar, S.A., Shivanna, K., Krishnamurthy, V. and Eappen, K.P.: Concentration of uranium levels in groundwater. *Int. J. Environ. Sci. Tech.*, 5(2), 263–266 (2008)
5. Bhalla, A., Singh, G., Kumar, S., Shahi, J.S. and Mehta, D.: Elemental analysis of groundwater from different regions of Punjab State (India) using EDXRF technique and the sources of water contamination. In: Proc. of International Conference on Environmental and Computer Science, pp. 156–164, IACSIT Press, Singapore (2011)
6. Brindha, K., Elango, L. and Nair, R.N.: Spatial and temporal variation of Uranium in a shallow weathered rock aquifer in southern India. *J. Earth Syst. Sci.*, 120(5), 911–920 (2011)
7. Central Ground Water Board: Water Quality Issues and Challenges in Punjab, CGWB (2014) <http://cgwb.gov.in>
8. Fontes, J.: Dating of groundwater. In: Guidebook of Nuclear techniques in Hydrology. Technical Report Series No. 91, International Atomic Energy Agency, Vienna (1983)
9. Geyh, M.: Environmental isotopes in the hydrological cycle—Principles and applications, IHP-V. Technical Documents in Hydrology, No. 39, Vol. IV, UNESCO, Paris (2000)
10. Hess, C.T., Michel, J., Horton, T.R., Prichard, H.M. and Coniglio, W.A.: The occurrence of radioactivity in public water supplies in the United States. *Health Phys.*, 48, 553–586 (1985)
11. International Atomic Energy Agency: Guidebook on nuclear techniques in hydrology. Technical Report Series 91, IAEA, Vienna (1983)
12. International Atomic Energy Agency: Isotope methods for dating old groundwater. STI/PUB/1587, IAEA, Vienna (2013)
13. Jurgens, B.C., Fram, M.S., Belitz, K., Burow, K.R. and Landon, M.K.: Effects of groundwater development on Uranium: Central Valley, California, USA. *Gwat*, 48(6), 913–928 (2010)
14. Kochhar, N., Gill, G.S., Tuli, N., Dadwal, V. and Balaram, V.: Chemical quality of groundwater in relation to incidence of cancer in parts of SW Punjab, India. *Asian J. of Water, Environ. Pollut.*, 4(2), 107–112 (2007)
15. Kochhar, N., Dadwal, V., Rishi, M., Sharma, N.K. and Balaram, V.: Evaluation of Chemical Quality of Groundwater in parts of Sirsa (Harayana), Mansa, Bhatinda and Muktsar Districts, SW Punjab with emphasis on Uranium in relation to human health. In: Proc. of IGWC-2012 on the Assessment and Management of Groundwater Resources in Hard Rock Systems with Special Reference to Basaltic Terrain, pp. 611–626, Aurangabad, Maharashtra, India (2012)
16. Kumar, A., Rout, S., Narayanan, U., Mishra, M.K., Tripathi, R.M., Singh, J., Kumar, S. and Kushwaha, H.S.: Geochemical modelling of Uranium speciation in the subsurface aquatic environment of Punjab State in India. *J. Geol. Min. Res.*, 3(5), 137–146 (2011)
17. Kumar, A., Usha, N., Sawant, P.D., Tripathi, R.M., Raj, S.S., Mishra, M., Rout, S., Supreeta, P., Singh, J., Kumar, S. and Kushwaha, H.S.: Risk Assessment for Natural Uranium in Subsurface Water of Punjab State, India. *Human Ecologil. Risk Assessment*, 17, 381–393 (2011)
18. LeMone, D.V., Goodell, P.C., Harris, A.H. and Winston, J.W.: Phosphate Rocks: Sustainable Secondary Source for Uranium and their Agricultural Impact – 9481. In: Proc. of Waste Management Symposium 2009 on Waste Management for the Nuclear Renaissance, vol. 2, pp. 1107–1119, Phoenix, Arizona, USA (2009)
19. Mook, W.G.: Environmental isotopes in the hydrological cycle—Principles and applications, IHP-V. Technical Documents in Hydrology, No. 39, Vol. 1, UNESCO, Paris (2000)
20. Osmond, J.K. and Cowart, J.B.: Ground water. In: Ivanovich, M., Harmon, R.S. (Eds.), Uranium Series Disequilibrium. Applications to Earth, Marine, and Environmental Science. Clarendon Press, Oxford, UK, pp. 90–333 (1992)
21. Singh, H., Singh, J., Singh, S. and Bajwa, B.S.: Uranium concentration in drinking water samples using the SSNTDs. *Indian J. Phys.*, 83(7), 1039–1044 (2009)
22. Singh, J., Singh, L. and Singh, S.: High U-contents observed in some drinking waters of Punjab, India. *J. Environ. Radioactiv.*, 26, 217–222 (1995)

23. Singh, S., Rani, A., Mahajan, R.K. and Walia, T.P.S.: Analysis of Uranium and its correlation with some physico-chemical properties of drinking water samples from Amritsar, Punjab. *J. Environ. Monit.*, 5, 917–921 (2003)
24. Stalder, E., Blanc, A., Haldimann, M. and Dudler, V.: Occurrence of Uranium in Swiss drinking water. *Chemosphere*, 86, 672–679 (2012)
25. Terwey, J.L.: Isotopes in groundwater hydrology. Challenges in African Hydrology and Water Resources. In: Proceedings of the Harare Symposium. IAHS Publication no. 144, pp. 155–160 (1984)
26. Tripathi, R.M., Sahoo, S.K., Mohapatra, S., Lenka, P., Dubey, J.S. and Puranik, V.D.: Study of Uranium isotopic composition in groundwater and deviation from secular equilibrium condition. *J. Radioanal. Nucl. Chem.*, 295, 1195–1200 (2013)
27. UNSCEAR: Ionizing Radiation: Sources and biological effects. UN Report. New York (1982)
28. Uranium: The McGraw-Hill Science and Technology Encyclopedia (5th ed.). The McGraw-Hill Companies, Inc. ISBN 0-07-142957-3.
29. World Health Organization: Uranium in drinking water. Background document for development of WHO guidelines for Drinking-water quality, Geneva, Switzerland, WHO/SDE/WSH/03.04/118/Rev/1, 29 (2012)
30. Yurtsever, Y. and Araguas, L.A.: Environmental Isotope Applications in Hydrology: An Overview of the IAEA's Activities, Experiences, and Prospects, Tracers in Hydrology (Proceedings of the Yokohama Symposium, July 1993) IAHS Publication no. 215, pp. 3–20 (1993)
31. Zapeca, O.S. and Szabo, Z.: Natural radioactivity in groundwater- a review. National Water Summary 1986—Ground-Water Quality: Hydrologic Conditions and Events, pp. 50–57 (1986)

Chapter 37

Groundwater Sources in Semi-Arid Regions and Their Vulnerability to Climate Change: Drâa Catchment, Morocco

S. Ouyse, José Joel Carrillo-Rivera, G.J. Hernández-García,
and M. Ramirez-Beltrán

Abstract Water availability in Drâa basin (*surface area* ~115,000 km²) depends on rainfall, melting snow in the High Atlas mountains and groundwater. The region has strong evidence of groundwater flow presence whose functioning is required to be fully understood to achieve an adequate water management for an expected rainfall reduction. Previous objectives of carried out studies in the region included the aquifer unit theory and water-balance, lacking a 3D groundwater flow understanding. A regional approach allowing a clearer perspective of groundwater dynamics in its geological context was applied: the Groundwater Flow Systems Theory, which identifies local, intermediate and regional flows hierarchy. The conceptual 3D model included: hydraulic heads, hydraulic properties of rock units, soil type, vegetation, and geomorphology which are in agreement with the physical, chemical and isotopic properties of groundwater. This model was implemented, calibrated and validated using Visual Modflow. Obtained initial-heads were subjected to different recharge conditions; results show that change in recharge is more affecting local flows. However, in the Middle Drâa sub-basin where intermediate flows were identified, the simulated heads lack immediate response to the variation of recharge. Results suggest that local flows are more likely to be affected by climate conditions than those of intermediate and regional nature.

Keywords Flow systems • 3D modelling • Groundwater • Recharge • Drâa basin

S. Ouyse (✉) • J.J. Carrillo-Rivera • M. Ramirez-Beltrán
Institute of Geography, UNAM, CU, Coyoacán, Mexico, DF
e-mail: ouyse_samira@yahoo.fr

G.J. Hernández-García
Institute of Geophysics, UNAM, CU, Coyoacán, Mexico, DF

37.1 INTRODUCTION

The High and Middle Drâa sub-basins are located in the South-East of Morocco between longitude $5^{\circ}30'29''$ - $7^{\circ}40'11''$ and latitude $29^{\circ}37'29''$ - $32^{\circ}0'0''$ (Fig. 37.1), it is characterized by a contrasting climate due mainly to the altitudinal gradient, and to the atmospheric circulations (*Tropical and extra-tropical interactions*). Population and agricultural practices are mainly concentrated in the oases, which are supplied by surface-water (*rainfall and dam release*) and groundwater (*importance of baseflow in drought conditions*). Statistical analyses of annual rainfall series over 40 years (*temporal distribution*) for the monitoring stations (*spatial distribution*) of High and Middle Drâa Sub-basins showed that rainfall distribution remains constant in time and that the probability to detect increasing or decreasing trends remains insignificant at 1 %, 5 % and 10 % significant levels [1]. Rainfall-runoff relation in a monthly time step in the High Drâa sub-basin shows an insignificant correlation, which could be due to the time scale determination (flash flood due to stormy events (*rainfall intensity*)), snow-melting fraction, and baseflow (*groundwater*) supplement which are not commonly integrated in a conceptual hydrological model. As groundwater extraction is increasing resulting to dry conditions which reduce surface-water supply, fundamental approaches are needed to develop a general understanding of Groundwater Flow Systems. Previous studies on the hydrogeological characterization of groundwater sources in the Drâa basin was based on the “aquifer unit” notion;

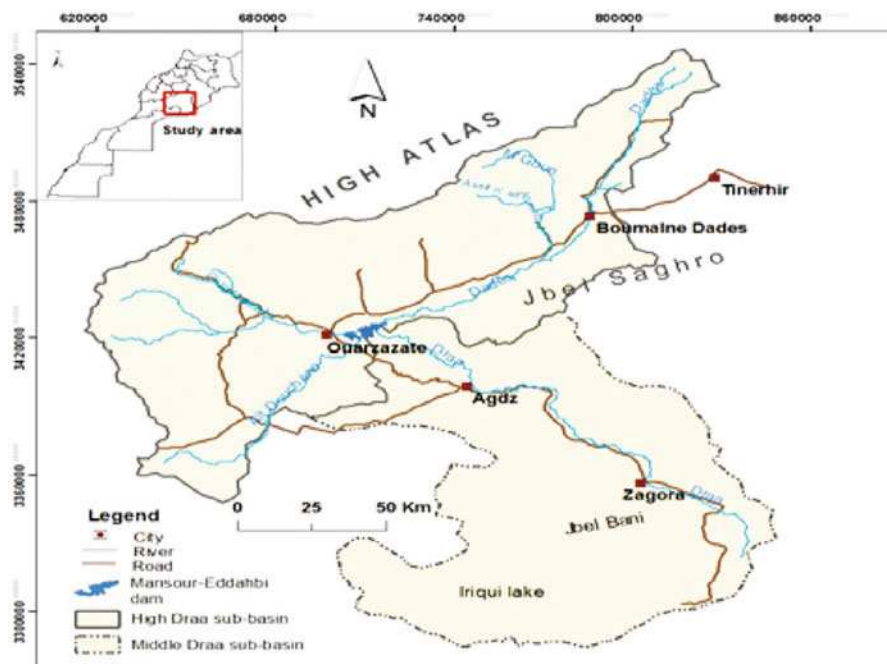


Fig. 37.1 Location of the study area

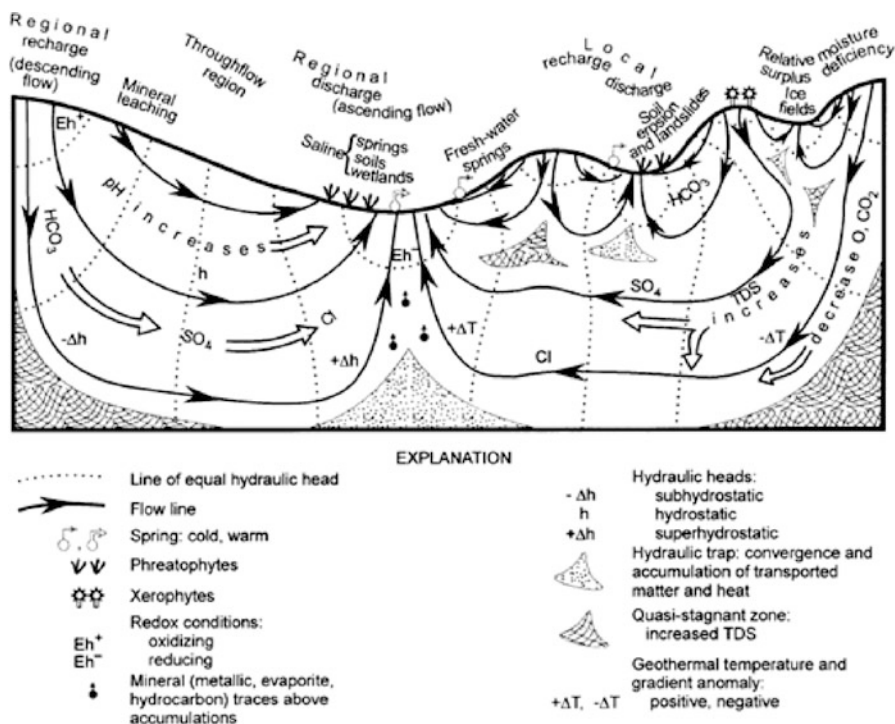


Fig. 37.2 Regional gravitational flow of groundwater [4]

which simplifies the relation among morphology, lithology and aquifer units. In the absence of information on the hydraulic conditions of the aquifer units; these studies do not give a comprehensive knowledge on the hydrodynamics of groundwater flow. This study shows the active role of groundwater as general geological agent; this was achieved by integrating Groundwater Flow Systems theory [2] (Fig. 37.2), which allowed a better understanding of groundwater functioning in Drâa basin, and provided a rational framework for studying groundwater behaviour in response to climate variability [1]. This wide system view approach integrates: i) hydrogeological properties of aquifer units and the depth to the basement rock, ii) water-rock interaction and hydrochemical evolution, iii) soil and vegetation cover characteristics, iv) isotopes and radiometric analyses.

37.2 MATERIAL AND METHODS

The conceptual hydrogeological model based on the gravity driven flow theory [2], [3], [4] was developed using Visual Modflow [5], which uses the finite differences method to solve groundwater flow equation. The regional boundary conditions of

the model were in agreement with the geological, hydrogeological and geochemical data. Several packages (*General-Head-boundary*, *River*, *Recharge*, *Evapotranspiration*, *wells*) were used to refine the model simulation output.

The domain consists of 17856 grid cells, distributed in 144 lines W-E, and 124 columns N-S. The geological boundary conditions (*geometry*) were presented by the topographic levels extracted from Digital Elevation Model (*DEM*) and the basement rock was presented by unfractured volcanic rocks of the Precambrian. Vertically the model consists of three layers, generating an anisotropic conditions; thus the top layer is presenting different (K_x , K_y) distribution which reflects the different geological formations of the study area. The second layer is presenting the fractured rhyolitic Precambrian with an estimated thickness of 300 m, it is characterized by a vertical hydraulic head (K_z) which is one magnitude greater than the horizontal (K_x , K_y); this condition is considering the importance of fractures and faults in inducing vertical flow. The third layer is presenting the basement rock and the deepest limit of the model. The hydraulic properties (K_v , K_x , K_y , S_s , S_y and *porosity*) were chosen according to [6], [7], and [8]. The regional aquifer system of Drâa basin can be considered as a multilayer aquifer system, where the preferential flow paths can be produced. The hydraulic characteristics of lithological units (alluvium, *shale*, *sandstone*, *basalt*, *limestone*, *volcanic rocks*), which are hydraulically connected, present unconfined, confined and semi-confined conditions [1]. The water-levels or initial heads are presenting an important input to simulate the hydrogeological processes influencing the groundwater flow. The model was developed to simulate the initial conditions previous to the period of Mansour-Eddahbi dam implementation. The initial heads (potentiometric surface) were estimated from water levels reported in wells and boreholes and from DEM values for springs and natural discharge zones suggested by vegetation and soil type. Boundary conditions were presented by other packages; the river module was used to simulate the exchange between the river and the groundwater system by comparing the head levels in the river to the riverbed cells threshold. The river module was requiring some control points (55 observation wells were selected) which allow a better calibration for the model. The discharge zones of groundwater were presented in the model by General Head Boundary (*GHB*), which is establishing a linear relation between groundwater's inflow and outflow. The *GHB* was applied to Iriki Lake, where saline soil (*Sierozem*) and vegetation (*Halophytes*) which are characteristic for discharge zones were mapped. The Recharge and Evapotranspiration (*ET*) packages were used to simulate the exchanged fluxes as a function of time within a stress period of 30 years. According to the conceptual model, the recharge is taken place in altitudes exceeding 2000 m a.s.l, with an estimated rate of 10 % of rainfall. In this model the altitudinal variation of precipitation was considered; thus, the recharge rate was contrasting from upstream to downstream (estimated rates were 80 mm/y for High Atlas, 10 mm/y for Anti-Atlas and 0 mm/y for the lower plain). For the Evapotranspiration module, the effective values were estimated to equal that of rainfall ($ETP = R$); the final accepted values were 200 mm/y for the domain where the hydraulic head is above the ET extinction depth, and 500 mm/y where discharge zones were manifested (*oases and Iriki lake*).

37.3 RESULTS AND DISCUSSION

The model calibration showed a good correlation between observed and model generated values, with an NRMSE of 1.8 % for 10 years of simulation, which presents reasonable initial results. The partial validation of the model was made through proxies, by comparing the obtained results to the field conditions (*springs, discharge to the rivers, regional discharge*). The validated model showed (Fig. 37.3) the coexistence of different flow systems (different velocities and directions), the hydraulic continuity manifested by flow distribution according to hydrological properties, and the importance of groundwater (33 % of *total storage*) discharge to rivers. Furthermore, the model showed the vertical flow response (*recharge and discharge conditions*) (Fig. 37.3); the recharge presented by downward flow occurs mainly in High Atlas mountains, where recharged water could attain 1500 m of depth. This flow is not limited to Drâa basin but travels towards adjacent basins (*Tafilalet, Haouz*) (Fig. 37.3) which indicates the hydrogeological continuity between aquifer systems. Although, the recharge in the Anti-Atlas Precambrian outcrop is less important; however, the recharged groundwater have a significant contribution to the changing of groundwater quality. The discharge zones are manifested by upwards flow towards valleys, rivers, and low altitudes plains (*Iriki lake*). To simulate the response of groundwater flow to climate variation, the original condition of groundwater heads calculated by the model were subjected to contrasting recharge scenarios (*recharge rate of 50 mm/y and 200 mm/y*). For 10 years of simulation, the results show (Fig. 37.4) a water-table recovery of more than 100 m during humid conditions (200 mm/y) in the limestone formation of the High Atlas mountains where local flow occurs. This pronounced temporal variation of the water-table (10 m/y) is due to the low values of primary porosity and hydraulic conductivity of the matrix, which are increasing the time of infiltration; consequently the water-levels in fractures and cavities can rise rapidly, while the matrix remains unsaturated [9].

In contrast, the equipotential lines do not show a significant change to recharge in the lower part of the basin (*Middle Drâa sub-basin*) (Fig. 37.4) where

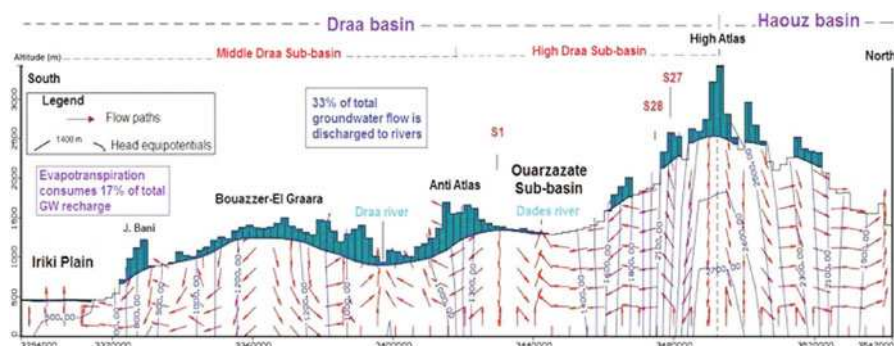


Fig. 37.3 Cross-section showing the hierarchy of groundwater flows and discharge zones in the calibrated and validated model [1]

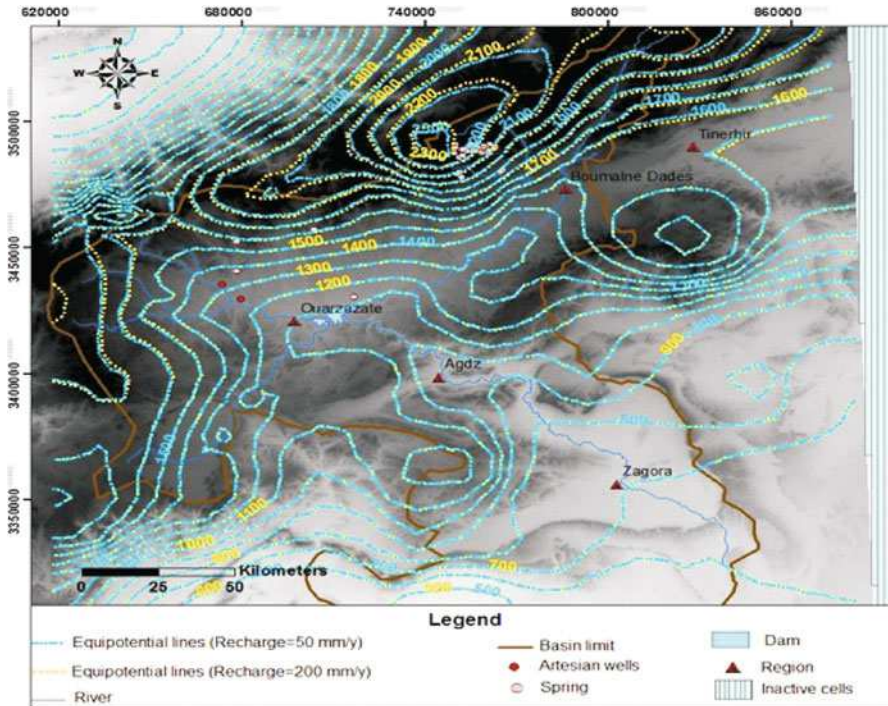


Fig. 37.4 The effect of recharge conditions on groundwater flow [1]

intermediate and regional flows were simulated by the model. This can be explained by the sensitivity of groundwater level to recharge in region dominated by local groundwater flow. Thus, a possible decrease in precipitation in the recharge zone will produce a lowering of the water table in the High Atlas in a short period, which may lead to the disappearance of several springs [1].

In addition, groundwater belonging to the intermediate or regional flows will require a long period of time (*hundreds to thousands of years*) to reveal the impact of actual climate conditions, which can be identified from isotopic signature of discharged groundwater [1]. Following characterization of the geology, hydrology and geochemistry of the groundwater flow systems and development of a conceptual description for groundwater flow in the system, numerical modelling is a logical follow-up that can augment understanding of the groundwater system. Numerical modelling may also be a source of the estimations and assessments needed to best characterize the groundwater system [10]. The running of the conceptual model of Groundwater Flow Systems Theory using Modflow had reproduced results which partially overlap with the multidisciplinary analyses and the actual conditions. The model has been partially validated by the identification of the relationship between the generated values and the existing data. This regional approach has allowed to characterize the discharge and recharge zones (*vertical*

flows), to identify the hierarchy of flow systems in Drâa basin (local, intermediate and regional flows), and to determine the groundwater flow systems response to various climate conditions. This understanding could assist in defining appropriate strategies to manage local flows against drought conditions, and to take advantage of intermediate and regional flows which are not directly affected by current climate conditions, but are facing other issues related to their chemical quality and original recharge zone position [1].

REFERENCES

1. Ouyse, S.: Simulation of surface water and groundwater flows in the High and Middle Drâa sub-basins. Dissertation, Cadi Ayyad University, Marrakech, Morocco (2012)
2. Tóth, J.: Theoretical analysis of groundwater in small drainage basins. *Journal of Geophysical Research*, 68, 4791–4812 (1963)
3. Tóth, J.: Las aguas subterráneas como agente geológico: causas, procesos y manifestaciones. *Boletín Geológico y Minero de España*, 111(4), 9–26 (2000)
4. Tóth, J.: From the artesian paradigm to basin hydraulics. Eötvös Loránd University. Institute of Geography and Earth Sciences. Hungary (2008)
5. McDonald, M.G. and Harbaugh, A.W.: A Modular Three-Dimensional Finite-Difference Ground-Water Flow Model. U.S. Geological Survey, Techniques of Water-Resources Investigations, Book 6, Chapter A1, TWRI 6-A1 (1996)
6. Freeze, R.A. and Cherry, J.A.: Groundwater. Prentice-Hall, Inc. Englewood Cliffs, NJ, USA (1979)
7. McWorter, D.B. and Sunada, D.K.: Groundwater Hydrology and hydraulics. Water Resources Publications, Ft. Collins, CO. (1977)
8. Morris, D.A. and Johnson A.I.: Summary of hydrologic and physical properties of rock and soil materials as analyzed by the Hydrologic Laboratory of the U.S. Geological Survey. U.S. Geological Survey Water-Supply Paper 1839-D (1967)
9. Cook, P.G.: A guide to regional groundwater flow in fractured rock aquifers. Bibliography. ISBN 1 74008 233 (2003)
10. IAEA: Isotope methods for dating old groundwater. International Atomic Energy Agency, Vienna. ISBN 978–92–0–137210–9 (2013)

Chapter 38

Assessment of Groundwater Recharge due to Monsoon in Ozar Watershed of Maharashtra State Using Isotopic Technique

S.K. Verma, S.P. Rai, M.S. Rao, and C.P. Kumar

Abstract The over exploitation of groundwater in India is increasing day by day due to ever increasing population and industrialization, resulting in progressive lowering of static water level and reduction of well yields. The estimation of recharge to groundwater is crucial to better water resources management particularly in arid and semi-arid regions. The tritium tagging technique has been widely used for the estimation of groundwater recharge in different regions of India. This technique provides fairly accurate estimate of vertical downward flow component of soil moisture through unsaturated zone. In the present paper, the groundwater recharge due to monsoon rains in Ozar watershed located in Nashik district (Maharashtra) in Godavari basin has been assessed using tritium tagging technique. The experiments have been carried out in cultivated agricultural fields. Artificial radioisotope (Tritium) was injected at four cultivated sites before the onset of monsoon and soil samples were collected from the injection points soon after the withdrawal of monsoon. In the study area, mainly three types of soils were found, namely clay, loam and sand in which sand predominants. The percentage of groundwater recharge varies from 9.77 % to 23.19 % in the study area depending on the type of soil and other geo-hydrological conditions of the study area.

Keywords Groundwater recharge • Irrigation • Tritium tagging • Particle size

38.1 INTRODUCTION

The recharge to groundwater from surface to the subsequent layers of soil is governed by the process of infiltration which is one of the most important parameters to study the movement of water through unsaturated soil. The infiltration may be defined as the process of the water penetrating from ground surface into soil

S.K. Verma (✉) • S.P. Rai • M.S. Rao • C.P. Kumar
National Institute of Hydrology, Roorkee, Uttarakhand, India
e-mail: skverma@nih.ernet.in

mass. Estimation of groundwater recharge is essential for evaluation of groundwater resources. In most of the cases, major source of recharge to groundwater is due to precipitation. However, in the irrigated areas the irrigation return flow also contributes to groundwater recharge significantly. In addition to the precipitation and irrigation inputs, which contribute to the direct or vertical recharge to groundwater, there is a lateral component of recharge through the sub-surface horizontal flow due to natural hydraulic gradient. The isotope techniques can be employed to estimate the vertical component of recharge. The vertical component of recharge to groundwater can be estimated using naturally injected environmental isotopes like oxygen-18, deuterium and tritium including artificial tritium which is required to be injected at the selected sites. In the present study, the artificial tritium has been used to estimate the vertical component of groundwater recharge due to monsoon and irrigation using tritium tagging technique [1–4].

38.2 STUDY AREA

The study area comprises of the parts of Niphad taluka of Nasik district, Maharashtra. It is located in the watershed GV 7 (designated and numbered by GSDA) of Godavari basin. The area of Ozar village under the study is 15.25 sq. km. The Ozar area is lying between the latitude $20^{\circ} 04'$ to $20^{\circ} 05'$ N and longitude $76^{\circ} 54'$ to $76^{\circ} 56'$ E. The locations of the test sites are shown in Fig. 38.1. The area is approachable and connected by road and lies on Mumbai-Agra Highway at a distance of 20 km from Nasik.

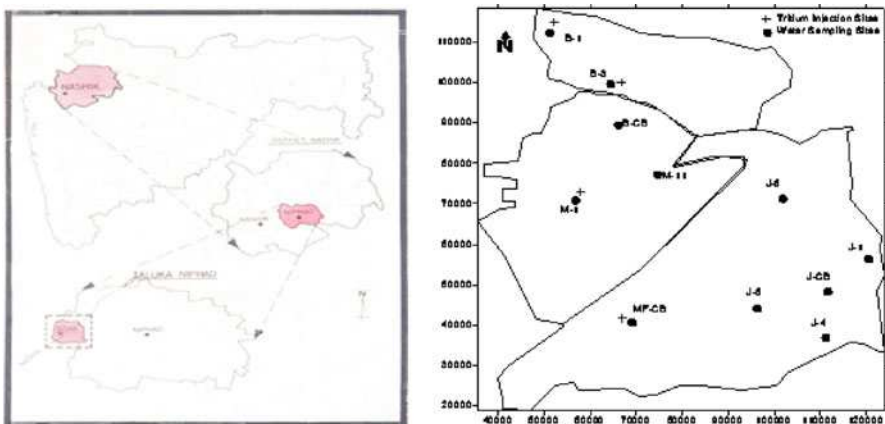


Fig. 38.1 Study area of region Ozar, Nasik

38.3 MATERIAL AND METHODS

38.3.1 Field Experimentation

Four sites were selected in the study area considering only the type of surface soil and accessibility of the area which are listed in Table 38.1. Two sets of tritium injection were made at each site during April 2000 well before the onset of monsoon. Each set of injection consisted of one central injection on the line and four injections in a circle of radius 10 cm around it. The drive rods (10 mm diameter) were first hammered into the soil, for making 70 cm deep holes. The drive rods were then pulled out and stainless steel pipe (injection pipe) was inserted into each hole. About 2 ml of tritium of specific activity of 40 $\mu\text{Ci/cc}$ was injected in each hole with the help of plastic syringe through the injection pipe care being taken that there was minimum disturbance to the natural condition of the soil due to the injection. Each hole was completely filled up with the soil after carrying out tritium injection in the same. The fields were left for normal use by the farmers for application of irrigation and/or precipitation.

The soil sampling was carried out at the time of tritium injection during the month of April 2000 before the onset of monsoon and during the month of November 2000 after the monsoon season. Soil samples were collected layer by layer (10 cm sections) with the help of a hand auger of 2" diameter starting from ground surface to about 200 cm and packed in properly sealed polyethylene bags. The moisture content of the soil samples on wet weight basis was estimated by gravimetric method in the laboratory. Volumetric moisture content for each soil sample was estimated by multiplying the moisture content obtained by the gravimetric method on wet weight basis and bulk density of the soil.

38.3.2 Laboratory Experimentation

The particle size distribution for the soil samples was carried out by sieve analysis and hydrometer analysis. Soil samples were washed with distilled water to remove the soluble salts. The washed samples were separated into two fractions i.e. +75 micron and -75 micron through wet sieving. Sieve analysis was performed for the fraction of soil retained on 75 micron sieve (+75 micron). The portion passed

Table 38.1 Particle size distribution for the experimental sites

S. No.	Name of Site	Gravel (%)	Sand (%)	Silt + Clay (%)
		(>2.0 mm)	(2 mm–0.075 mm)	(<0.075 mm)
1.	Chaurewasti	5.5	92.8	1.77
2.	Ganeshnagar	1.0	97.0	1.9
3.	Sonewadi	9.0	90.4	0.5
4.	Mahadevmuth	16.4	81.7	1.8

through the 75 micron sieve (-75 micron) was analysed by hydrometer. The particle size distribution for each experimental site is given in Table 38.1.

After determination of soil moisture content for the soil samples collected from each 10 cm depth by gravimetric method, each sample was subjected to distillation under low pressure. Water from the each soil sample was extracted and stored in the plastic/glass vials for further counting of the tritium activity in the distilled soil water. The tritium count rate (counts per minute or CPM) for each sample was obtained by the liquid scintillation counter. These count rates for all the samples were corrected for background counts in order to get net tritium counts per minute. The net tritium count rate (net counts per minute or net CPM) for various sites were plotted as a histogram against the individual depth intervals which shows position of the original and shifted peaks of injected tritium. After getting the shifted tritium peak, the centre of gravity of the peak was determined and the shift of the peak from original depth of injection of 70 cm was calculated for each site. The percentage of groundwater recharge for each site has been determined using equation (38.1) and is shown in Table 38.2.

$$R = \theta_v d(100/p) \quad (38.1)$$

where R is the percentage of ground water recharge, θ_v is the average volumetric moisture content in the tritium peak shift region, d is the shift of tritium peak in cm, and p is rainfall and/or irrigation in cm.

The recharge to groundwater for various sites were determined by multiplying the peak shift of tritium as calculated above and average volumetric moisture content in the peak shift region and are given in Table 38.2. The percentage of groundwater recharge at each site due to monsoon rain for the year 2000 and irrigation is given in Table 38.2.

38.4 RESULTS AND DISCUSSION

The values of recharge to groundwater estimated due to rainfall in monsoon season and irrigation during the year 2000 at each experimental site namely, Chaurewasti, Ganeshnagar, Sonewadi, Mahadevmuth, using tritium tagging technique (Radio-

Table 38.2 Peak shift, av. vol. moisture content, recharge (cm), rainfall (cm), irrigation (cm) and recharge (%)

Sr. N.	Name of Site	Peak shift (d) (cm)	Av. Vol. Moist. Content (θ_v)	Recharge (cm)	Rainfall (p) (cm)	Irrigation (p) (cm)	Recharge (R) (%)
1.	Chaurewasti	85.50	0.175	14.96	44.5	20.00	23.19
2.	Ganeshnagar	74.78	0.12	8.97	44.5	20.00	20.15
3.	Sonewadi	21.54	0.202	4.35	44.5	0.00	9.77
4.	Mahadevmuth	100.00	0.189	18.9	44.5	40.00	22.36

tracer method) are given in Table 38.2 along with other details. All the sites were located in cultivated land. The details of particle size analysis of soil samples collected from each site are shown in Table 38.1.

- 1) In general the percentage of recharge to groundwater is high in Ozar watershed i.e. Chaurewasti (23.19 %), Ganesh Nagar (20.15 %) and Mahadevmuth (22.36 %) hence these sites are suitable for artificial recharge.
- 2) It appears that the recharge to groundwater at few sites is higher due to the contribution of irrigation return flow. The data show that the recharge due to rainfall is only 9.77 % at Sonewadi site.
- 3) The particle size analysis indicates very high percentage of sand (~90 %). It reflects that the watershed is suitable for taking up artificial recharge activities. The groundwater recharge values obtained by Tritium Tagging Techniques only reflect the present recharge conditions in the light of limited availability of rainwater or surface water to recharge. If more water will be allowed to retain on the surface, the groundwater recharge percentage will certainly be higher.
- 4) The water level fluctuation corroborates the groundwater recharge values obtained in Ozar watershed.

38.5 CONCLUSIONS

The assessment of groundwater recharge due to rainfall and irrigation has been carried out at 4 sites in Ozar watershed situated in Niphad taluka of Nashik district, Maharashtra using Tritium tagging technique. The percentage of groundwater recharge at various sites, namely, Chaurewasti, Ganeshnagar, Sonewadi and Mahadevmuth due to monsoon rains and irrigation are given in Table 38.2 along with other details.

REFERENCES

1. Mookerjee, P.: New concept of profile moisture and depth of injection in tritium tagging technique for evaluation of groundwater recharge as a component of the water balance equation. *Bull. of Radiation Protection*, 13(1), 147–150 (1990)
2. Munnich, K.O.: Moisture movement measured by isotope tagging. *In: Guide book on nuclear techniques in hydrology*. IAEA, Vienna, 112–117 (1968a)
3. Munnich, K.O.: Use of nuclear techniques for the determination of groundwater recharge rates. *In: Guide book on nuclear techniques in hydrology*. IAEA, Vienna, 191–197 (1968b)
4. Zimmerman, U., Munnich, K.O. and Roether, W.: Downward movement of soil moisture traced by means of hydrogen isotopes. American Geophysical Union, Geophysical monograph no. 11, 28 (1967b)

Chapter 39

Application of Statistical Techniques to Identify the Hydrogeochemical Processes in Coastal Aquifers of Pondicherry Region, Tamil Nadu

R. Thilagavathi, S. Chidambaram, C. Thivya, S. Pethaperumal, K. Tirumalesh, and M.V. Prasanna

Abstract Groundwater pollution can be illustrated as degrading of water quality for any usage. The Eleven hydrochemical parameters of groundwater samples from different formation were used in this study to understand groundwater chemistry in this complex multilayer aquifer system. The statistical analysis of the results shows that dominant process of weathering of feldspar, pyroxene and ion exchange. The water flows along the formation dissolving these ions along its flow path through the process of leaching of the secondary salts inherited in the formation obtained by the mixing of several geochemical processes. The anthropogenic impacts in the groundwater are noted in the younger formation than that of Cretaceous and Lower Cuddalore.

Keywords Groundwater • Layered Aquifers • Hydrochemistry • Weathering

39.1 INTRODUCTION

Statistical approaches are very useful in the identification of relationships between variables. A correlation matrix is established based on method of covariance using Pearson's correlation coefficient between ion pairs. Factor analysis gives the

R. Thilagavathi (✉) • S. Chidambaram • C. Thivya
Department of Earth Sciences, Annamalai University, Annamalai Nagar, India
e-mail: thilagavathir1987@gmail.com

S. Pethaperumal
State Groundwater Unit and Soil Conservation, Department of Agriculture, Pondicherry, India

K. Tirumalesh
SOE, Isotope Hydrology Section, Isotope Application Division, BARC, Mumbai, India

M.V. Prasanna
School of Engineering and Science, Department of Applied Geology,
Curtin University of Technology, Sarawak, Malaysia

general relationship between measured chemical variables by elucidating and classifying the original data. Factor analysis can also be used to determine the geographical distribution of the resulting factors. Multivariate statistical methods have been applied to characterize and evaluate surface and groundwater [1–3].

39.2 STUDY AREA

Pondicherry region encompasses 293 km² areas with seven communes consisting of a total 179 villages [4]. The geographical coordinates of the study area are 11° 45' and 12° 02'N latitudes 79° 37' and 79° 53' E longitudes (Fig 39.1). The study area is intersected by the deltaic channel of River Gingee and Pennaiyar. In general this region is a flat peneplain with an average elevation of about 15 m above msl (mean sea level) [5]. Three major physiographic units are generally observed viz., i) Coastal plain, ii) Alluvial plain and iii) Uplands [5]. The area is covered with Quaternary, Tertiary and Cretaceous sediments with Archaeans as the basement rocks [5].

39.3 METHODOLOGY

Based on [5] and studies carried out by different researchers, the observation wells were selected for sampling groundwater from the specific formation. 81 groundwater samples for two different seasons of PRM and POM in order to cover different formation in the study area, it includes the samples from Alluvial (30), Upper Cuddalore sandstone (13), Lower Cuddalore sandstone (13) and Cretaceous (24) aquifers (Fig. 39.1). The major cations and anions were analysed using standard procedures [6]. Multivariate methods were applied to the original chemical data set of different formations using SPSS software (version 17). The hydrochemical variables incorporated in multivariate analysis are; Ca, Mg, Na, K, Cl, HCO₃, NO₃, F, PO₄, SO₄ and DOC.

39.4 RESULTS AND DISCUSSION

The maximum, minimum and average concentration for various ions for irrespective of formation was represented in the (Table). 004Ea, Ca and Cl, HCO₃ is the dominate cation and anion during PRM and POM (Table 39.1).

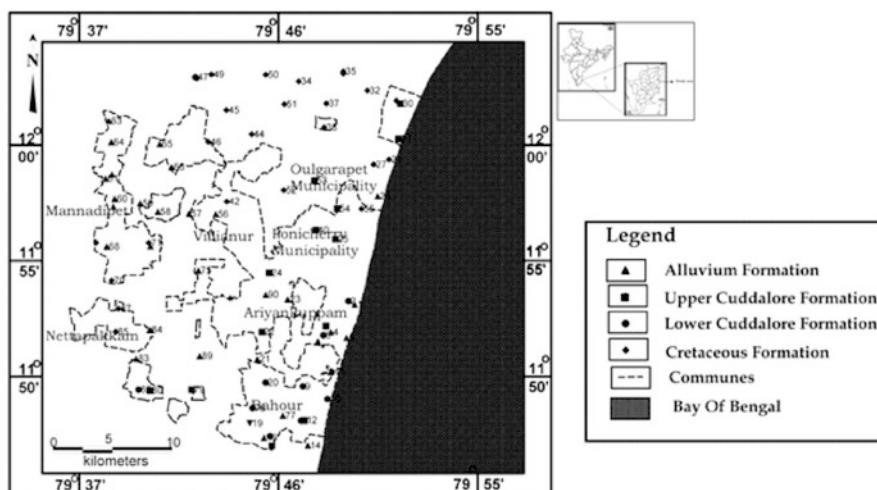


Fig. 39.1 Location map of the study area

39.4.1 Correlation among Hydrochemical Species

In alluvial aquifer during PRM and POM significant correlation of HCO_3 with Ca and Na indicates chemical weathering [7]. No strong negative correlations were established among ions. In the Upper Cuddalore aquifers, during PRM significant correlation between Ca, Mg, Na, DOC, EC and TDS is also noticed. In POM Good to excellent correlation exist between Ca, EC and TDS. Na and HCO_3 indicate the active chemical weathering process along with leaching of secondary salt. DOC, PO_4 has good correlation with Ca which may be due to the fertilizer activities. During PRM in Lower Cuddalore aquifers, good to excellent correlation exists for most of the parameter except DOC, TC, F. Significant correlation exhibits between Ca, Mg, Cl, HCO_3 , SO_4 , NO_3 and H_4SiO_4 . Oxidation of organic carbon in the aerobic environment results in the increase of HCO_3 concentration. During PRM, PO_4 and H_4SiO_4 are highly correlated with the agriculture activities [7]. Strong positive correlation between Na^+ and Cl^- ions, strengthens the assumption that dissolution of evaporates/contribution of saline sources govern the chemistry of groundwater, which is also noticed in the case of Upper Cuddalore aquifer. In Cretaceous formation, significant correlation is noticed between HCO_3 , SO_4 , Cl EC and TDS irrespective seasons.

39.4.2 Factor Analysis

The FA results for the groundwater samples in alluvial aquifer are shown in Fig 39.2 and 3 four factors with Eigen values ≥ 1 emerged accounting for total

Table 39.1 Maximum, minimum and average of the chemical constituents analysed in groundwater representing PRM and POM seasons (All values in mg l^{-1} except EC in μscm^{-1} and pH)

Formation			EC	TDS	pH	Temp °C	Ca	Mg	Na	K	Cl	HCO ₃	PO ₄	H ₄ SO ₄	NO ₃	F	SiO ₄	TC	DOC
Alluvium	PRM	Max	2596	1661	7.8	34.4	104	62.4	517.2	47.2	798	475.8	2	28.4	21.8	0.6	202	144.9	17
		Min	314	201.6	6.6	28.3	12	7.2	20	0.1	35.5	73.2	0	0	0	0.1	2	23.4	0
		Avg	1243.9	886.4	7.3	31.4	52.5	26.1	195.6	7.8	374	246.5	0.1	10	7.5	0.3	68.5	61.5	3.1
	POM	Max	2352	1269	8.2	32.7	147	91.2	314	70	833	732	2.7	180	41.6	3.4	106	189.3	10
		Min	300	188	6.8	28.4	28	7.2	48	3	88.6	61	0.1	1	0	0	10	15.5	0.5
		Avg	1261.3	726	7.5	31.1	76.5	38.2	133.8	29.6	287	365.5	0.4	80.5	10.2	0.4	70.3	88	2.7
	PRM	Max	2713	1735	7.8	33.2	88	33.6	567.5	18.1	745	402.6	0.2	11.6	21.8	0.6	115	73.8	13.3
		Min	221.7	174	6.6	28.4	28	0	7.1	0	53.2	73.2	0	0	0.1	0.1	3	15.8	0.8
		Avg	750.4	498.8	7.2	31.3	52.3	14.2	99.7	5.1	176	181.9	0	3.9	9.5	0.3	36.8	44.7	3.9
Upper Cuddalore	POM	Max	1367	774	8.1	32.8	92	41	193	42	532	390.4	0.3	160	26.4	1.4	97	97.8	5.4
		Min	168.4	106.9	6.3	30	27	1.6	20	1	70.9	61	0.1	1	0	0.1	17	17.1	0.4
		Avg	699.2	425.1	7.3	31.3	59.2	24.4	100.8	14.6	200	241.2	0.1	58	9.1	0.6	70.9	57	2.6
	PRM	Max	1432	946	7.7	33.7	112	48	146	8.1	390	268.4	0	4.4	21.5	0.4	148	55.1	13.6
		Min	270	179	6.2	30.5	16	7.2	12	0	26	85.4	0	0	0	0.2	2	21.6	0.9
		Avg	527.2	368.7	7.1	32.1	37.3	26.9	51.7	1.6	114	166.3	0	1	5.6	0.3	34.4	39.2	2.8
	POM	Max	1534	878	8	36.2	112	88.8	175	22	355	390.4	0.1	112.5	15.6	1	88	97.8	6.3
		Min	219.7	130.5	6.9	30.5	20	2.4	46	4	70.9	146.4	0.1	2	0	0	17	28.5	0.6
		Avg	582.2	352.7	7.4	31.9	50	21.1	81.7	9.1	136	255.3	0.1	30.2	2.5	0.5	40.5	59.6	3.1
Lower Cuddalore	PRM	Max	2164	1976	7.8	34.3	172	45	550.5	16.9	904	366	0.3	44	21.9	0.8	182	95.2	4.1
		Min	186.5	184	6.2	28.1	20	2.4	6.8	0.1	53.2	73.2	0	0.4	0	0.1	10	13	0.8
		Avg	905.1	630.3	7.4	31.4	70.2	22	98.5	3.6	198	243.4	0	7.6	11.2	0.3	79.8	52.6	2.1
	POM	Max	2241	1248	8.3	32.9	168	60	764	45	1524	878.4	0.4	250	57.6	1.9	106	161.7	6.5
		Min	202.4	129	6.4	27.4	24	0	33	4	35.5	109.8	0.1	5	0.2	0	25	13.9	0.3
		Avg	1055.9	651.5	7.5	30.8	83.5	36.3	131.6	16.2	236	413.3	0.1	75.9	10.6	0.6	76.1	98.3	2.7
Cretaceous	PRM	Max	2164	1976	7.8	34.3	172	45	550.5	16.9	904	366	0.3	44	21.9	0.8	182	95.2	4.1
		Min	186.5	184	6.2	28.1	20	2.4	6.8	0.1	53.2	73.2	0	0.4	0	0.1	10	13	0.8
		Avg	905.1	630.3	7.4	31.4	70.2	22	98.5	3.6	198	243.4	0	7.6	11.2	0.3	79.8	52.6	2.1
	POM	Max	2241	1248	8.3	32.9	168	60	764	45	1524	878.4	0.4	250	57.6	1.9	106	161.7	6.5
		Min	202.4	129	6.4	27.4	24	0	33	4	35.5	109.8	0.1	5	0.2	0	25	13.9	0.3
		Avg	1055.9	651.5	7.5	30.8	83.5	36.3	131.6	16.2	236	413.3	0.1	75.9	10.6	0.6	76.1	98.3	2.7

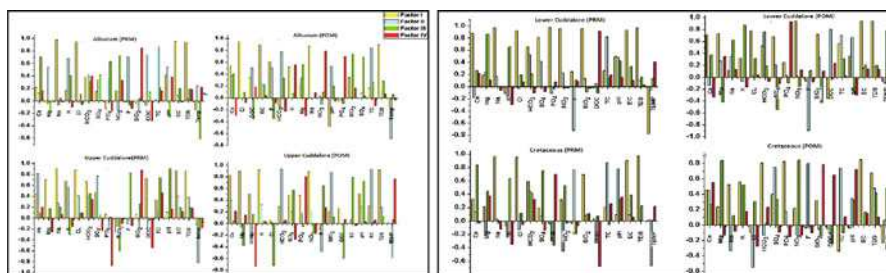


Fig. 39.2 Factor analysis for the groundwater samples

variances of PRM and POM of 86.30 % and 69.56 %. Upper Cuddalore formation also has the four factor loadings with Eigen values ≥ 1 accounting for total data variances (TDV) of 86.30 % and 83.43 %. Lower Cuddalore has the four factor component with Eigen values ≥ 1 representing the total variances during of 84.2 % and 82.95 %. Cretaceous has the three factors representing the total variances of 72.96 % and 69.97 % respectively for PRM and POM.

39.4.3 Factor I

In Alluvium Factor 1 explains about 33.88 % and 28.76 % of total data variance (TDV) for PRM and POM shows the saline source of the study area and ion exchange processes. Higher scores of Alluvium are located in the South east and South Western part of study area. In Upper Cuddalore Factor 1 is of 19.90 % and 31.29 % TDV and its mainly represented by of Ca, Na, Cl, SO_4 indicating leaching of secondary salts [8]. In Upper Cuddalore formation Factor 1 representation are noted along the coast line of the study area. In Lower Cuddalore Factor 1 is (PRM is 54.32 % and POM is 37.16 % of TDV) indicate leaching of secondary salts [7]. Factor 1 of Cretaceous during PRM and POM is 28.27 % and 22.60 % TDV and it shows mainly loading of Ca, Na, Cl, K, SO_4 , HCO_3 and DOC (Fig 39.2). Na and Cl association is generally due to the sea water intrusion; SO_4 and DOC is due to the anthropogenic process. High contribution of Cl and Ca in this factor indicates that the excessive interaction of water with the aquifer formation. The representation of several ions in this factor also indicates the mixing of different geochemical processes. Few of the Cretaceous samples are represented in North –western region and some representation on the North –Eastern part.

39.4.4 *Factor II*

Alluvium Factor 2 has TDV of (PRM) 19.90 % and (POM) 17.6 % with the high loading of Mg, PO_4 and DOC. Enrichment of organic carbon in subsurface and deeper layers suggests the deposition under calm conditions prevailed during slow accumulation in finer sediments and it is more associated in clay sized fraction. Most of the positive representation of Factor II in Alluvial samples represent on the North western region of the study area and few of the representations and noted in the south eastern region, which are due the agriculture activities. Factor II of Upper Cuddalore shows that the PRM (17.81 %) and POM (22.31 %) are represented with loading of K, pH, TC, HCO_3 and SO_4 mainly due to the process of weathering. Upper Cuddalore samples are represented along the North –Eastern region and southern part of the study area. In Lower Cuddalore of Factor II represents the 12.42 % and 20.13 % of TDV are mainly represented by the loading of HCO_3 , pH and DOC. Representation by HCO_3 indicates the weathering of carbonate as well as the anaerobic dissolution for followed by oxidation. During PRM Lower Cuddalore samples are represented along the South eastern region and in POM representations of samples are along the river course. Factor II of Cretaceous represents the 18.47 % and 18.16 % of total variances and mainly loading of EC, TDS, SiO_2 , NO_3 , TC, F and pH which is due to the ion exchange. Cretaceous samples are falls in North–Eastern region in both the seasons. The second factor is predominantly due the agriculture sources or due to the process of weathering.

39.4.5 *Factor III*

Factor III of Alluvium during PRM (17.81 % TDV) and POM (12.7 % TDV) (Fig. 39.1) are represented by PO_4 , NO_3 , Mg, SO_4 and SiO_2 . Most of the samples of alluvial formation are represented in the Factor III along the north western part of the study area and some of the samples represent in southern part. In Upper Cuddalore Factor III explains of PRM (17.81 % TDV) and POM (17.90 % TDV) shows the higher positive loading of the K, SO_4 , NO_3 , SiO_2 , pH, Mg and HCO_3 representing the incongruent dissolution. Upper Cuddalore samples are represented on the South–Eastern part of the study area. In Lower Cuddalore. Factor III explains of 10.0 % and 17.59 % of total variances during PRM and POM show the higher positive loading of Na, K due to dominance of agriculture activities. These Lower Cuddalore samples are represented on the southern region of the study area. During PRM and POM NO_3 and PO_4 have very high positive loading of factor III during PRM (explaining about 16.71 % of variance) and Na, Cl and EC is highly positively loading of the during POM (explaining about 15.29 % of variance). Cretaceous samples spread North western and Northern part.

39.4.6 Factor IV

In Alluvium aquifers Factor IV PRM (14.70 % TDV) and POM (10.42 % TDV) is represented by SiO_2 , PO_4 and NO_3 . In Upper Cuddalore Factor IV of the PRM and POM is 14.70 % TDV and 11.91 % TDV. Higher loading of the SiO_2 and Mg are characterized by more reducing condition and also due to the anthropogenic sources like agricultural activities. Factor IV of Lower Cuddalore with the total variances of the 7.37 % and 8.06 % represented by DOC and PO_4 . Factor IV of Cretaceous is mainly dominated by PO_4 during PRM with 9.48 % TDV and 13.65 % during POM. The alluvial samples are located on the central part of the study area. Upper Cuddalore samples are spread over the southern region along the river Ponnaiyar. The factor IV of Cretaceous and Alluvium are represented in the topographic high or in the elevated region of the study area.

39.5 CONCLUSIONS

The application of statistical analysis on data set represents the signature of the factor I; in alluvium is due to saltwater intrusion and interaction with the geological matrix resulting in the groundwater salinity. The higher factor loadings in Upper Cuddalore, Lower Cuddalore and Cretaceous are related with the leaching of salts and anthropogenic activities. These dominant factors of hydrogeochemical processes are represented on the south and south eastern part of the study area in all the aquifers which is mainly resulted due to groundwater flow according to the topographic.

REFERENCES

1. Bengraïne, K. and Marhaba, T.F.: Using principal component analysis to monitor spatial and temporal changes in water quality. *J. Hazard. Mater.*, 100(1–3), 179–195 (2003)
2. Love, D., Hallbauer, D., Amos, A. and Hranova, R.: Factor analysis as a tool in groundwater quality management: Two southern African case studies. *Phys. Chem. Earth*, 29(15–18), 1135–1143 (2004)
3. Razmkhah, H., Abrishamchi, A. and Torkian, A.: Evaluation of spatial and temporal variation in water quality by pattern recognition techniques: A case study on Jajrood River (Tehran, Iran). *Journal of Environmental Management*, 91, 852–860 (2010)
4. Govindaradjane, S., Reddy, S.S., Sivasankaran, M.A. and Ramakrishna, B.: The Study on Arsenic concentration in groundwater of Pondicherry region. *Pollution Research*, 26, 99–102 (2007)
5. Centre for Groundwater Board (CGWB): Groundwater Resources and Development Prospects in Pondicherry Region, Union Territory of Pondicherry, 63 (1993)
6. APHA: Standard methods for the examination of water and waste water, 19th edition, APHA. Washington DC, USA (1995)

7. Chidambaram, S., Ramanathan, AL., Prasanna, M.V., Loganathan, D., Badrinarayanan, T.S., Srinivasamoorthy, K. and Anandhan, P.: Study on the impact of tsunami on shallow ground-water from Portnova to Pumpuhar, using geoelectrical technique – south east coast of India. *Indian Journal of Marine Sciences*, 37(2), 121–131 (2008)
8. Prasanna, M.V., Chidambaram, S., Pethaperumal, S., Srinivasamoorthy, K., John Peter, A., Anandhan, P. and Vasanthavigar, M.: Integrated geophysical and chemical study in the lower subbasin of Gadilam River, Tamilnadu, India. *Environmental Geosciences*, 15(4), 145–152 (2008)

Chapter 40

Isotope Hydrogeological Factors Control Transport of Radon-222 in Hard Rock Fractured Aquifer of Bangalore, Karnataka

Md. Arzoo Ansari, Archana Deodhar, U. Saravana Kumar, Deljo Davis, and R.K. Somashekar

Abstract Radon-222 is a daughter element of radium-226 and are member of the uranium decay series. Radon-222 concentrations in groundwater of Bangalore city in different geological units were measured in 42 tube wells. The study area is underlain by Granite, Migmatite, Granodiorite and Gneiss rock and many dolerite dykes. The radon-222 concentration in groundwater is widely varying and ranging from 14 to 1000 Bq/L with an average value of 172.4 Bq/L. Significant differences in the radon-222 concentrations in groundwater among geological units were observed. The radon-222 distribution in groundwater is related to the presence of uranium in aquifer materials of the various rock types. Uranium concentration in groundwater is ranging from 0.2 to 523 $\mu\text{g/L}$. Transport of radon-222 through bedrock by water depends mainly on the percolation of water through the pore and along fractured planes of the rocks. Rn-222 cannot travel farther than several hundred meters away from their origin because of its short half-life of 3.8 days. It may travel the farthest within fractured or fissured geological formation where groundwater movement is fastest. The study shows that radon concentration in groundwater is controlled by geohydrological and hydrochemical characteristics of the study area.

Keywords Radon • Uranium • Groundwater • Hydrogeology • Bangalore

Md. A. Ansari (✉) • A. Deodhar • U.S. Kumar
Isotope Hydrology and Radiotracer Section, Isotope Applications and Radiopharmaceuticals
Division, Bhabha Atomic Research Centre, Trombay, Mumbai, India
e-mail: arzoo@barc.gov.in

D. Davis • R.K. Somashekar
Department of Environmental Science, Bangalore University, Bangalore, India

40.1 INTRODUCTION

Radon (^{222}Rn) is colorless, tasteless and odorless radioactive noble gas, formed by the decay of radium-226 in uranium (^{238}U) decay chain. The average concentration of uranium in the earth’s crust is about 4 mg/kg. The uranium decays into numerous other radioactive isotopes including ^{222}Rn . In hard rock aquifer, radon is ejected from the solid and into the adjacent pore space, mineral grain, or groundwater [1]. Because of short half-life (3.8 days) and the relatively slow flow of groundwater in most settings, radon is unlikely to be transported great distance in aquifers. Therefore when high levels of radon are found in groundwater, its source (uranium) is likely to be present in the surrounding rock or sediment. In addition to the uranium content of the underlying rock, radon concentration in groundwater is also a function of the physical properties of the rock and sediment comprising the aquifer. Several factors including uranium mineralization, fracture aperture, sediment porosity, and degree of metamorphism have been found to influence radon concentration in groundwater [2, 3].

The objective of the present study is to evaluate the distribution of radon in hard rock fractured aquifer in Bangalore (Fig. 40.1). Radon concentrations are known to be high in the granitic rock of this area and this study attempts to enhance our understanding of the distribution of radon in the highly fractured and non fractured granitic aquifers.

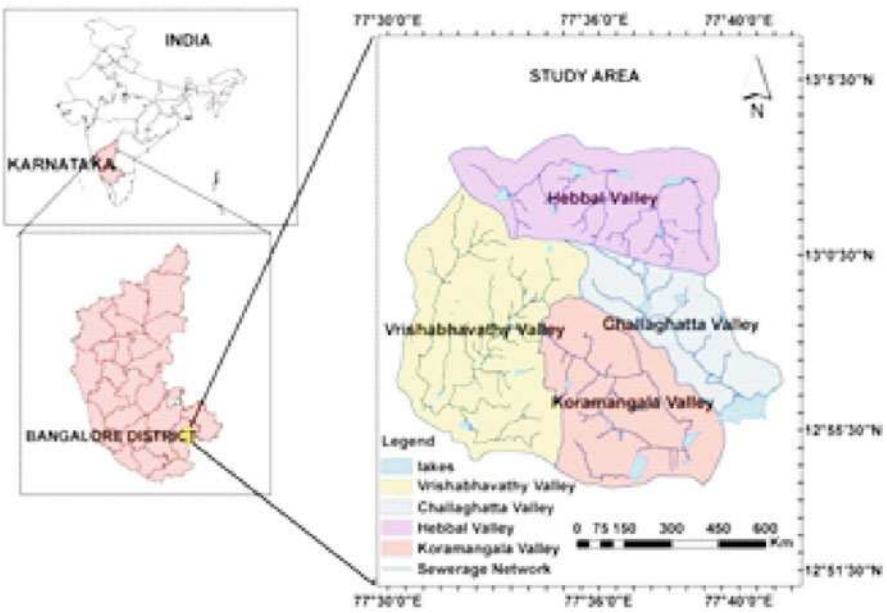


Fig. 40.1 Location map of the study area

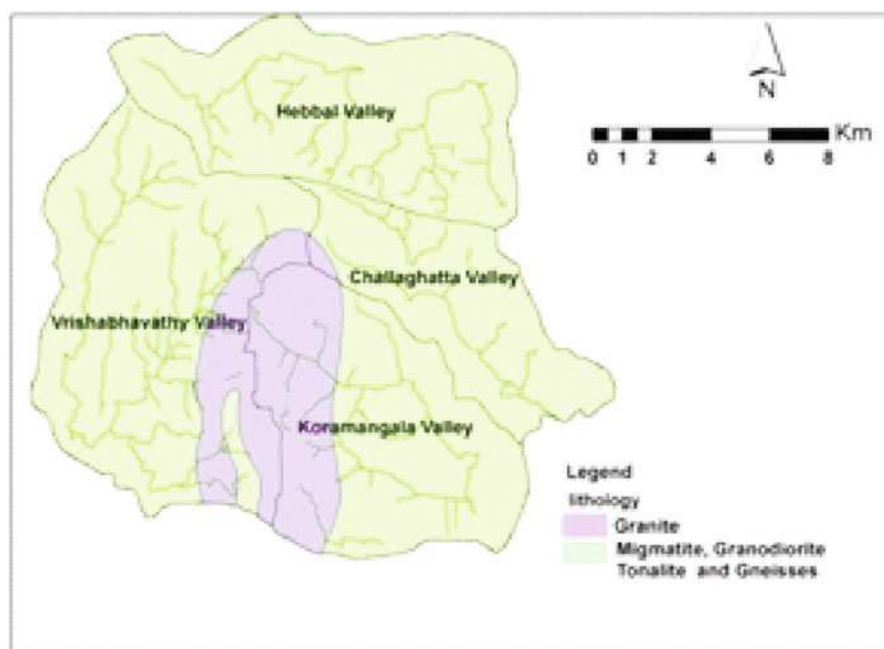


Fig. 40.2 Geology of the study area

40.2 STUDY AREA AND HYDROGEOLOGY

The study area is underlain by granite, migmatite, granodiorite and gneiss rock (Fig. 40.2). Numerous dolerite dykes are found in north, west and southwest part of the study area. The aquifer system is a combination of the shallow weathered zone, extended upto the depth of 60 m and deep fractured. The depth range 30 to 40 m is the most water bearing zone and from 40 to 90 m, there is very little occurrence of water, but beyond 90 m water bearing zone decreases rapidly [4]. The hard rock aquifer or fractured aquifers are present upto the depth of 100 m below ground surface.

40.3 MATERIAL AND METHODS

Water samples were collected from the 42 tube wells. Samples from shallow bore well were collected to obtain information concerning the distribution of radon within the surficial materials and deep bore well samples were collected to evaluate the radon potential of the granitic rock. Field analyses included temperature, pH, electrical conductivity and TDS. Radon in water is measured using RAD-7 (DurrIDGE Co., USA, Model No. 711) with a detection limit of 0.37 Bq/L. A sample

bottle is connected to the radon-in-air monitor (RAD7) in a closed air-loop mode, with a desiccant column before the air inlet of the counter. The ^{222}Rn from the water samples continuously circulates through the desiccant column, RAD7, and then back to the water sample so that it reaches an equilibrium between the water and the air. Then, the activity of the ^{222}Rn is determined by counting its alpha-emitting daughters in the monitor. The activity of ^{222}Rn in water is calculated from the distribution factor of radon concentration between water and air.

40.4 RESULTS AND DISCUSSION

From the results, it was found that the electrical conductivity (EC) of the groundwater falls in the range 501 to 1759 $\mu\text{S}/\text{cm}$, which is dependent on their travel path and the associated rock-water interaction (dissolution of rock minerals), whereas pH is found in the range from 6.8 to 8.1. Radon concentration in the groundwater is highly variable, ranging from 14 to 1000 Bq/L with an average mean value of 172.4 Bq/L (Table 40.1). Almost all the groundwater samples contained radon-222 concentration above permissible limit of 11.1 Bq/L (300 pCi/L) (USEPA, 1991) [5]. This variability is caused by chemical and/or physical processes. In order to evaluate which process have the most effect on the level of radon in a well, radon concentrations must be compared to both the chemical and physical properties of aquifer.

Uranium concentration in water samples is ranging from 0.2 to 523 $\mu\text{g}/\text{L}$. Although groundwater samples having more dissolved uranium concentration, did not measure high radon. So no statistical relationship was found between radon level and uranium in groundwater samples. Generally, dissolved uranium can account for only 1 to 10 % of the radon measured [6]. Hence, in the present study system, uranium in the rock is the source of the radon. Previous studies also indicated the same relationship [7]. Radon concentration in shallow well are significantly lower than the deeper wells, this may be due the presence of high fractures and lineaments in the shallow depth. The radon vs. the depth confirmed radon activity is a function of depth. The contour analysis of radon concentration (Fig. 40.3) in the bore well waters indicates that higher concentration of radon were found in SSW, NNE and eastern part of study area which might be due to changes in geological regime or exposure of younger granitic rocks associated with high abstraction of ground water (Fig. 40.4).

40.5 CONCLUSIONS

The main factors for radon concentrations in groundwater in hard rock aquifer are uranium mineralization in different rock type and presence of fracture, fault and thrust in the area. The high porosity and permeability at shallow depth do not allow

Table 40.1 In-situ physico-chemical parameters, isotopic and trace element results of water samples

Sample I.D.	Location	Well depth (m)	Temp. (°C)	pH	EC (μS/cm)	TDS (mg/L)	²²² Rn (Bq/L)	Uranium (μg/L)
CB1	Challaghata Valley	45.7	25.8	6.8	995	809	30	3.5
CB4		128	29.2	6.9	560	451	76.6	1.6
CB11		49.1	29.5	7.3	916	764	255	2.8
CB12		45.7	29.5	7.9	628	529	242	2.3
CB13		189	29.5	7.7	864	747	—	—
HB2	Hebbal Valley	121.9	28	7.6	900	568	84.1	14.7
HB4		243.8	27.9	8	510	322	114	3.5
HB7		99.1	28	7.2	1728	1090	68.7	5.5
HB9		137.2	28	7.1	721	455	68.7	8.7
HB10		61	27.9	7.3	629	397	126	6.7
HB14		36.6	27.9	7	477	301	131	4.8
HB17		91.4	27.9	7	806	509	407	1.4
HB19		30.5	28	8.1	419	264	717	68
HB22		91.7	27.9	7.2	1759	1110	131	4.8
HB23		243.8	27.9	7.9	841	531	1000	523
HB24		45.7	27.8	7.5	802	506	401	42.5
HB25		125	27.8	7	528	333	202	7.9
HB26		176.8	28	7.2	1728	1090	14	3.4
KB2	Koramagala Valley	106.7	26.5	7.8	659	507	247	102.5
KB3		103.6	25	7.3	625	593	85	0.2
KB5		125	25	7.5	546	450	57.6	111.9
KB8		103.6	29.5	6.9	645	510	58.9	13.6
KB10		76.2	28	7	594	468	57.6	111.9
KB11		140.2	28.7	6.9	563	508	89.4	3.7
KB12		91.4	29.5	7	556	423	72.9	44
KB16		109.7	28.7	6.9	565	461	36.8	1
KB17		30.5	27.2	7	603	490	17.3	2.1
KB19		30.5	27.3	7.4	908	737	414	1.3
VB2	Virshabhavathy Valley	61	27.2	7.5	576	595	26	6
VB3		48.8	23.6	7.4	528	659	116	17
VB5		64	25.4	6.9	656	556	16	8
VB6		97.5	24.2	7.8	685	597	72.5	3.5
VB7		137.2	25	7.8	1228	1156	29.7	3
VB10		36.6	28.5	7.4	1070	928	44.9	3.4
VB12		40.8	27.2	7.2	1006	898	39.8	6.8
VB14		109.7	27.2	7.3	788	679	14	3.8
VB15		67.1	27.2	7.1	677	617	44.9	3.4
VB18		103.6	24.7	7.4	713	591	261	36.8
VB22		121.9	26.4	7.1	476	490	105	1.4
VB24		61	27.2	7.2	875	773	825	16.2
VB26		61	26.4	7.1	851	699	151	6.7
VB28		121.9	23.5	7.7	501	440	111	3

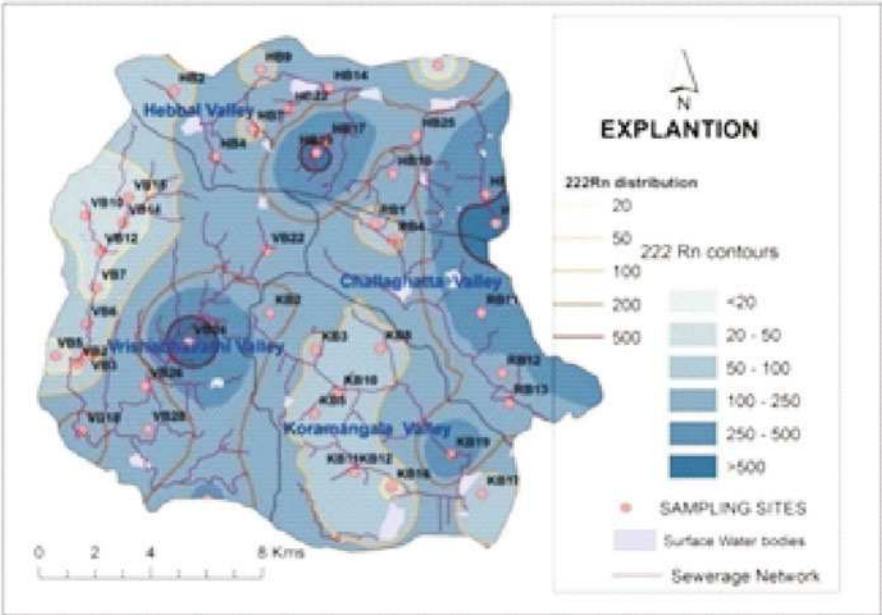


Fig. 40.3 Spatial distribution of radon in groundwater

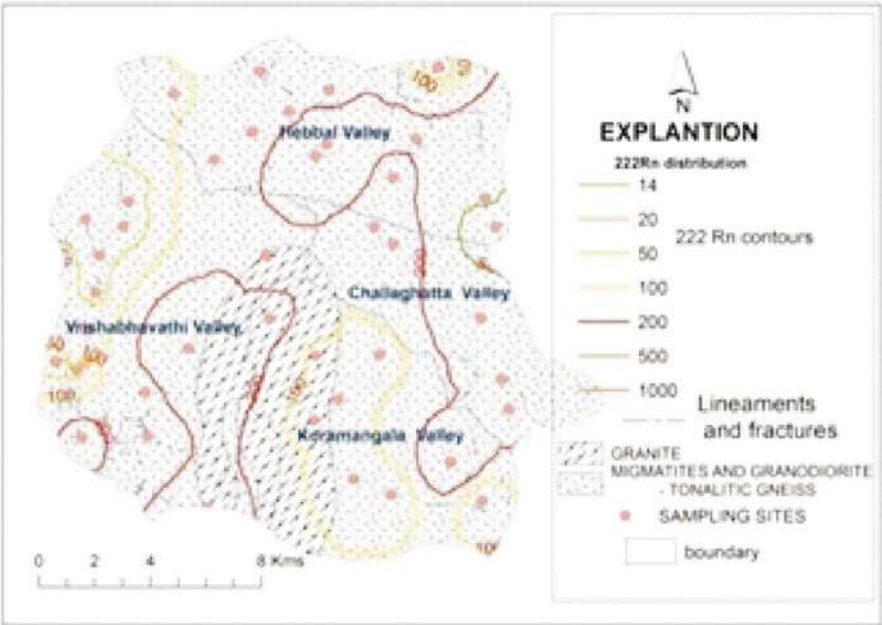


Fig. 40.4 Radon concentration vs geological distribution

the radon to accumulate and thus produce low radon concentration in the shallower bore well. Based on the present study, it is concluded that the radon occurrence in groundwater in hard rock fractured aquifer is controlled by geohydrological and hydrochemical characteristics of the study area.

ACKNOWLEDGEMENT This work has been carried out in collaboration with the Department of Environmental Science, Bangalore University under the DAE/BRNS (Board of Research in Nuclear Science) funded project. We thank Dr. Gursharan Singh, Associate Director (I) & Radiochemistry and Isotope Group for encouragement given during the investigation. The analytical support provided by Shri. H. V. Mohokar, Shri. Suman Sharma and T. B. Joseph, IA&RPhD, BARC and the help provided by the scientists and staffs of Bangalore University during field sampling are acknowledged.

REFERENCES

1. Wanty, R.B. and Nordstrom, D.K.: Natural radionuclides. *In*: Regional groundwater quality, ed. W.M. Alley, 423–441 (1993)
2. Hollocher, K. and Yuskaitis, A.: Chemical composition of surface and high-uranium well water, Lake Sunapee area, New Hampshire. *Northeastern Geology*, 15(2), 159–169 (1993)
3. Folger, P., Nyberg, P., Wanty, R.B. and Poeter, E.: Relationships between ^{222}Rn dissolved in ground water supplies and indoor ^{222}Rn concentrations in some Colorado front range houses. *Health Physics*, 67(3), 245–253 (1994)
4. CGWB: Central Ground Water Board, New Delhi (2007).
5. USEPA: National Primary Drinking Water Regulations; Radionuclides; Proposed Rule. Fed. Reg., 56(138), 33050–33127 (1991)
6. Veeger, A.I. and Ruderman, N.C.: Hydrogeological control on radon-222 in a buried valley fractured bedrock aquifer system. *Groundwater*, 36(4), 596–604 (1998)
7. Gall, I.K., Ritzi Jr., R.W., Baldwin Jr., A.D., Pushkar, P.D., Carney, C.K. and Talnagi Jr., J.F.: The correlation between bedrock uranium and dissolved radon in groundwater of a fractured carbonate aquifer in southwestern Ohio. *Groundwater*, 33(2), 197–206 (1995)

Chapter 41

Groundwater Arsenic Contamination Affecting Different Geological Domains in India: Its Relation to Fluvial Geomorphology and Quaternary Stratigraphy

Babar A. Shah

Abstract Groundwater arsenic (As) survey in tubewell was done from Bengal Delta (West Bengal), Middle Ganga Plain (Uttar Pradesh-Bihar), Ghaghara Valley (Uttar Pradesh), Imphal Valley (Manipur) and Barak Valley (Assam). About 51% of tubewells have As > 10 µg/l (WHO guideline) and 30% of tubewells have As > 50 µg/l (max. As 500 µg/l) in the Bengal Delta (West Bengal). In the Middle Ganga Plain (Uttar Pradesh-Bihar), about 73% of tubewells have As > 10 µg/l and 41% of tubewells have As > 50 µg/l (max. As 1300 µg/l). About 49% of tubewells have As > 10 µg/l and 29% of tubewells have As > 50 µg/l (max. As 510 µg/l) in the Ghaghara Valley (Uttar Pradesh). In the Manipur Valley, about 63% of tubewells have As > 10 µg/l and 40% of tubewells have As > 50 µg/l (max. As 502 µg/l). In the Barak Valley (Assam), about 66% of tubewells have As > 10 µg/l and 26% of tubewells have As > 50 µg/l (max. As 350 µg/l). Most of the As-contaminated (As > 10 µg/l) tubewells are located within the depth of 15 to 50 m in the Holocene Newer Alluvium aquifers. Arsenic affected villages are preferentially located close to abandoned or present meander channels and floodplains of the Ganga, Ghaghara, Bhagirathi, Barak and Imphal rivers.

Keywords Groundwater arsenic • Sediment arsenic • Older Alluvium • Holocene aquifer • Geomorphology

41.1 INTRODUCTION

Groundwater As contamination have been reported in many parts of the world such as Bangladesh, India, Pakistan, Nepal, China, Hungary, Vietnam, Thailand, Cambodia, Tiwan, Inner Mongolia, Ghana, Egypt, Japan, Argentina, Mexico, USA and

B.A. Shah (✉)

Department of Geological Sciences, Jadavpur University, Kolkata, India

e-mail: bashahju@yahoo.com

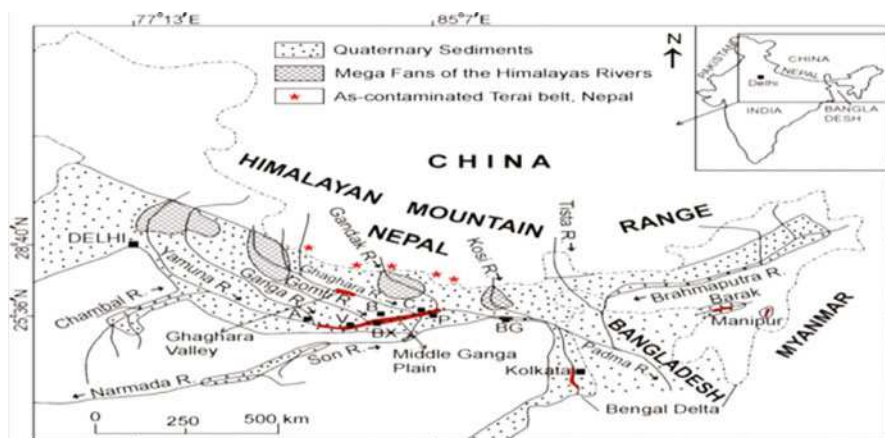


Fig. 41.1 Quaternary sediments in the Indo-Ganga foredeep and Bengal Basin. The study areas of five geological domains are shown in the map. Abbreviations: A - Allahabad, V - Varanasi, BX - Buxar, B - Ballia, C - Chhapra, P - Patna, BG - Bhagalpur

Chile [1]. Long-term intake of As-contaminated groundwater above 50 $\mu\text{g/l}$ has caused skin diseases, cardiovascular, neurological, hematological, renal and respiratory diseases, as well as lung, bladder, liver, kidney and prostate cancers [2]. The upper permissible limit of As in drinking water is 10 mg/l, as per the World Health Organisation [3], which has been endorsed by Bureau of Indian Standards [4]. A groundwater As survey was carried out from different Quaternary domains in India (Fig. 41.1) viz., Bengal Delta (West Bengal), Middle Ganga Plain (Uttar Pradesh-Bihar), Ghaghara Valley (Uttar Pradesh), Imphal Valley (Manipur) and Barak Valley (Assam). Groundwater As concentrations in tubewell waters were tested within the Holocene Newer Alluvium aquifers, as well as the Pleistocene Older Alluvium aquifers. The main objective of study is to investigate the distribution of groundwater As in entrenched channels and floodplains in Quaternary domains under fluvial geomorphologic setting.

41.2 MATERIAL AND METHODS

Hand tubewell water samples were collected for As analysis (Table 41.1). The geographic locations of all samples were recorded by a handheld Global Positioning System (GPS). The information of tubewell depth was acquired from owner of the tubewell. The Older and Newer Alluvium sediment samples were collected from Bengal Delta, Middle Ganga Plain, Ghaghara Valley, Imphal Valley and Barak Valley and GPS location of all samples were recorded. Analysis of As and

Table 41.1 Groundwater arsenic status (%) from five geological domains in India

Basins	Samples	As > 10 µg/l	As > 50 µg/l	Max. As µg/l
Bengal Delta (West Bengal)*	355	51	30	500
Middle Ganga Plain (Uttar Pradesh-Bihar)	224	73	41	1300
Ghaghara Valley (Uttar Pradesh)	231	49	29	510
Manipur Valley (Manipur)	628	63	40	502
Barak Valley (Assam)	80	66	26	350

iron (Fe) were carried out in the Older and Newer Alluvium sediments. Iron in sediment and tubewell water samples was analysed by 1,10 phenanthroline method by the use of UV spectro-photometer. Arsenic in tubewell water and sediments was analysed through flow injection hydride generation atomic absorption spectrometry (FI-HG-AAS) system. Details of the reagents and glassware were given elsewhere [5]. Groundwater As contaminations affecting different geological domains in India are presented below.

41.3 RESULT AND DISCUSSION

41.3.1 Bengal Delta (West Bengal)

The Bengal Basin is $\sim 1.4 \times 10^5 \text{ km}^2$ in area and covers most of Bangladesh and parts of West Bengal, India. Currently, nine districts east of the Bhagirathi River are As-contamination in groundwater [1], [6]. Arsenic affected areas confined to the western part of the Bhagirathi River are mainly discussed here. In this study, 355 tubewell water samples were analysed from Howrah and Hooghly districts in the western part of the Bhagirathi River (Table 41.1). About 51% of tubewells have As > 10 µg/l and 30% of tubewells have As > 50 µg/l. Maximum As and iron (Fe) concentrations in tubewell waters are 500 µg/l and 13 mg/l in Ulubaria and Balagrh blocks, respectively. Arsenic contaminated aquifers are mainly confined in the Holocene entrenched channels and floodplains of the Bhagirathi River. Many affected areas in the Balagarh Block of Hooghly district are located over the Damodar fan-delta, where maximum As concentrations of 85-90 µg/l have been recorded. The As-affected areas in Amta and Bagnan blocks of Howrah district are located on either side of the present Damodar channel but south of the Damodar fan-delta. Amta and Bagnan areas recorded maximum As concentrations of 50 and 90 µg/l, respectively [6]. Many coal seams from the Raniganj and Jharia coalfields of the Damodar Valley, which flank the Bengal Basin, have As concentrations from 65 to 360 mg/kg. Biogenic As bearing pyrite often grow as cement like overgrowth on iron rich heavy mineral like titaniferous magnetite [6].

41.3.2 Middle Ganga Plain (Uttar Pradesh-Bihar)

Narrow As-contaminated tracts have been recorded in the Middle Ganga flood-plains from the states of Bihar and Uttar Pradesh [7–11]. In this study, 224 tubewell water samples were analysed from Middle Ganga Plain (Table 41.1). About 73% of tubewells have As concentrations above 10 µg/l and 41% of tubewells have As above 50 µg/l. About 77% of As-contaminated tubewells are from shallower depth (21 to 40 m) in the Holocene aquifers. Maximum concentrations of As and Fe in tubewell waters are 1300 µg/l and 12.93 mg/l at Semariya Ojjha Patti and Pandey Tolla villages, respectively. Most of the As contaminated tubewells are located within the depth of 20 to 50 m in the Newer Alluvium aquifers. The Fe content in tubewell waters varies from 0.1 to as much as 12.9 mg/l. About 85% of tubewells have Fe beyond its permissible limit of 1 mg/l [9]. Arsenic contaminated tubewells in Vaishali, Patna, Ballia, Bhojpur, Buxar, Mirzapur, Ghazipur districts are mostly located in entrenched channels and floodplains of the Ganga River in the Holocene Newer Alluvium surfaces. Tubewells located in Ballia, Ara, Chhapra, Patna, Hazipur, Buxar, Muhammadabad, Ghazipur, Saidpur, Varanasi, Chunar and Mirzapur towns are As-safe in groundwater because of their positions on the Older Alluvium upland surfaces. Tubewells located in the Pleistocene Older Alluvium aquifers are virtually As-safe in groundwater, whereas tubewells located in the Holocene Newer Alluvium aquifers are As contaminated in groundwater [8, 9]. Arsenic concentrations in the Older Alluvium sediments varies from 5.65 mg/kg to 13.73 mg/kg. Iron concentration in the Older Alluvium sediments varies from 1.57 g/kg to 6.15 g/kg. As concentration in the Newer Alluvium sediments varies from 3.75 to 30.91 mg/kg [9]. Arsenic in suspended river sediments of the Yamuna, Ganga, Gomati, Ghaghara, Son, Gondak, Buri Gandak and Kosi Rivers varies from 5.61 mg/kg to 10.59 mg/kg and Fe content in suspended river sediments of these rivers varies from 1.17 g/kg to 5.65 g/kg [9]. Arsenic-bearing minerals deposits in the Himalayan hill range including hydrothermal pyrite-chalcopyrite-arsenopyrite-galena mineralization associated with quartz veins in Buniyal, Doda, Almora, J and K Hills [12]. The Indus-Tsangpo suture in north India is marked by ophiolitic rocks, including olivine serpentinites. These ophiolites are composed of serpentinized peridotite, layered mafic to ultramafic rock, volcanic and oceanic sediments that contain high As [13].

41.3.3 Ghaghara Valley (Uttar Pradesh)

In this study, 231 tubewell water samples were analysed from Ghaghara Valley (Table 41.1). About 38%, 61% and 42% of tubewells in Faizabad, Gonda and Basti districts, respectively have As > 10 µg/l. Moreover, 15%, 45% and 26% of tubewells in Faizabad, Gonda and Basti districts, respectively have As above 50 µg/l. Maximum concentrations of As in tubewells from Faizabad, Gonda and

Basti districts are 350 µg/l, 510 µg/l and 150 µg/l, respectively [14]. Faizabad and Ayodhya twin towns are located on the yellow-brown coloured oxidized Pleistocene Older Alluvium upland surfaces and tubewells are As-safe (<10 µg/l) in groundwater. However, tubewells in outskirts of Faizabad town near Pathan tolia and Kala Majhar have maximum As concentrations of 72 µg/l and 350 µg/l, respectively. About 47% As-contaminated (As > 10 µg/l) tubewells in these three districts are located within the depth of 10 to 35 m [14].

41.3.4 Manipur Valley (Manipur)

The Manipur Valley was infilled by thick Newer Alluvium sediments and composed of clay, sand, silt and carbonaceous matter, deposited mainly in the central and upper part of the Manipur Valley. About 628 tubewell water samples were analysed from Imphal East, Imphal West, Thoubal and Bishnupur districts of Manipur Valley (Table 41.1). About 63% of tubewells have As >10 µg/l and 40% of tubewells have As > 50 µg/l. Arsenic contaminated aquifers in the Manipur Valley are mainly located within the Holocene Newer Alluvium, where the depth of tubewells varies from 5 to 120 m [15].

41.3.5 Barak Valley (Assam)

The Barak Valley is located in the southern part of Assam and consists of three districts viz. Cachar, Karimganj and Hailakandi districts. Groundwater survey in Cachar and Karimganj districts (Table 41.1) shows that 66% of tubewells have As concentrations above 10 µg/l and 26% of tubewells have As above 50 µg/l (max. 350 µg/l). About 90% of installed tubewells in these two districts are from shallower depth (14 to 40 m). The Plio-Pleistocene Older Alluvium aquifers composed of shale, ferruginous sandstone, mottle clay, pebble and boulder beds, which at higher location or with thin cover of Newer Alluvium sediments are As safe in groundwater [16].

41.4 CONCLUSIONS

Groundwater As contamination occurred in different Quaternary domains in India. The river channels with the Newer Alluvium deposits are incised as narrow entrenched river valley terraces, which normally occur above the active flood plain. Tubewells in the Holocene Newer Alluvial aquifers are mostly As-contaminated in groundwater. The Pleistocene Older Alluvium upland surfaces are As-safe in groundwater. Most of the towns on the Quaternary geological

domains are As-safe in groundwater because of their locations on the Pleistocene Older Alluvium upland surfaces. Most of the As affected villages are preferentially located close to abandoned or present meander channels. The Pleistocene oxidizing yellow-brown coloured sediments are well flushed by groundwater flow due to high-hydraulic head and are low in As and devoid of organic matter. The environment of the Pleistocene aquifers is not favorable to release sorbed As to groundwater and aquifers are generally As-safe in groundwater.

ACKNOWLEDGEMENTS The author thanks to School of Environmental Studies, Jadavpur University for the As and Fe analyses. The financial support of this study came from DST Young Scientist Scheme, and CSIR Scientists' Pool Scheme, which is gratefully acknowledged.

REFERENCES

1. Ravenscroft, P., Brammer, H. and Richards, K.: As pollution: a global synthesis. Wiley-Blackwell, Chichester (2009)
2. Smith, A.H., Goycolea, M., Haque, R. and Biggs, M.L.: Marked increase in bladder and lung cancer mortality in a region of Northern Chile due to arsenic in drinking water. *Am. J. Epidemiol.* 147, 660–669 (1998)
3. World Health Organisation (WHO): Guideline for drinking water quality. Recommendations 2nd edn., 1993, 1, Geneva (1993)
4. Bureau of Indian Standards: Indian standard: drinking water. Specification (first revision), Amendment No. 2, New Delhi (2003)
5. Samanta, G., Roy Chowdhury, T., Mandal, B., Biswas, B., Chowdhury, U., Basu, G., Chanda, C., Lodh, D. and Chakraborti, D.: Flow Injection Hydride Generation Atomic Absorption Spectrometry for determination of arsenic in water and biological samples from arsenic-affected districts of West Bengal, India, and Bangladesh. *Microchem. J.* 62, 174–191 (1999)
6. Acharyya, S.K. and Shah, B.A.: Groundwater arsenic contamination affecting different geologic domains in India – a review: influence of geological setting, fluvial geomorphology and Quaternary stratigraphy. *Environ. Sci. Health. Part A* 42, 1795–1805 (2007)
7. Chakraborti, D., Mukherjee, S.C., Pati, S., Sengupta, M.K., Rahman, M.M., Chowdhury, U.K., Lodh, D., Chanda, C.R. and Chakraborty, A.K.: Arsenic groundwater contamination in Middle Ganga Plain, Bihar, India: a future Danger? *Environ. Health Perspect.* 111, 1194–1200 (2003)
8. Shah, B.A.: Role of Quaternary stratigraphy on arsenic-contaminated groundwater from parts of Middle Ganga Plain, UP-Bihar, India. *Environ. Geol.* 53, 1553–1561 (2008)
9. Shah, B.A.: Arsenic in groundwater, Quaternary sediments, and suspended river sediments from the Middle Gangetic Plain, India: distribution, field relations, and geomorphological setting. *Arab J. Geosci.* doi: [10.1007/s12517-013-1012-4](https://doi.org/10.1007/s12517-013-1012-4) (2013)
10. Kumar, M., Kumar, P., Ramanathan, A.L., Bhattacharya, P., Thunvik, R., Singh, U.K., Tsujimura, M. and Sracek, O.: Arsenic enrichment in groundwater in the middle Gangetic plain of Ghazipur district in Uttar Pradesh, India. *J. Geochem. Explor.* 105, 83–94 (2010)
11. Raju, N.J.: Arsenic exposure through groundwater in the Middle Ganga Plain in the Varanasi environs, India: a future threat. *J. Geol. Soc. India* 79, 302–314 (2012)
12. Tewari, A.P. and Gaur, R.K.: Geological conditions of formation of Pyrite-Polymetallic deposits of the Himalaya and the Great Caucasus – a comparison. *Him. Geol.*, 7, 235–245 (1977)
13. Guillot, S. and Charlet, L.: Bengal arsenic, an archive of paleohydrology and Himalayan erosion. *Environ. Sci. Health Part A* 42, 1785–1794 (2007)

14. Shah, B.A.: Status of groundwater arsenic pollution in Holocene aquifers from parts of the Ghaghara Basin, India: Its relation to geomorphology and hydrogeological setting. *Phy. Chem. Earth*, 58-60, 68–76 (2013)
15. Chakraborti, D., Singh, E.J., Das, B., Shah, B.A., Hossain, M.A., Nayak, B., Ahamed, S. and Singh, N.R.: Groundwater arsenic contamination in Manipur, one of the seven North-Eastern Hill states of India: a future danger. *Environ. Geol.* 56, 381–390 (2008)
16. Shah, B.A.: Role of Quaternary stratigraphy on arsenic-contaminated groundwater from parts of Barak Valley, Assam, North–East India. *Environ. Earth Sci.* 66, 2491–2501 (2012)

Chapter 42

Ground Water Sustainability in Varanasi District, Uttar Pradesh: Current Situation and Need for Effective Strategies

Prahlad Ram and N. Janardhana Raju

Abstract In recent times, there has been a tremendous increase in demand for fresh water and water shortage in arid and semi-arid regions due to population increase, industrialization and agricultural activities in parts of world. Comparative studies of ground water resources in Varanasi district have been carried out with the objective to identify reasons why groundwater resources is increasingly being exploited, and to explore ways through which the exploitation could be done sustainably. In study area, erratic rainfall, diminish of ponds and reduction of surface water create tremendous pressure on groundwater to fulfill increasing demands. The heavy withdrawal of ground water for sustainable development of agricultural practices, fast urbanization and industrialization led to problems of overdraft, falling water levels and failure/dried up of shallow tubewells/dugwells, degradation of ground water quality and shift of blocks from safe to critical and semi-critical.

Keywords Groundwater • Sustainability • Alluvium • Varanasi

42.1 INTRODUCTION

The sustainable management of aquifers is a burning problem in many countries. New scientific tools can assist in its solution, both in the analysis of whether the present management is sustainable and in the definition of strategies and measures to achieve sustainability. The impact of urbanization, agricultural activities and industrialization has led to over-exploitation of ground water resource and deterioration of ground water quality. The present trend of growth in population, resource use and environmental degradation of the ground water regime may not be sustainable for more than a few decades. Estimates of ground water resources of India as on 2011 shows that about 245 billion cubic meter (BCM) fresh water resource is

P. Ram (✉)

Central Ground Water Board, CHQ, Bhujal Bhawan, Faridabad, India

e-mail: prahlad_ism@yahoo.co.in

N.J. Raju

School of Environmental Sciences, Jawaharlal Nehru University, New Delhi, India

abstracted annually of which 91% is used in agriculture and remaining 9% is used in domestic and industrial purpose [1]. The use of ground water to agriculture is more as compared to other uses. Varanasi district is situated in the central Ganga alluvial plain and this alluvial formation is important sources of abundant and dependable ground water supplies because of large saturated thickness and high well yields. Intensive use of ground water from these formations has led to several quantity and quality problems [2–4].

42.2 STUDY AREA AND HYDROGEOLOGY

The study area is situated between latitudes $25^{\circ}5'00''\text{N}$ – $25^{\circ}35'00''\text{N}$ and longitude $82^{\circ}40'00''\text{E}$ – $83^{\circ}12'00''\text{E}$ in Varanasi district, Uttar Pradesh (Fig. 42.1). Study area falls in the sub-tropical region characterized by hot summer and severe winter and average annual rainfall is 1016 mm. Total geographical area of study area is 1535 km^2 with 3682194 population [1]. It is situated in the central Ganga plain is underlain by Quaternary alluvial sediments consisting of clay, silt, sand and gravel of various grades. The alternate sand and clay layers have created a multi-tier

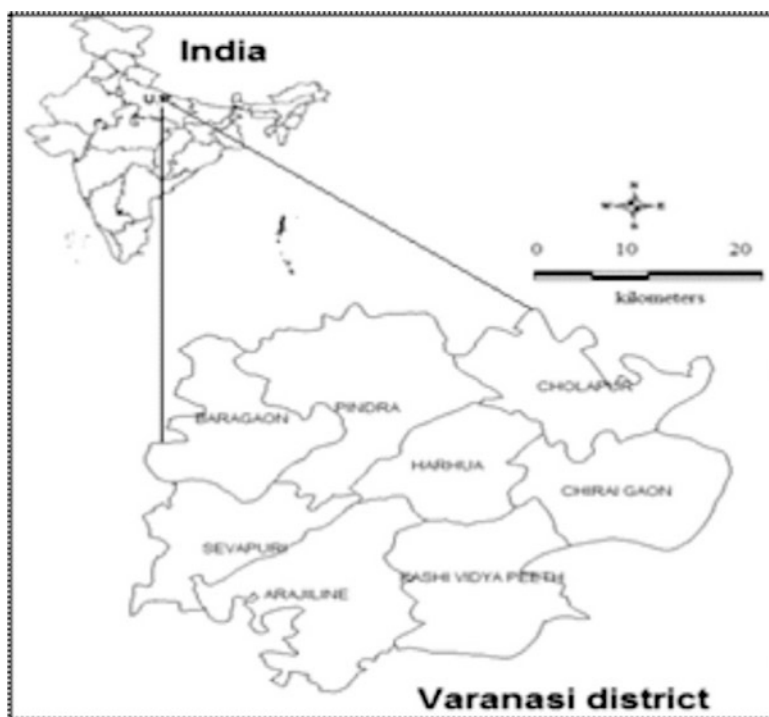


Fig. 42.1 Location map of Varanasi district

aquifer system [5]. Depth up to which aquifers are commonly developed ranges from 31-236 m.bgl. The yield of shallow borewells (hand pumps) and dug-wells puncturing unconfined aquifers within the depth of 50 m.bgl varies from 5 to 10 lps. The yield of tubewells cumulatively tapping shallow and deeper aquifers varies between 25 and 65 lps at moderate drawdowns. The groundwater resources of the area have been exploited mostly through shallows dug-wells, hand-pumps, dug-cum-bore wells and bore wells for both domestics and irrigation purposes.

42.3 MATERIAL AND METHODS

Ground water resource of Varanasi has been estimated using ground water resources estimation methodology. Ground Water Estimation Committee' 1997 is constituted by Ministry of Water Resources, Government of India to formulate the methodology (GEC-97) drawing the expert members from various organizations of ground water field. The methodology involves estimation of annual replenishable ground water resources(annual ground water recharge), annual ground water draft (annua lutilization) and the percentage of utilization with respect to recharge (stage of ground water development). Block has been taken as assessment unit is categorized based on stage of ground water development and long term water level trend. In order to know the changing scenario and remedy measure for sustainable ground water development of ground water resources and accordingly of Varanasi district comparative studies has been carried out based on data of years 2004, 2009 and 2011.

42.4 RESULT AND DISCUSSION

The comparative studies of ground water resources of Varanasi district has been carried out with the data of 2004, 2009 and 2011, keeping all parameters in consideration which influenced the ground water regime. The annual replenishable ground water resource (recharge) in 2004, 2009 were carried out 57375 ha m and 53302 ha m respectively whereas in 2011 it has been reduced to 53994 ha m. There is about 3381 ham (6%) decrease in the replenishable ground water resource from previous. The gross annual ground water draft for irrigation domestic and industrial uses for assessment years 2004 and 2009 were worked out 37786 ha m and 53302 ham where as it is 41927 ha m in 2011 estimation. There is about 11% increase in the ground water draft for all uses from 2004 estimation. The stage of ground water development for the assessment years 2004 and 2009 were worked out as 73% and 80% whereas it is 86% in assessment year 2011. There is 13% advancement in stage of ground water development. The long term water level fluctuation data indicates that the water level is significantly declining in major part of district. As per latest assessment (As on 2011), out of 8 blocks the 1 block is over-exploited, 2 Critical,



Fig. 42.2 Wells located at (a) Harhua Bazar, Harahua block and (b) Rohania Thana, Kashi Vidyapeeth block, Varanasi

3 semi-Critical, and 2 safe, whereas in 2004 all blocks were safe [6]. Ground water abstraction has increased to such an extent that in most part of the district dug wells have gone dry and hand pumps and shallow tube wells are at the verge of failure (Fig. 42.2). Current practice of abstraction of ground water resources in district is not sustainable. In order to manage water resources to meet the needs of people while sustaining functioning ecosystems we need to implement a more balanced and integrated approach to water management.

42.5 CONCLUSION

The alarming stage of ground water development, lowering of ground water level and failure of wells indicate that the present rate of abstraction puts a question mark on long-term sustainability of groundwater resources. Remedy measure should be taken for sustainable ground water development such as adaptation of Rainwater harvesting and artificial recharge to ground water, conjunctive utilization of surface and ground water, adaptation of micro-irrigation system like Drip and Sprinkler and raising of low water consuming crops and maintenance of existing water tanks by de-siltation and prevention of their encroachment as well as using them as artificial recharge system. Current situation reveal that *if immediate remedial measures are not taken to reverse the declining trend of water table, it would be difficult to sustain for long time.*

REFERENCES

1. Central Ground Water Board: Dynamic Ground Water Resources of India (As on March, 2009). Ministry of Water Resources, Govt. of India (2011)

2. Raju, N.J., Ram, P. and Dey, S.: Groundwater quality in the lower Varuna River basin, Varanasi district, Uttar Pradesh, India. *Jour. Geol. Soc. India*, 73, 178-192 (2009)
3. Raju, N.J., Shukla, U.K. and Ram, P.: Hydrogeochemistry for the assessment of groundwater quality in Varanasi: A fast urbanizing center in Uttar Pradesh, India. *Environ. Monit. Assess.*, 173, 279–300 (2011)
4. Raju, N.J.: Evaluation of hydrogeochemical processes in the Pleistocene aquifers of middle Ganga plain, Uttar Pradesh, India. *Environ. Earth Sci.*, 65, 1291–1308 (2012)
5. Shukla, U.K. and Raju, N.J.: Migration of the Ganga River and its implication on hydro-geological potential of Varanasi area, UP, India. *Jour Earth Syst. Sci.*, 117(4) (2008)
6. Central Ground Water Board: Dynamic Ground Water Resources of India (As on March, 2004). Ministry of Water Resources, Govt. of India (2006)

Chapter 43

Discharge Pattern in the Gunt Valley, Western Pamir, with respect to $\delta^2\text{H}$, $\delta^{18}\text{O}$ and Hydrochemistry

C. Meier, M. Knoche, M. Brehme, R. Merz, and S.M. Weise

Abstract A three years lasting isotope hydrological study has been performed in the 14,000 km² catchment of river Gunt in the western Pamir in Tajikistan to resolve the contributions of different components to the total run-off out of the catchment. River samples have been taken from about 30 locations and precipitation from five stations in this high-alpine and partly glaciated region both in a monthly interval. Precipitation as important initial parameter was shown to originate from different wind systems tracing regionally the isotopic composition in time. Within the catchment, the subcatchments group with respect to deuterium excess of their waters. This strengthens the assumption of the varying influence of different wind systems. Along with the isotopic composition, hydrochemistry of the river waters varies in an annual cycle as result of a varying contribution of groundwater and/or melt water. Similarly, with these tracers the low-energy flow of the eastern part of the valley can be clearly separated from the dominating fraction from the high-energy flow in the western part.

Keywords Isotope Hydrology • Hydrochemistry • River Water • Pamir • Arid Region

43.1 INTRODUCTION

Central Asia, and in particular the Aral Sea basin of it, is one region in the world which is strongly affected by water shortage. The rivers Amu Darya and Syr Darya are the main contributors to this region. These melt water dominated rivers have their origins in the Pamirs and Tien Shan[1]. As representative catchment for the headwaters of the Aral Sea Basin we investigated the River Gunt catchment in the Central Pamirs. The Gunt catchment is an east-west running basin that is located in the Gorno Badakhshan Autonomous Region of Tajikistan. It covers an area of about

C. Meier (✉) • M. Knoche • M. Brehme • R. Merz • S.M. Weise
Department Catchment Hydrology, UFZ Helmholtz Centre for Environmental Research,
Halle, Germany
e-mail: christiane.meier@ufz.de

14,000 km² and shows an altitude range of about 4,000 m with the highest elevations, Peak Karl Marx (6,726 m) and Peak Engels (6,510 m), at its southern border. Almost in the middle of the catchment there is a natural dammed lake (Yashilkul) situated with an extension of circa 40 km². It divides the study region into two parts; the western part is characterized by a pronounced relief with steep erosion valleys, while the eastern territory represents a high plateau with smaller altitude ranges and wider valleys. The discharge of the Lake Yashilkul through the natural dam leads to a relatively constant runoff of the River Gunt all over the year, also in the low flow period throughout the winter months. The study area is situated in a transition zone of different wind systems [2]. The influences of the Westerlies, the Indian Monsoon and further southern cyclones on precipitation in this region are detectable [3]. But it is still a challenge to define and to quantify the impacts of these wind systems.

Every month water samples were taken at about 30 sampling points for river water along the main stream of Gunt river and most of its tributaries. River water samples were analyzed for the stable water isotopes ($\delta^2\text{H}$ and $\delta^{18}\text{O}$) and for major ion concentrations.

43.2 ISOTOPE PATTERNS

The monitoring data show comparably high $\delta^2\text{H}$ (-103.5 to -96.5 ‰) and $\delta^{18}\text{O}$ (-14.8 to -14.0 ‰) values far in the west of the catchment, and the lowest values in the plateau area around the lake Yashilkul and in the east of the catchment ($\delta^2\text{H}$: -125.0 to -131.0 ‰, $\delta^{18}\text{O}$: -16.0 to -18.0 ‰). These differences result from the increasing altitude from west to east. The eastern part of the catchment is an cold alpine desert with precipitation sums of ≤ 160 mm/a while the western part is warmer and receives a little more precipitation (~300 mm/a). Further it was found that the isotopic signature of the Gunt River is mainly formed by lake water. Especially in the winter months the stream flow is dominated by heavier water due to evaporation, flowing through the natural landslide dam. An additional isotopic pattern in the catchment is a distinction between tributaries flowing from the northern boundary to the main stream and tributaries originating in the south of the catchment (Fig. 43.1). The altitudes of the northern and southern mountain ranges are similar, but however it occurs an enrichment of heavier stable isotopes in the northern tributaries. The distinction between northern and southern tributaries can also be detected in the deuterium excess. The enrichment bases on the atmospheric circulation that brings precipitation by southern cyclones originating in the Mediterranean and Caspian Sea especially to the northern catchments and causes their higher $\delta^2\text{H}$, $\delta^{18}\text{O}$ and d values. Lower $\delta^2\text{H}$ and $\delta^{18}\text{O}$ and d values can be explained by precipitation transported through Westerlies mainly to the southern subcatchments.

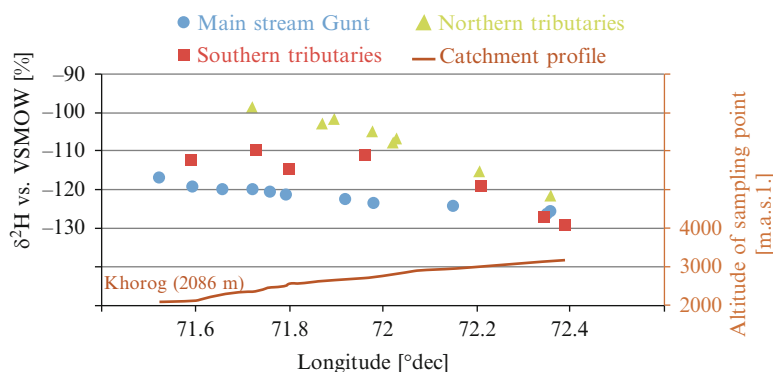


Fig. 43.1 Development of mean $\delta^2\text{H}$ values of water samples along the main river profile

43.3 HYDROCHEMISTRY

The hydrochemical data of the river water shows similar pictures as the isotopic data. In general the concentrations of major ions as chloride, sulphate, sodium, potassium, magnesium, calcium and hydrogen carbonate are fairly low as common in catchments with very little water-rock interaction [4]. The tributaries show their maximum in ion concentrations in the low flow period during winter and spring months, while the lowest mineralization of the waters is found in the late summer (Fig. 43.2). This fact can be explained by melting cycles; in winter and spring infiltrated higher mineralized subsurface water drains the catchments while in summer and autumn low mineralized water from snow- and glacier melt feeds the rivers.

Within the subcatchments a negative correlation between ion concentration and glaciation was found. This shows that river water in a glaciated subcatchment is strongly controlled by low mineralized melt water. The meltand in the end shrinking of the glaciers in the Gunt catchment is finally noticeable in the mineralization of river water and was also detected by an evaluation of satellite images [5].

43.4 SUMMARY

Over a time range of two years monthly river water samples of a high alpine drainage basin were analyzed for stable water isotopes and major ion concentrations to identify precipitation sources and to delineate runoff generation. We present stable isotope ($\delta^2\text{H}$ and $\delta^{18}\text{O}$) and hydrochemical data of river water samples from a nearly ungauged and at least isotopically and hydrochemically unexplored catchment in the Amu Darya headwaters, the Tajik Pamirs.

The main stream Gunt is clearly affected by water arising from the high plateau and the Lake Yashilkul. Seasonal differences in the measured values are mainly

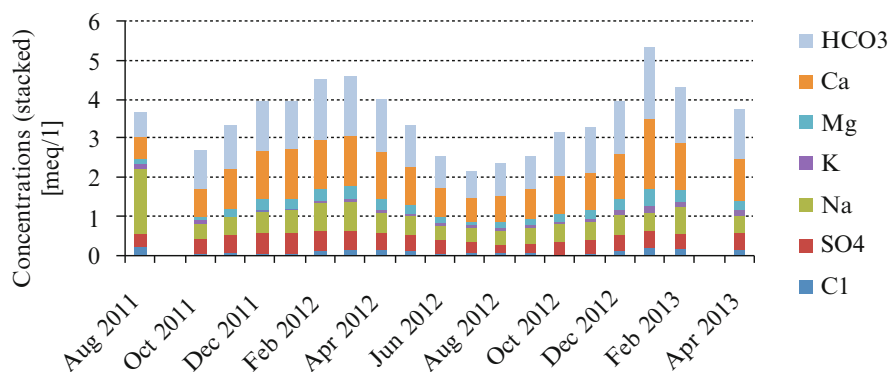


Fig. 43.2 Development of ion concentrations during the whole sampling period (Aug 2011–Apr 2013)

caused by melting processes as well as varying influences of different wind systems. Glacier melt plays a role for runoff generation in glaciated subcatchments and therefore in the whole Gunt basin, but it is still a question to distinguish and quantify the influences of snow melt and glacier melt.

ACKNOWLEDGEMENTS The authors would like to acknowledge the Federal Ministry of Education and Research (BMBF) for funding this project. This work was kindly supported by Helmholtz Impulse and Networking Fund through Helmholtz Interdisciplinary Graduate School for Environmental Research (HIGRADE) [6].

REFERENCES

1. Barlow, M. and Tippett, M.K.: Variability and predictability of Central Asia river flows: Antecedent winter precipitation and large-scale teleconnections. *J. of Hydrometeorology*, 9, 1334–1349 (2008)
2. Aizen, V.B., Mayewski, P.A., Aizen, E.M., Joswiak, D.R., Surazakov, A.B., Kaspari, S., Grigholm, B., Krachler, M., Handley, M. and Finaev, A.: Stable-isotope and trace element time series from Fedchenko glacier (Pamirs) snow/firn cores. *J. Glaciol.* 55, 275–291 (2009)
3. Meier, C., Knoche, M., Merz, R. and Weise, S.M.: Stable isotopes in river waters in the Tajik Pamirs: regional and temporal characteristics. *Isot. Environ. Health Stud.* 49, 542–554 (2013)
4. Brehme, M.: Statistische Auswertung der Flusswasserzusammensetzung im Einzugsgebiet des Gunt (Pamir-Gebirge) im Hinblick auf ihre räumliche und zeitliche Variabilität. Diplomthesis (unpublished), Martin-Luther-University Halle-Wittenberg (2014)
5. Lindner, M.: Rezente Gletscheränderung im Einzugsgebiet des Gunts (Tadschikistan). Diploma thesis (unpublished), University of Innsbruck (2013)
6. Bissinger, V. and Kolditz, O.: Helmholtz Interdisciplinary Graduate School for Environmental Research (HIGRADE). *GAIA* 1, 71–73 (2008)

Chapter 44

Environmental Isotope Investigation to Understand the Groundwater Recharge from Irrigation Tanks in Thirumal Area, Madurai

Noble Jacob, Diksha, Ajay Jaryal, and A. Gurunathan

Abstract Madurai is a water scarce, semiarid region in southern part of Peninsular India. Currently, tank-fed agriculture development programme is being implemented in this region by utilizing the large number of traditionally existing minor irrigation tanks. Hence, an isotope hydrological investigation has been conducted in the Thirumal village, Madurai district to demarcate the zone of influence (i.e., the command area) of the cascade of tanks (4 tanks) and to quantify the groundwater recharge to the downstream wells. Pre (October 2011) and post (February 2012) monsoon samples were collected from the irrigation tanks, open wells upstream and downstream of the tanks etc. and analysed for $\delta^2\text{H}$, $\delta^{18}\text{O}$ and hydrochemistry. The downstream well samples lie in a mixing line between the tank water and the rainwater in the $\delta^{18}\text{O}$ - $\delta^2\text{H}$ plot, indicating groundwater recharge from the irrigation tanks and the area of influence of these tanks were demarcated. The tanks contribution to the downstream wells varies from 97% at 20 m to 41% upto 880m for the first tank, 93% at 60m to 26% at 880m for the second tank, 95% at 30m to 18% at 940m for the fourth tank and varies from 25% at 20 m to 9% at 550m for the third tank.

Keywords Environmental Isotopes • Irrigation Tanks • Hydrochemistry • Madurai

N. Jacob • Diksha (✉) • A. Jaryal
Isotope Production and Applications Division, Bhabha Atomic Research Centre,
Mumbai, India
e-mail: diksha@barc.gov.in

A. Gurunathan
DHAN Foundation, Madurai, India

44.1 INTRODUCTION

The depletion in availability of groundwater and deterioration of its quality are some of the major problems the country is facing today, as they affect the lives of millions of people. To address the above problems, various artificial recharge methods are being implemented in recent years in order to augment the amount of groundwater available for use. But, it is often difficult and costly to evaluate the effectiveness of these artificial recharge methods, especially if only conventional hydrological methods are used. However, the environmental isotopes and geochemical tracers are proved to be powerful tools and can be effectively used to evaluate both the natural and artificial groundwater recharge. They have been successfully used to estimate the contribution of storm as well as annual precipitation to groundwater recharge [1], quantify the recharge from percolation tanks [2] etc. Madurai district is a water scarce, semiarid region in southern part of Peninsular India. Currently, tank-fed agriculture development programme is being implemented in this region by utilizing the large number of traditionally existing minor irrigation tanks. These irrigation tanks are being renovated and developed for water conservation in order to facilitate groundwater recharge and water usage during non-monsoon months. Hence, an isotope hydrological investigation has been initiated in the Thirumal village, Madurai district to demarcate the zone of influence (i.e., the command area) of the Urappareddi cascade of tanks and to quantify the groundwater recharge from these tanks to the downstream wells.

44.2 STUDY AREA AND HYDROGEOLOGY

Thirumal village (Area - 25 km²) is located about 45 km southwest of Madurai, Tamil Nadu (Fig. 44.1). Four minor irrigation tanks in cascade namely, NarayappanNayakan (Tank 1), Melakanmoi (Tank 2), Sandirankulam (Tank 3) and Urappareddi (Tank 4) tanks have been recently renovated and developed for conserving rainwater as part of a tank fed agriculture development program implemented by a community development NGO named DHAN (Development Human ActioN) Foundation. The annual average rainfall in this area is about 900 mm. It receives rainfall during northeast monsoon (47%), southwest monsoon (32%), summer rains (17%) and winter rains (4%). A declining trend of annual rainfall is noticed in the recent years. The climate is subtropical and the temperature varies from 15 to 41°C. Black clayey soil is generally found in this area which is underlain predominantly by crystalline formations. Ground water occurs under phreatic conditions in the weathered residuum and interconnected shallow fractures in the granitic rock. Large diameter open wells with depths ranging from 10 – 20 m are present in this region.

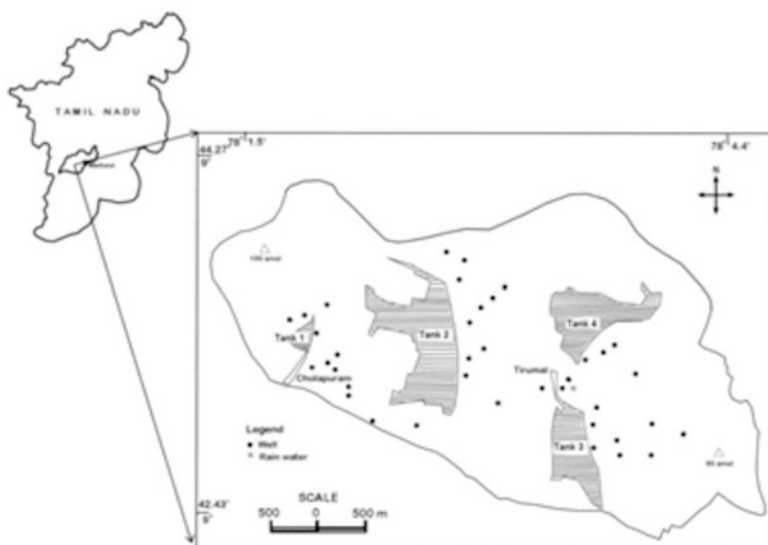


Fig. 44.1 Location map of Thirumangalam area, Madurai, showing the sampling locations

44.3 SAMPLING/METHODOLOGY

Two water sampling campaigns were conducted – pre-monsoon sampling was carried out during October 2011 and post monsoon sampling was done during February 2012. During the above sampling periods, physicochemical parameters such as groundwater levels, water temperature, electrical conductivity, pH, alkalinity etc. were measured insitu using Hanna made multiparameter probe. During the pre-monsoon period about 10 open well and 1 bore well samples were collected whereas, during post monsoon period about 22 open well and 2 bore well samples were collected for chemical and isotopic analysis as per standard protocol. The samples were measured in lab using DINOX Ion chromatography system for major cation and anions and using ISOPRIME Isotope Ratio Mass Spectrometer (IRMS) for $\delta^{18}\text{O}$ and $\delta^2\text{H}$.

44.4 RESULTS AND DISCUSSION

In general, the groundwater samples collected during the pre-monsoon period from the open wells near to the irrigation tanks have an electrical conductivity 400 to 1000 $\mu\text{S}/\text{cm}$, pH varies from 7.2 to 8.2 and alkalinity varies from 62 to 166 mg/L indicating that these waters are fresh. During the post monsoon period, the open well samples away from the tank show an EC of 936 to 1043 $\mu\text{S}/\text{cm}$; pH varies from 7.2 to 7.8, alkalinity varies from 158 to 224 mg/L while open well samples

close to the tank show an EC of 251 to 1092 $\mu\text{S}/\text{cm}$; pH varies from 5.5 to 8.2, alkalinity varies from 100 to 300 mg/L. The reduction in EC and pH show that the wells near to the irrigation tank are getting recharge from the tanks during the post monsoon period. The nitrate concentration in open wells during the pre-monsoon period varies from 21 to 81 mg/L while during the post monsoon period varies from 0.7 to 76 mg/L. Permissible limit of nitrate in drinking water is 20 mg/L [3]. Higher concentration of nitrate in groundwater is due to the use of fertilizers in this area. Reduction in nitrate is observed during the post monsoon period. During the pre monsoon period, a few open wells away from the tank have EC 1600 to 2560 $\mu\text{S}/\text{cm}$; pH varies from 7.2 to 7.5, alkalinity varies from 94 to 116 mg/L. These samples are brackish in nature. Post monsoon data of these samples show that there is no variation.

44.4.1 Hydrochemistry

Hydrochemical data of groundwater samples collected from Thirumal Village during the pre and post monsoon periods is plotted on a Piper's trilinear diagram (Fig. 44.2). Most of the ground samples fall in no dominant ion zones in Piper's diagram. The groundwater samples away from the tanks are Na-Mg-Cl- HCO_3 type while samples close to the influence of irrigation tanks are Na-Ca-Mg-Cl- HCO_3 type. Bore well samples are Na-Mg-Ca-Cl- HCO_3 type while brackish samples are Na-Ca-Mg-Cl type.

44.4.2 Stable Isotopes

Stable isotope techniques can be used to quantify the recharge from artificial recharge structures such as percolation tanks etc. due to the fact that these tanks are evaporating water bodies and have enriched isotopic signatures compared to the local groundwater. A plot of $\delta^{18}\text{O}$ vs. $\delta^2\text{H}$ was made for pre and post monsoon samples (Fig. 44.3).

The downstream well samples lie in a mixing line between the tank water and the rainwater in the $\delta^{18}\text{O}$ - $\delta^2\text{H}$ plot, indicating groundwater recharge from the irrigation tanks. From the distribution of EC and $\delta^{18}\text{O}$ in the groundwater, the areas of influence of these tanks were demarcated (Fig. 44.4). Using a two-component $\delta^{18}\text{O}$ mass balance model, the tanks contribution to the downstream wells was quantified using isotope ($\delta^{18}\text{O}$) balance equation.

$$ms = [\text{R pg} - \text{Rg, t}]/[\text{R pg} - \text{Rs, t}] \quad (44.1)$$

where ms is the fraction of artificial recharge water in the admixture, Rpg is the isotopic composition of pure groundwater, Rg,t is the isotopic composition of the

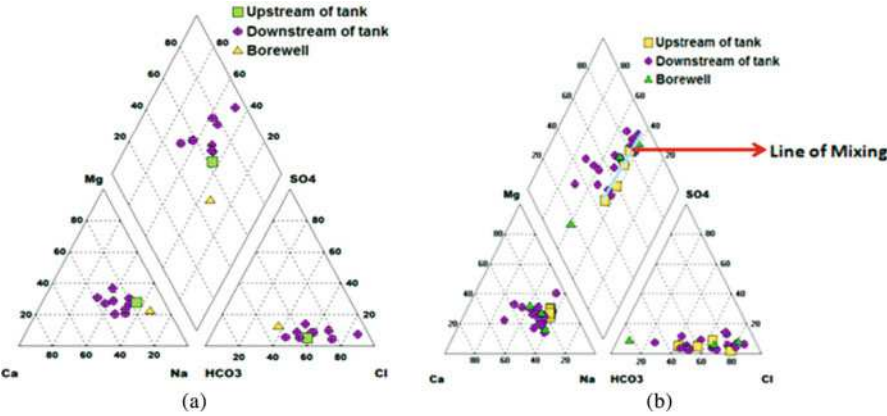


Fig. 44.2 Piper’s trilinear diagram for groundwater samples (a) pre-monsoon and (b) post monsoon periods

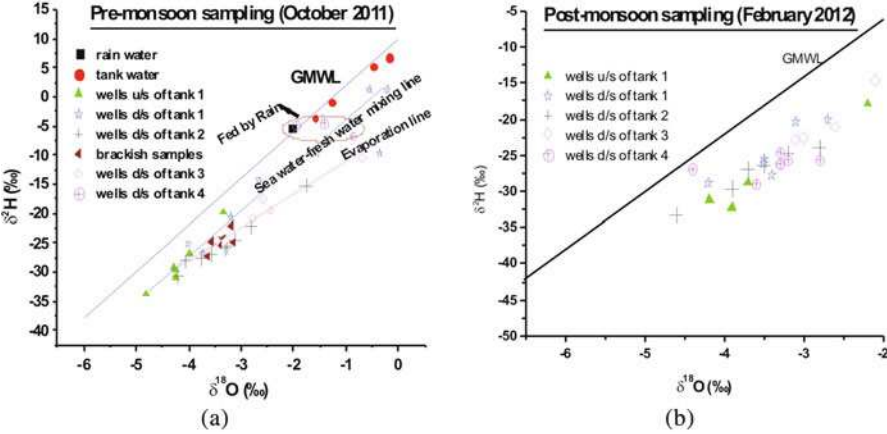


Fig. 44.3 Plot of $\delta^{18}\text{O}$ vs. $\delta^2\text{H}$ (a) pre-monsoon and (b) post monsoon periods

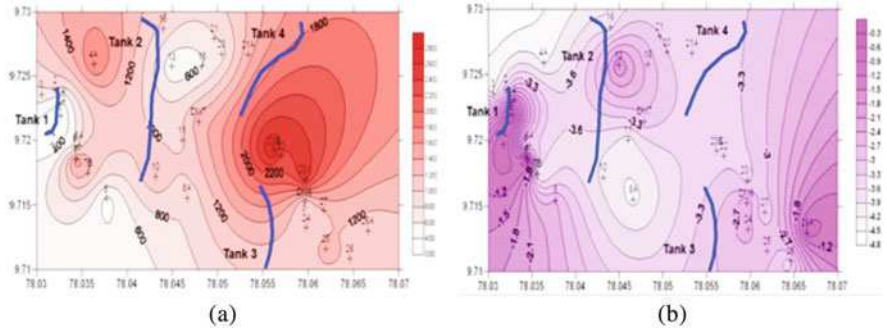


Fig. 44.4 Spatial distribution of (a) EC (μS/cm) and (b) $\delta^{18}\text{O}$ (‰) in Feb 2012

Table 44.1 Percentage tank water contribution to groundwater at various distances

Tank 1		Tank 2		Tank 3		Tank 4	
Distance (m)	Percentage contribution	Distance (m)	Percentage contribution	Distance (m)	Percentage contribution	Distance (m)	Percentage contribution
20	97	60	93	20	25	30	95
150	70	420	56	260	19	170	18
880	41	880	26	550	9	940	18

admixture at any distance and time t and $R_{s,t}$ is the isotopic composition of the artificial recharge water at time, t .

The calculated percentage tank water contribution to the groundwater at various downstream wells is given in Table 44.1. It is seen that the groundwater recharge from tanks 3 and 4 are comparatively lower than tanks 1 and 2. This is because of the difference in type of soils in that area.

44.5 CONCLUSIONS

From the study, it is concluded that the groundwater quality of open wells close to the irrigation tanks is fresh because of the recharge from the tanks, while open wells away from the tanks are brackish in nature. The observed high concentrations of nitrate in groundwater could be from the application of fertilizers. From the distribution of EC and $\delta^{18}\text{O}$ in the groundwater, the areas of influence of these tanks were demarcated. Using a two component $\delta^{18}\text{O}$ mass balance model, the tanks contribution to the downstream wells was calculated. It is seen that the groundwater recharge from tank 3 and 4 are comparatively lower than tank 1 and 2. This is because of the difference in type of soils in that area.

REFERENCES

1. Rao, S.M.: Practical isotope hydrology. New India Publishing, New Delhi (2006)
2. Shivanna, K., Kulkarni, U.P., Joseph, T.B. and Navada, S.V.: Contribution of storms to groundwater recharge in the semi-arid region of Karnataka, India. *Hydrol.Process*, 18, 473-485 (2004)
3. WHO: Guidelines for drinking water quality, Recommendations, World Health Organisation Geneva, 1, 188 (1996)

Chapter 45

Quantitative Provenance Analysis of Sediments in the Changjiang (Yangtze) River (China)

G. Vezzoli, M. Limonta, E. Garzanti, and S. Yang

Abstract We use quantitative provenance analysis (geochemical analysis; high-resolution bulk-petrography and heavy-mineral analysis, exploratory compositional data analysis and Aitchison distance) on present-day river sediments of the Changjiang (Yangtze) River to quantify the contributions of each tributary to the Changjiang River Delta, and thus to evaluate sediment provenance in the distinct parts of the drainage basin.

Keywords Present-day river sediments • Quantitative provenance analysis • Compositional data analysis • Log-Ratio • Changjiang (Yangtze) River

45.1 INTRODUCTION

Quantitative provenance analysis is a powerful tool for interpreting provenance of modern and ancient terrigenous wedges [1]. In the last ten years the progress towards a comprehensive quantitative model of clastic detritus production and dispersal has been driven by development and use of mathematically rigorous methods of statistical analysis of sediment composition. In fact, geological data are often presented in percentages that represent relative contributions of the single variables to a whole. This means that the relevant information is contained only in the ratios between variables of the data, hereinafter referred to as compositional data, or compositions [2]. Unfortunately, the natural properties of compositional data are in contradiction to most of the methods provided by standard multivariate statistics. In practice, standard statistical methods can lead to questionable results if they are directly applied to the original compositional

G. Vezzoli (✉) • M. Limonta • E. Garzanti

Department of Earth and Environmental Sciences, University of Milano-Bicocca, Milan, Italy

e-mail: giovanni.vezzoli@unimib.it

S. Yang

Laboratory of Marine Geology, Tongji University, Shanghai, China

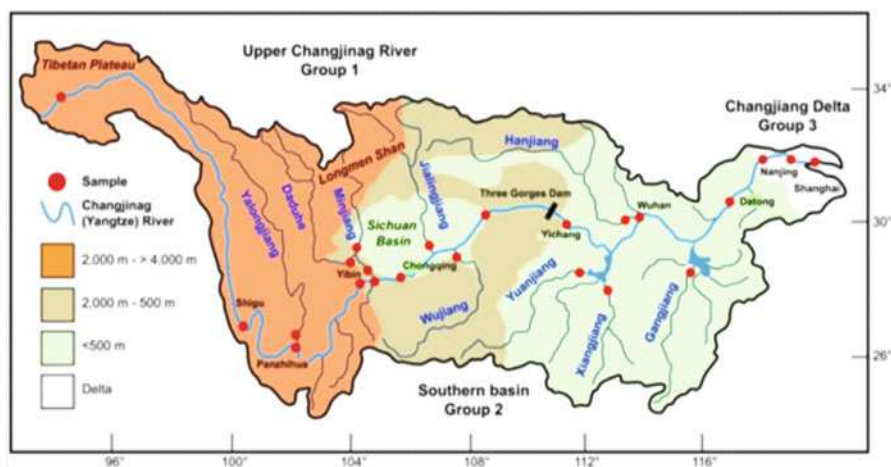


Fig. 45.1 Changjiang basin

data [e.g. 3]. As a suitable alternative, a family of log-ratio transformations from the simplex to the standard Euclidean space were introduced that make the standard statistical analyses viable [2, 3].

45.2 STUDY AREA

The Changjiang River is the third longest river in the world (6,300 km) and the largest river in Asia in term of water discharge (area $1.8 \cdot 10^6 \text{ km}^2$, average discharge $9 \cdot 10^{11} \text{ m}^3/\text{a}$). It drains a variety of different geological units and has a complex source-to-sink sediment-transport system (including the world's largest power station, the Three Gorges Dam, Fig. 45.1).

45.3 MATERIAL AND METHODS

22 sand-sized bedload sediment samples were collected from active fluvial bars of the Changjiang River and its tributaries. 65 suspended load samples (geochemical analysis [4]) were collected from the mainstream and major tributaries of the Changjiang River during the flood seasons of 2001, 2004, 2008 and 2009 (Fig. 45.1). Samples were collected in the upper part of the catchment (group 1, northwestern left-bank tributaries) from the Tibetan Plateau (mean elevation $> 4000 \text{ m}$), through the Longmen Shan fold-thrust belt, to the Sichuan Basin (mean elevation $< 500 \text{ m}$). In the southern part of the basin (group 2, right-bank tributaries) and in the Changjiang Delta (group 3).

45.3.1 Sand and Petrography and Heavy Minerals

In each sample, 400 points were counted by the Gazzi-Dickinson method on the whole sand fraction. Average rank for each sample is expressed by the Metamorphic Index (MI, [5]) which varies from 0 in detritus from unmetamorphosed cover rocks to 500 in detritus from granulite-facies basement rocks. In each sample, 200 to 250 transparent detrital minerals were counted in grain mounts by the area method on the very fine to fine sand fraction (63–250 μm). The abundance of heavy minerals in the sediment is expressed by the heavy-mineral concentration (HMC), which represents a fundamental parameter to be taken into account when estimating relative sediment budgets from heavy-mineral data [6].

45.3.2 Exploratory Compositional Data Analysis

Exploratory compositional data analysis (centre, variation matrix, total variance and biplot of a compositional dataset) was performed by CoDaPack [7] and was used to compute descriptive statistics [8]. Center (Table 45.1) is the closed geometric mean and represents a measure of central tendency for our compositional dataset. The total variance measures the whole relative variability of our compositional dataset (Table 45.2) whereas the variation matrix describes the dispersion in the dataset (i.e. the ratios between variables affected by high or low variability can be identified; Table 45.3).

In order to discriminate homogeneous provenance groups and discover special features related to subcompositions, compositional biplot was used [9] (Fig. 45.2, the problem of zero values was solved by the “multiplicative replacement strategy” [3]). Next, using ternary diagrams after centring data, subcompositional data analysis were performed to evaluate the compositional variability and the patterns of variation of interesting sub-compositions [10] (Fig. 45.2). Finally, in order to quantify the similarity between samples of the groups 1 and 2 with samples of the group 3, the Aitchison distance [2, 3] was calculated (Table 45.4).

45.4 RESULTS AND DISCUSSIONS

Suspended load of the group 1 (uppermost Changjiang reaches in Tibet, Yalongjiang, Daduhe, Minjiang, Jialingjiang and Hanjiang rivers) is characterized by high Al_2O_3 and CaO content. Bedload sands are feldspatho-litho-quartzose with a amphibole-dominated heavy-mineral assemblage including epidote, pyroxene and fibrolitic sillimanite. Suspended load of the group 2 (Wujiang, Yuanjiang, Xiangjiang and Ganjiang rivers) is characterized by high Al_2O_3 content, whereas the bedload includes litho-quartzose and feldspatho-quartzose sands with

Table 45.1 Centers of the compositional data of each group (*n* = sample size of each group)

Geochemistry					Sand petrography							Heavy minerals										
Na2O	CaO	Al2O3	K2O	<i>n</i>	Q	F	Lm	Ls	Lv	MI	<i>n</i>	ZTR	Hgm	P	G	E	A	HMC	<i>n</i>	Group		
0.040	0.234	0.607	0.119	5	0.272	0.085	0.045	0.137	0.051	0.411	10	0.021	0.000	0.172	0.041	0.205	0.505	0.057	10	1		
0.042	0.180	0.655	0.123	8	0.367	0.076	0.026	0.068	0.018	0.444	8	0.197	0.000	0.016	0.076	0.299	0.370	0.042	8	2		
0.039	0.132	0.718	0.111	52	0.278	0.126	0.041	0.052	0.024	0.480	4	0.022	0.000	0.072	0.033	0.211	0.639	0.022	4	3		

Table 45.2 Centred log-ratio variances and total variance (T.V.) of each group

Na ₂ O	CaO	Al ₂ O ₃	K ₂ O	T.V.	Q	F	Lm	Ls	Lv	MI	T.V.	ZTR	Hgm	P	G	E	A	HMC	T.V.	Group
0.004	0.008	0.007	0.004	0.022	0.250	0.217	0.507	0.212	0.831	0.864	2.879	0.561	3.580	0.740	0.367	0.252	0.211	0.396	6.107	1
0.030	0.070	0.008	0.002	0.111	0.335	0.876	0.499	1.110	1.158	0.909	4.887	3.459	11.801	9.085	0.549	1.328	1.268	2.000	29.489	2
0.023	0.079	0.027	0.013	0.141	0.034	0.015	0.049	0.371	0.034	0.057	0.560	0.215	12.704	0.269	0.317	0.828	0.380	1.575	16.288	3

Table 45.3 Variation matrix

	Na2O	CaO	Al2O3	K2O	Q	F	Lm	Ln	Ms	ZTR	ZTR	P	Q	E	A	HMC	HgM	Group
Na2O					0.270	1.488	0.302	0.578	1.823	0.990	0.928	0.409	0.900	1.333	0.900	1.333	0.409	1
CaO	0.0014				0.477	1.477	2.173	2.101	0.669	20.549	3.036	2.803	4.798	6.088	6.088	16.427	2	
Al2O3	0.182	0.024			0.114	0.173	0.041	0.028	0.028	0.435	0.180	1.079	0.748	1.079	1.079	1.344	3	
K2O	0.136	0.040	0.050															
Q	0.0018	0.012					0.934	0.459	1.314	0.985				3.041	3.253	1.321	0.485	4
F	0.119	0.039					2.246	3.875	3.196	0.328			10.749	15.635	14.199	10.306	21.642	5
Lm	0.131	0.189					0.131	0.107	0.436	0.490			0.190	0.450	0.450	0.190	0.447	6
Ln							1.049	3.265	2.845				0.407	0.333	0.770	23.18		7
Ms	0.003						0.709	1.632	1.799				0.877	0.968	0.819	16.893		8
ZTR	0.014						0.300	0.593	0.064				0.717	0.319	1.274	9.461		9
P																		
Q																		
E																		
A																		
HMC																		
HgM																		

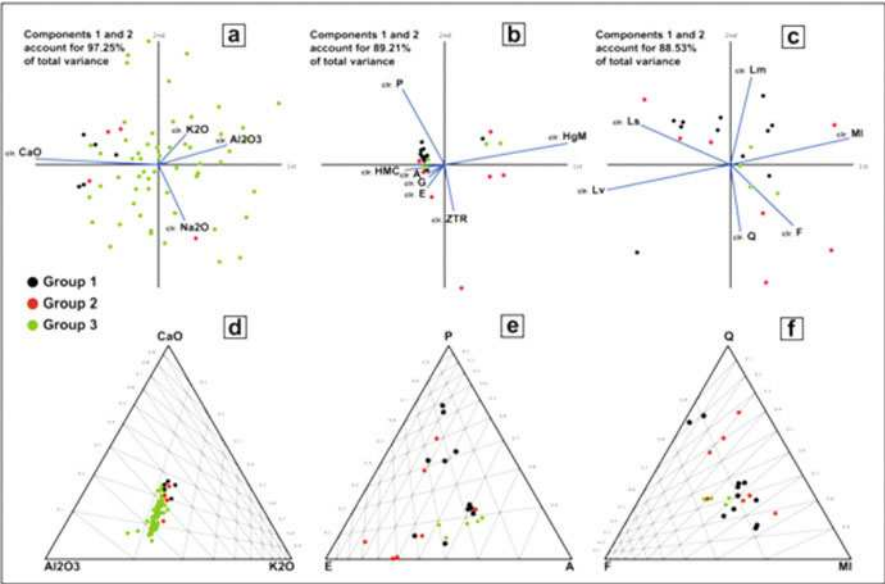


Fig. 45.2 Compositional Biplot.

Table 45.4 Aitchison distance

Group 3	Group 1	Group 2
Changjiang Delta	Tibetan Plateau	Left-bank tributaries
Aitchison distance	24.65	15.74

pyroxenes, zircon and tourmaline. Suspended sediments from the Changjiang Delta are characterized by their high Al_2O_3 content where as sands are litho-feldspatho-quartzose with amphiboles, epidote, pyroxenes and fibroliticsillimanite. The comparison among the centres of the three groups allowed us the identification of those variables that can have an important discriminatory character. The results reported in Table 45.1 showthat group 1 is well discriminated from the other two groups by the high CaO and minor Al_2O_3 contents. At the same time, group 1 is well

discriminated from group 2 by the low values of quartz, MI, zircon, tourmaline, rutile and epidote and high values of sedimentary lithic grains and pyroxenes. Analysis of the total variance reveals that CaO, sedimentary lithic grains and high grade metamorphic minerals (e.g. sillimanite) are the variables characterized by higher relative variability (Table 45.2). The analysis of the the variation matrices (Table 45.3) indicates that the ratios involving CaO, Ls, MI, HgM and P variables are characterized by high variability. In order to discriminate homogeneous provenance groups within our data set, we used the compositional biplot (Fig. 45.2). In Fig. 45.2a the three groups are clearly differentiated, with the samples from group 3 showing a high dispersion when compared with the two others. In general, the three groups maintain a quite good separation also in the mineralogical and petrographic biplots (Fig. 45.2b, 45.2c). Combining the information from Table 45.1 and biplots (variables whose centres are very different and whose rays form angles higher than 90) it was possible to select a “good” three-part subcomposition for obtaining a clear discrimination among the three groups (Fig. 45.2). The ternary diagram of subcomposition CaO, Al_2O_3 and K_2O discriminates samples from group 1 by their high CaO content, whereas samples of group 3 are characterized by higher content of Al_2O_3 (Fig. 45.2d). The ternary diagram of subcomposition P, E, and A discriminates samples of group 3 from samples of the others two groups by their amphiboles and epidote content (Fig. 45.2e). The ternary diagram of subcomposition Q, F, and MI differentiates samples of group 3, characterized by feldspars, from samples of the group 1 and 2 characterized by quartz and metamorphic lithic grains (Fig. 45.2f). Results from the Aitchison distance indicate the best similarity between samples of group 1 and samples of group 3 (Table 45.4). However, this result is not uniform. Within group 1, only the samples from the left-bank tributaries of the upper Changjiang River show the best similarity, instead, samples of the Tibetan plateau have a low similarity with Changjiang delta samples. The same small similarity was obtained for the samples of the right-bank tributaries of the Changjiang River in the southern part of the basin (group 2).

45.5 CONCLUSIONS

Quantitative provenance analysis (geochemical analysis; high-resolution bulk-petrography and heavy-mineral analysis, exploratory compositional data analysis and Aitchison distance) indicated that the left-bank tributaries in the northwestern part of the drainage basin (group 1; Daduhe, Minjiang, Jialingjiang and Hanjiang rivers) are the most important in supplying sediment to the Changjiang River Delta (group 3). The rivers draining the eastern edge of the Tibetan plateau (group 1) do not appear to dominate the modern sediment budget [11], as well as the right-bank tributaries (group 2) in the southern part of the basin (e.g. Wujinag, Gangjiang). Finally, we also observed no significant change in the river composition downstream of the Three Gorges Dam.

REFERENCES

1. Weltje, G.J. and von Eynatten, H.: Quantitative provenance analysis of sediments: review and outlook. *Sedimentary Geology*, 171, 1–11 (2004)
2. Aitchison, J.: The Statistical Analysis of Compositional Data. Chapman and Hall, London, 416 pp. (1986)
3. Buccianti, A., Mateu-Figueras, G. and Pawlowsky-Glahn, V. (Eds): Compositional Data Analysis in the Geosciences: from Theory to Practice: Geological Society, London, Special Publications, 264 (2006)
4. Shao, J.Q. and Yang, S.Y.: Does chemical index of alteration (CIA) reflect silicate weathering and monsoonal climate in the Changjiang River basin? *Chinese Science Bulletin*, 57, 1178–1187 (2012)
5. Garzanti, E. and Vezzoli, G.: A classification of metamorphic grains in sands based on their composition and grade. *J. Sediment. Res.*, 73, 830–837 (2003)
6. Garzanti, E. and Andò, S.: Heavy-mineral concentration in modern sands: implications for provenance interpretation. In: Mange, M., Wright, D. (Eds), Heavy Minerals in Use. Developments in Sedimentology Series, 58. Elsevier, Amsterdam, 517–545 (2007)
7. Comas-Cufí, M. and Thió-Henestrosa, S.: CoDaPack 2.0: a stand-alone, multi-platform compositional software. In: Egozcue, J.J., Tolosana-Delgado, R., Ortego, M.I. (Eds), CoDaWork'11: 4th International Workshop on Compositional Data Analysis. Sant Feliu de Guíxols (2011)
8. Daunis-I-Estadella, J., Barceló-Vidal, C. and Buccianti, A.: Exploratory compositional data analysis. In: Buccianti, A., Mateu-Figueras, G. and Pawlowsky-Glahn, V. (Eds.), Compositional data analysis in the geosciences: from theory to practice: Geological Society of London Special Publications, 264, 161–174 (2006)
9. Gabriel, K.R.: The biplot graphic display of matrices with application to principal component analysis. *Biometrika*, 58, 453–467 (1971)
10. von Eynatten, H., Pawlowsky-Glahn, V. and Egozcue, J.: Understanding perturbation on the simplex: a simple method to better visualise and interpret compositional data in ternary diagrams. *Mathematical Geology*, 34, 249–257 (2002)
11. He, Mengying, Zheng, Hongbo, Bookhagen, Bodo and Clift, Peter D.: Controls on erosion intensity in the Yangtze River basin tracked by U-Pb detrital zircon dating. *Earth Science Reviews*, doi: [10.1016/j.earscirev.2014.05.014](https://doi.org/10.1016/j.earscirev.2014.05.014) (2014)

Chapter 46

Textural Variation of Sediments in the Course of a Small River: A case study from Khurar River, Khajuraho, Chhaterpur District, Madhya Pradesh, India

S. Kanhaiya and B.P. Singh

Abstract Textural (grain size) analysis is one of the parameter that helps in determining sedimentary environment. In the present investigation, texture was analysed from sixteen stations in the Khurar River, Madhya Pradesh. Grain size analysis was carried out employing mechanical sieving method using a sonic shaker. Frequency and cumulative frequency curves were prepared from the grain size data on centimetre and arithmetic probability papers, respectively. The ϕ values were determined and used to calculate the statistical parameters such as mean, standard deviation, skewness and kurtosis. It is found that the mean value varies from -0.63 to 0.80 with a graphic mean distribution ranging from -0.27 to 0.40 ϕ , indicating that the size of the river sand is very coarse- to coarse-grained. The standard deviation (sorting) shows a range of 0.69 to 1.65 ϕ , while the skewness values of the sediment samples range from 0.19 to 0.29 ϕ , thus indicating the presence of fine fraction to near-symmetrical fraction in the population. The kurtosis varies between 1.03 and 1.09 ϕ , indicating that 25% of the samples are leptokurtic, 6.25% are very leptokurtic, 50% are mesokurtic and 12.5% are platykurtic. The platykurtic nature in few cases suggests mixing of the sediments from two sources. Bivariate plots prepared combining different textural parameters were used to interpret their behaviour in the river sediments. C-M plot was also prepared to understand the dominant mode of transportation in the Khurar River sediments. In this river all the sediments are dominantly characterized by the rolling process of deposition. This study reveals that sorting varies from poorly sorted to moderately well sorted from upstream to downstream part of the river may be because of dominance of winnowing and selective sorting in the lower reaches of the river.

Keywords Grain size • Kurtosis • Standard deviation • Sieving • Skewness

S. Kanhaiya (✉) • B.P. Singh

Centre of Advance Study in Geology, Banaras Hindu University, India

e-mail: shyamkanhaiya44@gmail.com

46.1 INTRODUCTION

Texture (grain size) is the most fundamental property of sediment particles, affecting their entrainment, transport and deposition [1]. It helps in determining depositional environment, besides others. Grain size analysis provides important clues to the sediment transportation history, depositional conditions and provenance [2, 3]. In this study, the stream sediments of Khurar River, have been collected (starting from upstream to downstream direction) and analysed. Grouped data of grain sizes, obtained by sieving technique are presented in a table. Different modes of sediment transportation have been identified by plotting the cumulative frequency distributions of grain sizes on probability paper. The net distribution is then divided into traction load (coarsest fraction), saltation load (medium fraction) and suspension load (finest fraction). The textural parameters were then computed graphically following Folk and Ward [2] and Friedman [3].

46.2 GENRAL AND GEOLOGICAL FEATURES OF THE RIVERS

The Khurar River flows exclusively on Archean rocks of Bundelkhand carton. This comprises over ~29, 000 km² area in north-central India. The carton consists of slivers of Archean greenstone successions within granitoids and gneisses. The origin of the Khurar River originates from the Beni Sagar reservoir (Lat. 24°48' 3.5" N and Long. 79°52'59.6" E), village Saddupura (Maharajganj) near Khajuraho town in Chhaterpur district, Madhya Pradesh, India. This river is serving as one of the tributaries of Ken River (tributary of river Yamuna). It is a small river and the length of the river is about 34 kilometres. It conflues with Ken river at Ghadiyal pond, near renneh fall in the area of Panna tiger reserve (Lat. 24°54' 13.9" N and Long. 80°2'6" E) and flows from SW to NE direction (Figure 46.1). The width of the river is ranging from 5 to 15 meter and average velocity is 2.5 meter/second. There are many small braid-bars (2-4 m large) in the middle of the channel.

46.3 SAMPLING AND METHODOLOGY

A total of forty-eight sediment samples from sixteen stations those occurs on the braid-bars were collected in the entire course of the Khurar River at an interval of about one kilometre (Figure 46.1). Sampling sites were positioned by GPS and all the samples were collected in the mid channel of the river and two hundred gram by weight. One each sample from each station was utilized for sieving analysis by coning and quartering method. Sieves being spaced at definite intervals were arranged on half phi (ϕ) intervals starting from 10 mesh (-1 ϕ), 14 mesh (-0.5 ϕ), 18 mesh (0 ϕ), 25 mesh (0.5 ϕ), 35 mesh (1.0 ϕ), 60 mesh (2.0 ϕ), 120 mesh (3.0 ϕ),

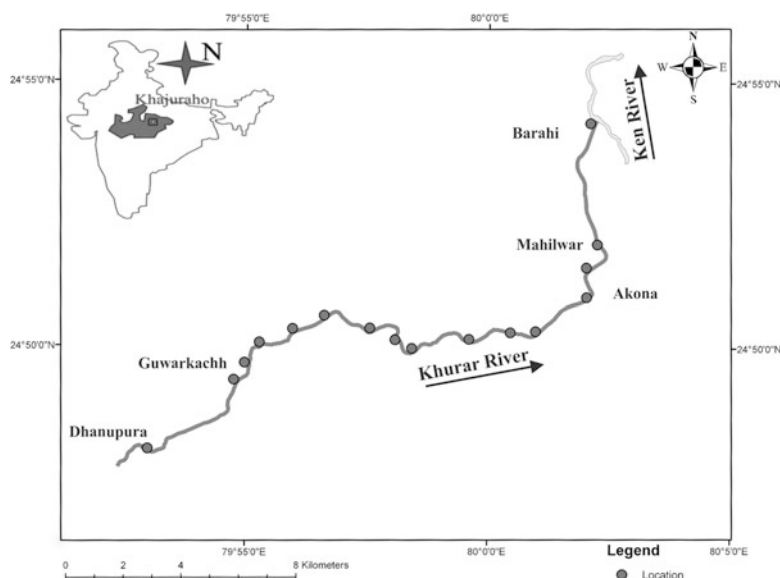


Fig. 46.1 Sampling location of the Khurar River

170 mesh (3.5 ϕ), 230 mesh (4.0 ϕ), and shook for fifteen minutes followed by weighing of each retained fraction. Individual weight percentages were recalculated to hundred for making them percentage. The frequency curves were prepared on simple graph paper. Cumulative curves were plotted on arithmetic probability graph paper. The graphic parameters proposed by Folk and Ward [1], C-M plot to evaluate the hydrodynamic force working during the deposition proposed by Passega [4] and log-probability values proposed by Friedman [3] were calculated from the percentile values (in Φ units) of the cumulative curves. Following folk and ward [2] bivariate plots were plotted considering various textural parameters.

46.3.1 Grain Size Distribution and Cumulative Frequency Curves

Grain size analysis is a classical tool and provides additional information regarding sediment transport, energy conditions and depositional environment. Various textural parameters such as graphic mean, standard deviation (sorting), skewness and kurtosis have environmental significance and are useful for understanding syn sedimentary hydrodynamic factors of transportation and deposition in a basin [2–4]. Frequency curves show that most of the samples are bimodal in nature, except few unimodal ones. On the basis of frequency curves it is observed that the sizes of the sediments are ranging from very coarse to coarse-grained. Sediments are ranging from poorly sorted at starting points and moderately-sorted to moderately well-sorted as we go towards confluence point of the river with Ken River (Figure. 46.2). The cumulative

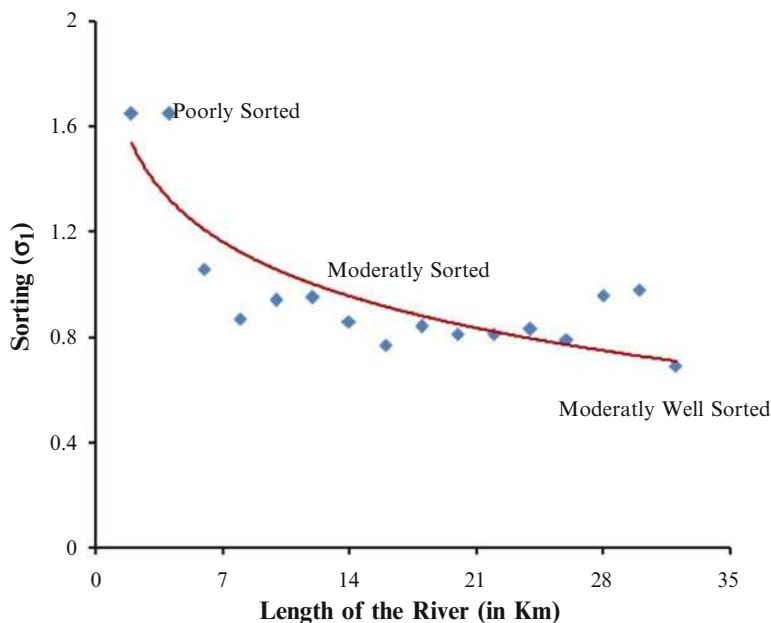


Fig. 46.2 Sorting of the sediment with length of the river

frequency curve show three to four segments in each case representing traction, saltation I, saltation II and suspension fraction within the sediments. In general, the traction and saltation loads dominate over the suspension load.

46.3.2 Log-probability Curves

Log-probability curves proposed by Visser [5] had been plotted on the log probability (ordinate) paper indicate the mode of transportation of sediments within a depositional medium [5]. These plot indicates two or three straight line rather than a single straight line. Each segment of the curve is interpreted to show different sub population of grain that were transported simultaneously but by different ways i.e. suspension, saltation and traction bed load. Grain size probability plots for river sands are uniquely segmented into three differently sloped components because river move material in three ways: by suspension, by saltation and as bedload [5]. All the sixteen samples had been plotted on log probability paper and compared with established trend for modern and ancient fluvial deposits proposed by Visser [5], generally showing the dominance of saltation with traction and suspension domain also. These plots also indicates sorting of the sediment, where most of the sediments are moderately sorted probably due to prolonged transport and winnowing processes. In the present case, the sediments show moderate sorting even in the coarse of short distance may be because of winnowing and selective sorting of the sediments within the river.

46.3.3 Textural Parameters and Their Inter-relationship

All the textural parameters were calculated from cumulative curves, based on different phi values. The formula given by Folk and Ward [2] is regarded as most suitable and used for calculation of different textural parameter in the present study. In the studied samples, the mean size varies from -0.63ϕ to 0.80ϕ , the sorting varies from 0.69 to 1.65ϕ , the skewness varies from -0.23ϕ to $+0.29\phi$ i.e. near-symmetrical to very fine-skewed and the kurtosis varies from 0.69 to 1.77ϕ . The inter-relationship plots between different parameters are recognisance tool to interpret various aspects of depositional environment [3]. Following folk and ward [2], six bivariate scatter plots are prepared by the combination of various textural parameters. The entire bivariate scatter plots suggest bimodal nature of sediments and a dominance of the sand mode mixed with a very small amount of silt.

46.3.4 C-M Plot

In the present study C-M plot proposed by Passega [4] is used to understand the dominant mode of transportation and the environment of deposition. All the hydrodynamic forces working during the deposition of the sediments have been analysed and interpreted by C-M plot [4]. The C and M show that these parameters are indicators of hydraulic conditions under which sediments are deposited. C-M diagrams in which C is the one-percentile, M the median of the grain-size distribution, characterize the coarsest fractions of the samples [6]. Percentile of the size distribution (C) in microns had been plotted against the median of the size distribution in microns (M) for the sediments (Figure. 46.3). It is observed that all the river sediments are above the CR line existing in segment N-O of the pattern. It

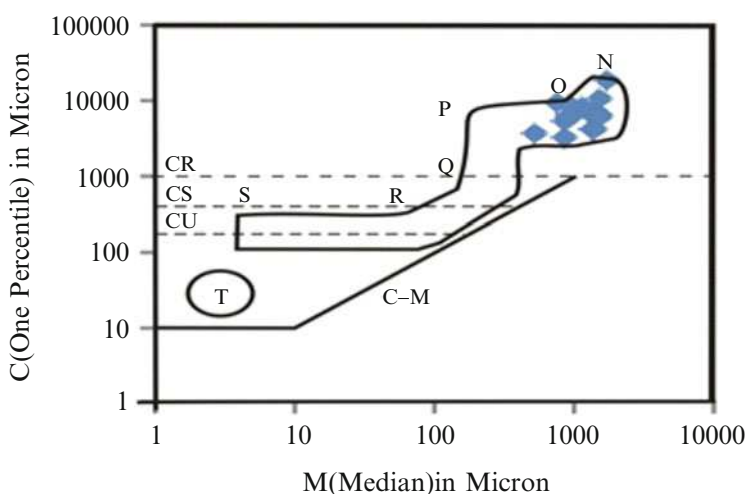


Fig. 46.3 C-M plot showing concentration of points in upper left corner

indicates fairly well sorted sediments, almost entirely transported by rolling. Thus, the sediments dominated by coarse and very coarse sand deposited by the process of rolling in the Khurar River.

46.4 CONCLUSIONS

The frequency curves are dominantly indicative of coarse to very coarse-grained nature of the sediments. The graphic mean value indicates the more or less equal distribution of both very coarse and coarse sand-size particles. In general, the samples show poor sorting in beginning followed by moderate sorting to moderately well sorting at last site where the river Khurar conflues with river Ken. In most of the samples, both peak and tails are equally sorted giving rise to mesokurtic condition. All the bivariate plots between mean, skewness, kurtosis and standard deviation are indicative of bimodal nature of sediments, among them sand-size (very coarse to coarse) is dominant with subordinate silt. All the sediments of Khurar River are characterized by the rolling process of deposition. The log-probability curves of samples are showing dominance of saltation with traction and suspension. The change of sorting from poorly-sorted to moderately-sorted and moderately well- sorted suggests that the winnowing and selective sorting is possible even in the small river depending upon the hydrodynamic conditions of the river.

REFERENCES

1. Flemming, B.W.: The influence of grain-size analysis methods and sediment mixing on curve shapes and textural parameters: Implications for sediment trend analysis, *Sedimentary Geology*, 202, 425–435 (2007)
2. Folk, R.L. and Ward, W.C.: Brazos River bar: a study in the significance of grain size parameters. *Journal of Sedimentary Petrology*, 27, 3–26 (1957)
3. Fraidman, G.M.: Differences in size distributions of populations of particles among sands of various origins. *Sedimentology*, 26, 3–32 (1979)
4. Passega, R.: Grain size representation by C-M pattern as a geological tool. *Journal of Sedimentary Petrology*, 34, 830–847 (1964)
5. Visher, G.S.: Grain size distributions and depositional processes. *Journal of Sedimentary Petrology*, 39, 1074–1106 (1969)
6. Passega, R.: Significance of C-M diagrams of sediments deposited by suspension. *Sedimentology*, 24, 723–733 (1977)

Chapter 47

Particle Size Characteristics of Ramganga Catchment Area of Ganga River

M.Y.A. Khan and G.J. Chakrapani

Abstract Rivers constitute the lifeline for any country. Both natural and anthropogenic processes influence the river processes. Recently, erosion processes and fluvial transport of materials have become a focus of reviving attention owing to their significance in land use and environmental aspects. To understand the erosion process and sediment geochemistry, more than 25 samples were collected from river Ramganga. Ramganga River originates from a Namik glacier in Gairsain village of Chamoli district in Uttarakhand lying at an elevation of 2926metres. Ramganga River flows in the Kumaon Himalayas and is the first major tributary of river Ganga in the Indo-Gangetic plains. The study area includes the entire catchment of river Ramganga covering a stretch of approx. 350 km from the Chamoli district in Uttarakhand to Farrukhabad district in Uttar Pradesh before joining with the Ganga River on its left bank at an elevation of 124 meters. The river bank sediments were evaluated for their size determination by using the particle size analyzer. All the sediments were treated with H_2O_2 to remove organic matter; the computed results were interpreted using the statistical approach mentioned by [2]. Most of the sediment were found to be of sand grade and are well sorted to poorly sorted in nature. Population of sediments varies from being coarse skewed to fine skewed. An attempt has been made to find out the factors controlling the sediment size. Multivariate analysis was performed to find out the relation of sediment size with discharge and climatic conditions such as rainfall. The results point out the role of topographical, lithological, and climatic factors in determining the grain size of sediments.

Keywords Ramganga River • Suspended sediment • Grain size

M.Y.A. Khan (✉)

Department of Earth Sciences, Indian Institute of Technology Roorkee, Roorkee, India
e-mail: yawar.gr44@gmail.com

G.J. Chakrapani

Department of Earth Sciences, Indian Institute of Technology Roorkee,
Roorkee, Uttarakhand, India

47.1 INTRODUCTION

Oceans intakes the major quantity of sediment loads from the rivers. It is expected that river transported about $15-16 \times 10^9$ tons of sediments annually to the oceans [5, 9]. [8] reported that about 1.2 billion tons of sediments are transported by Indian rivers to the ocean. Along the other Indian river, the Ganges River transports about 1600×10^{12} grams of total suspended sediments to the Bay of Bengal [7]. Particle size characteristics information of the suspended sediment transported by rivers played important role in order to quantifying and modelling the transport of sediment and sediment related pollutants, including nutrients, heavy metals, micro- organics and radionuclides in the course of river systems [10].

The Ramganga River (Fig. 47.1) is one of the most important northern tributary of Ganga River with mean annual discharge of $537 \text{ m}^3 \text{ s}^{-1}$ [1] ; drains the part of Kumaon Himalayas range and the parts Ganga Flood Plains in Uttar Pradesh, India. According to the report published by Central Water Commission, India in 2012, the average annual rainfall observed in the period from 1996 to 2000 is 900 mm with total number of rainy days being 75. Despite of the important geographical features of this river, there is no data available on grain size distribution of bottom sediments and suspended sediment matter. The focus of this paper is to gather information on the particle size characteristics of suspended sediment transport of Ramganga River, first major tributary of the Ganga River Basin, India.

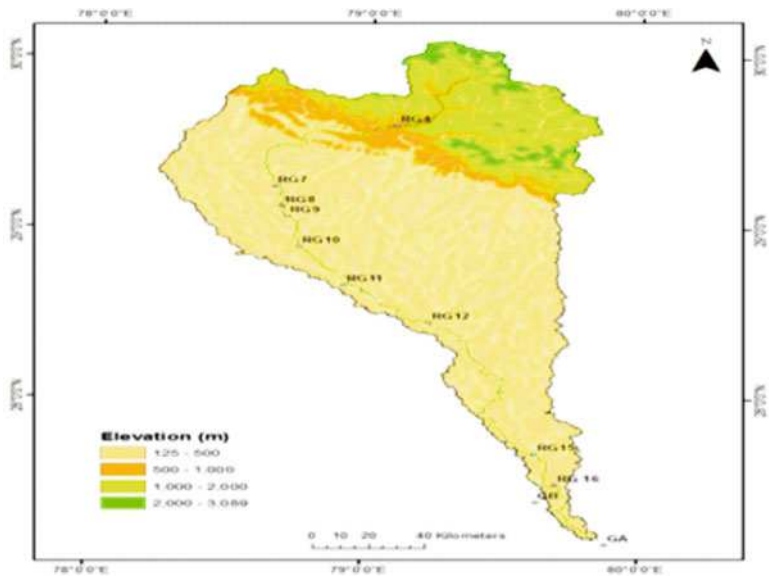


Fig. 47.1 Ramganga river catchment

47.2 STUDY AREA

The Ramganga river, is a part of Ganga river originating from Namik glacier, which rises from Dudhotali Mountain in the village named “Garsain” located Chamoli district of central Uttarakhand, at an elevation of 3024 meters above Mean Sea Level (MSL). The basin ($30^{\circ}06'02.22''$ N to $27^{\circ}10' 42.11''$ N and $79^{\circ} 16' 59.22''$ E to $79^{\circ} 50' 16''$ E) covers a total catchment area of 32,493 km² and has a total length of 350 km. During the monsoon period the discharge of the river is 10000 m³/Sec, whereas only 5 m³/Sec during summer. Geologically, Ramganga River constitutes of two major lithotectonic zone of Sub Himalayas and lesser Himalayas. The most important lithologies of the area in the hilly terrain are calcareous shales and siltstones of Blaini/Infrakrol formations; quartzites of Nagthat and Sandra formations; low-grade metamorphics of phyllites, slates and schists; limestones of Krol and Deoband formations; and high-grade metamorphics of granite gneisses [3]. In Ganga Flood Plains the important lithotectonic zones are Varanasi Older Alluvium and Newer Alluvium with major lithologies of sand, silt and clay [4].

47.3 MATERIAL AND METHODS

5 L Volume of sample was taken from 11 different locations for assessing the grain size characteristics of suspended sediments of sample. In the laboratory these samples were filtered through a 0.45 µm filter paper. The material which was retained on the filter paper after filtering the sample is suspended sediment. For grain size distribution these samples were analyze in the particle size analyzer.

47.4 RESULTS AND DISCUSSION

To interpret the grain size characteristics (Table. 47.1), the statistical method developed by [2] was applied. Generally, all the sediment samples from upstream to downstream are found to be poorly sorted due to high river energy, variable

Table 47.1 Statistical parameters of samples

Locations	Mean size (µm)	Sorting (µm)	Skewness (µm)	Kurtosis (µm)
RG4	48.28	2.631	−0.122	0.952
RG7	45.78	2.563	−0.125	0.953
RG8	117.1	3.297	−0.269	0.821
RG9	71.08	2.981	−0.253	0.823
RG10	73.96	3.757	−0.142	0.951
RG11	186.8	3.26	−0.349	0.876
RG12	219.9	2.592	−0.345	1.425
RG15	64.36	2.891	−0.116	0.817
RG 16	94.53	3.877	−0.379	0.737

source of sediments such as glaciers origin mask wasting and different lithologies along the river course [6]. Most of the sediments belong to the category of fine skewed to very fine skewed and mesokurtic to platykurtic except RG12 which is leptokurtic. Distribution of grain size in the suspended sediments has been examined in the samples taken from the Ramganga River during the Feb 2013 post monsoon period. Fine sands and silts are present in all suspended sediment samples whereas clay fractions are found to be absent.

In terms of the mean size, suspended sediments vary between 0.05 and 0.20 mm. There is no such variableness were found in suspended sediments d_{50} , from upstream to downstream (Fig. 47.2), except for two samples (RG11 and RG12), which shows a high increase in d_{50} value at 500 m. This individuality is may be due to the draining of highly polluted water into the river at these two locations

From Fig. 47.3 (a) it can be observed that there is no such high variation was found in the concentration of suspended sediment if we go from downstream to upstream but if highly concentrate on the given plot we found a little decrease in

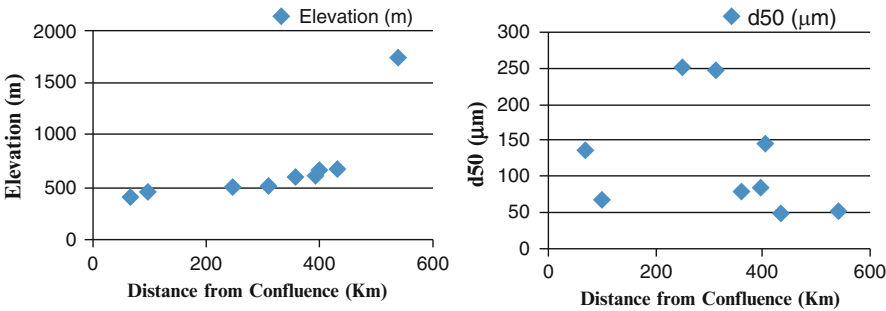


Fig. 47.2 Longitudinal section and suspended sediment median diameter (d_{50}) of the Ramganga river basin.

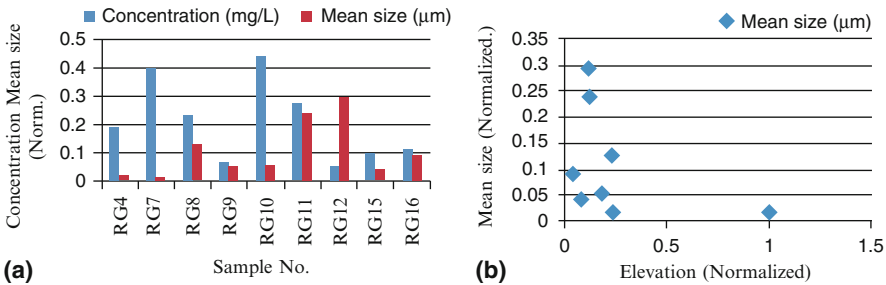


Fig. 47.3 (a) Concentration and mean grain size distribution at sample points and (b) Mean grain size vs elevation.

concentration from upstream to downstream. This is due to the differences in the geomorphology of the river in upstream and downstream. In upstream, the river crosses different bedrock geology of Lesser and Sub Himalayas while in downstream the rivers flows through Ganga Flood plains. The other reason of this variation in concentration was the construction of Ramganga dam in between the upstream and downstream of the river. The variation of mean grain size with elevation was plotted and shown in Fig. 47.3 (b). A linear relation with an inverse slope was clearly observed. It is assumed that as the elevation increases, the collision energy is higher and sediment storage capacity is low. Thus abrasion should dominate over selective sorting of grain sizes.

47.5 CONCLUSIONS

Suspended sediments of the Ramganga River are varies in between .003 mm to .4 mm in size. The d_{50} value of the sediment was not showing much variation except for two locations. There are significant spatial variations in the suspended sediments with no clear trend. However, there was considerable reduction in the concentration in suspended sediments as we went downstream. As the elevation increases, the collision energy increases and sediment storage capacity becomes low. Thus abrasion should dominate over selective sorting of grain sizes. The work is going on and has not been completed as of now and as such the authors cannot zero in to conclude the grain size distribution characteristics of Ramganga River. The sampling and analysis of particle size characteristics is being carried out for monsoon season and the results will be published in suitable journal and conferences.

REFERENCES

1. CWC (Central Water Commission): Environmental evaluation study of Ramganga major irrigation project. Central Water Commission. Vol 1 (2012)
2. Folk, R.L. and Ward, W.C.: Brazos river bar: a study in the significance of grain size parameters. *Journal of Sedimentary Petrology*, 27(1), 3–26 (1957)
3. Gupta, R.P. and Joshi, B.C.: Landslide hazard zoning using the GIS approach - A case study from the Ramganga catchment, Himalayas. *Engineering Geology*, 28, 119–131 (1990)
4. Khan, A.U. and Rawat, B.P.: Quaternary geology and geomorphology of a part of Ganga basin in parts of Bareilly, Badaun, Shahjahanpur and Pilibhit district, Uttar Pradesh. G.S.I. (1990)
5. Milliman, J.D. and Meade, R.H.: World-wide delivery of river sediments to the oceans. *Jour. Geol.*, 91(1), 1–21 (1983)
6. Pandey, S.K., Singh, A.K. and Hasnain, S.I.: Grain-size distribution, morphoscopy and elemental chemistry of suspended sediments of Pindari Glacier, Kumaon Himalaya, India. *Hydrological Sciences-Journal-des Sciences Hydrologiques*, 47(2), 213–226 (2002)

7. Richey, J.E.: Interaction of C, N, P, and S in river systems: A biogeochemical model. *In*: B. Bolin and R.B. Cook (Editors), *The Major Biogeochemical Cycles and Their Interactions*. Wiley, New York, pp. 365–383 (1983)
8. Subramanian, V., Biksham, G. and Ramesh, R.: Environmental geology of peninsular river basins of India. *Jour. Geol. Soc. Ind.*, 30, 393–401 (1987)
9. Walling, D.E. and Webb, B.W.: The spatial dimension in the interpretation of stream solute behavior. *Jour. Hydrol.*, 47, 129–149 (1983)
10. Walling, D.E.: Suspended sediment transport by rivers: A geomorphological and hydrological perspective. *Arch. Hydrobiol.*, 47: 1–27 (1996)

Chapter 48

Spatial and Temporal Variability in Grain Sizes of Alaknanda River

S. Panwar and G.J. Chakrapani

Abstract Recent studies have probed grain size analysis to understand the transport energy, deposition, source of the sediments in rivers. Sediment size also relates to the geochemical composition of the sediment and for predicting the response of climate and anthropogenic activities on watersheds. Following the approach of Folk and Ward, 1957 grain size characteristics were evaluated for the channel sediment sampled from river Alaknanda during different time periods. River Alaknanda is one of the major tributary of River Ganga flowing in Garhwal Himalayas. The erosion rate in the Alaknanda basin is very high, almost double the world's average; a large number of landslides occur in the entire watershed which are caused naturally due to steep slopes and lithology and nowadays promoted by increased anthropogenic disturbances and thus in this case grain size becomes the fundamental character to understand the river processes. Grain size was evaluated by using a particle size analyzer. The different time period data highlights the spatial and temporal variation in the statistical parameters of grain sizes. The values of mean size, sorting, skewness and kurtosis varies considerably. It was found that sand dominates in most of the samples. Well sorted to poorly sorted nature of the sediment was observed. The skewness and kurtosis values show the heterogeneous nature of grain sizes. An approach has also been followed to discriminate the grain size distribution of two different intervals by using the ANOVA test. A one way ANOVA test was performed to estimate the remarkable difference in the mean values of grain size parameters of two samples. ANOVA results confirm that significant differences exist between the samples. The outcome of the study demonstrates the influence of discharge, river energy, erosion rate and seasonal variability in determining the sediment size.

Keywords Grain size • Alaknanda River • skewness • kurtosis • ANOVA Test

S. Panwar (✉)

Department of Earth Sciences, Indian Institute of Technology Roorkee, Roorkee, India
e-mail: sugandha.panwar@gmail.com

G.J. Chakrapani

Department of Earth Sciences, Indian Institute of Technology Roorkee,
Roorkee, Uttarakhand, India

48.1 INTRODUCTION

The contribution of river Ganga and Brahmaputra to the world's annual suspended flux accounts for ~25% [1]. The Ganga River in its upstream fetches most of its water and sediment load from its tributary named Alaknanda that flows in the Garhwal Himalayas. The sediment erosion rate of Alaknanda River is $\sim 356 \text{ t-km}^2/\text{yr}$ that is double of the world physical denudation rate [2] at Devprayag. Alaknanda river has higher impact on the water chemistry of Ganga more than the companion river Bhagirathi [2–5]. The grain size analysis of a river is useful for understanding the river energy, geomorphology and anthropogenic disturbances [6, 7]. Spatial and temporal variation in discharge, lithology, climate, and vegetation are among the factors that influence the bed load grain size of a river [7, 8]. In this part of the Himalayas, where high discharge during the monsoon months is an attribute, the grain size studies are essential to understand the nature of sediment during the different seasons.

48.2 STUDY AREA

The study has been carried out for the Alaknanda River which is a major tributary of river Ganga. The river originates from the snout of Sanopath and Bhagirathi Kharak glaciers in the state of Uttarakhand, India. At Devprayag, the confluence of river Alaknanda with Bhagirathi River, gives river Ganga its formal name. The catchment area of river Ganga at Devprayag is $19.6 \times 103 \text{ km}^2$ of which Alaknanda watershed covers an area of $11.8 \times 103 \text{ km}^2$ [3]. The Alaknanda River originates in the Higher Himalaya and drains through the Central Crystallines and Lesser Himalayan formation comprising of granites, gneisses, schist, phyllite, carbonates, massive quartzite, slates, and greywacke [9]. The catchment area is characterized by steep slopes, high vegetation, vast drainage system and high monsoon rainfall. The study area map of Alaknanda basin is shown in Fig. 48.1.

48.3 METHODOLOGY

To study the grain size variability, six bed load sediments were collected from the Alaknanda River during October, 2012 (post-monsoon) and March, 2014 (pre-monsoon) to find out the spatial and seasonal variability in the grain size and factors influencing them. Grain size distribution was estimated by using a Particle Size Analyzer (Model Coulter LS230), which uses laser diffraction pattern to calculate the diameter of the grain. Grain size characteristics were evaluated by Folk and Ward, 1957 method [10]. To confirm the seasonal variability in the mean grain sizes, one-way ANOVA test was performed.

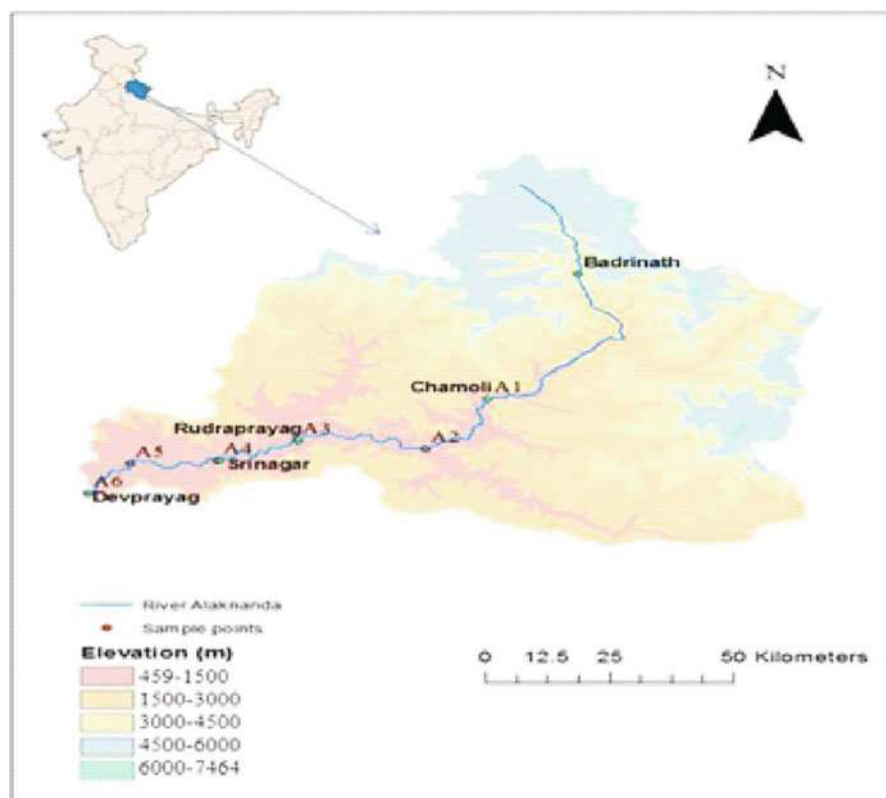


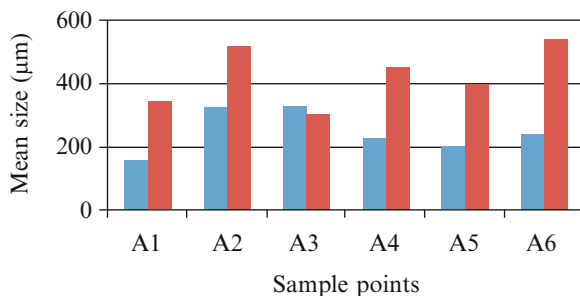
Fig. 48.1 Study area map showing Alaknanda watershed and the sample location sites

48.4 RESULTS AND DISCUSSION

48.4.1 Grain Size Parameters of River Sediments

Sediment size depends on stream flow conditions, climate, geology and anthropogenic activities. Folk and Ward, 1957 mentioned the statistical parameters to interpret particle size characteristics [10]. Considering the mean size, varying from 158.1-330 μm ($1.6-2.7\Phi$) during the post monsoon to 308.1-540 μm ($0.9-1.7\Phi$) during the pre-monsoon month; downstream decrease in grain size was not found (Fig. 48.2), revealing that there are many local factors influencing the river energy that determines the grain size esp. the slope. On certain locations, steep slope aids in increasing the river energy and helps in the transportation of larger grains. But a vast variation in grain sizes was found during the two seasons. This shows the climatic effect in governing the grain size. During the months of June-July, there is an intense monsoon rainfall in this part of the Himalayas that influence the river discharge and thus the texture of the river sediments. Fig. 48.3(a-l) shows

Fig. 48.2 Mean grain size (μm) variation in post- and pre-monsoon sample; blue (post-monsoon) and red (pre-monsoon) result



that sediments are moderately sorted in both the post-monsoon and pre-monsoon season except the sample from Chamoli (Sample no. A1) which shows poorly sorted nature during the pre-monsoon month due to low river energy. The high river energy during the post-monsoon months due to high glacial melt may result in sorting of the sediments. The skewness values also show the seasonal change, but mostly being fine-skewed. The kurtosis value that shows the peakedness of the probability distribution shows the mesokurtic range during the post monsoon season; but mesokurtic to leptokurtic value during the pre-monsoon months.

48.4.2 ANOVA Test and Grain Size Distribution

Statistical parameters mentioned above shows a significant variation in grain sizes both spatially and temporally. Significant difference between two seasonal samples was supported by performing the one way ANOVA test. Table 48.1 shows that for every grain size parameter (M_z , Φ , σ , Sk , KG), $F > F_{crit}$. Therefore, null hypothesis is rejected in this case and it can be inferred that there exist a significant difference in the grain size variability both spatially and temporally. The result confirms that slope, rainfall, tectonics and lithology are among the factors that may influence the bed load grain size.

48.5 CONCLUSIONS

Significant differences exist in the grain size parameters. The mean size of the sediment varies from being fine to medium grained during the post-monsoon month to medium to coarse grained during the pre-monsoon. The skewness value shows the dominance of fine grained fraction. But no generalized pattern was found considering the spatial variation in grain size, though a good seasonal variation was observed. The results point out the fact that there are many variables that influence the grain size characteristics in the Alaknanda catchment area. The foremost characteristic was found to be the discharge that varies seasonally; other

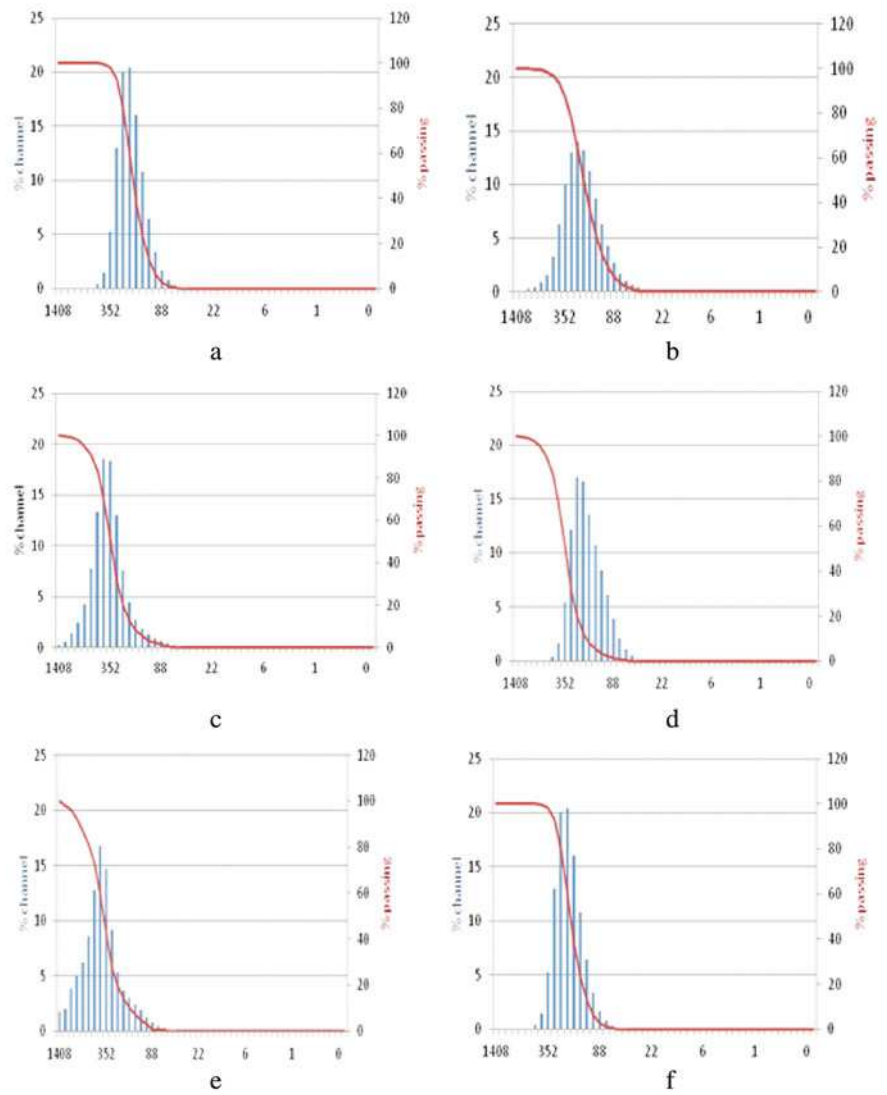


Fig. 48.3 Grain size variability of the Alaknanda sediments, (a-b) indicate sample A1; (c-d) indicate A2; (e-f) A3; (g-h) A4; (i-j) A5; and (k-l) A6 during the pre-monsoon and post-monsoon season respectively

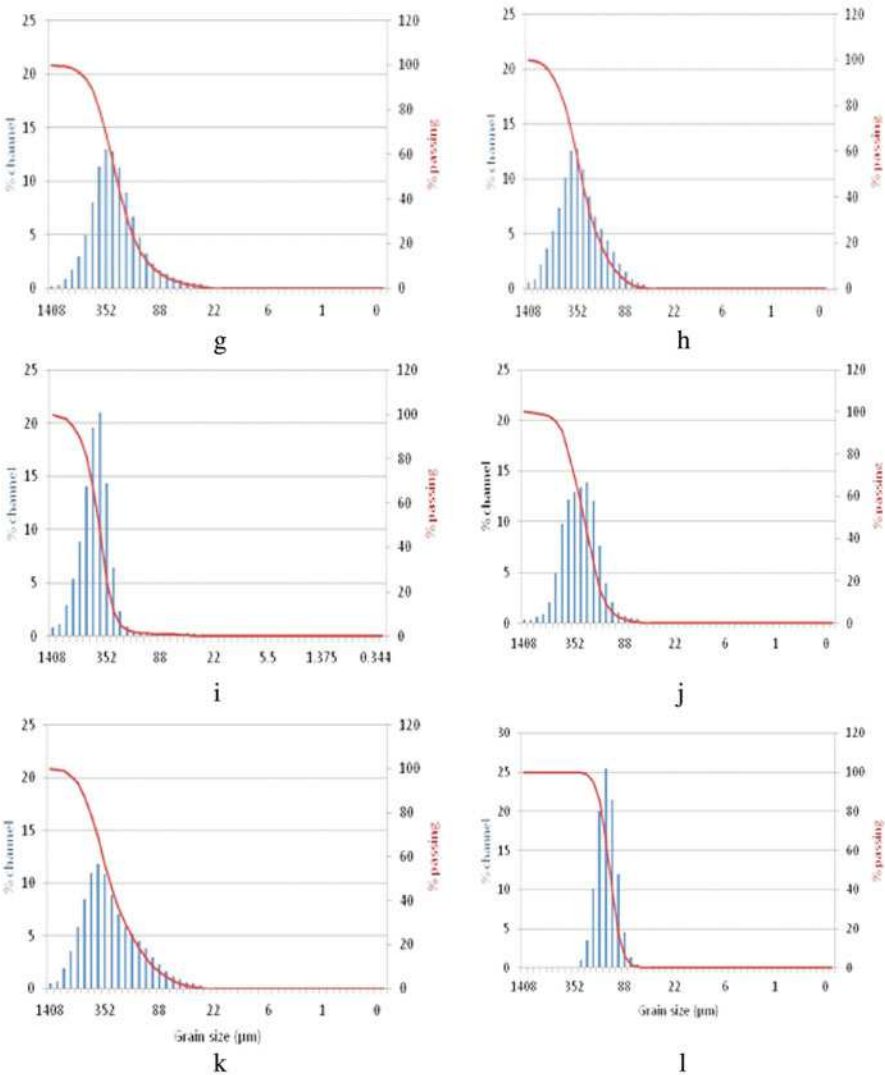


Fig. 48.3 (continued)

Table 48.1 ANOVA test for statistical significance between mean grain sizes (M_z), phi size (Φ), sorting (σ), skewness (S_k) and kurtosis (K_G)

Variable	F	F_{crit}	ρ
M_z	14.26	4.96	0.004
Φ	14.15	4.96	0.004
σ	19.43	4.96	0.001
S_k	4.31	4.96	0.064
K_G	12.96	4.96	0.005

factors determining the grain size are slope, climate, tectonics and lithology. The one-way ANOVA test confirms the finding that there exists a spatial and temporal inhomogeneity in the sediment size of the Alaknanda River.

REFERENCES

1. Folk, R.L. and Ward, W.C.: Brazos river bar: A study in the significance of grain size parameters. *J. Sediment. Petrol.* 27(I), 3–26 (1957)
2. Berner, E.K. and Berner, R.A.: The global water cycle: geochemistry and environment. Prentice-Hall, Englewood Cliffs, NJ (1987)
3. Singh, A.K. and Hasnain, S.I.: Major ion chemistry and weathering control in a high altitude basin: Alaknanda River, Garhwal Himalaya, India. *Hydrolog. Sci. J.* 43(6), 825–843 (1998)
4. Chakrapani, G.J.: Major and trace element geochemistry in upper Ganga river in the Himalayas, India. *Environ. Geol.* 48, 189–201 (2005)
5. Chakrapani, G.J. and Saini, R.K.: Temporal and spatial variations in water discharge and sediment load in the Alaknanda and Bhagirathi Rivers in Himalaya, India. *J. Asian Earth Sci.* 35, 545–553 (2009)
6. Slattery, M.C. and Burt, T.P.: Particle size characteristics of suspended sediment in hillslope runoff and stream flow. *Earth Surf. Proc. Land.* 22, 705–719 (1997)
7. Valdiya, K.S.: Geology of Kumaun Lesser Himalaya. WIHG Dehradun, pp. 291 (1980)
8. Cuen, S., Francus, P. and Lamoureux, S.F.: Estimation of grain size variability with micro X-ray fluorescence in laminated lacustrine sediments, Cape Bounty, Canadian High Arctic. *J. Paleolimnol.*, 44, 803–817 (2010)
9. Pandey, S.K., Singh, A.K. and Hasnain, S.I.: Grain-size distribution, morphoscopy and elemental chemistry of suspended sediments of Pindari Glacier, Kumaon Himalaya, India. *Hydrolog. Sci. J.* 47(2), 213–226 (2002)
10. Singh, V., Devrani, R. and Ansari, Z.: Estimation of the rate of erosion of valley fill deposits in a part of the NW Lesser Himalaya. *Episodes* 5(3), 445–451 (2012)

Chapter 49

Characterization of the Rainfall of Central Mozambique Based on Isotopes of Water

F. Steinbruch and S.M. Weise

Abstract This paper adds to the understanding of monsoon precipitation in Southern Africa as a contribution to isotope hydrological studies in that region. Central Mozambique's climate has a wet and a dry season, both controlled by the migration of the Inter-Tropical Convergence Zone (ITCZ). Two rain collectors were installed at an altitude of 34 m and 346 m about 60 km and 120 km west of the Indian Ocean. Both were operational from 02/2007 to 09/2010. Reference is made to the IAEA/GNIP stations Harare and Antananarivo. The local meteoric water line is $\delta D = 8.7 \delta^{18}O + 15.5\%$ ($R^2 = 0.97$). The mean annual rainfall in 2007-2010 is lower than for the period 1956-1984 and is most pronounced for the dry season. The observed high deuterium-excess values suggest contributions from different water vapour sources that evaporated under varying conditions over the trail of ITCZ. δ^2H and $\delta^{18}O$ ratios in dry season precipitation are more depleted in ^{18}O due to atmospheric recycling of evaporated and equilibrated water vapour in convective systems.

Keywords East African Rift System • Deuterium Excess • Monsoon • Stable Water Isotopes

49.1 INTRODUCTION

Stable water isotope analyses are used to investigate global precipitation cycles [1-4]. This paper contributes to the understanding of climate phenomena, especially monsoon precipitation in Southern Africa as a contribution to isotope hydrological investigations in that region. The study area is situated in the East African Rift System in central Mozambique between latitudes $10^{\circ}12'S$ and $26^{\circ}52'S$. The climate is influenced by the north-south migration of the Inter-Tropical Convergence Zone

F. Steinbruch (✉)

Indo-German Center for Sustainability, Indian Institute of Technology Madras, Chennai, India
e-mail: steinbruch@igcs.-chennai.org

S.M. Weise

Department Catchment Hydrology, UFZ Helmholtz Centre for Environmental Research, Halle, Germany

(ITCZ), dominantly in the form of warm monsoon rain between October and March. During the cool dry season from April to September precipitation is formed within continental and sub-polar convective systems. The influence of the Indian Ocean Zonal Mode, i.e. the rising and decreasing of the mean sea surface temperature known as El Niño and La Niña, on the southern African climate is well documented [5,6]. In the region El Niño is associated with below and La Niña with above normal precipitation. The years 2007/2008 were characterized by La Niña swinging into an El Niño phase in 2009/2010 and again into a La Niña phase in the second half of 2010 lasting with interruptions until 2011/2012 [7]. Furthermore the regional climate is influenced by orographic precipitation as a result of the forced uplift of moist air from the Indian Ocean at the flanks of the so-called Gorongosa Mountain, a massif associated with the East African Rift System, with an extension of about 800 km² and an altitude of 1883 m together with rain shadow effects due to the rift morphology.

49.2 METHODS

Two rain collectors, called *Gorongosa* and *Chitengo* were installed next to existing pluviometrical stations (Chitengo ID: P373, 34 m asl, about 60 km west of Indian Ocean; Gorongosa ID: P812 about 120 km west of the Indian Ocean at 346 m asl) and operational from February 2007 to September 2010. Chitengo recorded precipitation in 15 and Gorongosa 22 out of 44 months of observations of which monthly composite samples were collected for stable water isotope analyses. Samples were collected in 25 ml to 50 ml narrow-necked brown glass bottles. The measured stable water isotopes are normalized to the VSMOW-SLAP scale (Vienna Standard Mean Ocean Water and Standard Light Antarctic Precipitation, respectively). Data of the Global Network of Isotopes in Precipitation (GNIP; operated by WMO/IAEA) of sites at similar latitude, i.e. 18.9°S, like the project stations served as a reference. Harare is located about 380 km west of the study area at an altitude of 1471 m and recorded $\delta^2\text{H}$ and $\delta^{18}\text{O}$ in precipitation from 1961-2001, and Antananarivo is about 1380 km east of the study area at an altitude of 1300 m and has records from 1962-1974.

49.3 RESULTS

The Local Meteoric Water Line (LMWL) of the study area is $\delta\text{D} = 8.7 \delta^{18}\text{O} + 15.5\text{‰}$ ($R^2 = 0.97$) compared with Antananarivo: $\delta\text{D} = 8.3\delta^{18}\text{O} + 15.8\text{‰}$ ($R^2 = 0.98$) and Harare: $\delta\text{D} = 8.4 \delta^{18}\text{O} + 18.01\text{‰}$ ($R^2 = 0.94$) (Table 49.1, Fig. 49.1).

Table 49.1 Local Meteoric Water Lines (LMWL) of dry and wet seasons precipitation

Station	LMWL, wet season	LMWL, dry season	Linear regression
Antananarivo	$\delta D = 8.62 \delta^{18}O + 18.29\text{‰}$	$\delta D = 7.18 \delta^{18}O + 10.93\text{‰}$	$R^2 = 0.98 / 0.96$
Gorongosa	$\delta D = 7.14 \delta^{18}O + 9.10\text{‰}$	$\delta D = 9.16 \delta^{18}O + 17.68\text{‰}$	$R^2 = 0.99 / 0.8$
Chitengo	$\delta D = 8.95 \delta^{18}O + 15.68\text{‰}$		$R^2 = 0.89$
Harare	$\delta D = 7.52 \delta^{18}O + 11.65\text{‰}$	$\delta D = 7.32 \delta^{18}O + 17.74\text{‰}$	$R^2 = 0.92 / 0.81$

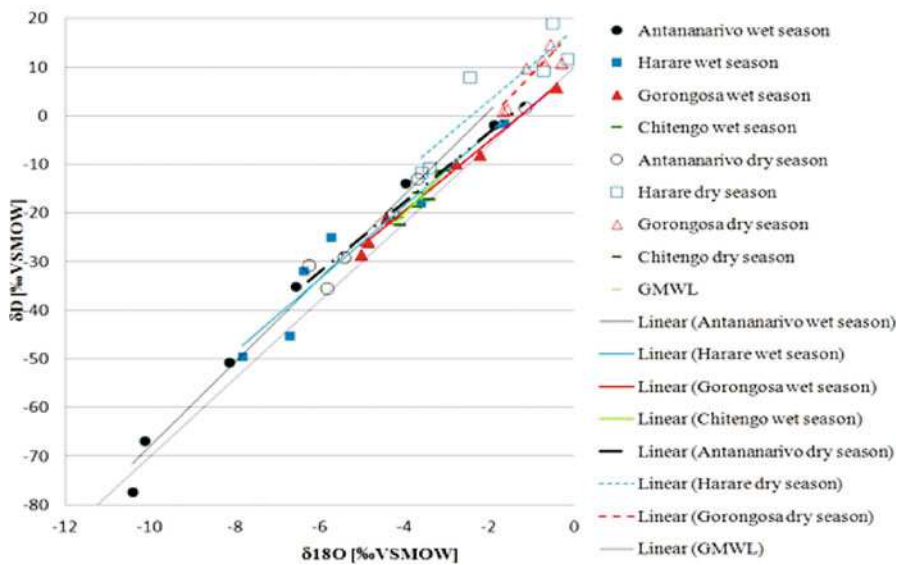


Fig. 49.1 Depth-weighted $\delta^{18}O$ - δ^2H plots of dry and wet seasons precipitation

49.4 PRECIPITATION PATTERNS AND STABLE WATER ISOTOPES

The mean annual rainfall has reduced at P812 to 1276 mm in 2007-2010 compared to 1338 mm in 1956-1982 and at P373 to 852 mm in 2007-2010 compared to 869 mm in 1956-1982. The observed decrease in the mean rainfall is most pronounced for the dry season, i.e. P812: 250 mm in 1956-1982, 180 mm in 2007-2010, P373: 155 mm in 1956-1982, 100 mm in 2007-1010. Gorongosa has a noticeably higher mean dry season precipitation compared to Antananarivo and Harare due to orographic rainfalls. Antananarivo and Harare have mean annual precipitations of 1387 mm and 865 mm. Peak monsoon is observed in Antananarivo and Gorongosa in the months of December and February. The wet season LMWL of Harare resembles the dry season LMWL of Antananarivo. The wet season LMWL of Harare and Gorongosa show enrichment in 2H and ^{18}O and slopes below 8 due to rainout and evaporation along the continental track. The wet season LMWL of Chitengo, located in the rift floor between the Indian Ocean coastline and

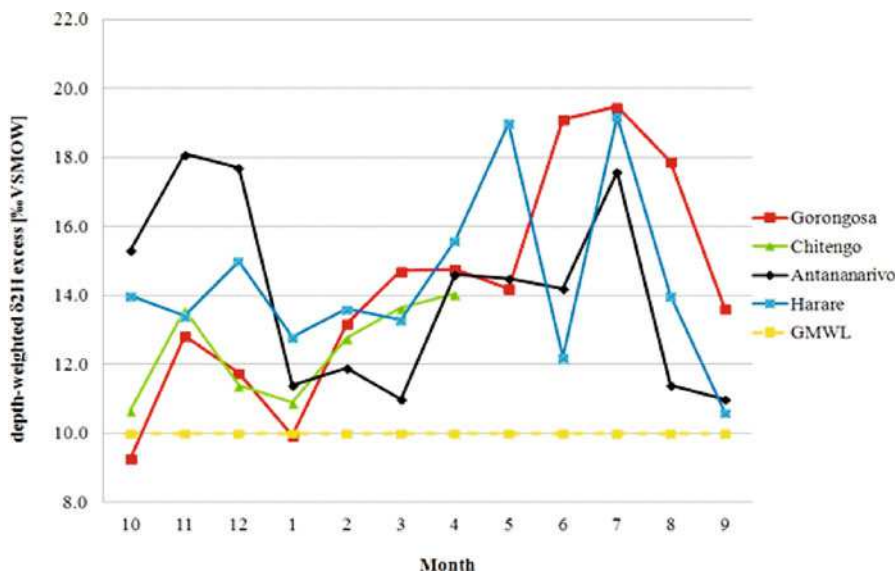


Fig. 49.2 Monthly deuterium-excess of study area and reference stations

Gorongosa, resembles the precipitation of Antananarivo (Fig. 49.1). The high deuterium-excess values for Antananarivo, Gorongosa and Harare result from a combination of water vapour sources that evaporated under varying conditions over the Indian Ocean and equatorial area of the African continent along the path of ITCZ. The $\delta^2\text{H}$ and $\delta^{18}\text{O}$ ratios in dry season precipitation of Gorongosa and Harare are depleted in ^{18}O due to atmospheric recycling of evaporated and equilibrated water vapour in convective systems (Fig. 49.2).

ACKNOWLEDGEMENT The authors acknowledge support by the International Atomic Energy Agency, Regional Water Authority of Mozambique, Carr Foundation, and Petra Blümel from UFZ Helmholtz Centre for Environmental Research.

REFERENCES

1. Goni, I.B.: Tracing stable isotope values from meteoric water to groundwater in the southwestern part of the Chad Basin. *Hydrogeology Journal*, 14, 742–752 (2006)
2. Kendall, C. and McDonnell, J.J.: Isotope tracers in catchment hydrology. Elsevier Science, Amsterdam (1998)
3. Rozanski, K., Araguas-Araguas, L. and Gonfiantini, R.: Isotope patterns of precipitation in the East African Region. In: Johnson, T., Odada, E.O. (eds.) *The limnology, climatology and paleoclimatology of the East African Lakes*, pp. 79–93. Gordon and Breach Publishers, Amsterdam (1996)

4. Vuille, M., Werner, M., Bradley, R.S., Chan, R.Y. and Keimig, F.: Stable isotopes in East African precipitation record Indian Ocean zonal mode. *Geophysical Research Letters*, 32, L21705 (2005)
5. WCRP: www.wcrp-climate.org/documents/monsoon_factsheet.pdf.
6. Sharon, E. and Nicholson: An analysis of the ENSO signal in the tropical Atlantic and Western Indian Ocean. *Int. J. Climatology*, 17, 345–375 (1997)
7. http://www.cpc.ncep.noaa.gov/products/analysis_monitoring/ensostuff/ensoyears.shtml
8. IPCC: http://www.climatechange2013.org/images/report/WG1AR5_ALL_FINAL.pdf

Chapter 50

Control of Deteriorating Water Quality in Extracted Boreholes by Flow Systems Definition

José Joel Carrillo-Rivera and Antonio Cardona

Abstract Climate change could be blamed on observed water quality decline. This is an undesirable response in any supply project based on groundwater that could produce negative effects as health hazards for the population, undesirable impacts to infrastructure, and increases of maintenance costs for economic activities. Climate change has created recent concern, also the increase in groundwater extraction resulting in enhancement of salinity and/or toxic element content. Results are significant in regions where aquifer thickness is ~1,000 m or more. The objective of this work is to propose the control of groundwater quality in extraction boreholes when the dynamics of the governing flow systems is defined by establishing their hierarchy as proposed by the Groundwater Flow Systems (GFS). Understanding GFS and their role in extracted groundwater provides adequate strategies for efficient water use and its corresponding planning and management. Usually boreholes response to groundwater extraction is a mixture of flows of different hierarchy. Vertical inflows increase their importance as drawdown progresses with extraction time. Results suggest climatic conditions may affect local flows. A joint groundwater monitoring for adequate managing is highly satisfactory *ie.* hydraulic data (water-level), physical (temperature) and chemical (specific element) data may be used to monitor expected response due to extraction.

Keywords Discharge Area • Groundwater Flow Systems • Water Quality Change • Monitoring

J.J. Carrillo-Rivera (✉)

Institute of Geography, Universidad Nacional Autónoma de México, C.U., Coyoacán, DF, México

e-mail: joeljcr@igg.unam.mx

A. Cardona

CSRSD, Earth Sciences, Universidad Autónoma de San Luis Potosí, Dr. Manuel Nava No. 8, San Luis Potosí, México

50.1 INTRODUCTION

Groundwater is the major source of potable water supply in arid and semi-arid regions. Its availability, however, may be limited by the inflow of contaminants through human activities at soil surface, as well as by processes such as saline water inflow in coastal regions, or by inflow of groundwater with different quality. The inflow of water salinity (total dissolved solids) as well as major (Na) and trace elements (*ie*, F, Fe, As, Cd, Pb) that change the quality of extracted water are substantial health hazard for humans [1] and can interfere with economical activities enhancing costs in management, infrastructure and maintenance. Groundwater extraction in Mexico is causing several negative environmental responses mainly in regions related to a basement rock depth of ~1,000, or more. The objective of this paper is to show the possibility to define groundwater quality controls in boreholes when the governing flows (*ie*. local, intermediate and regional) are defined. The presence of flows of different hierarchy, partial penetration of constructed boreholes (usually tapping 1/10 of the aquifer thickness) and extensive extraction result in a vertical ascending inflow of groundwater from beneath the aquifer unit, which, could be subject to its control.

50.1.1 *The San Luis Potosi Mexico, Study Area*

The San Luis Potosí Catchment (SLPC) is ~400 km north-west of México City at the south-eastern end of the Sierra Madre Occidental (SMO); it holds the capital of the state, with the same name.

The climate is semi-arid with average yearly summer rainfall of ≈ 400 mm. It is a closed catchment (Fig. 50.1) lacking perennial runoff. The mean annual and summer temperatures are 17 °C and 21 °C, respectively. The altitude of the catchment floor is between 1,850 to 1,900 m amsl; the surrounding sierras reach 2,750 m amsl.

Some ~1,700 m of Tertiary fractured lava flows, tuff and ignimbrite cover an inferred hydrogeological basement (Cretaceous calcareous mudstone, and a Tertiary quartz-monzonite intrusion). High F (>0.2 % weight) in the glassy matrix (≈ 80 % in volume) in rocks has been reported at the N of the SMO. A clastic sequence (gravel, sand, silt and clay derived from adjacent volcanic and sedimentary units) deposited on the volcanic units (Fig. 50.2) is referred to as TGU. A fine grained 50-150 m thick compact-sand bed with low permeability fully enclosed in the centre of the TGU has is ~ 300 km² in extent.

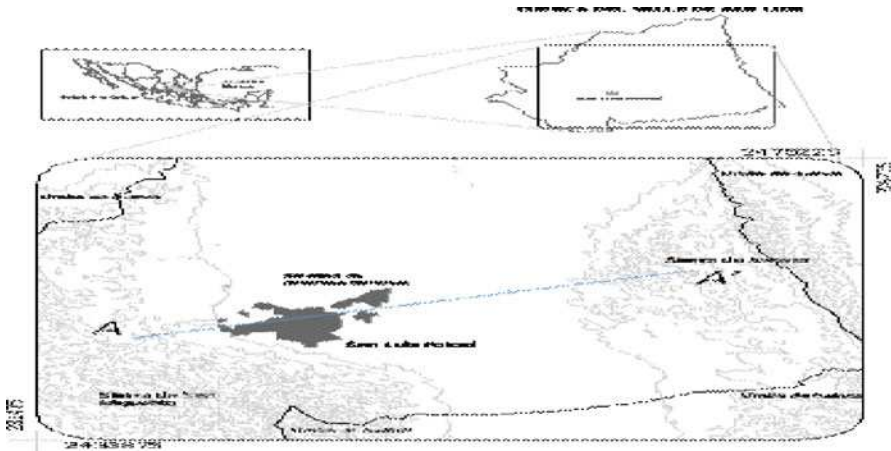


Fig. 50.1 Location of the San Luis Potosí study close Catchment

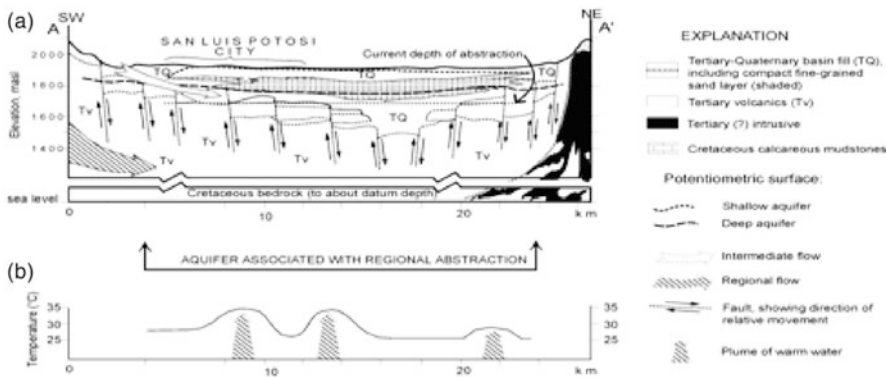


Fig. 50.2 Section showing (a) cross-section sketching the lithology and presence of current flow systems and (b) vertical rising of high temperature water (location of section in Fig. 50.1)

50.2 METHODOLOGY

Generally, the water of each flow differs in its chemistry and isotopes according to its recharge condition and subsequent travel depth and distance. A local flow has a short and shallow path, so its characteristics are closer to recent rainfall and it will be influenced by dissolved minerals from geologic units along its flow path. Regional flows travel the deepest and longest path, its recharge zone is in the highest continental region and its discharge in the lowest topographic zone. Intermediate flows circulate between those of local and regional type, showing intermediate chemical and physical characteristics between those flows. Water chemistry of different flows evolves along their path travelling separately. Water

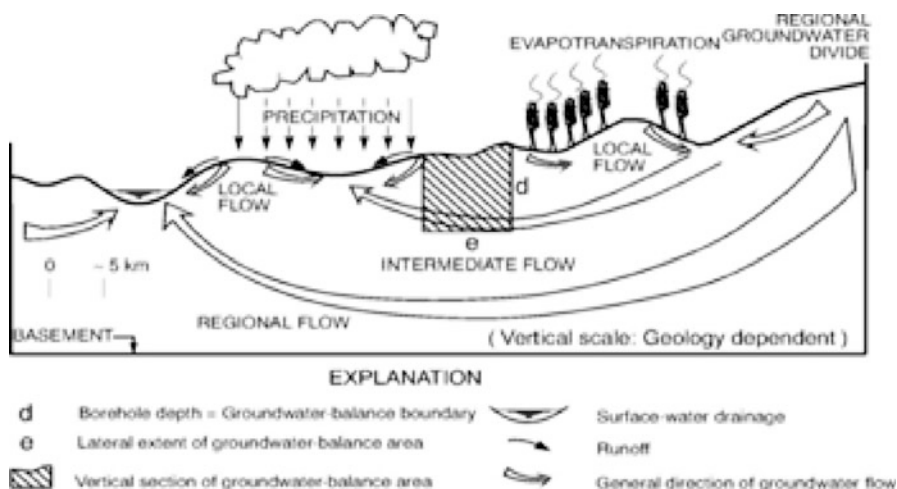


Fig. 50.3 Diagram representing the groundwater flow systems in a geological environment proposed by Tóth (1999). (Adapted from [4])

in a regional flow approaching its discharge zone grows chemically uniform disregarding the type of the geological units through which it has travelled [5].

The objective was achieved defining the presence of flow systems as proposed by the Groundwater Flow System Method (GFSM), also known as Modern Hydrogeology [3]. Under natural conditions there is direct and indirect field evidence of the interaction of groundwater movement with various elements of the environment; movement resulting from the hierarchical nature of groundwater flow in 3D within the prevailing boundary conditions (water-table and basement rock). Hence, local, intermediate and regional flow systems may be identify, each with its zone of recharge, transit and discharge (Fig. 50.3).

50.3 RESULTS

Carried out aquifer-tests in the SLPC showed two main responses (Fig 50.4). A classical horizontal flow suggested by borehole-61 of water travelling through a granular aquifer-unit showing constant values with extraction time (20 hrs) of electrical conductivity, EC (290 $\mu\text{mhos/cm}$); F^- (0.45 mg/L); Na^+ (25 mg/L); temp. (23.7°C). Borehole-34 (in fractured volcanic) had contrasting response along a 60 hrs test. Initial values of EC (200 $\mu\text{mhos/cm}$), F^- (0.47 mg/L), Na^+ (17 mg/L), temperature (30.5°C) rapidly evolved to higher values of EC (248 $\mu\text{mhos/cm}$), F^- (0.88 mg/L), Na^+ (32 mg/L), and temp (35.8°C) with pumping time (60 hrs). The yields of boreholes 61 and 34 were 45 L/s and 5 L/s, respectively. This contrasting response is helpful to plan a monitoring programme and an efficient water supply management. Any water sample collected in borehole-61

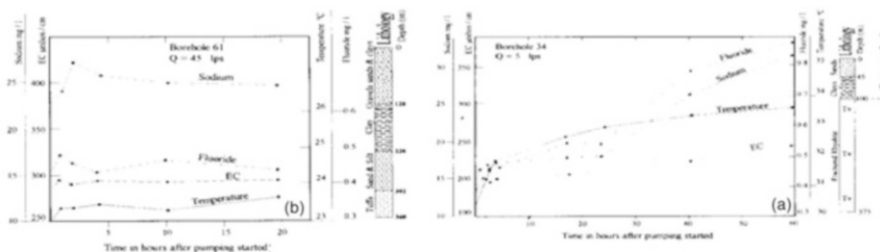


Fig. 50.4 Temperature, F^- , Na^+ and EC response to groundwater extraction in two partial penetrating boreholes with horizontal flow (B-61) and vertical flow (B-34)

after extraction started may show the water quality of the intermediate flow system and allow an efficient monitoring and water extraction programme to be established. However, in borehole-34 the change from an acceptable F^- and Na^+ content to impoverishing values as extraction progressed implies that a sampling procedure in this or similar responding boreholes would require precautions to define a suitable, stable and efficient water supply management and monitoring project.

The identified displacement in time of hot F^- regional flow proposes a simple control of water with high F^- content by stop pumping after two months (not in Fig. 50.4) when F^- content reaches the (WHO) recommended value of 1.5 mg/L and resume extraction in a nearby borehole. An additional identified F^- control is its relation to temperature in extraction boreholes (Fig. 50.5), suggesting that an acceptable F^- groundwater mixture of regional and intermediate flows to be obtained when temperature is lower than $30^{\circ}C$. Figures 50.4 and 50.5 suggest the presence of low temperature and salinity good quality water which is related along granular aquifer materials. This water tapped by boreholes is more related to a modern flow system than the regional flow. The more modern a flow system is the more vulnerable it becomes to modern changes in recharge conditions. Therefore, these flows could prove to be more vulnerable to changes in the climatic conditions, proposing a major concern to investigate the nature of the flow hierarchy of borehole water, especially when groundwater is used for a water supply project.

50.4 CONCLUDING REMARKS

The lack of understanding groundwater functioning related to the response of extraction boreholes is resulting in the deterioration of obtained water quality mainly due to vertical ascending flow from depth. Such response is more relevant in areas of volcanic fractured material where its thickness is about, or in the excess of 1,000 m. The application of the GFSM may provide adequate sound directions to control groundwater quality obtained in extraction boreholes. The use of standard

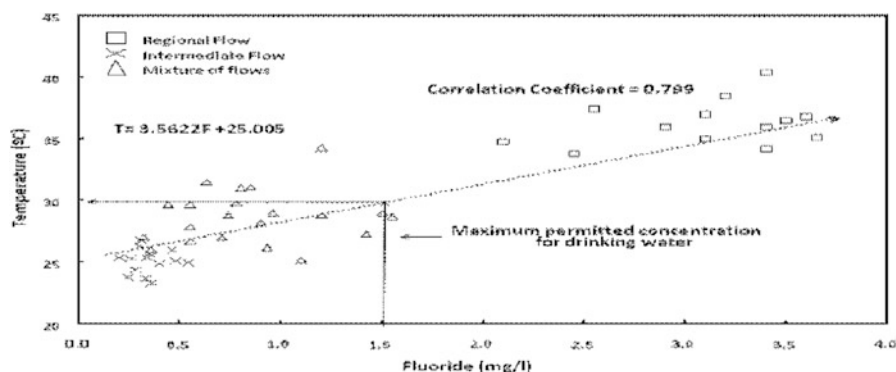


Fig. 50.5 Relationship of discharge temperature to fluoride content in extraction boreholes

aquifer-test hydraulic techniques coupled with water quality monitoring could assist in achieving a satisfactory groundwater extraction strategy for efficient water planning and improved groundwater management in agreement with the natural hydrogeological response of the system. Any long term alteration in the climatic conditions implies a direct effect on the prevailing local flow systems; flows containing the best quality water, which are subject to contamination processes at the surface. Consequently, local flows require their identification and protection for the adequate management of the water sources in any region.

REFERENCES

1. Edmunds, W.M. and Smedley, P.L.: Groundwater chemistry and health – an overview. In: Appleton, J.D., Fuge, R. and McCall, G.J.H. (Eds), *Environmental Geochemistry and Health Geological Society. Special Publication (113)*, 91–105 (1996)
2. Carrillo-Rivera, J.J., Cardona, A. and Edmunds, W.E.: Using extraction regime and knowledge of hydrogeological conditions to control high-fluoride concentration in obtained groundwater: San Luis Potosí basin, Mexico. *Journal of Hydrology*, 261, 24–47 (2002)
3. Tóth, J.: Groundwater as a geological agent: An overview of the causes, processes, and manifestations. *Hydrogeology Journal*, 7: 1–14 (1999)
4. Carrillo-Rivera, J.J.: Application of the groundwater-balance equation to indicate interbasin and vertical flow in two semi-arid drainage basins, Mexico. *Hydrogeology Journal*, 8(5): 503–520 ISSN: 1431–2174; Impact F. 1.675 (2000)
5. Carrillo-Rivera, J.J., Varsányi, I., Kovács, L.Ó. and Cardona, A.: Tracing groundwater flow systems with hydrogeo-chemistry in contrasting geological environments. *Water, Air and Soil Pollution*, (184): 77–103. DOI: [10.1007/s11270-007-9400-6](https://doi.org/10.1007/s11270-007-9400-6) (2007)

Chapter 51

Canal Irrigation and Its Impact on Spatial and Temporal Variation in Groundwater Level: A Case Study in Indira Gandhi Canal Project Stage I Command Area

Sandhya and S. Sreekish

Abstract The western part of India is hot desert, which is known as Thar Desert. The largest extent of this desert is spread over Rajasthan state. In order to increase agriculture potential of desertic soil Indira Gandhi Canal Project (IGCP) was introduced. The development of IGCP project has brought changes in the land use pattern in terms of increase in area under the agriculture. The increase in area under agriculture and under irrigation network has brought fluctuations in the groundwater level. This fluctuation in groundwater level is result of the seepage of water through the excessive irrigation and the seepage from the canal network. Thus the human impact in form of land-use pattern of a land is an important determinant of rise and fall in groundwater level. The spatial and temporal variation in groundwater level has been analysed Inverse Distance Weightage technique across different pentards for 128 observation wells of the Anupgarh, Vijayanagar and Suratgarh tehsil of Sriganganagar district of Rajasthan, which lies in the northwestern part of IGCP Stage I.

Keywords Irrigation • Waterlogging • Salinisation • Spatial Interpolation • Pentard

51.1 INTRODUCTION

“Water is our most neglected asset, more valuable than any of the metals and perhaps even more critical than soil. Too much or too little creates problems, especially in dry lands” [1]. To meet the global concern of food scarcity the large-scale development of irrigation projects in drylands has been done world-wide. Large scale inter-basin transfer of river water to these drylands, is combating the present problem of the food scarcity by facilitating the irrigation. Irrigation is

Sandhya • S. Sreekish (✉)
CSRDI, Jawaharlal Nehru University, New Delhi, India
e-mail: sreekish@mail.jnu.ac.in

generally considered an effective way of increasing agricultural production. But excessive recharge brought about by seepage losses from the irrigation network and deep percolation from irrigation has raised the underlying groundwater. A rise in groundwater level subsequently led to waterlogging and associated salinity problems in many irrigated areas around the world [2].

Rise in groundwater level was also found to be the major impact of large irrigation projects introduced in India also [3–5]. The introduction of Indira Gandhi Canal Project (IGCP) in the western part of Rajasthan, which is known as Thar Desert has extended irrigation facility. And this has not only increased the agriculture production but also provided drought proofing, and increased human settlement by providing the drinking water facility, created employment opportunities and provided requisite opportunities for overall economic development of Thar [6]. The increase in area under agriculture along with irrigation network has brought variations in the groundwater level [7]. This fluctuation in groundwater level is a result of the seepage of water through the excessive irrigation and the seepage from the canal network. The excessive irrigation applied to the agricultural fields results in the rise in groundwater level. At the same time the extraction of groundwater through tube-wells for the irrigation leads to decline in groundwater level. Thus the change in land-use pattern is an important determinant of rise and fall in groundwater level. However in most of the arid tracts intensive irrigation has led to the problem of waterlogging. Thus it is imperative to understand and analyse the spatial and temporal variations in the waterlogged regions after introduction of IGCP Stage I in the present study area has been analysed here through this paper.

51.2 STUDY AREA

The study has been carried out in the stage I of IGCP (Fig. 51.1) command area, which extends to Hanumangarh, Ganganagar and Bikaner districts of Rajasthan. However the present study confines only to southwestern part of the IGCP Stage I, that include the Anupgarh, Vijayanagar and Suratgarh tehsils (Fig. 51.1 and Fig. 51.2) of Ganganagar district. The study area has well distributed network of canal (Fig. 51.3).

51.3 MATERIAL AND METHODS

Groundwater level data in meters below ground level (bgl) for 128 observation wells (Fig. 51.2) has been collected from Groundwater Department, Command Area Development Authority, IGCP Stage I, Bikaner, Rajasthan. The analysis has been done for the period of 1982 to 2007 for pre-monsoon (March) and post-monsoon seasons (September). The analysis of groundwater level has been carried out by dividing the entire study period into different pentads (5 year time period).

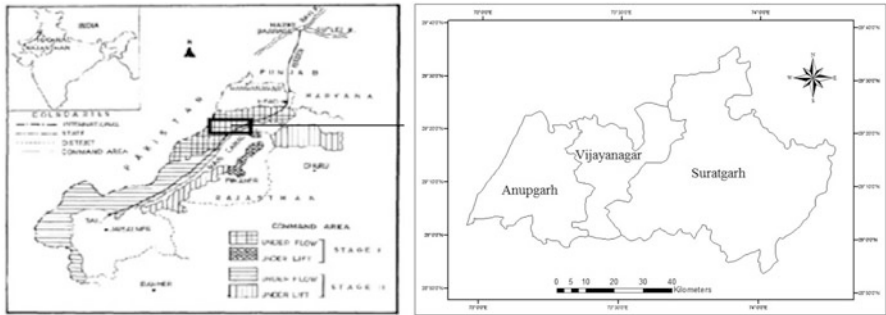


Fig. 51.1 Location of study area

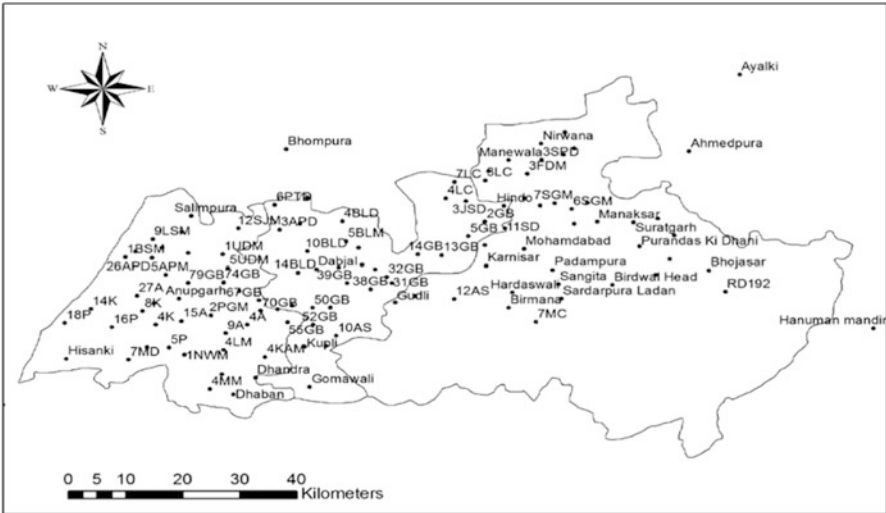


Fig. 51.2 Location of observation wells

The methodology used includes geo-referencing of map, spatial interpolation of spatial variations in the groundwater level using Inverse Distance Weightage (IDW) technique [8]. The spatial variation in groundwater level has been analysed following the categorization of Ministry of Water Resources [9] as given in Table 51.1. Further for detailed study of rise or fall in water level, other classes in safe zone have been demarcated at an interval of 3 meters.

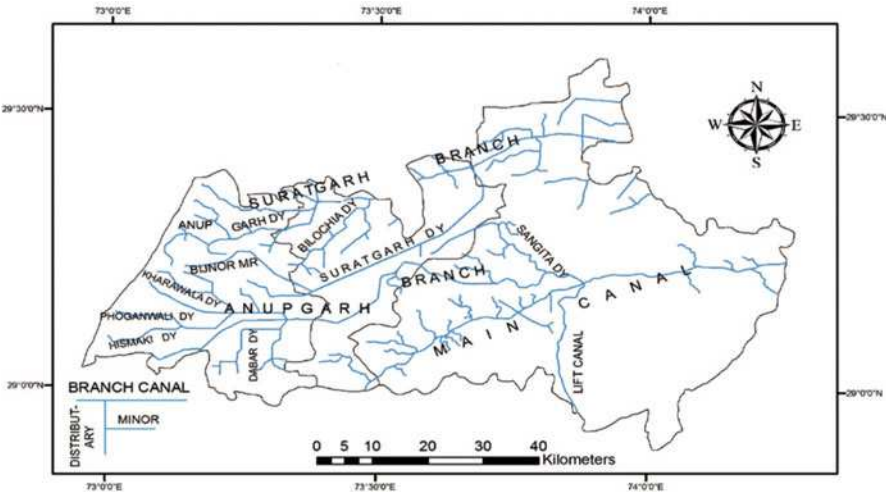


Fig. 51.3 Canal map

Table 51.1 Categorization of groundwater level for the analysis of waterlogged areas

Water table Zone	Water table in meters bgl
Waterlogged	Less than 2
Potentially Waterlogged	2 to 3
Safe	Above 3

51.4 RESULTS AND DISCUSSIONS

The analysis of groundwater level for 1982-1985 period pre-monsoon season shows that the Purandas Ki Dhani, Prema Ki Dhani and Rang Mahal observation wells are already waterlogged, with neighbouring area being in the potentially sensitive to waterlogging zones. This region lies in the Ghaggar river low lying region, which is having a hard-pan of Kankars below it, which restricts the seepage of water further through it. All other regions are in the safe zone. The south western parts of this region have the groundwater level at the deeper levels upto 20 m bgl. The south western parts of this region are covered with thick aeolian soils. During post-monsoon season none of the observation wells under waterlogged condition. Rang Mahal and Purandas Ki Dhani, which were in waterlogged zone in pre-monsoon period were turned to the potentially sensitive to waterlogging condition. During 1986-1990 pre-monsoon season rise in groundwater level has been observed in all the areas, which are in the safe zone, except the Ghaggar river depression. In post-monsoon season waterlogging conditions were observed at Purandas Ki Dhani, due to the seepage from the canal and excessive irrigation. Rang Mahal and the surrounding region of Purandas Ki Dhani were found to be potentially waterlogged (Fig. 51.4 and 51.5).

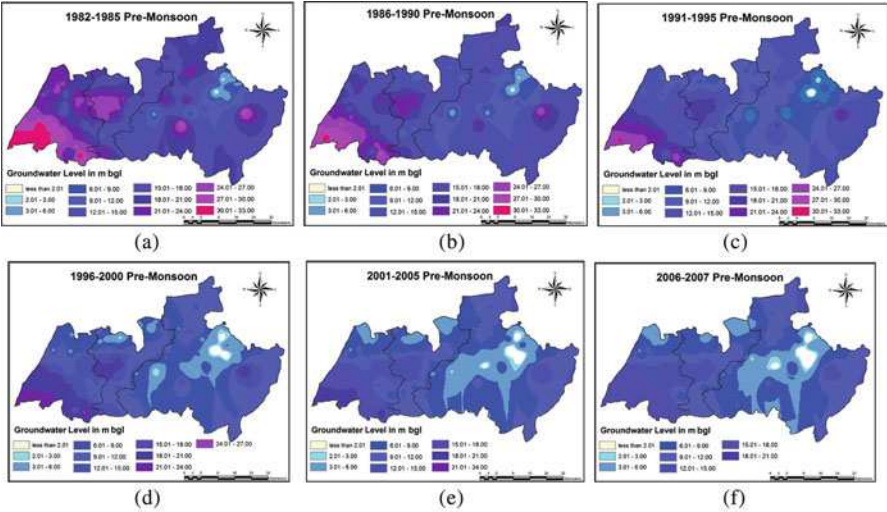


Fig. 51.4 Groundwater level in pre-monsoon season during time periods (a) 1982-1985, (b) 1986-1990, (c) 1991-1995, (d) 1996-2000, (e) 2001-2005, (f) 2006-2007

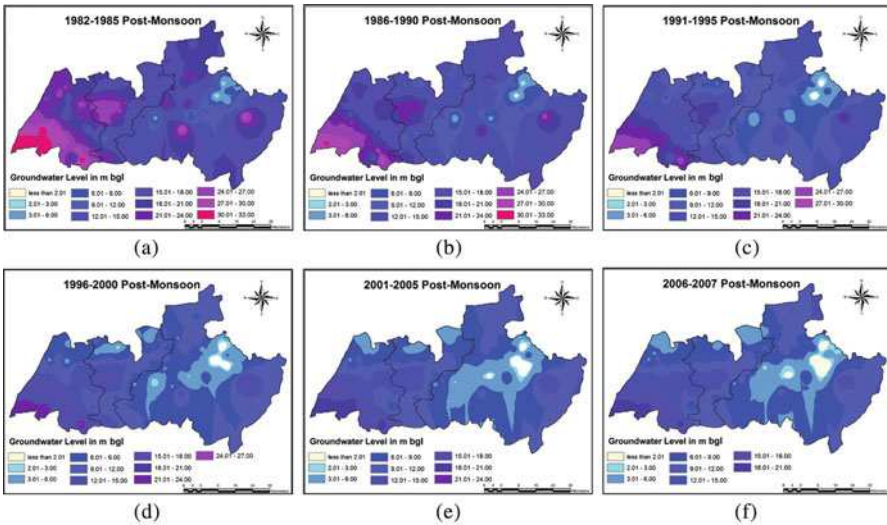


Fig. 51.5 Groundwater level in post-monsoon season during time periods (a) 1982-1985, (b) 1986-1990, (c) 1991-1995, (d) 1996-2000, (e) 2001-2005, (f) 2006-2007

During 1991-1995 pre-monsoon season the rise in groundwater level has continued, though most of the region was under the safe zone. The rise in groundwater level in the lower lying regions facilitated the agriculture in these areas. During post-monsoon season the extent of waterlogging conditions and potentially sensitive areas also increased to the surrounding areas. The extension of branches of

canal during this period has raised the groundwater level. This was result of expansion of agricultural and area under double cropping leading to increased seepage of water from the excessive irrigation. In 1996-2000 expansion of the waterlogged areas has been observed, which marks a spread to the neighbouring potentially sensitive to waterlogging regions. New potentially sensitive waterlogged areas have been observed in the northern part of Vijayanagar and also at 12AS observation wells of Suratgarh. During the 2001-2005 Sangita observation well has also been added under waterlogged category. During 2006-2007 an expansion of waterlogged and the potentially sensitive to waterlogging to surrounding areas has been observed. In the safe zone the maximum groundwater level depth has been reduced to 18 from around 21 m bgl. From 1996-2000 to 2006-2007 time periods the pre and post monsoon seasons has maintained the similar pattern in the groundwater table in the regions which are in more proximity to canal because the areas receiving continues irrigation water supply through canals generally sowing two to three crops annually. As the canal provides with assured the supply of water and the shallower groundwater levels have facilities of digging the tubewells.

51.5 CONCLUSIONS

The spatial variation in groundwater in the present study area shows that the northern and the north eastern region, which has Ghaggar river plain has shallow water table. However the sand dunes and the southwestern regions had water table at greater depth. The shallow groundwater level is due to the hard-pan of kankars lying underneath it. The areas under the safe zone has marked rise in ground water level over the time period of 1982-2006, though they have remained in the safe zone only. The impact of rainfall variability on the groundwater fluctuation is negatively correlated [10] for this region because other factors like seepage of water from canal and human induced activities like excessive canal irrigation and groundwater extraction through tubewells for drinking, household and agricultural purposes has major impact on the groundwater level fluctuations.

REFERENCES

1. Cressey, G.B.: Water in the Desert. *Annals of the Association of American Geographers*, 47(2), 105-124 (1957)
2. FAO: Agricultural Drainage Water Management in Arid and Semi Areas. Irrigation and Drainage Report 61, Rome (2000)
3. D'Souza, R., Mukhopadhyay, P. and Kothari, A.: Re-evaluating Multi-Purpose River Valley Projects: A Case Study of Hirakund, Ukai and IGCP. *Economic and Political Weekly*, 33(6), 297-302 (1998)
4. Thakkar, H.: Assessment of Irrigation in India, South Asia Network on Dams, Rivers and People, India. Thematic Review: Assessment of Irrigation Options in India, pp. 1-129 (1999)

5. Aggarwal, M.C. and Kumar, R.: Reclamation of Waterlogged and Saline Lands through Drainage. *Haryana Farming*, pp. 18–19 (1998)
6. Government of Rajasthan: IGNP Studies for the State of Rajasthan (Final Report), Annex H. *Environmental Review*. Jaipur (1999)
7. Jaglan, M.S. and Qureshi, M.H.: Irrigation Development and Its Environmental Consequences in Arid Regions of India. *Environmental Management*, 20(3), 323–336 (1996)
8. Burrough, P.A.: Principles of Geographic Information System for Land Resource Assessment. New York, Oxford University Press (1986)
9. GOI: Report of the working group on waterlogging, soil salinity and alkalinity. Ministry of Water Resources, New Delhi (1991)
10. Sandhya: Introduction of Canal to Drylands and its Impact on Land and Water Resources: A Case Study in Indira Gandhi Canal Project Stage I Command Area (Unpublished M.Phil. Dissertation). New Delhi, Jawaharlal Nehru University (2013)

Chapter 52

Impact of Canal Recharge on Groundwater Quality of Kolayat Area, District Bikaner, India

Sumant Kumar, N.C. Ghosh, R.P. Singh, Rajesh Singh, and Surjeet Singh

Abstract: Rajasthan is one of the water scarce states of India where the annual average rainfall varies from less than 100 to 1000 mm. Kolayat area of district Bikaner located in western part of the state, receives average annual rainfall of 275 mm. Owing to the less rainfall of this low magnitude, the water availability problem in the Kolayat area is critical in comparison to many other parts of the state. The water requirement, of the area, is mainly met by Indira Gandhi Nahar Project (IGNP) canal. The groundwater quality of the area through which IGNP canal passes has been studied to understand the effect of canal recharge on groundwater and subsurface movement of recharge pathways. The canal trends in NE-SW direction and flows towards SW. The study has been carried out across the canal 40 km in the eastern and 20 km in the western direction. The depth to water varies between 10 and 55 m bgl. The water levels are shallow in western direction and upto Bajju in eastern direction from the canal. The water levels become deeper as one moves towards eastern direction. This suggests that the groundwater regime receives recharge from the canal towards western direction and upto Bajju in eastern direction. The groundwater flow directions obtained from water table contours also reveal the presence of groundwater mound in the vicinity of the canal. The EC of the canal water is 302 $\mu\text{S}/\text{cm}$ where as the EC of groundwater varies from 563 $\mu\text{S}/\text{cm}$ to 23600 $\mu\text{S}/\text{cm}$. The EC of groundwater along the canal varies from 563 $\mu\text{S}/\text{cm}$ (Bajju) to 1916 $\mu\text{S}/\text{cm}$ except Modayat where as EC is high away from the canal. Water quality analysis confirms the same result as interpreted from groundwater contours. The groundwater of the area has high calcium, magnesium, sodium, potassium, chloride, sulphate, they range upto 634, 787, 5890, 1015, 7908, 2650 mg/L respectively. Further, fluoride in the areas around Chak 4 GMR (3.8 mg/L), Bajju (1.93 mg/L), Godu Krishi farm (4.12 mg/L), Godu village (1.93 mg/L) exceeds the permissible limit for drinking purpose. The study also reveals that recharge from IGNP canal has a long term influence in the study area where groundwater is withdrawn for various activities.

S. Kumar (✉) • N.C. Ghosh • R.P. Singh • R. Singh • S. Singh
National Institute of Hydrology, Roorkee, India
e-mail: sumantks@gmail.com

Keywords: Kolayat • Groundwater • IGNP • Rainfall • Water Quality

52.1 INTRODUCTION

The stage of ground water development in district Bikaner district is 94.65 %, which indicates that the annual ground water draft and recharge are nearly equal. In district Bikaner out of 5 blocks, 2 falls under “Over-exploited” category, 1 blocks under “Critical” category, 2 blocks under “Safe” category [1]. The Kolayat area falls under safe category due to less development of groundwater. The main ground water related problem in the area, is its salinity. The study area extends with a major irrigation project called Indira Gandhi Nahar project (IGNP). This is one of the most enormous projects (649 Km long) in the world aiming to transform the desert waste into agriculturally productive area. The water supply to IGNP is through 204 km long Indira Gandhi Feeder, takes off from Harike barrage, which lies on Sutlej River [3]. The main Indira Gandhi Canal enters the district of Bikaner north of village Bhansar and it passes through Khagabera, Lakharwara, Sisardesar Chattargarh, Sattasar, Siasar, Prithiraj Ka Bere, Karmisar and Modayat. With the implementation of IGNP, which involved large amount of water into the system through canal network, the hydrogeological situation in the command area has undergone significant changes [4]. Prior to the introduction of canal irrigation, the ground water levels, in the area, were deep varying from 40 to over 50 m bgl. The ground water levels started rising consequent to the release of water in canals and introduction of irrigation. With the expansion of area under irrigation, the IGNP command area witnessed an alarming expansion of water logging and soil salinity. The areas around Kharbara, Dantor, Manaksar, Modayat, Charanwala Bhikampur etc. are more prone towards water logging [2]. In this study the effect of I.G.N.P canal on groundwater viz. water quality, groundwater contours in Kolayat block has been brought out. It is also tried to replicate the path of groundwater recharge movement to the aquifer.

52.2 STUDY AREA AND HYDROGEOLOGY

The study area forms part of kolayat block of district Bikaner and lies in Survey of India Toposheet no. NG 43/1 between longitude 72° 14' 25.79" E & 72° 46' 52.38" E and latitude 28° 00' 25.57" N & 27° 49' 40.41" N as shown in Fig. 52.1. The IGNP canal trends NE-SW and flows in SW direction. The prominent places along the canal are Modayat and Bajju. The study has been carried out across the canal 40 Km in the eastern and 20 Km in the western direction. The study area located in the Thar Desert, has arid type climate with extremes of temperatures, erratic rainfall and high evaporation. Rainfall data (1973-2011) showed that the annual rainfall varies between 32 and 580 mm with mean value of 275 mm. The temperature varies from 48.5° C in summer to 5°C in winter. The atmosphere is generally dry except the

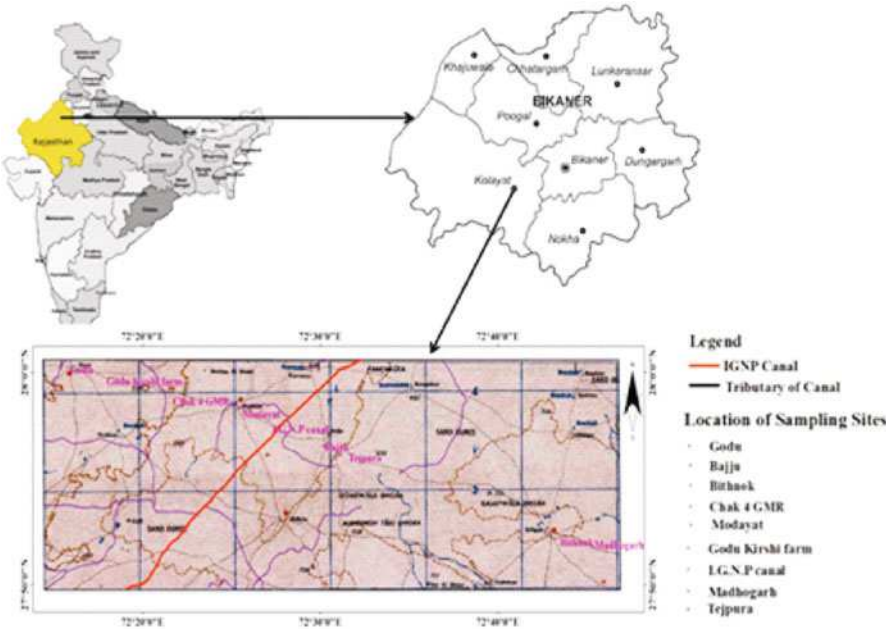


Fig. 52.1 Location map of the study area

monsoon period. Geologically the area is represented by the Nagaur formation of Marwar supergroup. The main rock types are bricked colored sandstone, siltstone with gypsum and clay beds. The rocks of Nagaur formation are overlain by alluvial and deposits.

52.3 METHODOLOGY

Groundwater levels are measured using water level sound recorder. Water samples from dug wells and main canal were collected in standard plastic bottles (period: April, 2013). The locations of the sampling sites are shown in Fig. 52.2. The physical parameters such as temperature, pH, electrical conductivity etc. were determined in the field using portable instruments. The water samples are analysed for their pH, EC, Ca^{++} , Mg^{++} , Na^{+} , K^{+} CO_3^{--} , HCO_3^{-} , SO_4^{--} and NO_3^{-} , Cl^{-} , F^{-} .

52.4 RESULTS AND DISCUSSION

The water levels were measured in the field and it was observed that groundwater level varies from 10 to 55 m (Fig. 52.3). The groundwater levels were available as the depth below ground surface; therefore, by measuring the R.L of the respective



Fig. 52.2 The location of sampling sites of Kolayat area, Distt., Bikaner

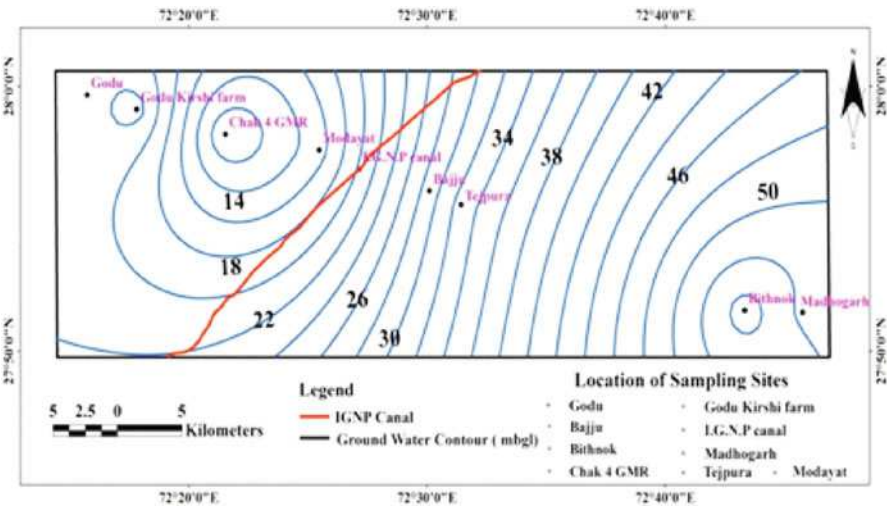


Fig. 52.3 Depth to water level map of the study area

well location, these data have been converted to groundwater level above msl and then geo-referenced with respect to their latitude and longitude to get groundwater contours. Fig. 52.4 shows the groundwater contours maps depicting the groundwater flow direction towards west direction and upto Bajju in the eastern direction from the canal.

The EC of the canal is 302 $\mu\text{S}/\text{cm}$ whereas the EC of the groundwater varies from 563 $\mu\text{S}/\text{cm}$ to 23600 $\mu\text{S}/\text{cm}$. The EC of groundwater along the canal varies from 563 $\mu\text{S}/\text{cm}$ (Bajju) to 1916 $\mu\text{S}/\text{cm}$ except Modayat. The EC plot of the study

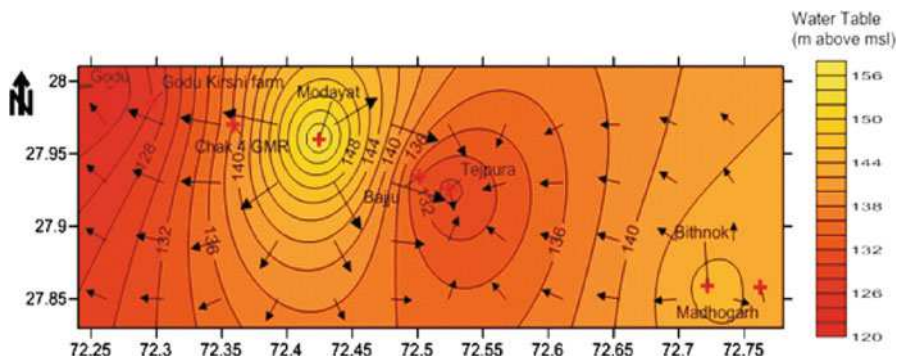


Fig. 52.4 Water table contours and flow direction of the study area

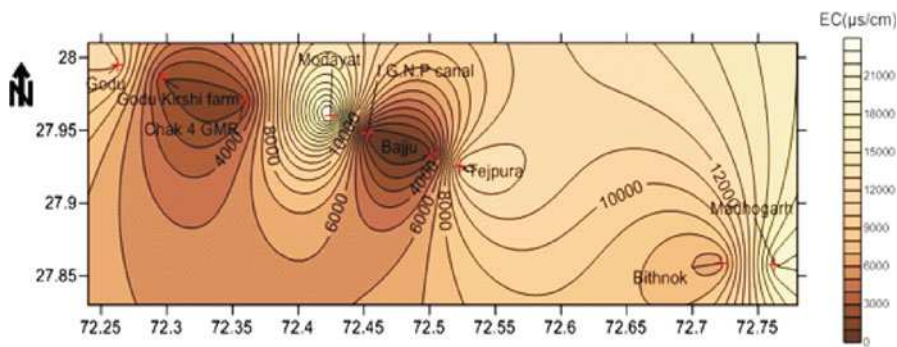


Fig. 52.5 Electrical conductivity (EC) distribution in Kolayat area, Distt. Bikaner

area is shown in Fig. 52.5. Water quality analysis confirms the same results as interpreted from groundwater contours.

The analyzed water quality parameters are given in Table 52.1. The constituents of water quality parameters analyzed include: pH, EC, total dissolved solids (TDS), hardness, calcium, magnesium, sodium, potassium, alkalinity, bi-carbonate, nitrate, sulphate, chloride, and fluoride. The results of the analyzed water quality parameters at different locations are compared with the permissible drinking water quality norms (IS: 10500-2012). A perusal of the data given in Table 52.1 reveals that of most of the locations EC values are very high except Chak 4 GMR, Godu Krishi farm and Bajju which indicates that recharge from the canal is reaching to these places. Modayat, locate close to the main canal is having anomalously high EC, this may be due to the gypsum bed. The ground water in the area has high calcium, magnesium, sodium, potassium, chloride, sulphate, they range upto 634, 787, 5890, 1015, 7908, 2650 mg/L respectively. Further, fluoride in the areas around Chak 4 GMR (3.8 mg/L), Bajju (1.93 mg/L), Godu Krishi farm (4.12 mg/L), Godu village (1.93 mg/L) exceeds the permissible limit for drinking purpose.

Table 52.1 Results of water quality constituents

Parameters	Sampling Locations									Permissible limit (IS:10500:2012)
	I.G.N.P Canal	Modayat	Chak 4 GMR	Godu Kirshi farm	Godu Village	Bajju	Tejpura	Bithnok	Madhogarh	
pH	7.22	7.15	7.65	8.76	7.32	8.77	7.38	7.77	8.95	6.5-8.5
EC ($\mu\text{S}/\text{cm}$)	302	23600	1551	1916	11270	563	13400	6340	19070	-
TDS (mg/L)	193	15104	992	1226	7212	360	8576	4057	12204	2000
Hardness (mg/L)	112	1746	120	20	1756	116	3700	1184	1700	600
Ca ⁺⁺ (mg/L)	30	633	30	5	629	30	184	282	281	200
Mg ⁺ (mg/L)	9	40	11	2	45	10	787	116	242	100
Na ⁺ (mg/L)	20	5890	261	261	1250	52	640	750	4940	-
K ⁺ (mg/L)	3.5	35	2.4	1.75	1015	18	190	194	90	-
Alkalinity (mg/L)	110	326	444	434	290	54	1100	576	74	600
HCO ₂ ⁻ (mg/L)	134	397	541	529	353	66	1342	702	90	-
NO ₃ ⁻ (mg/L)	4	1.4	12	22	20	19	25	21	3	45
SO ₄ ⁻⁻ (mg/L)	100	2650	134	155	2650	120	700	285	1400	400
Chloride (mg/L)	54	7908	300	228	2568	70	2500	1538	6538	1000
Fluoride (mg/L)	0.2	1.38	3.8	4.12	1.93	1.58	-	0.72	1.09	1.5

52.5 CONCLUSIONS

Impact of recharge from I.G.N.P canal on groundwater quality has been studied in Kolayat block. The area traversing IGNP canal (extends in NE-SW direction and flows towards SW) passes through Kolayat (Bajju field station) is studied to understand the characteristic of groundwater and its dynamics. The groundwater levels are measured and samples were collected from 40 Km in the eastern and 20 km in the western direction. The groundwater data analysis reveals that depth to water level varies between 10 and 55 m bgl. The water levels are shallow in western direction and upto Bajju in eastern direction from the canal. The water level become deeper as we move towards eastern direction from Bajju. The groundwater dynamics suggest that the canal is recharging towards western direction and upto Bajju in the eastern direction. Physiochemical water quality analysis of canal and groundwater samples confirms the same result. The EC of the canal is 302 $\mu\text{S}/\text{cm}$ where as the EC of groundwater varies from 563 $\mu\text{S}/\text{cm}$ to 23600 $\mu\text{S}/\text{cm}$. The groundwater in general is not suitable for drinking purposes as salinity and fluoride exceeds the limit from Indian standards drinking water.

REFERENCES

1. Central Ground Water Board (WR) – Western Region: Report on dynamic groundwater resources of Rajasthan (2005)
2. Central Ground Water Board (WR) – Western Region: Report on groundwater scenario, Bikaner District, Rajasthan (2009)
3. Mandal, S.K.: Climate, Sustainability and Development in Semi-arid Regions, 2nd International Conference, August 16-20, 2010, Fortaleza – Ceará, Brazil (2010)
4. Srivastava, M., Sharma, I.K. and Sharma, D.D.: Ground Water Scenario in Indira Gandhi Nahar Pariyojna (IGNP) in parts of Sri Ganganagar, Hanumangarh, Churu, Bikaner, Jaisalmer, Jodhpur and Barmer Districts, Rajasthan. Memoir Geological Society of India, No. 82, 2013, pp. 16–35 (2013)

Chapter 53

Domestic Wastewater Treatment Using Tanfloc: A Tannin Based Coagulant

Rajesh Singh, Sumant Kumar, and Megha Garg

Abstract Fresh water resources in most areas of world are shrinking at an alarming rate and may not meet the ever increasing demands for domestic, agriculture and industry in future. Moreover, estimates reveal an annual production of ~30 MT of wastewater in the World. In India, estimated sewage water generation from Class I and Class II cities is 38,255 MLD, out of which only 11,787 MLD is being treated. The untreated wastewater enters in groundwater, rivers, and other water bodies thereby making it unfit for human consumption. The projected wastewater generation in India will be 122,000 MLD by 2050, which necessitates strengthening of existing treatment plants and investment in new treatment plants for safeguarding fresh water resources and human health. Pre-treatment is an integral part of any wastewater treatment scheme and results in appreciable reduction in capital as well as operating cost associated with downstream units due to reduction in organic load. A tannin based natural flocculent (Tanfloc) along with ferric chloride was used for pre-treatment of domestic wastewater using jar-test. It was able to achieve reduction in turbidity, COD, and BOD up to 95%, 69%, and 60% respectively. The optimum dosage for treatment of municipal wastewater under investigation was 10 ppm ferric chloride with 15 ppm Tanfloc.

Keywords: Wastewater • Coagulant • Tannin • Organics

53.1 INTRODUCTION

Ineffective sanitation infrastructures facilitate every year 2.2 millions of deaths by diarrhoea, mainly among child under 3 years old, 6 million people blind from trachoma and 200 million people infected with schistosomiasis [1]. Obviously,

R. Singh (✉)

Environmental Hydrology Division, National Institute of Hydrology, Roorkee, India
e-mail: rs.chemistry@gmail.com

S. Kumar

Groundwater Hydrology Division, National Institute of Hydrology, Roorkee, India

M. Garg

Department of Biotechnology, DAV College, Chandigarh, India

most of them in developing countries, so appropriate technologies referring urban wastewater may be investigated in order to broaden the variety of technical possibilities of treatment. In this sense, many types of water treatment are being used. Their differences lay on economical and technical features. Several previous papers have pointed out the importance of urban wastewater management [2, 3]. This type of waste has been a target for social studies, as it involves several aspects that have to do with social structure and community organization [4, 5]. According to this dimension, it is very important to consider wastewater management as a social change factor in developing countries, as the relationship between wastewater treatment and production, on one hand, and human developing process, on the other, is rather known. Researching on other procedures of water treatment has been the scope of this work. For several years, investigators are concerned towards working on an alternative process for water treatment, mostly bearing in mind concepts such as sustainability, affordability and social feasibility. In this sense, natural coagulants/flocculants are wide-spread, easy-handling resources that are not difficult to work with by non-qualified personnel. There are some examples of this agent, such as *Moringa oleifera* [6] or *Opuntia ficus* [7]. Tannins may be a new source for coagulant and flocculent agents. The main aim of the present investigation is to characterize the coagulant and flocculent activity of this new tannin-based product (Tanfloc) as a municipal wastewater treatment. TANFLOC flocculent product is a trademark that belongs to TANAC (Brazil). It is a tannin-based product, which is modified by a physicochemical process, and has a high flocculent power. It is obtained from an *Acacia mearnsii* bark. This tree is very common in Brazil and it has a high concentration of tannins. According to TANAC specification, TANFLOC is vegetal water extract tannin, mainly constituted of flavonoid structures with an average molecular weight of 1.7 kDa. More groups such as hydrocolloid gums and other soluble salts are included in the TANFLOC structure. Chemical modification includes quaternary nitrogen that gives TANFLOC cationic character.

53.2 MATERIALS AND METHODS

53.2.1 *Chemicals*

TANFLOC has been kindly supplied by TANAC (Brazil). The reagents used throughout the investigations were A.R. grade and procured from Merck/Qualigens chemicals and all the solutions were prepared with deionized water. All the glassware used during the experiment were thoroughly cleaned by soaking in chromic acid solution and finally rinsed with de-ionized water several times prior to use.

53.2.2 Domestic Wastewater

The sewage/domestic wastewater was collected from Khanjarpur drain (Roorkee), which receives domestic effluent from IIT Roorkee and nearby habitation. Samples were collected immediately before conducting the experiments in order to avoid any change in the actual composition of sample.

53.2.3 Jar Test Procedure

Jar-test was selected as the standard treatment in order to study coagulation process. The procedure was: 0.5 L of sewage was put into a beaker. Certain dose of coagulant/ flocculent was added, and beaker was put into a magnetic stirrer (Remi Make). The solution was stirred at 500 rpm for 2 minutes after addition of chemicals followed by slow stirring at 150 rpm for 20 minutes in order to mimic the process taking place in solids contact clarifier. Treated water samples were obtained from the centre of beaker, 3 cm from the surface.

53.2.4 Analytical Methods

All analytical measures were made according to the Standard Methods for the Examination of Water and Wastewater [8].

53.3 RESULTS AND DISCUSSION

53.3.1 Effect of Tanfloc Dosage

As a first approach, different dosage of Tanfloc flocculent (2-20 ppm) was added to sewage sample to understand the efficacy of the chemical towards reduction of pollutants. Turbidity was reduced by 85.6% with 20 ppm Tanfloc dosage. The optimum dosage for COD reduction was found to be 10 ppm with 62.8% reduction. Higher does not yield any further reduction. Maximum BOD reduction (57.7%) was observed with 20 ppm dosage (Fig. 53.1).

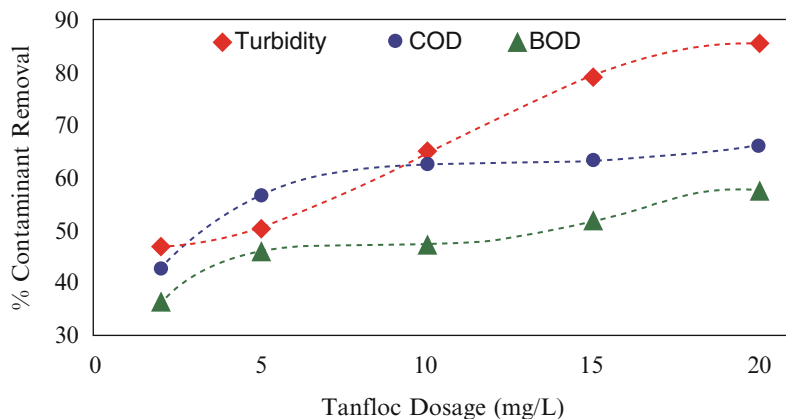


Fig. 53.1 Effect of Tanfloc doses on turbidity, COD, and BOD reduction

53.3.2 Synergistic of Ferric Chloride and Tanfloc Dosage

Tanfloc is a flocculent and hence, its efficiency can be improved by dosage of coagulant. To understand the effect of coagulant, Tanfloc was dosed in varying dosages (2-20 ppm) along with 10 ppm ferric chloride. Ferric chloride was selected based on pH of sewage, which is most suited for iron based coagulants. Prominent reduction in the contaminants was observed with the combined effect of ferric chloride (coagulant) and Tanfloc (flocculent). Maximum reduction in turbidity (96.9%) and COD (81.4%) was achieved with 15 ppm Tanfloc dosage whereas maximum reduction in BOD (80.7%) was achieved with Tanfloc dose of 10 mg/L (Figure 53.2). So, in this case the optimum dosage of Tanfloc was 15 ppm. Dosing Tanfloc, above 15 ppm resulted in reduced contaminant reduction efficiency. This may be due to formation of daughter aggregates as a result of addition of charge to the neutralized aggregates.

53.3.3 Optimization of Coagulant (Ferric Chloride) Dosage

For achieving the optimum dosage of ferric chloride, Tanfloc dosage was kept constant (15 ppm) and ferric chloride dosage varied (5-20 ppm). Percentage reduction of contaminates is shown in Fig. 53.3.

It can be concluded from this experiment that with 15 ppm Tanfloc, 5 ppm ferric chloride is sufficient to produce optimized result in terms of turbidity. For maximum reduction in COD and BOD, the dosage of ferric chloride is 10 ppm and 20 ppm respectively. Considering all the three parameters, the optimum dosage of ferric chloride is 10 ppm along with 15 ppm Tanfloc. This also result in appreciable reduction in sludge volume.

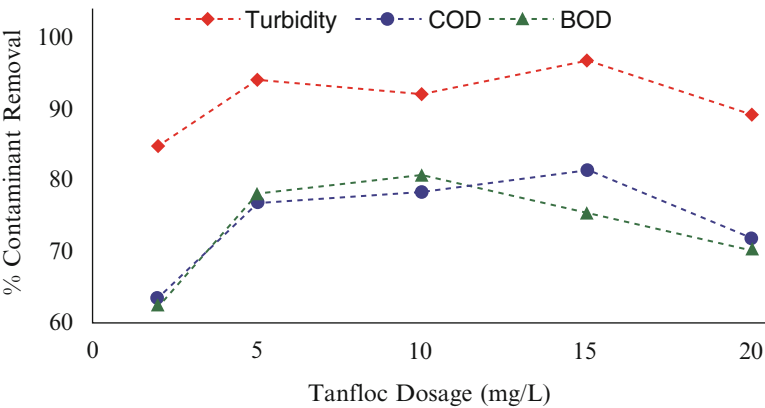


Fig. 53.2 Effect of Tanfloc and ferric chloride dosing on turbidity, COD, and BOD reduction

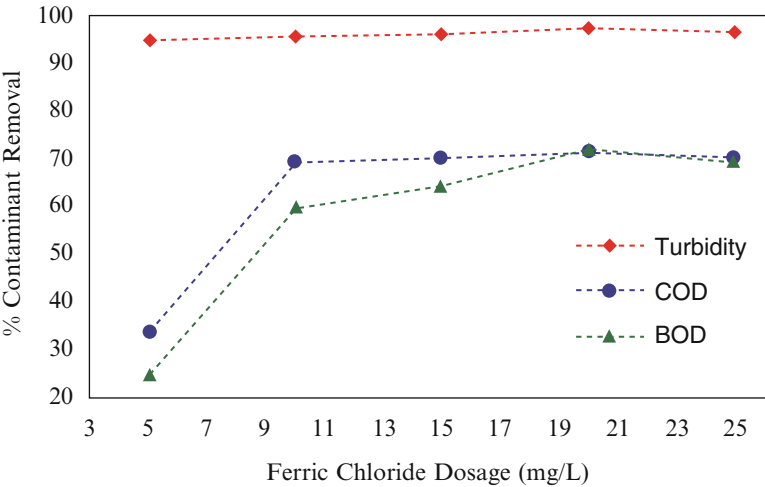


Fig. 53.3 Effect of ferric chloride doses on turbidity, COD, and BOD reduction

53.4 CONCLUSIONS

The conclusions that may be drawn from the present investigation are-

- The tannin based flocculant (Tanfloc) can be used for treating municipal wastewater (sewage).
- Efficiency of Tanfloc increases manifold with coagulant such as ferric chloride in for removing turbidity, COD, and BOD.
- Up to 95 % turbidity, 69 % COD, and 60 % BOD is removed with Tanfloc treatment along with ferric chloride.

- The optimum dosage for the sewage under investigation was 10 ppm ferric chloride with 15 ppm Tanfloc.

REFERENCES

1. WHO: UN-water global annual assessment of sanitation and drinking-water (GLAAS) 2012 report: The challenge of extending and sustaining services, Switzerland (2012)
2. Harleman, D.R.F. and Murcott, S.: The role of physical-chemical wastewater treatment in the mega-cities of the developing world. *Water Science and Technology*, 40, 75–80 (1999)
3. Karrman E.: Strategies towards sustainable wastewater management. *Urban Water*, 3, 63–72 (2001)
4. Starkl, M., Brunner, N. and Flogl W.: Feasibility versus sustainability in urban water management. *Journal of Environmental Management*, 71, 245–260 (2004)
5. Starkl, M., Brunner, N., Flogl, W. and Wimmer, J.: Design of an institutional decision-making process: The case of urban water management. *Journal of Environmental Management*, 90, 1030–1042 (2009)
6. Beltran-Heredia, J., Sanchez-Martín, J., Delgado-Regalado, A. and Jurado-Bustos, C.: Removal of Alizarin Violet 3R (anthraquinonic dye) from aqueous solutions by natural coagulants. *Journal of Hazardous Materials*, 170, 43–50 (2009)
7. Young, K., Anzalone, A. and Alcantar, N.: Using the Mexican cactus as a natural based process for removing contaminants in drinking water. *Polymeric Materials: Science & Engineering*, 93, 965–966 (2005)
8. APHA: Standard methods for the examination of water and wastewater, Washington (2005)

Chapter 54

Persistent Pesticides in Fluvial Sediment and Their Relationship with Black Carbon

Musarrat Parween, A.L. Ramanathan, N. Janardhana Raju,
and P.S. Khillare

Abstract: The persistence of Organochlorine pesticides (OCPs) and Black Carbon (BC) was studied in sediment samples from river Yamuna, a major tributary of the Ganges (one of the largest, most populated and intensively used rivers in Asia). High levels (21.41 to 139.95 ng g⁻¹) of sum of 20 OCPs (Σ_{20} OCPs) have been detected with β -HCH as the predominant component. Σ HCH and Σ DDT constituted ~86% of Σ_{20} OCPs. Lindane, DDT and technical grade HCH were recently used. Toxicological studies with reference to fresh water sediment quality guidelines showed alarming levels of γ -HCH and DDT. DDD, DDE, β -HCH, α -HCH, Endrin, Heptachlor epoxide and Chlordane exceeded some of the guideline levels. High levels of BC (0.46 ± 0.23 mg g⁻¹) constituted 1.25 to 10.56% of TOC. BC was correlated with isomers of HCH, p,p'-DDT and Methoxychlor; while TOC with Σ_{20} OCPs, γ -HCH, Endosulfan Sulfate and Methoxychlor. PCA enabled better understanding of the relationship between various OCPs, BC and TOC. The association of BC with various OCPs indicated its importance in retention of some OCPs into fluvial sediments; exhibiting the potential to reduce their bioavailability. The study is unique to report the role of BC in persistence of OCPs in fluvial sediments.

Keywords: Organochlorine Pesticide • Black Carbon • Sediment • Persistent • Correlation

54.1 INTRODUCTION

OCPs and BC constitute of the infamous groups of major global contaminants. OCPs can biomagnify and accumulate in living organisms, including animal tissue, blood and even milk. Most of them were banned several years ago, but are still used and are ubiquitous in environment. BC consists of an entire continuum including partly charred plant material, charcoal, graphite and soot with no unambiguously

M. Parween (✉) • A.L. Ramanathan • N.J. Raju • P.S. Khillare
School of Environmental Sciences, Jawaharlal Nehru University, New Delhi, India
e-mail: musarratparween@gmail.com

acceptable boundaries. It is ubiquitous in the atmosphere, sediment, soil, and water, and influence a wide range of biogeochemical processes. Recent studies have demonstrated BC to be capable of adsorbing several types of POPs (including dioxins, polycyclic aromatic hydrocarbons, polychlorinated biphenyls and various pesticides) much more strongly than bulk organic carbon. However, such relationships in context to OCPs have not yet been well established. Asia is the largest source for BC emission where India ranks second [1]. River Yamuna which is the lifeline of Delhi is amongst the most polluted cities of the world. It suitably represents a heavily polluted fluvial ecosystem and was thus selected for this study.

54.2 METHODOLOGY

Sediment samples were processed (methods 3540, 3630C, USEPA) and analyzed with GC-ECD (Shimadzu 2010, Japan) and GC/MS, QP2010 Plus (Shimadzu, Japan). Standard mixture of 22 OCPs (EPA 8081B, Sigma Aldrich, USA) was used for the quantification of OCPs after calibration ($R^2 > 0.99$). Samples were processed for TOC [2] and soot BC [3] and both analyzed with CHNSO analyzer (Euro Elemental Analyzer, Euro Vector EA3000) after calibrations ($R^2 > 0.98$) using Synthetic mixtures for soil#2 and soil#4 (EuroVector, E11036-A and E11038-A). Size fraction of sediment was analyzed using Laser Particle Size Analyser (Microtrac S3500, USA) after processing samples [4]. All methods are described elsewhere [5].

54.3 QUALITY ASSURANCE

Blank and a spiked matrix sample were analysed for OCPs to check contamination and for peak identification. LOD for OCPs was 0.01 ng g^{-1} and recovery between 84 and 95%. The relative standard deviations of replicate samples were $<10\%$, 12% and 7% for OCPs, BC and TOC. Carbon analysis in CHNS elemental analyser (detection limit 50ppm) gave recovery from 86 to 91%. Sample tray, tin capsules, samples and standards were heated overnight in an oven and kept in desiccators before analysis. Blanks and standards as samples were run with each batch of analysis.

54.4 RESULTS AND DISCUSSION

High levels of $\sum_{20}\text{OCPs}$ (21.41 to 139.95 ng g^{-1}) were detected in the study area. $\beta\text{-HCH}$ was the most predominant component (Fig. 54.1). $\sum\text{HCH}$ and $\sum\text{DDT}$ constituted $\sim 86\%$ of $\sum_{20}\text{OCPs}$. Sorption and desorption by soils and sediments

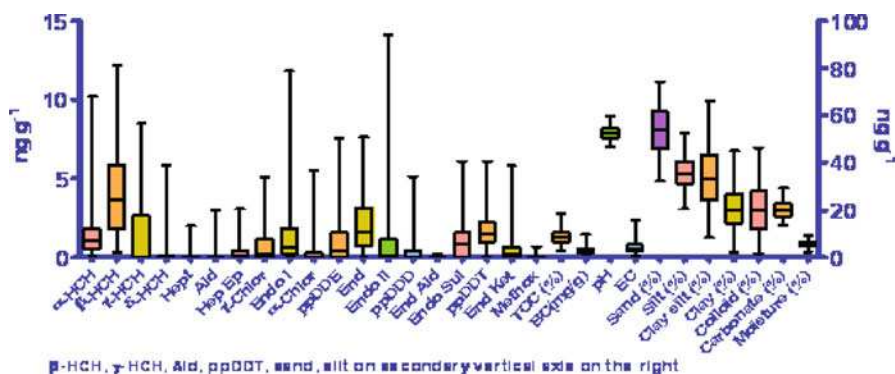


Fig. 54.1 Distribution of OCPs (ng g^{-1}) and BC (mg g^{-1}) along with physicochemical parameters (units specified) of river Yamuna sediment. The unit of EC is mS cm^{-1} . pH is unitless. Values for maximum, 75th percentile, median, 25th percentile and maximum (top to bottom)

are the basic processes controlling fate and transport of OCPs. Sorption was related to the structural and chemical characteristics of the pesticides and determined by properties such as volatility, water solubility, octanol-water partition coefficient, etc. Isomer ratios indicated fresh usage of Lindane, DDT and technical grade HCH. Aldrin and chlordane were speculated at few locations. All of these are banned since decades or restricted for use in India. Toxicological studies with reference to fresh water sediment quality guidelines showed alarming levels of γ -HCH and DDT. β -HCH, α -HCH, Endrin, Heptachlor epoxide, DDD, DDE and Chlordane also exceeded guideline levels. Soil properties such as, pH, EC, soil particle size composition and soil moisture determined the distribution of OCPs. Molecular weight and vapour pressure were observed as important properties which control the association of pesticides with sediment. TOC and BC had mean concentrations $1.37 \pm 0.51\%$ and $0.46 \pm 0.23 \text{ mg g}^{-1}$ respectively. BC constituted 1.25 to 10.56% of TOC. Identification of 10% of TOC as BC has implications for sedimentary carbon preservation [6].

Correlation studies indicated the role of BC and TOC in the retention of OCPs (Fig 54.2). Properties such as large surface area, hydrophobicity and persistence enables BC to bind strongly with OCPs, increase their persistence and lower the risk of bioavailability in tropical freshwater sediments. BC was correlated significantly with various OCPs (α -HCH, β -HCH, γ -HCH, Endrin, Endosulfan sulphate, Methoxychlor) in the study area. The study is thus unique in its observations with regard to strong relationships between OCPs and carbonaceous materials in freshwater sediment. The interactions involved in the process are forces like, van der Waals attraction and hydrophobic interactions. Covalent bonding and sequestration too may be involved. The study thus provides new avenue for investigating soot BC as an adsorbent of OCPs in sediment and an important component controlling bioavailability.

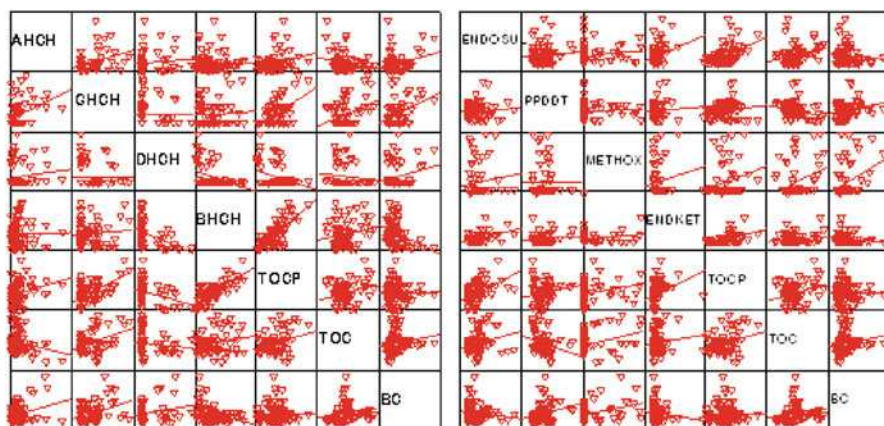


Fig. 54.2 Scatter plot diagram for correlated variables. BC in mg g^{-1} and TOC in percentage, all other variables in ng g^{-1} . A, G, D and B HCH stand for α , β , γ and δ -HCH respectively

54.5 CONCLUSIONS

The study indicated fresh usage of many OCPs that are banned since decades or restricted for use in India including lindane, technical grade HCH, DDT, Aldrin and Chlordane. The floodplain of Delhi which is extensively used for cultivating of crops and vegetables, may act as a potential threat to human health via the food chain. BC concentration was considerably high. Lack of data in freshwater sediment pertaining to BC content and its role in retention of OCPs which promoted this study has obtained results with moderate but significant correlation between TOC, BC and OCPs. The study is thus, unique in its observations with regard to strong relationships between OCPs and BC in tropical freshwater sediment. Due to its large surface area, hydrophobicity and persistence, BC may have the potential to bind strongly with OCPs, enhance their persistence and lower the risk of bioavailability in tropical freshwater sediments.

ACKNOWLEDGEMENT One of the authors is grateful to Indian Council of Medical Research, New Delhi, India, for funding for the research as JRF. Analytical facilities provided by the AIRF and CIF (SES), JNU, New Delhi are also duly acknowledged.

REFERENCES

1. Kroeger, T.: Black carbon emissions in Asia: sources, impacts and abatement opportunities. Contractor report prepared by International Resources Group for USAID, ECO-Asia Clean Development and Climate Program. Bangkok, Thailand (2010)

2. Hu, L., Zhang, G., Zheng, B., Qin, Y., Lin, T. and Guo Z.: Occurrence and distribution of organochlorine pesticides (OCPs) in surface sediments of the Bohai Sea, China. *Chemosphere*, 77(5), 663–672 (2009)
3. Gélinas, Y., Prentice, K.M., Baldock, J.A. and Hedges, J.I.: An improved thermal oxidation method for the quantification of soot/graphitic black carbon in sediments and soils. *Environ Sci Technol*, 35(17), 3519–3525 (2001)
4. Konert, M. and Vandenberghe, J.E.F.: Comparison of laser grain size analysis with pipette and sieve analysis: a solution for the underestimation of the clay fraction. *Sedimentology*, 44(3), 523–535 (1997)
5. Parween, M., Ramanathan, A.L., Raju, N.J. and Khillare, P.S.: Persistence, variance and toxic levels of Organochlorine pesticides in fluvial sediments and the role of Black carbon in their retention. *Environ Sci Pollut Res*, DOI [10.1007/s11356-014-2531-6](https://doi.org/10.1007/s11356-014-2531-6) (2014)
6. Gustafsson, Ö. and Gschwend, P.M.: The flux of black carbon to surface sediments on the New England continental shelf. *Geochim Cosmochim Acta*, 62(3), 465–472 (1998)

Chapter 55

Relationship between Physicochemical Parameters and Toxicity of Leachate from Municipal Solid Waste Landfill Site in Delhi

Anshu Gupta and R. Paulraj

Abstract: As landfills are used to dispose Municipal Solid waste (MSW) but due to lack of proper engineering facilities, these landfills have always been the source of pollution in the soil and water environment. The leachate samples were collected from Bhalaswa landfill site in Delhi in winter season. Leachates were characterized by measuring physicochemical parameters like pH, EC, TDS, concentrations of metals like Pb, Cu, Fe, Ni, Cr, Ca, K, Na, Mg. Toxicity tests such as germination inhibition and growth were tested and cell apoptosis was assessed by Flow cytometry. The toxicity tests were conducted by diluting the crude leachate with distilled water and toxicity was recorded against *Triticum aestivum* (Wheat). The results indicate that lower concentration stimulated germination as well as growth while higher concentrations inhibited the process in a time and dose dependent manner. This implies that leachate from the landfill is toxic to plants and exposure to the leachate in aquatic environment may pose a potential risk to the organisms. The results show that *Triticum aestivum* treated with different concentrations of leachate induces toxicity in *Triticum aestivum* in a time and dose dependent manner. The results further indicate the relationship between physicochemical parameters and toxicity.

Keywords: Municipal Solidwaste Landfill • Leachate • Bioassay • Toxicity

55.1 INTRODUCTION

Waste entering the landfill sites undergoes a number of transformations that include biological, chemical and physical. In the landfill three physical phases are present: the solid phase (waste), the liquid phase (leachate) and the gas phase. The liquid phase is enriched by solubilised or suspended organic matter and inorganic ions from the solid phase. In the gas phase mainly carbon (prevalently in the form of CO₂ and CH₄) is present. The main environmental aspects of landfill leachate are

A. Gupta • R. Paulraj (✉)

School of Environmental Sciences, Jawaharlal Nehru University, New Delhi, India

e-mail: paulrajrajamani@gmail.com

the impacts on surface as well as groundwater quality if leachate is discharged into these water bodies without any prior treatment [1]. Leachate is characterized by high concentrations of organic and inorganic compounds. The contact of such a complex mixture with the surrounding water bodies, could lead to environmental problems [2, 3], therefore it is considered as an environmental matter of concern. A number of studies have shown that the leachate has contaminated the underlying ground water in the vicinity of the landfill sites [4–6]. It has been reported earlier that a large volume of ground water can be contaminated by even a small amount of landfill leachate. This polluted water may ultimately affect the aquatic biodiversity of the aquatic ecosystem and can also lead to the contamination of food chain [7, 8]. It has been reviewed from the previous literature that a number of toxic as well as carcinogenic chemicals were present in the leachates of all the MSW landfills studied [9]. Traditionally, the risk assessment of MSW landfills is based only on the chemical analysis of some specific compounds present in the leachate. In contrast to chemical analysis alone, bioassays can be used to characterize the toxicological affects of the municipal solid waste leachates that would integrate the biological effects of all the constituents of the leachates. Thus, with the help of bioassays, bioavailability, synergistic, antagonistic, additive affects of the constituents of the leachate can be assessed directly without going for assumptions and extrapolation made from chemical analysis alone [10]. Plant bioassays are simple as compared to animal bioassays. These bioassays have been validated in international collaborative studies under the United Nations Environment Programme (UNEP), World Health Organisation (WHO), US Environment Protection Agency (USEPA). These plant bioassays have proved to be efficient for toxic monitoring of environmental pollutants [11–14]. The aim of the present study was to monitor the leachate composition of Bhalswa landfill site and its toxicity to *Triticum aestivum*.

55.2 MATERIALS AND METHODS

55.2.1 Landfill Leachate Sample Collection

According to the multi-spot collection principle, samples were collected at different depths and at different points. Collected samples from different points were mixed and sealed in a clean plastic barrel with a lid and ring clamp, and promptly transported to the laboratory for analysis and stored at 4°C. Measurement were followed by the procedures described in American Public Health Association. Physicochemical analysis such as pH, Electrical conductivity (EC), Total dissolved solids (TDS) were measured in the field without any delay by water analysis kit (PC-510, Eutech instruments). The samples for Heavy metal determination were preserved by the addition of 1ml HNO₃ /L of the leachate in order to arrest the microbial activities and to prevent precipitation of the metals in the leachate samples. Samples were brought to lab and kept at 4°C until further processed and

analysed according to the standard methods [15]. The digested samples were analysed for metals such as Cr, Cd, Cu, Zn, Pb and Fe and alkali metals such as Na^+ , K^+ , Ca^{2+} , Mg^{2+} by the Flame Atomic Absorption Spectrophotometer (Thermo Scientific).. The Chloride and Sulphate were analyzed by Spectrophotometer (HACH DR 2700) using the standard methods as given in APHA (2005). Chemical Oxygen Demand (COD) and Biochemical Oxygen Demand (5 day BOD) were also analysed by standard methods. The instrument was calibrated using the reference standards and suitable blank in order to produce high quality in the analysis.

55.2.2 Wheat Preparations

Wheat, supplied by Indian Agricultural Research Institute, Pusa, New Delhi was selected as the test plant. Dry seeds were soaked for 3 h in distilled water and allowed to germinate on moist germination sheet for the use in the test.

55.2.3 Germination Test

There were seven groups. Six treatment groups were exposed to the leachate of different concentration by diluting the crude leachate with distilled water (10%, 20%, 40%, 60%, 80% and 100%). The negative control group was exposed to distilled water. The germination ratio of 300 soaked seeds in each treatment was measured after exposure for 24, 48 and 72 h. The experiment was carried out in triplicate.

55.2.4 Root Tip Preparations for Early Seedling Growth Test

Triticum aestivum (Wheat) was selected as the test plant. Dry Wheat seeds were soaked for 24 h in distilled water and allowed to germinate between two layers of moist germination sheet at 25 ± 1 °C. When the newly emerged roots were about 1.0 cm in length, they were used for the test

Thirty seedlings, which reached 1 cm in root length, were treated for 120 h, and the seminal root in each treatment was measured after exposure. All the experimental groups were maintained in an incubator at 25 ± 1 °C.

55.2.5 Flow Cytometric Analysis for Cell Apoptosis

The cell apoptosis was measured on Flow cytometer (Beckman coulter) equipped with 15mW argon laser. It was carried out by the method given by [16].

55.3 RESULTS AND DISCUSSION

The leachate sample showed alkaline pH (pH=8.1). According to [17], the landfills that are very old generate leachates that are alkaline in nature with pH ranging from 8.0-8.5. The samples showed a very high EC (26500 $\mu\text{S}/\text{cm}$). Total dissolved solids (TDS) of the sample were also very high (21540 mg/L). Conductivity is an indicator of the abundance of the total concentration of the ions or the abundance of the dissolved inorganic species [18]. The leachate samples analysed showed a very high concentration of Fe (17.3 mg/L). Cu, Ni and Cd were found in the concentration of 0.409, 0.71, 0.79 mg/L, respectively. Chromium (5.34 mg/L) and Pb (7.038) were found beyond the permissible limits set by CPCB for leachate disposal [19]. High concentration of Fe in the leachate is the evidence of dumping of iron and steel scraps in the dump site [20]. The quantity of Pb in the leachate is attributed to the disposal of wastes such as batteries, paints and photography processing chemicals in the dump site [6]. Chloride and Sulphate were found to be 4922.4 and 5135 mg/L respectively. Also chloride is a conservative parameter of the landfill leachate, thus poses a serious threat to the ground water in the vicinity of the landfill [5]. Na, K, Ca and Mg were found as 10423, 13384, 1058 and 11334 mg/L respectively in the leachate of Bhalaswa landfill site. BOD of the samples was 900 mg/L and COD was 11000 mg/L. Both the parameters were beyond the standard limits.

55.3.1 Germination Inhibition

The seeds treated with the different concentrations of leachate showed germination inhibition in a time and dose dependent manner (Fig. 55.1). In the lower concentrations, the seeds germinated well with respect to the control. In the lower doses the number of seeds germinated increased with increase in time of treatment. Whereas in the higher doses (60%), the seed germination was inhibited. In 80% and 100% there was total inhibition of the process of germination which shows that the leachate is very toxic.

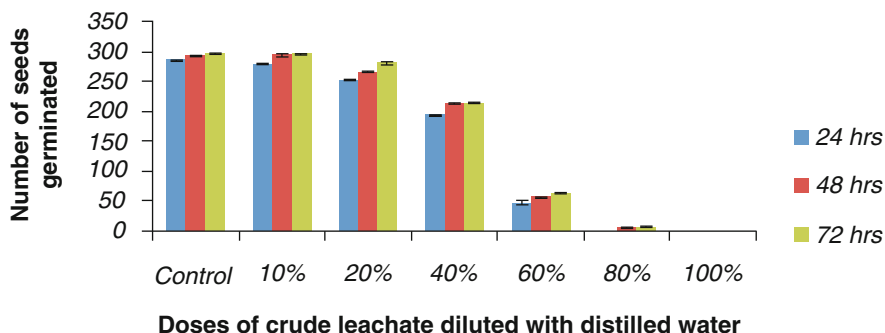


Fig. 55.1 Effect of landfill leachate on the germination of the seeds of *Triticum aestivum* in a time and dose dependent manner

55.3.2 Early Seedling Growth

The seedlings treated with leachate showed root elongation in a time and dose dependent manner. In the lower leachate concentrations the seedlings grew but as there was increase in the concentration, the root length growth was inhibited (Fig. 55.2). After 10% there was inhibition of root growth with respect to control and at 60%, 80% and 100% there was no root elongation as the growth was totally inhibited in these concentrations.

55.3.3 Landfill Leachate Induced Cell Apoptosis

The cell apoptosis was tested by Flow cytometry shown in Fig. 55.3, shows that after treating the root tips of *Triticum aestivum* with different concentrations of leachate for 72 hrs, the apoptosis increased in the cells of root tips in a dose dependent manner. In the root tips treated with 20% leachate for 72 hours, 8.04% of the total cells were apoptotic and it was 12.51% for 40% leachate treatment, 16.71% for 60%, 19.17% for 80% and 28.54% of the total cells in 100% leachate treatment where as in control the number of apoptotic cells were 0.87% only.

55.4 CONCLUSIONS

As the use of municipal solid waste landfills have become the most widely utilized method of solid waste disposal, contamination from municipal landfill leachate has become a serious problem for the aquatic environment because the leachates

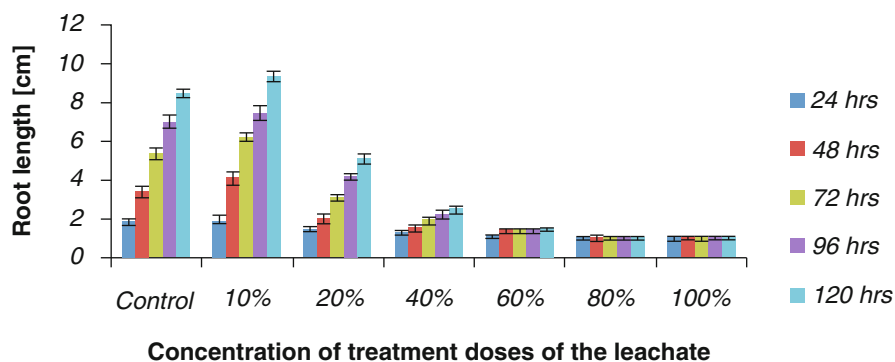


Fig. 55.2 Effect of leachate on the root elongation of the seedlings of *Triticum aestivum* in a time and dose dependent manner

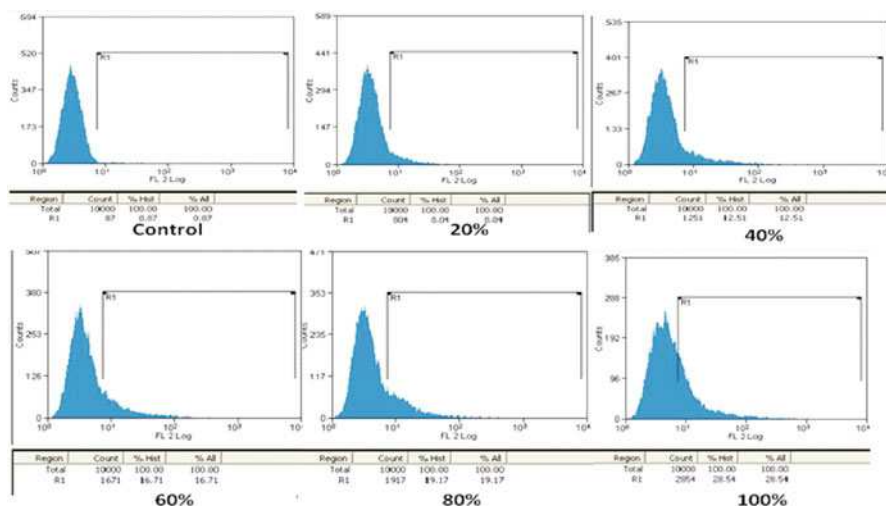


Fig. 55.3 The cell apoptosis in the cells of root tips of *Triticum aestivum* among the leachate treated groups and control

contaminate both surface as well as ground water, which is either due to faulty design or construction of the landfill site. Most of the parameters analysed like BOD, COD, Chloride, Cr, Pb were beyond the standard limits set by CPCB for leachates. The toxicity seen in the bioassay is directly related to the concentration of pollutants. In the lower leachate concentrations the level of pollutants is also lower so the toxicity is also less but as there is increase in the concentration of the leachate treatment the toxicological effects become more severe. It shows that the toxicity is directly related to the physical and chemical parameters of the leachate. It becomes very important for the appropriate risk assessment so that the various health risks to plants and animals as well as humans can be evaluated. The present study indicates that municipal solid waste leachate is very toxic and it should be treated before disposing it to the environment.

REFERENCES

1. Chistensen, T.H., Raffaello, C. and Rainer, S.: Landfill Leachate. In: Land Filling of Waste Leachate. Christensen, T.H. and R. Stengmann (Eds.). St. Edmundsbury Press, Bury St. Edmunds, Suffolk, Great Britain, pp: 14 (1992)
2. Olivero-Verbel, J., Padilla-Bottet, C. and De la Rosa, O.: Relationships between physico-chemical parameters and the toxicity of leachates from a municipal solid waste landfill. *Ecotoxicol. Environ. Saf.*, 70, 294–299 (2008)
3. Matejczyk, M., Plaza, G.A., Nalecz-Jawecki, G., Ulfig and Markowska-Szczupak, A.: Estimation of the environmental risk posed by landfills using chemical, microbiological and ecotoxicological testing of leachates. *Chemosphere*, 82, 1017–1023 (2011)

4. Jhamnani, B. and Singh, S.K.: Groundwater Contamination due to Bhalasawa Landfill site in New Delhi. *Inter. J. Civil Env. Eng.*, 3, 121–125 (2009)
5. Srivastava, S.K. and Ramanathan, A.L.: Geochemical assessment of groundwater quality in vicinity of Bhalswa landfill, Delhi, India, using graphical and multivariate statistical methods. *Environmental Geology*, 53(7), 1509–1528 (2008)
6. Mor, S., Ravindra, K., Dahiya, R.P. and Chandra, A.: Leachate characterization and Assessment of Ground water pollution near Municipal Solidwaste landfill site. *Environ. Monitoring and Assess.*, 118, 435–456 (2008)
7. Bakare, A.A., Mosuro, A.A. and Osibanjo, O.: Effect of stimulated leachate on chromosomes and mitosis in roots of *Allium cepa* L.. *Environ. Biol.*, 21, 251–260 (2000)
8. Christensen, T.H., Kjeldsen, P., Albrechtsen, H.-J., Heron, G., Nielson, P.H., Bjerg, P.L. and Holm, P.E.: Attenuation of landfill leachate pollutants in aquifers, *Crit. Rev. Environ. Sci. Technol.*, 24, 119–202 (1994)
9. Schrab, G.E., Brown, K.W. and Donnelly, K.C.: Acute and genetic toxicity of municipal landfill leachate. *Water, Air, Soil Pollut.*, 69, 99–112 (1993)
10. Kjeldsen, P., Rooker, M.A., Baun, A.P., Ledin, A. and Christenson, T.H.: Present and longterm composition of Municipal Solidwaste Landfill leachate: A review. *Critical reviews in Environmental Science and Technology*, 32, 297–336 (2002)
11. Grant, W.F.: Higher plant assays for the detection of chromosomal aberrations and gene mutations—a brief historical background on their use for screening and monitoring environmental chemicals. *Mutat. Res.*, 426, 107–112 (1999)
12. Grant, W.F.: Chromosome aberration assays in *Allium*. A report of the U.S. Environmental Protection Agency Gene-Tox program. *Mutat. Res.*, 99, 27–29 (1982)
13. Ma, T.H.: The international program on plant bioassays and the report of the follow-up study after the hands-on workshop in China. *Mutat. Res.*, 426, 103–106 (1999)
14. Ma, T.H.: *Vicia* cytogenetic tests for environmental mutagens. A report of the U.S. Environmental Protection Agency Gene-Tox program. *Mutat. Res.*, 99, 257–271 (1982)
15. APHA: Standard methods for the Examination of Water and Waste Water. 21st edn. American Public Health Association/American Water Works Association/Water Environment Federation, Washington, DC (2005)
16. Lee, T.J., Shultz, R.W., Bowdoin, L.H. and Thompson, W.F.: Establishment of Rapidly Proliferating Rice Cell Suspension Culture and Its Characterization by Fluorescence-Activated Cell Sorting Analysis. *Plant Molecular Biology Reporter*, 22, 259–267 (2004)
17. Slomczynska, B. and Slomczynski, T.: Physico-chemical and toxicological characteristics of leachates from Municipal Solid waste landfills. *Polish Journal of Environmental Sciences*, 13 (6), 627–637 (2004)
18. Banar, M., Aysun, O. and Mine, K.: Characterization of the leachate in an urban landfill by physicochemical analysis and solid phase micro extraction. GC/MS. *Environ. Monitor. Assess.*, 121: 439–459. DOI: [10.1007/s10661-005-9144-y](https://doi.org/10.1007/s10661-005-9144-y) (2006)
19. The Gazette of India. Municipal Solid Waste (Management and Handling) Rules, 2000. Notification issued by Ministry of Environment and Forests, Government of India (2000)
20. Asuma-Ohwoghere, O. and Aweto, K.E.: Leachate characterization and Assessment of Groundwater and surface water qualities near municipal solid waste dump side in Effurun, Delta State, Nigeria. *Int. J. of Environment and Earth Sc.*, 3(9), 126 (2013)

Chapter 56

Effects of Coal Mining Activities on Soil Properties with Special Reference to Heavy Metals

Bhanu Pandey, Madhoolika Agrawal, and Siddharth Singh

Abstract: Soil physico-chemical properties and concentrations of heavy metals in the soils around Jharia coalfield in Jharkhand state of India were determined to quantify the levels of contamination in the area. The extensive coal mining in the area altered physico-chemical properties of the soil. Sites near coal mining areas were heavily contaminated with all the measured heavy metals. The average concentrations of Fe, Mn, Zn, Pb, Cu, Ni, Cd and Cr were higher compared to the critical soil concentrations. At the sites near coal mining areas, Mn, Cu and Ni were near the toxic limits of the respective metals. Soil pollution assessment was carried out using enrichment factor, geo-accumulation index and pollution load index. Higher enrichment factor for Mn, Zn, Pb, Cu, Ni and Cd indicated significant inputs from mining activities in the soil. The geo-accumulation index values revealed that Cu, Pb and Ni are significantly accumulated in the study area. The pollution load index derived from contamination factor indicated that the sites near coal mining areas are most polluted. Multivariate statistical analyses, principal component and cluster analyses suggested that Ni, Cu and Pb were derived from anthropogenic sources, particularly coal mining activities and vehicular transport.

Keywords: Coal Mining • Soil Properties • Heavy Metal • Enrichment Factor • Geo-Accumulation Index • Soil Pollution Index

56.1 INTRODUCTION

In order to meet the energy necessities of the increasing population and industries, the overall coal production as well as coal mining have enormously increased in India, which ranks third amongst the top ten coal producing countries in the world

B. Pandey (✉) • M. Agrawal

Laboratory of Air Pollution and Global Climate Change, Department of Botany, Banaras Hindu University, Varanasi, India
e-mail: bhanubot@gmail.com

S. Singh

Central Institute of Mining and Fuel Research, Dhanbad, Jharkhand, India

[1]. The Indian reserve of coking coal is mainly found in the Jharia coal field (JCF) in Jharkhand state. The exhaustive coal mining activities and mine fires in the area have brought about various geo-environmental hazards such as soil and water pollution [2]. Coal mining activities are unavoidably linked with the excavation of huge amounts of dump rocks, which are of great environmental concern due to the potential for production of acidic and metal-rich drainage. Burning coal gives rise to airborne compounds such as fly ash and bottom ash, which contain heavy metals that settle down or wash out from the atmosphere into the land and thus contaminate soil.

56.2 STUDY AREA

Jharia coalfield (JCF) is located in Dhanbad district of Jharkhand state of India. It lies between latitudes $23^{\circ} 39'$ to $23^{\circ} 48'$ N, longitudes $86^{\circ} 11'$ to $86^{\circ} 27'$ E and 222 m above mean sea level (Fig. 56.1).

56.3 MATERIALS AND METHODS

Five sites were selected around JCF for soil sampling. At each site, five sub sites were selected and the soil samples were collected upto 15 cm depth during May 2011. Black shale and sandstone were collected from two sites. All the soil samples

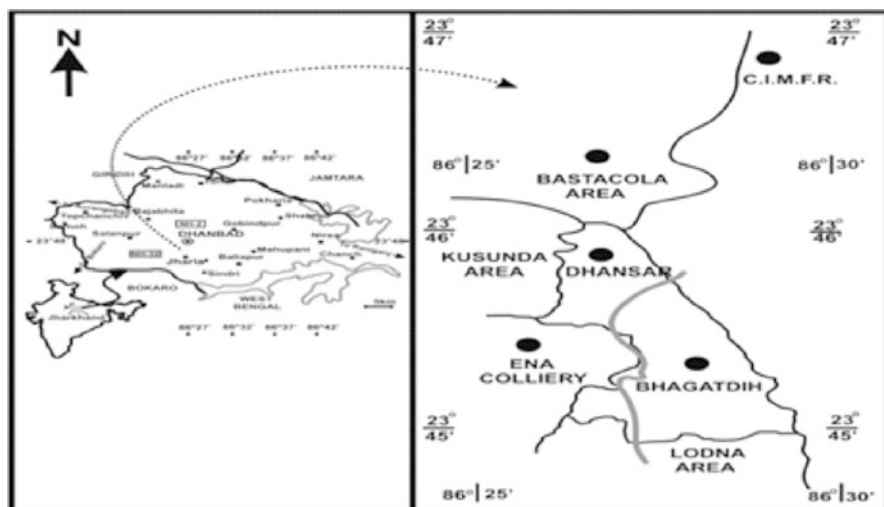


Fig. 56.1 Location of the study site and sampling stations

were analyzed for physico-chemical properties, while heavy metal concentrations analyses were done for soil samples and sediments.

56.4 RESULTS AND DISCUSSION

The coal mining activities increased the concentrations of potentially toxic heavy metals, which varied considerably with the locations due to distances from the mining area. Heatmap of z-score transformed physico-chemical properties and heavy metals reveals that except soil pH and Cr all showed their maximum (red color) in the soil of coal mining area (Fig. 56.2). The average concentrations of Fe, Mn, Zn, Pb, Cu, Ni and Cd were higher compared to the critical soil concentrations. At the sites near coal mining areas, Mn, Cu and Ni were near the toxic limits of the respective metals. Soil pollution assessment was carried out using enrichment factor, geo-accumulation index and pollution load index. Higher enrichment factor for Mn, Zn, Pb, Cu, Ni and Cd indicated significant inputs from mining activities in the soil. The geo-accumulation index values revealed that Cu, Pb and Ni are significantly accumulated in the study area. The pollution load index derived from contamination factor indicated that the sites near coal mining areas are most polluted. Principal component analysis (PCA) suggested that coal mining, atmospheric deposition and vehicular transport are the major sources of heavy metals in the soil (Fig. 56.3a). Cluster analysis revealed that soil contamination with respect to heavy metals varied considerably with the locations due to distances from the mining site (Fig. 56.3b).

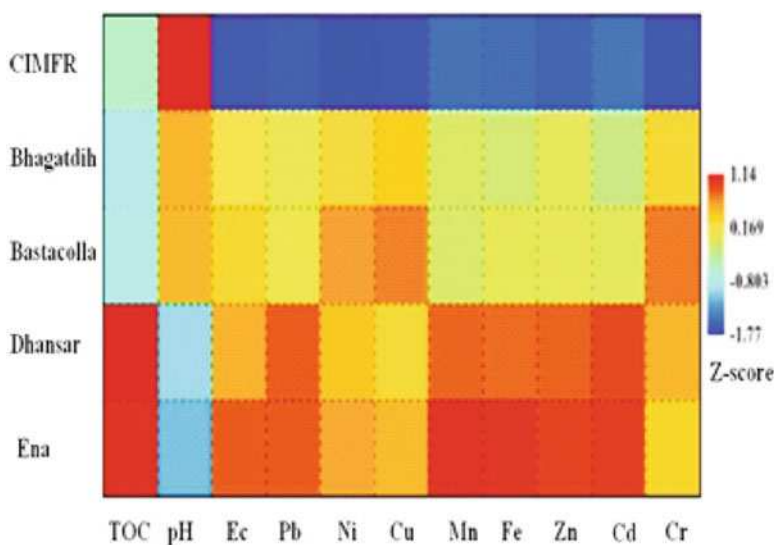


Fig. 56.2 Heatmap of z-score transformed physico-heavy metal conc. at heavy metals at different sites

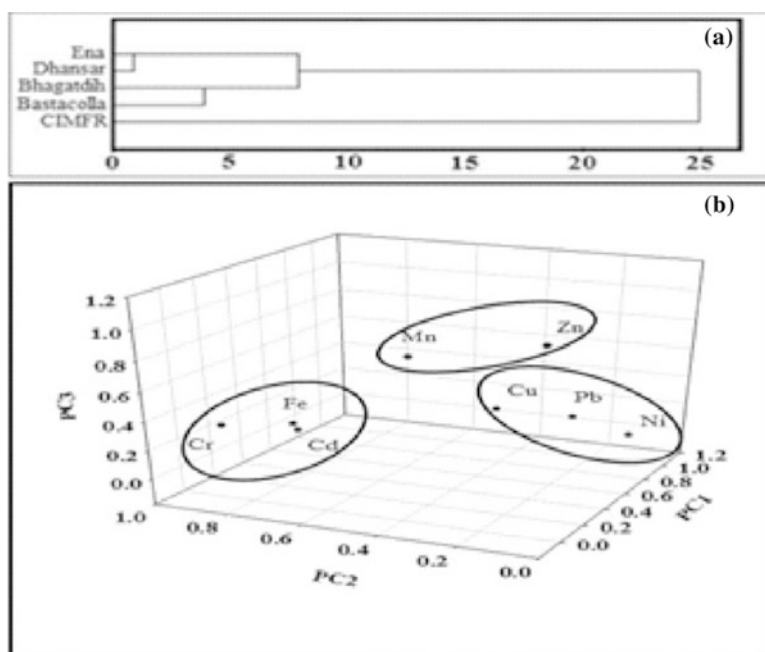


Fig. 56.3 Cluster analysis on the chemical properties and different sites (a) and rotated principal components loading for heavy metal (b) in soil

56.5 CONCLUSIONS

Distinct changes and spatial variations of heavy metals in the soil were recorded around coal mining areas. Anthropogenic sources especially coal mining activities are responsible for high concentration of heavy metals in the soil. High enrichment of heavy metals was found near coal mining areas. Cd, Zn and Pb enriched highly around JCF mostly near coal mining through anthropogenic sources ($EF > 1$). Among the environmentally most toxic heavy metals, Pb, Cd, Zn and Cu were accumulated in the soils at coal mining area and near to the coal mines. The soil of JCF contaminated in the terms of Cd, Cu, Zn and Pb.

REFERENCES

1. World Coal Association: Coal Facts 2011 (2011)
2. Rout, T.K., Masto, R.E., Padhy, P.K., George, J., Ram, L.C. and Maity, S.: Dust fall and elemental flux in a coal mining area. *J. Geochem. Explor.* <http://dx.doi.org/10.1016/j.gexplo.2014.04.003> (2014)

Chapter 57

Coal Mining and Organic Pollutants: A Case of Mahanadi Basin Coalfields, India

Amiya Shankar Naik

Abstract: Coal has been the leading fuel in the energy industry. Its usage has shown far reaching consequences to health and environment. Occurrence of PAH in coal is well known fact but its effect to the human health is least addressed. It is one of the dangerous carcinogens with its ubiquitous presence in the environment. The present investigation on few coal samples reveals presence of substantial amount of PAH in the Mahanadi basin coalfields. Proper mitigation of this substance is required to ensure proper health of the miners and personnel in coal industry. Among the PAH reported are Anthracene, Benzo(a)pyrene, Phenanthrene and Pyrene etc. According to International Agency for Research on Cancer (IARC) a study in 1936 by investigators in Japan and England showed lung cancer mortality among workers in coal carbonization and gasification processes. Later on studies in US was carried on coke oven workers which confirmed the lung cancer mortality, with the suggestion of excessive genitourinary system cancer mortality. Given these implications this investigation attempts to address PAH in the coals of Mahanadi basin.

Keywords: Coal • PAH (Polycyclic Aromatic Hydrocarbons) • Environment

57.1 INTRODUCTION

The Gondwana basins in India occupy a unique position in the physiographical set up of the Indian subcontinent. They are linear trending basin following the major river systems such as Godavari, Mahanadi, Son, Narmada and Damodar basin spanning across six states in the Indian union. The study of these basins is of great importance as 99 % of the coal reserves as per the Geological Survey of India (GSI) exploited in the country is located in the coalfields of these basins. It is thus obvious that the coal production activity in the country is mainly from these regions. Talcher coalfield is the principal coalfield with reserves over 48 billion tones and occupies the number one position in terms of coal production in the state (Fig. 57.1 and 57.2). The coal

A.S. Naik (✉)
Department of Geology, BHU, Varanasi, India
e-mail: amiyanaik@yahoo.co.in

concern to miners as well as the inhabitants of the region but the focus of research have been basically on suspended particulate matter (SPM), respirable particulate matter (RPM), SO_2 , NO_x etc. The focus of Central Pollution Control Board (CPCB) also emphasizes on the above parameters to evaluate the air pollution in the region. The present study highlights the need for characterization of the particulate matter in the air and specifically the polycyclic aromatic hydrocarbon (PAH). This investigation is the outcome of the research carried out on the petrology and geochemistry of the coals of Talcher coalfield. Selected samples were subjected to organic geochemical analysis to identify the aliphatic and aromatic hydrocarbons. World over there is a growing concern over the occurrence of PAH in the environment. These substances are strongest known carcinogens. These are derived through incomplete combustion of organic material arising partly from natural combustion such as forest and volcanic eruption also through anthropogenic emissions. Substantial research on the sources and effects of PAH on the human health has been carried out but the data on Indian context is still in its nascent stage.

57.2 PETROGRAPHIC PROPERTIES OF THE COALS

A quantitative assessment of maceral in these coals reveals that the concentration of vitrinite varies between 15.40% and 81.50%, mean 44.98% (18.40% and 91.96%, mean 49.93% on m.m.f. basis). Among the macerals of this group, collotelinite has been found most dominating with a concentration from 15.00% to 77.6%, mean 43.87% (17.92% to 91.03%, mean 48.69% on m.m.f. basis). Among the macerals of liptinite group the sporinite is the most common maceral ranging in concentration from 0.40% to 22.70%, mean 08.91% (0.47% to 24.46%, mean 09.88% on m.m.f. basis). The inertinite content of these coals ranges from 02.70% to 51.50%, mean 28.44% (5.05% to 53.17%, mean 31.47% on m.m.f. basis). The maceral of this group include fusinite ranging from 1.60% to 41.40%, mean 18.66% (2.99% to 41.99%, mean 20.63% on m.m.f. basis). The vitrinite content in Talcher coals (18.40% to 91.96%, mean 49.29% on m.m.f. basis) suggest that, barring few sections of the coal seams, these coals are vitrinite rich. In seam II of this coalfield, the macerals of vitrinite group show their maximum enrichment in the banded dull coal bands whereas inertinite shows its maximum concentration in the dull coal bands. The liptinite macerals have nearly similar distribution in all the bands except bottom most part of the of this seam where it shows higher concentration. The vitrinite reflectance R_{om} (from 0.42% to 0.52%) and fixed carbon are high and volatile matter is low in the lower part of the seam. In seam-III of the Talcher coalfield the concentration of vitrinite is relatively low in the upper part of the seam and high in the lower part. Liptinite shows low concentration in the lower and middle parts of the seam section. The macerals of inertinite group show uniform distribution in this seam but have relatively low concentration in the lower part. The vitrinite reflectance R_{om} (from 0.45% to 0.50%) and fixed carbon are high and volatile matter is low in the upper part of the seam. Seam-IV has maximum

concentration of vitrinite in the uppermost band of the seam while liptinite shows its minimum in this part. Inertinite has more concentration in the middle part of the seam. Fixed carbon shows high concentration in the upper part and volatile matter in the middle part of the seam. vitrinite reflectance Rom (from 0.38% to 0.50%) shows higher values in the upper part of the seam. Seam-V does not show any trend of distribution of vitrinite and inertinite group macerals from bottom to top. However, middle and upper few bands have significantly higher concentrations of inertinite. The liptinite group macerals show higher values in the lower-middle and upper bands of this section. Higher values of volatile matter content have been recorded in the upper and the lower-middle bands of the seam, and fixed carbon in the middle and the uppermost band of this section. Vitrinite reflectance (Rom) has a narrow range (from 0.46% to 0.50%) of variation. Seam-VI shows decrease of vitrinite content and increase of liptinite content from bottom to top of this section. The concentration of inertinite is higher in the upper part of the seam. Volatile Matter and Fixed carbon do not show any trend of their distribution. vitrinite reflectance Rom shows its maximum (0.50%) in the lowermost band of the seam. Seam-VIII shows richness in the vitrinite content in the lower part of the seam while relatively low concentration of liptinite in this part. Inertinite having low concentration in this seam shows very little variation in its concentration from bottom to top of the seam. Volatile matter has low concentration in the lower and upper parts of the seam while fixed carbon has higher concentration in lower and upper parts of the seam. vitrinite reflectance Rom ranges from 0.46% to 0.50%. The concentration of vitrinite decreases from bottom to the upper part of Seam-IX. The macerals of liptinite group have low concentration in the bottom of the seam. Inertinite content of the seam increases towards the upper part of it. Volatile matter increases from bottom to top while fixed carbon increase towards the bottom of the seam. Vitrinite reflectance Rom ranges from 0.46% to 0.51%.

57.3 QUANTITATIVE OCCURRENCE OF ULTIMATE CONSTITUENTS

The carbon content of coals of the Talcher coalfield ranges from 41.01% to 64.21%, mean 52.16% (63.29% to 80.39%, mean 73.85% on d.a.f. basis). The hydrogen ranges from 2.84% to 5.15% mean 4.10% (2.82% to 6.40%, mean 4.85% on d.a.f. basis). The Nitrogen in coals of the Talcher coalfield ranges from 0.42% to 2.89%, mean 1.28% (0.58% to 3.80%, mean 1.80% on d.a.f. basis). The content of oxygen in coals of the Talcher coalfield ranges from 13.38% to 25.92%, mean 18.02% (10.79% to 30.65%, mean 18.62% on d.a.f. basis). The Sulphur in coals of the Talcher coalfield ranges from 0.33% to 1.20% mean 0.62% (0.50% to 1.76%, mean 0.88% on d.a.f. basis)

57.4 QUANTITATIVE OCCURRENCE OF PROXIMATE CONSTITUENTS

The moisture content of coals of the Talcher coalfield varies between 4.00 and 8.00%, mean 5.92%. The ash content of Talcher coals ranges from 10.00% to 39.10% with a mean value of 20.74%. (Table 6.1 to 6.3). Volatile matter content of Talcher coals ranges from 20.00% to 37.60%, mean 30.9%. Fixed carbon is determined by subtracting the sum of moisture, ash and volatile matter from one hundred. In the Talcher coals, it ranges from 28.90% to 59.80%, with a mean value of 42.37%.

57.5 GAS CHROMATOGRAPHY-MASS SPECTROMETRY

Gas Chromatography Mass Spectrometry was used to identify the compound present in the coal namely the aliphatic and aromatics. The second objective was to identify the biomarkers to understand its precursor and depositional conditions. The samples indicate similar pattern of occurrence of almost all the compounds in the samples. The *n*-alkanes distribution in coal sample of Talcher is characterized by C₁₆-C₃₀ *n*-alkanes with a smooth unimodal distribution and maximizes at C₂₁ (Figs 57.3, 57.4). This pattern indicates organic matter derived mainly from terrestrial organic matter. The Pr/Ph ratio in the coal samples show value > 1. The concentration of low (and high) molecular weight aliphatic compounds in the chromatogram shows their low abundance. The inputs from middle order aliphatic (C₂₁-C₂₅) members are abundant in the samples. The inputs from higher plants (C₂₇-C₃₁ members) or terrestrial sources are small in concentration. The presence of biomarker, cadalene is recorded in the sample which is an indication of input from higher plants. The benzohopanes have been detected in the coal samples which are suggestive of secondary transformation products of C₃₅ bacteriohopanepolyol derivatives [1, 2, 4, 6]. Combustion-derived pyrolytic (Polycyclic aromatic hydrocarbons) PAH found in the coal samples include pyrene, flouranthene, benzo(a)anthracene, Benzo(a) pyrene, Benzo(e)pyrene, Perylene, Indeno(1,2,3-cd) pyrene, Benzo(ghi)perylene, Coronen, and Triphenylene + Chrysene.

57.6 DISCUSSION AND RECCOMENDATION

The coals of Talcher coalfield indicate high concentration of aromatic over aliphatic hydrocarbons and further reveal high carcinogenic PAH. Petrochemically the coals are sub-bituminous in rank, the low sulphur coal have high occurrence of PAH [8] which is true for the Talcher coals. The modern analytical tools revealed

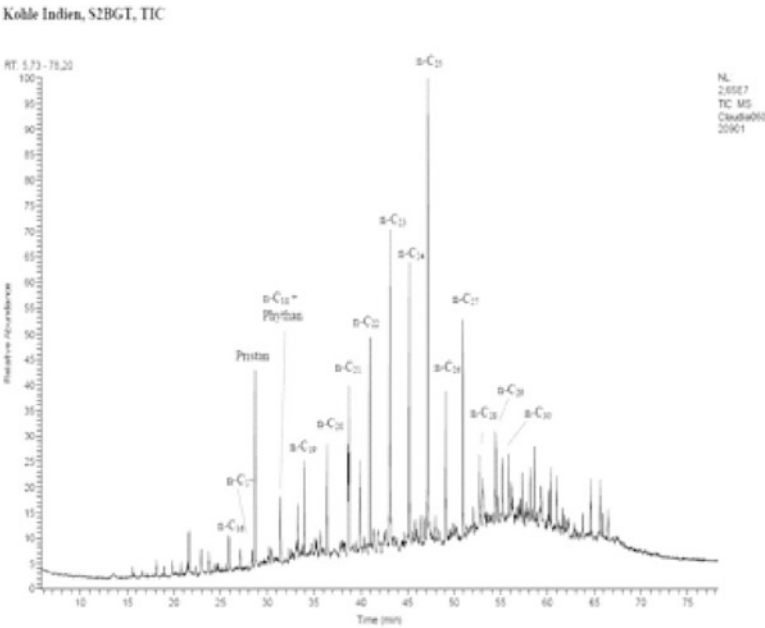


Fig. 57.3 Chromatogram showing aliphatic components

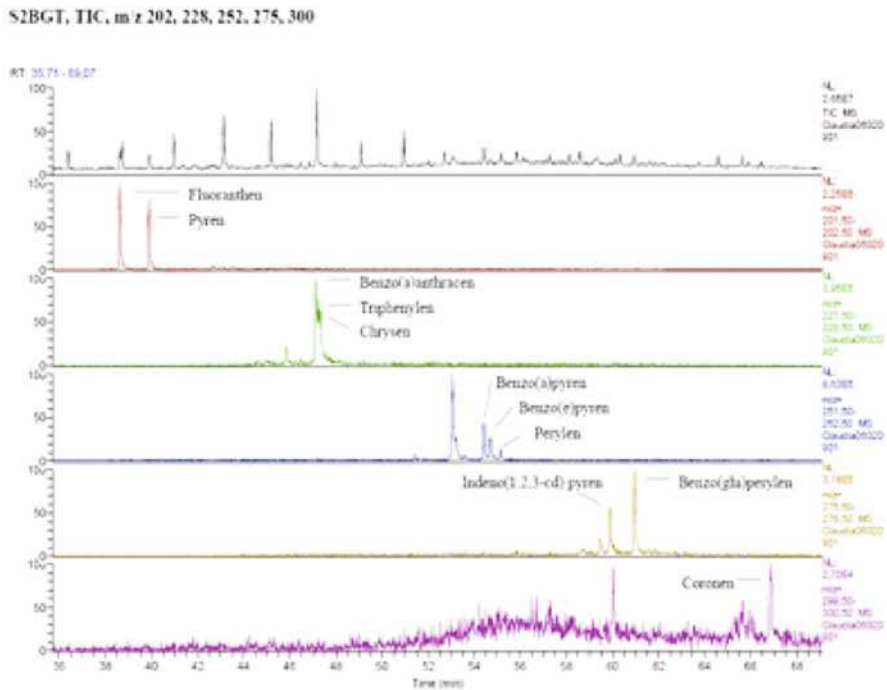


Fig. 57.4 Chromatogram showing aromatic components

these carcinogenic entities which were unknown with the previous analytical tools. Benzo(a)pyrene, not only harm the respiratory and immune system but also cause cell mutation and cancer, including lung and skin cancer [8]. Talcher coalfield is the largest coalfield in the state of Odisha producing almost 100 million tons of coal annually. The ambient air quality is a matter of concern in all the mining areas of the world and Talcher coalfield is no exception. The study conducted in areas such as Mumbai and Gangetic plain [5, 7] have reported PAHs but the focus was not on coal mining area. With the growing demand of coal and rising oil deficit the coal production is likely to increase in coming years with the increasing energy demands. If the economic growth is advocated at the cost of human health then it should be addressed properly so as to negate its adverse effect. PAH has ubiquitous presence but its presence in the atmosphere above the permissible level is a matter of concern. More research has to be focused in this direction to generate data sets and mitigation measures taken up to ensure safety of the inhabitants and the miners.

REFERENCES

1. Bechtel, A., Gawlick, H.J., Gratzner, R., Tomaselli, M. and Püttmann, W.: Molecular indicators of palaeosalinity and depositional environment of small scale basins within carbonate platforms: The Late Triassic Hauptdolomite Wiestalstausee section near Hallein (Northern Calcareous Alps, Austria). *Organic Geochemistry*, 38.1, 92–111 (2007)
2. Grice, K., Schouten, S., Nissembaum, A., Charrach, J. and Sinninghe Damsté, J.S.: A remarkable paradox: Sulfurised freshwater algal (*Botryococcus braunii*) lipids in an ancient hypersaline euxinic ecosystem. *Organic Geochemistry*, 28, 195–216 (1998)
3. Khaiwal, Ravindra, Sokhi, Ranjeet and Van Grieken, Rene: Atmospheric polycyclic aromatic hydrocarbons: Source attribution, emission factors and regulation. *Atmospheric Environment*, 42, 2895–2921 (2008):
4. Killops, S.D. and Killops, V.J.: Introduction to organic geochemistry. Second edition. U.K. Blackwell Publishing Limited (2005)
5. Kulkarni, Pramod and Venkataraman, Chandra: Atmospheric Polycyclic Aromatic Hydrocarbons in Mumbai, India. *Atmospheric Environment*, 34, 2785–2790 (2000)
6. Peters, K.E. and Fowler, M.J.: Applications of Petroleum geochemistry to Exploration and Reservoir management. *Organic Geochemistry*, 33, 5–36 (2005)
7. Singh, D.P., Gadi, Ranu, Mandal, T.K., Saud, T., Saxena, M. and Sharma, S.K.: Emissions estimates of PAH from biomass fuels used in rural sector of Indo-Gangetic Plains of India. *Atmospheric Environment*, 68, 120–126 (2012)
8. Wang, Ruwei, Liu Guijian, Zhang, Jiamei, Chou, Chen-Lin, and Liu, Jingjing: Abundances of Polycyclic Aromatic Hydrocarbons (PAHs) in 14 Chinese and American Coals and their relation to coal rank and weathering. *Energy Fuels*, 24, 6061–6066 (2010)

Chapter 58

Impact of Tillage and Residue Management Practices on Soil Aggregates and Soil Organic Carbon

P. Singh, J. Heikkinen, S. Mitra, and K. Regina

Abstract: Soil organic matter and soil aggregate stability are good indicators of soil quality and both can be positively affected by reduced tillage and residue management practices. A field study was conducted to find the impacts of tillage and residue management practices on soil carbon stock and distribution of SOC within different soil physical fractions. The study site was a 30-year experiment divided to six treatment classes, conventional tillage (CT) and reduced tillage (RT) with straw incorporated (S), straw removed (SR) and straw burned (SB). The soil was segregated into four different classes: large and small macroaggregates, microaggregates and silt and clay which were analyzed for total carbon. Reduced tillage or residue incorporation did not result in higher C sequestration but there were more water stable aggregates in the reduced tillage treatment.

Keywords: Soil aggregates • Macroaggregates • Microaggregates • Reduced tillage • Soil carbon

58.1 INTRODUCTION

Conventionally tilled soils are known to lose soil organic carbon (SOC) whereas reduced tillage is thought to increase soil aggregation, quality, fertility and sequestration of soil carbon (C) [1]. Straw management practices affect the amount of carbon input into the soil and hence the C sequestration rates of soils. Minimum

P. Singh (✉)

School of Environmental Sciences, Jawaharlal Nehru University, New Delhi, India

MTT Agrifood Research Finland, Jokioinen, Finland

e-mail: Pssinghpooja@gmail.com

J. Heikkinen • K. Regina

MTT Agrifood Research Finland, Jokioinen, Finland

S. Mitra

School of Environmental Sciences, Jawaharlal Nehru University, New Delhi, India

Department of Environmental Science, Tezpur University, Assam, India

tillage practices and increased residue inputs can increase SOM and soil aggregate stability [2]. No-tillage reduces the breakdown of macroaggregates, and as a result more microaggregates are formed within macroaggregates [3] which can store a considerable amount of SOC [1, 3] and are better protected against physical disturbance [4]. Previous studies have reported that the croplands of Finland have lost a considerable amount of SOC [5] and no-till practices have not increased SOC [6]. In these conditions, it would be beneficial if more of the existing C was stored within soil aggregates. The objective of this study was to quantify the effects of tillage and straw management practices on soil C, aggregation and aggregate-associated C in boreal conditions. We hypothesized that 1) reduced tillage (RT) has more stable aggregates than conventional tillage (CT), 2) RT has more C in microaggregates within macroaggregates (mM) and 3) treatments with straw left into the field has sequestered more C in the soil compared to plots with straw removed or burned.

58.2 STUDY AREA

The study site was a long-term experimental field maintained by MTT Agrifood Research Finland since 1980. The site is located in the boreal climatic region (60°48.15'N, 23°28.08'E) 90 m above mean sea level at okioinen in Southern Finland. The mean annual temperature and rainfall observed for the site were 4.6°C and 627 mm. The soil was classified as VerticCambisol (FAO).

58.3 MATERIAL AND METHODS

Soil samples were collected in early June 2013 from four soil layers: 0-5, 5-10, 10-15 and 15-20. Bulk density was determined by drying samples of known volume overnight at 105°C. The C and N content was determined from air dried, ground samples sieved through a 2 mm sieve and analyzed using the Leco CN-2000 analyzer (LECO, St Joseph, MI, USA). The soil was fractionated as in [1] to four different size fractions: (a) large macroaggregates (LM>2000 µm), (b) small macroaggregates (SM: 250- 2000 µm), (c) microaggregates (m > 53-250 µm) and (d) silt and clay (S+C < 53µm) (Part A). The contents of LM and SM were further fractionated to microaggregates (mM), silt and clay (s+cM) and coarse particulate matter (cPOM) (part B).

58.4 RESULTS AND DISCUSSION

Soil C stock was higher in conventional tillage than in reduced tillage ($p=0.045$) but straw management did not affect the carbon content of the top soil (Fig. 58.1). Agricultural management practices affect SOC storage capacities of soil but the

Fig. 58.1 Total C stock in the 0-20 cm layer of the soil in conventional (CT) and reduced tillage (RT) with straw incorporated (S), removed (SR) or burned (SB)

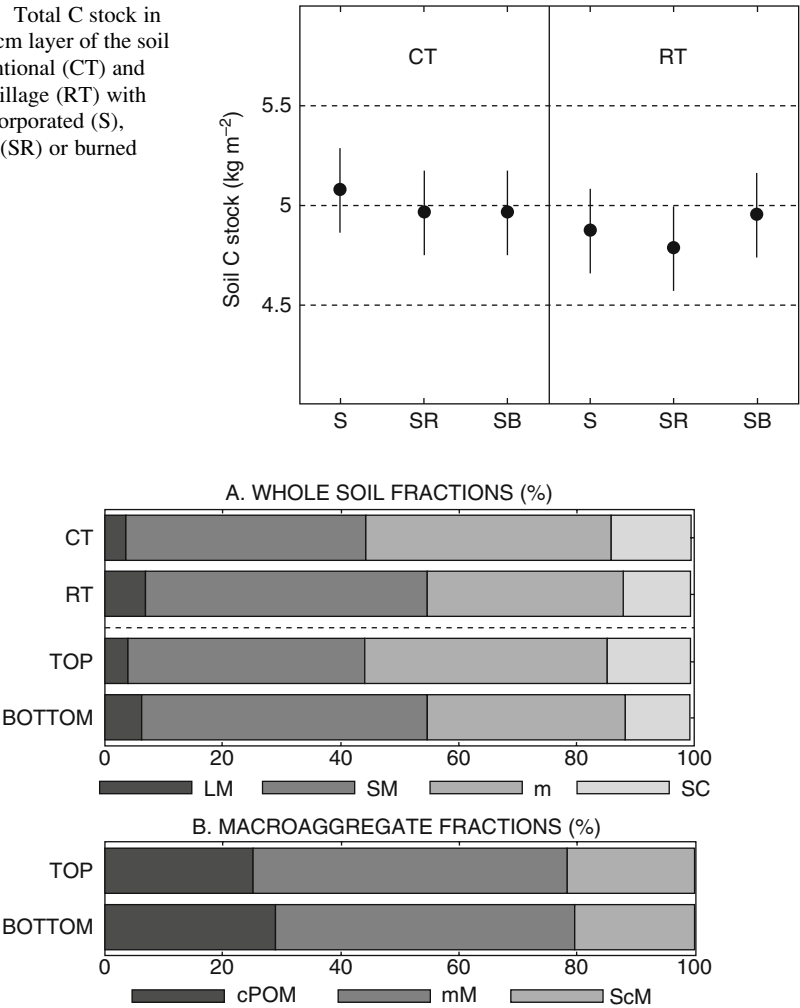


Fig. 58.2 Relative weights of (A) whole soil fractions in the conventional and reduced tillage treatments and in the 0-5 and 15-20 cm layers and (B) in fractions within the macroaggregates

effects vary with climate that influence soil and plant processes [7]. Reduced tillage is probably more effective in increasing SOC in arid conditions than in boreal humid conditions.

Majority of the soil weight consisted of SM and m fractions (Fig. 58.2A). Reduced tillage increased the amount of LM and SM ($p<0.001$) and more of these aggregates had accumulated to the deeper layer than to the top layer ($p<0.002$). The macroaggregate composition (Part B) was not affected by tillage, straw treatment or by their interaction but there was some indication of their differences between the layers (Fig. 58.2B). The treatments did not differ with respect to C content of the physical fractions (results not shown).

58.5 CONCLUSIONS

Reduced tillage enhanced the soil aggregation by increasing the LM and SM fractions in the soil. Total soil carbon stock, however, turned out to be slightly lower under reduced tillage than under conventional tillage. Straw management did not have statistically significant effect either on soil aggregation or soil carbon stock. Our study concludes that although reduced tillage can improve soil structure, generally the chances to increase soil carbon sequestration by tillage or by straw management practices are limited in boreal agroecosystems.

REFERENCES

1. Six, J., Elliot, E.T. and Paustian, K.: Soil macroaggregate turnover and microaggregate formation: a mechanism for C sequestration under no-tillage agriculture. *Soil Biology & Biochemistry*, 32, 2099–2103 (2000)
2. Paul, B.K., Vanlauweb, B., Ayukea, F., Gassner, A., Hoogmoeda, M., Hurissoa, T.T., Koala, S., Lelei, D., Ndabamenyea, T., Six, J. and Pulleman, M.M.: Medium-term impact of tillage and residue management on soil aggregate stability, soil carbon and crop productivity. *Agriculture, Ecosystems and Environment*, 164, 14–22 (2013).
3. Six, J., Elliott, E.T., Paustian, K. and Doran, J.W.: Aggregation and soil organic matter accumulation in cultivated and native grassland soils. *Soil Science Society of America Journal*, 62, 1367–1377 (1998)
4. Six, J., Bossuyt, H., Degryze, S. and Deneff, K.: A history of research on the link between (micro) aggregates, soil biota, and soil organic matter dynamics. *Soil & Tillage Research*, 79, 7–31 (2004)
5. Heikkinen, J., Ketoja, E., Nuutinen, V. and Regina, K.: Declining trend of carbon in Finnish cropland soils in 1974–2009. *Global Change Biology*, 19, 1456–1469 (2013)
6. Sheehy, J., Regina, K. and Six, J.: Aggregate stability and aggregate-associated carbon. In: No-till and reduced tillage practice in Finland. *Agrociencia*, 16(3) (2012)
7. Ogle, S.M., Jaybreidt, F. and Paustian, K.: Agricultural management impacts on soil organic carbon storage under moist and dry climatic conditions of temperate and tropical regions. *Biogeochemistry*, 72, 87–121 (2005).

Chapter 59

Effect of Land Cover on Soil Particle Size and Organic Carbon in the Plough Layer

Poushali Roy and S. Sreekesh

Abstract: Physical alteration of soil characteristics of especially the plough layer (0-20 cm) is brought about through land culture. The type of land cover, in fact, is an important factor controlling the soil texture, soil organic carbon (SOC) and soil erosion. The objectives of this paper are to analyze soil particle size distribution in the plough layer and quantify the SOC storage in the finer soil separate under native vegetation cover, cultivated land, eucalyptus plantations and barren land. A digital land cover map of the study area has been generated using Resourcesat-2 image. Soil samples from plots under different land cover types have been collected from depths of 0-10 cm and 10-20 cm. Particle size analysis has been done by dry sieving. SOC content of each soil separate – sand, very fine sand, silt+clay, under different land cover, has been done with the help of Walkley and Black method. Analysis of particle size distribution showed that proportion of sand particle is high. However silt+clay proportions have been found to vary with land cover types. SOC was high in silt+clay particles in general; but tended to increase in the sand fractions when particulate organic matter is incorporated. SOC decreased with soil depth under all land cover conditions but showed a reverse trend in some plots of cultivation.

Keywords: Soil particle size • Soil organic carbon • Particulate organic matter • Walkley and Black method

59.1 INTRODUCTION

The management and enhancement of soil organic carbon (SOC) is very important not only for carbon (C) sequestration as a measure of climate change mitigation but also for maintaining soil fertility to ensure food security [1]. Terrestrial soils

P. Roy

Department of Geography, Kashipur Michael Madhusudan Mahavidyalaya, Purulia, West Bengal, India

S. Sreekesh (✉)

CSRSD, Jawaharlal Nehru University, New Delhi, India

e-mail: sreekesh@mail.jnu.ac.in

store 1115 to 2200 Pg of organic C [2], two-third of it in the form of soil organic matter (SOM) [3]. The variability in the organic C content of soils is a function of soil texture [4-7] which is, in turn, determined and altered by land cover. Change in land cover can, therefore, alter the SOC stock [2, 8, 9] mainly in the top 10 to 20 cm of the soil profile [10] or the plough layer, which has a high concentration of SOC due to – high SOM content [11] and low density of SOC [12] in general, and is mostly influenced by tillage operations [13] in cultivated areas. The objectives of this paper are, therefore, to (a) analyze soil particle-size distribution in the plough layer and (b) quantify the SOC storage in the finer soil separates under different land cover conditions.

59.2 MATERIALS AND METHODS

The study area, Irga watershed, lies in the sub-humid tropics. Topography is flat to undulating with 0 to 7.5 percent slope (Fig 59.1a). Soil in the area, classified as Alfisols, is sandy in texture. The land cover in the area consists of about 37 percent cultivated land, 26 percent forest area, 12 percent area under plantation, and 18 percent barren land (Fig. 59.1b). The Survey of India topographical maps 72 H/15 (surveyed in 1978-79), L/3 and L/4 (surveyed in 1976-77) on a scale of 1:50,000, and Resourcesat-2 LISS III image of 28 December, 2012 for path 105 and row

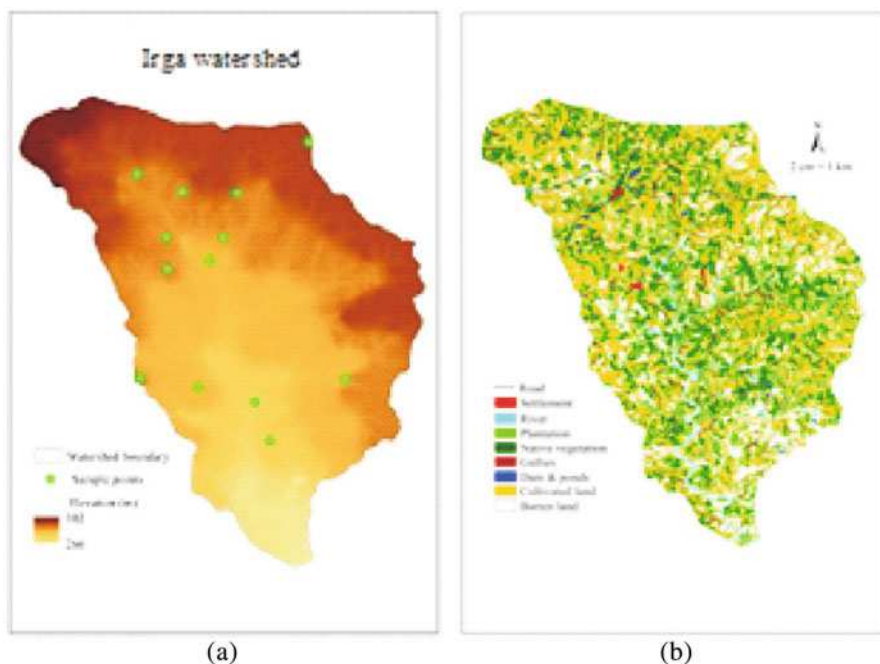


Fig. 59.1 (a) Elevation map with soil sample points and (b) land cover map of Irga watershed

55 (downloaded from <http://bhuvan-noeda.nrsc.gov.in/download/download/download.php>) were used. Four broad land cover classes were identified from geo-rectified satellite imageare: (1) native vegetation (NV); (2) Eucalyptus plantation (PL); (3) cultivated land (CL); and (4) barren land (BL). The number of plots chosen for each land cover was based on its distribution in the study area. Soil samples were collected from 0-10 cm and 10-20 cm depths during the non-growing phase, i.e. over summer (April, 2012), so as to minimize the influence of plant type and growth stage on SOC. Particle size analysis was done by dry sieving; three particle size fractions were identified – coarse sand (2-0.25 mm diameter), fine sand (0.25-0.05 mm) and silt +clay (<0.05 mm). Plant roots and crop residues <2 mm in size were not differentiated from soil particles so as to understand the effect of particulate organic matter (POM) on SOC content. Organic C content in each particle-size fraction was determined using the Walkley and Black (1934) method [14, 15].

59.3 RESULTS AND DISCUSSION

Particle-size fraction distribution was dominated by coarse sand fraction in the 0-10 cm and 10-20 cm depths (Fig 59.2) under all land cover conditions. Coarse and fine sand content, however, decreased with soil depth with a resultant increase in silt+clay content. A few plots in CL areas, however, showed a reverse trend that can be attributed to plowing which leads to the incorporation of POM into the deeper soil layers [16]. A significant textural transition from sandy soil to sandy clay loam was found in plots that have been brought under cultivation.

SOC content increased with decrease in fraction size in the plough layer (Fig. 59.3a). This indicates that silt+clay domain is the most stable SOC size pool. Some CL sites, however, showed a higher SOC concentration in the coarse sand fraction than in silt+clay fraction due to the presence of residue-derived POM

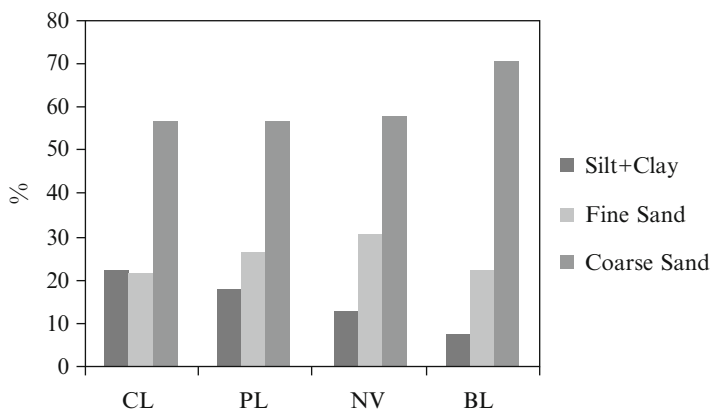


Fig. 59.2 Particle-size distribution under different land cover conditions

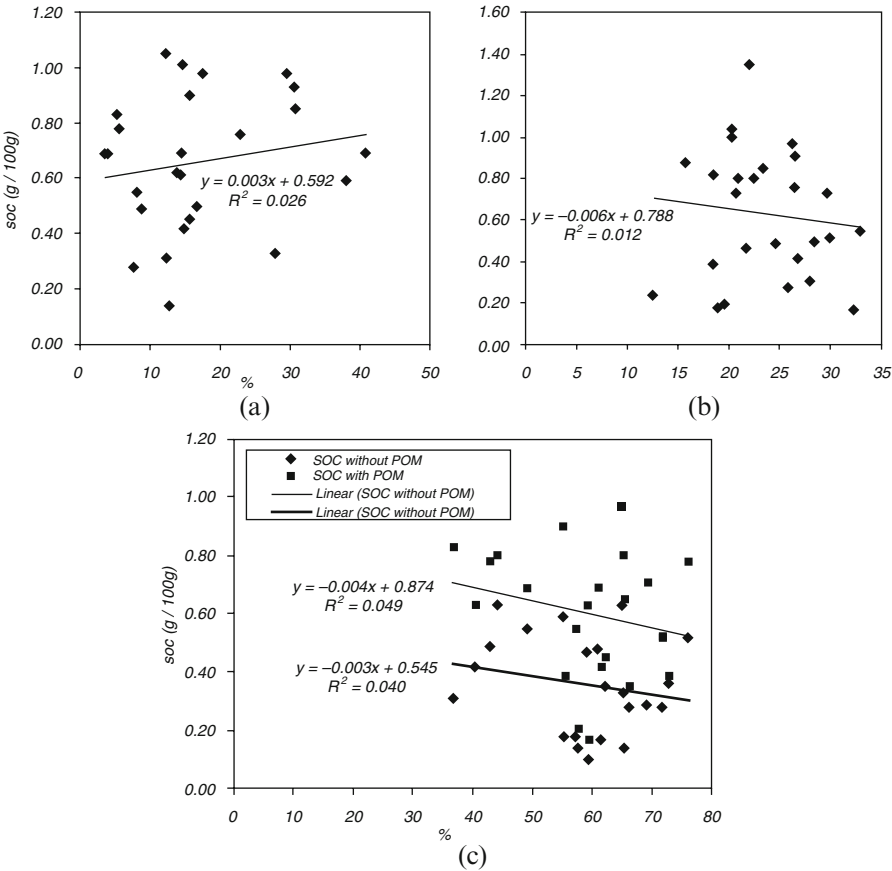


Fig. 59.3 Relation between SOC content and percentage (a) coarse sand, (b) fine sand and (c) silt +clay fractions in the plough layer

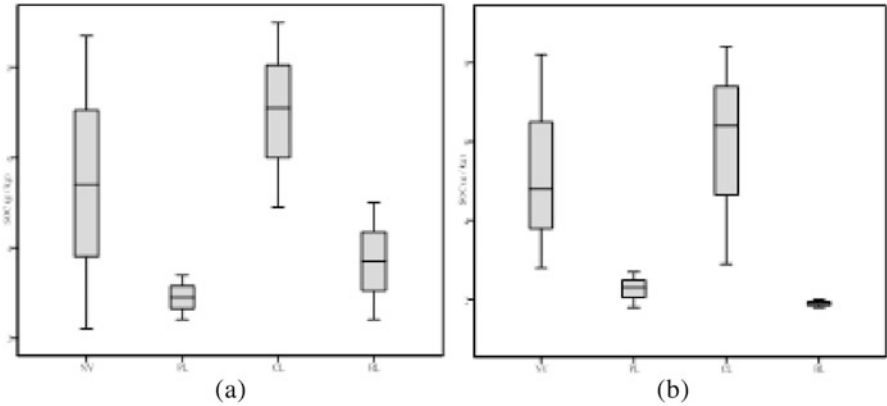


Fig. 59.4 SOC distributions under different land cover conditions at (a) 0-10 cm and (b) 10-20 cm

in the former [16]. SOC content was higher in CL areas than in the soils under NV (Fig. 59.4a & b). The higher SOC content in CL areas was due to the sandy clay loam texture that has been an effect of cultivation. It is also because of the high concentration of SOC in sand fractions due to the presence of residue-derived POM [16, 17]. The high SOC content in CL may also be attributed to the application of fertilizer and manure [18], and to the poor drainage conditions that are necessarily associated with CL that include paddy fields [16]. Overall the SOC content in the watershed is less varying from low (2-4 g kg⁻¹) to medium (4-6 g kg⁻¹).

59.4 CONCLUSIONS

Land cover is a significant factor influencing the texture and SOC content in the plough layer. The order of SOC content at 0–20 cm depth in the study area is: CL>NV>BL (with slight grass cover)>PL. C levels in CL have exceeded those under NV in the study area. Mango garden, however, have a high SOC content in the plough layer equivalent to CL. Maintenance of mango garden as well as native forests is, therefore, a priority in this watershed. SOC content, especially in the study area, can also be increased by converting BL to permanent pasture or orchards rather than bringing them under Eucalyptus plantation. Areas under Eucalyptus plantation, owing to low disintegration properties of leaves, have SOC content lower than BL, especially when the latter has a slight grass cover. Overall, the low SOC content in the study area indicates that the area has a high potential to sequester C, though not naturally, but if put to proper land management practices. Greater accumulation of organic C in these soils, especially in coarse sand fraction, can be obtained by increasing the incorporation of POM in these soils.

REFERENCES

1. Razafimbelo, T., Chevallier, T., Albrecht, A., Chapuis-Lardy, L., Rakotodrasolo, F.N., Michellon, R., Rabeharisoal, L. and Bernoux, M.: Texture and Organic Carbon Contents Do Not Impact Amount of Carbon Protected in Malagasy Soils. *Sci. Agric.* 70(3), 204–208 (2013)
2. Batjes, N.H.: Total Carbon and Nitrogen in the Soils of the World. *Eur. J. Soil Sc.* 47, 151–163 (1996)
3. Victoria, R., Banwart, S., Black, H., Ingram, J., Joosten, H., Milne, E. and Noellemeyer, E.: Benefits of Soil Carbon. In: UNEP Year Book: Emerging Issues in Our Global Environment, UNEP, pp. 19–33 (2012)
4. Parton, W.J., Schimel, D.S., Cole, C.V. and Ojima, D.S.: Analysis of Factors Controlling Soil Organic Matter Levels in Great Plains Grasslands. *Soil Sci. Soc. Am. J.* 51, 1173–1179 (1987)
5. Burke, I.C., Yonker, C.M., Parton, W.J., Cole, C.V., Flach, K. and Schimel, D.S.: Texture, Climate, and Cultivation Effects on Soil Organic Matter Content in U.S. Grassland Soils. *Soil Sci. Soc. Am. J.* 53, 800–805 (1989)
6. Parton, W.J., Scurlock, M.O., Ojima, D.S., Gilman, T.G., Scholens, R.J., Schimel, D.S., Kirchner, T., Menaut, J.C., Seasted, T., Garcia Moya, E., Kamnalrut, A. and Kinyamar, I.:

- Observations and Modeling of Biomass and Soil Organic Matter Dynamics for the Grassland. *Biome Worlwide. Gl. Biogeochem. Cy.* 7(4), 785–809 (1993)
7. Post, W.M. and Kwon, K.C.: Carbon Sequestration and Land-Use Change: Processes and Potential. *Global Change Biol.* 6, 317–328 (2000)
 8. Lal, R.: Soil Carbon Sequestration to Mitigate Climate Change. *Geoder.* 123, 1–22 (2004)
 9. Robert, M.: Global Change and Carbon Cycle: The Position of Soils and Agriculture. *In:* Roose, E.J., Lal, R., Feller, C., Barthes, B., Stewart, B. A. (eds.) *Soil Erosion and Carbon Dynamics. Advances in Soil Science*, pp. 3–12. CRC Press, BotaRacon (2006)
 10. Smith, G.: Toward An Efficient Method for Measuring Soil Organic Carbon Stocks in Forests. *In:* Lal, R., Kimble, J. M., Follett, R. F., Stewart, B.A. (eds.) *Assessment Methods for Soil Carbon. Advances in Soil Science*, pp. 293–310. CRC Press, Bota Racon (2000)
 11. Jenny, H.: *Factors of Soil Formation: A System of Quantitative Pedology*. Dover Publications Inc., New York (1994)
 12. Roose, E.J. and Barthes, B.: Soil Carbon Erosion and Its Selectivity at the Plot Scale in Tropical and Mediterranean Regions. *In:* Roose, E.J., Lal, R., Feller, C., Barthes, B., Stewart, B.A. (eds), *Soil Erosion and Carbon Dynamics. Advances in Soil Science*, pp. 55–72. CRC Press, Bota Racon (2006)
 13. Celik, I., Gunal, H., Budak, M. and Akpinar, C.: Effects of Long-term Organic and Mineral Fertilizers on Bulk Density and Penetration Resistance in Semi-arid Mediterranean Soil Conditions. *Geoderma*, 160(2), 236–243 (2010)
 14. Bhattacharya, T., Sarkar, D. and Pal, D.K.: *Soil Survey Manual*. NBSS Publ. 146, pp. 94–95. NBSS & LUP, Nagpur (2009)
 15. Jaiswal, P.C.: *Soil, Plant and Water Analysis*, pp. 96–100. Kalyani Publishers, Noida (2011)
 16. Lantz, A., Lal, R. and Kimble, J.: Land Use Effects on Soil Carbon Pools in Two Major Land Resource Areas of Ohio, USA. *In:* Scott, D.E., Mohtar, R.H., Steinhardt, G.C. (eds), *Sustaining The Global Farm*, pp. 499–502. 10th International Soil Conservation Organization Meeting, Purdue University (1999)
 17. Balesdent, J. and Balbane, M.: Major Contribution of Roots to Soil Carbon Storage Inferred from Maize Cultivated Soils. *Soil Biol. Biochem.* 28(9), 1261–1263 (1996)
 18. Qin, S., Hua, C., Hec, X., Donga, W., Cuia, J. and Wang, Y.: Soil Organic Carbon, Nutrients and Relevant Enzyme Activities in Particle-size Fractions under Conservational versus Traditional Agricultural Management. *Appl. Soil Ecol.* 45, 152–159 (2010)

Chapter 60

Sodicity Status of Salt-Affected Soils of Israna, Haryana, India

Seema and R. Paulraj

Abstract: Salt-affected soil (SAS) is a permanent problem inherited in landscape of arid and semi-arid region due to climatic conditions. Sodic soils are an important category of SAS which are characterized by excess levels of sodium ions (Na^+) in the soil solution phase as well as on the cation exchange complex. Soil sodicity is one of the major problems that deteriorates the quality and quantity of produce and limits the choice of cultivable crops. The objective of the study was to assess the sodicity status in the salt-affected area of Israna. Soil chemical properties related with sodicity viz., electrical conductivity (EC), exchangeable sodium (Na^+) concentration, exchangeable sodium percentage (ESP), sodium adsorption ratio (SAR) and soil pH were analyzed using standard methods. Results showed significantly ($P \leq 0.05$) higher values of pH, exchangeable Na^+ concentration, ESP and SAR in all the affected sites relative to the control sites. This study reveals that the salt-affected soils are sodic in nature which affects the growth and yield of crops.

Keywords: Sodic soils • ESP • SAR • Cation exchange complex

60.1 INTRODUCTION

Salt-affected soils (SAS) occupy nearly 7% of world land area and contain excess salts which impair soil productivity [1]. SAS are characterized into saline and alkali (sodic) groups on the basis of their physico-chemical and biological properties [2]. Salinization and sodication are the two most important global environmental problems leading to land degradation and it is being alleviated by many improper agricultural and forestry practices [3]. Sodic soils are essentially found in arid and semi-arid regions and occupy generally two billion hectares throughout the world [4]. In India, about 47% of the sodic soils are confined to Indo-Gangetic plains belonging to Uttar Pradesh, Haryana, Punjab and Bihar states [5]. These soils are known by different local terms in India like *usar*, *kallar* etc. Sodic soils are characterized by high pH, exchangeable sodium percentage (ESP) and sodium

Seema • R. Paulraj (✉)

School of Environmental Sciences, Jawaharlal Nehru University, New Delhi, India

e-mail: paulrajr@yahoo.com

absorption ratio (SAR) [6]. Excess amount of sodium salts often degrades the chemical, physical, hydrological and nutritional properties of these soils [7]. Many a times, the effects are so severe that lands eventually go out of cultivation posing a great challenge in view of shrinking agricultural land, particularly in developing countries. So the aim of the study is to evaluate the physico-chemical properties that lead to a better understanding of the sodicity status of the salt-affected soils of study area.

60.2 METHODS AND MATERIALS

60.2.1 *Study Area*

The study area is located in Israna block in Panipat district, Haryana. Panipat district has an area of 1250 sq. km and lies between latitude 29° 09' 15" N to 29° 27' 25" N and longitude 76° 38' 30" E to 77° 09' 15" E. The topography of district is plain and constitutes a part of Indo- Gangetic alluvial plains. The soils generally vary from sandy loam to loam but in many parts of the district, there is occurrence of salt-affected soils with alkaline patches of variable pH.

60.2.2 *Soil Sampling and Preparation*

The soil samples used in this study were collected from Israna, Panipat (India). For data collection random composite soil sampling was done. From the study area, a total of 9 composite samples (0-20 cm) were collected including 2 control samples of farmland soils of the same area. All soil samples were air-dried, ground in mortar-pestle and passed through a 2 mm sieve. The 2 mm sized soil samples were then further used for physical and chemical analysis.

60.2.3 *Soil Analysis*

Soil physical and chemical properties that are known to be affected by accumulation of salts viz. soil particle distribution, pH, EC, soluble cations (Na^+ , Ca^{2+} , Mg^{2+} and K^+), SAR, exchangeable bases (Na^+ , Ca^{2+} , Mg^{2+} and K^+) and ESP were determined using standard protocols. The proportions of sand, silt and clay were measured using Microtrac S3500 laser particle analyser described by Konert and Vandenberghe [8]. Soil pH and EC were measured in 1:2 soil-water suspensions using EUTECH cyberscan 510. Soluble cations concentrations were determined in 1:2 soil-water suspensions using Thermo scientific atomic absorption spectrophotometer (AAS) [9]. The exchangeable cations were extracted from the soil with

normal neutral ammonium acetate [9] and analyzed by AAS. SAR was calculated using Na^+ , Ca^{2+} and Mg^{2+} concentrations whereas ESP was calculated from concentration of exchangeable sodium ions and cation exchange capacity (CEC).

60.2.4 Data Analysis

Statistical analysis was done using SPSS version 16.0 for windows. Means were compared for significance using independent samples t-test ($p < 0.05$).

60.3 RESULTS AND DISCUSSION

Table 60.1 shows some physico-chemical properties of the salt-affected and control sites. According to the classification system of United States Department of Agriculture (USDA) for particle size distribution, the soils were found to be silt loam in texture. The pH, EC and SAR of affected soils ranged from 8.48 to 11.04, 0.76 to 1.99 dS/m and 19.53 to 30.48 (meq/L)^{1/2} with an average of 9.41 ± 0.66 , 1.38 ± 0.39 dS/m and 25.48 ± 3.21 (meq/L)^{1/2} respectively as shown in Fig. 60.1 (a, b and c). These soils thus can be classified as sodic in nature since pH, EC and SAR were found to be within the classification limits as described by Richards [10]. The percentage of exchange sites occupied by sodium (ESP) ranged from 49.86 to 66.64% with an average of 58.92 ± 5.00 % (Fig. 60.1d). The values of ESP were found to be approximately four times higher than the critical limit for sodicity [6]. An ESP of 15 (SAR~13) is considered as a threshold limits above which soils becomes dispersive in nature and suffer serious physical problems like slaking, swelling, surface crusting etc. [11]. Yield of many crops are reported to reduce by half their full potential at ESP values of 30 or above [12]. However, the average values of pH (7.39 ± 0.24), SAR (3.18 ± 0.04 (meq/L)^{1/2}) and ESP ($12.79 \pm 1.28\%$) of control sites were less than the critical limits defined for sodic soils and hence are non-sodic in nature. In this study, salt-affected soil pH, SAR and ESP were very significantly ($P \leq 0.01$) higher than the control farmland soils (Table-60.1). This may be due to high salt content especially Na^+ concentration in soil solution as well as on exchange sites of the affected sites as compared to controls. Whereas EC of the affected soils were found to be significantly lower than control sites (2.42 ± 0.17 dS/m). It has been reported previously that the ambient soil electrolyte concentration (EC) is the principal factor determining the adverse effects of Na^+ concentration on soil properties. Lower the concentration of EC, more exacerbating are the deleterious effects of exchangeable Na^+ [11]. Sodium was the dominant cation among all the soluble cations and accounted for over 87.19% of the total concentration in affected soils whereas the concentration of K^+ was observed to be the least. Similarly, the concentration of Na^+ was found to be highest and K^+ the least in control sites (Table-60.1). Soluble Ca^{2+} was significantly ($P \leq 0.05$) lower but

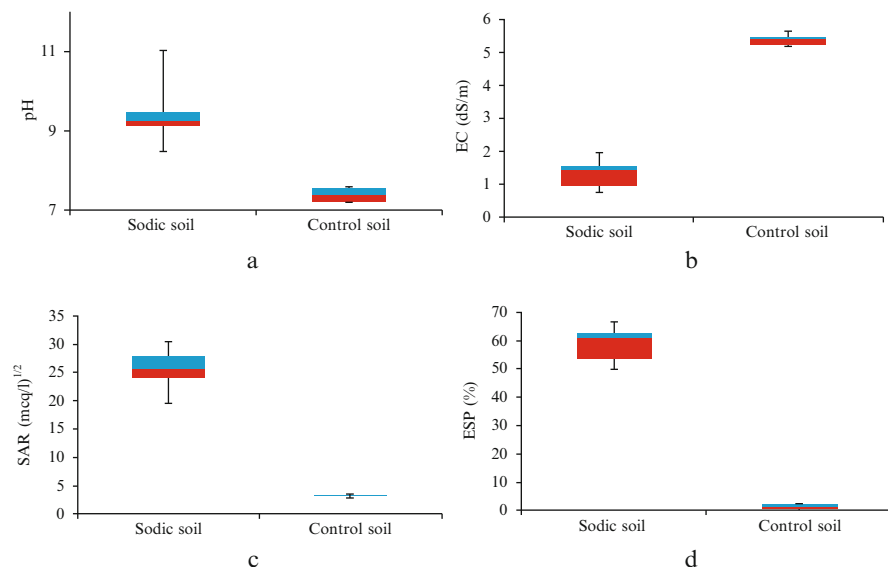


Fig. 60.1 Range of the important sodicity parameters of control and sodic soils is presented as box plots (a) pH (b) EC (c) SAR and (d) ESP. The lower edge of red and upper edge of blue box represents the 25th and the 75th percentiles respectively; line joining the two boxes presents the median value; upper and lower whiskers represent the maximum and minimum values

Table 60.1 Various physico-chemical properties of salt-affected and control soils of study area

Soil properties	Control sites	Affected sites
pH	7.39 ± 0.24^b	$9.41 \pm 0.66^{a*}$
EC (dS/m)	2.42 ± 0.17^a	$1.38 \pm 0.39^{b*}$
Soluble Na^+ (meq/L)	5.58 ± 0.13^a	8.37 ± 2.44^a
Soluble Ca^{2+} (meq/L)	2.72 ± 0.16^a	$0.11 \pm 0.07^{b*}$
Soluble Mg^{2+} (meq/L)	3.47 ± 0.01^a	$0.14 \pm 0.09^{b*}$
Soluble K^+ (meq/L)	0.10 ± 0.06^a	0.98 ± 0.92^a
SAR (meq/L) ^{1/2}	3.18 ± 0.04^b	$25.48 \pm 3.21^{a*}$
Exchangeable Na^+ (Cmol _c /Kg)	2.16 ± 0.38^b	$29.04 \pm 3.36^{a*}$
Exchangeable Ca^{2+} (Cmol _c /Kg)	6.82 ± 4.07^a	9.99 ± 2.72^a
Exchangeable Mg^{2+} (Cmol _c /Kg)	3.40 ± 0.62^a	8.65 ± 4.22^a
Exchangeable K^+ (Cmol _c /Kg)	0.20 ± 0.05^a	0.42 ± 0.17^a
ESP (%)	12.79 ± 1.28^b	$58.92 \pm 5.00^{a*}$
CEC (Cmol _c /Kg)	17.15 ± 4.71^b	$49.33 \pm 4.57^{a*}$

Figures represent mean \pm SD. Values in the same row bearing different superscripts are significantly different at $P \leq 0.05$. * implies significance at $P \leq 0.01$

exchangeable Na^+ concentration was significantly ($P \leq 0.05$) higher in affected soils than the control soils (Table-60.1). As reported by several researchers [11], [13] and [14], plants growing in sodic soils are associated with impaired uptake of Ca^{2+} as result of high concentrations of Na^+ in soil solution resulting in decrease in crop yield and quality.

60.4 CONCLUSION

Evaluation of physico-chemical properties of salt-affected soils revealed significantly elevated values of pH, SAR, exchangeable Na^+ and ESP as compared to control soils of farmland. Also the soluble Na^+ concentration was higher when compared to control soils. The study shows that the dominant salt problem associated with affected soils is sodicity. Under high pH and Na^+ condition, the tendency for structural instability would enhance and plant metabolism and nutrition is adversely affected [12]. These factors will collectively affect the crop productivity and yield. Therefore, it is suggested that management of these soils need to be considered.

ACKNOWLEDGEMENT Authors are thankful to technical staff of CIF, School of Environmental Sciences for their help in analysis and Council of Scientific and Industrial Research (CSIR), India for providing fellowship.

REFERENCES

1. Chhabra, R.: Classification of salt-affected soils. *Arid Land Res Manag.*, 19, 61–79 (2005)
2. Farifteh, J., Farshad, A. and George, R.J.: Assessing salt-affected soils using remote-sensing, solute modelling, and geophysics. *Geoderma*, 130, 191–206 (2006)
3. Singh, K., Singh, B. and Singh, R.R.: Changes in physico-chemical, microbial and enzymatic activities during restoration of degraded sodic land: Ecological suitability of mixed forest over monoculture plantation. *Catena*, 96, 57–67 (2012)
4. Singh, B. and Garg, V.K.: Phytoremediation of a sodic forest ecosystem: plant community response to restoration process. *Not. Bot. Hort. Agrobot. Cluj.*, 35(1), 75–85 (2007)
5. Mandal, A.K., Sharma, R.C. and Singh, G.: Assessment of salt-affected soils in India using GIS. *Geocarto Int.*, 24(6), 437–56 (2009)
6. Mzezwa, J., Gotosa, J. and Nyamwaza, B.: Characterisation of sodic soil catena for reclamation and improvement strategies. *Geoderma*, 113, 161–175 (2003)
7. Singh, K., Pandey, V.C., Singh, B. and Singh, R.R.: Ecological restoration of degraded sodic lands through afforestation and cropping. *Ecol Eng.*, 43, 70–80 (2012)
8. Konert, M. and Vandenberghe, J.: Comparison of laser grain size analysis with pipette and sieve analysis: a solution for the underestimation of the clay fraction. *Sedimentology*, 44, 523–535 (1997)
9. Pansu, M. and Gautheyrou, J.: Handbook of soil analysis: Mineralogical, organic and inorganic methods. Springer-Verlag, Berlin Heidelberg, New York (2003)
10. USDA: Methods for soil characterization, In: Richards, L.A. (ed.), Diagnosis and improvement of saline and alkali soils. Agriculture handbook no.60. U.S. Salinity Laboratory, Washington DC (1954)
11. Qadir, M., Noble, A.D., Schubert, S., Thomas, R.J. and Arslan, A.: Sodicty induced land degradation and its sustainable management: problems and prospects. *Land Degrad. Develop.*, 17(6), 661–676 (2006)
12. Hajkowicz, S. and Young, M.: Costing yield loss from acidity, sodicty and dryland salinity to Australian agriculture. *Land Degrad. Develop.*, 16, 417–433 (2005)

13. Curtin, D. and Naidu, R.: Fertility constraints to plant production. *In*: Sumner, M.E., Naidu, R. (eds.) *Sodic Soil: Distribution, Management and Environmental Consequences*. pp. 107–123. Oxford University Press, NY (1998)
14. Grattan, S.R. and Grieve, C.M.: Salinity–mineral nutrient relations in horticultural crops. *Scientia Horticulturae*, 78, 127–157 (1999)

Chapter 61

Characterizing and Quantifying the Effect of Aerosol Optical Depth over North Indian Plain during Harvesting Season

Prasenjit Acharya and S. Sreekish

Abstract: This paper analyses the dynamics of AOD over north-western part of northern Indian plain during the harvesting season its effect on surface reaching solar radiation from 2001 to 2009 using MODIS level 2 atmospheric data set. The analysis carried out for post monsoon season during rice harvesting period and is based on 8 days composite AOD, Ozone, Water vapour, and surface pressure data. Spatial variability of AOD has been shown in $0.47\ \mu\text{m}$ and $0.66\ \mu\text{m}$ in order to grasp the idea of relative difference in occurrence of fine and coarse mode aerosol. Analysis of the particles under SEM-EDX collected through air sampling in the agricultural field in Punjab and Haryana during rice harvesting season shows released particles from the residue burning have 72% of O, 8% of C, 7% of Si, 2% Al, and 7% F in significant amount and barely less than equal to 1% of other elements such as Na, K, Ba, Mg, Fe, Ca, Ti, Zn, P, and Cl. NOAA-HYSPLIT back trajectory analysis shows these emitted smoke and aerosol plumes which transport a long distance through active wind system affect insolation amount at the surface. AOD levels between 2003 and 2007 were moderate to high in the western part of North Indian plain, with an average of 0.8–1.8 at $0.47\ \mu\text{m}$ and 0.6–1.4 at $0.66\ \mu\text{m}$. Radiative forcing in this region during the study period vary pronouncedly amounting to $-20\ \text{Wm}^{-2}$ to $11\ \text{Wm}^{-2}$.

Keywords: AOD • Irradiance • Radiative Forcing • Elemental Composition • Back Trajectory

61.1 INTRODUCTION

Aerosol, the suspended microscopic particulate matter in air represents the nature of the atmosphere and has an important role in climate process. It has a strong influence in climate system by reflecting, scattering, and absorbing the incident radiation. The amount of incoming radiation that is taken away by the aerosol

P. Acharya • S. Sreekish (✉)

School of Social Sciences, Jawaharlal Nehru University, New Delhi, India

e-mail: sreekish@mail.jnu.ac.in

scattering and absorption is targeted to be the most important for climate change. Hence the role of aerosols in surface radiative forcing is considered as the most important for climate modeling and climate change studies. There is now clear and rapidly growing evidence that atmospheric aerosols have profound impacts on thermodynamics and radiative energy budgets of the earth [1-3]. The growing awareness of the potential climate impacts of anthropogenic aerosols has resulted in a large research effort that has significantly improved our understanding of their role in earth radiative balance [4]. Aerosol provides one of the largest uncertainties in climate forcing due to their variability in space and time and lack of detailed knowledge about their optical properties [5, 6]. Characterization of atmospheric aerosol is important for modelling and monitoring atmospheric processes. A number of studies carried out to explore the chemical properties of atmospheric aerosols from different sources using electron microscopy [7-11]. Size resolved morphology and chemical characterization of aerosol particles shows crustal materials are abundant in PM 10 whereas particles less than and equal to PM 2.5 contains high carbon aggregates [12, 13].

61.2 STUDY AREA

The study was carried out in the alluvial tracts of Punjab and Haryana in the western North Indian plain. This region comes under semi arid and tropical sub-humid climate. The maximum day time temperature during summer remains in the range of 32-46⁰ C and in the night it varies from 27-32⁰ C. While in winter, the values are between 10-25⁰ C in the day and 4-10⁰ C in night. Relative humidity remains 20-30% during dry season and 55-95% in wet season. Estimates shows that almost 70-80% of the rice-wheat system in Punjab is machine harvested [14] which it leaves an enormous amount of crop residue remains unused in the field and usually burned by the farmers [15, 16]. Harvesting of rice is usually done during mid of October to mid of November in post monsoon. A sample of total five burning field was done during October 2009 to 2010 covering two consecutive harvesting seasons.

61.3 MATERIAL AND METHODS

Field samples of the smoke and aerosol plume during the open field burning were collected by using APM 821 handy air sampler. The flow rate during the sampling was 0.3-1.4 liter per minute (lpm) for all the field locations. Whatman Glass Microfibre Filter (GF) paper (diameter 25 mm) with pore size 1.6 μ m was used in the sampler probe through which smoke was allowed to pass to go through NO₂ and SO₂ absorbing solutions in two glass impingers connected by tubes. The sampling time during the burning was set to 30-60 minutes depending on the size of the field.

The trapped particles emitted during burning of the crop residue in the filter paper were analyzed under SEM-EDX to derive the particle size distribution and the elemental composition. Around 30 X-ray spectra belong to 30 individual particles ($n = 30$) have been acquired to compute the variability of elemental concentrations. To model the irradiance at the surface all the necessary input data are taken from MODIS Level 1 atmospheric products. All such data that are used here are in daily basis. The time span that has been opted for the present study is 2001 to 2009 accounting five years of study i.e. 2001, 2003, 2005, 2007 and 2009. A sample of 8 days (14th to 21st) has been taken under consideration from the month of October which is representative for the post monsoon seasons. The algorithm used for modeling the surface irradiance is based on Gregg and Carder (1990) model which is suitable for terrigenous aerosol mode. Daily AOD have been analyzed at 0.47 and 0.66 μm along with daily modeled monochromatic direct irradiance at the surface in order to synchronize the modeled shortwave flux with response to optical depth.

61.4 RESULTS AND DISCUSSION

61.4.1 *Spatial Variability and Chemistry of AOD*

The spatial distribution of AOD shown in Figure 61.1 during this season shows that the western IG plain – especially the Punjab plain – is most affected by high optical depth and continuously showed high AOD values throughout the period of study. AOD varies spatially in this region with an average magnitude of 0.6 to 1.2 at 0.47 μm and 0.2 to 1.6 at 0.66 μm . AOD levels between 2003 and 2007 were moderate to high in the western part of North Indian plain, with an average of 0.8–1.8 at 0.47 μm and 0.6–1.4 at 0.66 μm . such high optical depth over the Punjab plain is attributed to burning of agricultural residues which produced a large amount of carbonaceous aerosols in association with smoke. From the analysis of individual particles under SEM-EDX (Figure 61.2) the observed average concentration in terms of atomic weight is given in Table 61.1. Such elemental composition however bring out that the particles are made up with compounds of Oxides, and pure carbon. Because of varying degree of absorption in the visible (i.e. 0.47, 0.55 and 0.66 μm) and infrared (0.7-1000 μm) spectrum, as well as water solubility, majority of the particles which are in coarse mode can act as an important moderator of incoming short wave and long wave flux ↓.

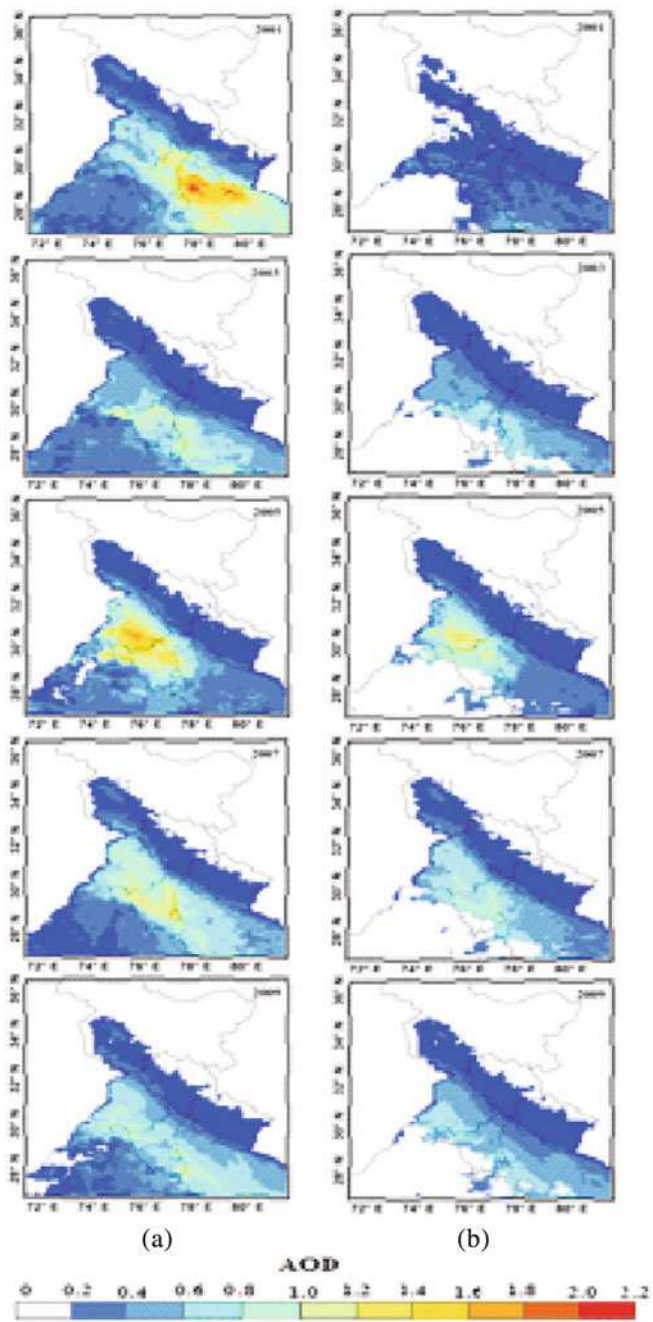


Fig. 61.1 Spatio-temporal variation of AOD during post monsoon season (2001–09). (a) $0.47\ \mu\text{m}$, (b) $0.66\ \mu\text{m}$

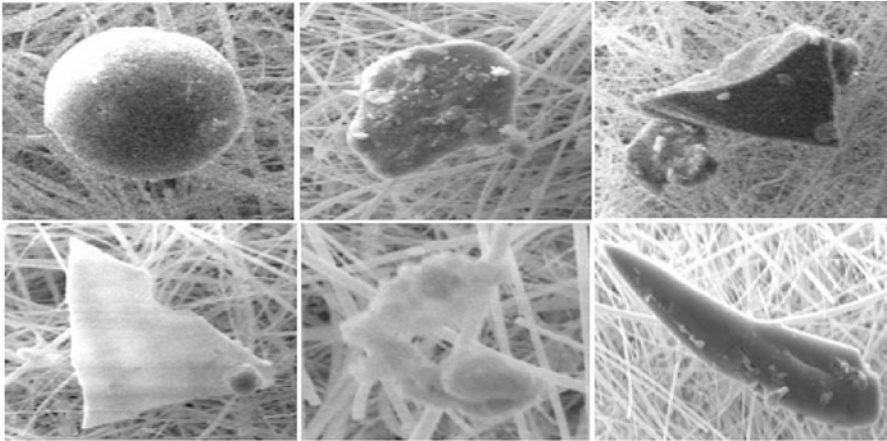


Fig. 61.2 Electron microscopic view of particles

Table 61.1 Average elemental concentration in aerosol (n = 30) measured in SEM-EDX

Elements	Average Concentration (%)	Elements	Average Concentration (%)
C	8.67	Zn	0.24
Na	1.77	Ba	0.05
Si	6.83	Mg	0.28
Al	2.06	Fe	0.65
K	0.67	P	0.07
Ti	0.08	Cl	0.48
Ca	0.18	F	6.63
O	73.63		

61.4.2 Variation of Surface Irradiance

Temporal variations of computed downward monochromatic direct shortwave flux along with its latitudinal component at both 0.47 and 0.66 μm are shown in Figure 61.3. It has been observed throughout the modeled output that the magnitude of low irradiance prevailed in the areas of high aerosol load explaining stronger correlation with AOD. Spatial average of shortwave flux varies significantly during 2001 to 2009. Table 61.2 summarizes the details of spatio temporal variability of modeled irradiance in both the channels. It appears from the modeled values and the image statistics; the year 2005 during the study period was mostly flourished with low flux \downarrow caused radiative forcing (RF) of -20 Wm^{-2} and -12 Wm^{-2} at 0.47 and 0.66 μm respectively. During field work it has been observed that the generated enormous amount of smoke and aerosol plume due to extensive burning of rice residue is transported with the wind system towards south east. Computed daily trajectories with 3 hrs of interval from NOAA HYSPLIT during this burning time confirm the transportation of this smoke plume towards Delhi National Capital

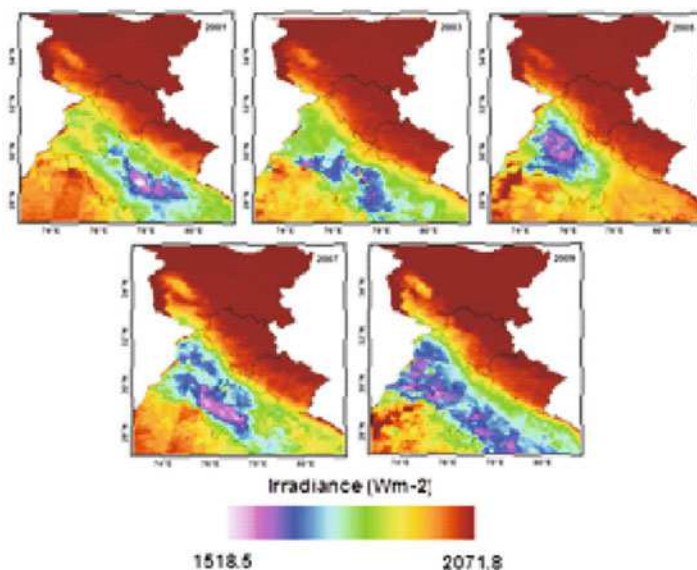


Fig. 61.3 Modeled short wave direct irradiance at the surface during post monsoon

Region (NCR) as a result of which it produces a wide scale effect on radiative forcing.

61.5 CONCLUSIONS

The analysis adequately exhibit the fundamental chemistry of the aerosol emitted due to the burning of crop residue in the open field during rice harvesting period. Emitted smoke particles are mostly composed of oxides of Na, K, Ca, P, Fe, Mg, Zn, Ba, Ti, Cl, F, Al and Si as well as pure carbon. Varying degree of absorption in the UV to the infra red spectrum as well as hygroscopicity of these fine to coarse mode particles make atmosphere sensitive to insolation if they are present at a large amount in the atmosphere. The emitted smoke consisted of SO_2 , NO_2 , CO_2 , CO and CH_4 etc in combination with aerosols increase the atmospheric turbidity and result of it is the low radiant energy flux \downarrow at the surface. Estimated radiant energy flux difference or the RF from the modeled irradiance at the surface which varied greatly from -20.38 Wm^{-2} to 11.21 Wm^{-2} during the period taken under study explained satisfactorily the effect of AOD on incoming solar radiation at the shortwave flux \downarrow .

Table 61.2 Statistics of modeled irradiance (Wm^{-2}) at the surface averaged over 8 days' period

	0.47 μm					0.66 μm				
Year	Min	Max	Range	Mean	Sd	Min	Max	Range	Mean	Sd
2001	1956.69	2064.78	108.08	2019.05	18.56	1524.56	1592.92	68.36	1561.50	11.23
2003	1977.16	2069.17	92.01	2027.37	14.36	1537.95	1592.92	54.97	1567.02	8.68
2005	1955.84	2064.93	109.09	2006.99	24.28	1523.12	1591.73	68.61	1554.74	14.69
2007	1977.09	2066.50	89.41	2015.61	16.53	1534.19	1592.79	58.59	1559.79	10.57
2009	2001.31	2067.86	66.55	2026.82	11.32	1547.22	1592.88	45.66	1566.28	7.91

REFERENCES

1. Houghton, J.T. et al. (eds): The scientific basis: contribution of working group I to the third assessment report of the intergovernmental panel on climate change. Climate Change, Cambridge University Press, pp 525–582 (2001)
2. Andreae, M.O. et al.: Strong present-day aerosol cooling implies a hot future. *Nature*, 435, 1187–1190 [10.1038/nature03671](https://doi.org/10.1038/nature03671) (2005)
3. Solomon, S., Qin, D., Manning, M., Chen, Z., Marquis, M., Averyt, K.B., Tignor, M. and Miller, H.L. (eds): Climate Change 2007: The Physical Science Basis, Contribution of Working Group I to the Fourth Assessment Report of the Intergovernmental Panel on Climate Change. Cambridge University Press, ISBN 978-0-521-88009-1 (2007)
4. Andreae, M.O. and Rosenfeld, D., Aerosol-cloud-precipitation interactions. Part 1. The nature and sources of cloud-active aerosols. *Earth Science Reviews*, 89, pp. 13–41 (2008)
5. Sathesh, S.K. and Ramanathan V.: Large differences in tropical aerosol forcing at the top of the atmosphere and Earth's surface. *Nature*, 405, 60–63 (2000)
6. Houghton, J.T., Ding, Y., Griggs, D.J., Noguer, M., van der Linden, P.J., Dai, X., Maskell, K. and Johnson, C.A. (eds): Climate Change 2001: The Scientific Basis, Contribution of Working Group I to the Third Assessment Report of the Intergovernmental Panel on Climate Change. Cambridge University Press, ISBN 0-521-80767-0 (2001)
7. Sheridan, P.J., Schnell, R.C., Kahl, J.D., Boatman, J.F. and Garvey, D.M.: Microanalysis of the aerosol collected over south-central New Mexico during the ALIVE field experiment, May–December, 1989. *Atmos. Environ.*, 27A, 1169–1183 (1993)
8. Posfai, M., Anderson, J.R., Buseck, P.R., Shattuck, T.W. and Tindale, N.W.: Constituents of a remote Pacific marine aerosol: A TEM study. *Atmos. Environ.*, 28, 1747–1756 (1994)
9. Posfai, M., Anderson, J.R., Buseck, P.R. and Sievering, H.: Compositional variations of sea-salt-mode aerosol particles from the North Atlantic. *J. Geophys. Res.*, 100, 23,063–23,074 (1995)
10. Buseck, R.P., Jacob, D.J., Posfai, M., Li, J. and Anderson, J.R.: Minerals in the air: An environmental perspective. *Int. Geol. Rev.*, 42, 577–593 (2000)
11. Li, J., Pósfai, M., Hobbs, P.V. and Buseck, P.R.: Individual aerosol particles from biomass burning in southern Africa, 2, Compositions and aging of inorganic particles. *J. Geophys. Res.*, 108(0), XXXX, doi:[10.1029/2002JD002310](https://doi.org/10.1029/2002JD002310) (2003)
12. Pachauri, T.: SEM-EDX Characterization of Individual Coarse Particles in Agra, India. *Aerosol and Air Quality Research*, 523–536. doi:[10.4209/aaqr.2012.04.0095](https://doi.org/10.4209/aaqr.2012.04.0095) (2013)
13. Pipal, A.S., Kulshrestha, A. and Taneja, A.: Characterization and morphological analysis of airborne PM_{2.5} and PM₁₀ in Agra located in north central India. *Atmospheric Environment*, 45(21), 3621–3630. doi:[10.1016/j.atmosenv.2011.03.062](https://doi.org/10.1016/j.atmosenv.2011.03.062) (2011)
14. Badrinath, K.V.S., Kiran Chand, T.R. and Krishna Prasad, V.: Agriculture crop residue burning in the Indo-Gangetic Plains – a study using IRS-P6 AWiFS satellite data. *Current Science*, 91(8), 1085–1089 (2006)
15. Gupta, R.: The economic causes of crop residue burning in western Indo-Gangetic Plains, ISI, New Delhi (2010)
16. Singh, C.P. and Panigrahy, S.: Characterisation of residue burning from agricultural system in India using space based observations. *Journal of Indian Society of Remote Sensing*, 39(3), 423–429 (2011)

Chapter 62

Evaluation of Urban Air Pollution Distribution in the Colombo Municipal Council Area, Sri Lanka

Samanmali Matharaarachchi, L. Manawadu, and Jagath Gunatilake

Abstract: Environmental pollution is one of the major health problems in both industrialized and developing countries including Sri Lanka. The main categories are water pollution, air pollution, land pollution and noise pollution etc. Out of this, air pollution is one of the severe and growing problem in worldwide and highly affects to the human health specially those who live in urban centers. It is a dangerous and silent hazard in comparison to other hazards since it is invisible. There are two types of air pollution respectively indoor air pollution and outdoor air pollution. Mainly indoor pollution is increasing with human domestic activities and outdoor air pollution is increasing with urbanization, industrialization and transport activities. The usage of motor vehicles in the Colombo City has been increased by over 300% in the last 20 years. The majority of these are motor cycles and three wheels and also other vehicles such as public transports. In that case recent results show that the city of Colombo is heavily polluted and the level of air pollution has been reached to its dangerous levels. During peak traffic hours (between 6 am to 8.30 am and 4 pm to 6 pm), Colombo area face to severe air pollution. Air pollution level was increase with rainfall variation of the area. Contamination of air pollutant was travel to another area using wind and Sea breeze. Main air pollutant emitter was Traffic and vehicles. It was clearly shows with monthly variation of pollutant distribution. Air pollution was increased with festival seasons and school holding time period.

Keywords: Environment pollution • Air pollution • Colombo city • GIS and RS

S. Matharaarachchi (✉) • J. Gunatilake

Postgraduate Institute of Science, University of Peradeniya, Peradeniya, Sri Lanka

e-mail: mataraarachchids@gmail.com

L. Manawadu

Department of Geography, University of Colombo, Colombo, Sri Lanka

62.1 INTRODUCTION

Over the past century, world has been an increasing trend towards urbanization. In that case many people living close to town areas. Urbanization and environmental pollution connected with together. Man had so many needs. They tried to achieve their needs. In that case increase in environmental pollutions. Air pollution is one of the environmental pollutants. Air pollution in Sri Lanka becoming on environmental concern with vehicle emission contributing to 80 percent of the country's as compared to other sources such as industrial pollution. With the increasing number of vehicles (Car, truck, buses and motorcycle) in Sri Lanka from 129,520 in 1970 to 1,374,144 in 1996, vehicles are alarmingly contributing to air pollution in a way they were not two decades ago [1]. In the present Sri Lanka was affected to the acid rain. Acid rain was not considered problem until recently in the country. Some research indicators that it occurs in some parts of Sri Lanka. For instance a high level of sulfur and nitrogen interception by fog in Horton Plains, support the suspicion that forest die-back at this site can be due to acid rain[2]. 1.4% of samples were recorded pH value between 4.40 – 4.80 and 30% of the samples had a pH range of 4.90 – 5.30 in island wide. They check out the other chemical parameters such as Na^+ , K^+ , Ca^{2+} and Mg^{2+} as well as nitrate. The overall concentration of nitrate in rain water ranged from 0.002 to 0.751 mg l^{-1} with highest value were recorded from Colombo [3]. National Building Research Organization was studied about air pollution trend in the largest industrial area of the Sri Lanka. Twenty locations were selected for the air sampling and passive sample technique was use to monitoring air quality. The parameter of SO_2 and NO_2 monitored within the study area. In this study aim to study spatial distribution of air pollution in Colombo city using GIS and Remote Sensing. As well as this study spatial distribution of annual average NO_2 and SO_2 between 2002 to 2008 periods in Colombo city. As well as aimed to examine the relationship between air pollution and land use pattern, relationship between air pollutant and human expose in this study using GIS and RS.

62.2 STUDY AREA

Colombo, the commercial capital of Sri Lanka is located on the southwestern coast of the island just south of the Kelani River. Colombo Municipal Council Area is situated between $99^\circ 50' - 79^\circ 54'$ Eastern longitude and $6^\circ 50' - 6^\circ 60'$ Northern latitude. The Study area falls within the Colombo district of the Western Province. The Colombo Core-Area (CCA) comprises the three contiguous Municipal Councils of Colombo; Colombo, Dehiwala-Mt.Lavinia and Kotte. Colombo Municipal Council Area (CMC) which has 47 municipal wards was selected for this study (Fig. 62.1). It is bounded to the North by Kelani River, to the South by the Dehiwala Channel, to the East by the Kelaniya, Kolonnawa and Sri Jayawardhanapura Kotte

Fig. 62.1 Study area



Pradeshiya Sabha area and to the West by the Indian Ocean. National Building Research Organization was started air quality monitoring programme in Colombo Urban Area in September 2012. Nineteen locations were established around the Colombo Urban Area for Air quality monitoring. Sample location shows Fig. 62.2.

62.3 MATERIAL AND METHODS

This study was carried out using secondary data collected from different government Agencies. These data were analysis by using Geographical Information System (GIS) and remote sensing software. Data was analysis using ArcGIS 10.1 package and Microsoft Excel 2010. Inverse Distance Weighted (IDW) technique of

Fig. 62.2 Sample location

Spatial Analysis tool was used in ArcGIS 10.1 version. All the data represent using maps and graph. Figure 62.3 shows data analysis technique in ArcGIS.

62.4 RESULTS AND DISCUSSION

Monthly variation of NO_2 levels from October, 2012 to June, 2013. It is apparent the increased distribution of NO_2 levels from October, 2012 to December, 2012. CL4 and CL 19 exist the highest NO_2 levels in most of the months. Concentration of NO_2 in December, 2012 is remarkable that total study area has emitted more than $30.2 \mu\text{g}/\text{m}^3$ amount of NO_2 . Associating areas of CL 17, CL 16, CL4, CL19, CL09 and CL13 undergo higher concentration of NO_2 . There is a considerable decrease of the NO_2 content by January, 2013. But there is rather an increase of NO_2 in February. Higher concentration of NO_2 levels in CL17, CL16 and suburbs is

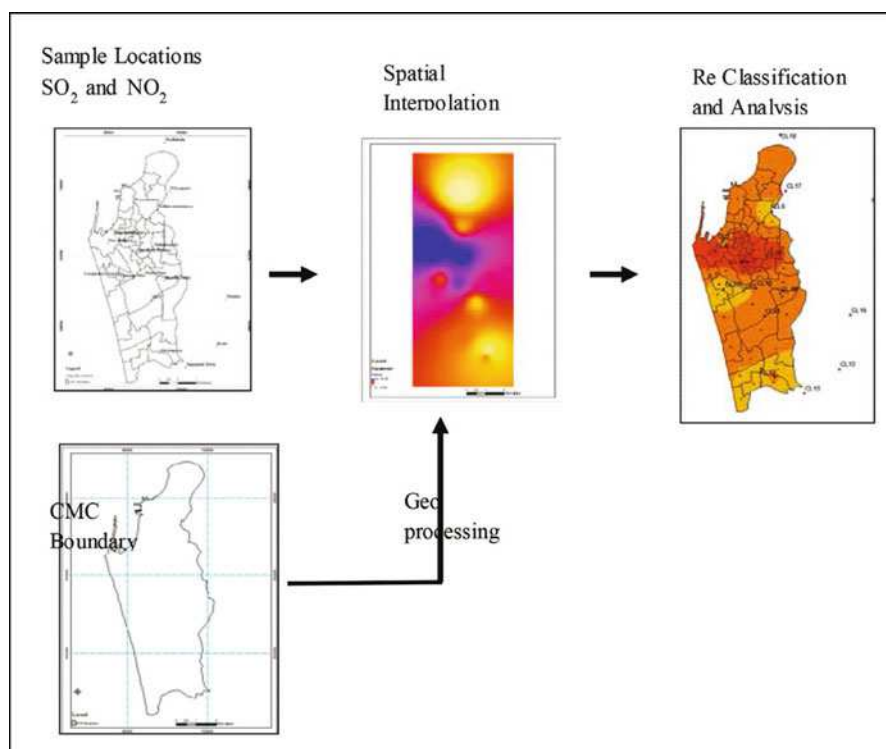


Fig. 62.3 Methodology of data analysis

outshining and since April to June there is also a highlighting increase of NO_2 levels over a considerable area of Colombo Municipal Council Area. CL10 exist with lower levels of NO_2 , while most of other surrounding regions are accounted by higher levels of NO_2 even in a case such as in June 2013 (Figure 62.4). But normally there are lower levels of NO_2 during May and June reasoned by southwest monsoon rains. In contrast this common phenomenon goes upside down in the year 2013. Hence, the distribution of NO_2 levels more than $90.8 \mu\text{g}/\text{m}^3$ covers a considerable area of CMC area during June, 2013. It is exceptional the cases related to CL 09 and CL 03 in June when compared with other locations. When considering the monthly variation of SO_2 from October, 2012 to June, 2013 northern parts of the Colombo MC area record higher levels of SO_2 among all locations (Figure 62.5). CL 19, CL 17, CL 4 are standing top levels of NO_2 concentration in most of the months considered in this study. There is relatively a higher concentration of SO_2 in most of the upper parts of the study area from May 2013 to June, 2013. April 2013 is peculiar due to the higher content of SO_2 in CL02 than other locations. Even though, this condition changes to lower amount by May, 2013. Instead higher levels of SO_2 are distributed throughout the upper parts onwards CL 02 and CL10. CL 19 and CL 04 revise with high levels of SO_2 by June, 2013.

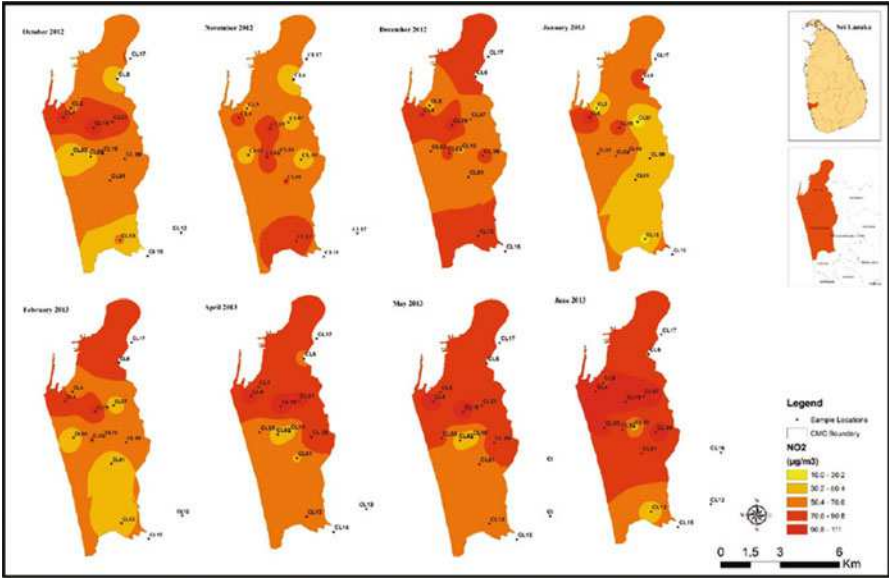


Fig. 62.4 Monthly variation of nitrogen dioxide in 2012 October to June 2013

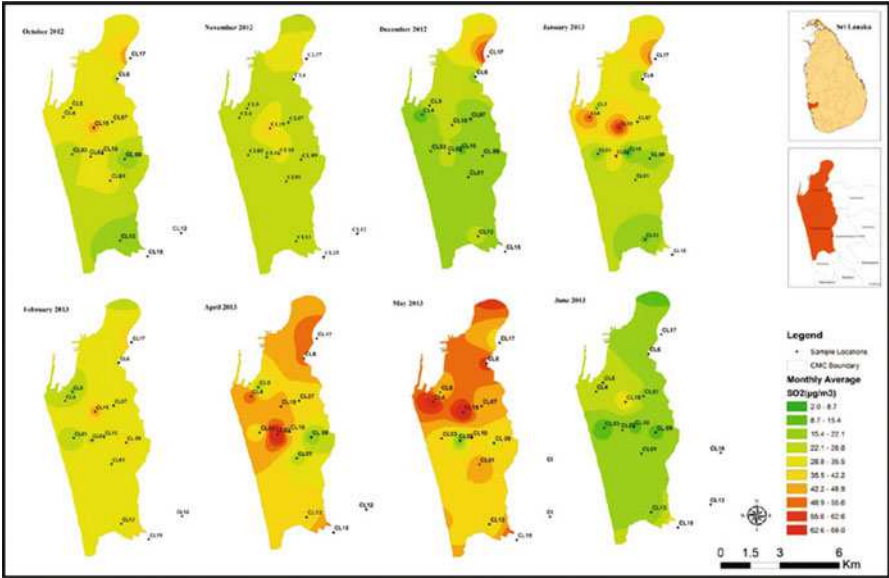


Fig. 62.5 Monthly variation of sulfur dioxide in 2012 October to June 2013

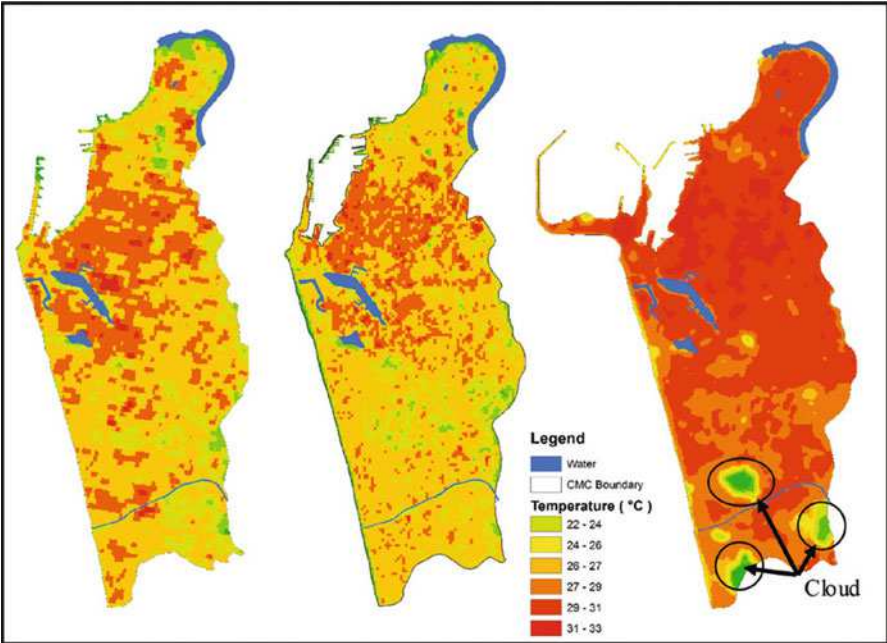


Fig. 62.6 Distribution of land surface temperature

Atmospheric temperature was calculated using Landsat 7 and Landsat 8 images. Landsat 7 ETM+ images consist with eight bands such as three visible, one NIR, two MIRs, and two thermals. Spectral Radiance Scaling Method used for data preparation. The LST ranged from 22°C to 33°C. Some of the high temperature zones are shows in Fort, Maradana area (Figure 62.6). Generally there was high building density (commercial and industrial) and traffic density in while the day. LST was an increasing past two decade. In 1987 high temperature recorded close to Fort and Maradana area. But it is increase step by step to the other area. Impact of that LST distribute to the South part of the CMC. In 2013 all the area of CMC generally LST was passed minimum 30°C while the day. In this situation called heat island effect.

The relationships of LST and air pollutant are calculated using Grid regression analysis method. The R² value of the NO₂ and LST regression was 0.508, and F-statistic equals 263.4, resulting p=0.00001, at the confidence level of 0.05. Figure 62.7 shows relationship between temperature and NO₂ contamination. The R² value of the SO₂ and LST regression was 0.52, and F-statistic equals 279.11, resulting p=0.00001, at the confidence level of 0.05. Figure 62.8 shows relationship between temperature and SO₂ contamination.

The relationship between traffic density and NO₂, SO₂ are calculated using Grid regression. The R² value of the traffic density and NO₂ regression was 0.18, and F-statistic equals 2720.30, resulting p=0.00001, at the confidence level of 0.05.

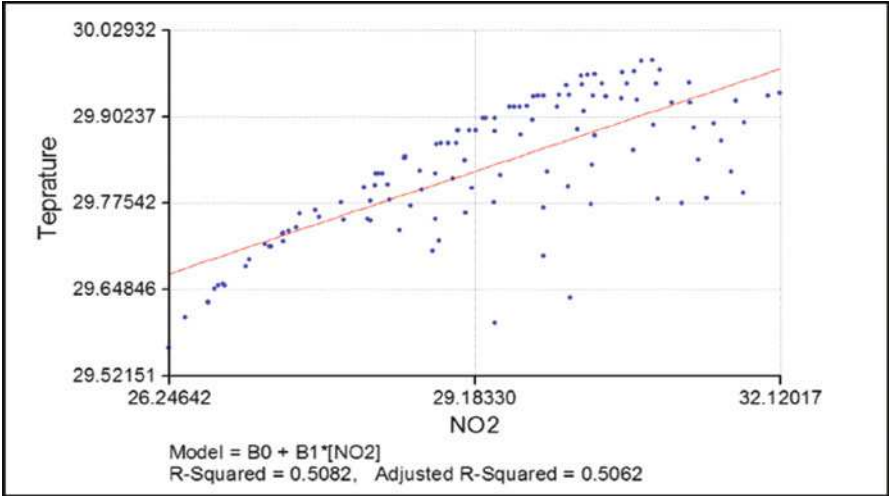


Fig. 62.7 Relationship between NO_2 and LST

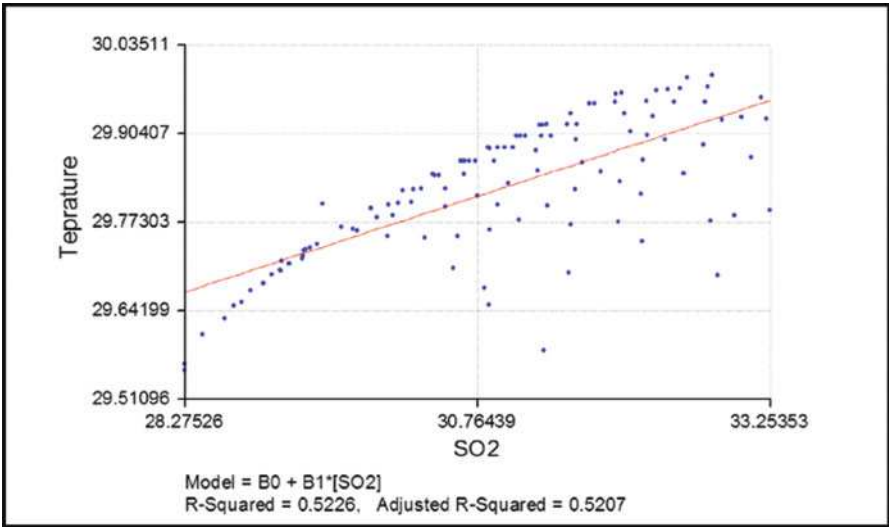


Fig. 62.8 Relationship between SO_2 and LST

Figure 62.9 shows relationship between traffic density and NO_2 contamination. The R^2 value of the SO_2 and traffic density regression was 0.38, and F-statistic equals 162.51, resulting $p = 0.00001$, at the confidence level of 0.05. Figure 62.10 shows relationship between traffic density and SO_2 .

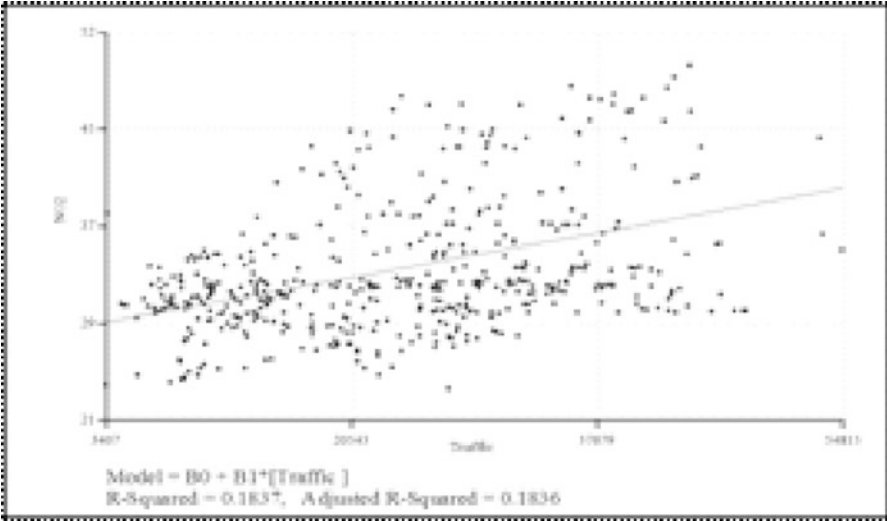


Fig. 62.9 Relationship between traffic density and NO₂

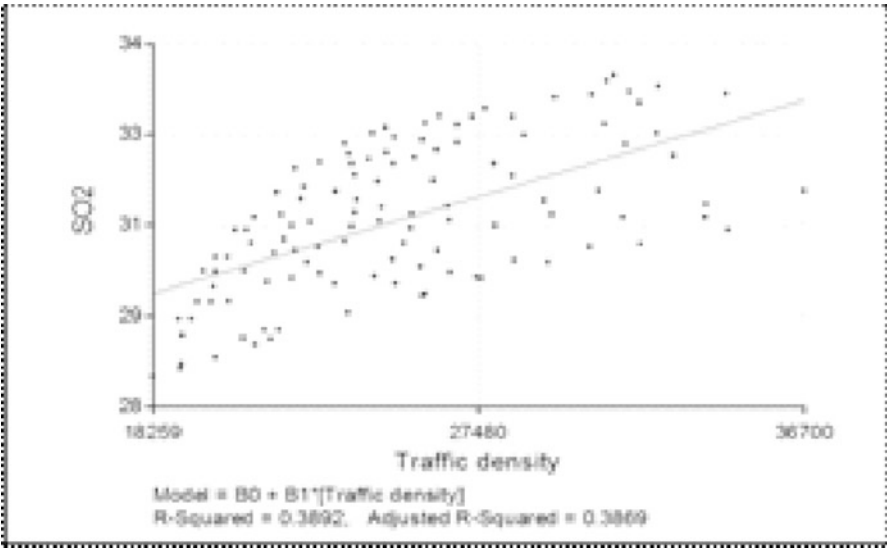


Fig. 62.10 Relationship between traffic density and SO₂

62.5 CONCLUSIONS

Air pollution level was increase with rainfall variation of the area. Contamination of air pollutant was travel to another area using wind and Sea breeze. Main air pollutant emitter was Traffic and vehicles. It was clearly shows with monthly

variation of pollutant distribution. Air pollution was increased with festival seasons and school holding time period. Road network cannot enlarge in Colombo MC Area. In that case Colombo MC Area will need to ordinarily traffic flows in the present. If established new vehicle flow, it not should be a traffic problem greater than past original road. Land cover/ Land use were change in past four decade in CMC Area. The general trend were observed in the built up areas increase temporally. The vegetation cover was decrease step by step in this commercial area. In effect of this case there was no natural filtration in Carbon particles. It was effect to the increasing air pollutant and land surface temperature.

REFERENCES

1. Ileperuma, A., Oliver, Aberatne and Vilani, D.K.: Air pollution monitoring in the city of Kandy: possible transboundary effects. *Jurnal of the National Science Foundation of Sri Lanka*, 34(3), 137–141 (2006)
2. Environmental Economics: Air quality management (AQM) programme, Environmental Economics and Global Affairs Division, Ministry of Environmental and Natural Resource, pp. 92–98 (2002)
3. Silva, E.I.L. and Manuweera, L.: Surface and Rainwater Chemistry in Sri Lanka – A Risk of Acidification. *Asian Journal of Water, Environment and Pollution*, 1(1 & 2), 79–86 (2004)

Chapter 63

Platinum, Palladium and Rhodium in Road Dust/Top Soils from Major South Indian Cities: Implications on Environment and Human Health

V. Balaram, C.T. Kamala, A. Sreenivasa Rao, M. Satyanarayanan, K.S.V. Subramanyam, and S.S. Sawant

Abstract: Pt, Pd and Rh emitted into the air through the exhausts of cars and trucks collected from Bangalore, Hyderabad and Visakhapatnam cities of south India were assessed in the context of their accumulation and resultant risks on human health and ecology. Apart from road dusts, respirable suspended particulate matter (RSPM) samples from these three cities were collected and studied. Road dust and top soil samples from road junctions and traffic signals with heavy and erratic traffic flow showed higher PGE levels than those from roads with low and free flow traffic suggesting that traffic flow conditions greatly influenced emissions of PGE from the auto-catalysts. Further studies on the exposure levels from Hyderabad, showed higher amounts of Pt, Pd and Rh in the blood samples of older people (for example, traffic police) who are exposed to extreme traffic conditions. Owing to the adverse health and ecological risk potential of PGE on humans, monitoring their levels, understanding the transformation paths and to find out mitigation methods are necessary.

Keywords: Platinum group elements • Auto-catalyst • Urban environment • Road dust • Sampling • ICP-MS

V. Balaram (✉) • C.T. Kamala • M. Satyanarayanan • K.S.V. Subramanyam • S.S. Sawant
CSIR-National Geophysical Research Institute, Hyderabad, India
e-mail: balaram1951@yahoo.com

A.S. Rao
Department of Chemistry, Alliance College of Engineering and Design, Alliance University,
Bangalore, India

63.1 INTRODUCTION

Today mankind is exposed to the highest levels of toxic metals such as Pb, Hg, As, Al, Ni, Sn, Sb, Bi and V particularly in the urban environment in recorded history. These toxic metals have no known function in the body and, in fact, are harmful particularly in excess concentrations. In addition, platinum group elements (PGE) are currently receiving world-wide attention because of their extensive utility in high technology applications including the use of Pt, Pd and Rh in automobile catalytic converters. Pt, Pd and Rh are emitted into the air through automobile catalytic converters. Part of it will settle down in the soil and dust on either side of the high ways. Consequently, their levels in air may be higher on certain locations, for instance in and around, traffic junctions, garages, in tunnels on national high ways and on roads with heavy traffic having a stop and go movement. In fact, the main emission source of PGE into the environment, except for the emissions of geogenic and cosmic origin, are human activities such as autocatalytic converters [1] in addition to their other industrial use and medical applications. Several studies are underway to understand the effects of these elements on humans and animals in many countries including India [2-5]. The concentrations and distribution patterns of PGE in road dust were an accurate reflection of the levels of pollution and were found to match with the local traffic conditions. Even the surrounding water bodies can be polluted with these elements due to rain and subsequent runoff as raining greatly contributes to the spread of contaminants in the environment. In fact, very little information is available on these processes due difficulties in the detection and determination of very low (ng/l) levels of these metals in different matrices such as dust, soils and water [6]. Recent studies indicated that platinum and palladium can accumulate in the roots of plants after uptake [7]. Whether eating platinum-containing plant roots can do any harm to animals and humans, is not yet clear. On the other hand it is likely that micro-organisms may be able to convert platinum substances to more dangerous species in soils [8], but on this subject very little information is available at present. The efforts to understand the effects of PGE emitted from catalytic converters on human health have prompted more researchers to focus on the accumulation of PGE in the environment including water, soil, plants, and dust. In the present study, an attempt is made to obtain information about anthropogenic emissions of PGE and other toxic elements, their concentration levels and distribution patterns in urban road dusts and other environmental segments, including humans exposed to different traffic conditions from different areas of three major cities of South India - Bangalore, Hyderabad and Visakhapatnam.

63.2 EXPERIMENTAL

63.2.1 *Instrumentation, Sampling, Sample Preparation and Analytical Methodology*

An ICP-MS Perkin-Elmer Sciex (Model ELAN DRC II Toronto, Canada) was used for sample analysis. The instrumental parameters and operating conditions of the ICP-MS were set using a procedure described by Balaram et al [9]. A Respirable Dust Sampler (RDS, EnviroTech) was used for the collection of RSPM in ambient air. The overall sampling sites are categorized based on the traffic flow into low traffic zone or control (sites in the interior of the residential area), medium traffic zone (away from the main city having only industrial trucks as traffic) and more traffic zone (covering both city traffic and industrial trucks). Details of the particular steps of analytical procedures for PGE quantification in environmental samples such as road dust, airborne particulate matter, soil, sediments, water, wastewater and biological samples are furnished elsewhere in a detailed way [10].

63.2.2 *Results and Discussion*

There are no reported data of PGE concentrations in ambient air prior to the introduction of motor vehicle catalytic converters. Ever since autocatalytic converters were introduced, they were termed mobile sources of platinum, palladium and rhodium due to loss of small quantities of these metals from the autocatalytic converters as a result of mechanical and thermal impacts. The overall sampling sites are divided based on the type of PGE input source i.e., automobile and automobile as well as industrial discharge in all three cities. The concentration of Pt, Pd and Rh in respirable suspended particulate matter (RSPM) in ambient air collected at six sampling stations from the highways of Bangalore, Hyderabad and Visakhapatnam cities are presented in Table 63.1. These data demonstrate that catalytic converter attrition is responsible for the elevated abundances and concentrations of PGE increased with traffic density, reaching values up to 43 ng/g Pt, 58 ng/g Pd and 10.8 ng/g Rh in road dust samples. The concentration levels of PGE appeared to be in the following order: Pt > Pd and Pd > Rh, with Rh having lesser abundances.

63.2.3 *Mobility and Bioavailability of PGE in the Environment*

Platinum concentrations in urban air have increased by more than two orders of magnitude in the last 20 years and pose a potential health risk [11]. The bioavailability of active form of platinum depends on oxidation state and/or ligand.

Table 63.1 Conc. range (ng/g) in road dust collected in high traffic areas in Bangalore, Hyderabad and Visakhapatnam

City	Concentration range (in ng/g) in road dust collected in high traffic areas		
	Pt	Pd	Rh
Bangalore	7.6–27.4	7.8–25.4	8.6–10.8
Hyderabad	4–43	6–58	0.4–7.2
Visakhapatnam	0.2–29.13	2.3–39.13	-
Background conc.	0.1–2.1	0.5–1.6	0.7–2.3

Platinum compounds provide an excellent illustration of the need to differentiate the chemical species of an element for example, when evaluating its allergenic potential. Allergic symptoms including rhinitis, asthma, and urticaria have been reported after World War II in workers employed in platinum refineries and in secondary users, mainly for the manufacture or recycling of catalysts [12]. Therefore, it was assumed that metals emitted in the oxidation state '0' do not enter in biogeochemical cycles due to their chemical inertness. However, the results of studies on the solubility of selected chemical forms of PGE have shown that many factors could increase their bioavailability. Significant increases in PGE bioavailability can be observed in the presence of some organic compounds such as humic acids, fulvic acids, acetates, or metabolic products of fungi, bacteria and plants [13]. The results of the speciation studies indicated that various naturally occurring ligands have the potential to increase the mobilities of Pt, Pd and Rh through the formation of soluble complexes which can easily be transported in environmental and biological systems [14]. Preliminary studies were carried out to investigate the concentration levels of PGE in blood samples of occupationally exposed people in Hyderabad city, clearly point to traffic as a main source of PGE contamination in the roadway environment. Pt levels are observed to be higher than Pd and Rh in general. When compared the levels of Pt, Pd and Rh in blood samples of exposed people in other countries (Table 62.2). PGE value ranges obtained in the present study are far higher than the values obtained in the earlier works in other countries. The Pt ranged from 150–6500 ng/l followed by Pd 220–1950 ng/l and Rh 400–4950 ng/l respectively.

63.3 CONCLUSIONS

Although further detailed investigation of Pt, Pd and Rh contents in dust, soil and plant samples along roadsides is required to define their distribution in space and time, present data led to the following conclusions: i) The concentrations of PGE in urban dusts from metro cities of south India are far higher than the natural background. A direct relationship between PGE concentrations and traffic volume could be established. ii) Significant abundances of Pt and Pd were recorded in each of the dust and soil samples, whilst Rh content was very low. iii) An increasing

Table 62.2 Pt, Pd and Rh concentrations (ng/l) in blood samples of exposed persons in Hyderabad, India in comparison with reported values, modified after Marcelo et al. [15]

Country	Matrix	Pt (ng/l)	Pd (ng/l)	Rh (ng/l)
Germany	Urine	6-91 (33 mean)	-	
Italy	Urine	<0.6-1.9 (1.02 median)	5.2 – 14.8 (9.5 median)	3.1 – 49.5 (11.7 median)
Italy	Urine	0.6 – 9.5 (0.9 median)	0.1 – 28.9 (8.8 median)	1.4 – 38.6 (8.9 median)
Germany	Urine	0.4 – 77.5 (1.6 median)	-	-
Germany	Urine		<90	<7 – 16 (< mean)
USA	Urine	<30	-	-
Sweden	Serum	<100 – 200 (<100 median)	<200-300 (200 median)	<100 - 580 (<100 median)
Sweden	Blood	<100 – 330 (<100 median)	<200-300 (200 median)	<100 - 580 (<100 median)
India	Blood	150 - 6500	220 -1950	400 - 4950

trend between Pt and Pd contents in blood samples of the exposed persons confirm their bioavailability, iv) There is greater potential for exposure to high concentrations of platinum, palladium and rhodium by the road users and those living in urban environments or along the highways and v) Although present emissions of PGE may not pose a serious threat, the growing number of motor vehicles equipped with catalytic converters and accumulation of PGE in the environment may become a problem in the near future. Therefore further research is required to better understand the behavior of PGE emitted from auto-catalysts in the urban environment of Indian Cities. PGE mobility, species, as well as bioaccumulation need to be understood further in a detailed way.

REFERENCES

1. Ravindra, K., Bencs, L. and Van Grieken, N.R.: Platinum group elements in the environment and their health risk. *Sci. Total Environ.* 318, 1–43 (2004)
2. Gomez, B., Palacios, M., Gomez, M.M., Sanchez, J., Morrison, G. and Rauch, S.: Levels and risk assessment for humans and ecosystems of platinum-group elements in the airborne particles and surface road dust of some European cities. *Sci. Total Environ.* 299(1-3), 1–19 (2002)
3. Zereini, F., Alt, F., Messerschmidt, J., vonBohlen, A., Liebl, K. and Puttmann, W.: Concentration and distribution of platinum group elements (Pt, Pd, Rh) in airborne particulate matter in Frankfurt and Mainz, Germany. *Environ. Sci. Technol.* 38, 1686–1692 (2004)
4. Mathur, R., Balaram, V., Satyanarayanan, M., Sawant, S.S. and Ramash, S.L.: Anthropogenic platinum, palladium and rhodium concentrations in road dusts from Hyderabad city, India. *Environ. Earth Sci.*, 62, 1085–1098 (2011)
5. Balaram, V., Kamala, C.T., Mathur, R., Mathur, R., Srenivasa Rao, A. and Satyanarayanan, M.: On a Sustainable Future of the Earth's Natural Resources. Ed. Ramkumar, Mu, Springer Earth System Sciences (2013)

6. Balaram, V.: Current developments in the quantitative determination of PGE for basic and applied geochemical studies. Spl. Pub. No. 2, Geol. Soc. India (2014) (in press).
7. Oke, S., Kikkert, J., Vasiluk, L. and Hale, B.: A study of platinum accumulation in radish (*Raphanus sativus*) and durum wheat (*Triticum durum*) plants, Studies by Undergraduate Researchers at Guelph (SURG), Vol 7, No 1 (2013)
8. Essumang, D.K., Dodoo, D.K., Obiri, S. and Oduro, B.A.K.: Analysis of vehicular fallouts from traffic in the Kumasi Metropolis, Ghana. *Bull. Chem. Soc. Ethiop.*, 20(1), 9–15 (2006)
9. Balaram, V., Mathur, R., Banakar, V.K., Hein, R.J., Rao, C.R.M., Rao, T.G. and Dasaram, B.: Determination of the platinum group elements (PGE) and of gold (Au) in the manganese nodule reference samples by nickel sulphide fire assay and Te coprecipitation with ICP-MS. *Indian J. Marine Sci.*, 35, 7–16 (2006)
10. Kamala, C.T., Balaram, V., Satyanarayanan, M. and Subramanyam, K.V.S.: Source identification studies of PGE and other heavy metals released into the urban environment and development of methods for their analysis. *J Appl Geochem*, 14, 16–25 (2012)
11. Zereini, F., Wiseman, C., Alt, F., Messerschmidt, J., Muller, J. and Urban, H.: Platinum and rhodium concentrations in airborne particulate matter in Germany from 1988 to 1998. *Environmental Sci. Technol.*, 35, 1996–2000. (2001)
12. Cristaudo, A., Sera, F., Severino, V., De Rocco, M., Di Lella, E. and Picardo, M.: Occupational hypersensitivity to metal salts, including platinum, in the secondary industry. *Allergy*, 60, 159–164 (2005)
13. Jackowska, A.D., Kudak, B., Polkowska, Z. and Namisenik, J.: Environmental Fate of Traffic-Derived Platinum Group Metals. *Crit. Rev. Anal. Chem.*, 39, 251–271 (2009)
14. Colombo, C.: The Speciation and Bioavailability of Platinum, Palladium and Rhodium in the Environment. Ph.D. Thesis. Department of Earth Science and Engineering, Imperial College London, pp. 201 (2008)
15. Morcelli, C.P.R., Figueiredo, A.M.G, Sarkis, J.E.S., Enzweiler, J., Kakazu, M., and Sigolo, J. B.: PGE and other traffic related elements in road side soils from Sao Paulo, Brazil. *Science of the Total Environment*, 345(1-3), 81–91 (2005)

Chapter 64

Longer Growing Season Decreases Peak Summer Vegetation Productivity in North American Ecosystems

B.R. Parida and W. Buermann

Abstract: During the last decades, snow-dominated Northern American (NA) ecosystems have experienced prolonged spring warming and earlier spring onsets. Recent studies showed that these changes have adverse effects on plant productivity due to water stress. In this study, we analyze relationships between longer non-frozen period, peak summer vegetation greenness index and a drought index by using the three decades of optical satellite data, microwave Freeze-Thaw record and climatic data. Results show that longer non-frozen period caused decline in summer soil moisture availability. This suggests a mechanism of ‘longer non-frozen period-summer drought’ which has led to widespread decline in peak summer vegetation greenness across large portions of NA’s mid- and high-latitude ecosystems. This mechanism may be exacerbated in the future under accelerated spring warming and associated longer growing season, and depending on the future precipitation pattern generally larger degrees of dryness during the peak of the northern growing seasons can be expected.

Keywords: Spring warming • Longer growing season • Summer drought

64.1 INTRODUCTION

Over Northern American (NA) mid- and high latitude continental regions, annual average temperatures have increased by 1-2 °C during the second half of the 20th century [1] and are projected to increase by 2-6.7 °C under the RCP4.5 scenario. The most pronounced warming trends have been observed in winter and spring, with peak warming in early spring over western Canada, the central Canadian Rockies and the interior Northwest of the U.S [2]. This spring warming has led to

B.R. Parida (✉)

Department of Civil Engineering, Shiv Nadar University, Dadri, India

e-mail: bikash.parida@snu.edu.in

W. Buermann

Institute for Climate and Atmospheric Science, University of Leeds, Leeds LS2 9JT, United Kingdom

increases in the length of the vegetation growing season by 2-4 days/decade since 1950 in NA [3]. Most regions of NA ecosystems rely on winter snowpack as an important source of water during the course of growing season [4]. However, early spring warming causes early snowmelt-runoff that leads to a disruption in the existing water supply systems in the summer season of high water use demand. Such changes in the hydrological flow regime favor winter and spring flooding that in turn lowers summer soil moisture and river flows and leads to reduction in summer photosynthesis by plants. Earlier spring onset has been associated with increasing carbon sequestration by high latitudes vegetation [5]. However, little attention has been given on how warmer springs influence the summer productivity over NA ecosystems (i.e. tundra, boreal and mixed forests, savannas, grasslands) and what are the corresponding key mechanisms involved between warmer springs and vegetation productivity. A recent study based on long-term satellite vegetation records by [6] provided a strong evidence of earlier spring onset and decline in peak summer forest greenness due to mid-summer moisture deficit over NA boreal forests. Even so, the mid-summer drought signal arises from earlier spring onset has not been confirmed with moisture or drought indicators. Here, we posit that these relationships could be more pronounced on the continental scales rather than regional scales or specific to boreal ecosystems as reported by [6].

64.2 STUDY AREA AND DATA USED

The study area lies between 30°N to 75°N in the snow-dominated NA regions encompassing land cover types viz. forests, shrublands, savannas, and grasslands. Long-term satellite vegetation records of Normalized Difference Vegetation Index (NDVI) have been used from the improved and extended GIMMS-NDVI data set. The third generation of the GIMMS-NDVI data are aggregated into monthly time steps at 0.25° x 0.25° spatial resolution spanning from 1982 to 2010 and obtained from measurements of NOAA's AVHRR sensors [7]. The length of the non-frozen (NF) period is closely linked to length of growing season which is obtained from the recently released daily Freeze-Thaw (FT) record from the microwave sensors [8]. A direct index of drought called Palmer Drought Severity Index (PDSI) is obtained (aggregated into 0.25° resolution) as a surrogate of soil moisture status and lower PDSI values generally indicate a drier climate [9].

64.3 METHODS

GIMMS-NDVI computed from near-infrared (0.72-1.0 μm) and red bands (0.58-0.68 μm) to monitor vegetation growth and known as a surrogate measurement of plant photosynthetic activity [5]. The NF period from January to August is derived from the daily FT record by summing the number of classified NF days [8]. This

indicator can capture the effect of frozen status of the land surface. Spatial grid-point Pearson's correlations are performed between length of NF period and NDVI based on first-differenced (FD) of time series of the original data. The FD method is adopted since it describes as a way to remove non-stationary in mean from the original data.

64.4 RESULTS AND DISCUSSION

64.4.1 *Decadal Trends in Length of NF Period and Peak Summer NDVI*

Figure 64.1 shows increasing in length of NF period trend in NA and Eurasia (EA) domain by 0.27 and 0.31 day yr^{-1} , respectively. This trend is coincident with global warming and largely driven by earlier spring thawing that translates into a 2.7 days/dec lengthening of the NF period from 1982 to 2010 in NA.

The spatially explicit grid-point trend of length of NF period shows that increasing trend is robust specifically in the high latitude regions ($>50^\circ\text{N}$) with dominant land cover types such as evergreen needle leaf forest, mixed forests and tundra (Fig. 64.2a). In other words, especially the ecozones of Boreal Shield, Hudson Plain and Boreal Cordillera portions show an increasing trend of about >5 days/dec. The increasing trend of length of NF period coincides in part with negative/browning trends in peak summer NDVI (Fig. 64.2b).

Previous findings based on shorter satellite vegetation records showed the positive or greening trend of summer NDVI up to mid 1990s over northern ecosystems [5]. However, this greening trend stalled or reversed during the latest period (1996-2010) because of warming induced summer drought and decreased summer precipitation [10]. Other than these two climatic drivers our findings also provide evidence that the browning trends of peak summer NDVI specifically over northern high latitudes ($>50^\circ\text{N}$) is also linked to the length of NF period in response to spring warming. Over the NA boreal forests, a recent study suggests that the mechanism 'earlier spring onsets-peak summer drought' has a contribution to the browning trends of peak summer productivity [6]. We infer that increasing trends in length of NF period may have a larger influence on browning trends of peak summer NDVI in future under accelerated spring warming.

64.4.2 *Linkages between Length of NF Period and Peak-to-Late Summer NDVI at Inter-annual Time Scales*

We analyze influence of length of NF period (as length of growing season) on peak summer vegetation greenness index (NDVI) across the NA ecosystems and explore

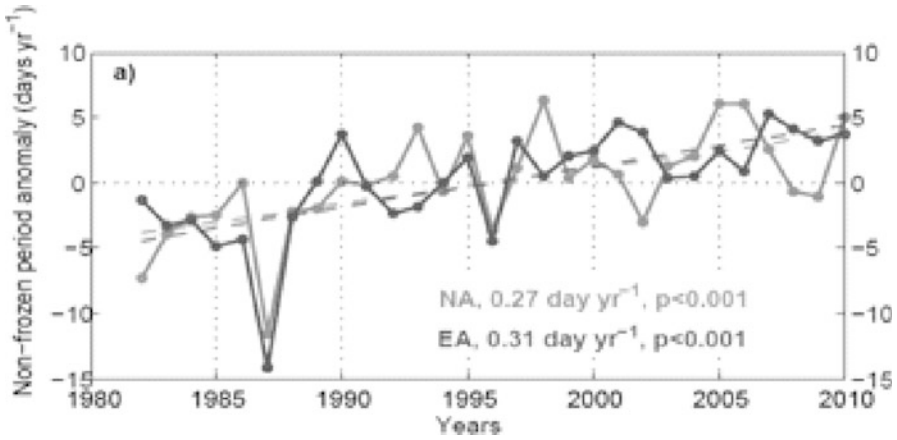


Fig. 64.1 Length of NF period trend for the NA and EA region as derived from the FT record over the period 1982–2010

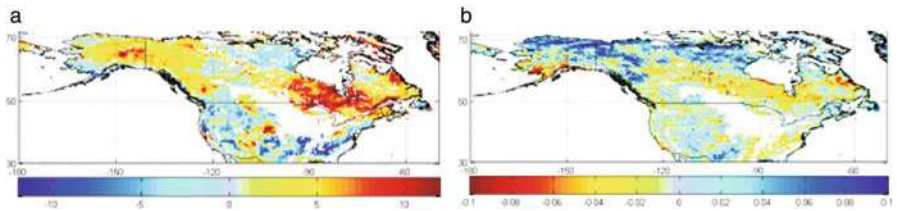


Fig. 64.2 Map depicts long term trends in length of NF period and peak summer NDVI in NA for 1996–2010. Changes are calculated through linear regression. In panel (a), changes larger or smaller than five days/dec are generally statistically significant whereas in (b) NDVI changes larger or smaller than 0.03 per dec are statistically significance at $p < 0.1$ level. For the high latitudes (above 50°N), peak summer is defined as July to August, whereas for the 30°N–50°N it is defined as August to September

corresponding relationships with drought index PDSI. Fig. 64.3 exhibits large-scale negative correlations (60% of areal proportions) and the pattern implies longer NF period corresponds to decline in peak summer NDVI and stronger effects are seen over climatologically drier regions of western U.S and Canada. By contrast, regions surrounding the Hudson Bay and Southwest of Alaska show positive correlations which indicate peak summer vegetation greenness continued to benefit from longer NF period. Earlier study has confirmed the adverse effect of earlier spring onset on peak summer productivity (using both NDVI and gross primary productivity) only for NA boreal forests [6] whereas our result suggests that this mechanism can operate in a larger-scale encompassing almost all NA ecosystems viz. tundra, boreal forest, mixed forest, savannas, and grasslands.

Further analyses of longer NF period and summer drought signal (not shown here) for 1982–2010 reveals that widespread co-location of negative correlation pattern with those based on NF period and its linkages with peak summer NDVI over the vast areas of northern ecosystems. This suggests longer NF period

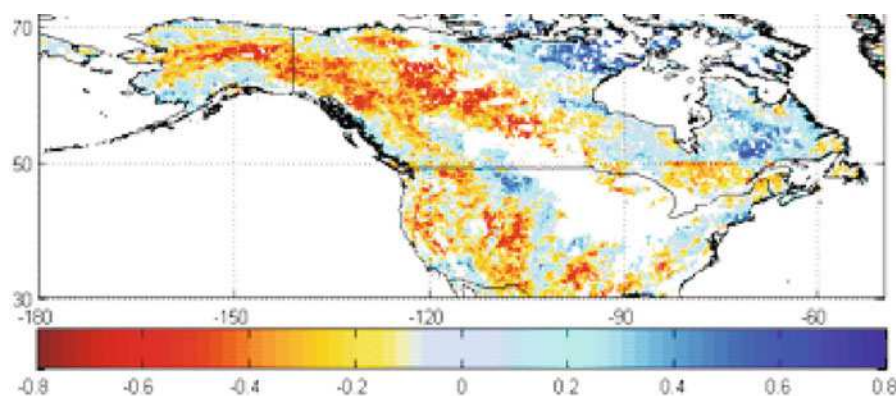


Fig. 64.3 Map depicts grid point correlations between length of NF period and peak summer NDVI for the period 1982-2010. Original data have been first differenced prior correlations. Correlation values greater or smaller than 0.32, are generally statistically significant ($p < 0.1$). Frequency histogram shows areal proportions (%) of corresponding correlations for every 0.2 interval

corresponds to lower summer soil moisture during peak growing season and led to mid-summer drought conditions. This provides an evidence for a pronounced shift into a more water-limited regime due to increasing length of growing season and earlier snowmelt-runoff in response to spring warming.

64.5 CONCLUSIONS

The identified mechanism ‘longer NF period-peak summer drought’ is playing a dominant role in the snow-dominated NA ecosystems and has an adverse effect on vegetation photosynthetic activity during peak summer growing season. Thus, NA ecosystems are becoming more vulnerable to this mechanism. Our results also indicate that increasing length of growing season particularly above 50°N is also linked to peak summer vegetation browning trends in the recent decades in conjunction with the summer drought related to rising summer temperature and decreased summer precipitation.

REFERENCES

1. Cayan, D.R. et al.: Changes in the onset of spring in the western United States. *Bull. Am. Meteorol. Soc.*, 82, 399–416 (2001)
2. Karl, T., Knight, R., Easterling, D. and Quayle, R.: Indices of climate change for the United States. *Bull. Am. Meteorol. Soc.*, 77, 279–292 (1996)

3. Easterling, D.R.: Recent changes in frost days and the frost-free season in the United States. *Bull. Am. Meteorol. Soc.*, 83, 1327–1332 (2002)
4. Barnett, T.P., Adam, J.C. and Lettenmaier, D.P.: Potential impacts of a warming climate on water availability in snow-dominated regions. *Nature*, 438, 303–309 (2005)
5. Myneni, R.B., Keeling, C.P., Tucker, C.J., Asrar, G. and Nemani, R.R.: Increased plant growth in the northern high latitudes from 1981 to 1991. *Nature*, 386, 698–702 (1997)
6. Buermann, W., Parida, B.R., Jung, M. and Burn, D.H.: Reichstein, M.: Earlier springs decrease peak summer productivity in North American boreal forests. *Environ. Res. Lett.*, 8, 024–027 (2013)
7. Tucker, C.J. et al.: An extended AVHRR 8 km NDVI data set compatible with MODIS and SPOT vegetation NDVI data. *Int. J. Rem. Sens.*, 26, 4485–4498 (2005)
8. Kim, Y., Kimball, J.S., Zhang, K. and McDonald, K.C.: Satellite detection of increasing Northern Hemisphere non-frozen seasons from 1979 to 2008: Implications for regional vegetation growth. *Remote Sens. Env.*, 121, 472–487 (2012)
9. Zhao, M. and Running, S.W.: Drought-induced reduction in global terrestrial net primary production from 2000 through 2009. *Science*, 329, 940–943 (2010)
10. Wang, X. et al.: Spring temperature change and its implication in the change of vegetation growth in North America from 1982 to 2006. *PNAS*, 108, 1240–1245 (2011)

Chapter 65

Species Diversity and Regeneration Status in Sabaiya Collaborative Forest, Nepal

Bikash Kumar Mishra and S.C. Garkoti

Abstract To assess the status of diversity and regeneration of Sabaiya collaborative forest phytosociological study of the forest was carried out and Species Diversity, Importance value index, basal area, density and regeneration status were accessed. Edaphic characteristics were also studied. A total of 51 species were recorded in the study, of which 15 were represented in tree group, 20 in the shrub group and 9 in the herb group. Both seedling and sapling were represented by 11 species each. The forest was dominated by *Shorea robusta* (68.8 %) and *Mallotus philipensis* (6.8 %). Occasionally *Terminaliatomentosa* (4 %) and *Syzygiumcumini* (4.8 %) were present in the canopy. The sub-canopy was dominated by *Lagerstroemia parviflora* and *Semecarpusanacardium*. The understory was quite sparse and dominated by *Shorearobusta* and *Daubangagrandifloraseedlings*; and shrubs such as *Clerodendroninfortunatum* and *Eupatorium oderatum*. Among herbs *Cyperusiria* and *Cynadondactylon* were dominant. Despite having satisfactory regeneration of seedlings of Sal (16960 stem/ha), very few (120 stem/ha) saplings were recorded. Similar was the case with other tree species. The soil was sandy loam to loamy sand, slightly acidic to near neutral (pH 5.34–6.88), soil Nitrogen moderate (0.12–0.25 %) and Organic carbon moderate (1.5–3.0 %).

Keywords Sal • Diversity • Regeneration • Forest

65.1 INTRODUCTION

Forest covered about 75 % of the Terai in the central and western Nepal until 1950s [1]. Since, the forests of Terai are an important resource for both commercial and subsistence purposes [2], human pressures has reduced the forested area to less than 50 % of total land area in Terai by 1988 [3]. *Shorearobusta* Gaertn.f. (locally known as ‘Sal’) dominates the vegetation of the Terai region [4, 5], with other important species being *Syzygiumcumini*, *Terminallia* spp., *Bombaxceiba*, *Lagerstroemia parviflora* and *Mallotusphilipensis*. Under suitable condition ‘Sal’ has enormous

B.K. Mishra (✉) • S.C. Garkoti

School of Environmental Sciences, Jawaharlal Nehru University, New Delhi, India

e-mail: rjbikash@gmail.com

regeneration capacity; however, only natural regeneration is relevant method for Sal [6]. ‘Sal’ is considered as a highly valuable timber species [2] and hence to meet timber requirements, the people of Nepal mainly depend on it [7]. Therefore, ‘Sal’ forests of Terai are under continuous anthropogenic pressure and consequently, at present are shrinking and exhibit very poor regeneration status. In order to benefit the large population of the forest command area and for the sustainable use of forest, the government of Nepal introduced a new policy in May 2000 [8]. This policy introduced a new concept of Collaborative Forest Management (CFM) for the forests of Terai which are in large blocks [9, 10] define Collaborative forest management (CFM) as a working partnership between the key stakeholders in the management of a given forest—key stakeholders being local forest users and state forest departments, as well as parties such as local governments, civic groups and nongovernmental organizations, and the private sector. The CFM approach addresses more terai specific issues such as inclusion of distant user.

65.1.1 Sabaiya Collaborative Forest, Parsa

The Ministry of Forest and Soil Conservation (MFSC) approved three pilot CFM schemes in 2004: one in each Bara, Parsa and Rautahat Districts [11]. This programme is being implemented under a programme called the Biodiversity Sector Programme for Siwaliks and Terai (BISEP-ST), funded by Dutch government. However, at present only one of the pilot schemes, **Sabaiya**, has started implementing its scheme with the active assistance of DFO office [9].

65.2 MATERIALS AND METHODS

65.2.1 Study Site

Study site, Sabaiya collaborative forest, is located in the Parsa District in the south-central lowland Terai of Nepal (27°8' N to 27°14' N latitude, 84°53'E to 85°57'E longitude, 200–230 m elevation) (Fig. 65.1). Tropical monsoon climate prevails in this region. The maximum temperature in this region is recorded upto 40 °C & minimum temperature up to 7 °C. Average rainfall in this region is 1760.3 ml. Out of the total area of the forest of Parsa district, it covers 3138.51 hectares.

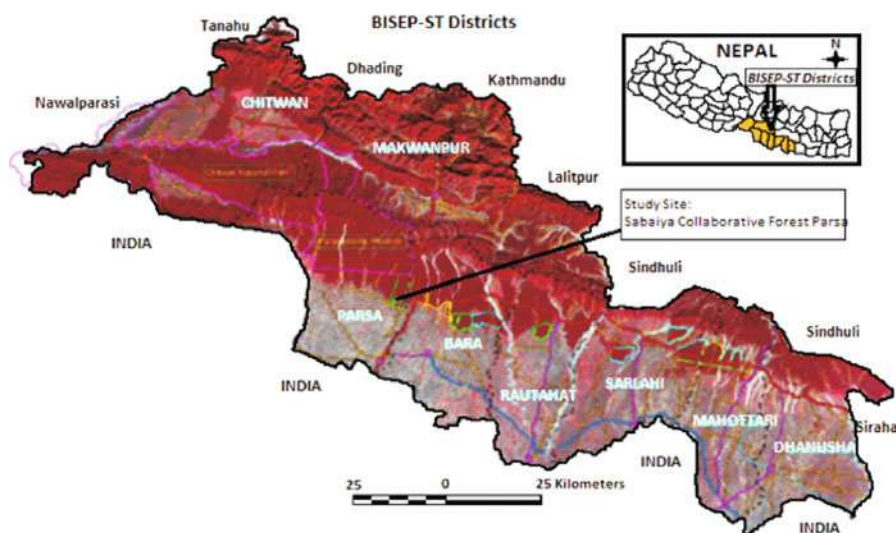


Fig. 65.1 BISEP-ST districts and the study site, Sabaiya collaborative forest

65.2.2 Methodology

A total of two transects were used for the study & each transect was 2 km long. Sampling locations were established every 200 m along the transect and thus a total of 20 locations were sampled. Starting points of the transects were established at the southern boundary of the forest. Sampling of tree species were done in three strata: trees (>5 cm DBH), saplings (1–5 cm DBH & > 1 m height), and seedlings (<1 m height) [3]. At each location a 10x10m square plots were established. Trees were sampled in 10x10m plot. Within each plot trees were identified to species and DBH of individuals of each species was measured. Within each 10x10m plot at one fixed corner 5x5m plot was established for shrubs, sapling and seedlings, & 1x1m for herbs. All the saplings, seedling, shrubs & herbs were also identified to species & the number of individuals of each species was counted. 5x5m plot was nested within 10x10m plot & 1x1m plot was nested within 5x5m plot. Diversity indices (Shannon–Wiener index and Simpsons index), Evenness and Species richness were calculated. Importance Value Index (IVI) was calculated following [12] and Abundance following [13].

From quadrat number one, five and nine, in each transect, soil was collected from three depths: 0–10 cm, 10–20 cm & 20–30 cm at two fixed locations by the help of soil core sampler and were bulked in polyvinyl bag and analyzed at plant ecology laboratory of Jawaharlal Nehru University, New Delhi, India. pH, texture, organic matter(%), total nitrogen, available phosphorus and moisture were determined for each sample following methods described in Laboratory methods of soil and plant analysis: A working Manual [14, 15].

65.3 RESULTS AND DISCUSSIONS

65.3.1 Results

65.3.1.1 Average Forest Structure and Composition

A total of 51 species were recorded in the study, of which 15 were represented in tree group, 20 in the shrub group and 9 in the herb group (Table 65.1). The forest was dominated by *Shorearobusta* and *Syzygiumcumini*. Occasionally *Terminalia tomentosa* and *M. phillipensis* were present in the canopy. The sub-canopy was dominated by *Lagerstroemia parviflora* and *Semecarpusanacardium*. The under-story was quite sparse and dominated by *Shorearobusta* and *Daubanga grandiflora* seedlings; and shrubs such as *Clerodendronin fortunatum* and *Eupatorium oderatum*.

65.3.1.2 Tree Density and Basal Area

The highest tree density was recorded for *Shorear obusta* (430 stem ha⁻¹), followed by *Mallotus philippensis* (40 stem ha⁻¹), *Syzygium cumini* (30 stem ha⁻¹) and *Terminalia tomentosa* (25 stem ha⁻¹). The species with the highest basal area was *Shorear obusta* (34.32 m²/ha) followed by *Syzygium cumini* (3.90 m²/ha), *Adina cordifolia* (2.28 m²/ha), *Bombax cieba* (2.08 m²/ha) and other species covered less than 2 m²/ha (Table 65.2).

65.3.1.3 Regeneration of Tree Species

In seedling group the highest density was recorded for *Shorear obusta* (16960 seedling ha⁻¹), followed by *Daubanga grandiflora* (5400 seedling ha⁻¹) and *Grewiasubin aqualis* (1540 seedling ha⁻¹). Though, seedlings of *Shorear obusta* was in appreciable number (16960 seedling ha⁻¹), saplings recorded were in very few number (120 sapling ha⁻¹). Neither tree nor saplings were recorded for *Daubanga grandiflora* which had good number of seedlings (5400 seedling ha⁻¹). Regeneration for other species was very poor (less than 450 seedling ha⁻¹ to even 0).

Table 65.1 Species diversity, richness and evenness in the Sabaiya collaborative forest

Community Statistics	Symbol/Unit	Values				
		Tree	Sapling	Seedling	Shrub	Herb
Species richness	no.	15	10	11	20	9
Diversity	Shanon index (H')	1.349	1.978	1.265	2.091	0.555
	Simpsons index	0.515	0.839	0.567	0.771	0.208
Evenness	e	1.147	1.97	1.21	1.607	0.581

Table 65.2 Density and basal area of tree species

S.N.	Species	Density (tree/ha)	Basal area (m ² /ha)
1	<i>Shorea robusta</i> (sal)	430 (68.8)	34.32435
2	<i>Syzygium cumini</i> (jamun)	30 (4.8)	3.90765
3	<i>Dalbergialatifolia</i> (satisal)	5 (0.8)	1.754685
4	<i>Terminalia tomentosa</i> (asna/saj)	25 (4)	1.76483
5	<i>Dillenia pentagyna</i> (tatari)	5 (0.8)	0.592215
6	<i>Lagerstroemia parviflora</i> (bot dhairo)	20 (3.2)	0.24482
7	<i>Holarrhena antidysenterica</i> (baadkule)	5 (0.8)	0.212035
8	<i>Grewiasubin aqualis</i> (fashro)	10 (1.6)	1.10744
9	<i>Adina cordifolia</i> (karma)	10 (1.6)	2.28105
10	<i>Aphanamixis polystachya</i> (royna)	5 (0.8)	1.79666
11	<i>Bombax cieba</i> (simal)	5 (0.8)	2.08656
12	<i>Semecarpus anacardium</i> (bhalayo)	25 (4)	1.72679
13	<i>Mallotus philippensis</i> (Sindure)	40 (6.4)	0.287475
14	sps A (unidentified)	5 (0.8)	0.02292
15	<i>Albizia procera</i> (siris)	5 (0.8)	0.183985
Total		625	52.293465

Figures in parenthesis indicate the relative dominance of the species in percentage.

65.3.1.4 Importance Value Index

Importance percentage is a measure of influence of each species on the forest community. IP was calculated from relative basal area (RBA), relative frequency (RF) and relative density (RD). *Shorea robusta* contributed to more than 56 % of the importance percentage in the collaborative forest, followed by *Syzygium cumini* (7.66 %), *Mallotus philippensis* (5.88 %), *Semecarpus anacardium* (5.4 %) and *Terminalia tomentosa* (4.83 %). The IP of all other species were below 4 %.

65.3.1.5 Edaphic Characteristics

The soil in the study site was reported mainly sandy loam and loamy sand. Organic carbon content in all sampling plots were moderate (1.5–3.0 %) except in one plot where it was high (>3.0 %) . Total nitrogen across all plots was moderate (0.12–0.25) to low (0.05–0.12). Soil moisture recorded at the sampling time (December) ranged from 11.23 % to 5.23 %. The soil was slightly acidic to near neutral as pH ranged between 5.34 and 6.88. Likewise phosphorus in the soil ranged between 21.68 % and 5.65 %.

65.3.2 Discussion

Stainton [16] described ‘Sal’ forests as species-poor. The per plot species richness observed for different life forms in present study supports this characterization. Likewise, the observation of tree density ($625 \text{ trees ha}^{-1}$) is consistent with densities reported by [17] ($745 \text{ trees ha}^{-1}$) in Churiyamai VDC in Makwanpur district and [18] ($408 \text{ trees ha}^{-1}$) in Gorakhpur India. Shanon Diversity Index (H') (1.349) was significantly higher than that reported by [17], 0.833 in community forest and 1.072 in national forest of Churiyamai VDC of Makwanpur district, Nepal but lower than that reported by [19], 2.502 in Nawalparasi district, Nepal. Total basal area in our study ($52.29 \text{ m}^2/\text{ha}$) was within the range $16.0\text{--}61.1 \text{ m}^2/\text{ha}$ reported by [20] in Corbett National Park, India. The high basal area observed in our study resulted from good density of mid and large sized trees. Regeneration of *Shorearobusta* at seedling stage was satisfactory (16960 stem/ha) but very few number was recorded for sapling.

‘Sal’ tree flourishes under wide range of soil types, but not on very sandy, gravely soils adjacent to a river which gets waterlogged. It can grow on alluvial to lateritic soils. ‘Sal’ tree can grow in slightly acidic to neutral sandy loam ($\text{pH} = 5.1\text{--}6.8$) [21–23]. The soil pH and texture (sandy loam and loamy sand) of the study site were consistent with the characteristic of ‘Sal’ forest reported by above mentioned authors.

65.4 CONCLUSION

The present study site is a *Shorearobusta* dominated forest. Shanon Diversity index indicated good species diversity in the study site. Species richness of herbs was very low which may be due the sampling in winter season. Though the regeneration of ‘Sal’ is satisfactory at seedling stage, their development into sapling is very poor. Though the soil in the study site is appropriate for the growth and development of ‘Sal’ forest, growth of sapling was not supported. Past disturbances, fire, flood, changing environment etc. seems to have affected the regeneration.

REFERENCES

1. Joshi, A.R.: Establishing biological monitoring system for Terai Arc Landscape. A report submitted to WWF Nepal programme, Kathmandu, Nepal (2002)
2. Webb, E.L. and Sah, R.N.: Structure and diversity of natural and managed sal forest in the Terai of Nepal. *Forest Ecology and Management*, 176, 337–353 (2003)
3. Timilsina, N., Ross, S.M. and Heinen, J.T.: A community analysis of sal (*Shorearobusta*) forests in the western terai of Nepal. *Forest Ecology and Management*, 241, 223–234 (2007)

4. Rautiainen, O.: Spatial yield model for *Shorear obusta* in Nepal. *Forest Ecology and Management*, 119, 151–162 (1999)
5. Shrestha, R., Karmacharya, S.B. and Jha, P.K.: Vegetation analysis of natural and degraded forests in Chitrepani in Siwalik region of central Nepal. *Tropical Ecology*, 41(1), 111–114 (2000)
6. Joshi, S.P., Rautiainen, O. and Suoheimo, J.: Silvicultural guidelines for the implementation of operational forest management plans in the Terai, Nepal. FMUDP Technical Report No. 15. HMGN/FINNIDA, Kathmandu (1995)
7. Acharya, K.P., Tamrakar, P.R., Gautam, G., Regmi, R., Adhikari, A. and Acharya, B.: Managing tropical sal forests (*Shorear obusta*) of Nepal in short rotations: findings of a 12-year long research. *Banko Janakari*, 12(1), 71–75 (2002)
8. MFSC: Revised forestry Sector policy. Kathmandu. Ministry of Forest and Soil Conservation, Nepal (2000)
9. Bampton, J.F.R., Ebregt, A. and Banjade, M.R.: Collaborative Forest Management in Nepal's Terai: Policy, Practice and Contestation. *Journal of Forest and Livelihoods*, 6(2) (2007)
10. Carter, J. and Gronow, J.: Recent Experience in Collaborative forest management. Review paper. CIFOR Occasional Paper no. 43 (2005)
11. Paudyal, D.: Collaborative forest management in Nepal: Stepping towards managing productive forests of terai with social inclusion. The Initiation Ministry of Forest and Soil Conservation (2007)
12. Curtis, J.T.: The vegetation of wisconsin: an ordination of plant communities. University of Wisconsin Press, Madison, pp 657(1959)
13. Curtis, J.T. and McIntosh, R.P.: The interrelations of certain analytic and synthetic phytosociological characters. *Ecology*, 31, 434–455 (1950)
14. Okalebo, J.R., Gathua, K.W. and Woome, P.L.: Laboratory methods of soil and plant analysis: A working manual – KARI – UNESCO – ROSTA (1993)
15. Zobel, D.B., Jha, P.K., Behan, M.J. and Yadav, U.K.R.: A practical manual for ecology. Ratna Book Distributors, Kathmandu, Nepal (1987)
16. Stainton, J.D.A.: Forests of Nepal. Hafner Publishing Company, New York, 181 p. (1972)
17. Karkee, K.: Effects of Deforestation on Tree Diversity and Livelihoods of Local Community: A Case Study from Nepal. A thesis submitted to the Lund University (2004)
18. Pandey, S.K. and Shukla, R.P.: Plant diversity in managed Sal (*Shorear obusta* Gaertn.) forests of Gorakhpur, India: species composition, regeneration and conservation. *Biodiversity and Conservation*, 12, 2295–2319 (2003)
19. Sapkota, I.P.: Species diversity, regeneration and early growth of sal forest in Nepal: Responses to inherent disturbances regime; doctoral thesis. Swedish University of Agricultural Sciences (2009)
20. Singh, A., Reddy, V.S. and Singh, J.S.: Analysis of woody vegetation of Corbett National Park, India. *Vegetatio*, 120, 69–79 (1995)
21. Gangopadhyay, S.K. and Banerjee, S.K.: The influence of vegetation on the properties of the soils of Sikkim. *Biological Sciences*, 53, 283–288 (1987)
22. Gangopadhyay, S.K., Nath, S., Das, P.K. and Banerjee, S.K.: Distribution of organic matter in coppice Sal (*Shorear obusta*) in relation to soil chemical attributes. *Indian Forester*, 116, 407–417 (1990)
23. Rana, B.S., Singh, S.P. and Singh, R.P.: Biomass and productivity of central Himalayan Sal (*Shorear obusta*) forest. *Tropical Ecology*, 29, 1–7 (1988)

Chapter 66

Treatment of Coke Oven Effluents by Duckweeds Ponds – A Laboratory Scale Study

Subodh Kumar Maiti and Arindam Halder

Abstract Duckweeds are small; floating aquatic plants belongs to Lemnaceae, capable to degrade phenol in wastewater. Synthetic wastewater, similar to the characteristics of coke-plant effluents, was prepared in the laboratory, and tested the degradation efficiency in terms of reduction of COD and phenol under different organic loading rate (OLR) at 4 d and 8 d of hydraulic detention time (HRT). Artificial duckweeds ponds were kept in outdoor conditions and meteorological parameters were monitored and used for the estimation of evapo-transpiration rate and degradation of phenol. From the present experiment, it can be concluded that, for phenol concentration of 250 mg/L, 4 d detention is sufficient for the removal of 91% phenol. At higher phenol concentration of 600 mg/L, a detention time of 8 d is essential. If phenol concentration in the effluent exceeds greater than 800 mg/L pre-treatments wastewater is required. A design example for the treatment of low temperature coal carbonization wastewater by duckweeds pond system also given.

Keywords Synthetic coke-plant effluent • Duckweeds • Organic loading rate • Phenol • COD

66.1 INTRODUCTION

Duckweeds are small, floating aquatic plants belongs to the family of Lemnaceae, has no leaf, stem or specialized structure, it has only “frond” suited for floating. Four general *Spirodela*, *Lemna*, *Wolffia* and *Wolffiella* are the typical genera of Duckweeds. *Lemna* and *Wolffia* have frond measurement of 6-8 mm and 2 mm respectively. Duckweeds have one of the fastest reproduction rates and their dry weight is 252 kg/ha. A small cell in the frond divides and produces a new frond; each frond is capable of producing at least 10 to 20 times during its life cycle [1–7]. Duckweeds pond has been used for recycling of wastewater, removal of nitrogen and phosphorus

S.K. Maiti (✉) • A. Halder

Department of Environmental Sc & Engg, Indian School of Mines, Dhanbad, India

e-mail: subodh_maiti@yahoo.com

and harvested duckweed could use as livestock feed [10, 11], textile wastewater treatment and removal of heavy metals [5], swine wastewater treatment, nutrient recovery and biomass production [6] and bio-oil production [7]. Maximum specific growth rate of 0.24 g/g/d was reported for COD and ammonia concentration of 600 mg/L and 50 mg/L under a HRT of 20 d [3]. Duckweeds could be used for the removal of various pollutants such as ammonia and phosphate. An integrated duckweeds and algal pond study reported that ammonia removal was due to uptake of duckweeds (18%), nitrification (3%), sedimentation (8%) and combined volatilization of NH_3 and denitrification (73%). Outdoor experiments were conducted by Oron [3] in a shallow mini-ponds (20-30cm deep) for evaluation of performance of duckweed species *Lemna gibba* as a purifier of domestic wastewater and reported that under adequate operational conditions, the quality of secondary effluents meets irrigation reuse standards. There has been reports from Bangladesh on a 500 m³/d duckweed based sewage treatment plant in which raw sewage (BOD = 360 mg/L) comes to a settling pond of 3 d detention time followed by duckweed ponds of 26 d detention time, gives overall BOD removal of 97.5% with an effluent BOD of 8.9 mg/L [4].

66.2 MATERIAL AND METHODS

66.2.1 *Preparation of Synthetic Wastewater, Experimental Set-up, Collection of Duckweeds*

The synthetic wastewater was prepared using phenol, ammonium sulphate, phosphate buffers and nutrient solution according to the composition given by [11]. The physico-chemical characteristics of synthetic wastewater were analysed as per Standard Methods [12]. Four tubs of cylindrical shape, made of PVC were used for the lab scale study. The total volume of each pond was around 20 L but the experiments were performed on a working volume of 10. Duckweed was collected at regular intervals in buckets by sieving with a sieve from a coke plant situated about 15 km from Indian School of Mines, Dhanbad. As the duckweed was collected from the quenching water pond of the coke plant, no acclimatization was required before the experiments were started. The moisture content of Duckweed was found to be 91.33% and volatile matter content was found to be 78.61 % [13].

66.3 RESULTS AND DISCUSSION

66.3.1 Efficiency of Duckweeds at HRT of 4 Days

The average HRT for duckweeds ponds is reported as 4 to 6 days [13], though other workers have worked at HRT of 3 to 10 days [3] and 10-20 days [9]. Initially, phenol removal efficiency of duckweed ponds was studied at 4 d HRT and phenol concentration of 250 mg/L and corresponding COD of 740 mg/L. The average OLR during the experiment was 18.54 kg BOD/ha-day or 35.71 kg Phenol/ha-day which is lower than the design OLR of 22.4 to 33.6 kg BOD/ha-day [13] (Fig 66.1). It has been noticed that the COD reduction efficiency increased with a reduction in the load and at a load of 86 kg COD/ha-day the reduction in COD was found to be a maximum of 53.33%.

The average OLR during the experiment was 21.0 kg BOD/ha-day or 42.85 kg Phenol/ha-day, which is lower than the design OLR of 22.4 to 33.6 kg BOD/ha-day [13]. Initially the density of Duckweed was maintained 480 g/m² or 4.8 tons/ha. The yield of Duckweed was observed differently at different phenol concentrations (Table 66.1). The average yield between 250 to 600 mg/L phenol concentrations

Fig. 66.1 COD reduction in different influent phenol concentration

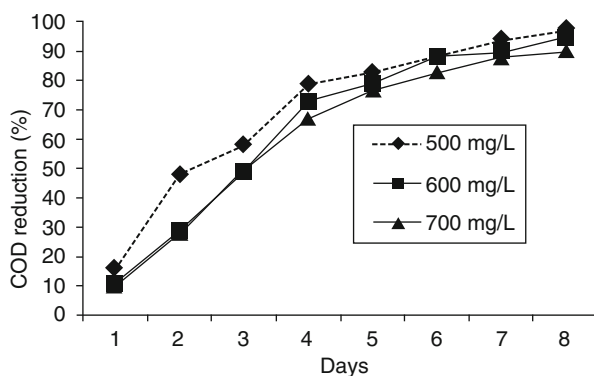


Table 66.1 Specific growth rate of duckweeds under different organic loads

Feed phenol (mg/L)	Initial COD (mg/L)	Organic loading rate (OLR)		Increase in the weight of duckweeds (g)	Increase in density (%)	Yield (g/g/day)
		kg phenol/ha-day	kg BOD ₅ /ha-day			
HRT (days)	(% reduction)					
250 (4)	740 (91)	35.7	18.54	13.4	16.0	0.50
500 (4)	1440 (74)	71.53	36.0	25.6	30.4	0.60
500 (8)	1380 (97)	35.7	17.3	60.3	72.0	0.57
600 (8)	1680 (91)	42.85	21.0	67.2	80.0	0.55
700 (8)	1960 (90)	50.0	24.60	35.6	43.0	0.26
800 (*)	2280 (*)	57.2	28.61	*No growth, all died		

was observed in the range of 0.55-0.60 /day. Maximum duckweed growth of 72-80 % was observed at a detention period of 8 days. At influent phenol concentration of 500-mg/L maximum removal efficiency of 94.2 % was observed. At maximum phenol removal efficiency, the duckweed growth was 72 % and corresponding yield was 0.57 g/g/day.

66.4 CONCLUSIONS

Based on the present laboratory investigation on duckweed pond treatment system following conclusion could be drawn:

- Duckweed ponds have the necessary potentiality to treat coke oven effluents especially with high phenol concentrations.
- A detention period of 4 days is required to treat coke plant effluents with phenol concentration of 250 mg/L.
- A detention period of 4 days is not enough to treat coke plant effluents containing 500 mg/L of phenol. It requires a higher detention period of 8 days.
- Duckweeds are not able to survive at phenol concentrations of 800 mg/L.
- Duckweed ponds do not affect substantial removal of other pollutants than COD, such as chloride, sulphate etc.
- The phenol removal efficiency of Duckweeds increases with decreasing OLR.

REFERENCES

1. Arceivala, S.J.: Wastewater Treatment for Pollution Control (2nd ed). TMGH, New Delhi, 239–253 (1998)
2. Fritz, J.J., Middleton, A.C. and Meredith, D.D.: Dynamic process modeling of wastewater stabilization ponds. *J WPCF*, 51(11), 2725–2743 (1979)
3. Oron, G., Porath, D. and Wildschut, R.: Wastewater treatment and renovation by different duckweeds species. *J Enot. Engg*, 112(2), 247–263 (1986)
4. Alaerts, G., Mahbubar, R. and Kelderman, P.: Performance analysis of a full-scale duckweed-covered sewage lagoon. *Water Res.*, 30(4), 843–852 (1996)
5. Sekomo, B.C., Diederik, P.L.R., Saleh, S.A. and Lens, P.N.L.: Heavy metal removal in duckweed and algae ponds as a polishing step for textile wastewater treatment. *Ecol Engg.*, 44, 102–110 (2012)
6. Xu, J. and Shen, G.: Growing duckweed in swine wastewater for nutrient recovery and biomass production. *Bioresource Tech*, 102, 848–853 (2011)
7. Muradov, N., Fidalgo, B., Gujar, A.C. and T-Raissi, A.: Pyrolysis of fast-growing aquatic biomass – *Lemna minor* (duckweed): Characterization of pyrolysis products. *Bioresource Tech*, 101, 8424–8428 (2010)
8. Reed, S.C., Middlebrooks, R. and Crites, R.W.: Natural systems for Waste Management and Treatment. McGraw Hill, New York (1988)
9. US Environmental Protection Agency: Design manual for constructed wetlands and floating aquatic plant system for municipal wastewater treatment. EPA 625/1-88-022, Cincinnati, OH (1988)

10. Hillman, W.S. and Culley, D.D.: The uses of Duckweeds. *American Scientist*, 66, 453–458 (1978)
11. Vermaat, Jan E. and Hanif, K.H.: Performance of common duckweed species (Lemnaceae) and waterfern *Azolla filiculoides* on different types of wastewater. *Water Res.*, 32(9), 2569–2576 (1998)
12. APHA: Standard Methods for the examination of water and wastewater. APHA, AWWA and WPCF (21th ed) (2005)
13. Metcalf and Eddy Inc.: Wastewater Engineering – Treatment, Disposal and Reuse, 3rd Ed. Tata McGraw-Hill, New Delhi (1995)

Part III
Tectonic Activity and Natural Disasters

Chapter 67

Zonal Crustal Movement

Xin Xian-wu

Abstract This paper describes the harmonic motion of the Earth and its calculation method. It based stress analysis of motion of Earth and generalized Hooke 's law, derived equations of motion of the crust, calculate the crustal movement of the major weft, and use the results to reproduce the original ancient land of before 250 Ma. By comparing the calculated results with measured values of the ITRF 2000, it proof: 1. Due to the mechanical properties of Earth's interior rock, tidal forces suffered there are differences, with the solid tidal advance from east to west, arise relative movement between the circle layer. This is the harmonic motion of the Earth. 2. Harmonic movement of the earth is the basic driving force to promote the evolution of the Earth. Its energy from the Earth's rotation. 3. Before 250 Ma, the Earth is only a piece of the original ancient land, it radius 7550 km, the north is slightly missing. 4. Earlier 250 Ma, continent began to split.

Keywords Earth • Evolution • Speed • Calculation

67.1 INTRODUCTION

Harmonic motion of the Earth is an energy of the Earth's rotation through tidal turned into a dynamic process of crustal movement. Use derived equations can be calculated crustal movement in drift distribution, power field and energy consumption, you can also calculate the position of each point of the mainland in different geological periods. Harmonic motion equations of the earth revealed the inner link of the crust movement phenomenon. For the systematic study that volcanoes, geothermal, earthquakes, continental drift, the Earth's rotation slows down and the moon regression and other natural phenomena, For the development of satellite positioning technology, earthquake prediction technology, and geology, astrophysics, and other areas of ancient geography provides a new way of thinking.

X. Xian-wu (✉)

Qianshan Science and Technology Office, Anshan, Liaoning, China

e-mail: xinxianwu@126.com

67.2 THE HARMONIC MOTION

Harmonic motion refers to when the wave advance, Relative movement between different media along forward direction. For example: Let go of the gas, when the bicycle wheel rolling, produce relative moving rim respect to the tire. When shaking body, hula hoop moving around the waist. When harmonic reducer work process [1], the rigidity wheel for the flexible wheel produce movement, etc.

We take a soft rubber tube set in a hard plastic rod outside, draw a straight line on the end face. Then, with two parallel boards, rubbing them in one direction (Fig. 67.1A). Turning several laps later, deviated from a straight line can be seen, with respect to the rigid plastic rods, soft rubber tube has moved opposite to the direction of rotation. Fig. 67.1B. That is: harmonic motion process, Softer circle is always relative to a hard circle, along the forward direction of the waves generated faster movement. Cut along the equator of the earth, see Fig. 67.1C. In the crust as an example: In the tidal force, Earth will be stretched along the opposite direction of the moon. With g, e, f three line, divided the crust in two layers. During the rotation of the earth, When the material passes through the point g, f between, must be compressed to a radial height equal to e, f the height. Therefore, g is actually advancing along e . This is similar to the movement shown in Fig. 67.1A, will cause the crust relative to the mantle do the reverse movement. The calculated results indicate that, In pull of the Earth's rotation resistance, the tidal at 1610 km per hour, advancing along the equator. This process, 0.000004 m/h is continent largest mobile average speed. This deceleration has gear ratio of 4×10^{11} , In other words, the continent moving force, not tidal force direct role, but is magnified 4×10^{11} times the Earth's rotation resistance moment.

67.3 EQUATIONS OF HARMONIC MOTION OF THE EARTH

In the space of the Cartesian coordinate system: Y axis pointing sun. Placed the center of the Earth coincides with the origin, and the North Pole is located in the positive Z axis position. All unit body of the same depth, constituting thickness is

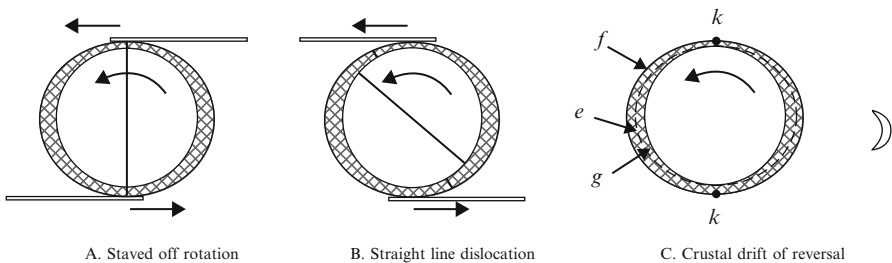


Fig. 67.1 Harmonic motion experiment and crustal harmonic movement

1 of hollow ball. When study the role of tidal force only, the ball in the tidal force role, in the force equilibrium state. Use plane of parallel XOZ to cut the ball, Calculate the tidal forces of suffered spherical shell, ΣF_1 . And caused by it, on the other side of the Spherical shell, per unit body tension. f_1 . f_1 decomposed into force f_a along tangential direction of the circle, and force f_b along a radial direction. And respectively produce stress σ_e and σ_r . According to the generalized Hooke's law [1], calculate the linear strain of unit body. Then export, in the tiny resistance force state, When $\zeta = 0$, Equations of Harmonic motion of the Earth. When $\beta \rightarrow 0$, $\omega t = 2\pi$. This equation can be expressed as

$$\begin{aligned}
 S_0 &= S_{10} + S_{20} \dots \\
 S_{10} &= \sum_{i=1}^n S_{1i} \quad (i = 1, 2, 3, \dots, n) \\
 S_1 &= 2.718624 (\nu + 2 \cdot \pi^{-1}) H^2 \rho E^{-1} \times 10^{-13} (m/m) \\
 S_{20} &= 2.718624 (1 + 2\nu \cdot \pi^{-1}) H^3 \rho E^{-1} \times 10^{-13} (m/r)
 \end{aligned} \tag{67.1}$$

where ρ is unit body density, $\text{kg} \cdot \text{m}^{-3}$, H is unit body to the geocentric distance, unit is m, E elastic modulus of unit body, P_a , ν Poisson's ratio. S_{1i} geometry movement amount, S_1 of i -layer the unit body; S_{10} geometry movement amount of unit body relative to reference axis. S_{20} compression movement amount of unit body relative to reference axis. S_0 zonal movement amount of unit body relative to reference axis.

Unit body circle of crustal, most of is the oceanic crust and continental crust Interphase composed. From (67.1) it can be seen, when ωt is an integer multiple of 2π , compression movement amount and geometry movement amount is proportional to the angle of rotation. Furthermore, each unit body motion segments of the same circle are mutually promote, pursuant to which, the above equation can be converted to crustal movement equation.

67.4 BASED ON THE PRINCIPLE OF HARMONIC MOVEMENT TO REPRODUCE THE EVOLUTION OF THE EARTH

The westward drift amount of the crust, is calculated using the equations motion of the crust. The circle calculation is the continent below 5 km. That is, on the ocean floor surface taken unit body. Oceanic crust and continental connection point: under the continental coastline. Different locations on each continent, relative to the reference axis drift amount S_{ZB} , can be respectively converted into New Zealand, America or London as the base year drift amount U_N , U_A , U_L .

After continent recovery, forming a complete ancient land. The shape of the ancient land, like a piece of moon cake is bitten off bite; see Fig. 67.2A. Using the current latitude and longitude to description, its location is: West from 63° E, east to 157° W; North from 59° N, south to 70° S, Center is 0° N, 133° E; Radius 7550 km. Center of missing part is 53° N, 133° E; Radius 3500 km.

relative to the benchmark. Weft italics below, it Is here relative to New Zealand datum, calculated amount of westward drift. ITRF 2000 stations measured values, write at the top of semicolon, the bottom is Monitoring Station code. From all continents drift of relative to New Zealand Benchmarks, are positive value can be seen, Continental is not Unordered Drift, But in New Zealand as a benchmark, westward drift. Furthermore, comparison that the vicinity of each of the weft, measured values of ITRF 2000 stations, with this weft, the calculating values of drift of continent with respect to South American Datum, Shows that, Both have good consistency in the mainland, On weft of more islands, deviation is larger; the velocity direction, The Americas west coast of the at compression process except, Entirely consistent two.

67.5 CONCLUSIONS

Motion analysis results, as well as its comparison with the measured values of ITRF 2000 part stations, showed:

1. Since simultaneous act by the tidal force with the rotation of the earth, various circle of the Earth would, along with tidal advance, relative to the center of the Earth, occur westward horizontal movement, i.e. the Earth's harmonic movement.
2. Harmonic motion of the Earth is a fundamental driving force in the evolution of the Earth, its energy from the Earth's rotation.
3. Harmonic movement is the universal law of evolution of celestial bodies.

ACKNOWLEDGEMENT Beginning from the first draft of 1994, many experts have put forward valuable suggestions. Thanks!

REFERENCES

1. Xu Hao (Editor): Mechanical Design Manual. Beijing: Mechanical Industry Press (1992)
2. Ma Zong Jin and Du Pin Ren: Symmetry and asymmetry of the Earth. Anhui: Anhui Education Press (2007)

Chapter 68

Tectonic Setting of Basic Rocks of Borborema Province, Brazil, Inferred from Multi-Dimensional Discrimination Diagrams

Sanjeet K. Verma and Elson P. Oliveira

Abstract Fifteen multi-dimensional diagrams [1–3] for basic and ultrabasic rocks, based on log-ratio transformations, were used to decipher tectonic setting for two case studies of Borborema province, NE Brazil. The applications of these diagrams indicated the following results: (1) a mid-ocean ridge setting for Forquilha Eclogite Zone during the Mesoproterozoic; (2) a transitional island arc to mid-ocean ridge setting for Algodões during the Paleoproterozoic. Our interpretations of main result for basic-ultrabasic magmas, along with the original authors' findings, were generally consistent.

Keywords Geochemistry • Tectonic setting • Borborema province • Log-Ratio transformation • Discrimination diagrams

68.1 INTRODUCTION

The Borborema Province of NE Brazil is made of several Precambrian geotectonic fold belts, domains, massifs, or terranes, and Phanerozoic sedimentary covers. The province contains units with ages protruding from the Archean to the Neogene time [4, 5]. To the understanding of the geotectonic domains and their tectonic setting, researchers have used several geological constraints. The most used ones were field relationship, high-resolution geochronology, isotope geology, thermobarometry, and geochemical modeling [6–11]. However, in several cases the proposed tectonic settings were not unambiguous, demanding new data or new approaches. For instance, on the basis of field relationship and structural geology D'el-Rey Silva [12] suggested an extension-related origin for the Sergipano belt in the southernmost part of Borborema Province, whereas Oliveira et al. [7] using field relationship combined with geochronology, isotope geochemistry and whole rock geochemistry, demonstrated that the region had a complex evolution with ocean basin

S.K. Verma (✉) • E.P. Oliveira

Department of Geology and Natural Resources, Institute of Geosciences, University of Campinas—UNICAMP, Campinas, São Paulo, Brazil

e-mail: sanjeetverma@ige.unicamp.br

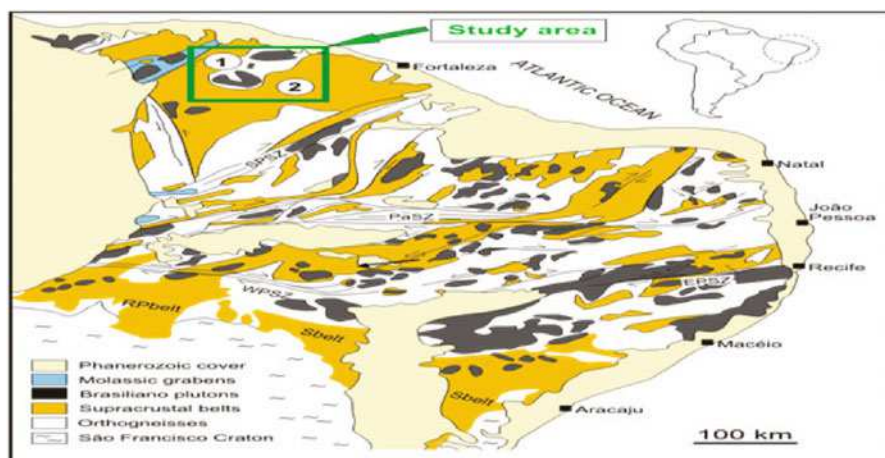


Fig. 68.1 Location map of investigated basic rocks in the Borborema Province. 1 - Forquilhaeclogite zone; 2 - Algodõesamphibolites. Sbelt - Sergipano Belt; RPbelt- Riacho do Pontal belt; WPSZ and EPSZ, stand respectively for west and east Pernambuco shear zone; PaSZ - Patos shear zone; SPSZ – Senador Pompeu shear zone.

opening, collision, post-collision indentation and foreland basin formation. Thus, controversies exist about the origin of the Sergipano belt as well as about other areas in the Borborema Province, and very often to resolve contentions new approaches are required. Therefore, the novelty of our approach lies in the multi-dimensional solution as a complement to try to decipher tectonic settings. Fifteen new multi-dimensional discrimination diagrams for a wide range of ultrabasic to basic magmas to infer their tectonic settings have recently been proposed from linear discriminant analysis of natural logarithm transformed ratios of chemical data [1–3], and were used in this work. A compilation of geochemical data for Forquilha Eclogite Zone and Algodões basic metavolcanic rock samples from the Borborema Province during Proterozoic (Fig. 68.1) is used to illustrate an application of these statistically coherent tectonomagmatic discrimination diagrams.

68.2 CALCULATION OF THE DISCRIMINANT FUNCTIONS DF1 AND DF2

To use fifteen multi-dimensional diagrams [1–3], we must calculate the DF1 and DF2 discriminant functions for each of them. These equations were already mentioned in the respective papers [1–3].

68.3 RESULTS AND DISCUSSION

The data from the above localities were plotted in the corresponding multidimensional diagram [1–3]. The results are summarized in Tables 68.1–68.2, with success percentage. Each tectonic setting (IA=Island Arc; CR=Continental Rift; OI=Ocean Island; and MOR=Mid–Ocean Ridge) were identified based on total success percentages (Tables 68.1–68.2).

68.3.1 Forquilha Eclogite Zone, Central Ceara Domain

Forquilha Eclogite Zone has been recently discovered in the Central Ceará Domain of the Borborema Province (Fig. 68.1), which is located in the northern region [13]. The zone has several boudin-like, or narrow layers of high-pressure mafic rocks within host paragneisses. The belt comprises three groups of rocks: (1) garnet amphibolites, (2) retrograded eclogites and (3) clinopyroxene–garnet amphibolites. According to original authors [13], the eclogites display flat REE patterns, and low Nb/La ratios suggesting MORB signature from ocean floor or intra-oceanic back-arc tectonic setting for the ForquilhaEclogite Zone, Central Ceará. For this area of ForquilhaEclogite Zone, 28 samples of Mesoproterozoic basic rocks (protolith age of 1570 Ma) were available, all of which had complete data sets for the all diagrams based on log-ratios [1–3]. The diagrams (Table 68.1) based on log-ratios of major elements and trace elements [1–3] showed mid–ocean ridge (MORB; Table 68.1). Thus, the expected mid–ocean ridge setting was clearly indicated for the ForquilhaEclogite Zone basic rocks. Our finding is also consistent with original authors [13].

Table 68.1 Results for basic magmas from the Forquilha Eclogite Zone, Central Ceará Domain [1–3]

Fig. [Ref.]	Total no. of samples (%)	Predicted tectonic affinity and no. of discriminated samples (%)				
		IAB	CRB+OIB	CRB	OIB	MORB
[1]	140 (100)	39 (28)	--	11 (8)	37 (26)	53 (38)
[2]	140 (100)	11 (8)	4 (3)	16 (11)	22 (16)	87 (62)
[3]	140 (100)	47 (33)	8 (6)	15 (11)	21 (15)	49 (35)

Table 68.2 Results of Algodões Amphibolites, Central Ceará Domain [1–3]

Fig. [Ref.]	Total no. of samples (%)	Predicted tectonic affinity and number of discriminated samples (%)				
		IAB	CRB+OIB	CRB	OIB	MORB
[1]	75 (100)	53 (71)		5 (6)	2 (3)	15 (20)
[2]	25 (100)	0 (0)	1 (4)	3 (12)	6 (24)	15 (60)
[3]	75 (100)	38 (51)	0 (0)	0 (0)	0 (0)	37 (49)

68.3.2 *Algodões Amphibolites, Central Cear  Domain*

The Algod es Sequence occurs in the eastern portion of the Central Cear  Domain (CCD), a typical sector of the Borborema Province situated between the Trans-Brasiliano Lineament and the SenadorPompeu shear zone [14]. The Algod es Sequence comprises the Algod esamphibolites, Chor paragneisses, and the Cip orthogneisses. Martins et al. [6] interpreted the Algod esamphibolites as a thick pile of basaltic lava, tuff and sill. They also indicate that no pillow structure has been recognized so far in this unit. On the basis of trace element geochemistry and positive $\epsilon\text{Nd}(t)$ values, authors [6] suggested that 2236 ± 55 Ma-old Algod esamphibolites are similar to oceanic plateau basalts and less often to back-arc basalts. For these Paleoproterozoic Algod esamphibolites, the first and third set of major element and trace element based diagrams [1, 3] showed an island arc setting (IAB; Table 68.2) whereas the second set of diagram [2] indicated a mid-ocean ridge (MORB; Table 68.2). In summary, two sets of diagrams [1, 3] showed an island arc setting whereas other diagrams [2] indicated a MORB setting. Thus, the expected back-arc setting is plausible for the Algod es basic rocks, in agreement with the original interpretation [6].

ACKNOWLEDGEMENT This work was supported by FAPESP grants [2012/07243–3 and 12/15824–6]. We are very grateful to an anonymous reviewer for constructive suggestions. Our sincere gratitude goes to Priyanka Patel for her prompt reply for any queries related with IAMG conference.

REFERENCES

1. Verma, S.P., Guevara, M. and Agrawal, S.: Discriminating four tectonic settings: five new geochemical diagrams for basic and ultrabasic volcanic rocks based on log-ratio transformation of major-element data. *J. Earth Sys. Sci.* 115, 485–528 (2006)
2. Agrawal, S., Guevara, M. and Verma, S.P.: Tectonic discrimination of basic and ultrabasic rocks through log-transformed ratios of immobile trace elements. *Int. Geol. Rev.* 50, 1057–1079 (2008)
3. Verma, S.P. and Agrawal, S.: New tectonic discrimination diagrams for basic and ultrabasic volcanic rocks through log-transformed ratios of high field strength elements and implications for petrogenetic processes. *Rev. Mex. Cienc. Geol.* 28, 24–44 (2011)
4. Almeida, F.F.M., Hasui, Y., BritoNeves, B.B. and Fuck, R.A.: Brazilian Structural Provinces: an introduction. *Earth-Sci. Rev.* 17, 1–29 (1981)
5. Van Schmus, W.R., Oliveira, E.P., Silva Filho, A.F., Toteu, S.F., Penaye, J. and Guimar es, I. P.: Proterozoic links between the Borborema Province, NE Brazil, and the Central African Fold Belt. *Geol. Soc. Lon Sp. Pub.* 294, 69–99 (2008)
6. Martins, G., Oliveira, E.P. and Lafon, J.-M.: The Algod es amphibolite-tonalite gneiss sequence, Borborema Province, NE Brazil: Geochemical and geochronological evidence for Palaeoproterozoic accretion of oceanic plateau/back-arc basalts and adakitic plutons. *Gondwana Res.* 15, 71–85 (2009)

7. Oliveira, E.P., Windley, B.F. and Araújo, M.N.C.: The Neoproterozoic Sergipano orogenic belt, NE Brazil: a complete plate tectonic cycle in western Gondwana. *Precambrian Res.* 181, 64–84 (2010)
8. Knesel, K.M., Souza, Z.S., Vasconcelos, P.M., Cohen, B.E. and Silveira, F.V.: Young volcanism in the Borborema Province, NE Brazil, shows no evidence for a trace of the Fernando de Noronha plume on the continent. *Earth Planet. Sc. Lett.* 302, 38–50 (2011)
9. Araújo, C.E.G., Cordani, U.G., Basei, M.A.S., Castro, N.A., Sato, K. and Sproesser, W.M.: U–Pb detrital zircon provenance of metasedimentary rocks from the Ceará Central and Médio Coreaú Domains, Borborema Province, NE-Brazil: Tectonic implications for a long-lived Neoproterozoic active continental margin. *Precambrian Res.* 206–207, 36–51 (2012)
10. Castro, N.A., Araújo, C.E.G., Basei, M.A.S., Osako, L.S., Nutman, A.A. and Liu, D.: Ordovician A-type granitoidmagmatism on the Ceará Central Domain, Borborema Province, NE-Brazil. *J S Am. Earth Sci.* 36, 18–31 (2012)
11. Neves, S.P., Monié, P., Bruguier, O. and Rangel da Silva, J.M.: Geochronological, thermochronological and thermobarometric constraints on deformation, magmatism and thermal regimes in eastern Borborema Province (NE Brazil). *J S Am. Earth Sci.* 38, 129–146 (2012)
12. D’el-Rey Silva, L.J.H.: Tectonic evolution of the Sergipano belt, NE Brazil. *Rev. Bras. Geo.* 25, 315–332 (1995)
13. Amaral, W.D.S., Santos, T.J.S. and Wernick, E.: Occurrence and geochemistry of metamafic rocks from the Forquilha Eclogite Zone, central Ceará (NE Brazil): geodynamic implications. *Geol. J.* 46, 137–155 (2011)
14. Trompette, R.: Geology of Western Gondwana, Pan-African/Brasiliano Aggregation of South America and Africa. A. A. Balkema, Rotterdam, Brookfield, 350 (1994)

Chapter 69

Tectonomagmatic Origin of Igneous Rocks from the Western Mexican Volcanic Belt

Surendra P. Verma and Kailasa Pandarinath

Abstract The origin of magmas in the western part of the Mexican Volcanic Belt (W-MVB) was constrained from tectonomagmatic discrimination diagrams under the assumption that the magmas originated from different tectonic settings are distinguishable from differences in their chemical compositions. For the W-MVB, the diagrams for basic rocks generally indicate a continental rift setting whereas those for intermediate and acid rocks show either an arc or a transitional arc to rift setting but with relatively low total percent probability values. Besides these diagrams, the conventional significance tests (Fisher F, Student t, and ANOVA) were also applied to understand the complex petrogenetic and tectonic processes in the W-MVB.

Keywords Tectonic setting • Geochemistry • Log-Ratio transformations

69.1 INTRODUCTION

The origin of the Mexican Volcanic Belt (MVB) is controversial and has been attributed to the conventional subduction and less conventional rifting or plume-related processes. In the western part of this belt (W-MVB), two major tectonic processes have been taking place simultaneously, which are the subduction of the small Rivera plate and a part of the Cocos plate and the operation of a well-developed triple rift system (Fig. 69.1). In this work, we have selected W-MVB to infer its tectonomagmatic origin by applying the recently (2006-2013) developed highly successful discrimination diagrams [1–6]. These diagram sets are capable of discriminating four tectonic settings at a time. We have compiled and created an integrated geochemical database of 1600 samples of igneous rocks from the W-MVB region, classified them into different rock types and applied the appropriate discrimination diagrams. The results related to the tectonomagmatic origin of the W-MVB are briefly discussed.

S.P. Verma (✉) • K. Pandarinath

Departamento de Sistemas Energéticos, Instituto de Energías Renovables, Universidad Nacional Autónoma de México, Priv. Xochicalco s/no., Col. Centro, Apartado Postal 34, Temixco, Mor., Mexico
e-mail: spv@ier.unam.mx

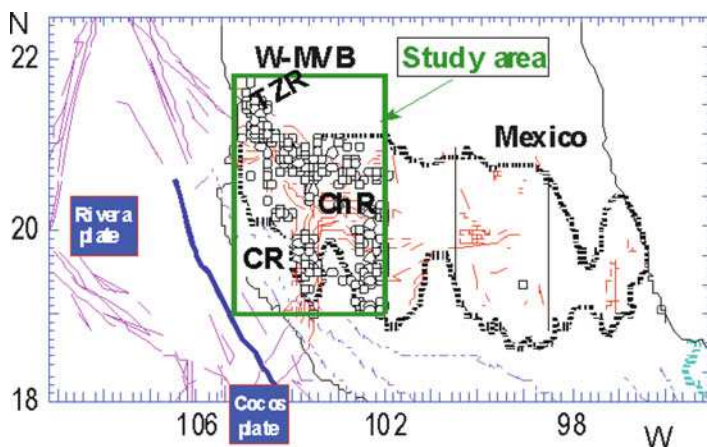


Fig. 69.1 Schematic regional tectonics and location of samples (open circles) in the western part of the Mexican Volcanic Belt (W-MVB); the three rift systems (CR – Colima Rift; ChR – Chapala Rift; TZR – Tepic Zacoalco Rift) shown are operating simultaneously to the subduction process of the Rivera and a part of the Cocos plate (south of the map area)

69.2 MULTI-DIMENSIONAL DIAGRAMS

For a total of 50 such diagrams for basic and ultrabasic (15 diagrams; [1–3]), intermediate (15 diagrams; [4]), and acid magmas (20 diagrams; [5, 6]) based on logratio transformation of major and selected trace elements and linear discriminant analysis, 100 complex equations are required, which are listed in the original sources [1–6].

69.3 RESULTS AND DISCUSSION

After deciding the magma types as basic, intermediate, and acid varieties [7], the appropriate tectonomagmatic discrimination diagrams were applied and respective probabilities were calculated. An example is provided of just one diagram for basic and ultrabasic rocks (Fig. 69.2) that discriminates four tectonic settings [1], in which about 76% (233 out of 305) samples plot in the CRB field. From all such diagrams [1, 2], the W-MVB basic rocks indicate a continental rift (CR) setting with percent values of about 67% [1] and 38% [2], respectively, or a continental arc (CA) setting with a low percent value of about 36% [3] (Table 69.1). The intermediate rocks indicate a continental arc to collision setting in two sets of diagrams and a continental arc setting in the third set ([4]; Table 69.2). Finally, the acid rocks from the W-MVB indicate a continental arc (CA) setting in major element based diagrams [5, 6] with relatively low percent probability values of about 39%-40% (Table 69.2). The two sets of diagrams based on relatively immobile major and

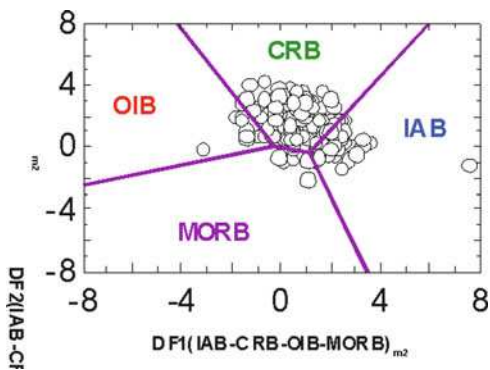


Fig. 69.2 An example of multi-dimensional diagram [1] applied to the basic rock (B) samples from the W-MVB; note that this diagram discriminates four tectonic settings of IA (island arc), CR (continental rift), OI (ocean island), and MOR (mid-ocean ridge), and that the subscript m2 stands for major elements; most of the samples plot in the CR setting

Table 69.1 Tectonic setting for basic and ultrabasic magmas from the W-MVB [1–3]

Fig. [ref.]	Samples (%)	Predicted tectonic affinity and number of discriminated samples (%)				
		IAB	CRB+OIB	CRB	OIB	MORB
[1]	1525(100)	247 (16.2)	---	1019 (66.8)	167 (11)	92 (6)
[2]	555(100)	159 (28.6)	57 (---)	208 (37.5)	125 (22.5)	63 (11.4)
[3]	870(100)	317 (36.4)	60 (---)	211 (24.3)	163 (18.7)	179(20.6)

Table 69.2 Tectonic setting for intermediate [4] and acid [5, 6] magmas from the W-MVB

(Type) Samples	Number of discriminated samples [total % probability for all five diagrams]				
	IA+CA	IA	CA	CR+OI	Col
[4] 5270	{530} [---]	{451} [9.2%]	{2032} [46.9%]	{626} [12.4%]	{1631} [31.5%]
[4] 2240	{170} [---]	{237} [11.3%]	{704} [36.1%]	{420} [20.6%]	{709} [32.0%]
[4] 930	{114} [---]	{107} [13.3%]	{409} [53.2%]	{153} [17.0%]	{147} [16.5%]
[5] 1310	{144} [---]	{201} [19.0%]	{424} [39.8%]	{265} [20.3%]	{276} [20.9%]
[6] 1310	{105} [---]	{115} [9.7%]	{408} [39.0%]	{476} [36.5%]	{206} [14.8%]
[6] 465	{37} [---]	{24} [6.5%]	{123} [30.4%]	{170} [41.7%]	{111} [21.4%]
[6] 325	{20} [---]	{23} [8.2%]	{84} [28.2%]	{160} [52.7%]	{38} [10.9%]

trace elements [6]showawithin-plate setting (CR+OI) with total percent probability values of about 42% and 53% (Table 69.2).

These differences reinforce our conclusion that the discrimination diagrams should be used in conjunction with the evaluation of petrogenetic processes. The origin of these different W-MVB rock varieties cannot be linked through simple magmatic processes such as fractional crystallization without assimilation of continental crust. To better constrain the origin of magmas in the W-MVB and explain their tectonomagmatic origin, we applied the significance tests of Fisher F, Student

Table 69.3 Confidence limits of the mean for Sr and Nd isotopes in basic to acid magmas from the W-MVB

(SiO ₂) _{adj}		⁸⁷ Sr/ ⁸⁶ Sr		¹⁴³ Nd/ ¹⁴⁴ Nd	
95%	99%	95%	99%	95%	99%
48.42- 49.62	48.21- 49.82	0.70349- 0.70371	0.70345- 0.70374	0.51289- 0.51292	0.51288- 0.51293
56.81- 58.21	56.58- 58.44	0.70372- 0.70383	0.70370- 0.70384	0.51286- 0.51289	0.51286- 0.51290
68.99- 72.98	68.48- 72.48	0.70402- 0.70424	0.70400- 0.70433	0.51281- 0.51285	0.51281- 0.51286

t, and ANOVA to the compiled data from the W-MVB, using the new precise and accurate critical values [8, 9]. Software UDASYs was efficiently used for this purpose [10]. The results for radiogenic Sr and Nd isotopes are summarized in Table 69.3 for the three major magma types. A visual examination of the confidence limits of the mean shows that there may be significant differences in both ⁸⁷Sr/⁸⁶Sr and ¹⁴³Nd/¹⁴⁴Nd for basic, intermediate, and acid magmas.

We confirmed that these isotope ratios significantly differ from each other at 95% confidence level and they do so also at 99% confidence level except for ¹⁴³Nd/¹⁴⁴Nd between basic and intermediate magmas. This implies that assimilation of the crust is certainly required as a major petrogenetic process in the W-MVB. In summary, the use of statistical tools such as multi-dimensional diagrams and discordancy and significance tests has been successfully demonstrated for the western part of the Mexican Volcanic Belt.

ACKNOWLEDGEMENT This work was supported by DGAPA-PAPIIT grant IN104813.

REFERENCES

1. Verma, S.P., Guevara, M. and Agrawal, S.: Discriminating four tectonic settings: five new geochemical diagrams for basic and ultrabasic volcanic rocks based on log-ratio transformation of major-element data. *J. Earth Sys. Sci.* 115, 485–528 (2006)
2. Agrawal, S., Guevara, M. and Verma, S.P.: Tectonic discrimination of basic and ultrabasic rocks through log-transformed ratios of immobile trace elements. *Int. Geol. Rev.* 50, 1057–1079 (2008)
3. Verma, S.P. and Agrawal, S.: New tectonic discrimination diagrams for basic and ultrabasic volcanic rocks through log-transformed ratios of high field strength elements and implications for petrogenetic processes. *Rev. Mex. Cienc. Geol.* 28, 24–44 (2011)
4. Verma, S.P. and Verma, S.K.: First 15 probability-based multi-dimensional discrimination diagrams for intermediate magmas and their robustness against post-emplacement compositional changes and petrogenetic processes. *Turk. J. Earth Sci.* 22, 931–995 (2013)
5. Verma, S.P., Pandarinath, K., Verma, S.K. and Agrawal, S.: Fifteen new discriminant-function-based multi-dimensional robust diagrams for acid rocks and their application to Precambrian rocks. *Lithos* 168–169, 113–123 (2013)

6. Verma, S.P. and Rivera-Gómez, M.A.: Computer programs for the classification and nomenclature of igneous rocks. *Episodes* 36, 115–124 (2013)
7. Cruz-Huicochea, R. and Verma, S.P.: New critical values for F and their use in the ANOVA and Fisher's F tests for evaluating geochemical reference material granite G-2 (U.S.A.) and igneous rocks from the Eastern Alkaline Province (Mexico). *J. Iber. Geol.* 39, 13–30 (2013)
8. Verma, S.P. and Cruz-Huicochea, R.: Alternative approach for precise and accurate Student's t critical values and application in geosciences. *J. Iber. Geol.* 39, 31–56 (2013)
9. Verma, S.P., Cruz-Huicochea, R. and Díaz-González, L.: Univariate data analysis system: deciphering mean compositions of island and continental arc magmas, and influence of underlying crust. *Int. Geol. Rev.* 55, 1922–1940 (2013)

Chapter 70

Global Sub-Crustal Stress Field

R. Tenzer and M. Eshagh

Abstract The sub-crustal stress has been traditionally computed using the Runcorn's formulae. This method allows computing the stress field only with a very limited spectral resolution. To overcome this problem, we apply a new method of computing the sub-crustal stress components based on utilizing the stress function with a subsequent numerical differentiation. This method increases the (degree-dependent) convergence domain of the asymptotically-convergent series and consequently allows evaluating the stress components to a higher spectral resolution compatible with currently available global crustal models. This method also facilitates the variable Moho geometry, instead of assuming only a constant Moho depth in the Runcorn's formulae. The crustal thickness and the sub-crustal stress are then determined directly from gravity and (seismic) crustal structure models. The numerical result reveals that the largest intensity of the sub-crustal stress occurs mainly along seismically active convergent tectonic plate boundaries, particularly along oceanic subduction zones and continent-to-continent collision zones.

Keywords Crust • Gravity • Stress • Moho

70.1 INTRODUCTION

The sub-crustal stress induced by mantle convection was investigated in the context of various geoscience studies. The examples can be given, but are not limited to the interpretation and better understanding of deep earthquake mechanisms, volcanism, subduction, mantle convection, heat flow, kimberlite magmatism, ore concentration and tectonic and magnetic features. Runcorn [1] found a direct relation between the sub-crustal stress and the gravity field. He simplified the Navier-Stokes' equations to derive the horizontal components of the sub-crustal stress field based on

R. Tenzer (✉)

Department of Engineering Science, University West, Trollhättan, Sweden

e-mail: rtenzenr@sgg.whu.edu.cn

M. Eshagh

School of Geodesy and Geomatics, Wuhan University, Wuhan, China

assuming a two-layered Earth's model. The principal disadvantage of this method is a divergence of the asymptotically-convergent series after a relatively low degree of spherical harmonics. To improve the convergence domain, Eshagh and Tenzer [2] modified the Runcorn's formulae by applying the stress function, which is defined by means of Laplace harmonics, instead of their partial derivatives. This modification allows computing the sub-crustal stress components with a spectral resolution compatible with the currently available global crustal models (up to degree 180 or more). This is significant improvement compared to the Runcorn's formulae, which has a limited spatial resolution up to a spherical harmonic degree of 25. Moreover, Eshagh and Tenzer [2] utilized the Vening Meinesz-Moritz (VMM) inverse problem of isostasy [3] in definition of the stress function. This definition thus takes into consideration the variable Moho geometry.

70.2 METHOD

Eshagh and Tenzer [2] presented the method of computing the horizontal components of the sub-crustal stress field in the following form

$$S_x \mathbf{e}_\theta + S_y \mathbf{e}_\lambda = S Y_{n,m}^{(2)}(\theta, \lambda) \quad (70.1)$$

where \mathbf{e}_θ and \mathbf{e}_λ are the meridional and prime-vertical components of the unit position vector \mathbf{e} respectively, S_x and S_y are the corresponding sub-crustal stress components. The tangential components of the spherical harmonic vector $Y_{n,m}^{(2)}$ of degree n and order m read

$$Y_{n,m}^{(2)}(\theta, \lambda) = Y_{n,m}^{(1)}(\theta, \lambda) \mathbf{e}_\theta + \frac{\partial Y_{n,m}^{(1)}(\theta, \lambda)}{\sin \theta \partial \lambda} \mathbf{e}_\lambda \quad (70.2)$$

where $Y_{n,m}^{(1)}$ are the surface spherical harmonic functions, and θ, λ are spherical coordinates (co-latitude and longitude). The stress function S is given by

$$S = \frac{g \Delta \rho^{c/m}}{S^2} \sum_{n=2}^N \frac{1}{(n-1)s^{n+1}} \left[\frac{2n+1}{n+1} \frac{(\bar{\rho}^c H)_n}{2 \Delta \rho^{c/m}} - (D_0)_n \right] \quad (70.3)$$

where g is the Earth's mean gravity, $\Delta \rho^{c/m}$ is the Moho density contrast, $s = 1 - D/R$, D is the Moho depth, and R is the Earth's mean radius. The (nominal) Moho-depths spherical functions $(D_0)_n$ are computed from

$$(D_0)_n = -\frac{g_0^i}{4\pi G \Delta \rho^{c/m}} \delta_{n,0} + \frac{1}{4\pi G \Delta \rho^{c/m}} \frac{2n+1}{n+1} [2\pi(\bar{\rho}^c H)_n - \Delta g_n] \quad (70.4)$$

where G is the Newton's gravitational constant, $\delta_{n,0}$ is the Kronecker's delta. The normal compensation attraction g_0 reads

$$g_0^i = \frac{4\pi}{3} G R \Delta \rho^{c/m} (s^3 - 1) \quad (70.5)$$

Laplace's harmonics of the solid topography are defined by

$$(\bar{\rho}^c H)_n = \frac{1}{4\pi} \sum_{m=-n}^n \iint \bar{\rho}^c H(\Omega') Y_{n,m}^{(1)}(\Omega') d\sigma' \bar{\rho}^c H = \begin{cases} \rho^c H & H \geq 0 \\ (\rho^w - \rho^c) H & H < 0 \end{cases}$$

where ρ^c is the topographic density, and ρ^w is the mean seawater density.

70.3 RESULTS

The crustal thickness and the sub-crustal stress were evaluated with a spectral resolution complete to degree 180 of spherical harmonics using the GOCO03S global gravity model Mayer-Guerr et al. (2012 [4]). The computation was realized globally on a 1×1 arc-deg grid. The Moho depths are shown in Fig. 70.1. The sub-crustal stress field is shown in Fig. 70.2.

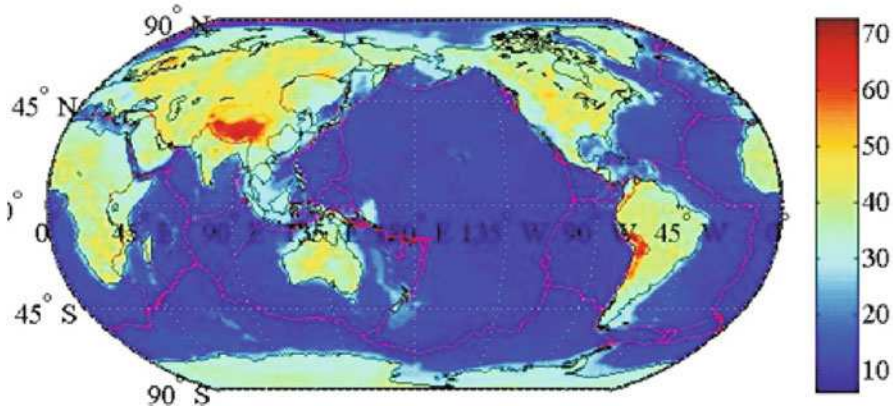


Fig. 70.1 The Moho depths (values are in km)

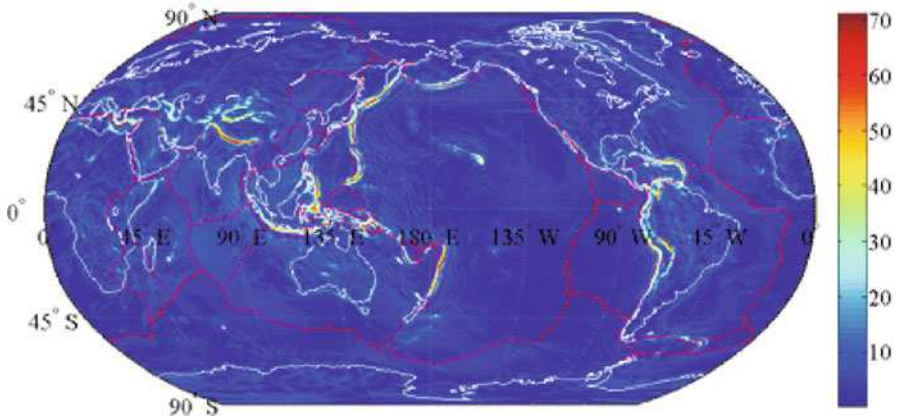


Fig. 70.2 The sub-crustal stress intensity (values are in MPa)

70.4 CONCLUSIONS

The sub-crustal stress field closely resembles the global tectonic configuration. Most of the stress is accumulated along tectonic plate boundaries. The intra-plate stress field is, on the other hand, much less pronounced or almost completely absent, except for some more localized features. Locations of these intra-plate stress anomalies over oceans typically coincide with hotspots (i.e., Island, Hawaii, Reunion, Mauritius). Additional intra-plate stress anomalies are detected along active strike-slip fault zones. Most of the sub-crustal stress field is concentrated along the convergent tectonic plate boundaries with the maximum intensity detected at oceanic subduction zones. Large shear stress intensity is also detected along the continent-to-continent collision zone between the Indian and Eurasian tectonic plates in Himalaya. The divergent tectonic plate boundaries along mid-oceanic ridges and continental rift zones (East-Africa, West-Antarctica and Baikal rift zones) are without the presence of a significant stress field. The stress field detected around hotspots is not directly related to volcanism, but is probably attributed to crustal flexure. This is justified by the fact that the maximum stress anomalies do not directly coincide with hotspot locations, but are distributed around them and further extend around seamounts (which were shifted from the original location by the ocean-floor spreading).

REFERENCES

1. Runcorn, S.K.: Flow in the mantle inferred from the low degree harmonics of the geopotential. *Geophys. J. R. astr. Soc.* 14, 375–384 (1967)

2. Eshagh, M. and Tenzer, R.: Sub-crustal stress determined using gravity and crust structure models. *Comput. Geosc.* (2014, submitted)
3. Sjöberg, L.E.: Solving Vening Meinesz-Moritz Inverse Problem in Isostasy. *Geophys. J. Int.* 179, 1527–1536 (2009)
4. Mayer-Guerr, T., Rieser, D., Höck, E., Brockmann, J.M., Schuh, W.-D., Krasbutter, I., Kusche, J., Maier, A., Krauss, S., Hausleitner, W., Baur, O., Jäggi, A., Meyer, U., Prange, L., Pail, R., Fecher, T. and Gruber, T.: The new combined satellite only model GOCO03s. Abstract, GGHS2012, Venice (2012)

Chapter 71

A Blind-wavelet Algorithm and Its Application to the Metal Mine Seismic Data Processing

Zhongli Zhou, Bin Liu, Feilong Qin, and Guangxin Huang

Abstract Inspired by the principle of wavelet analysis and blind signal separation in denoising, this paper presents a one-dimensional blind-wavelet algorithm. Some corresponding parameters of the blind-wavelet algorithm are discussed. In this paper, the blind-wavelet algorithm contains the following three main steps. Firstly, the multi-channel seismic signals are decomposed into multi-level wavelet, the scale coefficients and the multi-level wavelet coefficients can be obtained, then, the multi-level wavelet coefficients are processed by soft threshold method. Secondly, all the scale coefficients and the same depth wavelet coefficients of the signals are decomposed by the blind source separation, and the sequences of the decomposed signals can be correctly reflected through an appropriate method. Finally, the source signals are estimated via signal reconstruction. The results show that the organic combination of blind source separation and wavelet analysis (the blind-wavelet algorithm) can effectively eliminate the noise of the deep metal ores seismic data, it meets the requirements of the high resolution and fidelity after the denoising in the deep metal ores seismic exploration. The results of this research demonstrate that the blind-wavelet algorithm is quite fit for two adjacent channel signals processing of metal ore deposits seismic data denoising. It is shown that application of the blind-wavelet algorithm to seismic data processing is effective.

Keywords One-dimensional blind-wavelet algorithm • Wavelet analysis • Blind signal separation • Metal ore deposits seismic data denoising

71.1 INTRODUCTION

The geological environment of the metal mineralization region is complex. Because of the strong interference of the noise in metal deposits seismic data, low resolution and low signal to noise ratio (SNR), it is difficult to deal effectively with metal

Z. Zhou • B. Liu (✉) • F. Qin • G. Huang
Geomathematics Key Laboratory of Sichuan Province, Chengdu University of Technology,
Chengdu, China
e-mail: liubincim@163.com

deposits seismic data by the traditional denoising method. Wavelet threshold denoising [1] is an important method in seismic data processing. Wavelet analysis is a “signal microscope”, and the detailing of the signal in different frequency bands will be observed through the wavelet decomposition. The random noise is high frequency signal and it can be removed by the threshold method. But the coherent noise is too difficult to be removed, such as linear noise. The signal is more sophisticated and more conducive to process after the wavelet decomposition in different frequency bands [2]. Signal reconstruction can restore the source signal. Actually, wavelet decomposition is a deconvolution processing, the signal is decomposed into different frequency bands, and the reconstruction is a convolution processing. Currently, with the multi-channel blind source separation technique [3] in seismic data processing, the information of the useful signal and removed part irrelevant can be obtained. But in fact, because of the source signals in the linear mixture, the effect of blind source separation is not ideal. The observed seismic signal is the convolution of the source signal and noise, which does not meet the conditions of blind signal separation. Therefore, in order to overcome the limitation, it is necessary to further study blind signal separation and the wavelet analysis, considering their advantages and constructing a new denoising algorithm to denoise the interference signal. In this paper, inspired by the principle of wavelet analysis and blind signal separation in denoising, we introduce the one-dimensional blind-wavelet algorithm.

71.2 ONE-DIMENSIONAL BLIND-WAVELET ALGORITHM PRINCIPLE

71.2.1 The Design of the Blind-wavelet Algorithm

Through wavelet decomposition, the random noise is mainly in the high-frequency part of signal and the coherent noise appears in different frequency bands. In order to effectively eliminate the noise signal, the signal will be decomposed into different frequency bands. Then the corresponding wavelet coefficients of the scale space will be processed by the threshold method. Because the convolution processing is similar to the linear signal processing, wavelet decomposition satisfies the conditions of the signal separation. While the source signals are extracted by the blind signal separation, the signal of all the scale spaces can be reconstructed as the source signal by the wavelet inverse transformation. After the transformation of the blind-wavelet algorithm, the interference signal can be effectively eliminated. The design of the blind-wavelet algorithm is shown in Fig. 71.1.

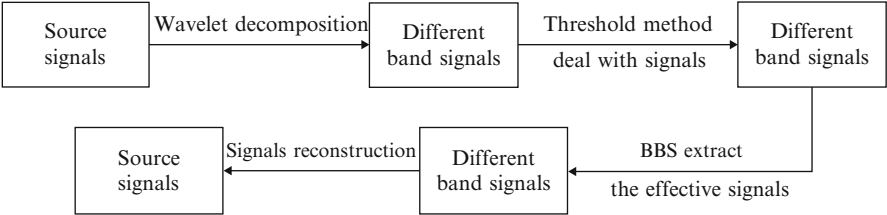


Fig. 71.1 The design of the blind-wavelet algorithm

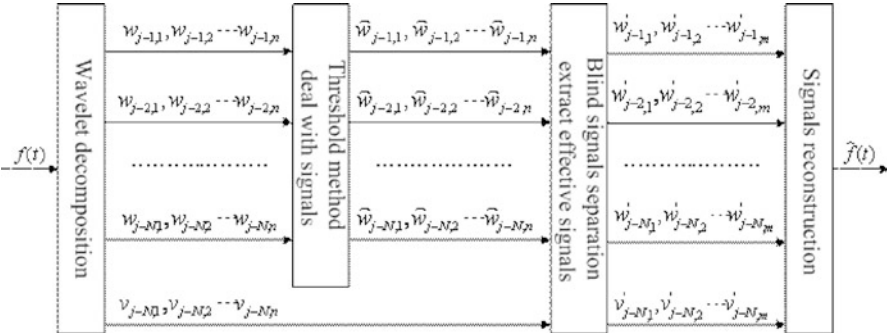


Fig. 71.2 The flow chart of the one-dimensional blind-wavelet algorithm

71.2.2 The Construction of the Blind-wavelet Algorithm

According to the design of the blind-wavelet algorithm. The flow chart of the one-dimensional blind-wavelet algorithm is shown in Fig. 71.2.

71.2.3 The Parameter Selection of Blind-wavelet Algorithm

In this part, the following parameters of the blind-wavelet algorithm will be discussed.

- (1) Proper wavelet basis. In the wavelet transformation, the common wavelet basis contains db wavelet series and sym wavelet series. The types of wavelet will be determined after decomposition and reconstruction of the signal wavelet. If the signal f_1 is a decomposition transform, the signal f_2 is a reconstruction transform. The minimum value can be obtained as follows:

$$\|f_1 - f_2\| = \sqrt{\sum_{i=1}^N (f_{1i} - f_{2i})^2} \quad (71.1)$$

- (2) Generally speaking, the number of the decomposition layers in the blind-wavelet algorithm is from 1 to 4.
- (3) Selection of the threshold [4]. Because the threshold coefficients depend on the number of decomposition layers, so it is different for the selection of wavelet coefficients threshold in different frequency bands. Consider

$$\lambda = \sigma \sqrt{2 \log N} / \log(j+1) \quad (71.2)$$

- (4) The selection of blind signal separation algorithm. The blind source separation algorithm used in this paper is the JADE algorithm [5–7].

71.3 THE RESULTS ON THE SEISMIC DATA OF SINGLE GUN METAL ORE

The blind-wavelet algorithm is used to process the seismic data of a metal ores (Fig. 71.3). The sample points are 6000, sampling interval is 1ms and the seismic data is with a total of 584 channel signals. From Fig. 71.3, it is easy to find that the SNR of the seismic data is very low, and the noise mainly includes the surface wave, linear noise and a large amount of random noise. There is almost no hyperbolic morphology on the data profile, and texture is not obvious. Figs. 71.4 and 71.5 show the results by blind signal separation algorithm and the wavelet threshold method for the seismic data shown in Fig. 71.3, respectively. Fig. 71.6 shows the results of the blind-wavelet algorithm.

From Fig. 71.4 and Fig. 71.5, the seismic section texture by the blind signal separation and wavelet threshold method is clearer than the original seismic texture. Some interference noises have been eliminated, but hyperbolic characteristic is still relatively vague and the SNR is low. Through wavelet threshold method, some random noise and interference noise are eliminated, and the surface wave, linear noise eliminated are relatively small. However, elimination effect of linear noise by blind source separation is good, and random noise is not ideal. From Fig. 71.6, the elimination effect of one-dimensional blind-wavelet algorithm is better than blind source separation algorithm and wavelet threshold algorithm. Not only the sound wave, the surface wave and linear noise are eliminated which were the legacy of noise by wavelet threshold method, but also the random noise is eliminated which is not eliminated by the blind source separation. Through one-dimensional wavelet algorithm, most of the noise was eliminated. The texture of entire section (Fig. 71.6) by the blind-wavelet algorithm is clear and fluent, the hyperbolic characteristic is obvious, and the high signal-to-noise ratio is derived.

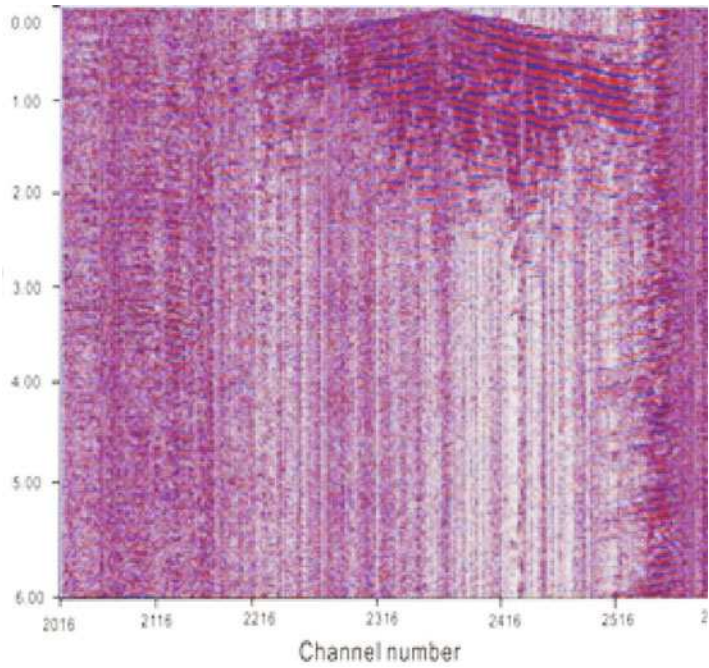


Fig. 71.3 The original seismic data profile

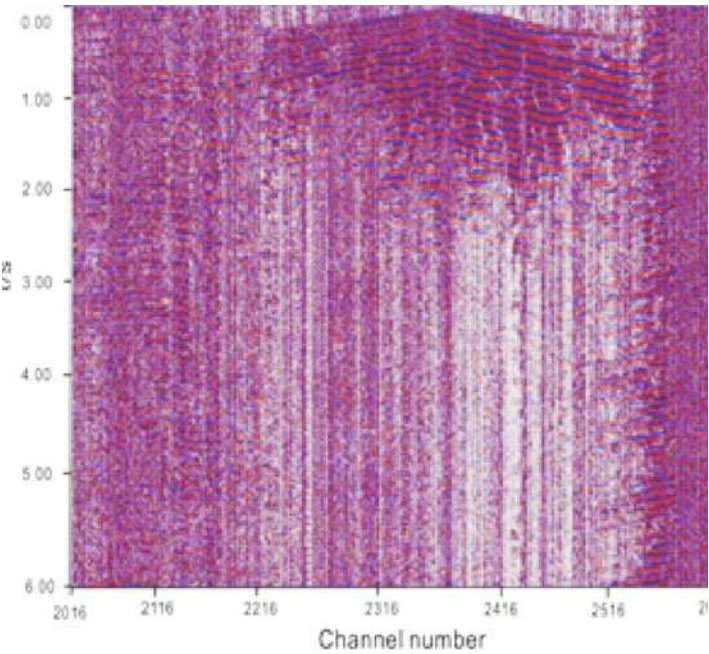


Fig. 71.4 Blind signal separation denoising profile (JADE)

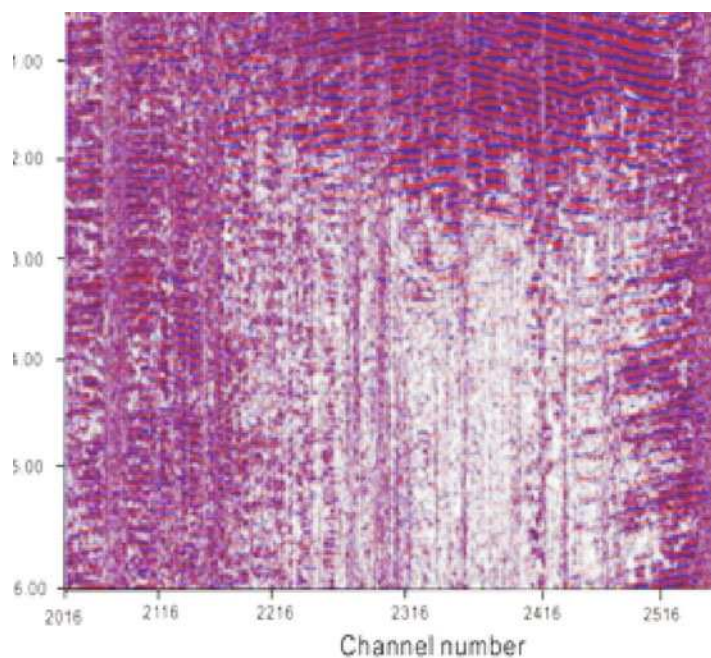


Fig. 71.5 Wavelet threshold denoising profile

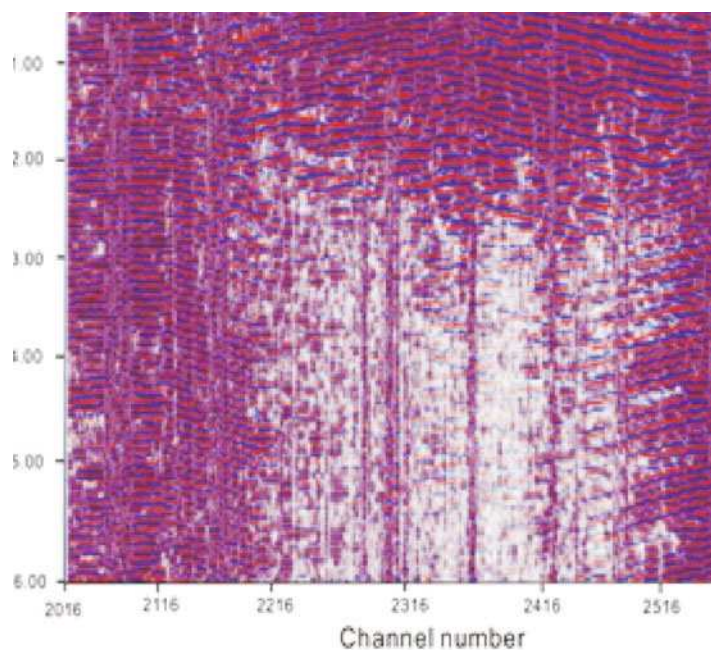


Fig. 71.6 1-D blind-wavelet algorithm denoising profile

71.4 CONCLUSION

In this study, a one-dimensional blind-wavelet algorithm is presented. The blind-wavelet algorithm is applied to process the seismic data. The results show that the denoising advantages of blind-wavelet algorithm is obvious, it can effectively eliminate the random noise, linear noise, surface waves and acoustic noise of the data. The hyperbolic characteristics of seismic data after denoising are more apparently, seismic profile is more clear and smooth, the signal to noise ratio becomes higher, which meets the requirements of the high resolution and fidelity. But we only give a one-dimensional blind-wavelet algorithm for two adjacent channel signals processing, the multi-channel signal processing will be a hot topic in the future.

REFERENCES

1. Liua, C.C., Sun, T.Y., Tsai, S.J., Yu, Y.H. and Hsieh, S.T.: Heuristic wavelet shrinkage for denoising. *Applied Soft Computing*, 11(1), 256–264 (2011)
2. Zhang, H., Blackburn, T.R., Phung, B.T. and Sen, D.: A Novel Wavelet Transform Technique for On-line Partial Discharge Measurements Part 1. WT De-noising Algorithm. *IEEE Trans. Dielectr. Electr. Insul.*, 14(1), 3–14 (2007)
3. Souloumiac, A.: Nonorthogonal Joint Diagonalization by Combining Givens and Hyperbolic Rotations. *IEEE Transactions on signal processing*, 57(6), 2222–2231 (2009)
4. Li, J., Cheng, C.K., Jiang, T.Y. and Grzybowski, S.: Wavelet De-noising of Partial Discharge Signals Based on Genetic Adaptive Threshold Estimation. *IEEE Transactions on Dielectrics and Electrical Insulation*, 19(2), 543–549 (2012)
5. Cardoso, J.F. and Antoine, S.: Blind Beamforming for Non-Gaussian Signals. *IEEE Proceedings*, 140(6), 362–370 (1993)
6. Cardoso, J.F.: High-order contrasts for independent component analysis. *Neural Computation*, 11(1), 157–192 (1999)
7. Zbynek, K., Tichavsky, P. and Oja, E.: Efficient Variant of Algorithm Fast ICA for Independent Component Analysis Attaining the Cramer-Rao Lower Bound. *IEEE Transactions on neural networks*, 17(5), 1265–1277 (2006)

Chapter 72

Study of N -dimensional Matrices and Its Application in Geology

Wei Shen and Haiyan Du

Abstract The definition and arithmetic (including add-subtract, bracket multiplication and Hadamard products) of N -dimensional matrices are studied and proved. The cubic matrices are a special case of N -dimensional matrices. The multi-dimensional data are expressed more brief and facility in theoretical analysis by the method of N -dimensional matrices. A geological example is given to illustrate the method and procedure of N -dimensional matrices in geological application. The method of N -dimensional matrices are considered a good tool in exploration and forecast.

Keywords N -Dimensional matrices • Bracket multiplication • Hadamard products • Cubic matrices • Metallogenic prediction

72.1 INTRODUCTION

In earth science research there are many multidimensional data, for example, we consider the stability of global scope in all directions for many complex geological phenomena, i.e. distinguishing between isotropic or anisotropic distribution, which contain more than one dependent variables and factors that have different statistical characteristics. We must use multivariables and multiple parameters (i.e. multidimensional data) to describe those. For ore deposits prediction there are a lot of difficult problems such as multi-dimension of mineral migration and spatial distribution, multi-level and multi-stage of the deposits evolution and ore-controlling structure, etc. [1–5]. Current methods for geological model are nonlinear logistic regression model, multiple log-linear model, multidimensional scaling and quantitative theory, etc. But these methods are primarily concerned with two-dimensional data [6]. Therefore putting forward new methods to process the multidimensional data is very useful and significant [7]. This manuscript

W. Shen (✉)

China University of Geosciences, Xueyuan Road 29, Beijing, P.R. China

e-mail: shenweihome@sina.com

H. Du

China Geological Library, Xueyuan Road 29, Beijing, P.R. China

presents a concept of N -dimensional matrices and common definitions and arithmetic such as add-subtract, bracket multiplication and Hadamard products and studies its proposition. The method of N -dimensional matrices can be used to deal with multidimensional data in earth sciences.

72.2 N -DIMENSIONAL MATRICES

DEFINITION 1.1 An n dimensional array $S_{r_1 \times r_2 \times \dots \times r_n} = (S_{i_1 i_2 \dots i_n})$ ($1 \leq i_1 \leq r_1, 1 \leq i_2 \leq r_2, \dots, 1 \leq i_n \leq r_n$) is call to be an N -dimensional matrices.

For example, when $n=4$, the subscript i_4 indicates horizontal ordinate and i_3 vertical coordinate (or latitude and longitude), the subscript i_2 indicates altitude (or elevation), $S_{i_1 i_2 i_3 i_4}$ ($i_1 = 1, 2, \dots, r_1$) indicates a value of i_1 -th geochemical element (such as Au) in three dimensional coordinates i_2, i_3, i_4 .

DEFINITION 1.2 Let $S_{r_1 \times r_2 \times \dots \times r_n}$ and $T_{r_1 \times r_2 \times \dots \times r_n}$ be N -dimensional matrices respectively. We denote add/subtract of, $S_{r_1 \times r_2 \times \dots \times r_n} \pm T_{r_1 \times r_2 \times \dots \times r_n} = (S_{i_1 i_2 \dots i_n} \pm T_{i_1 i_2 \dots i_n})$, ($1 \leq i_1 \leq r_1, 1 \leq i_2 \leq r_2, \dots, 1 \leq i_n \leq r_n$).

For example, when $n=4$ ($S_{i_1 i_2 i_3 i_4} + T_{i_1 i_2 i_3 i_4}$) ($i_1 = 1, 2, \dots, r_1$) indicates a sum of two geological variables ($S_{i_1 i_2 i_3 i_4}$ and $T_{i_1 i_2 i_3 i_4}$) (such as geophysical variables and geochemical variables) in three dimensional coordinates i_2, i_3, i_4 .

DEFINITION 1.3 Let A be a $m \times r_1$ matrix, and $S_{r_1 \times r_2 \times \dots \times r_n}$ be an N -dimensional matrices. Then we define bracket multiplication, denote $[]$, as N -dimensional

matrices $T_{m \times r_2 \times \dots \times r_n} = [A][S_{r_1 \times r_2 \times \dots \times r_n}]$, i.e. $t_{s i_2 i_3 \dots i_n} = \sum_{k=1}^{r_1} a_{sk} S_{k i_2 i_3 \dots i_n}$ ($1 \leq s \leq m, 1 \leq i_2 \leq r_2, 1 \leq i_3 \leq r_3, \dots, 1 \leq i_n \leq r_n$).

Especially when $n=4$ and $A=a$ is a r_1 -dimensional vector, $T=[a][S]$ is a three dimensional array with $r_2 \times r_3 \times r_4$, i.e.

$$t_{s i_2 i_3 \dots i_n} = \sum_{k=1}^{r_1} a_k S_{k i_2 i_3 \dots i_n} \quad (1 \leq i_2 \leq r_2, 1 \leq i_3 \leq r_3, 1 \leq i_4 \leq r_4).$$

For example, when $a=(a_1, a_2, \dots, a_{r_1})$ (where a_k is a weight number, $\sum_{k=1}^{r_1} a_k = 1$, $t_{i_2 i_3 i_4}$ ($1 \leq i_2 \leq r_2, 1 \leq i_3 \leq r_3, 1 \leq i_4 \leq r_4$) indicates a sum of weighted values of r_1 geochemical elements ($S_{i_1 i_2 i_3 i_4}, i_1 = 1, 2, \dots, r_1$) in three dimensional coordinates i_2, i_3, i_4 .

Proposition of bracket multiplication:

$$(i) \quad [A \pm B][S_{r_1 \times r_2 \times \dots \times r_n}] = [A][S_{r_1 \times r_2 \times \dots \times r_n}] \pm [B][S_{r_1 \times r_2 \times \dots \times r_n}] \quad (72.1)$$

$$(ii) \quad [A][S_{r_1 \times r_2 \times \dots \times r_n} \pm T_{r_1 \times r_2 \times \dots \times r_n}] = [A][S_{r_1 \times r_2 \times \dots \times r_n}] \pm [A][T_{r_1 \times r_2 \times \dots \times r_n}] \quad (72.2)$$

where $[S_{r_1 \times r_2 \times \dots \times r_n}]$ and $[T_{r_1 \times r_2 \times \dots \times r_n}]$ are N -dimensional matrices respectively, A and B are $m \times r_1$ matrix.

PROOF We prove part (i).

The right hand side and left hand side of Eq. (72.1) are N -dimensional matrices with $m \times r_2 \times \dots \times r_n$, the $si_2i_3 \dots i_n$ -th element of left hand side of Eq. (72.1) is

$$\sum_{k=1}^{r_1} (a_{sk} \pm b_{sk}) s_{ki_2i_3 \dots i_n} = \sum_{k=1}^{r_1} a_{sk} s_{ki_2i_3 \dots i_n} \pm \sum_{k=1}^{r_1} b_{sk} s_{ki_2i_3 \dots i_n} \quad (1 \leq s \leq m, 1 \leq i_2 \leq r_2, \dots, 1 \leq i_n \leq r_n), \text{ which}$$

show Eq. (72.1) right.

DEFINITION 1.4 Let $S_{r_1 \times r_2 \times \dots \times r_n}$ and $T_{r_1 \times r_2 \times \dots \times r_n}$ be N -dimensional matrices respectively. Then we define Hadamard products, denote \circ , as N -dimensional matrices,

$$S_{r_1 \times r_2 \times \dots \times r_n} \circ T_{r_1 \times r_2 \times \dots \times r_n} = (s_{i_1i_2 \dots i_n} t_{i_1i_2 \dots i_n}), \quad (1 \leq i_1 \leq r_1, 1 \leq i_2 \leq r_2, \dots, 1 \leq i_n \leq r_n).$$

Proposition of Hadamard products:

$$(i) \quad S_{r_1 \times r_2 \times \dots \times r_n} \circ T_{r_1 \times r_2 \times \dots \times r_n} = T_{r_1 \times r_2 \times \dots \times r_n} \circ S_{r_1 \times r_2 \times \dots \times r_n} \quad (72.3)$$

$$(ii) \quad (S_{r_1 \times r_2 \times \dots \times r_n} \circ T_{r_1 \times r_2 \times \dots \times r_n}) \circ U_{r_1 \times r_2 \times \dots \times r_n} = S_{r_1 \times r_2 \times \dots \times r_n} \circ (T_{r_1 \times r_2 \times \dots \times r_n} \circ U_{r_1 \times r_2 \times \dots \times r_n}) \quad (72.4)$$

$$(iii) \quad (S_{r_1 \times r_2 \times \dots \times r_n} + T_{r_1 \times r_2 \times \dots \times r_n}) \circ U_{r_1 \times r_2 \times \dots \times r_n} = S_{r_1 \times r_2 \times \dots \times r_n} \circ U_{r_1 \times r_2 \times \dots \times r_n} + T_{r_1 \times r_2 \times \dots \times r_n} \circ U_{r_1 \times r_2 \times \dots \times r_n} \quad (72.5)$$

where, $(S_{r_1 \times r_2 \times \dots \times r_n}, T_{r_1 \times r_2 \times \dots \times r_n}$ and $U_{r_1 \times r_2 \times \dots \times r_n})$ are N -dimensional matrices respectively.

PROOF We prove part (iii).

The right hand side and left hand side of Eq. (72.5) are N -dimensional matrices with $r_1 \times r_2 \times \dots \times r_n$, then

$$(S_{r_1 \times r_2 \times \dots \times r_n} + T_{r_1 \times r_2 \times \dots \times r_n}) \circ U_{r_1 \times r_2 \times \dots \times r_n} = ((s_{i_1i_2 \dots i_n} + t_{i_1i_2 \dots i_n}) u_{i_1i_2 \dots i_n}) = (s_{i_1i_2 \dots i_n} u_{i_1i_2 \dots i_n} + t_{i_1i_2 \dots i_n} u_{i_1i_2 \dots i_n}) \quad (1 \leq i_1 \leq r_1, 1 \leq i_2 \leq r_2, \dots, 1 \leq i_n \leq r_n), \text{ which show Eq. (72.5) right.}$$

DEFINITION 1.5 Let k be a constant, and $S_{r_1 \times r_2 \times \dots \times r_n}$ be an N -dimensional matrices, we denote $T_{r_1 \times r_2 \times \dots \times r_n} =$

$kS_{r_1 \times r_2 \times \dots \times r_n} = (k_{si_1 i_2 \dots i_n})(1 \leq i_1 \leq r_1, 1 \leq i_2 \leq r_2, \dots, 1 \leq i_n \leq r_n)$ as N -dimensional matrices with $r_1 \times r_2 \times \dots \times r_n$.

72.3 CUBIC MATRICES

The definition/conception and arithmetic of cubic matrices is presented by Bates and Watts [8] in 1980 based on the geometric concept of curvature. Cubic matrices have a wide range of applications in nonlinear regression analysis, game theory and economics. In fact, the cubic matrices are a special case of N -dimensional matrices (when $n=3$).

DEFINITION 2.1 A three dimensional array $X=(x_{kij})$ with $n \times p \times q$ ($1 \leq k \leq n, 1 \leq i \leq p, 1 \leq j \leq q$) is call to be a cubic matrices [8]. It can be written as

$$X = \begin{pmatrix} X_1 \\ X_2 \\ \vdots \\ X_n \end{pmatrix}, \text{ where } X_k = \begin{pmatrix} X_{k11} & \cdots & X_{k1q} \\ \vdots & \ddots & \vdots \\ X_{kp1} & \cdots & X_{kpq} \end{pmatrix}.$$

For example, the subscript j indicates horizontal ordinate and i vertical coordinate (or latitude and longitude), $x_{kij}(k=1,2,\dots,n)$ indicates a value of k -th geochemical element (such as Au) in two dimensional coordinates i, j .

DEFINITION 2.2 Let X with $n \times p \times q$ and Y with $n \times p \times q$ be cubic matrices respectively. We denote (add-subtract) $X \pm Y = (x_{kij} \pm y_{kij})$, ($1 \leq k \leq n, 1 \leq i \leq p, 1 \leq j \leq q$) [9].

For example, $x_{kij} + y_{kij}$ ($k=1,2,\dots,n$) indicates a sum of two geological variables x_{kij} and y_{kij} (such as geophysical variables and geochemical variables) in two dimensional coordinates i, j .

DEFINITION 2.3 Let A be an $m \times n$ matrix, and X with $n \times p \times q$ be a cubic matrices. Then we define bracket multiplication, denote $[]$, as cubic matrices $Y =$

$$[A][X] \text{ with } m \times p \times q \text{ [9], i.e. } y_{sij} = \sum_{k=1}^n a_{sk} x_{kij} (1 \leq s \leq m, 1 \leq i \leq p, 1 \leq j \leq q).$$

Especially when $A=a$ is a n -dimensional vector, $Y=[a][X]$ is an $p \times q$ matrix, i.e.

$$y_{ij} = \sum_{k=1}^n a_{sk} x_{kij} (1 \leq i \leq p, 1 \leq j \leq q) \quad . \text{ For example, when } a=(a_1, a_2, \dots, a_n)$$

(where a_k is a weight number, $\sum_{k=1}^{r_1} a_k = 1$), $y_{ij}(1 \leq i \leq p, 1 \leq j \leq q)$ indicates a sum of weighted values of n geochemical elements ($x_{kij}, k = 1, 2, \dots, n$) in two dimensional coordinates i, j .

Proposition of bracket multiplication (cubic matrices):

- (i) $[A \pm B][X] = [A][X] \pm [B][X]$
(ii) $[A][X \pm Y] = [A][X] \pm [A][Y]$

where X with $n \times p \times q$ and Y with $n \times p \times q$ be a cubic matrices respectively, A and B are $m \times n$ matrix.

DEFINITION 2.4 Let X with $n \times p \times q$ and Y with $n \times p \times q$ be cubic matrices respectively. Then we define Hadamard products [10], denote \circ , as cubic matrices $X \circ Y = (x_{kij}y_{kij})$, ($k \leq n, 1 \leq i \leq p, 1 \leq j \leq q$). Proposition of Hadamard products(cubic matrices):

- (i) $X \circ Y = Y \circ X$
(ii) $(X \circ Y) \circ Z = X \circ (Y \circ Z)$
(iii) $(X + Y) \circ Z = X \circ Z + Y \circ Z$

where X , Y and Z are cubic matrices respectively.

DEFINITION 2.5 Let k be a constant, and X with $n \times p \times q$ be a cubic matrices, we denote

$Y = kX = \begin{pmatrix} kX_1 \\ kX_2 \\ \vdots \\ kX_n \end{pmatrix} (1 \leq i_1 \leq r_1, 1 \leq i_2 \leq r_2, \dots, 1 \leq i_n \leq r_n)$ as cubic matrices with $n \times p \times q$.

72.4 EXAMPLE

The study on anomaly association of elements Cu-Zn-Ab-Ag-Sn-As in mid-west section of Jiangshan-Shaoxing suture zone

A three dimensional array (i.e. cubic matrices) $X = (x_{kij})$ with $6 \times 56 \times 99$ ($1 \leq k \leq 6, 1 \leq i \leq 56, 1 \leq j \leq 99$) is made up of 1:200,000 regional geochemical data on Cu, Zn, Ab, Ag, Sn and As (the number of each element is $5,544 = 56 \times 99$). The association of elements Cu-Zn-Ab-Ag-Sn-As are obtained by ore-forming elements and distribution of symbiotic combination of associated elements. Based on geochemical related elements data, the spatial distribution and anomaly geochemical element are studied by the cumulative indexes of multi geochemical element. The contour map of anomaly association of elements Cu-Zn-Ab-Ag-Sn-As is worked out by the cumulative indexes of geochemical association of elements Cu-Zn-Ab-Ag-Sn-As (Fig.72.1).

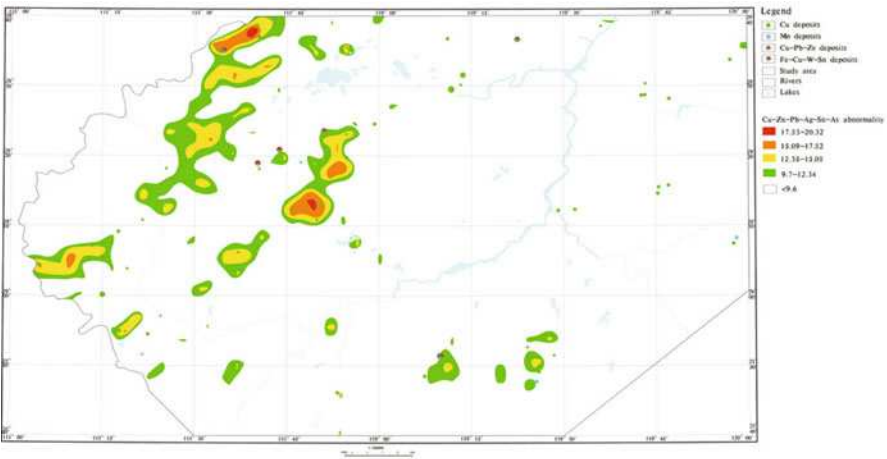


Fig. 72.1 Contour map of anomaly association of elements Cu-Zn-Ab-Ag-Sn-As in mid-west section of Jiangshan-Shaoxing suture zone.

The cumulative indexes : $(Z_{ij}) = \sum_{k=1}^6 \frac{X_{kij}}{\sum_{i=1}^{56} \sum_{j=1}^{99} X_{kij} / (56 \times 99)} = [a][X] \quad (72.6)$

where

$$a = \begin{pmatrix} \sum_{i=1}^{56} \sum_{j=1}^{99} X_{1ij} / (56 \times 99) \\ \sum_{i=1}^{56} \sum_{j=1}^{99} X_{2ij} / (56 \times 99) \\ \vdots \\ \sum_{i=1}^{56} \sum_{j=1}^{99} X_{6ij} / (56 \times 99) \end{pmatrix} \quad (1 \leq i \leq 56, 1 \leq j \leq 99)$$

72.5 CONCLUSIONS

- (a) The concept of *N*-dimensional matrices and common definitions and arithmetic such as add-subtract, bracket multiplication and Hadamard products are presented and its proposition are studied and proved.
- (b) A geological example, the study on anomaly association of elements Cu-Zn-Ab-Ag-Sn-As in mid-west section of Jiangshan-Shaoxing suture zone, is given to illustrate the method and procedure of *N*-dimensional matrices in geological

application. The method of N -dimensional matrices can be used to deal with multidimensional data in earth sciences.

- (c) The method of N -dimensional matrices has the advantage of more concise and convenient in representing and analyzing multidimensional data. N -dimensional matrices can be used to deal with space-time multidimensional data effectively.

ACKNOWLEDGEMENT This research was supported by the grant from the National Natural Science Foundation of China (Grant No. 41102208 and Grant No. 41172302).

REFERENCES

1. Zhao, P.-D.: Quantitative Mineral Prediction and Deep Mineral Exploration. *Earth Science Frontiers*, 14(5), 1–10 (2007)
2. Ye, T.-Z. and Xue, J.-L.: Geological Study in Search of Metallic Ore Deposits at Depth. *Geology in China*, 34(5), 855–869 (2007)
3. Zhai, Y.-S., Deng, J., Wang, J.-P. et al.: Researches on Deep Ore Prospecting. *Mineral Deposits*, 23, 142–149 (2004)
4. Shen, W.: Fractal and Chaos with Application in Mineral Resource Prediction. Geological Publishing House, Beijing (2002)
5. Shen, W. and Zhao, P.-D.: Multidimensional Self-affine Distribution with Application in Geochemistry. *Mathematical Geology*, 34(2), 109–123 (2002)
6. Wang, S.-C., Chen, Y.-L. and Xia, L.-X.: Theory and Method of Synthetic Information Mineral Resources Prognosis. Science Press, Beijing (2000)
7. Shen, W.: Progress in Nonlinear Quantitative Theory, Technology and Methods of Deep Exploration. *Earth Science Frontiers*, 17(5), 278–288 (2010)
8. Bate, D.M. and Watts, D.G.: Relative curvature measure of nonlinearity. *J. R. Statist. Soc.*, 42, 1–25 (1980)
9. Wang, X.-Z.: Theory and Application of Nonlinear Models Parameter Estimation. Wuhan University Publishing House, Wuhan (2002)
10. Ni, G.-X.: Theory and Method of Common Matrix. Shanghai Science & Technology Press, Shanghai (1984)

Chapter 73

Small- to Large-Scale Rock Fracture Patterns as Indicators of Shock-Related Fragmentation

Md. Sakawat Hossain and Jörn H. Kruhl

Abstract Shock-fragmentation of the Ries impact crater forms characteristic and complex fracture patterns from micro- to kilometre-scale. Outside the crater rim, prominent fractures are mainly vertical to sub-vertical, either in radial or tangential orientation to the crater. The traces of radial fractures from various outcrops around the Ries consistently point towards impact centre and, consequently, represent an excellent tool for locating the crater centre. The presence of prominent fractures in numerous outcrops outside the Ries crater indicates that impact-induced brittle deformation reaches as far as 70 km away from the crater centre. Time series analyses of fracture frequency reveals regularly spaced, ca. 3–4 m interval elongate vertical to sub-vertical zones of high deformation. This periodicity of increased fragmentation appears typical of impact fragmentation. The cyclic repetition of intensely fractured zones and their variations with distance are most likely the results of the interaction of rapidly evolving impact-induced shock waves.

Keywords Shock-fragmentation • Prominent fracture • Fracture-frequency • Power spectra

73.1 INTRODUCTION

Impact crater formation is an extremely complicated and dynamic process, which extends from micro-seconds during shock loading up to few minutes when gravity-driven collapse and resultant mass movements take place [1]. At the beginning of a kilometre-sized asteroid impact, pressures reaches up to several hundred gigapascals (GPa), temperature up to several ten-thousand degrees, and strain rate more than 10^{+6} s^{-1} [2]. Within few minutes, a large variety of deformation features are formed under very different and rapidly changing stress, temperature and strain-rate condition [2]. Impact initial impulse is carried to the target rock by stress waves of varying strength and direction of motion. Crater excavation, its ultimate

Md. S. Hossain (✉) • J.H. Kruhl

Tectonics and Material Fabrics Section, Technical University Munich, Munich, Germany

e-mail: sakawat.hossain@tum.de

morphology, and the extent of deformation are mainly controlled by the interaction of stress waves with free surface [1]. Moreover, as magnitudes of pressure and strain rate are enormously high and duration of deformation is extremely short, characteristics of impact deformation differ from those of tectonic deformation. From the point of impact, shock related micro- to kilometre-scale shattering and fracturing of the target rocks rapidly decrease outwards. At crater rim, large-scale fractures of vertical to sub-vertical orientations, with little or no displacement are dominant. During the early stage of cratering, when strain rates are very high, closely spaced fractures develop. They tend to be short, usually less than a cm, and displacements are less than 1 mm [2]. Fractures coalesce and increase in length occur during the intermediate stage. Large scale faults and fractures always develop during the final stage of cratering [3]. Presence of inherent flaws are very important as sites of weakness for the nucleation and coalescence of fractures [4]. After a certain threshold limit ($\sim 10^1\text{--}10^3\text{ s}^{-1}$) material inertia begins to affect the nucleation and propagation of the fractures [5]. Transition from narrow-spaced fracture networks to more localized large-scale fractures indicates the degree of heterogeneity in strain distribution [2]. Localized large-scale fracture network [6] may be able to provide important clues to identify the crater centre location and the brittle deformation extent. Moreover, current impact structure analyses mainly concentrate on the crater centre up to its outer rim [2]. However, in case of hypervelocity impact of a kilometre-sized asteroid, brittle deformation can reach far beyond the crater rim. In order to study the aspects of brittle deformation, mentioned above, we choose Ries meteorite crater (Nördlingen, Germany). Numerous quarries in and around this crater provide an excellent opportunity to study impact-related brittle deformation in the basement rocks and their sedimentary cover [7]. The 25 km diameter crater was formed 14.6 ± 0.1 (0.2) million years ago [8] by an oblique impact [9] of a ca. 1.5 km large meteorite on a two-layer target terrain that consisted of 620–750 m thick sub-horizontally layered sedimentary rocks of Triassic to Jurassic age, resting on Variscan basement [10]. Outside the inner crater ring, the upper sedimentary layer, consisting of Malm limestone, was subjected to brittle deformation far beyond the range and style typical for regional brittle deformation. Quantitative analyses of impact-fragmentation of the transiently loaded rocks in the target surrounding of Ries crater would help modelling dynamic impact deformation and their difference to the quasi-static tectonic deformation.

73.2 MATERIAL, METHODS AND MEASUREMENT

During field investigation in 9 different quarries around the Ries impact (Fig. 73.1), (i) prominent fracture orientation data were collected in conjunction with the section and bedding orientation and (ii) horizontal and vertical sections of the quarry outcrops were photographed. Fractures which are longer than 1 m and cut across several sedimentary beds are defined prominent. These fractures are assumed to be induced by impact and not by regional tectonics. The prominent fractures

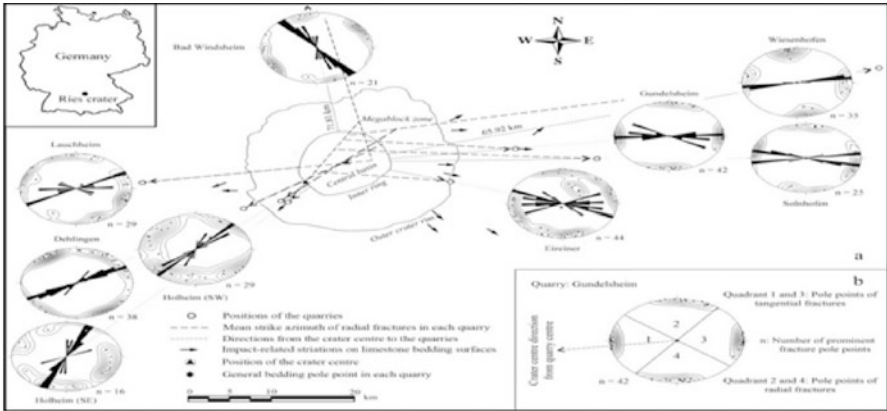


Fig. 73.1 Ries impact crater outline with prominent fractures orientation around the crater. (a) Prominent fractures from each quarry are represented in contoured pole-point diagrams. Strike directions of prominent radial fractures from each quarry are presented as length-weighted rose diagram. (b) Classification of prominent fractures (Fig. 73.1a) into radial and tangential fractures

orientation in each quarry is represented as contoured pole-point diagrams (Fig. 73.1a). Lines are drawn to connect the crater centre with each quarry centre. To identify and separate radial fracture set from prominent fractures, each connecting line is extended to the centre of the respective pole diagram. Two orthogonal lines are drawn through the centre of pole diagram, each of which makes 45° angle with the connecting line (Fig. 73.1b), produced 4 quadrants. Poles in quadrant 2 and 4 represent radial fractures. Strike of the radial fractures from each quarry is represented as rose diagram, which is then superimposed on respective pole diagram and finally their mean strike are extrapolated towards the crater centre. Fracture-frequency quantification is based on high resolution photographs from three vertical sections: NS oriented section-1 from Eireiner, 020° oriented section-2 from Solnhofen and 105° oriented section-3 from Wiesenhofen quarry. Photographs of each section were merged to a single image. Fractures were digitized manually and converted into binary images [7]. For each 25-cm interval, with 50% overlap, the number of fracture intercepts are recorded along a scan-line, and plotted against the section length. These raw data were smoothed and the linear trend was subtracted by using 'lowess' and 'detrend' function respectively [11] of Matlab Curve Fitting ToolboxTM.

Time series analysis of the fracture-frequency data was performed by using Fourier transform [12] and Wavelet power spectrum [13] methods to understand spatial-fracture-frequency distribution. In autospectrum analysis, powerspectra was estimated by using Fast Fourier Transformation (FFT) algorithm. Variations of the spectral peaks amplitude with distance were determined by Evolutionary powerspectra [14]. To map the changes in the time or spatial-frequency domain with a flexible standard resolution, wavelet power spectrum [13] method was used.

73.3 RESULT

Prominent fracture pole-point diagrams reveal two main sets of sub-vertical to vertical fractures in all 9 quarries (Fig. 73.1a). One is approximately tangential and the other one approximately radial to the crater centre. Most of the fractures are straight to curvilinear, with highly variable dips. Radial fractures mostly occur as single, often conjugate pairs and fracture branching is also observed. The extrapolated mean strike directions of the radial fractures from each quarry meet within a small area in the inner ring of the crater, which contains the impact centre deduced from impact-related striations on bedding surfaces (Fig. 73.1a) [15]. Variations of fracture frequency data along the scan line in three vertical sections are best matched by 7 - 8th order of Fourier fit determined based on correlation coefficient value, R^2 (ca. 0.631-0.58). Residual analysis of the Fourier fit model indicate that additional cycles might be present. This is true for all three sections. The autospectrum of these data reveals mainly three significant peaks at frequencies of ~ 0.0025 , ~ 0.0037 and ca. 0.0057-0.0081 cm^{-1} (Fig. 73.2b) and -3, the periods of the strong and weak amplitude spectrum are ~ 400 and ~ 170 cm, respectively. However, as in section-1, an intermediate amplitude power spectrum with period of ~ 270 cm is present in section-2. Evolutionary and wavelet power spectrum of section-1 show continuity of a ~ 270 cycle along the sections, and a relatively weak ~ 125 cm cycle in parts of the sections. In section-2 and -3, a ~ 400 cm cycle occurs in the entire sections, and relatively weak ~ 170 cm cycle is present in parts of sections.

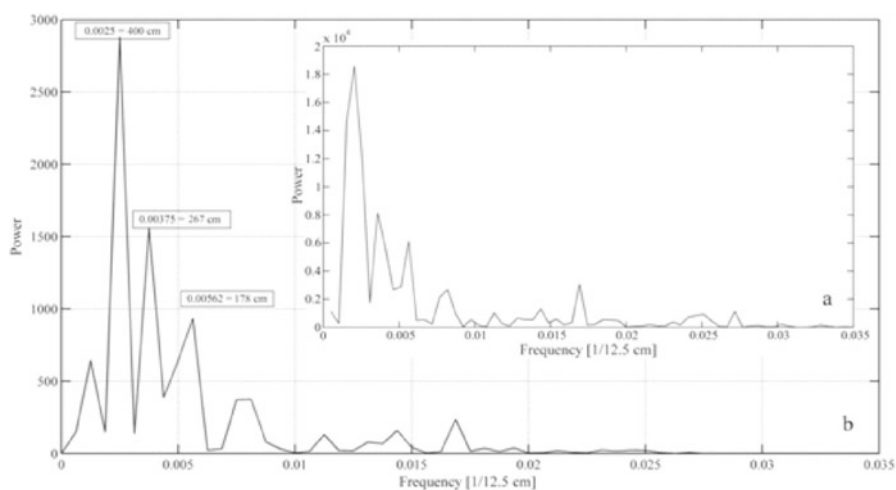


Fig. 73.2 The power spectrum of the fracture frequency transect across 2000 cm long section-2. (a) The autospectrum based on raw data. (b) The autospectrum based on processed data

73.4 DISCUSSION AND CONCLUSION

Prominent fractures of the Ries impact (Fig. 73.1a) can be compared with the fractures reported from (i) laboratory impact experiments [16, 6], (ii) micrometeoroid impact on the space craft solar panels [17], (iii) the nuclear test site in the Yucca flat region of Nevada [18], and (iv) other natural impact craters [19]. While most of the prominent fractures extend approximately several tens of metres into the subsurface, others extend farther over an indeterminable distance. In most cases, they are widest on the surface and generally narrow with depth, although the reverse is also observed. Some of the fractures also display evidence of offset. Due to local extent of the fractures, this offset is limited to the uppermost veneer of the surface material which probably does not return to its original position after passage of stress wave [18]. The radial and tangential sets of prominent fractures are attributed to rising and falling of the surface in response to the passage of shock and rarefaction waves produced by the impact [1]. Radial fractures (Fig. 73.1b) are Mode I tensional fractures, supposed to occur when high compressive stress (σ_1) is in radial orientation and minimum stress component (σ_3) is oriented concentrically as circumferential stress [20]. It is assumed that the above orientation of the principle stresses develop when the compressive wave front reaches the wall rock [16, 21]. Tangential fractures are formed upon relaxation due to elastic rebound of the rocks after the impact shock has passed, causes deformable material flows into the transient crater. They may also develop by differential movement of the free boundary as the rock is forced outward from the centre of the impact along shear planes intersecting the ground surface [22]. Faulting, formation of megablocks and slumping are related to mainly these circumferential tensional fractures. It seems that these fractures propagate outward while the shock wave interferes with the release wave which is reflected obliquely from the wall-rock surface. Geometry of “near surface” or so-called conical fractures as described by [20] and [1] resembles this kind of fractures. Although the extrapolated mean radial strike directions do not exactly intersect in a single point, most of them intersect within a small area that contains the crater centre (Fig. 73.1a) and are almost parallel to the impact-related striations [15]. The systematic variation of the strike orientation indicates that impact-induced radial fracture sets can be used to approximate the position of a crater centre which is not exposed. The presence of prominent fractures in numerous outcrops outside the Ries crater indicates that impact-induced brittle deformation reaches as far as 70 km away from the crater centre (Fig. 73.1a). However, the extent of deformation is most unlikely to be equal in all directions. Ries impact structure is interpreted to originate from a W-SW to E-NE oblique impact [9]. The enhanced damage in downrange directions [2] is observed in (i) other natural impacts, (ii) impact experiments, and (iii) numerical modelling. Therefore, the ca. 70 km extent of brittle deformation of the Ries impact in the NE-downrange direction would not necessarily be similar in other directions, specifically in the SW-uprange direction. Autospectrum of fracture frequency along the three sections indicate variation of spectral peak amplitude with distance (Fig. 73.2). The high

amplitude power spectrum with a period of ~ 270 cm adjacent to the crater rim (ca. 13 km) is weakened to half of its amplitude at a distance of ca. 30 km and almost disappears at a distance of ca. 65 km. On the contrary, an initial low amplitude power spectrum with a period of ~ 400 cm increases with distance from the crater centre (Fig. 73.2b). Besides, a very low amplitude power spectrum of ca. 125–170 cm cycle, slowly strengthens with distance but becomes less stronger compared to the 400 cm cycle. According to [1], thickness of the shock wave in solid rocks is up to a few meters and shock front is discontinuous. During expansion of the shock wave after its generation, it weakens and converts into an elastic wave. This elastic wave continues to travel through the target rocks, further weakened only by normal seismic attenuation [1]. Impact also excites surface wave that attenuates less rapidly than body waves. Therefore, it can be argued that the cyclic repetition of intensely fractured zones [7] and their variations with distance are most likely the results of the interaction of rapidly evolving shock waves.

REFERENCES

1. Melosh, H.J.: Impact Cratering: A Geological Process. Oxford University Press, New York (1989)
2. Kenkmann, T., Poelchau, M.H. and Wulf, G.: Structural geology of impact craters. *J. Struct. Geol.* 62, 156–182 (2014)
3. Spray, J.G.: Superfaults. *Geology*, 25(7), 579–582 (1997)
4. Griffith, A.A.: Phenomena of rupture and flow in solids. *Philos. Transact. Royal Soc. Lond.* 221A, 163–198 (1920)
5. Kipp, M.E., Grady, D.E. and Chen, E.P.: Strain-rate dependent fracture initiation. *Int. J. Fract.* 16(5), 471–478 (1980)
6. Polanskey, C.A. and Ahrens, T.J.: Impact spallation experiments: Fracture patterns and spall velocities. *Icarus* 87(1), 140–155 (1990)
7. Hossain, M.S. and Kruhl, J.H.: Fractal-Geometry-Based Quantification of Shock-Induced Rock Fragmentation in and around an Impact Crater. *Pure and Applied Geophysics* doi:10.1007/s00024-014-0922-8 (2014)
8. Schwarz, W.H. and Lippolt, H.J.: ^{40}Ar - ^{39}Ar Step heating of Nördlinger Ries Crater impact melts. *Meteorit. Planet. Sci. Suppl.* id.5191 (2013)
9. Artemieva, N.A., Wünnemann, K., Krien, F., Reimold, W.U. and Stöffler, D.: Ries crater and suevite revisited - Observations and modeling, Part II: Modeling. *Meteorit. Planet. Sci.* 48(4), 590–627 (2013)
10. Stöffler, D., Artemieva, N.A., Wünnemann, K., Reimold, W.U., Jacob, J., Hansen, B.K. and Summerson, I.A.T.: Ries crater and suevite revisited - Observations and modeling Part I: Observations. *Meteorit. Planet. Sci.* 48(4), 515–589 (2013)
11. Trauth, M.H.: MATLAB Recipes for Earth Sciences. Springer, Berlin Heidelberg (2010)
12. Bracewell, R.N.: The Fourier transform and its applications. McGraw Hill, Boston, USA (2000)
13. Lau, K.-M. and Weng, H.: Climate Signal Detection Using Wavelet Transform: How to Make a Time Series Sing. *Bull. Am. Meteorol. Soc.* 76(12), 2391–2402 (1995)
14. Oppenheim, A.V., Schaffer, R.W. and Buck, J.R.: Discrete-Time Signal Processing. Prentice Hall, Upper Saddle River, New Jersey (1999)
15. Schmidt-Kaler, H.: Geologische Übersichtskarte des Meteoritenkraters Nördlinger Ries 1:100 000. Bayerischen Geologischen Landesamt, München (2004)

16. Buhl, E., Kowitz, A., Elbeshausen, D., Sommer, F., Dresen, G., Poelchau, M.H., Reimold, W. U., Schmitt, R.T. and Kenkmann, T.: Particle size distribution and strain rate attenuation in hypervelocity impact and shock recovery experiments. *J. Struct. Geol.* 56, 20–33 (2013)
17. Graham, G.A., Kearsley, A.T., Drolshagen, G., McDonnell, J.A.M., Wright, I.P. and Grady, M.M.: Mineralogy and microanalysis in the determination of cause of impact damage to spacecraft surfaces. In: Pye, K., Kroft, D.J. (eds.) *Forensic Geoscience: Principles, Techniques and Applications. Geol. Soc. Lon. Special Publications*, 232, 137–146 (2004)
18. Allen, B.A., Drellack, S.L. Jr. and Townsend, M.J.: Surface effects of underground nuclear explosions. DE-AC08-96NV11718–122, Geotechnical Services Bechtel Nevada and U.S. Department of Energy, Nevada (1997)
19. Kumar, P.S. and Kring, D.A.: Impact fracturing and structural modification of sedimentary rocks at Meteor Crater, Arizona. *J. Geophys. Res. Planet.* 113(E9) (2008)
20. Ai, H. and Ahrens, T.J.: Dynamic tensile strength of terrestrial rocks and application to impact cratering. *Meteorit. Planet. Sci.* 39(2), 233–246 (2004)
21. Ahrens, T.J. and Rubin, A.M.: Impact-induced tensional failure in rock. *J. Geophys. Res. Planets*, 98(E1), 1185–1203 (1993)
22. Fulmer, C.V. and Roberts, W.A.: Rock induration and crater shape. *Icarus*, 2, 452–465 (1963)

Chapter 74

Distribution Study of Ore-Sourced Elements from a Long Drill-Core in a Loess-Covered Area

Deyi Xu, Bang Qin Feng, Changhai Tan, and Qiuming Cheng

Abstract This research aims at studying the vertical distribution modes of geochemical elements in the covering layer above a deposit. Seventy-eight samples were sequentially collected from a vertical loess drill core above Diyanqinamo Mo-deposit, which were equally separated in 1m's intervals. Each of the samples was screened into grains of grade 20, 40, 80, 120, 160, 200 and 200⁺ meshes to get 78×7 graded samples. The contents of 32 elements in each graded sample were measured by a handheld X-ray fluorescence analyzer to form a 78×7×32 dataset. Firstly, since the grain grades as attributes in a panel dataset are in orders, we regarded this dataset as a new type one and named it as Ordered-Attributes Panel Data (OAPD). Secondly, the non-parametric Friedman test was used to explore the correlation of the contents of the elements with both the distance from the ore and the grain grade separately. It turned out that among the 32 elements Mo, Zr, Sr, Rb, Th, Pb, Zn, Ni, Co, Fe, Mn, V, Ti, Sc, Ca, K, Ba, Cs, Te, Sb, Sn and Cd are correlated with both the distance and the grade. Then, varying coefficient-models were applied to the 22 elements to get the variation modes of the regression coefficients, reflecting the change rates of the contents with respect to the grain grades. At last, the variation modes were sketched and classified.

D. Xu (✉)

Department of Statistics, China University of Geosciences, Wuhan, China

State Key Laboratory of Geological Processes and Mineral Resources,
China University of Geosciences, Wuhan, China

e-mail: xdy@cug.edu.cn

B.Q. Feng

Department of Statistics, China University of Geosciences, Wuhan, China

C. Tan

Faculty of Earth Resources, China University of Geosciences, Wuhan, China

Q. Cheng

State Key Laboratory of Geological Processes and Mineral Resources,
China University of Geosciences, Wuhan, China

Faculty of Earth Resources, China University of Geosciences, Wuhan, China

Keywords Loess-covered area • OAPD • Friedman test • Varying-coefficient models

74.1 INTRODUCTION

The transportation modes of elements in a certain medium have been long and widely studied [1–6]. It is thought that the transportation of ore-sourced elements may be long in distance in various mechanisms. Following the work of [1, 2], this research aims at studying the long-term vertical distributions of ore-sourced elements in the statistics aspect, considering about the grain grades of loess samples.

74.2 DATA PREPARATION

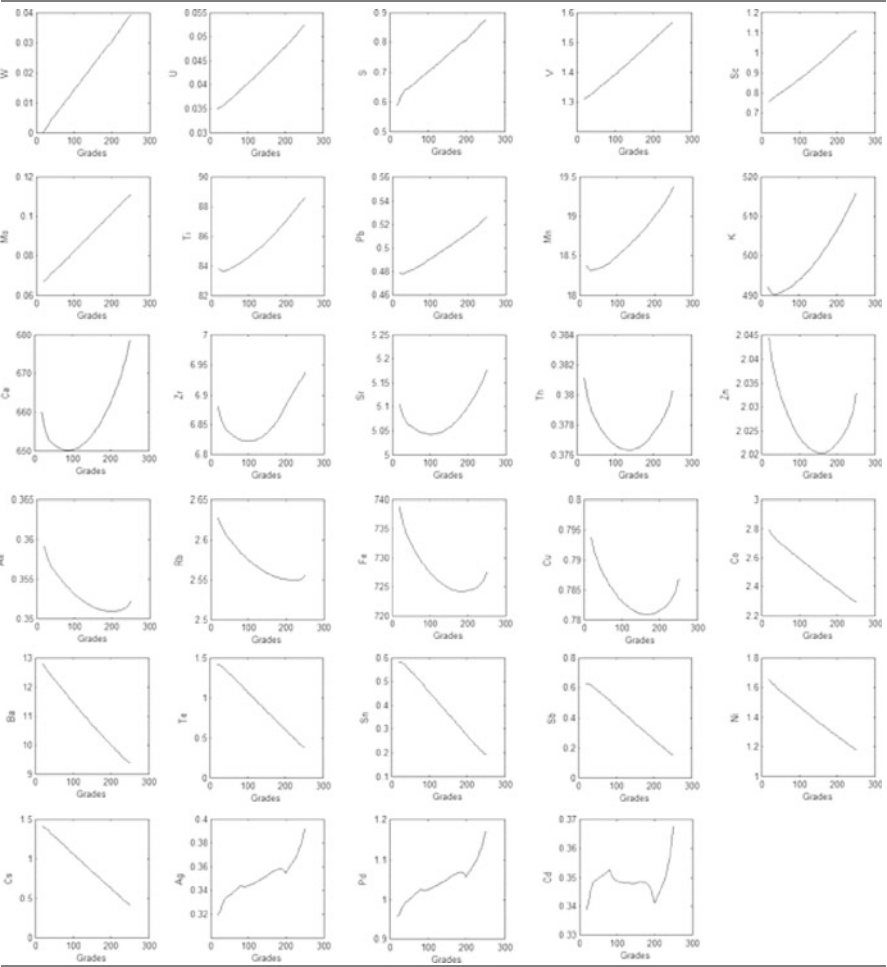
A 78 meters long loess drill-core taken above Diyanqinamo Mo-deposit was chosen. This deposit is located at Inner Mongolia grassland in northwest of China, which is covered by loess of meters to kilometers in thickness. Seventy-eight samples were sequentially collected equally separated in 1m intervals. Each of the samples was screened into grains of grade 20, 40, 80, 120, 160, 200 and 200⁺ meshes to get 78×7 graded samples. The contents of 32 elements in each graded sample were measured by a handheld X-ray fluorescence analyzer to form a 78×7×32 dataset. The dataset is a panel data set, however, the grain grades, as attributes in the panel dataset, are in orders (in other cases the attributes may be metric). Statistically, it is a new type of panel dataset, so that we name it as Ordered-Attributes Panel Data and OAPD in brief. To see whether the contents of the 32 elements are correlated with either the distance from the ore or the grade of the grain, the non-parametric Friedman test was conducted separately with respect to the distance and the grade. It turned out that 22 elements Mo, Zr, Sr, Rb, Th, Pb, Zn, Ni, Co, Fe, Mn, V, Ti, Sc, Ca, K, Ba, Cs, Te, Sb, Sn and Cd are correlated with both the distance and the grade. It implies that the vertical transportation of these 22 elements may result from the ore on one hand, and the transportation may depend on the grain grades on the other hand.

74.3 DISTRIBUTION MODES

There are three correlated variables, the content of element, the distance (or the depth from the surface) and the grade of the grain. Ignoring the grain grade, we obtained some of the distribution modes of the elements with respect to the depth by HP model [1, 2, 7]. Considering the depth, to see the change modes of the contents with respect to the grade, the varying-coefficient model [8] was applied to the

78×7×290APD set. The varying-coefficient model is a kind of non-parametric regression model, in which the regression coefficients are functions of a parameter. In this case, the content is the response variable, the depth is the explaining variable and the grade is the parameter. The model was realized by Matlab programming. The results of the model were sketched as in Table 74.1. In each graph in Tab. 74.1, the horizontal axis represents the grain grade, and the vertical axis represents the change rate of the content of the corresponding element with respect to the depth. Roughly, the modes could be classified into 4 types. Type 1 includes W, U, S, V, Sc and Mo. The change rates of the content with respect to the depth depend on the grain grades in an increasing linear way. Type 2 includes Ti, Pb, Mn, K, Ca, Zr, Sr,

Table 74.1 Change rate modes of elements



Th, Zn, As, Rb, Fe and Cu. The change rates of this type are in curves with only one minimum, from decreasing to increasing. Type 3 includes Co, Ba, Te, Sn, Sb, Ni and Cs. They change in a decreasing linear way. Type 4 includes Ag, Pd and Cd. They are irregular, but can be seen roughly increasing.

74.4 DISCUSSIONS

As we know, there are huge areas are covered by loess [9, 10]. To explore the mechanism for the transportation of ore-sourced or ore-related elements from the ore layer to the ground surface is very important. However, the process of the transportation could be very complicated. The scale of the process covers a range from the size of an atom to kilometers. The process may be related to chemistry, physics, geology, biology, meteorology, human activities and so on. In fact, there have been a lot of related achievements from different aspects. This research attempted to use statistics to reflect the distribution modes of ore-related elements in macro-scale with the consideration of the buried depth and the grain grades. The results about the change rate of the contents with respect to the depth along with grain grades might be helpful references to other studies, but a lot of detailed and systematic works need to be done. Even for the results of this work, the accuracy and efficiency remain to be verified and improved. That is because that the sample collection and content measurement were limited by present work conditions. Furthermore, the OAPD is new type of data in statistics; there still have no specified models to use for the analysis.

ACKNOWLEDGEMENT This work was financially supported by NSFC (No. 41272362, 40972205), China Geological Survey (No. 1212010633910, 1212011121101) and the “863” project (2009AA06Z110).

REFERENCES

1. Xu, D., Pei, H. et al.: Extraction and applications of the long-term vertical distribution trends of geochemical elements in the loess cover. *Earth Science—Journal of China University of Geosciences*, 37(6), 1135–1139 (2012) (in Chinese)
2. Xu, D., Pei, H. et al.: The extraction of long-term distribution trends of ore-sourced geochemical elements from a drill core in the loess covered area. *Lecture Notes in Earth Sciences. Mathematics of Planet Earth*, 9–13 (2014)
3. Cheng, Q.: Singularity theory and methods for mapping geochemical anomalies caused by buried sources and for predicting undiscovered mineral deposits in covered areas. *Journal of Geochemical Exploration*, 122, 55–70 (2012)
4. Anand, R.R. and Paine, M.: Regolith geology of the Yilgarn Craton, Western Australia: implications for exploration. *Australian Journal of Earth Sciences*, 49, 3–162 (2012)
5. Wang, X.: Conceptual model of deep-penetrating geochemical migration. *Geological Bulletin of China*, 24(10-11), 892–896 (2005) (in Chinese)

6. Tyler, G.: Vertical distribution of major, minor, and rare elements in a Haplic Podzol. *Environmental Pollution*, 119, 277–290 (2004)
7. Ahumada, H. and Garegnani, M.L.: Hodrick-Prescott Filter in Practice. *Jornadas de Economia Monetaria e Internacional*, FCE-UNLP (1999)
8. Hastie, T. and Tibshirani, R.: Varying-coefficient models. *Journal of Royal Statistical Society (Series B)*, 55(4), 757–796 (1999)
9. Cheng, Q. and Xia, Q.: Thoughts and practice for the integrated assessment of mineral resources in covered areas. *Mineral Journal*, suppl. 755–756 (2011) (in Chinese)
10. Liu, D.: Chinese loess. Science Press, Beijing (1965) (in Chinese)

Chapter 75

Hydrothermal Activity in the NE Portion of the Sewell Rise, Central Andaman Trough: Evidences from Multibeam and Petrographic Studies

S. Varghese, K.K. Bhat, and N. Subhash

Abstract The Sewell consists of NE-SW to nearly E-W trending flat topped mounts with intervening valleys with a more steeper SE slope than the NW due to the presence of boundary faults as indicated by the profiles studies. The subvolcanic textured rock is rhyolitic in composition with additional mineral phases of calcite, calcite veins, Fe-oxide veins, albite (An0-10), apatite and titanite which are identified as part of hydrothermal veins. Furthermore, this subvolcanic texture indicate these hydrothermal veins were emplaced at subcrustal level for sometime followed by migration to the surface along the crustal scale faults associated with the Sewell Rise. Fe-Mn-micronodules, Fe (19.81 to 30.82 wt%)-Mn (17.72 to 29.93 wt%) encrustations with Fe-Mn coronas having more or less the same mineral chemistry and close proximity of the Andaman Back Arc Spreading Centre (ABSC) suggests a large scale hydrothermal activity and consequent deposition of initial phase of development of ABSC related sea floor massive sulphide deposits formed at ~4 m.a at different pulses for a prolonged period on the Sewell Rise.

Keywords Multibeam • Sewell rise • Hydrothermal mineralization • Fe-Mn encrustation

75.1 INTRODUCTION

The 650 km wide Andaman basin lies between Burma and Sumatra and extends from the Malay Peninsula to the Andaman Nicobar Islands. The major tectonic processes in this basin are strike-slip faulting parallel to the Sunda trench, back-arc extension and basin formation due to the Andaman Sea Oblique subduction of the Indian plate and leaky transform tectonics driven Andaman back-arc spreading

S. Varghese (✉) • K.K. Bhat • N. Subhash
Operation East Coast-I, Marine and Coastal Survey Division, Geological Survey of India,
Kolkata, India
e-mail: saajuvarghese@gmail.com

[2]. Marine & Coastal Survey Division (M&CSD) mounted the cruise SM-227 onboard R.V. SamudraManthan on the Sewell Rise with the objective to establish the hydrothermal activity in the Sewell Rise.

75.2 METHODS

ResonSeaBat 7150 Multibeam Echo Sounder was used for Multibeam bathymetric survey whereas a Port Dredging Software 2000 (PDS 2000) software was used for acquisition of MBES data, processing to remove all the noises, to generate three dimensional grid models and bathymetric profile sections of the study area. After thin section study, mineral chemical analyses of selected phases of hydrothermal veins and Fe-Mn crust from Sewell Rise were carried out on a Cameca® SX100 Electron Probe Microanalyzer (EPMA), at the EPMA Lab, GSI, Kolkata.

75.3 RESULTS AND DISCUSSION

75.3.1 *Morphology of the Sewell Rise and East Basin*

The bathymetry of the area in general varied from about 760m to as deep as 2900m. In general, the area in the northern half i.e. Sewell Rise region (above 08° 30'N) is very rugged / undulatory with many flat topped (guoyts) mounts trending roughly in NE-SW to nearly E-W direction. For the detailed comparative studies, these ridges are named as Sewell Rise 1, Sewell Rise 2, Sewell Rise 3, Sewell Rise 4 and Sewell Rise 5 (Fig. 75.1). Profile studies indicate that comparatively the SE slope of Sewell Rise 1, Sewell Rise 2 and Sewell is steeper than NW slope (Fig. 75.2). The valley region between Sewell Rise 1 and 2 is very wider with a length of ~15km (Fig. 75.2). It is interesting to note that the slope along SE direction of the Sewell Rise 3 reduces towards the foot of the ridge due to talus deposits. Numerous landslides are picked up along the SE slope of the Sewell Rise 4. The East Basin in the study area is characterized by completely flat monotonous seabed (Fig. 75.1a). The bathymetry varies between 3200m near the Sewell to 2500m near the beginning of Mergui Ridge. So this basin is shallowing up towards the southeastern corner.

75.3.2 *Petrography*

Petrography of hydrothermal veins revealed its subvolcanic texture along with phenocrysts of quartz, plagioclase and calcite, in a matrix of same mineral

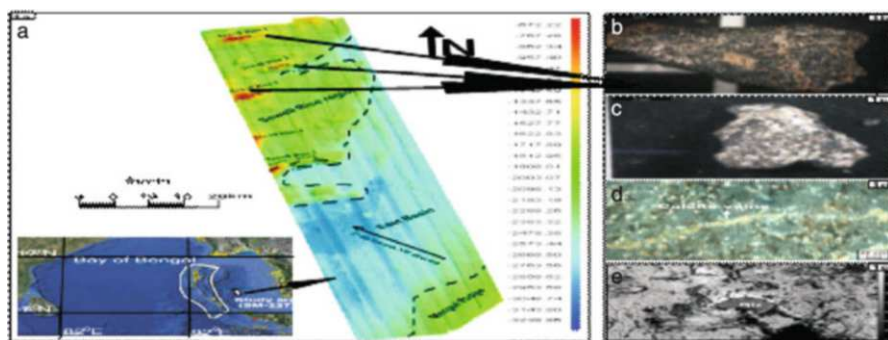


Fig. 75.1 (a) Interpreted 3D Grid Model of the study area. (b) Micro manganese nodule. (c) Fe-Mn encrust. (d) Hydrothermal vein with calcite vein. (e) SEM image of Fe-Mn encrust with entrapped quartz grain from a volcanic source

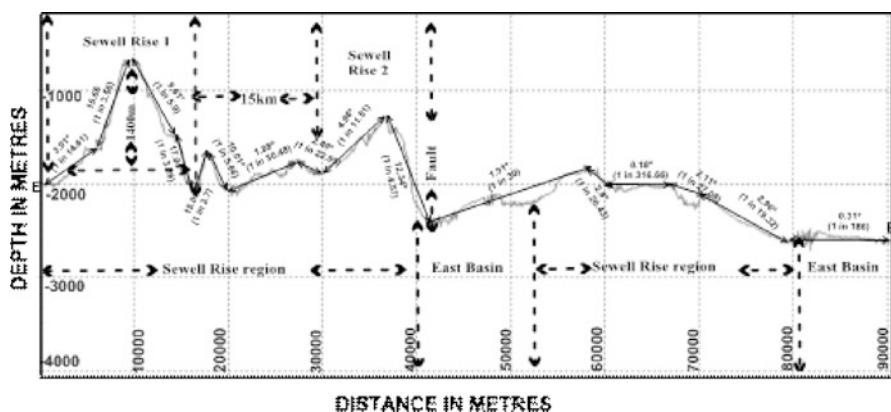


Fig. 75.2 Profile depicting different mounts of Sewell Rise and East Basin

composition. Calcite and Fe-oxide veins and monazite as accessory phase are also present (Fig. 75.1d). The micromanganese nodules (Fig. 75.1b) and Fe-Mn crust (Fig. 75.1c) consists of Fe-Mn corona with arrested phases of quartz grains of volcanic origin (Fig. 75.1e). EPMA studies shows that MnO varies from 22 to 29% whereas FeO ranges from 26 to 29% in the Fe-Mn crust with silica rich areas and identified additional mineral phases of albite (An0-10), apatite and titanite in the hydrothermal veins (Table 75.1).

75.3.3 Discussion

The steeper SE slope of all the seamounts of Sewell Rise, submarine landslides identified on the SE slope of Sewell Rise 4 and talus slope deposits on the Sewell

Table 75.1 Representative Electron Probe Micro Analysis (wt. %) of Fe-Mn encrust and mineral phases in hydrothermal veins from the Sewell Rise

Mineral	Fe-Mn crust	Fe-Mn Crust	Silica rich Fe-Mn crust	Calcite	Calcite vein	Apatite	Albite	Titanite
SiO ₂	11.41	3.17	51.06	2.51	23.65	0.34	65.82	50.02
Na ₂ O	0.54	0.32	0.18	0.05	0.03	0.07	10.85	0.06
MgO	2.16	2.41	4.14	0.17	0.91	0.26	0.01	0.87
Al ₂ O ₃	1.95	1.12	2.57	1.22	6.58	0.03	19.58	3.47
K ₂ O	0.4	0.22	5.1	0.4	4.05	0.09	0.02	0.55
CaO	4.73	4.07	1.19	55.62	24.6	55.1	0.26	1.32
TiO ₂	0.75	0.38	0.04	0	0	0	0.02	26.62
Cr ₂ O ₃	0	0.03	0	0	0.23	0	0	0.11
MnO	22.03	29.93	0.02	0.28	0.2	0.23	0	0.15
FeO	26.81	28.96	23.96	0.54	4.68	0.64	0.03	4.5
NiO	0.27	0.48	0	0	0.06	0	0.03	0
P ₂ O ₅	1.18	1.32	0.06	0.6	0.57	43.08	0.01	0.2
Total	72.25	72.4	88.32	61.39	65.57	99.85	96.62	87.88

Rise 3 are caused by the inferred occurrence of crustal scale faults. The subvolcanic texture of the hydrothermal veins indicate the emplacement at subcrustal level for some time and thereafter the migration of the partially crystallized veins along the faults bounding the Sewell Rise. In addition to these, unusual presence of ubiquitous calcite and calcite veins along with micro manganese nodules and Fe-Mn crusts are direct evidences of the hydrothermal activity persistent in the study area. This calcite veins might have developed due to regional scale CO₂ rich fluid influx associated with a major phase of tectonic event or a large scale volcanic activity associated with ABSC. Subtle changes in the chemistry of different coronas suggest a hydrothermal activity for a prolonged period without having much variation in their total bulk chemistry. These hydrothermal activity probably led to the formation of sea floor massive sulphide deposits (SMS) in the initial phases ABSC formation. All these evidences coupled with hydrothermal mineralization reported from back arc spreading centre and associated sea mounts world wide [1] as well reports of hydrothermal activity from the ABSC [3] near the present study area established the hitherto unidentified sea mount associated concealed SMS deposits on the Sewell Rise.

75.4 CONCLUSIONS

The Sewell Rise is not a single geomorphological unit, rather it encompasses numerous NE-SW trending seamounts and guoyts bounded by faults.

Large scale prolonged hydrothermal activity from a volcanic source driven by tectonic activity is also identified based on Fe-Mn encrustation, micromanganese

nodules and calcite veins probably formed the concealed SMS deposits on the Sewell Rise during the initial phases of ABSC formation ~4 m.a ago.

REFERENCES

1. Both, R.A., Crook, K., Taylor, B., Brogan, S., Chapell, B., Frankel, E., Liu, L., Sinton, J. and Tiffin, D.: Hydrothermal chimneys and associated fauna in the Manus back-arc basin Papua New Guinea. *American Geophy Union Trans*, 67, 489–490 (1986)
2. Curray, J.R.: Tectonics and history of the Andaman Sea region. *J. of Asian Ear Sci*, 25, 187–232 (2005)
3. Surya Prakash, L., Ray, D., Anil, L.P., Abhay, V.M., Satyanarayanan, M., Sreenivas, B., Chandrasekharam, D., Kota, D., Kamesh Raju, K.A., Kaisary, S., Balaram, V. and Gurav, T.: Distribution of REEs and yttrium among major geochemical phases of marine Fe–Mn-oxides: Comparative study between hydrogenous and hydrothermal deposits. *Che Geo*, 312–313, 127–137 (2012)

Chapter 76

Studies on the Seismicity in Garhwal Himalaya, India

Arun K. Shandilya and Anurag Shandilya

Abstract The studies on the basis of the seismic records of seismic events in Uttaranchal a review of the events have been done and a probability of the earthquake has been workout in the part of Garhwal-Kumaun-Himalaya in Uttaranchal. In the southern part of outer Himalaya thrust zones are expected to produce a long term probabilities of large earthquakes of magnitude more than 6, on Richter scale which have on an average 5 to 20 mm reactivation and neotectonic upliftments along the shear zones. These zones have estimated to have future probabilities of earthquakes on these areas which are based on the historical seismic records, the long term slip rate and the displacement caused by the previous seismic events. The historical records of seismic events in these part of the Himalaya have the earthquake intensities varying from 4 to 6.0 on Richter scale in the geological past. The Kangra earthquake (1905) was recorded more than 7.0 Richter scale, Garhwal Earthquake (1883), (6.0), 'Uttarkashi earthquake' (1920), 1991 (5.6, 6.8) respectively, Chamoli earthquake (1999), 6.5 and the Dehradun earthquake of (1970). The approach followed for calculations of probabilities employ the estimated recurrence times with a model that assumes probability increases with elapsed time from the large earthquake on the fault/thrust zone areas. Through the calculated probabilities the estimated natural disaster/hazards in the newly born state of Uttaranchal in Himalayan belt can be reduced.

Keywords Seismicity • Garhwal Himalaya Earthquake • Tectonic

76.1 INTRODUCTION

The past records of the Seismic events along the Himalayan belt in Himachal-Uttaranchal-Nepal, stated to the geological, structural, Seismic observation stations, provides the principle means for evaluating the potential for future earthquakes (Table 76.1, 76.2). After the Kangra (1905) earthquake, this area has experienced many earthquakes of lower magnitude, which has caused in many

A.K. Shandilya (✉) • A. Shandilya
Department of Applied Geology, Dr. Hari Singh Gour University, Sagar, M.P., India
e-mail: akshandilya_u@rediffmail.com

Table 76.1 Chronological listing of earthquakes of $M \geq 5.5$

Ref No.	Year	M	Dt.	Hr	Min	Sec.	Lat. N	Long E	Mar/ M	Depth	Source
1	1816	05	26	22	-	-	30.90	79.00	6.5	-	IMD
2	1842	03	05	21	10	-	30.70	78.00	5.5	-	IMD
3	1902	06	16	-	-	-	31.00	79.00	6.0	-	IMD
4	1906	06	13	-	-	-	31.00	79.00	6.0	-	IMD
5	1911	10	14	23	24	00.0	31.00	80.50	6.7	-	GR
6	1926	07	27	-	-	-	30.50	80.05	6.0	-	IMD
8	1935	03	05	10	34	28.0	29.75	80.25	5.8	-	GR
9	1945	06	04	22	15	53.0	30.30	80.00	6.5	60	IMD
10	1947	08	19	12	08	55.0	31.20	79.09	5.9	-	IMD
11	1949	02	05	20	07	06.0	31.20	79.05	5.5	-	IMD
12	1958	12	28	08	55	20.0	29.5	80.00	6.0	-	CGS
13	1961	12	24	05	34	36.0	29.43	80.83	5.6	59	ISS
14	1962	07	13	07	13	30.0	30.50	79.60	5.5	25	IMD
15	1962	07	14	05	01	06.6	30.40	79.50	5.5	40	IMD
16	1963	01	30	15	58	53.7	29.5	80.90	5.5	-	IMD
17	1964	09	26	10	33	50.0	29.96	80.46	5.8	50	ISC
18	1966	03	06	00	46	02.6	31.50	80.50	6.0	50	ISC
19	1966	06	27	02	15	57.2	29.62	80.83	6.0	06	ISC
20	1966	06	27	10	41	08.1	29.71	80.89	6.0	36	ISC
21	1966	12	16	10	59	18.1	29.62	80.79	5.7	19	ISC
22	1979	05	20	20	52	16.3	29.93	80.27	5.7	16	ISC
23	1991	10	19	22	59	11.6	30.77	78.79	6.4	15	ISC
24	1997	01	05	21	23	15.0	29.80	80.50	5.5	16	IMD/ ISC

Table 76.2 Record of seismic events in the part of Uttaranchal

	Dates		Msg.	Lat N	Long E
Sept.	1	1803	8.0	30.300	78.800
May	26	1816	6.5	30.900	79.000
June	6	1902	6.0	31.000	79.000
Oct.	14	1911	6.5	31.000	80.500
Aug.	28	1916	7.7	30.000	81.000
July	27	1926	6.0	30.400	80.400
Oct.	8	1927	6.0	30.500	80.500
Mar.	5	1935	6.0	29.700	80.200
June	4	1945	6.5	30.000	80.000
Dec.	28	1958	6.2	29.500	80.000
Dec.	31	1958	6.0	30.100	80.700
Sept.	26	1964	6.2	29.600	80.900
June	27	1966	6.0	29.600	80.900
Oct.	19	1991	6.8	30.700	78.770
Mar.	29	1999	6.4	30.550	79.424

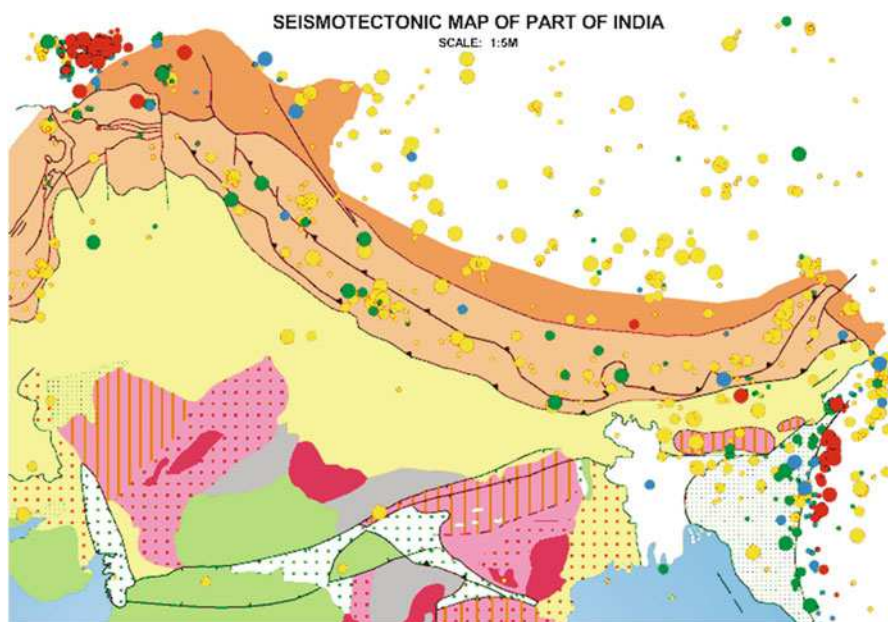


Fig. 76.1 Location of major thrusts/faults in Uttarakhand Himalaya.

areas formation of lakes by one earthquake and it was damaged by another earthquake, causes the flood (1978) in Bhagirathi and Alaknanda River in the geological past in Uttarakhand Himalaya. The Uttarkashi earthquake Oct., 1991, on 6.8 Richter scale and Chamoli Earthquake March 28, 1999, on 6.5 Richter scale caused an havoc with a lot of deaths, injuries and loss of properties and development of cracks on the ground, hill slopes and many neotectonic activities such as reactivation of landslides, hill slopes, and mass movement. Both these earthquakes located in the 200 km wide Main Central Thrust zone areas.

The main reasons for undertaking the calculation of 20 years probabilities due to the recent earthquakes and second consideration of several feature of regional seismicity that may indicate an increased potential of large earthquake, because of these earthquake the slip rate and neotectonic activities are higher. In the Uttarakhand area have wide zone of thrust trending NW-SE in Higher/Central Himalayan area as well as in lower Himalayan, which are characterized by the presence of MBT in the SW part and Krol/Garhwal thrust, Almora thrusts in the Lesser Himalaya and MCT distributed in the north (Fig. 76.1). For the harvesting and harnessing the water resources the Government has planned 62 majors/minor dams on the various river valleys, to generate the hydroelectricity and irrigation both. Since the rocks of terrain is highly sheared fractured with numbers of thrust zone, and fault zone, it may not be able to bear the weight of the water column and load of structure, it will also create the triggered induced earthquakes in near future.

Methods and models for estimated earthquake probabilities are at an early stage of development. Input parameters for the calculation of probabilities are their nature subject to alternative interpretation that may affect specific assessment of hazard. There is nonavailability of data for assessing the potentials for earthquake. However on the basis of few available earthquake-data these probabilities have been calculated and it lead to the conclusion that there is a significant chance of one or more large earthquake in the Uttaranchal region in the coming decades.

76.2 GEOLOGY AND STRUCTURE

The major structures in the rocks of Garhwal Himalaya are characterized by folding, faulting and thrusting and associated minor structures. The thrust tectonics dislocate, separates the rocks of two different geological ages and at places separates the rocks of higher grade metamorphics from low grade metamorphic or sedimentaries.

The important various thrust from South to North in the Uttaranchal are as follows - (1) Main Boundary Thrust (MBT), (2) Krol Thrust (3) Garhwal Thrust (GT) (4) North and South Almora Thrusts (NAT and SAT) (5) Chail Thrust (6) Vaikrita Thrust/Main Central Thrust and (7) Munsiri Thrust.

76.3 SEISMICITY RECORD IN GARHWAL

The seismic records in Garhwal is of violent earthquake of intensity VIII and >VIII occurred on 1st Sept. 1803 in the Central Region of Garhwal range ($30^{\circ}3'70^{\circ}18'$). This earthquake was highly destructive, a large part of the population perished and villages were buried by the fall of cliffs and landslides. Earthquake shocks of magnitude 5–6 on Richter scale have been recorded in 1809, 1816, 1966, 1967, 1968, 1969, 1979 and 1986, 1991, Chamba Earth quake (24th March 1995 on 4.5 Richter scale) respectively. [12] has investigated 252 microearthquake/seismic array in Garhwal, define a 140 km. long belt trending, NW -SE from Yamuna to Alaknanda Valley [6]. The Garhwal Seismic Belt (GSB) at it has been termed by [11] regional trends NW-SE. Over a distance of 35 km. between Yamuna and Bhagirathi valley the belt display a near E- W sinistral offset. This belt is defined by about 20 km. wide zone of numerous epicenters in the SE through a few epicenters fall outside, the zone in the vicinity of the North Almora Thrust. The northern boundary of GSB is better defined than the southern margin, where some epicenters are even located south of Tehri. The GSB cut across all the numerous thrust sheets located within higher Himalaya. The majority of earthquake in Garhwal are lie close to a south of MCT. The estimated depths of 193 local earthquakes were less than 10 km. and for 32 earthquakes were in the range of 10 to 15 km. In the overall

picture for the period 1984 to 1991 indicate the seismicity is concentrated in the between MCT zone and MBT zone (Table 76.1 and 76.2)

76.4 SEISMOTECTONICS

Seismic activity along the Bhagirathi and Alaknanda valley is ascribed to north word movement of Indian plate against the Tibetan Block of Eurasian plate at the rate of 0.05 to 0.06 in per year [4, 15]. The geological across section shows the various schuppens, floor and roof thrusts through, which have ridden over as duplexes. In the geological section correlation of the major tectonic units with the microseismicity is suggesting that most of the stress released through micro earthquakes occurred in the Himalaya, in south of MCT zone. North of MCT micro-seismic activity, is comparatively reduced, suggesting accumulation of stress, part of which was released in the recent Uttarkashi earthquake. Along the Bhagirathi valley in Uttarkashi region lies in a seismic gap between the rupture zones of 1895 earthquake of Garhwal, 1905 Kangra and 1934 Bihar earthquakes, [14] indicated an isolated contour of intensity VII surrounding. Dehradun-Mussouri, which are located 250 km SE of Kangra. A rupture zone through out the entire 250 km. Length from Kangra to Dehradun can be interpreted. The rupture zone runs NW -SE and is confined to the MBT zone, whereas the Uttarkashi earthquake and the local earthquakes in Garhwal are concentrated south of the MCT zone. It appears that both the thrust MBT and MCT are seismically active.

The epicentre of the Uttarkashi earthquake and Chamoli earthquake are located at a focal depth of 12 km (IMD) and 10.3 km (USGS) lies in the Vaikrita, Chail Thrusts. The micro earthquake activity is concentrated much further south of the MCT along the NAT and Pratap Nagar thrusts in Alaknanda valley. These two thrusts lie within the Tehri, and Srinagar dam sites. In the Uttarkashi area south of MCT the Dharasu fault and Jutogh fault are active and associated with the growth of antiform. These major thrusts MCT, Pratapnagar, and North Almora thrust become flattened at depth and become linked with the basement thrust.

[18] have evaluated the seismotectonics of NW Himalaya and classified them into Five seismotectonic domains of discrete deformation phases and seismic behaviour. These seismic zones are - (1) Main Himalayan seismic zone (2) High plateau seismic zone (3) High Himalayan seismic zone (4) Kashmir syntaxial seismic zone (5) Foot hill seismic zone. The Garhwal region were the Chamoli earthquake occurred on 28.03.1999, is located in the Main Himalayan seismic zone, the seismicity of which is predominantly related to the underthrusting decollement surface. [16] suggest that the MCT in north and MBT in south, displays a concentration of seismic events at different localities in Garhwal and Kumaun Himalaya.

[17] has divided the main longitudinal Himalayan seismic zone into discrete seismotectonic segments with will defined transverse boundaries marked by interpretative fundamental faults. The segments are - (1) Kashmir block (2) Chamba

Kishtwar block (3) Kangra block (4) Simla block (5) Garhwal block (6) Kumaun block.

The assessment of the Uttarkashi (20.10.1991) and Chamoli (1999) earthquakes source mechanism located near the intersection of the Himalayan transverse fault which has displaced the MCT in Bhagirathi valley near Uttarkashi and the fault propagation has taken place in south eastern direction and along the Alaknanda valley in Central Garhwal region. The seismicity defined by the local networks have indicated concentration of events in the vicinity of MCT and MBT. The seismicity is prominently north of the MCT and in Okhimath Gopeshwar area these are in either side of MCT [13], consistent with teleseismic concentration. The majority of the local network events are located within a depth of 15 km. [13] represent the deformation of the lesser Himalaya ranges and from seismic front roughly following the elevation front. It is therefore; clear that the Garhwal region have high level of seismic activity, the Chamoli earthquake 29 March, 1999 and Uttarkashi 20.10.1991 are the prominent seismic recent events in the area. Incidentally in 1962, two earthquakes of magnitude 5.5 on Richter scale were recorded from the same epicentrallocation.

76.5 MAIN SHOCK AFTER SHOCKS

The main shock on Oct. 20, 1991 of 6.6 on Richter scale in Uttarkashi area and 29 March 1999 of 6.5 on Richter scale in Chamoli area were followed by more than a thousand after shocks within a magnitude range 0.5 to 5.2, the later being the largest aftershock, which occurred on the next day. The Indian Meteorological Deptt. (IMD), New Delhi relocated the epicenter with 26 seismic station data within 300 km of the affected area and determined the epicenter as 30°75'N and 78°86'E for Uttarkashi Earthquake and 30°40'8"N and 79°41'6"E for Chamoli earthquake at the depth 12 km and 21 km. respectively. Based on the data from very close seismic station network (one of them being in epicentral region) operated by the Tehri Dam Project authority WIHG and NGRI. The WIHG has located the epicenter east of Uttarkashi. The US Geological based on 525 observation from global network data gave the epicenter east of Uttarkashi. The epicenter given by various organisations confirms its location east of Uttarkashi in spite of a discrepancy of the order of 10 km - 12 km between the various determinations. In the Chamoli region the maximum number of shocks were felt between Mandal and Chamoli. 30 after shocks of magnitude about 3 or more, occurred on the first day i.e., on 29/03/2000 and over 10 each on the next two days.

Field stations daily recorded 20–30 shocks of magnitude over 1.0 for about a month. Subsequently, the aftershocks gradually reduced an aftershock of 5.3 occurred an hour after mainshock. The largest aftershock of 5.5 occurred on 14.4.99. After Chamoli earthquake the after shocks of magnitude >4 and 5.0 which occurred in 20 days. In comparison to Uttarkashi earthquake have seven

aftershocks of magnitude >4.0 , which occurred in eight day (with 1 shock of >5.0). The total moment released for Chamoli after shock sequence is 6.2×10^{24} dynes cm., which is 7 times more than that of Uttarkashi aftershock segment, but 8 time less than that for the Chamoli main shock.

After shocks which continued for about two months in Uttarkashi area, occurred in are of 30×40 sq.km. between Bhagirathi and Bhilangana valleys and define a NW–SE trend. Most of the after shocks are less than 15 km. deep. The peak accelerations were highest at Bhatwari and Uttarkashi being of order of 30% of g. The maximum duration of acceleration or strong shaking with acedARATION more than 1% of was 40 second (Table 76.3).

Factors considered which affect the estimates of probabilities are:

(1) Faster fault slip rate - Estimate of the long term rates of slip on the MBT, MCT, Krol and Almora thrusts and associated faults are revised upward relative to the previous estimates. A higher slip rate shortens the expected time to the next earthquake and increases the likelihood of an earthquake. The estimates of slip rate on MBT in foot hills of Himalayas to be 20-22 mm/yr compared to the earlier estimates of 15-16 mm/yr. The slip rate on the NAT/SAT and MCT in lesser Higher Himalaya is estimated at 9 to 11 mm/yr. compared to earlier estimate of 6-7 mm/yr.

(2) Model of crustal deformation indicate that stress increased on nearby segment of MBT, KT, NAT, SAT and MCT after the Kangra earthquake (1905), Uttarkashi earthquake (1991), Chamoli earthquake (1999), recent earthquake. The stress increase shortens the time to the next earthquake on these segments.

Recurrence model: The earthquake proability estimates in this paper are based on current stochastic recurrence models of characteristic earthquake, including explicit consideration of the uncertainty in the values of the parameters of these models. By characteristic earthquake's it mean the relative narrow range of large events associated with successive complete ruptures of a specific segment [24]. The frequency of occurrence of such events is not necessarily predicted by extrapolation of the conventional (Gutenberg Richter) Linear (log) frequency vs. magnitude relationship. Further, because characteristic earthquakes are associated with a cycle of major stress drop and stress recovery, it is believed that the interevent or recurrence, times of these events may follow a temporal pattern associated with a relatively narrow probability distribution (Poissonian recurrence model). In contrast to the Gutenberg-Richter magnitude-frequency distribution and familiar poisson recurrence model, the two general characteristics are - (1) a relatively

Table 76.3 Earthquake probability in thrusts zone areas

Thrust zone	Approx. length in km.	Approx. width zone in km.	Expected magnitude or Richter scale
MCT	400	5 to 10.0	6to 7
Almora thrust	350	1.0 to 4.0	5.5 to 6
Krol thrust	250	1.0 to 4.0	5.5 to 6
MBT	400	0.5 to 2.0	6to 7

narrow magnitude (slip per event) range and (2) a relatively narrow recurrence time distribution are consistent with the notions of near constant strain rate and a nearly deterministic characteristic earthquake cycle.

There are many probabilistic models that display these two basic characteristics— (1) Renewal model (2) Time predictable model.

76.6 SUMMARY

By using the available information, reasonable assumption, and simple models, recurrence models, renewal models, it strives to make projections about the location size and times of future earthquakes. The types of basic information used are as follows:

1. Identification major thrust /fault zone judges to be capable of producing large earthquake in future.
2. Estimate of the amount of displacement and thus the magnitude of future large earthquakes likely to occur during rupture these thrust zones.
3. Estimate of the median recurrence intervals and their uncertainty for major earthquake on the thrust zones.
4. Earthquake of the date of most recent large earthquake for each of the thrust zone.

There are considerable uncertainties associated with each of these types of basic earthquake information. In particular, knowledge of the average time interval between segment rupturing earthquakes, which might be learned from palaeo seismic studies, might permit major revisions of the consensus forecast presented here. In the part of Uttarakhand Himalaya the possibilities of earthquakes have been calculated that in the coming 20 years there is a chance of experiencing a major earthquake of more than 7.0 magnitude in the Thrust zone areas. In the present calculation for the 20 year probability of one or more earthquake of magnitude 6.0 to 7.0 in Uttarakhand Himalaya along MCT zone and MBT zone to be 5.0 to 7.0 value. The probability was aggregated from the probabilities computed for individual thrust zone, which includes the Almora thrust (3.0 – 4.0), Garhwal-Krol thrust zones (4.0 to 5.0) and MCT-MBT zone have higher probability 5.0 to 7.0 value.

REFERENCES

1. Auden, J.B.: Structure of Himalaya in Garhwal. *Rec. Geol. Surv. Ind.* 71 (1937).
2. Benjamin, T.R. and Cornell, C.A.: Probability, statistics & decision for Civil Engineers, New York, McGraw Hill (1970)

3. Budding, K.E., Schwartz, D.P., Ostergren, C.L. and Hoirup, D.F.: Preliminary sliprate and earthquake recurrence Northern California (abs) EOS. *Transaction of AGU*. 70, 121 (1989)
4. Dewey, J.F. and Bird, J.M.: Mountain belt and the Global tectonics. *Jour. Geophys. Res.* 75, 2625–2647 (1970)
5. Gansser, A.: *Geology of Himalaya*. Interscience Publrs. London (1964)
6. Gour, V.K., Chander, R., Sarkar, L., Khattri, K.N. and Sinvahal: Seismicity and the state of stress from investigation of local EQ in Kumaun Himalaya (1985)
7. Gupta, H.K. and Gupta, G.D.: Uttarkashi earthquake. *Geol. Soc. of Ind. Mem.* (1995)
8. Gupta, H.K. and Gupta, G.D.: The Uttarkashi Earthquake Oct. 20, 1991. *Geol. Soc. of Ind Memoir* 30 (1995)
9. Gutenberg, Richter Schwartz, D.P. and Coppersmith, K.J.: Fault behaviour and characteristic earthquake example for Wasatch and SanAndreas Fault Zone. *Jour. of Geol. Res.* 89, 5681–5698 (1984)
10. Hagiwara, I.: Probability of earthquake occurrence as obtained from weibull distribution analysis of crustal strain. *Tectonophysics*, 23, 313–318 (1974)
11. Jain, A.K. and Chander R.: Geodynamic model for Uttarkashi earthquake of Oct. 1991. *In: Uttarkashi EQ*, *Geol. Soc. Ind.* (1995)
12. Khattri, K.N.: Great earthquake seismicity gaps and potential for EQ along the Himalayan plate boundary. *Tectonophysics*, 38, 79–92 (1987)
13. Khattri, K.N.: Seismic hazards in Indian region. *Current Science*. 62, 109–116 (1992)
14. Middlemiss, C.S.: Crystalline and Metamorphic rocks of Lower Himalaya. *Rec. Geol. Surv. Ind.* 30(i), 134–143 (1888)
15. Molnar and Tapponnier: Cenozoic tectonics of Asia: effect of a continental collision. *Science* 489, 419–426 (1975).
16. Narula, P.L.: Seismotectonic evaluation of NW Himalaya. *Rec. Geol. Surv. Ind.* 124, 8 (1991)
17. Narula, P.L.: Neotectonic activity, seismicity and related contemporary deformation in the NW Himalaya. *Symp. on Himalayan Geol.* Shimane, Japan, 33–36 (1992)
18. Narula, P.L., Ravishankar and Chopra, S.: Rupture deformation of Chamoli earthquake on 29.03.1999 and its implication for seismotectonics of Garhwal Himalaya. *Jour. Geol. Soc. Ind.* 55, 493–503 (2000)
19. Nishenko, S.P. and Buland, R.: A generic recurrence interval distribution earthquake forecasting. *Seis. Soc. of Am. Bull.* 77, 1382–1399 (1987)
20. Reid, H.F.: The mechanics earthquake in Lawson, A.C. Chairman. The California earthquake. AP of the 18. 1906. Report of state earthquake investigation commission, Carnegi. Instt. of Washington 87 (1910)
21. Saklani, P.S.: Structure and Tectonics of Pratapnagar area G. Himalaya. *Him. Geol.* 1, 75–91 (1971)
22. Sibson, R.: Roughness at the base of seismogenic zone: contributing factors. *Jour. of Geophys. Res.* 84, 5791–5800 (1984)
23. Schwartz, D.P. and Copper Smith, K.J. Fault behaviour and characteristics earthquake examples for Wasatch and San Andreas Fault zone. *Jour of Geology Res.* 89, 5681–5698 (1984)
24. Shimazaki, K. and Naketa, T.: Time predictable recurrence model for large earthquake. *Geophy. Res. Letters* 7, 279–282 (1980)
25. Shandilya, Arun K.: Studies on Structure and Morphotectonic between Srinagar thrust and Alaknanda fault G. Himalaya. Unpubl. D.Phil. Thesis, HNBBG University, Srinagar Garhwal, Utranchal (1984)
26. Shandilya, Arun K.: Analysis of thrusts around Srinagar Garhwal. *Jour. Madhyabharti*, Dr. HSGVV/Sagar University, Vol. 39 (1994)
27. Shandilya, Arun K.: Seismotectonic and geotechnical studies of some Himalayan dams in Garhwal. *Proc. Indian Geophy. Union Vol. 36 Pondicherry* (1999)
28. Shandilya, Arun K.: Seismotectonic model for recent earthquakes in Garhwal Himalaya. *Proc. ASC.* 2000. Uni. of Tehran. I.R. Iran (2000)

29. Shandilya, Arun K. and Negi, R.S.: Seismotectonic model for recent Earthquakes in Garhwal Himalaya. *Qtrly Jour. of GARC*, 9(4), 73–82 (2001)
30. Shandilya Arun K. and Negi, R.S.: (2003) Probabilities of Earthquakes in Uttaranchal Himalaya. *In: Central Himalaya Environ. and Development V 01.11* Ed. Dr. MSS Rawat. HNB G University, Srinagar Garhwal (2003)
31. Thakur, V.C.: Geology and Seismo aspects in Himalaya in U. Proc. Environ. Impact of WRD. Instt. of Engineers, New Delhi, Tata McGraw Hill Publ., New Delhi (1994)
32. USGS: Report no 1053 Probability earthquake in San Francisco Bay Region (1990)
33. Valdiya, K.S.: Geology of Kumaun Lesser Himalaya. WIHG Dehradun (1980)

Chapter 77

Shear Seam in Dam Foundation System

Abhishek Singh and Shilpa Pal

Abstract Dams are the hydraulic structures built with impervious material across river which provides water impounding for various purposes. These structures are constructed on rock formation so proper stress deformation analysis should be done. So it is important to analyze different stress concentration which results into undesirable deformation in dam foundation system. The paper presents analysis of dam foundation system under the shear seam using explicit finite difference method. Seams not only change the physical properties of the rock in and near the discontinuous zones, but they substantially affect the distribution of stresses and the overall stability of dam foundation. With different inclination of seam, stress deformation is concluded in the dam foundation system. These seams originate from the heel and software used for the analyses is FLAC 3D (Fast Lagrangian Analysis of Continua in 3 Dimensions). From the study it was concluded that the most critical case is the dam-foundation system with 120° inclined shear seam.

Keywords Shear seam • Flac 3D • Explicit finite difference • Dam foundation system • Stress contours • Concrete plugs

77.1 INTRODUCTION

Concrete dams are constructed on rock foundations because of their huge weight or high density. Rock foundations have a very large load bearing capacity which resist erosion and reduce permeability. Dams are hydraulic large structures which apply load to geological media or foundation system which lead to significant failures. These failures can be excessive settlement, presence of undetected weak seam, deterioration of rock with time. Faults and seam results in distribution of stresses, displacements and had an adverse effect on dam foundation system. Low modulus value create zone of stresses results to small openings. Numerical models are used in the analysis of the global mechanical behavior of dam foundation systems under normal operating conditions. Since structural behavior get strongly influenced by

A. Singh (✉) • S. Pal
Gautam Buddha University, Ghaziabad, Uttar Pradesh, India
e-mail: abhi23193@gmail.com

rock deformability which further results in large displacements. This paper focuses on stress deformation of dam foundation system carried out using FLAC 3D

77.2 PROBLEM GEOMETRY

A concrete gravity dam, 80m high and 72m base width is founded on 400m wide and 200 m deep rock foundation. The upstream face of the dam is vertical. The foundation is considered to have a shear seam of $1/10^{\text{th}}$ of the base width of the dam originating at the heel of the dam. The strength properties of the seam are taken $1/5^{\text{th}}$ the strength of the intact rock mass. Different inclinations of shear seams in the foundation have been considered for the study.

77.2.1 Analysis

The dam foundation system has been analyzed with a loading condition of self-weight of dam. The shear seam is assumed to exhibit $1/5^{\text{th}}$ the strength properties of the intact rock mass. Further the width of seam is taken $1/10^{\text{th}}$ the width of dam. The concrete and intact rock is assumed to exhibit linear elastic behavior, whereas joints are assumed to exhibit nonlinear elasto-plastic behavior. As seam originate at the heel with inclination varying from 60° to 120° with an increment of 30° in anticlockwise direction.

77.2.2 Software Used

The analysis has been carried out using the software FLAC 3D (*Fast Lagrangian Analysis of Continua in 3 Dimensions*) which is a three dimensional numerical program based on the explicit finite difference program. It simulating the behavior of three-dimensional structures built of soil, rock or other materials that undergo plastic flow when their yield limits are reached.

77.2.3 Material Properties

The dam foundation is considered to consist of quartz mica schist with the following properties of the rock mass [2], concrete, shear seam and concrete-rock interface in Table 77.1.

77.3 RESULT AND OBSERVATION

Shear seam in Dam foundation system assumed to originate at the heel with inclination varying from 60° to 120° with increment of 30° in downstream direction. Each condition is identified by the case number. The various cases are made as follows:

Case 1: Intact rock with no seam Case 3: Intact rock with shear seam at 90° Case 2: Intact rock with shear seam at angle 60° Case 4: Intact rock with shear seam at angle 120° The contours of principal stresses about Z axis in dam foundation system in respect of all cases presented in figure (77.1), (77.3), (77.5), (77.7) and in figure (77.2), (77.4), (77.6), (77.8) maximum unbalanced force can be derived in account to total force applied. Here, unbalanced force approaches a very small value; this indicates that an equilibrium state is reached. Displacement caused at toe of dam

Table 77.1 Material and their properties

Material	Properties
Intact Rock	Unit weight = 27.23 KN/m ³ , Bulk Modulus = 4780 MPa, Shear Modulus = 3580 MPa
Concrete	Young's Modulus = 201 x 10 ⁴ MPa, Poisson's Ratio = 0.15 Unit weight of concrete = 24 KN/m ³
Seam	Unit weight = 26.5 KN/m ³ , Bulk Modulus = 956 MPa, Shear Modulus = 716 MPa, Joint normal Stiffness = 100 MPa/m, Joint shear Stiffness = 100 MPa/m, Friction angle = 16°, Cohesion = 0 MPa
Concrete and rock Interface	Joint normal stiffness = 1200 MPa/m, Joint shear stiffness = 1000 MPa/m, Friction angle = 45°, Cohesion = 0.1 MPa

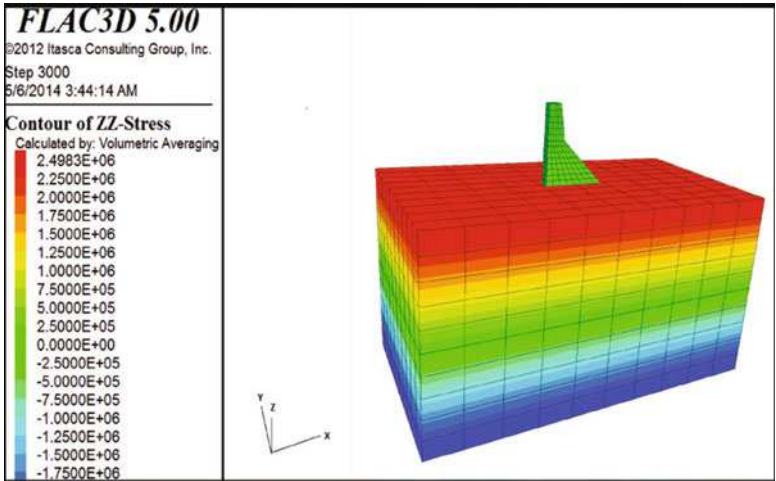


Fig. 77.1 Contours in dam foundation system with no seam

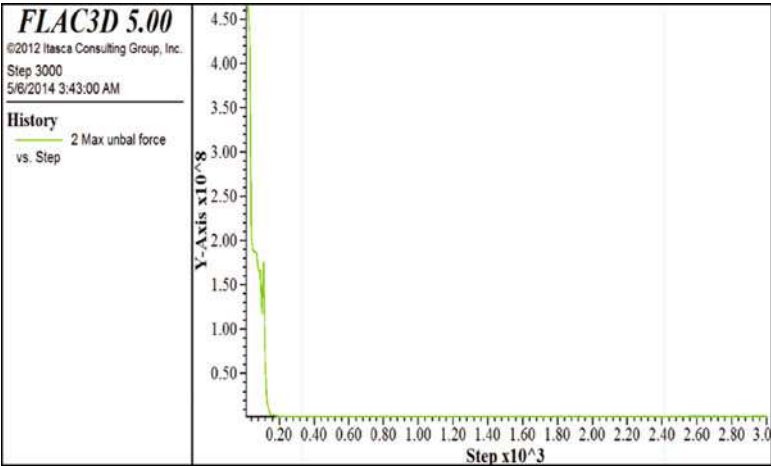


Fig. 77.2 Unbalanced forces in dam foundation system

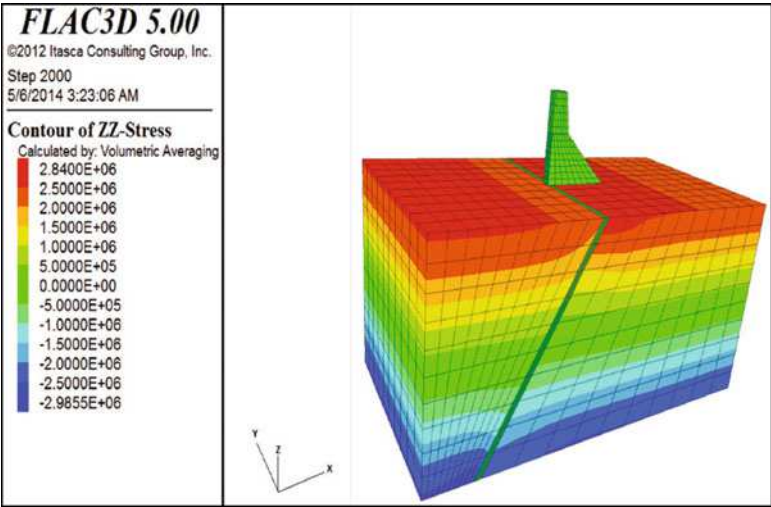


Fig. 77.3 Contours in dam foundation system with seam at 60°

with respect to the stresses in intact rock foundation presented in table 77.2,77.3,77.4,77.5 in respect of all cases. Grid ID (33, 34, 53, 71, 89, 107, 125, 143, and 161) represents the location of toe of the Dam.

- Case I - Intact Rock with No Seam
- Case II - Intact Rock with Seam at 60°
- Case III - Intact Rock with Seam at 90°
- Case IV - Intact Rock with Seam at 120°

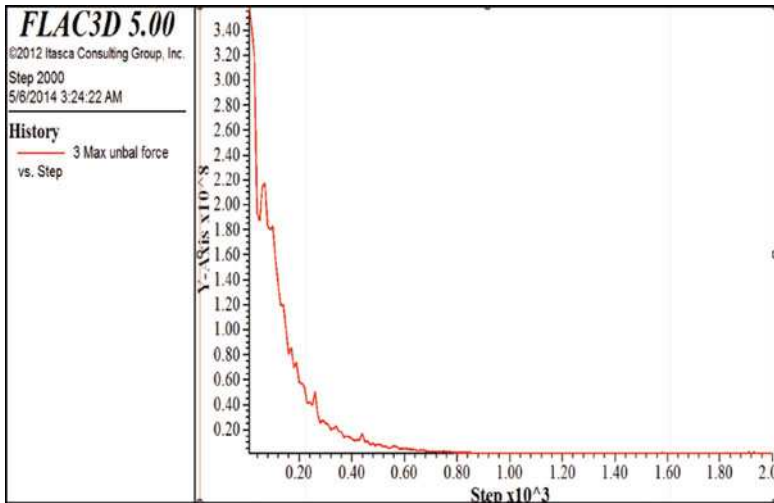


Fig. 77.4 Unbalanced forces in dam foundation system

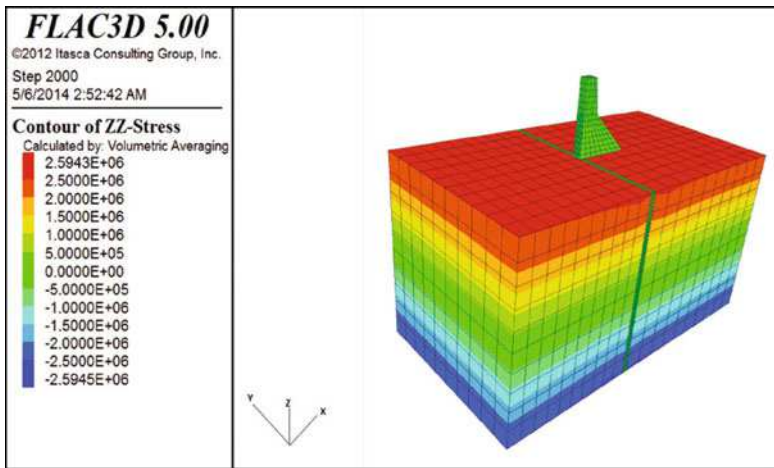


Fig. 77.5 Contours in dam foundation system with seam at 90°

77.3.1 Graphical Interpretation

As the toe of Dam is most stressed zone, displacement analysis has been carried out for the Dam foundation system using FLAC 3D. From graphical interpretation shown in Fig. 77.9, it is clearer that displacement would be maximum in case of the rock foundation system with shear seam at an angle of 120° (about both X and Y axis) and the most unstable one.

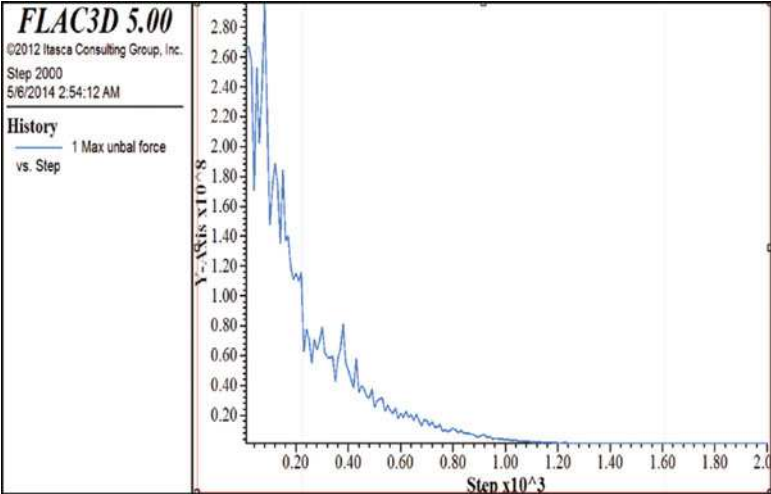


Fig. 77.6 Unbalanced forces in dam foundation system

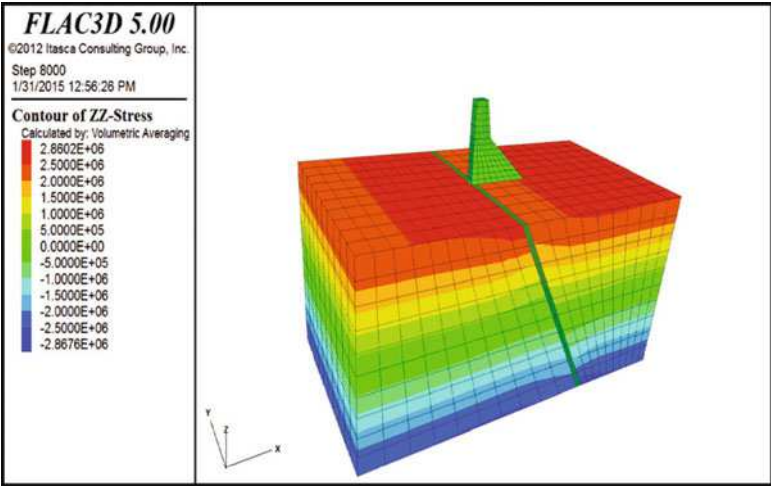


Fig. 77.7 Contours in dam foundation system with seam at 120°

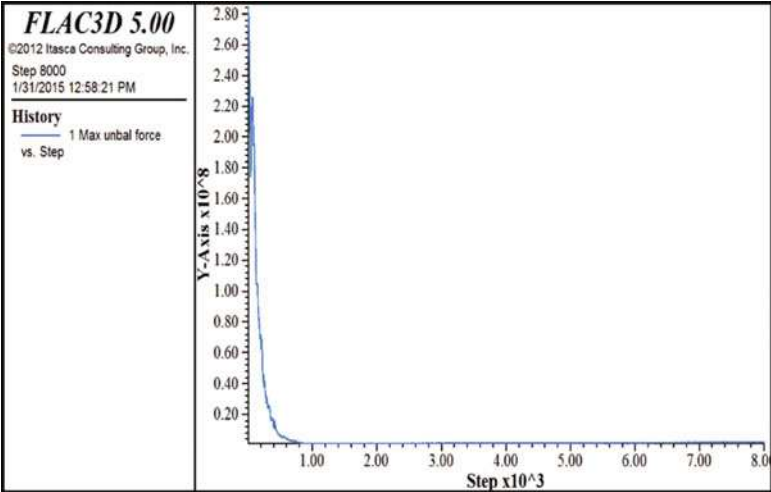


Fig. 77.8 Unbalanced forces in dam foundation system

Table 77.2 Represent displacement with respect to Grid ID

Grid ID	Position	Displacement
33	2.36e+02, 1.0e+02, 2e+02	1.392421e-02, -7.885761e-02, 0.000000e+00
34	2.36e+ 02, 1.0125e+02, 2e+02	1.564695e-02, -5.482387e-02, 0.000000e+00
53	2.36e+02, 1.025e+02, 2e+02	2.032476e-02, -3.191151e-02, 0.000000e+00
71	2.36e+02, 1.0375e+02, 2e+02	2.762869e-02, -1.283753e-02, 0.000000e+00
89	2.36e+02, 1.05e+02, 2e+02	3.956766e-02, -5.362415e-05, 0.000000e+00
107	2.36e+02, 1.0625e+02, 2e+02	2.781667e-02, 1.290489e-02, 0.000000e+00
125	2.36e+02, 1.075e+02, 2e+02	1.983278e-02, 3.119687e-02, 0.000000e+00
143	2.36e+02, 1.0875e+02, 2e+02	1.502705e-02, 5.378027e-02, 0.000000e+00
161	2.36e+02, 1.10e+02, 2e+02	1.433510e-02, 7.783233e-02, 0.000000e+00

Table 77.3 Represent displacement with respect to Grid ID

Grid ID	Position	Displacement
33	2.36e+02, 1.0e+02, 2e+02	6.478118e-03,-3.488744e-02, 0.000000e+00
34	2.36e+02, 1.0125e+02, 2e+02	7.252285e-03,-2.376733e-02, 0.000000e+00
53	2.36e+02, 1.025e+02, 2e+02	8.944550e-03,-1.307675e-02, 0.000000e+00
71	2.36e+02, 1.0375e+02, 2e+02	1.261159e-02,-5.159923e-03, 0.000000e+00
89	2.36e+02, 1.05e+02, 2e+02	1.796979e-02,-1.531693e-05, 0.000000e+00
107	2.36e+02, 1.0625e+02, 2e+02	1.262484e-02, 5.182731e-03, 0.000000e+00
125	2.36e+02, 1.075e+02, 2e+02	9.095631e-03, 1.347064e-02, 0.000000e+00
143	2.36e+02, 1.0875e+02, 2e+02	7.933462e-03, 2.434929e-02, 0.000000e+00
161	2.36e+02, 1.10e+02, 2e+02	6.601992e-03, 3.546004e-02, 0.000000e+00

Table 77.4 Represent displacement with respect to Grid ID

Grid ID	Position	Displacement
33	2.36e+02, 1.0e+02, 2e+02	8.034637e-03, -3.798558e-02, 0.000000e+00
34	2.36e+02, 1.0125e+02, 2e+02	8.451180e-03, -2.477007e-02, 0.000000e+00
53	2.36e+02, 1.025e+02, 2e+02	9.857878e-03, -1.290962e-02, 0.000000e+00
71	2.36e+02, 1.0375e+02, 2e+02	1.402840e-02, -4.555093e-03, 0.000000e+00
89	2.36e+02, 1.05e+02, 2e+02	1.982239e-02, -7.270726e-05, 0.000000e+00
107	2.36e+02, 1.0625e+02, 2e+02	1.402669e-02, 4.805443e-03, 0.000000e+00
125	2.36e+02, 1.075e+02, 2e+02	1.003062e-02, 1.331856e-02, 0.000000e+00
143	2.36e+02, 1.0875e+02, 2e+02	8.773085e-03, 2.506099e-02, 0.000000e+00
161	2.36e+02, 1.10e+02, 2e+02	8.073573e-03, 3.803793e-02, 0.000000e+00

Table 77.5 Represent displacement with respect to Grid ID

Grid ID	Position	Displacement
33	2.36e+02, 1.0e+02, 2e+02	5.907357e-02, -5.379596e-01, 0.000000e+00
34	2.36e+02, 1.0125e+02, 2e+02	5.148338e-02, -3.852864e-01, 0.000000e+00
53	2.36e+02, 1.025e+02, 2e+02	7.903634e-02, -2.409398e-01, 0.000000e+00
71	2.36e+02, 1.0375e+02, 2e+02	1.187020e-01, -1.053522e-01, 0.000000e+00
89	2.36e+02, 1.05e+02, 2e+02	1.880790e-01, -2.865273e-03, 0.000000e+00
107	2.36e+02, 1.0625e+02, 2e+02	1.194648e-01, 9.991623e-02, 0.000000e+00
125	2.36e+02, 1.075e+02, 2e+02	8.051871e-02, 2.334286e-01, 0.000000e+00
143	2.36e+02, 1.0875e+02, 2e+02	5.842167e-02, 3.805848e-01, 0.000000e+00
161	2.36e+02, 1.10e+02, 2e+02	6.489267e-02, 5.355769e-01, 0.000000e+00

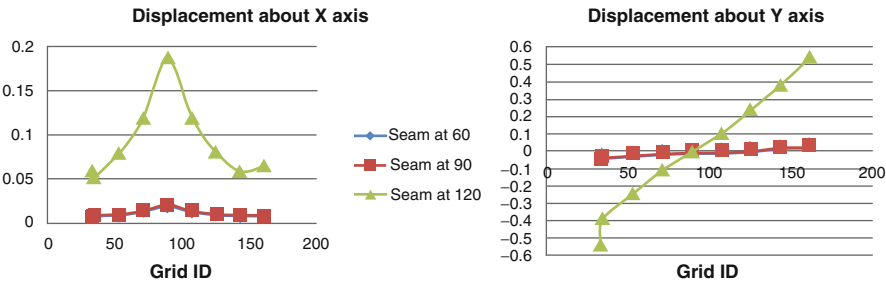


Fig. 77.9 Graphical interpretation of the displacement caused by shear seam in dam foundation system at different inclination

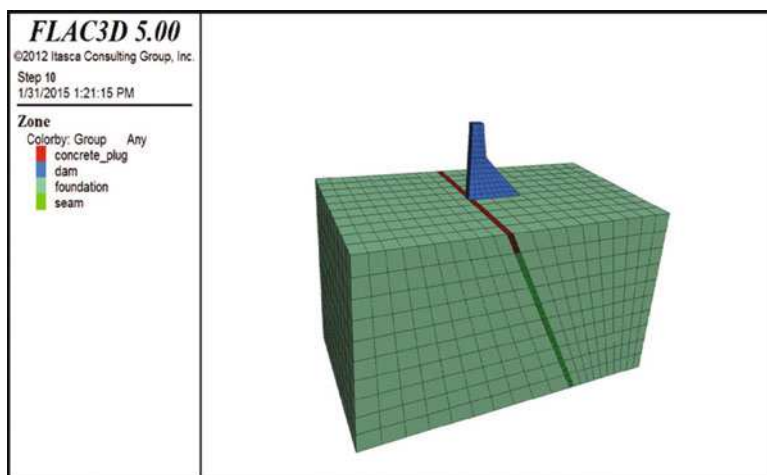


Fig. 77.10 Concrete plug remedy

77.4 CONCLUSION

The presence of seam in the dam foundation system has considerable effect on the foundation behavior. The present study indicates that:

- The stresses and displacement in the dam foundation system with shear seam increase considerably up to a certain depth with respect to the intact rock.
- Presence of shear seam at any inclination in dam-foundation weakens the system, the foundation with seam inclination 120° is the most critical one.
- From the figures it is clear that dam fails when seam is at downstream side. This show the results which we procured are correct and verified.

Remedy

- The shear seams in the foundation are treated by providing concrete plugs as shown in Fig. 77.10.
- The stresses can be reduced due to the placement of concrete plug. The efficiency can also be seen from the reduction of the deformation at the heel.

REFERENCES

1. Gupta, Manish and Dhawan, A.K.: Effect of shear seam in Dam Foundation. Central Soil and material research station.
2. Varadarajan, A., Sharma, K.G. and Kumar, Rakesh: Analysis of Masonry Dam Foundation by Distinct Element Method (2002)
3. Itasca Consulting Group Inc. FLAC 3D (2012)
4. User's manual Version 5.0, Minneapolis IS 6512 (1984)

Chapter 78

Geothermobarometry and Barrovian Metamorphism of Darjeeling-Mangpu Region, Eastern Himalaya

Suparna Tewari and Divya Prakash

Abstract Along the Darjeeling–Mangpu region, polyphase deformation and barrovian metamorphism has been delineated in relation to the Main Central Thrust (MCT). The different parageneses of pelitic rocks containing chlorite, muscovite, biotite, garnet, staurolite, kyanite, sillimanite, k-feldspar and plagioclase show various texture resulting by the continuous and discontinuous reactions in the different zones. From the Microprobe data of the coexisting minerals show that X_{Mg} varies in order garnet < staurolite < biotite < chlorite. White mica which is the solid solution between muscovite and phengite is the commonest mineral within the lower grade; garnet is almandine rich showing normal zoning in the lower part of the MCT and in the upper parts shows reverse zoning. In the lower grade rocks the oriented chlorite, mica grains and rolled garnet formed syntectonically and after succeeded by cross cutting mica, chlorite and idioblastic garnet. P-T condition estimated by different models of geothermobarometry, the temperature value range from 570°C for garnet zone and 780°C for sillimanite zone and the pressure range from 5 kbar to 7.5 kbar. Different models have been proposed to explain inverted metamorphism but recently the channel flow model which defines a flow of a weak crustal layer in between relatively rigid yet deformable crustal slab is most appropriate. If the channel flow is operating at the same time of focused denudation, this can result in exhumation of channel material within a narrow, nearly symmetric zone.

Keywords Geothermobarometry • Barrovian metamorphism • Darjeeling-Mangpu • Lesser Himalaya

S. Tewari (✉) • D. Prakash

Centre of Advanced Study in Geology, Banaras Hindu University, Varanasi, India

e-mail: suparnatewari87@gmail.com

78.1 INTRODUCTION

The area under investigation is about 35 km from Darjeeling main town (Fig. 78.1). The area constitutes a portion of lesser Himalaya probably of Precambrian to Palaeozoic age. The area constitutes the rocks of Daling and Darjeeling group, [1] first distinguishes the two main lithological units. These are thrust over the Lower Gondwana Damuda Formation of Permian age by Daling Thrust. The area has undergone multiple deformation and at least three phases of deformation viz. D_1 , D_2 , D_3 have been recognized which presumably occurred during the Tertiary Himalayan orogeny.

In this part of the region, numbers of workers have provided detailed geological study [2–6]. The aim of this study is to carry out a detail account of petrography, mineral chemistry and geothermobarometry of metapelites.

78.2 PETROGRAPHY

Under the microscope the rocks display a prominent S_1 foliation defined by the prominent preferred orientation of white mica, inequant quartz and ilmenite. At some places tight F_1 microfolds are seen in which S_1 has developed along the axial-plane of F_1 folds. S_1 is approximately parallel to the compositional layering except to the hinges. In most of the thin sections of the rocks, S_1 is microfolded (F_2) with development of crenulation cleavage S_2 along the axial plane of the F_2 folds. The foliation S_2 is defined by sericite (Muscovite) encloses the lenticles of quartz and plagioclase (Fig. 78.2a) in chlorite-sericitephyllite. Muscovites are aligned parallel to S_1 , as well as microfolded S_1 and S_2 schistosity. Biotite is present sporadic amounts in the phyllites. Garnet commonly occurs as porphyroblasts which are sieved with inclusion of quartz, biotite, ilmenite and rarely staurolite, kyanite and plagioclase. In zone B the porphyroblast of garnet wrapped by the foliation with pressure shadow area of quartz (Fig. 78.2b). In zone E garnet contains corroded core containing small inclusion of quartz. The junction between the rim and core garnet is demarcated by inequant quartz grains arrange around it (Fig. 78.2c).

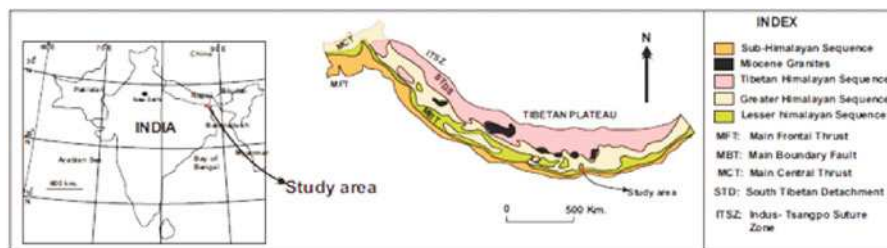


Fig. 78.1 Regional map of the Himalaya showing the major longitudinal lithotectonic subdivisions separated by major faults [7]

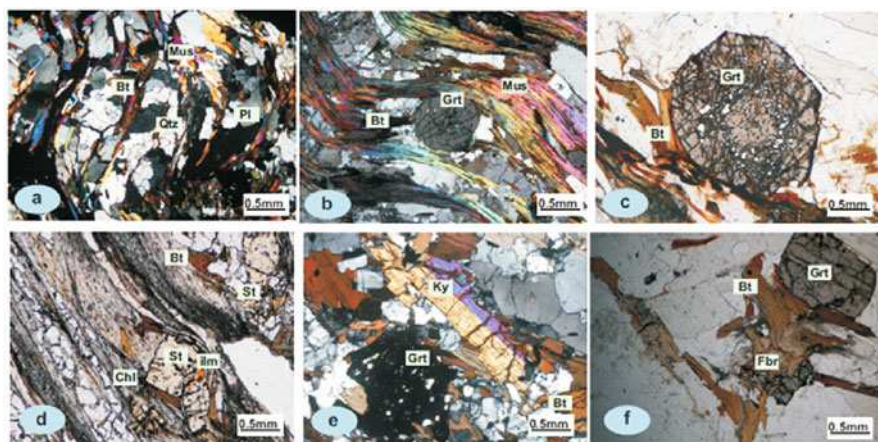


Fig. 78.2 a. Microfolded S_1 with development of S_2 in chlorite-sericite-phyllite (XPL); b. Porphyroblast of garnet wrapped by foliation with pressure shadow area of quartz (XPL); c. The junction between the rim and core garnet is demarcated by inequant quartz grains arranged around it (XPL); d. Staurolite porphyroblast present within the theschistosity S_1 defined by the orientation of chlorite and micas (PPL); e. Coarse bladed kyanite present along with garnet, mica and feldspars (XPL); f. Corroded poikiloblast of garnet replaced by sillimanite (PPL)

Staurolite occurs as sub-idioblastic in significant modal amount in the zone C and decreases in zones D and E. It lies on the S_1 foliation defined by the micas and chlorite (Fig. 78.2d). Kyanite occurs in the zones D and E as coarse bladed crystals (Fig. 78.2e) and sillimanite commonly occurs as fibrolite mats. Fibrolites are randomly oriented and intergrown with biotite (Fig. 78.2f).

78.3 MINERAL CHEMISTRY

The electron microprobe has been carried out by GEOL-JXA-8800L electron microprobe at the University of Wurzburg (Germany) using beam diameter $5\eta\text{A}$ beam current at an accelerating voltage 15kv. The relative X_{Mg} in the minerals varies in the order: chlorite>biotite>staurolite>garnet, and X_{Mn} decreases in the order: garnet>staurolite>chlorite>biotite.

The garnets do not reveal any prograde compositional changes. The X_{Mg} of garnets decreases with an increase in X_{Mn} in garnet and increases with rise in Ca/Mn ratio of garnet. Weak zoning in the garnet from the zone C from the sample collected in the vicinity of the staurolite-biotite isograd has been attributed to the Fe-Mg reaction. On the other hand, the garnets from the zones D and E are characterized by normal growth zoning with ball-shaped Mn and Ca profiles with Mn and Ca decreasing, and Fe, Mg and X_{Mg} increasing from the core towards the periphery. However, near the rim the pattern of zoning is reverse of the growth

zoning, i.e. increase in Mn and decrease of X_{Mg} and Mg. The normal growth zoning pattern of garnet has been attributed to continuous Fe-Mg-Mn reaction.

78.4 GEOTHERMOBAROMETRY AND CONCLUSION

The metamorphic conditions estimated through the different models of geothermometry and geobarometry and experimentally determined equilibria suggest pressures between 4.6-5 kbar for zone B, 5.5-6 kbar for zone C, 5.5-6.5 kbar for zone D and 7-7.5 for zone E and temperature between 450-550°C for zone A, 540-580°C for zone B, 580-600°C for zone C, 660-700°C for zone D and 680-780°C for zone E.

The reverse metamorphic zoning pattern, with successive higher rocks lying at greater elevation and structural level, has been attributed to migration of metamorphic front due to abnormally high heat flow in the regions of the MCT in the Central Crystalline Zone of Himalaya where the rocks of Daling-Darjeeling group were metamorphosed, prior to their transportation by thrusting to the present position in the Lower Himalaya.

REFERENCES

1. Mallet, F.R.: On the geology and mineral resources of the Darjeeling district and the western Duars. *Mem. Geol. Surv. Ind.*, 11(I), 1–50 (1874)
2. Lal, R.K., Mukerji, S. and Ackerman, D.: Barrovian metamorphism of Takdah, Darjeeling Himalaya (Eastern Himalaya). In: P.S. Saklani (Ed.), *Geological Aspects*, 2, 529–573 (2005)
3. Tewari, S. and Prakash, D.: Petrology of the Pelitic schists and gneisses of the area around Mangpu, district Darjeeling, West Bengal. National Seminar on “Geology and Geo-resources of the Himalaya and Cratonic Regions of India”, Department of Geology, Kumaun University, Nainital, 108 (2012)
4. Tewari, S. and Prakash, D.: A classic example of barrovian metamorphism around Mangpu, district Darjeeling, West Bengal. 3rd International Conference on “Precambrian Continental Growth and Tectonism”, Department of Geology, Bundelkhand University, Jhansi, 196 (2013)
5. Prakash, D. and Tewari, S.: Field and textural relationship in gneisses and schists from the area around Mangpu, Darjeeling district, West Bengal. *Journal of Geological Society of India*, 81, 451–454 (2013)
6. Prakash, D., Tewari, S., Singh, P. Chandra and Frimmel, H.W.: A classic example of Barrovian metamorphism around Mangpu, district Darjeeling, West Bengal, Eastern India. *Lithos* (In preparation)
7. Sorkhabi, R.B. and Macfarlane, A.: Himalaya and Tibet: mountain roots to mountain top. In: Macfarlane, A., Sorkhabi, R.B. and Quade, J. (Eds.), *Himalaya and Tibet: Mountain roots to mountain top*. Geological Society of America Special Paper, 328, 1–7 (1999)

Chapter 79

High Pressure and Ultrahigh Temperature Metamorphism at Diguva Sonaba, Eastern Ghats Mobile Belt (India): New Constraints from Phase Equilibria Modelling

Divya Prakash and Deepak

Abstract The investigated area around Diguva Sonaba represents a part of granulite facies terrain of Eastern Ghats Mobile Belt (India). The Precambrian metamorphic rocks of the area consist of mafic granulite (\pm garnet), khondalite, leptynite (\pm garnet, biotite), charnockite, enderbite, calc-granulite, migmatic gneiss and sapphirine-spinel-bearing granulite, which comprise the major rock types of the area. Sapphirine-spinel-bearing granulite occurs as lenticular bodies in khondalites, leptynites and calc-granulites. Textural relations such as presence of corroded blebs of biotite within garnet and orthopyroxene, resorbed hornblende within pyroxenes, and coarse prisms of sillimanite presumably pseudomorphs after kyanite, provide evidence of either, an earlier episode of upper amphibolites facies metamorphism or represent relict of a single prograde event leading to granulites facies metamorphism. In the sapphirine-spinel granulite, osumilite and sapphirine + spinel + quartz were stable during the thermal peak of granulite facies metamorphism (early stage) but were later replaced by the (Crd-Opx-Qtz-Kfs) - symplectites and variety of reaction coronas respectively during the retrograde episode (middle stage). Variable amounts of retrograde biotite or biotite + quartz symplectite replace orthopyroxene, cordierite, (Opx-Crd-Kfs-Qtz)-symplectite (late stage). The prograde path was followed by peak metamorphism at a temperature of c. 1000 °C and a pressure of c. 12 kbar as computed by isopleths of X_{Mg} garnet and X_{Al} orthopyroxene. The sequence of reactions as deduced from the corona and symplectites assemblages, together with petrogenetic grid and pseudosection considerations, records a clockwise P-T evolution.

Keywords High pressure • Ultra-high temperature • Diguva Sonbha • Phase equilibria modelling • Eastern ghats mobile belt

D. Prakash (✉) • Deepak

Centre of Advanced Study in Geology, Banaras Hindu University, Varanasi, India

e-mail: dprakashbhu@yahoo.com

79.1 INTRODUCTION

The Eastern Ghats Mobile Belt (EGMB) of Indian subcontinent occupies an important position and received considerable attention from petrologists over the last decade [1–5]. Nevertheless, pseudosection based studies on granulites of EGMB are still awaited posing a challenging task ahead. P-T pseudosections have proved to be a popular and powerful means of predicting and explaining mineral paragenesis of metamorphic rocks. Development of spectacular reaction texture and symplectitic intergrowths in Mg-Al granulites preserves a record of their evolutionary stages because of the strong refractory nature and varied mineralogy of these rocks. Our new results, in comparison with those from other localities of the EGMB, make it possible to re-evaluate the regional tectonothermal evolution of the EGMB [5].

79.2 GEOLOGICAL SETTING

Eastern Ghats Belt constitutes the eastern part of the southern Indian shield. It is separated from the Eastern Dharwar and Bastar cratons in the west and Singhbhum-Orissa craton in the north by a thrust. Precambrian rocks of the belt display prograde metamorphism from green schist to granulites facies. Green schist facies of rocks are exposed in the south-western part of the Eastern Ghats Belt, and towards the west of Nellore. Towards the east the greenschist facies belt of Nellore grades into the amphibolite facies. The amphibolite facies rocks are also exposed in the Khammam area and these grades into higher granulite facies towards the north-east.

The rocks of the granulites facies of the belt are included in the Eastern Ghats Group which subdivided into older Khammam formation and Younger Charnockite Formation. The whole rock and mineral dates of charnockite, khondalite and associated granulites in the Eastern Ghats Belt ranges from 3100 to 1000 Ma. The wide range of dates of granulites facies in the Eastern Ghats may be attributed to resetting of radiometric clock due to several events of intrusive igneous rocks post-dating an earlier episode of granulite facies metamorphism around 2600/2500 Ma. The 3090 Ma date of khondalite indicates that it retains the memory of an earlier event of high-grade metamorphism (M_1) documented in Karnataka craton. Thus the khondalite may correspond in age to the Sargur Group (>3000 Ma) of Karnataka which predate the granulite facies metamorphism (M_2) around 2600/2500 Ma. These phases of deformations affected the rocks of the Eastern Ghats Mobile Belt : (a) deformation and F1, NE-SW trending isoclinal folds around 2600/2500 Ma., (b) deformation, F2 NW-SE cross folds between 2000 and 1900 Ma, and (c) D3 deformation, F3, E-W folds formed at ~ 1400 Ma.

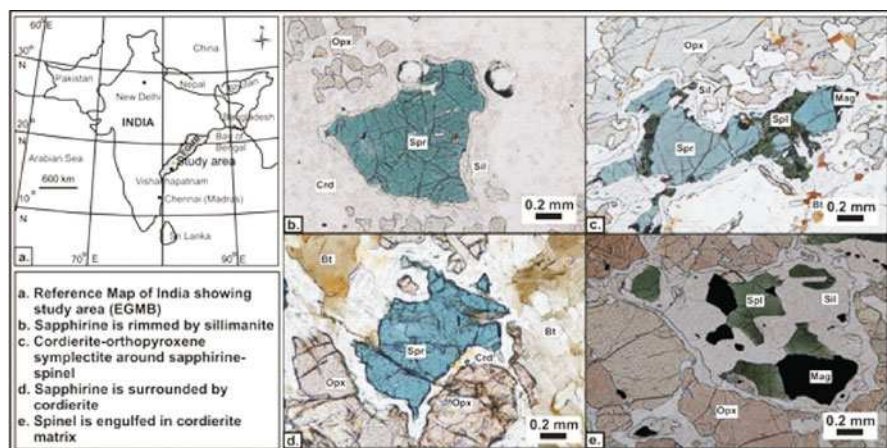


Fig. 79.1 Textural relationships of mineral

79.3 TEXTURAL RELATIONSHIPS

Textural relations (Fig. 79.1.) such as presence of corroded blebs of biotite within garnet and orthopyroxene, resorbed hornblende within pyroxenes, and coarse prisms of sillimanite presumably pseudomorphs after kyanite, provide evidence of either an earlier episode of upper amphibolites facies metamorphism (M_1) or represent relict of a single prograde event leading to granulites facies metamorphism (M_2). In the sapphirine-spinel granulites, osunilite and sapphirine + spinel + quartz were stable during the thermal peak of granulite facies metamorphism (early stage) but were later replaced by the (Crd-Opx-Qtz-Kfs) - symplectites and variety of reaction coronas respectively during the retrograde episode (middle stage). Variable amounts of retrograde biotite or biotite + quartz symplectite replace orthopyroxene, cordierite, (Opx-Crd-Kfs-Qtz) - symplectite (late stage). Post-crystalline deformation after the granulite facies event (M_{II}) is displayed by the common presence of deformed twin lamellae in plagioclase, deformed pyroxenes and biotite and cataclastic texture with coarse-grained porphyroclasts of plagioclase and pyroxenes in a fine-grained matrix of quartz, feldspar and pyroxenes.

79.4 MINERAL CHEMISTRY

The range of $X_{Mg}[Mg/(Mg + Fe^{+2})]$ of orthopyroxene in different rock types varies in the order: sapphirine-spinel granulite (0.55-0.72) > sapphirine granulite (0.59-0.72) > charnockite (0.45-0.49) > basic granulite (0.33-0.38). While in clinopyroxene the range of X_{Mg} is calc granulite (0.71-0.72) > basic granulites (0.44-0.58). Pyrope contents indicate following decreasing trends in the garnets

from the different rocks: Sapphirine-spinel-bearing granulite > garnet-leptynite > khondalites > basis granulite. While the grossularite content suggests a reverse trend: basic granulite > khondalite > garnet-leptynite > sapphirine-bearing granulite. The garnets are generally homogeneous. The composition of sapphirine lie between the 7:9:3 and 2:2:1 ($\text{MgO}:\text{Al}_2\text{O}_3:\text{SiO}_2$) solid solution join except one exception which lie between 7:9:3 and 3:5:1 indicating that it is per aluminous. The trends of X_{Mg} in biotite in the different rock types is as follows: sapphirine-spinel-bearing granulites (0.078-0.94) > basic granulites (0.40-0.89) > garnet-leptynite (0.55-0.71). The high TiO_2 content in biotite (more than 5.0 wt %) is similar to those from other granulite facies terrains. The X_{Mg} of biotite is affected by octahedral occupancy of Ti and Al^{VI} , and shows a significant decrease in X_{Mg} with an increase in $\text{Al}^{\text{VI}} + \text{Ti}$. The trends of X_{Mg} in spinel is as follows: spinel from sapphirine-spinel granulites (0.030-0.61) > leptynite (0.41). Fe^{3+} content of spinel ranges between 0.01 and 0.14 p.f.u. The X_{Mg} in cordierite ranges between 0.80 and 0.92.

79.5 DISCUSSIONS AND CONCLUSION

Despite the wide spread in estimated temperature, the thermal peak of metamorphism obtained through different models of geothermometry is 900 ± 50 °C. Estimated pressure for the thermal peak of metamorphism in the study area is 9 ± 1 kbar. The lower P-T estimate of about 800 °C and ~5 kbar is obtained from the geobarometry model involving in the spinel-quartz-cordierite equilibrium.

The pressure estimate varies from 9 kbar to about 5 kbar at temperature between 900° to 800 °C. The different geothermobarometry estimates and various evolutionary stages from the textural studies were combined to portray the pressure (P), temperature (T), time (t) path of, metamorphism in the study area. A nearly isothermal decompression path presumably related to rapid uplift of 14 km is evident from the clock wise P-T-t path. The above estimate suggest an overburden of 32 km. if we consider an average thickness of 35 km of the crust preserved in the Precambrian terrain of Southern India, the total crustal thickness is estimated to be 67 km in this region during 2.6-2.5 Ma.

The theoretical calculation of England & Thompson [6] (1984) and others have demonstrated that a clockwise P-T-t loop is likely consequence of concurrent thermal relaxation and erosion following continent-continent collision tectonics.

REFERENCES

1. Dasgupta, S. and Sengupta, P.: Indo-Antarctic correlation: a perspective from the Eastern Ghats Granulite Belt, India. *In: Proterozoic East Gondwana: Supercontinent Assembly and Breakup*

- (eds M. Yoshida, B.F. Windley and S. Dasgupta), *Geo. Soc.*, London, Spec. Pub., 206, 131–143 (2003)
2. Lal, R.K.: Metamorphic evolution of granulites from southern Indian Shield. *In: Milestones in petrology and future perspectives*. Mohan, A. (ed.), Mem. Geo. Soc. of India, Bangalore, 52, 61–108 (2003)
 3. Dasgupta, S., Raith, M. and Sarkar, S.: New perspective in the study of the Precambrian continental crust of India: An integrated sedimentologic, isotopic, tectonometamorphic and seismological appraisal. *Prec. Res.*, 162, 40–58 (2008)
 4. Mukhopadhyay, D. and Basak, K.: The Eastern Ghats Belt – A Polycyclic Granulite Terrain. *J. Geo. Soc. of India*, 73, 489–518 (2009)
 5. Prakash, D., Deepak, Singh, P. C., Singh, C. K., Tewari, S., Arima, M. and Frimmel, H.E.: Reaction textures and metamorphic evolution of sapphirine-spinel bearing and associated granulites from Diguva Sonaba, Eastern Ghats Mobile Belt, India. *Geo. Mag.*, in press (2014)
 6. Thompson, A.B. and England, P.C.: Pressure-Temperature-Time Paths of Regional Metamorphism II. Their Inference and Interpretation using Mineral Assemblages in Metamorphic Rocks. *J. of Petrol.*, 25, 929–955 (1984)

Chapter 80

Spatial Distribution of Seismic Site Coefficients for Guwahati City

Jagabandhu Dixit, S.T.G. Raghukanth, and Sujit Kumar Dash

Abstract The spatial distribution of seismic site coefficients at Guwahati is presented in this article. Estimated site coefficients consider different site types in the city and several level of ground shaking consider average of probable seismic event. The evaluation of site coefficients is based on the standard penetration test data at 105 boreholes distributed over the city. Equivalent linear one dimensional site response analyses are performed to predict the site amplification and to determine the spectral acceleration response. Due to the unavailability of recorded ground motion data for the region, synthetic ground motions simulated at the bedrock level for the city corresponding to several combinations of magnitude (M_w) and source-to-site distance (R) are used as input excitation. Simulated synthetic ground motion data with varying levels of excitation have been used to take care of the uncertainties in the input ground motions. The analyses depict the modification of the seismic ground motion due to the presence of soil overlying the bedrock.

Keywords Site response • Ground motion • Site coefficient • Guwahati city

80.1 INTRODUCTION

Amplification of ground motion due to local site conditions has been demonstrated during several destructive earthquakes. Depth of soil column and type of soil stratigraphy at a site significantly influences the seismic intensity and severity of structural damages. Focusing and resonance of seismic waves due to soil deposit

J. Dixit (✉)

Department of Civil Engineering, Shiv Nadar University, Gautam Budh Nagar,
Uttar Pradesh, India

e-mail: jagabandhu.dixit@snu.edu.in

S.T.G. Raghukanth

Department of Civil Engineering, Indian Institute of Technology Madras, Chennai,
Tamil Nadu, India

S.K. Dash

Department of Civil Engineering, Indian Institute of Technology Kharagpur, Kharagpur,
West Bengal, India

and the impedance contrast prevailing between horizontally layered soil deposit and underlying bedrock are the causes of ground motion amplification. Overall, amplification of ground motion is generally influenced by stiffness and damping of the medium, amplitude and frequency content of the waves propagating through the soil medium. Soft soil deposits substantially amplify the ground motion leading to visible structural damage during earthquakes [1]. In view of this, it is important to consider the local soil conditions at a given site in the estimation of surface level input ground motion for proper seismic analysis and design of structures. This paper presents the spatial distribution of seismic site coefficients at Guwahati city for different combinations of moment magnitude and source-to-site distance. These coefficients corresponding to different structural periods do take care of the local site effects and the variation in the ground motions.

80.2 STUDY AREA

Guwahati city is situated in the bank of river Brahmaputra over an area of about 600 km² (latitude 26.08°-26.25°N, longitude 91.58°-91.92°E). Most of the buildings in the city are unplanned and lack earthquake resistance capacity. The city is situated on Shillong plateau and its landscape is dominated by hills and wetlands. The city lies on the Shillong plateau spreading at the junction of Himalayan colliding zone to the north and sliding Burmese arc to the east. Northeast India being situated in one of the active intra-continental region is one of the most active earthquake prone zones in the world and has a number of intra-plate active faults capable of producing high seismic risk in the region. It is placed in zone V, the most severe zone of the country [2]. Over the last 120 years, it has witnessed 22 large earthquakes ($M_w \geq 7$) including 2 great earthquakes and hundreds of small earthquakes. According to the hazard map by Global Seismic Hazard Assessment Programme (GSHAP), Assam is expected to have peak ground acceleration (PGA) of 0.24g to 0.48g. The area is under high compressive stress due to north-eastward movement of the Indian plate.

80.3 SEISMIC SITE COEFFICIENTS

One dimensional site response analyses are performed at 105 soil sites in the city for which borehole data are available. The analysis is performed by SHAKE91 [3] for 700 times at each site using 700 synthetic time histories. The artificial ground motion data simulated for the city are used due to unavailability of ground motion records of past earthquakes. Ground motion is greatly affected by earthquake source, path and site conditions. Synthetic acceleration time histories used in the present site response analysis are generated by the stochastic finite fault simulation method of ground motion modeling [4–7]. The damping ratio, shear modulus, layer

thickness, density and shear wave velocity of each layer are the input parameters. Earthquake ground motion is excited at the bedrock level or stiff soil considered as bedrock. The spectral acceleration of bedrock motion and surface motion is estimated assuming 5% damping. Excitation is given at the bottom of soil column. Ground motion at the surface in terms of displacement, velocity, acceleration and corresponding response spectra are found from the analysis. The site effects can be quantified by the seismic site coefficients, defined as the ratio of spectral acceleration at a site at varying periods to that of the assumed reference outcropping rock site at those corresponding periods [8]. In the present study, the site coefficients are expressed as,

$$F_s = \frac{S_a^s(T)}{S_a^r(T)}$$

where $S_a^s(T)$ and $S_a^r(T)$ are the acceleration response spectra at different periods at the surface level and reference bedrock level respectively. F_s is the site coefficients at a given period.

The frequency dependent site amplification factors are represented in terms of short period site coefficient (F_a) and long period site coefficients (F_v). No amplification condition is considered at the rock sites. Hence, short period (F_a) and long period (F_v) site coefficients at each of the rock sites are taken to be 1.0. Site coefficients at PGA, 0.3 s, and 1.0 s for shaking intensities of 0.1g and 0.36g are presented in the form of contour maps in Figure 80.1 through Figure 80.3. The values of site coefficient at PGA for soft soil sites are found to be relatively smaller at higher level of bedrock acceleration that indicates de-amplification possibly due to the nonlinear behaviour of soil at higher strains. The coefficients are observed to be very high at 0.3 s as compared to that at 1.0 s. Spatial distribution of seismic response estimated in terms of seismic site coefficients for the city based on lower PGA values poses safety problem and higher PGA values seem to be uneconomical in the point of view of design of structures. Therefore, mathematical average of seismic responses due to an ensemble of ground motions is considered for the evaluation of site coefficients.

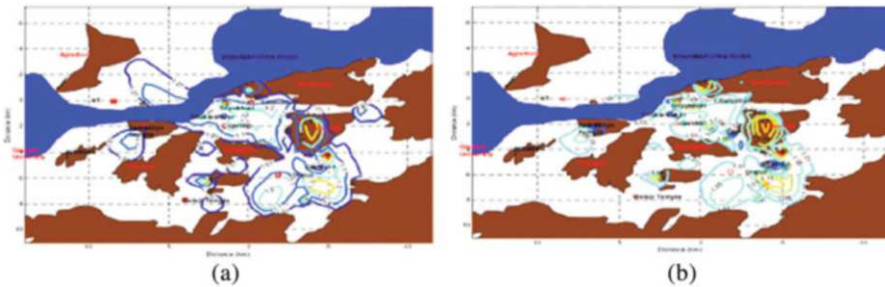


Fig. 80.1 Contour map of site coefficients at PGA (a) for 0.1 g and (b) for 0.36 g

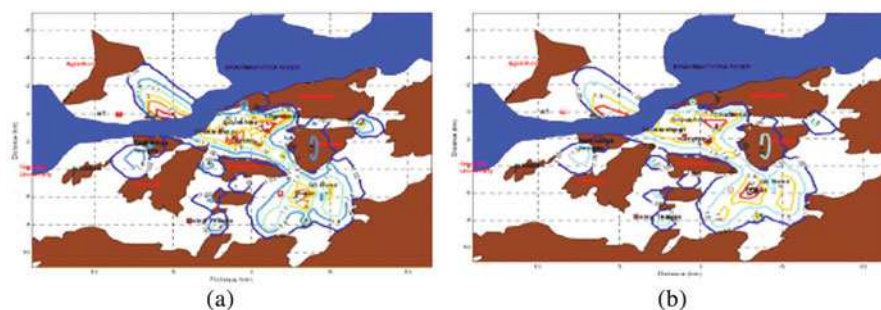


Fig. 80.2 Contour map of site coefficients at 0.3 s (a) for 0.1 g and (b) for 0.36 g

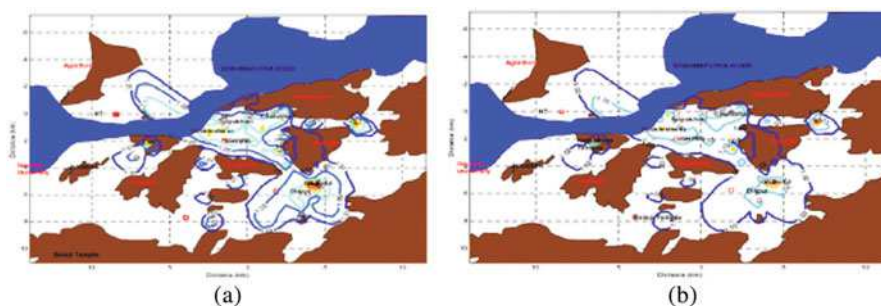


Fig. 80.3 Contour map of site coefficients at 1.0 s (a) for 0.1 g and (b) for 0.36 g

80.4 CONCLUSIONS

Equivalent linear one dimensional analysis depicts the modification of the seismic ground motion due to the presence of soft soil overlying the bedrock. The modification of ground motion is found to be dependent on the amplitude and frequency of input shaking, dynamic properties of soil, geometry of soil stratification and the depth of soil column. 700 synthetic ground motion data with varying levels of excitation have been used to take care of the uncertainties in the input ground motions. Several levels of ground shaking used in the estimation of site coefficients consider probable seismic events in the region. The spatial distribution of site coefficients presented in the form of contour maps can be used to estimate the design seismic force for earthquake resistant design of various structures in the city.

REFERENCES

1. Aki, K.: Local site effects on weak and strong ground motion. *Tectonophysics*, 218, 93–111 (1993)

2. Boore, D.M.: Stochastic simulation of high-frequency ground motions based on seismological models of the radiated spectra. *Bulletin of Seismological Society of America*, 73, 1865–1894 (1983)
3. Boore, D.M. and Atkinson, G.M.: Stochastic prediction of ground motion in eastern North America. *Bulletin of Seismological Society of America*, 4, 460–477 (1987)
4. Boore, D.M.: Simulation of ground motion using the stochastic method. *Pure and Applied Geophysics*, 160, 635–675 (2003)
5. Hwang, H.H.M., Lin, H. and Huo, J. R.: Site coefficients for design of buildings in eastern United States. *Soil Dynamics and Earthquake Engineering*, 6, 29–40 (1997)
6. Idriss, I.M. and Sun, J.I.: A computer program for conducting equivalent linear seismic response analysis of horizontally layered soil deposits. User's manual for SHAKE91 (1992)
7. IS 1893-Part I: Criteria for earthquake resistance design of structures. Fifth revision, Part-I; Bureau of Indian Standard, New Delhi (2002)
8. Raghukanth, S.T.G., Dixit, J. and Dash, S.K.: Ground motion for scenario earthquakes at Guwahati city. *Acta Geodaetica et Geophysica Hungarica*, 46(3), 326–346 (2011)

Chapter 81

Application of GIS-Based Weights of Evidence Method for Metallogenic Prediction to Copper Resources in Western Region of Zhejiang, China

Wei Shen and Haiyan Du

Abstract In western region of Zhejiang province, structure and magma activity occur frequently; Proterozoic eon and Paleozoic era of copper mineralization favorable layers are distributed in those regions; the NE orientation deep fractures develop and move; the Shengong period and early Yanshanian of magma activity closely relate to mineralization. There are well metallogenic conditions of Au, Ag and Cu minerals in the regions according to the long-term and complex geological evolution, tectonism and magmatic activity. Based on analysis of tectonism, stratum, rock, fractures and minerogenetic map in the region, the geological variables are obtained by the multi-source information of geological abnormality, minerogenetic abnormality using MAPGIS and MORPAS software. The study regions are divided into 1755 grid cells with 5km×5km. The five minerogenetic prospect regions of Cu deposits are obtained by weights of evidence modeling, which show that weight of evidence method is a good tool for minerogenic prediction.

Keywords Weights of evidence • Minerogenic prediction • Mineral deposits • Metallogenic belts

81.1 INTRODUCTION

The weights of evidence (WofE) is one of the most popular methods for mapping mineral prospectivity, which use the Bayesian theory of conditional probability to quantify spatial associations between evidence layers (or geological factors) and known mineral occurrences. It combines the prior probability of mineral occurrence with the conditional probability of mineral occurrence for each evidential layer using Bayes' rule to derive posterior probabilities of mineral occurrence [1, 2].

W. Shen (✉)

China University of Geosciences, Xueyuan Road 29, Beijing, P.R. China

e-mail: shenweihome@sina.com

H. Du

China Geological Library, Xueyuan Road 29, Beijing, P.R. China

In WofE modeling, a map pattern consisting of points (e.g., mineral deposits on 1:200,000 map) is related to one or more map patterns that are continuous in that they assume values at all points in the study area. Suppose that a study area is digitized as a number (n) of pixels and that X_i ($i = 1, 2, \dots, p$) are a number of binary explanatory variables used to predict a dichotomous random variable Y representing the presence ($Y_k=1$) or the absence ($Y_k=0$) of mineralization at the k -th pixel. Provided that n is very large, we can redefine the situation in terms of binary sets B_i corresponding to the X_i , and a set D corresponding to Y . In most WofE applications, the B_i are binary with or without missing data, but the method also can be used with multi-state explanatory variables [3].

WofE is based on the idea of prior and posterior probability; the former is the probability that a terrain unit contains an event before considering any existing predictor variables (the favorable conditioning factors); the latter is an “adjustment” or response of the prior probability, taking into account the evidence from one or more spatial patterns. Positive and negative weights (W^+ and W^-) are initially calculated; the magnitude of these weights depends on the measured association between the response variable and each class of each predictor variable. The difference between W^+ and W^- defines the contrast ($C=W^+ - W^-$), an overall measure of the degree of the spatial association between each class of the predictor variables and the response variable. The MORPAS (Metal Ore Resource Prediction and Assessment System) that provides tools for weights of evidence, logistic regression, fuzzy logic, and neural networks based on MAPGIS, has been used in this study as a useful tool for automatically calculating the mentioned parameters [4].

81.2 OVERVIEW OF WEIGHTS OF EVIDENCE

When there is a single pattern B , the odds $O(D|B)$ (i.e., $O = p/(1 - p)$) for occurrence of mineralization if B is present is given by the ratio of the following two expressions of Bayes’s rule:

$$P(D|B) = \frac{P(B|D)P(D)}{P(B)}, P(\bar{D}|B) = \frac{P(B|\bar{D})P(\bar{D})}{P(B)} \quad (81.1)$$

where the set \bar{D} represents the complement of D . Consequently,

$$\ln O(D|B) = \ln O(D) + W^+ \quad (81.2)$$

where the positive weight for the presence of B is

$$W^+ = \ln \frac{P(B|D)}{P(B|\bar{D})} \quad (81.3)$$

The negative weight for the absence of B is

$$W^- = \ln \frac{P(\overline{B}|D)}{P(\overline{B}|\overline{D})} \quad (81.4)$$

When $p = n$, there are two relations:

$$P\left(D \middle| \bigcap_{i=1}^n B_i\right) = \frac{P\left(\bigcap_{i=1}^n B_i | D\right) P(D)}{P\left(\bigcap_{i=1}^n B_i\right)} P\left(\overline{D} \middle| \bigcap_{i=1}^n B_i\right) = \frac{P\left(\bigcap_{i=1}^n B_i | D\right) P(\overline{D})}{P\left(\bigcap_{i=1}^n B_i\right)} \quad (81.5)$$

Conditional independence of D with respect to B_1, B_2, \dots, B_n implies that

$$P\left(\bigcap_{i=1}^n B_i | D\right) = \prod_{i=1}^n P(B_i | D) P\left(\bigcap_{i=1}^n B_i | \overline{D}\right) = \prod_{i=1}^n P(B_i | \overline{D}) \quad (81.6)$$

$$\begin{aligned} \text{Consequently, } P\left(D \middle| \bigcap_{i=1}^n B_i\right) &= P(D) \frac{\prod_{i=1}^n P(B_i | D)}{P\left(\bigcap_{i=1}^n B_i\right)} P\left(\overline{D} \middle| \bigcap_{i=1}^n B_i\right) \\ &= P(\overline{D}) \frac{\prod_{i=1}^n P(B_i | \overline{D})}{P\left(\bigcap_{i=1}^n B_i\right)} \end{aligned} \quad (81.7)$$

From these two equations it follows that

$$\frac{P\left(\overline{D} \middle| \bigcap_{i=1}^n B_i\right)}{P\left(D \middle| \bigcap_{i=1}^n B_i\right)} = \frac{P(D) \prod_{i=1}^n P(B_i | \overline{D})}{P(\overline{D}) \prod_{i=1}^n P(B_i | D)} \quad (81.8)$$

This expression is equivalent to

$$\ln O\left(D \middle| \bigcap_{i=1}^n B_i\right) = \ln O(D) + \sum_{i=1}^n W_i^+ \quad (81.9)$$

The log-odds on the left side of this expression is also known as the posterior logit. It is simply the sum of the prior logit and the weights of n map layers. The posterior probability follows from the posterior logit. Similar expressions apply when either one or both patterns are absent [5].

81.3 EXAMPLE OF APPLICATION

WofE modeling of mineral potential involves a three-stage process: (a) estimation of prior probability (P_{prior}) of prospect occurrence, (b) estimation of weights to be assigned to presence and absence of spatial evidence with respect to the prospects, and (c) updating of P_{prior} by using these weights to estimate the posterior probabilities ($P_{\text{posterior}}$).

Based on regional geological background analysis relationship and between minerals and geological background, the study regions are divided into 1755 grid cells with $5\text{km} \times 5\text{km}$ and the eleven geological variables (or evidential layers) are obtained by 1:200 000 geological maps and related minerals distribution maps (or layers). The weights for each geological variable (or evidential layer) are implemented in a GIS environment using MORPAS and MAPGIS (see Table 81.1). Based on proximity analysis, the posterior probability map and the five metallogenic prospective regions of Cu deposits are worked out by tectonism, stratum, rock, fractures, geological abnormality, minerogenetic abnormality, the values of posterior probability and the measures of the association of training sites (Fig. 81.1).

Table 81.1 Weights for each geological variable (or evidential layer)

Variable (or layer)	Criteria	W^+	W^-	Contrast
Percentage of favorable stratum areas	1 for $>15\%$	0.738	-0.354	1.092
	0 for $\leq 15\%$			
Entropy of stratigraphic combination	1 for $>20\%$	0.026	-0.686	0.712
	0 for $\leq 20\%$			
Values of factor abnormality for metallogenic element cluster	1 for presence	1.052	-0.122	1.175
	0 for absence			
Syntectonic type granite	1 for presence	0.357	-0.086	0.443
	0 for absence			
Yanshanian rock mass	1 for presence	0.449	-0.384	0.833
	0 for absence			
Fracture equidensity	Calculated values	0.212	-0.243	0.455
Number of fracture intersection points	Calculated values	0.113	-0.006	0.118
Number of Ag deposits occurrences	Calculated values	1.534	-0.109	1.644
Number of Au deposits occurrences	Calculated values	1.712	-0.126	1.838
Number of Pb-Zn deposits occurrences	Calculated values	0.129	-0.003	0.132
Number of Fe deposits occurrences	Calculated values	0.385	-0.031	0.416

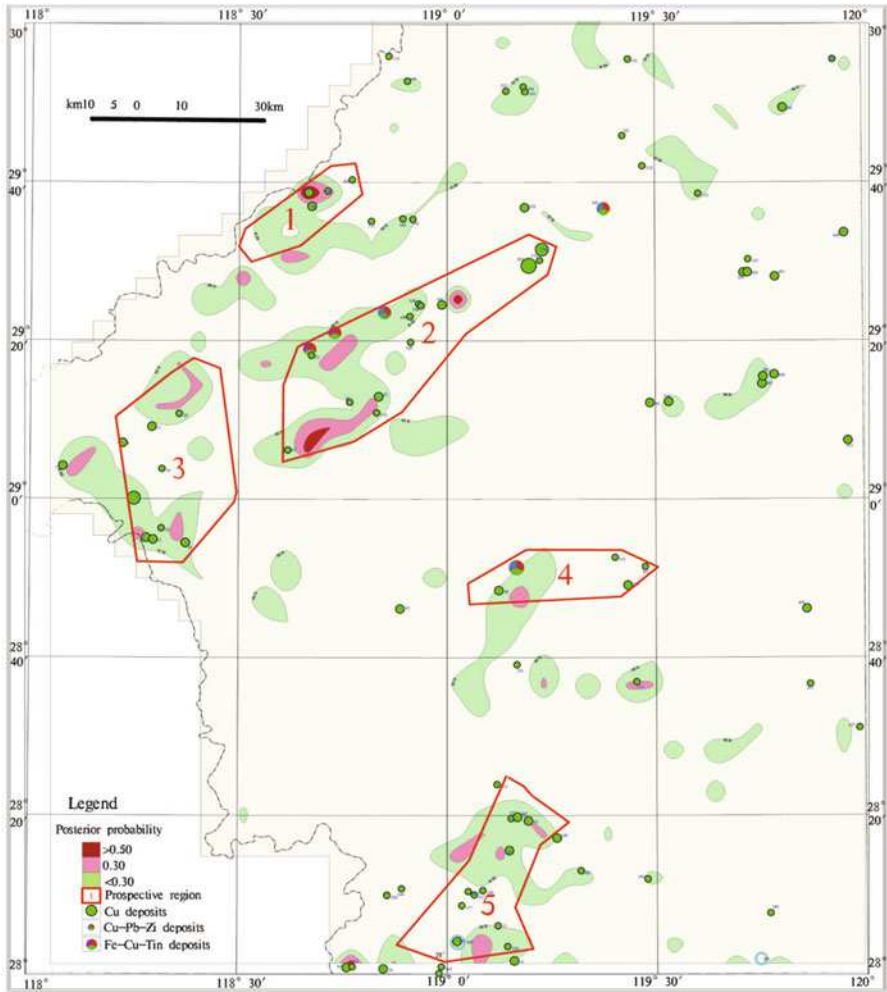


Fig. 81.1 Posterior probability map and five metallogenic prospective regions of Cu deposits

81.4 CONCLUSIONS

The study regions are divided into 1755 grid cells with 5km×5km and the eleven geological variables (or evidential layers) are obtained by 1:200 000 geological maps and related minerals distribution maps and based on regional geological background analysis relationship and between minerals and geological background. The weights for each geological variable (or evidential layer) are implemented in a GIS environment using MORPAS and MAPGIS. The weights of evidence model is considered as reasonable and delineates permissive regions for Cu deposits. The weights of evidence model has the additional characteristics that it is well defined, reproducible, objective, and provides a quantitative measure of confidence.

ACKNOWLEDGEMENT This research was supported by the grant from the National Natural Science Foundation of China (Grant No. 41102208 and Grant No. 41172302).

REFERENCES

1. Agterberg, F.P., Bonham-Carter, G.F., Cheng, Q.-M. et al.: Weights of Evidence Modeling and Weighted Logistic Regression for Mineral Potential Mapping. *In*: Davis, J.C. and Herzfeld, U.C. Computers in Geology: 25 Years of Progress, pp. 13–32. Oxford Univ. Press, New York (1993)
2. Porwal, Alok and Carranza, E.J.M.: Extended Weights-of-Evidence Modelling for Predictive Mapping of Base Metal Deposit Potential in Aravalli Province, Western India. *Explor. Mining Geol.*, 10(4), 273–287 (2003)
3. Bonham-Carter, G.F., Agterberg, F.P. and Weight, D.F.: Weights of Evidence Modeling: A New Approach to Mapping Mineral Potential. *In*: Agterberg, F.P., Bonham-Carter, G.F. Statistical applications in the earth science. *Geological Survey of Canada Paper*, 171–183 (1989)
4. Agterberg, F.P.: Combining Indicator Patterns in Weights of Evidence Modeling for Resource Evaluation. *Nonrenewable Resources*, 1(1), 39–50 (1992)
5. Agterberg, F.P.: A Modified Weights-of-Evidence Method for Regional Mineral Resource Estimation. *Natural Resources Research*, 20(2), 95–101 (2011)

Chapter 82

Application of Fuzzy Gamma Operator in Landslide Susceptibility Mapping along Yercaud Ghat Road Section, Tamil Nadu, India

V. Ramesh, Thanchuipou Phaomei, M. Baskar, and S. Anbazhagan

Abstract The present study emphasizes the application of fuzzy operators in landslide susceptibility mapping along Yercaud ghat road section in the state of Tamil Nadu, India. Yercaud is one of the important hill stations and tourist spot in Tamil Nadu. In recent times, it faces frequent landslide occurrences. There is a urgent need for detail study of landslides along the ghat road to prevent further slope failure. The study has been conducted through integrated remote sensing, GIS and field investigations. The existing landslide locations were collected from previous study and verified in the field. The slope gradient, slope aspect, relief, lithology, land cover, geomorphology, proximity to road, proximity to drainage and proximity to lineament were analyzed with the help of Survey of India topo map, published geology map and satellite data. The relationship between various causative factors with past landslide locations were compared using frequency ratio method. These frequency ratio values were normalized to get fuzzy membership values between 0 to 1. The parameter maps with membership values were integrated using fuzzy algebraic product, fuzzy algebraic sum and fuzzy gamma operators to get final landslide susceptibility map. The produced map was verified by comparing with existing landslide locations for calculating prediction accuracy. The fuzzy gamma operator ($\gamma=0.975$) showed the highest accuracy of 0.7895.

Keywords Landslide susceptibility • Fuzzy operators • Remote sensing • GIS

V. Ramesh • T. Phaomei • M. Baskar • S. Anbazhagan (✉)
Centre for Geoinformatics and Planetary Studies, Department of Geology,
Periyar University, Salem, India
e-mail: anbu02@gmail.com

82.1 INTRODUCTION

Landslide is one of the most frequently occurring disasters in hilly regions, which affects human life, property, economy and environment. The occurrence of landslides are influenced by various causative factors and triggered by several external factors, such as intense rainfall, earthquake shaking, water level change, and rapid stream erosion etc., [1]. Anthropogenic activities like building road network, urban development, deforestation, and rapid land use modification, may also influence occurrence of landslides [2]. Landslide susceptibility refers to the probability of occurrence of landslide in an area based on the correlation between causative factors and spatial distribution of landslides [3]. Landslide susceptibility map shows the stable and possible zones for future landslide occurrence [4].

Various landslide hazard assessment techniques were categorized under two broad categories viz., qualitative and quantitative [5]. The quantitative approaches includes statistical [6], probabilistic [7], and distribution free methods such as fuzzy logic [8, 9] and artificial neural network [10] methods. In the present case, landslide susceptibility mapping along ghat road of Yercaud hills were carried out using fuzzy algebraic product (FAP), fuzzy algebraic sum (FAS), and fuzzy gamma operators (FGO). The resultant susceptibility maps were compared with previous landslide locations and prediction accuracy were evaluated.

82.2 STUDY AREA

Yercaud is one of the important tourist spots in Tamil Nadu and situated on the Shevaroy Hills in Salem district. Pleasant climate prevailing in Yercaud hills throughout the year. The highest altitude of 1437m above mean sea level (amsl) is present near the Longlipettai area. Yercaud ghat section exposes with a less to moderately weathered charnockites under Archean formations. The ghat road is constructed in southwestern slope of Shevaroy hills by cut slopes. The length of the ghat road is 20 km built with 20 hairpin bends. It is located between 11°42'27" N and 11°46'57" N latitudes and 78°10'39" E and 78°12'21" E longitudes (Fig. 82.1). The ghat road section associated with mild soil erosion, intensive rainfall, weathering, and other anthropogenic activities in the form of widening of roads, which leads to slope failure.

82.3 GEOSPATIAL DATABASE

The landslide incident details were collected from previous [11]. The previous landslide locations were placed along ghat road sections, which were mapped out from IRS P6 LISS IV satellite data. The total numbers of previous landslides are 15.

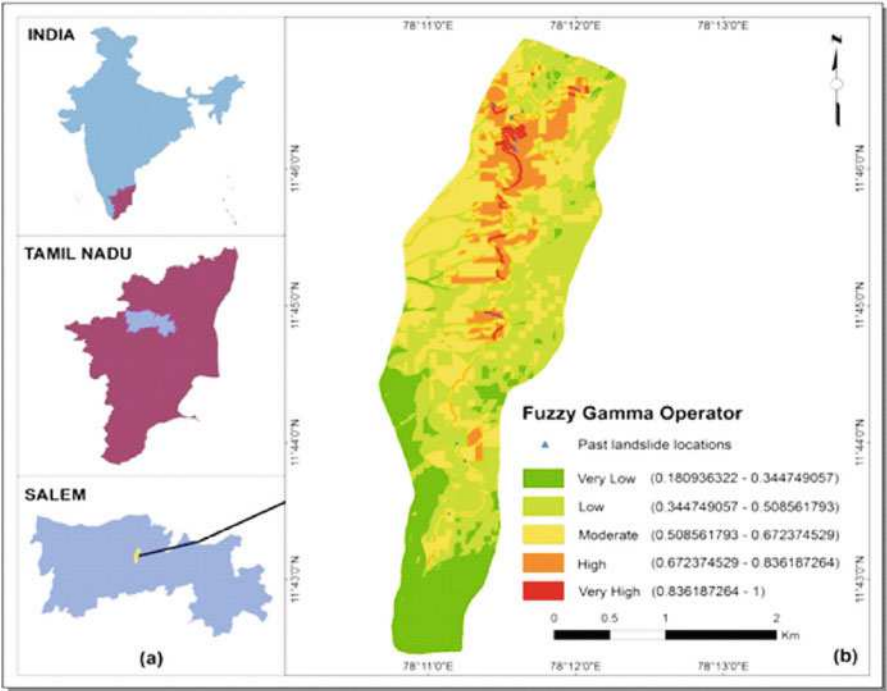


Fig. 82.1 (a) Location map of Yercaud Ghat Road Section in the State of Tamil Nadu, and (b) Landslide susceptibility map with the fuzzy gamma operator ($\gamma = 0.975$)

Most of the landslides were occurred in the mid section of ghat road, where hairpin bends are more with high relief condition. The entire section of ghat road is covered by charnockites [12]. The geomorphology and land cover maps were interpreted from IRS-P6 LISS IV satellite image. The ghat road mostly covers structural hill systems and intermontane valley. The topographical factors such as slope, slope aspect, and relief were derived from SRTM DEM data. The relief in the ghat road ranges between 312 and 1437 m amsl and divided into five equal interval classes (Table 82.1). Road buffer of (10m) was prepared using proximity analysis tool in GIS environment. The drainage map was prepared with topographical map on 1:50,000 scale and updated with satellite data. Various buffer zones were created from drainage map to generate proximity to drainage map. Lineaments were interpreted from satellite imagery and different buffer zones were created to do proximity analysis.

Table 82.1 Fuzzy membership values for causative factors

Parameter/ Class	Pixels in Class	Class Ratio	Landslide pixels in class	Slide Ratio	Frequency Ratio	Fuzzy Membership Value
Land Cover						
Crop Land	11507	3.07	0	0.00	0.00	0.00
Steep Slope	2559	0.68	0	0.00	0.00	0.00
Mixed Forest Plantation	61059	16.30	4	26.67	1.64	0.93
Fairly Dense Scrub	15319	4.09	0	0.00	0.00	0.00
Mining Area	654	0.17	0	0.00	0.00	0.00
Mixed Settlement	25442	6.79	0	0.00	0.00	0.00
Scrub Land	38945	10.40	0	0.00	0.00	0.00
Deciduous Forest	3604	0.96	0	0.00	0.00	0.00
Degraded Forest	6226	1.66	0	0.00	0.00	0.00
Open Mixed Forest	166888	44.56	8	53.33	1.20	0.68
Fairly Dense Forest	42347	11.31	3	20.00	1.77	1.00
Geomorphology						
Structural Hills	299441	79.89	15	100	1.25	1.00
Intermontane Valley	13976	3.73	0	0.00	0.00	0.00
Bazada Zone	18914	5.05	0	0.00	0.00	0.00
Shallow Pediment	42467	11.33	0	0.00	0.00	0.00
Lithology						
Charnockite	374798	100	15	100	1.00	1.00
Slope Gradient						
0 - 15 Degree	147856	39.47	2	13.33	0.34	0.02
16 - 25 Degree	136975	36.57	1	6.67	0.18	0.00
26 - 35 Degree	76295	20.37	8	53.33	2.62	0.34
36 - 45 Degree	13441	3.59	4	26.67	7.43	1.00
Slope Aspect						
North	5049	1.35	0	0.00	0.00	0.00
Northeast	1521	0.41	0	0.00	0.00	0.00
East	8142	2.17	0	0.00	0.00	0.00
Southeast	31145	8.31	1	6.67	0.80	0.24
South	58052	15.50	0	0.00	0.00	0.00
Southwest	98423	26.28	5	33.33	1.27	0.38
West	127814	34.12	3	20.00	0.59	0.18
Northwest	44421	11.86	6	40.00	3.37	1.00

(continued)

Table 82.1 (continued)

Parameter/ Class	Pixels in Class	Class Ratio	Landslide pixels in class	Slide Ratio	Frequency Ratio	Fuzzy Membership Value
Relief						
312–536	135593	36.20	3	20.00	0.55	0.00
537–761	66169	17.67	2	13.33	0.75	0.16
762–986	69929	18.67	5	33.33	1.79	1.00
987–1210	53023	14.16	3	20.00	1.41	0.69
1211–1437	49853	13.31	2	13.33	1.00	0.36
Proximity to road						
Road Buffer	11433	3.05	15	100	32.76	1.00
Other Area	363134	96.95	0	0.00	0.00	0.00
Proximity to drainage						
0–50 m	64326	17.17	3	20.00	1.16	0.31
50–100 m	50179	13.40	2	13.33	1.00	0.24
100–150 m	35453	9.47	3	20.00	2.11	0.72
150–200 m	27136	7.24	3	20.00	2.76	1.00
200–250 m	23893	6.38	1	6.67	1.05	0.27
>250 m	173580	46.34	3	20.00	0.43	0.00
Proximity to lineament						
0–50 m	97984	26.16	7	46.67	1.78	1.00
50–100 m	89342	23.85	3	20.00	0.84	0.47
100–150 m	68120	18.19	4	26.67	1.47	0.83
150–200 m	46601	12.44	1	6.67	0.54	0.30
>200 m	72520	19.36	0	0.00	0.00	0.00

Total No. of pixels in the study area – 374798; Total No. of landslide pixels – 15

82.4 FUZZY SET THEORY

Fuzzy set theory was first introduced by [13], which differs from the conventional Boolean set theory in such a manner objects within a set is definite. In fuzzy set, the extent of membership values of an object can have values ranges between 0 to 1, instead of having complete membership 0 or 1 as in a conventional set. The assignment of membership values between 0 and 1 plays a vital role in the fuzzy logic analysis. There is no regulation to assign the fuzzy membership values. The only thing is the selected values must imitate the extent of membership of a set. It can be user-defined based on subjective investigation [14] or the values can be derived from statistical analysis like information value [15] and from frequency ratio [16] or it can be assigned by various functions representing the reality such as J-shaped, Sigmoidal and Linear [17] or by using analytical hierarchical method [18]. With respect to a given data set (a thematic map), a membership can be assigned to each map category according to its direct/indirect relationship with the

phenomena in consideration [18]. Five operators were discussed by [14] viz., the fuzzy AND, fuzzy OR, fuzzy algebraic product, fuzzy algebraic sum, and fuzzy gamma operator. This study uses the fuzzy algebraic product, fuzzy algebraic sum, and fuzzy gamma operator for combining the fuzzy membership values.

$$\text{The fuzzy algebraic product is defined as : } \mu_{\text{combination}} = \prod_{i=1}^n \mu_i \quad (82.1)$$

The fuzzy algebraic sum is defined as:

$$\mu_{\text{combination}} = 1 - \prod_{i=1}^n (1 - \mu_i) \quad (82.2)$$

where μ_i is the fuzzy membership function for the ' i ' th map, and $i = 1, 2, 3, \dots, n$ maps to be combined.

$$\mu_{\text{combination}} = (FAS)^{\gamma} * (FAP)^{1-\gamma} \quad (82.3)$$

where γ is a value chosen in the range 0 to 1; FAS = Fuzzy Algebraic Sum and FAP = Fuzzy Algebraic Product.

In the present study, the membership values for each thematic layer were derived by normalizing the probability frequency ratio values calculated using Eq. 82.4 (Table 82.1).

$$\text{Frequency Ratio} = \frac{\text{Slide Ratio}}{\text{Class Ratio}} \quad (82.4)$$

where,

$$\text{Slide Ratio} = \frac{\text{Number of landslide grids in class}}{\text{Total number of landslide grids}} \quad (82.5)$$

$$\text{Class Ratio} = \frac{\text{Number of grids in individual class}}{\text{Total number of grids in whole class}} \quad (82.6)$$

However, the zero membership values has been assigned as 0.0001 in order to avoid the complete slackness of a class in a thematic map LHZ analysis [9].

82.5 RESULTS AND DISCUSSION

For the purpose of integration using fuzzy operator models, all the nine landslide influencing factors were converted to a raster format with 5.8m x 5.8m size grids to calculate the landslide susceptibility index. The total number of grids are 374798,

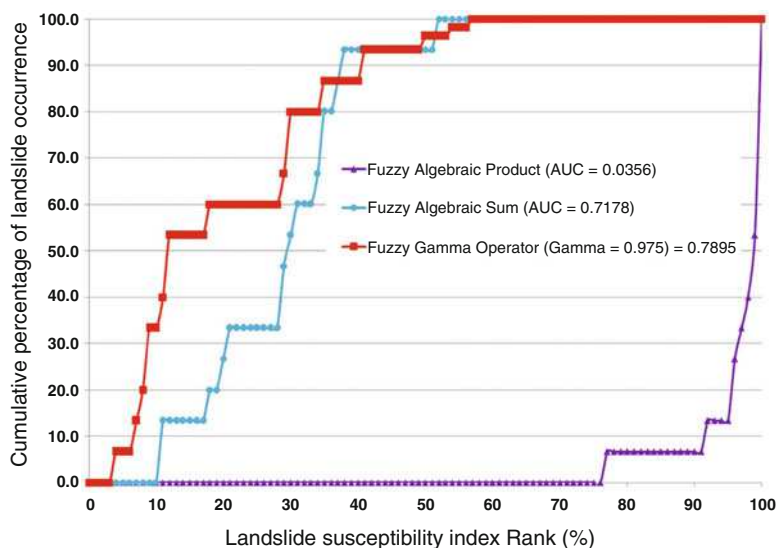


Fig. 82.2 Illustration of success rate curve showing landslide susceptibility index rank (x-axis) occurring in cumulative percent of landslide occurrence (y-axis).

and the total number of landslide grids are 15 in the study area. All the influencing factors were taken to the spatial analysis extension module of the ArcGIS software for integration. The landslide susceptibility index (LSI), were calculated based on the integration rules as shown in Eq. 82.1, Eq. 82.2, and Eq. 82.3. If the LSI value is high, it means a higher susceptibility to landslide; a lower value means a lower susceptibility to landslides. For fuzzy algebraic product, LSI values had a minimum value of 0 and a maximum value of 1, with a standard deviation of 0.0156 and the mean is 0.0007. For fuzzy algebraic sum, LSI values had a minimum value of 1.0208 and a maximum value of 10, with a standard deviation of 1.5809 and the mean is 4.3377. In the case of fuzzy gamma operator, the value of γ was set to 0.1, 0.2, 0.3, 0.4, 0.5, 0.6, 0.7, 0.8, 0.9, 0.975, 0.98, 0.985, and 0.99 to observe its effect on the landslide susceptibility map. The integrated result with the gamma value of $\gamma=0.975$ have shown highest accuracy than other values tested in the present study. In the case of applying the gamma operator ($\gamma=0.975$) the minimum, mean, maximum, and standard deviation values of LSI are 0.1809, 0.4737, 1, and 0.1492, respectively. The landslide susceptibility map is classified into equal intervals and grouped into five susceptibility classes for visual interpretation viz. very low, low, moderate, high and very high (Fig. 82.1).

Model validation is performed using the known locations of landslides and the landslide susceptibility map. The Area Under Curve (AUC) is one of the most commonly used qualitative accuracy assessment method for the prediction models in natural hazard assessment [19]. The success rate describes how well the model and factor predict the landslide [20]. The accuracy of fuzzy operator models in landslide susceptibility mapping along the Yercaud ghat road section was evaluated

by calculating “area under the curve (AUC)”. The AUC value of success rate curve for FAP, FAS, and FGO respectively 0.0356, 0.7178, and 0.7895, where FGO (using $\gamma=0.975$) has shown were shown highest accuracy value (Fig. 82.2).

82.6 CONCLUSIONS

The fuzzy logic approach is one of the easiest and simplest methods to prepare a landslide susceptibility map. In the present study, nine causative factors were combined using fuzzy algebraic product, fuzzy algebraic sum, and fuzzy gamma operator models. The fuzzy gamma operator with a γ value of 0.975 produces the best success rate accuracy of 79%. The landslide susceptibility map produced using fuzzy gamma operator model predicted 60% of the past landslide locations in very high susceptible class, while the high susceptible zone predicted 26.67% of the past landslide locations. The results point out fuzzy gamma operator model shows good prediction pattern than FAP and FAS operators of landslide susceptibility in the study area.

REFERENCES

1. Ayalew, L., Yamagishi, H. and Ugawa, N.: Landslide susceptibility mapping using GIS based weighted linear combination, the case in Tsugawa area of Agano River, Niigata Prefecture, Japan. *Landslides*, 1, 73–81 (2004)
2. Begueria, S.: Validation and evaluation of predictive models in hazard assessment and risk management. *Natural Hazards*, 37, 315–329 (2006)
3. Bonham-Carter, G.F.: Geographic information systems for geoscientists: modelling with GIS. Pergamon, Oxford, New York, pp. 292–302 (1994)
4. Brabb, E.E.: Innovative approaches to landslide hazard and risk mapping. In: Proceedings of 4th International Symposium on Landslides, Toronto, Canada. Volume 1, pp. 307–324. BiTech Publishers, Canada (1984)
5. Chauhan, S., Sharma, M., Arora, M.K. and Gupta, N.K.: Landslide Susceptibility Zonation through ratings derived from Artificial Neural Network. *International Journal of Applied Earth Observations and Geoinformation*, 12, 340–350 (2010)
6. Choi, J., Oh, H.J., Lee, H.J., Lee, C. and Lee, S.: Combining landslide susceptibility maps obtained from frequency ratio, logistic regression, and artificial neural network models using ASTER images and GIS. *Engineering Geology*, 124, 12–23 (2012)
7. Chung, C-J.F. and Fabbri, A.G.: Probabilistic prediction models for landslide hazard mapping. *Photogrammetric Engineering and Remote Sensing*, 65(12), 1389–1399 (1999)
8. Corominas, J. and Moya, J.: A review of assessing landslide frequency for hazard zoning purposes. *Engineering Geology*, 102, 193–213 (2008)
9. Dai, F.C., Lee, C.F. and Ngai, Y.Y.: Landslide risk assessment and management: an overview. *Engineering Geology*, 64(1), 65–87 (2002)
10. Das, I., Stein, A., Kerle, N. and Dadhwal, V.K.: Probabilistic landslide hazard assessment using homogeneous susceptible units (HSU) along a national highway corridor in the northern Himalayas, India. *Landslides*, 8, 293–308 (2011)
11. GSI: Geological and Mineral Resources map of Tamil Nadu and Pondicherry (1995)

12. Hearn, G.J.: Landslide and Erosion Hazard Mapping at Ok Tedi Copper Mine, Papua New Guinea. *Quarterly Journal of Engineering Geology*, 28, 47–60 (1995)
13. IDRISI: The decision support ring. IDRISI user manual version-4 (1995)
14. Kanungo, D.P., Arora, M.K., Sarkar, S. and Gupta, R.P.: Landslide Susceptibility Zonation (LSZ) Mapping – A Review. *Journal of South Asian Disaster Studies*, 2(1), 81–105 (2009)
15. Kayastha, P., Bijukchhen, S.M., Dhital, M.R. and Smedt, F.D.: GIS Based Landslide Susceptibility Mapping using a Fuzzy Logic Approach: A Case Study from Ghurmi-Dhad Khola Area, Eastern Nepal. *Journal Geological Society of India*, 82, 249–261 (2013)
16. Lee, S., Choi, J. and Min, K.: Landslide susceptibility analysis and verification using the Bayesian probability model. *Environmental Geology*, 43, 120–131 (2002)
17. Lee, S. and Min, K.D.: Statistical analysis of Landslide Susceptibility at Yongin, Korea. *Environmental Geology*, 40(9), 1095–1113 (2001)
18. Lee, S.: Application and verification of fuzzy algebraic operators to landslide susceptibility mapping. *Environmental Geology*, 52, 615–623 (2007)
19. McKean, J., Buechel, S. and Gaydos, L.: Remote sensing and landslide hazard assessment. *Photogrammetric Engineering and Remote Sensing*, 57(9), 1185–1193 (1991)
20. Saranathan, E., Rajesh Kumar., Kannan, M. and Anbalagan, R.: Landslide Macro Hazard zonation of the Yercaud Hill slopes ghat sections – km 10/4 to 29/6. *Indian Landslides*, 3(1), 9–16 (2010)
21. Satty, T.L.: Exploring the interface between hierarchies, multiple objectives and fuzzy set. *Fuzzy Sets Syst.*, 1, 57–68 (1978)
22. Srivastava, V., Srivastava, H. and Lakhera, R.C.: Fuzzy gamma based geomatic modeling for landslide hazard susceptibility in a part of Tons river valley, northwest Himalaya, India. *Geomatics, Natural Hazards and Risk*, 1(3), 225–242 (2010)
23. Van Westen, C.J., Rengers, N. and Soeters, R.: Use of Geomorphological Information in Indirect Landslide Susceptibility Assessment. *Natural Hazards*, 30, 399–419 (2003)
24. Wieczorek, G.F.: Preparing a detailed landslide-inventory map for hazard evaluation and reduction. *Bulletin Association Engineering Geology*, 21, 337–342 (1984)
25. Yin, K.L. and Yan, T.Z.: Statistical prediction model for slope instability of metamorphosed rocks. In: Proceedings of the 5th International Symposium on Landslides. *Lausanne*, 2, 1269–1272 (1988)
26. Zadeh, L.A.: Fuzzy sets. *IEEE Information and Control*, 8, 125–151 (1965)

Chapter 83

A Benchmark Synthetic Dataset for Fractured Reservoir

Yongduk Shin, Ankur Roy, Orhun Aydin, Tapan Mukerji, and Jef Caers

Abstract A benchmark synthetic fractured reservoir dataset is built as an initial step towards evaluating methodologies for using deterministic Discrete Fracture Network (DFN) models from an explored area in predicting performance in relatively underexplored adjacent zones. In this exercise we create a robust synthetic dataset comprising about seven million grid cells with details on geology, geomechanical and geophysical properties. It starts with a simple three-layered subsurface geology reflecting aeolian, fluvial and coastal environments and four major sealing faults that dissect the domain into a “core”, “graben” and a “horst” area. The entire reservoir is populated with relevant facies properties, porosity and permeability. Fracture intensity and orientation distributions are computed from geomechanical constraints. A subset of this data within the middle-layer of the core region is considered to be the “area of interest”. This region is populated with fractures invoking a DFN model by taking into account fracture intensity and orientations from geomechanical constraints. The influence of these fractures on seismic responses is evaluated based on computation of the effective elastic stiffness tensor. The seismic response can then be used as templates to interpret the characteristics of the fractured reservoir in the unexplored areas. Finally, the feasibility of production within the “area of interest” is evaluated by adding a set of injector and producer wells and simulating flow over a 10-year time period.

Keywords Faults • DFN • Rock physics • Seismic impedance • Streamline simulator

Y. Shin • A. Roy (✉) • O. Aydin • J. Caers
Energy Resources Engineering Department, Stanford Center for Reservoir Forecasting,
Stanford, CA, USA
e-mail: royankur@stanford.edu

T. Mukerji
Energy Resource Engineering and Geophysics, Stanford University, Stanford, CA, USA

83.1 INTRODUCTION

Reservoir forecasting is an important and difficult challenge in both conventional and unconventional resources that comprise fractured rocks. Unlike un-fractured systems, where the modeling comes down to structure and rock properties, the addition of planar features in the modeling workflow poses considerable challenges. Building a detailed Discrete Fracture Network (DFN) model from geological understanding and interpretations is one avenue. While very complex and accurate in terms of geology, these offer a deterministic perspective with little room for assessing uncertainty. This is because it can become computationally infeasible to run hundreds of deterministic models that may be required to estimate uncertainty with reasonable bounds. It has been shown that a DFN model can be upscaled to a binary indicator grid identifying those cells acting as a dual medium, as well as all effective matrix and fracture properties [1]. It can be then used as a training image for generating flow models with multiple-point statistics that enables quantification of uncertainty. It remains to be tested whether this concept can be applied to more complex and realistic problems. Here we document the workflow established as part of a broader project that addresses the following question: can a detailed deterministic fracture network (DFN) model of a reservoir with data from one production phase be used to forecast recovery during a later phase in a new, relatively underexplored zone, thereby answering questions related to uncertainty? The technique outlined in [1] can be potentially applied to this problem but creating a training image in this case is a major challenge because a hydrocarbon reservoir is a complex earth system delineated by various types of characteristics, for example geological, petrophysical, geophysical, and fluid dynamic properties. Synthetic data are therefore very useful for extensive testing of any proposed algorithms for reservoir modeling, characterization, forecasting, and management before applying them to real cases. Such a synthetic dataset is thus generated by creating a “geologically realistic” generic fractured reservoir assuming complete knowledge of the subsurface. The present research deals with this aspect of the problem and endeavors to take an atypical approach thereby bypassing standard “modeling” strategies.

83.2 GENERATING THE DATA SET

83.2.1 *Structure, Stratigraphy and Reservoir Properties*

To keep things simple yet meaningful, the reservoir is created with a “layer-cake” like stratigraphy within a 6 km x 7 km domain, comprising three units or layers, each about 150m thick and bounded by five horizons that define them. A number of faults are added that dissect the entire domain into a “core”, “graben” and “horst” conforming to an extensional setting (Fig. 83.1). After the structural components

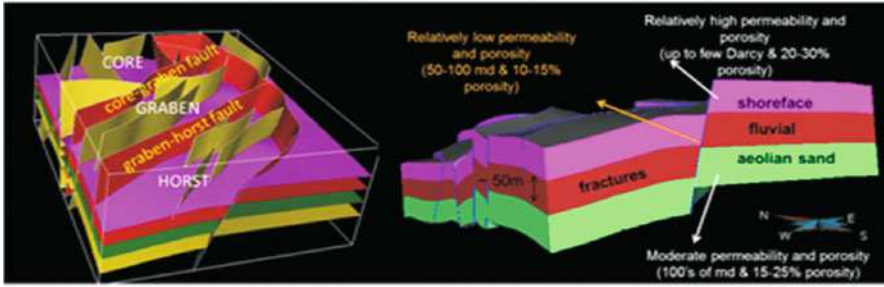


Fig. 83.1 Structure and stratigraphy. Faults separating core, graben and horst are shown in red. Middle layer has low porosity and permeability and has fractures

are created and the domain is gridded, the reservoir is populated with facies that represent different depositional environments – aeolian, fluvial and coastal from bottom to top (Fig. 83.1). A set of seven facies were created implementing object based modeling: fan and fan-channels in lower section of middle layer, channels in the upper section (running perpendicular to fans) and channels, lobes, drapes in the top layer (coastal). Remaining areas where none of the three facies are present are considered as floodplain, this comprises about 80% of the facies proportion in the top layer and about 50% in the middle layer. The bottom layer is aeolian sandstone.

Matrix porosity is simulated by using sequential Gaussian simulation (SGSIM) for each facies individually with different distributions across facies boundaries. The porosity of middle layer is kept low because we wish to study the effect of presence of fractures in a low porosity-permeability unit. The matrix permeability is assumed to be isotropic and is computed as a function of porosity. The difference in permeability between the three layers is kept quite distinct even without introducing the oil-water contact or generating fractures. The bulk density of matrix filled with pore water is calculated by using simple volumetric average of mineral component in each facies and pore fluid. Velocities are calculated assuming brine saturation. A theoretical model, the constant-cement model, is used for calculating P-wave velocity of sand facies [2]. Established empirical V_p - V_s relations are used for S-wave velocity of sand facies and P- and S-wave velocity of non-sand facies [3, 4]. The background unfractured medium is considered isotropic and values of shear modulus, bulk modulus, Lamé's parameter, Poisson's ratio and Young's modulus are calculated from the P- and S-wave velocities and density.

83.2.2 Generating Fractures

Fractures are considered to be present only within the sand facies of the middle-layer. Since it not a modeling exercise, generating fractures is noticeably different compared to modeling DFNs in a reservoir model. Where statistical data on fractures exist, such as fracture intensity, scale, and their directions, the information

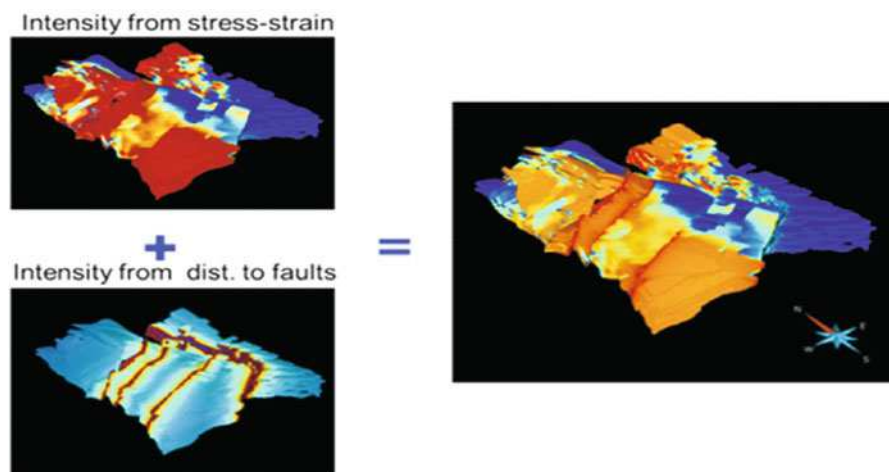


Fig. 83.2 Fracture intensity of middle-layer (right) calculated from two sources

on how the fractures have been generated is not required to run a DFN model. However, since this is an exercise in *creating ab initio* a synthetic dataset it is assumed that the fractures were formed when the horizons were deformed and faulted to their current shapes. Restoration analysis returns the current geological structure to its syn-depositional condition of flat un-faulted horizons. Principal strain components and their directional vectors are found from restoration/deformation vectors [5]. Principal stress components of induced deformation are calculated from elastic properties of rocks by invoking Hooke's law. The most tensile strain direction (max. principal strain) can be assumed to be the normal to a fracture plane and is used for finding fracture orientation in each grid block. The median value for dip for the fracture plane for the entire sand facies of the middle-layer thus calculated is about 41° . Fracture intensity arising out of stress/strain induced rock failure and fault induced damage (a power-law function distance from major faults) are linearly added as shown in Fig. 83.2.

Information on fracture orientation and fracture intensity thus generated is used for building a DFN within a smaller, 2 km x 2.2 km "region of interest" in the middle-layer of the core. A uniform length distribution is chosen such that the mean length remains around 5m and a median aperture value of ~ 1 mm, the length to height ratio being set to one. After the DFN is generated, effective fracture properties e.g., porosity, permeability, shape factor and intensity are computed. Following the steps laid down in [1], a binary indicator grid is generated by thresholding the fracture porosity values. This grid will be used for identifying cells to be modeled with dual porosity-permeability and single media (matrix only) cells. This step in the workflow is illustrated in Fig. 83.3.

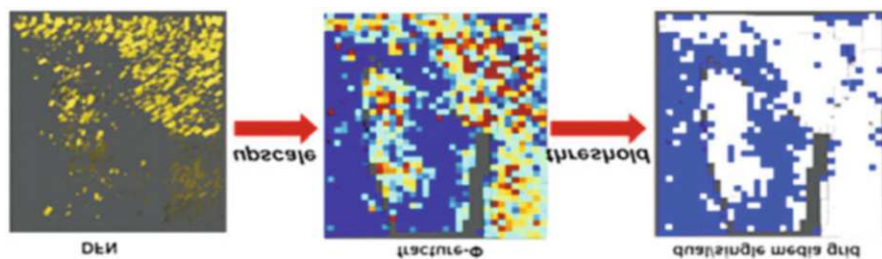


Fig. 83.3 Binary indicator grid (blue: single media; white: dual media) from DFN

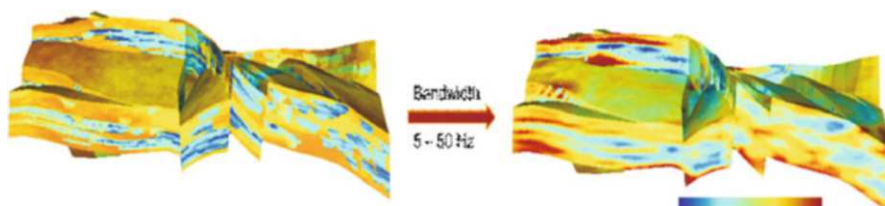


Fig. 83.4 Filtering P-wave impedance to seismic scale (EW section) S-wave velocity splitting (seismic scale) shows values in the middle layer indicate presence of fractures (Fig. 83.5)

83.2.3 Seismic Responses

Various effective medium models can be used for computing the effective elastic tensor of rocks with aligned fractures. All of them involve idealizations with respect to the fracture geometry and different approximations related to multiple fracture-to-fracture elastic interactions. As an example here Hudson's model [6, 7] is chosen for calculating elastic properties of fractured media, though any other appropriate effective medium model can also be used in this step. Hudson's model, like many other crack models, assumes penny-shaped cracks and calculates effective medium stiffness tensors by superposing correction terms on a background isotropic medium. Effective elastic properties with a single fracture set are transversely isotropic, but the symmetry axis is tilted since the median dip of the fracture plane is around 41° . The fracture orientation and intensity is spatially heterogeneous and varies from grid-block to grid-block. Once the elastic tensor is obtained at every grid block, the seismic phase velocity in any arbitrary direction of wave propagation is calculated using the Christoffel equation [7]. In order to obtain seismic signature at field resolutions, a forward seismic model is created from the grid-block seismic velocities. This is done by a low-pass filter derived from a Born approximation to generate representations of seismic imaging responses of velocity and impedance field [8]. The source-receiver spread is -6000m to +6000m, target depth is 2.5km and frequency used is 25-50 Hz. Figure 83.4 shows the effect of upscaling P-wave impedance for velocities parallel to the vertical axis to seismic scale.

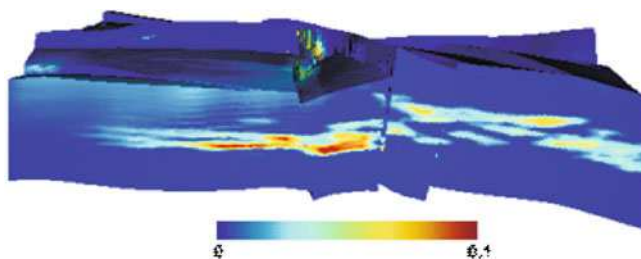


Fig. 83.5 NS section of S-wave velocity splitting

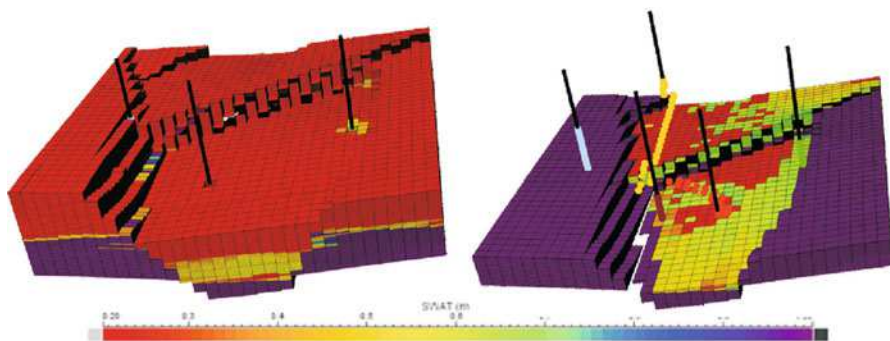


Fig. 83.6 (Left) Effect of adding three vertical wells. (Right) Adding deviated wells (colored dots mark trajectories) helps in enhancing production

83.2.4 Flow Simulation

Dynamic response of the synthetic reservoir is generated by means of flow simulation in order to create the true production data set of the synthetic reservoir. A commercial streamline simulator is chosen for this purpose because of computational time considerations. Permeability anisotropy for presence of fractures is computed by using permeability tensors from Oda's method [8]. Five wells are drilled in the "region of interest" within the core area, two of which are deviated (one injector and the other, producer) and three being vertical wells (two injector and one producer). Their locations are selected so that the vertical wells are drilled into less promising parts of the reservoir in terms of permeability. On the other hand, deviated wells are drilled so that they contact multiple reservoirs thus proving the feasibility of the field. The flow is simulated for a 10-year time period. The effect of adding deviated wells is shown in terms of a water saturation map (SWAT) in Fig. 83.6.

83.3 SUMMARY AND FUTURE WORK

The synthetic dataset thus generated includes details on geology, geophysical properties and flow responses. The exercise demonstrates how a binary indicator grid comprised of single and dual media cells can be generated and populated with effective fracture properties as in [1]. The results also delineate how the presence of fractures can influence seismic attributes, and hence how seismic attributes can be used to delineate the unexplored zones of the fractured reservoir. An important aspect of the modeling is the integration of geological restoration analysis with geomechanical and rock physics models for assessing the spatially varying seismic response of fractured reservoirs. During the next phase of our research, this grid thus created from the synthetic data will be used as a training image with seismic attributes (e.g. S-wave splitting) as “auxiliary variables” in creating multiple realizations of the subsurface that would ultimately help in evaluating uncertainty.

REFERENCES

1. Jung, A., Fenwick, D.A. and Caers, J.: Training image-based scenario modeling of fractured reservoirs for flow uncertainty quantifications. *Computers and Geosciences*, 17, 1015–1031 (2013)
2. Avseth, P.: Rock physics diagnostic of North Sea sands: Link between microstructure and seismic properties. *Geophysical Research Letters*, 27(17), 2761–2764 (2000)
3. Castagna, J.P. and Backus, M.M.: Petrophysical imaging using AVO: The Leading Edge, 12, 172–179 (1993)
4. Castagna, J.P.: Batzle, M.L. and Eastwood, R.L.: Relationships between compressional-wave and shear-wave velocities in clastic silicate rocks. *Geophysics*, 50(4), 571–581 (1985)
5. Mallet, J.L.L.: *Geomodeling*. Oxford University Press, Inc. (2002)
6. Hudson, J.A.: Overall elastic properties of isotropic materials with arbitrary. *Geophysical Journal International*, 102(2), 465–469 (1990)
7. Mavko, G., Dvorkin, J. and Walls, J.: A theoretical estimate of S-wave attenuation in sediment. 75th Annual Meeting, SEG, Expanded Abstracts (2005)
8. Mukerji, T., Mavko, G. and Rio, P.: Scales of reservoir heterogeneities and impact of seismic resolution on geostatistical integration. *Mathematical Geology*, 29(7), 933–950 (1997)
9. Oda, M.: Permeability tensor for discontinuous rock masses.

Part IV

Modelling and Simulations

Chapter 84

Three-Dimensional Metallogenic Prediction in Tonglushan Region Based on Digital Ore Deposit Model

N. Li Cheng and Liu Bing-li

Abstract Based on the geological background of Tonglushan region, and combining with the metallogenic theory, this paper reorganizes and analyzes the regional metallogenic model systematically, then determines the ore-prospecting criteria respectively from the strata, magmatic rocks, structure and wall rock alteration. Then guided by prospecting model, the paper selects favorable ore-forming strata, fault buffer, center symmetrical, fault density, tectonic intersection, the geochemical information etc. as evidence factors. Using the MICROMINE software as a platform and combining with the concealed geological body to build the digital geological model of surrounding areas, which is realize the 3D visualization, and viewers can watch the predictive result from different angles and positions. Through materialization of ore block model, then the materialization of each cell line interpolation and assignment, the final weight is obtained by 3D evidence model. By the primary halo zoning features of ore deposits, indicator of the geochemical exploration, forecasts the deep concealed ore, and realizes the geological and geochemical comprehensive prediction; Finally Marks out three of metallogenic prospect. The prospective areas show that the study area has a good potential for prospecting minerals and the method of ore prediction is very effective. The application of the analysis method which is quantitative information of structures as new prospecting variables achieve a new breakthrough in 3D prospecting minerals.

Keywords Tonglushan • Digital geological model • Geochemical comprehensive prediction

N.L. Cheng (✉) • L. Bing-li

Key Lab of Geomathematics of Sichuan Province, Chengdu University of Technology, Chengdu, China

e-mail: leecheng88@qq.com

84.1 INTRODUCTION

In the 1980s to now, the Tonglushan region of surface mining, shallow mining dwindling, deep concealed deposits and ore finding has become the main prospecting direction. Along with the development of science and technology, the use of a computer can directly recognize and deal with data mining knowledge, the form of symbols and rules, set up in the computer and the matching of the digital mineral deposit models, but most 3d metallogenic prediction [1, 3] method based on digital mineral deposit models on the basis of the study, concealed deposits of three dimensional metallogenic prediction has become a major bright spot in the field of mineral exploration in recent years.

84.2 STUDY AREA AND ESTABLISHMENT MODEL

The Tonglushan Cu-Fe deposit is located at the middle part of the Neocathaysian compound mole track and the northwestward of the Yangxin complex massif [2]. Data were collected in the study area is 1:100000 miner genetic map, geological map of 1:1 million, 1:2000 topographic maps, the prospecting line section, acquisition and collect the samples. In this paper, by using the existing geological data in the study area, select modeling method based on parallel section and the drilling, established the terrain, stratum, structure and magmatite mass in 3D entity model.

84.3 MATERIAL AND METHODS

In the study area is a West-East length 1882.69m, north-south length 2280.25m, and 1767.37m for high cube, and the scope of the three-dimensional cube. Fill in block (cube rows and columns * layer is 10m * 10m * 10m), a total of 1746383 unit block model. Cu, Au, Ag, Fe, data volume is established (Figure 84.1 Model of color from blue to cyan is to increase the content of Cu).

According to the analysis of metallogenic conditions of extraction of ore deposits and metallogenic information, combined with regional existing 3D data, establish the study area mineral prediction and assessment model (Table 84.1).

The relevant study information superposition compound through the analysis on the mineral formation, the comprehensive information metallogenic prediction method to calculate the weight of each ore, the ore body model of the study area was two value, namely the set unit block ore controlling of the attribute value is 1, does not exist for the 0, the weight of evidence weight formula to calculate the weight value of C (Table 84.2).

The weights are calculated by the value assigned to the unit blocks in each advantage factor, and then each unit block contains the favorable factor weights

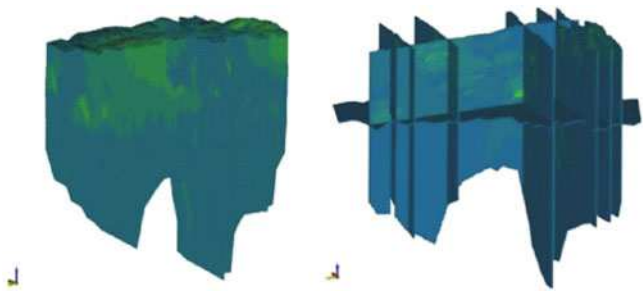


Fig. 84.1 The study area Cu grade interpolation element

Table 84.1 Prospecting prediction model in the study area

The ore controlling factors	Factor of metallogenic prediction	Characteristic variable	Characteristic value
Strengthen	Favorable strata information	Favorable metallogenic strata	Jialingjiang Fm, Daye Fm
Structural	structural character	Fault inference region	Around the faults of 300m buffer
	Analysis of tectonic characteristics	The main fault analysis	(0.10,0.30)
	Structural confluence point features	The fracture intersection	(0.78,1.58)
	Tectonic magmatite activities	Constructing the center symmetry	(0.21,0.96)
Geochemical exploration	Ore-forming element anomaly	Cu	≥0.0410
		Au	≥0.0015
		Ag	≥0.0120
		Fe	≥0.0410

Table 84.2 The study area the ore-prospecting criteria weights

Evidence study	W^+	W^-	C
Cu	3.148358282	-0.226542583	3.374900865
Au	3.075086325	-0.354568715	3.429655040
Ag	3.092517462	-0.127457554	3.219975016
Fe	2.583548282	-0.985658217	3.569206499
Jialingjiang Fm	1.953610289	-1.393737979	3.347348268
Daye Fm	-0.731785656	-1.625051814	0.893266158
Fault inference region	3.475251216	-0.542542533	4.017793749
The main fault analysis	2.253076224	-1.054058312	3.307134536
Constructing the center symmetry	1.792213494	-1.474675056	3.266888550
The fracture intersection	2.083037723	-1.289056510	3.372094233

Table 84.3 Delineation of Target Areas

Exploratory line	Target site	Basis For Projections					Predicted
		Position	primary halo	Structural	Fault	Fold	
4	4-1	250 meters below CK254	Abnormal display	contact zone	No. 61 fault footwall	anticlinal core west wing	deep mineral
	4-1	Neighbor of ZK406	Abnormal display	contact zone	No. 11 fault footwall	anticlinal core east wing	Target validation

were obtained with superposition weight [3]. According to the similarity to determine the weighted value is greater than the block 10.12 is the predicted prospective areas [4] analogy principle and subjective probability method, and according to the spatial position of the optimal prediction of block 2 forecasting target areas (Table 84.3).

84.4 CONCLUSIONS

This study will be 2D mineral traditional prediction was extended to 3D space, the geological conditions of Tonglushan study area and metallogenic regularity of understanding. In the selection of prospecting prediction elements in geological prospecting signs and geochemical data, the 2D structure of mature quantification information analysis applied to the 3D forecast, provide predictive variables. By statistical method considering the delineation of prospective areas were selected 3 target areas.

ACKNOWLEDGEMENTS This research benefited from a research project by China Geological Survey (No.12120114002001), the National Natural Science Foundation of China (No. 41272363).

REFERENCES

1. Chen Jianping: Large-scale 3D metallogenic prediction of concealed ore body in Gejiu, Yunnan province. *Chinese Journal of Geology*, 44(1), 324–337 (2009)
2. Liu Zhiguo: The Geology Feature and The Relation of ore-formation to magmas of the Tonglushan Cu-Fe deposit. *Geology of Chemical Minerals*, 24(4), 207–214 (2002)
3. Shi Rui and Chen Jianping: 3D positioning and quantitative prediction of the Xiaolinling gold belt in Tongguan area, Shaanxi. *Geology Bulletin of China*, 30(5), 711–721 (2011)
4. Liu Jishun: Discovery of cryptoexplosive breccia type Cu (-Au) ore bodies in Tonglushan skarn-type Cu-Fe deposit of Hubei Province and ore-searching vista. *Mineral Deposits*, 24(5), 527–536 (2005)

Chapter 85

The Integration Model of Deep Structure and Ore-Forming Systems of the Pechenga District (Baltic Shield)

K.V. Lobanov, M.V. Chicherov, I.A. Chizhova, and N.V. Sharov

Abstract The problems correlation of data of the Kola Superdeep Borehole was hampered by an imbalance between extremely detailed borehole studies and more piecemeal observations on the day surface in the Pechenga ore district. The rock density and anisotropy in Vp, geological, gravity, and geochronological data were employed for the formalization and correlation of the borehole section and the reference profile on the day surface using computer-based technologies. The integrated deep geodynamic model accounts for the modern structure of the Pechenga ore districts to a depth of 15 km and entails a new interpretation of its geological boundaries, development stages, and metallogeny. Ore-forming systems of the Pechenga ore district are known for large deposits of Cu-Ni ores deposits and occurrences of Pt, U, Au, Pb, and Zn.

Keywords Kola superdeep borehole • Correlation of the borehole section • The reference profile • Integrated deep geodynamic model • Ore-forming system

85.1 INTRODUCTION

Correlation of geological, geophysical, and metallogenic data for the border regions between Russia, Norway, and Finland has made it possible to suggest that the Pechenga ore district is an isolated segment of the Pechenga-Imandra-Varzuga metallogenic zone. In the northeast, the district is bound by the Voron'ya-Kolmosersk fault, in the southeast by the Litsk-Aragubsk fault, in the northwest by the Inari-Kirkines fault system, and in the southwest by a system of poorly known northwest-trending faults. It should be emphasized that the main tectonic

K.V. Lobanov (✉) • M.V. Chicherov • I.A. Chizhova
Institute of Geology of Ore Deposits, Petrography, Mineralogy and Geochemistry, Russian Academy of Sciences, Moscow, Russia
e-mail: lobanov@igem.ru

N.V. Sharov
Institute of Geological, Karelian Center, Russian Academy of Sciences, Petrozavodsk, Russia

elements of the Pechenga ore district are clearly reflected in the regional gravity field [1, 2].

Within the suggested boundaries the Pechenga ore district, besides the Pechenga and Allarechka Cu-Ni ore fields, incorporates the Archaean banded iron ores of Sydvaranger, the Early Proterozoic PGE and Ni occurrences of the Gora General'skaya, Karik, the Late Archaean-Early Proterozoic radioactive mineralization of different types (Litsevska), the hydrothermal Pb-Zn veins of probable Riphean age, and enigmatic Au-Ag mineralization discovered at deep levels of the SG-3 borehole and on the surface in the South Pechenga structural zone (Djevanet, Poroyarvi and others).

85.2 THE INTEGRATION MODEL OF THE PECHENGA ORE DISTRICT

The investigation of the Kola Superdeep Borehole (SG-3) was not restricted to the study of the drill core. Its general geological position was also taken into consideration, derived from long-term comprehensive research aimed at the creation of a deep model of the Pechenga district. This work was based on specialized documentation of the borehole section and included structural-petrological and petrophysical studies of core samples supplemented by studies of adequate parts of the bedrock surface for correlations with the borehole section and the surface reference profile [3].

The studies aimed at identifying the relationships between deformation and metamorphism as well as petrophysical properties of rocks and ore deposits. The database consists of 2000 SG-3 core and 3400 samples, collected from the ground surface. Rock density and their Vp anisotropy were used as the main parameters for comparison of the borehole SG-3 section and the reference profile on the surface. The first parameter reflects the rocks' lithology, the second accounts for the intensity of synmetamorphic tectonic deformations. In addition, new age data and morphology of the gravity field of the Pechenga district were considered. Special computer-based programs were used for the parameter calculations. Data for individual samples were compiled for rock types and processed by the weighted average method for the reference borehole section and the surface collected rocks selected for comparison.

The Cu-Ni-bearing Pechenga structure is best studied in the Pechenga ore district. A series of integration models were proposed in the mid-1980s based on the same geological map of the Pechenga ore field and the SG-3 borehole section. These models consider the Pechenga structure as a graben-syncline, asymmetrical syncline, explosive volcanic center, and continent-continent collision suture zone. The computer-based technology allowed revising these alternative models by comparing the observed and calculated gravity profiles passing through the SG-3 site [1–3].

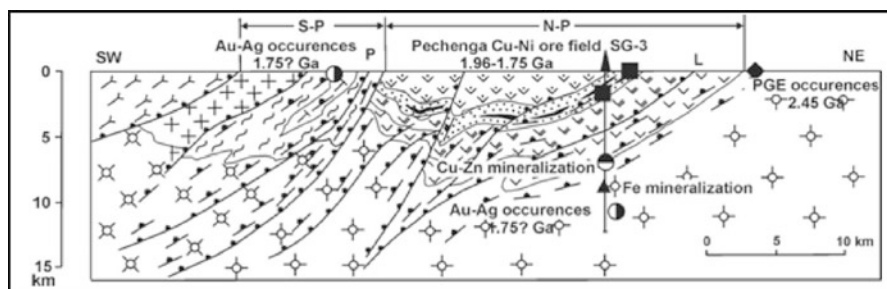


Fig. 85.1 Schematic section of the integrated geodynamic model of the Pechenga ore district in section through Kola Superdeep Borehole and correlation of ore-forming systems [3]

Geological constraints of the Integration model, density data and AVp values in the borehole section and on the surface were first used for the reappraisal of the integrated geodynamic model to a depth of 15 km. The reappraisal of the geodynamic model was mainly based on the comparison of observed and calculated gravity profiles along the section going through the SG-3 borehole. The computer-based technology allowed calculation of gravity profiles for various models from the morphology and size of tectonic units and the corresponding average rock densities. In other words, a reverse problem of simulation and fitting of a field caused by an object with known parameters was investigated. In the integrated model, the calculated and observed gravity profiles are in the best agreement with each other. An important result from elaboration of the integral model of the Pechenga ore district is the conclusion about a relatively shallow depth of its northern limb (i.e. of the North Pechenga series), which in the vertical extent do not exceed 10-12 km (Fig. 85.1).

The same is characteristic of the southern limb (or the South Pechenga series). According to the computerized analysis of the gravity data, there are no thick basic and ultrabasic feeder dykes under the central part of the Pechenga structure. Variations of the elastic anisotropy coefficient in the cross-section of the Pechenga structure indicate a more intense deformation of the southern limb compared to the northern limb. In the northern limb, synmetamorphic shearing and faulting mainly influenced the ore-bearing Productive member and the lower suites of the North Pechenga series. Judging from the distribution of rock densities, the maximal depth of the lower contact of the Productive member is less than 5-6 km. In the south, the distribution of the Productive member is limited by the Por'itash fault.

The integrated model regards the Pechenga ore district as a horizontal section of a mantle-derived volcano-plutonic ore-forming system of a centrally symmetric type. The model defines the northern limb of the Pechenga structure as an imbricated fragment of a volcanic caldera and describes its Southern limb as a sheeted monocline in juxtaposition with rheomorphic granitoid domes. Development of the system was preceded by rifting of the consolidated sialic crust. The model implies a co-genetic relationship between the Early Proterozoic volcanism and the nickel-bearing basic-ultrabasic plutonism. The basic and younger intermediate volcanic

rocks filled two volcano-tectonic depressions traced by a thick zone of northwestern faults. Later on, the volcano-tectonic depressions experienced intense compression and metamorphism, which also affected the basement rocks. Finally, steep-dipping zones of cataclasis and retrograde metamorphism were caused by an extension environment [1, 2].

85.3 ORE-FORMING SYSTEM OF THE PECHENGA DISTRICT

The Early Proterozoic Ni- and PGE-bearing Gora General'skaya massif consists of gabbro-norites and a small portion of olivine-plagioclase cumulates. Sulfo-arsenides are characteristic of its low-sulfide PGE mineralization, and prevalence of heavy and rare PGE testify to the existence of a spreading center which was probably associated with a hot spot or a mantle plume.

In the frames of the integrated model, the northern limb of the Pechenga structure (where Cu-Ni ores are concentrated), was presumed to be a sheared fragment of a volcanic caldera and its southern limb – a combination of a steeply dipping imbricated monocline with overthrust granitoid domes. The vertical extent of the Pechenga structure was estimated to be about 10 km. It was also assumed that the present erosion level of the Pechenga ore district may be considered as a horizontal section of a mantle-derived ore-forming system of central type (Fig. 85.1). The Cu-Ni deposits not only occupy a regular position in the Paleoproterozoic volcano-sedimentary complex. The Ni-bearing gabbro-wherlite intrusions are and Cu-Ni deposits are concentrated within the so-called “structural trench” oriented across the general strike of the Pechenga structure [4]. The Productive member also reaches maximum thickness in the structural trench. There were several attempts to discover Cu-Ni ores along the extension of the Pechenga structure in the Pasvik belt. The exploration boreholes penetrated several gabbro-wherlite bodies at the bottom of the Productive member. The bodies have the same petrological characteristics as in the Pilgularvi intrusions but only traces of Ni and Cu.

This inference allows relating the Pechenga Cu-Ni deposits, overprinted by metamorphism, to the volcano-plutonic types and provides a new insight into their setting, environment and origin. A summary of structural, petrological, mineralogical and geochemical data suggests that at the upper levels the Cu-Ni ore-forming system developed in two stages: 1) emplacement of mantle-derived gabbro-wherlite sills into heterogeneous Productive formation, their differentiation and generation of magmatic Cu-Ni ores; 2) dislocation and metamorphism of gabbro-wherlite sills and deposition of remobilized Cu-Ni ores in synmetamorphic shear zones.

Formation of epigenetic Cu-Ni ore zones, related to synmetamorphic secondary shearing, occurred in Svecofennian tectonomagmatic resulting in redeposition of primary magmatic sulfides at 1750 Ma [3].

Productive member on textural and structural features, mineral composition and genesis of ores are similar to those which fall to the surface, which proves the consistency of Cu-Ni mineralization down dip for at least 2.5 km.

A uranium mineralization was discovered in the Pechenga district in the 1970-s [2]. It is genetically linked to ferropicrites of the Pilgjarvi formation overlying the Productive member. Within the northern limb, three quarters of Ni-bearing intrusions established that the prolonged and multistage attack of metamorphic and magmatic processes on the Archean basement resulted in the successive migration and concentration of uranium. The Au-Ag mineralization in the context established by the SG-3 on the surface of the rocks South Pechenga series. The genetic association with gold mineralization and magmatic metasomatic processes was established by [3, 5]. The discovery of gold mineralization at the depth of 9.5-11 km has become an important result of the SG-3. Within this interval, gneisses and amphibolites of Archean age are crossed by fracture and retrograde zones. Small particles of native gold are disseminated in biotite, hornblende and plagioclase. In this zone were observed the dyke-like body porphyritic granite Litsk-Aragubsk complex (1.76 Ga). The origin of gold mineralization remains obscure: the redistribution of primary concentration in the metamorphic rocks; the deposition from reducing subcrustal fluids.

85.4 CONCLUSION

Geological constraints of the integration model, rock density data and their anisotropy of longitudinal waves in the borehole section and on the surface were first used for the reappraisal of the integrated geodynamic model to a depth of 15 km. The reappraisal of the geodynamic model was mainly based on the comparison of observed and calculated gravity profiles along the section going through the SG-3. According to the model of the Pechenga ore district, the nickel-bearing gabbro-wherlite intrusions primarily were formed as sills and occupied a subhorizontal position like to the ore-bearing intrusives of the Norilsk district. Ores of the Pechenga ore district formed at the collision development stage of the Svecofennian cycle and are controlled by shear zones in the Productive member. Epigenetic Cu-Ni ore in secondary shear zones, hydrothermal U and Au ores occurred in Svecofennian tectonomagmatic activation of the Fennoscandian Shield.

ACKNOWLEDGEMENTS The present research was executed under financial support of the Russian Foundation for Basic Research (project 14-05-00535).

REFERENCES

1. Kazansky, V.I., Kuznetsov, O.L., Kuznetsov, A.V., Lobanov, K.V. and Cheremisina, E.N.: Deep Structure and Geodynamics of the Pechenga Ore District: an Experience of the Kola Superdeep Borehole Studies. *Geology of Ore Deposits*, 36(6), 500–519 (1994)
2. Kazansky, V.I., Lobanov, K.V., Isanina, E.V. and Sharov N.V.: The Paleoproterozoic Pechenga Cu-Ni ore field (Fennoscandian Shield): A fault-bound volcanic center. *Izvestiya Earth Sciences section, Russian academy of Natural Sciences 33 International Geological Congress*. Oslo, Norway, Moscow, Special Issue, N 17, 43–46 (2008)
3. Lobanov, K.V., Kazansky, V.I., Kuznetsov, A.V. and Zharikov, A.V.: Integrated geodynamic model of the Pechenga ore district based on the correlation of geological, petrological, and petrophysical data from the Kola super-deep borehole and the reference profile at the surface. *In: Modern Problems of Ore Geology, Petrology, Mineralogy and Geochemistry*. IGEMRAS, Moscow, pp. 258–300. In Russian (2010)
4. Gorbunov, G.I.: Copper-Nickel Deposits of the Pechenga, Moscow. GEOS, 236 p. In Russian (1999)
5. Lobanov, K.V., Kazansky, V.I. and Chicherov, M.V.: The mantle-crustal ore-forming systems of the Pechenga ore district (Fennoscandian shield). *In: Mineral deposits research for a high-tech world. Proceedings of the 12th Biennial SGA Meeting, 12–15 August 2013, Uppsala, Sweden*. Elander Sverige AB, Volume 4, pp. 1657–1660 (2013)

Chapter 86

Joint Conditional Simulation of an Iron Ore Deposit Using Minimum or Maximum Autocorrelation Factor Transformation

N.L. Mai, O. Erten, and E. Topal

Abstract Considering the multivariable deposits that consist of various attributes that are frequently spatially correlated, the uncertainty associated with the grade-tonnage curves is assessed through the joint conditional simulation techniques. This paper presents the joint simulation of five attributes using the Minimum/Maximum Autocorrelation Factors (MAF). The methodology for joint simulation is three-fold: (1) MAF is used to transform the attributes to non-correlated factors; (2) the variograms for each MAF are computed and modelled; (3) the independent MAFs are individually simulated and back-transformed to the original data space. The methodology is demonstrated in an iron ore deposit in Western Australia, where the attributes of an iron ore deposit are successfully decorrelated and simulated independently. The grade-tonnage curves for each realisation are plotted and compared with the generated one by the kriging estimate. The MAF approach proves itself to be an efficient method for joint simulation of multivariable deposits.

Keywords Multivariate simulation • Minimum/maximum autocorrelation factors • Iron ore deposit • Grade-tonnage curves

86.1 INTRODUCTION

Iron ore deposits generally include different elements, typically Fe, Al_2O_3 , SiO_2 , CaO, LOI (Loss on Ignition) and others. As the iron ore is a raw material for steel making process, the uncertainty associated with its grade variability needs to be assessed. The conditional simulation algorithms are generally used to generate equiprobable realisations for the uncertainty assessment. However, as all attributes are spatially correlated, the joint simulation is required to preserve the correlation among the simulated attributes. Several techniques are developed to preserve the

N.L. Mai (✉) • O. Erten • E. Topal

Department of Mining Engineering and Metallurgical Engineering, Western Australian School of Mines, Kalgoorlie, WA 6433, Australia

e-mail: ngocluan.mai@postgrad.curtin.edu.au

correlation of variables during joint simulation process. They are generally divided into two groups:

A. Cosimulation Method

Simulation algorithms run directly on correlated variables using cross-variograms and co-kriging matrices [1, 2], thus the inter-variable correlations are preserved in the output realisations. Main drawbacks of this method are: 1) complexity when fitting the coregionalisation models; 2) correlation of variables must be linear [3]; 3) computational intensiveness to solve large co-kriging. Cosimulation technique easily becomes computationally inefficient when there are more than three variables.

B. Data Transformation Method

Prior to importing data into simulation process, the correlated variables are transformed to non-correlated factors and these factors are then simulated as independent variables. After simulation, simulated values are back transformed to gain original characteristics. There are several well-tested methods, some of which include Principal Component Analysis (PCA) [4, 5]; Minimum/maximum Autocorrelation Factors (MAF) [6, 7] and Stepwise Conditional Transformations (SCT) [8, 9].

The typical features of iron ore dataset are: 1) at least five spatially correlated variables need to be modelled and simulated; and 2) the number of samples is not very abundant. Cosimulation is tedious and computationally intensive when dealing with five variables; PCA only successfully decorrelates at zero or small lag distance; SCT requires impractical number of samples for five variables and also is not effective when lag distance is more than zero. MAF has the highest potential for iron ore deposits and is tested in this paper. After transformation, sequential Gaussian simulation (SGS) is chosen for running simulation in this paper.

86.2 SEQUENTIAL GAUSSIAN SIMULATION USING MAF

1. Primary Gaussian transformation: $Y(x) = \phi(Z(x))$
2. MAF transformation: $M(x) = A^T Y(x)$
3. Secondary Gaussian transformation (if necessary): $N(x) = \phi'(M(x))$
4. SGS simulation: $N^*(u) = \gamma(N(x))$
5. Back transformation.

where $Z(x)$: original data; $Y(x)$: normal scores; $M(x)$: MAF factors and A^T : trans-formation matrix (read more at [6, 7]).

86.3 CASE STUDY

86.3.1 Dataset Information

The iron ore dataset includes 610 boreholes with 3358 samples. 5-m-composite is used to regularise samples. The available borehole data (Fig. 86.1) is divided into two domains: Internal domain includes 589 regular boreholes with 3203 composites and external domain includes 21 irregular boreholes with 152 composites. The internal domain is used to characterise variography then simulation is implemented for the entire dataset.

86.3.2 MAF Transformation

MAF transformation is used to decorrelate five variables, Fe, Al₂O₃, SiO₂, CaO, and LOI (Fig. 86.2). The resulting factors are then used for variography

$$M(x) = A^T Y(x)$$

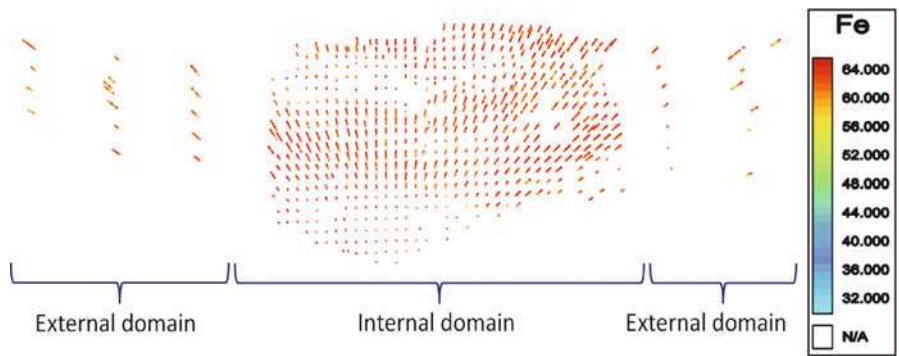


Fig. 86.1 Borehole system of deposit and domain division

$\begin{bmatrix} \text{MAF1} \\ \text{MAF2} \\ \text{MAF3} \\ \text{MAF4} \\ \text{MAF5} \end{bmatrix}$	$=$	$\begin{bmatrix} -0.1339 & -0.0394 & -0.6790 & 0.9923 & 2.8289 \\ -0.9081 & -1.0675 & -0.1982 & -0.6446 & 0.5208 \\ -1.1079 & 0.5553 & 0.5697 & -0.9887 & 1.1814 \\ -0.4178 & -0.4737 & -0.9210 & -0.0986 & -0.0788 \\ 0.2934 & 0.8316 & -1.0287 & -0.5790 & 1.0717 \end{bmatrix}$	$\begin{bmatrix} \text{Fe} \\ \text{Al}_2\text{O}_3 \\ \text{SiO}_2 \\ \text{CaO} \\ \text{LOI} \end{bmatrix}$
---	-----	--	--

Fig. 86.2 MAF transformation matrix

Table 86.1 Parameters of variogram models of five factors

Variable	Nugget	1 st spherical structure				2 nd spherical structure			
	C0	Sill	Range	Range	Range	Sill	Range	Range	Range
		C1	U	V	W	C2	U	V	W
MAF1	0.1	0.35	100	60	20	0.55	680	390	55
MAF2	0.1	0.4	100	50	15	0.5	260	200	40
MAF3	0.1	0.55	60	30	18	0.35	150	150	55
MAF4	0.1	0.5	50	40	10	0.4	150	60	18
MAF5	0.5	0.25	120	40	8	0.25	210	90	25

86.3.3 Variography

The variograms for each factor are computed and modelled using two spherical structures at three directions: Along strike (U), cross strike (V) and vertical (W) (Table 86.1).

86.3.4 Simulation and Validation

After transformation, since the factors are no longer spatially correlated, they are simulated individually by SGS. 20 realisations are generated.

A. Reproduced Correlation Coefficients

The simulation process has well preserved the correlation of variables, except CaO. The reason could be the weak correlation of CaO with other elements. In this situation, CaO can be excluded to be simulated independently (Table 86.2).

B. Reproduced Variogram

Variograms of simulated factors are reproduced at three directions. As represented in Fig. 86.3, variograms of 20 realisations of MAF1 are computed along strike direction (North 90). It is well demonstrated that realisations have honoured the spatial features of original data.

86.3.5 Grade-tonnage Curves

The grade-tonnage uncertainty of Fe₂O₃ content of the deposit is assessed by comparing grade-tonnage curves generated by ordinary kriging (OK) estimation and 20 SGS realisations (Fig. 86.4).

Table 86.2 Correlation coefficients (left: composite, right: 1st realisation)

Variable	Fe		Al ₂ O ₃		SiO ₂		CaO		LOI	
Fe	1.00	1.00								
Al ₂ O ₃	-0.89	-0.79	1.00	1.00						
SiO ₂	-0.88	-0.82	0.85	0.80	1.00	1.00				
CaO	-0.26	0.01	0.22	-0.19	0.31	-0.09	1.00	1.00		
LOI	-0.74	-0.70	0.59	0.60	0.52	0.53	0.09	-0.31	1.00	1.00

Fig. 86.3 Reproduced variograms.
(black lines: reproduced realisations' variograms, thick red line: variogram model from Table 86.1)

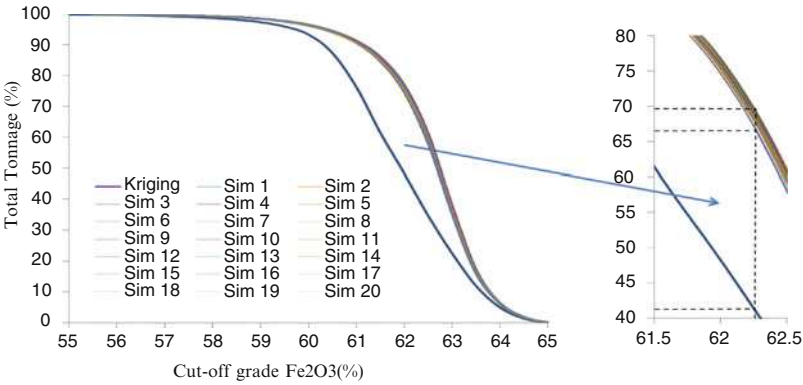
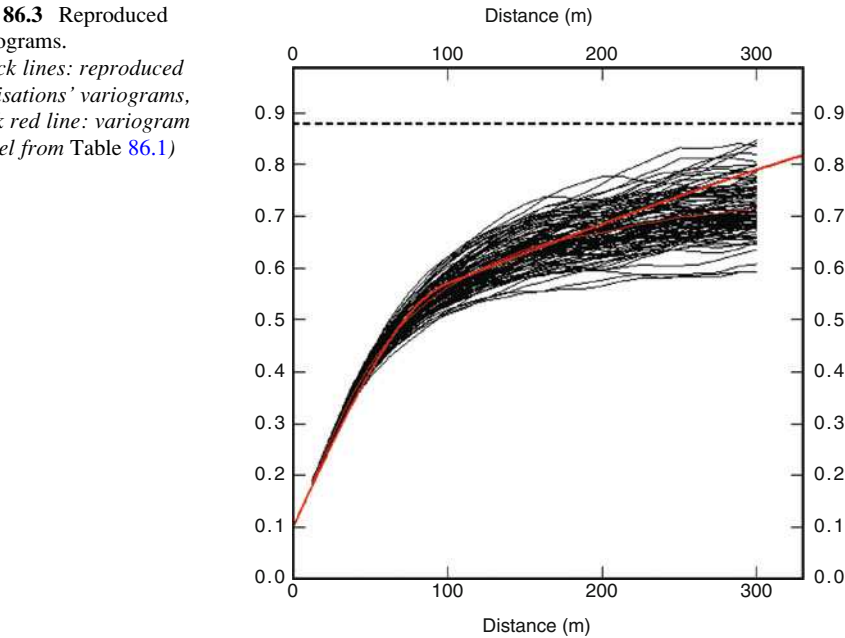


Fig. 86.4 Grade-tonnage curves of OK and 20 SGS realisations

- Two methods have similar range of total tonnage: From 55% to 65%
- OK has underestimated grade at locations where the estimated values are higher than mean of composite value. For instance, at cut-off 62.26%, the tonnage estimated by OK is 41.2% meanwhile SGS ranges from 66.5% to 69.7%.
- The variability of tonnage based on simulation is around 3% for several cut-offs.

86.4 CONCLUSIONS

MAF transformation is an efficient tool for multivariate conditional simulation. Incorporated into SGS, the simulated grade-tonnage curves show that the estimated result by OK is highly risk to resource evaluation procedure.

REFERENCES

1. Carr, J.R. and Myers, D.E.: COSIM: A FORTRAN IV program for conditional simulation. *Computers & Geosciences*, 11(6), 675–705 (1985)
2. Matheron, G.: Recherche de simplification dans un probleme de cokrigeage. Publication N-628, Centre de Géostatistique, Ecole des Mines de Paris, Fontainebleau, (1979)
3. Dowd, P.: Generalized covariances and structural analysis: a comparison. *Sciences de la Terre, Série Informatique Géologique*, 24, 95–128 (1985)
4. Davis, J.C.: Statistical and data analysis in geology: J. Wiley. (1986)
5. Goovaerts, P.: Spatial orthogonality of the principal components computed from coregionalized variables. *Mathematical Geology*, 25(3), 281–302 (1993)
6. Desbarats, A.J. and Dimitrakopoulos, R.: Geostatistical simulation of regionalized pore-size distributions using min/max autocorrelation factors. *Mathematical Geology*, 32(8), 919–942 (2000)
7. Vargas-Guzmán, J.A. and Dimitrakopoulos, R.: Computational properties of min/max autocorrelation factors. *Computers & Geosciences*, 29(6), 715–723 (2003)
8. Leuangthong, O. and Deutsch, C.V.: Stepwise conditional transformation for simulation of multiple variables. *Mathematical Geology*, 35(2), 155–173 (2003)
9. Leuangthong, O.: Stepwise conditional transformation for multivariate geostatistical simulation. NQ88013 (Ph.D.). University of Alberta (Canada), Ann Arbor. (2003).
10. Erten, O., Kizil, M.S., Beamish, B.B. and McAndrew, L.: Assessment of an in grade-tonnage curves of a multivariate lateritic bauxite deposit through min/max autocorrelation factor transformation. Paper presented at the 22nd IMCET (2011).

Chapter 87

Digital Modeling in the Study of Heavy Mineral Placers

N.P. Laverov, I.A. Chizhova, D.P. Khrushchov, A.V. Lalomov,
and E.A. Remezova

Abstract For comprehensive study of heavy mineral placers the modern methods are needed for integrated analysis. The generalization of methodological approaches and techniques has done for two kinds of modeling, widely used in the study of placers. The digital structural-lithological (DSL) modeling [1] is based on the principles of authoring partition for geological objects using a wide range of lithological, geochemical, metallogenic properties and other features. DSL-model is built as the result of computer processing of the target database, prepared on the basis of these principles. Methodology of geological-dynamic modeling of heavy mineral placers [2] is based on the study of the dynamic mechanisms of the main stages of placer formation processes - from the mobilization in the load sources of placer-forming material to deposition in the terminal sedimentary basin. Technology of hybrid expert systems [3] is the best for development of expert systems based on digital models for target prediction and evaluation of placer objects, because it permits the using of different knowledge about the object of study in various forms, allowing their automatically applying during expert system operation. The experimental sample model have shown a high level of target function.

Keywords Digital modeling • Structural-lithological modeling • Geological-dynamic modeling • Heavy mineral placers • Hybrid expert systems

87.1 INTRODUCTION

Formulation of the problem is connected with need to improve methods of informational provision for R&D, aimed at involving of heavy minerals placers for the development of raw materials base of titanium, zirconium, tin, gold and other

N.P. Laverov • I.A. Chizhova (✉) • A.V. Lalomov
Institute of Geology of Ore Deposits, Petrography, Mineralogy and Geochemistry, Russian Academy of Sciences, Moscow, Russia
e-mail: tchijova@igem.ru

D.P. Khrushchov • E.A. Remezova
Institute of Geological Sciences, National Academy of Sciences of Ukraine, Kiev, Ukraine

metals according to demands of pertinent industrial issues progress. The target of the paper is the presentation of theoretical basis, methods and obtained results of digital modeling for heavy minerals placers as well as defining of prospects for this methodology farther development.

87.2 THEORETIC BASIS AND METHODOLOGY

Modern version of the modeling methodology is based upon the combination of two authoring directions: digital structural-lithological modeling of sedimentary formations and geological-dynamical modeling of heavy minerals placers.

The methodology of DSL modeling is based on the combination of three theoretic directions: geological structural analysis, system approach and general principles of computer modeling. Digital structural-lithological model is built as the result of computer processing of the target database, prepared on the basis of these principles. It represents the most adequate volume mapping of structural and physical characteristics of geological object reflecting the spatial distribution of different elements of its structure and composition, including mineralization characteristics, processability, etc. To develop structural-lithologic models the procedure of their construction includes such landmark tasks as: development of a hierarchical structure of the object, the allocation of structural elements; the setting of lithological (including ore) filling of the structural elements; development of two-dimensional layout of the model; development of digital three-dimensional model, its verification; use model (derivatization, etc.).

Methodology of geological-dynamic modeling of heavy mineral placers [2] is based on the study of the dynamic mechanisms of the main stages of placer formation processes - from the mobilization in the load sources of placer-forming material to deposition in the terminal sedimentary basin.

- The concrete geological-dynamic models according to the various material and genetic types at consecutive stages of geological-prospecting survey are defined;
- The method of “mass balance” is offered for creation of two-dimensional models at a prospecting-estimated stage;
- The method “diffusion-convection migration of tracer” will be used for the creation of three-dimensional models for detailed estimation of deposits.

The purpose of modeling is to build a predictive-oriented spatial (3D) model of placers in the zonal and local rank (fields and deposits) with the mapping of the real (mineral and geochemical) composition and other properties and structure of the ore bodies (and surrounding deposits) by establishing hydrodynamic mechanisms, lithodynamic conditions and tectonic modes of their formation.

The combining of these two areas of author's modeling provides the different scales, increasing resolution and predictive functions for final model, which we named: Digital structural-lithological model with geological-dynamic filling. The result may be considered as retrospective-static modeling.

Retrospective-static modeling consists of two elements. The first one reflects the dynamics of objects in time (in the reverse order – from a study of modern state to decors like lylast). The second element (static) describes a stationary object structure now or simulated condition at short stages in the past, when the system variability can be neglected without significant error.

Both elements are interrelated: the identification of placer environments and paleo evolution based on its existing structure, the reconstruction of geological and dynamic processes allows giving a predictive assessment of metal-bearing placer.

87.3 LOGIC-INFORMATION MODELING

The creation of forecasting-search models of placer deposits and construction of decision rules to estimate the area, promising to detecting placer, are priorities in deposit predicting.

The evaluation of placers is carried out consistently by solution of following tasks:

1. An estimation of prospects of area;
2. In case of revealing of a prospecting area the estimation of productivity of perspective area is spent.

We have applied logic-information analysis [3,4]: a special algorithm of the pattern recognition method, based on the study of variation object range and the similarity concept. The essence of this method is to outline the informative tags to distinguish different groups of data sets and estimate their significance for evaluation of this difference and similarity. The identification of the informative tags is based on the principle of the common features of sites, belonging to the same class.

To distinguish the tags that are informative for description of class A_k and separate it from other classes, we have used the functions, based on: probability that tag j presents at the sites of class A_k and does not present at the sites of other classes; probability that tag j does not present at the sites of class A_k and presents at the sites of other classes. They are used for construction of the decision rule for the site identification: the site belongs to that class which has the maximum value of the function. As a result, we have a relationship of coefficients for an examined site, which characterizes the similarity degree of this site with other classes.

The mathematical processing of data has allowed us to compile logic-information models (the set of tags, informative for indicated tasks, with weights of theirs importance for solving of the problem). For example, solving the first task for gold alluvial placers, we have received the model “prospecting area” as the set of 14 tags from meta tags: basis, ore, morphostructure, substrat, structure of valleys - with weights in diapason from 0.046 to 0.58.

The rules for making decision have allowed creating expert system and determining correctly all placer deposits from database. Technology of hybrid expert systems [4,5] is the best for development of expert systems based on digital models

for target prediction and evaluation of placer objects, because it permits using different kinds of knowledge about the object of study in various forms, allowing their automatically applying during operation of the expert system.

87.4 EXAMPLES OF STRUCTURAL-LITHOLOGICAL MODELS

There are examples of DSL-models for titanium-zirconium placer deposit Centralnoe, Tambov region, Russia on Fig. 87.1-87.3. They are constructed by method of “mass balance”. Model “mass balance” uses the minimum data: source parameters of the ore are estimated using the results of litho chemical testing ([2], p.98); lithodynamic placer conditions are determined on the base of geomorphological characteristics of the coast and the composition of sediments.

The modeling results allow to solve the following tasks: establishing the morphology of the ore bodies and their spatial distribution, establishing the relationship of mineralization with lithofacies, facies, and forms of relief; development of

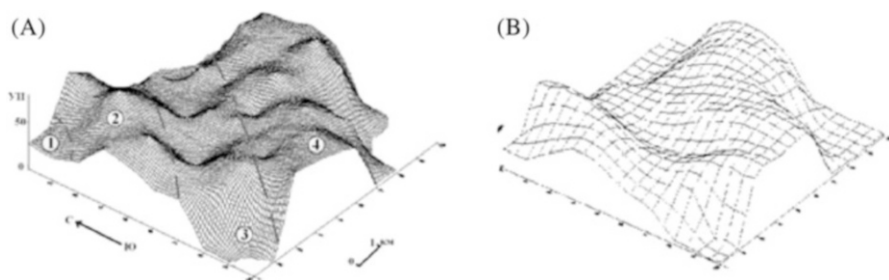


Fig. 87.1 Block-diagram of conditional ilmenite distribution (deposits Centralnoe, Tambov region, Russia; coastal marine complex, horizon 170), actual (A) and model (B) data. Facies zones: 1 – delta, 2 – littoral, 3 – coastal sea with active hydrodynamics, and 4 – coastal marine with moderate hydrodynamics

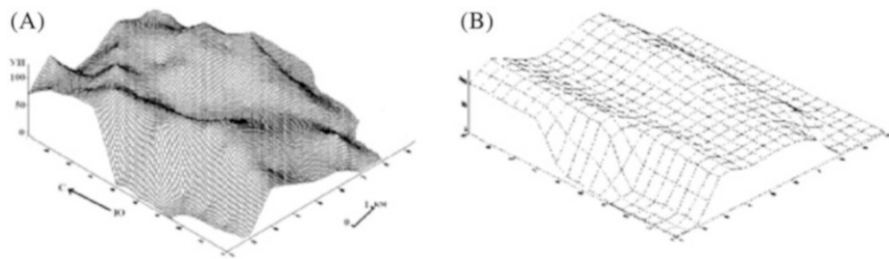


Fig. 87.2 Block diagram of conditional ilmenite distribution (deposits Centralnoe, Tambov region, Russia; dyunno-eolian complex, horizon 180), actual (A) and model (B) data

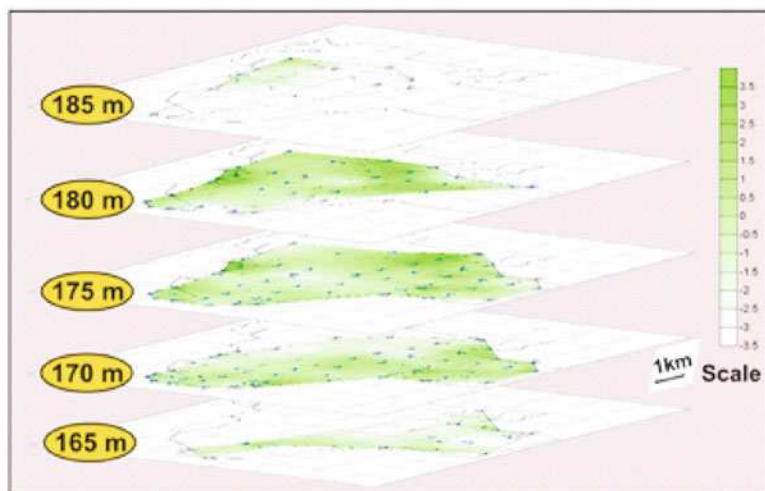


Fig. 87.3 3D-model of I Principal component distribution, characterizing the overall ordering of mineral assemblages and ore process direction on Centralnoe placer deposit

predict methods and deposits evaluation of given geological and industrial-type in the neighboring territories.

87.5 CONCLUSION

Obtained results show that the Retrospective-static methodology (Digital structural-lithological model with geological-dynamic filling) represents modern, efficient technology of information management of all R&D stages, which aimed at the development of placer titanium-zirconium, cassiterite, gold and rare metals ores deposits. Further modeling perspectives comprise on the one hand the methodology introducing into the investment projects implementation, and on the other - to further its development for a wide range of genetic types of deposits and its transformation into a permanently functioning models and expert systems which provide a solution of the complex issues related to deposits operation and environmentally reasonable mining closure with remediation of disturbed territories.

ACKNOWLEDGEMENTS The present research was executed under financial support of the Russian Foundation for Basic Research (project 14-05-90420Ukr_a)

REFERENCES

1. Khrushchev D.P. and Lobasov A.P.: Principles for the development of digital structural-lithological models of sedimentary formational units. *Geological Journal*, 213, 90–102 (2006). In Russian
2. Lalomov, A.V. and Tabolich, S.E.: Local geological-dynamic formation factors of integrated coastal-marine placers of heavy minerals. 223 p. GEOS, Moscow (2013). In Russian
3. ChizhovaI, A.: Logic-information modeling for prospecting metallogenic analysis of promising areas. *In: Research papers published by the RAS Institute of Geology of Ore Deposits, Petrography, Mineralogy and Geochemistry: new series Issue 4: Current problems of ore geology, petrology, mineralogy and geochemistry.* pp. 59–84. IGEM RAS, Moscow (2010). In Russian
4. Strujkov, S.F., Konstantinov M.M. and Chizhova, I.A.: Computer Expert System for Epithermal Gold-Silver Deposit Prognostication (Okhotsk-Chukchee Volcanic Belt, Northeast Russia). *Natural Resources Research*, 8(4), 315–343 (1999)
5. ChizhovaI, A.; Formation specifics of intellectual expert systems for forecasting express assessment of promising areas. *In: Yu, M., Arskiyi et al. (eds). The electronic Earth: Using information resources and modern technologies to increase precision of scientific forecast by means of modeling solutions in integral information fields.* pp. 323–331. RAS All-Russian Institute for Scientific and Technical Information, Moscow (2009). In Russian

Chapter 88

Working with Hierarchical Databases in R to Model Geometallurgical Data

S. Matos Camacho and K.G. van den Boogaart

Abstract For the demands of geometallurgy a vast amount of data in multifaceted shape is needed. There are high resolution images from the MLA, data tables with information on the chemistry of some mineral phases, statistics on the distribution of the grain size, and so on. This data needs to be stored in a database, which reflects the often hierarchical structure of it and is flexible enough to be extended with almost any potential occurring information. We provide a MySQL template for such a database. Finding the desired data there can be a tough task, since queries might be highly complex and confusing. Therefore, we developed an easy accessible R interface for accessing this database.

Keywords R • Geometallurgy • MySQL

88.1 INTRODUCTION

The task of geometallurgy [1] is the adaptive optimisation of mineral processing. Therefore it relies on the collaboration with several different disciplines, e.g. geology, mineralogy, mineral processing and metallurgy. Information on the microfabric, i.e. chemistry, mineralogy, microstructure, texture, etc. of raw or processed material, no matter if it is ore or a secondary resource, is examined in order to establish, e.g., a connection between the microstructure of sampled raw material and later milling results.

There are many sources for obtaining the needed data, as well as different kinds of this data (images, data tables, strings, binary data, etc.). For example the MLA (Mineral Liberation Analyser), which is a scanning electron microscope with

S.M. Camacho (✉)

HIF, Department of Modelling and Valuation, Helmholtz Institute Freiberg for Resource Technology, Freiberg, Germany
e-mail: s.matos@hzdr.de

K.G. van den Boogaart

HIF, Department of Modelling and Valuation, Helmholtz Institute Freiberg for Resource Technology, Freiberg, Germany

TUBAF, Institute of Stochastics, Technical University “Bergakademie”, Freiberg, Germany

automated software, is often used in a mineralogical context to obtain high resolution images of grain mounts or thin section slices. These images are usually divided into different frames. Again each frame contains a certain number of mineral particles consisting themselves of grains of different mineral phases. This information is encapsulated in a MS Access file, where a direct access on the data is only possible by a certain program. But for further purpose these information has to be freely accessible, complete and partially, since for certain samples these data can easily exceed the available main memory.

We developed a template for a Geometallurgical database in order to guarantee a structural data access, which realises a strictly hierarchical approach arising from most of the data occurring in this context. On the other hand we introduce an R package providing a fast and comfortable interface to query information in this database. It avoids complicated SQL statements and introduces slim R-like expressions instead.

88.2 A GEOMETALLURGICAL DATABASE

88.2.1 *The Database Scheme*

Since Geometallurgical data can be very diverse, a database storing such data must be flexible enough. Our approach distinguishes data into two types: atomic data, that consists of a single value, e.g., an integer or a string, and composite data, that is always stored as an object in the table *gmObject* (see Fig. 88.1). One may think of classes, where atomic data represents an attribute and composite data is the class itself.

Everything stored in the database is a variable. Every variable has a variable type, which defines if it is composite (type: set) or atomic (type: int, string, real, etc.). These are defined in the tables' *gmVar* and *gmVarType*.

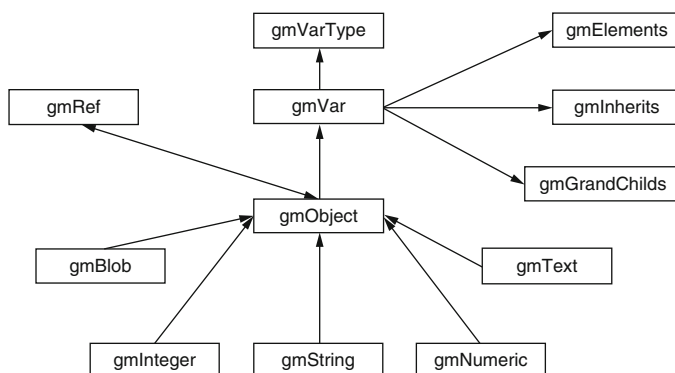


Fig. 88.1 The database scheme

If we want to create a new object (*gmObject*), it has to be of variable type set. Atomic data is always stored, with a reference to the object it belongs to, in the tables' *gmInteger*, *gmNumeric*, *gmString*, *gmText* or *gmBlob*. Thus, every single value has to be associated with a set containing it.

We also allow inheritance, meaning that a variable of a certain kind may have the same properties as another one (his parent) and some additional, too. Therefore, the table *gmElements* gives all the members of a variable, *gmInherits* defines the inheritance and *gmGrandChilds* even declares inheritance of second order (the parent of the parent).

Finally, we can construct data consisting of several kinds of composite data. This is defined in *gmRef*, where we may refer for an object if it is contained in some greater object.

Instead of using an object-orientated database [2], we used a relational one, MySQL. That allows an efficient access of huge amounts of statistical data and, on the other hand, is flexible enough in terms of different data types.

88.2.2 Example: MLA Data

MLA data is an example to demonstrate the hierarchical approach, and at the same time, to illustrate the database structure. As mentioned before, the MLA delivers images of certain samples. But every sample belongs to some measurement series, which itself may be part of a bigger project.

Figure 88.2 shows such a structure. For organisational reasons there is a super set called *root*, where you can find all the composite variables of first order, meaning that they are not part of any other variable. In the example we have projects, some mineral phases occurring in the MLA images, and users, who created the stored data. For every set we also stored some additional information, representing metadata.

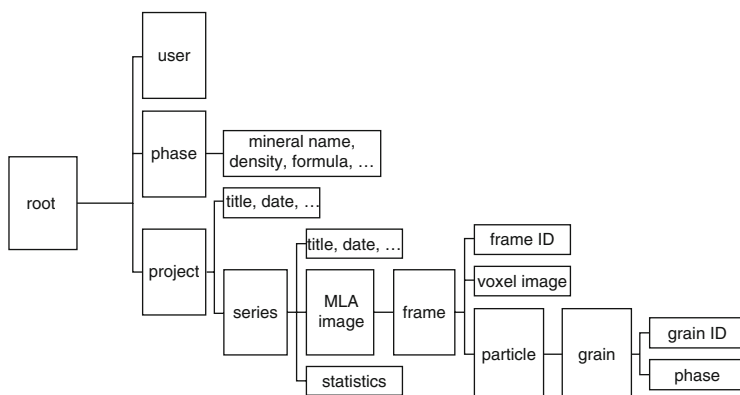


Fig. 88.2 Hierarchy of the geometallurgical database illustrating the example of MLA data: a red frame marks composite data, a blue frame atomic data

88.3 THE R PACKAGE *gmDATABASE*

The R package *gmDatabase* provides an interface for accessing the geometallurgical database in an easy way. Queries in such a database are likely to end up in highly complex SQL statements due to its hierarchical structure. Therefore we implemented an R package delivering a handful of functions for writing and retrieving data, using R-like representations instead of actual SQL commands. We use the package RMySQL [3] for connecting and communicating with the database.

Level 0: Functions for the Common User

These functions allow the user to communicate with the database using R. We provide functions for reading, writing and manipulating data. For example there is the main query function *gmRead(expr)*. Here *expr* specifies the thing we are looking for. For example, if we want to get the 6th frame of an MLA image in the series “X1” of the “Test project”, we can access it by

```
gmRead(root$project[gmTitle = "Test project"]$series[gmtitle = "X1"]
$MLAimage$freme[frameID = 6])
```

Level 1: The Interface between R and SQL

On this level we have functions for the manipulation of *expr*. Mainly we decompose this sequence to distinguish between variables in the database and actual values defining the desired object we are looking for. These functions can be also used for string manipulation and creation of calls in R.

Level 2: Constructing an SQL Query and Get the Result

The last level consists of internal functions, which are not meant for being executed by the user directly. They use the decomposed *expr* to create an SQL expression, which represents the query.

REFERENCES

1. Dunham, S. and Vann, J.: Geometallurgy, Geostatistics and Project Value—Does Your Block Model Tell You What You Need to Know? *In: Project Evaluation 2007*, pp 189–196 (2007)
2. Elmasri, R. and Navathe, S.B.: Fundamentals of Database Systems. 6th ed. Addison-Wesley (2011)
3. The Comprehensive R Archive Network: RMySQL, <http://cran.r-project.org/web/packages/RMySQL/index.html>

Chapter 89

Application of Empirical Model Decomposition and Independent Component Analysis to Magnetic Anomalies Separation: A Case Study for Gobi Desert Coverage in Eastern Tianshan, China

Chengbin Wang, Jianguo Chen, and Fan Xiao

Abstract Traditional mineral resources prospecting and information extraction method cannot satisfy the complexity of geological and multi-stages of ore-forming processes. In this paper, empirical model decomposition (EMD) and independent component analysis (ICA) are applied to separate and reconstruct magnetic data so as to extract the signals from different sources. Firstly, original magnetic data is sifted to get intrinsic mode functions (IMFs) from high to low frequency. Secondly, ICA is utilized to reconstruct the former IMFs which obtained by removing background and get independent components (ICs). Finally, nine IMFs and three ICs are obtained by the combining method that is used to process magnetic data of Gobi desert coverage in Eastern Tianshan. IC1 discriminates igneous rocks, and may be related to magmatic intrusion, IC2 tracks the distribution of plates and may be related to plate subduction, IC3 indicates the basite-ultrabasic rocks which are distributed in the middle of area and may be related to crustal thickening.

Keywords Empirical model decomposition (EMD) • Independent component analysis (ICA) • Magnetic data • Gobi desert coverage • Eastern Tianshan

C. Wang

Faculty of Earth Resources, China University of Geosciences, Wuhan, China

J. Chen (✉)

State Key Laboratory of Geological Processes and Mineral Resources, China University of Geosciences, Wuhan, China

e-mail: jgchen@cug.edu.cn

F. Xiao

Department of Earth Sciences, Sun Yat-sen University, Guang Zhou, China

89.1 INTRODUCTION

Because of the complexity of geological processes and multi-stages of ore-forming processes, original magnetic anomalies are composed of a mixture of various geological factors including background and local anomalies which may be caused by ore deposits or other geological anomalies. Separating magnetic anomalies is one of most difficult and important issues in mineral prospecting and potential resource assessment. In recent years, the means to predict mineral resources is using interaction information such as geology, mineral products, remote sensing, physical geography, exploration geochemistry and so on. Moreover, exacting the valid information is the pivotal and the most difficult step in mineral resources prediction and assessment [1]. Lots of new methods such as wavelet, fractal, and non-negative matrix factorization, Empirical Model Decomposition and independent component analysis have been introduced into the mathematical geology field. This paper mainly introduces an application of EMD and ICA combining method to magnetic anomalies separation.

89.2 PRINCIPLES AND METHODS

89.2.1 *Empirical Model Decomposition*

Empirical Model Decomposition, which was recently proposed by E. Huang, is nonlinear and unstable signal processing method which introduced the concept of intrinsic model function (IMF). Compared with Fourier transform and wavelet, EMD completely gets rid of the shackles of linearity and stability. So it has many successfully applications in meteorology, biomedical, structural mechanics, finance, communication, signal processing, image processing and others. Any complex time (space) signals (data) are composed by IMFs from high to low frequency. An IMF is a function that satisfies two conditions: (1) in the whole data set, the number of extreme and the number of zero crossings must either equal or differ at most by one; and (2) at any point, the mean value of the envelope defined by the local maxima and the envelope defined by the local minima is zero [2]. Nunes et al. proposed a modified bidimensional empirical mode decomposition (BEMD) on the basis of one-dimensional empirical model decomposition [3].

89.2.2 *Independent Component Analysis*

Independent component analysis is a multicenter signal processing method and it tries to transform an observed multidimensional vector into components that are statistically independent from each other as possible [4]. ICA is widely applied in

signal processing, sound signal separation, communication, face identification, remote-sensing information processing etc. ICA model is a basic generative model, and it describes how the observed data is generated by a mixing process. To guarantee that ICA model is solvable, the following assumption and limitations must be made: (1) statistical independence, (2) non-Gaussian distribution, (3) the unknown mixing matrix is square [5]. Assume n mutually independent random variables s_1, s_2, \dots, s_n , whose linear combination generates n random variables x_1, x_2, \dots, x_n , i.e.

$$x_i = a_{i1}s_1 + a_{i2}s_2 + \dots + a_{in}s_n \quad i = 1, 2, 3, \dots, n \quad (89.1)$$

where a_{ij} , $i, j = 1, 2, \dots, n$ are real coefficients. For convenience, define $\mathbf{x} = [x_1, x_2, \dots, x_n]^T$, $\mathbf{s} = [s_1, s_2, \dots, s_n]^T$, and \mathbf{A} as the matrix with elements a_{ij} , the composite model can be written as

$$\mathbf{x} = \mathbf{A}\mathbf{s} \quad (89.2)$$

The independent components \mathbf{s} can be solved by computing the inverse matrix \mathbf{B} of matrix \mathbf{A} , i.e.

$$\mathbf{s} = \mathbf{B}\mathbf{x} \quad (89.3)$$

In conclusion, EMD and ICA separate signals according to scale features and independence of data instead of pre-set base functions.

89.2.3 Technique Process

The process of combining method includes following three steps:

1:200,000 magnetic data are decomposed into IMFs by BEMD. Algorithm employs enveloping surface method and biharmonic spline interpolation.

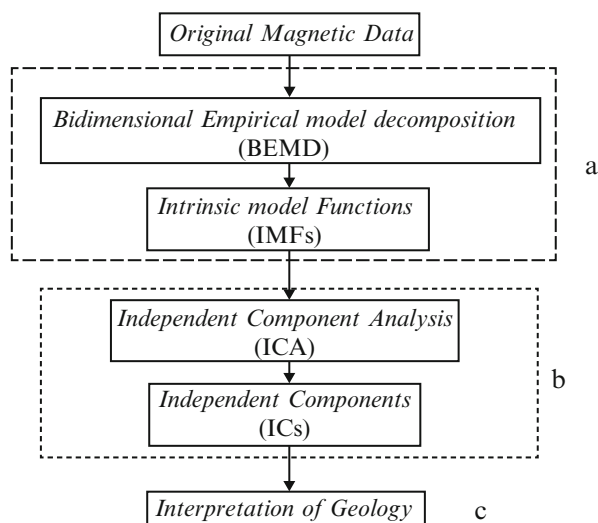
ICA is utilized to reconstruct the former IMFs which obtained by removing background and get ICs.

Geological interpretation of ICs combined with geological information.

89.3 CASE STUDY

Eastern Tianshan contains a number of Paleozoic terrains that amalgamated between the Tarim and Siberian blocks, and experienced a series of complex tectonic evolution events mainly during Paleozoic accretion and collision, Mesozoic thermal subsidence and Cenozoic thrusting and uplift. The study area is composed of three tectonic zones consisting of the late Paleozoic Ha'erlike–Dananhu

Fig. 89.1 Flow chart of EMD and ICA combining method



island arc, late Paleozoic Jueluotage rift and central Tianshan terrine systems, which are separated by the regional-scale deep Dacatan–Dananhui and Aqikkuduk–Shaquanzi faults, respectively. This paper applies EMD and ICA (Fig. 89.1) to analyze magnetic data which was collected in Gobi desert coverage in Eastern Tianshan, China. Firstly, using BEMD to sift magnetic data so as to get IMFs. Secondly, Fast ICA method [6] is applied to reconstruct the IMFs to obtain useful information. The magnetic separation results display the change from high frequency to low frequency. IMF1 indicates the high frequency maybe caused by noises while Res represents the low frequency maybe caused by background. Nonetheless, it is difficult to explain IMFs's geological significance because of too many IMFs. So we utilize the Fast ICA to reconstruct the local IMFs which obtained by removing background, then, three independent components (ICs) are obtained (Fig. 89.2).

We find that results of ICA are concise and easy to geological interpretation. IC1 discriminates igneous rocks from stratum, and may be related to magmatic intrusion, IC2 tracks the distribution of plates and may be related to plate subduction, IC3 indicates the basite-ultrabasic rocks which are distributed in the middle of area and may be related to crustal thickening.

89.4 CONCLUSION

This paper proposed a new method combining EMD and ICA to separate and reconstruct magnetic data. It is obviously that the combining method is effective to extract signals from different sources which may be related to geological events. Furthermore, it is necessary to deepen the geological interpretation in the further.

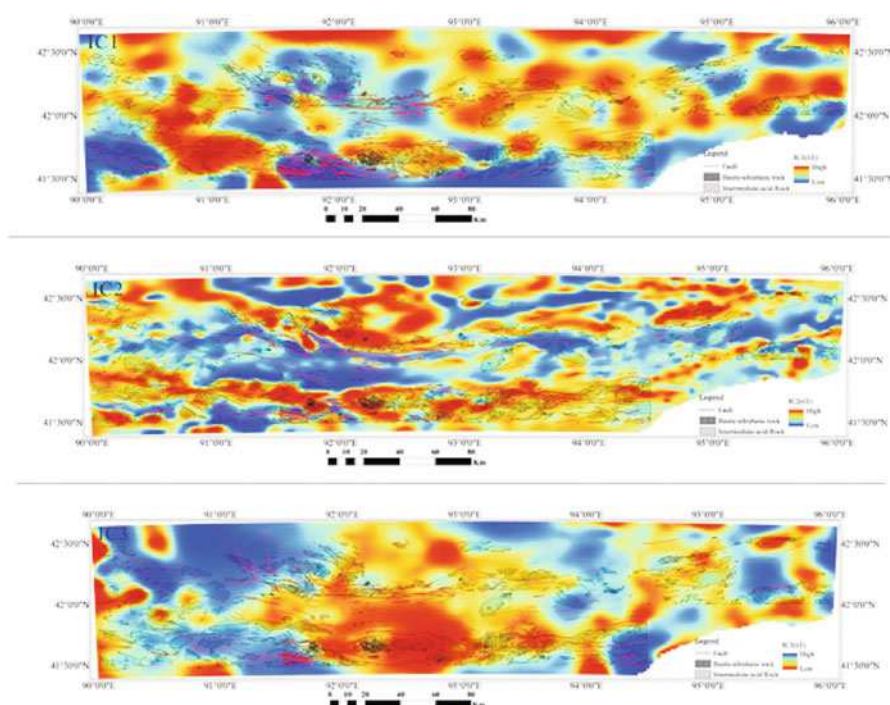


Fig. 89.2 Results of ICA

ACKNOWLEDGEMENTS This research has been financially supported by Chinese Geological Survey Program (1212011120986), National Key Technology R&D Program (No. 2011-BAB06B08-2) and Special fund program of Institute of Geophysical and Geochemical Exploration CAGS (WHS201205).

REFERENCES

1. Yu, X.C., Liu, S.H., Ren, J.M. and Zhang, T.: Robust Fast Independent Component Analysis Applied to Mineral Resources Prediction. *In: Geomathematics and GIS Analysis of Resources, Environment and Hazards, Proceedings of IAMG 94–97* (2007)
2. Huang, N.E., Shen, Z., Long, S.R. et al.: The Empirical Mode Decomposition and the Hilbert Spectrum for Nonlinear and Non-stationary Time Series Analysis. *Proceedings of the Royal Society of London. Series A: Mathematical, Physical and Engineering Sciences*.454 (1971), 903–995 (1998)
3. Nunes, J.C., Guyot, S. and Deléclle, E.: Texture analysis based on local analysis of the bidimensional empirical mode decomposition. *J. Machine Vision and Applications*, 16 (3), 177–188 (2005)

4. Hyvärinen, A.: Survey on independent component analysis. *J. Neural Computing Surveys*, 2 (4), 94–128 (1999)
5. Shi, X.Z.: Blind Signal Processing—Theory and Practice. Shanghai Jiao tong University Press & Springer, Shanghai China & Berlin Germany (2011)
6. Hyvärinen, A. and Oja E.: A fast fixed-point algorithm for independent component analysis. *Neural Computation*, 9 (7), 1483–1492 (1997)

Chapter 90

3D Modeling of Urban Geological Body Based on the KDA Method for Beijing City, China

Chen Jian-ping, Tian Yi, and Chen Yu-Chen

Abstract In order to evaluate the quantity and quality of city's underground space resources effectively, this paper puts forward a new three dimensional modeling for the city geology body of the Knowledge Driven Analysis (KDA) method. Based on the professional knowledge analysis of city engineering geology, hydrogeology, it selects geology, road, explored underground resources and so on, as the affecting factors to evaluate the urban geological body. By using a 3D software platform, this paper discusses the comprehensive modeling details for these factors even from non-spatial entities. The case of Beijing City shows this method can effectively describe the spatial and non-spatial properties for the city geological body.

Keywords Knowledge Driven Analysis (KDA) • 3D modeling • Geological body • Quantity evaluation

C. Jian-ping (✉)

Beijing Key Lab. of Land Resources Information Research & Development,
Beijing 100083, China

School of Earth Sciences and Resources, China University of Geosciences,
Beijing 100083, China

e-mail: 3s@cugb.edu.cn

T. Yi

Beijing Key Lab. of Land Resources Information Research & Development,
Beijing 100083, China

School of Land Science and Technology, China University of Geosciences,
Beijing 100083, China

e-mail: tianyi@cugb.edu.cn

C. Yu-Chen

School of Land Science and Technology, China University of Geosciences,
Beijing 100083, China

90.1 INTRODUCTION

Recently, the rapid promotion of metropolis results in a seriously problems, such as the sharp urban population increasing and the very shortage of living space, which had hindered the mega-cities' long term sustainable development [1–3]. In order to solve such issues, some developed countries have tempted on exploiting underground spaces. Their experiences proved that the exploitation of underground space resources is a must to the city sustainable development [4–6]. For the same reason, several Chinese cities have explored the urban underground space to support their city space development since 1980's [2]. However, due to the lack of a comprehensive geological model support, it is difficult to carry out the underground space resources' quantity evaluations. For example, the existing urban geological modeling, based on the TIN, DEM and other surface model in general, can't reflect the total entity affecting elements of the city geological body development [5]. Therefore, this paper is to get a new method to express the affecting elements of city geological body within a comprehensive model.

90.2 BASIS OF THE STUDY AREA

The study area lies in the city of Beijing, north of China, which has been expanded without fail since 1980s'. Because there isn't enough free space available for the old city's and major city's development (Fig. 90.1), Beijing had to explored the underground geological body in the last decades. However, for the lack of information for the city geological body, the developed underground structures had led to building subsides and land cracks. Learning the underground spaces by the professional knowledge in 3D is becoming an urgent need for Beijing.

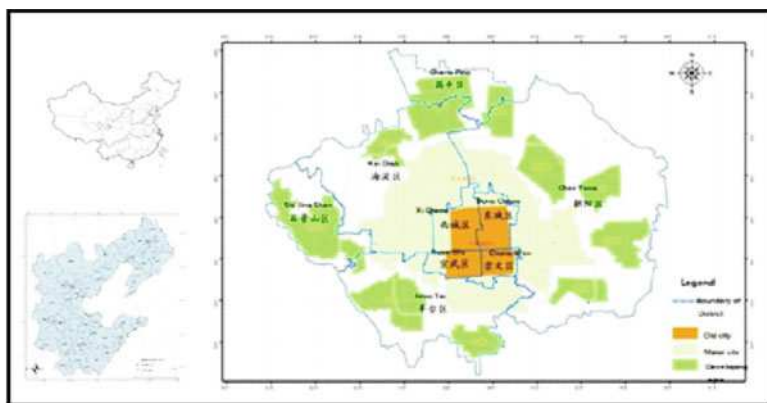


Fig. 90.1 Study area of Beijing, a city had to explore the underground geological body to get more developing spaces in China

90.3 METHODOLOGY

Usually, city planners need some engineering geological models to evaluate city geological bodies. However, the experience of city development in China indicates it as a complicated process. Therefore, the factors of economy and cultural protection and planning also should be fully taken into account for the city geological body development based on the professional knowledge of the city's history, the utilization of current status and so on. Within this paper, the process of those elements selecting and evaluation is named the Knowledge Driven Analysis (KDA). In practical terms, it can be broken down into three steps as follows.

Step 1: Key elements selecting. In general, the elements to drive or restrain the city geology body development, no matter in spatial and non-spatial format, should be identified clearly. Thus, this paper selects them rather than simply from the natural features, but also from some social and economic features, such as engineering geology, land use type, existing constructions or buildings above or under the surface, ecology, environment construction and so on to express the geological body utilizations (Table. 90.1).

Step 2: Factors' weighted value evaluating. For the selected factors, it is difficult to know how it works on the geological body exploration. Through the questionnaire survey of more than 100 experts of geology, history, hydrology, economy, city planning, this study gets the relative weighted values of those factors. When those factors were modeled in spatial format within a coordinate system, we can use the multi-factor weighted assessment model in ArcGIS software to get the quantity and quality of a city geological body for the city's underground development.

Step 3: Factors' modeling in a three dimensional platform. Considering the specific characters of the city geological bodies, the goal of geological bodies modeling is to analyse their availabilities as accurately as possible within the Micro-Mine software platform. For the non-spatial factors, for example, the historic reservation above a geological body needs to form a 1 to 2 kilometer horizontal protecting buffer area and 10 to 30 meter deep protecting buffer area based on the knowledge of the geology and rainfall. It is to avoid the potential collapses and damages for the ground buildings after the underground spaces exploring (Fig. 90.2). For the geological factors, this paper uses a series of geological profiles from the geological knowledge to form real body by the geological spatial relationships and lithology combination rules (Fig. 90.3).

90.4 RESULTS AND DISCUSSION

In order to evaluate the modelings affects, this paper analysis the potential quantity of underground space resources in the Beijing central city. Within the modeled areas, every evaluated factor is mixed into millions of cubes. The un-available cubes, based on the influences of underground resources developing, would be removed from the total underground space resources in Beijing central city by the

Table 90.1 Contents and their weight values of city geological body modeling in Beijing

Type	Index	Sub-index	Weight Value
Geology	1 Fracture structure		-10
	2 Major Stratum	2.1 Quaternary Period	10
		2.2 Tertiary Period	30
		2.3 Jurassic Period	30
		2.4 Cretaceous Period	60
		2.5 Carboniferous Period	30
		2.6 Ordovician Period	40
		2.7 Cambrian Period	40
		2.8 Proterozoic Eon	40
Road	3 Major Road	3.1 Circle Road	-5
		3.2 Major Road	-3
	Underground resources	4 Exploring Underground Resources	
5 Subway		-5	
6 Shallow Planning of the city		5	
7 Deep Planning of the city		3	
8 Underground space of the city building		8.1 Low building	-2
		8.2 Middle building	-4
		8.3 High building	-6
		8.4 High rise building	-8
	8.5 Very high building	-10	
Environment	9 Public Green Land		-5
	10 Water protection	10.1 Core Protecting Area	-10
		10.2 Major Protecting Area	-8
		10.3 Protection Area	-6
		10.4 Potential Area	-4
	11 Landfill of waste		-5
	12 Rivers and Lakes		-5
Others	13 Heritage conservation	13.1 State level	-5
		13.2 City level	-3
		13.3 Sub-city level	-1
Total			0

geological KDA rules. According to the total values, the low value cubes, not suitable for development, would be wiped off. In the end, it calculated that Beijing city have total developable underground space resources of 318,062 million cubic meters within the range of 300 meters under the ground, which could completely make up the land demand gap for future 20 to 50 years of Beijing. Of course, if there is more professional knowledge used for these model, the evaluating results of city potential underground spaces resources would be more accuracy.

Fig. 90.2 3D model of heritage conservation (top) and the underground limitation area of building (down)

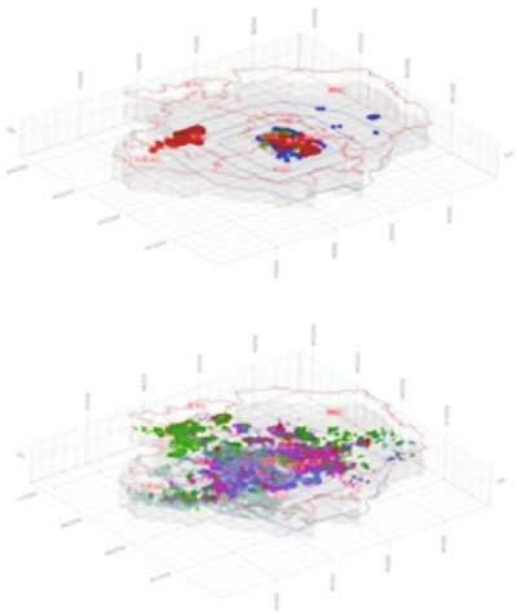
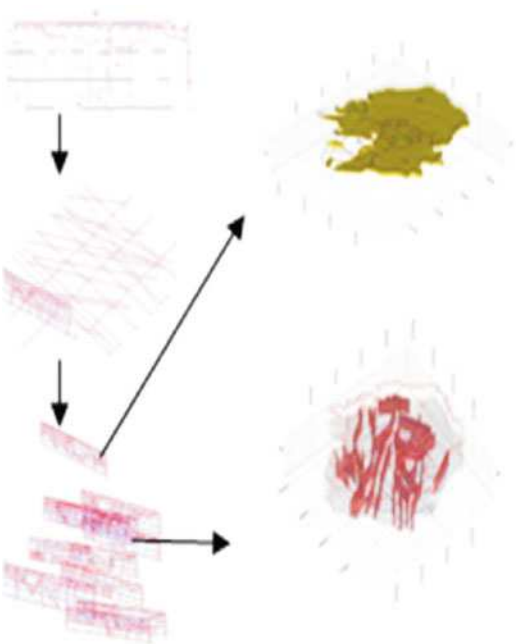


Fig. 90.3 Use of the geological profiles to form the 3D model of geological factors



90.5 CONCLUSIONS

This dissertation, combining real ground and underground 3D model, is a tentative research in city geological body modeling in China. It gives a set of 3D modeling method based on the city planning knowledge driven analysis and a case study in the central of Beijing City. It concluded that this method could guide the spatial and non-spatial in within a comprehensive model.

REFERENCES

1. Roberts, Don V.: Sustainable development and the use of underground space. *Tunnelling and Underground Space Technology*, 11(4), 383–390 (1996)
2. Xiuhua, Zheng, Chengbiao, Wang and Fuzong: Beijing's demonstration activities in geothermal source heat pumps in China. Geothermal Resources Council—Annual Meeting of the Geothermal Resources Council 2007, 487–491 (2007)
3. Niini, Heikki: Classification and development of bedrock resources in Finland. *Bulletin of the Geological Society of Finland*, 58(1), 335–350 (1986)
4. Parriaux, L. and Tacher, P. Joliquin: The hidden side of cities—towards three-dimensional land planning. *Energy and Buildings*, 36, 335–341 (2004)
5. Sterling, Raymond L. and Nelson, Susan: Planning the Development of Underground Space. *Underground Space*, 7(2), 86–103 (1982)
6. Narvi, S., Vihavainen, U., Korpi, J. and Havukainen, J.: Legal, administrative and planning issues for subsurface development in Helsinki. *Tunnelling and Underground Space Technology*, 9(3), 379–384 (1994)

Chapter 91

Generalized Compensation Model for the Gravimetric Moho Recovery

R. Tenzer and W. Chen

Abstract A constant value of the Moho density contrast is often assumed in methods for a gravimetric determination of the Moho geometry. This assumption might be sufficient in some regional studies. In global studies, however, this assumption is not reasonable due to the fact that the Moho density contrast vary significantly. Large errors then can be expected in the Moho geometry determined globally from gravity data. In this study we utilize a generalized compensation scheme based on variable depth and density of compensation. The Moho depths are determined based on assuming the variable Moho density contrast. We demonstrate that this assumption (instead of a uniform model) significantly improves the agreement between the global gravimetric and seismic Moho models; the RMS fit of the gravimetric result with the CRUST1.0 seismic Moho model is 4.5 km (for a uniform model) and 3.0 km (for a variable model).

Keywords Crust • Gravity • Isostasy • Mantle • Moho

91.1 INTRODUCTION

In gravimetric methods for a global recovery of the Moho depths a uniform density contrast at the Moho interface is often assumed. However, the results of seismic and gravimetric studies revealed that the Moho density contrast varies significantly [1], for instance, estimated that the Moho density contrast varies globally from 81.5 kg m^{-3} (in the Pacific region) to 988 kg m^{-3} (beneath the Tibetan Plateau). They also provided the average values of $678 \pm 78 \text{ kg m}^{-3}$ and $334 \pm 108 \text{ kg m}^{-3}$ for the continental and oceanic areas respectively. [2] reported a similar range of values between 82 and 965 kg m^{-3} , with a mean of 441 kg m^{-3} . They also demonstrated that the Moho density contrast under the oceanic crust is highly spatially correlated with age of the oceanic lithosphere; the density contrast minima are located along the oceanic rift zones and the corresponding maxima are along the oceanic subduction zones. These large density contrast variations at the Moho interface

R. Tenzer (✉) • W. Chen

School of Geodesy and Geomatics, Wuhan University, Wuhan, China

e-mail: rtenzenr@sgg.whu.edu.cn

indicate that the assumption of a uniform model might not be sufficient for an accurate determination of the Moho geometry from gravity data, especially in global studies and in regions with the complex lithospheric structure. A possible method of dealing with this problem was proposed by [1]. They developed and applied a least-squares approach, which combined seismic and gravity data in the Vening Meinesz-Moritz isostatic inverse scheme for a simultaneous estimation of the Moho depth and density contrast. In this study, we propose an alternative method, which incorporates the variable Moho density contrast as the a priori information in the gravimetric determination of the Moho depth.

91.2 METHOD

The Moho density contrast $\Delta\rho^{c/m}$ is defined as the difference between the (laterally varying) upper mantle density ρ^m and the (constant) reference crustal density ρ^c :

$$\Delta\rho^{c/m}(\theta, \lambda) = \rho^m(\theta, \lambda) - \rho^c \quad (91.1)$$

The relation between the gravity and Moho depth is then defined as follows

$$\delta g^{m, \Delta\rho}(r, \theta, \lambda) = \frac{GM}{R^2} \sum_{n=0}^{\bar{n}} \left(\frac{R}{r}\right)^{n+2} \frac{n+1}{2n+1} \sum_{m=-n}^n F_{n,m}^{\Delta\delta D} Y_{n,m}(\theta\lambda) \quad (91.2)$$

where GM is the geocentric gravitational constant, R is the Earth's mean radius, r , θ , λ are spherical coordinates (radius, co-latitude, longitude), $Y_{n,m}$ are the spherical harmonics, \bar{n} is the upper summation index, and $\delta g^{m, \Delta\rho}$ is the isostatic gravity disturbance [2]. The Moho-depth correction coefficients $F_{n,m}^{\mathcal{O}\rho\delta D}$ read

$$F_{n,m}^{\Delta\rho\delta D} = \frac{3}{\bar{\rho}_{\text{Earth}}} \sum_{k=0}^{n+2} \binom{n+2}{k} \frac{(-1)^k}{R^{k+1}} (\Delta\rho^{c/m} \delta D)_{n,m}^k \quad (91.3)$$

where

$$\sum_{m=-n}^n (\Delta\rho\delta D)_{n,m}^{(k)} Y_{n,m}(\theta, \lambda) = \frac{2n+1}{4\pi} \iint_{\phi} \Delta\rho^{c/m}(\theta', \lambda') D_0^k(\theta', \lambda') \delta D(\theta', \lambda') P_n(t) d\Omega' \quad (91.4)$$

The coefficients $F_{n,m}^{\mathcal{O}\rho\delta D}$ of the design matrix are generated from the a priori Moho depths D'_0 and the (laterally varying) values of the Moho density contrast $\Delta\rho^{c/m}$ (Eqs. 91.3, 91.4). The inverse solution of a system of observation equations (Eq. 91.2) yields the Moho-depth correction terms $\delta D'$.

91.3 RESULTS

The Moho depths were determined for the constant (455 kg m^{-3}) and variable Moho density contrast models. The values of the Moho density contrast were taken from the CRUST1.0 global seismic crustal model [3]. The results are shown in Fig. 91.1. These results were validated using the CRUST1.0 Moho depths (Fig. 91.2). The statistics of the Moho depth differences are summarized in Table 91.1.

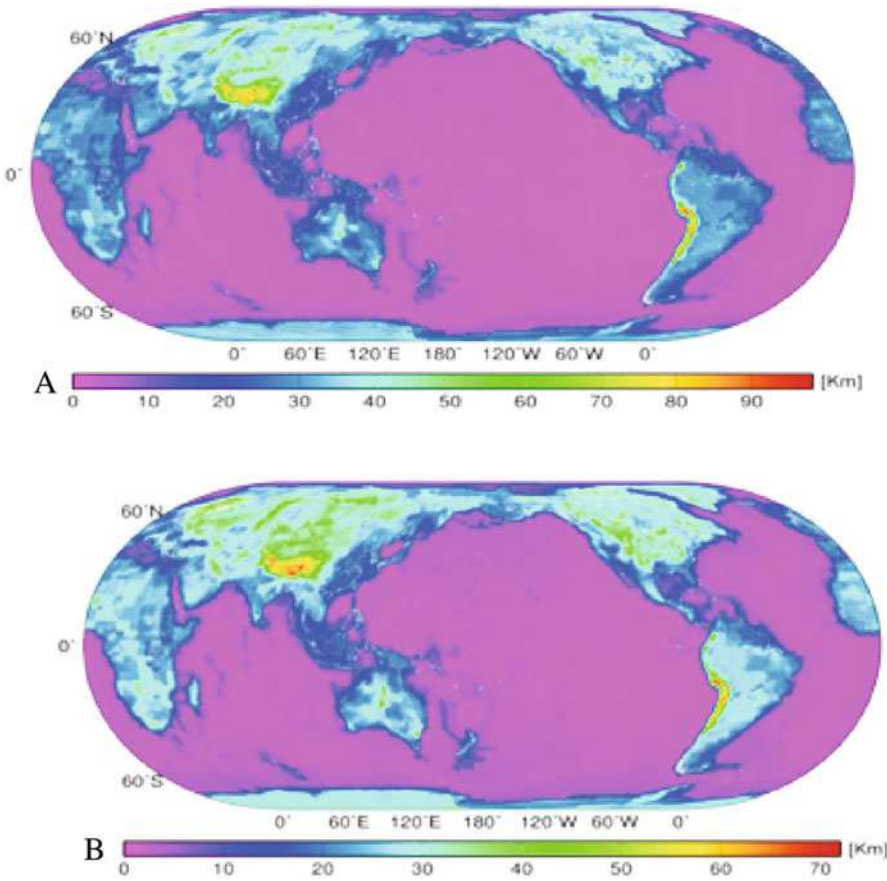


Fig. 91.1 Gravimetric Moho depths: (a) D and (b) $D_{\Delta\rho}$ determined using the constant and variable Moho density contrast respectively

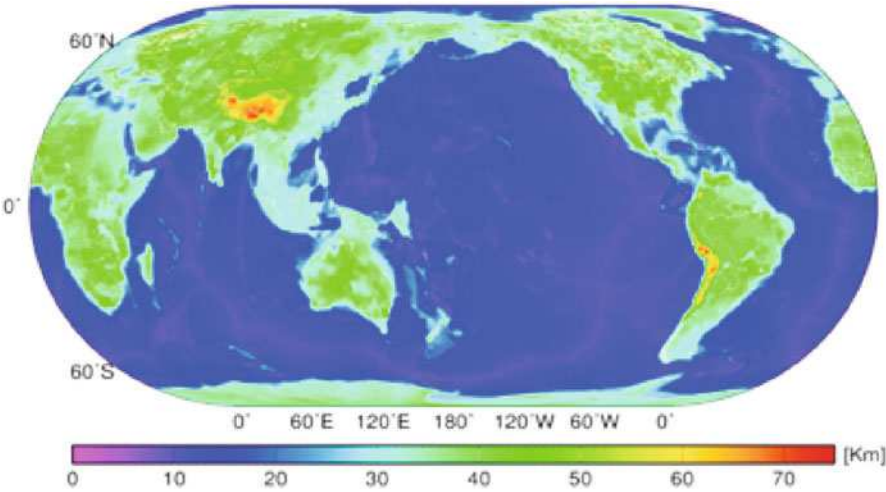


Fig. 91.2 CRUST1.0 seismic Moho model

Table 91.1 Statistics of the Moho depth differences

Moho depth differences	Min [km]	Max [km]	Mean [km]	RMS [km]
$D_{\Delta\rho} - D$	-26.3	8.1	-1.9	2.6
$D_{\text{CRUST1.0}} - D_{\Delta\rho}$	-11.7	30.7	9.7	3.0
$D_{\text{CRUST1.0}} - D$	-34.6	29.2	7.8	4.4

91.4 CONCLUSIONS

The RMS of differences between the gravimetric and seismic Moho depths (for a uniform model) is 4.4 km (Table 91.1). The variable Moho density contrast improved the RMS fit of the gravimetric solution with the seismic model more than 30%; the RMS of differences is in this case only 3.0 km. Both gravimetric solutions are significantly biased with respect to the CRUST1.0 seismic model; the mean of differences is 9.7 km (for a variable model) and 7.8 km (for a uniform model). This bias is attributed to the gravitational signal of (unmodelled) mantle heterogeneities. There are also additional uncertainties in the used gravity and crustal structure models, which caused the disagreement between the gravimetric and seismic models.

REFERENCES

1. Sjöberg, L.E. and Bagherbandi, M.: A Method of Estimating the Moho Density Contrast with a Tentative Application by EGM08 and CRUST2.0. *Acta Geophys.*, 58, 1–24 (2011)

2. Tenzer, R., Bagherbandi, M. and Gladkikh, V.: Signature of the upper mantle density structure in the refined gravity data. *Comput. Geosci.*, 16(4), 975–986 (2012)

3. Laske, G., Masters, G., Ma, Z. and Pasyanos, M.E.: CRUST1.0: An updated global model of Earth’s crust. *Geophys. Res. Abs.*, 14, EGU2012-3743-1, EGU General Assembly (2012)

Chapter 92

Colloidal Transport under Nonlinear Sorption in a Single Variable Fracture Aperture

Nikhil Bagalkot and G. Suresh Kumar

Abstract Transport of colloids in fractured media has gained a considerable importance in recent years, mainly in the field of chemical pollutant transport and in nuclear waste management in groundwater system. The major reason being, colloids assist in migration of radionuclides through fractured rocks. Field studies and experiments have shown that natural fractures have apertures which are complex in geometry and vary spatially. An attempt has been made to numerical model the colloidal transport in a single fracture-matrix system to investigate the mobility of colloids in the presence of variable fracture apertures. To capture the effect of variation of fracture aperture, two different geometrical distributions logarithmic and sinusoidal, have been developed to generate the variations of fracture aperture. Analysis for both linear and nonlinear sorption isotherm cases has been carried out. The nonlinear sorption isotherm has been carried out given by Langmuir and Freundlich of isotherms. Cauchy type of boundary condition is applied at the fracture inlet to better represent the field scenario. The results indicate that colloidal migration in fracture and rock matrix is sensitive to fracture aperture variation and the parallel plate model exaggerates the colloid concentration in fracture. Further the results also suggest that the type of colloid source condition has a profound effect on the migration of the colloids in fracture and rock matrix.

Keywords Colloidal transport • Fractured media • Variable aperture • Rock-matrix • Boundary condition • Nonlinear sorption isotherm

92.1 INTRODUCTION

Groundwater is becoming increasingly vulnerable to contamination both by natural and human activities, with potentially disastrous effects on human life. Recent studies [1, 2] have established that colloids act as carriers that transport contaminants which have leached into the subsurface water systems, thereby enhancing

N. Bagalkot (✉) • G.S. Kumar
Department of Ocean Engineering, IIT-Madras, Chennai, India
e-mail: nikhilbagalkot@gmail.com

their sweep through the system. This might be further accelerated by the presence of high permeability fractures. Hence a contamination at one point might still reach a distant water producing well located in a populated area carried by colloids through the subsurface fractured water system. This makes it extremely important to understand the nature of the transport of colloids in a subsurface fractured water system to accurately assess groundwater contamination. The fate of the colloidal transport and hence the contaminant transport in fractured media is dependent on retardation mechanism of colloids. The retardation mechanism are mainly dependent on adsorption of colloids on the solid surface and nature of variation of fracture aperture or fracture width. Adsorption plays a vital role in retarding the colloidal transport in fractured media. Several studies on colloidal transport have been carried out, Johnson et al. [3] incorporated both patch wise geochemical heterogeneity and random sequential deposition dynamics in a one-dimensional colloid transport model. Heecheul and Yavuz [4] presented a mathematical model based on mass balance equation for transport of colloids in unsaturated porous media, both first and second order kinetics were used. Johnson and Elimelech [5] incorporated linear and nonlinear adsorption in colloid transport modeling to account for the phenomenon of blocking. Most of the above studies and studies carried out so far are for conventional porous media, a very few studies have applied the concept of nonlinear adsorption to the multi-continuum fractured porous media consisting of high permeability fracture with adjoining low permeability rock matrix. Although the linear adsorption model has been used widely [6, 7] for colloidal transport in fractured media, it has become clear in recent times that this model fails to provide an adequate representation of effects of adsorption [8]. [8, 9] proved that the nonlinear adsorption isotherm represent adsorption phenomena adequately. Most of the studies carried out on colloid facilitated transport in single fracture matrix system are with assumption of the conventional parallel plate model. The parallel plate model is based on the assumption that the fracture aperture remain constant along the length of fracture. This assumption ignores a very vital nature of fracture geometry, the spatial variation of the fracture aperture along the fracture length and roughness of the fracture walls which have a significant effect on the colloidal transport. Experiments and field studies conducted by [10, 11] pointed out that the aperture width varies along the length of the fracture. Advection, dispersion, adsorption and mass flux transfer from fracture to rock matrix all are either directly or indirectly function of fracture aperture. Hence the variation of fracture aperture effects the colloidal transport and for near to accurate study of colloidal transport in fractured media the variation of fracture aperture has to be considered. In the present study a one dimensional approach has been used to investigate the effect of various non-linear adsorption (Langmuir and Freundlich) models on the transport of colloidal in a single coupled fracture – matrix system. Sensitive analysis of the coefficients governing the adsorption isotherms are carried out. Further applying the self-similarity concept [12] in the current research, a logarithmically and sinusoidally varying aperture have been used to describe the variation of the fracture aperture. Comparison of the concentration profiles of both

variable aperture and the parallel plate model has been carried out for each of the adsorption models used in the present work. And finally a Cauchy type of boundary condition has been used for the source.

92.2 PHYSICAL SYSTEM AND GOVERNING EQUATIONS

Figure 92.1 and 92.2 illustrates the schematic diagram representing the transport of the colloids in a single horizontal fracture-matrix system. High permeability fracture and low permeability porous rock matrix are depicted in Fig. 92.1 and 92.2. Figure 92.1 corresponds to transport of colloids for a variable fracture aperture model where the fracture aperture varies sinusoidally along the fracture length. Figure 92.2 depicts the transport of colloids for a variable fracture aperture model where the fracture aperture varies logarithmically along the fracture length. Both immobile and mobile colloids are shown in the Fig 92.1 and 92.2. In Fig. 92.1 and 92.2, $b(x)$ represents half fracture aperture for variable fracture aperture model; B is the half fracture spacing, and l_f is the length of the fracture.

Advection, dispersion and irreversible adsorption (linear and nonlinear) are the main transport processes in fracture. Matrix diffusion and irreversible adsorption are the transport processes in porous rock matrix. Additionally there occurs a mass flux transfer between high permeability fractures to porous rock matrix.

Following assumption which are adopted from [6, 13] are applied in present study:

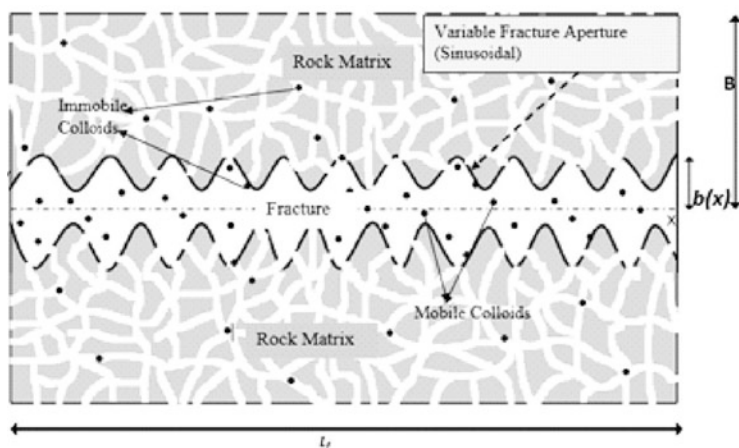


Fig. 92.1 Schematic diagram of single fracture-matrix system for colloidal transport with sinusoidal aperture variation

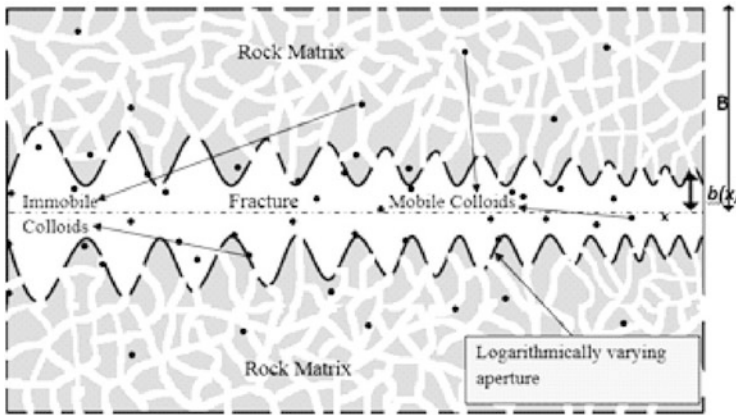


Fig. 92.2 Schematic diagram of single fracture-matrix system for colloidal transport with logarithmic aperture variation

1. Transport in fracture is assumed to be 1D with fluid flowing horizontally.
2. Transport in rock matrix is assumed to be 1D with transport of the fluid is perpendicular to flow in fracture.
3. The fracture aperture is much smaller in comparison with fracture length ($b(x) \ll L_f$)
4. Advection is dominant in fracture and may not exist in porous rock matrix.
5. Transport of colloids along the fracture is much faster as compared to that in porous rock matrix.
6. Colloids can be transported both in fracture and rock matrix.
7. The colloidal transport into rock matrix is primarily due to matrix diffusion and the diffusion occurs in transverse direction (Y axis) to that of fracture axis (along X axis).
8. A complete mixing is ensured at all times due to transverse diffusion and dispersion across the fracture, and a concentration gradient does not occur across the width of the fracture.

The governing equation used to represent the transport of colloids in fracture is adopted from Li. et al. (2004) with modification to account for the varying fracture aperture model.

$$\frac{\partial c_f}{\partial t} + \frac{1}{b(x)} \frac{\partial \sigma}{\partial t} = -\frac{Q}{A} \frac{\partial c_f}{\partial x} + D_f \frac{\partial^2 c_f}{\partial x^2} + \frac{\varepsilon \cdot \theta \cdot D_m}{b(x)} \frac{\partial c_m}{\partial y} \Big|_{y=b(x)} \quad (92.1)$$

where c_f (kg/m³) and σ (kg/m³) are the mobile and immobile colloid concentration in fracture respectively; C_m is the concentration of colloid in rock matrix; $A = b(x) \cdot l$ (m²) is the cross-sectional area; Q (m³/day) is the flow rate into the fracture; D_f (m²/day) and D_m (m²/day) are dispersion coefficient of fracture and diffusion coefficient of rock matrix respectively; ε is percentage of matrix diffusion flux of colloids; θ is

porosity of rock matrix; x represent the flow direction in fracture and y represents the direction of transport in rock matrix. The effect of adsorption is represented by the concentration of the immobile colloids (colloids adsorbed on to the fracture wall). Equilibrium sorption phenomena is often better represented by nonlinear isotherm. Most commonly used sorption isotherm relationship is Freundlich isotherm expressed as in Eq. 92.2.

$$\frac{\partial \sigma}{\partial t} = K_f p c_f^{p-1} \frac{\partial c_f}{\partial t} \quad (92.2)$$

where K_f relates to sorption capacity; while p is Freundlich exponent (0.7 - 1.2)

The Langmuir isotherm is another type of nonlinear isotherm expressed as in Eq. 92.3.

$$\frac{\partial \sigma}{\partial t} = \frac{K_L \cdot \sigma_{\max}}{(1 + K_L c_f)^2} \frac{\partial c_f}{\partial t} \quad (92.3)$$

where K_L is Langmuir constant.

The governing equation for colloidal transport in rock matrix is given by Eq. 92.4.

$$(1 + K) \frac{\partial c_m}{\partial t} = D_m \frac{\partial^2 c_m}{\partial y^2} \quad (92.4)$$

where K is the sorption partition coefficient for colloids within porous rock matrix.

The initial and boundary conditions of Eq. 92.1 and Eq. 92.4 are adopted from [14].

92.3 NUMERICAL MODEL

A fully implicit finite difference method has been used. A first order implicit forward difference is used to discretize the advective term (first term on RHS of Eq. 92.1). Second order implicit central difference is used to discretize the dispersion terms (second term RHS of Eq. 92.1). Two point backward finite difference is used to discretize the temporal term (first term on LHS of Eq. 92.1) and an implicit first order forward difference is used to discretize the coupling term (third term on the RHS of Eq. 92.1). A second order implicit central difference is used to discretize the condition term in the Eq. 5. Iterations are performed at each time step to satisfy the continuity at the fracture-matrix interface. A uniform grid spacing is adopted along fracture and a geometrically increasing grid spacing is used along the rock matrix in the transverse direction. The present numerical model is verified with that of available analytical solution given by [14] for the case of one dimensional colloidal transport for a fracture-matrix system with the inclusion diffusion of colloids into rock matrix for a parallel plate model.

92.4 RESULTS AND DISCUSSION

Figure 92.3 provides the comparison of spatial distribution of relative concentration of mobile colloids along the fracture for parallel plate model and variable aperture model consisting of sinusoidal and logarithmic variations. Simulation time of 100 days and a linear adsorption model is used. It can be observed from Fig. 92.3 that a larger amount of colloids have been retained within the fracture for a parallel plate model with reference to varying fracture apertures, while logarithmic variation of fracture aperture retains the least amount of colloids. This difference in concentration is due to the presence of curvature or zigzag surface for the variable aperture model as seen in Fig. 92.1 and 92.2. The presence of curvature increases the fracture wall surface area which leads increased surface for the adsorption sites, causing greater retardation of colloids as compared to parallel plate model, where in there is absence of any such curvature. Figure 92.4 provides the comparison of spatial distribution of relative concentration of mobile colloids along the fracture for sinusoidally varying aperture at different values of Freundlich exponent (p). Simulation time of 100 days and a Freundlich nonlinear adsorption isotherm at different values of Freundlich exponent ($p = 0.7, 0.9, 1.2$) has been used. It can be observed from Fig. 92.4 that as the exponent value (p) increases from 0.7 to 1.2 the colloid retainment in fracture decreases and is least for $p = 1.2$. When compared to sinusoidal colloidal profile in Fig. 92.3 (linear isotherm), a different profile is seen for the case of Freundlich nonlinear adsorption isotherm in the Fig. 92.4. This shows that there is difference in colloidal retainment in fracture when nonlinear adsorption is applied as against liner. The zero concentration point is further away from fracture inlet for the liner adsorption case (around 12 m, Fig. 92.3) as

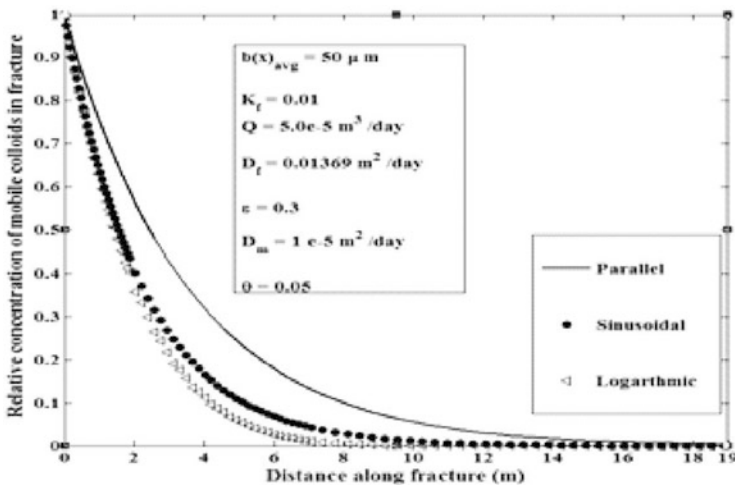


Fig. 92.3 Comparison of colloidal concentration in fracture for parallel plate model with that of variable aperture model (sinusoidal and logarithmic)

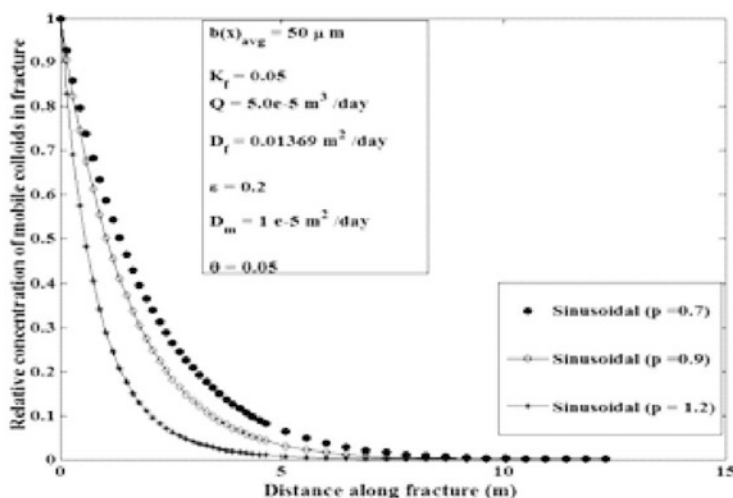


Fig. 92.4 Comparison of colloidal concentration in fracture at various values of Freundlich exponent (p) for sinusoidally varying fracture aperture

compared to nonlinear (max is 10 m, Fig. 92.4). Thus the linear adsorption isotherm overestimates the mobile colloidal concentration in fracture.

92.5 CONCLUSIONS

A numerical model has been developed to simulate colloidal transport in a coupled fracture-matrix system with variable fracture aperture. The effect of nonlinear adsorption on colloidal transport in fracture-matrix system has been analyzed using Langmuir and Freundlich nonlinear adsorption isotherms. The model results have been compared with the conventional parallel plate model, and subsequently. The models have also been tested under relatively complex boundary conditions using sinusoidal and logarithmic functions. The significance of considering the variable aperture fracture aperture and nonlinear adsorption is emphasized. The following specific conclusions have been deduced from the present study.

The numerical results clearly point out that parallel plate significantly overestimates the concentration of mobile colloids along the fracture, while the proposed variable fracture apertures (sinusoidal and logarithmic functions) has a significantly lower colloidal concentration, especially nearer to the fracture inlet.

The results also suggest that for sinusoidally varying aperture there is considerable difference in colloidal concentration in fracture when nonlinear adsorption isotherm is considered as compared to linear. In fact the linear adsorption isotherm clearly overestimates the colloidal concentration in rock matrix.

REFERENCES

1. Baek, I. and Pitt Jr, W.W.: Colloid-facilitated radionuclide transport in fractured porous rock. *Waste Management*, 16(4), 313–325 (1996)
2. Champ, D.R., Merritt, W.F. and Young, J.L.: Potential for the rapid transport of plutonium in groundwater as demonstrated by core column studies. *Scientific basis for radioactive waste management*, 5, 745–754 (1982)
3. Johnson, P.R., Ning, S. and Menachem, E.: Colloid transport in geochemically heterogeneous porous media: Modeling and measurements. *Environmental Science & Technology*, 30(11), 3284–3293 (1996)
4. Choi, H. and Yavuz, C.M.: Transport of a non-volatile contaminant in unsaturated porous media in the presence of colloids. *Journal of Contaminant Hydrology*, 25(3), 299–324 (1997)
5. Johnson, P.R. and Menachem, E.: Dynamics of colloid deposition in porous media: Blocking based on random sequential adsorption. *Langmuir*, 11(3), 801–812 (1995)
6. Natarajan, N. and Suresh Kumar, G.: Evolution of fracture permeability due to co-colloidal bacterial transport in a coupled fracture-skin-matrix system. *Geoscience Frontiers*, 3(4), 503–514 (2012)
7. Chrysikopoulos, C. V. and Assem Abdel-Salam: Modeling colloid transport and deposition in saturated fractures. *Colloids and Surfaces A: Physicochemical and Engineering Aspects*, 12 (2), 189–202 (1997)
8. Weber Jr, W., Paul, J., McGinley, M. and Lynn, E.K.: Sorption phenomena in subsurface systems: Concepts, models and effects on contaminant fate and transport. *Water Research*, 25 (5), 499–528 (1991)
9. Abulaban, A., John, L.N. and Debasmita, M.: Modeling plume behavior for nonlinearly sorbing solutes in saturated homogeneous porous media. *Advances in Water Resources*, 21 (6), 487–498 (1998)
10. Keller, K. and Bonner, B.P.: Automatic, digital system for profiling rough surfaces. *Review of Scientific Instruments*, 56(2), 330–331 (1985)
11. Hakami, E. and Barton, N.: Aperture measurements and flow experiments using transparent replicas of rock joints. *Rock Joints*, 383–390 (1990)
12. Feder, J.: *Fractals*, Plenum, New York, 283 pp (1988)
13. Sudicky, E.A. and Frind, E.O.: Contaminant transport in fractured porous media: Analytical solutions for a system of parallel fractures. *Water Resources Research*, 18(6), 1634–1642 (1982)
14. Abdel-Salam, A. and Chrysikopoulos, C.V.: Analytical solutions for one-dimensional colloid transport in saturated fractures. *Advances in Water Resources*, 17(5), 283–296 (1994)

Chapter 93

A Markov Chain Monte Carlo-based Particle Filter Approach for Spatiotemporal Modelling of an Environmental Process

L. Linguet and J. Atif

Abstract The knowledge of the global solar surface irradiance (SSI) incident on the earth's surface and its spatiotemporal distribution is important to numerous solar-based applications. However, spatiotemporal modelling of SSI (a non-linear process) from Earth observation data is unfortunately not straightforward. From a signal processing perspective, it is a non-stationary, non-linear/non-Gaussian dynamical inverse problem. In this paper, we propose an MCMC particle filter approach that combines satellite images and in situ data for space-time-referenced SSI modelling. We propose original observation and transition functions taking advantage of the characteristics of the involved types of data. A simulation study of solar irradiance is conducted in parallel with this method and a map of SSI potential in French Guiana for the year 2012 is provided.

Keywords Bayesian filter • Monte Carlo • Spatiotemporal modelling

93.1 INTRODUCTION

Climate science needs reliable and sufficiently detailed data to understand the radiative forcing of climate change. Solar energy systems such as photovoltaic systems and solar thermal systems require reliable spatiotemporal modelling of SSI for their monitoring and design. Earth observation data from meteorological satellites are often used to provide spatiotemporal information for solar resource assessments at high spatial and temporal resolutions because they produce better estimates than the ground-based radiometric networks [1]. However, spatiotemporal modelling of SSI (a non-linear process) from Earth observation data is unfortunately not straightforward [2]. Different approaches to estimating SSI from satellite images have evolved into complex models by incorporating additional observation

L. Linguet (✉)

UMR Espace-Dev, University of French Guiana, 97300 Cayenne, French Guiana, France
e-mail: linguetlaur@gmail.com

J. Atif

LMI TAO, INRIA/CNRS, University Paris Orsay, Paris, France

data, empirical information and physical information. Despite the models' increasing complexity, recurring obstacles still introduce significant uncertainty into their estimates [3]. We consider a Monte Carlo filtering approach to the dynamical estimation of SSI at ground level from satellite images. We defend the idea that an inverse approach based on Sequential Monte Carlo filtering [4, 5] (Particle Filter) assists in relaxing several assumptions and constraints while keeping estimation results aligned with those of existing methods. In addition to the dynamical estimation of the spatiotemporal values of SSI, the Bayesian filtering approach simulates missing values and estimates forecasting.

93.2 MATERIAL

To develop and validate the MCMC particle filter, a simulation study was conducted. The study area is located in French Guiana (South America) and covers an area between 51°W and 55°W longitude and between 1°N and 6°N latitude. A set of 5226 high resolution satellite images (GOES EAST) from the visible channel ($0.4\mu\text{m}$ - $1.1\mu\text{m}$) covering a 223-day period from the year 2012 was selected. The selection allows for various sky coverages. The spatial resolution of the satellite data is $15\text{ km} \times 15\text{ km}$, and the temporal resolution is 0.5 h. In situ measurements were provided by six weather stations of the French national weather service Meteo-France. Meteo-France offers access to hourly means of the global irradiance measured on the horizontal plane.

93.3 METHODOLOGY

State space models (SSM) are commonly used to describe the behaviours of many processes. Model variables can be divided into hidden variables (that are not measured) such as predicted clearness index at the surface (the clearness index is the global solar radiation on the earth's surface divided by the extra-terrestrial radiation at the top of the atmosphere; the index is a weekly stationary stochastic process) and observed variables such as the satellite image pixels. To model spatiotemporal behaviour of SSI, a recursive Bayesian filter called an MCMC

Particle Filter [6] was implemented using a Sequential Monte Carlo method. The particle filter relies on a non-linear and non-Gaussian model-based algorithm and allows estimation of dynamic hidden states based on a sequence of observations.

93.3.1 *State Space Model*

The hidden process, also defined as the state variable, is the clearness index and the observations were extracted from digital satellite images via an observation model. We used a stochastic observation model based on a joint probability distribution (pdf) between historic surface data (clearness index) and historic satellite data (apparent pixel albedo). The task was to obtain an estimate of the unknown x_k where only the value of z_k was known. One approach for estimating x_k is modelling the joint distribution $p(x, z)$ with a learning dataset of clearness index data and apparent pixel albedo data.

93.3.2 *MCMC Particle Filter*

The MCMC particle filter relies on a combination of MCMC and sequential Monte Carlo (SMC) methods which takes advantage of the strengths of its two components. The MCMC particle filter recursively computes the Bayesian “posterior” at time k using the posterior at time $(k-1)$ and the current observation (the probability density function of the current state conditioned on all observations until the current time). Stated differently, the particle filter discovers an update formula from $p(x_{k-1} | z_{1:k-1})$ to $p(x_k | z_{1:k})$ where $z_{1:k}$ denotes all observations $\{z_1, \dots, z_k\}$. Global irradiance estimates at the surface were retrieved by multiplying clearness index estimates by extra-terrestrial radiation at the top of the atmosphere. The method has been validated by comparison of SSI estimates derived from the MCMC particle filter with SSI measurements performed at ground radiometric stations.

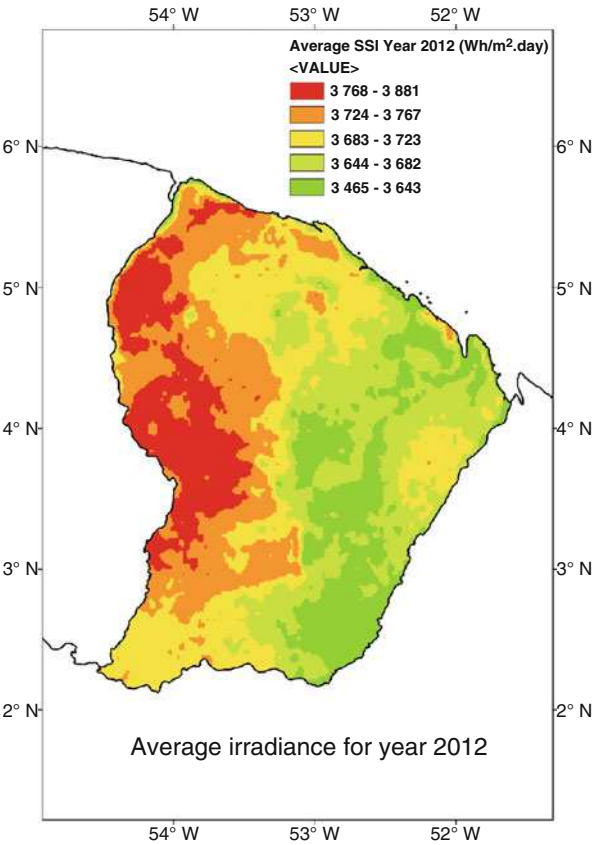
93.4 RESULTS AND DISCUSSION

Hourly SSI estimates derived from the MCMC particle filter model were compared with hourly irradiance measurements from six ground radiometric stations operated by the French National Meteorological Service of French Guiana. Statistical performances of hourly estimated irradiance (RMSE, MBE and correlation coefficient) show the effectiveness of the method: the absolute relative bias is below 15% and the coefficient correlation varies between 0.85 and 0.91 (Table 93.1). We estimated the average irradiance on a daily basis for the entire year 2012 across the territory of French Guiana in South America. We processed all observed pixels to estimate the SSI and established a map of irradiance estimates using ArcGIS software, as shown in Fig. 93.1. The initial results show that the optimal sites for solar irradiance potential are in the western region of French Guiana. In this region, the mean daily potential reaches its maximum value of 3880 Wh/m² day.

Table 93.1 Comparisons between MCMC particle filter SSI estimates and hourly irradiance measurements for six ground radiometric stations in French Guiana

Year 2012			
	RMSE	MBE	CC
St-Georges	28%	12%	0.85
Rochambeau	28%	4%	0.86
Ile-Royale	26%	-3%	0.91
Kourou	35%	-15%	0.89
St-Laurent	27%	1%	0.87
Maripasoula	24%	6%	0.89

Fig. 93.1 Average daily irradiance in French Guiana for the year 2012



93.5 CONCLUSIONS

The MCMC particle filter incorporates a statistical model for the observation process. The joint probability distribution of the state variable and the observation variables is not restricted by any prior assumption and gives a probabilistic perspective based on conditional distribution estimates. The methodology consists of a broad set of principles and techniques which may be used to advance the knowledge

of solar energy potential. This knowledge is critical to evaluating applied sustainability initiatives and the deployment of solar energy systems. This method can be used for real-time estimates and solar irradiance forecasts at the surface.

ACKNOWLEDGEMENTS The authors are grateful to Météo-France for supplying ground measurement data. The authors thank the European Feder program and the Conseil Regional of French Guiana.

REFERENCES

1. Gurtuna, O. and Prevot, A.: An overview of solar resource assessment using meteorological satellite data. *Proceedings of Recent Advances in Space Technologies*, IEEE Conference Publications, Istanbul, pp. 209–212 (2011)
2. Marie-Joseph, I., Linguet, L., Gobinddass, M.L. and Wald, L.: On the applicability of the Heliosat-2 method to assess surface solar irradiance in the Intertropical Convergence Zone, French Guiana. *International Journal of Remote Sensing*, Taylor & Francis, 34(8), 3012–3027 (2013)
3. Cebecauer, T., Suri, M. and Gueymard, C.: Uncertainty Sources in Satellite-Derived Direct Normal Irradiance: How Can Prediction Accuracy be Improved Globally? *In: Proceedings of the Solar PACES Conference*, Granada, Spain (2011)
4. Doucet, A., de Freitas, N. and Gordon, N.: *Sequential Monte Carlo methods in practice*. Springer-Verlag, New York (2001)
5. Arulampalam, S., Maskell, S., Gordon, N. and Clapp, T.: A tutorial on particle filters for online nonlinear/non-Gaussian Bayesian tracking. *IEEE Transactions on Signal Processing*, 50(2), 174–188 (2002)
6. Andrieu, C., Doucet, A. and Holenstein, R.: Particle Markov chain Monte Carlo methods. *Journal of the Royal Statistical Society B*, 72(3), 269–342 (2010)

Chapter 94

Using Stratigraphic Forward Modeling to Model the Brookian Sequence of the Alaska North Slope

Alina Christ, Oliver Schenk, and Per Salomonsen

Abstract Basin and petroleum system modeling allows geoscientists to examine the dynamics of sedimentary basins and their associated fluids to determine if past conditions were suitable for hydrocarbons to fill potential reservoirs and be preserved there. Commonly geological models are created using simple assumptions about the superposition of sedimentary layers during deposition. However, for prograding sequences foreland basin and passive margin settings in particular, this results in simplistic models with limited geological validation of thicknesses or facies distribution. Stratigraphic forward modeling is a quantitative approach to create a geological model by simulating dynamic sedimentary processes, such as erosion, sediment transport, and deposition, while maintaining mass balance. By suitably varying parameters that represent paleogeographic conditions (such as sea level, sediment input, and major tectonic events) stratigraphic forward modeling can generate a realistic three-dimensional model and predict the distribution of sediments and their properties.

Keywords GPM (Geologic process modeler) • Stratigraphic forward modeling • Alaska north slope

94.1 INTRODUCTION

For this study we used Geologic Process Modeler (GPM), a plugin within the Petrel E&P software platform that incorporates the principles of stratigraphic forward modeling. With GPM sediment transport and erosion, all in a water environment, can be modelled as well as carbonate redistribution and growth. This software uses

A. Christ (✉)
Schlumberger, Aslakveien 14E, 0753 Oslo, Norway
e-mail: achrist@slb.com

O. Schenk
Schlumberger, Ritterstrasse 23, Aachen, Germany

P. Salomonsen
Schlumberger, Risabergveien 3, 4068 Stavanger, Norway

numerical simulation based on the underlying physical processes that act during sedimentary processes [1].

The aim of the study was to show how GPM and the principles of stratigraphic forward modeling can be used to provide geologic details for an existing basin model. Input to GPM is taken from a basin evolution model within PetroMod petroleum systems modeling software that already included the progradation of foresets and multiple erosional events in the Brookian sequence. Reconstruction was mainly based on geological concepts and controlled by limited seismic and well data over most of the North Slope region, but without consideration of quantitative sedimentary processes.

94.2 REGIONAL GEOLOGY AND STUDY AREA

The Alaska North Slope is a prosperous hydrocarbon province with numerous discoveries and significant resources. Cretaceous and Tertiary sediments derived from the Brooks Range Orogen belong to the Brookian Sequence. They progressively filled the Colville foreland basin from west-southwest with a total present-day thickness of more than 6 km in the basin center decreasing towards the rift shoulder in the north (Barrow Arch). Siliciclastic material accumulated as condensed marine mudstone (Hue Shale), turbiditic sandstone (Torok, Seabee and Canning Fm) and shallow marine sandstone, mudstone and conglomerate (Nanushuk, Tuluvak, Prince Creek, Schrader Bluff and Sagavanirktok Fms) [2]. Organic-rich beds of the Hue Shale represent important oil source rocks, and Brookian mudstones may contain gas source rocks. Reservoir rocks consist of turbidite and shallow-marine to nonmarine sandstone, and known oil and gas accumulations occur in both structural and stratigraphic traps within the Brookian sequence. The case study described here involves the reconstruction of the first successions of the progradational Brookian Sequence during Aptian (Lower Cretaceous). The model comprises a total area of $2.11 \times 10^6 \text{ km}^2$ with a distance of 1600 km in E-W direction (Fig. 94.1a). In total we modeled a period of 7Ma, from 122Ma to 115Ma.

94.3 MODEL INPUT AND METHODS

The input to the model is a base surface originating from an existing PetroMod model by Schenk et al. (2012). This surface was extended towards the W and S to include the provenance areas of the sediment and to reconstruct the paleotopography at 122 Ma. Four different sedimentary point sources were positioned on this surface at locations indicated by both topography and paleocurrent information from Houseknecht et al. (2008). Sediment diffusion was also taken into account. To simulate erosion and deposition in our study area and we assigned a

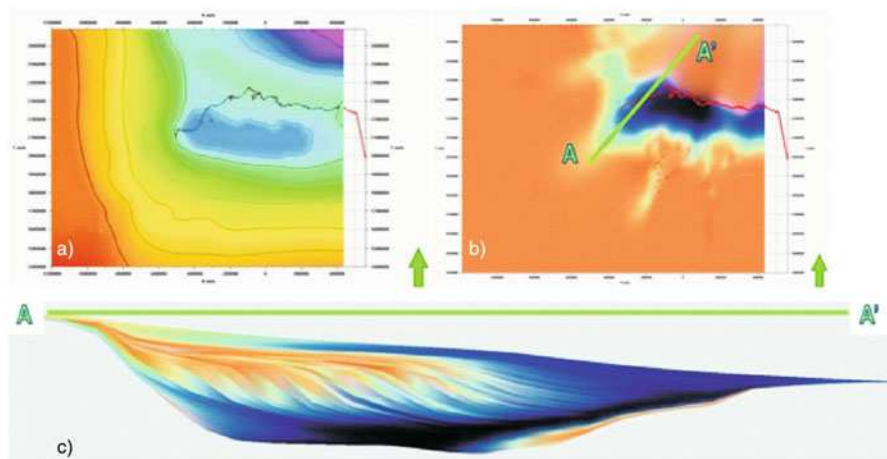


Fig. 94.1 Alaska North Slope model. The present-day shoreline is shown in red. 1a: Initial surface. 1b: Final model in plan view and location of cross section. 1c: Cross section showing predicted stratigraphy and sediment composition (coarse sediments in red and green, fines in blue and black)

tectonic map with uplift rates from 0.05 mm/a in the Brooks Range and subsidence in the basin area reaching 0.2 mm/a. These values are derived from conversion of a thickness map into tectonic movement per year derived from PetroMod data.

94.4 RESULTS AND DISCUSSION

The result of this GPM study is a fine-scale realistic model of the time-transgressive Brookian sequence and a process-oriented reconstruction of facies variations based on several geological parameters, such as sediment transport, erosion, and simultaneous uplift on a regional scale. The model shows the prograding foresets coming from the Brooks Range. The grain sizes closer to the sources are bigger, and the greater the distance to the sources the smaller the grains. It takes about 3Ma until the coarser grain fraction has reached the center of the Colville foreland basin. Validation of the extent and thickness of the modeled sequences was done with comparison to the surfaces derived from the PetroMod model. A workflow incorporating the Petrel platform, PetroMod software, and GPM plug-in was established, allowing the generation of geologically more reasonable models.

94.5 CONCLUSIONS

The GPM model facilitates a better process-oriented understanding of diachronous deposition, facies variations, and thickness distribution of the Brookian sequence. Additional use of GPM-based output in PetroMod software will improve geological validation, and will allow for more precise assessment of remaining potential hydrocarbon resources in this remote Arctic region.

REFERENCES

1. Tetzlaff, D.M. and Priddy, G.: Sedimentary Process Modeling: From Academia to Industry. *In: Geologic Modeling and Simulation, Sedimentary Systems* (Ed. by D.F. Merriam and J.C. Davis). Kluwer Academic/Plenum Publishers, New York (2001)
2. Schenk, O., Magoon, L.B., Bird, K.J. and Peters, K.E.: Petroleum system modeling of northern Alaska. *In: K.E. Peters, D.J. Curry and M. Kacwicz (eds), Basin Modeling: New Horizons in Research and Applications*. AAPG Hedberg Series, no. 4, 317–338 (2012)
3. Houseknecht, D.W., Bird, K.J. and Schenk, C.J.: Seismic analysis of clinoform depositional sequences and shelf-margin trajectories in Lower Cretaceous (Albian) strata, Alaska North Slope. *Basin Research* (2008)

Chapter 95

Numerical Simulation of Migration of Seismic Activity (On the Example of Kamchatka)

A. Naumovich Chetyrbotsky

Abstract The distribution of seismic activity in the area of Pacific volcanic ring. The mathematical model of its seismic activity cost based Burridge Knopoff (Burridge-Knopoff). Discuss the results of numerical experiments.

Keywords Seismic activity • A closed loop related oscillatori • Numerical experiments

95.1 INTRODUCTION

Seismic activity (SA) causes the movement of the masses and the destruction of material systems. The importance of studying is required for the forecast estimates of the consequences of earthquakes. Problems of their composition are connected with the lack of precise information on the mechanisms SA, lack of regular instrumental measurements, spatial and temporal heterogeneity of their distributions and etc. Meanwhile, for most of the period are accumulated huge archives of registered earthquakes. In addition, is developed and constantly is updated with the appropriate mathematical tools. During its development requires the observance of correctness and interpretability components of the model. There are a number of works in which violated their interpretability. For example, in [4] for presentation of SA is used model of FitzHugh-Nagumo, which describes the processes of ion transport through the membrane and the passage of the pulse potential across the membrane [2]. It is clear that, despite the plausibility obtained in [4] results, is incorrect analogy (and interpretation) between the SA and ion transport (dynamics in this model is defined by 3 types of ion currents, which are absent in the processes of the SA). In this situation of relevance study the manifestations of SA on the boundaries of lithospheric plates. An important object of this type is the path of the Pacific Ocean or the so-called Pacific volcanic ring. For this type of objects here

A.N. Chetyrbotsky (✉)

Far East Geological Institute Feb RAS, Vladivostok, Russia

e-mail: Chetyrbotsky@yandex.ru

first formulated in a simple statement of the problem. Next, we present and discuss results of numerical experiments.

95.2 THE MODEL OF RING CHAINS OF COUPLED OSCILLATORS

The physical mechanisms of the SA are usually presented by a chain of interrelated oscillators. Different configurations of their units correspond structured models considered environments. So the model of a solid YA Frenkel and T.Kontorova is the set of layers atoms which are related elastic forces. For interaction between atoms are used the respective “springs” [3]. The influence of neighboring layers on each other is modeled by a periodic potential, the easiest option which is a periodic function. This occasion corresponds to the model Scott, which in the long-wave limit gives the equation Sin-Gordon [9]. In [1] is learned a simple linear chain of blocks floating in a viscous fluid. It is believed that the blocks are connected by a springs with a certain stiffness. Contiguous blocks are located on the plate which moves in the horizontal direction with some speed. The wording here is made on the basis of the model of Burridge-Knopoff [5] and the model Fermi-Pasta-Ulam [7, 6],

$$m_i \frac{d^2 X_i}{dt^2} = F(X_{i+1} - X_i) - F(X_i - X_{i-1}) + f \left(\frac{dX_i}{dt} \right),$$

where the offset of the i -th block, relative to its equilibrium state, and its mass is supposed to occur (the entire set of N blocks); F characterizes the interaction of blocks; the last member is the power of the resistance movement of the block. Here he set according to [8]. The simplest case this model takes the form

$$\left(\frac{d^2 X_i}{dt^2} \right) = C_K (X_{i-1} - 2X_i + X_{i+1}) + f \left(\frac{dX_i}{dt} \right), \quad (95.1)$$

When matching start and end points (ring) record the model takes the form

$$\left(\frac{d^2 X_i}{dt^2} \right) = C_K (X_j - 2X_i + X_k) + f \left(\frac{dX_i}{dt} \right).$$

where $j = i - 1$ for $i > 1$ and $j = N$ if $i = 1$; $k = i + 1$ if $i < N$ and $k = 1$ if $i = N$. In this case, the approximation $\frac{dX_i}{dt}$ is determined by the entry: $(X_2 - X_N)/2\Delta t$ for $i = 1$ and $(X_1 - X_{N-1})/2\Delta t$ for $i = N$ (here Δt the time step). The calculation settings accepted values: $N = 100$, $\Delta t = 0.01$, $C_K = 30$.

Figure 95.1 presents the results of the research. Left 3D image matches the distribution of correlation of displacements of the positions, and the right 3D image - distribution correlations their velocities.

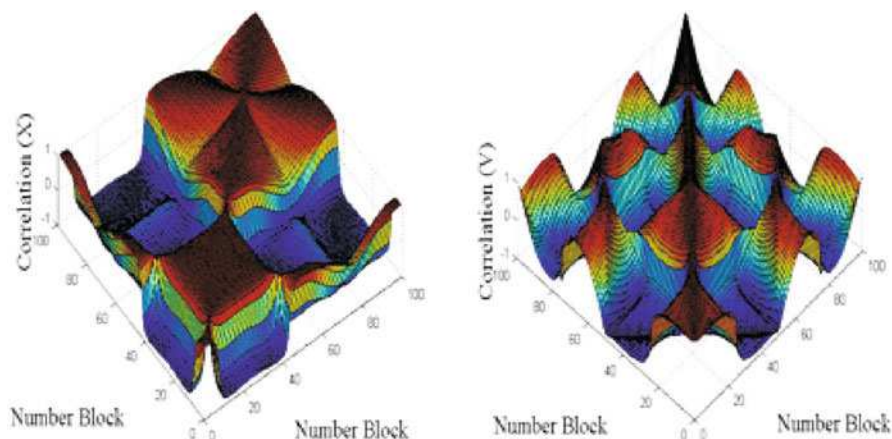


Fig. 95.1 Distribution correlation for position (X) and velocity (V)

The analysis of these distributions indicates compact splitting of population units at the individual group units, within each of which their displacement, agreed between themselves and flare to a synchronous. An indication of the absence of full synchronization of the distribution of the correlations for speed shift. It seems reasonable that the interpretation of results. If blocks distributed along the contour of the Pacific volcanic ring and they are the generators of the SA, the volcanic activity on different areas of the ring appears asynchronously.

REFERENCES

1. Zakharov, V.S.: Blokov model with dry friction. Electronic scientific edition ôgeorazrezö. 7, 1–25 (2010)
2. Ivanitsky, G.R., Krinsky, V.I. and Selkov, E.E.: Mathematical Biophysics of the cell. *M. Nauka*, 1978.310 S.
3. Antonova, T.A. and Frenkel, Y.A.: The theory of plastic deformation and twinning. *CHAT*, 8(1), S.89-95 (1938)
4. Spertus, V.B.: Study of geo solutions in the Crimean-black sea region in type models the Fitzhugh-Nagumo. *Geophysics. Zhur.* 30(5), 91–100 (2008)
5. Burridge, R. L.: Knopoff Model and theoretical seismicity. *Bull. of the Seismological Society of America*, 57(3), 341–371 (1967).
6. Ferguson, C.D., Klein, W. and Rundle, J.B.: Long-range earthquake fault models. *Computers in Physics*, 12(1), 34–40 (1998)
7. Fermi, E., Pasta, J. and Ulam, S.: Studies of nonlinear problems. Los Alamos Science Laboratory (1955)
8. Langer, J.S., Carlson, J.M., Myers, C.R. and Shaw, B.E.: Slip complexity in dynamics of earthquake faults. *Proc. Natl. Acad. Sci. USA*, 93, 3825–3829 (1996)
9. Rabinovich, M.I. and Trubetskov, D.I.: Oscillations and waves in linear and nonlinear systems. Kluwer Academic Publishers, 577 p (1989)

Chapter 96

Comparative Performance of Thirteen Single Outlier Discordancy Tests from Monte Carlo Simulations

Mauricio Rosales-Rivera, Lorena Díaz-González, and Surendra P. Verma

Abstract We evaluated the performance of thirteen single extreme outlier statistical discordancy tests (Grubbs-type N1, N2, N4; Dixon-type N7, N8, N9, N10; and high-order moment statistics skewness N14 and kurtosis N15) using highly precise and accurate Monte Carlo simulations for 20,000,000 replications and 102 independent simulation experiments. Our simulation errors and total uncertainties were extremely low for normal samples of sizes 5 to 20 involving a simple statistical contamination of one datum resulting from a parameter called δ from ± 0.1 up to ± 20 for modeling the slippage of central tendency or another parameter ϵ from ± 1.1 up to ± 200 for the slippage of dispersion. Both criteria — Power of Test proposed by Hayes and Kinsella [1] and Test Performance Criterion of Barnett and Lewis [2] were used. Our results indicate that the Dixon tests perform less well than the Grubbs-type, skewness, and kurtosis tests.

Keywords Discordancy tests • Outlier rejection • Monte Carlo • Grubbs • Dixon • Skewness • Kurtosis

96.1 INTRODUCTION

A considerable number of discordancy tests are available for determining an outlier (an extreme value) as a discordant observation in normal samples [2]. However, only a few studies exist about the use of Monte Carlo simulation for accurate and

M. Rosales-Rivera

Posgrado en Ciencias, Facultad de Ciencias, Universidad Autónoma de Estado de Morelos, Cuernavaca, Morelos, Mexico

L. Díaz-González

Facultad de Ciencias, Universidad Autónoma de Estado de Morelos, Cuernavaca, Morelos, Mexico

S.P. Verma (✉)

Departamento de Sistemas Energéticos, Instituto de Energías Renovables, Universidad Nacional Autónoma de México, Priv. Xochicalco s/no., Col. Centro, Apartado Postal 34, Temixco, Mor., Mexico

e-mail: spv@ier.unam.mx

objective evaluation of these tests. Recently, [3] discussed the performance of four single extreme outlier type discordancy tests. In the present work we used Monte Carlo simulations to evaluate comparative efficiency of thirteen discordancy tests (two-sided N2, N8, N14, N15 and one-sided N1, N4, N7, N9, N10) for normal samples of 5 to 20, using 20,000,000 replications and 102 independent experiments with low simulation errors. Following [4], the simulation error for the 20,000,000 replications used routinely in our work can be estimated approximately as $2 \times \sqrt{0.5 \times 0.5 / 20000000} = 0.00022$ in each of the 102 experiments.

96.2 DISCORDANCY TESTS AND MONTE CARLO SIMULATIONS

For a data array $x_1, x_2, \dots, x_{n-1}, x_n$ observations, with mean and standard deviation s , thirteen statistical tests were objectively evaluated in this work (Grubbs-type N1, N2, N4; Dixon-type N7, N8, N9, N10; and high-order moment statistics skewness N14 and kurtosis N15). For a contaminated sample of small size of 5 to 20, the $n-1$ observations were drawn from one stream of $N(0,1)$, and the remaining observation x_n was added from a different stream ($N(0 \pm \delta, 1)$ or $N(0, 1 \pm \varepsilon)$) where δ was varied from ± 0.1 up to ± 20 for slippage of central tendency or ε from ± 1.1 up to ± 200 for slippage of dispersion; then we arranged the complete array [2], as follows: $x_{(1)}, x_{(2)}, \dots, x_{(n-1)}, x_{(n)}$. All discordancy tests under evaluation could then be applied to this data array. For an uncontaminated sample, the simulations were for $\delta = 0$ and $\varepsilon = \pm 1$. In order to achieve an unbiased comparison, the application of the tests was always forced to the upper outlier $x_{(n)}$ for positive and $x_{(1)}$ for negative values of the parameters δ and ε [3]. All the tests were applied at 99% confidence level from highly precise and accurate critical values [5, 6], which permitted an objective comparison of their performance. The high level of 99%, instead of 95%, would result in a low type I error.

96.3 RESULTS AND DISCUSSION

After the application of the thirteen discordancy tests, we used two performance criteria: (i) Power of Test (Ω) defined by [1]; and (ii) Test Performance Criterion ($\pi_{D/C}$) [2]. The two performance criteria used in this work provide similar estimates [3]; any of them can be used to evaluate numerous other discordancy tests. Hence, the Barnett and Lewis criterion is plotted as a function of δ and ε in Figures 96.1 and 96.2 and the most important results are presented in Tables 96.1 and 96.2.

We can see in Figures 96.1(a)-(b) and Table 96.1 for different sizes of n that tests N4 and N1 showed a value of 0.5, whereas the other discordancy tests show values less than 0.5 for $\delta = 4 - 8$.

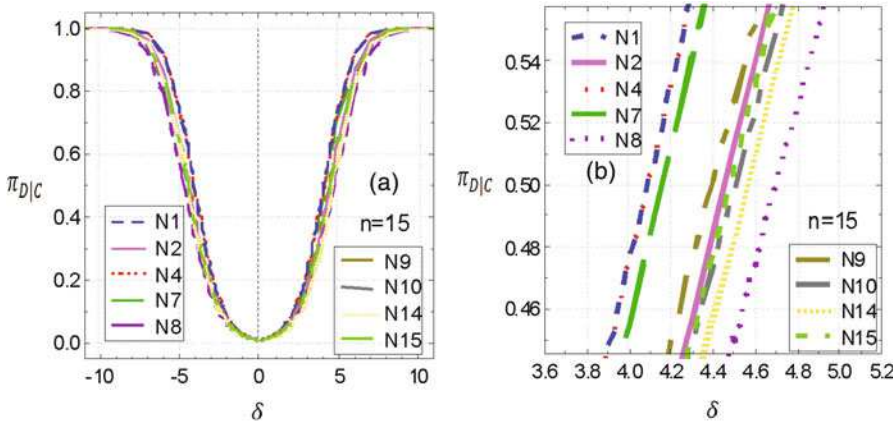


Fig. 96.1 Test Performance Criterion P5 ($\pi_{D|C}$) as a function of δ for all tests for $n = 15$. (a) δ from -10 to $+10$ for all tests; and (b) δ from 3.8 to 5.0 to specific values.

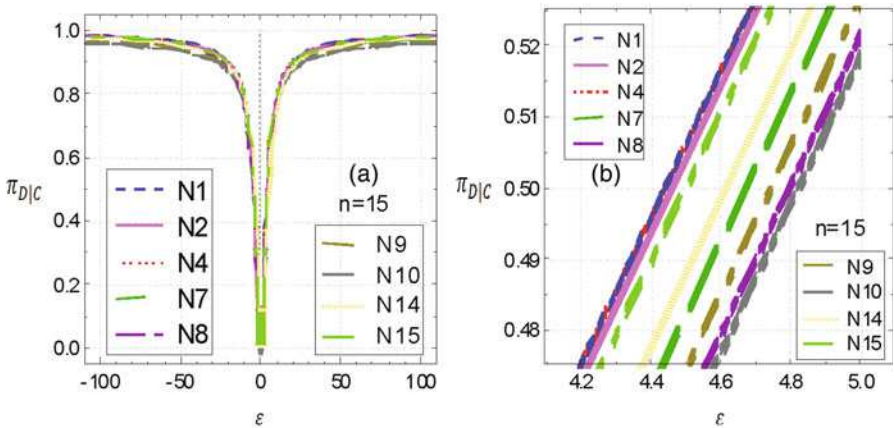


Fig. 96.2 Test performance criterion P5 ($\pi_{D|C}$) as a function of ϵ for all tests for $n = 15$ (a) ϵ from -100 to $+100$ for all tests; and (b) ϵ from 4.0 to 5.0 to specific values.

For ϵ and different sizes n , the behaviour of the discordancy tests remained practically the same. With the best performance, tests N4 and N1 reached the value of 0.5 before the other discordancy tests; these were followed by N2 with similar values by N15, and then N14, N7, N9, N8, and N10. For δ values greater than 8, the performance for the discordancy tests changed and the efficiency of the Dixon tests decreased by a small proportion against N2, N15, and N14.

Table 96.1 Test performance criterion P5 ($\pi_{D/C}$) specific values for thirteen single outlier discordancy tests as a function of δ .

<i>n</i>	δ	<i>N</i> 1	<i>N</i> 2	<i>N</i> 4	<i>N</i> 7	<i>N</i> 8	<i>N</i> 9	<i>N</i> 10	<i>N</i> 14	<i>N</i> 15
		<i>N</i> 1	<i>N</i> 2	<i>N</i> 4	<i>N</i> 7	<i>N</i> 8	<i>N</i> 9	<i>N</i> 10	<i>N</i> 14	<i>N</i> 15
5	± 8.07	0.5003	0.3165	0.5005	0.4884	0.3092	0.2279	0.0648	0.3149	0.3160
10	± 4.56	0.5006	0.3809	0.5007	0.4871	0.3511	0.4176	0.3578	0.3740	0.3782
15	± 4.1	0.5038	0.4042	0.5043	0.4843	0.3530	0.4241	0.3996	0.3798	0.3982
20	± 3.94	0.4998	0.4320	0.5010	0.4875	0.3656	0.4163	0.4025	0.3900	0.4231

Table 96.2 Test performance criterion P5 ($\pi_{D/C}$) specific values for thirteen singles outlier discordancy tests as a function of ϵ

n	ϵ	$N1$	$N2$	$N4$	$N7$	$N8$	$N9$	$N10$	$N14$	$N15$
		$N1$	$N2$	$N4$	$N7$	$N8$	$N9$	$N10$	$N14$	$N15$
5	± 10.8	0.5019	0.4796	0.5024	0.4497	0.4324	0.4345	0.4297	0.4520	0.4678
10	± 5.1	0.5010	0.4896	0.5014	0.4747	0.4545	0.4584	0.4495	0.4788	0.4825
15	± 4.42	0.5012	0.4990	0.5015	0.4802	0.4611	0.4640	0.4610	0.4825	0.4856
20	± 3.9	0.5004	0.5001	0.5006	0.4790	0.4624	0.4940	0.4611	0.4797	0.4995

96.4 CONCLUSIONS

Our simulation study clearly demonstrated that for a slippage of central tendency, the discordancy tests showed the following behaviour: $N4N1 \approx N7 > N9 \approx N2N15 \approx N10 > N14 > N8$ for $\delta \leq 6$ and $N4N1 > N2 \approx N15 > N14 > N7 > N9 > N10 > N8$ with δ up to 8 for samples sizes 5 to 20; and for a slippage of dispersion the performance could be summarized as: $N4N1N2 > N15 > N14 > N7 > N9 > N8 > N10$ in general for ε aimed at samples sizes 5 to 20.

ACKNOWLEDGEMENTS The first author (MRR) is grateful to Conacyt for a Master's fellowship during 2013–2014 when most of the computer programming work was carried out. We are also much grateful to Alfredo Quiroz-Ruiz who provided help during the programming. This work was supported by DGAPA-PAPIIT grant IN104813 to the third author (SPV). We appreciate the constructive comments from the reviewer of IAMG-2014.

REFERENCES

1. Hayes, K. and Kinsella, T.: Spurious and non-spurious power in performance criteria for tests of discordancy. *The Statistician*, 52, 69–82 (2003)
2. Barnett, V. and Lewis, T.: Outliers in Statistical Data. John Wiley & Sons, Chichester UK, 3rd edition (1994)
3. Verma, S.P., Díaz-González, L., Rosales-Rivera, M. and Quiroz-Ruiz, A.: Comparative Performance of Four Single Extreme Outlier Discordancy Tests from Monte Carlo Simulations. *The Sci. World J.*, 2014, Article ID 746451, 27 pages (2014)
4. Krishnamoorthy, K. and Lian, X.: Closed-form approximate tolerance intervals for some general linear models and comparison studies. *J. Stat. Comput. Simul.*, 82, 547–563 (2012)
5. Verma, S.P., Quiroz-Ruiz, A. and Díaz-González, L.: Critical values for 33 discordancy test variants for outliers in normal samples up to sizes 1000, and applications in quality control in Earth Sciences. *Rev. Mex. Cienc. Geol.*, 25, 82–96 (2008)
6. Verma, S.P. and Quiroz-Ruiz, A.: Corrigendum to Critical values for 22 discordancy test variants for outliers in normal samples up to sizes 100, and applications in science and engineering [*Rev. Mex. Cienc. Geol.*, 23, 302–319], *Rev. Mex. Cienc. Geol.*, 28, 202 (2011)

Chapter 97

3D Crustal Temperature Modeling over Japan for Geothermal Resource Assessment

Bingwei Tian and Katsuaki Koike

Abstract Maximum of the utilization of sustainable and recyclable energy sources could be an effective way for the reduction of carbon dioxide emission, which is mainly caused by energy consumption. In this study, the characterization of the heat stored underground and the analysis of the deep geothermal potential was performed for different geothermal systems based on various geology structures, fault zones and volcanic zones, including Hokkaido, Northeast of Honshu, Center of Honshu, Southwest of Honshu, Shikoku, and Kyushu geothermal systems. Geothermal energy potential maps were firstly produced at different depth intervals using two dimension kriging interpolations. The temperature distribution was then modeled in the three dimension to a depth of 1 km from the surface underground. In addition, the dataset from multi-sourced well loggings was used to improve the accuracy of 3D model and furthermore, predict the geothermal properties. Finally, based on the analysis of the deep geothermal potentials, location of high potential areas where further exploration and future exploitation of the geothermal resources is feasible in Japan were detected.

Keywords Geothermal resource • 3D • Temperature distribution • Upper crust

97.1 INTRODUCTION

Geothermal energy, not only applicable for electricity generation but also for direct heating, has been recognized as clean, sustainable and low-emission energy sources [1]. Japan is ranked as the world's third-richest country in geothermal energy [2, 3]. Assessment of deep geothermal potential is of great help for further exploration and exploitation of such energy resource in Japan. Due to various geological settings, faults, volcanic zones and topographies, the geothermal systems are widely distributed under different conditions. Therefore, it is difficult to make a variogram or geostatistical modeling in the wide area for this lack in stationarity. Based on different tectonic settings (Plate, Arc, and Tectonic Line), volcano front, fault zones

B. Tian (✉) • K. Koike

Graduate School of Engineering, Kyoto University, Kyoto 615-8540, Japan

e-mail: bwtian@gmail.com

and geography, we divided the Japan land into six zones of different geothermal systems: Hokkaido, Northeast of Honshu, and Center of Honshu, Southwest of Honshu and Shikoku, Kyushu, Nansei Islands and Izu-Bonin geothermal systems (Fig. 97.1). The details of each system are summarized in Table 97.1 and shown in Fig. 97.2.

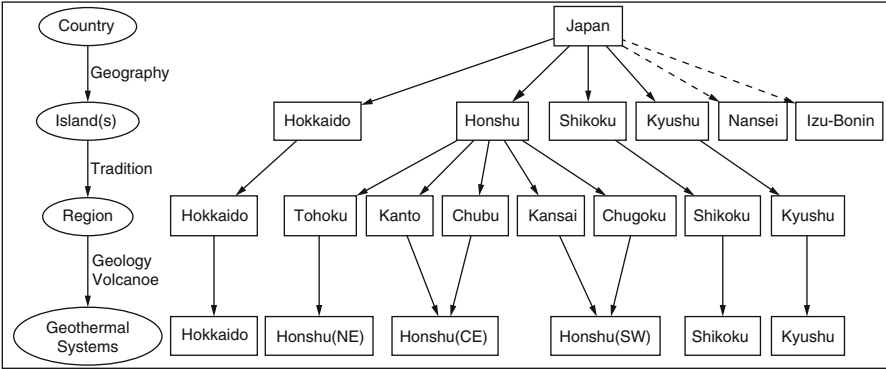


Fig. 97.1 Geothermal systems of Japan due to geography, geology and active volcanoes.

Table 97.1 Geothermal system in main island of Japan GPP represent for geothermal power plants

Geothermal Systems	Hokkaido	Honshu (NE)	Honshu (CE)	Honshu (SW)	Shikoku	Kyushu
Tectonic Arc	Kuril, Japan(NE)	Japan(NE) Japan(NE)	Japan(NW) Izu-Bonin	Japan(SW)	Japan(SW) CTL	Japan(SW) Ryukyu
Main Islands	Hokkaido	Honshu	Honshu	Honshu	Shikoku	Kyushu
Regions and (Prefectures)	Hokkaido (1)	Tohoku (6)	Kanto(7) Chubu(9)	Kansai(7) Chugoku(5)	Shikoku (4)	Kyushu (6)
Area(km ²)	83,460	63,860	92,470	64,680	18,790	39,600
Boreholes	434	271	223	64	8	214
Data (JAEA)	28,485	34,512	8,020	1,517	134	15,948
Active volcanoes	18	18	19	2	0	17
Hot Springs	2,220	3,870	7,800	3,100	570	9,640
GPP Units	1	9	1	0	0	11

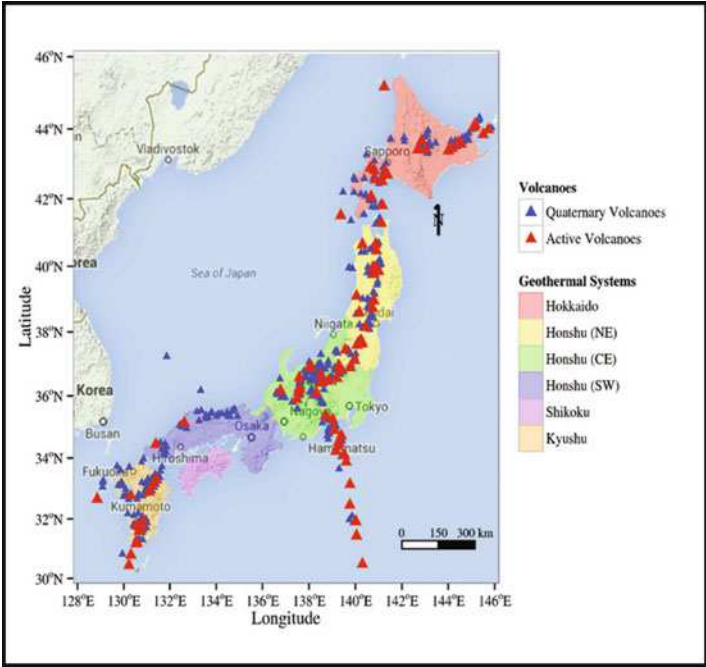
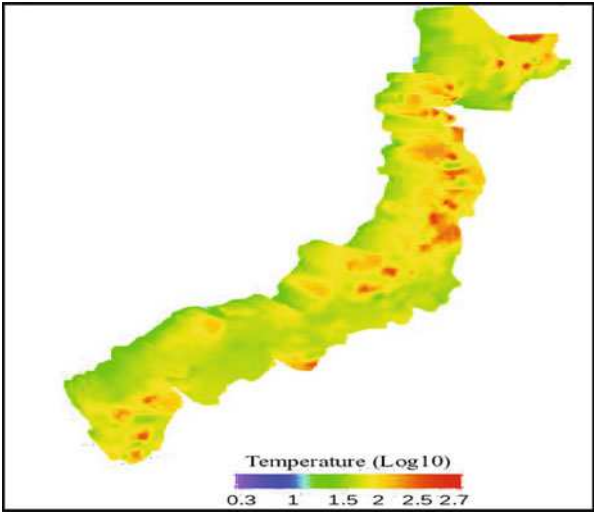


Fig. 97.2 Study area map with active volcanoes.

Fig. 97.3 Estimated 3D temp. distribution from the depth of 100 to 1000 m (log10 °C).



97.2 DATA RESOURCES

The borehole data set was acquired from the “temperature profiles in Japan” dataset (<http://www.jaea.go.jp/04/tono/siryou/welltempdb.html>) which was compiled by Japan Atomic Energy Agency in 2004. The active volcanoes data acquired from the key hole markup language (KML) file provided by the website of Japan Meteorological Agency (http://www.seisvol.kishou.go.jp/tokyo/STOCK/souran/appendix/active_volcanoes.zip). There are more than 110 active volcanoes and 27,000 hot springs located in Japan. The statistics of hot spring data is from the website of Ministry of the Environment Government of Japan (<http://www.env.go.jp/nature/onsen/index.html>).

97.3 METHODOLOGIES

Kriging with trend (KT) is normally called universal kriging (UK)(1) which is one kind of kriging methods by Matheron (1963) [4]. KT is often used for the regionized data with a significant spatial trend, such as a geothermal gradient in this study. KT is an extension of ordinary kriging (OK) by incorporating the local trend within the neighborhood search widow as a smoothly varying function of the coordinates, and then estimates the trend components within each search neighborhood window and then performs simple kriging (SK) on the corresponding residuals.

$$\hat{Z}(x_0) = \sum_{l=0}^L a_l f_l(x) + \sum_{i=0}^N \lambda_i (Z(x_i) - \mu(x_0)) \quad (97.1)$$

Where $\sum_{l=0}^L a_l f_l(x)$ is deterministic function with known function $f_l(x)$ and unknown function a_l , $L \ll N$. λ_i is kriging weight; N is the number of sampled points used to make the estimation and depends on the size of the search window; and (μ_{x_0}) is the mean of samples within the search window.

97.4 RESULTS AND DISCUSSION

After calculation based on a $1000 \times 1000 \times 100$ m mesh in Japan main islands, Fig. 97.3 shows temperature distribution from 100 m to 1000 m depth from the surface. The high temperature zones present in Eastern Hokkaido, Northeast Honshu, Center of Honshu and Southern Kyushu Island, especially in Northeast Honshu region, where the most concentrated high temperature zones are characterized. On the other hand, low temperature zones are mainly around the Shikoku Island and Southwest Honshu, despite the fact that there are few volcanoes in Southwest Honshu region. The volcanic activity in these regions is related to the Philippine

Sea Plate which subduct at the Nankai Trough. This part of the Philippine Sea Plate is younger and warmer than another part of the plate. Therefore, the slab is at shallow depths under the Southwest Japan Arc and the volcanic activity is dormant. Generally, deep temperature distribution is consistent with surface manifestations, especially active volcanoes. In Japan, the largest number of volcanoes and corresponding concentrated deep high temperature make the Northeast Honshu region be the most volume of volcanic products.

97.5 CONCLUSIONS

We characterized the crustal temperature of the heat stored underground in different geothermal systems based on various geological structures, fault zones and volcanic zones, including Hokkaido, Northeast of Honshu, Center of Honshu, Southwest of Honshu, Shikoku, and Kyushu geothermal systems in Japan. The temperature distribution with a cell resolution of $1000 \times 1000 \times 100$ m was estimated using kriging with trend method in the three dimension at the depth from 100 m of 1 km. Based on the result of the deep geothermal potentials, Eastern Hokkaido, Northeast Honshu, Center of Honshu and Southern Kyushu Island where further exploration and future exploitation of the geothermal resources is feasible in Japan were detected. Of these regions, the Northeast Honshu region owns the highest geothermal potential.

REFERENCES

1. Barbier, E.: Geothermal energy technology and current status: an overview. *Renewable and Sustainable Energy Reviews*, 6(1), 3–65 (2002)
2. Fridleifsson, I.B.: Geothermal energy for the benefit of the people. *Renewable and Sustainable Energy Reviews*, 5(3), 299–312 (2001)
3. Stefansson, V.: World geothermal assessment. Proceedings of the World Geothermal Congress, 24–29 (2005)
4. Matheron, G.: Principles of geostatistics. *Economic Geology*, 58, 1246–1266 (1963)
5. Wackernagel, H.: Multivariate Geostatistics: An Introduction with Applications. Springer, Berlin (2003)

Chapter 98

A Nonstationary Nonlinear Geostatistical Model and Its Application in a Beach Sand Deposit for Recoverable Reserve Estimation

M. Thakur, B. Samanta, and D. Chakravarty

Abstract The standard geostatistical models, both linear and nonlinear, require the data to be stationary, which is very rare in reality. The changing of means and variances, and spatial covariance structure are evident in the real life data. The so called global non-stationarity over a spatial field is captured by a model which is considered to be locally stationary but globally non-stationary. The proposed model is simultaneously defined everywhere in the concerned domain not only in the defined areas, but again the model behaves like a local stationary process in small areas. For this purpose, the smoothly varying local multivariate spatial distribution function has been derived by weighting all the data values in the spatial field using kernel function and consequently represented by Hermite polynomial expansions. The locally varying spatial covariance structure is modeled by a local covariance function defined by semi-variance parameters estimated experimentally by the local samples present in the local stationary region. The local recoverable reserve is estimated by calculating conditional cumulative distribution function using nonlinear geostatistical techniques such as disjunctive kriging and multi Gaussian kriging. The proposed method has been applied in an Indian beach sand deposit for local recoverable reserve estimation. An appropriate support effect model has been incorporated for designing this estimation algorithm. The impacts of support effect and nonstationarity in terms of local recoverable reserve are analyzed for the deposit.

Keywords Disjunctive Kriging • Selectivity curve • Cumulative distribution function • Nonstationarity

M. Thakur (✉) • B. Samanta • D. Chakravarty
Department of Mining Engineering, Indian Institute of Technology, Kharagpur, India
e-mail: 4u.mainak@gmail.com

98.1 INTRODUCTION

The concept of the geostatistical modeling techniques generally relies on the important assumption of stationarity, but real life spatial domains are rarely stationary. The local changes in mean and variance are therefore usually overlooked in the estimation process and hence often lead to an unreliable estimation when applied to real life nonstationary spatial data. An extensive research has been going on for a long time on how to deal with nonstationarity in the spatial processes. A deformation approach was introduced by Sampson and Guttorp [8]. The parametric maximum likelihood estimation approach, in this context, was used by Mardia and Goodall [5]. Nonstationary spatial kriging based on moving windows was presented by Haas [3]. A high frequency kriging approach for nonstationary environmental processes was established by Fuentes [2]. Again, Fuentes and Smith [1] explained another nonstationary spatial covariance modeling approach assuming the nonstationary process observed over the domain as convolution of local stationary processes and tried geostatistical as well as Bayesian approach to estimate the spatial structure. Machuca-Mory and Deutsch [4] proposed a methodology based on the assumption of local stationarity where the local distributions and variograms were inferred using distance weighting kernel functions and further used in estimation. The methodology used in this article is closely related to Machuca-Mory and Deutsch [4]. Here the reflection of the local changes has been incorporated in the cumulative distribution function (cdf) and the variogram parameters those have been used in the nonlinear geostatistical techniques like multi-gaussian and disjunctive kriging. It is assumed that the cdfs and the characteristics of the spatial process are stationary with respect to some key points in the domain. The local cdfs were evaluated using the distance kernel function applied to all the samples based on their distance from the corresponding key point in order to make the function smooth enough. The generation of the necessary local normal scores and local Hermite polynomials as well as Hermite coefficients allow for the nonlinear estimation in the locally stationary structure. In this approach, the nonlinear geostatistical techniques with a proper change of support model have been applied to estimate the selectivity curves of an Indian beach sand deposit. Application of geostatistics in estimating the recoverable reserves of beach sand deposit is rare. Sahin [7] reported that the placer sand deposits in India is in the tune of 340 million ton of ilmenite, 107 million ton of garnet, 21 million ton of zircon, 18 million ton of rutile, 8 million ton of monazite, and 130 million ton of sillimanite. These resources represent 35% of world resources of ilmenite, 10% of rutile, 14% of zircon, and 71% of monazite. This article made an attempt to estimate local recoverable reserves for a beach sand deposit located in the eastern part of India through the grade-tonnage curves using locally stationary nonlinear geostatistical techniques with an appropriate change of support model. The comparison between the results due to the locally stationary nonlinear techniques and that of usual globally stationary disjunctive kriging and multi-gaussian kriging has been investigated through the grade tonnage curve.

98.2 OVERVIEW OF THE DEPOSIT

The beach sand deposit investigated in this study is located in the eastern part of India. To maintain confidentiality, the name, geographical locations and other details of the deposit are not disclosed. For the same reason, the grade values of the deposit in actual scale are not divulged and a known multiplying factor is used to transform the original values. The new transformed values have been used in the modeling procedure. The concerned deposit is approximately 4,000m long and 1,000m wide. The sand deposit present here is geologically recent (Quaternary) origin that has been reworked partially to completely by the wind action to form Aeolian sand deposits, containing titanium and zirconium minerals. The deposit was drilled in wider grid interval of approximately 200m by 200m. Figure 98.1 gives two dimensional view of bore hole locations of the deposit where the small black dots are the bore holes.

98.2.1 Statistical Analysis of the Deposit

The assay data which are available for the resource evaluation study consist of 108 drill holes. The data contain Easting and Northing coordinates, borehole collar information, and HM (heavy metal) percentage of drill cores. Holes have been drilled up to a depth of 5.5 m, with sample cores collected at 1.0 m interval down to a depth of 4 m and the last core at 1.5 m length. As per the requirement for the deposit evaluation, the reserve estimation has been carried out for the topmost slice i.e. depth of 1 m from the top. Table 98.1 presents the summary statistics of assay values for HM% for the deposit. Six different statistical indices are used to characterize the data. Figure 98.2 presents the histogram plot of the HM % for

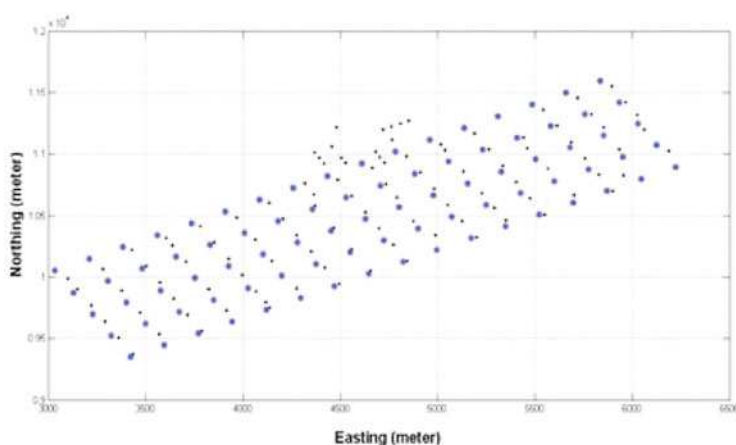
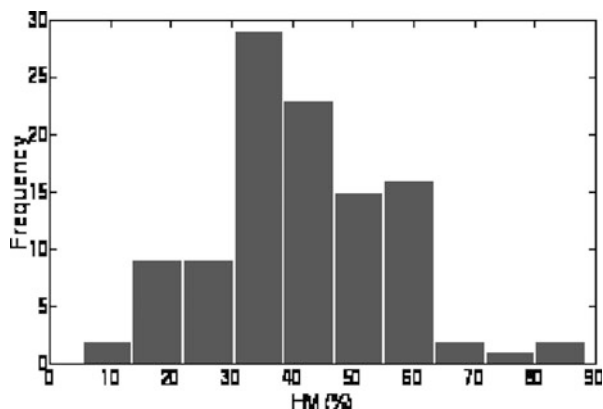


Fig. 98.1 Borehole locations and the panel centers (key points) of the deposit

Table 98.1 Statistical summaries of drill hole composite data

Samples	Mean HM (%)	Variance (%)	Standard Deviation (%)	Coefficient of Variation (%)	Skewness	Kurtosis
108	41.08	224.04	14.97	36.43	0.30	3.40

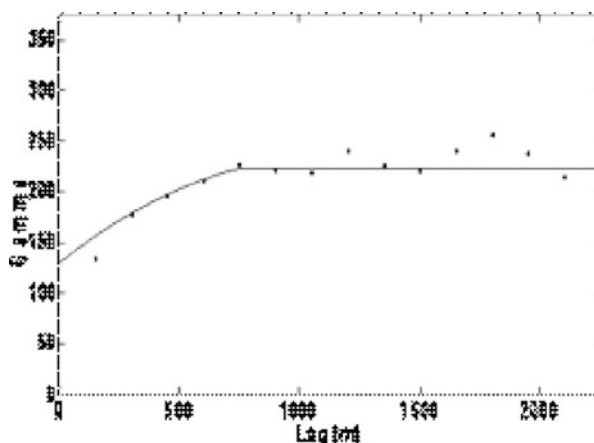
Fig. 98.2 Histogram of the deposit

the deposit. The histogram plots suggest that the frequency distribution of HM % akin to symmetric, bell shaped curve of Gaussian distribution.

98.2.2 Variography Analysis

The variogram is considered to be the heart of geostatistics based on which the grade/reserve estimation is carried out. The variography study captures the spatial continuity of a deposit, which is indicative of spatial correlation of sample values separated by a certain distance. A detailed analysis of the variogram study of the concerned deposit demonstrates that the spatial continuity is higher somewhat along the direction of N 60° E. Actually this direction is the coastal-line direction along which deposition of heavy minerals take place. In any other directions, the spatial continuity is lesser. In fact, it has been very difficult to construct a reasonable good variogram in other directions due to inadequate sample pairs on account of elongated formations of this nature. Therefore, only the omni-directional variogram models have been used for the ore reserve estimation (globally stationary method) purpose. Figure 98.3 presents the omni-direction point variogram of the whole deposit. The variogram analysis indicates that the point variogram shape is quite consistent and modeled by spherical variogram. It can also be noticed that semi-variogram is highly dominated by nugget component with an average relative nugget effect (nugget/sill) to be almost 0.6.

Fig. 98.3 Variogram of the deposit



98.3 METHODOLOGY

This section of the case study deals with how the locally stationary nonlinear methodology has been applied to the concerned beach sand deposit. For the local estimation of the recoverable reserve, two non-linear kriging techniques have been applied with a change of support model (DGM) to each of the area under chosen 85 key stationary points which, in this particular deposit, are assumed as the panel centers of 200×200 sq. meters anels. The bigger dots in the Figure 98.1 are the different key points (i.e. the panel centers) around which the local stationarity is defined.

Firstly, the local variogram parameters were estimated through experimental variogram modeling for each key stationary point using the samples within a reasonable radius and the values were stored for future use. Then the local cdfs are obtained for each of the key stationary point using the kernel function assigning weights on all the sample values based on their distance from the key stationary point. According to Machuca-Mory and Deutsch [4], the most suitable distance kernel in this context is the Gaussian kernel. The local normal scores transformation of the original sample data has been obtained as they are required to apply nonlinear geostatistical methods. Again, the local Hermite coefficients were saved for their further use in the nonlinear estimation process. Here, DGM is used as the change of support model in the modeling process. The SMU size here is assumed as $25 \text{ m} \times 25 \text{ m}$ for the estimation. Now the change of support coefficients are obtained for each of the stationary key points and shown in Figure 98.4 below. For each of the key stationary points, the tonnage figures are obtained for each local panel using nonlinear kriging techniques like disjunctive kriging and multi-gaussian kriging as shown by Rivoirard [6]. Then the tonnage figures are summed up to estimate the total tonnage for the deposit.

Fig. 98.4 Change of support coefficients

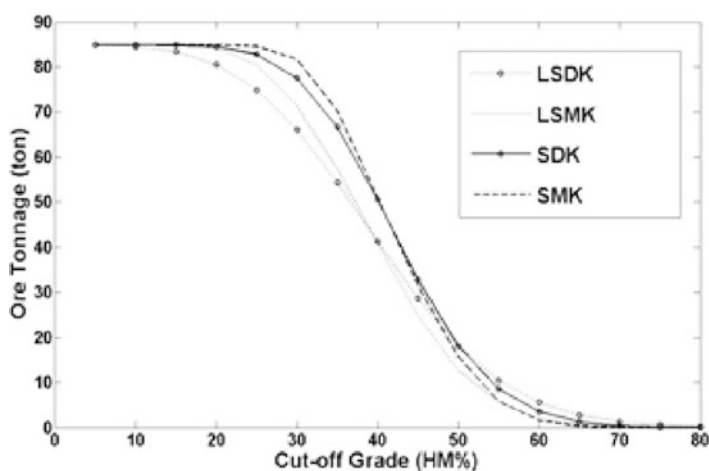
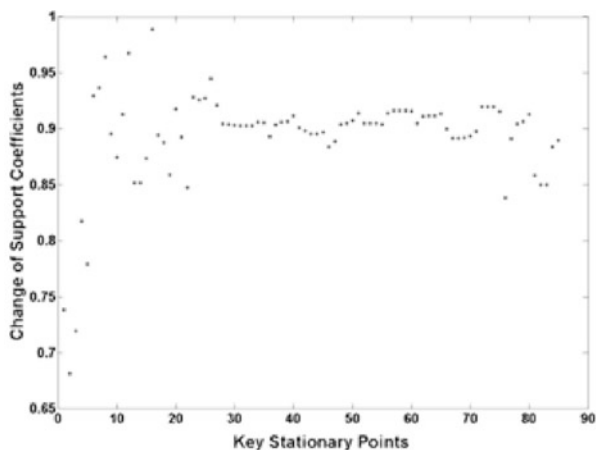


Fig. 98.5 Grade tonnage curves of the deposit evaluated for each key point

98.4 RESULTS

From the Figure 98.4, it can be observed that the local change of support coefficients lie between 0.85 and 0.95 mostly. Figure 98.5 shows the grade tonnage curves of the deposit due to both the kriging techniques: disjunctive kriging (DK) and multigaussian kriging (MK), using the locally stationary method as well as with the usual global stationary assumption. The ore tonnage (Y-axis) is scaled here in the Figure 98.5 by dividing the original tonnage by the product of the area of the panel and the specific gravity of the ore. The LSDK and LSMK stand for the locally stationary disjunctive kriging and locally stationary multigaussian kriging grade-tonnage curves respectively, where as SDK and SMK stand for the

same in the usual global stationary case. It can be seen that for the same cut-off grade, the ore tonnage obtained for LSDK and LSMK are less than SDK and SMK respectively except for few high cut-offs. The result shows that, for this particular deposit, if the local changes are considered in the modeling process then the estimated tonnage decreases.

98.5 CONCLUSIONS

The local information of the data is often ignored in the usual geostatistical techniques due to their strict stationarity assumptions. From the results, it can be noticed that if the local changes can be incorporated in the modeling process, the overestimation or the underestimation can be avoided. Though the local stationary estimation process is more expensive in terms of time and space, the results would be more reliable. However, the result becomes more accurate if there are plenty of samples available for the estimation.

REFERENCES

1. Fuentes, M. and Smith, R.L.: A new class of nonstationary spatial models. Technical report, North Carolina State University, Raleigh, NC (2001)
2. Fuentes, M.: A high frequency kriging approach for non-stationary environmental processes. *Environmetrics*, 12(5), 469–483 (2001)
3. Haas, T.: Local Prediction of a Spatio-Temporal Process with an Application to Wet Sulfate Deposition. *Journal of American Statistical Association*, 90, 1189–1199 (1995)
4. Machuca-Mory, D.F. and Deutsch, C.V.: Non-stationary geostatistical modeling based on distance weighted statistics and distributions. *Mathematical Geosciences*, 45(1), 31–48 (2013)
5. Mardia, K.V. and Goodall, C.R.: Spatial-temporal analysis of multivariate environmental monitoring data. *Multivariate Environmental Statistics*, 76, 347–385 (1993)
6. Rivoirard, J.: Introduction to disjunctive kriging and nonlinear geostatistics. Oxford University Press, Oxford (1994)
7. Sahin, A.: Global estimates of ore reserves in a beach sand deposit. *CIM Bulletin*, 94(1047), 43–47 (2001)
8. Sampson, P.D. and Guttorp, P.T.: Nonparametric estimation of nonstationary spatial covariance structure. *Journal of American Statistical Association*, 87, 108–119 (1992)

Chapter 99

Contextualized Geographically Weighted Principal Components Analysis for Investigating Baseline Soils Data on the North Wyke Farm Platform

P. Harris, N.J.K. Howden, S. Peukert, V. Noacco, K. Ramezani, E. Tuominen, B. Eludoyin, R. Brazier, A. Shepherd, B. Griffith, R. Orr, and P. Murray

Abstract The UK's North Wyke Farm Platform (NWFP) for sustainable grassland farming is set up as a large agriculture modelling system of 15 hydrologically-isolated catchments, where in each catchment, water chemistry, precipitation and soil moisture data are continuously monitored. This spatio-temporal data are then interrogated with respect to climatic timings and changes in crop, livestock and farm management, across the NWFP. Complementary data sets are also found via spatial field surveys, remote sensing and greenhouse gas studies. This study focuses on one such field survey, consisting of soils data at 495 sites. We spatially explore this data using a geographically weighted principal components analysis, where we provide a novel adaptation of the technique to deal with the distinctly partitioned nature of the data, which is collected across 20 fields, spread over the 15 catchments.

Keywords Grasslands • Livestock production • Non-stationarity • Local models

99.1 INTRODUCTION

The North Wyke Farm Platform (NWFP) at Rothamsted Research in the South-West of England, is a large, farm-scale experiment for collaborative research, training and knowledge exchange in agro-environmental sciences; with the aim

P. Harris (✉) • A. Shepherd • B. Griffith • R. Orr • P. Murray
North Wyke, Rothamsted Research, Okehampton, Devon EX20 2SB, UK
e-mail: paul.harris@rothamsted.ac.uk

N.J.K. Howden • V. Noacco • K. Ramezani • E. Tuominen
Faculty of Engineering, University of Bristol, Bristol BS8 1TR, UK

S. Peukert • B. Eludoyin • R. Brazier
Department of Geography, University of Exeter, Exeter, Devon EX4 4RJ, UK

of addressing agricultural productivity and ecosystem responses to different management practices. The 70 ha NWFP site, captures the data necessary to develop a better understanding of the dynamic processes and underlying mechanisms that can be used to model how agricultural grassland systems respond to different management inputs. Here, via beef and sheep production, the underlying principle is to manage each of three farmlets (each consisting of five hydrologically-isolated catchments) in three contrasting ways: (i) improvement through use of mineral fertilizers; (ii) improvement through use of legumes; and (iii) improvement through innovation.

The connectivity between the timing and intensity of different management operations and the transport of nutrients and potential pollutants from the farm is evaluated using sensor technology (providing numerous catchment-specific, temporal data sets) coupled with traditional field studies. For this study, we focus our attention on the latter with the statistical analysis of a 2012 soils survey (for the following seven variables: Bulk Density, Total Carbon, Total Nitrogen, Soil Organic Matter, pH, Isotope 13 for Carbon and Isotope 15 for Nitrogen), covering all 15 NWFP catchments. Height and slope are also included, taking the study data to nine variables in total. The design of the NWFP precedes this survey, where catchments were allocated to each farmlet based on: (a) historical farm practices; (b) expert knowledge of the physical properties of the North Wyke site; and (c) a need for a certain spatial connectivity between the five catchments of each farmlet. The soils data is viewed as baseline data before different management inputs were set in motion in early 2013. The soils data can be analyzed in a number of ways, where for this study we apply a geographically weighted principal components analysis (GWPCA) [1, 2]. A GWPCA can: (1) provide insights into how the dimensionality and structure of the soil variables varies across space, (2) identify local data anomalies; and (3) direct future soil sampling campaigns. For this study, we focus our attention on how GWPCA can be used as a local dimension reduction technique, where we introduce an adaptation of GWPCA to deal with the partitioned nature of the data.

99.2 METHODOLOGY

In a GWPCA, a series of localized PCAs are computed, where the local component outputs are mapped, permitting a local identification of any change in the structure of the multivariate data. The choice of kernel weighting function and the type and size of its bandwidth are all crucial. Fixed bandwidths (constant distance) suit data sets that are sampled over a fairly regular grid, whilst adaptive bandwidths (constant local sample size) suit irregular sample configurations. With this in mind, we calibrate our GWPCAs with a bi-square kernel using adaptive bandwidths, whose sizes are found (automatically and objectively) via cross-validation. We find the GWPCA results only at the sample sites, but variances and loadings could have been found at un-observed sites, also. As in any GWPCA, we report the results of

the global PCA, so that we can gauge the extent of spatial heterogeneity. In addition to the application of a standard GWPCA, we demonstrate an adapted GWPCA that attempts to deal with the partitioned nature of the soils data; data which is collected across 20 distinct fields spread over the 15 catchments. Field partitions include roads, hedges, fences, and the man-made French drains needed to hydrologically-isolate the catchments. Thus the soils data is not expected to be fully-continuous across the NWFP site (and in parts, may reflect historical farm practices). Instead continuity is only really expected within each of the 20 fields. Observe here, that is not viable to apply separate, local PCAs within each field, as some fields are highly under-sampled with as few as six observations (whilst some fields are relatively rich in information with over 100 observations). Also observe that a degree of continuity is still likely across all 15 catchments, and this study-scale process would not be accounted for if a piecemeal PCA approach was followed. To adapt GWPCA, we follow an approach similar in spirit to that used in the contextualized GW regression [3], where for our study, the weighting is a combination of the usual geographical weighting, together with a second geographical weighting that groups data by the field that they are located in. Thus the usual bi-square kernel is used for the first weighting, with:

$$w_{ij} = \left(1 - (d_{ij}/r_1)^2\right)^2 \quad \text{if } d_{ij} \leq r_1 \quad \text{and } w_{ij} = 0 \quad \text{otherwise,} \quad (99.1)$$

where the bandwidth is the geographic distance r_1 ; d_{ij} is the geographic distance between spatial locations of the i^{th} and j^{th} rows in the data matrix; and, w_{ij} is the geographic weight attached to an observation point indexed by j , for a calibration point indexed by i . This first weighting is multiplied by a second weighting, again using a bi-square kernel, with:

$$w_{kl} = \left(1 - (d_{kl}/r_2)^2\right)^2 \quad \text{if } d_{kl} \leq r_2 \quad \text{and } w_{kl} = 0 \quad \text{otherwise,} \quad (99.2)$$

where the bandwidth is the geographic distance r_2 ; d_{kl} is the geographic distance between the centroids of the k^{th} and l^{th} fields; and, w_{kl} is the geographic weight attached to an observation point that is field indexed by l , for a calibration point that is field indexed by k .

This second weighting function entails that data within each field are given the same second weighting, regardless of their location in that field (i.e. there are only ever 20 distinct second weights). Only the bandwidth r_1 is found optimally, as r_2 is user-specified so that all observations are given a (non-zero) second weighting. The combined weighting function is such, that for a GWPCA calibration point near to a boundary, a near-by observation that is within its field will be given a larger weight (i.e. more importance) than a near-by observation that is at the same distance from the GWPCA calibration point, but located in a different field. This contextualized GWPCA should reflect the expected discontinuities in the soils data.

99.3 RESULTS

For our PCA and GWPCA fits, the same globally standardized data is used (see [2] for some consequences of this). The PCA results (Fig. 99.1a) reveal that the first four components collectively account for 76.7% of the variation in the data. Thus proceeding with the same number of retained components for our GWPCA calibrations is natural, as it directly corresponds to that of a reasonable PCA specification. An optimal bandwidth for GWPCA using the single, standard weighting function is found to be 69.3% (i.e. the nearest 343 observations are weighted), with a minimum cross-validation score = 1.41. An optimal bandwidth for the contextualized GWPCA, using the combined weighting function is much tighter at 28.9%, with a minimum cross-validation score = 1.15.

Figs. 99.1b-d present the percentage of total variance (PTV) maps (again, with four retained components) for both GWPCAs, together with a second, standard GWPCA using the smaller bandwidth of the contextualized GWPCA. This third GWPCA acts as a control to gauge the effects of using different bandwidths between our standard and contextualized GWPCAs. It is clear that both standard

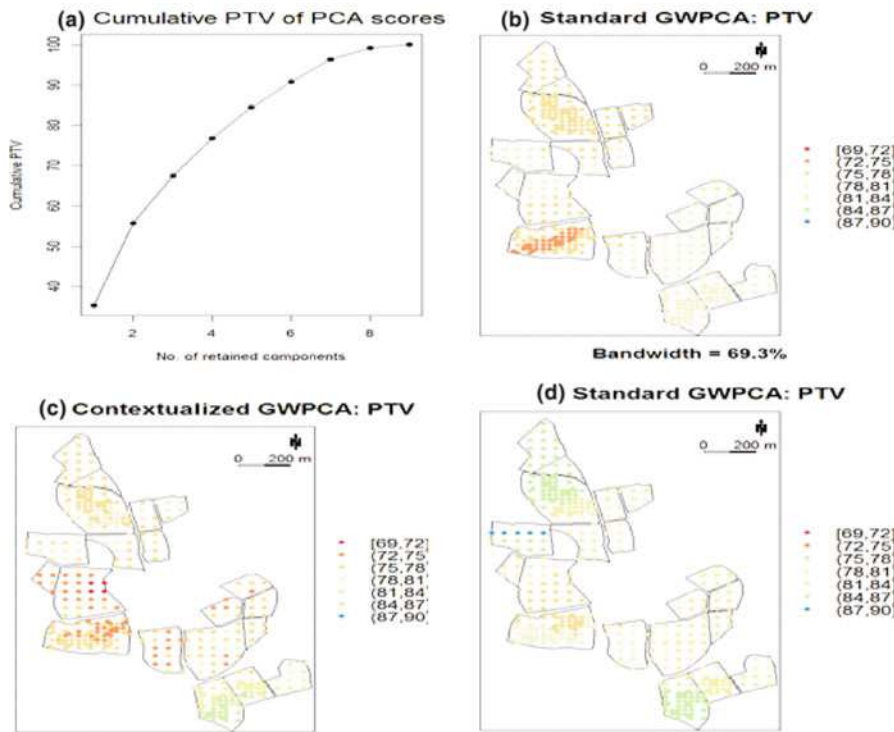


Fig. 99.1 (a) PCA cumulative PTV plot; (b) standard GWPCA PTV map (69.3% bandwidth); (c) contextualized GWPCA PTV map (28.9% bandwidth); and (d) standard GWPCA PTV map (28.9% bandwidth)

GWPCAs are representative of some smoothly-varying continuous multivariate process, where the GWPCA with the larger bandwidth tends to an over-smoothing, whilst the GWPCA with the smaller bandwidth tends to an under-smoothing. Neither reflects the expected discontinuities in the soils data at the field boundaries or strongly different variances between fields. Conversely, the contextualized GWPCA behaves as expected, where clear discontinuities are present according to the field boundaries. Considering the contextualized GWPCA provides the smallest cross-validation score, we tentatively assume that its PTV map provides the truest representation of changes in local data dimensionality in the soils data.

99.4 CONCLUDING REMARKS

For this study, we have outlined an adapted form of GWPCA to deal with the partitioned nature of the NWFP baseline soils data. Only changes in local data dimensionality were reported, but future work will report changes in the local relationships of the nine variables. The use of contextualised GWPCA to detect local outliers and direct future sampling campaigns will also be considered.

REFERENCES

1. Harris, P., Brunson, C. and Charlton, M.: Geographically Weighted Principal Components Analysis. *Int. J. Geogra Inf Sci*, 25(10), 1717–1736 (2011)
2. Harris, P., Clarke, A., Juggins, S., Brunson, C. and Charlton, M.: Enhancements to a geographically weighted principal components analysis in the context of an application to an environmental data set. In press *Geogr Anal* (2014)
3. Harris, R., Dong, G. and Zhang, W.: Using Contextualized Geographically Weighted Regression to Model the Spatial Heterogeneity of Land Prices in Beijing, China. *Transactions in GIS*, 17(6), 901–919 (2013)

Chapter 100

Downscaling of Precipitation in Mahanadi Basin, India Using Support Vector Machine, K-Nearest Neighbour and Hybrid of Support Vector Machine with K-Nearest Neighbour

Manjula Devak and C.T. Dhanya

Abstract The climate impact studies in hydrology often rely on climate change information at fine spatial resolution. Downscaling is a practice for obtaining local-scale hydrological variables from regional-scale atmospheric data that are provided by General Circulation Models. Among two downscaling methods, Statistical Downscaling is taken into account, as it offers less computational work as compared to Dynamic Downscaling and also provides us with a platform to use ensemble GCM outputs. In the present study, a Support Vector Machine (SVM), K-Nearest Neighbor (KNN) and Hybrid of Support Vector Machine (SVM) with K-Nearest Neighbor (KNN) approaches are proposed for Statistical Downscaling of precipitation at monthly time scale. To reduce the dimensionality of the dataset, the Principal Component Analysis (PCA) is also performed. The CanCM4 simulations are run through the calibrated and validated SVM, KNN and hybrid of SVM with KNN downscaling models to obtain future projections of precipitation values. A comparison is made between the models in this study.

Keywords Downscaling • General circulation models • Support vector machine • K-nearest neighbour • Equidistant CDF matching method

100.1 INTRODUCTION

In the arena of changes, the Climate Change is the subject of utmost concern. It is imperative to consider different time scales while investigating climate change because climate varies over a gamut of time scales: from a few years to hundreds of millions of years. These changes play a vital role in the study of hydrological processes. General Circulation Models (GCMs) are used to study the impact of climate change. The gap between the simulations obtained from global climate

M. Devak (✉) • C.T. Dhanya

Department of Civil Engineering, Indian Institute of Technology, New Delhi, India

e-mail: manjulaiitd@gmail.com

models and the information which is needed at local scales that is what is required by decision makers and impact assessors is minimized by downscaling techniques. In this study Statistical Downscaling is adopted as it offers less computational work and large number of realizations can be generated in order to gauge ambiguities. Many researchers in the past compare various methods of statistical downscaling like Artificial Neural Network (ANN), Conditional- Random Field (CRF) model, K-Nearest Neighbour (KNN), Support Vector Machine (SVM), Non-homogeneous Hidden Markov Model (NHMM) etc. and revealed that SVM is unable to arrest extreme rainfall event as SVM is regression based model generally does not illustrate entire variance of the downscaled variable (Wilby et al., 2004). The biggest limitation of the support vector approach lies in choice of the kernel (Burgess et al., 1998). Although SVM directly operates on kernel but it involves time consuming training on whole data set and also with extreme event forecasts SVM is sidelined. A particularly popular approach, K- nearest neighbour (KNN) is endorsed by many researchers in the past. Many authors adopted KNN method for downscaling [1–4] The studies mentioned above admit the dependency of KNN approach on the selection of a “good value” for K. Perhaps the most easy and candid approach in machine learning is K- Nearest Neighbour but when attributes increases certainty in the prediction decreases and also in context with narrow sample space it experiences high variance. Despite pleasant aspects in both the models there is a room for improvement so we come up with the hybrid of SVM with KNN with a view to curtail discordant nature of both the model to some extent. Main principle on which the proposed model works is the shear use of KNN with refinement in SVM. Hybrid of SVM with KNN couples the performance of SVM with improved boundaries and KNN with smooth distance function. Hence, the objective here is to scale down the drawbacks of SVM and KNN model by fusing it together which is applicable in all conditions. The results from the hybrid of SVM and KNN are then compared with both SVM and KNN models.

100.2 STUDY REGION AND DATA DESCRIPTION

The Mahanadi Basin is considered for the study purpose, which is located between 19°N and 23.7°N latitude and 80.4°E and 86.9°E longitude (Figure 100.1) with a basin area of 141589 Sq km. Based on the study conducted by Anandhi et al. [5] eleven predictor variables, viz, Air temperature (at 200, 500, 700, 925 mb), Geo-potential height (at 200, 500, 925 mb), Eastward wind (at 200, 925 mb) and Northward wind (at 200, 925 mb), are selected for downscaling precipitation in Mahanadi basin. National Centre for Environmental Protection (NCEP) prepared a gridded data (<http://www.cdc.noaa.gov/>) from which predictor data set for the period ranging from January 1961 to December 2004 for nine grid points is extracted at monthly time scale. Gridded precipitation data of resolution 1° by 1° is taken from Indian Meteorological Department (IMD) for five downscaling locations (Fig. 100.1). For the study region GCM data is taken from the website

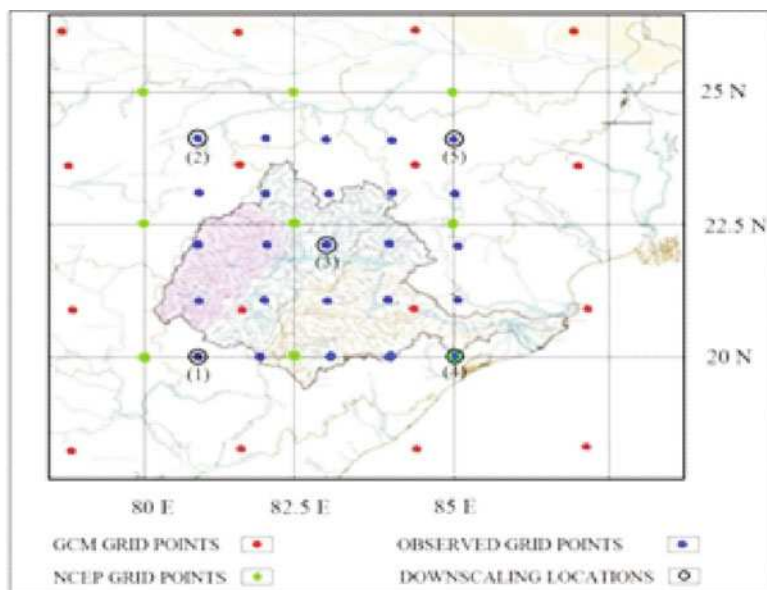


Fig. 100.1 Location of Mahanadi Basin in India with grid points and location number

www.cccma.bc.ec.gc.ca/. These are the simulations from CanCM4 model of the Canadian centre for climate modelling and analysis of Coupled modelled Inter comparison project-5 (CMIP-5). Historical and RCP 4.5 scenarios are used in the study. The predictor set for historical scenario is extracted from January 1961 to December 2004 and for RCP 4.5 scenario predictor set is extracted from January 2016 to December 2035 for sixteen grid points. Latitudes and longitudes of NCEP, GCM and IMD data is shown in Fig. 100.1.

100.3 METHODOLOGY

The detailed methodologies are described as under:

100.3.1 SVM Downscaling

The predictor dataset taken from NCEP database and is used for calibrating (from Jan 1961-Dec 1995) the model. The resolution of NCEP data is $2.5^\circ \times 2.5^\circ$ and that of GCM data is $2.8^\circ \times 2.8^\circ$ so GCM grid points are interpolated over NCEP grid points. The data sets from NCEP and GCM constituting eleven predictor variables for each grid point (total predictor = $11 \times 9 = 99$), is first standardized, by subtracting

the mean and dividing by standard deviation. Principal component analysis is then performed to reduce the size of the matrix and to eliminate redundancies in the data. Model is then calibrated by adjusting the kernel width (σ) and penalty term C. The calibrated model is then validated (from Jan 1996-Dec 2004). Precipitation is then simulated for future scenario using (RCP4.5 predictor set) from January 2016 to December 2035. The predictors are first bias corrected using EDCDF method [6]

100.3.2 KNN Downscaling

For downscaling the precipitation using KNN considers the same predictor set as SVM downscaling. First compile all predictor variables for nine grid points. Then perform principal component analysis with training set and preserve the principal directions (PDs) for future reference. Standardize the testing set by subtracting the mean and dividing by standard deviation as done for SVM model before. Multiply the standardized set with PDs preserved earlier to form feature vectors. For each time element i , calculate the Euclidian distance between the feature vectors and the PCs. Retain only first K distances after sorting the distance d_i in ascending order. From the observed data of precipitation select the K neighbors corresponding to the particular Euclidian distance for each day. The weight to each of the K neighbors is then assigned using Bisquare weighting function. Then apply weighted average technique to find the precipitation for particular month. Repeat the steps for each time element and for each grid. The same procedure is adopted, after preserving PDs of training set, to generate projections.

100.3.3 Hybrid of SVM and KNN

The underlying idea behind the fusion of SVM model and KNN is to calibrate the SVM model with nearest neighbors to a variable which is queried. The first step to find the neighbors which are close to the sample is the same as described in section 3.2. After finding the nearest neighbors, the SVM model is trained by incorporating these neighbors as predictor set.

100.4 RESULTS AND DISCUSSION

100.4.1 Calibration and Validation Results

SVM model is calibrated by selecting the optimum parameter value of kernel width (σ) and penalty term (C) by grid search method. The value of σ and C thus obtained are 10 and 10000 respectively. The optimum number of nearest neighbors, K is

fixed through an empirical formula, $K = (\text{length of dataset})^{0.5}$. Hybrid model takes into account all the three parameters. All the three parameters are selected based on Normalized mean square error (NMSE) and Correlation coefficients (CC). From the study it was found that first six principal components together preserve more than 95% of the variability of the original 99-dimensional dataset. All the results in this paper are presented for location 2 and 4. A comparison is made between the observed precipitation and precipitation generated from all the three models. As can be viewed from the box-plot (Fig. 100.2) the precipitation is better captured by hybrid model also this model better simulates the mean. The width of the box illustrates the uncertain behavior of the model, in figure 100.2 hybrid model shows nearly same box-width as that of the observed data. CDF plot is better captured by the hybrid of SVM with KNN (Fig. 100.3) and also it captures the peak values better than the other two models. Mean values are calculated for both locations (Fig. 100.4) which depicts that at both locations hybrid model shows mean values close to the observed data while SVM and KNN model overestimates the results. The results are also analyzed for monsoon n non-monsoon months separately (Fig. 100.5) which depicts that the absolute deviation (shown by bars) between mean of observed and mean of hybrid model result is less than the other two models. Complete testing set shows less NMSE values and higher CC values than monsoon months, this can be the explanation that model is unable to capture

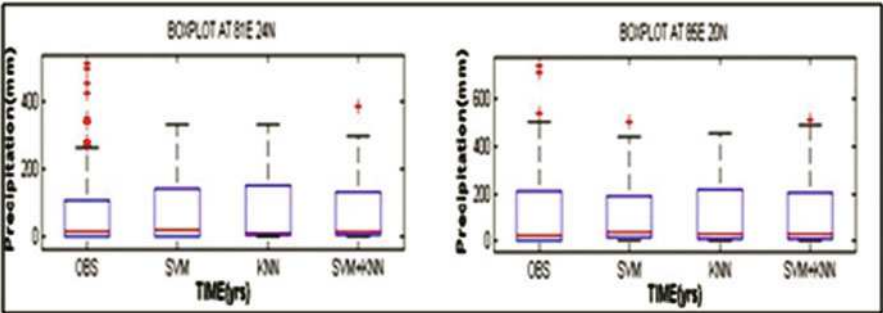


Fig. 100.2 Box plot for testing period

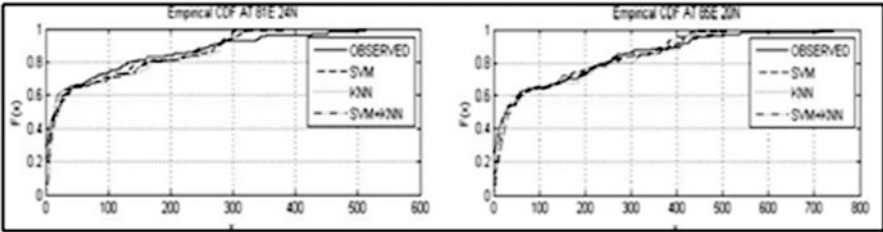


Fig. 100.3 CDF plot for testing period

Fig. 100.4 Mean and Standard Deviation plot for testing period

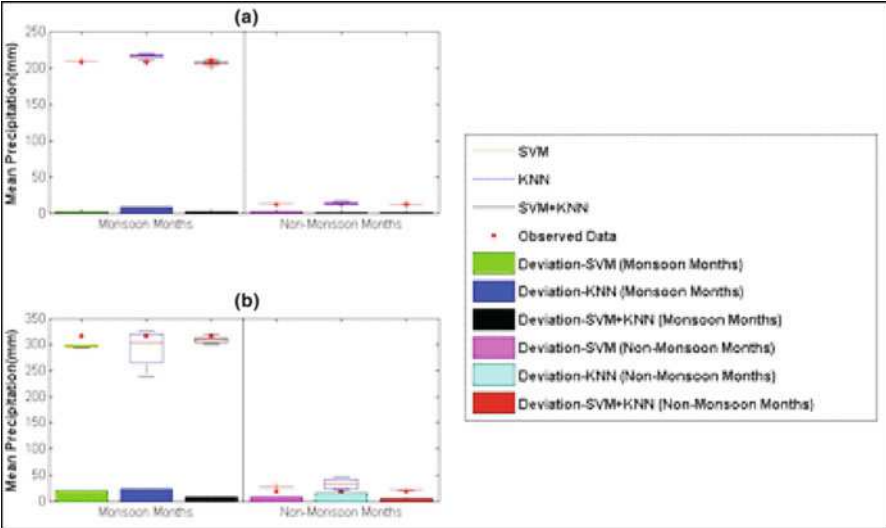
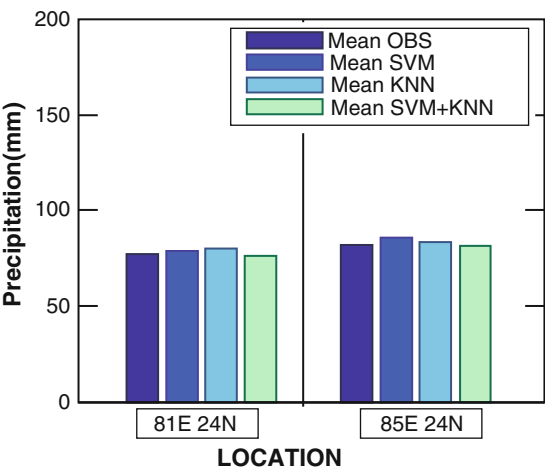


Fig. 100.5 Comparison of box plots of the average monthly precipitation values for monsoon and non-monsoon months separately from the SVM, KNN and SVM+KNN models: (a) 81E 24 N and (b) 85 E 20 N

the extreme values of precipitation but follows good behavior for non- monsoon months. All the results prove that hybrid model shows fairly good results than the other two models also there is the presence of regional variation in the results. Therefore, sometimes the applicability of the model also depends on the location of site. These models can also be used to downscale other parameters like maximum temperature, specific humidity, minimum temperature etc. which further helps in the valuation of climate changes with time and location both.

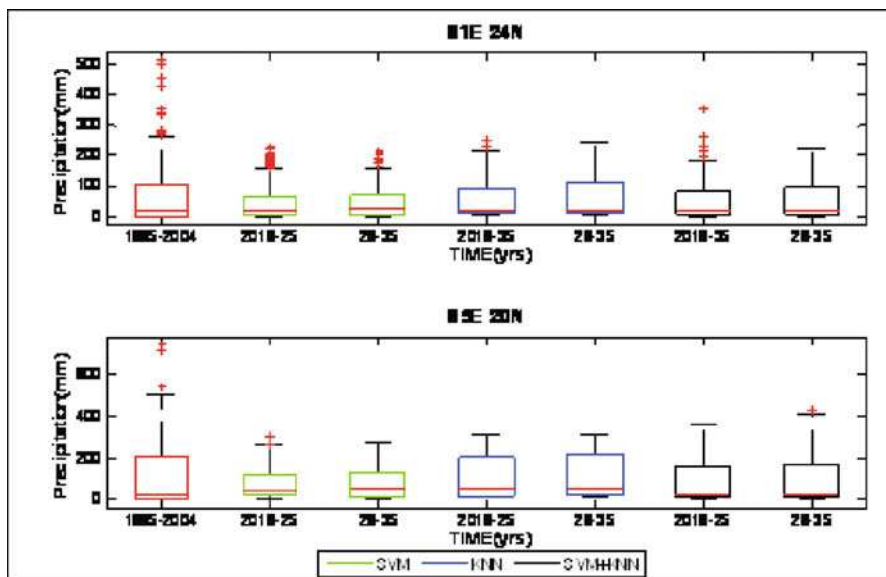


Fig. 100.6 Box plot for future projection

100.4.2 Future Projections

Figure 100.6 shows box-plot for future projections at both locations. At both locations, all the models show there is decreases in decadal precipitation. Hybrid model shows median value of the box-plot close to the observed data also able to capture the higher events.

REFERENCES

1. Lall, U. and Sharma, A.: A nearest neighbour bootstrap for time series resampling. *Water Resources Research*, 32(3), 679–693 (1996)
2. Buishand, T.A. and Brandsma, T.: Multisite simulation of daily precipitation and temperature in the Rhine (2001)
3. Yates, D., Gangopadhyay, S., Rajagopalan, B. and Strzepek, K.: A technique for generating regional climate scenarios using a nearest neighbour algorithm. *Water Resources Research*, 39 (7), 1199 (2003)
4. Gangopadhyay, S. and Clark, M.: Statistical downscaling using K-nearest neighbours. *Water Resources Research*, 41, W02024 (2005)
5. Anandhi, A., Srinivas, V.V. and Nanjundiah, R.S.: Downscaling precipitation to river basin in India for IPCC SRES scenarios using support vector machine. *International Journal of Climatology*, 28, 401–420 (2008)
6. Li, H., Sheffield, J. and Wood, E.F.: Bias correction of monthly precipitation and temperature fields from Intergovernmental Panel on Climate Change AR4 models using equidistant quantile matching. *Journal of Geophysical Research*, 115 (2010)

Chapter 101

A Precipitation-Runoff Simulation Model for Flood Forecasting of River Tel, Odisha, India

Prabeer Kumar Parhi

Abstract Flood forecasting is considered as an important component of non structural measures for flood management planning. Hence it is of immense importance to accurately estimate the flood hydrographs resulting from storm events for all the tributaries of a river system which causes flood. In the present study simulation of precipitation-runoff process for the Tel Sub basin of Mahanadi Basin is carried out and various important parameters of the model are calibrated. It is pertinent to mention that Tel (catchment area 22800 km²) is an important tributary of Mahanadi system and contributes significantly to the flood peak at the delta head of Mahanadi at Munduli. Historical flood records show that the River Tel alone contributed 74.85% and 71.1% of the total flood peak at the delta head of Mahanadi during the floods of 2008 and 2009 respectively. For precipitation-Runoff simulation study of Tel Sub basin of Mahanadi Basin the HEC-HMS model, developed by Hydrologic Engineering Center of US Army Corps of Engineers is used. Using the model and available data some important model parameters which significantly affect precipitation-runoff process are calibrated considering the storm event of 29 August 2006 to 4 September 2006. Further, using the calibrated model parameters, the model is run to estimate the flood peak and time to peak for the storm event of Sept 2008 flood (14 Sep 2008 to 25 Sep 2008) and July 2009 flood (14 July 2009 to 25 July 2009). The observed and computed values of flood peaks and time to peaks are compared and it is seen that there is a close agreement between the observed and computed values. The result shows that there is an error of 4.8% and 0.82% between the observed and computed flood peaks respectively for the storm events of 2008 and 2009.

Keywords Precipitation-runoff simulation • Tel river • HEC-HMS parameters • Calibration and validation • Flood forecasting

P.K. Parhi (✉)

Center for Water Engineering and Management, Central University of Jharkhand,
Ranchi, India

e-mail: prabeer11@yahoo.co.in

101.1 INTRODUCTION

The River Mahanadi, largest in Odisha has experienced large numbers of severe and devastating floods, endangering both life and property. As an important component of non structural measures (flood forecasting), it is very much essential to accurately estimate the flood hydrograph resulting from a storm event for all the tributaries of Mahanadi system. Earlier study shows that River Tel, which is an important tributary of Mahanadi system, has contributed very significantly to the flood peak at the delta head of Mahanadi at Munduli. It has been observed that in the year 2008 and 2009 River Tel alone contributed respectively 74.85% and 71.1% of the total flood peak at the delta head of Mahanadi at Munduli [1]. Hence in the present study it is proposed to calibrate and validate a precipitation-Runoff simulation model for the Tel Sub basin of Mahanadi Basin using HEC-HMS, developed by Hydrologic Engineering Center of US Army Corps of Engineers [2]. The proposed model will be used to calibrate various parameters of the model using available data and will also be validated using different data sets. The proposed model will also be used to estimate the flood peak and time to peak for the different tributaries of the River Tel.

101.2 STUDY AREA

The River Tel is one of the major tributaries of the River Mahanadi. It lies between $82^{\circ} 09' 48''$ to $84^{\circ} 17' 53''$ East longitude and $19^{\circ} 15' 08''$ to $20^{\circ} 53' 31''$ North latitude. During its course of 296 km, it drains an area of 1496 km² in Chhatisgarh and 21285 km² in Orissa, totaling to 22781 km². The River Tel intercepts 16.13% of the drainage area of River Mahanadi which is 32.34% of the drainage area of Mahanadi in Odissa [3].

101.2.1 Use and Analysis of Available Data

For precipitation runoff simulation of Tel sub-basin, the whole sub-basin is divided into 6 catchments representing various rivers. The catchment wise representation of Tel sub-basin is presented in Table 101.1. Various RG stations coming under each sub-catchments of Tel and their contribution as a percentage of sub-catchment area is determined using Thiessen Polygon approach. Table 101.2 represents sub-catchment wise Thiessen weights of each rain gauge (RG) stations.

Table 101.1 Sub-catchment of Tel sub-basin

Name of Sub-catchments under Tel	Catchment area (km ²)	Rivers coming under the Sub-catchments
SB-1	3381	Moter
		Hati
		Banjari
SB-2	3733	Ret
		Utei
		Sandul
SB-3	4192	Khadga
		Buda
		Bagh
SB-4	3712	Udanti
		Sukhatel
SB-5	4695	Indra
		Lanth
SB-6	3068	Suktel
Total	22781	Total Contribution from Tel

Table 101.2 Sub-basin wise rain-gauge weights for Tel river

Sub-catchment	R.G Station	Area (km ²)	Thiessen Weight
SB-1	Jaipatna	2164.00	0.64
	Junagarh	1217.00	0.36
SB-2	Lanjigarh	1124.00	0.30
	Bhawanipatna	785.00	0.21
	Kesinga	624.00	0.17
	Madanpur	1200.00	0.32
SB-3	Madanpur	787.00	0.19
	Tikabali	1720.00	0.41
	Sonepur	322.00	0.08
	Baliguda	1363.00	0.33
SB-4	Junagarh	952.00	0.26
	Khariar	2760.00	0.74
SB-5	Komna	1310.00	0.28
	Tureikela	694.00	0.15
	Khariar	584.00	0.12
	Titlagarh	939.00	0.20
	Belgaon	640.00	0.14
	Patnagarh	528.00	0.11
SB-6	Patnagarh	2047.00	0.67
	Baliguda	440.00	0.14
	Sonepur	581.00	0.19

101.3 CALIBRATIONS OF MODEL PARAMETERS

In the present study to simulate precipitation-runoff and routing process of a storm event using computer programme HEC-HMS, various model parameters are calibrated considering the flood event of September 2006 [4]. Various model parameters calibrated for Tel Sub-basin are as follows. The calibration of parameters is done considering soil type, topographical conditions, and channel characteristics. Some parameter values are calibrated/adjusted using trial and error so as to minimize the gap between the observed and computed flood peak and time to peak.

101.3.1 Initial Loss and Constant Loss Rate

Due to lack of detail soil information, the initial loss is considered as 20 mm which shows the amount of water that will infiltrate to the soil before surface runoff begins. The constant rate is assumed as 2.3 mm/hour, which shows the rate of infiltration that will occur after initial loss is satisfied.

101.3.2 Synthetic Unit Hydrograph Parameters

The software generates Unit Hydrograph (UH) for the basin with Clark's methodology such that empirical Snyder relationship is maintained. The standard lag and peaking coefficient calibrated for the basin are 6.7 hours and 0.42 respectively.

101.3.3 Recession Constant

To specify the rate at which the recession flow decreases with time, a recession constant is used which shows the ratio of base flow at constant time to base flow one day earlier. In the present study recession constant is calibrated as 0.92.

101.3.4 Routing Parameters

The Muskingum routing is used to route the flood through channel to the gauge discharge point of interest through stream reaches. The Muskingum K is essentially the travel time through the reach. It can be estimated from knowledge of the cross section properties and flow properties. In the present study the Muskingum K is estimated considering flow velocity as 6 to 8 kmph. The Muskingum X is the

Table 101.3 Comparison of observed and computed flood peaks at Patharla GD site

Flood Event (Year)	Event Duration (Period)	Observed Peak Discharge (cum)	Computed Peak Discharge (cum)	Observed Time to Peak	Computed Time to Peak	% Error
Sept-2008	14 Sep 2008, 09.00 hrs to 25 Sep 2009, 09.00 hrs	33560	31944	18 Sep, 2008, 03.00 hrs	18 Sep, 2003, 09.00 hrs	−4.81
July-2009	14 July 2009, 09.00 hrs to 25 July 2009, 09.00 hrs	17630	17488	04 July, 2009, Time 12.00 hrs	04 July, 2009, 09.00 hrs	−0.80

weighting factor between inflow and outflow influence; it ranges from 0.0 up to 0.5 [5]. In practical application, a value of 0.0 results in maximum attenuation and 0.5 results in no attenuation. In the present study it is calibrated as 0.23.

101.4 VALIDATIONS OF MODEL PARAMETERS

Using the calibrated parameters the flood peaks and time to peaks for the flood events for the storm event of Sept 2008 flood [6] (14 Sep 2008 to 25 Sep 2008) and July 2009 [7] flood (14 July 2009 to 25 July 2009) are estimated. The observed and computed values of flood peaks and time to peaks are compared and it is seen that there is a close agreement between the observed and computed values. Table 101.3 shows the observed and computed values of flood peaks and time to peaks for the flood events of Sept 2008 and July 2009.

101.5 CONCLUSIONS

The study shows that the HEC-HMS model can be used very effectively for the calibration of the catchment parameters those influences precipitation-runoff simulation process. The calibrated parameters can be used to simulate the precipitation-runoff process for the Tel sub-basin of Mahanadi basin for any storm event up an accuracy of 99 percent. The simulation model can be used for flood forecasting and flood plain mapping with sufficient lead lime so that flood hazard can be minimized to an appreciable extent.

REFERENCES

1. Flood Bulletin: Department of Water Resources Odisha, Bhubaneswar (2010)
2. US Army Corps of Engineers: HEC-HMS, User Manual. Hydrologic Engineering Center, Davis Version 3.2 (2008)
3. Das, G.: Flood Management in Mahanadi Basin. Water Resources Department, Odisha (1998)
4. Flood Bulletin: Department of Water Resources Odisha, Bhubaneswar (2006)
5. Subramanya, K.: Engineering Hydrology. Tata McGraw Hill, India (2008)
6. Flood Bulletin: Department of Water Resources Odisha, Bhubaneswar (2008)
7. Flood Bulletin: Department of Water Resources Odisha, Bhubaneswar (2009)

Chapter 102

Dynamics of Overland Flow under Changing Cropping Pattern: A Spatial Modeling Approach in Penganga Sub-watershed

Abira Dutta Roy and S. Sreekesh

Abstract A simulation study using SWAT hydrological model has been carried out to evaluate the impacts of changing cropping pattern and agricultural expansions on overland flow in Penganga Sub watershed, Maharashtra. Remote sensing data combined with ground-truthing and extrapolation of pixel signatures were done for generation of spatial crop inventory for the years 2011, 1999, 1990 and 1976. The crop inventory analysis showed a significant change in the cropping pattern over the decades. Less water intensive crops like Jowar, Tuarand Gram were heavily replaced by water intensive crops like Cotton and Wheat. Over 30% of the open scrubs were also converted for cultivation. These four different scenarios were modeled without hydrological structures under constant climatic conditions of 1975-76. The resultant simulated runoff showed higher peak discharges (~2000 cumecs in July, ~1500 cumecs in September) under the cover conditions of 1975. Under similar climatic conditions the consecutive scenarios showed gradual decline in runoff. The flow generated under the cover conditions of 2011 showed lowest and delayed peak discharges (~1000 cumecs in July and ~700 cumecs in September). The study showed that the shift in cropping pattern to water intensive crops reduced surface flow. This calls for appropriate crop combination for better utilization of available water.

Keywords Crop inventory • Overland flow • Runoff simulation • SWAT • Land use/Land cover

102.1 INTRODUCTION

Human utilization of territory, especially the plains for agricultural activities has been the main factor in the land use dynamics [1]. Changes such as deforestation, reclamation of wetlands, etc. with the aim of increasing agricultural production has affected watershed hydrology by altering the rates of interception, infiltration,

A.D. Roy • S. Sreekesh (✉)
CSRSD, Jawaharlal Nehru University, New Delhi, India
e-mail: sreekesh@mail.jnu.ac.in

evapotranspiration, and groundwater recharge that has resulted in changes to the timing and amounts of surface and river runoff [2]. Vegetation removal has also resulted in increased base flows if soil infiltration capacities remain constant [3]. On the other hand, if vegetation clearing is followed by land use practices that compact soils and expose them to erosion, then decreased percolation to groundwater can occur [4–6]. Numerous factors such as forest type, rainfall regime, soil type, soil depth and topography also play significant role in determining the impact of land use land cover changes on watershed hydrology [7]. Yet little has been proved so far regarding any established quantitative relationship between the land use properties and the runoff generation mechanism. Different methodologies have been implemented to fill in the deficiency of the knowledge in this subject, but no general model has been established to predict the effect of land use changes [8]. This paper attempts to understand the impacts of conversion of barren to agriculture land and changes in cropping pattern on the runoff of Penganga River using SWAT (Soil Water Assessment Tool) hydrological model assuming topographic and climatic conditions as constant.

102.2 STUDY AREA

Penganga River, with an area of 7996.26 sq km, is a tributary of the Wardha River which ultimately joins the Godavari River. Figure.102.1 shows the location of the study area. Much of the region is underlain by basaltic rocks of lava origin. It receives a highly variable annual rainfall of 50-200 cm. During January and April it receives rainfall around 2.5 cm. Periodic droughts are frequently observed here. The mean temperature in January ranges between 20-25 °C and in April it is above 30 °C.

The area is mostly plain except near to the water divided and the Buldana ranges from where the river origins. The area has high drainage density. Figure.102.2 (a) shows the relief pattern of the watershed. The soil map generated from NBSSLUP (National Bureau of Soil Survey and Land Use Planning) has been shown in Figure 102.2 (b) with the mapping codes denoted as per NBSSLUP norms.

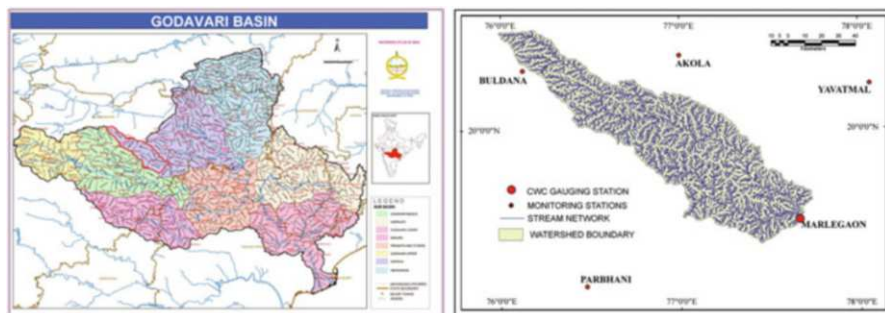


Fig. 102.1 Location map of Penganga subwatershed

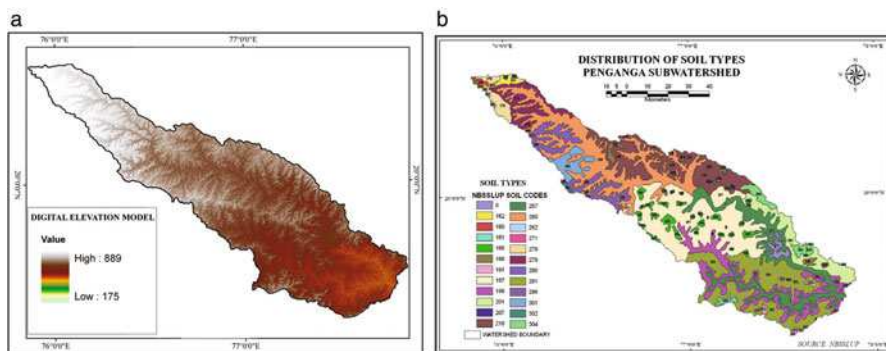


Fig. 102.2 (a). Relief map. (b). Soil map of Penganga subwatershed

About 60 % of the area is under cultivation; of which nearly 1/10th receives irrigation. Wells account for 60 % of the irrigated areas, canals for 20 %, and tanks for the remaining 20 %. Sorghum occupies 1/3rd of the cropped area, millet 1/10th, and pulses 1/6th. Cotton is the major cash crop occupying 1/8th of the cropped area. The irrigation system is fast changing the cropping pattern of the area [9].

102.3 METHODOLOGY

102.3.1 Data Preparation

In order to estimate the changes in cropped area and cropping pattern a crop inventory was done, using satellite images of 1976 (Landsat MSS), 1990 (Landsat TM), 1999 (Landsat TM), 2011 (IRS P6 LISS-III). Cloud free satellite images corresponding with the dates on the crop calendar of the region were selected such that both Rabi and Kharif crops at different growth stages are found. Supervised classification [10, 11] and accuracy assessment were done using Transformed Divergence Matrix [12], confusion matrix [13] of all the images. Transition matrix method [14] was subsequently used to obtain change in cropping pattern. Runoff simulation was done in SWAT [15–17]. SWAT, is a physical model and incorporates the entire hydrological cycle, its interaction with the surface and sub-surface conditions and also interactions between the variables constituting the hydrological cycle can be modeled by incorporating land use land cover data, digital elevation model, soil data, hydro-meteorological and plant growth data [18]. The model on the basis of soil, slope and land use/land cover types segregates the basin in to unique HRUs (Hydrological Response Units) and with the help of daily time step data on maximum minimum temperature, precipitation, solar radiation, humidity and wind speed simulates the runoff based on the water balance equation given below:

$$SW_t = SW_0 + \sum_{i=1}^t (R_{day} - Q_{surf} - E_a - w_{seep} - Q_{gw}) \quad (102.1)$$

where SW_t is the final soil water content (mm H₂O), SW_0 is the initial soil water content on day i (mm H₂O), t is the time (days), R_{day} is the quantity of precipitation on day i (mm H₂O), Q_{surf} is the quantity of surface runoff on day i , E_a is the quantity of evapotranspiration on day i (mm H₂O), W_{seep} is the quantity of water entering the vadose zone from the soil profile on day i (mm H₂O), and Q_{gw} is the quantity of return flow on day i (mm H₂O).

For all the different land use scenarios the model was run. The runoff simulated under the land cover conditions of 1976 was validated with the observed runoff using NashSutcliffe [19] as shown through equation below.

$$NS = 1 - \frac{\left[\sum_i^n (Q_{simi} - Q_{obsi})^2 \right]}{\left[\sum_i^n (Q_{obsi} - Q_{avg})^2 \right]} \quad (102.2)$$

where n is equal to number of time steps, Q_{simi} is equal to simulated runoff at time step i , Q_{obsi} is equal to observed runoff at time step i and Q_{avg} is equal to average observed stream flow over the simulation period. Subsequent to the validation, different crop cover scenarios were incorporated, eliminating the hydrological structures from the modeling environment keeping topographic and weather parameters constant.

102.4 RESULTS AND DISCUSSION

102.4.1 Cropping Pattern Change

Significant increase in the area under irrigation structures are seen from 1976 to 2011. Isapur Dam which became operational since 1982 inundated large acres of arable and open scrub land, as a result area under water bodies increased. A few medium irrigation projects namely Koradi and Pentaklihad come up during 2000. In 1990 the area under built up too showed an increase by 712.57 ha. During the years 1990 to 2011 further increase in the built up area by 9641.30 ha was observed. The built up areas and irrigation projects have increased at the cost of arable land and open scrub land in its vicinity. After irrigation facilities were introduced, area under wheat increased by 4813.91 ha from 1976 to 1990. On the other hand the area under cotton, tuar, jowar and gram observed a decline by 36617.79 ha, 28743.29 ha, 375.73 ha and 12049.07 ha respectively in the above period. With further up communing irrigational facilities the area under cotton, wheat, and jowar increased

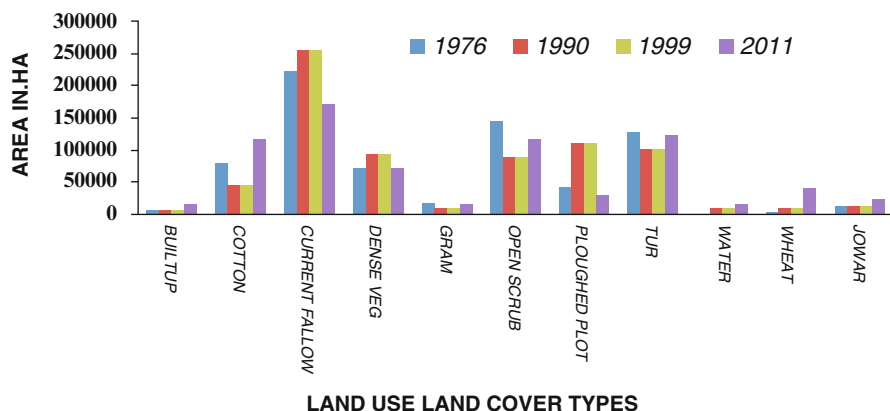


Fig. 102.3 Land use land cover changes from 1976 to 2011

during 1999 and 2011. On the other hand the area under crops like tur and gram declined. The area under current fallow, ploughed plot and open scrub showed fall in area during 2011 in comparison to that of the previous years. Thus agricultural intensification, expansion and cropping pattern changes became evident from the land use land cover change analysis. Figure 102.3 shows the trend in land use land cover change across 1976, 1990, 1999 and 2011.

102.4.2 Impact of Cropping Pattern Change on Runoff

Subsequent to the land use land cover change analysis the simulation of runoff was done. Runoff simulated under land cover conditions of 1976 and hydro-meteorological conditions of 1975-76 produced a NSE coefficient of 0.31. The low goodness fit can be attributed to absence of rain gauge stations inside the catchment. With this efficiency in model performance the scenarios of 1990, 1999 and 2011 were modeled to understand the impact of cropping pattern changes. Figure 102.4 shows the simulated overland flow under different land use land cover conditions.

The scenario of 1975-76 generated higher peaks from dominant open scrub and fallow land present during that year. The similar rainfall generated a lower peak under the land cover condition of 1990. The gradual decline in the peaks and increase in base flow is a result of gradual decline in the area under open scrub and current fallow and an increase in area under cropcover. The cropping pattern change has led to higher crop water requirement as more area was incorporated under water intensive crops.

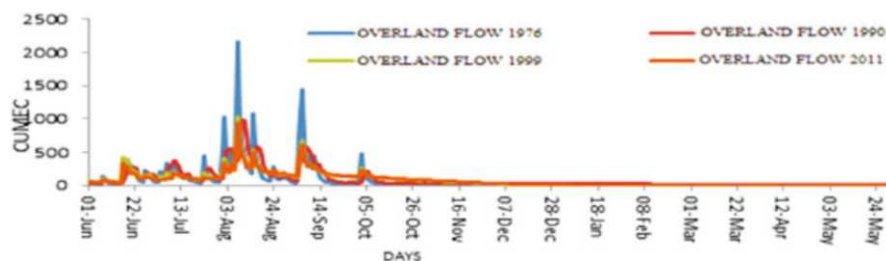


Fig. 102.4 Simulated runoff under land use land cover scenarios of 1976, 1990, 1999 and 2011

102.5 CONCLUSION

This research highlights that changing cropping pattern and conversion of barren open scrub land for agricultural purpose has negative impacts on the natural flow conditions of the region. The shift of agricultural practices from less water intensive to more water intensive crop in an existing water stressed arid region is highly unsustainable. The increased crop water requirement, the dynamic sowing density adversely impacts the overland flow. Such results call for appropriate crop combination and cropping practices that are suitable and resilient to the climatic condition of the region.

REFERENCES

1. Grove, A.T.: The historical context: Before 1850, in C. Jane Brandt and J.B. Thornes (eds.) *Mediterranean desertification and land use*. John Wiley & Sons, Chichester, United Kingdom (1996)
2. (b) Baker, W. L.: A review of models of landscape change. *Landscape Ecology*, 2, 111-133 (1989)
3. Bruijnzeel, L.A.: Deforestation and dry season flow in the tropics: A closer look. *Journal of Tropical Forest Science*, 1 (3), 229-243 (1989)
4. Bonnell, M., Purandara, B.K., Venkatesh, B., Krishnaswamy, J., Acharya, H.A.K., Sungh, U. V., Jayakumar, R. and Chappell, N.: The impact of forest use and reforestation on soil hydraulic conductivity in Western Ghats of India: Implications for surface and sub-surface hydrology. *J. Hydrol.*, 391, 47-62 (2010)
5. Chandler, D.G.: Reversibility of forest conversion impacts on water budgets in tropical karst terrain. *For. Ecol. Manage.*, 224, 95-103 (2006)
6. Zimmermann, B., Elsenbeer, H. and De Moraes, J.M.: The influence of land-use changes on soil hydraulic properties: implications for runoff generation. *For. Ecol. Manage.*, 222 (1-3), 29-38 (2006)
7. Bosch, J.M. and Hewlett, J.D.: A review of catchment experiments to determine the effect of vegetation changes on water yield and evapotranspiration. *Journal of Hydrology*, 55, 3-23 (1982)

8. Kokkonen, T.S. and Jakeman, A.J.: Structural effects of landscape and land use on streamflow response. *In*: Beck, M.B. (eds.), *Environmental Foresight and Models: A Manifesto*. Netherlands: Elsevier Science BV, pp. 303-321 (2002)
9. Tirtha, Ranjit: *Geography of India*, 2nd edition. Rawat Publication, Jaipur (2001)
10. Joice, A.T.: Procedure for gathering information for a supervised approach to computer implemented land cover classification of Landsat, acquired multispectral scanner data. NASA Reference Publication 1015, Houston TX, USA (1978)
11. Singh, V.K., Dwivedi, B.S., Shukla, A.K., Chauhan, Y.S. and Yadav, R.L.: Diversification of rice with pigeon pea in a rice-wheat cropping system on a Typic Ustochrept: Effect on soil fertility, yield and nutrient use efficiency. *Field Crops Research*, 92, 85-105 (2005)
12. Swain, P.H. and Davis, S.M.: *Remote Sensing: The Quantitative Approach*. McGraw-Hill, New York (1978)
13. Vyas, S.P., Manjunath, K.R., Kalubarme, M.H. and Gupta, P.C.: Remote sensing of dryland farming pulse crop in Hamirpur district of U.P. *In*: *Proceedings of National Symposium on RS Applications for Resource Management*. November 25-27, Guwahati, pp. 314-320 (1993)
14. Jensen, J.R.: *Introductory Digital Image Processing: A Remote Sensing Perspective* (2nd edn). Upper Saddle River, NJ: Prentice Hall (1996)
15. Govender, M. and Everson, C.S.: Modelling Stream flow from Two Small South African Experimental Catchments Using the SWAT Model. *Hydrological Processes*, 19(3), 683-692 (2005)
16. Bingner, R.L.: Runoff simulated from Goodwin Creek watershed using SWAT. *Trans. ASAE*, 39(1), 85-90 (1996)
17. Anand, S., Mankin, K.R., McVay, K.A., Janssen, K.A., Barnes, P.L. and Pierzynski, G.M.: Calibration and validation of ADAPT and SWAT for field-scale runoff prediction. *Journal of the American Water Resources Association*, 43(4), 899-910 (2007)
18. Neitsch, S.L., Arnold, J.G., Kiniry, J.R. and Williams, J.R.: *Soil and Water Assessment Tool – Theoretical Documentation*, Version 2005. Texas, USA (2005)
19. Nash, J.E. and Sutcliffe, J.V.: River flow Forecasting through Conceptual modes Part-I, A discussion of principles. *Journal of Hydrology*, 10, 282-290 (1970)

Chapter 103

Challenges of Including Groundwater Depth in a Liquefaction Loss Model

T. Ancheta and Seung-Jae Lee

Abstract The near surface or depth to the first occurrence of groundwater is vital in evaluating liquefaction initiation and therefore a liquefaction loss model. If groundwater is below a susceptible layer, that layer is unlikely to liquefy. This study will discuss the challenges in modeling near surface groundwater depths over a large region, using the Canterbury region of New Zealand as an example, and its importance to loss estimation relative to liquefaction hazard. Estimating the depth to near surface groundwater is an emerging discipline that benefits from geostatistics and hydrology. While accounting for spatial randomness in the groundwater depth, we develop a site-specific mean trend model assimilating secondary datasets correlated with the primary variable and process it through the Kriging system. Secondary datasets considered are a continuous map of distance to a water body (DWB) and ground surface elevation through a digital elevation model (DEM). Resulting estimation improves upon a Kriging method not incorporating the secondary information (Mean Square Error reduction ranges from 47.5 to 73.8 %). The estimation of the groundwater depth at unsampled locations leads to enhanced understanding of liquefaction over a region and thus of spatial distribution in the loss uncertainty. The findings of this study would be of great help to investigate the importance of the location of groundwater monitoring networks near concentrations of building exposures.

Keywords Liquefaction loss • Groundwater depth • Auxiliary variable • Kriging • Natural catastrophe

T. Ancheta (✉)

Model Development Department, Risk Management Solutions, Inc., Newark, CA, USA

e-mail: tim.ancheta@rms.com

S.-J. Lee

Geospatial Development Department, Risk Management Solutions, Inc., Newark, CA, USA

103.1 INTRODUCTION

Required to improve the performance of liquefaction loss models is an accurate spatial representation of the near surface or depth to the first occurrence of groundwater. Monitored groundwater depth, in general, becomes sparse and discontinuous over space, which leads to inaccurate geostatistical estimation. Fortunately, auxiliary digital elevation model output (DEM) correlated with the ground water elevation becomes available over much of the earth's surface. At the same spatial grids another auxiliary distance to water body (DWB) can be obtainable through the use of GIS techniques, namely a Euclidean distance calculation. While there are numerous existing geostatistical methods that model spatially non-homogeneous environmental phenomena by integrating auxiliary information, it is yet emerging to implement such geostatistical estimation in discipline of quantifying liquefaction hazard. The goal of this study is to create a groundwater depth map over a large region using a geostatistical method which takes advantage of the auxiliary databases. We constructed a drift model that benefits from the secondary datasets, processed it through a Kriging method, and compared estimation accuracy with that of a counterpart Kriging method not assimilating the secondary information. The finding of this study facilitates not only to identify exposures susceptible to the risk of liquefaction, but also to improve subsequent liquefaction loss analytics.

103.2 DATA

The ground surface elevation, median groundwater elevation, and distance to a water body were collected for the development of the proposed Kriging system in the Canterbury plain of New Zealand. To derive the necessary variables a digital elevation model, polygons of water bodies, and data from monitoring wells were collected as shown in Figure 103.1. Ground surface elevation is represented in digital elevation models (DEM) of the north and south island available from Landcare New Zealand [1, 2] while other variables were derived as described below. The primary variable, median groundwater elevation was derived from data recorded at 136 long-term (up to 40 years) monitoring wells managed by Environmental Canterbury [3] and the DEM. Median groundwater depths evaluated from time series of depths recorded from the monitoring wells. Distance to a water body is the minimum Euclidean distance to all selected rivers, lakes, or swamps. The river, lakes, and swamp polygons were available from Land Information New Zealand [4–6]. The lake and swamp polygons were filtered as to use only bodies of water with a minimum surface area of 50,000 m². This filter was selected arbitrarily but was intended to remove most of the smaller water bodies.

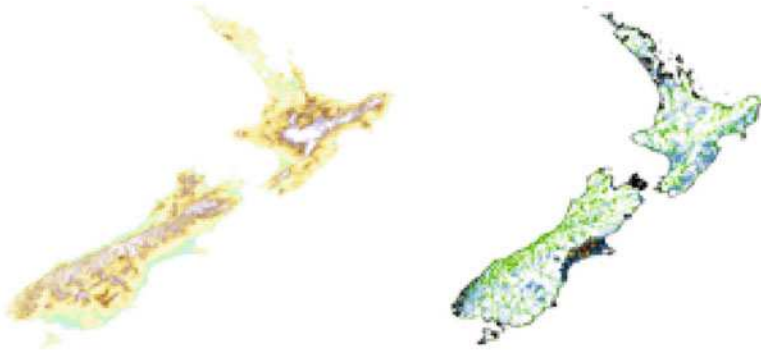


Fig. 103.1 North and south island digital elevation map plots (left). North and south island coast (black), rivers (green), lakes (blue) and swamps (red) (right). The colored circles are the location of the 136 monitoring wells

103.3 METHODS

103.3.1 Drift Models (*Measurement-driven Drift vs. External Drift*)

The first drift model ($m_{YI}(s)$ at spatial point s) relies upon utilizing the measurements of ground water elevation (GWE). It applies an exponential decaying filter to nearby measurements to produce $m_{YI}(s_j)$ at spatial point s_j :

$$M_{YI}(s_j) = \sum_{i=1}^N w_i Y(s_i) / \sum_{i=1}^N w_i, \quad (103.1)$$

where $Y(s_i)$ is GWE measurement at point s_i such that the Euclidean distance between s_i and s_j , $d(s_i, s_j) \leq 100$ km, and the weight w_i is equal to $\exp[-d(s_i, s_j)/a_r]$, where a_r is the spatial range of the exponential smoothing function ($a_r = 150$ km).

To take advantage of the auxiliary datasets available at points other than monitoring stations we select the expected value of a regression model as an external drift model:

$$m_{Y2}(s_j) = X_1(s_j) (\hat{\beta} X_2(s_j) + 1), \quad (103.2)$$

where $\hat{\beta} = [\sum X_I(s_k) X_2(s_k) Y(s_k) - \sum X_I(s_k)^2 X_2(s_k)] / \sum (X_I(s_k) X_2(s_k))^2$ is regression parameter, $X_I(s_k) X_2(s_k)$, and $Y(s_k)$ are ground surface elevation, DWB, and GWE respectively at collocated locations (s_k).

The functional form in equation 103.2 above assumes that GWE is linearly related to ground surface elevation and the distance to a water body (DWB) alters the slope ($\hat{\beta}$). The constant, 1, allows the function to predict GWE along and within water bodies. When along a water body boundary DWB is 0, GWE is equal to

ground surface elevation. Using the median GWE, DWB and ground surface elevation at the collected well locations $\hat{\beta}$ was found to be -0.00004. The parameter, $\hat{\beta}$, is likely region specific and will vary due to differences in the variation of GWE as a function of DWB related different recharge conditions and average aquifer depths at far distances from water bodies. Additionally, equation 103.2 allows for GWE to equal the ground surface elevation at the land/ocean boundary.

103.3.2 Cross-validation Procedure

Cross-validation is method of evaluating the relative performance of different possible Kriging systems or the so called drop-one prediction. The cross validation procedure used to test the performance of the two possible kriging systems as listed below.

1. Prepare two geostatistical Simple Kriging (SK) methods to compare: Method 1 using Eq. (103.1) as its drift and Method 2 using Eq. (103.2) as its drift.
2. Remove one measured GWE at a time, calculate each method's estimates at the location.
3. Iterate step 2 for the remaining 135 monitoring stations
4. Use estimates and removed measurements to calculate Mean Square Error (MSE) as an indication of estimation accuracy

103.4 RESULTS

The results presented are the correlation structure and a cross-validation of both methods in Section 3. Depending upon a type of drift model different residuals can be obtained. Figure 103.2 presents the model correlation structure used in the SK system for both methods. Cross-validation results (MSE in m^2) are summarized as shown in Table 103.1. There are significant improvements from Methods 1 to 2 regardless of distances between data and estimation points, which demonstrate that the external drift model we adopted increased estimation accuracy in a remarkable way (47.5 to 73.8 %). As the distance between data and estimation points increases, the impact of measurements on estimation decreases because 1) estimation errors keep increasing with longer separations and 2) estimates at longer separations are almost same as values of the drift models –estimation contribution from not measurements but mean trend values derived from the secondary datasets (not shown here though)

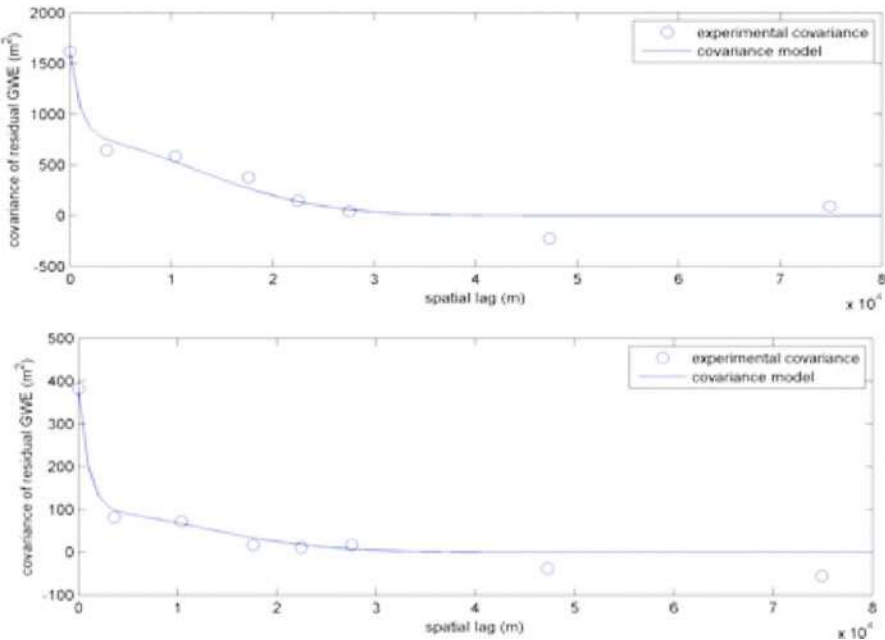


Fig. 103.2 Covariance model used for SK’s estimation. The top plot and the bottom plot are for Method 1 and Method 2 respectively

Table 103.1 Cross-validation results by geostatistical method and separation of data points from an estimation point

Distances b/w data and estimation points (km)	Method 1	Method 2
<5	3.11×10^2	1.17×10^2
5 – 20	4.98×10^2	2.61×10^2
20 – 35	1.45×10^2	3.85×10^2
35 – 50	1.65×10^2	4.32×10^2
50 – 65	1.62×10^2	4.27×10^2
65 – 80	1.62×10^2	4.27×10^2
80 – 95	1.62×10^2	4.27×10^2
>95	1.62×10^2	4.27×10^2

103.5 CONCLUSIONS

Given lack of the measurements of a primary variable, auxiliary information correlated with the primary variable may alternatively increase estimation accuracy. The secondary datasets ground surface elevation and distance to a water body are efficiently processed through a mean trend model within a geostatistical estimation framework. Use of both secondary datasets was shown to increase the prediction accuracy over a simpler model typically used. Improved representation

of groundwater elevation continuously over a large region will be useful to liquefaction sensitivity estimation spatial distribution in the loss analytics caused by the natural hazard under an event of earthquake.

REFERENCES

1. New Zealand National Digital Elevation Model (South Island). Landcare Research. <http://iris.scinfo.org.nz/layer/127-nzdem-south-island-25-metre/>.
2. New Zealand National Digital Elevation Model (North Island). Landcare Research. <http://iris.scinfo.org.nz/layer/131-nzdem-north-island-25-metre/>.
3. Dsfd
4. New Zealand Mainland River Polygons. Land Information New Zealand. <https://data.linz.govt.nz/layer/328-nz-mainland-river-polygons-topo-150k/>.
5. New Zealand Mainland Lake Polygons. Land Information New Zealand. <https://data.linz.govt.nz/layer/293-nz-mainland-lake-polygons-topo-150k/>.
6. New Zealand Mainland Swamp Polygons. Land Information New Zealand. <https://data.linz.govt.nz/layer/293-nz-mainland-swamp-polygons-topo-150k/>.

Chapter 104

Stochastic Quantification of Low-Resolution Geocoding Uncertainty and Its Application to Catastrophe Modeling

Seung-Jae Lee and David Carttar

Abstract Essential to developing a robust risk-management model is to clarify first “where are the exposed properties”. Geocoding is a process that binds property exposure in a built-in environment to spatiotemporal dynamics of natural catastrophes. While addresses geocoded to the finest possible spatial resolution lead to relatively precise estimation of losses from surrounding perils, incomplete/invalid input addresses must fall back to coarser spatial scales (postal code, city, and county etc.), resulting in less precise loss estimation. This work aims at providing the foundation to place the low-resolution geocoding outcomes into gridded locations at a targeted finer resolution. We take advantage of auxiliary information such as land use/cover to infer the likelihood of an exposure placement at the gridded locations. This development is showcased with a postcode in Florida to understand loss changes from low-resolution geocoding uncertainty perspectives.

Keywords Low-resolution • Geocoding uncertainty • Catastrophes • Loss estimation • Location intelligence

104.1 INTRODUCTION

Geocoding is a process that returns the latitude and longitude of a property exposure based on its address elements. A geocoder attempts to match the address elements with its geographic reference database at highest possible resolution. If this matching process succeeds at building-, parcel-, or street-level, its geocoding resolution is the so-called high-resolution geocoding. In contrast the initial attempt fails and its subsequent matching is accomplished at spatial resolutions coarser than street-level, it is called low-res (resolution) geocoding. A typical possible low-res geocoding outcome is a postal-code centroid.

Low-resolution geocoding reflects incomplete information about the location of an individual property, instead representing it as one of hundreds or thousands in a

S.-J. Lee (✉) • D. Carttar

Geospatial Development Department, Risk Management Solutions, Inc., Newark, California, USA

e-mail: sean.lee@rms.com

broader area. As a result, analytical efforts based on low-res geocoding may cause problematic conclusions in numerous disciplines [1, 2]. In property-based catastrophe risk assessment; low-res outcomes embody greater uncertainty than high-resolution geocoding cases. If treated as direct proxies for single locations, low-res results can retrieve incorrect hazard information and, consequently, produce inaccurate damage estimates. All of these become inputs to modeling and anticipating financial loss to a property, and therefore low-res geocoding uncertainty should be recognized as one of the uncertainty layers affecting loss estimates with respect to natural disasters.

This article aims at disaggregating exposures that are geocoded to the postcode level. The main thrust to achieve this goal is to better distribute the monetary value of exposed properties within the associated postcode. Based on prior experience, we interpret auxiliary land use and land cover data to produce distribution weights at gridded locations. In addition we quantify uncertainty in the weights by evaluating the translation procedure from land use/cover categories to the weights.

As a result, each of our targeted 50-m grids contains a downscaling weight and its associated uncertainty, all of which is used for constructing a parameterized distribution. With the distribution, we implement simulation studies to quantify the impact of low-res geocoding uncertainty on loss changes. We demonstrate the capability to disaggregate exposures with the case of Florida under the situation of low-res geocoding uncertainty.

104.2 QUANTIFYING UNCERTAINTY IN DOWNSCALING WEIGHTS

Our results are showcased in the postcode 33139 in Florida. We first created 50-m estimation grids covering the entire postcode, then superimposed auxiliary land use or land cover onto the 50-m grids. Per each grid cell an overlapping surface area with the layers of land cover or land use became a probability set. Based on the probability set we sampled 1000 random realizations of land use or land cover, each of which was translated into weights by line of business. Finally two sets of weights (one for land use and the other for land cover) were multiplied to come up with composite downscaling weights for the cell. The 1000 downscaling weights led to a density-scaled histogram (downscaling weights against their probability density) and then a Weibull distribution fit the histogram (i.e., parameterized distribution as illustrated in Figure 104.1). We selected the Weibull distribution thanks to its versatility to address a wide variety of shapes of the histogram with relative mathematical simplicity.

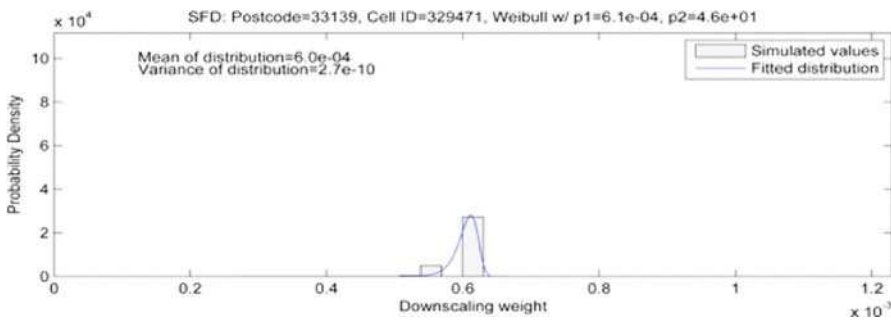


Fig. 104.1 An example of 1000 realizations of SFD (Single Family Housing) downscaling weights for a 50-m cell in 33139, Florida (Among 1000 were 161 cases below 0.5569×10^{-3} , no simulated cases between 0.5569×10^{-3} and 0.6×10^{-3} , and 839 cases above 0.6×10^{-3}) and fitted Weibull distribution with its scale parameter $p1$ and shape parameter $p2$. The Weibull distribution was selected since it is flexible and scalable enough to handle a wide variety of distribution shapes

104.3 SENSITIVITY ANALYSIS AROUND LOW-RES GEOCODING UNCERTAINTY

We used 14,850 exposures for earthquake (EQ) and 15,000 exposures for hurricane (HU) analyses. For illustration purposes only the exposures consist of multiple counts of same exposures in the postcode 33139 and their EQ/HU values (building, content, business interruption monetary values)do not necessarily represent real monetary values. All of these exposures were initially geocoded to street-level or finer (low-res geocoding percent = 0), and we consider 20% and 80% as a fraction of low-res geocoding by replacing a fraction of high-res geocoded locations with simply the postal centroid. Next, for assigning a 50-m cell to an exposure representing low-res geocoding we draw a set of same percentiles of downscaling weights from the Weibull distributions at 50 m-gridded locations, and utilize it as a probability set to randomly select a 50-m cell. It is also possible to choose a different set of percentiles (as in Table 104.1) to have a different probability set for another random sampling. Table 104.1 describes testing cases for evaluating low-res geocoding uncertainty and its impact on modeled loss of a portfolio of exposures.

Tables 104.2 and 104.3 show modeled loss (resulted from using Risk Management Solutions’ catastrophe modeling platform, Risk Link v13.0) due to HU and EQ respectively.

The metric compared in Table 104.2 and Table 104.3 is the average annualized loss (AAL) from all of the stochastic peril events that affect the locations in question. The percent AAL barely changes over percentile extractions (Case 2 to

Table 104.1 Two-parameter (percentage of low-res geocoding in a portfolio and percentile extraction from the Weibull distributions for simulation) setting by which to analyse loss changes. Case 1 is a baseline case where all of the exposures were geocoded to high-res (street-level or finer) whereas Cases 2-4 indicate possible low-res geocoding cases

	Case 1	Case 2	Case 3	Case 4	Case 5
Low-Res Geocoding %	Na	20	20	80	80
% Tile Used for Simulation	Na	10	90	10	90

Table 104.2 HU average annualized loss (AAL) changes from low-res geocoding uncertainty perspectives

	Case 1	Case 2	Case 3	Case 4	Case 5
AAL	130,188,099.61	132,158,867.38	132,207,880.54	138,108,705.04	138,266,033.18
% Change from Case 1		1.51	1.55	6.08	6.2

Table 104.3 EQ AAL changes from low-res geocoding uncertainty perspectives

	Case 1	Case 2	Case 3	Case 4	Case 5
AAL	884,464.04	884,820.57	885,037.10	885,908.80	886,633.64
% Change from Case 1		0.04	0.065	0.16	0.25

3 or Case 4 to 5), but the percent changes increase greatly as the portion of low-res geocoding outcomes increase (Case 2 or 3 to Case 4 or 5). Earthquake loss is much less affected by low-res geocoding uncertainty for this postcode because of the lower degree of location sensitivity (and lower overall hazard) of theEQ peril in South Florida. In contrast, HU loss changes due to low-res geocoding uncertainty are relatively remarkable (~6.2% increase in loss relative to the baseline Case 1). When we draw an aggregate exceedance probability (AEP) curve (the probability exceeding a loss level in a given year) due to HU by return periods, loss increases from Case 1 to Case 5 range between 0.35% and 9.48% (Figure 104.2).

104.4 CONCLUSIONS

This work not only disaggregated exposures, which were initially geocoded to the postcode level, to finer gridded locations, but also investigated the impact of the disaggregation procedure on loss changes. This work provided possible disaggregation options such as using 1) downscaling weights translated directly from land use and land cover and 2) both downscaling weights and their associated uncertainty. The degree of uncertainty in the downscaling weight and its subsequent loss

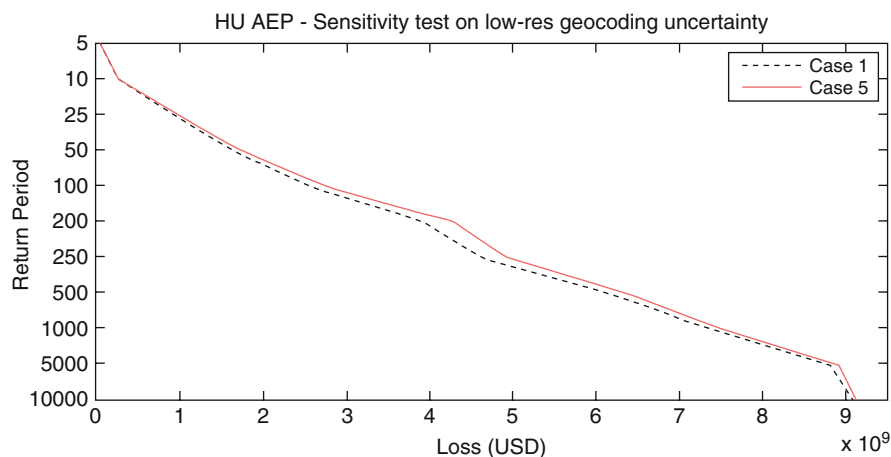


Fig. 104.2 HU sensitivity analysis on low-res geocoding uncertainty; AEP curves by return period (i.e., dotted curve: AEP for HU loss analysis under no low-res geocoding uncertainty and solid curve: AEP for HU loss analysis under a case of low-res geocoding uncertainty - Case 5 in Table 104.2)

changes would vary region by region, and thus the second option the work additionally offered could be also valuable in understanding low-res geocoding uncertainty. Our sensitivity analysis demonstrated that low-res geocoding uncertainty significantly affected loss changes when there are many cases of low-res geocoding outcomes in a portfolio.

REFERENCES

1. Sheehan, T.J., Gershman, S.T., MacDougal, L., Danley, R.A., Mroszczyk, M., Sorensen, A.M. and Kulldorff, M.: Geographic Surveillance of Breast Cancer Screening by Tracts, Towns and Zip codes. *J. Public Health Man.*, 6, 48–57 (2000)
2. Hurley, S.E., Saunders, T.M., Nivas, R., Hertz, A. and Reynolds, P.: Post Office Box Addresses: a Challenge for Geographic Information System-Based Studies. *Epidemiol.*, 14(4), 386–391 (2003)

Chapter 105

An Improvised Effective Oceanography Monitoring Using Large Area Underwater Sensor Networks

Burla Rajesh and K. Aanandha Saravanan

Abstract The deployment of Wireless Sensor Networks at ocean provides on-site, distributed sensing of some specific events. To the existing satellite and airborne radar scrutinizing, providing incessant and real-time data feed. Due to the unforeseen conditions, it is not possible to imagine the location, size or weather circumstances affecting the region. We present a novel framework for a large-scale sensor network deployment at ocean. Our main objective is to develop communication algorithm to localize maritime monitoring using realistic channel and weather models. The design choices are based on the present application situations, through a bottom-up approach. Wireless channel and physical layer are fundamental for dependability of results, thus particular focus is given to their model assortment. The network architecture is based on a cluster model protocol with an application-specific decision. The aim is to provide the best compromise between, message delivery, energy consumption and network connectivity under dynamic change in environments.

Keywords Ocean monitoring • Cluster model • Energy efficient

105.1 INTRODUCTION

The increasing demand in Wireless Sensor Networks (WSN) can be promptly, a tiny sensing material self powered which gather information or detect special events and communicate in a wireless pattern with the end goal of handling the processed data to a base station. Its senses the information, process it and communicate through any medium. These tiny devices are capable of detecting various application fields [1], a wireless sensor network (WSN) consists of battery-operated sensor devices with computing, data processing, and communicating components. The application of WSN to the underwater gives a enormous perspective for monitoring the marine regions. The oceans alone cover 70% of our planet and

B. Rajesh (✉) • K.A. Saravanan
Department of ECE, Vel Tech Dr. RR & Dr.SR Technical University, Chennai, India
e-mail: raaz.burla@gmail.com

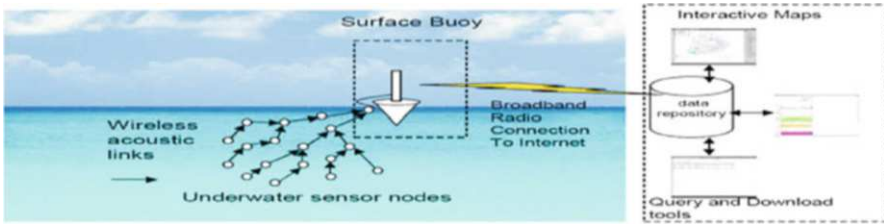


Fig. 105.1 One possible approach to UWSN deployment

along with rivers and lakes[2], monitoring these regions is difficult and expensive for humans: divers are regulated in the hours and depths at which they can work, and require a boat on the surface that is costly to operate and subject to weather conditions[3]. A sensor network installed underwater could monitor water temperature, pressure as well as variables such as conductivity, turbidity and certain pollutants Fig.105.1 shows a possible approach to UWSN deployment. The network could track plume of silt due to search operations or pollutants remaining in land, and it could monitor and model the behavior of underwater ecosystems [4]. Image sensors are used to monitor visible changes inside the water or count, and perhaps even classify species. In this paper, we propose a framework for the development of a WSN to monitor localized maritime events. We derive the basis for a simulation framework, describing and justifying the decisions taken.

105.2 THE NETWORK SIMULATION AND DEVELOPMENT

Simulation is the most professional alternative to develop a network prior to its deployment in remote environments. It allows predictable and minimizing the effects of obstacles and challenges [5], as well as discovering unexpected issues to assess and modify algorithms accordingly. WSN simulators are classified into three categories: custom-built, general purpose and OS-specific. Custom-built simulators are solutions purposely designed for a particular set of algorithms. They are exhaustive in specific areas of interest to the development and simplified in other areas. Their advantages are in the detail essential models to the simulations [6]. However, the over simplification of non-essential areas and the highly customized interface and output makes it difficult to practically compare with other normal solutions. General-purpose simulators are flexible and support different algorithms, protocols and environments. Their objective is to provide standard inbuilt models of existing protocols that can be customized to fit the demands. The most widely adopted simulators are NS-2 [7] and OMNeT++ [8]. NS-2 is built on a free, open-source platform that allows users to develop new modules and share them with the community. Its recognition as a tool for WSN development means that it is possible to achieve complete execution of routing algorithms. The biggest drawbacks arise

due to the simplified energy model, overly complex nodes, limited scalability and the potentially distorted results due to the number of modified modules. OMNeT++ is a component-based, modular simulator built for wired networks and later incremented with wireless extensions. Like NS-2, OMNeT++ is an open-source, general purpose simulator with contributions from the community [9]. We chose to design a custom-built simulator for this work, since it provides a greater flexibility and focus in the development of algorithms and solutions for the particular application circumstances described above.

105.3 SIMULATION

The simulation is based on a modular approach, where every module represents a different component of the network: nodes, sink and communication channel. In addition, a Real- Time Clock (RTC) and packet handler are required to provide the correct simulation environment. Fig. 105.2 provides a simplified architecture of these modules and their interactions.

The sink nodes have extra computational power, memory and energy reserves than standard nodes. This allows them to remain listening continuously for the duration of the deployment [10]. Furthermore, if the network uses a hierarchical algorithm, the additional processing power allows it to manage the network, storing routing tables and schedules. The RTC manager works as a discrete, pseudo-real-time clock, where each new action is stored as a pair $\langle nodeID, time \rangle$, making its operation closer to that of an internal timer. Each node is triggered sequentially, and once the RTC reaches its time. Each node decides its following task and status individually, according to stored triplets $\langle time, node, nextStatus \rangle$, where *time* is the event absolute starting time, *node* is the destination of the next event, and *nextStatus* identifies the type of event, whether reply, transmission, or relay. To simplify the communication process, improve simulation speed and reduce memory footprint [11], all active packets are stored in the Packet handler. The channel handler deals with each individual transmission over the wireless channel. The Physical (PHY) and Medium Access Control (MAC) layers are derived from IEEE 802.15.4 [12] standard and are common to all devices in the network. As such,

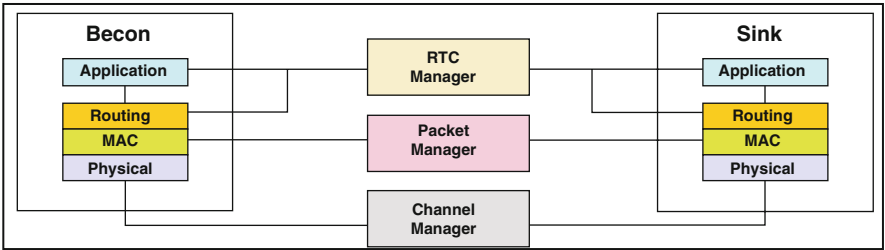


Fig. 105.2 Simulation architecture

interoperability between nodes and sinks is secured. Furthermore, the standard also describes the expected channel Path Loss (PL) equation, adopted in this simulation, with variable PL exponent.

105.3.1 Wireless Channel

The communication model is an essential part of simulation: depending on its detail, it can provide a correct understanding of how the packets are sent across the network. Due to random obstacles and variable path losses, broadcasts are calculated on a per-node basis, c independently with additive effect [13]. Water molecules resonate at approximately 2.4 GHz, therefore a signal is strongly attenuated if a wave blocks the line of sight, to the point that no transmission gets to the receiver with enough strength to be decoded. A simplistic approach is to consider waves as perfect sinusoidal curves. In these conditions, it can be said that the probability of a node receiving a packet is $pRx = h/H$, where h is the antenna height and H is the wave height. If a wave is higher than the antenna, there is the probability of blocking the signal. As there is no direct ratio between wave height and length, it is not possible to estimate if this probability is dependent on distance. PL, noise and interference are dependent on the transceiver used. In the case of an IEEE 802.15.4 [14] compliant transceiver, the standard provides equations to estimate these values.

105.3.2 Medium Access Control

In practice, the decisions taken while setting up the network will be fundamental to assist this statement. Having independent tiers and hierarchies can lead to different routing algorithms in each. A central issue with clustering is the ratio between CHs and sensing nodes [15]. Increasing the number of clusters provides reduces the load management in the lower tier, transferring it to upper tiers. Fewer, larger clusters, on the other hand, reduce the network management and overhead in upper tiers, at the cost of increasing contention and collision inside each cluster. In this work, we will consider the use of amplified transceivers, a theoretical outdoor range of 1000 meters under low PL. Network algorithms provide means of further improving usability and performance through careful design and adaptation to the application requirements.

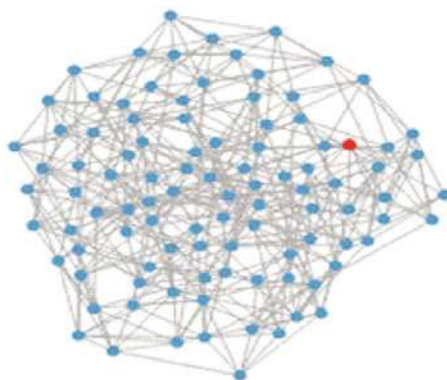
105.3.3 Cluster Formation

The ideal cluster formation would have a uniform CH distribution and transmission range, allowing the creation of a cell-like CH displacement. However, with maritime monitoring, scenario nodes and CHs are expected to be thrown from an aero plane, hence it is unlikely that they will be perfectly located. Cluster overlapping allows a degree of freedom at the best location, at the cost of added collision in overlapping areas. Fig. 105.3 shows an example of a random network deployment. It uses the $3R$ ideal distance between CHs to form a perfect hexagonal cluster, with a maximum deployment error of 150 meters around the ideal location [16]. The deployment consists of 2500 nodes with 1000 metres communication range, randomly deployed in a square area with 7000 x 7000 meters. The number of sensor nodes used in the figure serves only as example for visibility purposes, where a real deployment is expected to have a denser deployment [17]. Nodes in overlapping areas transmit to the closest CH.

105.3.4 Routing

Clustering allows the use of different routing algorithms inside and outside the cluster. Nodes subscribing a CH will be using a routing strategy defined by it. - Single-hop routing is used to test the simulation and weather effects over the communication [18]. It is the simplest routing algorithm where nodes transmit directly to the CH. Considering the CH deployment and coverage, all nodes (with minor gaps expected, as shown in Figure 105.3) are able to transmit to a CH. Single-hop also gives an insight regarding the energy usage across the network. Routing will consist of two messages: one from the CH, advertising itself and the amount of time nodes have to send back a reply with sensed data; and another from the node, transmitting its sensed data to the CH [19]. The routing algorithm receives the CH advertisement message from the MAC layer and, after a random delay, prepares a

Fig. 105.3 Example of a cluster formation and node-CH connectivity



message with updated data. As support for additional routing algorithms, all nodes can receive incoming packets and process them locally. The decision process is done at Routing level and it leads to either dropping the message or search for an adequate receiver. In the case of the CH, if the message has sensed data, it is stored for either inter-cluster or inter-network transmission.

105.4 RESULTS

To test the simulator, experiments were conducted on a cluster level, by randomly displacing 300 nodes around a CH, within 1000 meters circular area. The simulation time is 1 hour, during which the CH broadcasts one advertisement every 40 seconds, requesting nodes to send data back within 30 seconds of receiving the advertisement message. The PL exponent was set between 2 (clear weather) and 5 (harsh weather, comparable to indoors communication), while the wave height changed between 0.2 and 2 meters. Since the communication is single hop, there is no considerable latency between origin and destination. Fig.105.4 shows the variation of packet delivery with variations in PL exponent and H . It is visible how packet delivery is affected by weather changes. Between $PL = 2$ and $PL = 3$ the number of delivered packets decreases between 28% and 36% (for $H = 0.2$ m and $H = 2$ m, respectively). The steeper delivery loss occurs between $PL = 3$ and $PL = 4$, with a decrease of nearly 70%. This greater difference comes from node distribution: while peripheral nodes are divided between adjacent overlapping clusters, intermediate range nodes contact a single CH, making this the area with higher impact on cluster density. Nodes closer to the CH are fewer in number, hence the difference between $PL = 4$ and $PL = 5$ suffers a smaller loss, since the number of nodes is naturally smaller. On the other hand, the difference between wave heights is consistently lower for higher waves, due to the reduced time nodes have with clear line of sight to the CH. Another way to understand the simulation behavior and cluster communication is through average transmission range between nodes and CH. Fig.105.5 shows how the transmission range changes with PL and H . The curve follows a trajectory similar to that of packet delivery. The differences between maximum and minimum range for a given PL were minimal, with approximately 7 % maximum variation between values. This proves that that range is completely independent from wave height. On the other hand, range is severely affected by PL, going below 60 meters for $PL = 5$. Using this knowledge along with effect of path loss in range, we can estimate the routing algorithm effectiveness when affected by different environmental factors. The total estimated delivered packets for a uniformly distributed network is

$$\Sigma Delivered = h/H \times 80^{5.88/PL} \quad (105.1)$$

Fig. 105.4 Total packets delivered with different wave heights

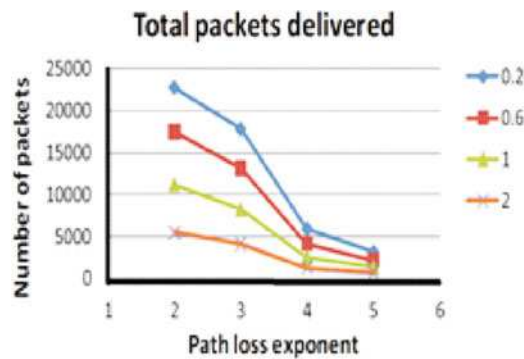


Fig. 105.5 Average transmission range for the delivered packets

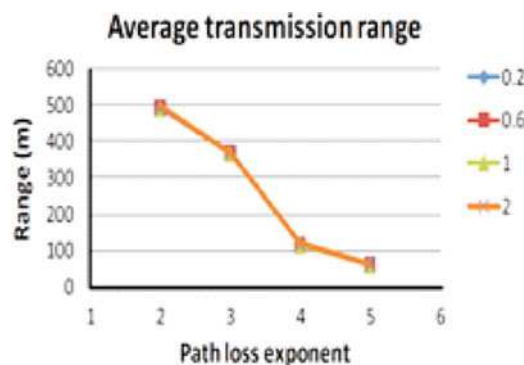


Fig. 105.6 Ratio between maximum estimated and delivered packets



Considering (105.1), we can estimate the packet delivery loss due to collision or back-off, as shown in Fig 105.6. With lower H , the packet delivery rate is 85% of the theoretical maximum, mainly due to contention and collisions. The drop with $PL=3$, with a minimum of 65.7% when $H=0.2$ shows that for the particular distribution, the network was not uniformly distributed, and the number of peripheral nodes was greater than what would be theoretically expected.

105.5 CONCLUSIONS

We conclude, simulation of WSNs is a quick and effectual mean of testing and optimizing network. This work shows the simulation development with focus on the communication process and the modular approach provides the basis for the development of routing algorithms and communication models, while the use of independent noise and interference sources lead to a more realistic outcome. Water and waves is another relevant issue for node communication. When a wave obstructs the line of sight, then the signal is considered too weak to be decoded. Cluster algorithms provide a reliable, distributed infrastructure for network management and are energy efficient.

REFERENCES

1. Culler, D., Estrin, D. and Srivastava, M.: Guest Editors' Introduction: Overview of Sensor Networks. *Computer*, 37, 41–49 (2004)
2. Akyildiz, I.F., Su, W., Sankarasubramaniam, Y. and Cayirci, E.: Wireless sensor networks: a survey. *Computer Networks*, 38, 393–422 (2002)
3. Baker, C.R. et al.: Wireless sensor networks for home health care. 21st International Conference on Advanced Networking and Applications Workshops/Symposia. Vol 2, Proceedings, pp. 832–837 (2007)
4. Estrin, D., Govindan, R., Heidemann, J. and Kumar, S.: Next century challenges: scalable coordination in sensor networks. Presented at the 5th annual ACM/IEEE international conference on Mobile computing and networking, Seattle, United States (1999)
5. Pottie, G.J. and Kaiser, W.J.: Wireless integrated network sensors. *Communications of the Acm*, 43, 51–58 (2000)
6. Raman, B. and Chebrolu, K.: Sensor networks: a critique of “sensor networks” from a systems perspective. *SIGCOMM Comput. Commun. Rev.*, 38, 75–78 (2008)
7. The Network Simulator NS-2. Available: <http://www.isi.edu/nsnam/ns/>
8. OMNeT++ Community Site. Available: <http://www.omnetpp.org/>
9. Robbe, N. and Hengstermann, T.: Latest trends in airborne pollution surveillance. *Sea Technology*, 4 (2007)
10. Cobham Tracking & Locating Ltd. (2008), RF-700C2 – Combo Oil Spill Tracker. Available: <http://www.seimac.com/>
11. I. EnviroWatch Global Enviro Network. (2002), Genesis Alert System Available: <http://www.genalert.com/>
12. Maciejewska, I.: Real Time Oil Spill Detection and Tracking Based on Air-Borne and Satellite Remote Sensing Technologies (2007)
13. Murray, S.P.: Turbulent Diffusion of Oil in Ocean. *Limnology and Oceanography*, 17, 651–660 (1972)
14. Britton, M. and Sacks, L.: The SECOAS Project: Development of a Self-Organising, Wireless Sensor Network for Environmental Monitoring. Presented at the Second International Workshop on Sensor and Actor Network Protocols and Applications (SANPA 2004) (2004)
15. Nittel, S. et al.: A drift-tolerant model for data management in ocean sensor networks. Presented at the 6th ACM international workshop on Data engineering for wireless and mobile access. Beijing, China (2007)
16. Luo, J., Wang, D. and Zhang, Q.: Double mobility: coverage of the sea surface with mobile sensor networks. *SIGMOBILE Mob. Comput. Commun. Rev.*, 13, 52–55 (2009)

17. I.W.-L.T. Group: Standard for part 15.4: Wireless MAC and PHY specifications for low rate WPAN. ed: IEEE Computer Society (2006)
18. Chen, C., Ma, J. and Yu, K.: Designing Energy-Efficient Wireless Sensor Networks with Mobile Sinks. World-Sensor-Web at SenSys (2006)
19. Vljajic, N. and Xia, D.: Wireless sensor networks: To cluster or not to cluster. *In: World of Wireless, Mobile and Multimedia Networks* (2006)

Part V
Remote Sensing and Geoinformatics

Chapter 106

The Extraction of Oil and Gas Information by Using SAS Imagery in the Jimusaer Field, Xinjiang-Clay Alteration Minerals

Peng Tao and Wang Maozhi

Abstract Using SASI aerial hyperspectral image data combining with the field measured spectral information and spectroscopic data in the USGS standard mineral spectral library, this paper studied the information extracting method for the clay alteration minerals which is related to the oil gas in the Jimusaer Area, Xinjiang Province, P.R. China. To begin with, based on the data calibration and spectral reconstruction of the SASI hyper-spectral images, the image dimension judgement and noise separation were made by minimum noise fraction (MNF). And then with the pixel purity index (PPI), the automatic matching recognition and information extraction of the images was performed, straight after which, two common clay alteration minerals—Kaolinite and Illite. At last, the mineral alteration mapping for the two clay alteration minerals was carried out by mixing tuning matched filtering (MTMF) technology. This exploring and method proposed in this paper point out an effective approach for oil and gas exploration by hyperspectral remote sensing technology.

Keywords SASI • Oil and gas • Hyperspectral remote sensing • Clay alteration minerals • Information extraction

106.1 INTRODUCTION

In the process of micro leakage, hydrocarbons and their concomitants shall interact to the rock mineral and soil on the surface to acidify the surface environment, leading to clay mineralization, carbonate lithification, pyritization and plant lesion. These surface alteration and variation phenomena are closely associated with underground oil and gas reserves and their bearings, among which the kaoline enrichment caused by change and loss of clay minerals is a potential sign for the existence of hydrocarbon, where the hydrosulfate and hydrocarbons contained in

P. Tao (✉) • W. Maozhi

Chengdu University of Technology, Geomathematics Key Laboratory of Sichuan Province,
Chengdu, China

e-mail: pengtao890114@sina.com

the materials under micro leaking shall change the oxidation-reduction environment at upper overlaying rocks, thus leading to the acidification, and these acid solutions can make the feldspar minerals replaced by the clay minerals to change the distribution and structure of clay mineral, and finally make the content of surface clay minerals increased significantly above the oil and gas [1, 2]. The early information on the detection of oil and gas micro leakage is dominated by the multispectral remote sensing such as LANDSAT TM and LANDSAT MSS, and the useful information is highlighted according to its best working band and by the calculation of ratio, conversion of chromaticity, separation of minimum noise, analysis of principal component and others, thus mapping and making a prospective evaluation for micro leakage area of oil and gas. The useful subtle information of the ground object spectral may not be presented well in the images due to the limited multispectral bands, the relatively wide range of spectral wavelength and the weak continuity, thus limiting the application of multispectral image in the information extraction of oil and gas. The hyperspectral imaging spectrometer provides dozens or even hundreds of narrow bands, which may produce a spectral curve superior than that of multispectral in both integrity and continuity [3, 4]. More surface materials of diagnostic spectral characteristics could be recognized by its ultrahigh spectral resolution, and rich information resources on space image would be available, thus providing more favorable conditions for identification of oil and gas alteration minerals.

Taking Jimusaer Sag Region in Xinjiang as the study area, this paper utilizes SASI aerial hyperspectral image data in combination with the ground object spectral information actually measured in field and spectrum in USGS standard mineral spectral base, to extract and recognize the clay alteration minerals on the basis of spectral reconstruction. Some interference anomalies are eliminated eventually through image processing to narrow the scope of field artificial validation and improve the accuracy for the information extraction of alteration minerals within the study area, thus providing a favorable and directional guidance for oil and gas exploration [5].

106.2 PRETREATMENT OF SASI DATA

106.2.1 The Basic Characteristics of the SASI Data

SASI spectral resolution of hyperspectral remote sensing image is 7.5 nm. The spatial resolution is 3.6 m, with 101 bands, The specific parameters are shown in Table 106.1. In this paper, using SASI imaging spectrometer in Jimusaer Sag Region in Xinjiang of airborne hyperspectral remote sensing bands data on October 1, 2013.

Table 106.1 Specifications of airborne imaging meter of SASI

Parameter	Spectral range	Each row pixel number	Continuous spectrum channel number	The spectral bandwidth	Frame frequency/ s^{-1}	Total field of view Angle / ($^{\circ}$)	The instantaneous field of view Angle / ($^{\circ}$)	SNR	Absolute accuracy of radiation /%
SASI-600	950-2450 nm	640	100	15 nm	100	40	0.07	>1000	$\pm 5-10$

106.2.2 Image Preprocessing

Using the experience software linear regression model of the ENVI, combining with the field measured punctuation feature of spectral information, calculate the image digital quantitative values with the experience of the linear relationship between reflectance, for SASI image reflectance image conversion and spectral reconstruction. In order to further evaluate the efficacy of the spectral reconstruction, using the method of PPI for reconstruction after image processing, on the basis of the result extracted reconstruction images could be pixel of vegetation spectral curve, comparing with USGS standard spectral library vegetation spectrum. As can be seen from the figure 106.1 on reconstruction of vegetation as pixel spectral curve and the USGS vegetation spectral curve of standard spectral library has achieved high alignment, spectral reconstruction have been achieved good results.

106.3 INFORMATION EXTRACTION OF CLAY ALTERATION MINERALS

Spectral matching technique based on the overall waveform is the most widely used in currently of imaging spectral data for mineral alteration information extraction, Such as hybrid modulation matched filtering technique, Spectral Angle (SAM) technique and Spectral Mixture Analysis etc. In this paper we use Mixture Tuned Matched Filtering technique, SASI Jimusaer Sag Region in Xinjiang in the airborne hyperspectral image data related to the oil and gas of clay alteration minerals.

The main process is as follows:

- (1) THE PIXEL EXTRACT: Using Spectral Hourglass Wizard of the ENVI software, After adjustment for SASI data first use Minimum Noise Fraction change, judge image dimension, to separate the noise in the data; Second to use Pixel Purity Index, to carry out the extraction processing and components in 2000-2400 nm, and then look for in the image spectrum the most “pure” pixel.
- (2) SPECTRAL ANALYSIS: The pixel is utilized to extract the spectral curve with the USGS standard spectrum in the library known pixel spectrum curve within the range of 2000-2400 nm range with respect to its absorption peak position and overall waveforms were analyzed. In Fig. 106.2, according to SASI data extraction of feature spectrum curve at 2160 nm and 2210 nm and USGS spectral library kaolin spectrum curve of 2165 nm and 2210 nm of characteristic absorption peak and strongest peaks show good consistency, And the overall waveform also fits in. In Fig. 106.3, according to SASI data extraction of feature spectrum curve at 2200 nm and 2350 nm and USGS spectral spectrum curve of illite in the library at 2220 nm and 2345 nm absorption peak position and the overall waveform also show a strong consistency. And

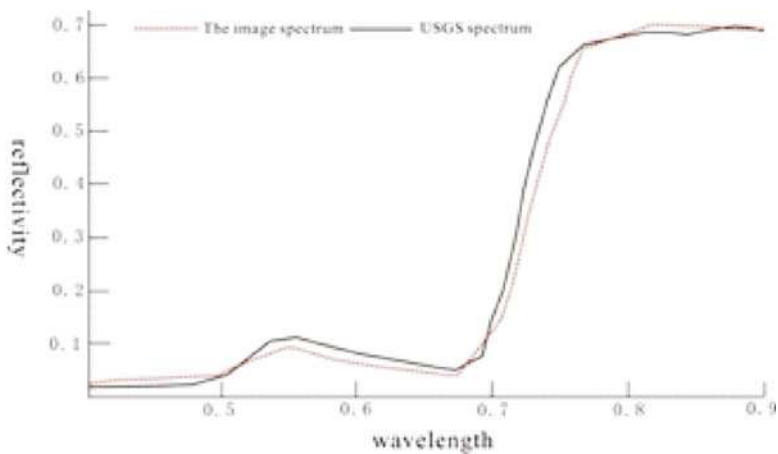


Fig. 106.1 The image spectral contrast with USGS spectrum

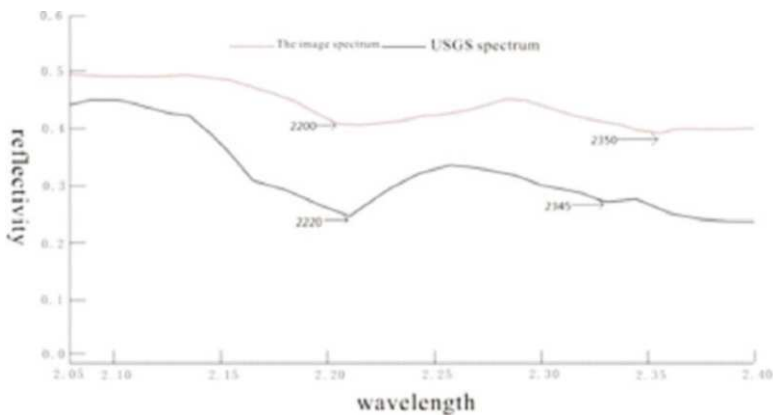


Fig. 106.2 Kaolin in USGS spectrum contrast with image spectra

- then the study area were determined with kaolinite and illite both clay alteration minerals.
- (3) Using Mixture Tuned Matched Filtering technique mapping clay alteration mineral, the result is shown in Fig. 106.4.

Among them, the yellow part is kaolinite, blue part is illite. Combined with the research area of geological data, Will be part of the mapping results and the geological background and stack on the geological background of known oil and gas information to verify the mapping results, the corresponding mapping results showed that the area has a large area of clay alteration minerals, and then confirms the area with hydrocarbon and its along the leakage, in accordance with the geological background. In conclusion, through minerals information extraction method (MTMF) has achieved ideal result.

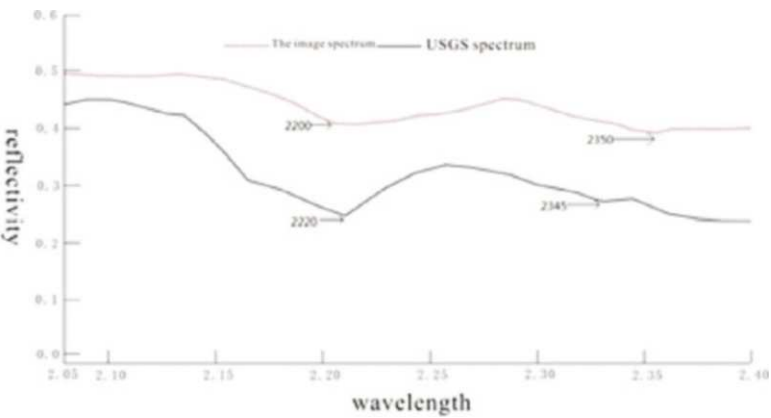


Fig. 106.3 Illite in USGS spectrum contrast with image spectra

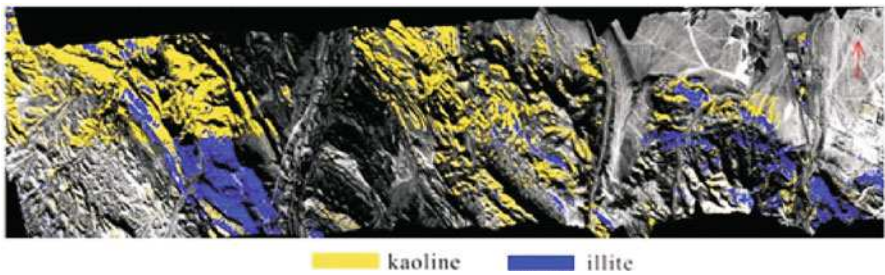


Fig. 106.4 Local clay alteration minerals in the study area of the mapping results

106.4 CONCLUSIONS

We can see that based on hyperspectral imaging, due to the alteration or mutation of hydrocarbon micro-seepage under different geological environment as a result of the analysis, making the use of spectral characteristics alteration of information, determining the most favorable oil and gas information interval band to identify, and ultimately making the use of technology to MTMF alteration mineral mapping is an effective technical means and worthy of further study. However, due to the limited conditions of remote sensing alteration information extraction with the ground cannot be completely consistent with the actual situation, the study area is dotted with a large area of clay alteration minerals exception, for these anomalies pend to be further studied, to facilitate a more precise delineation of the predicted target and better service for the oil and gas exploration.

REFERENCES

1. Saunders, D.F., Burson, K.R. and Thompson, C.K.: Model for Hydrocarbon Microseepage and Related Near-surface Alterations. *AAPG BULL.*, 83(1), 170–185 (1999)
2. Hou, W.G.: Research of geochemical and remote-sensing techniques to the exploration of oil and gas in northern Tarim Basin. *Computing Techniques For Geophysical and Geochemical Exploration*, 24(1), 6–11 (2002)
3. Zhang, J., Liu, L.J., Huang, Y. et al.: Jimusaer sag in Junggar basin of Permian series on the characteristics of sedimentary facies. *Xinjiang Geology*, 21(4), 412–414 (2003)
4. Wang, X.C., Tian, Q.J. and Guan, Z.: The extraction of oil and gas information by using hyperion imagery in the Sebei gas field. *Remote Sensing for Land Resources*, 1, 36–40 (2007)
5. Ye, F.W., Liu, D.C. and Zhao, Y.J.: Airborne hyper spectral survey system CASI/SASI and its preliminary application in uranium exploration. *World Nuclear Geoscience*, 28(4), 232–236 (2011)

Chapter 107

Characterization of Sampling Error in Instantaneous Orbital Data Products of TRMM over Indian Subcontinent

J. Indu and D. Nagesh Kumar

Abstract Rainfall estimates from low earth orbiting satellites like Tropical Rainfall Measuring Mission (TRMM) will be subjected to sampling errors of non negligible proportions owing to the satellite swath coupled with a lack of continuous coverage due to infrequent satellite visits. In the present work, the authors investigate relative sampling errors of space-time averaged rainfall in the active and passive sensors of TRMM namely, Precipitation Radar (PR) and TRMM Microwave Imager (TMI) using the data products of PR 2A25, TMI 2A12 and PR 2B31. A statistical bootstrap technique was found to provide good estimates of relative sampling errors for PR 2A25 data products [Indu and Kumar, 2014]. This study investigates the effect of different sampling techniques in estimating relative sampling errors using the monsoonal rainfall of 6 years [2002–2007] over the basin of Mahanadi, India. Results verify that the spatial distributions of relative sampling errors were affected by sampling technique employed. These findings clearly document that proper characterization of error structure from TMI and PR has wider implications for decision making prior to incorporating the resulting orbital products for basin scale hydrologic modeling.

Keywords TRMM • Bootstrap • Sampling • Basin • Uncertainty

107.1 INTRODUCTION

Rainfall products derived from microwave remote sensing is known to suffer from various sources of uncertainties, a major portion of which can be attributed to sampling uncertainty. Infrequent satellite visits cause difficulty in measuring the spatio-temporal variability of rainfall. In order to provide quantitative confidence on the rainfall estimates from satellites, estimates of sampling errors are crucial. Sampling errors not only depend on the type of satellites (e.g., geostationary or low earth orbiting) but also on precipitation type, season etc. The Tropical Rainfall

J. Indu (✉) • D.N. Kumar
Indian Institute of Science, Bangalore, India
e-mail: indusj@civil.iisc.ernet.in

Measuring Mission (TRMM) is a low earth orbiting satellite which carries an active sensor namely precipitation radar (PR) and a passive sensor called TRMM Microwave Imager (TMI). To date, studies related to TRMM sampling uncertainty have focused on comparing rainfall rates from a surface based dense network of rain gauges with that from TRMM. This technique suffers from a disadvantage over regions lacking in in-situ validation data. To circumvent this issue, attempts have been made to estimate sampling errors on a global scale using available satellite rainfall data products themselves. Recently, *Iida et al.* [1] have developed a technique using bootstrap approach to evaluate relative sampling errors of PR observed tri-monthly rainfall. This technique has successfully evaluated relative sampling errors globally for $5^\circ \times 5^\circ$ grid sizes without relying on rainfall from a dense network of ground instruments. *Indu and Kumar* [2] have investigated the potential of this approach in estimating sampling uncertainty for Mahanadi basin in India. The present study analyses 6 year data of TRMM seasonal rainfall from June 2002 to September 2006. Three data products are being examined namely the TMI derived 2A12 data, PR derived 2A25 data and TMI-PR combined data of 2B31. Post 2001 data products are considered for the analysis owing to the TRMM orbital boost from 350 km to 402.5 km in August 2001 which altered the data quality significantly.

107.2 METHODOLOGY

In the present study, the individual overlapping coincident snapshots of rain events in various orbital passes are examined during 6 years of daily seasonal rainfall over Mahanadi basin for a grid size of $1^\circ \times 1^\circ$. If $i = 1, 2, 3, \dots, n$ denote the number of times the satellite visits an area ($1^\circ \times 1^\circ$ grid), $R(1), R(2), R(3), \dots, R(n)$ be the corresponding area averaged rain rates in mm/hr from all footprints that are in the box and $N(1), N(2), N(3), \dots, N(n)$ be the number of PR footprints associated with each visit. Then, the average seasonal rainfall (mm) observed within each grid

$$\text{(of area } A) \text{ can be expressed as: } R_S = \frac{\sum_{i=1}^n N(i) \times R(i)}{\sum_{i=1}^n N(i)} \times 24 \times 122$$

The value of relative sampling error σ can be calculated using, say 1000 bootstrap samples of R_S . In the bootstrap technique by *Iida et al.* [2010], standard deviation is regarded as a measure of sampling error and the value of relative standard deviation is considered as a measure of relative sampling error.

107.3 RESULTS

The relative sampling errors (%) were estimated for 1° grid boxes over Mahanadi basin using bootstrap technique for seasonal rainfall during the data period of 6 years [2002 to 2006]. Comparative evaluation of results (Fig. 107.1) show that

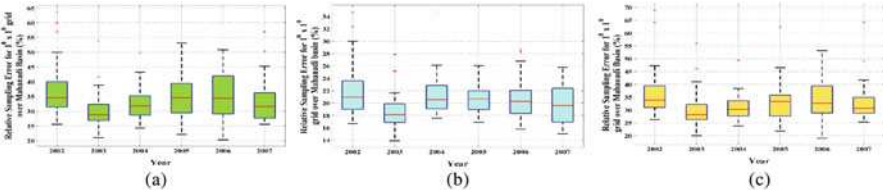


Fig. 107.1 Time series for Mahanadi basin for $1^{\circ} \times 1^{\circ}$ grid size for the 11-year data period showing relative sampling errors (%) for (a) 2A25, (b) 2A12 and (c) 2B31

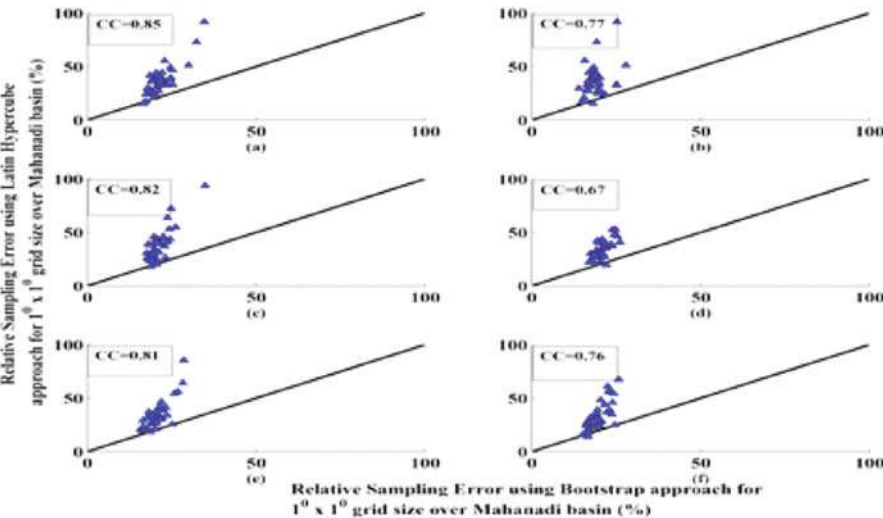


Fig. 107.2 Scatter plots showing relative sampling errors estimated using bootstrap approach versus those estimated using LHS technique for 2A12 product during the years of (a) 2002, (b) 2003, (c) 2004, (d) 2005, (e) 2006 and (f) 2007 [In the above figure, CC denotes correlation coefficient and the continuous line (—) denotes one-to-one line]

the sampling uncertainty from the TMI derived 2A12 data product is less compared to 2A25 and 2B31 data products. This can be attributed to a difference in sampling swath between the instruments of TMI and PR. The TMI data swath of 780 km enables a superior overview of the synoptic rainfall events than PR (having data swath of only 215 km). The wider TMI swath enables greater number of observations to be available for each spatial domain (grid box). This implies that despite the limitation of TMI radiometer retrieved rainfall from 2A12 product, their land rainfall will possess comparatively low bias due to sampling uncertainty when compared to the 2A25 and 2B31 products. In order to study the effect of sampling type on relative sampling errors, the approach was conducted using Latin hypercube sampling. Results for 2A25 data product are shown in Fig. 107.2. It can be observed that relative sampling errors estimated using LHS technique were similar to those from bootstrap technique. LHS technique tends to slightly overestimate the relative sampling errors. This slight overestimation pertaining to orbital data

products needs to be further studied before any clear conclusion can be drawn of its significance.

107.4 CONCLUSIONS

The present study examined the relative sampling errors over the catchment of Mahanadi basin, India for three TRMM orbital data products based on radar (PR), radiometer (TMI) and combined product of both (PR-TMI). Results indicate that the radiometer derived rainfall estimates from 2A12 incurred the least range of sampling uncertainty when compared to 2A25 and 2B31 rainfall estimates. Also, retrieval of sampling uncertainty using latin hypercube sampling was shown to have implications for wide scale assessment of satellite rainfall retrievals for hydrological applications. The present methodology can also be implemented for future missions of Global Precipitation Measurement.

REFERENCES

1. Iida, Y., Kubota, T., Iguchi, T. and Oki, R.: Evaluating sampling error in TRMM/PR rainfall products by the bootstrap method: Estimation of the sampling error and its application to a trend analysis. *Journal of Geophysical Research*, 115, D22119, doi:[10.1029/2010JD014257](https://doi.org/10.1029/2010JD014257) (2010)
2. Indu, J. and Nagesh Kumar, D.: Evaluation of TRMM PR Sampling Error over a Sub Tropical Basin using Bootstrap Technique. *IEEE Transactions on Geoscience and Remote Sensing*, [10.1109/TGRS.2014.2304466](https://doi.org/10.1109/TGRS.2014.2304466) (in print) (2014)

Chapter 108

Estimation of Regional Groundwater System in a Granitic Body by 3D Permeable Zone Modeling and Flow Simulation

T. Kubo, N. Matsuda, K. Kashiwaya, C. Liu, and K. Koike

Abstract Because clarifying a regional groundwater system is required for development and management of groundwater resources, it is important to evaluate the hydraulic property of a fracture system and alteration zones which act as the pass of groundwater flow in a rock body. For a case study of such hydraulic characterization, we selected an area in which the basement rock is composed of Cretaceous granite. We first constructed a 3D fracture model by a geostatistical method to simulate the regional fracture distribution by incorporating the orientation of the sampled fracture data obtained from the borehole investigations, and this model revealed the features of this fracture system in that area. We then incorporated a dataset of hydraulic conductivity obtained from single borehole hydraulic tests and rock-core tests using a N₂ gas permeameter and found a positive correlation with the size of simulated fractures. Finally, a numerical simulation using MODFLOW was applied to this hydraulic conductivity model for estimating the regional groundwater flow system. Anisotropic behavior of flows near the fault was revealed by this simulation.

Keywords Fracture system • Altered zone • Groundwater system • Permeability • Groundwater flow simulation

108.1 INTRODUCTION

Concern for the stable utilization of groundwater resources has been arose recently on a global scale. To perform the appropriate management of groundwater re-sources, clarifying a regional groundwater system including recharge and discharge area is required. For this purpose, numerical simulation of groundwater flow

T. Kubo (✉) • N. Matsuda • K. Kashiwaya • K. Koike
Graduate School of Engineering, Kyoto University, Kyoto 615-8540, Japan
e-mail: kubo.taiki.32n@st.kyoto-u.ac.jp

C. Liu
School of Urban Management, Resources and Environment, Yunnan University of Finance and Economics, Kunming 650221, China

is adopted in general. These simulations essentially need estimation of the hydraulic structure of the aquifer and the periphery. When the fractured rock body, such as granite, is selected as the target area, it is important to integrate the result of hydraulic test through rock body and the 3D fracture modeling, for the accurate estimation of hydraulic parameter, because a fracture acts as the pass of groundwater flow. Here we apply GEOFRAC (the GEOstatistical FRACTure simulation method), a geostatistical method using observed fracture dataset: location and orientation (strike and dip). Moreover, to characterize the hydraulic properties of rock body, the results of hydraulic test using borehole investigations and permeable test using rock-core sample were integrated with the fracture model. We defined the hydraulic property of each fracture and calculated the hydraulic conductivity. Finally, we constructed the spatial hydraulic conductivity model using the sequential Gaussian simulation (SGS) and performed the groundwater flow simulation to clarify the groundwater flow system and its connection with the fracture system.

108.2 STUDY AREA AND DATA SET

We selected the Tono area of Gifu Prefecture in central Japan as the study area of this research. In this area, interdisciplinary scientific researches for deep geological environments by the Japan Atomic Energy Agency (JAEA) have been carried out [1]. Therefore, a substantial accumulated geological data is available to use for our research. The main target covers an area 12 km (E–W) by 8 km (N–S), and extends to a depth of 1.5 km, the Mizunami underground research laboratory of JAEA (MIU-site) is located near the center. This area contains 26 borehole investigations ranging from 500 to 1000 m in depth. The basement rock of this area consists of the late Cretaceous granite called Toki-granite.

A total of 50,900 fracture picks were obtained at the 19 out of the 26 sites by the analysis of borehole video images. This fracture dataset, position, dip and angle, are available to construct the 3D fracture simulation model. In addition, 394 hydraulic conductivity (H_c) data were obtained by sequential packer hydraulic tests on sections in the boreholes at 25 sites [2].

108.3 FRACTURE MODELING

GEOFRAC is a stochastically simulation composed of plural geostatistics methods for spatial fracture modeling.

The greatest advantage of GEOFRAC is that it can incorporate the orientations (strikes and dips) of a sampled fracture data into a simulation. In GEOFRAC, fracture planes are depicted as an interconnected set of fracture facets that have a disk shape with a defined orientation and a uniform size. GEOFRAC consists of three main steps: (1) positioning of facet centers, (2) assignment of orientations, and (3) connection of facets to form fracture planes [3].

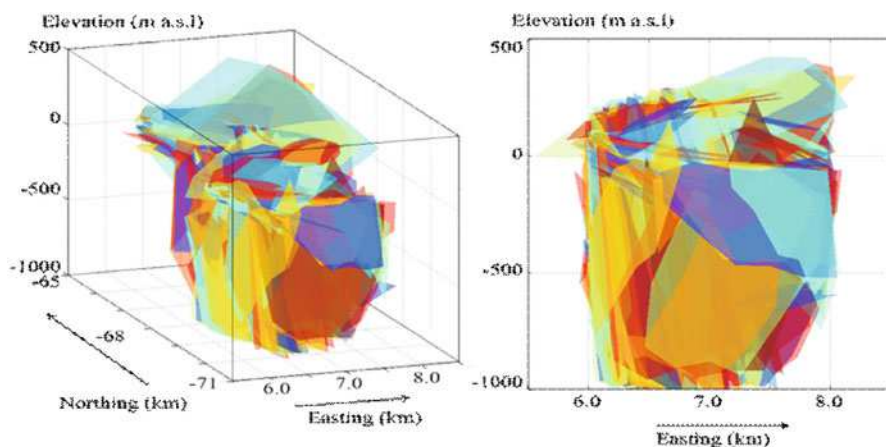


Fig. 108.1 3D Fracture distribution model showing the simulated fracture plane by GEOFRAC. Each fracture is colored randomly to be distinguished respectively. Left and right figures are the perspective views from south-west and north, respectively

Figure 108.1 shows the simulated fracture planes around the MIU-site. The accuracy of the simulation is verified by comparing the simulated fractures with the planar observation of the shaft wall which was drilled within the MIU-site. In the fracture model of the whole study area, the fracture distribution was characterized as that low-angle fractures mainly exist in the shallow part of the study area, while high-angle fractures are concentrated around the fault with corresponding strike.

108.4 CHARACTERIZING THE HYDRAULIC PROPERTY AND SPATIAL MODELING

To characterize the hydraulic property of rock body, we considered two hydraulic test data. One is permeable test using the rock-core sample: permeabilities of 35 samples obtained from every 25 m interval in one borehole were measured by N_2 gas permeameter. As the result, permeabilities of the altered and fault zone were larger than the intact rock cores. Therefore, such weak zone can form high-permeability zones within rock mass and has a significant role for the hydraulic structure. Next, we compared the hydraulic test data obtained from the borehole investigation with the area of fracture plane calculated by GEOFRAC model, and found positive correlation between the hydraulic conductivity (H_c) and the fracture area. H_c values of each fracture were calculated based on this co-relation and spatial distribution of whole area was modeled by SGS using the estimated H_c distribution.

108.5 GROUNDWATER FLOW SIMULATION

Finally, groundwater flow simulation by MODFLOW (finite-difference groundwater model) was implemented using the *Hc* model constructed. One remarkable feature revealed by the simulation is anisotropic behavior of the flows near the large scale fault located in the middle study area trending generally ENE–WSW. The fault acts as the flow barrier to the groundwater flow along the orthogonal direction against fault strike.

108.6 CONCLUSION

In this research, we characterized the hydraulic property of granite body to clarify the regional groundwater flow system by integrating the 3D fracture model and hydraulic test data. The fracture model revealed the feature of spatial fracture distribution in study area and positive relationship between the fracture area and the hydraulic conductivity. Using this co-relation, a hydraulic conductivity model was constructed, which was combined with a groundwater flow simulation. The simulation clarified a fault function as the barrier to the groundwater flow.

ACKNOWLEDGEMENTS The authors wish to express their gratitude to Dr. Tadahiko Tsuruta of JAEA and Dr. Shinji Takeuchi of Nihon University for devoted cooperation. This work was supported by JSPS KAKENHI Grant Numbers 20360408 and 23360402 and NSFC Project 40902058.

REFERENCES

1. Tsuruta, T., Tagami, M., Amano, K., Matsuoka, T., Kurihara, A., Yamada, Y. and Koike, K.: Geological investigations for geological model of deep underground geoenvironment at the Mizunami underground research laboratory (MIU). *Jour. Geol. Soc. Japan*, 119, 59–74 (2013)
2. Takeuchi, S., Kunimaru, T., Ota, K. and Frieg, B.: Development of the quality management system for borehole investigations: Part I—Quality assurance and quality control methodology for hydraulic packer testing. *Proceedings of the ASME 13th Int. Conf. Environmental Remediation and Radioactive Waste Management*, pp. 251–260 (2010)
3. Koike, K., Liu, C. and Sanga, T.: Incorporation of fracture directions into 3D geostatistical methods for a rock fracture system. *Environmental Earth Sciences*, 66, 1403–1414 (2012)

Chapter 109

Hyperspectral Image Classification Using a New Dictionary Learning Approach with Structured Sparse Representation

Zhen-tao Qin, Wu-nian Yang, Xiao-pin Wu, and Ru Yang

Abstract This paper introduces a new dictionary learning approach for hyperspectral images classification with structured sparse representation based on Compressed Sensing (CS). An important contribution of our paper is partition the pixels of a hyperspectral image into a number of spatial neighborhoods called pixel groups and the pixel group can be modeled of different size. The idea is to use of hyperspectral remote sensing image spatial correlation between pixels and the aim is to obtain a dictionary of each pixel. The dictionary is a linear combination of a few dictionary elements learned from the hyperspectral data and can accurately represent hyperspectral remote sensing images with less coefficients. The pixels are induced a common sparsity pattern and have a implicitly spectral correlation between pixels which are in a identical pixel group. The sparse coefficients are then used for classification hyperspectral images by a linear Support Vector Machine. The experiments show that the proposed method can get a better representation of hyperspectral images and has a higher overall accuracy and Kappa coefficients.

Keywords Hyperspectral imagery • Structured sparse representation • Representation features • Linear support vector machines • Classification

Z.-t. Qin

Key Laboratory of Geo-special Information Technology, Ministry of Land and Resources/
Institute of Remote Sensing & GIS, Chengdu University of Technology, Chengdu 610059,
China

Panzhihua College, Panzhihua, Sichuan, China

W.-n. Yang (✉) • X.-p. Wu

Key Laboratory of Geo-special Information Technology, Ministry of Land and Resources/
Institute of Remote Sensing & GIS, Chengdu University of Technology, Chengdu 610059,
China

e-mail: ywn@cdut.edu.cn

R. Yang

Panzhihua College, Panzhihua, Sichuan, China

109.1 INTRODUCTION

In recent years, with the development of electronic spectrum theory, electronic technology and computer technology, hyperspectral remote sensing (HRS) is developed at full speed. Hyperspectral Imagery (HSI) captures detailed terrestrial information with high resolution in both the spatial and spectral dimensions. Analysis of HSI data can find very abundant spectral information and features in detail.

In this paper, we incorporate both the spectral and contextual characteristics of a hyperspectral sample by clustering remote sensing images to obtain a dictionary of pixels and present a structured dictionary-based method for HSI sparse representation using a linear SVM as a classifier, completed the classification of hyperspectral remote sensing images.

109.2 DICTIONARY-BASED MODEL OF HSI

In recent years, Song et al. used sparse representation method for hyperspectral image classification [2]. The sparse representation coefficients y_i is considered to be independent from each other; in fact, this ignores the large correlation of HSI pixels. In order to solve this problem, and further improve the classification accuracy, the idea is to partition the pixels of HSI into a number of spatial neighborhoods called pixel groups, which is shown in Fig. 109.1, Pixels that belong to the same pixel group are often made up of the same material. Figure 109.1 shows how the pixels of a hyperspectral image be partitioned into 3×3 squares of pixels. Accounting for the above assumption, the establishment of a sparse representation model can now be written as (109.1).

$$X_H = DY_{H_i} + E_{H_i}$$

(109.1)

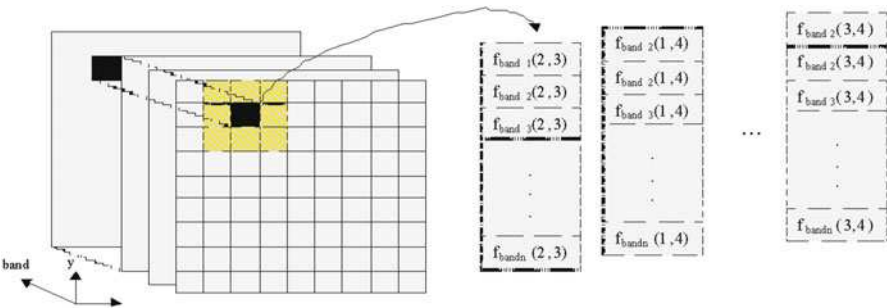


Fig. 109.1 The pixels of a hyperspectral image partitioned into 3×3 image patches. The pixels in the same pixel groups have revealed a hidden relationship of the spectral

In this model, the columns of Y_{H_i} and E_{H_i} are donated as the sparse representations and error vectors corresponding to the samples respectively. In order to get the dictionary and sparse representations, we employ the ℓ_2/ℓ_1 convex joint sparsity inducing regularizer to arrive at:

$$\arg \min_{D,Y} \frac{1}{2} \|X - DY\|_F^2 + \sum_{i=1}^g \gamma_{H_i} \|Y_{H_i}\|_{2,1} \text{ s.t. } \forall_i \|d_i\|_2 \leq 1 \quad (109.2)$$

Where γ_{H_i} is the regularization parameter for the i th group and $\|Y_{H_i}\|_{2,1}$ is the ℓ_2/ℓ_1 norm of the Y th row. For solving the problem, we have empirically adopted regularized M-FOCUSS algorithm. By estimating each row of the ℓ_2 norm.

Then update γ_H according to the estimated value. Setting the gradient of the objective function to zero, we arrive at: $\Lambda D^T DY_H - \Lambda X_H^T D + \gamma_H Y_H = 0$ where $\Lambda = \text{diag}(\|Y_{H,T}^i\|_2)$, Solving it and arrive at: $Y_H = \Lambda D^T (D \Lambda D^T + \gamma_H I)^{-1} X_H$.

To learn the dictionary D from hyperspectral data, let x_1, \dots, x_N , denote the sparse representation of the training data with respective labels l_1, \dots, l_N . Specific steps are as follows:

- (1) Structure dictionary learning, applying the SPAMS toolbox to solve formulation (109.2), learn the hyperspectral data x_1, \dots, x_N , yields dictionary D and corresponding sparse representations coefficient y , with respective labels l_1, \dots, l_N .
- (2) Linear SVM classifier is trained on the sparse representations and their corresponding labels l_1, \dots, l_N , to obtain the optimal classifier.
- (3) For any hyperspectral pixel, use the classifier to get its label l based on its sparse representations.

109.3 EXPERIMENTAL RESULTS AND ANALYSIS

In this section, in order to validate and test the effectiveness of the proposed structured dictionary-based Algorithm. we provide experimental results on real hyperspectral images. We compare the classification accuracy of the basic SVM classification(SVM) and the Structural Dictionary Learning(SDL), The experiment adopted four indicators to evaluate, respectively are Overall Accuracy(OA), Average Accuracy(AA), kappa and execution time.

The hyperspectral data was collected over an agricultural/forested area in NW Indiana by the AVIRIS sensor, called Indian Pines image. The results are show in Table 109.1. The SVM classification result and SDL result show in Fig. 109.2 (c, d)

The classification accuracy and execution time(s) of HSI by different classifiers are shown in Table 109.1.

Table 109.1 Classification accuracy and execution time(s)

Classifier	SVM	SDL	The method in [2]
OA	0.7678	0.9679	0.933
AA	0.6752	0.9234	unmeasured
Kappa	0.7301	0.9634	0.880
Time(s)	1.9765	19.4878	117.349

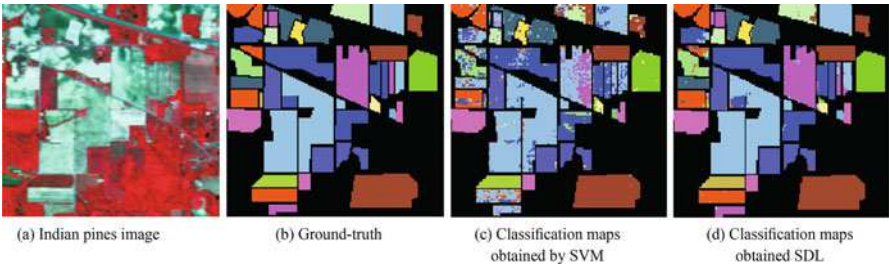


Fig. 109.2 Indian pines hyperspectral image and the comparison different classifiers are shown in Table 109.1. Indian pines image Ground-truth Classification maps obtained by SVM Classification maps obtained SDL

109.4 RESULT AND DISCUSSION

According to the experimental results, the structural dictionary learning algorithm proposed in this paper can significantly improve the classification accuracy. In the experiment, SDL can improve the classification accuracy from 0.7678 which don't use structured dictionary learning algorithm to 0.9679. From the perspective of execution time, the execution time of SVM algorithm is less than the execution time of SDL algorithm, this also illustrates the structural dictionary learning improved the classification accuracy by increasing the running time.

ACKNOWLEDGEMENT The author was sponsored by the National Natural Science Funds (NO.41372340) and Key Laboratory of Geo-special Information Technology, Ministry of Land and Resources, Chengdu University of Technology, China (NO. KLGSIT2014-03). Thanks Soltani-Farani A and Paolo Gamba offeredvery friendly help.

REFERENCES

1. Charles, A.S.: Learning sparse codes for hyperspectral imagery. *Selected Topics in Signal Processing, IEEE Journal of Selected Topics in Signal Processing*, 5(5), 963–978 (2011)

2. Song, X.F.: Classification of Hyperspectral Remote Sensing Image Based on Sparse Representation and Spectral Information. *Journal of Electronics & Information Technology*, 34(2), 268–272 (2012)

Chapter 110

Estimating Land Surface Temperature and its Lapse Rate over Kashmir Valley Using MODIS Data

Mohammd Rafiq, Irfan Rashid, and Shakil A. Romshoo

Abstract The study of the Land Surface Temperature (LST) is very important for its applications in many fields of natural sciences and is often used as input data in climate, agro-meteorological or hydrological models for forecasting ecosystem responses. Due to sparse and irregular distribution of meteorological station over Kashmir Himalayas, climate forecasting using interpolation of meteorological air temperature data (T_{air}) is not scientifically robust option. Remotely-sensed LST is, therefore, a good option to supplement the scanty network of the ground-based temperature observations for understanding and modelling a variety of environmental and ecological processes and phenomena. In the present study, an attempt was made to estimate LST and its lapse rate over Kashmir Himalayas using MODIS data and relate it with air temperature (T_{air}) from Indian Meteorological Department. Comparison between LST and T_{air} shows a very close agreement with MAE of $\pm 2^{\circ}\text{C}$. The calculated correlation coefficient between T_{air} and LST is above 0.9. Using ASTER DEM, LST was used to estimate the Lapse rate along various transects across the Kashmir Himalaya, which showed variations in space and time (from 0.3°C to 1.2°C per 100m change in the altitude). The information and knowledge generated from this research are going to improve the understanding and quantifications of various processes related to climate, hydrology and ecosystem where the use of temperature and lapse rate is an important and critical driving force.

Keywords MODIS • Land surface temperature • T_{air} • Lapse rate • Kashmir Himalayas

M. Rafiq (✉) • I. Rashid • S.A. Romshoo
Department of Earth Sciences, University of Kashmir, Srinagar, Jammu and Kashmir, India
e-mail: emidamls6@gmail.com

110.1 INTRODUCTION

Assessment and monitoring of various land surface processes in complex terrains such as Himalayas is hampered by the scanty distribution of meteorological stations. The problem is compounded by the difficulties in conducting field measurements of hydro meteorological parameters in order to derive a spatially representative distribution of the hydro meteorological parameters [1,2]. In Kashmir Himalayas, meteorological stations are scanty and sparsely located and for that reason, it is difficult to generate a good understanding of the hydrological processes [3]. Remotely sensed hydrometeorological parameters are routinely used for assessing various hydrological and meteorological processes at different spatial scales [4,5]. Remotely sensed Land Surface Temperature (LST) is of major interest for a variety of environmental and ecological applications. [6], including vector-borne disease bionomics, terrestrial hydrology, biosphere processes, climate change, biogeochemical studies, urban climate studies, and agricultural applications. LST is an important factor in modelling large scale hydrological systems, global primary production, and the greenhouse effect.

110.2 STUDY AREA

The state of Jammu and Kashmir is located in the northern part of the Indian sub-continent in the vicinity of the Karakoram and western mountain ranges. Kashmir valley is a longitudinal depression in the great northwestern complex of Himalayan ranges. It constitutes an important relief feature of tremendous geographic significance. Carved out tectonically, Kashmir valley has a strong genetic relationship with the Himalayan complex, which exercises an all-pervading influence on its geographic entity. Territorially, it forms the interior part of the state of Jammu and Kashmir. The latitudinal extent of the state is 32.17°N to 37.6°N, whereas the longitudinal extent is 73.26°E to 80.30°E (Fig. 110.1).

110.3 MATERIAL AND METHODS

DATA SETS USED: In this study different data from satellites, weather stations and also from the field was used. MODIS LST data was downloaded and processed from 2002- 2011 i.e. for 10 years and this data was related with IMD data with same date. IMD of 2002-2011. MODIS land surface temperature data was downloaded from (<https://lpdaac.usgs.gov/>):

- (1) MODIS 8 days land surface temperature at 1km resolution of Collection-5 (MOD11A2.L3) from 2002-2012.

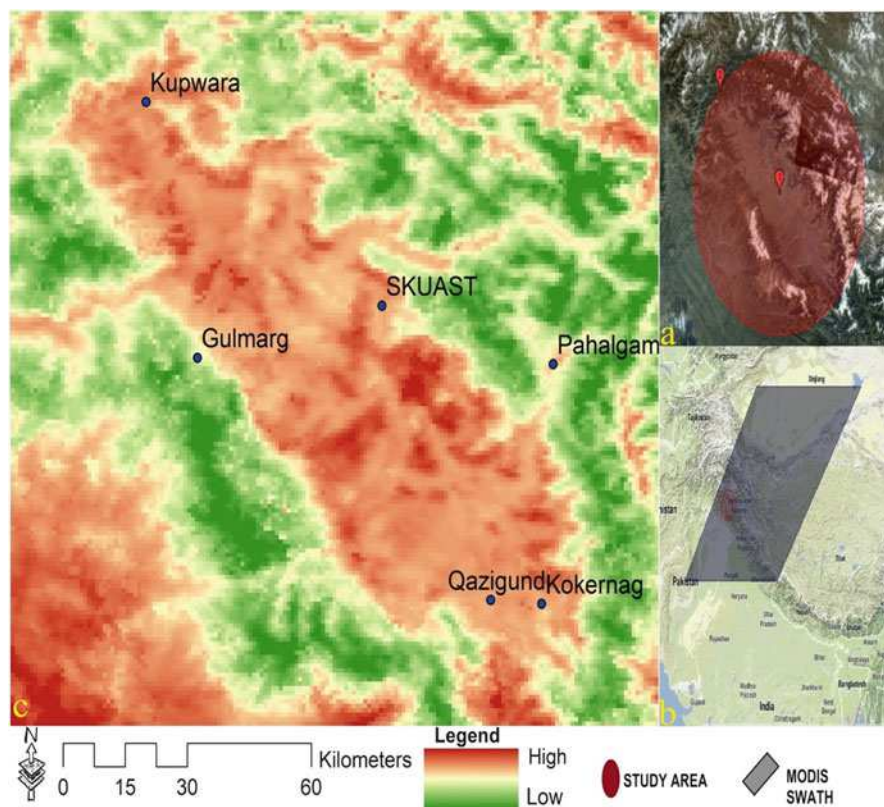


Fig. 110.1 Shows the study area (a), MODIS swath (b) and also the location of IMD stations (c)

- (2) Daily surface air maximum temperatures (T_{air}) from 6 meteorology stations over Kashmir valley.
- (3) MODIS Snow Cover 8-Day L3 Global 500m Grid (MOD10A2).
- (4) ASTER DEM 90 m.

110.4 METHODOLOGY

In this study an automated extraction of LST from MODerate Resolution Imaging Spectroradiometer MODIS (MOD11A2) imagery has been made to suffice the much needed spatially distributed temperature maps, which can replace the metrological point data. For LST data sets each HDF image contained multiple 'bands' of data (i.e. several images in one file) and so were imported into ArcGIS 10.1 to extract individual image files for each environmental variable. The processing of data was then divided into two steps preprocessing and post processing.

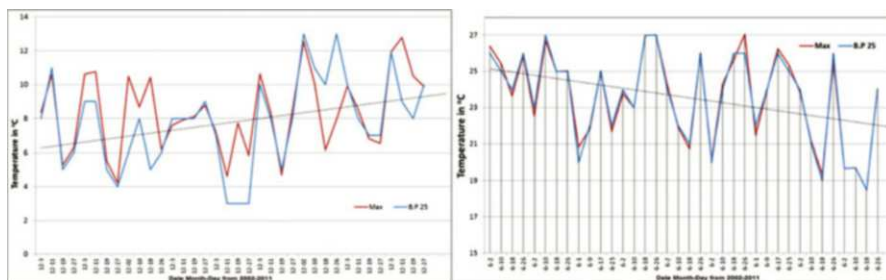


Fig. 110.2 Graphs showing the LST and Tair (IMD Data) of December from 2002-2011 and July 2002-2011

110.5 RESULTS

After analyzing the results from 2002-2011 the monthly trends showed that the temperature in winters is increasing with high R^2 values from September to December (Fig. 110.2) while as in summers (May–August) the temperature shows a decreasing trend (Fig. 110.2). The increase in the winter temperature is alarming due to the existence of glaciers in the area. There is a clear increase in overall temperature when we compared our 10 years data to past data from 1979. Due to increase in winter temperature the form of precipitation has also changed. We are now receiving more rain than snow. Due to which there is change in the flow of water in streams as our base flow highly depends on snow. If this situation continues our streams will become seasonal and the impact will be on the agriculture, horticulture and also the hydroelectricity, which is the backbone of our economy and also it will disturb the tourism sector of valley.

NASA provides the real-time satellite track for both terra and aqua satellites. The terra satellite track was retrieved from <http://rapidfire.sci.gsfc.nasa.gov/cgi-bin/imagery/realtime.cgi>. And those observation were taken into consideration where the observation time of IMD (UTC 06:00) and satellite over pass (UTC 06:00) was same. The result showed very close relationship (except some months with cloud cover and snow) (Fig. 110.3). When compared to the exact time of data retrieved from MODIS and metrological station i.e. around 11:30hrs (UTC06:00) am the correlation is up to .99 and the RMSE error is just 0.86°C.

110.6 LAPSE RATE ESTIMATION RESULTS

After analyzing the correlation results and errors in measurement of temperature with respect to LST, lapse rate was also estimated. In this study the US Geological Survey Digital Elevation Model (USGS-DEM) was used over Kashmir valley. Than the contour maps where generated having an interval of 1 km. Land surface Temperature along 8 different transacts located uniformly and containing at least 3 different contours were analyzed for TRL. Figure 110.4 the results showed that

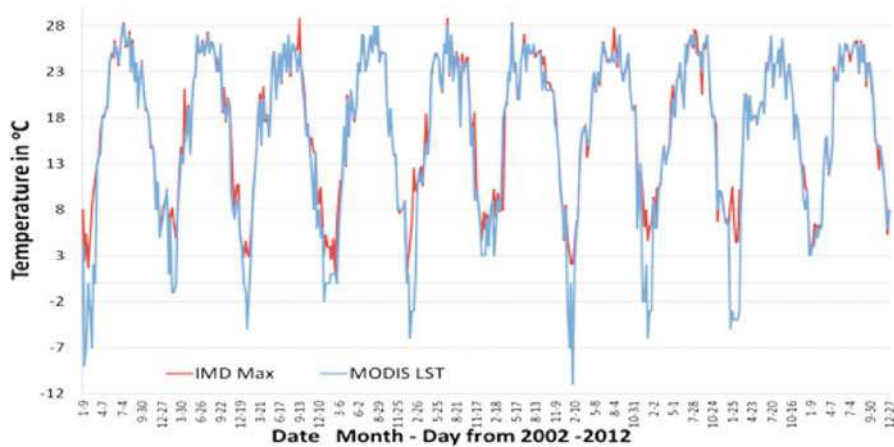


Fig. 110.3 The comparison between Tair and LST having the same observation time from 2002-2012

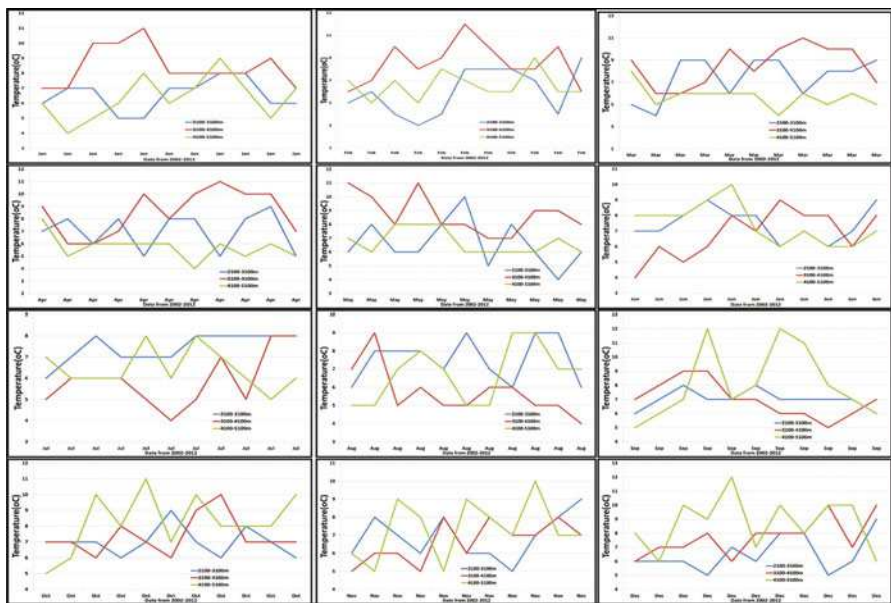


Fig. 110.4 Graphs showing the year round change in TRL of lidder transect during 2002-2012

the lapse rate along different environmental settings varied in space and time (from 0.3 °C–1.2 °C per 100 meters). Keeping in view the influence of aspect similar aspects (e.g. southern or northern) along the transect were analyzed. Also the information was taken from only those pixels having a similar type of Lu/Lc These observations are at variance with the commonly used TRL and hence can

improve the understanding and quantifications of various processes related to climate, hydrology and ecosystem where the use of temperature and TRL is an important and critical driving force. Change in TRL can affect the Snow melt runoff and will help us to understand the glacier system of our valley more effectively. By knowing the exact temperature of glacier site and TRL in the area we can better estimate the runoff and other important factors for glacier monitoring

110.7 CONCLUSIONS

We can use reconstructed LST time series data substituted for meteorological observations, especially in modelling approaches where data is typically aggregated. LST data along with snow cover data is very important for monitoring the temperature of different LU/LC and in turn can be used for checking and predicting crop yield and also the necessary measures to be taken, as this data can be used as an input to various hydro-metrological models.

REFERENCES

1. Hachem, S., Duguay, C.R. and Allard, M.: Comparison of MODIS-derived land surface temperatures with ground surface and air temperature measurements in continuous permafrost terrain. *The Cryosphere*, 6(1), 51–69 (2012)
2. Romshoo, S.A. and Rashid, I.: Potential and Constraints of Geospatial Data for Precise Assessment of the Impacts of Climate Change at Landscape Level. *International Journal of Geomatics and Geosciences*, 1(3), 386–405 (2010)
3. Romshoo, S.A., Bhat, S.A. and Rashid, I.: Geoinformatics for assessing the geomorphological control on the hydrological response at watershed scale in Upper Indus basin. *Earth System Science*, DOI: [10.1007/s12040-012-0192-8](https://doi.org/10.1007/s12040-012-0192-8), 121(3), 659–686 (2012)
4. Montanari, M., Hostache, R., Matgen, P., Schumann, G., Pfister, L. and Hoffmann, L.: Calibration and sequential updating of a coupled hydrologic-hydraulic mode using remote sensing-derived water stages. *Hydrological Earth System Science*, 13, 36–38 (2009)
5. Crow, W.T. and Ryu, D.: A new data assimilation approach for improving runoff prediction using remotely sensed soil moisture retrievals. *Hydrol. Earth Syst. Sci.*, 13, 1–16 (2009)
6. Neteler, M.: Estimating daily Land Surface Temperatures in mountainous environments by reconstructed MODIS LST data. *Remote Sensing*, 2(1), 333–351 (2010)

Chapter 111

Combining Quantitation of Remote Sensing Information of Local Structures and Calculation of Structural Stress Field

Wu-nian Yang, Xin Yang, Han-hu Liu, Zhen-tao Qin, and Xiao-ping Wu

Abstract The tectonic stress field is crucial to the study of tectonics, engineering geology, seismology and mineral exploration. In this paper, the author proposed a new theory and method for calculating the structural stress field using the composite quantitative data of remote sensing information on circular structures and related linear structures to approximate the iso-elevation line map of local structures bearing oil or gas on the basis of the phase-separation analysis of remote sensing information field and the theory of elastic mechanics.

Keywords Combining quantitation of remote sensing information • Circular or ring structure • Linear structure • Structural stress field • Quantitative analysis

111.1 INTRODUCTION

Structural stress field is important in the study of tectonics, engineering geology, seismology and mineral exploration[1–3]. In the mineral exploration, it often needs to investigate deformation features and mechanics of the crust's rock. An iso-elevation line map of fold structural layer is a basic map to indicate shape features of the fold, which is more important especially in the petroleum exploration engineering, but it needs for drawing this map to get a great deal of data of structural profiles or drilling. In this paper, the authors proposed a new theory and method for calculating the structural stress field using the composite quantitative data of remote sensing information on circular structures and related linear structures to approximate the iso-elevation line map of local structures on the basis of the phase-separation analysis of remote sensing information field and the theory of elastic mechanics[1]. The theory and method have been practically applied in many tested areas and effects are remarkable.

W.-n. Yang (✉) • X. Yang • H.-h. Liu • Z.-t. Qin • X.-p. Wu
Key Laboratory of Geo-spatial Information Technology, Ministry of Land and Resources/
Institute of Remote Sensing & GIS, Chengdu University of Technology, Chengdu 610059,
China
e-mail: ywn@cdut.edu.cn

111.2 RELATIONSHIP BETWEEN CIRCULAR AND RELATED LINEAR STRUCTURES AND CONCEALED STRUCTURAL RISES BEARING OIL OR GAS IN SPACE

It has been demonstrated that a concealed structural rise bearing oil or gas generally displays a circular structure in remote sensing image, which accompanies some multi-layer circular fractures and radial joints in space, and their development density increases from the edge of the circular structure to its center (Fig. 111.1). According to the mechanics property of rocks, this kind of joints mainly develop in brittle rocks, the area of the highest information abnormality on the pattern has certain correspondent relation with the highest point of the rise, and the abnormal values gradually decrease from the highest point of the rise to its edge. Under the thought, 2-D and 3-D quantitatively analyzing patterns of the local structures bearing oil or gas were established by the author through phase-separation analyzing of remote sensing information field and combining quantity of circular structures and related radial lineaments combined with GIS and geophysical data, based on the interpretation result of circular structures and lineaments and field study in the evaluation and quantitative analysis of concealed structures bearing oil or gas in Qiliba region, Xichang, China (show in Fig 111.3). According to the theory above, the pattern maps may be regarded as natural models calculating the local structural stress fields[1–3].

111.3 MECHANIC MODEL OF FOLDS AND CALCULATION OF STRUCTURE STRESS FIELD

After an isovalue-line map (as the 2-D map bottom the Fig. 111.3) of remote sensing information of structural layers of a fold is drawn, the structural stress field can be calculated and reconstructed on the theory of elastic mechanics. A mechanics model of a normal fold is that rock beds are curved and form a fold under a

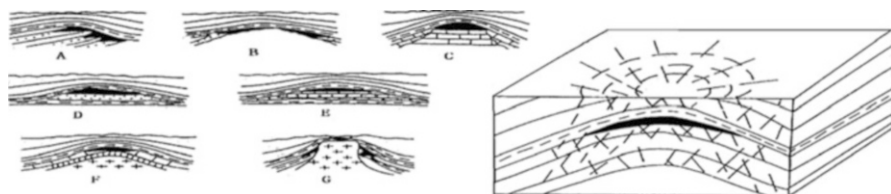


Fig. 111.1 Sketch map showing the relationship between circular and radial major joints and local structural rise underground. (The patterns in the Left of the map are some concealed structures bearing oil or gas)

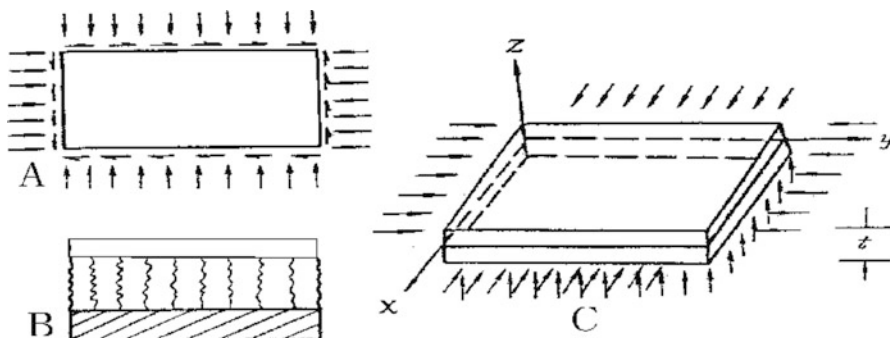


Fig. 111.2 Mechanics pattern of a plate acted on by forces

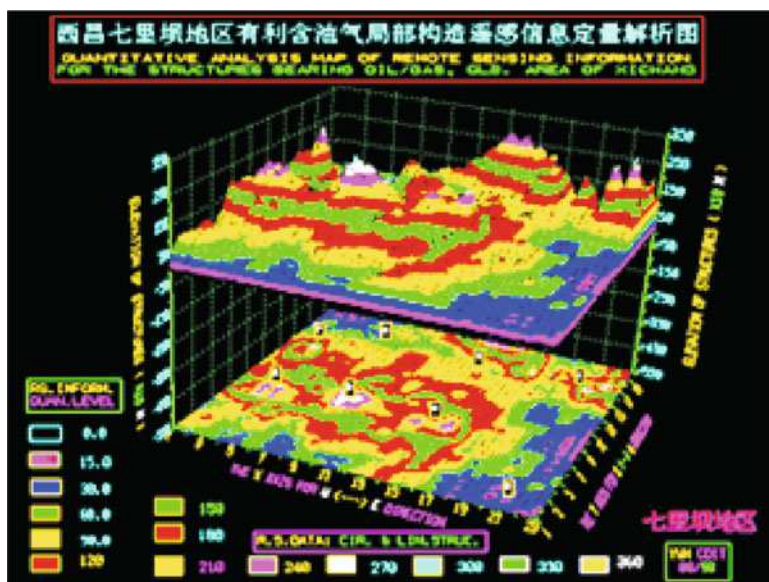


Fig. 111.3 3-dimension color patterns of quantitative analysis for local structures bearing oil/gas, Qiliba region of Xichang, southwestern Sichuan, China, observing from SE directions

horizontal compressive stress, similar to the deformation of a curved elastic slice acted on its plane by side pressures (Fig. 111.2A). If the function to the fold acted on by upper rock beds and lower rock beds is regarded, deformation of the slice is equal to lying on an elastic basement (Fig. 111.2B). So, apart from lateral pressures, the slice is also acted on by inversely elastic force of the basement at the same time. Therefore, the mechanics model of a rock layer to be folded should be a slice in curve balance state under jointly acting by horizontal force and vertical force (inversely elastic force). As it is shown in Fig. 111.2C, the middle plane of the

slice is $x - y$ plane, after the slice is twisted, the deflection $w(x, y)$ should fit the differential equation of the deflection:

$$\begin{aligned} D \times & \left(\frac{\partial^4 w}{\partial x^4} + 2 \frac{\partial^4 w}{\partial x^2 \partial y^2} + \frac{\partial^4 w}{\partial y^4} \right) \\ & - \left(N_x \frac{\partial^2 w}{\partial x^2} + 2 N_{xy} \frac{\partial^2 w}{\partial x \partial y} + N_y \frac{\partial^2 w}{\partial y^2} \right) + kw \\ & = 0 \end{aligned} \tag{111.1}$$

where N_x, N_y and N_{xy} are three components of internal force on the middle plane of the slice, and kw express inversely elastic force on folds from upper and lower restraining layers, k is a constant, which is called elastic impedance and based on M. Biot formula, its value may be estimated according to the elastic parameters of upper and lower restraining layers and fold scale; $D = Et^3/12(1-\nu^2)$, that is curved stiffness of the slice; E, ν are elastic modulus and Bosong ratio respectively.

In this study, the authors calculated paleo-tectonic stress field and obtained a contour graph of the distribution of tensional stress (Fig. 111.4) on the basis of the isodensity graph of circular and radial joints of Qiliba region of Xichang, China. In the calculation, $t = 0.3 \text{ km}$, $E = 500\text{Mpa}$, $\nu = 0.315$. In the Fig. 111.4, several high density abnormal areas are identical with above mentioned circular structures such

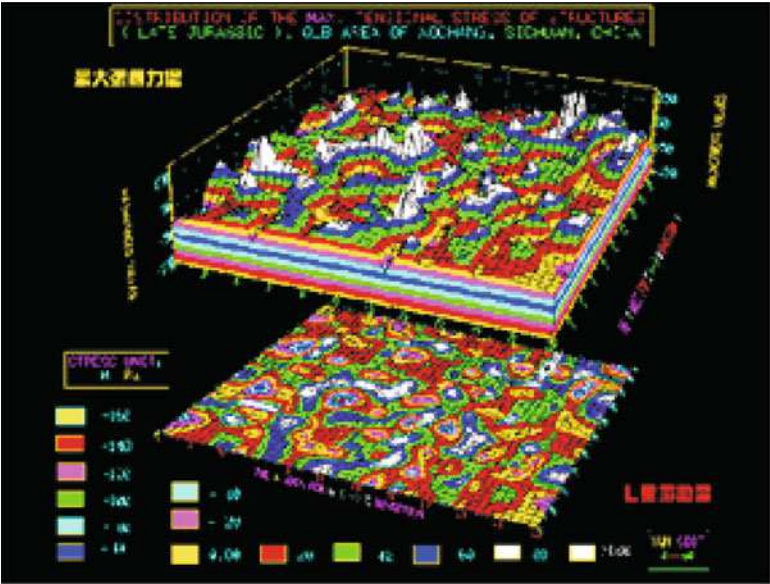


Fig. 111.4 Maximum tensional stress distribution map of the Qiliba region, Xichang, southwestern Sichuan. (stress unit: Mpa)

as Qiliba, Erwu and so on. The maximum of tensional stress could be 372Mpa, the major axis indicates the direction of maximum tensional stress. Theoretically, the area of high density of tensional stress is often the area of tensional cracks to be developed which is beneficial to oil or gas reserve.

According to the characteristics of information field showing in Fig. 111.1-111.3 and Figs. 111.4, we can glean the following information: the higher information abnormal belt in the east-west direction indicates an existing of larger structural rise belt underground. Several highest abnormal areas in a string of beads are the high points of some local structural rises which form through overlaying of the folds in the south-north direction. In space they have respondent relation with above mentioned circular structures, and are characteristics of multi-ring complex circular construction with positive anticlines or structural dome developing circular and radial joints.

111.4 CONCLUSION AND DISCUSSION

Because circular structures and related linear structures in circular or radiating patterns correspond in space to the rising of concealed structural, the authors propose a new theory and method with which a natural model of the concealed structural rise can be established and then the structural stress field can be calculated using composed quantitative data of remote sensing information on circular structures and related linear structures, on the basis of the phase-separation analysis of remote sensing information field and the theory of elastic mechanics.

ACKNOWLEDGEMENT The author was sponsored by the National Natural Science Funds (NO. 41372340). Sincerely thanks to the Committee of Development Foundation of Sciences and Technology for Geology and Minerals, Ministry of Land and Resources (MLR), China, that supported the finance for doing an advanced research of the project.

REFERENCES

1. Yang Wunian: Separate analysis of remote sensing information of structures of different geological periods and quantitative study of corresponding tectonic stress field. *Acta Geologica Sinica*, 71(3), 344-355 (1997)
2. Yue Guangyu, Du Siqing, Huang Jijun and Yang Wunian: Principle of structural compounding-combine, analysis of structural association - superposition in Sichuan basin and Guizhou plateau, China. Chengdu, Press of Chengdu University of Science and Technology (1996) (in Chinese with abstract of English)
3. Duan, X., Tian, Z., Ding, M. and Zhao, W.: Registration of remote-sensing images using robust weighted kernel principal component analysis. *AEU-International Journal of Electronics and Communications*, 67(1), 20-28 (2013)

Chapter 112

Research on GIS-Based 3D Prospectivity Mapping and a Case Study of Jiama Copper-Polymetallic Deposit in Tibet, China

Keyan Xiao, Nan Li, Alok Porwal, Eun-Jung Holden, Leon Bagas, and Yongjun Lu

Abstract This paper reports a deposit-scale GIS-based 3D mineral potential assessment for Jiama copper-Polymetallic deposit area in Tibet, China. The assessment is achieved through the combined use of a metallogenic model, and 3D geological, geochemical modelling and Prospectivity modelling. In this contribution, a metallogenic model for the Jiama deposit and a 3D modelling flow chart are used to construct multiple 3D layers of volumetric and triangular mesh models to represent geology, geochemistry and ore-controlling features in the study area. GIS-based 3D weights-of-evidence analysis is used to quantify and target the subsurface Prospectivity for Cu(-Mo) ore-bodies in the area, which defined three prospective deep-seated exploration targets. This contribution ends with a discussion on the potential fluid flow pathways based on the 3D zonation of major geochemical elements and their ratios, such as Zn / Pb ratios. The discussion confirms the GIS-based 3D quantitative assessment of the Prospectivity of the Jiama copper-Polymetallic deposit.

Keywords 3D • Geological modelling • Jiama copper-polymetallic deposit • Prospectivity mapping

K. Xiao

MLR Laboratory of Metallogeny and Mineral Resource Assessment, Institute of Mineral Resources, Chinese Academy of Geological Sciences, Beijing 100037, China

N. Li (✉) • A. Porwal • E.-J. Holden • L. Bagas • Y. Lu

Centre for Exploration Targeting, Core to Crust Fluid Systems, School of Earth and Environment, The University of Western Australia, 35 Stirling Highway, Crawley, WA 6009, Australia

e-mail: Superln1980@126.com

112.1 INTRODUCTION

Prospectivity mapping typically involves an integrated analysis of multiple layers of information including geological, geochemical, and geophysical data to estimate the likelihood of mineralization in a spatial framework using an empirical model. GIS-based prospectivity mapping at a deposit-scale is one of the most efficient ways of the quantitatively assessing mineral deposit models. This contribution documents a deposit-scale prospectivity analysis for the polymetallic Jiama copper deposit in Tibet. Firstly, we collected and sorted out geological and metallogenic models and extracted targeting elements. Secondly, using available geological and drill-hole data in the area along with constraints derived from the local geology, we reconstructed 3D geological models representing geology, ore-controlling structures, and geochemistry. These models include intrusions, contact zones, ore bodies, topographical surface, alterations and geochemical zones separated by chemical element signatures. Thirdly, this paper demonstrated quantification of contact zone for skarn-type ore bodies through using statistical analyses. Fourthly, this paper used a GIS-based W-o-E model to target potential mineral mapping. Finally, we used, geochemistry halos as another indicator for deposit to define potential hydrothermal fluid pathways and the prediction of fluid flow directions based on the 3D zonation of geochemical elements such as Cu, Mo, Zn, Au, Ag and Pb and element ratios between them. Element ratios can indicate the characteristics of changes in physical and chemical attributes of hydrothermal fluids with distance from the source intrusions. We think this is an underlying proof in verifying the mineral potential mapping of the W-o-E models.

112.2 WORKFLOW ON GIS-BASED 3D PROSPECTIVITY MAPPING UNDER DEPOSIT-SCALE

This contribution discusses and summarizes various references to construct a workflow on GIS-based 3D prospectivity mapping [1–16]. Specifically, using this workflow, we first collected and sorted the geological information and metallogenic models for the Jiama deposit and defined targeting elements. Secondly, using geological, drill-hole, cross sections data in the area along with some constraints or rules derived from the local geology, we generate 3D geological models representing geology, ore-controlling structures, and geochemistry. These models include intrusions, contact zones, ore bodies, topographical surface, alterations and geochemical volumes. Thirdly, the first part of Section 5 demonstrated the procedure of setting values to prospectivity volumes. Fourthly, we used W-of-E modeling to target potential mineral mapping. Finally, we used geochemistry halos to discuss the hydrothermal fluid pathways and prediction of fluid-flow directions based on the 3D zonation of Cu, Mo, Zn, Au, Ag and Pb and their relative element

ratios. Element ratios can indicate the characteristics of changes in the physical and chemical attributes of hydrothermal fluids with distance from the source intrusions.

112.3 DATA AND 3D MODELLING

Based on surface geology (including the nature of the host rocks, alteration mineral-assemblages and other mineralization-related geological features), topography and drill-hole lithology logs, cross sections, we constructed 3D models for the Jiama deposit. We then constructed 3D models of the geochemical volumes. These models were used to target potential mineral mapping, and then delineate the location and direction of fluid flow pathways for mineral potential modelling as evidence. The specific data and modelling methods are listed as shown in Fig. 112.1. In addition to topographic data, exploration datasets used in 3D modelling include various geological elements such as cross sections, stratigraphy, intrusions and ore-controlling structures, geochemistry such as soil geochemistry, drill hole data, and mineral alterations. In relationship to the Jiama, the data include geological and topographic maps at the scale of 1:2000, 26 geological cross-sections represented by exploration lines, 10 trenches (representing >300 samples), soil samples, and 218 drill holes.

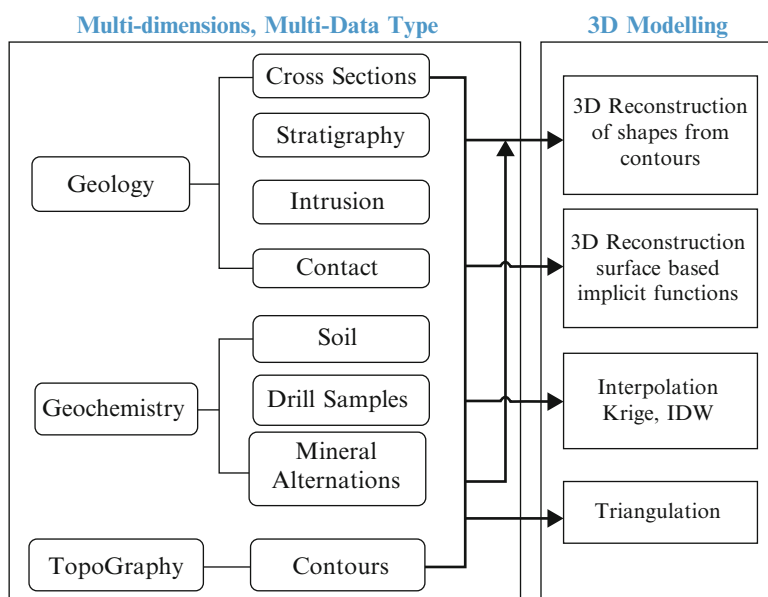


Fig. 112.1 Specific data and modelling methods in this paper

112.4 QUANTITATIVE ANALYSIS AND ASSESSMENTS

The volumetric and surface mesh models representing geological formations, geological contacts, alteration and geochemical variations were used for GIS-based W-o-E mineral prospectivity mapping. On the basis of quantitative assessments and 3D geological multi layers, we sorted 3 kinds of all of voxels. Specifically, class A is located in the northeastern part of the Jiama Deposit. Here the average Cu content is 0.38 % while the average Mo content is 0.055 %; it is therefore a Mo-Cu potential area. Class B is located in the northwest of the Jiama Deposit with an average Cu content of 0.54 % and an average Mo content of 0.017 %; it is therefore a Cu potential area. Class C is located in the south of the Jiama Deposit with an average Cu content of 0.47 % and an average Mo content of 0.019 %; it is therefore a Cu potential area.

112.5 DISCUSSION ON THE 3D GEOCHEMICAL MODEL

In this paper, we will use geochemical halo as indicator to delineate the location and direction of fluid flow pathways and as evidence for mineral potential mapping. The key findings of this research about geochemistry halos are discussed below.

- Well-defined vertical and strike geochemical zonation have been deciphered at Jiama. The vertical zonation from top to bottom is: $\text{Zn} \rightarrow \text{Pb} \rightarrow \text{Ag} \rightarrow \text{Au} \rightarrow \text{Cu} \rightarrow \text{Mo}$. The strike zonation from northeast to southwest is $\text{Mo} \rightarrow \text{Cu} \rightarrow \text{Au} \rightarrow \text{Ag} \rightarrow \text{Pb} \rightarrow \text{Zn}$. Since the older stratigraphic units outcrop in the southwest, the vertical section is consistent with a strike zonation.
- The spatial variation of Zn/Pb ratios at Jiama indicate that the hydrothermal fluid pathways were directed from northeast to southwest, and from bottom to top, and that the source was located at a <4400 m level above MSL. These results are consistent with the above geochemical zonation, which indicate the presence of high temperature elements in the northeast and at deeper levels.
- (Element ratios such as Zn/Pb, Cu/Pb, Ag/Pb, Au/Pb and Mo/Pb show similar vertical and strike trends. However, only the Zn/Pb ratio is used to characterize the fluid flow pathways for the reasons explained below. The fluid flow directions as inferred from the Zn/Pb ratios are consistent with those inferred from geochemical elements distribution.

The W-o-E analyses are also consistent with the geochemical zonation and the spatial distributions of the Zn/Pb ratios. Prospective Mo-Cu zones have been delineated northeast of the known Mo-Cu ore bodies at Jiama in the deeper levels, while the prospective Cu zones are delineated northwest and south of the Jiama Mo-Cu ore bodies.

112.6 SUMMARY

This paper presents a study that harnesses the power of 3D GIS technology and quantitative assessment for brown field exploration targeting for the Jiama Cu-Mo-Au deposit in Tibet. This is an active exploration area where large volumes of data are available including drill-holes, trenches, cross sections and soil geochemistry, as well as detailed surface geological map includes raw data of geology and topography. The metallogenic model of the deposit is well defined by geologists previously. On basis of it, we used 3D GIS technology and quantitative assessment methods to construct 3D models to represent key targeting elements for Cu-polymetallic deposits. Firstly, this paper collected and ordered parts of GIS-based 3D mineral potential mapping based on previous papers and authors' works. Secondly, this paper demonstrates that GIS-based 3D W-o-E modelling of the 3D models demarcate Cu-polymetallic prospective zones. This study has resulted in the delineation of three zones: one for Mo-Cu in the northeast of the known Jiama ore bodies and two others for Cu in the northwest and south of the ore bodies. Section 5 of this contribution discussed the delineation of geochemical gradients to determine hydrothermal fluid-flow directions. This study showed that the fluids were directed from bottom to top in the vertical plane and from northeast to southwest in a horizontal plane. Furthermore, it was determined that the source of fluids lie at depth of <4400 m above MSL with the use of W-of-Evidence.

REFERENCES

1. Bonham-Carter, G.F. and Agterberg, F.P.: Weights of evidence modelling: a new approach to mapping mineral potential. *Geological Survey of Canada*, 89, 171–183 (1989)
2. Bonham-Carter, G.F.: Geographic Information systems for Geoscientist: Modeling with GIS. Oxford Elsevier (1994)
3. Brown, W.M., Gedeon, T.D., Groves, D.I. et al. Artificial Neural Networks: A new Method for Mineral Prospectivity Mapping. *Australian Journal of Earth Sciences*, 47, 757–770 (2000)
4. Carranza, E.J.M. and Sadeghi, M.: Predictive mapping of prospectivity and quantitative estimation of undiscovered VMS deposits in Skellefte district (Sweden). *Ore Geology Reviews*, 38, 219–241 (2010)
5. Chen, J., Lv, P., Wu, W., Zhao, J. and Hu, Q.: A 3D method for predicting blind ore-bodies based on a 3D visualization model and its application. *Earth Science Frontiers*, 14, 54–62 (in Chinese with English abstract) (2007)
6. Cheng, Q.M., Agterberg, F.P. and Bonham-Carter, G.F.: Fractal pattern Integration for Mineral Potential Estimation. *Natural Resources Research*, 5, 117–130 (1996)
7. Cheng, Q.M. and Agterberg, F.P.: Fuzzy Weights of Evidence Method and Its Application in Mineral Potential Mapping. *Natural Resources Research*, 8, 27–35 (1999)
8. Cheng, Q.M.: Integration of Ada Boost and Weights of Evidence Model for Mineral Potential Probabilistic Mapping. Session MG3 “Geo-Process Modeling” at IAMG 2011 Annual Conference. Salzburg (2011)
9. Chen, J.P. and Wang, C.: Three-dimensional Metallogenic Prediction in Yongmei Region Based on Digital Ore Deposit Model. *Scientific and Technological Management of Land and Resources*, 29, 14–20 (2012)

10. Mao, X.C., Tang, Y.H. and Deng, H.: Three-dimensional morphological analysis method for geologic bodies and its application. *Journal of Central South University (Science and Technology)*, 43(2), 588–595 (2012)
11. Porwal, A. and Carranza, E.J.M.: Hale M. A Hybrid Fuzzy Weights-of-Evidence Model for Mineral Potential Mapping. *Natural Resources Research*, 15, 1–14 (2006)
12. Singer, D.A.: Basic concepts in three-part quantitative assessments of undiscovered mineral resources. *Nonrenewable Resources*, 69–81 (1993)
13. Singer, D.A. and Kouda, R.: Application of a Feed-forward Neural Network in the search for Kuruko Deposits in the Hokuroku District, Japan. *Mathematical Geology*, 28, 1017–1023 (1996)
14. Singer, D.A.: Typing mineral deposits using their associated rocks, grades and tonnages using a probabilistic neural network. *Mathematical Geology*, 38, 465–474 (2006)
15. Singer, D.A. and Menzie, W.: Quantitative Mineral Resource Assessments: An Integrated Approach. Oxford University Press (2010)
16. Wang, G.W., Zhang, S.T. and Yan, C.H.: Mineral potential targeting and resource assessment based on 3D geological modeling in Luanchuan region, China. *Computers & Geosciences*, 37, 1976–1988 (2011)

Chapter 113

Inferring Land Surface Processes from Watershed Characterization

Gowhar Meraj, Shakil A. Romshoo, and Sadaf Altaf

Abstract This research has integrated the use of the Linear Imaging Self Scanner (LISS-III) satellite data and Advanced Space borne Thermal Emission and Reflection Radiometer (ASTER) Digital Elevation Model (DEM) for assessing the surface hydrological behavior of Lidder and Rembiara watersheds of the Jhelum Basin. The results reveal that the Lidder watershed exhibits lesser basin lag time compared to Rembiara watershed for a same magnitude storm event. Moreover higher population density in the downstream regions of Lidder makes it more vulnerable to flooding than Rembiara. The methodology and results of this study intends to help in formulating better flood mitigation strategies in this part of the Himalayan region where the observation network of hydro-meteorological and estimation of other land surface parameters is either missing or very scanty.

Keywords Kashmir Himalaya. Jhelum basin • Hydrology • Morphometry • Runoff potential • Flood vulnerability • ASTER • LISS III

113.1 INTRODUCTION

Due to the inadequate data necessary for understanding the mountainous land surface and hydrological processes, the assessment of floods is often hindered in Himalaya [1]. Moreover, the application of physically based models is limited due to the complex nature of the related events as well as the limitation of the observational data [2]. In this research, we have evaluated watershed characteristics (morphometry, land cover and slope) which make the downstream areas of a

G. Meraj (✉)

Land Surface Processes Group (LSPG) & Glaciology and Climate Change Group (GCCG), Remote Sensing Lab. Department of Earth Sciences, University of Kashmir, Hazratbal, Srinagar, India

Department of Environmental Science, University of Kashmir, Hazratbal, Srinagar, India
e-mail: gowharmeraj@gmail.com

S.A. Romshoo • S. Altaf

Land Surface Processes Group (LSPG) & Glaciology and Climate Change Group (GCCG), Remote Sensing Lab. Department of Earth Sciences, University of Kashmir, Hazratbal, Srinagar, India

watershed, prone to flooding [3, 4]. The study has been carried out in the two watersheds of Jhelum basin (upper Indus basin) i.e. Lidder and Rembiara. The former is a right bank tributary watershed of the Jhelum basin in the greater Himalayan range and latter is the left bank tributary in the Pir Panjal range. This study has used a comparative qualitative index (total runoff score) in the two watersheds to determine the extent and magnitude of the flood vulnerability downstream. It is very important to assess the relative flood vulnerability in the left and right bank tributary watersheds of the Jhelum basin since both the sides have demonstrated different flood vulnerability due to the differential socio-geoenvironmental setting. These two watersheds are the representative watersheds among the 24 watersheds of the Jhelum Basin. This study is based on the integrated use of satellite remote sensing, geographic information system (GIS), and advanced field observation techniques for better understanding of the influences of watershed characteristics on hydrological processes and flooding. The findings of this research shall be of tremendous practical use in planning flood hazard management and mitigation strategies in the Himalaya in general and Kashmir Himalaya in particular, as there is scarcity of ground based observational data which often hampers the parameterization of the more complex physically based flood models [5, 6].

113.2 STUDY AREA

The unique geomorphological setup of the Jhelum basin with heterogeneous lithology and varied hydrological conditions render the basin all the more vulnerable to natural hazards particularly floods. Keeping in view the above facts, two representative watersheds - Lidder and Rembiara, on either banks of the axial river Jhelum have been chosen for the detailed study involving morphometry, land cover and slope analysis in order to understand their influences on the surface hydrological behaviour.

113.3 MATERIAL AND METHODS

For accomplishing the research objectives outlined for this research, a number of approaches were employed that included the use of satellite remote sensing data, digital elevation data, detailed field observations integrated in a knowledge-driven analytical framework using geospatial tools. For multi-criteria analysis we have used total run off score (*TR*) method. This approach is based on the principles of knowledge-driven modelling and converts the qualitative understanding of a phenomenon based on scientific knowledge into a quantitative estimation. In absence of a robust numerically or physically based approaches, which often relies on the detailed estimation and parameterization of the processes involved, this method is

113.5 CONCLUSIONS

It is concluded that during heavy rain spells, downstream of Lidder watershed will be more vulnerable to flooding than the downstream of the Rembiara watershed. Moreover, the differential topographic attribution in the two watersheds is going to have differing impacts on the transport of water and sediments. As a result, the flooding behavior shall also vary and depend among other things, on the amount and pattern of the precipitation. This research demonstrates that the differential geomorphologic, morphometric, topographic and land cover characteristics of these two watersheds have a strong influence on the hydrological functionality and response. In absence of adequate instrumentation and field data, these are unswerving and reliable indicators to infer hydrological information including flooding and flood vulnerability at the watershed scale [8].

ACKNOWLEDGEMENTS This research work has been accomplished under a research grant provided by the Department of Science and Technology, Government of India (DST-GOI) for the project titled “Integrated Flood vulnerability Assessment for Flood Risk Management and Disaster Mitigation”. The authors express their gratitude to the funding agency for the financial assistance.

REFERENCES

1. Mirza, M.M.Q.: Hydrologic modeling approaches for climate impact assessment in South Asia. *Climate Change and Water Resources in South Asia*. Balkema Press, Leiden, 23–54 (2005)
2. Chaponnière, A., Boulet, G., Chehbouni, A. and Aresmouk, M.: Understanding hydrological processes with scarce data in a mountain environment. *Hydrological processes*, 22(12), 1908–1921 (2008)
3. Diakakis, M.: A method for flood hazard mapping based on basin morphometry: application in two catchments in Greece. *Natural hazards*, 56(3), 803–814 (2011)
4. Meraj, G., Yousuf, A.R. and Romshoo, S.A.: Impacts of the Geo-environmental setting on the flood vulnerability at watershed scale in the Jhelum basin. M Phil dissertation, University of Kashmir, India (2013) <http://dspace.uok.edu.in/jspui/handle/1/1362>
5. Van De Wiel, M.J., Coulthard, T.J., Macklin, M.G. and Lewin, J.: Modelling the response of river systems to environmental change: Progress, problems and prospects for palaeo-environmental reconstructions. *Earth-Science Reviews*, 104(1), 167–185 (2011)
6. Romshoo, S.A., Bhat, S.A. and Rashid, I.: Geoinformatics for assessing the morphometric control on hydrological response at watershed scale in the Upper Indus basin. *Journal of Earth System Science*, 121(3), 659–686 (2012)
7. Zhang, Y.L. and You, W.J.: Social vulnerability to floods: a case study of Huaihe River Basin. *Natural Hazards*, 71(3), 2113–2125 (2014)
8. Patton, P.C.: Drainage basin morphometry and floods. In: *Flood Geomorphology*, 51–64. Ed. by V.R. Baker, R.C. Kochel and P.C. Patton. John Wiley, New York (1988)

Chapter 114

Investigation of Seepage Channel Using Remote Sensing Technique in Jodhpur City, Rajasthan

Birendra Pratap, N. Janardhana Raju, and G.S. Yadav

Abstract Jodhpur city has been experiencing rising ground water levels. The water levels in many parts of the city especially in the old city area, Tripoliya market, Gantaghar, Nai Sarak, Chandpole, Sajoti Gate, Shivanchi Gate and housing busy markets have touched to even 1-2 mbgl., causing seepage in underground basement of shops and houses in these areas and weakening the foundations and reducing the lives of the buildings due to dampness of the walls. Traditional field survey methods for detection of seepage channel are costly and time consuming. In this study, a rapid, cost-effective remote sensing technique was used for finding out the seepage channel in these parts of Jodhpur city and adjoining areas. In the present study Landsat-7 ETM, multi-date image and survey of India toposheets were used for generation of different thematic maps of the study area. A three- step process, image acquisition, processing and analysis have been applied for identification of seepage channel through visual interpretation of the satellite imagery. Finally based on the prepared thematic maps, analysis of remote sensing imagery and delineation of major structural control over ground water seepage flow channel was done along the lineaments. These lineaments are providing easy conduit for movement of ground water and seepage path of flow of ground water towards the city area.

Keywords Satellite imagery • Landsat-7 • Thematic map • Image processing • Lineament

B. Pratap (✉)

Central Soil and Materials Research Station, New Delhi, India

e-mail: bpcsmrs@gmail.com

N.J. Raju

School of Environmental Sciences, Jawaharlal Nehru University, New Delhi, India

G.S. Yadav

Department of Geophysics, Banaras Hindu University, Varanasi, Uttar Pradesh, India

114.1 INTRODUCTION

Jodhpur is the second largest city of the Rajasthan founded by Rao Jhodhaji in 1459 A.D. The city has a unique water management system of ancient times and has a number of traditional water impounding structures, such as Baories (step wells) ponds, Jhalaras and open wells etc. and major water reservoirs Kailana – Takht sagar. The water supply was primarily designed to arrest rain water in impounding structure to provide sustained water supply to the population. Due to vagaries of monsoon these reservoirs were further connected with the Rajiv Gandhi Lift Canal (RGLC) which continuously supplies water to these reservoirs. However, to fulfill the ever increasing demand of growing population the storage capacity of these reservoirs has been increased resulting in enhancement of the water level of these reservoirs. Due to unforeseen conditions, some part of the city is facing rise in water table causing seepages in underground basements of houses and shops. Proper investigations in the affected area and its surroundings are therefore desirable in order to find out the seepage channel which supports the rise in water table.

The application of space technology has made remote sensing technique a very powerful tool for the solution of ground water problems and systematic analysis of various geomorphical units/landforms/lineaments due to the synoptic and multi-spectral coverage of a terrain. The synoptic coverage helps in delineating lithological, geomorphological and structural features of local, regional and continental extent depending upon the spatial resolution. Such informations are essentially required for planning and executing to solve the ground water problems, especially in inaccessible and hard rock terrain. Remote sensing technique is the most cost-effective and time saving. The special advantage of remote sensing observation from satellites is to provide data about the earth and its natural resources [1] in spatial format and large area coverage.

In this study, a rapid, cost-effective technique was applied for identification of seepage channel, which is the cause of rising of ground water table in Jodhpur city and adjoining area.

114.2 GEOLOGY AND HYDROGEOLOGY

The geological formation of Jodhpur city and adjoining areas are mainly composed of sedimentary rocks like sandstone, shale and limestone of Vindhyan super group with certain areas occupied by rhyolite suite [2,3]. These formations are highly deformed due to tectonic activities. It is believed that during these tectonic processes have resulted in the development of some major lineaments that have extended up to several kilometres towards the city area. Jodhpur city has a standard urban area and peculiar geomorphological setting. The old walled city part is located on hill slope area and in the base of the fort hill ridge. The land gradually turns to plain alluvium terrain towards south, east and S-W. The study area consists of a number of flat-topped hills of sandstone and rhyolite trending NE-SW direction. Rhyolite hills have

an irregular relief and rough surfaces, whereas sandstone hills have erosional flat tops. Some of the rhyolite hills have a few meter thick capping of sandstone exhibiting clear junction between the two types of the rock formations.

In the city, the geological formations like Malani rhyolite and Jodhpur sandstone are inter-layered with shales. The lower flow of Malani rhyolite are highly faulted, folded, weathered and fractured due to tectonic processes. Kailana lake and Takht Sagar are also situated on this type of rock formation. The Jodhpur group of rocks like shale and sandstone cover maximum area of old walled city. The shale and sandstone are deformed due to Neotectonic activity in the area.

Malani rhyolites, Jodhpur sandstone and quaternary alluvium are hydrogeological formation in the study area. Ground water in the area occurs under water table conditions. The different sets of joints, faults and fractures as well as clayey material and ash beds play very important roles in the circulation, distribution and movement of ground water.

114.3 MATERIALS AND METHOD

In this study Landsat-7 Enhance Thematic Mapper (ETM), multi-date image and survey of India toposheets 45F/3, 45F/4, 45B/15 and 45B/16 at 1:50,000 scale each was used for generation of thematic maps such as base map, relief map, slope map, aspect map and lineament map of the study area through visual interpretation of the satellite imagery. The identification and delineation of various units on the thematic maps were based on the image elements like tone/colour, shape, size, texture, pattern, association etc. The inferences drawn from the remote sensing technique has been cross checked in a few selected sites and confirmed from other scientific studies that have been carried out in the study area [4]. Geomorphological features and lineaments are deciphering attributes of ground water occurrences, movements and potentiality.

114.4 RESULTS AND DISCUSSION

Based on the interpretation of satellite imagery, together with available information on geology of the area and water level data of different water bodies [5,6] are inferred the results. The finding indicates a number of lineament sets traversing NNE-SSW has been identified from the imagery. The prominent water bodies viz. Kailana-Takht Sagar and Bal Samand and many of the ridges and hills lie along these lineament sets. Apart from these large numbers of prominent Joints traversing E-W direction and other sets in NW-SE, WNW-ESE and NNW-SSE directions are clearly visible in the imagery. Due to urbanization activity in the city the signature of these lineaments sets are not clear in the city area. It is expected that many of these joint sets continue in same direction in the city area below the ground. Two very prominent lineaments are seen in the lineament map. One originates near

Kailana-Takht sagar and continues for quite a long distance eastward and central alignment of Baiji ka talav and other water body east of it, the second lineament is aligned along the Gulab Sagar and Fateh sagar in the city area. Most of the lineaments coming from Kailana-Takht sagar and passing towards city area may affect the water movement in the city area bor surrounding aquifers providing zones of enhanced infiltration/seepage towards city.

114.5 CONCLUSIONS

The remote sensing techniques have been applied to study the surface features such as lineaments with the help of Landsat-7 ETM multi date image. Presence of joints and sets of lineament in ryolites was the major contributor to seepage of water from reservoir and resulting in the rise of ground water level in the Jodhpur City area. The continued existence of two major and several minor lineaments originating from Kailana-Takht sagar and passing through Dau ki Dhani and Ahkeraj ji ka talab towards city area. This lineament provide easy conduit for the movement of ground water in the city area from the Kailana-Takht sagar, which needs further confirmation by geophysical techniques and through ground truth verification.

ACKNOWLEDGEMENTS Authors are extremely grateful to Chief Engineer, Ground Water Department, Jodhpur, Rajasthan for his kind permission to share the data collection part as well as field work.

REFERENCES

1. Kasturirangan, K., Aravamudan, R. and Deekshitulu, B.L.: Indian remote sensing satellite (IRS-1C) the beginning of new era. *Current Science*, 70(7), 495–500 (1996)
2. Blanford, W.T.: Geological Notes on the Great Indian Desert between Sind and Rajasthan. *Rec. Geol. Surv. India*, 10(1), 1–54 (1877)
3. Paliwal, B.S.: Tectonics of the Post-Aravalli Mountain Building Activity and its Bearing on the Accumulation of Sediments along the Western Flank of the Aravalli Range, Rajasthan, India. *In: R. Ahmed and A.M. Sheikh (eds.), Geology in the South Asia-I Proc. of GEOSAS-I Islamabad, Pakistan, Feb. 23–27, 1992. Hydrocarban Development Institute of Pakistan, 1994, pp. 52–60.5 (1992)*
4. Pratap, Birendra: Some Problems of Ground Water and its Management Using Geophysical Techniques around Jodhpur city of Rajasthan, India. Ph. D. Thesis, Banaras Hindu University, Varanasi (2006)
5. Report on the water level fluctuations in observation wells existing in the Jodhpur city and surroundings. Unpublished report of the Ground Water Department, Govt. of Rajasthan, Jodhpur (2001)
6. Annual Report for the year 2001: Central Ground Water Board, Western Region, Jaipur (2001)
7. Pratap, Birendra and Yadav, G.S.: Identification of Recharge Source for Jodhpur City. *In: National Symposium on Water Resources Management in Changing Environment (WARMICE-2012), pp. 121–125 Proceedings WARMICE (2012)*

Chapter 115

Monitoring Snow Cover Area Using Different Algorithms on Indian Remote Sensing Data

Farjana Birajdar, Gopalan Venkataraman, and Hrishikesh Samant

Abstract In the present study, Advanced Wide Field Sensor (AWiFS) of Indian remote sensing satellite data is used to monitor seasonal snow cover measurement in Bhaga basin of Western Himalaya, Himachal Pradesh, India. The AWiFS images are being corrected topographically using ASTER Digital Elevation model. An attempt has been made towards estimation of snow cover using algorithms based on Normalized Difference Snow Index (NDSI), Normalized Difference of Cloud Index (NDCI) and Snow Under Vegetation (S3). Algorithm S3 is used for estimation of snow pixels in vegetation area without reference data. Algorithms NDSI and NDCI are involving NIR band of reflectance for snow pixel area. Comparison of the estimated snow cover using all the three algorithms is carried out which represent that the results estimated using S3 algorithm are more accurate than NDSI and NDCI algorithms.

Keywords Snow cover • Himalaya • NDSI • NDCI • S3

115.1 INTRODUCTION

Areal extent of snow cover area changes with time. However, slight variation of snow also affects the electric power generation, reservoir management, irrigation practices and flood control etc. which contribute to the national economy. The elements of snow are ice crystals, liquid water and air [6]. Due to the harsh and rugged terrain of Himalaya, it is very difficult to map and monitor seasonal snow cover using field methods [7]. Hence Remote-sensing techniques have been extensively used for snow-cover monitoring. Monitoring of Snow-cover using satellite

F. Birajdar (✉) • G. Venkataraman
Centre of Studies in Resources Engineering, Indian Institute of Technology Bombay,
Mumbai, India
e-mail: farjanabirajdar@gmail.com

H. Samant
Department of Geology, St. Xavier's College (Autonomous), Mumbai, India

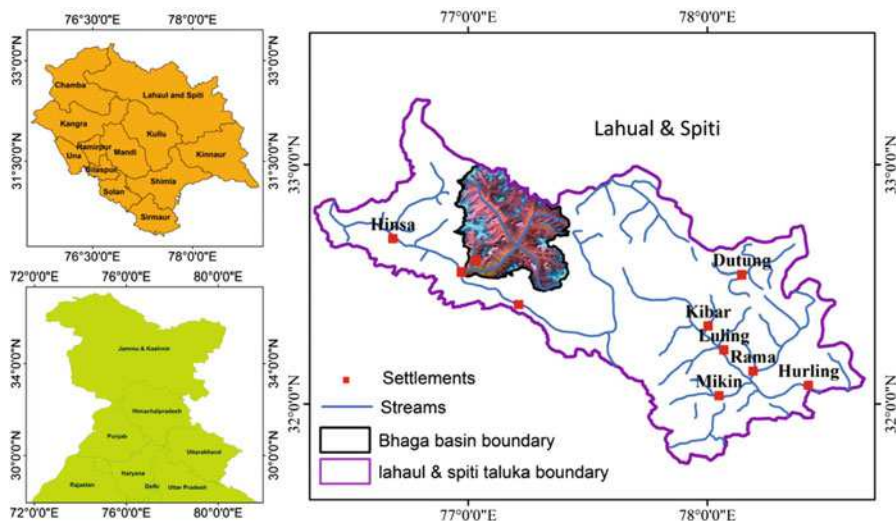


Fig. 115.1 Location map of study area

images started during April 1960 using the TIROS-1 satellite data [7]. The data from GOES, Meteosat, NOAA, AWiFS and Resourcesat have been used successfully for mapping of snow cover [1],[2]. 2

115.1.1 STUDY AREA

The study area comprises Bhaga basin ($76^{\circ}56'16.253''\text{E}$ to $77^{\circ}25'23.73''\text{E}$ longitude and $32^{\circ}28'19.656''\text{N}$ to $33^{\circ}0'9.887''\text{N}$ latitude), which is located at the north western Himalayan range. The Bhaga basin is the sub basin of Chenab basin lying under Lahaul - Spiti district of Himachal Pradesh, India (Fig. 115.1).

115.2 MATERIAL AND METHODS

Advanced wide field sensor (AWiFS) data of Indian remote sensing satellite has been used to monitor seasonal snow cover measurement. Geometric correction of AWiFS images have been carried out using IRS P6 LISS III images of 23.5 meter resolution. All the AWiFS images are being corrected radiometrically for atmospheric and topographic correction [5]. The slope matching technique is reported as most appropriate technique for measuring of snow cover in the harsh and rugged

Himalayan terrain [4]. Slope matching technique is applied on the topographically corrected AWiFS images and reflectance is estimated [4]. An algorithm, based on normalized difference snow index (NDSI), normalized difference of cloud index (NDCI) and snow under vegetation (S3) has been used to monitor snow cover area in Bhaga basin.

115.2.1 NORMALIZED DIFFERENCE SNOW INDEX (NDSI)

$$\text{NDSI} = (\text{Green} - \text{SWIR}) / (\text{Green} + \text{SWIR}) \quad (115.1)$$

NDSI is defined by above relation and it ranges from -1 to $+1$, where Green and SWIR are the reflectance of the Green and shortwave infrared bands respectively. A threshold value for NDSI has been defined for the pixels that are approximately 50-59% covered by snow from the imageries of different sensors. This threshold has been set by visual interpretation [3]. This computed reflectance value which is used for the calculation of the NDSI.

115.2.2 NORMALIZED DIFFERENCE CLOUD INDEX (NDCI)

$$\text{NDCI} = (\text{Red} - \text{SWIR}) / (\text{Red} + \text{SWIR}) \quad (115.2)$$

where Red and SWIR are the reflectance of the Red and shortwave infrared bands respectively. A threshold value for NDCI has been defined for the pixels that are approximately 60% or more covered by snow [4].

115.2.3 SNOW UNDER VEGETATION INDEX (S3 INDEX)

$$\text{S3 Index} = \text{NIR} (\text{Red} - \text{SWIR}) / (\text{NIR} + \text{Red}) (\text{NIR} + \text{SWIR}) \quad (115.3)$$

where NIR, Red and SWIR are the reflectance of the near-infrared, red (visible) and shortwave infrared bands respectively. S3 uses the reflectance characteristics of snow and vegetation to reduce the errors caused by snow covered area mixed with vegetation. Using visual interpretation technique, the threshold value of S3 index is defined for the pixels that are approximately 0.18% or more covered by snow and snow under vegetation has been defined [4].

115.3 RESULTS AND DISCUSSION

Snow cover mapping has been done by using AWiFS sensors data. The False Colour Composition (FCC) of the AWiFS data has been generated (Figure 115.2). The final snow cover map obtained by processing the AWiFS images and applying the threshold conditions for discriminating snow, cloud and snow under vegetation. The threshold value of 0.4 is defined for NDSI algorithm for the pixels those are approximately 50-59% covered by snow, The threshold value of 0.5 is assigned for NDCI for the pixels that are occupied by approximately 60% or greater by snow. Whereas, for S3 index the threshold value is distributed from 0.05 to 0.18 and assigned for snow cover area greater than 0.18%. Based upon the threshold values, the final snow cover map has been generated by assigning the threshold conditions of NDSI, NDCI and S3. Accuracy assessment is carried out on all the images and it is observed that S3 algorithms gives better accuracy on estimating the snow cover area (Table 115.1).

115.4 CONCLUSIONS

The estimation of snow cover under vegetation with high percentage of accuracy is possible in the hilly terrain like Himalaya. In the present study, after applying the topographic corrections using slope matching techniques on AWiFS images, NDSI

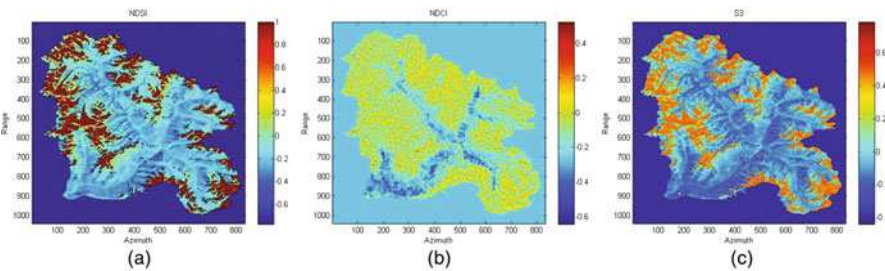


Fig. 115.2 (a) NDSI map, (b) NDCI map, and (c) S3 map of Bhaga basin

Table 115.1 Accuracy assessment of estimated snow covers area

Index	Date	Threshold	Precision	Error	Accuracy
NDSI	03/10/10	0.40	181	19	90.50
	25/03/10	0.40	182	18	91.00
NDCI	03/10/10	0.50	180	20	90.00
	25/03/10	0.50	188	12	94.00
S3	03/10/10	0.05-0.18	189	11	94.50
	25/03/10	0.05-0.18	191	09	95.50

and NDCI requires the reference data for identifying the snow under dense vegetation region, whereas S3 index does not require any reference data for identifying the snow area. Hence, S3 index is most suited for automatic identification of snow covered area with higher accuracy than NDSI and NDCI algorithms.

REFERENCES

1. De Ruyter de Wildt, M. and Seiz G. Gruen, A.: Operational snow mapping using multitemporal Meteosat SEVIRI imagery. *Rem. Sens. Environ.* 109 (1), 29–41 (2007)
2. Hall, D.K., Riggs, G.A. and Salomonson, V.V.: Development of methods for mapping global snow cover using Moderate Resolution Imaging Spectroradiometer (MODIS) data. *Rem. Sens. Environ.* 54(2), 127–140 (1995)
3. Khosla, D., Sharma, D.K. and Mishra, V.D.: Snow cover monitoring using different algorithm on AWiFS Sensor data. *Int. J. Adv.Eng. Sci. Tech.* 7 (1), 042–047 (2011)
4. Mishra, V.D., Sharma, J.K., Singh., K.K., Thakur, N.K. and Kumar, M.: Assessment of different topographic corrections in AWiFS satellite imagery of Himalaya terrain. *J. Earth Syst. Sci.* 118 (1), 11–26 (2009)
5. Nichol, J., Hang, L.K. and Sing, W.M.: Empirical correction of low sun angle images in steeply sloping terrain: a slope matching technique. *Int. J. Rem. Sens.* 27 (3–4), 629–635 (2006)
6. Rees, W.G.: Remote Sensing of Snow and Ice. In: CRC Press, Taylor & Francis Group: Boca Raton, FL, USA, pp. 99–117 (2006)
7. Singer, F.S. and Popham, R.W.: Non-meteorological observations from satellites. *Astronaut. Aerosp. Eng.* 1 (3), 89–92 (1963)

Chapter 116

Optimization of Neural Networks for Multisource Classification in a Glaciated Terrain

Aparna Shukla and Bisma Yousuf

Abstract In the present study, Artificial Neural Network (ANN) based semi-automatic multisource classification approach has been applied for the glacier terrain mapping in the Kashmir Himalayas (Kolahoi glacier) using integrated dataset comprising of multispectral Landsat TM data and several ancillary data layers (topographic attributes and transformed spectral bands). Terra ASTER data has been used for accuracy assessment. The study aims at selecting the best multisource dataset for classification and to investigate the impact of various neural network parameters on classification accuracy. The present study clearly demonstrates that selection of appropriate multisource dataset; network model and parameter values have a major influence on the performance of the ANN classification process.

Keywords Multisource classification • Glacier terrain mapping • Artificial Neural Network • Network parameters • Momentum factor • Training sample size

116.1 INTRODUCTION

Glacier component mapping is of utmost importance as it allows the quantification of glacier areas, volumes and mass balance. These measurements along with the estimation of debris cover over glaciers are considered to be key indicators of glacier health [5, 6]. Due to the remoteness, vastness and inaccessible nature of the mountain glaciers, remotely sensed data are likely the best and the only effective tool for regular mapping of glaciers in a comprehensive and effective manner [3]. Although various image processing techniques (band ratios, indices and classification based approaches) have been developed and employed by workers for glacier component mapping, some difficulties still exist in automatic mapping of glaciers due to the presence of spectrally similar classes such as debris, water, shadows and ice-mixed debris [1, 4]. Therefore additional information like

A. Shukla • B. Yousuf (✉)

Department of Earth Sciences, University of Kashmir, Srinagar, India

e-mail: bismaqazi13@gmail.com

topographic attributes, texture features, band ratios and indices, image transformations etc. have to be included in the classification process. Therefore, this study aims at exploring the potential of neural networks to select the best multisource. dataset for glacier terrain mapping (in Kolahoi glacier and adjoining areas, Jammu & Kashmir; latitude $34^{\circ} 15' N$ to $34^{\circ} 30' N$ and longitude $75^{\circ} 30' E$ to $75^{\circ} 45' E$) and the optimum structure for ANN that can produce better classification accuracy.

116.2 MATERIAL AND METHODS

The data used in this study comprises mainly of multispectral satellite images from Landsat-TM acquired on October 17, 2010, TERRA-ASTER dated October 18, 2010 & ASTER DEM. For performing the multisource classification for glacier terrain mapping, a series of sequential steps have been applied. Images have been first co-registered with each other. Then, the DN values in VNIR and SWIR bands of Landsat TM image have been converted to Top of Atmosphere reflectance units [2]. Further, ancillary data layers have been generated. Morphometric attributes like slope, aspect, profile and plan curvatures have been generated using ASTER DEM, while image transformations like band ratios (NIR/SWIR, Red/SWIR and Red/NIR), spectral indices (NDGI and NDSI), principal components (i.e. PC 2 of PC 124 and PC 2 of PC 345) and decorrelation stretch (DS2 of DS 124 and DS 345) have been derived from Landsat TM TOA reflectance image. The layers so generated have then been normalized. Subsequently, different training samples of varying sizes (discussed later) have been extracted for eight glacier terrain classes viz. snow, water, shadow, vegetation, bare, ice-mixed debris (IMD), supraglacial debris (SGD) & periglacial debris (PGD). Thereafter, 15 different cases have been formulated by adding one ancillary data layer to spectral data each time and classification has been performed using Idrisi software. The maps so generated have been evaluated for their accuracy against the reference dataset (855 testing pixels using the stratified random sampling technique) prepared from the ASTER image of the area. The highest overall accuracy and kappa coefficient i.e. 83.74% & 0.8066 resulted from a combination of spectral bands and NIR/SWIR layer. Eventually parameterization has been carried out on this dataset.

116.3 RESULTS AND DISCUSSION

116.3.1 *Effect of Number of Hidden Nodes*

To investigate the effect of number of hidden nodes on the classification accuracy, the default number of nodes in the hidden layer (7) has been increased and decreased by a value of 1 while keeping other parameters constant. In this way,

13 neural network models were configured here with the number of hidden nodes ranging from 3-16. Results reveal that the overall accuracy rises to 83.98% and kappa coefficient to 0.8089 as the number of hidden nodes is increased to 8. This accuracy gradually decreases as the number of hidden nodes is increased from 8 up to 11 and then it suddenly drops to as low as 75.09% when 12 hidden nodes have been used. After this, the accuracies again rise to 80% for 13 & 14 hidden nodes and then finally decrease for 15 & 16 hidden nodes to the lowest.

116.3.2 Effect of Learning Rate

In these experiments, the default value of learning rate i.e. 0.2 has been altered by an interval of 0.05, and ranging from 0.05 to 0.3. However the results obtained in this case show deviation from those obtained by various researchers and therefore, some more experiments have been carried out in this case using small learning rate intervals of 0.025, 0.075 & 0.125. It has been observed that as the learning rate is increased to 0.2, the overall accuracy and kappa coefficient gets increased by more than 3% and 0.0458 respectively. As the learning rate is further increased to 0.25, the accuracy temporarily decreases & then slightly increases again at a learning rate of 0.3, thus showing minor fluctuations.

116.3.3 Effect of Momentum Factor

Momentum factors have been altered from 0.3 to 0.9 at an interval of 0.1, thus forming 6 experiments. Results obtained here show that the overall accuracy increases from 81.87% to 83.74% and kappa coefficient from 0.7845 to 0.8066 on increasing the momentum factor from 0.3-0.5, however the accuracy plunges to 66.32% when the value is further increased to 0.8 and with a momentum factor of 0.9, the network training fails to converge. From these results, it can be concluded that the overall classification accuracy tends to increase with increase in momentum factor up to a certain point beyond which it does not give satisfactory results.

116.3.4 Effect of Number of Iterations

Here, the default value of iterations (1000) has been altered by 500 in a range of 500 to 4500 which result in 8 neural network models. The highest overall accuracy and kappa coefficient of 84.21% and 0.8126 respectively have been achieved on increasing the number of iterations to 2500; however, between two iteration numbers (1000 & 2000), it temporarily decreases to 82.22%. On further increase, the trend becomes quite unsteady and finally the accuracy decreases to 81.40% or

below (79.18%) at 3000 or above iterations (4500). In a nutshell, increase in the number of iterations up to 2500 leads to a significant increase in the classification accuracy but this trend slows down with further increase in number of iterations.

116.3.5 Effect of Training Sample Size

In case of training data, 3 different architectures have been developed with 20, 30 and 37 training pixels per class respectively. Results obtained here confirm that overall classification accuracy shows a slight improvement by 0.35% & kappa coefficient by 0.0062 with increase in the training sample size (20pixels/ class). However this improvement is not gradual and continuous; between two sample sizes (20 and 37pixels/ class), the accuracy temporarily decreases to 83.98% and then again shows an increase to 84.09% as achieved with 20 training pixels/ class. This indicates that there is a scope for classification accuracy to increase with increase in the training sample size.

116.4 CONCLUSIONS

The utilization of multisource data in image classification shows considerable potential for increasing the classification accuracy. The integration of NIR/SWIR layer with the spectral data has enhanced the overall accuracy by more than 9% than that produced by spectral data alone. With the parameterization of this network, there has been a significant improvement in the classification accuracy from 83.74% to 84.80% as compared to non- parameterized network of this dataset. Further, the individual accuracies (PA) of snow, water, SGD & PGD have remarkably enhanced by 5.32%, 35.9%, 17.95% & 3.77% respectively when the spectral and NIR/SWIR dataset was subjected to parameterization. Apparently, three neural net parameters viz. number of hidden nodes, number of iterations and training sample size have been found to have a significant effect on classification accuracy. Besides, there exists an optimal range for all the neural net parameters within which a neural network can classify and offer satisfactory results.

REFERENCES

1. Bolch, T. and Kamp, U.: Glacier Mapping in High Mountains Using DEMs, Landsat and ASTER data. *Grazer Schriften der Geographie und Raumforschung*, 41: 37–48 (2006)
2. Chander, G. and Markham, B.: Revised Landsat-5 TM Radiometric Calibration Procedures and Post-calibration Dynamic Ranges. *IEEE Transactions on Geoscience and Remote Sensing*, 41 (11): 2674–2677 Part 2 (2003)

3. Kaab, A.: Glacier volume changes using ASTER optical stereo. A test study in Eastern Svalbard. *IEEE Transactions on Geosciences and Remote Sensing* 10: 3994–3996 (2007)
4. Paul, F., Huggel, C. and Kaab, A.: Combining Satellite Multispectral Image Data and a Digital Elevation Model for Mapping Debris-Covered Glaciers. *Remote Sensing of Environment*, 89(4): 510–518 (2004)
5. Racoviteanu, A.E., Williams, M.W. and Barry, R.G.: Optical Remote Sensing of Glacier Characteristics: A Review with Focus on the Himalaya. *Sensors*, 8, 3355–3383 (2008)
6. Tiwari, R.K., Gupta, R.P., Gens, R. and Prakash, A.: Use of optical, thermal and microwave imagery for debris characterization in Bara-Shigri glacier, Himalayas, India. Geoscience and Remote Sensing Symposium (IGARSS), 2012 I.E. International, 4422–4425 (2012)

Chapter 117

Generation of Stream Length Gradient Index Map Using Visual Basic Program – A Case Study from South India

A.C. Dinesh, Vipin Joseph Markose, and K.S. Jayappa

Abstract This study investigates the spatial variations of SL using visual basic computer program called R. Profiler. The graphical interface of R. Profiler allows the user to calculate the SL easily and draw the river long profiles. In order to check the efficiency and accuracy, R. Profiler is validated by using the drainage networks data of Kali River basin of southern India. The digitized data were converted into .txt format and imported into R. Profiler. Using query option, streams of third order and above have been selected and calculated the SL automatically. The calculated SL values of each portion of the river were converted into point shapefile and prepared the spatial map by using Inverse Distance Weighted (IDW) interpolation method available in ArcGIS 9.3. The results show that, R.Profiler is effective in calculating SL using the text data of ESRI line shapefile as an input.

Keywords Visual basic 6 • R.profiler • DEM • GIS • Kali river • India

117.1 INTRODUCTION

Stream length-gradient index describes the morphology of stream network using distribution of topographic gradients along rivers. This was first used to reflect stream power or differential rock erodability [1]. At present it became an important tool in the identification of neotectonic deformation along the stream channel network [2]. Along with SL, longitudinal river profiles are also used as a key topographic signature to identify lithologic, tectonic, climatic, and base level effects. SL analysis has been used for detecting the impact of differential uplift on drainage systems using DEM to understand landforms in relation to the tectonics of Normandy intra plate area of NW France [3]. A MATLAB toolbox called TecDEM was developed which includes a suite of algorithms to analyze various

A.C. Dinesh (✉)

M&CSD, Geological Survey of India, Kolkata, India

e-mail: acdinesh@rediffmail.com

V.J. Markose • K.S. Jayappa

Dept. of Marine Geology, Mangalore University, Mangalore, India

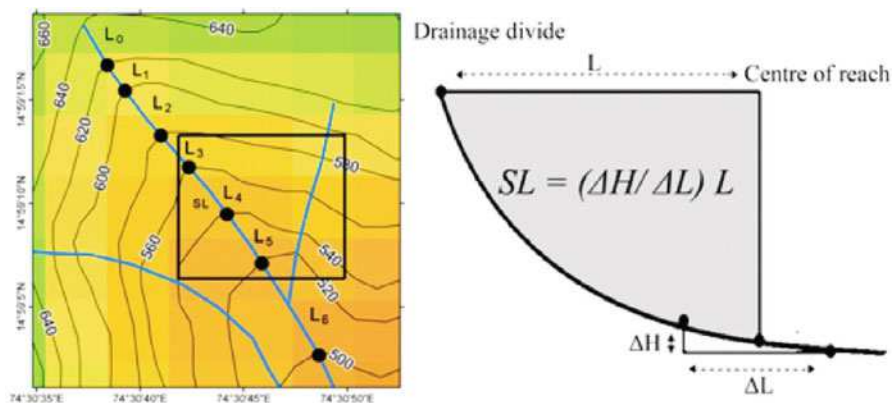


Fig. 117.1 Methodology for SL calculation

geomorphic indices including SL [4]. The program R. Profiler was developed in Visual basic 6 which can be used for calculation of stream length gradient index. The package consists of several modules developed for drainage network processing and SL calculation.

117.2 SL CALCULATION

Stream length-gradient index can be calculated using the following formula [117.1]:

$$SL = (\Delta H / \Delta L) L \quad (117.1)$$

where SL is stream length gradient index, L is the total channel length from the midpoint of reach where the index is calculated to the highest point in the upstream of the channel, $\Delta H / \Delta L$ is the channel slope or gradient of the reach, and ΔH represents the change in elevation for a particular channel of the reach with respect to ΔL that symbolizes length of the reach (Fig. 117.1).

117.3 R. PROFILER DEVELOPMENT

The program R.Profiler was developed in Visual basic 6 which can be used for calculation of stream length gradient index. The package consists of several modules developed for drainage network processing and SL calculation. The described package is designed to work on networks with Strahler's stream order in ESRI line shapefile format. For performing the analysis; one can use digitized contours and

drainage networks with the stream order of Strahler method [5] or extracted from the Digital Elevation Model (DEM) data. In the case of DEM derived drainage networks; one particular order of the stream is split into different segments whenever a lower-order stream joins. Using 'R.Profiler, the split lines will merge into a single line feature. In order to calculate SL, it is necessary to identify a trunk stream within the drainage networks. In large watersheds several trunk streams of different orders needed for SL calculation. In this study a new method of trunk stream selection is implemented based on the length of the channel. The interface coupled with the algorithm can easily identify the trunk stream within the watersheds. The tracing start from the last river segment of highest order in the basin, which has no downstream connections. Then the software traces the next longest lower order stream which connects the first selected channel. This procedure will continue until it reaches the first order stream. Once the tracing is over it is necessary to merge the traced features into a single feature. After merging, the process of tracing will start with the next lower order stream. This process can continue up to second order streams. Once the process is over a group of major channels of different orders can be generated which can be used for SL calculation. First, the user converts the shapefile into .txt format in ArcGIS and then imports into R.Profiler. In the *data window*, the user is asked for the location of the data which contains the starting and ending coordinates of the lineaments. The .txt data file contains the FID of the feature class, latitude and longitude of each node. Once, the data is imported, press the sub-menus '*All points*' and '*end points*' that allow the program to read and format the data. Then the user has to press '*stream order*' button. Drainage lines have been split at a point where the line intersects with the contour and given the elevation value for each segment. The length ΔL was measured along the main stream, between the intersections of two successive contours.

117.4 TESTING AND EVALUTION

The Kali River, one of the west flowing rivers of Karnataka, originates in the Western Ghat (Sahyadri) at an altitude of 900m forms the study area. It covers a total drainage area of 4,837km², extending from 14°43'1.8" to 15°33'44.9" N latitudes and 74°05'7.63" to 74°57'39.05" E longitudes in the Uttara Kannada district of Karnataka, India. The calculated SL values of each reach of the analyzed streams were converted to point shapefile. The spatial map of SL was prepared by SL point shapefile by Inverse Distance Interpolation method available in ArcGIS 9.3. The SL values of the study area range from 0.017 - 9700 and grouped into nine classes (figure 117.2). In the upper part of the basin, SL shows low Fig. 117.2 values compared to the middle and lower parts where it shows increasing trend. The Kali River has captured the east flowing river and expanded its watershed boundary up to 130km from the coast when compared to other west flowing rivers which have about 40 to 60km. The river capture area shows high SL values with deep V shaped valley and gorges which are deeper up to 300m. and 3 to 5km long. In an analysis of

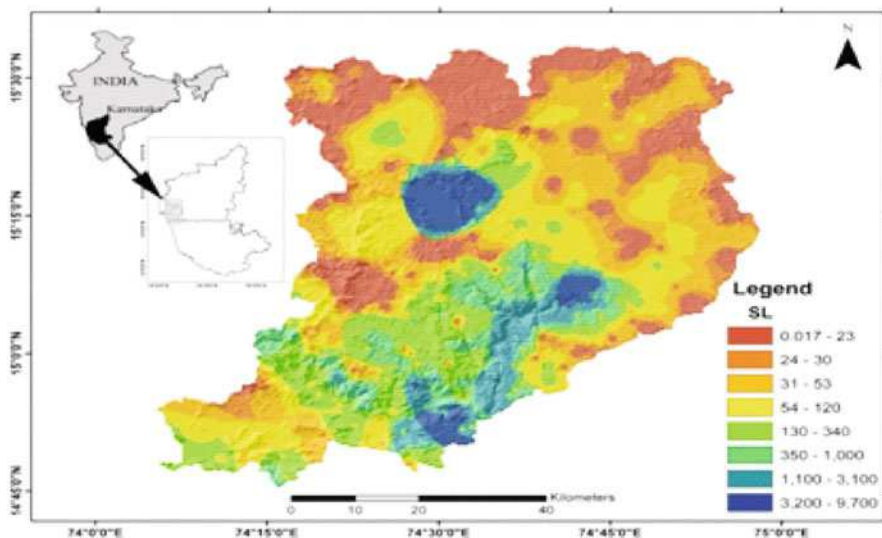


Fig. 117.2 Map showing location and spatial distribution of SL in Kali river basin

river profile, it is difficult to identify the locations of knick points, but SL map overcome this limitation. Another advantage of SL map is that it can be used for identification of steeper river segments which do not have well defined knickpoints. The disadvantage of this map is irregular distribution of high density SL points near riverheads where contours are closely spaced. Geostatistically, constant spacing of SL points in a horizontal plane will yield better results in interpolation.

117.5 CONCLUSIONS

In this attempt, GIS utility software R.Profiler is developed that allows users to calculate the stream length gradient index. An experimental results show that, R. Profiler is effective in calculating SL. The tool can handle a large number of line features at any scale and presents the analytical results quantitatively. We have tested R.Profiler in an investigation of morphometric parameters of the Kali river basin of southern India.

REFERENCES

1. Hack, J.T.: Stream-profile analysis and stream-gradient index. U.S. Geol. Sur. Jour. Res. 1, 421-429 (1973)

2. Font, M. Amorese, D. and Lagarde, J.L.: DEM and GIS analysis of the stream gradient index to evaluate effects of tectonics: The Normandy intra plate area (NW France). *Geomorphology*, 119, 172–180 (2010)
3. Missura, R.: Análise morfoestratigráfica da Bacia do Ribeirão dos Poncianos/MG. Rio Claro, 2005. 136 p. Tese (Mestrado) – Universidade Estadual Paulista. Unpublished. (2005)
4. Shahzad, F. and Gloaguen, R.: TecDEM: A MATLAB based toolbox for tectonic geomorphology, part 1: drainage network preprocessing and stream profile analysis. *Computers & Geosciences*, 37, 250–260 (2011a)
5. Strahler, A.N.: Quantitative analysis of watershed geomorphology. *Transactions of the American Geophysical Union* 38, 913–920 (1957)

Chapter 118

Three Dimensional Quantitative Extraction and Integration for Geosciences Information: A Case Study of Nannihu Mo Deposit Area

Li Ruix, Wang Gongwen, Zhu Yanyan, and Qu Jianan

Abstract Mineral prospectivity mapping (MPM) is one of the most crucial steps in mineral resources exploration and assessment, which aims to delineate prospective areas within the region of interest through integrating and analyzing diverse geoscience datasets including geological data, geophysical data, geochemical data and remote sensing data. With the help of geographic information system (GIS), we have realized many MPM methods in 2D in the past few decades. Now, with the development of 3D geological modeling and the requirement of deep prospecting, mineral resources potential evaluation also extends to 3D space. In this paper, we establish relevant solid models of study area and rasterize them into block models with Micromine, then, we use a single standalone mineral resources prediction and evaluation application GeoCube to integrate the anomaly information exported from Micromine and evaluate the mineralization potential of study area.

Keywords Mineral prospectivity mapping • 3D geological modelling • Multi-source information integration

118.1 INTRODUCTION

Due to the constraints of detection techniques, data mining capabilities and degree of geological exploration, the type of data we can acquire are generally based on 2D, with the development of GIS, many GIS-based MPM methods have been realized in 2D by some software packages, such as ArcWofE, ArcSDM and GeoDAS. However, geological information essentially exists in 3D space, and the depth is especially indispensable under the need of deep ore prospecting. 3D geological modeling has been regarded as an essential method to interpret and present the surface and subsurface geology. Several software systems have been developed for 3D geological modeling, such as GOCAD, Micromine and Surpac.

L. Ruix (✉) • W. Gongwen • Z. Yanyan • Q. Jianan
State Key laboratory of Geological Processes and Mineral Resources,
China University of Geosciences, Beijing, China
e-mail: lrsgis@gmail.com

In this study, 3D geological models are constructed with a series of boreholes, geological maps, geological exploration cross sections and digital terrain model (DTM) data, geochemical models is according to 26000 geochemical sampling point data and 3D geophysical models (e.g., gravity and magnetic data) is constructed by 4095 geophysical exploration point data. We must convert the solid models to block models for quantitative calculation even though the former is closer to reality, and most 3D geological modeling software provide the function of rasterisation.

118.2 STUDY AREA

The case study area is Luanchuan ore field (Fig. 118.1), which is situated in the southwest of Henan province, China. It mainly consists of Nannihu porphyry-type Mo (W) deposit, Sandaozhuangskarn-type Mo (W) deposit, Shangfanggou porphyry-type Mo (Fe) deposit and other porphyry-type or skarn-type polymetallic deposits (e.g., Shibaogou, Yuku, Maquan) around them.

The study area is tectonically located in the east of the Nannihu Mo polymetallic-metallogenic belt along the southern margin of the North China Craton [1-3]. The main hosted strata in the study area are the Middle Proterozoic Guandaokou Group and the Upper Proterozoic Luanchuan Group. The Guandaokou Group (ca. 100 m thick) is composed by fluvial-neritic facies clastic-carbonate rocks, or carbonate rocks containing stromatolites. The Luanchuan Group (ca. 3100 m thick) consists of shallow marine carbonate-clastic rocks, of which approximately 2050 m (i.e., the Meiyaogou, Sanchuan and Nannihu Formations) is associated with mineralization

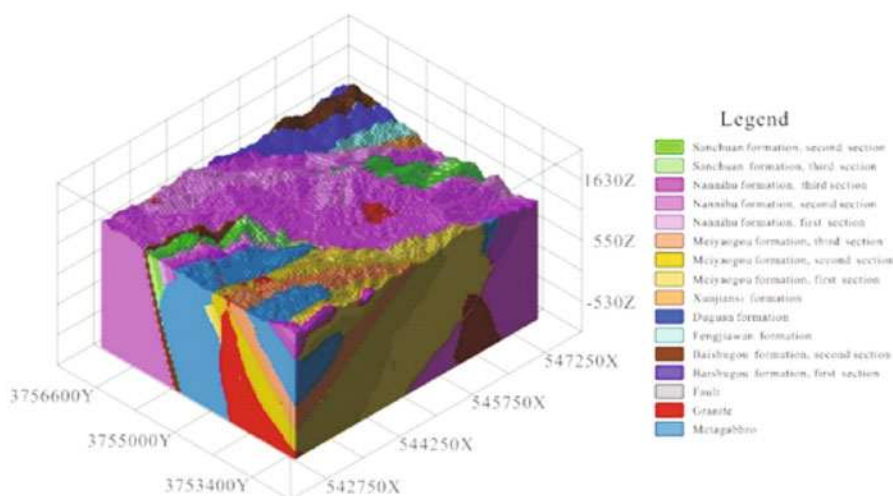


Fig. 118.1 3D geological model of study area

[2, 3]. Regional fault structures and fold structures are well-developed in the study area. There are small rocks formed in the intersection of the NWW-trending and NNE-trending faults, which control the formation of Mo deposits. Late Proterozoic syenite, metamorphic gabbro, and Jurassic granite porphyry are associated with mineral resources in the study area. Porphyry-skarn Mo (W) deposit and skarn-type polymetallic sulfide deposit are mainly distributed in the center belt of the geochemical anomaly [4]. According to Re-Os isotopic dating, large-scale Mo mineralization occurred about 140 Ma [1, 4].

118.3 METHODOLOGY

118.3.1 *Three Dimensional Geological Modeling*

Combined with the genesis model of typical porphyry-skarn deposit of this study area, we collect diverse of datasets including geology, geophysics and geochemistry data, with the help of 3D visualization geological modeling software, we can establish 3D geological model (e.g., stratum, rock, fault), 3D geophysical model (e.g., gravity continuation, gravity inversion, magnetism continuation, magnetism inversion), 3D geochemical model (Mo anomaly) and 3D Mo ore body model.

118.3.2 *Comprehensive Information Integration*

In this case, we will use weights of evidence (WofE) method to integrate diverse geoscience datasets and calculate the posterior probability of study area. WofE is a kind of multivariate statistical model based on Bayes rule and probabilistic uncertainty theory [5, 6]. WofE is a knowledge-driven MPM method, we need a known deposit layer as training layer and several indicator layers related to mineralization as evidential layers. The computing processes of WofE can be divided into two steps: (1) Calculating the weights of each evidence layer, for the i th evidence layer, represents the weight on its presence, and represents the weight on its absence. (2) Calculating the posterior probability of each unit cell based on the weights obtained in step (1).

118.4 CONCLUSIONS AND DISCUSSION

The result of information integration is not the entire study area but the union of all of the valid evidential layers, and the prediction result is composed of a number of unit cells which have a value between 0 and 1, represents the posterior probability.

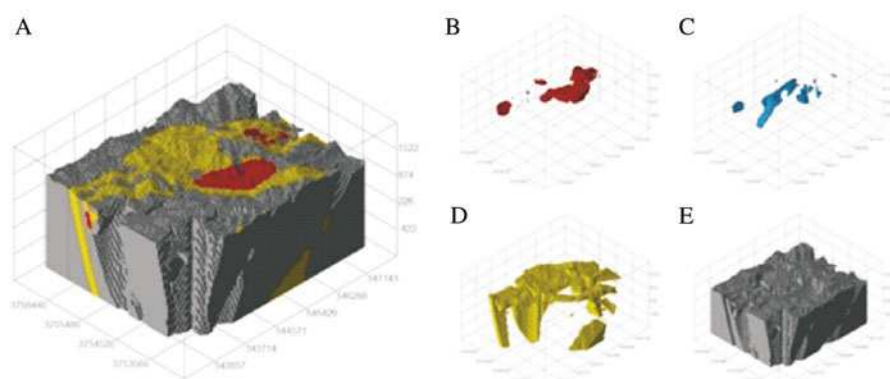


Fig. 118.2 A: Overall view of prospect area. B: First level prospect area. C: Second level prospect area. D: Third level prospect area. E: Background value

In this study, the range of posterior probability is from 0.0038 to 0.7881, of which about 68% of unit cells (457612 cells) distribute in the minimum 1% interval of posterior probability range, about 97% of unit cells (646786 cells) distribute in the minimum 10% interval of posterior probability range and less than 1% of unit cells (6280 cells) distribute in the maximum 73% interval of posterior probability. The study area is divided into three levels of prospect areas and background by the fractal method, the classification result is as shown in Fig. 118.2.

In this case, we build relevant 3D solid models and convert them to block models with Micromine. Then, we apply weights of evidence method to integrating diverse of abnormal information and calculating the posterior probability with GeoCube. Finally, we use fractal method to delineate prospecting target area. According to the geometric relation between the ore body model and other models (e.g., stratum, fault and rock) of the study area, we can find that the north, northwest and southeast of known Nannihu ore body are favorable for prospecting, the mainly strike of ore body in study area is northwest, and the northeast area is the mineral area.

REFERENCES

1. Ye, H.S., Mao, J.W., Li, Y., Yan, C.H., Guo, B.J., Zhao, C.S. and Chen, L.: Characteristics and metallogenic mechanism of Mo–W and Pb–Zn–Ag deposits in Nannihu ore field, Western Henan Province. *Geoscience*, 20(1), 165–174 (2006)
2. Wang, G., Zhang, S., Yan, C., Song, Y., Sun, Y., Li, D. and Xu, F.: Mineral potential targeting and resource assessment based on 3D geological modeling in Luanchuan region, China. *Computers & Geosciences*, 37(12), 1976–1988 (2011)
3. Wang, G., Zhang, S., Yan, C., Xu, G., Ma, M., Li, K. and Feng, Y.: Application of the multifractal singular value decomposition for delineating geophysical anomalies associated with molybdenum occurrences in the Luanchuan ore field (China). *Journal of Applied Geophysics*, 86, 109–119 (2012)

4. Mao, J., Ye, H. and Wang, R.: Mo and vein-type Pb–Zn–Ag ore deposits in the eastern Qinling, Central China and its implication for prospecting. *Geological Bulletin of China*, 28(1), 72–79 (2009) (in Chinese).
5. Agterberg, F.P.: Combining indicator patterns in weights of evidence modeling for resource evaluation. *Nonrenewable Resources*, 1(1), 39–50 (1992).
6. Bonham-Carter, G.: Geographic information systems for geoscientists: modelling with GIS (No. 13). Elsevier (1994)

Chapter 119

Multi-Classifer Fusion for Land Use Land Cover Mapping in Jharia Coal Field

Sumit Kumar Chaudhary, Dheeraj Kumar, and M.K. Jain

Abstract Open cast mining process destroys landscapes, forests and wildlife habitats due to clearance of trees, plants, and topsoil. This results in ecological degradation such as soil erosion, destruction of agricultural land, water pollution, etc. Therefore mapping and monitoring of landscapes for temporal detection is extremely essential. A study of application of data fusion techniques for mapping of land use cover has been carried out for a mining coalfield in order to ascertain potential impact of mining activities on flora and fauna. The study has incorporated pixel level Image fusion process as well as decision level fusion procedures. High Pass Filter (HPF) method based on pixel level fusion is applied to fuse the multispectral (MS) and panchromatic (PAN) image of Landsat ETM+ data. The fused MS image is classified into seven land use categories viz. agricultural land or open shrub, water bodies, dense vegetation, built-up land, barren land, mining area and overburden dump area using different classifiers. The selected classifiers are maximum likelihood, mahalanobis distance and support vector machine. The Naive Bayes classifier fusion rule on abstract level is applied to integrate the decisions from each classifier. The result of accuracy assessment shows an little increment of 0.41% and 0.73% in both classification accuracy as well as kappa coefficient in comparison to single classifier with the highest accuracy.

Keywords Multi-classifier fusion • Mapping • Land use land cover • Temporal • Multispectral image

S.K. Chaudhary (✉) • D. Kumar
Department of Mining Engineering, Indian School of Mines, Dhanbad, India
e-mail: sumit.mathe@gmail.com

M.K. Jain
Department of Environmental Science and Engineering, Indian School of Mines,
Dhanbad, India

119.1 INTRODUCTION

Assessing and monitoring the Land Use/Land Cover (LU/LC) mapping is key requirement in scientific research, planning and management of natural resources in rapidly changing ecosystem [1–3]. Remote sensing (RS) techniques paved the path in the study of LU/LC mapping and change analysis in practical and economical point of view. Because of the inherent capacity of systematic observations at various resolutions, RS technology extends possible data archives from present time to over several decades back [2]. Image classification is one of the most important steps in extracting LU/LC information for RS datasets. There are numerous methods of classification available in literature viz. Maximum Likelihood Classifier (MLC), Minimum Distance Classifier (MDC), Mahalanobis Distance Classifier (MahDC), Support Vector Machine (SVM), Spectral Angle Mapper (SAM), Neural Network (NN), etc. In most of the cases, one single classifier could not perform well in all the sample characteristics. It was further observed that different classifiers resulted in separate misclassified groups [4]. That means different classifiers used complementary information for decision-making in classification procedure. Multi-classifier fusion used such complementary information for integration of decision maps [4, 5]. In this paper, an experiment was carried to analyse the ability of multi-classifier fusion techniques for accurate assessment of land use pattern of Jharia Coalfield (JCF), one of the major coalfields of India.

119.2 STUDY AREA

The study area (approximately 280 sq. km) falls in the vicinity of Damodar River valley nearby Dhanbad town towards north-west of Kolkata. The field accounts for 100% of the country's prime coking coal production. It includes a diversity of land cover classes, which are changing very rapidly due to widespread of mining activities.

119.3 METHODOLOGY

The methodology comprises data fusion of high resolution panchromatic (PAN) and multispectral (MS) images, then classification of fused data using selected classifiers, and finally classifier fusion procedure applied on single classifier decision map. Geo-corrected Landsat-7 ETM+ data acquired during Feb, 2003 were downloaded from U.S. Geological Survey (USGS) website and the pertaining study area was extracted. The high pass filter (HPF) method of pixel based image fusion was selected to enhance the spatial resolution of MS image at the PAN image resolution [6]. The classes were recognised as dense vegetation, sparse vegetation,

water bodies, built-up land, barren land, quarries, and overburden land after visual image interpretation, and signatures for each class were created. MLC, MahDC and SVM based classifications were performed on spatially enhanced image. Contingency (or Confusion) matrices for each method were also determined by utilising training samples. The Naive Bayes Combination (NBC) method [7] was applied to integrate the decision maps and result was compared with Majority Voting (MV) method [4, 5]. The pixel based accuracy assessment of output maps from single classifiers and multiple classifier fusion methods has been carried out with the help of 1233 reference points. The entire work was carried out using ERDAS IMAGINE and MATLAB software.

119.4 RESULTS AND CONCLUSIONS

The total accuracy and Kappa statistics for each of the methods are given in Table 119.1. A slight increment of 0.41% and 0.73% in the classification accuracy as well as kappa coefficient were observed with NBC method over MLC method. The highest classification accuracy was also observed with NBC method in comparison to all other selected methods as depicted in Table 119.1. An approximately similar result was also found in case of the MV and single classifier MLC method. However, NBC yielded better result than all single classifier methods as well as MV method of multi-classifier fusion. The LU/LC statistics in case of NBC, MV and MLC are given in Table 119.2. Fig. 119.1 shows the resultant LU/LC map of JCF. Based on the analysis of the results obtained from the study, following conclusions

Table 119.1 Comparison of classification accuracy

	Single Classifier			Multi-classifier fusion	
	MLC	MahDC	SVM	MV	NBC
Total Accuracy	78.75%	76.97%	76.97%	78.75%	79.16%
Kappa Statistics	0.7500	0.7293	0.7301	0.7506	0.7555

Table 119.2 LU/LC statistics for different methods output map

Class	NBC		MV		MLC	
	Area (km ²)	% Area	Area (km ²)	% Area	Area (km ²)	% Area
Forest vegetation	57.2	14.90	58.54	15.25	54.97	14.32
Non-Forest vegetation	231.31	60.26	233.25	60.77	230.37	60.02
Water bodies	12.87	3.35	10.04	2.62	7.16	1.87
Barren land	4.37	1.14	4.56	1.19	8.11	2.11
Built-up land	30.76	8.01	32.96	8.59	48.42	12.62
Quarries	25.55	6.66	26.91	7.01	19.16	4.99
Overburden	21.77	5.67	17.55	4.57	15.62	4.07
Total	383.83	100.00	383.81	100.00	383.81	100.00

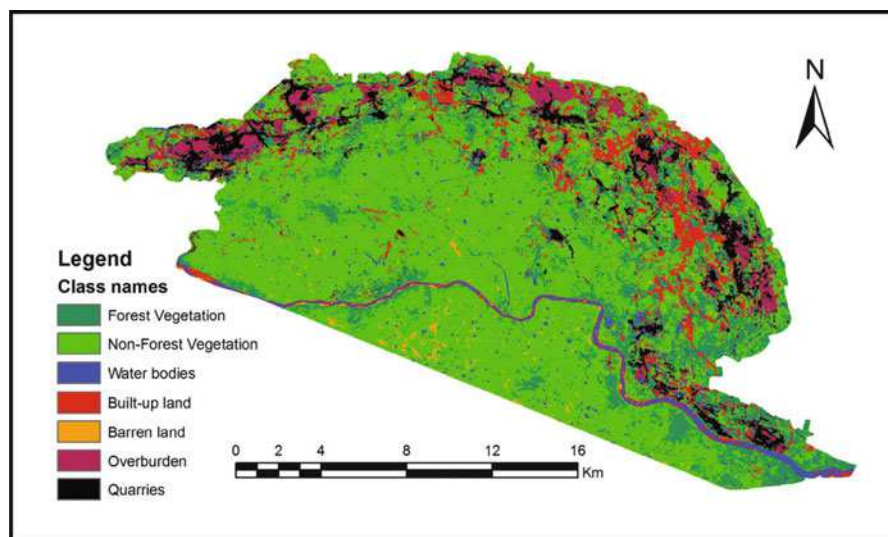


Fig. 119.1 The LU/LC map of JCF in case of NBC method

may be drawn. The NBC method gives better performance in comparison to the MV method for improving the accuracy in land use/land cover assessment of an area undergoing rapid changes due to mining activities, but in fact these methods don't show significant increment in accuracy over single best classifier. The performances of these methods can be further improved by choosing suitable classifiers for fusion with the help of diversity analysis. There are a number of methods of classifier fusion, which needs to be understood and analysed by comparing their performances. The sturdy evaluation of these techniques ultimately results into improved image analysis and land cover mapping.

ACKNOWLEDGEMENTS We are grateful to US Geological Survey, USA for providing the Landsat-7 ETM+ imagery of my study area. We are also thankful to Indian School of Mines, Dhanbad for their infrastructural support.

REFERENCES

1. Foody, G.: Status of land cover classification accuracy assessment. *Remote Sensing of Environment*, 80(1), 185–201 (2002)
2. Xie, Y., Sha, Z. and Yu, M.: Remote sensing imagery in vegetation mapping: A review. *Journal of Plant Ecology*, 1(1), 9–23 (2008)
3. Yuan, F., Sawaya, K., Loeffelholz, B. and Bauer, M.: Land cover classification and change analysis of the Twin Cities (Minnesota) Metropolitan Area by multitemporal Landsat remote sensing. *Remote Sensing of Environment*, 98(2), 317–328 (2005)

4. Ma, H., Zhou, W., Dong, X. and Xu, H.: An empirical research of multi-classifier fusion methods and diversity measure in remote sensing classification. *In: First International Workshop on Knowledge Discovery and Data Mining (WKDD)*, (2008)
5. Zhao, Q. and Song, W.: Remote sensing image classification based on multiple classifiers fusion. *In: 3rd International Congress on Image and Signal Processing (CISP)*, vol. 4, pp. 1927–1931 (2010)
6. Kuncheva, L.: Combining pattern classifiers: Methods and algorithms. John Wiley & Sons (2004)
7. Chavez, P., Sides, S. and Anderson, J.: Comparison of three different methods to merge multiresolution and multispectral data – Landsat TM and SPOT panchromatic. *Photogrammetric Engineering and Remote Sensing*, 57(3), 295–303 (1991)

Chapter 120

Land Use and Land Cover Changes and Their Impacts on Floods in Pampa River Basin in Kerala: A Remote Sensing Based Analysis

N.A. Mayaja and C.V. Srinivasa

Abstract The basin characteristics of Pampa River – the third largest river of the State of Kerala, flowing through the heart of central region of the State – has undergone tremendous variations in the recent past. Alternating cycles of recurring flood and drought has become a predominant feature of this river, which, once used to be a rich and sustainable source of water throughout the seasons and lifeline for a population. The rapid pace of urbanization, massive encroachment of river banks, deforestation, transition in the agricultural pattern etc transformed the land use pattern of this river basin. A large number of villages and densely populated regions on the bank of this river face the ravage of flood every year. In this context, this study attempts to evaluate the land use and land cover (LULC) changes occurred in Pampa river basin during the last decade i.e., 2001-2010, identify the human intervention factors as well as the possible impacts of these factors on the floods occurring in this river basin.

Keywords Land use land cover • Pampa river basin • River floods

120.1 INTRODUCTION

The extensive socio-economic transitions that happened during the last decades in the State of Kerala in general and the Travancore region (the mid-region of the State) in particular lead to increased rate of infrastructure development and profuse landscape changes. The basin characteristics of Pampa River – flowing through the heart of Travancore region – have undergone tremendous variations. Alternating cycles of recurring flood and drought has become a predominant feature of this

N.A. Mayaja (✉)

Dept. of Civil Engineering, Atria Institute of Technology, Bangalore, India

e-mail: mayaja@hotmail.com

C.V. Srinivasa

Dept. of Civil Engineering, Global Academy of Technology, Bangalore, India

river, which, once used to be a rich and sustainable source of water throughout the seasons and lifeline for a population. A good number of villages and densely populated regions on the bank of this river face the ravage of flood every year. Analyzing the spatial and temporal changes in land use and land cover (LULC) is one of the effective ways to understand the causes of flood. In this context, this study attempts to evaluate the LULC changes occurred in Pampa River basin during the period from 2001 to 2010, identify the human intervention factors as well as their possible impacts on the floods occurring in this river basin.

120.2 LAND USE FEATURES OF THE STUDY AREA

Pampa river encompasses a basin area of approximately 2235sq.km, and four districts of the State of Kerala, viz., Idukki, Kottayam, Pathanamthitta and Alappuzha. As per the latest census 2011, the total population in the above four districts is about 6.40 millions [1]. The area extends over thick tropical forests, wasteland, built up (urbanized and semi-urbanized) settlements, a few water bodies and a rich agricultural bowl of Kerala called Kuttanad. The land use pattern of this river basin is unique, distinctive and diverse. Physiographically, the terrain can be classified in to three categories viz., lowland, midland, and highlands. The high land consists of high altitude areas of thick forests whereas midland consists of cash crops like rubber and tea. The low land is basically providing agrarian crops like paddy and coconut. Out of total geographical area half share is accounted for agriculture and one fourth for forest. While the high land area occupies about 50%, the mid land and low land have about 40% and 10% shares respectively.

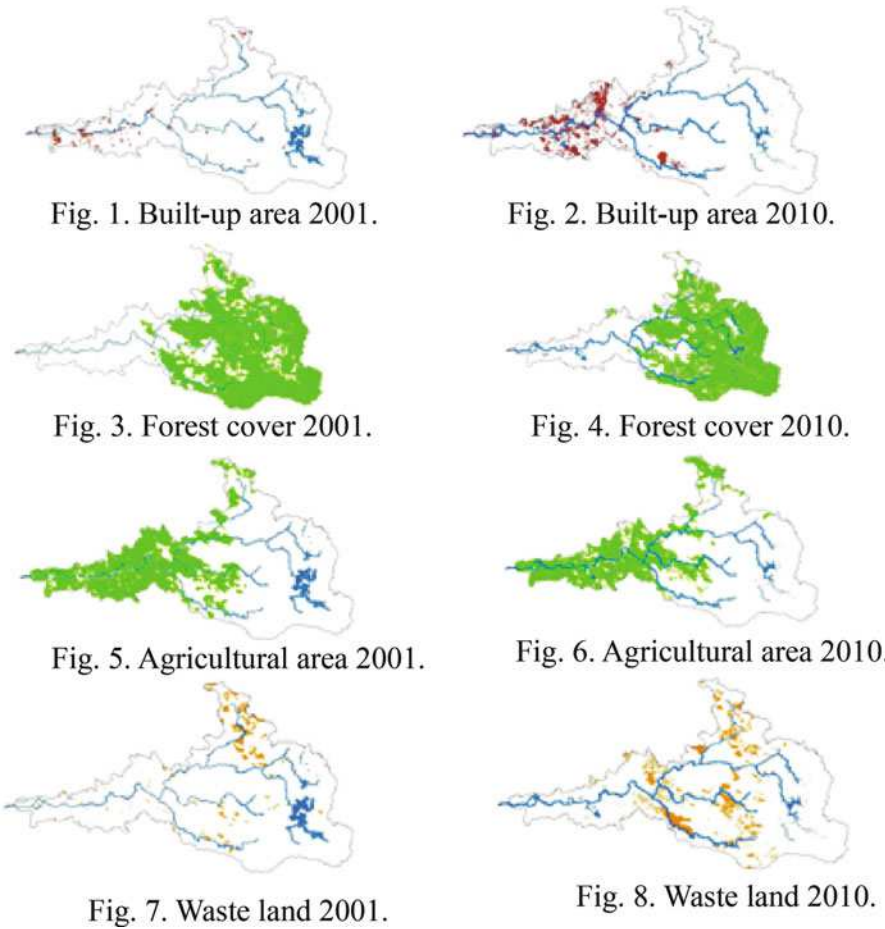
120.3 METHODOLOGY

For the purpose of analysis in this study, initially, the Pampa river basin area was delineated using the relevant Survey of India (SOI) topographic maps. Subsequently, the multispectral Remote Sensing (RS) images of the basin obtained from the Indian Remote Sensing (IRS) satellite for the period 2000 to 2010 is processed and analyzed. For the purpose of detailed analysis, the images of land use have been classified in to four categories, viz; built up area, forest cover, agriculture area and waste land. The comparison and evaluation of percentage variation have been primarily made with the land use images captured during June 2001 and June 2010.

120.4 RESULTS AND DISCUSSION

The land use changes in the river basin in above four categories have been mapped and shown in Figs 120.1–120.8. The summary of results is depicted in Table 120.1.

During the period of study, the built up area of 19 sq.km in the year 2001 has exponentially increased to 68 sq.km by the year 2010 indicating a 354% growth. This was happening in the downstream regions, densely populated, and undergoing a high rate of urbanization (7.64% decennial growth, provisional statistics). The phenomenal increase in the built up area of the river basin is increasing the flood havoc of this region. The forest cover, which was approximately 1234 sq.km in the year 2001, has dwindled to 1054 sq.km by 2010, involving a reduction of about 14.52%. The reasons are deforestation, encroachments, and irrational expansion



Figs 120.1–120.8 Comparison of satellite imageries showing land utilization 2001 and 2010

Table 120.1 Summary of results of LULC mapping (Area in sq.km)

No.	Land use	Area in 2001	Area in 2010	% variation
1	Built up area	19	68	(+) 354
2	Forest	1234	1054	(-) 14.52
3	Agriculture	554	511	(-) 7.73
4	Waste land	48	97	(+) 200

plans of Sabarimala – the famous pilgrimage Centre in this river basin. The agricultural area has reduced only marginally (7.73%) and is limited to the downstream and middle regions. A few studies have identified that this slow down of agriculture dynamism in Central Travancore region are on account of socio-economic factors and ‘political climate’ non-conducive for labour oriented agricultural activities [2, 3]. An area of 48 sq.km mapped in 2001 as waste land has substantially increased to 97sq.km by 2010 indicating a two fold increase. The wasteland in 2001 was sparsely distributed in the upstream alone, whereas by 2010 it has spread to the rich downstream basin also. The phenomena of rapid transition of such productive land to waste land in Indian scenario, due to socio-economic and environmental factors has been addressed in a few recent studies [4, 5]. According to a study, specific to Kerala, the main reasons for such severe land degradation can perhaps be attributed to the following reasons [6].

1. Agriculture became non-economic and hence land leveling and massive conversion of paddy fields to non-cultivated areas.
2. Degradation of forests due to encroachments.
3. Fast pace of urbanization and consequently roads and infrastructure grabbed a high share of cultivatable land
4. Unchecked soil erosion consequent to the poor land management. All these four factors are well testified in the case of Pampa river basin.

A study on this issue conducted by Pampa ParirakshanaSamithy – an NGO in Kerala – has identified many regions in the river basin, which has turned into wasteland [7].

120.5 CONCLUSIONS

The radical variations in the land use pattern of pampa river basin revealed in this study over the period from 2001-2010 are ‘strong negative changes’, directly aggravating the flood situation of this river basin. The three fold increase in built up area, fast transition of river to waste lands, increased deforestation, changing agrarian crop intensity etc calls for an urgent need for a diligent policy formulation to protect the river and the basin. Also there should be a conscious urban planning policy to cap the rate of urbanization on the river banks. The impact of the negative factors may be irreparable, if left unchecked. This may result in recurring flood and

drought havocs with unprecedented intensities. Perhaps the only prescription is an urgent comprehensive policy planning with diligent implementation.

REFERENCES

1. Census of India: Provisional population totals: website <http://censusindia.gov.in>
2. Economic Review. Annual publication of Planning Board, Govt. of Kerala (2007)
3. Kerala State Council for Science, Technology and Environment: website kscste.kerala.gov.in
4. Mohammad Afsar Alam: Regional Planning and Waste Land Development in India: An overview. *Asia-Pacific Journal of Social Sciences*, V(1), 152–166 (2013)
5. Sundar, I.: Waste land development through regional planning. *Indian Journal of Millennium Development Studies*, 6(1), 19–25 (2011)
6. Kerala State Council for Science, Technology and Environment. State of environment report – Kerala. Vol. 1, Report (2007)
7. Sukumaran Nair, K.: Pampa River: An ecological study. Report of Pampa Parirakshana Samithi (2009)

Chapter 121

Spatio-Temporal Study of the Distribution of Land Use and Land Cover Change Pattern in Chandigarh, India Using Remote Sensing and GIS Techniques

Neelam Sidhu, Madhuri S. Rishi, and Rakhi Singh

Abstract Chandigarh is among the most important city of the northern India in terms of socio-economic growth due to upcoming major projects, modernization of industrial activities and development of Information Technology sector so many people immigrated to the city and this resulted in greater load on the city population, thus, was selected for this study. Landsat TM and ETM+ images were used to characterize the land cover type and land cover changes in Union Territory of Chandigarh. The analysis revealed that the urban development of the city has been very rapid during the last decade and more recently, vegetation has greatly declined. The results demonstrated that the pressure of increased commercialization has driven change in land use pattern over a period of time and has resulted in widespread environmental degradation.

Keywords Urbanization • Population growth • Remote sensing • GIS

121.1 INTRODUCTION

Rapid urbanization brings opportunities for new urban development, however it also has brought serious losses of arable land, forest land and water bodies. Although remotely sensed images have been used to study urban growth pattern the world over, very few studies have been employed these methods to examine the growth of Indian cities. Remote sensing and GIS are recognized worldwide as valuable technologies in environmental application and are very useful in monitoring the environmental changes due to human activities [3,4,6]. A satellite image provides low cost and up to date spatial data that can be used to derive useful information to city managers and planners [7]. The present study was undertaken with objective of analysis of land use/land cover changes in the city Chandigarh

N. Sidhu (✉) • M.S. Rishi • R. Singh
Department of Environmental Studies, Panjab University, Chandigarh, India
e-mail: neelamsidhu87@gmail.com

between 1989 to 2011 with a view to detect the land consumption rate and the changes that has taken place particularly in the built-up land using both Geographical information system and Remote sensing data. This paper will also assist in monitoring the dynamics of land use resulting out of changing demand of increasing population.

121.2 STUDY AREA

Union Territory of Chandigarh which was earlier planned for the finite population of half a million and now has reached beyond its planned capacity to the total population of 10,54,686, one of densely populated city in India and the urbanization of the city accounts for 95.3%. The Union territory of Chandigarh has an area of 114 sq.km. It has emerged as a regional hub for education, health, information and technology. In the Union Territory of Chandigarh, the majority of land is under urban area (97%) and 2.9% in rural area [2] (Fig. 121.1).

121.3 MATERIAL AND METHODS

121.3.1 General Procedure for Data Processing

Three cloud free Landsat TM and ETM+ images and survey of India toposheets drawn on 1:50000 scale were used for analysis. Three images acquired on 11 October 1989, 4 November 2000 and 27 December 2011 were selected from data available for this study.

121.3.1.1 Data Processing

Pre processing involved the scanning and digitization of Survey of India Toposheets at 1:50000 scale to serve as the base map. To establish the relationship between an image coordinate system and a map coordinates system we need to align or georeference the raster data. The images were geometrically rectified and registered to the same projection namely, Transverse Mercator WGS 1984 to lay them over each other. After georeferencing the base map, remote sensing image is registered with base map using the same technique. Arc GIS 9.3 and ERDAS Imagine 9.1 are powerful tools for extracting land use and land cover layers has been employed.

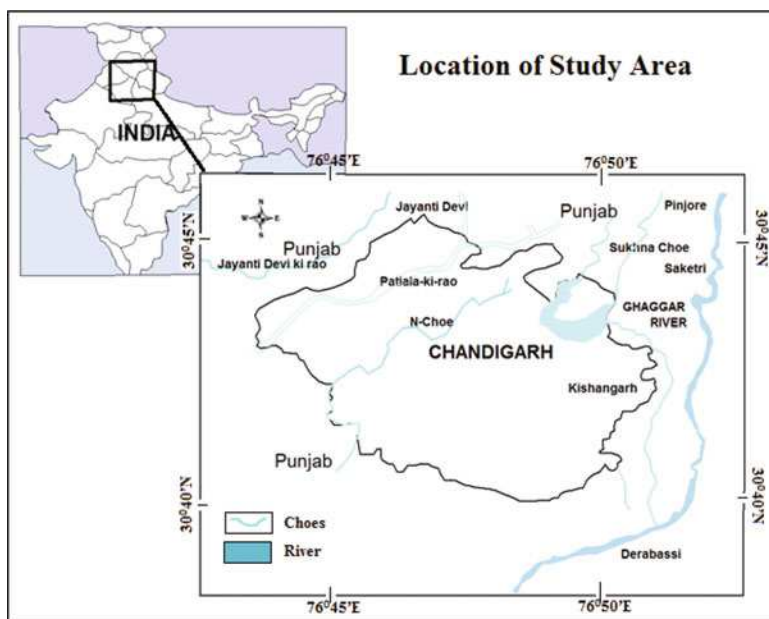


Fig. 121.1 Location map of the study area

121.3.1.2 Image Classification

The initial Landsat (1989) and final (2011) imageries were subjected to a classification zones. Supervised classification of remotely sensed data has been done for all the images. In order to classify the images, four classes were delineated in the images namely, built up area, water bodies, vegetation and others. The overall testing accuracy for year 1989 was 80%, for year 1990 it was 84% and for year 2001 it was 88%.

121.4 RESULTS AND DISCUSSION

121.4.1 *Land Use Change Pattern in Union Territory of Chandigarh*

The change analysis presented in this paper is based on the statistics extracted from the land use /land cover maps of the Union Territory of Chandigarh with using GIS (Table 121.1). The land use map prepared for the year 1989, 2000 and 2011 are shown in figure 121.2, 121.3 and 121.4 respectively. Urban development change is

Table 121.1 Land use statistics of Chandigarh city, 1989-2011

Years	1989		2000		2011	
Land Use	ha	%	ha	%	ha	%
Urban/built-up	4271.50	37.46%	4285.06	37.58%	5194.71	45.56%
Water body	141.01	1.23%	138.90	1.21%	218.25	1.91%
Vegetation	2810.06	24.64%	3295.08	28.90%	3131.55	27.46%
Others	4399.15	36.64%	3861.90	32.28%	3075.75	25.04%
Total	11400.00	100	11400.00	100	11400.00	100

Fig. 121.2 Landuse map of 1989

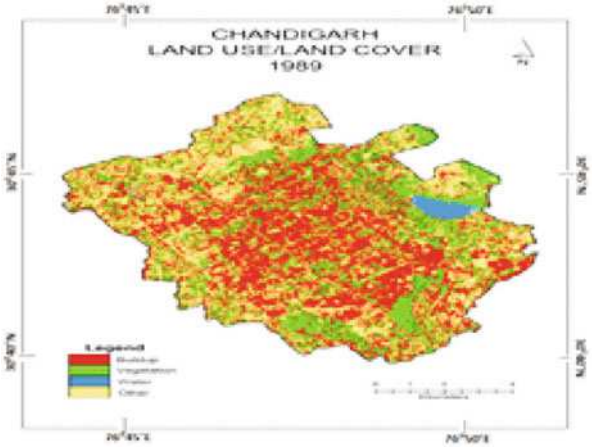
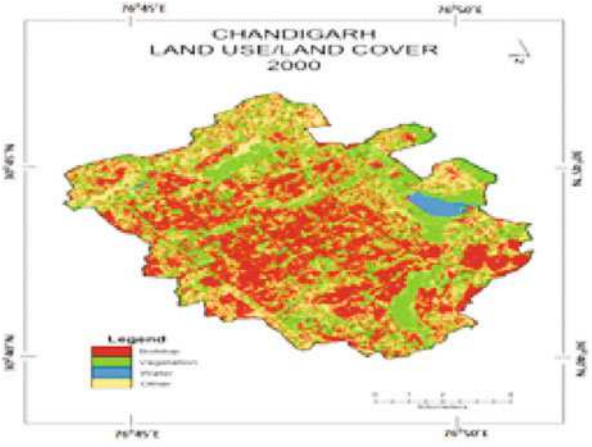
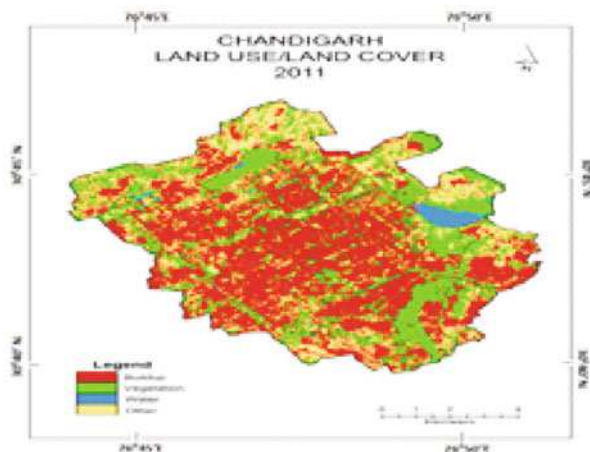


Fig. 121.3 Landuse map of 2000



very high in the city area, from 37.46% of total area in 1989 to 45.56% in 2011. On the other hand vegetation data has shown the increasing trend from 1989 to 2000 i.e. 24.64% of total area in 1989 to 28.90% while study observed the decrease in the vegetative land from 28.90% to 27.46% due to acquisition of land for various purposes.

Fig. 121.4 Landuse map of 2011



121.5 CONCLUSIONS

Chandigarh has witnessed rapid population growth from 1961 to 2011 i.e. from 1,19,881 to 10,54,686. It has witnessed a big leap taken in commercialization and urbanization in a short span of few decades. This pressure has driven change in land use pattern over the period of time. Many major projects are going on in Chandigarh which may further reduce the agricultural activities of the study area. Therefore urban land expansion has been largely driven by elevation, population growth and economic development.

REFERENCES

1. Button, K.: City management and urban environmental indicators. *Ecological Economics*, 40, 217–233 (2002)
2. Census of India: <http://www.censusindia.net> (2011)
3. Gao, J. and Skillcorn, D.: A GIS remote sensing approach to detection of land cover change in Auckland urban-rural fringe. *Proceedings of Geoinformatics '95 Hong Kong*, 1, 222–229 (1995)
4. Miguel-Anyanz, J.S. and Biging, G.S.: Comparison of single-stage and multi-stage classification approaches for cover type mapping with TM and SPOT data. *Remote sensing of Environment*, 59, 92–104 (1997)
5. Mundia, C.N. and Aniya, M.: Analysis of land use/cover changes and urban expansion of Nairobi city using remote sensing and GIS. *International Journal of Remote Sensing*, 26(13), 2831–2849 (2005)
6. Riaza, A., Martinez-Torres, M.L., Ramon Lluch, R., Alonso, J. and Heras, P.: Evolution of equatorial vegetation communities mapped using Thematic Mapper images through a geographical information system (Guinea, Equatorial Africa). *International Journal of Remote Sensing*, 19, 43–54 (1998)
7. Sarvestani, M.S., Ibrahim, A.L. and Kanaroglou, P.: Three decades of urban growth in the city of Shiraz, Iran: A remote sensing and geographical information systems application. *Cities*, 28, 320–329 (2011)

Chapter 122

Development of Technique to Characterize TROF

Vidit Mohan, Ashwin P. Ramesh, and Anirudh Toshniwal

Abstract Trees Resources Outside Forests (TROF) is an important natural resource and comprises tree formations in agro-forestry systems. However, determining suitable remote sensing technique to represent TROF for semi-urban to rural environment in India is a challenge. A research is undertaken to develop this technique for a study area existing at the outskirts of Rae Bareilly, UP. A classification based approach is tried to be evaluated. The study tried to understand importance of resolution and date of data captured for effective classification of TROF. As classification algorithms can significantly alter accuracy of classification, different classification techniques are analyzed as well. Results are compared statistically with ground truth data for accuracy assessment. The images are geocoded using GPS coordinates of control points. The result of accuracy assessment is summarized using Kappa coefficient. Explanatory statistics is used to compare classified data correspond to classification done with different algorithms over images of various resolution and to comment on efficacy of combinations of resolution of satellite image and classification technique.

Keywords Land resources • Remote sensing • TROF mapping

122.1 INTRODUCTION

TROF is defined as trees having diameter of 10cm or more at breast height and are not notified as forests [1]. Considering its inherent and substantial contribution to the national bio-resource stock, TROF spatial distribution, form, and chronological changes must be precisely and periodically determined [2]. Space borne remote sensing is an effective surveying tool as it provides data with different resolutions; specific in time and space; and cover large areas economically.

However, it is essential to account for TROF characteristics relevant to large area inventories because of a series of statistical and non-statistical concerns. Due

V. Mohan (✉) • A.P. Ramesh • A. Toshniwal
Department of Petroleum Engineering, Rajiv Gandhi Institute of Petroleum Technology,
Rae Bareilly, UP, India
e-mail: mohanvidit@gmail.com

to the TROF's rapid dynamics, current aerial photographs were used for inventory. The tree density varies largely and trees have erratic growth conditions with respect to inter-individuum competition [3]. In this regards, this paper enumerates to characterize and evaluate the tree resources through a standardized method using satellite images supplemented by extensive field assessment.

122.2 MATERIALS AND METHODS

122.2.1 Study Area

The study area selected is situated in the eastern part of Uttar Pradesh ($26^{\circ}10'05''\text{N}$ to $26^{\circ}16'05''\text{N}$ latitude and $81^{\circ}14'00''\text{E}$ to $81^{\circ}15'00''\text{E}$ longitude). The study area comprises of natural vegetation; tree species such as, Dhak, Khair, Babul, Shishum, Neem, Vilayti Babul, Arjuna, Kanji, Siras, Eucalyptus, Mango and Jamun; and scrubs interspersed with grasses. The principal crops grown are rice, pulse, wheat, barley, millet and poppy.

122.2.2 Satellite and Ancillary Data

The present study utilized the digital Google Earth Satellite imagery (Spatial resolution of 30 m) of November 2, 2013. Published climatic data, Geology Map, etc. were also used as collateral data.

122.2.3 Methodology

The TROF boundary was delineated in Erdas Imagine 9.1 software along with pre-processing of procured satellite data for visual analysis of images and preparation of various classified maps. The well defined and evenly distributed Ground Control Points (G.C.P) from the field assessments have been used for the geo-referencing of the raw image and to locate the ground verification points [2]. The Global Positioning System (GPS) coordinates collected during field validation was laid over the classified image to validate the overall accuracy of the classifier and for managing training data. The classified image is analyzed for editing and refinement for inclusion and omission of misclassified patches. Finally, the final TROF map was generated by stratifying the area based on the geometrical formation of tree resources into varied TROF classes. The various classification techniques were analyzed to account for the accuracy of classification. The classified index images are calculated for k (Kappa)-coefficient.

122.3 RESULTS AND DISCUSSION

122.3.1 *TROF Spatial Distribution and Characterization*

TROF is distributed throughout classified datasets except barren land and in rural/urban settlement (Figure 122.1). TROF presence increases as the distance to human settlements decreases. The textural information was used to differentiate the cases where neighborhood TROF class had an impact on the classification of particular type of TROF.

122.3.2 *Accuracy Assessment*

An accuracy assessment was carried out based on the generated confusion matrix (Table 122.1). The columns contain ground reference data while the rows contain classified information. The intersection of the rows and columns summarize the number of sample units (ie. pixels) assigned to a particular class relative to actual category as verified in the field. Within the diagonal of the matrix, the numbers represent the number of pixels that were correctly identified. Numbers not found within the diagonals are errors. The overall accuracy is determined by summing all

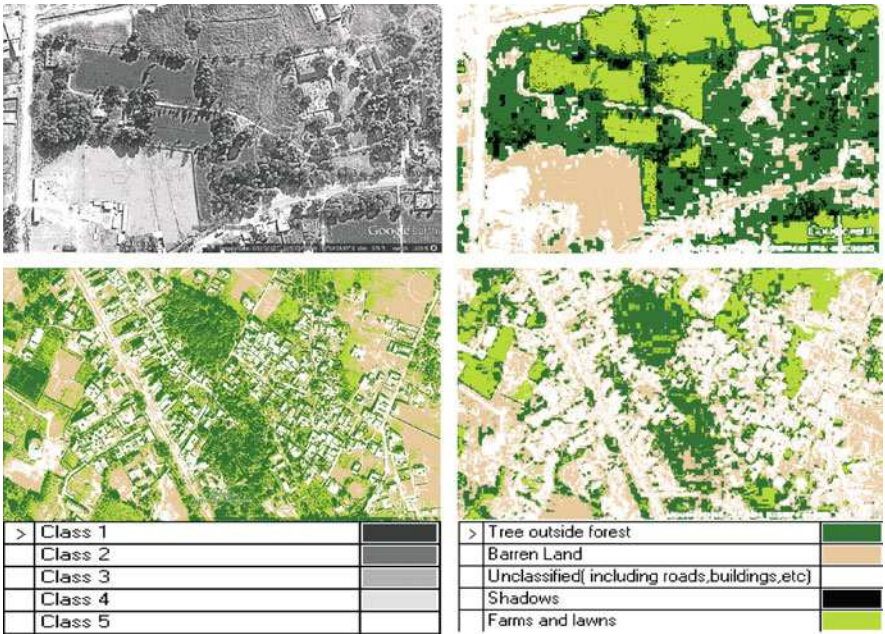


Fig. 122.1 The various classification techniques discussed in the text (clockwise). SODATA classification; Maximum likelihood classifier; Minimum distance classifier; Mahalanobis classifier

Table 122.1 Confusion matrixes using the discussed classification method

	A	B	C	D	E	SUM	UA%
A	230	0	0	37	0	267	86.1
B	0	290	0	0	26	316	91.8
C	0	0	264	0	0	264	100
D	34	0	0	219	0	253	86.6
E	0	79	0	0	228	307	74.3
SUM	264	369	264	256	254	1407	
PA%	87.1	78.6	100	85.5	89.8		
OVERALL ACCURACY	87.5	KAPPA = .84					
AVERAGE RELIABILITY	88.2						
AVERAGE ACCURACY	87.8						

Classes: **A** = Trees Outside Forest. **B** = Unclassified (includes houses, roads, etc). **C** = Barren land. **D** = Shadows. **E** = Farm/Green patches. **PA** = Produce Accuracy. **UA** = User Accuracy.

the numbers within matrices diagonal and dividing by the sum of errors. The producer's accuracy is a statistic that specifies the probability of ground reference datum being correctly classified. It is calculated by dividing the diagonal number from a class's column by the sum of the entire column including the number found within diagonal. The user's accuracy is a statistic that indicates the probability of how well the classified sample represents what is found on the ground. This measure is calculated by dividing the diagonal of class by the sum of the numbers within row of that class.

Kappa coefficient of agreement and its variance are estimated under stratified random sampling method for field inventory. This statistic measures the agreement between classification map and associated reference data [3]. The value of 0.84 shows strong agreement among the two. The sub-pixel comparison approach was also adopted to determine expected overlap among the classes based on land-cover fractions. It accounted for over- or underestimation of each class. A cross-tabulation formed by overall agreement–disagreement, where row and column labels of the matrix represent assessed categories and reference categories, respectively was generated. Thus, agreement values correspond to diagonal cells, whereas disagreement values correspond to off-diagonal cells. The average overlapping is around 12.28%.

122.4 CONCLUSION

The identification of TROF is possible through interpolation of the land appraisal data, training data management and accuracy assessment [3]. The reclassification is possible through derived interferences. *First*, it is based on time domain and is influenced by sensor characteristics and pattern recognition techniques [2]. *Second*, the study suggests that the region has a vast potential of increasing its tree cover. Thus, this study should be used for future investigation in the area.

ACKNOWLEDGEMENTS The authors express their sincere appreciation to the Department of Geoinformatics of RGIPT for facilitating and monitoring the study.

REFERENCES

1. Food and Agricultural Organization of the United Nations: FAO: Tree Outside Forest. Rome (2005)
2. Tripathy, G.K. and Ghosh, T.K.: Monitoring of desertification process in Karnataka State of India using GIS. *International Journal of Remote Sensing*, 17(12), 224–225 (1996)
3. Narasimhan, R.L. and Chandra, H.: Application of Remote Sensing in Agricultural Statistics. *Indian Journal of Agricultural Economic*, 55(2), 120–124 (2000)

Chapter 123

Study of the Urban Green Space Planning Using Geographic Information Systems and Remote Sensing Approaches for the City of Colombo, Sri Lanka

M.S.P.M. Sirirwardane, Jagath Gunatilake, and S. Sivanandarajah

Abstract With the growth of human population and their demands, constructed environment has replaced the natural environment in a significant way. Urban forestry, Urban Green Spaces (UGS) and natural parks are very important which urban planners and designers are interested in. This study is focused on the sustainable development of green spaces. Therefore Identification and analyzing of existing urban green areas was done through supervised image classification method by using high resolution satellite images. Central place theory and spatial analytical techniques were combined to understand the existing patterns of the green spaces. The green areas were analyzed with the other critical natural and human factors and weighted under existing urban regulations and standards in Sri Lanka and developed a multi criteria model for analyzing the suitability and probability of expansion of existing urban green spaces for sustainable green space planning activities. The results were presented in cartographical maps as well as web based maps which encourage the citizen engagement activities for nature conservation.

Keywords Urban Green Spaces (UGS) • Geographic Information Systems (GIS) • Remote Sensing (RS) • Central place theory

M.S.P.M. Sirirwardane (✉)

Postgraduate Institute of Science, University of Peradeniya, Peradeniya, Sri Lanka

e-mail: supunsiriwardane@gmail.com

J. Gunatilake

Department of Geology, University of Peradeniya, Peradeniya, Sri Lanka

S. Sivanandarajah

GIS Division, Survey Department of Sri Lanka, Peradeniya, Sri Lanka

123.1 INTRODUCTION

Urbanization is a rapidly increasing phenomenon in modern world. With the growth of human population and their demands, constructed environment has replaced the natural environment in a significant way. As a result, urban heat islands, air pollution and sound pollution have become some critical issues for the citizens. Therefore people reconsider to build up natural environment rather than artificial constructions. But most of the time the priority has given to construction and natural environment is ignored. The green spaces are very important part of the natural environment of an urban area as they add values in several ways. They are defined as the open spaces which consisting different levels of vegetation cover. These studies are focused on the sustainable development of the Urban Green Spaces (UGS). Following objectives were defined in this study.

- Identification and analyzing of existing urban green areas and their patterns by using GIS and remote sensing techniques.
- Develop a model for analyze the suitability and expansion probability of urban green space planning activities by considering natural and human factors.

The study area was Colombo Municipal Council (CMC) administrative area and it is considered as one of the major urbanized area in Sri Lanka.

123.2 MATERIAL AND METHODS

Identification and analyzing of existing urban green areas and their patterns is the starting approach of the study. This process was done through supervised image classification method by using high resolution GeoEye satellite images. After extracting the vegetation cover, the central place theory and other spatial analytical techniques were combined to understand the existing patterns of the green spaces (Fig. 123.1).

As the second objective the green areas were analyzed with the other critical natural and human factors, such as, buildings, transportation networks, bare lands, urban heat hot spots, air pollution contaminations etc. These factors were weighted under existing urban regulations and standards in Sri Lanka and developed a multi criteria model for analyzing the suitability and probability of expansion of existing urban green spaces. For this approach the topographic maps from survey department were used with several other data sets such as air pollution data from National Building Research Organization (NBRO). The final results were presented in cartographical maps as well as web based maps which encourage the modern trends in GIS and citizen engagement activities for nature conservation. Planners, Designers and decision makers can use the results as decision support system with the comments submitted by the community.

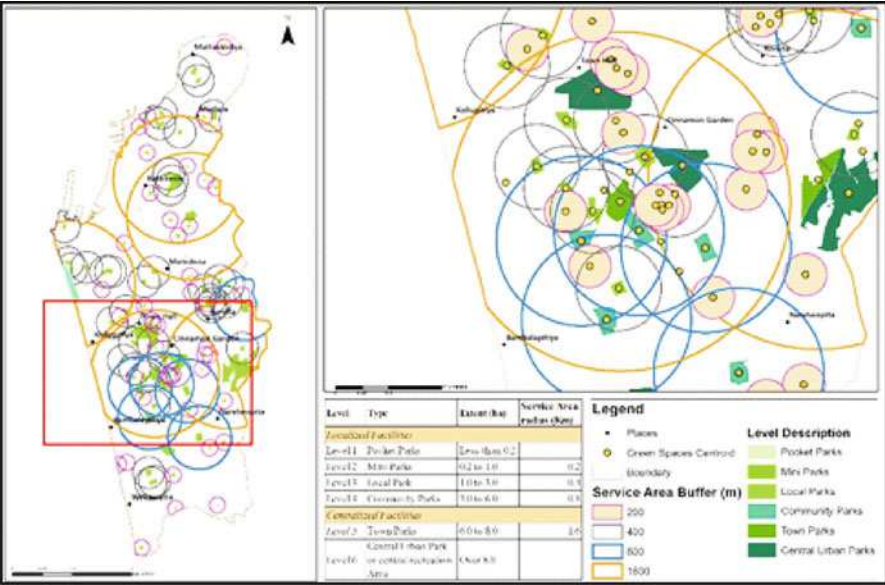


Fig. 123.1 Analyzing the existing patterns (Created by the results of present research)

123.3 RESULTS

The completion of the first objective, gave a layer of vegetation cover. The accuracy assessment was 82% for the supervised classification and the vegetation cover was extracted. This layer was introduced to the suitability model with other layers which represent physical and human factors. A weighted overlay model was created using expertise inputs and research experience. The suitability was categorized into five sectors which can be identified as “most suitable, suitable, moderate suitable, less suitable and not suitable”. According to the results, most suitable area is less than 2% of the total study area. But there are 30% of the land is suitable for expanding green spaces while another 38% cannot be expanded. Moderate suitable area is around 30%.

123.4 CONCLUSIONS

The results expressed that the expansion of green spaces is a huge challenge. The suitable area and moderate suitability conditions can be improved towards the sustainable green areas. Urban planners, designers are very important for analyzing this sort of suitability using models. The model can be reused with several other factors such as advanced soil conditions, aesthetic aspects and socio economic conditions etc. And also it can be used to analyze another study area. However these

results are more worth when the other stakeholders are involved in the planning process. Therefore, building a web application to achieve citizen comments is very useful and that information is a critical source for decision makers who usually finalize projects to be implemented.

REFERENCES

1. Luo, Y., Xu, J. and Yue, W.: A Model for the Evaluation of Urban Green Spaces' System Using RS and GIS Methods. Department of Geography, East China Normal University, Shanghai, 200062, China (2006)
2. National Physical Planning Department.: Revision of all the reservations and buffer zones. http://www.nppd.gov.lk/attachments/article/72/Buffer_Zones.pdf (2009)
3. Peng, H.: Analysis of the Beijing Greenbelts Plan Using Geographic Information Systems (GIS). Washington State University (2004)
4. Ruangrit, V. and Sokhi, B.S.: Remote Sensing and GIS for Urban Green Space Analysis – A Case Study of Jaipur City, Rajasthan (2004)
5. Shah, M. and Haq, A.: Urban Green Spaces and an Integrative Approach to Sustainable Environment. Department of Asian and International Studies, City University of Hong Kong, Hong Kong, China (2011)
6. Urban Development Authority: Public Outdoor Recreation Space Planning as an integral part of Landscape Master Plans for Urban Areas in Sri Lanka. <http://www.uda.lk/pdf/PORS%20-%20urban%20areas.pdf> (2011)
7. Ukwattage, N.L. and Dayawansa, N.D.K.: Urban Heat Islands and the Energy Demand: An Analysis for Colombo City of Sri Lanka Using Thermal Remote Sensing Data. Department of Agricultural Engineering, Faculty of Agriculture, University of Peradeniya, Sri Lanka (2012)

Chapter 124

Prediction of Crop Suitability of Certain Indian Spices – A GIS Approach

Utpala Parthasarathy, O.P. Nandakishore, K. Jayarajan, K.V. Saji, and K. Nirmal Babu

Abstract GIS technology is a computer-based data collection, storage, and analysis tool that combines previously unrelated information into easily understood maps. GIS can perform complicated analytical functions and then present the results visually as maps, tables or graphs. This allows decision-makers to virtually see the issues before them and then select the best course of action. The database prepared from existing field survey can be compiled using digital map for monitoring the availability of the species in the unknown locations through Ecocrop model of DIVA GIS. The spatial analysis thus helps in choosing the best location for the crop depending on the environmental parameters. The plotting of *Piper* species and *Garcinia* species collected from Western Ghats gave information of the species richness sites as well as the diversity of the species. Based on these results the prediction of the distribution of *piper* species and *Garcinia* species in North Eastern India was done and confirmed the availability with survey. The climatic parameters, important for crop suitability, The studies indicated that area under the natural habitat or the cultivation of the crop has a positive relation with the environmental suitability.

Keywords GIS technology • Ecocrop model • Prediction • *Piper* species • *Garcinia* species

124.1 INTRODUCTION

The genus *Piper*, the largest in the family Piperaceae consisting of more than 1000 species, occurs throughout the tropical and subtropical regions. The distribution of *Piper* ranges from sea level to the high ranges of Western Ghats and Sub Himalayas in India. The sub mountainous tracts of the Western Ghats are believed to be the centre of origin of black pepper, *Piper nigrum* L. *Piper* species occurring in India are economically important. The genus *Garcinia* (Family: *Clusiaceae*) consists of over 200 species distributed in the tropics of the world, chiefly in Asia, Africa, and Polynesia. They are evergreen polygamous trees, shrubs and herbs. About

U. Parthasarathy (✉) • O.P. Nandakishore • K. Jayarajan • K.V. Saji • K.N. Babu
Indian Institute of Spices Research (ICAR), Marrikunnu, Calicut, Kerala, India
e-mail: Utpala@spices.res.in

35 species are reported to exist in India, many of which are endemic and economically important, with immense medicinal properties (Roberts, 1984). *Garcinia* is the source for a natural diet ingredient (-) hydroxycitric acid, HCA which is an anti obesity compound. Geographical Information System (GIS) has been successfully used to study geographic distribution of cultivated species as well as pests of agricultural crops 10, 11. Hence the present study was undertaken to investigate morphological grouping of the species and species richness of *Piper* and *Garcinia* using GIS, to describe the geographic distribution of the *species*. This study will provide baseline data for further analysis on exploration, conservation and use of germplasm of wild crop relatives as well as for studies on the factors that explain the geographic distribution of species.

124.2 MATERIAL AND METHODS

The geographical information (altitude, longitude and latitude) of the collection sites of *Piper* and *Garcinia* species were obtained by GPS, imported and was converted to shape file in which each spots representing the geographical location of the collection, using DIVA-GIS tool. The grid maps of temperature, rainfall and elevation were superimposed on the shape file to analyse the temperature, rainfall and altitude of all the sample collection locations. The diversity of *Garcinia* and *Piper* species were determined using tool Shannon's Diversity index method (Shannon and Weaver, 1949) and species richness in the collection area was determined by method of DIVA-GIS. Using 'ECOCROP' model, and the climatic information the domain of the two crops in India was predicted and confirmed by survey.

124.3 RESULTS AND DISCUSSIONS

Systematic surveys were conducted in 483 sites to collect *Piper* species in the Western Ghats, the major centre of diversity for the species in India. Live specimens were collected and established in the black pepper germplasm conservatory of the Indian Institute of Spices Research, Calicut. The altitude, longitude and latitude of the collection site were recorded using GPS. The data were plotted using DIVA-GIS software to study the distribution, diversity and richness of *Piper* species. Altitude map and rainfall map were prepared with the help of point-to-grid cells of the climatic data map option of DIVA-GIS, using a grid size of $18' \times 18'$ km cells and superimposed with the species distribution map (Fig. 124.1) to compare with the cluster groups and study the possibility of any specific pattern. For the rainfall map BIOCLIM model of annual precipitation was used. Altitude and rainfall are considered to be the most important aspects influencing the distribution of *Piper* [1] Species diversity and richness map was prepared with the help of point-to-grid analysis option of DIVA-GIS, using circular neighbourhood method with a radius of 50 km. The superimposed map of BIOCLIM annual precipitation and species distribution indicates that *P.longum* naturally occurs in the high-rainfall zones

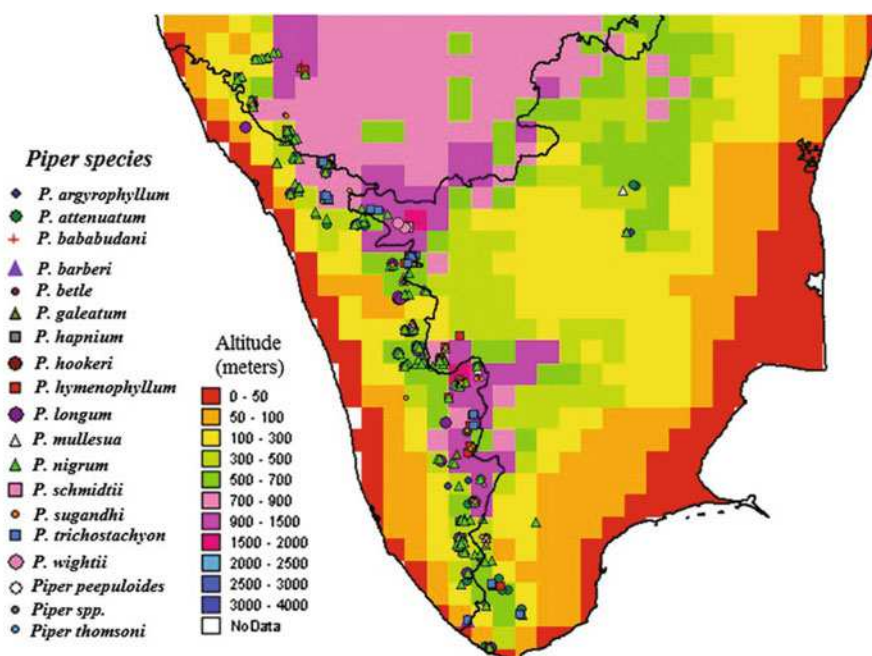


Fig. 124.1 Altitude map of southern India and *piper* species distribution

(more than 4000 mm), while the rest of the species is present within 1500–3000 mm rainfall zone. A well-distributed rainfall within the range of 1000–3000 mm is best suited for proper growth and development of pepper. [2] The annual rainfall in all the collection sites ranged from 1500 to 4000 mm. Species such as *P. babubudani*, *P. thomsoni*, *P. longum* and *P. galeatum* are found in areas receiving rainfall over 2000 and up to 4000 mm.

Species richness map (Figure 124.2) shows two hot spot areas. One is between 75°92'–77°06'E long. and 10°95'–11°03'N lat., consisting of Achankovil, Kulathapuzha, Silent Valley and Tiunelly, Kerala, and Nilgiris, Tamil Nadu. Another is in the extreme south, between 76°92'–77°45'E long and 8°07'–9°10'N lat., consisting of Neyyar and Poovanathmodu, Kerala and Brymore, Kanyakumari district and Kodayar; Kariardam and Kannikatty; Tirunelvely district, Tamil Nadu, where 7–8 species are available in the same site.

Based on our study, the species can be broadly divided into three groups. The first group occurs in high altitude (300–1000 m), the second group at medium altitude (100–500 m) and the third group at lower altitudes (50–150 m). About 15 qualitative characters were recorded from the 16 samples collected (both live specimen and herbarium). These were computerized using SPSS software for cluster analysis (15 characters of 16 species) by hierarchical clustering to spatially group the species based on similarity matrix (Figure 124.3). A scatter diagram was prepared using SPSS software to understand species distribution along the environmental gradients. The scatter diagram of species distribution (Figure 124.4) prepared with rainfall and

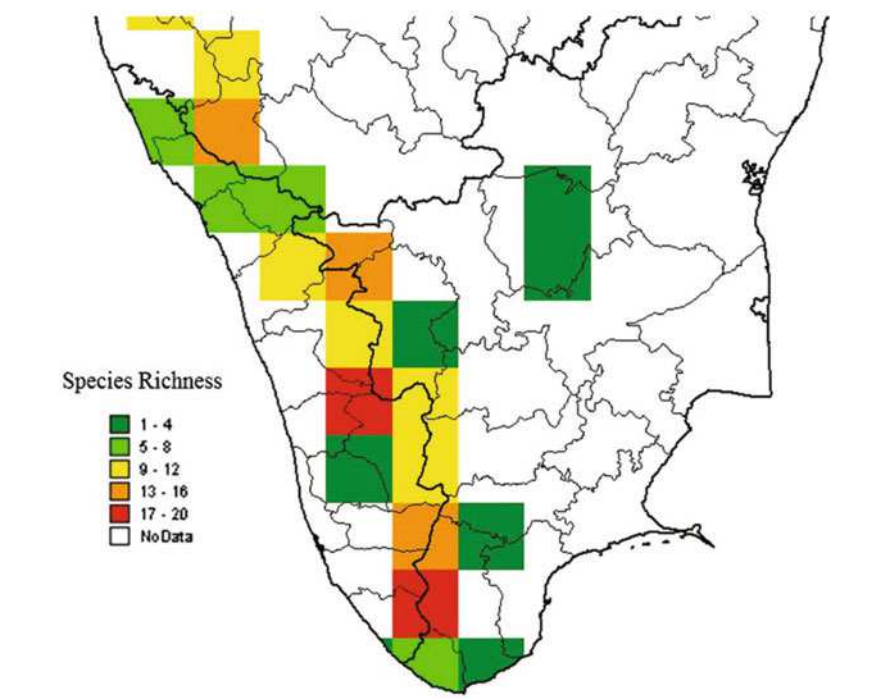


Fig. 124.2 *Piper* species richness map at S. India

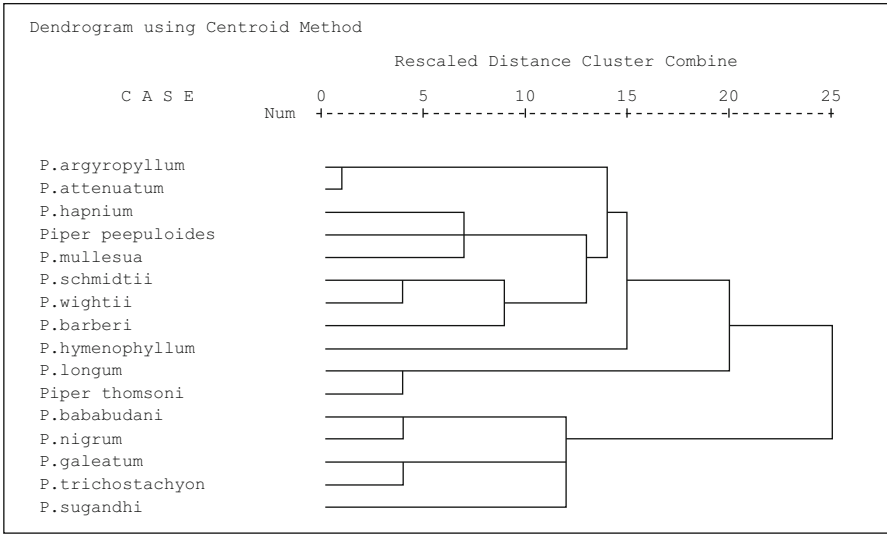


Fig. 124.3 Hierarchical cluster of 16 species

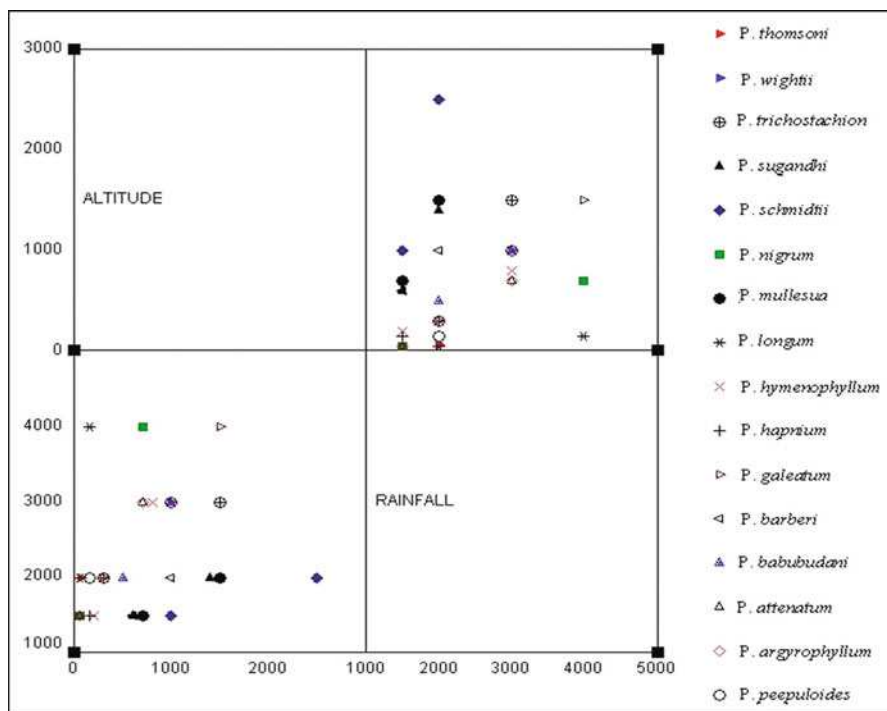


Fig. 124.4 A scatter diagram

altitude shows that the high altitude species are falling in comparatively low-rainfall grids of the BIOCLIM map. In southern India, coastal areas which received more rainfall are at low altitude areas. The species clustered in the same cluster are showing same altitude and rainfall in the scattered diagram indicates that morphological characters are influenced by the environmental parameters.

124.4 GARCINIA

The environmental information like altitude, temperature and precipitation information of the garcinia collection sites of western Ghats were plotted in the India map and with the help of Ecocrop model of DIVA GIS. The map predicted that North Eastern Himalayan foot hills are also excellent habitats for *Garcinia*. Survey in the states of North east was done based on the prediction and 5 species were collected which are all different from the Western Ghats species. A visit to the Herbarium of the Botanical Survey of India, Shibpur, Kolkata, gave a very clear idea about the species identity. It is very interesting to report that these species were reported by Hooker and Kings from N.E. States on 17th century. Our survey receded that these species are only known to the local people where it is available and by different local names. *Garcinia* is one among a few genus in the plant kingdom showing a great diversity in

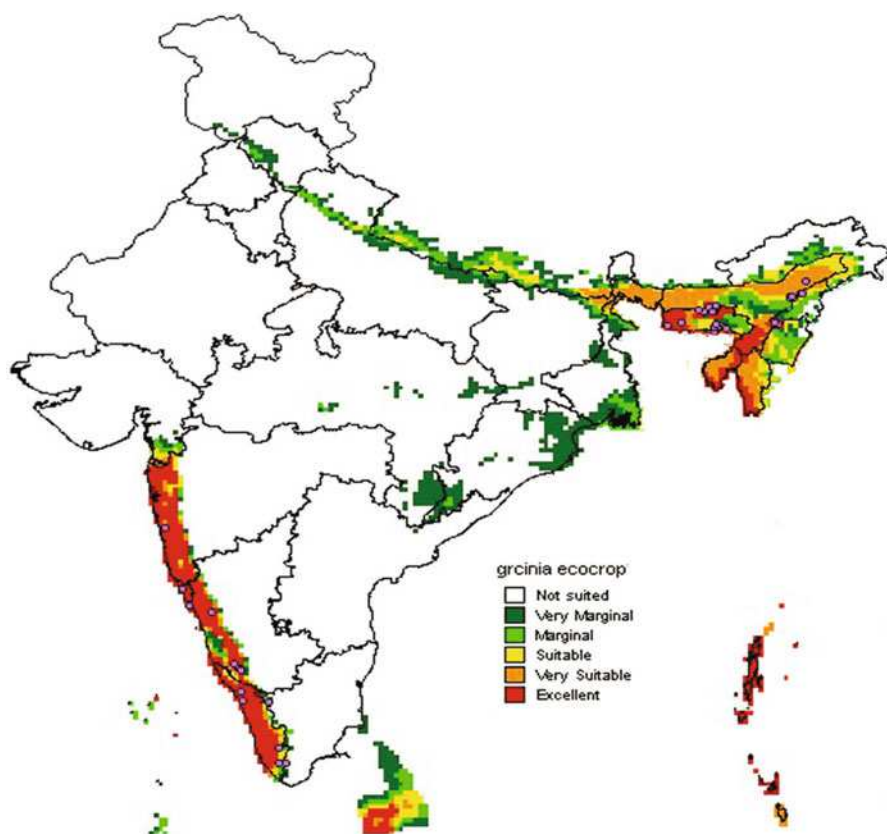


Fig. 124.5 *Garcinia* domain prediction by ECOCROP model

the morphology especially of leaves and flower [3]. Many species of *Garcinia* are threatened due to habitat destruction [4] and many species of *Garcinia* falls in IUCN red list. Another issue faced by the researchers is the synonymy of certain species [5]. This study reported that though the two ecosystems like Western Ghats and Himalayan foot hills are wide apart from each other the weather patterns of *Garcinia* adobes is similar. The *Garcinia* species showed a wide range in the altitudes of occurrence (10–1500 m MSL); there was specificity in average annual temperature (17–23°C) and total rainfall (2000 – 4200 mm). After collecting 5 species from Western Ghats and 5 species from Himalayan foot hills the genetic set up of the species studied with the help of markers and the sequences of some specific genomic DNA region. In the phylogenetic similarity cluster two species appeared and it was very interesting to note that between them, one is from Western Ghats species and another from the Himalayan species. It shows that the morphological variation the species containing is due to the variation of the ecosystems otherwise the types of species recorded in the two different ecosystems are almost same and may have originated themselves in the two different ecosystems when they have found the same type of environmental conditions (Figs. 124.5, 124.6 and 124.7).

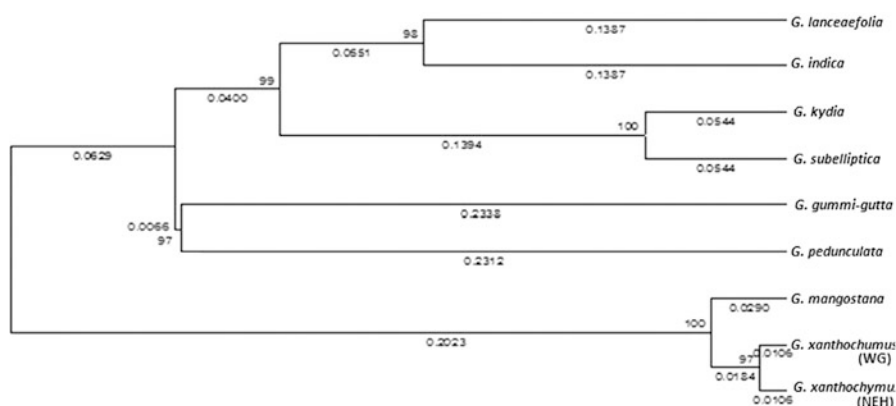


Fig. 124.6 Evolutionary relationship of selected *Garcinia* species using Neighbor-joining method



Fig. 124.7 Photographs of the species of the different sub clusters

REFERENCES

1. Marquis, R.J.: Biogeography of neotropical *Piper*. In: *Piper: A Model Genus for Studies of Phytochemistry, Ecology and Evolution* (eds Dyer, L.A. and Palmer, A.D.N.), Kluwer Academic/Plenum Publishers, New York (2004)
2. Utpala Parthasarathy, Saji, K.V., Jayarajan, K. and Parthasarathy, V.A.: Biodiversity of *Piper* in South India - application of GIS and cluster analysis. *Current Science*, 91(5), 652–657 (2006)
3. Osman, M.B. and Rahman, M.A.: *Mangosteen–Garciniamangostana*. Southampton Centre for Underutilised Crops, University of Southampton (2006)
4. Cheek, M.: *Garcinia kola*. In: IUCN 2004. IUCN Red List of Threatened Species. www.iucnredlist.org/apps/redlist/details/34715/0 (2004)
5. The Plant List: Version 1. <http://www.theplantlist.org/>; Accessed on 1 January 2013 (2010)

Chapter 125

Morphometric and Hydrological Study of Alaknanda and Bhagirathi Basins

Vikas Kamal, Ritesh Sipolya, Rajesh Kumar, and S. Mukherjee

Abstract The river Ganges has its practical origin from the confluence point of its two tributaries the Alaknanda and Bhagirathi at a place known as Devprayag. These two rivers have their own very large catchments or drainage basin. Both of them have their own drainage characteristics in terms of physical area and ecological habitats. The variability of discharge from both the catchments determines the flow regime in the river Ganga. The international nature of river Ganga and its huge basin makes its study complicated and its hydrological data difficult to obtain. For the sake of studying the flood behavior downstream in period of emergency like that in 2013 Uttarakhand tragedy, an indirect approach is to obtain the flow regime through morphometry. The various novel and traditional approaches gives us a unique opportunity to predict the flow regime in 30 year to more than 100 year return period flood conditions. In this study the DEM of ASTER and SRTM have been utilized to analyze morphometry using D-8 method. The drainage basin shape, area, perimeter, density, river network, river length, vertical distances, slope, hypsometric curves and longitudinal profiles are calculated for both the basins using both ASTER DEM of 30 m and SRTM DEM of 90 m resolution. Further using empirical equations an attempt is made to calculate discharge at outlet point for both the basins. This is correlated statistically with different morphometric parameters to know which factors are best representing the basin flow regime of the basins.

Keywords Flood hydrograph • Return period • Alaknanda • Bhagirathi • Morphometry

125.1 INTRODUCTION

The holy Ganga is popularly known to originate in Gangotri glacier's snout Gaumukh at height of 4000 m amsl as river Bhagirathi which later joins Alaknanda at Devprayag at height of 1000 m amsl. The catchment characteristics

V. Kamal • R. Sipolya • R. Kumar • S. Mukherjee (✉)
School of Environmental Sciences, Jawaharlal Nehru University, New Delhi, India
e-mail: saumitramukherjee3@gmail.com

of Alakhnanda and Bhagirathi differ to a large extent though both lie in the same hydrometeorological subregion. Drainage characteristics are being widely studied through morphometric analysis over a GIS platform. The present work is on two mega catchments at the beginning of the river Ganga. D8 method has been utilized here to process the SRTM-DEM (Shuttle Radar Topography Mission – Digital Elevation Model) of 90 m spatial resolution. After experimenting with both ASTER (Advanced Spaceborne Thermal Emission and Reflection Radiometer) DEM data of 30 m and SRTM-DEM of 90 m, it was found that to avoid the inclusion of small rills, SRTM was suitable for study. Hydrological data availability is highly scarce for this region because of international character of Ganga River and the water sharing among the Indian states. So in order to study runoff of these catchments, an indirect approach involving SUH (Synthetic Unit Hydrograph) was adopted. SUH are derived using SCS (Soil Conservation Service), Snyder's method and dimensionless unit hydrograph approach. The dimensionless unit hydrograph method is preferred for this work keeping in mind the dearth of free data available [1].

125.2 STUDY AREA AND GEOLOGY

The Bhagirathi and Alakhnanda catchment of Ganga watershed in Uttarakhand state lies in North-Western Himalayas of India (Fig. 125.1). The total calculated geographical area of Bhagirathi catchment till Devprayag is 7644 sq km and Alakhnanda watershed till Devprayag is 11071 sq km approximately. Bhagirathi river originates at Gangotri glacier which is at the base of Chaukhamba peak. Alakhnanda river originates from the eastern slopes of Chaukhamba from the Bhagirathi, Kharak and Satopanth glaciers. Alakhnanda flows along the Badrinath temple shrine. The state of Uttarakhand falls into three broad stratigraphical zones:

- Outer or Sub-Himalayan zone composed of sediments mostly of tertiary age,
- Central or Lower Himalayan zone, composed of granite and other crystalline rocks of unfossiliferous sediments and
- Higher Himalayan zone, composed of a series of highly fossiliferous sediments.

Alakhnanda and Bhagirathi catchment falls into the area of Lower and Higher Himalayan zone.

125.3 MATERIAL AND METHODS

Morphometric analysis of Alakhnanda and Bhagirathi catchments were done in a sequential manner.[2] First SRTM DEM was filled using hydrology tool of ArcGIS. The flow direction and flow accumulation raster was calculated, following which stream links were determined [4]. Characteristics like length of each segment, relief, order, drainage density, slope, drop etc were calculated for 4th and higher

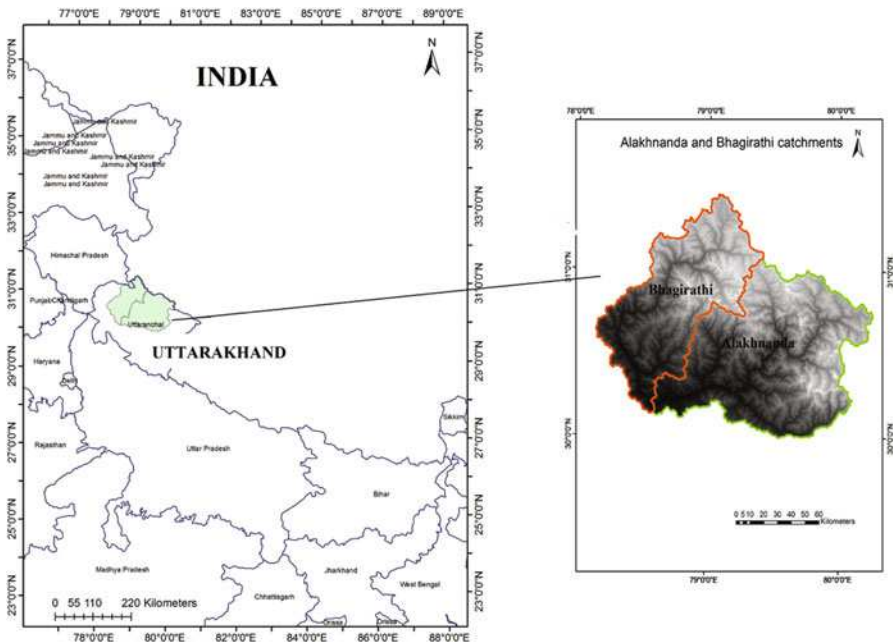


Fig. 125.1 Study area showing the Alaknanda and Bhagirathi catchments

order watershed only because 1st, 2nd and 3rd order watershed have scattered coverage and usually ridges and valleys are missed out in them. This was carried out in RiverTools software v3.0. Flood peak hydrographs were generated for Bhagirathi and Alaknanda at their outlet point which is at Devprayag. As already mentioned, dimensionless unit hydrograph approach was used here. Physiographic parameters were used for both the catchments to generate a synthetic unit hydrograph based on studies already done on gauged catchments. Following this, hydrographs were generated for flood peak discharges of 25 year, 50 year and 100 year return period. Linear rational approximations of following were used for fitting the data to the near normal curve:

$$y = (a + cx^2 + ex^4 + gx^6 + ix^8 + kx^{10}) / (1 + bx^2 + dx^4 + fx^6 + hx^8 + jx^{10})$$

.Rational approximation have shown to outperform both spline and polynomial approximation [3].

125.4 RESULTS AND DISCUSSION

125.4.1 Morphometry Analysis (Table 125.1)

Table 125.1 The statistical summary of different morphometric parameters determined

	6th order basins				5th order basins				4th order basins			
Alaknanda Basin Parameter	Max	Min	Mean	SD	Max	Min	Mean	SD	Max	Min	Mean	SD
Area	1892.88	271.65	1035.34	567.38	546.49	39.36	167.67	103.38	211.26	6.21	41.86	29.50
Perimeter	279.95	98.84	171.36	60.98	134.17	28.21	64.29	21.61	71.36	10.55	29.99	11.17
Basin Length	96.32	32.87	51.11	22.07	44.75	9.25	20.98	7.18	25.04	3.67	10.02	3.80
Shape Factor	0.74	0.45	0.63	0.11	0.72	0.47	0.60	0.07	0.78	0.39	0.62	0.07
S-L 2/1	0.55	0.40	0.46	0.05	0.64	0.30	0.49	0.08	1.23	0.20	0.51	0.16
S-L 3/2	0.49	0.39	0.45	0.04	1.00	0.16	0.44	0.15	1.54	0.05	0.54	0.29
S-L 4/3	0.81	0.41	0.56	0.14	3.34	0.17	0.70	0.55	13.76	0.02	1.12	1.38
S-L 5/4	0.81	0.38	0.61	0.15	3.68	0.03	1.01	0.81	-	-	-	-
S-L 6/5	1.28	0.27	0.69	0.34	-	-	-	-	-	-	-	-
Stream freq.	2.57	2.21	2.39	0.13	3.33	1.78	2.50	0.34	4.62	1.07	2.55	0.51
Drainage density	1.53	1.34	1.42	0.08	2.03	1.22	1.49	0.18	11.74	0.88	2.48	1.54
Drainage texture	18.26	6.77	13.51	3.86	9.39	3.33	5.91	1.52	14.15	2.18	4.63	1.54
Mean bif. factor	2.25	1.72	1.94	0.21	4.44	1.67	2.10	0.57	5.18	1.63	2.20	0.72
Elongation ratio	16.43	5.26	12.38	3.69	8.24	2.09	4.73	1.45	5.37	0.87	2.42	0.81
Circulatory ratio	0.56	0.30	0.43	0.08	0.63	0.37	0.48	0.07	0.71	0.26	0.54	0.08
Compactness constant	0.21	0.08	0.11	0.04	0.45	0.14	0.26	0.08	1.12	0.19	0.50	0.18
Length of the overland flow	0.37	0.33	0.35	0.02	0.41	0.25	0.34	0.04	0.58	0.20	0.35	0.06
	6th order basins				5th order basins				4th order basins			
Bhagirathi basin parameter	Max	Min	Mean	SD	Max	Min	Mean	SD	Max	Min	Mean	SD
area	1483.27	245.26	662.04	504.90	792.14	80.19	193.76	155.33	177.11	7.31	41.07	29.00
perimeter	243.07	77.98	138.68	63.35	192.54	42.23	70.17	31.27	67.00	13.39	29.85	10.30
basin length	73.02	22.41	39.73	19.42	61.18	14.17	22.70	9.78	20.55	4.57	10.01	3.41
shape factor	0.72	0.50	0.63	0.11	0.75	0.46	0.60	0.08	0.75	0.45	0.62	0.07
S-L 2/1	0.63	0.42	0.53	0.09	0.68	0.36	0.51	0.08	0.94	0.27	0.50	0.15
S-L 3/2	0.76	0.37	0.52	0.15	0.81	0.14	0.46	0.14	1.62	0.09	0.58	0.31

S-L 4/3	0.58	0.36	0.47	0.10	2.79	0.30	0.68	0.53	5.41	0.04	1.03	0.89
S-L 5/4	0.87	0.49	0.71	0.14	2.43	0.10	0.89	0.57	-	-	-	-
S-L 6/5	0.75	0.04	0.36	0.30	-	-	-	-	-	-	-	-
Stream freq.	2.81	2.14	2.46	0.26	3.01	1.90	2.45	0.27	4.65	1.76	2.58	0.44
Drain. density	1.72	1.25	1.48	0.20	1.78	1.17	1.45	0.17	7.94	1.22	2.30	1.09
Drain. texture	15.44	6.12	10.46	3.38	10.62	4.26	6.14	1.57	9.56	1.93	4.57	1.44
Mean bifurfactor	7.88	1.83	3.52	2.56	5.87	1.71	2.15	0.88	5.14	1.64	2.17	0.71
Elongation ratio	12.94	4.98	9.73	3.47	8.32	2.87	5.01	1.52	5.49	0.90	2.40	0.82
Circulatory ratio	0.52	0.30	0.41	0.10	0.63	0.27	0.47	0.08	0.72	0.23	0.54	0.08
Compactness constant	0.23	0.09	0.15	0.06	0.34	0.14	0.24	0.06	1.15	0.21	0.50	0.16
Length of the overland flow	0.40	0.29	0.34	0.05	0.45	0.29	0.37	0.04	0.45	0.19	0.34	0.05

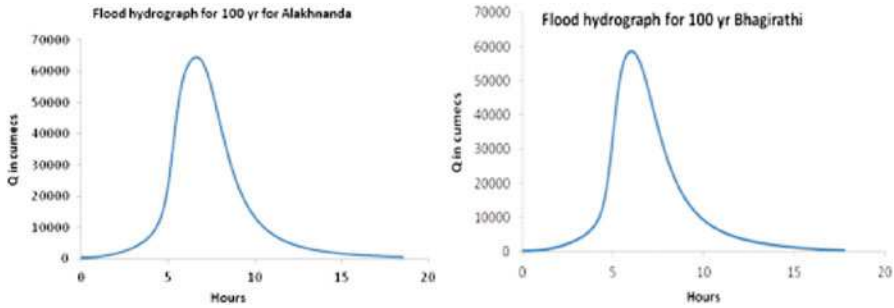


Fig. 125.2 Flood peak discharge of 100y return period

125.4.2 Flood Hydrographs

Synthetic Unit hydrograph approach resulted in the generation of hydrographs as given in Fig. 125.2. Only 100 year return period flood hydrograph are given, which show that peak flood of both the catchments vary by a margin of 7000 cumecs and that of Alaknanda is larger owing to its 45% larger area. The shortfall in discharge is accounted for by the rainfall data used in the study.

125.5 CONCLUSIONS

The morphometric analysis of the 4th, 5th, 6th order catchments of both the Alaknanda and Bhagirathi watershed shows that for 4th and 6th order basins Alaknanda has higher drainage density, texture and stream frequency but the trend is reversed in 5th order basins. Mean bifurcation factor is higher for Bhagirathi basin in all order basins showing that it is structurally more disturbed. The flood hydrographs of both the basins for different return period successfully shows the peak discharge values that fit well according to the morphometric characteristics of the basins, but due to limitation of methods being followed and data availability the outcome is not reliable and needs validation.

REFERENCES

1. Bhuyan, P.K., Mishra, S.K. and Berndtsson, R.: Simplified two parameter gamma distribution for derivation of synthetic unit hydrograph. *Journal of Hydrological Engineering*, July/Aug, 226–230 (2003)
2. Strahler, A.N.: Quantitative analysis of watershed geomorphology. *Trans. Am. Geophysical Union*, 38, 913–920 (1957)

3. Vendersteen, G.: Curve fitting using splines, polynomials and rational approximations, a comparative study. NORSIG 96, 1996 I.E. Nordic Signal Processing Symposium, Espoo, Finland, September 24–27, 41–44 (1996)
4. Pareta, K. and Pareta, U.: Quantitative morphometric analysis of a watershed of Yamuna basin, India using ASTER DEM and GIS. *International Journal of Geomatics and Geosciences*, 2 (1) (2011)

Chapter 126

Role of Remote Sensing Data in Geoenvironmental Mapping: Case Studies from Syria

Mohamad Rukieh

Abstract Remote Sensing techniques play a pioneer role in this field, where space images have special characteristics and properties which are not found in the traditional methods, since wide and valuable information can be acquired about the geoenvironmental systems which adequately reflect the recent situation of the natural environment, and the impact of human activity effect. In comparison between old and recent remote sensing data, it is possible to study and determine the direction and intensity of the negative and positive processes which are related to both natural or human made factors and their impact on the environment, as well as the characteristics and extent of environment damage and pollution. We have carried out by these techniques. Geoenvironmental survey of the southern area of Syria on 1/100000 scale, with 10000square km2 Preparing geoenvironmental maps that reflect the natural components of ecosystems and the impact of human activity, in addition to the effect of the geological factors and those of geochemical pollutants. Also it was preparing maps of geoenvironmental assessment of the study area. We had digital processing for Russian and land sat TM images which we used, by using IRDAS software, especially those related to natural anomalies determination. The work is completed through field actions, which are represented by the checking the result of space images interpretation, collecting more than 4000 samples of soil, plants, ground and surface water, bottom sediments, rocks, for analysis. The results reflected in geochemical pollution maps.

Keywords Space images • Spectral band • Environmental mapping • Analysis • Syria

M. Rukieh (✉)
Damascus, Mazeh, Syria
e-mail: rukiehm@gmail.com

126.1 INTRODUCTION

During 1996-1997, in General Organization of remote sensing (GORS) a comprehensive geoenvironmental survey had been done to the southern part of Syria using remote sensing techniques, for 10000km² area of 1/100000 scale, (Fig. 126.1) This is for preparing geoenvironmental maps which show the environmental status of the study area as resulted from natural and artificial environmental systems resulted of human different activities. The geoenvironmental System represented a homogeneous area in its formation; of organized structure having specific phenomena resulted from the exchanged effect for the internal natural and artificial factors [1, 5] The natural elements in one geoenvironmental system are characterized in geological structure unity, relief, surface and ground water, soil, plants, conditions of new tectonic processes, and they form geodynamic and geochemical balance determining the direction of the affected artificial load[5]. The artificial elements were determined by samples of human manners which differ in the level of shape and effect on the environment. It is important here to refer that the geoenvironmental system may be formed in pure natural circumstances without any effect of the artificial factors to human activities [5] the study showed that using data of space and spatial survey in geoenvironmental mapping doesn't only allow the analysis of the available maps data but getting additional information about

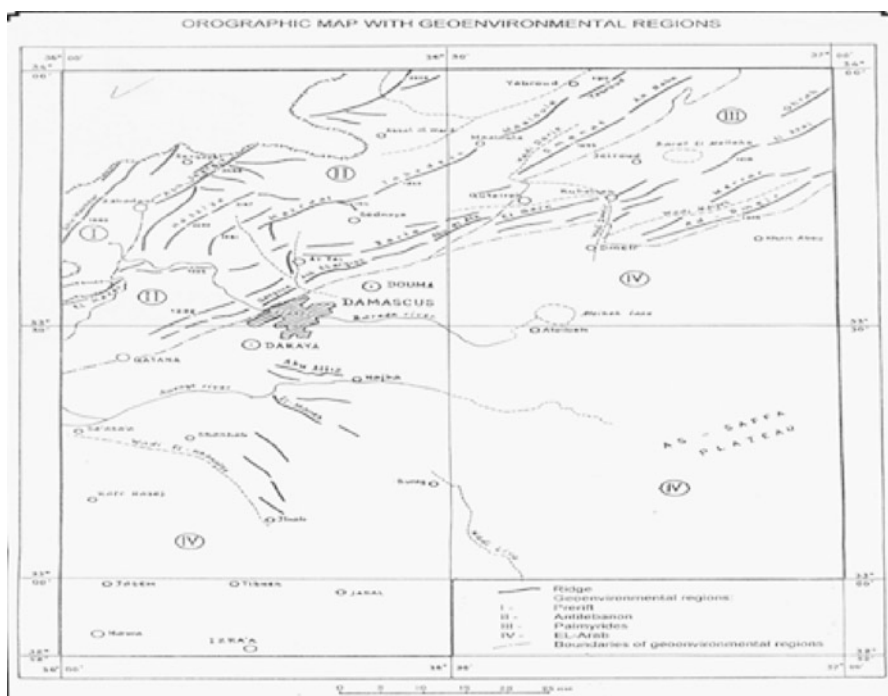


Fig. 126.1 Orographic map with geoenvironmental regions

geoenvironmental systems. The comparison between the old and new sensed data is useful in determining the direction and severity of environmental changes. As well as, it is available to increase the quantity of information through later digital processing the space images using programmes which could be followed by field works to specific areas. [5]

126.2 MATERIAL AND METHODS

We used space images of different scales, of various spectral channels /500-980/ nanometer, of different resolution /5-8 m to 45 m/, in different dates /1973-1995/, and in different seasons in the one year. Most of the images were taken by Russian satellite (Fig. 126.2).

The digital processing of space Images had been done by Sun station using ERDAS programme. The following data had been processed

- MCY data, 1995 which represented 6 images in three spectral bands registered digitally, and collected in one image for each spectral field.
- MCY 1992 data, image in three spectral fields registered digitally in addition to using filters in order to removal the deformation.

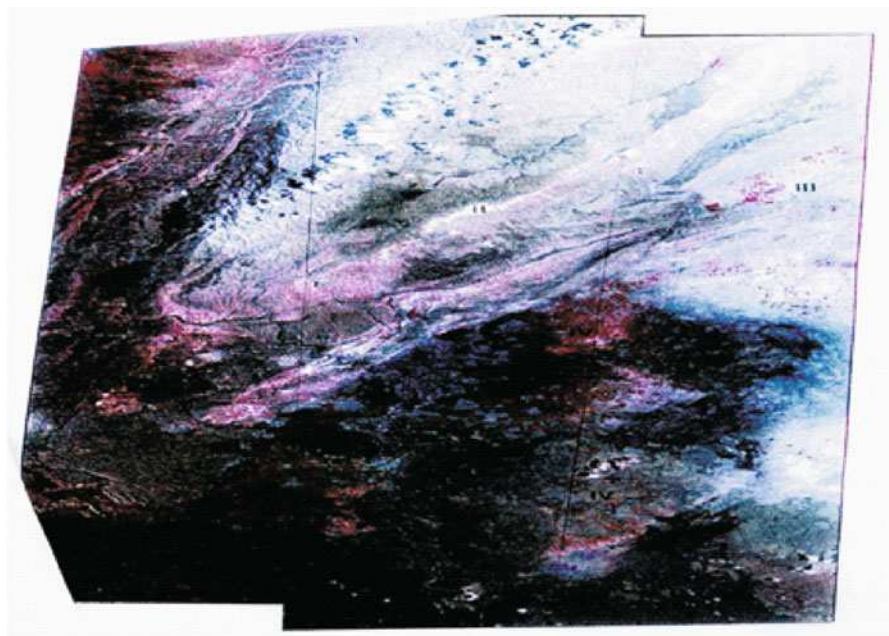


Fig. 126.2 Color Russian space image covers the study area and shows the natural geoenvironmental system (I-IV)

- Photographic space image taken by MK4 camera loaded on Resource F1 satellite and composed of two images in two spectral bands /640-690/ to /810-900/ nanometres, 1 / 800000 scale. The images had been changed to digital values keeping the resolution 7m. These data had been joint through referential points, and the necessary geometrical correction were made, this is a main process for showing the composite images later. The mechanical processing was made by using two main methods:

1- Synthesis colour for three spectral channels with (red, green, and blue). 2- colour symbolizing processes for specific narrow fields or for parts of them.

126.3 DISCUSSION

126.3.1 Preparing of Geoenvironmental Maps

Geoenvironmental maps had been prepared for a number of sheets to the study areas of 1/100000 figs. (1), each of them consisted of many sections, the most important:

Natural environmental system maps which reflect the natural characteristics and the geodynamic stability degree towards physical and mechanical effects, as well as towards soil pollution. Where a determining to four main geoenvironmental areas had been done: 1- the area of front rift, 2- eastern Lebanon series and Al-Kalamoon (Antilebanon), 3- western Palmyride, 4- southern volcanic area and Damascus basin (Jabal El-Arab) [2, 4] In addition to distinguish more than fifty primary environmental system. (Figs, 126.1, 126.2)

Phenomena and external and internal geological processes maps which reflect the tectonic breaks and active faults by which seismic zones are connected [2] As well as they show the parts in which external processes like sliding, erosion, karst, phenomena of wind effect, wetness, saltiness... etc are activated.

Land use maps which demonstrate 14 kinds of artificial systems resulted from human activities.

Maps of toxic and geochemical analysis results which show the pollution degree of soil, plants, surface and ground water and deep sediments

126.3.2 Estimation of the Geoenvironmental Status of the Study Area

Geoenvironmental estimation maps had been prepared to the study area depending on the natural geoenvironmental ability and the deformation degree of the natural environment, where determining the degree of deformation and anomalous through studying new space images, whereas determining the pollution degree had been

done through geochemical and toxic analysis research. The geoenvironmental ability had been divided to 9 groups depending on geochemical and geodynamic stability degree. As a sequence four main cases to environment had been distinguished: normal, accepted, dangerous and very dangerous.

126.4 RESULTS

For the first time in Syria, a group of geoenvironmental maps for the southern part of Syria had been prepared of 1/ 100000 using remote sensing data and field works which showed the recent environmental status in south of Syria and give the following:

More comprehensive estimation to the study area status. Determining the characteristics of the environmental deformation through group of quantitative and qualitative factors, as well as defining the pollution degree of different environmental surroundings such as: soil, plants, surface and ground water, bottom sediments. Etc., dividing the natural environmental milieu to four samples: stable, accepted, moderately and threatened. Estimation of geoenvironmental ability through geochemical and geodynamic stability degree in addition to preparing map of geoenvironmental ability and status of milieu., Determining the dangerous area which is characterized by huge pollution, it covers part of Damascus and its surroundings, Ghota, Darya, Doma, Qatana and industrial areas., Showing the boundary of the huge anomalous zones through space images., Determining the natural factors which cause desertification. And the role of human activity in this processes which include: climate dryness, low surface flow, saltiness of deep and surface soil, formation of carbonate and plaster crust on the surface of land, and plant rarefaction which is represented by:

Arbitrary grazing in the low productive grassland.

Retraction of forestry.

Irregular irrigation to the arable lands [3]

The strong active of cities growth, industrial production

126.5 CONCLUSIONS

The Research shows the importance and effectiveness of remote sensing data Integrated with field work in Geoenvironmental survey and preparing the Geoenvironmental and Estimation maps. The methodology which we used may be able to demonstrate in other areas for likes studies.

REFERENCES

1. Fenogradov, B.F.: Aerospace Monitoring for the Environmental Systems. Book, Moscow (1984)
2. Ponikarov: The Geological Map for Syria (1966)
3. The Use of Water Resources for Barada and Al-Awag Basins for Irrigation purposes in Syria: Report. A group of Russian experts, Leningrad (1986)
4. Kouzlov, F.F.: The History of Geologic Development in Neogene, Quaternary and the Recent Tectonic in Syria: Report. Moscow (1966)
5. Mernova, A.F.: Remote Sensing and Geoenvironmental Mapping Depending on Space Images. Book, Moscow (1994)

Chapter 127

Integrating Smart Platforms to Analyze Energy Patterns in Academic Building

Prasad A. Pathak, Bakul Budhiraja, and Deepika Mann

Abstract Commercially available software for energy monitoring provide the output in terms of graphs and tables, however, they are limited in visualization of spatial distribution of energy consumption. In this study we have used Samsung Galaxy S4 as the relatively cheaper platform to collect data for temperature and humidity inside an academic block of Shiv Nadar University and visualized it in 3D with other datasets. This study has been treated as an exploration of cellphone based sensors to collect data and integrate it into GIS domain for effective visualization. It was found that the smartphone based data collection is easy, has a potential of crowd sourcing for data collection and can be integrated with GIS with certain additional steps. This study is a part of a grant received by Shiv Nadar University from Dept. of Electronics and IT, Govt. of India.

Keywords Temperature • Humidity • GIS • Visualization • 3D analyst

127.1 INTRODUCTION

It has been observed and proved in many studies that large buildings are inefficient in terms of energy consumption and conservation [1, 2, 3]. Educational institutes have several types of buildings, i.e. academic blocks, hostels, administrative buildings, library, etc. According to the type of building, its usage is different and hence, the energy consumption would be different. Building structure and components are crucial factors in determining the thermal mass of a building which is an indicator of heat gain/loss and help us calculate cooling or heating demand. Usually, this analysis is performed in the preliminary design evaluation steps. A lot of software programs are available for the same [4]. In the functional buildings, wired sensors have been used to monitor temperature and humidity in individual rooms of academic and commercial buildings. A step further is to install smart meters to

P.A. Pathak (✉)
Shiv Nadar University, Dadri, Uttar Pradesh, India
e-mail: prasad.pathak@snu.edu.in

B. Budhiraja • D. Mann
TERI University Vasant Kunj, New Delhi, India

obtain electricity consumption data at frequency of even 30 seconds to identify the patterns of energy consumption [5]. Most of them provide the results in graphs which have “time” component as one of the axes, however, are not indicative of the context why the consumption of electricity has happened. Moreover, this kind of continuous monitoring demands infrastructure investment, software investment and deciphering the results to identify high and low energy consumption patterns. In academic building set up, we assumed the energy consumption patterns may be dependent on usage of various areas at any particular time, i.e. number of occupants in the given instance, and the use, i.e. use of computers, etc. These factors along with concurrent temperature and humidity would determine the energy demand and definitely, would generate spatial and temporal patterns. GIS has been used to analyze energy consumption patterns at the scale of city or a large region. However, indoor studies have rarely used GIS. Recently, [1] adopted GIS to map energy consumption across a university campus in Malaysia. The study was carried out for all the buildings, a single measure of energy consumption was obtained per building and details within each building were not studied separately. In another study, [6] integrated GIS along with sensor network based data collection system and a simulation software. The study has explored capacity of GIS to store data and convert building CAD drawings into a spatial database. Analysis was not carried out in GIS. One of the forte of GIS is 2D and 3D visualization, which has not been explored in providing visual context to the energy patterns. With availability smartphones such as Samsung Galaxy S4, sensors for temperature and humidity are easily available and help us cross over the problem of data availability. According to Sensirion [7], the manufacturer of the temperature and humidity sensor in this phone, the sensor has accuracy of 0.5°C and 4% in temperature and relative humidity, respectively. Approximately 3 seconds is the frequency at which it can recognize change in the parameters but allow data collection even every second. In this study, we have used the android based application, developed by Computer Sciences team in the same project, to collect temperature and relative humidity data. The next sections would describe the data collection and results.

127.2 STUDY AREA AND DATA COLLECTION

A floor of an academic block in Shiv Nadar University was used as a testbed in this study. It represents various usage areas, such as classrooms, computer labs, lounge, conference rooms, faculty cabins, and open corridors. Thus, it has both controlled and uncontrolled environments (Fig 127.1).

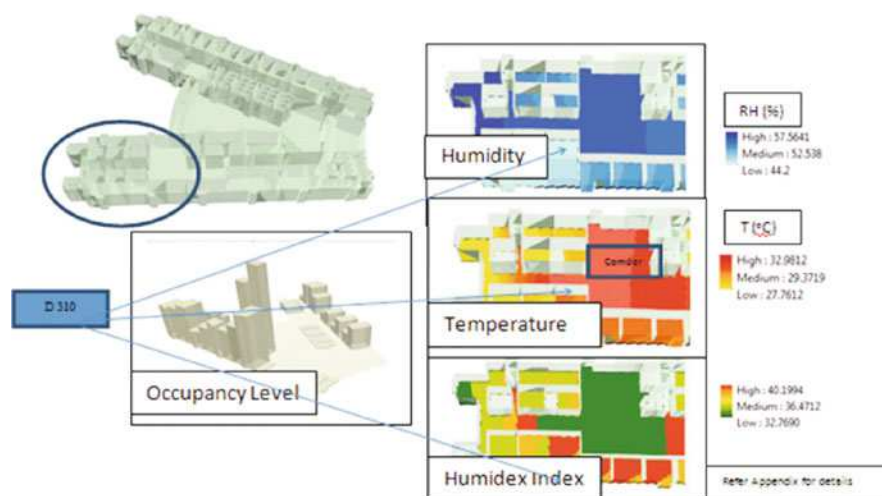


Fig. 127.1 3D visualization of an entire floor, humidity, temperature, humidex, and occupancy for a portion of the floor

127.3 MATERIAL AND METHODS

One of the major limitation which was realized in designing the data collection method was unavailability of GPS signal for this indoor measurements. Hence, locations were predetermined to collect data. A team of researchers was staying at each location for 15 seconds to make sure that the sensor has recognized the parameters and then the data was stored (May 1st, 2014, 1 pm). A unique identification number of assigned to each location and was used while storing the data on phones. This data was then imported into GIS domain in .csv file format. Other parameters collected: occupancy of everyroom at hourly basis, no. of machines (computers) installed in each room. The spatial database was created using ArcGIS 10 suite. Temperature and humidity data was collected for one time. The data was stored on the phone in .csv format and then it was attached to sampling point layer in GIS using their ids. Diffused interpolation with barriers technique was adopted to create interpolation surface for temperature and humidity. Further, Humidex index was calculated from these parameters for the entire floor as an indicator of zones demanding more energy for cooling. ArcScene was used to develop a 3D model of the study area. The Fig. 127.1 shows various zones of the floor in 3D and the parameters observed, it also shows the Humidex index surface for each zone. Fig. 127.2 shows a graph with all the variables for the group of rooms shown below. The graph shows that high occupancy, temperature, and humidity kick start the “Noticeable Discomfort zone” category.

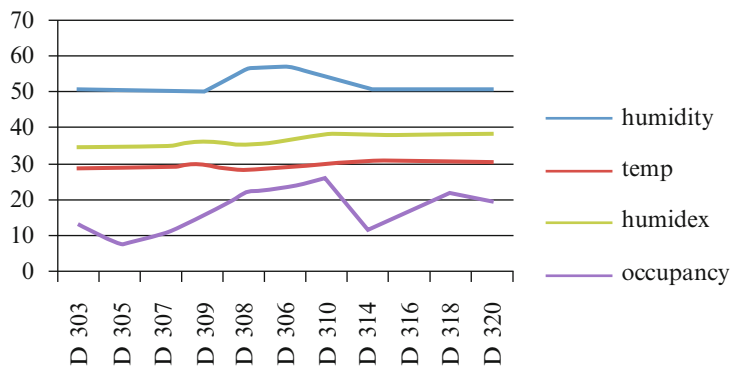


Fig. 127.2 Graphical representation of environmental parameters and humidex index

Table 127.1 Comfort zones according to Humidex

Humidex (°C)	Degree of comfort and discomfort
Less than 29	Little or no discomfort
30 to 34	Noticeable discomfort
35 to39	Evident discomfort
40 to 45	Intense discomfort: avoid exertion
45 to 54	Dangerous discomfort
Above 54	Heat stroke probable

127.4 RESULTS AND DISCUSSION

It is clear from Fig. 127.2 that as all the parameters (Occupancy, Temperature, and Humidity) indicate, a discomfort zone is obtained in the class room D 310. However, unless, the 3D visualization is carried out, the relative location of the room and spatial distribution of the variables in its neighboring areas is not clear. The 3D visualization in Fig. 127.1 clearly shows that the corridor area has higher temperature and humidity which has generated zones of discomfort according to humidex index (Table 127.1) and there is no role of occupancy. However, classrooms such D 310 develop zones of discomfort during a particular time of the day such as around 1 pm, when they experience higher occupancy (which adds to relatively higher temperature, humidity even in controlled environment) along with the exposure to sun.

127.5 CONCLUSIONS

Graphical representation with location information suggests the exact location of areas of discomfort where more energy demand would generate to regulate temperature. However, 3D visualization of spatio-temporal data suggests or provides

more logical reasoning to justify such demands because of other related factors like sun exposure, conditions in the immediate vicinity, etc. Integration of smart phone as a tool to collect indoor data is easy, supports infrastructure for data transfer and GIS conversion for visualization. Automatic capturing of indoor location was the major limitation in this study. The 3D visualization is extremely useful in understanding the small scale variations in environmental parameters, i.e. temperature and humidity in a broader context. The study will be further extended to calculate thermal mass and suggest structural changes to conserve energy of the academic block where 3D visualization of spatio-temporal data collected over larger period of times will be utilized.

REFERENCES

1. Rasam, A., Hanif, F., Samad, A. and Hadi, R.: Spatial Information Management System for Building Energy Consumption. Proceedings 2013 I.E. 3rd International Conference on System Engineering and Technology, 19–20 Aug. 2013, Shah Alam, Malaysia (2013)
2. Doukas, H., Patlitziannas, K.D., Iatropoulos, K. and Psarras, J.: Intelligent building energy management system using rule sets. *Building and Environment*, 42, 3562–3569 (2007)
3. Zhao, H. and Magoules, F.: A review on the prediction of building energy consumption. *Renewable and Sustainable Energy Reviews*, 16, 3586–3592 (2012)
4. ECOTECT: Building Performance Simulation Software obtained at <http://www.zigersnead.com/current/blog/post/ecotect-building-performance-simulation-software/08-05-2008/1307/> dated 01/05/2014
5. Zenatix: Start-up co-founded by Dr. Amarjeet Singh on energy data analytics, obtained at <http://www.iiitd.ac.in/news/zenatix> on 08/06/2014
6. Agnolotti, V. and Giger, C. (unknown).SIMGIS: GIS for Thermal Simulations in the Built Environment. ESRI User Conference Proceedings. Obtained at <http://proceedings.esri.com/library/userconf/proc05/papers/pap2402.pdf>, dated 08/06/2014
7. Sensirion: SHTC1 – Digital Humidity Sensor. Obtained at <http://www.sensirion.com/en/products/humidity-temperature/humidity-sensor-shtc1/> date 08/06/2014

Chapter 128

An Integrated Golden Spike Information Portal Enabled by Data Visualization and Semantic Web Technologies

Xiaogang Ma, Linyun Fu, Peter Fox, and Gang Liu

Abstract The purpose of the portal (<http://geotime.tw.rpi.edu/>) described in this paper is to provide formal background information of Golden Spikes. Golden Spike is the nickname for Global Boundary Stratotype Section and Point, or GSSP, which a stratigraphic section is serving as the reference unit for a particular boundary on the geologic time scale. In this work we deployed a number of state-of-the-art information technologies, such as semantic modeling and encoding, data visualization, SPARQL query, and online map layers from Web Map Services. The portal received positive feedbacks from researchers in the domain of stratigraphy and we are assembling further information and updating the portal to make it more useful.

Keywords Stratigraphy • Geochronology • Geologic time ontology • Semantic web • Geoinformatics

128.1 INTRODUCTION

An important output of international stratigraphic study is the International Chronostratigraphic Chart released by the International Commission on Stratigraphy [1]. The chart sets up a coordination of geologic time scale among various countries and has been widely used in geologic works [2]. An essential part of the International Chronostratigraphic Chart is the information about Global Boundary Stratotype Section and Point (GSSP), or Golden Spike. In the past few years, geoinformatics researchers have taken efforts to build computer-readable models for the geologic time scale [1,3-4]. Most recently, works have been done on the modeling and encoding of geologic time onto logics and vocabularies that can be used in the Semantic Web [3-5]. In a recent review paper [6] we analyzed those

X. Ma (✉) • L. Fu • P. Fox

Tetherless World Constellation, Rensselaer Polytechnic Institute, 110 8th Street, Troy, NY, USA

e-mail: max7@rpi.edu

G. Liu

School of Computer Science, China University of Geosciences, Wuhan, China

works and gave comments on further efforts. The work presented in this paper is a part of the efforts following the directions discussed in that review. The purpose of this paper is to present the work we have done for an integrated information portal of golden spikes. The background information of golden spikes covers various topics such as geochronology, stratigraphy, paleontology, petrography, etc. Careful modeling and encoding are needed if we want to present those topics in a single user interface. The Semantic Web provides new approaches for the modeling and encoding work. A key feature of the Semantic Web, comparing with the conventional Web, is that it provides a space in which the data in the Web can not only read and understood by humans but also can be read and processed by computers. To achieve that feature, onto logies and vocabularies are modeled and encoded to underpin the data. In this work, we reused the ontology and vocabulary developed by Cox and Richard [7] and we followed the approach we adopted for visualizing the geologic time scale [8] but with a new method to realize the interactions. The following sections will present the methods we applied the functions realized, as well as the feedbacks from the community of stratigraphic studies.

128.2 METHODS APPLIED AND FUNCTIONS REALIZED

128.2.1 Geologic Time Ontology and Vocabulary

As discussed in [6], there are two key concepts to know in the geologic time scale: interval and boundary. An interval is equal to a period of time and a boundary is equal to a certain time. The golden spike is a concept of boundary in this sense. They are ratified (by IUGS – International Union of Geological Sciences) stratigraphic section serving as reference units that divide intervals in the geologic time scale. Understanding the two concepts will help us read the modeling and encoding of the geologic time ontology and vocabulary in [7]. The ontologies and vocabularies discussed in that paper are corresponding to different versions of the International Chronostratigraphic Chart, and are accessible at [9]. We loaded a version of the geologic time ontology and vocabulary into a triple store (i.e. a database for the Semantic Web) and used it as the knowledge base for the portal.

128.2.2 Visualization

In [8] we developed a visualization of the geologic time scale by using the Action Script language and the Flare library [10], and developed interactions between the visualization and online geologic map layers by using the JavaScript language. A downside of [8] is that we need an interface between the ActionScript and

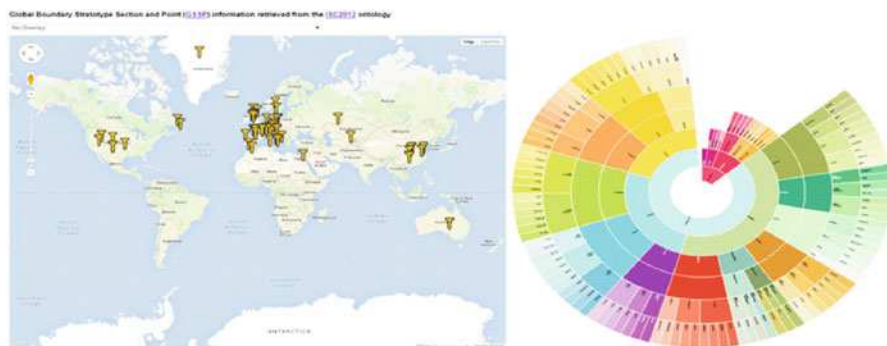


Fig. 128.1 User interface of the developed golden spike information portal (accessible at: <http://geotime.tw.rpi.edu>)

JavaScript programming languages to setup a channel for transferring data and this hinders the efficiency in programming. In this work we use the D3 library [11] for developing a visualization of the geologic time scale. D3 is a JavaScript library and this provides convenience for us to develop the interactions between the visualization and symbols of golden spikes distributed in a Google Map window. Figure 128.1 shows the layout of the user interface of the developed portal.

128.2.3 Interactions

When the portal is initialized, it will show a map window with all the golden spikes inside. The data of all golden spikes are from the result of a SPARQL query sent to the triple store. Users can zoom in to see the detailed location of one or a few of them. If a user clicks a spike, a small window will pop up (see Fig. 128.2), showing the primary guiding criterion, age information and a link to more details of the golden spike. Clicking that link will show an image with formal description of that golden spike (Fig. 128.3).

When the spike symbol is clicked, such as the Base Darriwilian in Fig. 128.2, in the visualization chart on the right part of the user interface a node of the corresponding chronostratigraphic unit will be highlighted (Fig. 128.4), to show the location of this unit in the geologic time scale. If a user clicks a node in the visualization chart, the map window will zoom into the corresponding golden spike and the information window will pop up. Each click in the visualization chart initiates a SPARQL query and the interactions in the map window are based on the query result. On the top left part of the user interface we also provide a drop down list of online geologic map layers. Users can load them into the map window to see more information about the area where a golden spike is located.



Fig. 128.2 Pop-up window of the golden spike of Base Darriwilian

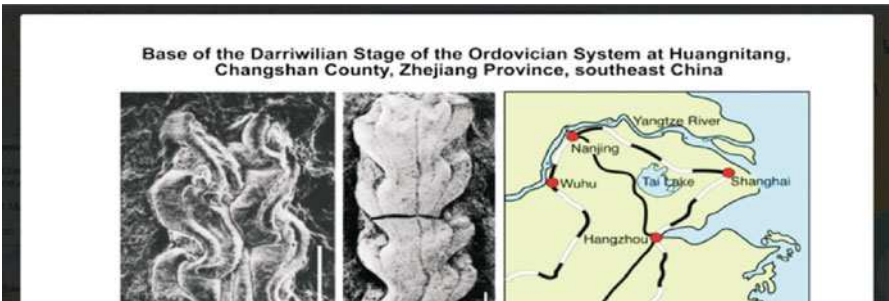


Fig. 128.3 Formal description of the golden spike of Base Darriwilian



Fig. 128.4 A highlighted chronostratigraphic unit in the visualization chart

128.3 FEEDBACKS FROM COMMUNITY

In early 2014 we invited researchers in the domain of stratigraphy to use the portal and received positive feedbacks from them. They thought this is a nice tool for reference in research and education. They also offer suggestions on how to improve it. For example, one suggestion on the visualization chart is to use a table-style layout to replace the current sun-burst style.

128.4 CONCLUSIONS

By using data visualization, geoinformatics and Semantic Web technologies, we developed an informational portal of golden spikes, which is a useful tool for reference in research and education of stratigraphy.

ACKNOWLEDGEMENTS This work is partly supported by the National Science Foundation of China (NSFC No. 41172300).

REFERENCES

1. <http://www.stratigraphy.org/index.php/ics-chart-timescale>
2. Gradstein, F.M., Ogg, J.G. and Smith, A.G. (eds): A Geologic Time Scale 2004. Cambridge University Press, Cambridge (2004)
3. NADM Steering Committee: NADM Conceptual Model 1.0—A conceptual model for geologic map information: U.S. Geological Survey Open-File Report 2004–1334, North American Geologic Map Data Model (NADM) Steering Committee, Reston, VA, USA (2004)
4. Cox, S.J.D. and Richard, S.M.: A formal model for the geologic time scale and global stratotype section and point, compatible with geospatial information transfer standards. *Geosphere*, 1(3), 119–137 (2005)
5. Michalak, J.: Topological conceptual model of geological relative time scale for geoinformation systems. *ComputGeosci*, 31(7), 865–876 (2005)
6. Perrin, M., Mastella, L., Morel, O. and Lorenzatti, A.: Geological time formalization: an improved formal model for describing time successions and their correlation. *Earth Sci Inform*, 4(2), 81–96 (2011)
7. Cox, S.J.: OWL representation of the geologic timescale implementing stratigraphic best practice. Abstract IN31B-1440 presented at 2011 Fall Meeting, AGU, San Francisco, CA (2011)
8. Ma, X., Carranza, E.J.M., Wu, C., van der Meer, F.D. and Liu, G.: A SKOS-based multilingual thesaurus of geological time scale for interoperability of online geological maps. *Computers & Geosciences*, 37(10), 1602–1615 (2011)
9. Ma, X. and Fox, P.: Recent progress on geologic time ontologies and considerations for future works. *Earth Science Informatics*, 6(1), 31–46 (2013)
10. Cox, S.J.D. and Richard, S.M.: A geologic timescale ontology and service. *Earth Science Informatics*, In press (2014)
11. Ma, X., Carranza, E.J.M., Wu, C. and van der Meer, F.D.: Ontology-aided annotation, visualization and generalization of geological time scale information from online geological map services. *Computers & Geosciences*, 40(3), 107–119 (2012)
12. <http://resource.geosciml.org/vocabulary/timescale/>
13. <http://flare.prefuse.org/>
14. <http://d3js.org/>

Chapter 129

Web-based Facility Management System Using Open Source GIS

P. Naga Vineet and L. Gnanaphazzam

Abstract Organizations use facility management as an important management tool and also as strategy for resource and facility management. But, question arises in defining facility management and how GIS can help improvising FM? Such systems require three dimensional data alongside time. GIS can provide a solution to the lacuna. In organizations, the demand for additional space and resources increases through time. Indian Institute of Space Science and Technology plans to use GIS for FM of the campus. A methodology has been developed for FM utilizing GIS platform. This paper proposes the methodology utilizing ArcGIS, proprietary software for data preparation and open source software's such as Geoserver, Unity 3D Game Engine, C++, JavaScript, CSS and XML for developing various components of the Web based facility management.

Keywords Geographic information system • Facility management • 2D and 3D GIS on web • Web mapping service • Indian Institute of Space Science and Technology

129.1 INTRODUCTION

GIS has transformed the way organizations use geographical information. It presents geographical information in a meaningful way to analyze and answer spatial questions. Governments, Industries, Organizations and Universities are some examples of users who implement GIS in their day to day activities. Specifically, these require a unified system which can provide single point access to all secure administrative information, both graphical and non-graphical information. Some of the objectives can be achieved through Facility Management. But, question arises in defining FM and the extent of productive use of information and how GIS can help improvising FM? FM provides project planners, managers and administrators manage infrastructure information, while GIS helps to analyze, visualize and

P.N. Vineet (✉) • L. Gnanaphazzam

Department of Earth and Space Sciences, Indian Institute of Space Science and Technology,
Thiruvananthapuram, India

e-mail: vineeth.naga@gmail.com

manage information in spatial mode. Thus, combining FM and GIS can lead to meaningful and productive use of information and also as a strategy tool for resource management. Such systems require three dimensional data alongside time. Aforementioned, due to the need of spatial mode FM for universities, web based GIS system can be a possible solution for the lacuna. The system objective is to collect both graphic and non-graphic information related to university and its sub-departments and transform to a computer platform to store, analyze, query and present in various formats of charts, reports, maps and web-based views aiming to increase efficiency and progress of the university. Information retrieved is productive, if three-dimensional information is available in spatial information. Thus, visualizing 3-dimensional information gives productive information. 3D technologies in WebGIS have many hurdles which are yet to be solved. However, a methodology is developed utilizing ArcGIS, proprietary software for data preparation and open source software's such as Geoserver, Unity 3D Game Engine, C++, JavaScript, CSS and XML for developing various components of the Web based facility management.

129.2 STUDY AREA

The study area is Indian Institute of Space Science and Technology campus situated at coordinates 8°37'31"N, 77°02'02"E at Valiamala, Thiruvananthapuram, Kerala, India. It is Asia's first Space Institute well known for programmes with specific focus to space science, technology and applications.

129.3 DATA AND SOFTWARES USED

Primary data used for this research are

- CAD drawings of infrastructure information (buildings, roads, etc.)
- Hard copy of electrical and water lines.

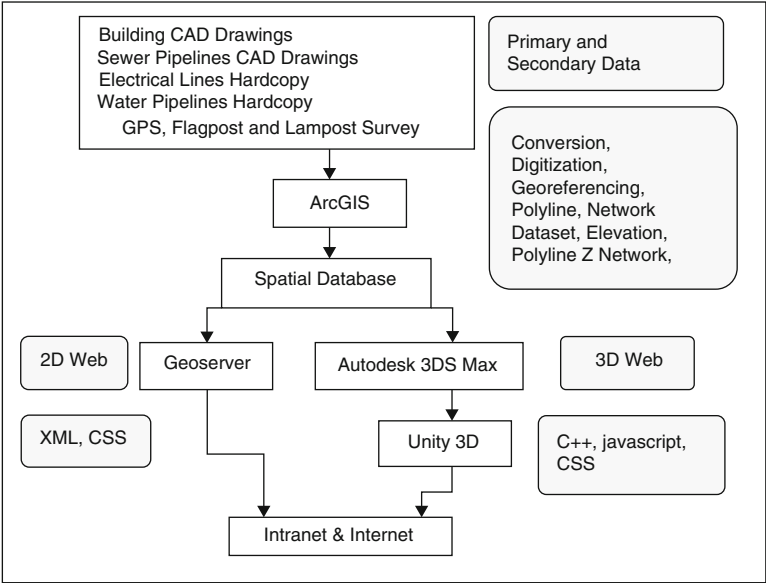
Secondary data used were

- Manual survey (floor wise details, student records, etc.)

Software's utilized for this research were:- ArcGIS, AutoCAD, Geoserver, Unity 3D Game Engine

129.4 METHODOLOGY

ArcGIS was used for generating geodatabase utilizing raw data from primary and secondary data. Important information which were necessary for facility management such as floor wise details of buildings and information of utilities and other



Flowchart 129.1 Methodology developed for 2D and 3D GIS facility management of IIST

manual survey information were incorporated as attributes. After the geodatabase has been created, 2D spatial web deployment was done through Geoserver. Web mapping service has been generated using CSS and XML and controls for query and map download options were incorporated on the web interface. Although, there were technical hurdles in 3D web deployment, it was successful utilizing Unity 3D game engine with C++, JavaScript and CSS. Walkthrough of the campus was an important feature which was required in the objectives of the research project. Thus a character was created and controls were through arrow combinations of keyboard for navigation and cursor for direction. The methodology developed is presented in Flowchart 129.1.

129.5 RESULTS AND DISCUSSION

129.5.1 Spatial Database and 2D Web GIS

Spatial geodatabase which was generated was successfully deployed on web for 2D using Geoserver. (Fig 129.1. and Fig 129.2.). The query feature successfully displayed the relevant information of the buildings at the bottom of the webpage. Such information can be utilized for resource and facility management of the future needs of the campus.



Fig. 129.4 Web page view of 3D GIS and room view of walkthrough with information

129.6 CONCLUSIONS

The research mainly focused on facility management with implementation of 3D graphics into WebGIS. With 3D graphics into GIS, it created a new potential which is immense and can make users use WebGIS more efficiently. Through advancements in technology, we can ensure 3D WebGIS to become easier to implement and can find unique applications. The results obtained answer the question which was focused in the article. The proposed methodology and obtained results are of promising quality which can be used for further developments in this sector.

REFERENCES

1. Stuart Rich and Kevin H Davis.: Geographical Information Systems (GIS) for Facility Management (2010)
2. Dr. Shankar Kumar Sinnakaudan et al.: Geocampus: UiTM Penang Campus Management System. Geospatial World Map Asia (2007)
3. Bruce Boyd and Rainbolt, Eric S.: GIS for University campus planning and Facilities Management. ESRI International User Conference (1998)
4. Tein-Yin Chou et al.: An Implementation of 3D GIS on web, AARS (2000)
5. Siyka Zlatanova and Klaus Tempfli: Modelling for 3D GIS: Spatial Analysis and visualization through web. ISPRS, XXXIII, Part B4, Amsterdam (2000)
6. T. Schürl, Boy, A. and Fritsch, D.: Geographic Information Systems and Facility Management, ISPRS, XXXII, Part 4, Germany (1998)
7. Dieter Fritsch and Martin Kada: Visualization using Game Engines. ISPRS, XXXV, Commission 5, 621–625, Istanbul (2004)
8. U. Baaser, Laudein, R. and Bareth, G.: Campus Routing – A Web based LBS for the University of Cologne. ISPRS, XXXVIII, Part 2, 302–306, Hong Kong (2010)

Part VI
Meteorology and Climate Change

Chapter 130

Estimation of Wind Speed in the Suburban Atmospheric Surface Layer

Tanja Likso

Abstract The main goal of this paper is to examine a possibility of application of Monin-Obukhov similarity theory for the wind speed estimation at 2 m above the ground using the routine weather elements. Consequently, for this purpose the meteorological data for the year 2005 at the Zagreb-Maksimir Observatory, located in a suburban setting was used. The similarity theory is adopted for the purposes of estimation of the wind speed at 2 m above the ground, that is, for calculation of turbulence parameters. One of the most important results is the classification of effective roughness length according to wind direction. The comparison between measured and estimated wind speed at 2 m above the ground ignoring and taking into account the dependence of effective roughness length on wind direction was performed. The verification parameters for estimation of wind speed at 2 m are bias, mean absolute error and root mean squared error between measured and estimated values of wind speed. Taking into account the dependence of effective roughness length on wind directions, all three parameters decreased, especially the bias.

Keywords Wind speed • Similarity theory • Effective roughness length

130.1 INTRODUCTION

The measurement of wind speed and direction is highly sensitive to flow distortion by obstacles. This is the reason why the standard height for wind observations is set at 10 m above the ground. However, many studies are based on the wind speed data at lower level, for example at 2 m. Due to the lack of such observed wind speed data, only an indirect approach for their estimation is possible, using routinely observed weather elements. The Monin-Obukhov (M-O) theory is adopted for the purposes of estimation of the wind speed at 2 m above the ground, that is, for calculation turbulence parameters following improvements that were introduced by [1–5]

T. Likso (✉)

Department for Climate Monitoring, Meteorological and Hydrological Service of Croatia,
Zagreb, Croatia

e-mail: likso@cirus.dhz.hr

130.2 MONIN-OBUKHOV SIMILARITY THEORY APPLICATION

The method for estimating the surface layer parameters at the edge of suburban area is described in detail by [6, 7], only the basic ideas are repeated here. For estimation of M-O length L an iterative and empirical procedure are used. In the iterative procedure the computation starts with estimates for the typical quantities of turbulence scales, i.e. friction velocity u^* and temperature scale θ^* with the assumption about neutral atmospheric static stability (M-O stability parameter $\zeta = z/L \rightarrow 0$). Using new values of u^* and θ^* an updated value of M-O length is calculated. Depending on the sign of M-O length, new values of u^* and θ^* enter the calculation where appropriate stability corrections are introduced. Taking into account these new, improved values of u^* and θ^* , the new improved value of M-O length is obtained, and so on. It appears that usually not more than three iteration steps are needed to achieve a sufficient accuracy of 1 % in successive values of M-O length. On the other hand, the mentioned empirical procedure is based on approximate solutions for the relationship between M-O stability parameter ζ and bulk Richardson number Ri proposed by [5]. If wind speed is available at the height z_2 , then, an estimation of wind speed at other level in surface layer can be obtained using:

$$u(z_1) = u(z_2) \left[\frac{\ln\left(\frac{z_1}{z_0} - \psi_m\left(\frac{z_1}{L}\right)\right)}{\ln\left(\frac{z_2}{z_0} - \psi_m\left(\frac{z_2}{L}\right)\right)} \right] \quad (130.1)$$

If $L < 0$ (statistically unstable conditions), stability correction functions are calculated as [3]:

$$\psi_m\left(\frac{z_1}{L}\right) = 2\ln\left(\frac{1+x}{2}\right) + \ln\left(\frac{1+x^2}{2}\right) - 2\tan^{-1}(x) + \frac{\pi}{2} \quad (130.2)$$

$$\text{where} \quad \psi_h\left(\frac{z}{L}\right) = 2\ln\left(\frac{1+x^2}{2}\right) \quad (130.3)$$

$$x = \left(1 - 16\frac{z}{L}\right)^{\frac{1}{4}} \quad (130.4)$$

According to [4], if $L > 0$ (statistically stable atmospheric conditions) then ψ_m and ψ_h can be calculated according to relations:

$$-\psi_m \frac{az}{L} + b\left(\frac{z}{L} - \frac{c}{d}\right)\exp\left(-\frac{dz}{L}\right) + \frac{bc}{d} \quad (130.5)$$

$$-\Psi_h \left(1 + \frac{2az}{3L} \right)^{\frac{3}{2}} + b \left(\frac{z}{L} - \frac{c}{d} \right) \exp \left(-\frac{dz}{L} \right) + \left(\frac{bc}{d} - 1 \right) \quad (130.6)$$

where $a = 1$, $b = 0.667$, $c = 5$ and $d = 0.35$.

Before introducing improvements [4] for stability correction functions, there were a certain number of errors in convergence of L under stable conditions. After taking into account corrections (5, 6), there were only a low number of cases with error in convergence of L and consequently errors in calculations of u^* and θ^* . In order to avoid such unacceptable results of L in mentioned iterative procedure the value $L = 0.001$ m as a low limit was used.

130.2.1 Effective Roughness Length Estimation

In this paper three approaches for effective roughness length z_0 estimation are used: root mean squared errors (RMSE) between estimated and corresponding measured values of wind speed at 2 m above ground, relationship between the standard deviation of wind speed and z_0 as well as the relationship between the median of wind gust factor and z_0 . According to all three methods used, z_0 values obtained are higher for western than for eastern quadrants of wind direction, as expected.

130.3 RESULTS

The comparison between measured and estimated wind speed at 2 m height ignoring and taking into account the dependence of z_0 on wind directions was performed. Table 130.1 shows three verification parameters of wind speed at 2 m: bias, mean absolute error and root mean squared error between measured and estimated values of wind speed. Taking into account the dependence of z_0 on wind directions, all three parameters (estimation errors) decreased especially the bias in comparison with corresponding parameters of wind speed estimation without any classification according to wind direction.

130.4 CONCLUSION

One-year period of special observation during 2005 at the Zagreb-Maksimir Observatory made possible the application of M-O similarity theory for estimation of the wind speed at 2 m above the ground, that is, for calculation surface layer parameters using both improved iterative and empirical method. Both methods are in excellent agreement with the exception of statically very stable conditions, i.e. when the bulk

Table 130.1 Verification parameters of wind speed at 2 m height for the Zagreb-Maksimir Observatory for the year 2005: bias (BIAS), mean absolute errors (MAE) and root mean squared errors (RMSE). The results refer to the cases of wind speed > 2 m/s and under neutral conditions

Wind direction sectors*	Verification parameters: BIAS, MAE, RMSE, Zagreb-Maksimir			
	z_0 (m)	BIAS (m/s)	MAE (m/s)	RMSE (m/s)
N-NE	0.15	-0.09	0.30	0.40
NE-E	0.15	-0.07	0.24	0.20
E-SE	0.13	0.00	0.14	0.15
SE-S	0.13	0.01	0.24	0.28
S-SW	0.20	-0.06	0.33	0.41
SW-W	0.35	-0.04	0.33	0.41
W-NW	0.25	0.00	0.25	0.39
NW-N	0.20	0.01	0.18	0.19
Mean	0.20	-0.03	0.25	0.31
All directions**	0.18	-0.11	0.32	0.41

*Classification according to wind direction sectors

**Estimation without any classification according to wind direction

Richardson number $Ri > 1$. This limitation of the presented method in reproducing intermittent turbulence is directly caused by the use of a stability correction functions under very stable conditions [8]. The most important result is the estimation of effective roughness length z_0 . Dependence of z_0 on wind direction has been established. The highest values appeared for the western and the lowest for the eastern wind directions, representing suburban terrain of about 1 km in the upwind direction. The estimation of wind speed at 2 m height is satisfying irrespective of the fact that obtained values underestimated observed values. Obtained results are in accordance with expectations. Taking into account the dependence of z_0 on wind directions, all the three verification parameters decreased especially the bias in comparison with corresponding parameters of wind speed estimation without any classification according to wind direction. The obtained results suggest that the wind observation at the standard level (10 m) is representative for the area of about one kilometre in the upwind direction. The wind data extrapolation at lower or higher levels, based on standard measurements at 10 m, can provide values of the wind representative for wider inhomogeneous (regarding surface roughness) suburban area of the city of Zagreb. This data can be used for atmospheric modelling, estimation of turbulent fluxes, wind energy, civil engineering and air pollution applications, etc.

REFERENCES

1. Paulson, C.A.: The Mathematical Representation of Wind Speed and Temperature Profiles in the Unstable Atmospheric Surface Layer. *J. Appl. Meteor.* 9, 857–861 (1970)
2. Businger, J.A., Wyngaard, J.C., Izumi, Y. and Bradley, E.F.: Flux-profile Relationships in the Atmospheric Surface Layer. *J. Atmos. Sci.* 28, 181–189 (1971)
3. Dyer, A.J.: A Review of Flux-profile Relationships. *Bound.-Layer Meteorol.* 7, 363–372 (1974)
4. Beljaars, A.C.M. and Holtslag, A.A.M.: Flux Parameterization over Land Surfaces for Atmospheric Models. *J. Appl. Meteor.* 30, 327–341 (1991)
5. Lee, H.N.: Improvement of Surface Flux Calculations in the Atmospheric Surface Layer. *J. Appl. Meteor.* 36, 1416–1423 (1997)
6. Likso, T. and Pandžić, K.: Determination of Surface Layer Parameters at the Edge of a Suburban Area. *Theor. Appl. Climatol.* 108, 373–384 (2012)
7. Likso, T.: Estimation of Wind Speed in the Suburban Atmospheric Surface Layer. Doctoral thesis (in Croatian), Faculty of Science, University of Zagreb, 98 pp (2012)
8. Costa, F.D., Acevedo, O.C., Mombach, J.C.M. and Degrazia, G.A.: A Simplified Model for Intermittent Turbulence in the Nocturnal Boundary Layer. *J. Atmos. Sci.* 68, 1714–1729 (2011)

Chapter 131

Role of Arabian Sea Surface Pressure on Indian Northeast Monsoon

Ramesh Kumar Yadav

Abstract Indian northeast monsoon season (October to December) is the major period of rainfall activity over south peninsula. The season is also referred to as “Post-Monsoon Season” or “Retreating Indian Summer Monsoon (ISM) Season”. This study examines the role of Arabian Sea surface pressure on the inter-annual variability (IAV) of Indian northeast monsoon rainfall (INEMR). For establishing the teleconnections, sea surface temperature (SST), rainfall, mean sea level pressure (MSLP), and lower troposphere zonal and meridional wind data have been analyzed. The study reveals that during excess INEMR years, similar to ISM semi-permanent low and monsoon trough, the anomalous semi-permanent surface low pressure and trough are observed over Arabian Sea and peninsular India, respectively. These anomalous low and trough intensifies the tropical storms, depressions and cyclones over Bay-of-Bengal, which hits peninsular India and gives widespread rainfall, affecting the IAV of INEMR.

Keywords Northeast monsoon • Tropical storms • Trough • Cyclonic circulation • Low pressure

131.1 INTRODUCTION

The season, October to December is considered as northeast (NE) monsoon season in India. Airflow reverses and wind blows northeasterly across the Indian Ocean. A trough of low pressure gets established over the south Bay-of-Bengal (BoB). Tropical disturbances such as lows, depressions, cyclonic storms, easterly waves (disturbances associated with perturbations in the wind field and progressing through the tropics from east to west) and cyclones occasionally form in this trough giving widespread rainfall over South India. During the NE monsoon (NEM) season, India receives about 11% of its annual rainfall, while south peninsula, south of 15°N receive 17–49% of their annual rainfall. The Indian north-east

R.K. Yadav (✉)

Indian Institute of Tropical Meteorology, Pashan, Pune, Maharashtra, India

e-mail: yadav@tropmet.res.in

monsoon rainfall (INEMR) displays considerable interannual variability (IAV), significantly affecting the agricultural activity in the region [1, 2].

131.2 DATA & METHODOLOGY

Monthly rainfall data, for the meteorological subdivisions of peninsular India, for the period 1871-2012 (142-years), has been obtained from the Indian Institute of Tropical Meteorology (IITM) rainfall records [3]. The INEMR region for the country is considered for the largest possible spatially coherent area comprising six meteorological subdivisions of peninsular India [4]. For studying the global precipitation, the GPCP data is used [5]. The simultaneous correlation coefficient (CC) between NEMR series and GPCP data for the period 1982-2012 over southern peninsular India is 0.85 which suggests the consistency and accuracy among the datasets. To examine the observed behavior of anomalous Indian NEM circulation, the SST data used is the optimally interpolated Reynolds version-2 monthly mean dataset [6], available from 1982-2013. The monthly mean zonal and meridional wind data have been provided by the NCEP/NCAR global atmospheric reanalysis dataset [7]. For understanding the dominant modes of variability simultaneous correlations and regressions analyses of SST, MSLP, precipitation and wind fields have been examined.

131.3 RESULTS AND DISCUSSION

131.3.1 Interannual Variability of Indian Northeast Monsoon Rainfall

The INEMR time series have been prepared as the area weighted seasonal (OND) rainfall over six meteorological sub-divisions of peninsular India (Fig 131.1a), for the period 1871-2012, expressed as the rainfall anomaly (Fig. 131.1b) from the long period normal (1871-2012). In this study, INEMR is considered to be normal if the rainfall anomaly is within ± 1 standard deviation (SD). The flood and drought years have been defined if the rainfall anomalies are greater than $+1$ SD and less than -1 SD, respectively. There are 24 flood years and 22 drought years in 142 years period from 1871-2012. The average rainfall is 345.6 mm with standard deviation (SD) 90.76 mm and coefficient of variation (CV) 26.26%. The 11-year running mean curve are super-imposed on INEMR series to show the epochs of above and below normal rainfall. The curve shows more undulating features from 1871 to 1925 and 1980 to till date. The trend analysis shows the rate of increasing of 0.23 mm of rainfall per year for the period 1871 – 2012, but the trend is not significant.

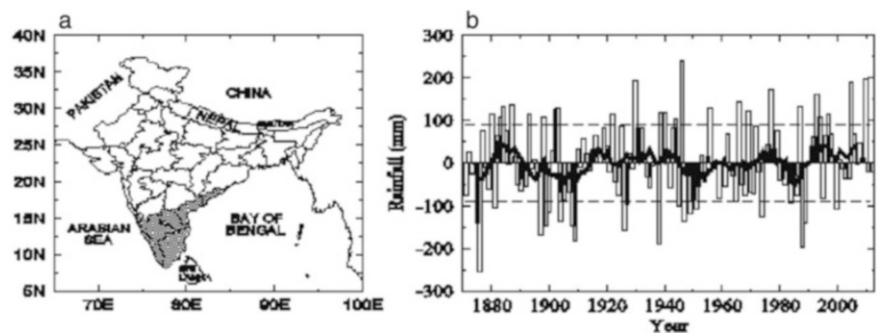


Fig. 131.1 (a) Shaded regions geographical locations of six meteorological sub-divisions of north-east monsoon (NEM). (b) The time-series of Indian north-east monsoon rainfall (INEMR) for the period 1871-2012 expressed as the rainfall anomaly of area weighted seasonal rainfall from the long period normal (1871-2012). The horizontal dash lines are +1 and -1 standard deviation (SD). The thick curve is the 11-year running mean

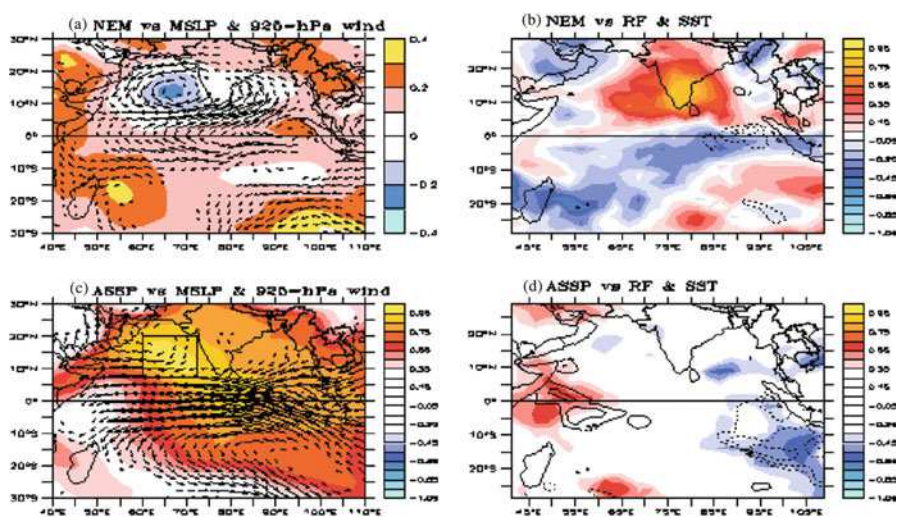


Fig. 131.2 Spatial pattern of simultaneous (a) correlation of MSLP (shaded) and regression of 925 hPa winds (arrows) with INEMR and (b) correlation of rainfall (shaded) and SST (contours) with NEMR during the period 1982-2012. Similarly, (c) and (d) are same as (a) and (b), respectively but for ASSP during the period 1982-2013. MSLP are shown as (hPa), SST as ($^{\circ}\text{C}$) and winds as (m/s). The box (c) over Arabian Sea indicates ASSP region

131.3.2 Teleconnections of Indian Northeast Monsoon Rainfall

The simultaneous correlation coefficient (CC) of MSLP and SST with INEMR and regression of 925-hPa zonal and meridional winds onto INEMR for the period 1982-2012 are calculated and shown in Fig. 131.2a. Similarly, CC of rainfall and

SST with INEMR are shown in Fig. 131.2b. All the data series have been detrended before carrying out analysis. In Fig. 131.2a, The 925-hPa wind pattern shows westerlies anomalies over north of equatorial Indian Ocean (IO) and easterlies anomalies over south of equatorial IO. Anti-cyclonic circulation anomaly is observed over south-east tropical IO. Trough and cyclonic circulation anomalies are observed over peninsular India and Arabian Sea (AS), respectively. These trough and low are similar to Indian summer monsoon (ISM) season (JJAS) trough and low pressure formed over north India and Pakistan, respectively. Similar to ISM, during the season (OND) the trough is responsible of the formation of tropical lows, storms, depression and cyclones which hits the peninsular India and hence excess INEMR. Fig. 131.2b, shows significant positive CC of rainfall over peninsular India and surrounding and negative anomaly over south of equator. The SST pattern shows significant cool anomaly over east equatorial IO and warm anomaly over Bay-of-Bengal (BoB). The trough and the associated wind anomalies are responsible for the above said SST anomalies over the eastern IO.

131.3.3 Role of Surface Pressure over INEMR

In the previous subsections, we have seen that INEMR has strong and robust association with surface low pressure anomaly over Arabian Sea. Based on that, MSLP box has been selected ($60^{\circ}\text{E} - 72.5^{\circ}\text{E}$; $7.5^{\circ}\text{N} - 20^{\circ}\text{N}$) as shown in Fig 131.2c and index have been prepared by averaging the grid values of this box (representing Arabian Sea Surface Pressure; named as ASSP). Further, to examine the circulation features associated with ASSP, similar CCs and regression analysis have been carried out and shown in Fig. 131.2c&d, respectively. The spatial patterns shows significant positive surface pressure anomaly all over the Indian subcontinent, significant equatorial easterlies, anti-cyclone over AS and elongated ridge over BoB. The SST (contours) shows significant warm anomaly over tropical western IO and significant cool anomaly over southeast IO. The rainfall anomaly shows significant excess anomaly over south BoB, west AS, east equatorial IO and southeast IO and significant deficient anomaly over tropical west IO. This suggests that the weakening of surface low over AS produces ridge anomaly over BoB and deficient rainfall anomaly over south BoB, which affects INEMR. Also, strong easterlies over equatorial IO produces warm SST anomaly over tropical western IO and cool SST anomaly over southeast IO.

131.4 CONCLUSIONS

Indian Northeast Monsoon (INEM) season (OND) is the major period of rainfall activity over south peninsula. It is also called as “Post-Monsoon Season” or “Retreating ISM Season”. A similarity in circulation pattern is found between

ISM and INEM. As ISM is strongly associated to low pressure and trough over Pakistan and north India, the INEM is also strongly associated to the anomalous semi-permanent surface low pressure and trough over Arabian Sea and peninsular India, respectively. The tropical disturbances, such as lows and depressions formed along the monsoon trough during ISM and gives copious rainfall over north India. Similarly, the trough over peninsular India, during INEM season is conducive for the formation of tropical storms, depressions and cyclones, which hits the peninsular India and gives copious rains affecting the IAV of INEMR.

REFERENCES

1. Yadav, R.K.: Why is ENSO influencing Indian northeast monsoon in the recent decades? *Int. J. Climatol.* 32, 2163–2180 (2012) doi: [10.1002/joc.2430](https://doi.org/10.1002/joc.2430).
2. Yadav, R.K.: Emerging role of Indian ocean on Indian northeast monsoon. *Climate Dynamics* 41, 105–116 (2013) doi: [10.1007/s00382-012-1637-0](https://doi.org/10.1007/s00382-012-1637-0).
3. Parthasarathy, B., Munot, A.A. and Kothawale, D.R.: All India monthly and seasonal rainfall series : 1871–1993. *Theor. and Appl. Climatol.*, 49: 217–224 (1995)
4. Parthasarathy, B., Rupa Kumar, K. and Munot, A.A.: Homogeneous Indian Monsoon Rainfall: variability and prediction. Proceedings of the Indian Academy of Sciences. *Earth and Planetary Science Letters* 102, 121–155 (1993)
5. Huffman, G.J., Adler, R.F., Arkin, P.A., Chang, A., Ferraro, R., Gruber, A., Janowiak, J., McNab, A., Rudolf, B. and Schneider, U.: The Global Precipitation Climatology Project (GPCP) Combined Precipitation Dataset. *Bulletin of American Meteorological Society* 78, 5–20 (1997)
6. Reynolds, R.W., Rayner, N.A., Smith, T.M., Stokes, D.C. and Wang, W.: An improved in situ and satellite SST analysis for climate. *J. Climate* 15, 1609–1625 (2002)
7. Kalnay, E., Kanamitsu, M., Kistler, R., Collins, W., Deaven, D., Gandin, L., Iredel, M., Saha, S., White, G., Woollen, J., Zhu, Y., Chelliah, M., Ebisuzaki, W., Higgins, W., Janowiak, J., Mo, K. C., Ropelewski, C., Wang, J., Leetmaa, A., Reynolds, R., Jenne Roy and Joseph Dennis: The NCEP/NCAR 40-year reanalysis project. *Bull. Amer. Meteor. Soc.* 77, 437–470 (1996)

Chapter 132

Effect of Dust on the Indian Summer Monsoon

P. Maharana, A.P. Dimri, and A. Choudhary

Abstract The atmospheric dust plays a major role in deciding the radiation balance over the earth. This property of the dust has a long term effect on the Indian summer monsoon and its spatial distribution. Two sets of simulations (control and dust chemistry simulation) are made to analyze the effect of dust on the Indian summer monsoon. The analysis of the pre-monsoon and May temperature climatology reflects that the heating of the land mass is more in the dust chemistry simulation as compared to the control simulation, which is providing the strength to the monsoon flow during JJAS.

Keywords Indian summer monsoon • Dust • Control simulation • Dust chemistry simulation • Climatology

132.1 INTRODUCTION

India receives 80% of its rainfall during the summer season, which comprises of months from June to September (JJAS) [1, 2]. The rainfall during the summer has an important contribution to the agriculture, industry, water resource, ground water recharge, provide relief from the heat and also play a major role in deciding the socio-economic condition of a major part of the population. The atmospheric dust acts as cloud condensation nuclei, and hence directly affects the formation of the cloud cover over a region. The clouds alter the incoming and outgoing solar radiation of the earth and directly affect the energy balance over the earth surface. This misbalance in the energy can have a pronounced effect on the Indian summer monsoon. In India, the rest of the season besides the monsoon are mostly dry or having less rainfall. During post-monsoon, the northeast monsoon causes rainfall over the southern part of India and during winter, the rainfall over the northern India caused by the winter disturbances. During the pre-monsoon season (Mar-May; MAM) the temperature starts to rise over the Indian continent, and also the dust concentration [3]. The dust aerosol, whether absorbing or non-absorbing, block the

P. Maharana • A.P. Dimri (✉) • A. Choudhary
School of Environmental Sciences, Jawaharlal Nehru University, New Delhi, India
e-mail: apdimri@hotmail.com

radiation coming towards the surface of the earth and it cause cooling. This phenomenon is called the solar dimming effect. Global dimming causes the long term decrease of the south Asian monsoon by reducing the meridional surface temperature [4] whereas Lau et al. shows the absorbing black carbon may intensify the Indian summer monsoon by elevated heat pump theory [5].

132.2 STUDY AREA

The whole south-Asian region is considered for this modeling study.

132.3 METHODOLOGY

Two sets of simulation are made using a regional climate model (RegCM4.0), where model is forced with same lateral boundary conditions, over exactly same domain, for the same period. The only difference is the first simulation doesn't have the effect of dust on the model simulation (control experiment) and second simulation has the dust module on dust chemistry simulation.

132.4 RESULTS AND DISCUSSION

The land and sea over the Indian region starts to get heated up from the pre-monsoon period. As the land gets heated up quickly as compared to the sea, the temperature over the Indian land is very high during monsoon. The higher temperature over the region leads to low pressure and form a monsoon trough over north India and a pressure gradient from land towards sea. The pressure difference is the cause of the flow of the wind from sea, which carries moisture towards Indian land mass and cause heavy monsoonal precipitation. So the temperature can be the major indicator of the energy balance over the earth which decides the amount of rainfall during monsoon. The model is nicely able to reproduce the spatial distribution of the rainfall climatology in both the simulations with the major rainfall peaks over India. The pressure difference between the sea and land provides the necessary pressure gradient force for the movement of the large scale south westerly which brings in moisture in to the Indian land mass. The sea level pressure climatology depicts that pressure gradient exists between the low pressure land and high pressure sea, which is in close agreement with the observation analysis. The comparison of the two simulations (bias plot) shows that the pressure gradient is less in the control experiment as compared to the dust chemistry simulations over the Indian region (Fig. 132.1a). The model simulation with dust chemistry option shows more intensity of the precipitation over the central India, western India and

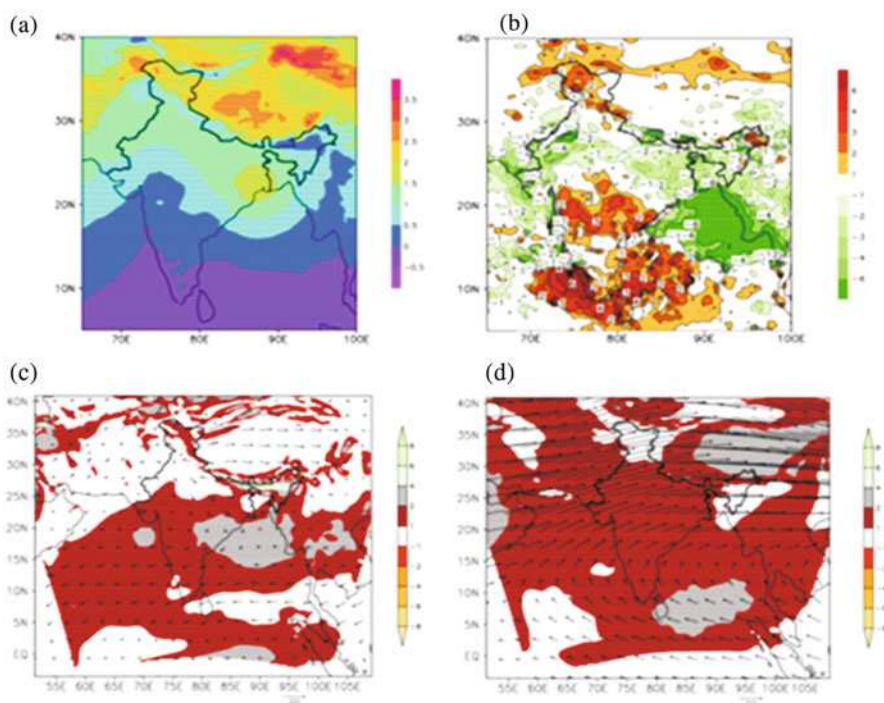


Fig. 132.1 The bias between the JJAS climatology of the control and dust chemistry simulation of (a) sea level pressure (hPa), (b) precipitation (mm/day), (c) 850hPa wind (m/s) and (d) 200hPa wind (m/s)

over the ocean region near the Burma coast. The difference between the control simulation and the dust chemistry simulation shows that the control simulation has higher rainfall over the monsoon core zone and lesser precipitation over the sea, Indo-Gangetic plains and the Rajasthan region (Fig. 132.1b). The model nicely captures the JJAS climatology of the lower level wind (850hPa) such as the Findlater jet, its core and position over India and upper level wind (200hPa) the tropical easterly jet, sub-tropical westerly jet and position of the Tibetan anticyclones over the Indian region. The comparison between the control run and dust chemistry simulation reveals that the strength of the Findlater jet is more over the Arabian sea, Bay of Bengal and central Indian region in the dust chemistry simulation at 850hPa (Fig. 132.1c). The analysis at 200hPa shows that in the sub-tropical westerly jet stream and tropical easterly jet are stronger in control run as compared to the dust chemistry simulation (Fig. 132.1d).

The JJAS temperature distribution over the India depicts that the temperature is well represented in the both of the simulation. The bias plot of the simulations shows that the temperature in the control run is more as compared to the dust chemistry simulation. But in the earlier discussion, it was found out that the pressure gradient, wind strength and the precipitation is more in the case of dust

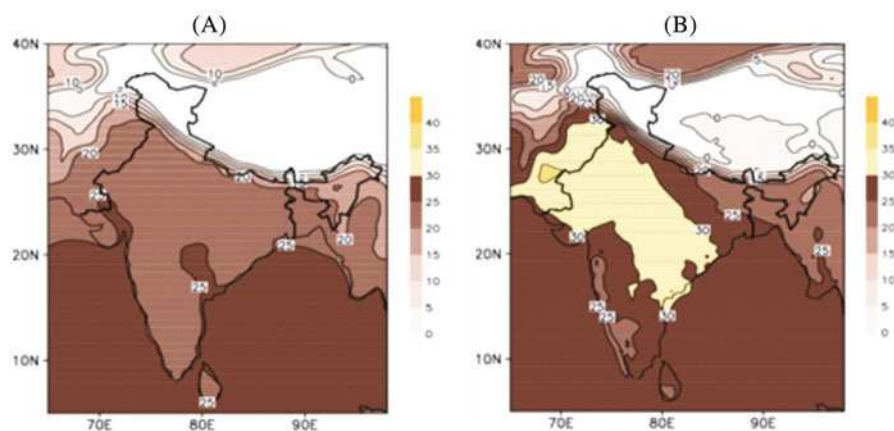


Fig. 132.2 The temperature climatology ($^{\circ}\text{C}$) of May month for (a) control and (b) dust chemistry simulation

chemistry simulation. To analyze the higher values of these parameters in the dust chemistry simulation, the pre-monsoon temperature pattern is analyzed for both the simulations. The MAM spatial distribution over India shows that the temperature shows more value over Indian land mass in the dust chemistry simulation, similarly the temperature distribution of the May (last month of pre-monsoon season) depicts that the heating over the Indian land mass is very high in the as compare to the control simulation (Fig. 132.2a-b).

132.5 CONCLUSIONS

This heating over the land during May month may lead to the strong pressure gradient, south-westerly and heavy precipitation in the dust chemistry simulation during JJAS. Once the monsoon hits the Indian landmass the heavy precipitation and its evaporation cools the surface and also the evaporation brings the temperature down in the dust chemistry option. This is why the JJAS surface temperature is less in the dust chemistry simulation as compared to the control simulation.

REFERENCES

1. Guhathakurta, P. and Rajeevan, M.: Trends in rainfall pattern over India. *Int. J Clim*, 28(11), 1453–1469 (2008)
2. George, G., Charlotte, B.V. and Ruchith, R.D.: Interannual variation of northeast monsoon rainfall over southern peninsular. *J Mar Sci*, 40(1), 98–104 (2011)
3. Lau, K.M. and Kim, K.M.: Observational relationships between aerosol and Asian monsoon. *Geo Res Let*, 30, 1–5 (2006)

4. Stanhill, G. and Cohen, S.: Global dimming, a review of the evidence for a wide spread and significant reduction in global radiation with a discussion of its probable causes and possible agricultural consequences. *Agri Met*, 107, 255–278 (2001)
5. Lau, K.M., Kim, K.M. and Kim, M.K.: Asian monsoon anomalies induced by aerosol direct effects. *Clim Dyn*, 26, 855–864 (2006)

Chapter 133

Study of Physical and Dynamical Processes in the Ionosphere at Equatorial Anomaly Crest Region during Magnetic Storm for High and Low Solar Activity Period

Bornali Chetia, M.K. Barman, M. Devi, and A.K. Barbara

Abstract The ionosphere represents one of the most important error sources that affecting GPS positioning. It is strongly related to solar activity and geomagnetic field. The GPS satellites and dual frequency receivers can be used to measure the Total Electron Content (TEC) of the Earth's ionosphere. In this paper, the total electron content (TEC) profile features, have been utilized for extraction of parameters like profile factor, P and anomaly factor, PEA separately for three seasons (summer, winter and equinox) and the parameters are used for assertion of a certain day as quiet (Q) or disturbed (D). The ionospheric Total electron content (TEC) is used to examine the influence of solar activity by taking advantage of the dispersive nature of the ionospheric medium. The definitions of Q and D days are made through profile features and the threshold values of ΣKp for each season are evaluated. The relations between Disturbed storm time (Dst) and P factor, ΣKp and P factor are established after corrections for solar activity condition. The prediction and assertion of Q/D days are then made by examining IEC profiles for the cases where IEC data were not used for the parameter extraction. A few case studies using these methods are also presented in these papers. Work is based on TEC/IEC data collected from VHF Radio Beacon (RB) technique from geostationary satellite and GPS receiver at Guwahati (26.20N, 91.750E), an equatorial anomaly crest station.

Keywords RB • TEC profile • Anomaly crest • Q-D days • Magnetic storm • Dst • Kp

B. Chetia (✉) • M. Devi • A.K. Barbara
Department of Physics, Gauhati University, Guwahati, India
e-mail: bonmi000@rediffmail.com

M.K. Barman
Department of Physics, MC College, Barpeta, India

133.1 INTRODUCTION

The effect of ionosphere on GPS applications such as satellite communication, tracking and navigation are directly proportional to the Total Electron Content (TEC). Therefore it is necessary to study the physical and dynamical processes of the ionosphere. It is well known that sun solar radiation is the primary energy source for upper atmospheric dynamics and ionization. The magnitude of solar radiation varies with various timescales, which will significantly change the structure and behavior of the ionosphere [1, 2]. TEC variations with respect to the local time, season and solar activity have been studied extensively over the past few decades. Pandey and Dashora [5] reported the effect of geomagnetic storm of November 2004 and May 2005 on variation of GPS derived TEC at Udaipur, India. In the result they pointed that during the geomagnetic storm of November 2004 the vertical TEC values decreases where as for the storm of May 2005, it increases during the main phase of storm. The studies over equatorial anomaly regions are very important because the equatorial plasma fountain is highly sensitive to the disturbance electric fields. In this paper, we have studied the physical and dynamical processes in the ionosphere at Guwahati (26.2°N, 91.75°E) during magnetic storm for high and low solar activity period. For the experiment the GSV4004 receiver have been employed for collection of TEC at Guwahati University Laboratory. The system is obtained from GPS Silicon Valley, USA and it can track up to 11 GPS signals at the L1 frequency (1575.42 MHz) and the L2 frequency (1227.6 MHz). It measures phase and amplitude (at 50-Hz rate) for each satellite and computes TEC from combined L1 and L2 carrier phase measurements which also collects Ionospheric Scintillation data.

133.2 DATA AND ANALYSIS

The diurnal pattern of TEC shows that the TEC values increases from about sunrise to an afternoon maximum and then falls to attain a minimum just before sunrise. The diurnal characteristic of TEC depends on seasonal variations, sun solar activity, geomagnetic activity and latitudinal dependence. From the past observation [3, 4] it is observed that the TEC values are high in equinoctial months followed by more or less similar values in summer and winter. Due to the thermospheric neutral composition TEC values depends on the seasonal variations. During the daytime, the equator is hotter than the pole which causes meridional wind flows towards the pole from the equator and it changes the neutral composition and O/N₂ decreases at equatorial and low latitude stations. In equinox, this decrease will be very high. At F2 layer, N₂ dissociation is the important process which removes ambient electrons. Therefore, the decrease in O/N₂ ratio will result in higher electron density and therefore in equinox TEC values will be highest. Because of the Sun emits a

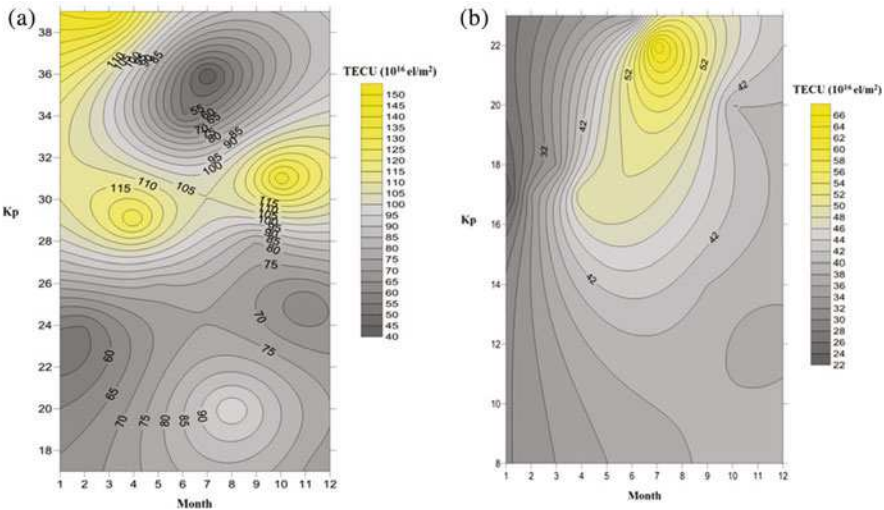


Fig. 133.1 (a) Kp vs TEC during high solar activity period (2012) and (b) Kp vs TEC during low solar activity period (2009)

wide spectrum of radiation along with high energy particles the sunspot number and the flux of the radio emission of the Sun at a wavelength of 10.7 cm (2.8GHz) is a useful parameter of solar activity relevant for ionospheric effects. It is observed that the solar activity controls the ionization level [6], i.e. higher values during a high solar activity period and low value during a low solar activity period. From our experiment it is observed that there is an enhancement of TEC during high solar activity period except for summer month which shows a large decrease in TEC with respect to Q-days (Figure 133.1) during strong geomagnetic condition ($Dst = -127nT$) as compared to the low solar activity period for the same summer month with geomagnetic storm ($Dst = -101nT$) which shows a positive TEC effect. However the TEC difference between summer and autumnal equinoxes is less significant in low solar activity situation compared to high solar activity period. It is also noted that the TEC profile shape changes with respect to the solar geomagnetic activities. Therefore, it is important that the profile shape is to be examined with respect to geomagnetic activity at different solar ambiances. For this purpose a parameter called Profile factor (P-factor) is defined from the TEC diurnal variation. It is the period of the profile that maintains 70% of noon time TEC peak. A large number of TEC profiles are then examined for each day of a month and P-factor is extracted for each case. This exercise is done for both high and low solar activity periods. The relation between this P-factor with magnetic activity at both high and low solar activities are presented in the following article.

133.2.1 *Relation Between P-Factor and Kp During High and Low Solar Activity Period*

Once the P factor is obtained from the diurnal TEC plots, its relation with Kp is examined individually for vernal equinox, summer and autumnal Equinoctial month during High and Low Solar Activity period. A few representative plots between P-factor and Kp are shown in the Figure 133.2. The Figure 133.2(a, b) show variation of P-factor with Kp values for one of the vernal equinoctial months, during high and low solar activity periods respectively. The figure shows that the P-factor is independent of Kp for low solar activity, but a significant increase in P-factor with Kp is seen when solar activity increases. Similar relations between P-factor and Kp is also observed during summer months. As a case representation, the associations to these two parameters for summer months are shown in Figure 133.2(c, d) for high and low solar activity condition respectively. A relatively strong relation of Kp and P-factor is seen during high solar activity period, a large decrease in the P-factor is observed with the increase in Kp during the high solar ambience whereas for low solar ambience P-factor seems to increase with increasing Kp. The P-factor and Kp relations for the autumnal equinoctial months for high and low solar ambience are shown in Figure 133.2(e, f). During autumnal months of low solar activity conditions it is seen that a significant increase in P-factor with Kp is noted. In high solar activity period the relation between P-factor and Kp remains same as observed in other seasons.

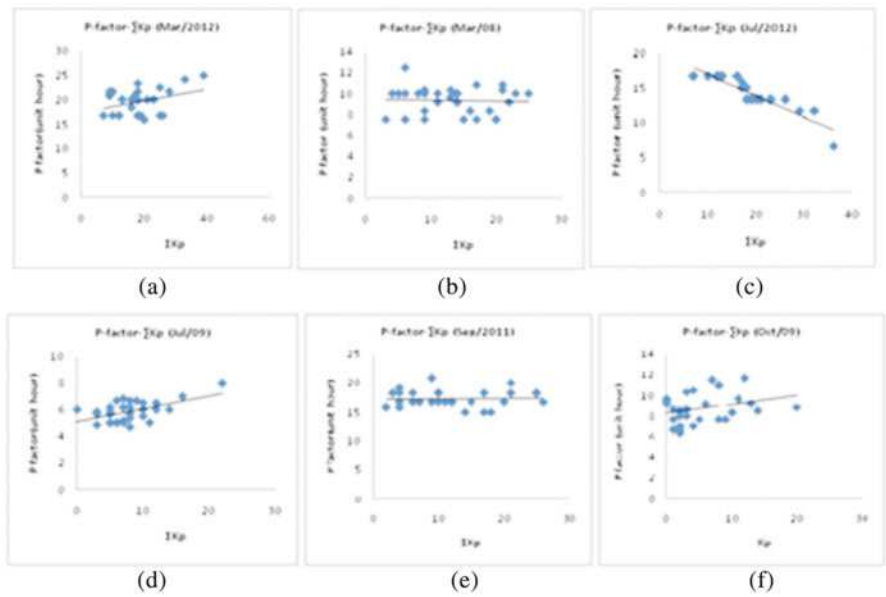


Fig. 133.2 Relation for P-factor with geomagnetic parameter Kp during high and low solar conditions

133.2.2 Relation Between P-Factor and Dst During High and Low Solar Activity Period

In present study, we have used Disturbed Storm Time (Dst) data, that record the number and severity of geomagnetic storms during High and Low solar activity periods. Figure 133.3(a, b) shows the relation between Disturbed storm time (Dst) and P-factor for vernal equinoctial month during high and low solar activity condition. It can be seen that the strength of the magnetic storm is more intense during high solar activity period where P-factor increases with the strength of the storm. On the other hand, for low solar activity condition, P-factor shows a slight decrease with the increasing strength. Taking the concept of Dst in mind, same analysis is also done for summer month. Figure 133.3(c, d) shows the relation between Dst and P-factor for summer month during High and Low solar activity period. Here we can see that there is a large decrease in P-factor with the increasing strength of the geomagnetic storm i.e. Dst = -127nT for High solar ambience where for vernal equinoctial month Dst = -131nT but with increasing P-factor. On the other side for low solar activity period, Dst increases with the increasing P-factor. The relation between Dst and P-factor is also carried out for autumnal equinoctial month for both High and Low solar activity period representing Figure 133.3(e, f). It can be seen that P-factor is more or less independent of Dst for both High and Low solar activity period. The only difference is that the strength of the occurring geomagnetic storm is more intense during High solar activity period.

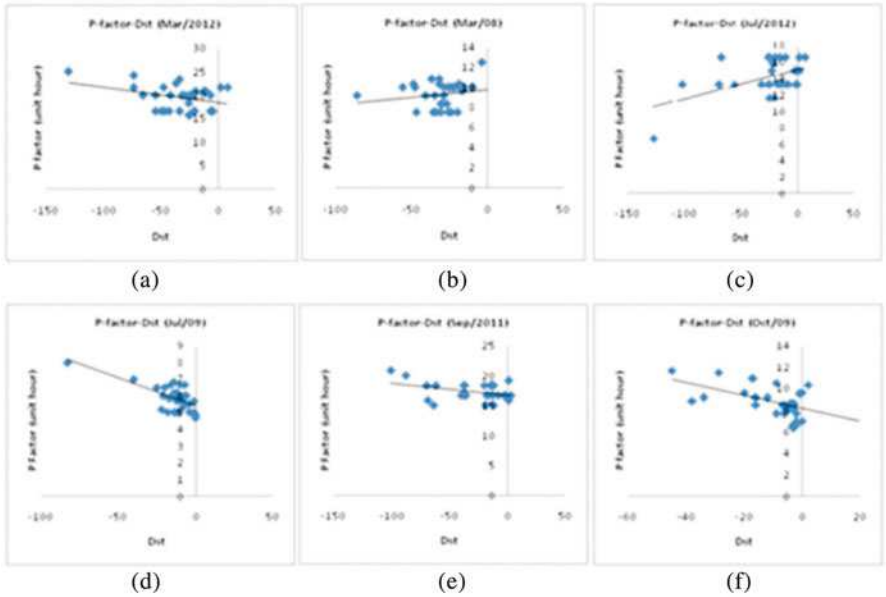


Fig. 133.3 Relation for P-factor with geomagnetic parameter Dst during high and low solar conditions

133.3 CONCLUSIONS

The present paper describes the diurnal and seasonal TEC variations during high and low sun solar activity period under disturbed geomagnetic conditions for Guwahati. The results presented in this paper show a good positive correlation between solar activity and TEC values. This paper also shows the relation between Disturbed storm time (Dst) and P-factor, ΣKp and P-factor during high and low sun solar activity condition. Our results indicate that P-factor is independent of Kp for low solar activity, but a significant increase in P-factor with Kp is seen when solar activity increases and the P-factor is more or less independent of Dst for both High and Low solar activity period. It is also seen that in low solar activity period geomagnetic disturbances have little influence on TEC value and it is found that Solar and geomagnetic control on profile shape during high solar activity period is found to be very significant.

REFERENCES

1. Gorney, D.J.: Solar cycle effects on the near-earth space environment. *Rev. Geophys.*, 28(3), 315–336, doi:[10.1029/RG028i003p00315](https://doi.org/10.1029/RG028i003p00315) (1990)
2. Liu, L. and Chen, Y.: Statistical analysis of solar activity variations of total electron content derived at Jet Propulsion Laboratory from GPS observations. *Journal of Geophysical Research*, 114, A10311, doi:[10.1029/2009JA014533](https://doi.org/10.1029/2009JA014533) (2009)
3. Bagiya, Mala, S., Joshi, H.P., Iyer, K.N., Aggarwal, M., Ravindran, S. and Pathan, B.M.: TEC variations during low solar activity period (2005–2007) near the Equatorial Ionospheric Anomaly Crest region in India. *Ann. Geophys.*, 27, 1047–1057 (2009)
4. Modi, R.P. and Iyer, K.N.: IEC and slab thickness near the peak. *Indian J. Radio Space Phys.*, 18, 23–26 (1989)
5. Pandey, R. and Dashora, N.: Space weather studies at the crest of the equatorial ionization anomaly using GPS receiver. Proceeding of XXVIIIth URSI 23–29 Oct New Delhi, India (2005)
6. Rama Rao, P.V.S., Niranjan, K., Ramana Rao, B.V., Rao, B.V.P.S. and Prasad, D.S.V.V.D.: Proc. URSI/IPS Conference on the Ionosphere and Radiowave Propagation Sydney, Australia (1985)

Chapter 134

Winter Hailstorm over New Delhi, India

A. Chevuturi, A.P. Dimri, and U.B. Gunturu

Abstract This study describes unusual winter hailstorm occurring over New Delhi, India. Cold and dry conditions during winter are not conducive for generating a hailstorm, thus making them a rare meteorological occurrence. This study uses numerical simulation to understand the dynamics of a winter-time hailstorm occurrence. The cause of a hailstorm during winter is attributed to low level convective available potential energy and moisture incursion that causes rising of air till the mid-tropospheric level and then further rising takes place due to the western disturbance in the mid-troposphere causing baroclinic instability.

Keywords Winter • Hailstorm • Western disturbances • Baroclinic instability

134.1 INTRODUCTION

An unusual winter hailstorm occurred over National Capital Region (NCR)/New Delhi, India on 17Jan2013 (1600–1800 UTC) with extensive cloud cover over the north Indian region. Heavy precipitation was observed over NCR and surrounding regions with freak hail incidence. For a time series analysis of the hailstorm cases over NCR [1], it is observed that no hailstorm cases occurred during months of Feb and Oct and that the hailstorm events dominate during summer months. Primarily, the Indian climate is divided into four seasons; pre-monsoon (Mar-Apr-May), monsoon (Jun-Jul-Aug-Sep), post-monsoon (Oct-Nov) and winter (Dec-Jan-Feb) [2]. With such a classification, a pattern is observed, where most hailstorms cases over Delhi occur during the warmer periods of pre-monsoon and monsoon months. However, during winter months a very few hailstorm cases occur. Out of the 33 hailstorm cases only 5 occur during the colder/winter period; with Jan showing only 2 cases. With such distinction between summer and winter hailstorms, it can be hypothesized that the mechanisms of these two kinds of hailstorms are different,

A. Chevuturi • A.P. Dimri (✉)

School of Environmental Sciences, Jawaharlal Nehru University, New Delhi, India

e-mail: apdimri@hotmail.com

U.B. Gunturu

King Abdullah University of Science and Technology, Thuwal, Saudi Arabia

and that the winter hailstorms are rare. Over north Indian region, pre-monsoon storms occur during convectively unstable atmospheric conditions culminating due to transient disturbances observed in the air mass due to the surface heating causing vertical wind shear, ideal for hail formation [3]. During monsoons development of deep convection because increased surface temperature associated with moisture incursion from the south-westerly flow over India can cause hailstorms [4]. In the context of hailstorms, it can be concluded that convection due to high surface temperatures and moisture laden flow are important for hailstorm formation. Hail is precipitation in the form of hard, rounded pellets of irregular lumps of ice formed due to deposition of ice over the condensation nuclei as the hailstones cycle travels through strong convective clouds [5]. The winter months are associated with absence of increased surface temperatures or low level of moisture incursion, making it a cold and dry season [2]. These conditions are not conducive for generation of deep convection required for sustaining a hailstorm. Though rare in occurrence, hailstones destroy crop, infrastructure, property and in extreme cases may cause injuries to humans [6]. Studying such unusual winter hailstorms may have high socio-economic impact. With these considerations, the objective of the study is to understand the cause of unusual winter hail formation over NCR. Numerical weather prediction technique is utilized for understanding the above discussed storm event. This storm is simulated with Weather Research and Forecasting (WRF) model with Advanced Research WRF (ARW) dynamical core [7].

134.2 RESULTS AND DISCUSSION

A deep trough was formed over the western Indian and Pakistan region on 17Jan2013 which corresponds to an incoming western disturbance (WD) [8]. This system along with the moisture incursion from Arabian Sea and Bay of Bengal develops instability to form the extensive cloud cover during the storm. The model simulated precipitation output shows localized storm formation over NCR with the axis of the storm to be oriented along NE to SW direction with the storm cluster progressing in an eastward direction. The peak of precipitation intensity around NCR region was observed around 1700UTC (Fig.134.1). For a focused analysis of the winter hailstorm formation vertical cross sections of parameters analyzed along the axis of core precipitation zone of the storm region as demarcated by a green line and area averaged over the $1^{\circ} \times 1^{\circ}$ grey box around NCR (77.2°E and 28.6°N) as drawn in Fig. 134.1.

Over NCR the geopotential height anomaly shows an increase around 400–200 hPa (Fig.134.2A). This increase is associated with the dipping in the perturbation geopotential height contour lines. These changes are due to the tropopause fold penetrating the troposphere. This tropopause lowering is associated with baroclinic instability occurring over the region [9]. The increase storm intensity over the region is caused by the baroclinic instability due to the migratory WD and the development of cyclonic circulation [10]. This instability in the mid- to upper

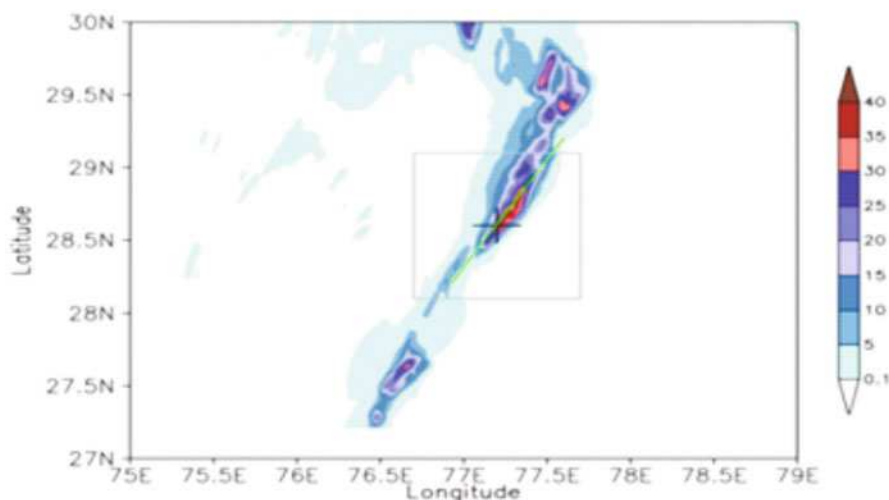


Fig. 134.1 Model precipitation (mm/half-hour) at 1700UTC 17 Jan 2013 at 1 km horizontal model resolution, +sign denoting NCR. (Green line drawn across maximum precipitation zone is along which vertical cross sections of various variables are analyzed and $1^\circ \times 1^\circ$ grey box around NCR over which area averaged parameters are discussed in following sections)

tropospheric levels generates the turbulent convective energy required for the development of updrafts during storm occurrence. With the availability of moisture in the atmospheric column the instability leads to heavy precipitation. But a WD over northern India does not always lead to hail formation during winter. The updrafts driven by the instability developed over the region, cycles the hail through the cloud. Thus, vertical wind velocity is an important factor for the hail formation. Strong convective updrafts ($>5\text{--}10$ m/s) suppress homogenous nucleation to form ice particles which grow to form hail [11]. Whereas, lower wind speeds would not attain enough energy to develop a strong hailstorm. The model simulated vertical wind updraft speeds over NCR show a magnitude of 4–6 m/s which provide sufficient time for ice particle growth by dry or wet growth.

The instability developed in the mid-tropospheric levels due to the WD develops propensity for baroclinic atmosphere in the upper half of troposphere. When the temporal variation of temperature profile of the region is analyzed, a dip is observed in the -60°C isotherm around 1600–1700UTC (Fig. 134.2B). The lowering is the tropopause fold that causes incursion of colder stratospheric layers into warmer troposphere. This in turn develops a steep temperature gradient, which enhances upper level instability. Still the reasons for instability in the lower layers are yet not clearly defined. In this Fig. 134.2B, an increase of moisture over NCR in the lower levels of atmospheric column is observed along with development of convective available potential energy (CAPE) from around 1300UTC. The moisture convergence develops the propensity of increased CAPE in the atmospheric column. There is reduction in CAPE values in subsequent time periods after 1300UTC. The increase of CAPE defines the potential energy that is available to drive a storm

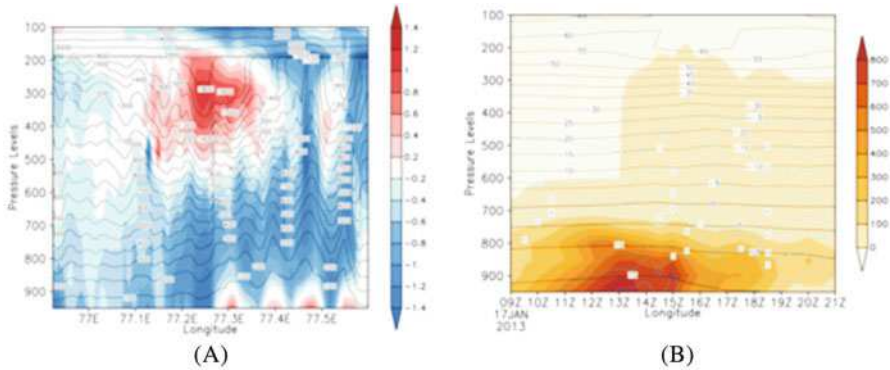


Fig. 134.2 (A) Longitude-pressure cross section (over green line shown in Fig. 134.1) at 1 km horizontal model resolution at 1700UTC 17 Jan 2013 for geopotential height anomaly (shaded) and perturbation geopotential height (m; contour). (B) Time-pressure cross section (area averaged over the grey box shown in Fig. 134.1) at 1 km horizontal model resolution for CAPE (J/kg; shaded), temperature ($^{\circ}\text{C}$; black contours) and specific humidity (g/kg; blue contours)

and release of CAPE in form of kinetic energy promotes storm development. Along with this the low level moisture incursion provides the buoyancy required for the air parcel to rise. Thus, upper level instability is predominantly by the existing WD embedded with the low level instability due to moisture incursion and development of CAPE lead to instability spanning the troposphere which makes it conducive conditions for hailstorm formation. Studies describe the “continental” clouds having three zones in the vertical direction based on temperature variation: diffusional droplet growth zone (up to -10°C), mixed phase zone (-10°C to -38°C) and glaciated zone (above -38°C) [12]. The isotherm of -38°C is termed as homogeneous freezing isotherm beyond which homogenous nucleation occurs. As per Fig. 134.2B, it can be concluded that the mixed phase zone for the current hailstorm can be considered within 600–350 hPa, where hail particles grow by deposition of water particles. This zone in the model simulated output coincides with region having strong convergence influence and higher specific humidity, promoting hail formation along with raindrop growth. The region of glaciation in the upper levels of troposphere is imperative for the development of small ice particles through homogenous nucleation. These particles further grow to form the various ice precipitation forms, in this case hail. The problem with winter storms is that instability is not sufficient enough for the cloud to extend to this height or form an anvil. But in the 17 Jan 2013 hailstorm, the instability extending from low to upper levels of troposphere discussed above allows the formation of ice nuclei in the glaciations zone leading to winter hail formation.

REFERENCES

1. NNDC-CDO: NOAA National Data Center Climate Data Online, <http://www7.ncdc.noaa.gov/CDO/cdo>
2. Attri, S.D. and Tyagi, A.: Climate profile of India, Meteorological Monograph No. Environment Meteorology-01/2010, IMD, http://www.imd.gov.in/doc/climate_profile.pdf (2010)
3. Orville, H.D. and Kopp, F.J.: Numerical Simulation of the Life History of a Hailstorm. *J. Atmos. Sci.*, 34, 1596–1618 (1977)
4. Lau, W.K., Waliser, D.E. and Goswami, B.N.: South Asian monsoon. *In: Intraseasonal variability in the atmosphere–ocean climate system*, pp. 21–72. Springer Berlin Heidelberg (2012)
5. Pruppacher, H.R. and Klett, J.D.: Microphysics of clouds and precipitation. *Atmos. Oceanographic Sci. Lib.*, 18 (2010)
6. De, U.S., Dube, R.K. and Rao, G.P.: Extreme weather events over India in the last 100 years. *J. Ind. Geophys. Union*, 9, 173–187 (2005)
7. Skamarock, W.C., Klemp, J.B., Dudhia, J., Gill, D.O., Barker, D.M., Duda, M.G., Huang, X., Wang, W. and Powers, J.G.: A Description of the Advanced Research WRF Version 3, UCAR. http://www.mmm.ucar.edu/wrf/users/docs/arw_v3.pdf (2008)
8. Dimri, A.P. and Chevuturi, A.: Model sensitivity analysis study for western disturbances over the Himalayas. *Meteorol. Atmos. Phys.*, 123, 155–180 (2014)
9. Bush, A.B.G. and Peltier, W.R.: Tropopause Folds and Synoptic-Scale Baroclinic Wave Life Cycles. *J. Atmos. Sci.*, 51, 1581–1604 (1994)
10. Singh, M.S. and Agnihotri, C.L.: Baroclinity over India in winter and its relation to western disturbances and jet streams – Part 1. *Ind. J. Meteorol. Hydrol. Geophys.*, 28, 303–310 (1977)
11. Heymsfield, A.J., Miloshevich, L.M., Schmitt, C., Bansemer, A., Twohy, C., Poellot, M.R., Fridlind, A. and Gerber, H.: Homogeneous ice nucleation in subtropical and tropical convection and its influence on cirrus anvil microphysics. *J. Atmos. Sci.*, 62, 41–64 (2005)
12. Muller, C.L., Kidd, C., Fairchild, I.J. and Baker, A.: Investigation into clouds and precipitation over an urban area using micro rain radars, satellite remote sensing and fluorescence spectrophotometry. *Atmos. Research*, 96, 241–255 (2010)

Chapter 135

Spatio-Temporal Variability of Rainfall and Temperature in Northeast India

S. Sreekish and Manasi Debnath

Abstract This paper deals with the spatial and temporal pattern in monthly rainfall and temperature (maximum and minimum) distribution over the Northeast India. Five meteorological stations have been chosen for this study. The stations considered for analysis of temperature are Dibrugarh (1952–2000), Guwahati (1951–2000), Cherrapunji (1952–2000), Imphal (1954–2000), and Darjeeling (1952–2000). The rainfall analysis has been done for all the above stations for the period 1951–2010. The Mann-Kendall trend test was carried out to assess the trend in rainfall and temperature for different seasons during study period. The analysis has shown that these stations of Northeast India have not experienced any specific trend in rainfall in winter and monsoon seasons. The pre-monsoon season has an increasing trend in rainfall while during post-monsoon season a declining trend in rainfall was observed in two stations. All the stations experienced insignificant rise in maximum temperature during the post monsoon period while rest of the seasons have not shown any persistent trend over the region. An increasing trend in minimum temperature was observed in these stations during post-monsoon season, except Imphal and Cherrapunji. Dibrugarh is the only station which observed an increasing trend in minimum temperature in all of the seasons except winter. In winter minimum temperature increased insignificantly in Guwahati and Darjeeling stations. Even though insignificant, the later indicated a warming tendency for the region.

Keywords Mann Kendall test • Trend in maximum and minimum temperature • Rainfall • Northeast India

135.1 INTRODUCTION

An understanding of spatial and temporal changes in rainfall and temperature is essential for the water resource management, food production and security as well as the balanced economic development of a region. Northeast India is a unique region due to its heterogeneous topography and resultant climatic diversity within

S. Sreekish (✉) • M. Debnath
CSRSD, Jawaharlal Nehru University, New Delhi, India
e-mail: sreekish@mail.jnu.ac.in

the region. The region has meteorological significance because it receives the highest rainfall in the planet Earth [1]. The variations in the climatic parameters are also not homogeneous over the region. The region observed different pattern of change in climate variables in different point of time. It has been already proven, after a study of 30 years data, that different parts of India have been facing dissimilar pattern of change in various climatic parameters such as a general increasing trend of rainfall in North Assam, Western Madhya Pradesh, Konkan and Andhra Pradesh whereas South Assam, Gangetic West Bengal, Haryana, and Mysore has experienced general decreasing trend in rainfall [2, 3]. The Northeast region of India has observed arise in maximum temperature at the rate of 0.11°C per decade and mean temperature at the rate of 0.04°C per decade [4–7]. A range of variability in several climatic parameters or simply climate change led to the risk in several socio-economic aspects; more flood or drought induced agricultural production reduction, food insecurity, climate induced mobility of marginalized social community, water unavailability etc. [8]. Thus there is a growing need to assess the variability and trend in climatic variables within a region for the purpose of mitigation and adaptation and also for policy formulation. Such an assessment is more relevant in environmentally, tectonically and economically vulnerable North-east India. The present study attempted spatial and temporal analysis of the monthly rainfall and maximum and minimum temperature for the selected stations of Northeast of India.

135.2 STUDY AREA

The study area lies in the eastern Himalayas. Meteorological stations considered for the analysis are Darjeeling (Darjeeling Himalaya) in northwest, Dibrugarh (upper Brahmaputra valley) in the east, Guwahati (middle Brahmaputra valley) in the centre, Cherrapunji (Meghalaya Plateau) in east and Imphal in southeast.

135.3 MATERIAL AND METHODS

The data used for this study was collected from the various digital data set compiled by the India Meteorological Department. Data were available in the form of daily as well as monthly series. The data were collected from the inception of the station which varied for different stations. Consequently temperature data has been collected for the period 1961 to 2000 while the rainfall data for the period 1951 to 2010. The pattern and trend of rainfall and temperature are examined using the non-parametric Mann-Kendall test [9, 10]. The test would also help in identifying the starting year of positive or negative trend in the time series data. The Mann-Kendall test is one of the widely used distribution-free test of trend in time series data. Distribution-free tests have the advantage that their power and significance are

not affected by the actual distribution and extremities of the data. The analysis has been carried out for monsoon, post-monsoon, winter, and pre-monsoon seasons as per the scheme of classification of India Meteorological Department.

135.4 RESULTS AND DISCUSSION

135.4.1 Rainfall

The analysis of seasonal rainfall in the Northeastern stations of India is not showing any significant trend (Table 135.1). There is no change in rainfall pattern during monsoon and winter seasons in the study region. However insignificant positive trends are observed at Dibrugarh and Cherrapunji during post-monsoon season and at Dibrugarh, Cherrapunji and Guwahati during pre-monsoon season. It indicates that there is a tendency to have more rainfall during summer months in the region. The stations which experienced a trend began to show changes either during earlier part (prior to 1960) or later part (post 2005) except in Imphal, during pre-monsoon season, where insignificant negative trend began in 1980.

Table 135.1 Trend in seasonal rainfall over different stations of the study area

Stations	Season	Change	Year	M.K. value	Significances at 90 % confidence level
Dibrugarh	Monsoon	NC			
	Post_monsoon	CP	1958	+0.173	INSIGNIFICANT
	Winter	NC			
	Pre_monsoon	CP	1953	+0.068	INSIGNIFICANT
Guwahati	Monsoon	NC			
	Post_monsoon	NC			
	Winter	NC			
	Pre_monsoon	CP	2010	+0.529	INSIGNIFICANT
Cherrapunji	Monsoon	NC			
	Post_monsoon	CP	2009	+0.702	INSIGNIFICANT
	Winter	NC			
	Pre_monsoon	CP	1958	+0.49	INSIGNIFICANT
Imphal	Monsoon	NC			
	Post_monsoon	NC			
	Winter	NC			
	Pre_monsoon	CN	1980	-1.15	INSIGNIFICANT
Darjeeling	Monsoon	NC			
	Post_monsoon	NC			
	Winter	NC			
	Pre_monsoon	CN	2000	-0.25	INSIGNIFICANT

NC = No change, CP = Change with positive trend, CN = Change with negative trend.

Table 135.2 Trend in seasonal maximum temperature at different stations of study area

Stations	Season	Change	Year	M.K. value	Significances at 90% confidence level
Dibrugarh	Monsoon	NC			
	Post_monsoon	CP	1992	+0.834	INSIGNIFICANT
	Winter	NC			
	Pre_monsoon	NC			
Guwahati	Monsoon	CP	1992	+0.422	INSIGNIFICANT
	Post_monsoon	CN	1995	−0.215	INSIGNIFICANT
	Winter	NC			
	Pre_monsoon	NC			
Cherrapunji	Monsoon	NC			
	Post_monsoon	NC			
	Winter	CP	1953	+0.38	INSIGNIFICANT
	Pre_monsoon	NC			
Imphal	Monsoon	CP	1977	+0.84	INSIGNIFICANT
	Post_monsoon	CP	1978	+0.66	INSIGNIFICANT
	Winter	CP	1977	+0.78	INSIGNIFICANT
	Pre_monsoon	NC			
Darjeeling	Monsoon	NC			
	Post_monsoon	CP	1964	1.08	INSIGNIFICANT
	Winter	NC			
	Pre_monsoon	NC			

NC = No change, CP = Change with positive trend, CN = Change with negative trend

135.4.2 Maximum Temperature

There is no significant trend in maximum temperature during different seasons in the study area even though increasing trends are observed in many stations at different seasons (Table 135.2). During monsoon season, Guwahati and Imphal stations point towards an increasing trend which is statistically insignificant while other stations are not experiencing any change. During post-monsoon season all stations, except Cherrapunji, experienced an insignificant increasing trend in maximum temperature. In winter season Cherrapunji and Imphal stations showed insignificant increasing trend while there is no change in maximum temperature in other stations. The Imphal experienced more warming tendency in non-summer seasons than other stations. In contrast to other seasons, pre-monsoon is not showing any trend in all stations indicating that the summer maximum temperature remained unchanged in this region.

The different stations as well as different seasons experienced changes either during early period or latter period (post 1990) of the study with an exception at Imphal (Table 135.2). At Imphal the increasing trend, even though insignificant, started around 1977–78 period in all seasons except pre-monsoon season. In contrast, the Cherrapunji station started showing signs of increasing trend as early as

1953 during winter season while at Darjeeling it began in 1964 for the post-monsoon season. In other stations the sign of change are noticed only after 1990's. However the year of change in trend of maximum temperature was not concurrent across the stations or among the seasons in the study area.

135.4.3 Minimum Temperature

There is no significant trend in minimum temperature in all the stations during different seasons in the study area even though increasing trends are observed in many stations at different seasons (Table 135.3). During monsoon season, Dibrugarh experienced significant positive trend which started from the year 1985. This is the only station and season which has a significant positive trend in minimum temperature. The Imphal and Darjeeling had an insignificant increasing and declining trends in minimum temperature respectively while at Guwahati and Cherrapunji stations trend was absent during monsoon season. The post-monsoon season also showed insignificant positive trend at Dibrugarh, Guwahati, and Darjeeling stations while no trend in other stations. The trend was absent in winter season at Guwahati, Cherrapunji and Imphal stations while Dibrugarh had negative

Table 135.3 Trend in seasonal minimum temperature at different stations of study area

Stations	Season	Change	Year	M.K. value	Significances at 90% confidence level
Dibrugarh	Monsoon	CP	1985	2.07	SIGNIFICANT
	Post_monsoon	CP	1994	0.450	INSIGNIFICANT
	Winter	CN	1989	-0.411	INSIGNIFICANT
	Pre_monsoon	CP	1994	1.05	INSIGNIFICANT
Guwahati	Monsoon	NC			
	Post_monsoon	CP	1987	0.841	INSIGNIFICANT
	Winter	CP	1980	0.362	INSIGNIFICANT
	Pre_monsoon	NC			
Cherrapunji	Monsoon	NC			
	Post_monsoon	NC			
	Winter	NC			
	Pre_monsoon	NC			
Imphal	Monsoon	CP	1998	0.11	INSIGNIFICANT
	Post_monsoon	NC			
	Winter	NC			
	Pre_monsoon	NC			
Darjeeling	Monsoon	CN	1967	-0.0832	INSIGNIFICANT
	Post_monsoon	CP	1961	0.60	INSIGNIFICANT
	Winter	CP	1967	1.34	INSIGNIFICANT
	Pre_monsoon	CN	1967	-0.037	INSIGNIFICANT

NC = no change, CP = Change with positive trend, CN = Change with negative trend

and Darjeeling had positive trends both of which are insignificant. Similarly pre-monsoon season is also not showing any trend at Guwahati, Cherrapunji and Imphal stations while Dibrugarh and Darjeeling had insignificant positive and negative trends respectively. The minimum temperature at Cherrapunji was devoid of any trend in all seasons.

It is observed that the insignificant positive or negative trends in minimum temperature experienced in some stations are in different years (Table 135.3). There is no uniformity in year of change in minimum temperature in the study area or the seasons in which it occurred. Except Darjeeling all other stations experienced change in different years after 1980 while Darjeeling experienced the change during mid 1960's in all seasons. At Dibrugarh, Guwahati and Imphal stations the positive trends, except during winter at Dibrugarh (Table 135.3), were observed between 1980 and 1997. It is also to be noted that positive trends in this region is closer to 90% confidence level. This indicates the possibility of a statistically significant increasing trend in minimum temperature in near future.

135.5 CONCLUSIONS

There is no significant increasing or decreasing trend in rainfall or temperature in the Northeastern stations of India considered for the present study during the second half of the last half of last century. The analysis indicates that the changes in rainfall and temperature are seasonal as well as site specific and not uniform across stations or seasons. The pre-monsoon season had an increasing trend in rainfall while post-monsoon season had a declining trend in two stations. The insignificant increasing trend in rainfall during the pre-monsoon indicates an increase in summer rainfall while there is no significant trend in rainfall in other seasons. Maximum and minimum temperature is showing insignificant increasing trend during monsoon season only at Imphal and during post-monsoon at Dibrugarh, Guwahati and Darjeeling stations indicating a warming tendency in these consecutive seasons. Persistent increasing trend in maximum temperature was observed at all the stations (except Cherrapunji) only in post monsoon. On the other hand general increasing trend in minimum temperature was observed in most of the stations more frequently during the winter months. Imphal and Cherrapunji observed less increasing trend while Darjeeling and Dibrugarh observed higher degree of positive trend in minimum temperature. Darjeeling experienced the insignificant positive trend in maximum and minimum temperature during post monsoon season while only minimum temperature showed positive trend during winter. Overall temperature (both minimum and maximum) in post-monsoon period has been continuously increasing throughout the region except Cherrapunji during the study period. However, it is observed that there is no concurrence in the starting period of the trend of maximum and minimum temperature in these stations. It is to be noted that most of the positive trends, especially after 1980's, are near to the 90 % confidence level which denotes the possibility of a firm increasing trend in the temperature in the

near future. However, lack of persistent trend in rainfall, temperature (both maximum and minimum), and difference in starting periods of trend, even though insignificant, made it difficult to attribute such changes to an indication of climate change in this area.

REFERENCES

1. Jain, S.K. and Kumar, Vijay: Trend analysis of rainfall and temperature data for India. *Current Science*, 102, 1 (2012)
2. Parthasarathy, B. and Dhar, O.N.: Secular variations of regional rainfall over India. *Quart. J. R. Met. Soc.*, 100, 245–257 (1974)
3. Dash, S.K., Jenamani, R.K., Kalsi, S.R. and Panda, S.K.: Some evidence of climate change in twentieth-century India. *Climatic Change*, 85, 299–321 (2007)
4. Pant, G.B. and Rupa Kumar, K.: *Climates of South Asia*. John Wiley and Sons, New York (1997)
5. Jain, S.K. et al.: Analysis of rainfall and temperature trends in Northeast India. *International Journal of Climatology*, Published online in Wiley Online Library (wileyonlinelibrary.com), DOI: [10.1002/joc.3483](https://doi.org/10.1002/joc.3483) (2012)
6. Das, P. J. and Goswami, D.C.: Long-term variability of rainfall over northeast India. *Indian Journal of Landscape System Ecological Studies*, 26(1), 1–20 (2003)
7. Das, P.J.: Rainfall regime of Northeast India: A Hydrometeorological Study with special emphasis on the Brahmaputra basin. Unpublished PhD thesis. Guwahati University, Assam (2004)
8. IPCC: Summary for policymakers. In: *Climate Change 2014: Impacts, Adaptation, and Vulnerability. Part A: Global and Sectoral Aspects. Contribution of Working Group II to the Fifth Assessment Report of the Intergovernmental Panel on Climate Change* [Field, C.B., V.R. Barros, D.J. Dokken, K.J. Mach, M.D. Mastrandrea, T.E. Bilir, M. Chatterjee, K.L. Ebi, Y.O. Estrada, R.C. Genova, B. Girma, E.S. Kissel, A.N. Levy, S. MacCracken, P.R. Mastrandrea, and L.L. White (eds.)]. Cambridge University Press, Cambridge (2014)
9. Mann, H.B.: Nonparametric tests against trend. *Econometrica*, 13, 245–259 (1945)
10. Kendall, M.G.: *Rank Correlation Methods*. Griffin, London (1975)

Chapter 136

Surface Energy and Mass Balance on the Ablation Zone of Chorabari Glacier, Central Himalaya, India

**Kapil Kesarwani, D.P. Dobhal, Alok Durgapal, Indira Karakoti,
and Manish Mehta**

Abstract The energy balance at the glacier-atmosphere interface is the key control of the interaction between glaciers and climate. Melting at the glacier surface is controlled by the surface energy balance. Here we report, the energy and mass balance study carried out on Chorabari Glacier, Mandakini basin, Central Himalaya for the period of one year (Nov 2011-Oct 2012). The meteorological data collected from an Automatic Weather Station (AWS) were used to compute the annual cycle of local surface energy balance in the ablation zone. The average energy flux is calculated 28.5 Wm^{-2} for surface melting. In addition, the net radiation component is the largest contributor (52%) to the total surface energy heat flux followed by turbulent sensible (26%) and latent (9%) fluxes and the remaining 13% is only from subsurface heat. The study shows that the modelled ablation is well matched with ground measurement by 2% relative error.

Keywords Himalaya • Glacier • Meteorology • Energy-mass balance

136.1 INTRODUCTION

The Surface Energy Balance (SEB) of the glacier describes a very close physical relationship between snow/ice ablation and climate forcing, particularly the solid precipitation (snowfall) and air temperature [1]. The relation between meteorological parameters and the mass balance of glacier surface is important for understanding the physical processes governing by snow/ice melt [2]. The energy balance studies on mountain glaciers such as Andes [3], European Alps [4], Rocky Mountains [5] and Tien Shan [6] are very fairly documented but in the Himalaya very less attention has been given on this issue. Here we report, the energy and mass balance

K. Kesarwani (✉) • D.P. Dobhal • I. Karakoti • M. Mehta
Centre for Glaciology, Wadia Institute of Himalayan Geology, Dehradun, Uttarakhand, India
e-mail: kapilcfg@gmail.com

A. Durgapal
D.S.B. Campus, Kumaun University, Nainital, Uttarakhand, India

study for one year (Nov 2011-Oct 2012) on Chorabari Glacier, Central Himalaya. The SEB has been estimated by using standard equation;

$$Q = R_n + H_s + H_L + G \quad (136.1)$$

where Q is total energy for Snow/ice melting, R_n is net radiation, H_s is sensible heat flux, H_L is latent heat flux, and G is the subsurface heat flux.

136.2 STUDY AREA

Chorabari Glacier is located at 30°46'20.58"N; 79°2'59.38"E in Mandakini basin of Alaknanda catchment (a tributary of river Ganga) Central Himalaya, India (Fig. 136.1). It is medium-sized compound valley type glacier covering an area of ~6.6 Km² and having a length 6.5 Km. It has a small accumulation area below from Bhartkhunta peak (6578 m asl) and Kedar peak (6940 m asl) flows from North to South between 6400 and 3895 m asl with an average slope of 20° [7].

136.3 METHODOLOGY

136.3.1 AWS Description

For studying the weather parameters, we have installed an Automatic Weather Station (AWS) on the upper ablation zone (4270 m asl) of the Chorabari Glacier in October 2011 (Fig. 136.1). The meteorological station is equipped with sensors of air temperature (Pt100RTD), relative humidity (Hygromer IN-1), net radiometer (NR-LITE-L), upward-downward looking pyranometer (CMP3-L), wind monitor (Young 05103), air pressure (RM Young-61302V), acoustic distance sensor (SR50A) for measurement of snow depth and tipping bucket rain gauge (TE525M) [8].

136.3.2 Mass Balance Observation

The mass balance of Chorabari Glacier on the ablation zone was measured using standard glaciological stake network method [9]. A network of 40 stakes was set up and each stake was fixed to a depth of 5-6 m to measure the accumulation and ablation in October 2011. Average densities of 0.15, 0.56 and 0.85 g cm⁻³ were calculated for snow, firn and ice, respectively [7].

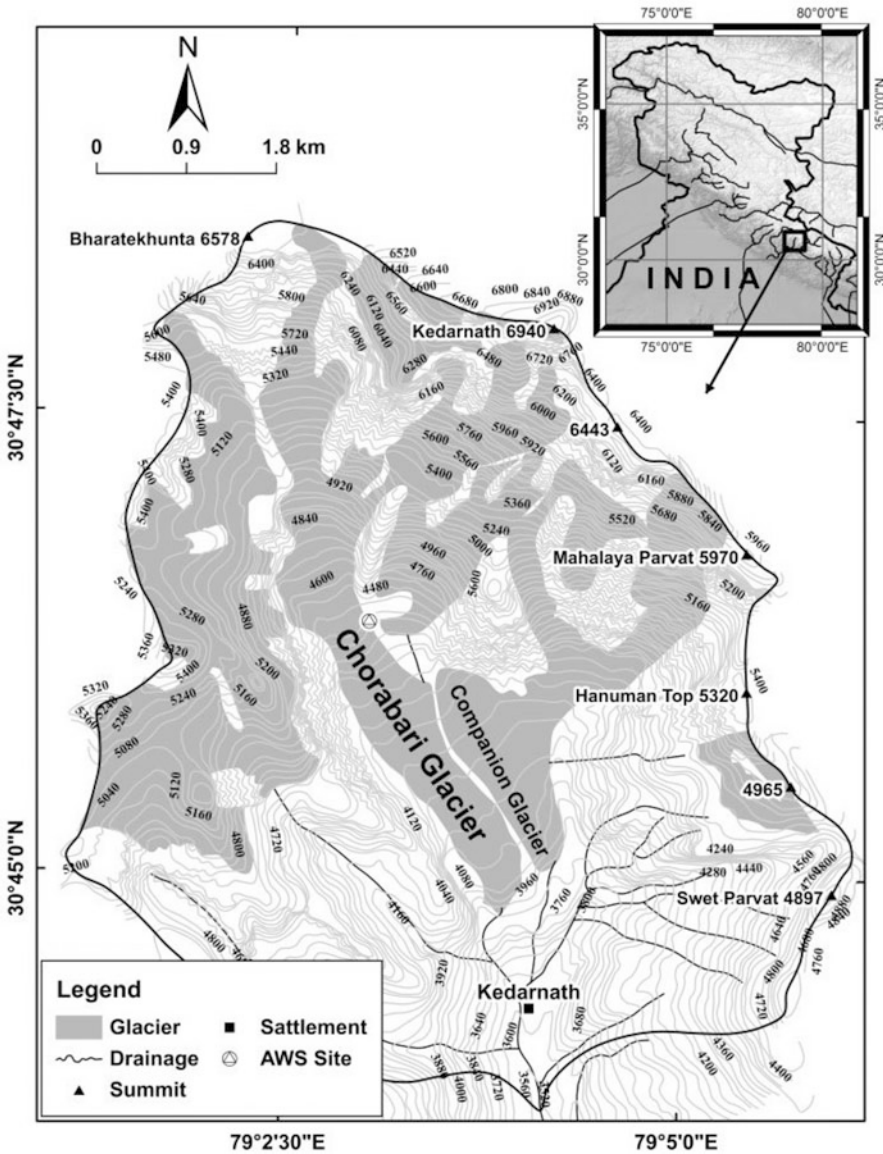


Fig. 136.1 Location map of Chorabari glacier and automatic weather station site

136.4 RESULTS

During the study period, the net radiation is the most important energy source for melting at the glacier surface which was estimated 52% to the total surface energy heat flux. The turbulent sensible and latent heat flux are calculated by using bulk

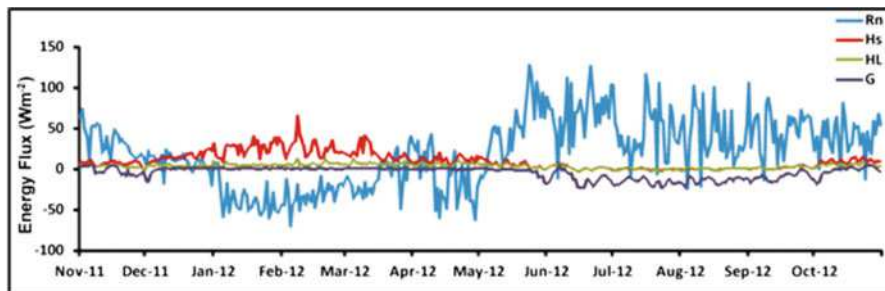


Fig. 136.2 Daily mean values of energy-balance components

dynamic approach, contributing 26 and 9% respectively to the total heat flux. The subsurface conductive heat flux is to be estimated 13% (Fig. 136.2). The heat flux provided by rain to melt the glacier surface is very small and is estimated to be 5.5 MJ.

The mass loss estimated through SEB approach in the ablation zone was $-6.2 \times 10^6 \text{ m}^3 \text{ w.e.}$ whereas, based on ground measurement (stakes data), the mass loss was calculated to be $-5.7 \times 10^6 \text{ m}^3 \text{ w.e.}$

136.5 CONCLUSIONS

In this study, we have used a physically based energy-balance modelling to estimate the surface energy balance on the ablation zone of Chorabari Glacier from AWS data. The net radiation component is the largest contributor to the total surface energy heat flux. In addition, the study shows that the modelled ablation has a good correlation with the ablation, measured from glaciological method having 2% relative error.

ACKNOWLEDGEMENTS Authors are grateful to Director, Wadia Institute of Himalayan Geology (WIHG), Dehra Dun for providing the necessary facilities. We are thankful to Shri Deepak Srivastava, Retd. Deputy Director General, Geological Survey of India and Dr Rakesh Bhambri, Scientist, Centre for Glaciology, WIHG for their guidance and valuable suggestions. Thanks are also due to Department of Science & Technology, Government of India, New Delhi for funding this work.

REFERENCES

1. Mölg, T. and Hardy, D.R.: Ablation and associated energy balance of a horizontal glacier surface on Kilimanjaro. *J. Geophys. Res.*, 109(D16), 1–13 (2004)
2. Reid, T.D. and Brock, B.W.: An energy-balance model for debris-covered glaciers including heat conduction through the debris layer. *J. Glacio.*, 56(199), 903–916 (2010)

3. Favier, V., Wagnon, P., Chazarin, J.P., Maisincho, L. and Coudrain, A.: One-year measurements of surface heat budget on the ablation zone of Antizana Glacier 15, Ecuadorian Andes. *J. Geophys. Res.*, 109(D18), D18105 (doi: 10.1029/2003JD004359) (2004)
4. Pellicciotti, F., Carenzo, M., Helbing, J., Rimkus, S. and Burlando, P.: On the role of subsurface heat conduction in glacier energy-balance modeling. *Ann. Glacio.*, 50(50), 16–24 (2009)
5. Nakawo, M. and Young, G.J.: Estimate of glacier ablation under a debris layer from surface temperature and meteorological variables. *J. Glaciol.*, 28(98), 29–34 (1982)
6. Hong, M., Zongchao, L. and Yifeng, L.: Energy balance of snow cover and simulation of snow-melt in the western Tien Shan mountains, China. *Ann. Glaciol.*, 16, 73–78 (1992)
7. Dobhal, D.P., Mehta, M. and Srivastava, D.: Influence of debris cover on terminus retreat and mass changes of Chorabari Glacier, Garhwal region, central Himalaya, India. *J. Glaciol.*, 59 (217), 961–971 (2013)
8. Kesarwani, K., Pratap, B., Bhambri, R., Mehta M., Kumar, A., Karakoti, I., Verma, A. and Dobhal, D.P.: Meteorological observations at Chorabari and Dokriani glaciers, Garhwal Himalaya, India. *J. Ind. Geol. Cong.*, 4(1), 125–128 (2012)
9. Østrem, G. and Brugman, M.: Glacier mass-balance measurements: a manual for field and office work. (NHRI Science Report 4) National Hydrology Research Institute, Environment Canada, Saskatoon, Sask (1991)

Chapter 137

Monitoring the Status of Siachen Glacier Using Multi Temporal Remote Sensing Approach

Snehmani, Mritunjay Kumar Singh, Krishnanjan Pakrasi,
Anshuman Bhardwaj, and A. Ganju

Abstract The temporal monitoring of any glacier is important for observing the effects of changing climate. This study reports the decadal changes in Siachen glacier. Analysis was carried out on decadal basis by processing and analyzing Landsat images from 1978 to 2013. Images were co-registered within Root Mean Square Error (RMSE) limit of 0.5 pixel. An object based classification approach was adopted to perform temporal semi-automated areal change detection. The glacier inventory of 1978 showed around 74976 ha of glacier area which further decreased by around 1302 ha in 2013 with a shift of 1.5 km in the snout position.

Keywords Landsat • ASTER GDEM • NDSI • Thermal band • Object based classification

137.1 INTRODUCTION

Global warming and climate change are constantly in center of most of the glaciological studies in Indian Himalayan context. Glacier retreat is an indicator of ongoing climate change [1]. The changes in glacier and snow cover areas are very prominent in many parts of the Himalayas [2]. Remote sensing has emerged as a very effective tool for year round monitoring of difficult to approach high altitude glaciers. But in the case of Himalayan glaciers, the presence of debris cover, which has the same spectral reflectance as the surrounding non glaciated surface, makes any semi-automated remote sensing based mapping approach very difficult. Some efforts have recently been made towards developing a remote sensing based glacier inventory of Nepal and Bhutan Himalayas [3, 4]. Such efforts in Indian Himalayan context are needed to be revised. This paper focuses on an object based classification approach to perform temporal semi-automated areal change detection in case

Snehmani (✉) • M.K. Singh • K. Pakrasi • A. Bhardwaj • A. Ganju
Snow and Avalanche Study Establishment, Him Parisar, Chandigarh, India
e-mail: snehmani@gmail.com; jay_rsgis@yahoo.co.in; p.krishnanjan@gmail.com;
anshuman.teri@gmail.com; ashwagosha@gmail.com

of Siachen glacier over a temporal span of 35 years (1978–2013). The approach was validated with respect to manually digitized boundaries of the glacier for all the years and the observed RMSEs in areal differences were very less ($<5\%$). In addition, the snout recession (~ 35 m/yr) and diminishing glacier area over this time period were clearly seen. These observations were tried to be explained through the available meteorological records for the glacier, in order to establish their link with the changing climate.

137.2 STUDY AREA

The Siachen glacier is located on the north-facing slopes of the Karakoram mountain range in the state of J&K, India [5]. As seen on the Google Earth, it is located between 78.73° and 77.4° longitudes and 35.68° and 35.15° latitudes. It originates as an ice fall at a height of around 6,300 m and is joined almost immediately by two streams, also originating as ice falls in the West and in the East at heights of around 6,000 m and 5,800 m respectively. The three ice falls, at the head of this glacier, combine lower down into a large ice field which at its widest, is around 5 km. This glacier, from head to its terminus at the head of the Nubra Valley, exhibits a length of around 74 kilometers. It feeds the Muztagh or Shaksgamriver that flows parallel to the Karakoram range before entering into Tibet.

137.3 DATA USED

Landsat images of 1978, 1990, 2001, 2010, 2013 were downloaded and processed. Landsat image of 1978 was MSS image with 60 m spatial resolution. Landsat images of 1990 and afterwards were TM and ETM+ with better 30 m multispectral bands. ASTER GDEM V2 was used for 3D visualization and manual boundary delineation. The SASE (Snow and Avalanche Study Establishment) observatories' meteorological data were used for further analysis of the classification outcomes.

137.4 METHODOLOGY

Preprocessed and co-registered Landsat images were used to obtain a new Normalized Difference Debris Index (NDDI) which along with the slope parameter obtained from ASTER GDEM V2, helped in differentiating supraglacial debris cover from snow/ice as well as surrounding non-glacial barren rocks:

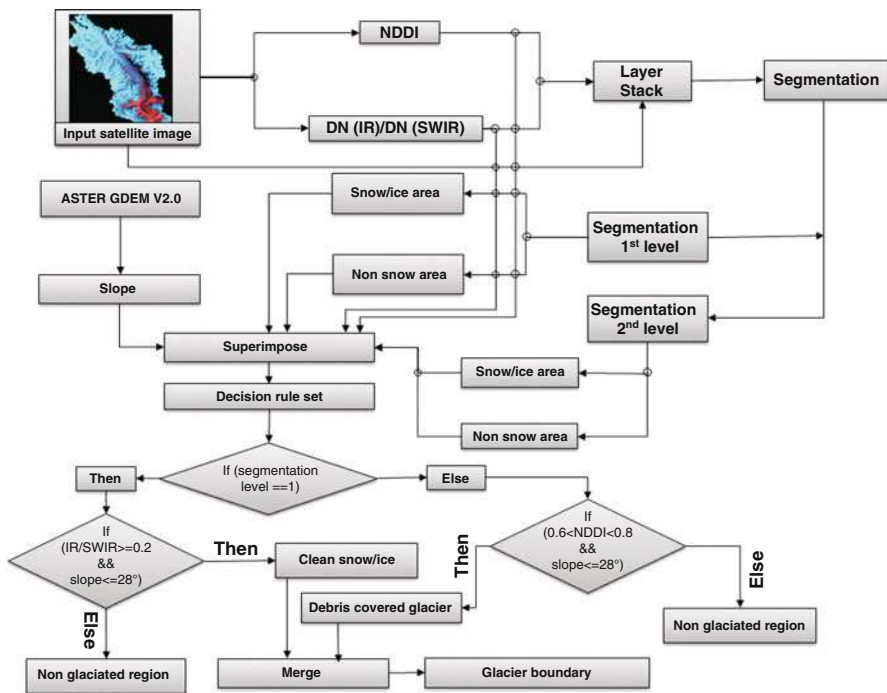


Fig. 137.1 Methodology followed

$$NDDI = \sqrt{\frac{DN(\text{Thermal}) - DN(\text{Red})}{DN(\text{Thermal}) + DN(\text{Red})}} \quad (137.1)$$

A semi-automated and object based method (Fig. 137.1) was developed with some empirical thresholding based on literature [6] and visual observations to obtain final glacier boundaries. For the year 1978, manually delineated boundary was used as MSS lacked thermal band to apply the methodology.

137.5 Accuracy Assessment

$$RMSE = \sqrt{\frac{\sum_{i=1}^n (a_i - \hat{a}_i)^2}{n}} \quad (137.2)$$

where a_i is the manually digitized area, \hat{a}_i is the area of glacier extracted through object based classification approach and n is the total number of years observed (Table 137.1).

Table 137.1 Observed % RMSE for different years

Year	RMSE (%)
1990	3.2
2001	2.5
2010	2.3
2013	2.1

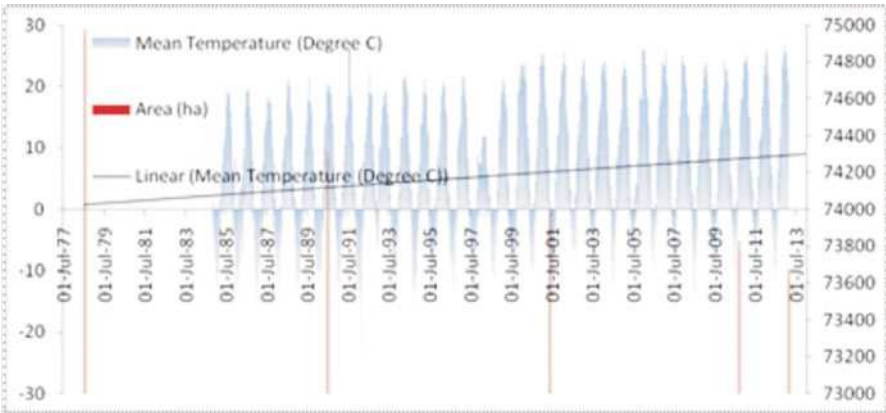


Fig. 137.2 Trends of changes in glacier area and temperature in past three decades

137.6 RESULTS

The total glacier area decreased from 74976 ha in 1978 to 73674 ha in 2013 (Figs. 137.2 and 137.3). During this period, the snout of the glacier also retreated with a rate of about 35 m/yr (Fig. 137.3). Figure 137.2 also depicts past 30 years’ trend of daily mean temperature for this glacier.

137.7 DISCUSSION

The suggested semi-automated method of glacier area extraction was found to be working well in case of this glacier with negligible RMSE. Very few of the small polygons were misclassified and could be easily removed by manual editing. The interesting finding was a new normalized difference index called NDDI which was able to map and differentiate supraglacial debris cover from other glacier features and surrounding rocky areas. It has the potential to further speed-up the process of such monitoring studies in future. The glacier area was found to be decreasing with a rate of 37 ha/yr and the receding rate of snout was about 35 m/yr during past 3.5 decades. During these decades, the average trend of daily mean temperature obtained from 4 weather observatories on this glacier showed an alarmingly increasing temperature rate (Figure 137.2). Thus, we can conclude that even the

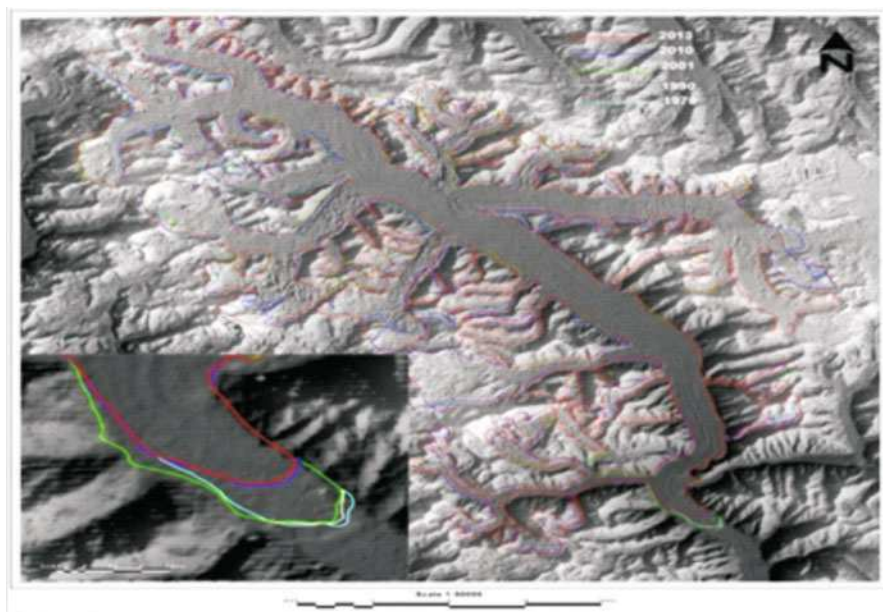


Fig. 137.3 Temporally changing glacier boundaries and snout positions

glaciers which have very large accumulation area and which are located in relatively higher elevations are getting affected by the increasing air temperature.

ACKNOWLEDGEMENT We are thankful to the MoES project (Number: MoES/P.O(Sismo)/1/(83)/2010) for providing the grants to carry out this research.

REFERENCES

1. Haeberli, W., Frauenfelder, R., Hoelzle, M. and Maisch, M.: Rates and acceleration trends of global glacier mass changes. *Geografiska Annaler*, 81A, 585–591 (1999)
2. Nie, Y., Zhang, Y., Liu, L. and Zhang, J.: Glacial change in the vicinity of Mt. Qomolangma (Everest), central high Himalayas since 1976. *J. Geogr. Sci.*, 20(5), 667–686 (2010)
3. ICIMOD Research Report: Glacier Status in Nepal and Decadal Change from 1980 to 2010 Based on Landsat Data. ISBN 1978929115311 [Printed] 97892115312 (electronic) (2014)
4. Bajracharya, S.R., Maharjan, S.B. and Shrestha, F.: The status and decadal change of glaciers in Bhutan from the 1980s to 2010 based on satellite data. *Annals of Glaciology*, 55(66), 159–166 (2014)
5. Snehamani, Bhardwaj, A., Singh, M.K., Gupta, R.D., Joshi, P.K. and Ganju, A.: Modelling the hypsometric seasonal snow cover using meteorological parameters. *J. Spatial Sci.* Doi: [10.1080/14498596.2014.943310](https://doi.org/10.1080/14498596.2014.943310) (2014)
6. Paul, F., Huggel, C. and Kaab, A.: Combining satellite multispectral image data and a digital elevation model for mapping debris-covered glaciers. *Remote Sens. Env.*, 89, 510–518 (2004)

Chapter 138

Monitoring Glacial Parameters in Parts of Zaskar Basin, Jammu and Kashmir

Iram Ali, Aparna Shukla, and Junaid Qadir

Abstract Alteration in glacial parameters are pertinent indicators of glacier health and their response to climate change. In the present study, five glaciers of Zaskar basin including Pensli-lungpa, Durung Drung, Kangi, Hogshu and one unnamed glacier have been studied for temporal changes in glacial extent, glacial mass balance via accumulation area ratio (AAR) and ELA. For this purpose various multi-temporal satellite datasets of the study area and ASTER DEM have been used. ELA has been derived by using normalized difference glacier index (NDGI) technique and DEM together. Glacier boundaries have been derived by manual digitization. The mapping of glaciers during the period 1980–2000 & 2000 to 2011 reveals that the glacier cover reduced from 291.98 km² to 259.11 km², and 259.11 km² to 250.96 km² witnessing deglaciation of 11.25% and 3.14% respectively. Moreover, that there has been an increase in SLA of the sub basin from 5126 m a.s.l to 5297 m a.s.l from 1977 to 2000 and 5297 m a.s.l to 5361 m a.s.l from 2000 to 2011. Besides, the minimum and maximum AAR derived mass balance for the study area during the period of study has been 42.61 cm and -13.17 cm, respectively. An increase in the mean ELA in the area is followed by pronounced glacier recession and deglaciation.

Keywords Equilibrium line altitude (ELA) • Accumulation area ratio (AAR)

138.1 INTRODUCTION

Snow and glaciers are very important components of the Earth's surface. Spatial extent of glaciers and its components are sensitive to climatic conditions and climate change [4]. Glacier length, mass balance and snow melt runoff are some of the glacier parameters that are directly or indirectly related with the climate. Any change in the climate is reflected by the glacier and can be studied by analyzing the glacier parameters. This necessitates active mapping and monitoring of glacier parameters. Deglaciation, retreat, variations in equilibrium line altitudes (ELA),

I. Ali (✉) • A. Shukla • J. Qadir

Department of Earth Sciences, University of Kashmir, Srinagar, India

e-mail: geoiram@gmail.com

accumulation area ratio (AAR), glacier thickness and volume are some of the inter-linked and vital glacier parameters with reference to scrutinizing impacts of climate variability on glaciers in a region. Considering the vastness and inaccessible nature of mountain glaciers, and the repetitive observations required, satellite remote sensing technology offers a highly viable tool for monitoring the different glacier parameters in an effective way [1]. More recently [2] analyzed the glacier retreat and morphometric parameters in Doda valley, Zaskar basin in Jammu & Kashmir of the glaciers using multi-temporal satellite data and concluded that the total glacier area loss from 1962 to 2001 is 18.16% and the mass balance for the years 1975 and 1992, is positive but in the year 2001, specific mass balance of all glaciers was negative. The present work is aimed at deriving retreat, deglaciation, variations in the ELA & AAR for five glaciers (Pensli-lungpa, Durung-drung, Kangi, Hogshu and one un-named glaciers) of Zaskar basin using time series LANDSAT MSS, TM, & ETM+ from 1977 to 2013.

138.2 STUDY AREA

The study area includes Zaskar valley Ladakh, Jammu & Kashmir in the Great Himalayan Range extending from $33^{\circ}5'24''$ N $-77^{\circ}10'12''$ N to $34^{\circ}5'24''$ N $-75^{\circ}59'23''$ E. The elevation in the area ranges between 3700–6400 m above MSL. The important glaciers constitute Pensilungpa, Durungdrung, Kangi and Hogshu among which Durungdrung glacier is the largest one.

138.3 MATERIAL AND METHODS

In order to carry out the present study, multi-temporal satellite data of years 1977, 1980, 1999, 2000, 2011 and 2013 from LANDSAT MSS, TM, ETM+ and ASTER DEM have been used as primary datasets. For the purpose of deriving snowline, normalized difference glacier index (NDGI) was applied and a threshold value of 0.32 has been found suitable for mapping and differentiating between accumulation and ablation zones. The mapping of the glaciers was carried out by manual digitization from the period 1977 to 2013 which was aided by using various spectral band combinations and false colour composited (FCCs). For the current study accumulation area ratio (AAR) was firstly derived from the below equation $AAR = S_C / S_G$. Where S_C represents surface area of accumulation zone and S_G the total surface area of the glacier respectively [3] which later on was converted to specific mass balance using equation given below:

$$Y = 243.01 \cdot X - 120.187$$

where Y is the specific mass balance in water equivalent (cm) and X is the accumulation area ratio [5].

138.4 RESULTS AND DISCUSSION

138.4.1 Glacier Area Changes

The results reveal that the glacier areas of Pensilungpa (G1), DurungDrung (G2), G3, Kangi (G4) and Hogshu (G5) were reduced from 21.39 km², 82.45 km², 44.72 km², 65.57 km² and 78.65 km² to 18.28 km², 71.72 km², 35.50 km², 56.59 km² and 66.51 km², respectively, from 1977 to 2013 Fig.138.1 (a). This results to a total deglaciation of 14.53%, 13.01%, 20.61%, 13.69% and 15.43% for Pensilungpa, DurungDrung, G3, Kangi and Hogshu for past 36 years (1977 to 2013) Fig. 138.1(b).

138.4.2 Variations in Snow Line Altitude (SLA)

An in depth analysis of SLA of five main glaciers in Zaskar basin reveal that there has been an increase in SLA of the sub basin from 5126 m a.s.l to 5297 m a.s.l from 1977 to 2000 and 5297 m a.s.l to 5361 m a.s.l from 2000 to 2011 Fig 138.2 (a). The mean SLA of each glacier is represented in Fig. 138.2(b).

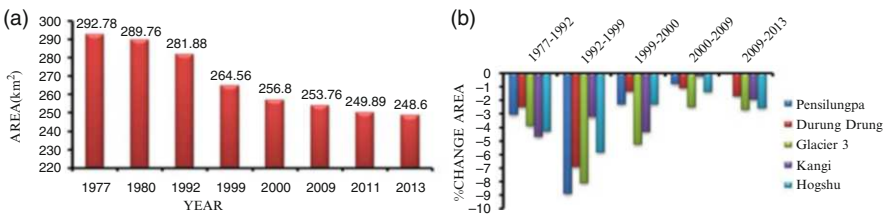


Fig. 138.1 (a) Variation in the glacier area from 1977-2013. (b) Change in area (%) for individual glaciers from 1977–1992, 1992–1999, 1999–2000, 2000–2009 and 2009–2013

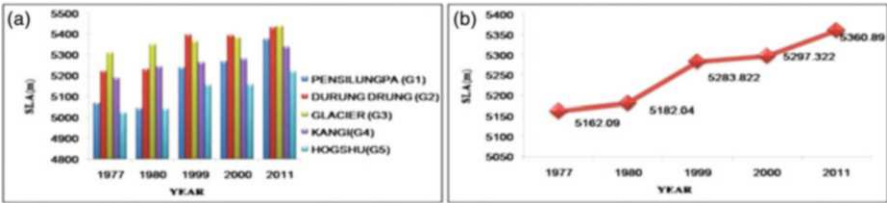


Fig. 138.2 (a) Variations in snow-line altitudes (SLA) of all glaciers from 1977–2011. (b) Mean snow line altitude (SLA) of each glaciers from 1977–2011

Table 138.1 Summary statistics of individual mass balance and AAR values of glaciers for year 1999, 2000 and 2011

Glacier name	Mass Balance (cm)	AAR	Mass Balance (cm)	AAR	Mass Balance (cm)	AAR
	1999	1999	2000	2000	2011	2011
Pensilungpa (G1)	17.81	0.56	13.94	0.55	5.9	0.51
Durungdrung (G2)	17.83	0.56	−5.28	0.47	12.6	0.54
Glacier (G3)	17.58	0.56	−9.83	0.45	5.92	0.51
Kangi(G4)	11.62	0.54	−26.84	0.38	−5.19	0.47
Hogshu(G5)	13.58	0.55	−16.89	0.42	4.56	0.51

138.4.3 Mass Balance

After analyzing the mass balance of all the glaciers it has been depicted that the mass balance for the years 1977 and 1980 is positive for all the glaciers whereas the mass balance in year 1999 shows moderately positive mass balance Table 138.1.

138.5 CONCLUSIONS

The study reveals that NDGI has proved to be the best semi-automatic method for differentiating between snow and ice. Additionally it has been found that the total glacierized area of basin reduced from 292.78 km² to 248.74 km² from 1977 to 2013. Consequently the mean SLA of the sub-basin has increased from 5126 m a.s.l to 5297 m a.s.l from 1977 to 2000 and 5297 m a.s.l to 5361 m a.s.l from 2000 to 2011. Besides, mass balance for the years 1977 and 1980 is positive for all the glaciers where as the mass balance in year 1999 shows moderately positive mass balance. The results obtained here are in good confirmation with one another. Additionally, the results from the glacier parameters indicate a general degeneration of glaciers in the study area which necessitates their continuous and regular monitoring. This emphasizes the fact that these parameters are important indicators of glacier health.

REFERENCES

1. Bolch, T. and Kamp, U.: Glacier Mapping in High Mountains Using DEMs, Landsat and ASTER data. *Grazer Schriften der Geographie und Raumforschung*, 41, 37–48 (2006)
2. Chander, G. and Markham, B.: Revised Landsat-5 TM Radiometric Calibration Procedures and Post-calibration Dynamic Ranges. *IEEE Transactions on Geoscience and Remote Sensing*, 41 (11), 2674–2677 Part 2 (2003)
3. Dyurgerov, M.B. and Meier, M.F.: Glaciers and the changing Earth system. A 2004 snapshot. Boulder, CO, University of Colorado. Institute of Arctic and Alpine Research. INSTAAR Occasional Paper 58 (2005)
4. Kaab, A.: Glacier volume changes using ASTER optical stereo. A test study in Eastern Svalbard. *IEEE Transactions on Geosciences and Remote Sensing*, 10, 3994–3996 (2007)
5. Kulkarni, A.V., Rathore, B.P., Mahajan, S. and Mathur, P.: Alarming retreat of Parbati glacier, Beas basin, Himachal Pradesh. *Current Science*, 88, 1844–1850 (2005)

Chapter 139

An Analysis of Pattern of Changes in Snow Cover in the Upper Beas River Basin, Western Himalaya

Seema Rani and S. Sreekesh

Abstract This study is an attempt to look at intra seasonal and inter annual variations in temperature and in snow covers area (SCA) of the Upper Beas river basin (up to Pandoh dam) of the Western Himalaya. The SCA was assessed based on Normalized Differential Snow Index (NDSI) using representative images of MODIS Snow Cover Daily L3 Global) data for the period 2000–2010. Air temperature data from adjacent India Meteorological Department stations were used to examine the relationship between the snow cover and air temperature. It has been observed that the SCA showed large scale fluctuations both in time and space.

Keywords Snow cover area (SCA) • MODIS • River run-off

139.1 INTRODUCTION

Study of spatial and temporal variability of cover area (SCA) is of paramount importance in the context of climate variability and water supply and proper management of water resources. SCA is considered as important component of the climate system to assess the climate variability in the Cryosphere [1, 2] as it is considered to be highly sensitive to the fluctuations in temperature and the changes in the extent of snow cover would also affect the seasonal distribution of river flow and water supply for hydroelectric generation, agriculture, hydrologic systems, soil stability and related socio-economic systems [3]. There are evidences of changes in snow cover area around the globe. The fourth assessment report of IPCC [6] highlighted that Northern Hemisphere snow cover extent has been consistently below the 21 years (1974–1994) average since 1988. Several studies [4–8] have also been done on the Indian Himalayas to examine the changes in SCA by using remote sensing data (Landsat, IRS and MODIS). They found high intra-seasonal variability in the SCA in different regions of the Himalayas. The present study assessed the annual, seasonal and monthly trends in the SCA of the upper Beas river

S. Rani • S. Sreekesh (✉)

Centre for the Study of Regional Development, Jawaharlal Nehru University, New Delhi, India

e-mail: sreekesh@mail.jnu.ac.in

basin during 2000–2010 and the relationship between SCA and air temperature. The study would be helpful to manage the water resources in the upper Beas river basin and ensure environmental security in the region.

139.2 STUDY AREA

The area of study is the upper Beas river basin up to Pandoh dam. It is bounded between latitude $31^{\circ} 31' 00''$ – $32^{\circ} 45' 00''$ N and longitude $76^{\circ} 44' 00''$ – $77^{\circ} 52' 00''$ E. Beas River up to Pandoh has a length of 116m and catchment area of about 5300 sq. km.

139.3 MATERIAL AND METHODS

Daily maximum and minimum air temperature data of Manali and Bhuntar for the period 1980–2010 was collected from the India Meteorological Department (IMD). MODIS/Terra Snow Cover Daily L3 Global 500m Grid (MOD10A1) data of upper Beas river basin from 2000 to 2010 was obtained from the Distributed Active Archive Center (DAAC) located at the National Snow and Ice Data Center (NSIDC). The MOD10A1snow cover product is a classified image. For development of snow covered products, the Normalized Difference Snow Index (NDSI) [9] approach, using band 4 and 6, has been used to compute snow cover area. Present study considered middle of the month snow covered area, obtained from NDSI, is considered as the representative of the month. Descriptive statistics were used to characterize the SCA at monthly, seasonal and annual basis. Ordinary least-squares (OLS) regression test was used to assess the direction and magnitude of trend in the annual, seasonal and monthly SCA.

139.4 RESULTS AND DISCUSSION

139.4.1 *Annual Trends*

Mean annual SCA in the upper Beas river basin was 31.44% during 2000–2010. Annual SCA of the study area shows a positive trend, but the trend is not statistically significant (Table 139.1).

Table 139.1 Descriptive statistics and trend in SCA of the upper Beas river basin during 2000-2010

Time Scale	Mean	Std. Deviation	CV (%)	Rate of Change (%/yr.)
January	53.73	7.92	14.75	-0.004
February	62.03	15.10	24.34	-0.29
March	64.10	11.18	17.44	-0.318
April	46.83	7.20	15.37	-0.526*
May	34.69	7.53	21.71	-0.367
June	20.02	6.35	31.74	-0.5
July	10.60	5.41	51.00	0.538*
August	6.50	2.68	41.29	-0.06
September	7.38	3.28	44.37	0.328
October	19.05	7.46	39.13	0.172
November	21.04	8.96	42.60	0.48
December	36.96	16.24	43.92	0.048
Winter Season	54.13	5.93	10.95	-0.247
Pre-monsoon Season	33.85	3.48	10.29	-0.525*
Monsoon Season	8.16	2.46	30.07	0.523
Post-monsoon Season	20.05	6.82	34.01	0.41
Annual	31.44	2.96	9.43	0.1757

* significant at 0.10 level

139.4.2 Seasonal Trends

On an average, SCA in winter was 54%, and in monsoon, 8% (Table 139.1). This difference is because monsoon is the season of abundant rain and snow and glaciers at very high altitudes continue melting during this season [10]. The variation of seasonal mean SCA was observed to be least in the monsoon season and maximum in the winter season (Table 139.1). The SCA trends shows a decline in the winter and pre-monsoon season and rise in the monsoon and post-monsoon season (Table 139.1). The trend in the pre-monsoon SCA was statistically significant at the 90% level of confidence.

139.4.3 MONTHLY TRENDS

The monthly trend analysis in the snow cover area shows an increasing trend from September to December and decreasing trend from January to August (except July that shows increasing trend) during the period 2000–2010. The trend was only significant in April and July (Table 139.1). The variation in the SCA may be attributed to changes in the air temperature and form of precipitation as these two determine the rate of snow accumulation and ablation.

139.5 CORRELATION BETWEEN SCA AND AIR TEMPERATURE

Correlation shows negative correlation of SCA with mean minimum, mean maximum and mean air temperature in all the seasons. Annual, seasonal and monthly trend analysis shows higher variability in the mean minimum air temperature at Manali and mean maximum air temperature at Bhuntar during 1980–2010. Overall, a warming trend is observed in the upper Beas river basin [11]. On the basis of correlation analysis, it can be inferred that warming trend during the pre-monsoon season would decrease snow cover.

139.6 CONCLUSIONS

High intra-seasonal variability has been observed in the SCA of the upper Beas river basin during 2000–2010. Correlation analysis indicates that the warming trend during the pre-monsoon season would decrease snow cover area in the basin. There is need of detailed study of the influence of climate variability on the SCA of the study area with more data of climate variables particularly snowfall as snow has direct effect on the SCA changes.

REFERENCES

1. IPCC: Climate Change 2007: Impacts, Adaptation and Vulnerability. Contribution of Working Group II to the Fourth Assessment Report of the Intergovernmental Panel on Climate Change, M.L. Parry, O.F. Canziani, J.P. Palutikof, P.J. van der Linden and C.E. Hanson, Eds., Cambridge University Press, Cambridge, UK (2007)
2. IPCC: Climate Change 2013: The Physical Science Basis: Contribution of Working Group I to the Fifth Assessment Report of the Intergovernmental Panel on Climate Change (IPCC), Cambridge University Press, Cambridge, UK (2013)
3. IPCC: Climate Change 1995: The IPCC Scientific Assessment. Contribution of Working Group I To Second Assessment Report of Intergovernmental Panel on Climate Change (IPCC). Cambridge University Press, Cambridge, UK (1996)
4. Gupta, R., Duggal, A., Rao, S., Sankar, G. and Singhal, B.: Snow cover area vs. snowmelt runoff relation and its dependence on geomorphology- a study from the Beas catchment (Himalayas, India). *J Hydrol (Amst)*. 58, 325–339 (1982)
5. Jain, S., Rathore, D. and Chaudhry, A.: Snow Cover Estimation in Himalayan Basins using Remote Sensing. A Report by the National Institute of Hydrology, Roorkee (2001)
6. Kulkarni, A., Mathur, P., Rathore, B., Alex, S., Thakur, N. and Kumar, M.: Effect of global warming on snow ablation pattern in Himalaya. *Curr Sci*. 83(2), 120–123 (2002)
7. Kulkarni, A.: Monitoring Himalayan Cryosphere using remote sensing techniques. *Journal of the Indian Institute of Science*. 90(4), 457–469 (2010)
8. Gurung, D., Kulkarni, A., Giriraj, A., Aung, K., Shrestha, B. and Srinivasan, J.: Changes in seasonal snow cover in Hindu Kush-Himalayan region. *The Cryosphere Discuss.* 5, 755–777 (2011)

9. Hall, D., Riggs, G. and Salomonson, V.: Development of methods for mapping global snow cover using moderate resolution imaging spectrometer (MODIS) data. *Remote Sens. Environ.* 4, 127–140 (1995)
10. Jain, S., Goswami, A. and Saraf, A.: Role of Elevation and Aspect in Snow Distribution in Western Himalaya. *Water Resour. Manage.* 23, 71–83 (2009)
11. Rani, S.: Assessment of the influence of Climate variability on the snow cover area of the upper Beas river basin. Unpublished M.Phil. Dissertation, CSRD, JNU (2014)

Chapter 140

Stream Flow Changes and Glacier Recession in the Upper Indus Basin

Nahida Ali and Shakil A. Romshoo

Abstract Trend analysis for 8 stations of Lidder watershed was performed using 3 Non-parametric and 2 parametric tests. It was found that upstream and downstream stations didn't showed much variation except one downstream station i.e Ader station which showed significant decreasing trend for spring, winter and Autumn season. It was observed during last 40 years, the glacier area in the basin has decreased from 45.82 km² in 1969 to 38.98 km² in 2010. Differential response has been observed between the upstream downstream region streamflow of the River. The insignificant decreasing trends in the downstream of the Lidder and the increasing observed trends of discharge at Ader discharge stations downstream could be primarily attributed to the Karst topography of the region.

Keywords Parametric • Non-parametric • Krast • Cryosphere

140.1 INTRODUCTION

Himalayan rivers are key source of fresh water to more than one billion people [1]. They support one of the most heavily irrigated regions in the world in the northern India [2]. The much controversial statements [3] about rapid retreat and disappearance of Himalayan glaciers and consequent drastic reduction in downstream river flows has created vigorous debate on changes in glacier mass balance [4, 5] and river flow, and the nature and role of climate trends and variability [6, 7]. In this research upstream and downstream variation in streamflow were determined and tried to understand this variability in term of seasonal, monthly and annual. Impact of changes in Glacier area which are one of the important sources of streamflow in the Lidder watershed was also determined to make better understanding of the upstream and downstream streamflow variation.

N. Ali (✉) • S.A. Romshoo

Department of Earth Sciences, University of Kashmir, Srinagar, Jammu and Kashmir, India

e-mail: geonahida@gmail.com

140.2 STUDY AREA

The study was carried out in Lidder watershed in the upper Jhelum basin, a tributary of the Indus river system, located in the western Himalaya between latitudes $33^{\circ} 59'$ and $34^{\circ} 12'$ and longitude $75^{\circ} 09'$ and $75^{\circ} 23'$ and covering an area of 653 km^2 . The watershed is one of a few cathments within Jhelum basin with permanent snow, and permanent ice/glaciers occupy about 3% of the entire Lidder watershed and 6% of the upper Lidder watershed area.

140.3 MATERIAL AND METHODS

Discharge data was collected for 8 discharge stations of Lidder watershed out of which Aru, Sheshnag and Batakoot were upstream stations while Akura, Kirkadal, Gur, Ader and Khanbal tail were Downstream stations. Five statistical tests were used on discharge data from 1971–2012 time series, out of which 3 tests were Non-Parametric (Mann-Kendall, Sperman's Rho and Distribution free cusum test) and 2 were Parametric (Linear regression and Cumulative deviation). Glacier were digitized from 1969 to 2010 using On-screen digitization approach on scale of 1: 30000.

140.4 RESULTS AND DISCUSSION

140.4.1 *Streamflow Changes*

Streamflow changes were analysed for Monthly, Annual and Seasonal variation in the discharge data for 8 stations of Lidder watershed. Statistical trend test result (Table 140.1) showed that upstream stations Aru and Gur showed statistical decreasing trend for annual and seasons while Batakoot showed decreasing non-significant trend for annual and summer season. Downstream station Akura, Kirkadal and Gur showed significant decreasing trend while only Ader station showed significant increasing trend for spring, winter and autumn season; a reason for this increase could be the Krast topography of that area. Khanbal tail showed increasing trend but non-significant.

140.4.2 *Glacier Area Change*

During the last 40 years, the glacier area in the basin has decreased from 45.82 km^2 in 1969 to 38.98 km^2 in 2010. Kolahoi, the biggest glacier in the basin has shrunk

Table 140.1 Summary statistics of significant values for eight stations of Lidder watershed

Station	Statistical test name	Annual	Winter	Spring	Summer	Autumn
Aru	Mann-Kendall	S (0.01)	S (0.01)	S (0.01)	S (0.01)	S (0.01)
	Spearman's Rho	S (0.01)	S (0.01)	S (0.01)	S (0.01)	S (0.01)
	Linear regression	S (0.01)	S (0.01)	S (0.01)	S (0.01)	S (0.01)
	Cusum	S (0.01)	S (0.01)	S (0.05)	S (0.1)	S (0.1)
	Cumulative deviation	S (0.01)	S (0.01)	S (0.01)	S (0.01)	S (0.05)
Sheshnag	Mann-Kendall	S (0.01)	S (0.01)	S (0.01)	S (0.05)	S (0.01)
	Spearman's Rho	S (0.01)	S (0.01)	S (0.1)	S (0.1)	S (0.05)
	Linear regression	S (0.01)	S (0.01)	S (0.01)	S (0.05)	S (0.01)
	Cusum	S (0.01)	S (0.01)	S (0.01)	S (0.01)	S (0.01)
	Cumulative deviation	S (0.01)	S (0.01)	S (0.01)	S (0.01)	S (0.01)
Batakoot	Mann-Kendall	NS	S (0.01)	S (0.1)	NS	S (0.05)
	Spearman's Rho	NS	S (0.01)	S (0.1)	NS	S (0.05)
	Linear regression	NS	NS	NS	NS	S (0.05)
	Cusum	NS	S (0.01)	NS	NS	S (0.01)
	Cumulative deviation	S (0.05)	S (0.01)	NS	NS	S (0.01)
Akura	Mann-Kendall	S (0.01)	S (0.01)	S (0.05)	S (0.01)	S (0.01)
	Spearman's Rho	S (0.01)	S (0.01)	S (0.1)	S (0.01)	S (0.05)
	Linear regression	S (0.01)	S (0.01)	S (0.05)	S (0.01)	S (0.05)
	Cusum	S (0.05)	S (0.01)	NS	S (0.01)	S (0.01)
	Cumulative deviation	S (0.01)	S (0.01)	S (0.05)	S (0.01)	S (0.05)
Kirkadal	Mann-Kendall	NS	S (0.01)	S (0.01)	S (0.01)	NS
	Spearman's Rho	NS	S (0.01)	S (0.01)	S (0.01)	NS
	Linear regression	NS	S (0.01)	S (0.01)	S (0.05)	NS
	Cusum	NS	S (0.05)	S (0.01)	S (0.01)	NS
	Cumulative deviation	NS	S (0.01)	S (0.01)	S (0.01)	NS
Gur	Mann-Kendall	S (0.01)	NS	S (0.05)	S (0.01)	NS
	Spearman's Rho	S (0.01)	NS	S (0.1)	S (0.01)	NS
	Linear regression	S (0.01)	NS	S (0.05)	S (0.01)	NS
	Cusum	S (0.01)	NS	NS	S (0.01)	S (0.1)
	Cumulative deviation	S (0.01)	NS	NS	S (0.01)	S (0.1)
Ader	Mann-Kendall	NS	NS	S (0.1)	NS	NS
	Spearman's Rho	NS	S (0.1)	S (0.1)	NS	S (0.1)
	Linear regression	NS	S (0.05)	S (0.05)	NS	S (0.05)
	Cusum	NS	NS	NS	NS	NS
	Cumulative deviation	NS	S (0.1)	S (0.05)	NS	S (0.1)
Khanbal tail	Mann-Kendall	NS	NS	NS	NS	NS
	Spearman's Rho	NS	NS	NS	NS	NS
	Linear regression	NS	NS	NS	NS	NS
	Cusum	NS	NS	NS	S (0.05)	NS
	Cumulative deviation	NS	NS	NS	NS	NS

from 14.27 km² in 1969 to 12.00 km² in 2010. As a result of the shrinking cryosphere in the basin, the stream discharge, comprising predominantly of snow and glacier-melt, is showing declining trend despite the melting of these glaciers.

140.5 CONCLUSIONS

The insignificant decreasing trends in the downstream of the Lidder and the increasing observed trends of discharge at Ader discharge stations downstream could be primarily attributed to the Karst topography of the region which allows recharge of the springs from the precipitation and increased melting of the snow and ice-melt in the glaciated areas. These surface-ground water interactions in this karst region and the emergence of these springs in the vicinity of these measuring station is a major factor responsible for the different streamflow trends observed downstream. The understanding of the interplay of the observed glacial recession, streamflow changes and the surface-groundwater interactions is imperative for knowing the variability of the streamflow in the upstream and downstream of the Indus basin under similar meteorology.

REFERENCES

1. Ives, J.D. and B. Messerli: The Himalayan Dilemma: Reconciling Development and Conservation. John Wiley, London, doi:[10.4324/9780203169193](https://doi.org/10.4324/9780203169193) (1989)
2. Tiwari, V.M., J. Wahr and S. Swenson: Dwindling groundwater resources in the northern India, from satellite gravity observations. *Geophys. Res. Lett.* 36, L18401, doi: [10.1029/2009GL039401](https://doi.org/10.1029/2009GL039401) (2009)
3. IPCC: Clim. Change: Impacts, Adaptation and Vulnerability. Contribution of Working Group II to the Fourth Assessment Report of the Intergovernmental Panel on Clim. Change, edited by M.L. Parry et al., 976 pp. Cambridge University Press, Cambridge (2007)
4. Berthier, E., Arnaud, Y., Kumar, R., Ahmad, S., Wagnon, P. and Chevallier, P.: Remote sensing estimates of the glacier mass balances in the Himachal Pradesh (Western Himalaya, India). *Remote Sens. Environ.*, 108, 1327–1338. (2007)
5. Eriksson, M., Jianchu, X., Sheresthe, A.B., Vaidya, R.A., Nepal, S. and Sandstorm, K.: The Changing Himalayas: Impact of Climate Change on Water Resources and Livelihoods in the Greater Himalayas, ICIMOD, Kathmandu (2009)
6. Immerzeel, W.W., Droogers, P., de Jong, S.M. and Bierkens, M.F.P.: Large scale monitoring of the snow cover and run off simulation in Himalayan river basin using remote sensing. *Remote Sens. Environ.*, 113, 40–49 (2009)
7. Bookhagen, B. and Burbank, D.W.: Towards a complete Himalayan Hydrological Budget: Spatiotemporal distribution of snow melt and rainfall and their impact on river discharge. *J. Geophys. Res.*, 115, F03019, doi: [10.1029/2009JF001426](https://doi.org/10.1029/2009JF001426). (2010)

Chapter 141

Hydrological Modeling and Streamflow Characterization of Gangotri Glacier

Manohar Arora, Rakesh Kumar, Naresh Kumar, and Jatin Malhotra

Abstract High mountain basins provide high specific discharges to headwaters of major continental rivers. Glacierised catchments show a discharge regime that is strongly influenced by snow and glacier melt waters. Many of the major rivers in India originate from the Himalayas. These rivers have significant contribution from snow and ice which makes these rivers perennial. Himalayan region has high concentrations of mountain glaciers. Large extent of this region is covered by seasonal snow during winter. Runoff generates from melting of these snow and glaciers is one of the important sources of water for the Himalayan rivers. Glaciers and snowfields are distributed throughout the Himalayas and form a source of numerous streams. Considering this aspects, in this study a snowmelt runoff simulation model SNOWMOD suitable for Himalayan basins developed earlier has been modified and applied for simulation of flows from the Gangotri Glacier, the headwaters of River Bhagirathi in the Uttarakhand Himalayas. The flow data for the year 2010 has been considered for calibrating the model whereas the year 2011 and 2012 have been considered for validating the model for simulating the daily flows. The efficiency of the model has been computed based on the daily simulated and observed flow values for three years. The values of the model efficiencies are 86%, 87% and 90% respectively for the years 2010, 2011 and 2012.

Keywords Himalayas • Runoff • Glaciers • Modeling • Calibration • Validation

141.1 INTRODUCTION

In the Himalayan streams 40–70% water is contributed by the snow and glacier melt [1, 5, 6] and this happens during the summer session when water requirement is more. On one hand multi-purpose projects are being planned over the Himalayan rivers, on the other hand climate change studies indicate the loss of glaciers area over the few decades [4, 3, 2]. This emphasizes the need of more reliable estimations of snow/glaciers runoff. However, till now snow hydrology studies carried out

M. Arora (✉) • R. Kumar • N. Kumar • J. Malhotra
National Institute of Hydrology, Roorkee, India
e-mail: arora@nih.ernet.in

in India are few and not up to the mark. Most of the models applied to the Indian Himalayas are index based models. These models require hydrological parameters like lapse rate melt factor, snow cover, critical temperatures and runoff coefficients. Most of the studies derive these parameters by calibration procedure that too based on a few months to a few years. This may be due to insufficient collection of data, mainly snow cover information and hydro-meteorological data at higher altitudes due to highly variable terrain. Hence, it is necessary to develop a suitable methodology and models for estimation and forecasting snowmelt/glacier melt runoff for the Himalayan region including accurate estimation of snow cover and model parameters. The primary object of this paper is to apply SNOWMOD snow melt runoff model and study the characteristics of streamflow.

141.2 STUDY AREA

The proglacial melt water stream, known as Bhagirathi River, emerges out from the snout of the Gangotri Glacier at an elevation of 4000 m. The snout of the Gangotri Glacier is known as “Gomukh”. The Gangotri Glacier system most commonly known as Gangotri Glacier, is a cluster of many glaciers comprising main Gangotri Glacier (length: 30.20 km; width: 0.20 to 2.35 km; area: 86.32 km²) as trunk part of the system. The flow data was collected from field observations near the snout of the glacier at Bhujbas. Location of study area is shown in Fig. 141.1.

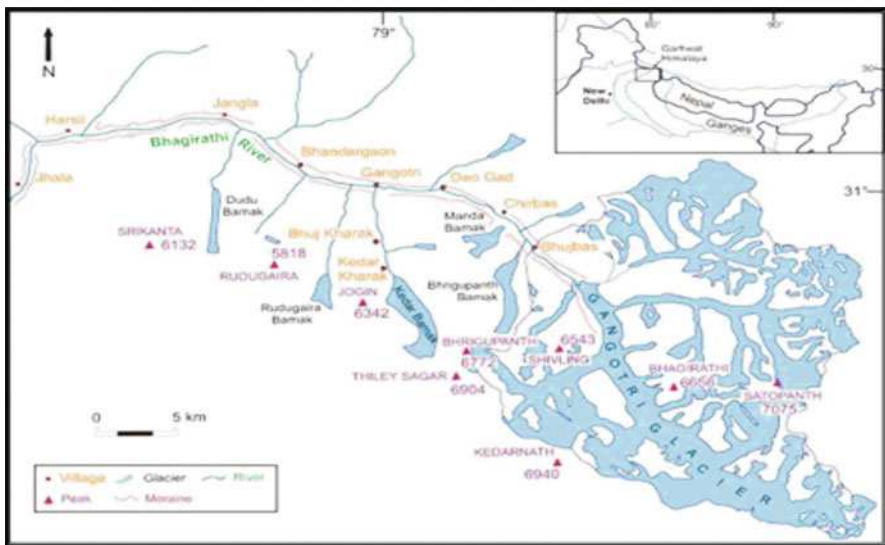


Fig. 141.1 Location of the study area

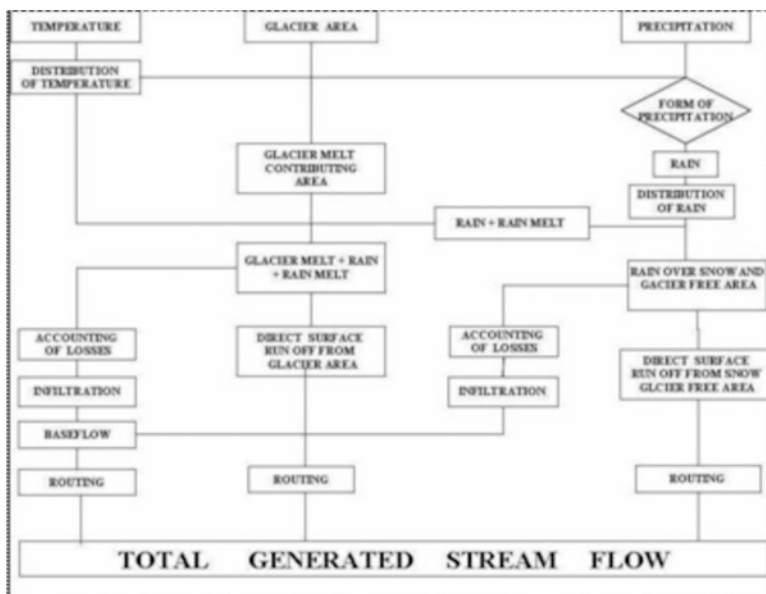
141.3 METHODOLOGY

The process of generation of streamflow from such basins involves primarily the determination of the input derived from the melt and rain, and its transformation into runoff. For simulating the streamflow, the basin is divided into a number of elevation zones and various hydrologic processes relevant to the melt and rainfall runoff are evaluated for each zone. The model deals with melt and rainfall runoff by performing the following three operations at each time step:

- (i) extrapolate available meteorological data to the different elevation zones,
- (ii) calculate rates of melt and/or rainfall at different points, and
- (iii) integrate melt runoff from snow and glacier covered area (SCA) and rainfall runoff from snow free area (SFA), and route these components separately with proper accounting of baseflow to the outlet of the basin. The model optimises the parameters used in routing of the melt runoff and rainfall runoff.

Input to the model such as glacier cover, permanent snow cover, and seasonal snow cover generated through remote sensing techniques were used in conjunction with daily maximum and minimum temperature, rainfall and discharge. The information on SCA can be easily obtained from the satellite imageries/digital data. These days there are a number of satellites available and provide SCA data with a reasonably high frequency. SCA for each elevation zone was plotted against the elapsed time to construct the depletion curves for the various elevation zones in the basin. In order to simulate daily runoff, daily SCA for each zone is required as input to the model. Daily values of SCA can be obtained by interpolating/extrapolating the derived depletion curves. It is to be pointed out that the depletion of snow covered area is controlled by the accumulated snow during preceding winter and patterns of the temperature during the melt period. Because amount of snowfall/snow covered area and temperature conditions fluctuate from year to year, snow covered area and depletion trends also vary from year to year. A seasonal snow cover will disappear at a faster rate during warmer climatic conditions, while it will follow slow depletion under a colder temperature regime. The amount of melt water produced from each altitude zone indicates the total amount of solid precipitation in that zone. However, in the present study, differentiations in melting from SCA and glaciated area were not considered because information on SCA is not available and it was not included in the budget of the project. Glaciated area in each elevation zone was determined using toposheets and satellite data. For the computations of snow melt, normal range of degree day factor varies between 1 to 4. It depends upon the exposure of the main body of the glaciers. Since Gangotri Glacier is debris covered glacier, higher values of degree day factor can be used for the computation of glacier melt. The different values of the degree day factors are used in the model for each month of the ablation season. These values are determined through the calibration of the model. These values are kept the same during the simulation of flows for different years. The flow data are generated for three times in a day utilizing the measurements of velocity, gauge and river cross sections using the

velocity area method. Subsequently daily flow values are computed taking the average of the three flow values. The daily flow values have been computerized and processed before considering the modeling. The daily maximum and minimum temperature monitored at the site have been computerized and preliminary processing has been carried out for the consistency and the reasonable accuracy of the measurement. Subsequently the daily mean temperature has been computed for the ablation season of each year by averaging the values of daily maximum and minimum temperature. The structure of the SNOWMOD model is presented in the following flowchart.



In order to divide the study basin in different elevation zones, Digital Elevation Model (DEM) has been prepared using the ILWIS GIS package. The study basin has been divided in nine elevation zones considering the different ranges of the elevations.

141.4 RESULTS AND ANALYSIS

The flow data for the year 2010 has been considered for calibrating the model whereas the year 2011 and 2012 have been considered for validating the model for simulating the daily flows. The DEM of the basin was prepared and the area under each elevation zone was determined. Table 141.1 represents the area under each elevation zone. The snow and glaciated area in each elevation was also determined.

Table 141.1 Area in each elevation band of the basin

Elevation zone	Elevation range (m)	Area of different zones (km ²)
1	>3800	0.40
2	3800-4200	8.84
3	4200-4600	31.93
4	4600-5000	90.65
5	5000-5400	122.72
6	5400-5800	141.45
7	5800-6200	109.60
8	6200-6600	43.92
9	6600-7000	5.98

Fig. 141.2 Comparison of observed and simulated discharge for the calibration year 2010

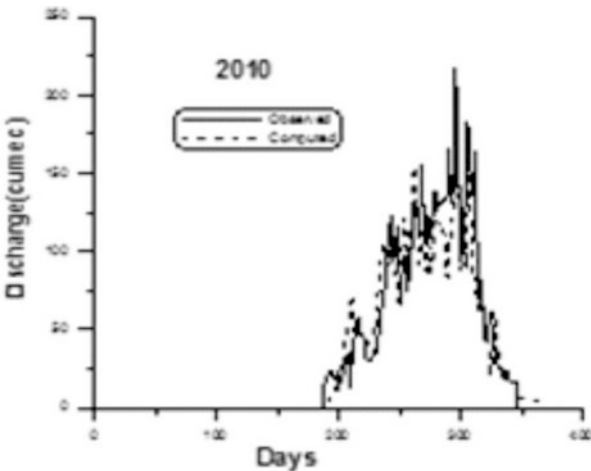


Figure 141.2 shows the comparison of observed and simulated hydrograph for the calibration period. After calibration the parameters were fixed and the model was run on the observed flow data for the validation period. Figure 141.3 (a & b) shows the comparison of the observed and simulated hydrograph for the validation period. The efficiency of the model has been computed based on the daily simulated and observed flow values for three years. The values of the model efficiencies are 86%, 87% and 90% respectively for the years 2010, 2011 and 2012. The performance of the model in preserving the runoff volume of entire ablation season has been tested based on the criteria computed as percentage difference in observed and simulated runoff (D_v) during the ablation season. Their values computed for the year 2010, 2011 and 2012 are 6.01%, 7.61% and -1.29% respectively. It is observed that the total snowmelt contribution in the streamflow is about 85%. The total rainfall contribution is about 4% and the sub surface flow contribution is 11% of the total streamflow.

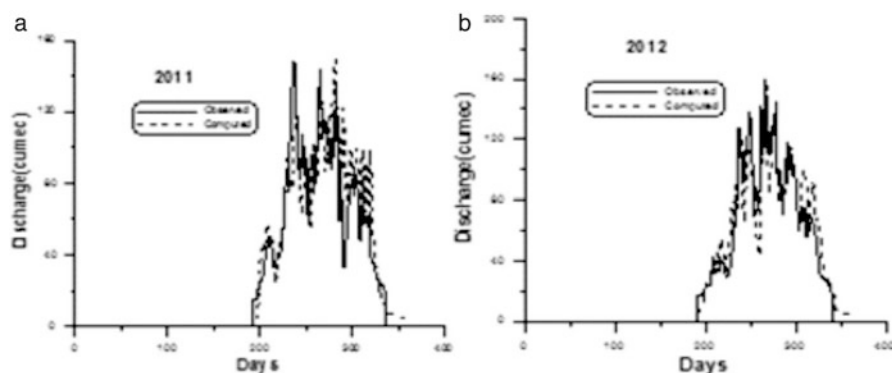


Fig. 141.3 (a). Comparison of observed and simulated discharge for the validation year 2011. 3 (b). Comparison of observed and simulated discharge for the validation year 2012

141.5 CONCLUSION

The results obtain form the SNOWMOD are satisfactory. In SNOWMOD runoff measured after integration of glacier melt runoff and rainfall generated runoff from glacier free area, and route these components separately with proper accounting of base flow to the outlet of the basin. As calibration has been done based only 1 year data, the accuracy of calibrated parameters is limited. It is observed that the total snowmelt contribution in the streamflow is about 85%. The total rainfall contribution is about 4% and the sub surface flow contribution is 11% of the total streamflow. It has been observed that the glaciers in the Bhagirathi river basin are substantially covered with debris compared to the other glaciers and snow regions. This affects the process of glacier melting, which ultimately affects the discharge. For future studies, other river basins may be considered for testing the applicability of the models in the Himalayan region. The debris cover on the glaciers and intermittent snowfall in the melting season need to be considered to improve the models.

REFERENCES

1. Arora, M., Rathore, D.S., Singh, R.D., Kumar, R. and Kumar, A.: Estimation of melt contribution to total stream flow in river Bhagirathi and river Dhauri Ganga to Loharinag Pala and Tapovan Vishnugad project sites. *J. Water Resource and Protection*, 636–643 (2010)
2. Bergström, S.: Development and application of a conceptual runoff model for Scandinavian catchments. Bulletin Series A No 52, Department of Water Resources Engineering, Lund Institute of Technology, 134 (1976)

3. Central Water Commission and National Institute of Hydrology: Preliminary consolidated report on effect of climate change on water resources. Ministry of water resources, Government of India (2008)
4. Marshall, S.J., White, E.C., Demuth, M.N., Bolch, T., Wheate, R., Menounos, B., Beedle, M.J. and Shea, J.M.: Glacier Water Resources on the Eastern Slopes of the Canadian Rocky Mountains. *Canadian Water Resources Journal* (Taylor & Francis), 109–134 (2011)
5. Singh, P., Jain, S.K. and Kumar, N.: Estimation of snow and glacier melt runoff contribution to the Chenab river, Western Himalaya. *Mountain Research Development*, 17(1), 49–56 (1997)
6. Singh, P., Haritashya, U.K. and Kumar, N.: Modelling and estimation of different components of stream flow for Gangotri Glacier basin, Himalayas. *Hydrological Sciences Journal*, 55(2), 309–322 (2008)

Chapter 142

Abundance of *Cycladophora davisiana* Used as an Indicator for Paleoenvironment of Kerguelen Plateau, Southern Ocean Region

Girish Kumar Sharma and Sheetal Kanojia

Abstract The ODP Site 738B Leg 119 is located on the base of southern slope of Kerguelen Plateau. Twenty nine samples from two sections viz., 1H1-1H2 were used to carry out the present study. The polycystine radiolaria *Cycladophora davisiana* Ehrenberg first appears in upper Pliocene sediments in North Pacific at approximately 2.7 Ma. Peaks and curves of *C. davisiana* abundance are used as stratigraphic and Paleooceanographic markers indicating glacial period during the Quaternary and over the last 425 Kys. The two zones were established viz. Omega and Psi and which are equivalent to NR1 and NR2 of upper Quaternary. On the basis of abundances, *C. davisiana* having one peak in omega while eight in the Psi zone. Further, it is interpreted that in the Psi zone more cooling or glacial periods were present compared to Omega.

Keywords Quaternary paleoenvironment • *Cycladophora davisiana* • Southern ocean region

142.1 INTRODUCTION

The study area lies in the southern part of Kerguelen Plateau at latitude 62°42.54'S and longitude 82°47.25'E (Fig. 142.1). The identified species shows well preserved Antarctic assemblage collected at a water depth of 2252.5 mbsf. Twenty-nine samples from two sections (1H1-1H2) were used for this study. The total length of studied samples is 2,850 m (Figure 142.2). The Leg 119 site 738B consists of nanofossil ooze, calcareous chalk and limestone. They began the study on radiolarian bearing sediments in the Southern Ocean and described twenty species from the Antarctic sector of the Indian Ocean. They reported some species of radiolaria from Indian Ocean sector of Antarctica. They studied the radiolaria from the

G.K. Sharma (✉) • S. Kanojia

Department of Geology, Kumaun University, Nainital, India

e-mail: gksharma61@yahoo.com

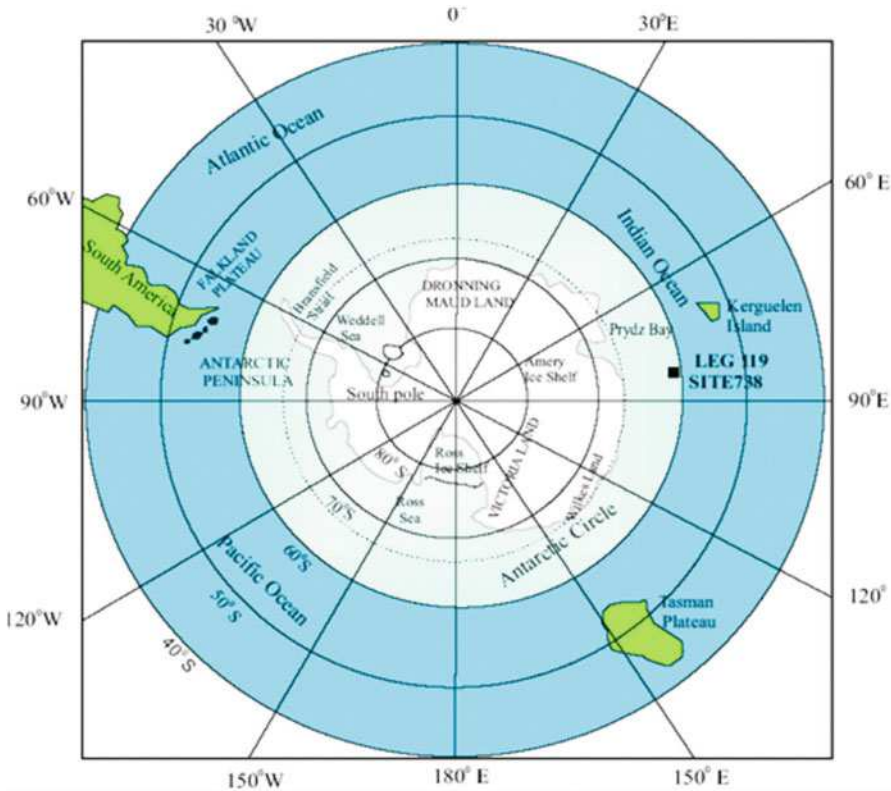


Fig. 142.1 The position of study area of Leg 119 Site 738 B

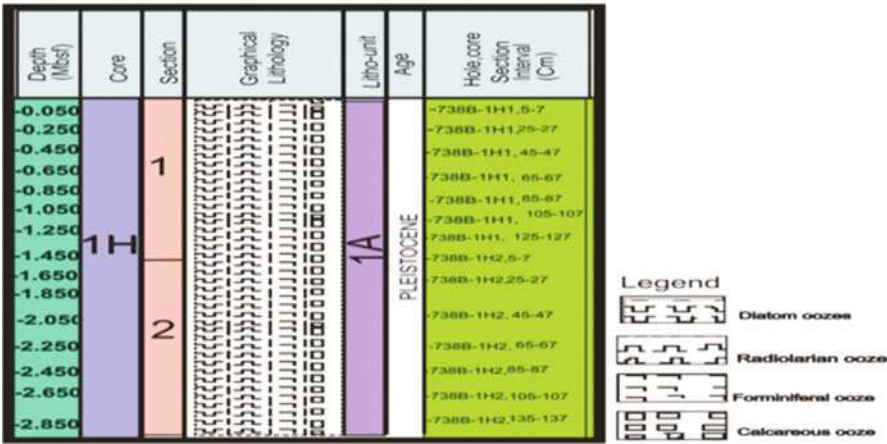


Fig. 142.2 Age, position of the samples, lithostratigraphic succession and depth of leg 119 sites 738B

Wilhelm II Coast of Antarctica and Kerguelen Island and worked on the B.A.N.Z. Antarctic Research Expedition and collected sediment samples to carry out detail study on radiolaria. They described Antarctic radiolarian species from the Super family Liosphaericae and established Neogene radiolarian biostratigraphy along with illustrations and descriptions of important taxa. They carried out the detailed study on Antarctic Neogene radiolarian biostratigraphy and proposed radiolarian biostratigraphy of late Tertiary Antarctic Seas of the Southern Ocean Region. They marked radiolarian zones of Quaternary and Upper Tertiary deposits of middle Asia. They worked on biostratigraphy and paleoclimate of the Antarctic region and established Pliocene-Pleistocene radiolarian biostratigraphy and paleoclimatic history from the samples collected near the Antarctic and subtropical convergence of the Southern Ocean region. They studied the bottom sediments of the Bellingshausen Basin in the Antarctic Sea and established Neogene biostratigraphy of Falkland Plateau and Weddell Sea. They did the study on radiolarian biostratigraphy and magnetostratigraphy of siliceous microfossils from Antarctic sediments and identified two new genera and seventeen new species from the Neogene sediments of the Kerguelen plateau and carried out work on the biochronology and magnetostratigraphy of the Antarctic sediments. Established radiolarian from Eocene to Recent biostratigraphy, biogeography, diversity, and history of Southern Ocean and carried out detail study on Neogene radiolaria from ODP Legs 119 and 120. Work on sections of ODP Site 745 in the Kerguelen Plateau and placed the last occurrence datum of *Stylatractus universus*. Reported Antarctic Neogene radiolaria from ODP Leg 119 and described environmental control of radiolarian diversity, evolutionary rates and taxa longevities. They identified and described 83 radiolarian taxa and established two Pleistocene zones of Tasman region. Work on radiolarian assemblage proxies for productivity in the 0 - 6 Ma on DSDP Site 532, ODP Site 1084 and carried out the work on radiolarian paleoproductivity.

142.2 METHODOLOGY

Twenty nine samples from two sections (1H1-1H2) of leg 119 site 738B were used to carry out the present study. Sediment samples of about 3-4g were disaggregated in dilute Hydrogen peroxide (H_2O_2) for 1-2 hour followed by heating to just below the boiling point. One teaspoonful of Calgon (Hexametaphosphate) was added to further boil and disaggregate the sediment samples for 1-2 hours and complete the treatment. The samples were sieved through a 63 micron mesh sieve and dried. The strewn slides were prepared by using an eye dropper and Canada balsam as a mounting medium. Generally, minimum 2-3 slides (of cover slip size 22:22mm) were examined for taxonomic and stratigraphic work, depending on their abundance i.e. generally between 950-1000 individual radiolarians.

142.3 OBSERVATIONS

It is observed that the two sections (1H1-1H2) of Leg 119 Site 738B of Southern Ocean region having the typical Antarctic assemblage. On the basis of appearance, disappearance and abundance of taxa, viz. Omega and Psi zones are established. On the basis of abundance of *Cycladophora davisiana* {Plate 142.I}, one peak is

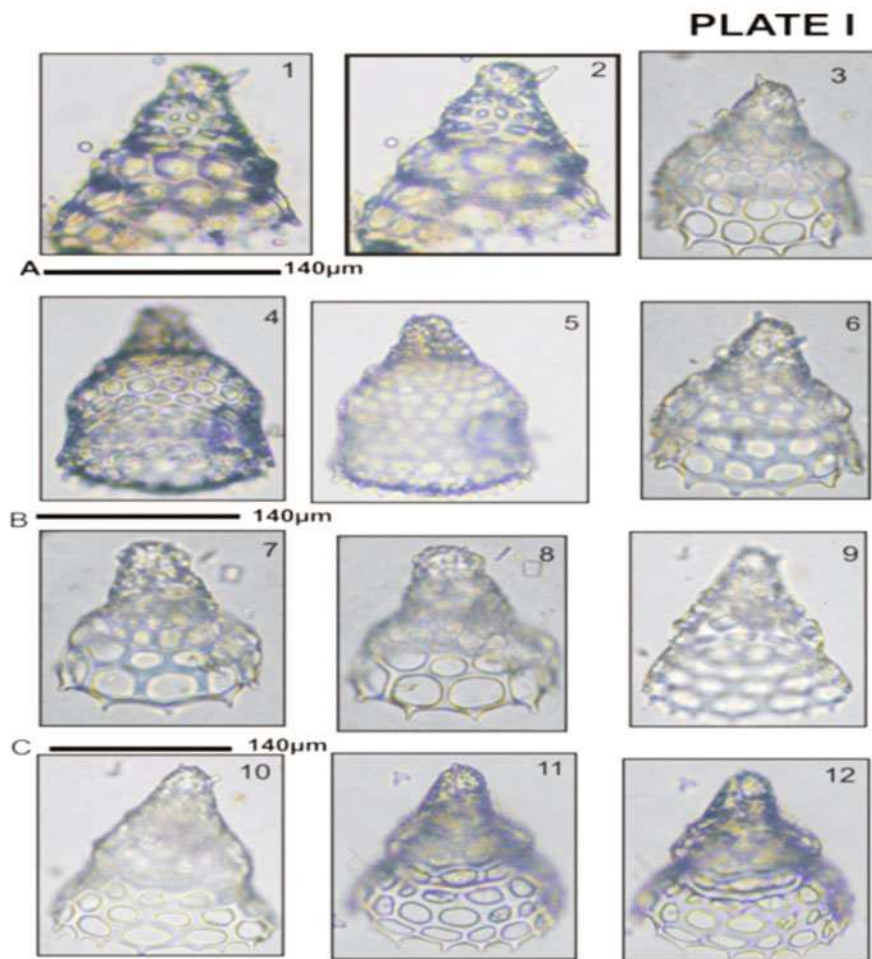


Plate 142.I *Cycladophora davisiana* Ehrenberg. Figs 1, 2: Focused on inner pore and outer pores of shell Sample 738B-1H1, 5-7 cm; scale bar A. Figs 3, 6: Focused on inner and outer shell sample 738B-1H2, 55-57 cm; scale bar A. Figs 4, 5: Focused on inner shell and outer shell sample 738 B-1H1, 35-37 cm; scale bar B. Figs 7, 8: Focused on inner and outer shell sample 738 B-1H2, 15-17 cm; scale bar C. Figs 9, 10: Focused on inner and outer shell respectively sample 738B-1H2, 115-117 cm; scale bar C. Figs 11, 12: Focused on inner and outer shell sample 738B-1H2, 135-137 cm; scale bar C

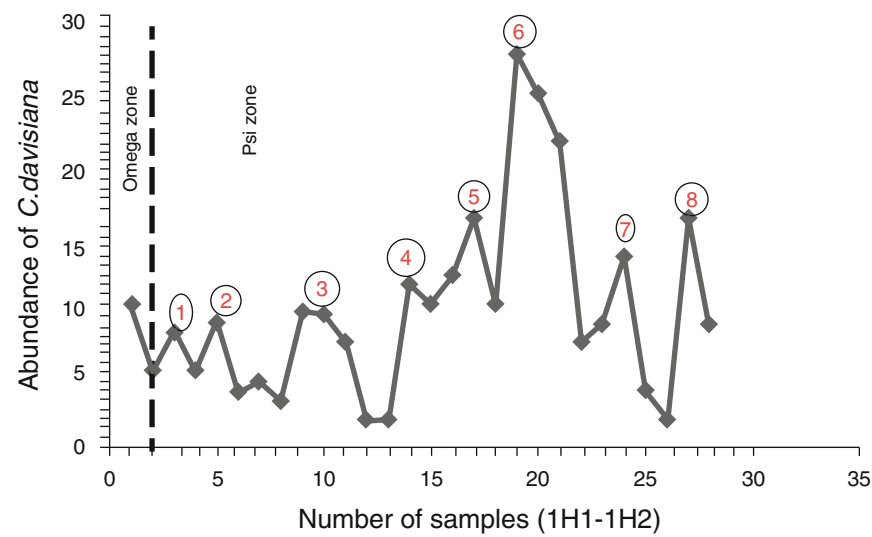


Fig. 142.3 Relative abundance peaks of *Cycladophora davisiana* in Leg 119 Site 738B section (1H1-1H2)

observed in the Omega zone while eight peaks in the Psi zone (Fig. 142.3). It is interpreted that during uppermost part of Pleistocene in Omega zone, the glacial periods were ceased while in the Psi zone the glacial cycles were active. It means that between 0.8~0.4 Ma the active glaciations was going on.

Chapter 143

Conservation Agriculture – A New Paradigm for Climate Change Mitigation in Rainfed Indian Agriculture

G. Pratibha, G.R. Korwar, I. Srinivas, K.V. Rao, B.M.K. Raju, M. Maheswari, A.K. Indoria, K. Srinivasa Rao, D.K. Choudhary, and B. Rama Devi

Abstract A field experiment was carried out in rainfed semi-arid tropics of India to develop sustainable conservation agriculture (CA) practices as an alternative to conventional agriculture practices to increase yields, soil fertility in pigeon pea – castor cropping system. But this may offset the benefits by increasing greenhouse gas (GHG) emissions; hence the GHG emissions were monitored. A replicated trial was laid out in split plot design with three tillage practices viz., conventional tillage (CT), reduced tillage (RT) and zero tillage (ZT) and three anchored residue height (0 cm, 10 cm and 30 cm). The pooled analysis of data showed that seed yield and biological yield are influenced by tillage practices and anchored residue height. ZT recorded significantly lower yields (seed and biological yield) in both crop (pigeonpea and castor) compared to conventional and reduced tillage. In general, with increase in anchored residue height seed yield increased. CT recorded the higher harvest index as compared to the ZT. A higher CO₂ emission was recorded in ZT whereas the N₂O emission was lower and no significant difference was observed in methane oxidation between tillage practices.

Keywords Conservation agriculture • Biological yield • GHG emission • Climate change mitigation

143.1 INTRODUCTION

Improved crop productivity achieved with intensive tillage, increased use of fertilizers, improved crop protection practices and burning of crop residues to meet the needs of growing population is a major driver to resource degradation and climate change. The IPCC report on climate change [1] indicates that agriculture

G. Pratibha (✉) • G.R. Korwar • I. Srinivas • K.V. Rao • B.M.K. Raju • M. Maheswari • A.K. Indoria • K.S. Rao • D.K. Choudhary • B. Devi
Central Research Institute for Dryland Agriculture, Santosh Nagar, Hyderabad, India
e-mail: pratibhaagro65@gmail.com

contributes 13.5% of the annual greenhouse gas (GHG) emissions due to human activities in 2004. Scenario studies suggested that it is technically feasible to stabilize greenhouse gas concentrations in the atmosphere at current levels, provided a range of mitigation technologies are developed and implemented. Agriculture is one of the important sectors, having substantial mitigation potential with high cost competitiveness than other sectors viz., energy, transportation and forestry. Hence, the major challenge for agriculture in 21st century is to enhance the productivity by efficient use of natural resources with minimal impact on the resources and environment in general and rainfed agriculture in particular as these regions contribute 44% of total crop production and moreover it is uncertain in these regions due to aberrant weather conditions, degraded soil with low soil fertility and water holding capacity. Hence this may be a tall order for the agricultural scientists and farmers but this is possible by the use of sustainable management practices like conservation agriculture. Conservation agriculture with three agronomic principles like significant reduction of soil tillage, a permanent soil cover through crop residues and increased biodiversity through diversification of crop rotations and/or intercropping is an alternative strategy to the conventional agricultural practices for climate change mitigation by increasing carbon sequestration and reducing the greenhouse gas emissions in rainfed regions. However there are some key constraints like appropriate implement to sow the crop in residues, sparing of crop residues due to competing demands of residues for fodder and fuel wood, etc. for adoption of CA [2]. Moreover several studies were conducted on conservation agriculture (CA) in irrigated rice - wheat system but such studies are lacking in rainfed regions of India. Keeping the constraints in view a study was conducted to develop a holistic sustainable CA practices and its potential role in mitigation of GHG emission in pigeonpea – castor cropping system.

143.2 MATERIAL AND METHODS

143.2.1 Cropping Systems and Treatments

Field experiments were initiated in 2009 at Hayathnagar Research Farm (HRF) of the Central Research Institute for Dryland Agriculture (CRIDA), Hyderabad (17°23'N latitude, 78°29'E longitude, altitude 540 m above mean sea level) in the semi-arid region of southern India. Average seasonal (June- January) rainfall during the experimental period was 720 mm, which accounts for approximately 42% of annual potential evapo-transpiration. Average annual maximum and minimum temperature during experimental period was 32 °C and 20 °C respectively.

Pigeon pea (*Cajanus cajan*) – castor bean (*Ricinus communis*) annual crop rotation was followed during rainy season from 2009-10 to 2013-14. The experiment was laid out in split-plot design with three tillage system as main plot treatment and residue levels as subplot treatments in three replications. Tillage treatments were

assigned to the main plots (300 m²) which were split randomly into three sub plots (100 m²) based on the harvest height (anchored residues). The three tillage treatments include (1) Conventional tillage (CT), consists of one pass with disc plough (15–20 cm depth) in off season during May with summer showers, followed by one pass of cultivator (10 cm depth) and disc harrow after the onset of monsoon in second fortnight of June just before sowing of the crop. (2) Reduced tillage (RT) consists of one pass of cultivator followed by disc harrowing before sowing with onset of monsoon in June. (3) Zero tillage (ZT) consists direct sowing without any tillage. In all the three tillage systems, crop was sown with precision planter cum herbicide applicator developed at CRIDA. The sub plot treatments involved harvesting the crop at different heights which resulted in different heights of anchored residues i.e., harvesting at base (0 cm), above 10 cm (10 cm) and above 30 cm (30 cm) resulted in different quantities of residues. Seed, stalk, yields of pigeonpea and castor were recorded during all the experimental years.

143.2.2 Greenhouse Gas Measurement

Greenhouse gas measurements were done with insulated static vented chambers. The chamber contained an anchor and a cover as two-piece system which were made of aluminum. The anchor (15 cm tall) was inserted into the soil at a nearly leveled surface to a depth of 7.5 cm in each treatment. Measurements were made at 3-d intervals during the first 4 months after planting to measure CO₂ flux due to root and microbial respiration during active crop growth, N₂O flux due to N fertilization, and GHG fluxes (CO₂, N₂O and CH₄) due to major precipitation events. As the rate of crop growth and precipitation events declined and the effect of N fertilizer on N₂O flux diminished due to N uptake by crop, measurements were made at 7-d intervals thereafter until crop harvest. The CO₂, CH₄ and N₂O concentrations were measured in the sample using fully automated gas chromatograph (Bruker 450) equipped with TCD, FID and ECD respectively. Soil gas emission rates were calculated as the change in headspace gas concentration over time within the enclosed chamber volume and these changes in either linear or curvilinear concentration gradient over time [3]. Cumulative seasonal GHG emissions were estimated by linear interpolation of flux rates between sampling dates then summing daily rates over each growing season. The statistical analysis for seed and biological yield was carried out using procglm of SAS software version 9.2. Tukey's studentized range test (HSD) was employed to offer corrections to p- values while doing multiple comparisons.

143.3 RESULTS AND DISCUSSION

143.3.1 *Seed and Biological Yield*

The seed and biological yield in castor and pigeonpea were significantly influenced by tillage practices. The CT and RT recorded significantly higher seed yield over ZT. However the difference in the yields between tillage treatments was narrowing down over the years (Data not shown). This relative yield increase over time and transition period has been attributed to improved soil conditions with residue retention, such as organic carbon, soil enzyme activity, microbial biomass, porosity and structural stability [4]. The pooled analysis of seed, biological yield and harvest Index (HI) showed that yields in different tillage treatments, residue heights and their interaction after four years was significant. The interaction data revealed that grain and straw yield increased significantly in residues treatment under both tillage and no-tillage treatment (Table 143.1). Significantly higher seed yield was obtained in CT in pigeon pea (1191 kg/ha) and castor (2037 kg/ha) and this was on par with RT. ZT recorded 19 and 20% lower yield as compared to CT and 17 and 18% over RT in both pigeon pea and castor respectively. These results are in agreement Alvarez and Steinbach [5]. Anchored residue height of 30 and 10 cm registered highest seed yield and were on par with each other but they were statistically superior to 0 cm anchored residue. Similar increase in yield and growth with either standing or flat residues was reported by Cutforth et al. [6].

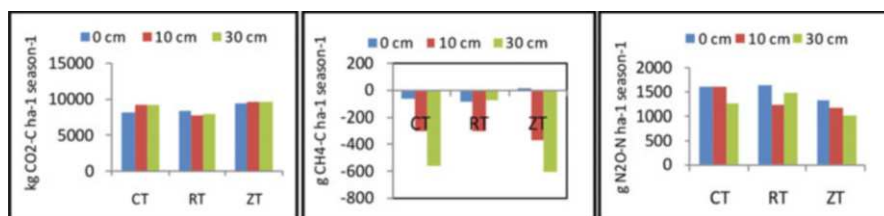
In pigeonpea no significant interaction was observed between tillage and residue heights in seed yield, but in castor significant interaction was recorded. The effect of crop residues on yield is more clearly indicated in no-till system as compared that of CT. Moreover the soils of the experimental site are alfisols and they have hard setting tendencies and low infiltration rate [7]. Hence the crop residues on the soil surface in general and minimum/zero-tillage practices in particular play an important role to sustain soil fertility, improving water use efficiency, physical conditions of soils and enhance crop productivity [8]. Similar trend was observed in both the crops in biological yield and harvest index (HI). The HI varied with tillage and anchored residue height treatments in both pigeonpea and castor. Among the tillage practices, CT recorded significantly higher HI than ZT.

143.3.2 *Seasonal Fluxes of CO₂, CH₄ and N₂O*

The present study revealed that CO₂, CH₄ and N₂O fluxes were influenced by tillage and anchored residue (Fig. 143.1). The ZT recorded 8% higher CO₂ fluxes as compared to CT and RT. This low emission in CT indicates that there was low storage of CO₂ in the soil air. Similar results were observed by Regina and Alakukku [9]. Moreover, the CO₂ measurements done after off season tillage and rainy season tillage just after ploughing was found to increase CO₂ flux

Table 143.1 Seed yield, biological yield and harvest index in different tillage and residue management practices in pigeon pea-castor system

Treatments		Pigeon pea			Castor		
Tillage	Residue heights (cm)	Seed yield (kg/ha)	Biological yield (kg/ha)	HI (%)	Seed yield (kg/ha)	Biological yield (kg/ha)	HI (%)
CT	0	1057 ^{Ab}	4655 ^{Ab}	22.7	1902 ^{Ab}	8188 ^{Ac}	23.22
	10	1265 ^{Aa}	4968 ^{Aab}	25.46	2068 ^{Aa}	8827 ^{Aa}	23.43
	30	1251 ^{Aa}	5102 ^{Aa}	24.52	2140 ^{Aa}	8904 ^{Ab}	24.04
RT	0	1061 ^{Ab}	4766 ^{Ab}	22.25	1841 ^{Ab}	7968 ^{Ac}	23.1
	10	1164 ^{Aa}	4615 ^{Bab}	25.21	2045 ^{Aa}	8821 ^{Aa}	23.18
	30	1255 ^{Aa}	5171 ^{Aa}	24.26	2038 ^{Aa}	8965 ^{Ab}	22.74
ZT	0	854 ^{Bb}	3983 ^{Ab}	21.45	1628 ^{Ab}	6833 ^{Bc}	23.82
	10	1039 ^{Ba}	4172 ^{Aab}	24.89	1726 ^{Ba}	7781 ^{Ba}	22.17
	30	997 ^{Ba}	4149 ^{Ba}	24.02	1520 ^{Ba}	6685 ^{Bb}	22.74
Mean							
Tillage	CT	1191	4908	24	2037	8640	23.56
	RT	1160	4851	24	1975	8585	23
	ZT	963	4101	23	1625	7100	22.91
Residue height	0 cm	991	4468	22.13	1790	7663	23.38
	10 cm	1156	4585	25.19	1946	8476	22.93
	30 cm	1168	4807	24.27	1899	8184	23.17

**Fig. 143.1** Seasonal fluxes of CO₂, CH₄ and N₂O in different tillage and residue management practices in pigeon pea-castor system

immediately after tillage and this increase was only for few hours and decreased later [10]. Crop residue removal, reduced CO₂ fluxes as the crop residue serves as a C substrate for soil microorganisms. The CT has recorded 22% higher N₂O emissions as compared to ZT. The higher N₂O emissions under CT could be due to a strong disaggregation and enhanced soil aeration, which help in improving the living conditions of aerobic nitrifying bacteria [11]. Influence of crop residues on GHG emissions is more pronounced in ZT than in CT and RT. Anchored residues of 10 and 30 cm in ZT reduced the N₂O emissions whereas in CT significant difference in emissions between residues was not observed. In all the treatments, both release and uptake of methane was observed but there was net efflux of CH₄ rather

than CH₄ fluxes. The latter occurred during continuous rainfall events when anaerobic conditions prevailed [12]. In general methane oxidation increased with increase in crop residues and the effect of crop residues is more pronounced in ZT. Methane flux was observed in 0 cm anchored residues whereas oxidation was recorded in 10 and 30 cm.

Due to significant interaction between tillage and residue levels, the effect of tillage has been analysed at the same level of residue, the effect of residue at the same level of tillage; Capital letters indicate the effect of tillage, lower case letters the effect of residue levels; Means followed by the same letter are not significantly different at $P = 0.05$.

143.4 CONCLUSIONS

The results of this five year study revealed that yields in CT are higher under rainfed conditions but these yields were on par with RT. However, the yield gap between the tillage treatments is narrowing down over years. Similar results were reported by several authors in transition phase of the experiment and it takes time to realize the benefits of the ZT. Hence, it may take time for the ZT to out yield CT and RT. Keeping in view, yield and environmental impacts, RT with 10 cm anchored residue may be recommended. Further, the harvesting height at 10 cm adds residue to the soil which improves the soil quality and also helps to overcome the competing use of residue.

REFERENCES

1. Intergovernmental Panel on Climate Change (IPCC).: Climate change 2007, Synthesis report. Edited by Pachauri, R.K. and Reisinger, A. IPCC, Geneva (2007)
2. Hobbs, P.R., Sayre, K. and Gupta, R.: The role of conservation agriculture in sustainable agriculture. *Philos. Trans. R. Soc. Lond. Biol.* 363, 543–555 (2008)
3. Hutchinson, G.L. and Mosier, A.R.: Improved soil cover method for field measurement of nitrous oxide fluxes. *Soil Sci. Soc. Am. J.* 45, 311–316 (1981)
4. So, H.B., Grabski, A. and Desborough, P.: The impact of 14 years of conventional and no-till cultivation on the physical properties and crop yields of a loam soil at Grafton, NSW, Australia. *Soil Till. Res.* 104, 180–184 (2009)
5. Alvarez, R. and Steinbach, H.S.: A review of the effects of tillage systems on some soil physical properties, water content, nitrate availability and crops yield in the Argentine Pampas. *Soil Till. Res.* 104(1), 1–15 (2009)
6. Cutforth, H.W., McConkey, B.G., Ulrich, D., Miller, P.R. and Angadi, S.V.: Yield and water use efficiency of pulses seeded directly into standing stubble in the semiarid Canadian prairie. *Can. J. of Plant Science*, 82(4), 681–686 (2002)
7. Sharma, K.L., Mandal, U.K., Srinivas, K., Vittal, K.P.R., Mandal, B., Grace, J.K. and Ramesh, V.: Long-term soil management effects on crop yields and soil quality in a dryland Alfisol. *Soil Till. Res.* 83(2), 246–259 (2005)

8. Shah, Z., Shah, S.H., Peoples, M.B., Schwenke, G.D. and Herridge, D.F.: Crop residue and fertiliser N effects on nitrogen fixation and yields of legume–cereal rotations and soil organic fertility. *Field Crops Res.* 83(1), 1–11 (2003)
9. Regina, K. and Alakukku, L.: Greenhouse gas fluxes in varying soils types under conventional and no-tillage practices. *Soil Till. Res.* 109(2), 144–152 (2010)
10. Reicosky, D.C., Dugas, W. A. and Torbert, H.A.: Tillage-induced soil carbon dioxide loss from different cropping systems. *Soil Till. Res.* 41(1), 105–118 (1997)
11. Gregorich, E.G., Rochette, P., St-Georges, P., Mckim, U.F. and Chan, C.: Tillage effects on N₂O emissions from soils under corn and soybeans in Eastern Canada. *Can J Soil Sci.* 88, 153–161 (2007)
12. Johnson, J.M.F., Franzluebbers, A.J., Weyers, S.L. and Reicosky, D.C.: Agricultural opportunities to mitigate greenhouse gas emissions. *Environ Pollut.* 150, 107–124 (2007)

Chapter 144

Perspective of the Agriculture Development of the Mountain Areas in Modern Condition of Climate Change

I. Normatov, P.I. Normatov, and A. Muminov

Abstract Considering importance of weather conditions for development of agricultural grades influence of the Nurek reservoir on formation of a microclimate of the Dangara district with the developed agricultural branch investigated. It has observed that the natural trend of temperature in summer and the winter periods before construction of a reservoir transformed to the return, i.e. temperature increases in the winter and decreases in the summer. Analysis of annual precipitation shows the cyclical their fluctuations by interval of 3-5 years. Humidity reduction for the considered periods that is connected with increase of temperature at almost invariable trend of the precipitation change in Dangara was observed.

Keywords Water reservoir • Agroclimatic condition • Agriculture • Mountain • Irrigation

144.1 INTRODUCTION

Hydropower along with agriculture is the basic economical branch of the Republic of Tajikistan. The total annual of hydropower resources of the Tajikistan is 527 Bln. kWt · h that now is using only 5%. The presence of the rich potential of the production of electricity in Tajikistan suggests that in the short term expected to build a number of small and large hydroelectric power plants (HPP) with reservoirs [1]. Therefore, at planning prospects for agriculture coastal areas to the reservoirs should take into consideration the influence of water reservoirs in the transformation of the meteorological conditions of the area and make correction to the irrigation norm of the relevant agriculture crops. The aim of the present paper is a retrospective comparative analysis of statistical parameters of 60-year time series

I. Normatov (✉)

Institute of Water Problems, Hydrophober and Ecology, AS Tajikistan, Dushanbe, Tajikistan
e-mail: inomnor@gmail.com

P.I. Normatov • A. Muminov

Tajik National University, Dushanbe, Tajikistan

of temperature, humidity and monitoring of the Nurek reservoir influences on trend changes of these parameters.

144.2 METHODOLOGY

To determine the influence of mountain reservoirs on agroclimatic conditions we analyzed the trend of meteorological parameters the Dangara district of Tajikistan with developed agriculture that is a coastal to the Nurek reservoir. We used meteorological data 1950-2012 years from station located in the research area. Nurek dam construction has started in 1961 year. The water level at 1979 has reached 890 m, and the normal water level (NWL) equal to 910 m has achieved in September 1983. Therefore, we can assume that the influence of the reservoir on meteorological parameters area has been observed after 1980 years. Based on this assumption, we analyzed meteorological parameters of the two periods - before (1950-1980) and after (1981-2012) the construction of the dams.

144.3 RESULTS AND DISCUSSION

Temperature change in the Dangara district for the period 1950-2010 years is characterized by its uniform increase without any extreme evidences about influence of the Nurek reservoir (Fig. 144.1).

Natural to expect that the manifestation of any signs of the influence of the reservoir on the temperature variation due to smoothing them for such a long period are very difficult. For a more detailed study of the influence of the reservoir on the average temperature, we carried out separately systematization of meteorological parameters of Dangara district before and after the construction of the reservoir.

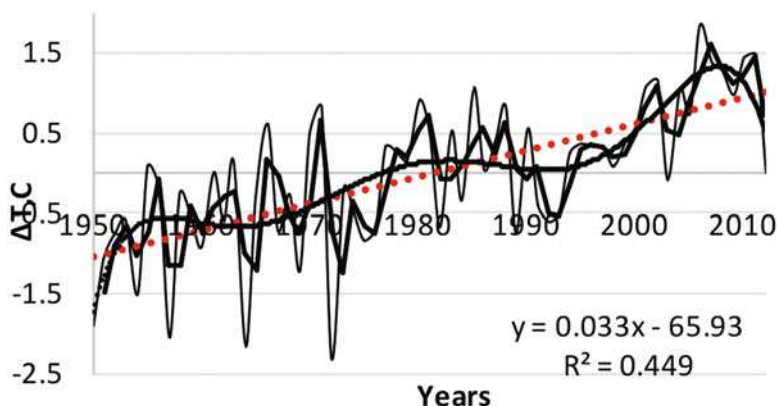


Fig. 144.1 Long-term course of mean annual temperature deviations from the average values for the period 1950-2012

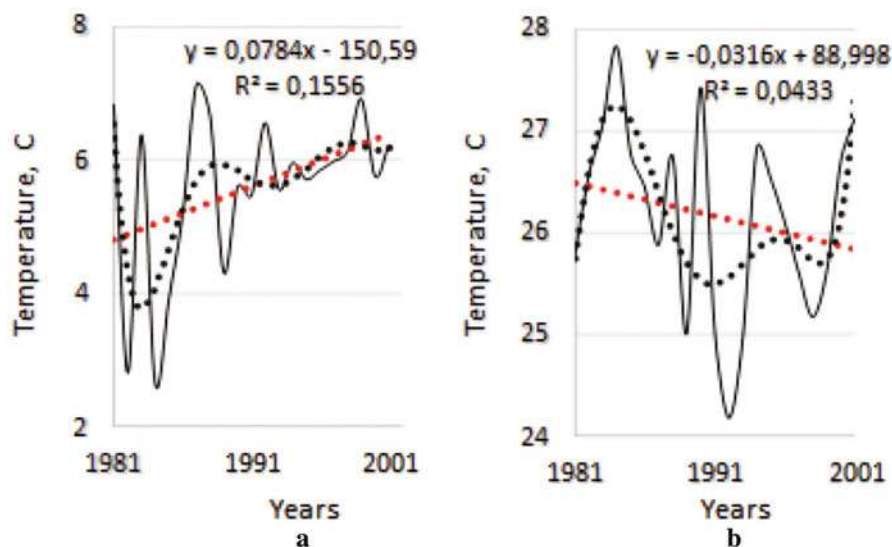


Fig. 144.3 Long-term average annual temperature of Dangara in winter (a) and the summer (b) for the period 1981-2001

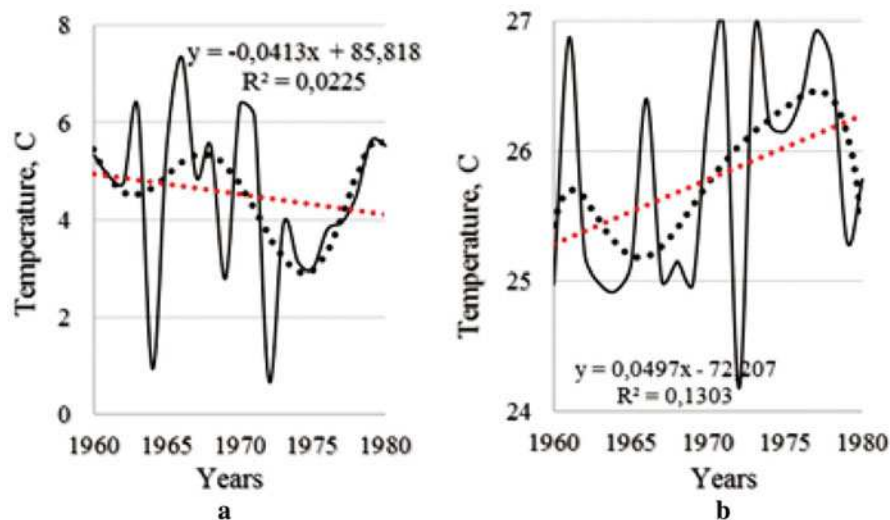


Fig. 144.2 Long-term average annual temperature of Dangara in winter (a) and the summer (b) for the period 1960-1980

Taking into consideration that the weather of Tajikistan is continental, we considered the trend of temperature change in winter and summer seasons of the considering periods. Annual average temperature change in winter (XI-II) (a) and summer (V-VIII) (b) before and after construction of the Nurek reservoir shown in Figs 144.2, 144.3.

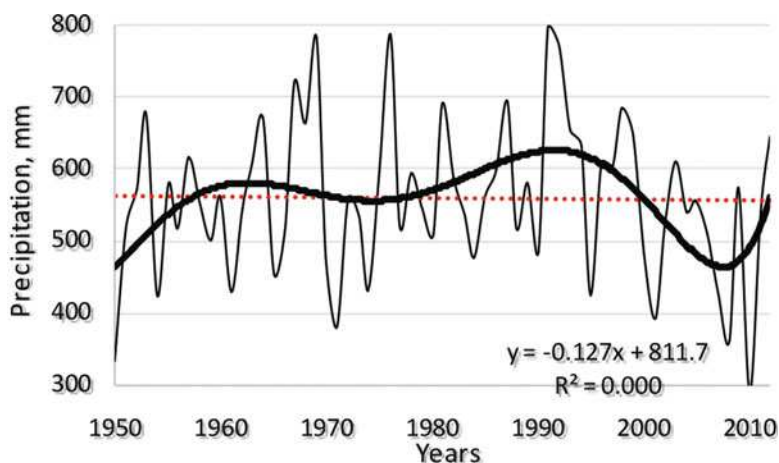


Fig. 144.4 Long-term change of mean annual precipitation deviations for the period 1950-2012

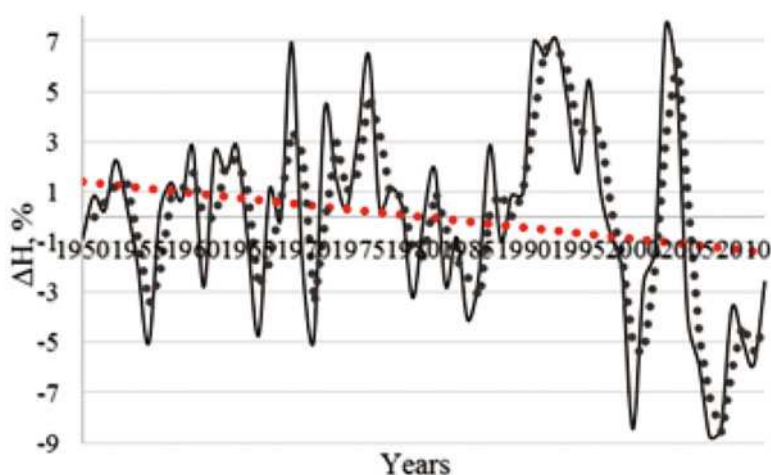


Fig. 144.5 Long-term course of mean annual humidity deviations from the average values for the period 1950-2012

The data on Fig. 144.2, 144.3 show that before 1980 when water level did not reach Normal water level (NWL) has observed increase in temperature occurs mainly in summer. After filling the reservoir by water to full mark (after 1980), the picture will change to the opposite, i.e. to increase the temperature in the winter. The obtained results give reason to believe that the reservoir acts as a conditioner weather conditions in the settlement areas. Analysis of annual precipitation shows that for the period 1960-2010 the cyclical fluctuations by interval of 3-5 years have observed (Fig. 144.4).

Humidity reduction for the considered periods that has connected with increase of temperature at almost invariable trend of the precipitation change in Dangara has observed (Fig. 144.5).

144.4 CONCLUSION

Research has shown the important role of reservoirs on climate change and the transformation of a microclimate of the coastal to reservoirs areas. In turn, climate change leads to changes in the dynamics of growth of crops and their productivity. Remedy the situation is only possible through the development of adaptation mechanisms crops to new climatic conditions and selection of species steady to climatic stresses.

REFERENCE

1. Petrov, G.N. and Normatov, I. Sh.: Conflict of interests between water users in the Central Asian Region and possible ways to its elimination. *J. Wat. Res.* 37, 113–120 (2010)

Chapter 145

In the Face of Changing Climate: Groundwater Development through Artificial Recharge in Hard Rock Terrain of Kumaun Lesser Himalaya

M. Tripathi

Abstract The study indicates that abnormal weather phenomena in the form of less rainfall with no snowfall and reduction in number of rainy days, short span heavy rainfall, hydrogeologic and geomorphologic conditions of the aquifer system and availability of surface water resource are the major limitations for groundwater recharge in the study area. A detailed study of the seven micro-watersheds of Western Ramganga River in the Kumaun Lesser Himalayan terrain has been carried out to identify and propose area specific artificial groundwater recharge structures (AGRS) using remote sensing, geographical information system, field survey and multi criteria decision making techniques (MCDM). The small-scale AGRS structures can be built across lower order streams in order to enhance infiltration into the subsurface formations. The results of the present study can serve as guidelines for planning future artificial recharge projects in the area in order to ensure dependable water supply and sustainable groundwater utilization on a long-term basis.

Keywords Kumaun Himalaya • Groundwater • Water harvesting • Artificial recharge

145.1 INTRODUCTION

Groundwater plays an important role in the Himalayan mountain system. In the Kumaun Lesser Himalayan terrain mostly groundwater found at depths varying from a meter in valleys to more than 30 meter at the water divides [1]. Beneath the riverbed the groundwater occurs largely in disconnected local bodies in favorably perched aquifers in both confined and unconfined conditions and also in zones of jointing, fracturing and faulting. The hydraulic properties of the formations have a strong bearing on the movement and storage of water. Metamorphic rocks have a

M. Tripathi (✉)

Department of Geograph, Kumaun University, Nainital, Uttarakhand, India

e-mail: manishatripathi.jnu@gmail.com

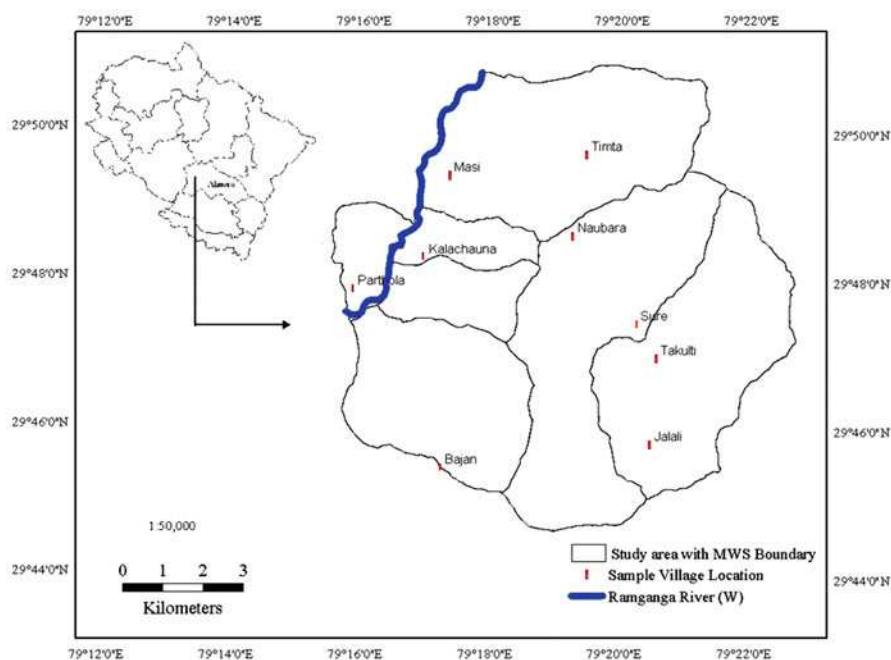


Fig. 145.1 Location of the study area

very low hydraulic conductivity 10^{-9} . The secondary porosity due to faults and fractures constitute the principal mechanism for groundwater flow in metamorphic rocks. Furthermore, the permeability of crystalline rocks varies widely, depending on the degree of weathering, nature of weathered materials and intensity of fracturing and open spaces in the fractures. In most of the granite/gneiss area, the weathered zone serves as an effective groundwater reservoir.

The rise in groundwater level is a direct consequence of precipitation, particularly in the monsoon season, when the groundwater withdrawal is minimum [2] whereas the water level at a particular place is a characteristic feature of unsaturated zones [2, 3, 4, 5, 6]. The village communities of the study area (Fig. 145.1) have had acute water shortages for many decades as a result of increase in temperature, change in rainfall patterns and snowfall and reduction in no of rainy days. This has resulted in the drying up of the springs which are the only source of water in the upslope areas. Although the uppermost areas in the watershed along the water divide receive fair amount of monsoon rains, they are the areas with least access to perennial water sources such as streams and major river (Ramganga). In many places, residents of these areas have to walk long distances for their drinking water. In lower areas, water availability may be affected by upstream extraction of water mainly during the dry season. In terms of vulnerability, the survival of the communities of Ramganga valley is at stake because of the acute shortage of water in the area whose intensity is increasing day by day. In the present study an attempt

has been made to decipher groundwater prospect zone and artificial recharge zone for augmenting groundwater in the area with the help of the integration of various thematic layers such as geology, geomorphology, hydrogeomorphology, lineament, slope, soil, drainage density, stream order, by applying weight index overlay analysis (WIOA) method in GIS environment. Water shortages in the study area comprising seven micro-watersheds; have been progressively increasing over the last 30-40 years. It is very essential to carefully handle and store the runoff generated through rainfall in surface and groundwater storage structures, in hard rock terrain, the ultimate source of surface and groundwater resources is the precipitation. Rainwater harvesting and artificial recharge of groundwater has been advocated and practiced in the hard-rock regions to come up with falling groundwater. The artificial water-harvesting structures will be helpful for establishing efficient use of available groundwater resources in the study area. These are innovative in the sense that they increase the groundwater recharge, and in turn, reduce loss of water through surface runoff.

145.2 MATERIAL AND METHODS

Data and research studies about the natural resources especially groundwater resource depletion in the study area are almost non-existent therefore, the study was required to rely on the field survey (spring monitoring) and human observations from different part of the study area. Due to the lack of proper monitoring system in the study area it is not sure whether the variations in the precipitation received are part of an abnormal weather cycle or are results of modifying and changing landscape conditions as a whole. The methodology involves the study and identification of the ideal geo-hydrological conditions prevailing in the area within the regional geological setup with respect to the adjacent geological formations based on the high resolution LISS III and PAN merged satellite data (IRS 1D), Survey of India maps at 1:50,000 scale followed by field surveys and previous studies carried out in the region to delineate groundwater prospect and artificial recharge zones and identifying suitable artificial groundwater recharge structures (AGRS) from entire study area. To achieve this objective a set of nine representative sample villages have been selected on the basis of physical-environmental setting including topography, terrain, aspect, geology and social and economic setup with accessibility, and natural resource conditions such as water facilities available there. It is observed that the environment, people, and their socio-economic characteristics are more or less same in the adjoining areas therefore, it was necessary to spread the sample villages quite widely to have representations of physical-social and cultural dimensions quite accurately at small scale. Therefore, few indicators such as number of households, number of natural springs, terrain are basic criteria to select the nine sample villages from different micro-watersheds. Attempts are made to enumerate maximum number of households in the selected villages.

145.3 STUDY AREA

145.3.1 Hydrogeology

Hydrogeological conditions of the area are more important in planning artificial recharge schemes. The youngest geological formations of Pleistocene-Quaternary, which are fluviatile in origin, and occur as loose valley, fill deposits, covers the hard crystalline igneous and metamorphic rocks in the area which occupies the central part of the synclinal AlmoraNappe (a thick folded sheet of Precambrian metamorphic rocks and associated granite-that has been southward dislocated considerably from its original place). The Almoragroup, that constitute the AlmoraNappe (Fig. 145.2) is composed of garnetiferous “mica-schist” interbedded with micaceous-quartzites, augen gneisses and carbonaceous phylliteinterbedded with black metagraywackes with graphite schist. The rugged hills of the AlmoraNappe represent severely compressed complex layers, divided into blocks by transverse faults, resulting in extensive strong crushing of the rocks. The zone of the frasctured rocks provides very good aquifers of tremendous water potential. Prevalent joints and fractures of rocks together with cleavage have greatly increased the water-bearing capacity of the surface rocks. Furthermore, these provide easy passage to the groundwater flow.

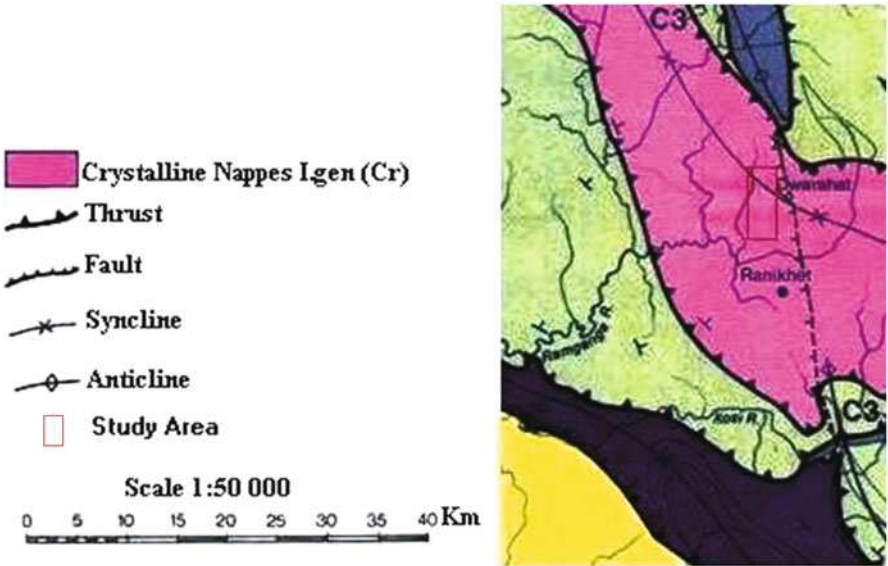


Fig. 145.2 Tectonic and structural setting of the study area

145.3.2 Hydrogeomorphology

The hydrogeomorphological set-up of the study area controls the retention period of surface and groundwater within a topographic unit. The gradients are very steep in the runoff zones, with very little possibility of infiltration. Such areas on hill-slopes may be suitable only for water conservation measures like gully plugging, bench terracing or contour trenching, aimed at slowing down surface runoff and thereby causing more infiltration, which may go as delayed subsurface seepage either to the unconfined or deeper confined aquifer systems. The adequate groundwater resources are generally available only during the monsoon while major component of the monsoon rains goes as surface runoff in the area. Thus, groundwater recharge is normally not sufficient to saturate the aquifers in short periods. Moreover the lower order streams (2nd and 3rd order streams) are normally do not have any flow during the major part of winter and only higher order streams (4th and 5th order) having some flow in the lower reaches during summer. The broad valley floor and the zone of lowest elevation occurring along the river Ramganga typically have typically gentle to very gentle gradients. The movement of both surface and groundwater in these areas is sluggish and retention time, in general, is high. These areas are generally categorized as groundwater potential zones as all the water moving down the water table gradient converges in this zone. Moderate topographic slopes are occurring on valley sides. Surface and subsurface retention of water in these areas are for longer durations depending upon depth of soil profile, hydrogeology, land-use/land-cover etc. The piedmont zones, with comparatively deep water table is located immediately within the break in slope of foot hill zone and flood plain of the Ramganga River. The surface drainage is generally located above the water table. These areas are suitable for constructing recharge basins and percolation ponds to recharge the aquifer. At elevations just below the piedmont zone, artificial recharge through percolation ponds, recharge pits, trenches and recharge basins is normally feasible [7].

145.4 RESULTS AND DISCUSSION

In the study area, even though the monsoon rainfall is high, scarcity of water is felt in post-monsoon season. Due to steep gradients, a large quantity of water flows out to low elevation areas as surface runoff. The dependence on groundwater has increased many-times, and the natural recharge to groundwater has decreased due to reduction in recharge. The Ramganga River with its very wide catchment area receives its flow from snow melt, rainfall and through base flow. Since the slopes are high and hills are barren a major part of rainwater goes as surface runoff. Another part which percolates downward through cracks, fissures and joints in the rocks, appear on surface as springs and in the gadheras/gads (small rivulets) under favorable circumstances.

145.4.1 Artificial Groundwater Recharge Measures (AGRM)

145.4.1.1 Prioritization of Areas for Artificial Recharge

Prioritization of areas for artificial recharge is prerequisite for the development and management of groundwater resources in the study area. Normally, areas having deeper water levels are given higher priority. Areas having shallow water levels with rising water level trends during certain periods (post-monsoon period) are considered for small structures (check dams, percolated ponds, etc.) instead of large structures in artificial recharge plan.

145.4.1.2 Hydrogeomorphological Demarcation of Recharge Area

Regional geology combined with local hydrogeological and morphometrical understanding leads to systematic understanding of different zones like recharge protection zones, direct recharge zones, zones for soil-water conservation etc. These recharge zones can then be selected for the artificial recharge structures.

145.4.1.3 Location Specific Measures

Location specific measures are preferably associated with greater degree of fracturing in rocks such as quartzites, structure and slope should be such that it allows for faster infiltration (Fig. 145.2).

145.4.1.4 Ridge to (Top-down) Valley Approach

In this approach, watershed treatment measures are initiated from the highest level and progressively move downward. The upper catchment areas including forest area and lands of marginal farmers (located usually on the ridges and upper reaches) are treated first. These results in reduction in velocity of water, soil conservation and prevention of silt deposition in artificial groundwater recharge structures on the downstream site.

145.4.1.5 Scarp VS. Dip Slope Approach

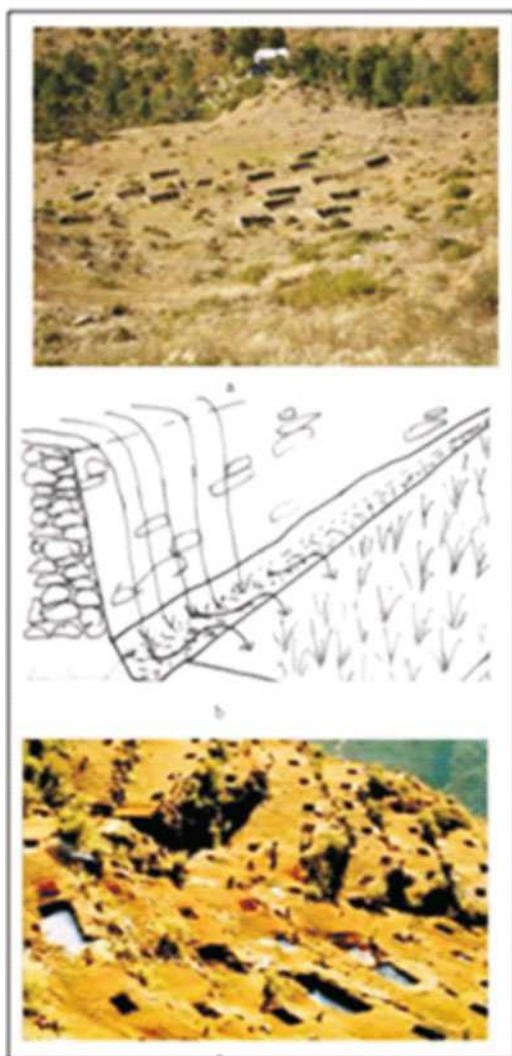
Thus recharge structures recommended on scarp slopes, while harvesting structures on dip slope. As scarp slopes are lithologically more conducive to recharge and more sustainable, number of permeable horizons on the scarp slope is greater in number and such slopes are having greater potential sites for recharge as compare to dip slope. While dip slopes are best suited for the water harvesting structures

instead of scarp slopes as the streams on the scarp slope tend to dry up quicker as compare to dip slopes. Percolation pits or ponds can be constructed along the scarp slope to recharge groundwater, while storage tanks and pond and check dams can be constructed on dip slope (Fig. 145.5a).

145.4.2 Artificial Groundwater Recharge Structures (AGRS)

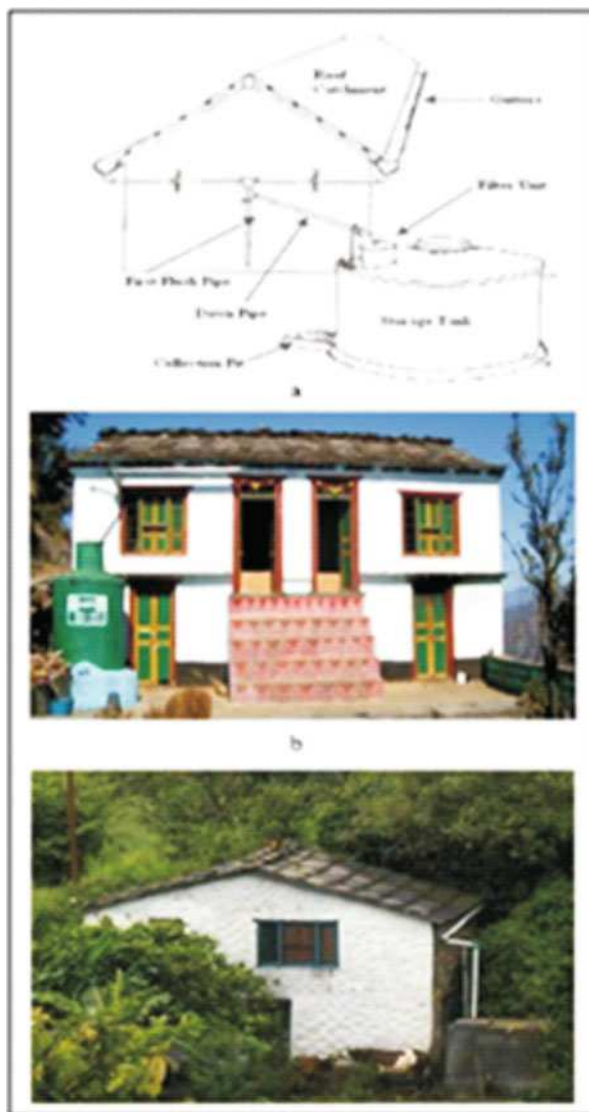
In the study area where source of water is only rainfall, entire efforts of water conservation are to be concentrated on in-situ rainfall (Fig. 145.4). Gully plugging, contour bunding, bench terracing and gabion structures are the common water conservation structures applicable in runoff zone. Harvesting water by building micro-structures is one of the key strategies for adapting to water stress in the study area (Fig. 145.5). These harvesting structures are locally called khal (water reservoir) and are built by individuals as well as by the village as a whole. Rainwater harvesting to recharge groundwater to revive mountain springs holds lot of promise for the whole Himalayan region. Percolation pits are made to make the rainwater enter directly into the aquifer. Roof water and surface water can be diverted to percolation pits. It is good to have a minimum of one percolation pit for every 3-4 Km² in the study area (Fig. 145.5d). Gully plugs may be chosen wherever there is local break in slope to permit accumulation of adequate water behind the bund. A number of gully plugs may be provided on the same gully or small gadhera, one below the other at every 50-100 m separation. Gabion structure can be constructed across small streams in the study area to conserve stream flow, with practically no submergence beyond stream course. The preferred height of gabion structure can be between 1-0.5 m and it can be built in the stream with width of less than 10 m. The excess water overflows this structure storing some water to serve as source at recharge. In the study area, it is observed that rectilinear drainage is common not only in the higher order streams, but also in the lower order streams (1st and 2nd). The long linear stretches of the streams and rivulets courses effectively lead to quick flow of water which gets little time for infiltration. In such cases, the most suitable recharge technique would be the construction of a series of en echelon dams which check the flow of water while allowing the water to flow with a reduced velocity, thus enabling it more time for infiltration. En echelon dams have been suggested at 5 places in the study area across streams and rivulets which flow linearly for a considerable distance. Contour trenches can be constructed on hill slopes as well as on degraded and barren waste lands in both high- and low-rainfall areas. The water retained in the trench will help in conserving the soil moisture and groundwater recharge. Contour bunding involves construction of narrow-based trapezoidal embankments (bunds) along contours to impound water behind them, runoff-recharge zones of all the seven micro-watersheds, with low to moderate slopes. These areas exhibit high fluctuation in the water table and have poor to moderate which infiltrates into the soil and ultimately augment groundwater recharge (Fig. 145.3). Check dams are recommended at 13 locations across the

Fig. 145.3 Design of:
 a. Infiltration trenches,
 b. Siltation trenches,
 c. Staggered contour
 trenches with square pits in
 between



3rd order streams and rivulets in the groundwater potential. It is expected that the check dams would prevent the water from flowing down to join the higher order streams and instead permit the water to spread out around the lower order streams and recharge the aquifer (Fig. 145.5b). Water percolation tanks can be made for plantation and infiltration on fracture zones, at the contacts of quartzites and phyllite and along the scarp slope, for rapid infiltration. In the study area, percolation tanks can be constructed on 3rd order streams, in Jalali and Gagas micro-watershed. Bench terraces helps in soil conservation and holding runoff water on terraced area for longer duration giving rise to increased infiltration recharge on the top of the hills, and mid slope of the valley wall. The vertical interval of such

Fig. 145.4 a. In situ water conservation method, Roof water harvesting, b. Modern collection tank, c. Old collection tank



terraces should not be more than 1m. Such measures can be adopted where soil depth is more than 1m. The infiltration of rainwater into the recharge zone can be increased through vegetative measures also [8]. Among the vegetative measure a few seedlings of *Alnusnepalensis* (utis), *Prunuscerasoides* (padam) and *Quercusleucotrichophora* (banj oak) can be planted at 2×2m spacing at the lower end of recharge zone.

Fig. 145.5 a. Scarp vs. ridge approach, Storage of runoff water in conservation ponds, b. Check dam, c. Water storage tank, d. Percolated tanks, e. Plastic lined conservation ponds instead of cemented pond, f. Khal



145.5 CONCLUSIONS

A sound resources database using remote sensing and GIS technique has been generated to understand the resources situation which was then followed by critical analysis of groundwater scenario to arrive at identification of appropriate site for construction of water conservation structure. The study indicates that hydrogeomorphic conditions of the aquifer system and availability of surface water resource are the major limitations for artificial groundwater recharge plans.

The aquifers are deep and yield is very poor. This work through the monitoring of rural hill environment would be helpful to produce information for policy-makers and planners and aid their understanding of development processes in the complex Himalayan environment.

REFERENCES

1. Valdiya, K.S.: Developing a paradise in peril. VII G.B. Pant Memorial Lecture, G.B. Pant Institute of Himalayan Environment and Development, Kosi-Katarmal, Almora, p. 26 (1997)
2. Raj, P.: Trend analysis of groundwater fluctuations in a typical groundwater year in weathered and fractured rock aquifers in parts of Andhra Pradesh. *Jour. Geol. Soc. India*, 58, 5–13 (2001)
3. Todd, D.K.: Ground water hydrology. John Wiley & Sons, New York.
4. Athavale, R.N., Rangarajan, R. and Murlidharan, D.: (1992). Measurement of natural recharge in India. *Jour. Geol. Soc. India*, 39, 235–244 (1980)
5. Moon, S.K., Woo, N.C. and Lee, K.S.: Statistical analysis of hydrograph and water-table fluctuation to estimate groundwater recharge. *J. Hydrol.*, 292, 198–209 (2004)
6. Lee, J.Y., Yi, M.J. and Hwang, D.: Dependence of hydrological responses and recharge estimates on water-level monitoring locations within a small catchment. *Geosci. Jour.*, 9(3), 277–286 (2005)
7. Central Ground Water Board: Manual on artificial recharge of ground water. Ministry of Water Resources, Government of India (2007)
8. Valdiya, K.S. and Bartarya, S.K.: Hydrological Studies of Springs in the Catchment of the Gaula River, Kumaun Lesser Himalaya, India. *Mount. Res. Dev.* 11(3), 239–258 (1991)

Chapter 146

Sustainable Biochar - A Tool for Climate Change Mitigation, Soil Management and Water and Wastewater Treatment

Dinesh Mohan, Abhishek Kumar, and Charles U. Pittman

Abstract Global threats including climate change, land degradation, environmental contamination, and water shortages lead to economic, social and environmental damage. These need to be addressed to overcome the major disaster occurring now and in near future. Sustainable Biochar (BC) from biomass and wastes can be an environmentally-friendly option for carbon sequestration, soil fertility improvement, pollution remediation and agricultural by-product/waste recycling. Pyrolysis of lignocellulosic biomass to bio fuels and other value-added products including biochar has attracted considerable attention since the mid-1970s due to petroleum price spikes, climate change and increasing energy demand [1]. Fast and slow pyrolyses are promising routes to renewable liquid fuels, biochars and chemicals. Fast pyrolysis is a promising route to recover renewable liquid fuels. Fast pyrolysis employs short residence time (<3 s) at 400-5000C in absence of oxygen to generate bio-oil or pyrolytic oil, bio-char and gas [1, 2].

Keywords Biochar • Climate change mitigation • CO₂ sequestration • Water treatment

146.1 INTRODUCTION

Agricultural crops and residues can easily be converted into bio-energy with bio-char as a byproduct using slow or fast pyrolysis [1, 3-5]. This biochar can be burned or sequestered into soils. Its long-term sequestration duration, while uncertain, can exceed centennial timescales while simultaneously improving soil fertility and structure and possibly reducing fertilizer run-off [5-8]. The beneficial

D. Mohan (✉) • A. Kumar

School of Environmental Sciences, Jawaharlal Nehru University, New Delhi, India

e-mail: dm_1967@hotmail.com

C.U. Pittman

Chemistry Department, Mississippi State University, Mississippi State, USA

application of biochar has attracted increasing multidisciplinary interest in science and engineering. Biochar has a potential to remediate soil and water contaminated with organic and inorganic contaminants [3, 4, 7, 8]. In the present investigation, both slow and fast pyrolysis biochars were developed, characterized and utilized for environmental management. Magnetic biochars were also prepared and used for water treatment. The objectives were (1) to convert biomass into biochar by slow and fast pyrolysis (2) to characterize the developed biochars (3) to remediate organic and inorganic contaminants from water (2) to improve the soil fertility (3) to investigate carbon sequestration as a strategy for climate change mitigation.

146.2 RESULTS AND DISCUSSION

Fast pyrolyses of pine wood, pine bark, oak wood, oak bark were conducted in an auger fed reactor at 400 and 450°C. Slow pyrolyses of corn stover, rice husk were carried out in an indigenously designed reactor. The biochars' composition and morphology were studied by FTIR, XRD, FT-Raman, SEM, TEM, elemental analysis, surface area, density, swelling and ^{13}C NMR measurements. Removal of fluoride using slow [9] and fast pyrolysis biochars [10] were reported. More fluoride was removed using fast pyrolysis pine wood and pine bark biochars than slow pyrolysis corn stover biochar [9, 10]. Magnetic corn stover biochar was also prepared and successfully used for fluoride removal [9] (Table 146.1).

Sorption studies demonstrated that low surface area biochars have excellent adsorption capacities for chromium, cadmium, lead, arsenic, fluoride, ibuprofen and salicylic acid removal from water. These contaminants were recovered and biochars were successfully regenerated and reused through several cycles.

Biomass derived biochar is one environmentally friendly option to mitigate CO_2 emission by storing them in soils. In the present research, CO_2 emission from soils treated with biochar was compared to identical soils where the equivalent amount of fresh biomass was added. In addition, the changes in soil properties on biochar addition were investigated. The biochar was applied to soil in different proportions 0.5%, 1.5% and 3% (w/w). The same amount of fresh biomass was applied to different soil samples. Blanks were also taken. The soil/biochar and soil/biomass samples were placed into a CO_2 chamber. Incubation was conducted for 150 days at 25°C and 65% relative humidity to determine the biochars' effect on physical and chemical properties of soil conditioned with biochar. The CO_2 emission from biochar-treated versus biomass-treated soil was measured using an automated CO_2 flux analyzer. CO_2 emission from biomass-treated soils samples was significantly higher than from soils treated with BC. Cumulative CO_2 emissions from soil treated with BC-treated soils was ~90% less than emissions from biomass-treated soils. Water holding capacity, bulk density, pH, electrical conductivity,

Table 146.1 Biochar application in contaminants remediation

Adsorbents	Adsorbate	pH	Temp. (°C)	Conc. range (mg/L)	Adsorption capacity (mg/g)	References
Corn stover biochar	Fluoride	2.0	25	1-100	6.42	[9]
			35	1-100	5.17	
			45	1-100	5.00	
Magnetic Corn stover biochar	Fluoride	2.0	25	1-100	4.11	
			25	1-100	3.45	
			25	1-100	3.41	
Pine wood biochar	Fluoride	2.0	25	1-100	7.66	[10]
Pine wood biochar		2.0	35	1-100	6.34	
Pine wood biochar		2.0	45	1-100	4.46	
Pine bark biochar		2.0	25	1-100	9.77	
Pine bark biochar		2.0	35	1-100	10.53	
Pine bark biochar		2.0	45	1-100	8.40	
Oak wood char	Chromium	2.0	25	1-100	3.03	[11]
		2.0	35	1-100	4.08	
		2.0	45	1-100	4.93	
Oak bark char	Chromium	2.0	25	1-100	2.45	
		2.0	35	1-100	3.95	
		2.0	45	1-100	4.0	
Oak wood	Lead	5.0	5		0.30	[12]
		5.0	25		2.62	
		5.0	35		11.30	
Oak bark	Lead	5.0	5		14.84	
		5.0	25		13.10	
		5.0	35		22.61	
Oak wood char	Cadmium	5.0	25		0.37	
Pine bark char		5.0			0.34	
Oak bark char		5.0			5.40	
Pine wood char	Arsenic	3.5	25		1.20	
Oak wood char		3.5			5.85	
Pine bark char		3.5			12.15	
Oak bark char		3.5			7.40	

organic matter, organic carbon, and cation exchange capacity were measured and analyzed for untreated soil and biochar-treated soil. Biochar-treated soils had significantly increased water holding capacities, organic carbon, organic matter and cation exchange properties. Thus, biochar developed from agricultural residues successfully improved the soil fertility. This indicates a sustainable direction for crop production.

146.3 CONCLUSIONS

These studies demonstrated that biochars have been successfully used for contaminants (heavy metals, fluoride, pharmaceuticals and pesticides) removal from water and soil. Furthermore, biochar has the capability to serve as a green environmental approach to mitigate CO₂ emission by storing them in soils, to improve soil and remediate organic and inorganic contaminants from water.

REFERENCES

1. Mohan, D., Pittman, Jr., C.U. and Steele, P.H.: Pyrolysis of Wood/Biomass for Bio-oil: A Critical Review. *Energy & Fuels*, 20, 848–889 (2006)
2. Pittman, Jr., C.U., Mohan, D., Eseyin, A., Li, Q., Ingram, L., Hassan, E.-B.M., Mitchell, B., Guo, H. and Steele, P.H.: Characterization of Bio-oils Produced from Fast Pyrolysis of Corn Stalks in an Auger Reactor. *Energy Fuels*, 26, 3816–3825 (2012)
3. Mohan, D., Sarswat, A., Ok, Y.S. and Pittman, C.U.: Organic and Inorganic Contaminants Removal from Water with Biochar, a Renewable, Low Cost and Sustainable Adsorbent – A Critical Review, *Bioresource Technology*, Accepted (2014)
4. Ahmad, M., Rajapaksha, A.U., Lim, J.E., Zhang, M., Bolan, N., Mohan, D., Vithanage, M., Lee, S.S. and Ok, Y.S.: Biochar as a sorbent for contaminant management in soil and water: A review. *Chemosphere*, 160, 191–202 (2014)
5. Lehmann, J.: Bio-energy in the black. *J. Frontiers in Ecology and the Environment*, 5, 381–387 (2007)
6. Lehmann, J.: A handful of carbon. *Nature*, 447, 143–144 (2007)
7. Lehmann, J., Gaunt, J. and Rondon, M.: Bio-char sequestration in terrestrial ecosystems – A review. *Mitigation and Adaptation Strategies for Global Change*, 11, 403–427 (2006)
8. Liang, B., Lehmann, J., Solomon, D., Kinyangi, J., Grossman, J., O'Neill, B., Skjemstad, J.O., Thies, J., Luizão, F.J., Petersen, J. and Neves, E.G.: Black Carbon Increases Cation Exchange Capacity in Soils. *Soil Science Society of America Journal*, 70, 1719–1730 (2006)
9. Mohan, D., Kumar, S. and Srivastava, A.: Fluoride Removal from Ground Water using Magnetic and Nonmagnetic Corn Stover Biochars. *Ecological Engineering*, In Press (2014)
10. Mohan, D., Sharma, R., Singh, V.K., Steele, P. and Pittman, Jr., C.U.: Fluoride Removal from Water using Biochar, a Green Waste, Low-Cost Adsorbent: Equilibrium Uptake and Sorption Dynamics Modeling. *Industrial and Engineering Chemistry Research*, 51, 900–914 (2012)
11. Mohan, D., Rajput, S., Singh, V.K., Steele, P.H. and Pittman, Jr., C.U.: Modeling and evaluation of chromium remediation from water using low cost bio-char, a green adsorbent. *Journal of Hazardous Materials*, 188, 319–333 (2011)
12. Mohan, D., Pittman, Jr., C.U., Bricka, M., Smith, F., Yancey, B., Mohammad, J., Steele, P.H., Alexandre-Franco, M.F., Gómez-Serrano, V. and Gong, H.: Sorption of arsenic, cadmium, and lead by chars produced from fast pyrolysis of wood and bark during bio-oil production. *Journal of Colloid and Interface Science*, 310, 57–73 (2007)

Chapter 147

Modelling Paleo-Geomorphology of Wave-Dominated Sandy and Tide-Influenced Muddy Coastal Embayments on the Decadal to Centennial Scale: A Comparative Study

J. Deng, J. Harff, Y. Li, and W. Zhang

Abstract In front of the modern changing climate, an integrated coastal zone management requires future scenarios of coastal evolution that can be projected by multi-scale Long Term Morphodynamic Models (LTMMs). A realistic initial Digital Elevation Model (DEM) assigned to the historical starting time is essential for calibrating and validating these models. By using the information of historical coastline changes, relative sea level record and modern DEM, the inverse modelling method (i.e. Dynamic Equilibrium Shore Model, DES Model) has been developed and validated for approximately estimating historical morphology at the Pomeranian Bay, southern Baltic Sea. This model bears also the potential for future projection of coastal morphogenesis based on sea level rise scenarios. The Pomeranian Bay is a wave-dominated sandy coast where sand remains within the coastal area and fine-grained suspended matter discharged by rivers is transported cross-shore basinward. A Long-shore Sediment Transport Capacity Model (LSTC) has proven the area to be semi-enclosed – one of the main preconditions for applying the inverse model to coastal environments. For comparison the Laizhou Bay (Bohai Sea) has been selected as a research area. Here, joint factors such as river discharge, tides, waves, and sea level variations shape the nearshore bottom morphology. In addition to the wind-wave driven Long-shore Sediment Transport Capacity, tidal residual currents are also important for estimating long-shore sediment flux to determine the boundary of the semi-enclosed area. At the Laizhou Bay, the muddy sediments at the sea bottom descend from numerous rivers' discharges. So, the riverine sediment source has to be taken into account here when balancing the sediment mass as distinguished from the Pomeranian Bay. In

J. Deng (✉) • J. Harff

Institute of Marine and Coastal Research, University of Szczecin, Szczecin, Poland

e-mail: junjie.deng@univ.szczecin.pl

Y. Li

Yantai Institute of Coastal Zone Research, Chinese Academy of Sciences, Yantai, China

W. Zhang

MARUM - Center for Marine Environmental Sciences, University of Bremen, Bremen, Germany

terms of modelling coastal morphogenesis, the comparative study carried out here helps to understand different formation mechanisms of wave-dominated sandy coast and tide-influenced muddy coast.

Keywords Comparative study • modelling • paleo-geomorphology • Laizhou Bay • Pomeranian Bay

147.1 INTRODUCTION

Future scenarios of coastal geomorphological changes are particularly required for the areas having subsiding coasts against sea level rise, coastal erosion driven by storms (changing dynamics of atmospheric circulation) and changes in sediment budget. Parameterization of a long-term multi-scale morphodynamic model to generate future scenarios has to base on the information derived from the reconstruction of paleo-coastal geomorphological changes. This fact highlights the importance of modelling paleo-coastal geomorphology at the corresponding time span to future projection (i.e. ca. 100 years according to climate modelling period).

A model to generate paleo-Digital Elevation scenarios has been elaborated for the wave-dominated sandy coast (i.e. the Pomeranian Bay, southern Baltic Sea) [1]. This model, named Dynamic Equilibrium Shore (DES) model generates paleo-Digital Elevation Models (DEMs) on the decadal to centennial time scales. The basic concept is a dynamic equilibrium coastal profile evolution in adaption to the sediment budget in a spatially three-dimensional domain.

The application of this model at a distinct coastal sedimentary environment (i.e. tide influenced muddy coast) requires not only calibrating this model, but sometimes also iteratively adjustment of the model. This adjustment needs scientific background knowledge at the research area. Therefore, a comparative study of modeling different geological and oceanographic coastal settings can help to generalize the model but also to uncover its limitations.

Here, the Pomeranian Bay, southern Baltic Sea, and the Laizhou Bay, Bohai Sea, northeast China are compared. The first one is regarded a sample of a wind-wave dominated sandy coast, whereas the Laizhou Bay stands for tide influenced muddy coast. Coastal erosion serves as main source for coastal sediment transport and accumulation at the Pomeranian Bay. For the Laizhou Bay, fluvial sources supply most of the sediments accumulated as sinks along the Laizhou Bay coast. The sediment sink area coincides with the subsiding belt along the Laizhou Bay coast, whereas the uplifting belt situates along the eastern coast of Shandong Peninsula [2]. Among numerous rivers merging the southern Bohai Sea, the Yellow River dominates fluvial sediment sources. It is notable that besides natural forces, during the last decades anthropogenic factors influence increasingly coastal morphogenesis. Dams and reservoirs erected upstream diminish continuously the suspended matter load delivered to the receiving marine basins [3]. This decrease makes sea level change and wind-wave dynamics becoming increasingly important

for the coastal development compared to fluvial factors. As the same time the tide starts to play the dominant role in transporting sediments out of the sheltered embayment system to deep shelf and Yellow Sea [4, 5].

147.2 METHODS

147.2.1 *Wave-dominated Sandy Coast*

At the semi-enclosed coastal system in terms of sediment budget, the model domain consists of an eroded coastal segment and an accreted coastal one. This model domain is bounded alongshore by the nodal points where time-averaged long-shore sediment flux is zero. The seaward boundary is determined by the so-called closure depth limiting seaward sea bottom morphological change. The whole model domain is thus discretized alongshore into $n+m$ zones, each zone represented by one cross-shore profile [1]. By using the data of a modern Digital Elevation Model, historical coastline changes, and relative sea level records, the paleo-coastal morphology can be simulated under the constraint of sediment mass conservation. The mathematical expression is given below:

$$\left| \sum_{i=1}^m V_{erosion,i}(const1) \right| = \left| \sum_{j=1}^n V_{accretion,j}(const2) \right| \quad (147.1)$$

In this equation, the Left Hand Side (LHS) represents the total mass volume lost from the eroded coastal zones and the Right Hand Side (RHS) represents the total accreted mass volume at the prograded coastal zones. Const1 is the uniform ratio between paleo and present curvature coefficients of all cross-shore profiles at the eroded coastal zones, and const2 is the ratio at the accreted coastal zones. The value of const1 can be determined by iterative inverse procedure when const2 is set to 1, or const2 can be determined by iterative inverse procedure when const1 is set to 1. Fig. 147.1a shows an example of a dynamic equilibrium evolution of coastal profiles at the eroded coastal segment.

147.2.2 *Tide-influenced Muddy Coast*

At the muddy coast, the whole model domain includes the river mouth system. The seaward boundary is determined by the closure depth as well. At the alongshore direction it is bounded by the location of transition from coastal progradation to coastal erosion. The tide and wind driven hydrodynamic forces are responsible for the transport of suspended sediment out of the model domain. The mathematical equation can be expressed as follow:

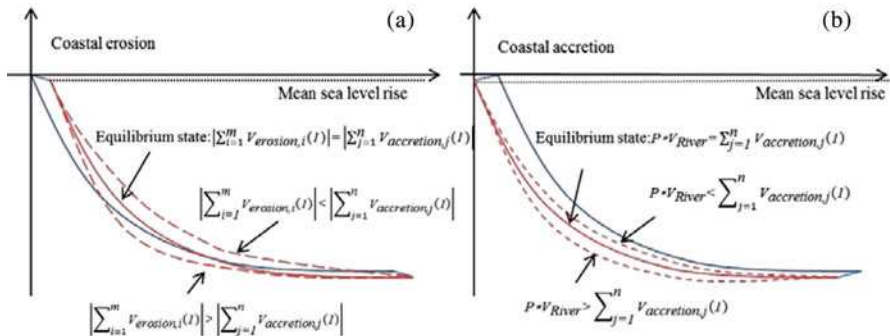


Fig. 147.1 Examples showing how sediment sources and sinks affecting coastal bathymetrical profile morphology in the DES model (Blue curve: present coastal profile; Red curve: paleo-coastal profile)

$$P * V_{River} = \left| \sum_{j=1}^n V_{accretion,j}(const2) \right| \quad (147.2)$$

In this equation, V_{River} is the sediment flux from the river and P stands for the percentage of this flux controlling deposition at the model domain. P is a function of tide and wind. By using the information of a modern DEM, historical coastline changes, and relative sea level records, Equation 147.2 describes how the coastal profile shape (i.e. $const2$) is determined by the riverine sediment sources V_{River} and hydrodynamic forces P at the research area.

If the alongshore boundary is determined by the nodal points where long-shore sediment flux is zero, then Equation 147.2 should be re-written as follow:

$$P * V_{River} = \left| \sum_{j=1}^n V_{accretion,j}(const2) \right| - \left| \sum_{i=1}^m V_{erosion,i}(const1) \right| \quad (147.3)$$

In this case, either $const1$ or $const2$ has to be assumed to equal to 1 so as to obtain the solution of Equation 147.3.

The variation of the riverine sediment sources V_{River} and hydrodynamic forces P induces a dynamic equilibrium evolution of coastal profiles (Fig. 147.1b).

147.3 MODEL APPLICATIONS

The coast at the Pomeranian Bay (southern Baltic Sea) as a subsiding coast is also threatened by rising sea level and storm induced erosion [6]. The application of the DES model at this coast [1] indicates that coastal evolution at a dynamic equilibrium state: $\left| \sum_{i=1}^m V_{erosion,i}(1) \right| < \left| \sum_{j=1}^n V_{accretion,j}(1) \right|$ at the eroded coastal segment by comparing historical bathymetrical data in 1980s AD [1]. This mode

is schematically depicted by Fig. 147.1a. By using this paleo-DEM in ca. 1900 AD as a starting point, the application of multi-scale process-based model Baltic Sea Long-term Morphodynamic Model tell that sediment sources from the coastal erosion is mainly caused by long-term wind induced wave dynamics and frequent storms from the north.

At the Laizhou Bay, southern Bohai Sea, wave-tide-circulation modelling studies shows that about 70% of Yellow River sediment flux is deposited in the Bohai Sea [4]. Anthropogenic influences have caused a decrease of Yellow River sediment flux from up to $20 \cdot 10^8$ t/yr in 1950s AD to ca. $2 \cdot 10^8$ t/yr in 2010AD at the Lijing station [3]. Relative sea level rise is about 2.1mm/yr from 1950AD to 1994AD at the western subsiding coast [7], while there is only 1.7mm/yr from 1950AD to 2010AD at the eastern uplifting coast. The preliminary result indicates that coastal submarine morphological change coincides with the dynamic equilibrium state: $P \cdot V_{River} < \left| \sum_{j=1}^n V_{accretion, j}(1) \right|$ in Fig. 147.1b. This tendency in sea bottom morphological evolution coincides with the measured data [8].

147.4 CONCLUSIONS

The application of the DES model to two distinct coastal environments reveals the different stages of coastal profile dynamic equilibrium evolution. According to the model results, none of both coasts is in an equilibrium stage. For times of more than 100 years ago when measured data is scarce, paleo-DEMs generated by the DES model can substitute empirical data. These paleo-DEMs are to be regarded scenarios which serve as initial coastal morphologies for process-based morphodynamic modelling. The comparison of modelling approaches applied to different geological and oceanographic coastal settings proves that the DES model originally developed for sandy wave-dominated coasts is a valuable tool for displaying coastal morphodynamics at muddy river-dominated coasts too. This study proves that cooperation between marine geologists, oceanographers, environmental scientists and modelers serves as a prerequisite for successful modeling of coastal morphodynamics.

ACKNOWLEDGMENTS This study is carried out in the frame of the bilateral co-operation between University of Szczecin, Poland and Yantai Institute of Coastal Zone Research, CAS, China. The authors express their thank to the Polish National Science Centre (Narodowe Centrum Nauki: NCN) for the financial support with the No. DEC-2011/01/N/ST10/07531 as well as to the Chinese Academy of Sciences for financing the exchange of scientists.

REFERENCES

1. Deng, J., Zhang, W., Harff, J., Schneider, R., Dudzinska-nowak, J., Terefenko, P. and Furmańczyk, K.: A numerical approach for approximating the historical morphology of wave-dominated coasts—A case study of the Pomeranian Bight, southern Baltic Sea. *Geomorphology*, 204, 425–443 (2014)
2. Li, C., Chen, G., Yao, M. and Wang, P.: The influences of suspended load on the sedimentation in the coastal zones and continental shelves of China. *Marine Geology*, 96, 341–352 (1991)
3. Wang, H., Yang, Z., Saito, Y., Liu, J., Sun, X. and Wang, Y.: Stepwise decreases of the Huanghe (Yellow River) sediment load (1950–2005): Impacts of climate change and human activities. *Global and Planetary Change*, 57, 331–354 (2007)
4. Lu, J., Qiao, F., Wang, X., Teng, Y., Jung, K.T. and Liu, Y.: Modeling the Yellow River sediment flux and its deposition patterns under climatological conditions. *Ocean Dyn.* 63, 709–722 (2013)
5. Bian, C., Jiang, W. and Greatbatch, R.J.: An exploratory model study of sediment transport sources and deposits in the Bohai Sea, Yellow Sea, and East China Sea. *Journal of Geophysical Research*, 118, 5908–5923 (2013)
6. Harff, J. and Meyer, M.: Coastlines of the Baltic Sea—zones of competition between geological processes and a changing climate: examples from the Southern Baltic—Springer. In: Harff, J., Björck, S., Hoth, P. (eds), *The Baltic Sea Basin*. pp. 149–164. Springer-Verlag, Heidelberg (2011)
7. Zhang, J. and Wang, J.: Combined impacts of MSL rise and the enlarged tidal range on the engineering design standard in the areas around the Huanghe River Mouth in Chinese. *Marine Science Bulletin*, 18(5), 1–9 (1999)
8. Liu, F., Chen, S., Peng, J. and Chen, G.: Temporal variability of water discharge and sediment load of the Yellow River into the sea during 1950–2008. *Journal of Geographical Sciences*, 21 (6), 1047–1061 (2011)

Chapter 148

A First-order Non-linear Differential Equation Characterizing Multiple Types of Probability Distributions

Q. Cheng

Abstract A non-linear first-order differential equation is proposed to describe the decay function of probability density around the mean values. Assume the decay rate of probability density function is negatively proportional to the density itself, with a functional coefficient dependent on the value of the random variable. Applying Taylor series expansion to the coefficient function, the differential equation can be approximated by multiple simple dynamic systems, each with explicit solutions. These functions can be utilized either as separate and combined solutions to generate various commonly used probability distributions including but not limited to Gaussian, power-law, gamma, inverse gamma, Pareto, Weibull, Rayleigh, and Maxwell-Boltzmann distributions.

Keywords Gaussian distribution • Gamma distribution • Power-law distribution • Pareto distribution • Weibull distribution

148.1 INTRODUCTION

Probability distributions or probability density functions (PDF) are commonly used in numerous applications in sciences for purposes ranging from characterization, estimation, extrapolation, assessment to prediction. Each type of probability distribution is found suitable for describing certain types of phenomena and processes, for example, the normal distribution is used, ensured by the classical Central Limit Theorem, to characterizing physical quantities summed many independent processes such as measurement errors, gamma distribution is frequently used to model waiting times, Pareto distribution to extreme events, power-law distribution to frequency-size distribution of earthquakes, inverse gamma distribution for self-

Q. Cheng (✉)

Earth and Space Science and Engineering, York University, 4700 Keele Street, Toronto, Canada, M3J1P3

State Key Lab of Geological Processes and Mineral Resources,
China University of Geosciences, Beijing and Wuhan, China
e-mail: qiuming@yorku.ca; qiuming@cug.edu.cn

organized criticality description of landslides, Weibull distribution is often used to describe a particle size distribution, the Rayleigh distribution is used for describing wind velocity, and the Maxwell-Boltzmann distribution is a probability distribution for the speed of a particle within the gas in physics, to just name a few. Understanding the associations of these types of probability distributions is essential not only for determining usage of these distributions but also for interpretation of their applications. In the literature there are many attempts to derive certain types of probability distribution and to interpret the mechanism related to the formation of the probability distribution. Famous examples include Fokker-Planck differential equation or Kolmogorov forward equation which provides a general differential equation for characterizing the derivation of various probability distributions [1][2].

In the current paper, a simple first order non-linear differential equation was proposed to describe the decay function of probability density around the mean values of a random variable. Assume the decay rate of probability density function is negatively proportional to the density itself, with a functional coefficient dependent on the value of the random variable. Applying Taylor series expansion to the coefficient function, the differential equation can be approximated by multiple simple dynamic systems, each with explicit solutions including Gaussian functions, exponential functions, power-law functions and exponential functions with inverse random variable. These functions can be utilized as either separate or combined probability distributions to fit observed data by means of simple linear regression or multivariate regression. The combined model can be considered as a general model from which many other distributions such as Gaussian, power-law, gamma, inverse gamma, pareto, Weibull, the Rayleigh, and the Maxwell-Boltzmann distributions can be derived as special cases. This result may provide insight into multiple types of commonly used probability distributions and new way to interpret applications of these types of distributions.

148.2 FIRST-ORDER DIFFERENTIAL EQUATION AND PROBABILITY DISTRIBUTIONS

148.2.1 First-order Differential Equation

In study of characterization of end products of “multiplicative cascade geo-processes” of various types, including earthquakes, floods and mineralization etc. the author of the paper originally proposed a non-linear model for characterizing extreme river flow and flood event [3] as well as for modelling upward migration of ore materials from depth to the surface of the earth due to various mechanisms including electrochemistry, diffusion, groundwater pumping, convection, capillary rise and vegetation effects [4]. From a multiplicative cascade processes (MCP) point of view, MCP can cause highly irregular energy and density distribution of multiscale singularities that can be characterized by multifractal models [5]. Based on the assumption of MCP non-linear dynamics the decay of

density as a function of scale x (distance for 1D, area for 2D and volume for 3D problems) can be described by the following equation [5].

$$\frac{dC(x-x_0)}{dx} = -\frac{1}{\lambda(x)}C^\gamma(x-x_0) \quad (148.1)$$

where the coefficient $\lambda(x)$ is a function of scale x and γ is an index of non-linearity. This differential equation indicates the decay rate of density proportional to density itself with a variable coefficient that is a function of x . To solve equation (148.1), one needs to know the functional form of $\lambda(x)$.

148.2.2 Simplified Coefficients and Explicit Solutions

It is usually not possible to know the exact expression of the coefficient function involved in (148.1) without assuming certain processes such as diffusion or a variety of processes depending upon the complexity of the system. However, the coefficient function $1/\lambda(x)$ can be approximated by means of a Taylor series expansion of $1/[\lambda(1/x)]$ and assuming $\gamma = 1$, then the solution can be derived as [3][4][6]

$$C(x-x_0) = cx^{-\lambda_1} e^{-\sum_{k \neq 1} \lambda_k (x-x_0)^{-k+1}} \quad (148.2)$$

The model (148.2) gives a new function of combined forms of power-law term and exponential terms, where the parameter C is a constant and λ_k representing the coefficients of the increment terms.

148.2.3 Multiple Probability Density Functions

In this section, it shows that several probability density functions can be associated to the general solutions (148.2). Here we just name a few examples as shown below. More probability distributions can be similarly derived.

Gaussian distribution - if letting $\lambda_{-1} = 1/(2\sigma)^2$ and $\lambda_k = 0$, $k \neq 1$.

Pareto distribution - if letting $\lambda_1 = \alpha + 1$ and $\lambda_k = 0$, $k \neq 1$.

Gamma distribution - if letting $\lambda_0 = 1/\theta$, $\lambda_1 = 1-k$ and $\lambda_k = 0$, $k \neq 1$ and $k \neq 0$.

Inverse Gamma distribution - if letting $\lambda_1 = 1+\alpha$, $\lambda_2 = \beta$, and, $\lambda_k = 1$, $k \neq 2$.

Weibull distribution - if letting $\lambda_1 = 1-k$, $\lambda_{-(k-1)} > 0$ and other $\lambda_k = 0$.

Rayleigh distribution - if letting $\lambda_1 = 1$, $\lambda_{-1} = 1/2\sigma^2$, and $\lambda_k = 0$, $k \neq 1$ and $k \neq -1$.

Maxwell-Boltzmann distribution - if letting $\lambda_1 = -2$, $\lambda_{-1} = m/(2kT)$ and $\lambda_k = 0$, $k \neq 1$ and -1 .

148.3 AN EMPIRICAL EXAMPLE

In order to demonstrate how the general model (148.2) can be applied as either individual type of distribution or mixing distributions to fit the frequency-grade distribution of about 380 porphyry copper mineral deposits from the world mineral deposits database [7]. Two modes were experimented: cumulative frequency distribution (A) and (B) and noncumulative mode (C). For the cumulative frequency distribution the calculated parameters are: $\lambda_{-1} = -0.85$, $\lambda_0 = 4.01$, $\lambda_1 = -1.51$ with the goodness of fit by log-transformed observed values and log-transformed estimated values $R^2 = 0.996$. For noncumulative frequency distribution the calculated parameters are $\lambda_{-1} = -2.56$, $\lambda_{-1} = 10.32$, $\lambda_0 = -7.36$ with $R^2 = 0.974$. The functions with the above parameters are fixed to the data as shown in Fig. 148.1 (A)–(C), respectively.

The upper range of grade is fitted by a power-law distribution with parameter $\lambda_1 = 3.4$ and $R^2 = 0.98$ [8]. The results indicate that the distribution of the discovered porphyry copper mineral deposits follow a mixing distribution.

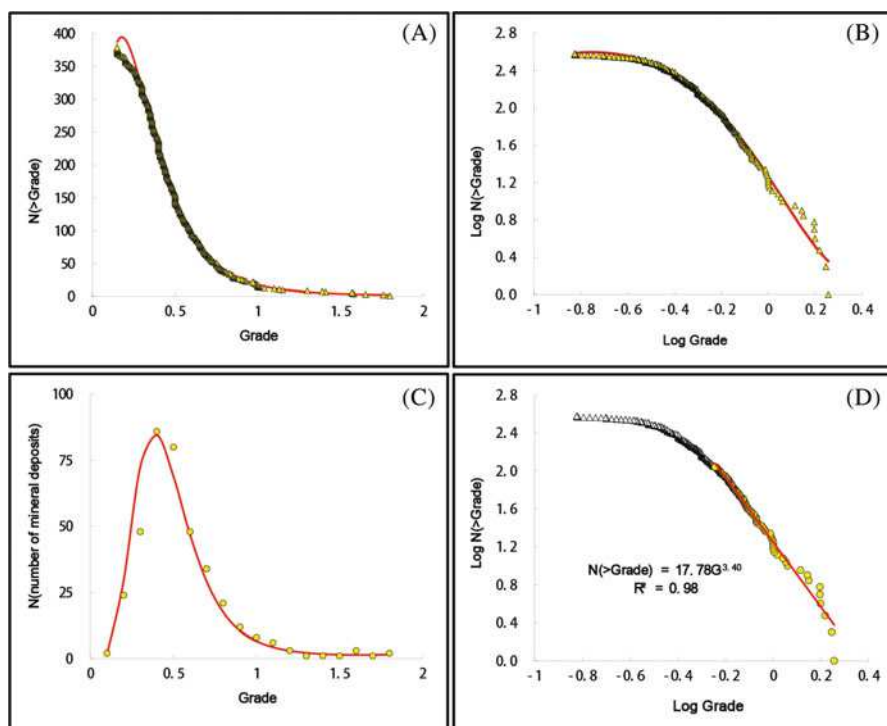


Fig. 148.1 Grade-frequency distribution of porphyry copper mineral deposits. (A) Cumulative number of mineral deposits with grade greater than a threshold; (B) Same data plotted as log-log scale; (C) Frequency distribution of mineral deposits; and (D) Cumulative frequency distribution. The red curves in (A) – (C) are fitted by four-parameter models as seen in text. Red curve in (D) is fitted by power-law model for the upper range of grades

148.4 CONCLUSIONS

The first-order differential equation introduced in the current paper can be used to associate various types of commonly used probability distributions including but not limited to diffusion-convection processes related Gaussian distribution, extreme events related Pareto distribution, Gamma distribution, Inverse Gamma distribution, Weibull distribution, Rayleigh distribution, Maxwell–Boltzmann distribution. The case study has demonstrated that the frequency distribution of ore grade from 380 porphyry copper mineral deposits in the world can be modeled by a combined model involving power-law, exponential and Gaussian distribution whereas the cumulative frequency distribution of grade in its upper range can be fitted by power-law distribution.

REFERENCES

1. Fokker, A.D.: Die mittlere Energierotierendelektrischer Dipole im Strahlungsfeld., *Ann. Phys.* 348, 810–820 (1914)
2. Feller, W.: On boundaries and lateral conditions for the Kolmogorov differential equations. *Annals of Mathematics*, 65(3), 527–570 (1957)
3. Cheng, Q.: A combined power-law and exponential model for streamflow recessions. *J. of Hydrology*, 352, 157–167 (2008)
4. Cheng, Q.: Singularity theory and methods for mapping geochemical anomalies caused by buried sources and for predicting undiscovered mineral deposits in covered areas. *J. of Geochem.Expl.* 122, 55–70 (2012)
5. Cheng, Q. and Agterberg, F.P.: Singularity analysis of ore-mineral and toxic trace elements in stream sediments. *Computers & Geosciences*. 35, 234–244 (2009)
6. Cheng, Q.: Vertical distribution of elements in regolith over mineral deposits and implications for mapping geochemical weak anomalies in covered areas: Geochemistry: Exploration, Environment, Analysis. doi:10.1144/geochem2012-174.
7. Singer, D., Berger, V.I. and Moring, B.C.: Porphyry copper deposits of the world: database, map, and grade and tonnage models. U.S. Geological Survey Open-File Report 02–268 (2005)
8. Cheng, Q.: Singularity of mineralization and multifractal distribution of mineral deposits. *Petrology, Mineralogy and Geochemistry*, 27(3), 298–305 (2008) (in Chinese with English abstract).

Author Index

A

Acevedo, A., 89–93
Acharya, P., 397–403
Adler, P.M., 111–114
Agrawal, M., 369–372
Ali, I., 893–896
Ali, N., 905–908
Al-Ruwaih, F., 199–205
Altaf, S., 741–744
Anbazhagan, S., 545–552
Ancheta, T., 679–684
Ansari, M.A., 259–265
Arachchi, D.S.M., 213–219
Arora, M., 909–914
Atif, J., 617–621
Aydin, O., 555–561

B

Babu, K.N., 801–807
Bagalkot, N., 609–615
Bagas, L., 735–739
Bakimchandra, O., 159–167
Balaram, V., 415–419
Barbara, A.K., 861–866
Barman, M.K., 861–866
Basistha, A., 159–167
Baskar, M., 545–552
Bhardwaj, A., 887–891
Bhat, K.K., 497–501
Bing-li, L., 565–569
Birajdar, F., 749–753
Brazier, R., 651–655
Brehme, M., 281–284
Budhiraja, B., 823–827

Buermann, W., 421–425
Burgess, P., 89–93

C

Caers, J., 555–561
Camacho, S.M., 589–592
Cao, H., 140–145
Cardona, A., 327–332
Carrillo-Rivera, J.J., 237–243, 327–332
Carttar, D., 685–689
Chae, B.-G., 45–49
Chakrapani, G.J., 121–126, 307–311, 313–319
Chakravarty, D., 643–649
Chaudhary, S.K., 773–776
Chen, J., 593–597
Chen, W., 605–608
Chen, Z., 29–34
Cheng, N.L., 565–569
Cheng, Q., 3–9, 29–34, 491–494, 959–963
Chetia, B., 861–866
Chetyrbotsky, A.N., 627–629
Chevuturi, A., 867–870
Chicherov, M.V., 571–575
Chidambaram, S., 251–257
Chizhova, I.A., 571–575, 583–587
Choi, J., 45–49
Choudhary, A., 855–858
Choudhary, D.K., 923–928
Christ, A., 623–626

D

Dash, S.K., 533–536
Davis, D., 259–265

Daya Sagar, B.S., 57–64

Debnath, M., 873–879

Deepak, 527–530

Deng, J., 953–957

Deodhar, A., 259–265

Deutsch, C.V., 39–43

Deutsch, J.L., 83–87

Devak, M., 657–663

Devi, B.R., 923–928

Devi, M., 861–866

Dey, S., 221–228

Dhanya, C.T., 657–663

Díaz-González, L., 631–636

Diksha, 285–291

Dimri, A.P., 855–858, 867–870

Dinesh, A.C., 761–764

Divi, R.S., 199–205

Dixit, J., 533–536

Dobhal, D.P., 881–884

Du, H., 475–481, 539–543

Durgapal, A., 881–884

Dutta, S., 173–180

E

Eludoyin, B., 651–655

Erten, O., 577–582

Eshagh, M., 461–464

Etsell, T.H., 83–87

F

Feng, B.Q., 491–494

Fox, P., 829–833

Fu, L., 829–833

G

Ganju, A., 887–891

Garg, M., 349–354

Garkoti, S.C., 427–432

Garzanti, E., 293–299

Ghosh, N.C., 341–347

Gnanaphazzam, L., 835–839

Gongwen, W., 767–770

Griffith, B., 651–655

Guadagnini, A., 65–68

Gunatilake, J., 405–414, 797–800

Gunturu, U.B., 867–870

Guo, K., 15–19, 21–27

Gupta, A., 361–366

Gurunathan, A., 285–291

Gurung, D., 191–197

H

Halder, A., 435–438

Harff, J., 953–957

Harris, P., 651–655

Heikkinen, J., 381–384

Hernández-García, G.J., 237–243

Holden, E.-J., 735–739

Hossain, Md.S., 483–488

Howden, N.J.K., 651–655

Huang, G., 467–473

I

Indoria, A.K., 923–928

Indu, J., 711–714

J

Jacob, N., 285–291

Jain, M.K., 773–776

Jaryal, A., 285–291

Jayappa, K.S., 761–764

Jayarajan, K., 801–807

Jianan, Q., 767–770

Jian-ping, C., 599–604

K

Kamal, V., 809–814

Kamala, C.T., 415–419

Kanhaiya, S., 301–306

Kanojia, S., 917–921

Karakoti, I., 881–884

Kashiwaya, K., 715–718

Kesarwani, K., 881–884

Khan, M.Y.A., 307–311

Khillare, P.S., 355–359

Khramtsov, A., 89–93

Khrushchov, D.P., 583–587

Knoche, M., 281–284

Koike, K., 637–641, 715–718

Korwar, G.R., 923–928

Krishan, G., 183–187

Kruhl, H., 483–488

Kubo, T., 715–718

Kulkarni, P., 173–180

Kulkarni, S., 173–180

Kumar, A., 949–952

Kumar, C.P., 183–187, 245–249

Kumar, D., 773–776

Kumar, D.N., 711–714

Kumar, G.S., 609–615

Kumar, N., 909–914

Kumar, R., 809–814, 909–914
Kumar, S., 341–347, 349–354
Kumar, U.S., 259–265
Kumari, M., 159–167

L

Lalomov, A.V., 583–587
Laverov, N.P., 583–587
Lee, S.J., 679–684
Lee, S.-J., 685–689
Leung, J.Y., 115–120
Li, N., 735–739
Li, Y., 953–957
Likso, T., 843–846
Limonta, M., 293–299
Linguet, L., 617–621
Liu, B., 15–19, 21–27, 467–473
Liu, G., 135–140, 829–833
Liu, H.-h., 729–733
Lobanov, K.V., 571–575
Lohani, A.K., 183–187
Lu, Y., 735–739

M

Ma, X., 829–833
Madhoo, H.A., 89–93
Maharana, P., 855–858
Maheswari, M., 923–928
Mai, N.L., 577–582
Maiti, S.K., 435–438
Malhotra, J., 909–914
Manawadu, L., 405–414
Mann, D., 823–827
Maozhi, W., 703–708
Markose, V.J., 761–764
Matharaarachchi, D.S., 405–414
Matsuda, N., 715–718
Mayaja, N.A., 169–172, 779–783
Mehta, M., 881–884
Meier, C., 281–284
Menafoglio, A., 65–68
Meraj, G., 741–744
Merz, R., 281–284
Mishra, B.K., 427–432
Mitra, S., 381–384
Mohan, D., 949–952
Mohan, V., 791–794
Mueller, U., 11–14
Mukerji, T., 105–110, 555–561
Mukherjee, A., 207–210
Mukherjee, S., 809–814

Mukhopadhyay, S., 173–180
Muminov, A., 931–935
Murray, P., 651–655

N

Naik, A.S., 373–379
Nandakishore, O.P., 801–807
Noacco, V., 651–655
Noomee, L., 89–93
Normatov, I., 931–935
Normatov, P.I., 931–935

O

Oliveira, E.P., 449–452
Orr, R., 651–655
Ortiz, J.M., 147–152
Ouyse, S., 237–243

P

Pakrasi, K., 887–891
Pal, S., 513–521
Palchik, V., 77–80
Pandarinath, K., 455–458
Pandey, B., 369–372
Panwar, S., 313–319
Parhi, P.K., 665–669
Parida, B.R., 421–425
Parthasarathy, U., 801–807
Parween, M., 355–359
Patel, P., 191–197
Pathak, P.A., 823–827
Paulraj, R., 361–366, 391–395
Pazdniakou, A., 111–114
Peredo, O., 147–152
Perfect, E., 129–133
Pethaperumal, S., 251–257
Peukert, S., 651–655
Phaomei, T., 545–552
Pittman, C.U., 949–952
Piyadasa, R.U.K., 213–219
Porwal, A., 735–739
Prakash, D., 523–526, 527–530
Prasanna, M.V., 251–257
Pratap, B., 745–748
Pratibha, G., 923–928

Q

Qadir, J., 893–896
Qiang, W., 140–145

Qin, F., 467–473
 Qin, Z.-t., 719–722, 729–733
 Qiuming, C., 95–99

R

Rafiq, M., 723–728
 Raghukanth, S.T.G., 533–536
 Rai, S.P., 245–249
 Rajesh, B., 691–698
 Raju, B.M.K., 923–928
 Raju, N.J., 191–197, 221–228, 275–278,
 355–359, 745–748
 Ram, P., 275–278
 Ramanathan, A.L., 355–359
 Ramesh, A.P., 791–794
 Ramesh, V., 545–552
 Ramezani, K., 651–655
 Ramirez-Beltrán, M., 237–243
 Rani, S., 899–902
 Rao, A.S., 415–419
 Rao, K.S., 923–928
 Rao, K.V., 923–928
 Rao, M.S., 183–187, 245–249
 Rashid, I., 723–728
 Regina, K., 381–384
 Remezova, E.A., 583–587
 Rishi, M., 785–789
 Rishi, M.S., 231–234
 Romshoo, S.A., 723–728, 741–744, 905–908
 Rosales-Rivera, M., 631–636
 Roy, A., 129–133, 555–561
 Roy, A.D., 671–676
 Roy, P., 385–389
 Ruix, L., 767–770
 Rukieh, M., 817–821

S

Sahu, B.K., 153–157
 Saji, K.V., 801–807
 Salomonsen, P., 623–626
 Samant, H., 749–753
 Samanta, B., 643–649
 Sandhya, 333–338
 Saravanan, K.A., 691–698
 Satyanarayanan, M., 415–419
 Sawant, S.S., 415–419
 Schenk, O., 623–626
 Secchi, P., 65–68
 Seema, 391–395
 Shah, B.A., 267–272
 Shandilya, A., 503–510
 Shandilya, A.K., 503–510
 Sharma, A.D., 231–234

Sharma, G.K., 917–921
 Sharma, R., 57–64
 Sharov, N.V., 571–575
 Shen, W., 475–481, 539–543
 Shepherd, A., 651–655
 Shin, Y., 555–561
 Shukla, A., 755–758, 893–896
 Sidhu, N., 785–789
 Singh, A., 513–521
 Singh, B.P., 301–306
 Singh, C.K., 159–167
 Singh, M.K., 887–891
 Singh, N., 121–126
 Singh, P., 381–384
 Singh, R., 341–347, 349–354, 785–789
 Singh, R.P., 341–347
 Singh, S., 341–347, 369–372
 Sipolya, R., 809–814
 Sirirwardane, M.S.P.M., 797–800
 Sivanandarajah, S., 797–800
 Snehamani, 887–891
 Somashekar, R.K., 259–265
 Sreekesh, S., 333–338, 385–389, 397–403,
 671–676, 873–879, 899–902
 Srinivas, I., 923–928
 Srinivasa, C.V., 169–172, 779–783
 Steinbruch, F., 321–324
 Subhash, N., 497–501
 Subramanyam, K.S.V., 415–419
 Suk, H., 45–49
 Szymanski, J., 83–87

T

Takshi, K.S., 183–187
 Tan, C., 491–494
 Tao, P., 703–708
 Tenzer, R., 461–464, 605–608
 Tetzlaff, D., 89–93
 Tewari, S., 523–526
 Thakur, M., 643–649
 Thilagavathi, R., 251–257
 Thivya, C., 251–257
 Tian, B., 637–641
 Tirumalesh, K., 251–257
 Tolosana-Delgado, R., 11–14
 Topal, E., 577–582
 Toshniwal, A., 791–794
 Tripathi, M., 937–947
 Tuominen, E., 651–655

V

van den Boogaart, K.G., 11–14, 589–592
 Varghese, S., 497–501

Velasco-Tapia, F., 71–74
Venkataraman, G., 749–753
Verma, M.P., 51–54, 101–104
Verma, S., 207–210
Verma, S.K., 245–249, 449–452
Verma, S.P., 35–38, 71–74, 455–458,
631–636
Vezzoli, G., 293–299
Vineet, P.N., 835–839
Vishal, V., 115–120

W

Wang, C., 593–597
Wang, W., 3–9
Weise, S.M., 281–284, 321–324
Weng, Z., 135–140
Wikramasinghe, D., 213–219
Wu, F., 21–27
Wu, X.-p., 719–722, 729–733

X

Xian-wu, X., 443–447
Xiao, F., 593–597
Xiao, K., 735–739

Xu, D., 491–494
Xu, S., 105–110

Y

Yadav, G.S., 745–748
Yadav, R.K., 849–853
Yang, R., 719–722
Yang, S., 293–299
Yang, W.-n., 719–722, 729–733
Yang, X., 729–733
Yanyan, Z., 767–770
Yi, T., 599–604
Yongguo, Y., 95–99
Yousuf, B., 755–758
Yuhua, C., 95–99

Z

Zagayevskiy, Y., 39–43
Zhang, L., 15–19
Zhang, W., 953–957
Zhang, Z., 135–140
Zhao, J., 3–9
Zhou, Q., 135–140
Zhou, Z., 467–473